DESY 96-235
November 1996

Future Physics at HERA

Proceedings of the Workshop 1995/96

Edited by

G. Ingelman, A. De Roeck, R. Klanner

Volume 1

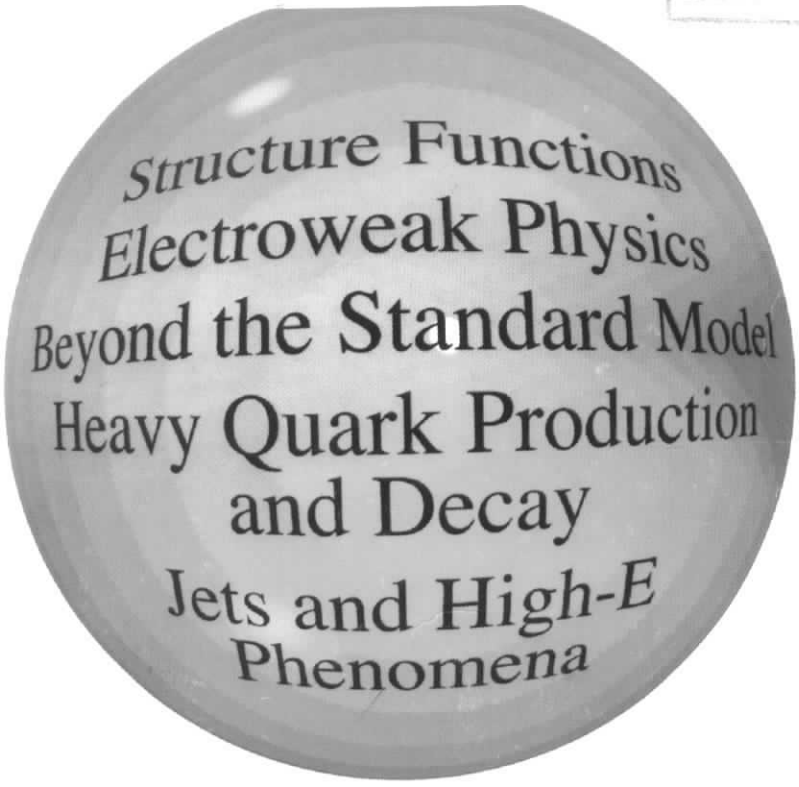

http://www.desy.de/~heraws96

Future Physics at HERA

Proceedings of the workshop 1995/96

Edited by

G. Ingelman, A. De Roeck, R. Klanner

Volume 1

Structure Functions

Electroweak Physics

Beyond the Standard Model

Heavy Quark Production and Decay

Jets and High-$E_\perp$ Phenomena

Published by

Deutsches Elektronen-Synchrotron **DESY**
Notkestraße 85
D-22607 Hamburg
Hamburg
Germany

Proceedings of the workshop on Future Physics at HERA Volume 1

Electronic version available on http://www.desy.de/~heraws96

The help of C. Hartmann and L.A.T. Bauerdick in designing the covers is gratefully acknowleged. The picture of the sailboat in front of Hamburg's Speicherstadt is a courtesy of Jan Hladký, Inst. of Physics, Czech Academy of Sciences, Prague.

PRINTING COMPANY: HB-DRUCK, H. BUNG, D-22149 HAMBURG

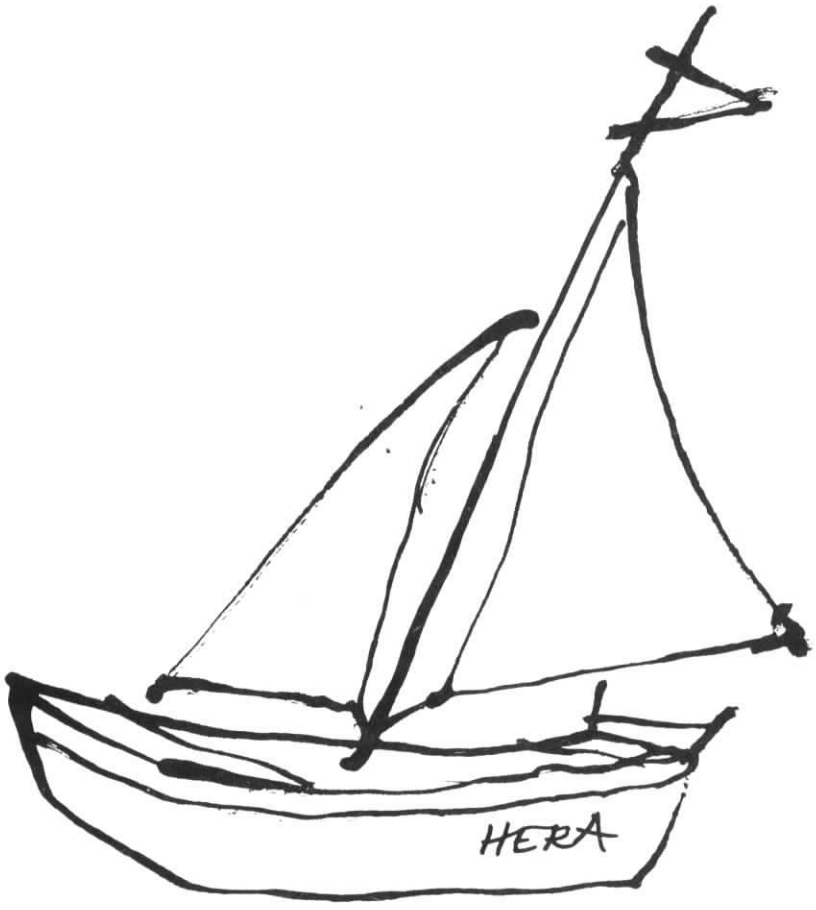
HERA

Foreword

The workshop on 'Future Physics at HERA' started with a general meeting at DESY in September 1995 and is now completed a year later with these proceedings. With the experience of the first years of HERA running, it was the appropriate time to consider how to go ahead for the coming years. The HERA program must be carefully planned based on physics priorities and realism of what is feasible with possible upgrades of the accelerator complex and the detector systems, or even entirely new experiments. Thus, the aim of the workshop has been: 'To work out and review prospects for future physics at HERA, running in collider and fixed target modes. Options to be considered include high luminosity, polarized beams, light and heavy nuclei.'

With the assistance of the Advisory Committee (W. Buchmüller, J. Feltesse, A. Levy, H. Schröder, J. van den Brand, A. Wagner) we organized the work in nine study groups to cover different topics: HERA upgrades and impacts on experiments, structure functions, electroweak physics, heavy quark production and decay, jets and high-$E_\perp$ phenomena, diffractive hard scattering, polarized protons and electrons, light and heavy nuclei in HERA and, last but not least, physics beyond the standard model. For each working group conveners were appointed, both theorists and experimentalists to promote collaborative efforts. In February 1996 a mid-term plenary meeting was held to communicate the progress and the final general workshop meeting took place at DESY May 29-31, 1996, with summaries of the results from the working groups. The complete reports of the groups are now available in these proceedings.

An overview of all the interesting and important results can be obtained from the summary reports for each of the working groups. Some totally new aspects compared to what was treated in the 1987 and 1991 HERA workshops should be noted. Beams in HERA of polarized protons as well as light and heavy nuclei were studied seriously both regarding machine aspects and physics potential. New fixed target experiments were considered and the machine aspects of possible HERA upgrades and their impacts on experiments were studied.

It is our hope that these proceedings will be a valuable basis for the future of HERA. In particular, that they contribute to wise decisions concerning upgrades and running programs of HERA and the experiments.

These proceedings represent an enormous effort and dedication of the many participants. As organizers, we are particularly grateful to the conveners of the working groups, who shared our responsability to carry through the workshop. We are much indebted to our workshop secretary Ms. H. Haertel and also thank Ms. B. Bahr, Mr. A. Edin, Ms. S. Guenther, Ms. I. Harm, Ms. S. Lefay and Dr. G. Soehngen for their assistance. Finally, we gratefully acknowledge the strong support to this workshop from the DESY directorate.

Hamburg, September 1996

Gunnar Ingelman Albert De Roeck Robert Klanner

Introduction

HERA is a world wide unique facility which supports a broad and exciting programme in experimental particle physics. The HERA performance has been steadily improving and is now starting to approach the design value with an integrated luminosity of 4 pb^{-1} per month, an overall efficiency of 50% and a longitudinal positron polarization of more than 50%. However, the request for a luminosity well beyond its design value of 35–40 $pb^{-1}year^{-1}$ is clearly justified by this study. A design group with members from both the accelerator division and the HERA experiments has recently completed a conceptual design study which shows that it should be possible to reach a yearly integrated luminosity of order 150 pb^{-1} by moving the low beta quadrupoles closer to the interaction point. The directorate considers the luminosity upgrade to be of high priority and expects that the upgrade can be carried out during the 1999/2000 winter shutdown.

A conceptual design study has shown that it may be possible to store polarized proton beams in HERA. However, to carry out a programme on nucleon spin physics requires major modifications to both the preaccelerators and to HERA proper. A decision how to proceed will be taken after the completion of the luminosity upgrade, i.e. in 2000/2001, and also after the completion of a more technical study. The construction time is estimated to be 4 years such that polarized protons could in principle be available around 2005, after the first part of the high luminosity programme has been completed.

Colliding heavy and light nuclei with high energy electrons opens up a new field of research. DESY and GSI are now exploring how such a facility could be realized as a collaborative effort between the two institutions. As a first step a joint workshop on electron-nuclei interaction at high energies is planned for the spring of 1997.

This study not only shows that we have just scratched the surface of the HERA physics potential, it also provides a guide towards its realisation. On behalf of the DESY Directorate I thank the organizers and all the participants in the study for a job well done.

Bjoern H Wiik

VOLUME 1

VOLUME 2

Working Group on

Structure Functions

Conveners:

J. Blümlein (DESY), A.T. Doyle (Glasgow), F. Hautmann (Oregon),
M. Klein (DESY), A. Vogt (DESY, Würzburg).

Participants:

D. Bardin (DESY-Zeuthen), V. Barone (Torino), U. Bassler (Paris), L. Bauerdick (DESY), G. Bernardi (Paris), J. Blümlein (DESY-Zeuthen), M. Botje (NIKHEF), J. Chyla (Prague), P. Christova (Shoumen), A.M. Cooper-Sarkar (Oxford), U. D'Alesio (Torino), S. Dasu (Wisconsin), K. Daum (Wuppertal), A. DeRoeck (DESY), R. Devenish (Oxford), A.T. Doyle (Glasgow), M. Fleischer (Dortmund), J. Fleischer (Bielefeld), J. Forshaw (Manchester), M. Genovese (Grenoble), A. Glazov (DESY-Zeuthen), G. Gustafson (Lund), F. Hautmann (Oregon), L. Kalinovskaya (Dubna), A. Kataev (Dubna), M. Klein (DESY-Zeuthen), P. Kooijman (NIKHEF), B. Kopeliovich (Heidelberg), M. Krämer (DESY), M. Lancaster (Oxford), S.A. Larin (NIKHEF, Lisbon), E. Levin (Rio de Janeiro), G. Levman (Toronto), L.N. Lipatov (Gatchina), A.D. Martin (Durham), M. McDermott (DESY), M. Meyer-Hermann (Frankfurt), W.N. Murray (York), T. Naumann (DESY-Zeuthen), H. Navelet (Saclay), W.L. van Neerven (Leiden), P. Nogueira (Lisbon), C. Pascaud (Orsay), R. Peschanski (Saclay), B. Povh (Heidelberg), A. Prinias (Imperial College), S. Riemersma (DESY-Zeuthen), T. van Ritbergen (NIKHEF), R.G. Roberts (RAL), C. Royon (Saclay), G.P. Salam (Cambridge), A. Schäfer (Frankfurt), A. Sidorov (Dubna), E. Stein (Frankfurt), U. Stoesslein (DESY-Zeuthen), P. Sutton (Manchester), O. Tarasov (DESY), R.S. Thorne (RAL), M. Tokarev (Dubna), L. Trentadue (Parma), W.-K. Tung (East Lansing), A. Vogt (DESY, Würzburg), J.A.M. Vermaseren (NIKHEF), S. Wallon (Saclay), T. Weigl (TU Munich), R. Yoshida (Bristol), F. Zomer (Orsay)

Structure Functions — Working Group Reports:

Structure Functions in Deep Inelastic Scattering at HERA[1]

J. Blümlein (DESY), T. Doyle (Glasgow), F. Hautmann (Oregon)
M. Klein (DESY), A. Vogt (Würzburg)

Abstract

An introduction and summary is given of the main results achieved by working group 1: Structure Functions in Deep Inelastic Scattering at HERA. The prospects were discussed of future measurements of the structure functions F_2, F_L, xG_3, $F_2^{Q\overline{Q}}$ and F_π at HERA. The results represent a long term programme of experimentation with high luminosity, different lepton beam charges, proton and deuteron beams, allowing for precision measurements. The theoretical investigations focussed on QED corrections, higher order QCD corrections for different observables, resummation of small x contributions, and the detailed understanding of NLO QCD evolution codes, to allow for a high precision analysis of the forthcoming deep inelastic data.

1 Introduction

The discussion of prospects of structure function physics has taken place for the third time in a HERA physics workshop. In 1987, the emphasis was put mainly on high Q^2 structure function simulations, and the determination of parton distributions [1]. In 1991, the experimental part concentrated on the reconstruction of the deeply inelastic event kinematics and Monte Carlo simulations, while the theoretical investigations began to focus on the physics of the parton densities at very low x [2].

This workshop was based on the experience gained in the first four years of running at HERA, and on recent important theoretical developments, in particular the extension of next-to-leading order (NLO) calculations to more observables, and on small x resummations. One of the major goals on the theoretical side was to summarize the progress towards high–precision calculations, and to point out which further theoretical investigations are most important in order to match the accuracy expected in future high–statistics structure function data from HERA.

On the experimental side, the scope of the studies has been extended to the charm contribution to the proton structure functions at low x, and to the pion structure function. The knowledge of existing HERA data allowed for much more reliable simulations than in previous workshops. Demands on the future HERA running were derived, which are contained in the

[1]Summary report of Working Group 1 of the 1996 HERA Physics Workshop

experimental section of this paper. A challenging scenario of running HERA for many years has been developed. It requires the accumulation of high luminosity for both lepton beam charges and also to accelerate deuterons. This will permit to reach very high precision, i.e. an error level of only a few % for the proton stucture function F_2, and also accurate results for F_L, F_2^c and F_π. On the basis of this data high precision studies of QCD in the regions of very small x and of very large Q^2 can be carried out. In the following, we summarize the main results obtained in the theoretical and experimental investigations of the working group.

2 Theoretical Studies

Since the 1991 HERA Physics Workshop, various theoretical developments have taken place in the field of deep–inelastic scattering (DIS). These include the extension of QED radiative corrections to more observables, the calculation of various QCD coefficient functions and scattering cross sections to $O(\alpha_s^2)$, determinations of the 3–loop corrections of a series of moments of coefficient functions and anomalous dimensions for non–singlet as well as singlet structure functions, and the resummation of certain classes of logarithmic corrections at small x. During the present workshop, applications of these results have been considered to future HERA data. Comparisons have been performed of the experimental requirements and the theoretical accuracy achieved at present.

2.1 QED Radiative Corrections

The understanding of the $O(\alpha)$ QED corrections for a few choices of kinematical variables was already obtained at the time of the 1991 HERA workshop [3]. In a contribution to the present workshop [4], recent developments in the semianalytical approach by the HECTOR collaboration [5] have been summarized. These include the $O(\alpha)$ corrections for a wide variety of kinematical variables as well as leading–log $O(\alpha^2)$ results. Recently also the QED corrections due to the resummation of the $O(\alpha[\alpha \ln^2(1/x)]^l \log[Q^2/m_e^2])$ terms were calculated [6]. For leptonic variables, their contribution is of similar size as the second order corrections $\sim \alpha^2 \log(Q^2/m_e^2)$ and diminishes the effect of these terms. A first complete $O(\alpha)$ calculation was reported also for neutral current polarized–lepton polarized–hadron scattering [7] accounting for photon and Z-boson exchange. This calculation covers the cases of both longitudinal and transverse nucleon polarization for the twist–2 contributions to the Born term [8].

2.2 Comparisons of NLO QCD Evolution Codes and the Theoretical Error of $\alpha_s(M_Z^2)$

A major effort within the working group concerned a detailed comparison of next-to-leading order (NLO) QCD evolution codes. The aim of this comparison was to understand the accuracy of the different numerical solutions of the evolution equations and their conceptual differences. A numerical agreement of better than $\pm 0.05\%$ of the parton densities has been achieved between five of the evolution programs. For these codes, previous deviations due to different theoretical assumptions on the truncation of the perturbative series at NLO are now completely understood. The results of this study are summarized in ref. [9].

Precision measurements of F_2 allow for detailed QCD tests and an improved extraction of $\alpha_s(Q^2)$. The theoretical uncertainties of the α_s measurement from scaling violations have been investigated for NLO analyses in the HERA range [10, 11]. The different representations of the evolution within NLO lead to a shift of up to $\Delta\alpha_s(M_Z^2) = 0.003$. The largest theoretical errors at NLO are due to the renormalization (R) and factorization (M) scale uncertainties, resulting in $\Delta\alpha_s(M_Z^2) = {}^{+0.004}_{-0.006}\,|_R\,{}^{-0.003}_{+0.003}\,|_M$, for a Q^2–cut of $Q^2 \geq 50\,\mathrm{GeV}^2$. The contribution of mass threshold uncertainties to $\Delta\alpha_s(M_Z^2)$ was conservatively estimated to 0.002 in ref. [12]. Due to the large statistics at low Q^2 it appears to be desirable to include also the range down to a few GeV^2 in the QCD analyses. To exploit this region fully, however, requires to carry out next-to-next-to leading (NNLO) analyses, for which the 3–loop splitting functions still have to be calculated.

2.3 $O(\alpha_s^2)$ and $O(\alpha_s^3)$ Corrections

Since the 1991 HERA Physics workshop, various two–loop calculations have been performed for quantities related to structure functions. A survey on the status of these calculations, and recent three–loop results, was presented to this working group [13]. The NLO corrections turn out to be essential for the quantitative understanding of most of the observables.

Numerical studies during this workshop were devoted to the behaviour of $F_L(x, Q^2)$ [14] and $F_2^{Q\overline{Q}}$ [15, 16]. An update of the parametrization of the NLO heavy flavour coefficient functions is also given in [15]. Moreover, a calculation of the heavy flavour structure functions in charged current interactions has been presented [17]. Besides of the twist-2 contributions to the structure function F_L, also higher–twist terms for its non–singlet part have been investigated, accounting for renormalon contributions [18]. Also the NLO corrections to the scattering cross section $\sigma(\gamma + g \to J/\psi + X)$ are available now [19].

First results on the behaviour of structure functions in NNLO were reported by the NIKHEF group [20, 21]. The first moments for both the non–singlet and singlet combinations of unpolarized DIS structure functions have been calculated. By the same group also a phenomenological analysis was presented [22], estimating the x-dependence of the corresponding splitting functions by a fit allowing for a set of functions which are known to contribute. Also a phenomenological application of the non–singlet results to xF_3 was reported [23].

2.4 Resummations for Small x

The measurement of DIS structure functions remains one of the major methods to investigate the small-x physics at HERA. Various aspects have been considered in the working group. A possible approach has been discussed which relies on the $k_\perp$-factorization method [24]. It consists of combining systematically the resummation of the small-x logarithmic corrections, as given by the BFKL formalism [25] and the QCD corrections to it, with the QCD mass factorization theorem, dictated by the renormalization group. This approach enables one to study the small-x effects by solving improved evolution equations which include resummed kernels. A first numerical analysis along these lines was carried out in ref. [26]. A review of these equations and the current status of resummed calculations, covering also the non–singlet cases, can be found in ref. [27].

During the workshop numerical studies of structure functions at small x have been performed by two groups [28, 29]. One contribution to the workshop [30] dealt with the resummation of the small-x contributions on the level of a double–log approximation. In the flavour non–singlet sector resummation effects are small, less than 1% [31]. In the singlet sector, however, they may give rise to large contributions [28, 29]. The question of assessing the importance of unknown sub–leading terms has also been addressed in ref. [28], comparing several different models. The outcome is that these terms seem to be able to affect the result sizeably. This indicates that at present the uncertainties on the theoretical predictions at small-x are fairly large, and more accurate calculations (next-to-leading small-x logarithms as well as exact 3-loop contributions) are necessary. The analysis in ref. [29] has emphasized the role of a combined determination of F_2 and F_L to pin down the behaviour of the QCD perturbative series at small x. The effects of small-x resummations on the photon structure functions were also discussed [28].

On the leading–order level, predictions for the structure functions, covering the BFKL effects at small x, can also be obtained starting from a different equation, which was introduced a few years ago [32] to describe the detailed structure of the gluon radiation associated to small-x events. In ref. [33], the solution to this equation has been investigated numerically for the structure function F_2.

In the working group also the properties of the BFKL resummation equation itself were discussed with emphasis on the transverse momentum cut–off [34]. Recent progress in calculating NLO corrections to the BFKL kernel was reported in ref. [35], see also [27] for other ongoing investigations.

An alternative formulation of QCD at small x has been proposed in a series of papers, based on a colour dipole concept [36]. The theory has been worked out for the case of scattering of two quarkonia, in which non-perturbative effects are suppressed by the smallness of the quarkonium radius. First attempts to apply the colour dipole formulation to deep–inelastic scattering have been reported at this workshop [37, 38]. The suitability of this approach to investigate unitarity corrections and parton saturation has been emphasized, and an explicit parametrization of multi-pomeron exchange contributions has been presented [38].

3 Experimental Studies

The future HERA measurements of structure functions using electron and positron, proton and deuteron beams promise to be of great interest, since the envisaged increase of luminosity will allow for reducing the statistical and the systematic errors, especially for the proton case, to the level of a few per cent in almost the full accessible kinematic range. Within this working group, detailed simulation studies have been performed of various structure function measurements, in order to estimate their expected accuracy and to analyze their physics impact.

3.1 The Proton Structure Function F_2

A thorough simulation has been carried out [39] of future HERA measurements of the proton structure function $F_2(x, Q^2)$ for a nominal kinematic range given by $y < 0.8$, $\theta_e < 177°$, $Q^2 > 0.5\ \mathrm{GeV}^2$, and $\theta_h > 8°$. The following assumptions were made on the future measurement accuracies: 0.5-1% for the scattered electron energy E'_e, 0.5-1 mrad for the polar angle θ_e, 2% on

the hadronic energy E_h, 1-2% for the photoproduction background uncertainty at high y, and 2% due to trigger and detector efficiencies. The luminosity was assumed to be known within 1%. Moreover, control of the radiative corrections at the level of 1% has been assumed. These conditions lead to an estimated systematic error of F_2 of about 3% in almost the full kinematic range of $2 \cdot 10^{-5} \leq x \leq 0.7$ and $0.5 \leq Q^2 \leq 5 \cdot 10^4$ GeV^2. The anticipated accuracy represents an improvement by about a factor of two compared to the present results but extended to a much wider region. The current H1 and ZEUS structure function analyses served as a basis for the simulations and were summarized in various talks presented to this working group [40].

In a detailed NLO QCD analysis [39], possible determinations of the strong coupling constant α_s and of the gluon distribution have been considered using the H1 and the ZEUS QCD analysis programs and fitting techniques. The error of α_s strongly depends on the minimum Q^2 which can be included into such analysis. While perturbative QCD seems to work down to 1 GeV^2 at low x, the theoretical scale uncertainties in NLO become very large, see above. With only HERA proton data an α_s error of about 0.004 can be expected for $Q^2 > 3$ GeV^2. As described in [39] the measurement of α_s requires very accurate control of the dependence of the systematic errors on the kinematic variables. This will permit to largely reduce their effect in the fit procedure like it has been practiced in the BCDMS/SLAC data analysis [41] which lead to an experimental α_s error of 0.003. Combination of the high x fixed target F_2 data with the low x HERA data promises to yield a precision measurement of α_s with an estimated experimental error of 0.0013 for $\alpha_s(M_Z^2)$. Simultaneously the gluon distribution can be measured very accurately with an estimated error of e.g. 3% for $x = 10^{-4}$ and $Q^2 = 20$ GeV^2 [39] using HERA data only. This potential measurement can only be reliably interpreted if the theoretical description is extended to NNLO.

3.2 High Q^2 Structure Functions

For $Q^2 \gtrsim 500$ GeV^2 and with both electron and positrons beams employed, there are two neutral current and two charged current reactions, i.e. four cross sections to be measured. This permits to extract various structure functions and combinations of parton densities, as was already thoroughly studied in the previous HERA workshops [42, 43] and summarized in the discussion [44]. The main conclusions remain valid: i) the charge asymmetry in neutral current $e^{\pm}p$ scattering allows to determine the interference structure function $xG_3 = 2x \sum Q_q a_q \cdot (q - \bar{q})$ for large y; ii) the charged current cross sections directly determine the valence quark distributions for $x \geq 0.3$; iii) with a high precision measurement of the four cross sections, various combinations of parton distributions can be unfolded, e.g. the singlet distribution or the strange quark density. All these measurements require highest luminosities, $\mathcal{L} \geq 500\ pb^{-1}$, about equally shared between electron and positron runs.

3.3 Deuteron Structure Functions

Interest has been expressed in the structure function working group [39, 45] in measuring the electron–deuteron DIS cross section at HERA. At low x, despite a few % structure function extraction uncertainty due to shadowing effects [46], the proton–deuteron F_2 difference will permit to constrain the up-down quark difference. This is expected to vanish towards low x but has not been measured yet in the domain of $x < 10^{-3}$. Deuteron structure function data

are important for a self consistent QCD analysis of HERA data as they constrain the non-singlet distributions in the α_s and gluon determination. Even with a luminosity of $\mathcal{L} = 50\text{pb}^{-1}$ only, interesting parton distribution combinations as $s - c$ [43] at high $Q^2 > 100$ GeV^2 can be measured.

3.4 Changing the Beam Energies

With the maximum possible energies of $E_p \simeq 1000$ GeV and $E_e \simeq 35$ GeV, the cms. energy squared can be increased by about a factor of 1.5 as compared to the nominal energy runs. Hence x values lower by this factor can be accessed at a given Q^2. It should be stressed that this high-energy option is the only way to explore this extended kinematical range in the foreseeable future. It requires only modest luminosity $\mathcal{L} \simeq 5$ pb^{-1} for the exploration of the low x region.

Because of the relation $Q^2 \simeq (2E_e \cot \theta_e/2)^2$, the decrease of the electron beam energy can be employed to reach very low values of $Q^2 < 1$ GeV^2. Using a small luminosity, $\mathcal{L} \simeq 1$ pb^{-1}, only this will allow for a high precision measurement of the transition region to photoproduction even after the foreseen luminosity upgrade which may limit the detector acceptance close to the beam pipe.

A run at lowest possible proton beam energy with $\mathcal{L} \simeq 10$ pb^{-1} is required in order to ensure maximum overlap of the HERA F_2 data with the fixed-target results. This is important for the precision measurement of α_s. Lowering E_p is also a necessity for measuring the longitudinal structure function F_L.

3.5 The Longitudinal Structure Function F_L

Various, partially complementary studies were presented to the workshop on the estimated measurement accuracy of the longitudinal structure function F_L [47, 48]. The joint conclusion of these studies is that an F_L precision measurement requires a set of about four different proton beam energies, $E_p = 250, 350, 450$ and 820 GeV, for instance, with luminosities around 5–10 pb^{-1} per energy setting. In a wide range of Q^2, between about 4 and 100 GeV^2, F_L should be measurable with an absolute error of typically 0.08 [48]. That accuracy largely depends on the maximum y, i.e. the minimum electron energy which can be controled in view of background and trigger requirements. The availability of various proton energies and the use of the subtraction method [49] will permit a significant measurement of the x dependence of $F_L(x, Q^2)$ which is important to distinguish between different predictions for F_L. A run at highest proton energy, $E_p \simeq 1000$ GeV, would represent an important gain in sensitivity to F_L, and lower E_e data would provide useful systematics cross checks.

3.6 The Charm Contribution to F_2

At low x, the charm contribution to the inclusive DIS cross section has been measured to be about one quarter [50]. Its understanding is crucial for the interpretation of F_2 and interesting for an independent measurement of the gluon distribution. With a luminosity of several 100 pb^{-1}, the charm structure function will be measurable with an estimated accuracy of 10%, the error being mainly due to the limited knowledge of the charm fragmentation probability $P(c \to D)$ into D mesons, and the detector and analyses uncertainties [51, 15]. This will permit

a detailed investigation of the charm production mechanism as a function of Q^2 and x and a complementary determination of the gluon distribution. The measurement relies on the observation of open charm production at HERA which should profit from Silicon detectors installed near the interaction vertex in order to enhance the charm tagging efficiency.

3.7 Structure of the Pion

HERA provides an interesting opportunity to study the structure of the pion [52, 53] as was presented to this working group [54]. Finite values of momentum transfer squared from the incoming proton beam to the outgoing neutron can be measured in the H1 and ZEUS neutron calorimeters with mean values of the order of 0.1 GeV^2. Studies were performed prior to the workshop [53], and a complete Monte Carlo simulation of the performance of the H1 forward neutron calorimeter is described in [55]. A modest luminosity of 10 pb^{-1} would yield about 5000 events in the range $10 < Q^2 < 15$ GeV^2. This would enable the structure of the virtual pion to be determined as a function of the longitudinal momentum of the exchanged pion for $0.6 > x_\pi > 10^{-4}$. Higher luminosities may allow the separation of the longitudinal structure of the pion and the determination of the structure of higher mass resonances.

References

[1] Proceedings of the 1987 HERA Physics Workshop, ed. R. Peccei, (DESY, Hamburg, 1988), Vol. **1**, pp. 1–181.

[2] Proceedings of the 1991 HERA Physics Workshop, eds. W. Buchmüller and G. Ingelman, (DESY, Hamburg, 1992), Vol. **1**, pp. 17–127.

[3] Proceedings of the Workshop Physics at HERA (DESY, Hamburg, 1992) Vol. **2**, p. 798.

[4] D. Bardin, J. Blümlein, P. Christova, and L. Kalinovskaya, these Proceedings; hep-ph/9609399, DESY 96–198.

[5] A. Arbuzov, D. Bardin, J. Blümlein, L. Kalinovskaya, and T. Riemann, Comp. Phys. Commun. **94** (1996) 128.

[6] J. Blümlein, S. Riemersma, and A. Vogt, DESY 96–120 (1996).

[7] D. Bardin, J. Blümlein, P. Christova, and L. Kalinovskaya, DESY 96–189.

[8] J. Blümlein and N. Kochelev, Phys. Lett. **B381** (1996) 296; DESY 96–175.

[9] J. Blümlein, M. Botje, C. Pascaud, S. Riemersma, W.L. van Neerven, A. Vogt, and F. Zomer, these Proceedings; hep-ph/9609400, DESY 96–199, INLO-PUB-20/96, WUE-ITP-96-018.

[10] J. Blümlein, S. Riemersma, W.L. van Neerven, and A. Vogt, DESY 96–172, hep-ph/9609217, Proceedings of the Workshop on QCD and QED in Higher Orders, Rheinsberg, Germany, April 1996, eds. J. Blümlein, F. Jegerlehner, and T. Riemann, Nucl. Phys. **B** (Proc. Suppl.) **51C** (1996) 96.

[11] J. Blümlein, S. Riemersma, W.L. van Neerven, and A. Vogt, these Proceedings.

[12] J. Chyla, talk presented at the workshop; Phys. Lett. **B351** (1995) 325.

[13] W.L. van Neerven, these Proceedings, hep-ph/9609243.

[14] J. Blümlein and S. Riemersma, these Proceedings, hep-ph/9609394.

[15] K. Daum, S. Riemersma, B.W. Harris, E. Laenen, and J. Smith, these Proceedings.

[16] A. Vogt, talk presented at the workshop; DESY 96-012, hep-ph/9601352, May 1996, Proceedings of the International Workshop on Deep Inelastic Scattering and Related Phenomena (DIS 96), Rome, April 1996, to appear.

[17] V. Barone, U. D'Alesio, and M. Genovese, these Proceedings.

[18] M. Meyer–Hermann, A. Schäfer, and E. Stein, these Proceedings;
E. Stein, M. Meyer–Hermann, L. Mankiewicz, and A. Schäfer, Phys. Lett. **B376** (1996) 177.

[19] M. Krämer, talk presented at the workshop;
M. Krämer, J. Zunft, J. Stegborn, and P. Zerwas, Phys. Lett. **B348** (1995) 657;
M. Kämer, Nucl. Phys. **B459** (1996) 3.

[20] S.A. Larin, T. van Ritbergen, and J.A.M. Vermaseren, Nucl. Phys. **B427** (1994) 41.

[21] S.A. Larin, P. Nogueira, T. van Ritbergen, and J.A.M. Vermaseren, NIKHEF 96–010, hep-ph/9605317.

[22] S.A. Larin, P. Nogueira, T. van Ritbergen, and J.A.M. Vermaseren, these Proceedings.

[23] A. Kataev, talk presented at the workshop.

[24] S. Catani, M. Ciafaloni and F. Hautmann, Phys. Lett. **B242** (1990) 97, Nucl. Phys. **B366** (1991) 135;
J.C. Collins and R.K. Ellis, Nucl. Phys. **B360** (1991) 3;
E.M. Levin, M.G. Ryskin, Yu.M. Shabel'skii and A.G. Shuvaev, Sov. J. Nucl. Phys. **53** (1991) 657;
S. Catani and F. Hautmann, Nucl. Phys. **B427** (1994) 475.

[25] L.N. Lipatov, Sov. J. Nucl. Phys. **23** (1976) 338; E.A. Kuraev, L.N. Lipatov and V.S. Fadin, Sov. Phys. JETP **45** (1977) 199; Ya. Balitskii and L.N. Lipatov, Sov. J. Nucl. Phys. **28** (1978) 822.

[26] R.K. Ellis, F. Hautmann and B.R. Webber, Phys. Lett. **B348** (1995) 582.

[27] J. Blümlein, S. Riemersma and A. Vogt, DESY 96–131, hep-ph/9608470, Proceedings of the Workshop on QCD and QED in Higher Orders, Rheinsberg, Germany, April 1996, eds. J. Blümlein, F. Jegerlehner, and T. Riemann, Nucl. Phys. **B** (Proc. Suppl.) **51C** (1996) 30.

[28] J. Blümlein, talk presented at the Workshop;
J. Blümlein, S. Riemersma and A. Vogt, hep-ph/9607329, Proceedings of the International Workshop on Deep Inelastic Scattering and Related Phenomena (DIS 96), Rome, April 1996, to appear;
J. Blümlein and A. Vogt, DESY 96–096.

[29] R.S. Thorne, these Proceedings.

[30] J.R. Forshaw, talk at the workshop;
J.R. Forshaw, R.G. Roberts and R.S. Thorne, Phys. Lett. **B356** (1995) 79.

[31] J. Blümlein and A. Vogt, Phys. Lett. **B370** (1996) 149; Acta Phys. Pol. **B27** (1996) 1309.

[32] M. Ciafaloni, Nucl. Phys. **B296** (1988) 49; S. Catani, F. Fiorani and G. Marchesini, Nucl. Phys. **B336** (1990) 18;
G. Marchesini, Proceedings of the Workshop QCD at 200 TeV Erice, Italy, 1990, eds. L. Cifarelli and Y. Dokshitser, (Plenum Press, New York, 1992), p. 183.

[33] P.J. Sutton, these Proceedings.

[34] M. Mc Dermott, talk presented at the workshop; J.R. Forshaw and M. Mc Dermott, DESY 96–103, hep-ph/9606293.

[35] L.N. Lipatov, talk presented at the workshop;
L.N. Lipatov, Proceedings of the Workshop on QCD and QED in Higher Orders, Rheinsberg, Germany, April 1996, eds. J. Blümlein, F. Jegerlehner, and T. Riemann, Nucl. Phys. **B** (Proc. Suppl.) **51C** (1996) 110;
DESY 96–132.

[36] A.H. Mueller, Nucl. Phys. **B415** (1994) 373;
A.H. Mueller and B. Patel, Nucl. Phys. **B425** (1994) 471, and references therein.

[37] G. Gustafsson, talk presented at the workshop.

[38] R. Peschanski and G. Salam, these Proceedings; SPhT-96/087; Cavendish-HEP-96-010; hep-ph/9607474.

[39] M. Botje, M. Klein and C. Pascaud, these Proceedings.

[40] G. Bernardi, A. Glazov, H1 Results on F_2, talks presented at the workshop.
R. Yoshida, ZEUS Results on F_2, talk presented at the workshop.

[41] A. Milstaijn and M. Virchaux, Phys.Lett. **B274** (1992) 221.

[42] M. Klein and T. Riemann, Z. Phys. **C24** (1984) 151;
G. Ingelman and R. Rückl, Z. Phys. **C44** (1989) 291;

[43] J. Blümlein, M. Klein, Th.Naumann and T.Riemann, Proceedings of the Workshop Physics at HERA (DESY, Hamburg, 1987) Vol. **1**, p. 67.

[44] Th. Naumann, talk presented at this workshop.

[45] V. Sidorov and M. Tokarev, these proceedings;

[46] M. Strikhman, contribution to this workshop.

[47] H. Blaikley, A. Cooper-Sarkar and S. Dasu, contributions to this workshop.

[48] L. Bauerdick, A. Glazov and M. Klein, these Proceedings.

[49] H1 Collaboration, Determination of the Longitudinal Structure Function F_L at Low x at HERA, Contributions to the Rome and Warsaw Conferences, 1996, to be published.

[50] C. Adloff et al., H1 Collaboration, DESY 96-138, Z. Phys. **C**, to appear.

[51] K. Daum, H1 collaboration, talk at the workshop;
A. Prinias, ZEUS collaboration, talk at the workshop.

[52] B. Kopelevich, B. Povh and I. Potashnikova, DESY 96-011 (1996).

[53] G. Levman and K. Furutani, ZEUS Note 92-107, unpublished and DESY 95-142 (1995).

[54] B. Povh, F_π with H1, talk presented at this workshop.
W.N. Murray, F_π with ZEUS, talk presented at this workshop.

[55] M. Beck et al., H1–collaboration, Proposal for a forward neutron calorimeter for the H1 experiment at DESY.

Recent Developments in Radiative Corrections at HERA

Dima Bardin[a,b], Johannes Blümlein[a], Penka Christova[c]
and Lida Kalinovskaya[b]

[a] DESY–Zeuthen, Platanenallee 6, D-15735 Zeuthen, Germany
[b] Bogoliubov Laboratory for Theoretical Physics,
JINR, ul. Joliot-Curie 6, RU–141980 Dubna, Russia
[c] Konstantin Preslavsky University of Shoumen, 9700 Shoumen, Bulgaria

Abstract: We describe several numerical results for radiative corrections for deep inelastic ep scattering at HERA which are calculated using the HECTOR package. We present radiative corrections for ten different choices of kinematical variables for unpolarized neutral and charged current deep inelastic scattering. Radiative corrections for neutral current scattering off polarized protons are calculated in leptonic variables and compared to those obtained by the POLRAD code for the kinematic regime of the HERMES experiment.

1 Introduction

The precise knowledge of QED radiative corrections is indispensable in the determination of nucleon structure functions. The forthcoming high statistics measurements of $F_2(x,Q^2)$, $F_L(x,Q^2)$ and $F^{c\bar{c}}(x,Q^2)$ at H1 and ZEUS require knowing the radiative corrections at the % level. In some of the measurements particularly, the range of high y is essential. Here the radiative corrections turn out to be large for some choices of the kinematical variables and higher order corrections can be necessary.

In the present note we summarize the status reached in the calculation of the QED radiative corrections. In section 2, we present a short description of main features of the recently released code HECTOR [1].

For the first time also polarized nucleon structure functions can be measured at HERA with the HERMES experiment Also here the radiative corrections are large. Recently a dedicated new calculation [2] was performed including both γ and Z-boson exchange and accounting for all twist-2 contributions to the structure functions contributing to scattering cross sections both for the case of longitudinally and transverse polarized nucleons.

In section 3, we present a discussion of numerical results summarized in a collection of figures. A particular emphasis is given on the high y range by presenting and discussing the results for ten different choices of the kinematical variables. A first comparison between the results of HECTOR and earlier results of POLRAD [3]-[5] is presented.

2 HECTOR 1.00 and its recent upgrade

The code HECTOR was created at DESY–Zeuthen in 1995. Version 1.00, November 1995 [1], accumulates and comprises results collected over the course of 20 years (1975-1994) by the Dubna-Zeuthen Radiative Correction Group (DZRCG) [6], based on a *semi-analytic, model-independent* (MI) approach and results by J. Blümlein (1990-1994), based on an inclusive *leading logarithmic approach* (LLA).

The branches of HECTOR include earlier codes for treatment of selected parts of radiative corrections:

- HELIOS – an inclusive LLA treatment of *leptonic* QED radiative corrections including second order initial state radiation, $\mathcal{O}((\alpha L)^2)$, and *soft-photon exponentiation* to all orders for a variety of measurements: leptonic, mixed, Jaquet-Blondel, double angle variables, the Σ method and others [7];
- TERAD – a complete $\mathcal{O}(\alpha)$ MI treatment of *leptonic* QED radiative corrections for several types of measurements, for a detailed description see [8];
- DISEP – a complete $\mathcal{O}(\alpha)$ quark-parton model treatment of QED radiative corrections and *one-loop electroweak* radiative corrections [9] for leptonic and mixed variables;
- TERADLOW – a MI treatment of *leptonic* QED radiative corrections in the photoproduction region for leptonic variables [8].

HECTOR makes use of extensive access to existing libraries of the structure functions and parton densities, both via the PDF-library [10] and directly, and to recent *low* Q^2-libraries.

The QCD corrections are implemented in the framework of different factorization schemes, as the $\overline{MS}$ and DIS schemes, in order to ensure a proper use of available parton densities. The LO option is also available.

Currently one may access ten different choices of kinematical variables for neutral and charged current deep inelastic scattering, see figures 2a-j.

Simple kinematical cuts are possible within the complete $\mathcal{O}(\alpha)$ MI approach.

The upgrade of HECTOR, version 1.11, will contain the following additions:

- The option to calculate radiative corrections for neutral current deep inelastic polarized lepton – polarized nucleon scattering has been incorporated [2]. It includes both γ and Z-boson exchange. The Born cross section contains all twist-2 contributions to the polarized structure functions – for the cases of longitudinal and transverse proton polarization.
- The radiative corrections for a *tagged photon measurement* based on a mixture of complete MI, deterministic and LLA approaches are being incorporated [11].

Version 1.11 will be released by the end of 1996.

3 Numerical Results

3.1 QED radiative corrections at high y

The radiative corrections (RC) at high y are presented in two sets of figures, 1 and 2, at HERA collider energies. Here for the structure functions, we used the CTEQ3M LO parametrization [12].

In figures 1a-d, we show the comparison between complete $\mathcal{O}(\alpha)$ MI calculations and those in LLA, for 4 types of measurements for which the complete results are available.

In *leptonic* variables at small x and high y, where the correction is big, the difference between complete and LLA calculations reaches tens of percent.

In *mixed* variables we registered an almost constant, x, y-independent shift between the two calculations, which is quite small, $\leq 0.5\%$.

An interesting phenomenon is observed in *Jaquet-Blondel* and *hadronic* variables. There the difference between the two calculations grows with growing y, reaching several percent for $y \approx 1$, i.e. in the soft photon corner of hadronic y. This could be a reflection of the fact that in these variables the final state radiation leading log correction is absent and non-logarithmic terms can be important.

So, one can conclude, that although the LLA approximates the gross features of radiative corrections in all 4 variables, its precision is not sufficient if one aims at an accuracy of measurement of the order of 1%.

In figures 2a-j, we show the comparison between lowest order and higher order LLA calculations of radiative corrections for ten measurements: eight – for neutral current (NC) and two – for charged current (CC). Although we have presented figures for all ten choices of measurements available in HECTOR, we will discuss only several of the most popular kinematic variables.

In *leptonic* variables at small x and high y, the higher order corrections reach tens of percent. Since LLA qualitatively decribes the lowest order corrections, one may trust the reliability of higher order corrections estimation.

In *Jaquet-Blondel*, *mixed*, and *hadronic* variables, the higher order corrections exhibit very similar properties. They grow with increasing x and y, reaching $1-2\%$ at high x and high y, i.e. in the soft photon corner.

The constant positive shift, growing with increasing x, is distinctly seen in *double angle* and Σ variables. It may reach 1% for $x = 0.1$ and goes down rapidly with decreasing x.

In the $e\Sigma$ method, the higher order corrections are surprisingly large, but this method is not so popular.

From figures presented, we may conclude that higher order corrections are in general rather important for the precision measurement of deep inelastic scattering at HERA.

Both sets of figures prove that a realistic radiative corrections procedure must take into account both the complete lowest order calculations and higher order corrections, at least within LLA. This is exactly the strategy that the HECTOR code follows.

3.2 Comparison of HECTOR and POLRAD15 for Polarized Deep Inelastic Scattering

In this section we compare the results of the codes HECTOR and POLRAD15. We refer to the kinematic range of the HERMES experiment and consider only leptonic corrections in leptonic variables for scattering off polarized protons. Both the cases of longitudinal and transverse polarizations were studied. We used the parametrizations of Schäfer'88 [13] and GRSV'96 [14] to describe the polarized structure functions.

To simplify the first comparison between the two codes, we neglect Z-boson exchange, account only for one structure function ($g_1^{\gamma\gamma}$) for the case of longitudinal proton polarization, and at most for two ($g_{1,2}^{\gamma\gamma}$) for the case of transverse polarization. Furthermore, we neglect the vacuum polarization correction (the running α), higher order radiative corrections, hadronic corrections and electroweak corrections.

The comparison for *unpolarized*, *longitudinal* and *transverse* parts of deep inelastic scattering (DIS) radiative corrections normalized by corresponding Born cross sections is presented in figures 3a-d. They are denoted in figures as UNPOL, LONG, TRAN, correspondingly. Further details may be found in [2].

The results of the comparison may be summarized as follows:

- Very good agreement was found for all values of x and y in the *unpolarized*-case.
- We registered some disagreement for small x and high y, i.e. in the Compton region, for *longitudinal*- and *transverse*-cases.
- We observed an amazing agreement between complete and LLA calculations in the considered set-up. This suggests the use of a fast, LLA code for HERMES measurements in leptonic variables.

Further work on the comparison, aimed at the resolution of the above-mentioned disagreement, is in progress.

Acknowledgments

The authors are very much obliged to I. Akushevich for pleasant and fruitful collaboration on the comparison with POLRAD. We are thankful to A. Arbuzov and T. Riemann for an enjoyable common work within the HECTOR project. We are indepted to T. Riemann and S. Riemersma for a critical reading of the manuscript.

References

[1] A. Arbuzov, D. Bardin, J. Blümlein, L. Kalinovskaya, T. Riemann, *Computer Phys. Commun.* **94** (1996) 128.

[2] D. Bardin, J. Blümlein, P. Christova, L. Kalinovskaya, DESY 96–189.

[3] T. Kukhto and N. Shumeiko, *Nucl. Phys.* **B219** (1983) 412.

[4] N. Shumeiko, In Proceedings of the 1992 Zeuthen Workshop on Elementary Particle Theory: Deep Inelastic Scattering, Teupitz/Brandenburg, Germany 6-10 April 1992; J. Blümlein and T. Riemann Eds, *Nucl. Phys. B (Proc. Suppl.)* **29A** (1992) 236.

[5] I. Akushevich and N. Shumeiko, *J. Phys.* **G20** (1994) 513.
I. Akushevich, N. Shumeiko et al. Internal Report DESY-Zeuthen-94-02.

[6] In the field of deep inelastic scattering, the following physicists worked within DZRCG: A. Akhundov, D. Bardin, C. Burdik, P. Christova, O. Fedorenko†, L. Kalinovskaya, T. Riemann. N. Shumeiko participated in the long first period of work in this direction.

[7] J. Blümlein, *Z. Physik* **C47** (1990) 89; *Phys. Letters* **B 271** (1991) 267; *Z. Physik* **C65** (1995) 293.
J. Blümlein, G. Levman and H. Spiesberger, in: E. Berger (ed.), Proceedings of the Workshop on Research Directions of the Decade, Snowmass 1990 (World Scientific, Singapore, 1992), p. 554; *J. Phys.* **G19** (1993) 1695.

[8] A. Akhundov, D. Bardin, L. Kalinovskaya and T. Riemann, *Fortschr. Phys.* **44** (1996) 373.

[9] D. Bardin, C. Burdik, P. Christova and T. Riemann, *Z. Physik* **C42** (1989) 679; *Z. Physik* **C44** (1989) 149.

[10] H. Plothow–Besch, *Computer Phys. Commun.* **75** (1993) 396.

[11] D. Bardin, L. Kalinovskaya and T. Riemann, in preparation.

[12] H.L. Lai, J. Botts, J. Huston, J.G. Morfin, J.F. Owen, J.W. Qiu, W.K. Tung and H. Weerts, *Phys. Rev.* **D51** (1995) 4763.

[13] A. Schäfer, *Phys.Lett.* **B208** (1988) 175.

[14] M. Glück, E. Reya, M. Stratmann and W. Vogelsang, *Phys. Rev.* **D53** (1996) 4775.

[15] S. Wandzura and F. Wilczek, *Phys. Lett.* **B72** (1977) 195.

†Deceased

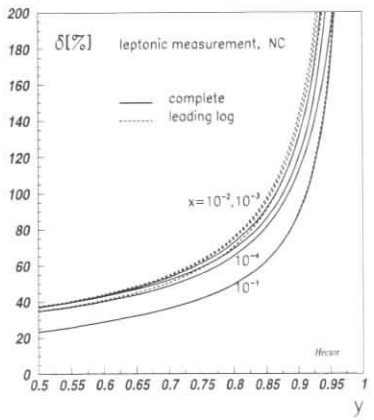

Fig. 1a: A comparison of complete and leading log calculations of RC for NC DIS at HERA for *leptonic* variables.

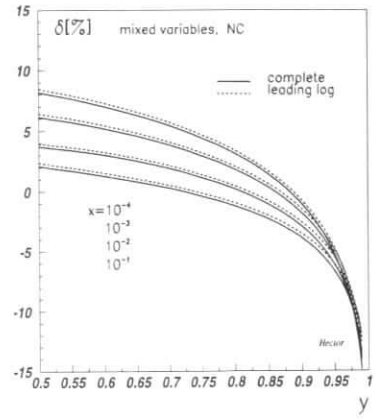

Fig. 1c: The same as Fig.1a but for *mixed* variables.

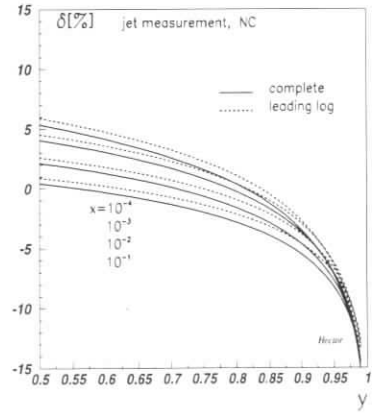

Fig. 1b: The same as Fig.1a but for *Jaquet-Blondel* variables.

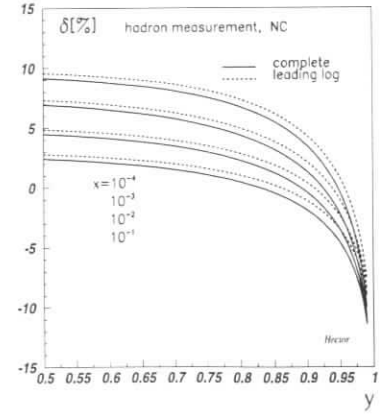

Fig. 1d: The same as Fig.1a but for *hadronic* variables.

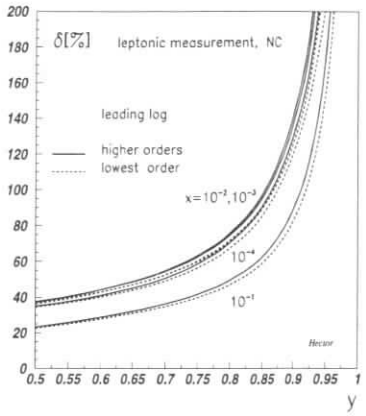

Fig. 2a: A comparison of lowest order with higher order leading log calculations of RC for NC DIS at HERA for *leptonic* variables.

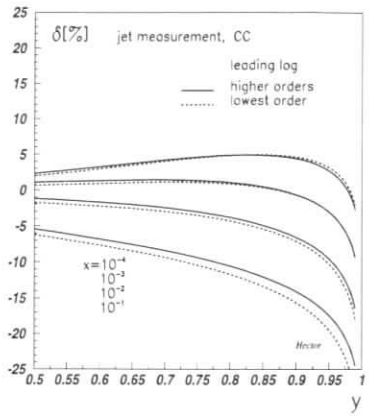

Fig. 2c: The same as Fig.2b but for CC DIS.

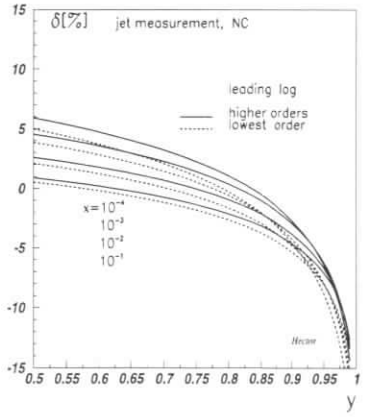

Fig. 2b: The same as Fig.2a but for *Jaquet-Blondel* variables.

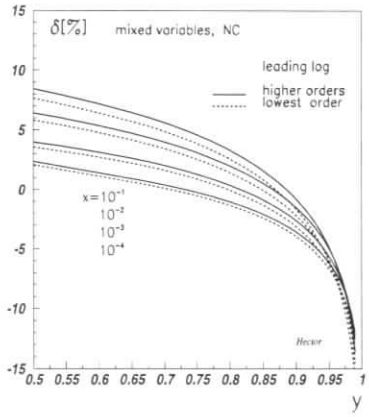

Fig. 2d: The same as Fig.2a but for *mixed* variables.

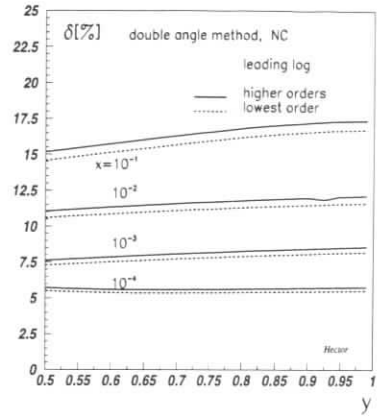

Fig. 2e: The same as Fig.2a but for the *double angle* method.

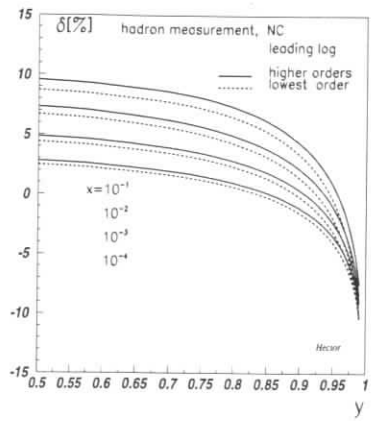

Fig. 2g: The same as Fig.2a but for *hadronic* variables.

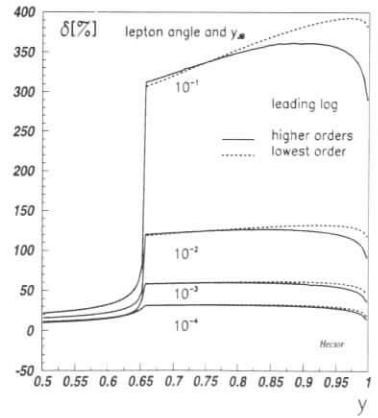

Fig. 2f: The same as Fig.2a but for the *lepton angle and* $y_{\rm JB}$ method.

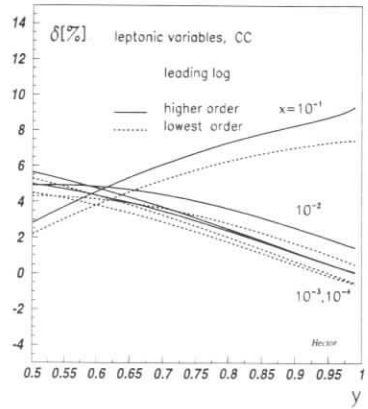

Fig. 2h: The same as Fig.2b but for *leptonic* variables.

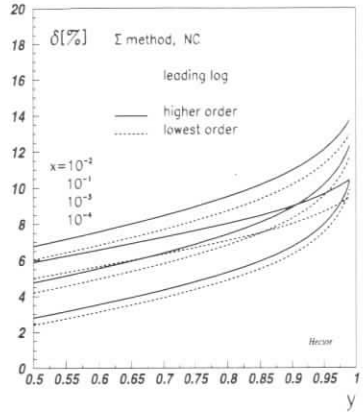

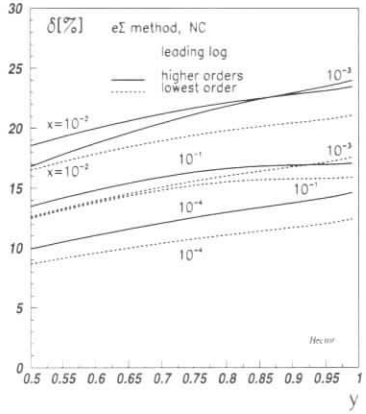

Fig. 2i: The same as Fig.2a but for the Σ method. Fig. 2j: The same as Fig.2a but for the $e\Sigma$ method.

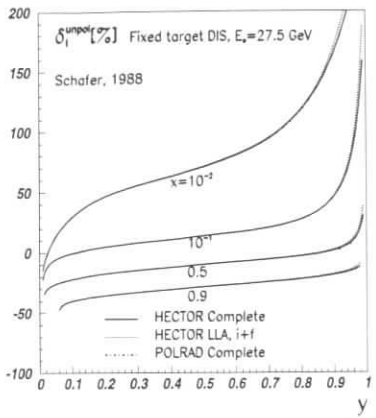

Fig. 3a: A comparison of RC between HECTOR and POLRAD for NC *unpolarized* DIS for *leptonic* variables.

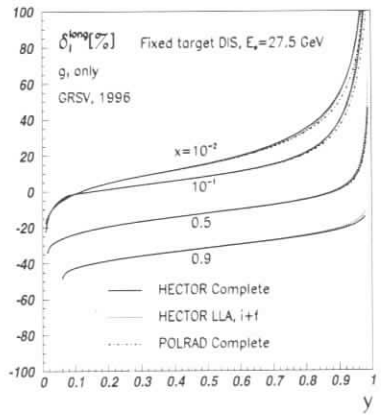

Fig. 3b: The same as Fig.3a but for *longitudinal* DIS.

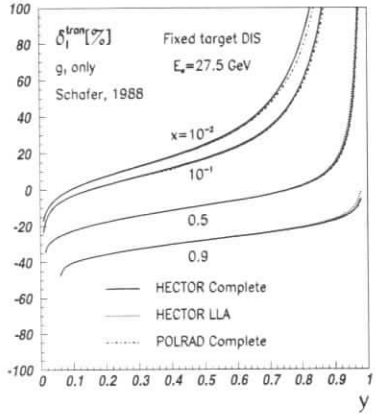

Fig. 3c: The same as Fig.3a but for *transverse* DIS.

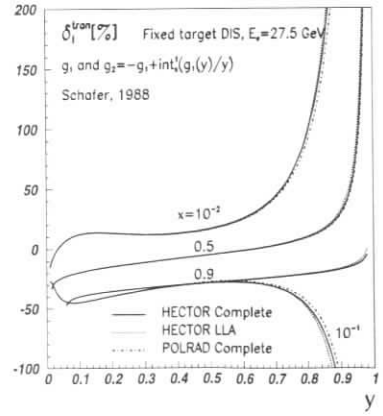

Fig. 3d: The same as Fig.3c but for another assumption on g_2 [15].

A Detailed Comparison of NLO QCD Evolution Codes

J. Blümlein[a], M. Botje[b], C. Pascaud[c], S. Riemersma[a],
W.L. van Neerven[d], A. Vogt[e,f], and F. Zomer[c]

[a] DESY-Zeuthen, Platanenallee 6, D–15738 Zeuthen, Germany
[b] NIKHEF, PO Box 41882, 1009 DB Amsterdam, The Netherlands
[c] LAL, IN2P3-CNRS et Université de Paris-Sud, F–91495 Orsay Cédex, France
[d] Instituut Lorentz, Rijksuniversiteit Leiden, PO Box 9506, 2300 RA Leiden, The Netherlands
[e] Deutsches Elektronen-Synchrotron DESY, Notkestraße 85, D–22603 Hamburg, Germany
[f] Institut für Theoretische Physik, Universität Würzburg, D–97074 Würzburg, Germany

Abstract: Seven next-to-leading order QCD evolution programs are compared. The deviations of the results due to different theoretical prescriptions for truncating the perturbative series are clarified, and a numerical agreement between five codes of better than 0.1% is achieved. Reference results for further comparison are provided.

1 Introduction

In order to exploit the full potential of HERA for deep–inelastic scattering (DIS), the highest possible luminosities and considerable efforts for the reduction of experimental systematic uncertainties are necessary. This will finally allow a measurement of the proton structure function F_2 over a wide range, with errors on the level of very few percent [1]. To make full use of such results, and to allow even for combined analyses using the high–precision fixed–target data as well, the structure function evolution programs required for the necessary multi–parameter QCD fits have to be numerically and conceptually under control to a much higher accuracy. At least one order of magnitude is desirable. This accuracy is necessary to safely rule out contributions to the theory error of $\alpha_s(M_Z^2)$ which arise from the particular technical implementation of the solution of the NLO evolution equations. Due to the current apparent difference in $\alpha_s(M_Z^2)$ as determined in e^+e^- and DIS experiments [2], this question is of particular importance for the future QCD analyses based on the HERA structure function data.

So far no high–precision comparison of next-to-leading-order (NLO) programs has been performed including the full HERA range. In previous studies partial comparisons were carried out demanding a considerably lower accuracy (see e.g. ref. [3]). Other comparisons focussed on the valence range and compared the effect of different codes used for the QCD fit on $\Lambda_{\rm QCD}$ only, see ref. [4]. The required accuracy cannot be easily reached by just comparing results to published parametrizations, due to their inaccuracies, caused by respective numerical representations. Often also the physical and technical assumptions made are not fully documented.

In this paper, we present the results of a dedicated effort, comparing the results of seven NLO codes under perfectly controlled conditions. The paper is organized as follows. In Section 2 we recall the basic formulae, and sketch the most commonly used approaches to the

evolution equations. Section 3 compares the differences of six 'global' evolution programs. The clarification of the deviations found there, using also a seventh program especially suited for the 'local' evolution of F_2, is described in Section 4. The size of the numerical differences which persist after this development is investigated in Section 5, where also reference results for further comparison are provided. Finally Section 6 contains our summary.

2 Approaches to the Next-to-Leading Order Evolution

The evolution equations for the parton distributions $f(x,Q^2)$ of the proton are given by

$$\frac{\partial f(x,Q^2)}{\partial \ln Q^2} = \left[a_s(Q^2)\, P_0(x) + a_s^2(Q^2)\, P_1(x) + O(a_s^3)\right] \otimes f(x,Q^2)\,. \tag{1}$$

Here x stands for the fractional momentum carried by the partons, and $\otimes$ denotes the Mellin convolution. For brevity, we have introduced $a_s(Q^2) \equiv \alpha_s(Q^2)/4\pi$. Eq. (1) is understood to represent, in a generic manner, the non–singlet cases as well as the coupled quark and gluon evolutions. $P^{(0)}$ and $P^{(1)}$ denote the corresponding leading order (LO) and NLO splitting functions, respectively (see, e.g., ref. [5]). Only these two coefficients of the perturbative series are completely known so far, hence the solution of the evolution equations is presently possible only up to NLO. To this accuracy, the scale dependence of the strong coupling $a_s(Q^2)$ reads

$$\frac{\partial\, a_s(Q^2)}{\partial \ln Q^2} = -\beta_0 a_s^2(Q^2) - \beta_1 a_s^3(Q^2) + O(a_s^4)\,. \tag{2}$$

Throughout our comparisons, we will identify the renormalization and factorization scales with Q^2, as already indicated in eqs. (1) and (2). For different choices see refs. [6, 7]. Introducing the QCD scale parameter Λ, the solution of eq. (2) can be written as

$$a_s(Q^2) \simeq \frac{1}{\beta_0 \ln(Q^2/\Lambda^2)} - \frac{\beta_1}{\beta_0^3} \frac{\ln\left[\ln(Q^2/\Lambda^2)\right]}{\ln^2(Q^2/\Lambda^2)}\,. \tag{3}$$

Two approaches have been widely used for dealing with the integro–differential equations (1). In many analyses, they have been numerically solved directly in x-space. We will exemplify some techniques applicable in this case for one particular program, choosing 'QCDNUM', which is based on the programs of ref. [8], and is planned to become publicly available [9]. See, for example, ref. [10] for a description of a differing x-space implementation.

In QCDNUM, the Q^2 evolution of the parton momentum densities is calculated on a grid in x and Q^2, starting from the x-dependence of these densities at a fixed reference scale Q_0^2. The logarithmic slopes in Q^2 are calculated from eq. (1). To compute the convolution integrals, the assumption is made that the parton distributions can be linearly interpolated (at all Q^2) from one x gridpoint to the next. With this assumption the integrals can be evaluated as weighted sums. The weights, which are essentially integrals over the splitting functions, are numerically calculated (by Gauss integration) to high precision at program initialization. From the value of a given parton distribution and the slopes at Q_0^2, the distribution can be calculated at the next gridpoint $Q_1^2 > Q_0^2$ (or $Q_1^2 < Q_0^2$). This distribution then serves to calculate the slopes at Q_1^2 etc., and the evolution is continued over the whole x–Q^2 grid. The evolution algorithm makes use of quadratic interpolation in $\ln Q^2$.

In this way, a fast evolution of parton densities is obtained, entirely based on look-up weight tables which are calculated at program initialization. The numerical accuracy depends on the density of the x grid and, to a lesser extent, on that of the Q^2 grid. In the comparisons presented here, 370 gridpoints in x covering $10^{-5} \leq x < 1$ have been used: 230 points distributed logarithmically for $x < 0.2$, and 140 points distributed linearly for $x > 0.2$. A logarithmic Q^2 grid with 60 points covered the range $4 < Q^2 < 10^4$ GeV^2.

An important alternative to the direct x-space treatment, employed in the analyses of refs. [11, 12] based upon ref. [13], is to transform the evolution equations to Mellin-N moments. The main virtue of this transformation is that the convolution is reduced to a simple product. Hence eq. (1) turns into a system of ordinary differential equations at fixed N, which allows for an analytic solution. Rewriting the evolution equations in terms of $a_s \equiv a_s(Q^2)$ using eq. (2), and expanding the resulting r.h.s. into a power series in α_s, one arrives in NLO at

$$\frac{\partial f(x,a_s)}{\partial a_s} = -\frac{1}{\beta_0 a_s}\left[P^{(0)}(x) + a_s\left(P^{(1)}(x) - \frac{\beta_1}{\beta_0}P^{(0)}(x)\right) + O(a_s^2)\right] \otimes f(x,a_s)\,. \tag{4}$$

After transformation to N-moments, its solution can be written down in a closed form for the non-singlet cases, with $a_0 \equiv a_s(Q_0^2)$, as

$$f_N(a_s) = \left[1 - \frac{a_s - a_0}{\beta_0}\left(P_N^{(1)} - \frac{\beta_1}{\beta_0}P_N^{(0)}\right) + O(a_s^2)\right]\left(\frac{a_s}{a_0}\right)^{P_N^{(0)}/\beta_0} f_N(a_0)\,. \tag{5}$$

For the notationally more cumbersome, corresponding relation for the singlet evolution, the reader is referred to refs. [11, 12].

From these analytic solutions, one can acquire the x-space results by one contour integral in the complex N-plane, see ref. [12]. Using a chain of Gauss quadratures, a numerical accuracy of this integration at better than 10^{-5} is readily achieved. In our comparisons, at most 136 fixed support points at complex N-values have been used, with this maximal number employed only for very large values of x [14]. Due to the required non-trivial analytic continuations of the NLO anomalous dimensions [12], this approach is technically somewhat more involved than the numerical x-space solution. On the other hand, since the Q^2 integration is done in one step, regardless of the evolution distance, and the use of fixed support points allows for performing the calculation of the anomalous dimensions only once at program initialization, this method is competitive in speed to the x-space iterations.

A partly independent N-space program has been developed during this workshop [15], implementing an iterative numerical solution of the Mellin-transformed eq. (4). Since one of the advantages of the N-space approach is not exploited here, this program is so far not competitive in speed with the ones discussed before. It has however been of considerable value for cross-checks and theoretical investigations, see below.

Before we now turn to the comparisons, it should be emphasized that a perfect agreement between the results based upon eqs. (1), (4), and (5) is not to be expected, since they all differ in terms of next-to-next-to leading order (NNLO), hidden under the $O(a_s^3)$ and $O(a_s^2)$ signs.

3 The Initial Comparisons

All our comparisons are performed under somewhat simplified, but sufficiently realistic conditions. We assume four massless flavours, in eq. (1) as well as in eq. (2), at all scales considered,

i.e. effects due the non-zero charm mass and the existence of the bottom quark are not taken into account. All our results below will refer to the $\overline{\rm MS}$ renormalization and factorization schemes, and the corresponding scales are identified with Q^2. The reference scale Q_0^2 for the evolution, and the four-flavour QCD scale parameter Λ in eq. (3) are chosen as

$$Q_0^2 = 4 \text{ GeV}^2\,, \quad \Lambda_{\overline{\rm MS}}^{(4)} = 250 \text{ MeV}\,. \tag{6}$$

The following initial conditions are selected for the (anti-) quark and gluon densities:

$$\begin{aligned} xu_v(x,Q_0^2) &= A_u x^{0.5}(1-x)^3\,, \; xd_v(x,Q_0^2) = A_d x^{0.5}(1-x)^4\,, \\ xS(x,Q_0^2) &= [x\Sigma - xu_v - xd_v](x,Q_0^2) = A_S x^{-0.2}(1-x)^7\,, \\ xg(x,Q_0^2) &= A_g x^{-0.2}(1-x)^5\,, \; xc(x,Q_0^2) = x\bar{c}(x,Q_0^2) = 0\,. \end{aligned} \tag{7}$$

The SU(3)-symmetric sea S is assumed to carry 15% of the nucleon's momentum at the input scale, and the remaining coefficients A_i are fixed by the usual sum rules. Finally F_2 is determined by simply convoluting the resulting parton densities with the appropriate coefficient functions.

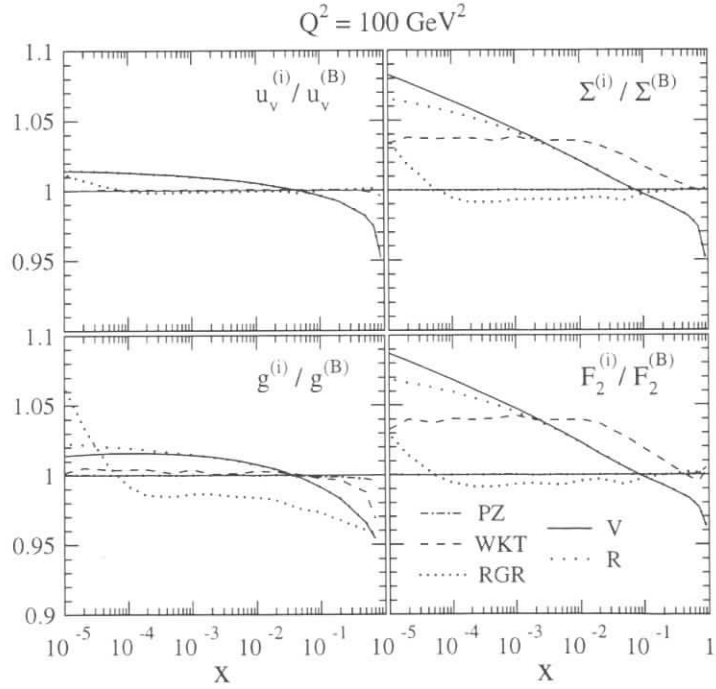

Figure 1: The differences between the up-valence, singlet quark and gluon densities, u_v, Σ and g, and the proton structure functions F_2, as obtained from evolving the input (7) with various NLO evolution programs [9, 10, 14, 15, 16, 17] to $Q^2 = 100$ GeV^2. All results have been normalized to those of ref. [9]. For a detailed discussion see the text.

The results of our first comparisons are shown in Figure 1. One notices the very good agreement between the programs [9, 10] used by the HERA collaborations. The differences are always much less than 1%, and the curves can hardly be distinguished, except for large x, with the present resolution. A similarly excellent agreement is seen between the two N-space programs [14, 15], except for very low x, where offsets up to 1.5% show up. The most striking feature of the figure, however, is the very sizeable differences between these two groups of programs: the scaling violations, increasing (decreasing) the distributions at small (large) values of x, are considerably stronger in the results of refs. [14, 15], although, of course, the same values for α_s are employed as in refs. [9, 10]. This effect reaches a magnitude of as much as 8% for the structure function F_2 at the smallest x-values considered.

As stated above, perfect agreement had not been expected due to theoretical differences, but the size of this offset was a surprise to most of us. It initiated quite some checking and programming activity, which will be summarized in the next section.

Also shown in the figure are the results obtained by the x-space evolution programs of the MRS and CTEQ global fit collaborations [16, 17]. Very good agreement to the results of refs. [9, 10] is found for the valence quarks, except for ref. [16] at extremely low values of x. In the singlet sector, however, significant differences are observed for some quantities: 1.5 – 3% on the gluon density in ref. [16], and up to 4% on the sea quark distributions in ref. [17].

4 Pinning Down the Differences

Besides checks and comparisons of the numerical values of the NLO splitting between the codes of refs. [9, 14, 15], the large differences discussed in the previous section led to three program developments, which together allowed for their full understanding on an unprecedented level.

- A program for a local representation of the evolution of F_2 close to the initial scale, completely independent of all previous ones, was added to the comparisons [18].
- The code of ref. [15] was extended to include, still in moment space, an option for evolving also on the basis of eq. (1) instead of (4).
- The program of ref. [14] was used to simulate an iterative solution of eq. (4) as performed in ref. [15], and additionally two new iterative options, one of them equivalent to eq. (5), were introduced into this package.

The results of these efforts are displayed in Figure 3, where we show the evolution of F_2, close to our reference scale $Q_0^2 = 4$ GeV^2, for three typical values of x. The differences, depicted in the previous figure for $Q^2 = 100$ GeV^2, build up very quickly near Q_0^2: already around 10 GeV^2 they are close to their final level. The second important observation is the perfect agreement of the local representation [18] with the x-space codes [9, 10], which immediately stopped any speculations on possible problems in the latter programs. Next one notices that the 1% small-x difference between refs. [14] and [15] is perfectly understood in terms of the slightly different contributions truncated away in eqs. (4) and (5), cf. ref. [6]. The concluding step is the comparison of the modified evolution of [15] with the results of [9, 10, 18]. This reveals that in fact virtually all offsets between the results of refs. [9, 10, 14, 15] in Figure 1 are

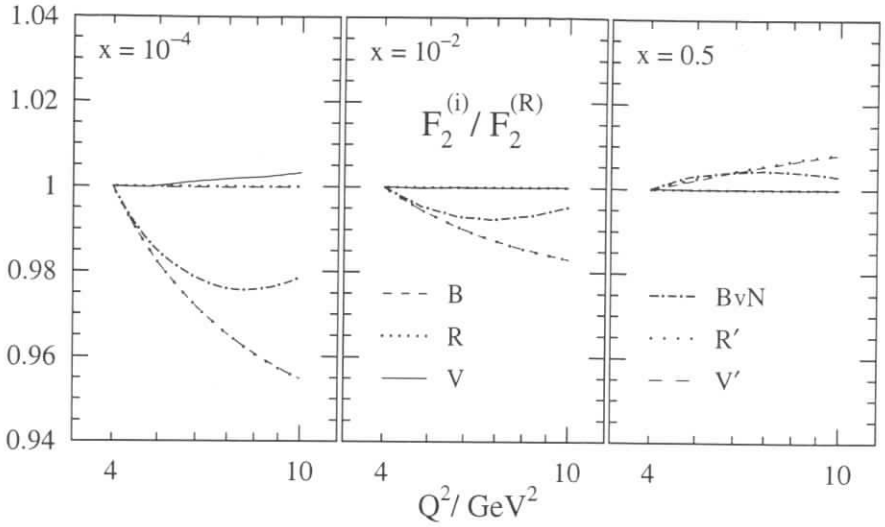

Figure 2: A comparison of results on the Q^2 evolution of F_2 close to the reference scale $Q_0^2 = 4$ GeV^2. The results of refs. [9, 15, 12] (denoted by **B**, **R**, and **V**) are as in the previous figure. **BvN** represents a local representation of the F_2 evolution [18], and the curves **R**′ and **V**′ check the numerical consistency by adapting to the theoretical assumptions of refs. [9] and [15], respectively.

due to the differences introduces by the employed truncation prescriptions for the perturbative series the NLO level, i.e. by terms of NNLO and beyond.

The origin of the differences between the results of refs. [16, 17] and our programs could not be clarified during this workshop. Hence for the very precise comparisons to which we now turn, we will keep only our five program packages, which agree, at least, sizeably better than to 1%.

5 The Achieved Numerical Accuracy

Armed now with at least two different codes for any of the truncation prescriptions of Section 2, we can proceed to explore the limits of the agreement of our five program packages under consideration. This complete coverage will be used for comparing all programs, even those with conflicting theoretical treatments, in one figure. For this purpose, the results of refs. [9, 10] have been normalized to the modified evolution of ref. [15] (based upon eq. (1)), whereas the 'iterated' evolution of ref. [14] is normalized to the original results of ref. [15] (based upon eq. (4)).

The results are shown at two fixed Q^2 values in Figure 3 for the parton distributions, and in Figure 4 for Q^2 evolution of the proton structure function F_2 at three fixed values of x. The total spread of the results at $Q^2 = 100$ GeV^2 amounts to at most about 0.05%, except for very large x, where the distributions, especially the gluon density, become very small. Even after

evolution to 10^4 GeV^2, the differences are still on the level of 0.1%, meeting the goal formulated in the introduction. Moreover, there is no reason for failing to reach an even higher accuracy, at least to 0.02% as already achieved between the N-space programs, also in x-space, e.g. by increasing the still not too high number of Q^2 grid points in the program of ref. [9].

Finally, for the convenience of those readers who want to check their own existing of forthcoming NLO evolution program to an accuracy well below 0.1% over a wide range in x, we show in Table 1 two sets of reference results, which represent the evolution of the initial distributions (7) under the conditions (6), according to eq. (1) and eq. (5) to $Q^2 = 100$ GeV^2.

x	xu_v	xd_v	xS	$2xc$	xg	F_2
10^{-5}	9.2793 E-3	5.2115 E-3	2.6670 E1	5.0866 E0	9.6665 E1	7.0270 E0
10^{-4}	2.8777 E-2	1.6134 E-2	1.3862 E1	2.4694 E0	4.7091 E1	3.5868 E0
10^{-3}	8.7208 E-2	4.8678 E-2	6.7508 E0	1.0663 E0	2.0801 E1	1.7271 E0
10^{-2}	2.4598 E-1	1.3494 E-1	2.8562 E0	3.5762 E-1	7.5998 E0	7.9497 E-1
0.1	4.7450 E-1	2.3215 E-1	5.7924 E-1	4.6496 E-2	1.4260 E0	3.5397 E-1
0.3	3.1152 E-1	1.1662 E-1	5.7780 E-2	3.5268 E-3	1.9173 E-1	1.6536 E-1
0.7	2.5048 E-2	3.9486 E-3	8.0219 E-5	4.0111 E-6	1.1276 E-3	1.4359 E-2
x	xu_v	xd_v	xS	$2xc$	xg	F_2
10^{-5}	9.4109 E-3	5.2848 E-3	2.8893 E1	5.6465 E0	9.8060 E1	7.6417 E0
10^{-4}	2.9144 E-2	1.6336 E-2	1.4755 E1	2.6954 E0	4.7859 E1	3.8325 E0
10^{-3}	8.8083 E-2	4.9146 E-2	7.0516 E0	1.1434 E0	2.1110 E1	1.8094 E0
10^{-2}	2.4723 E-1	1.3553 E-1	2.9226 E0	3.7584 E-1	7.6627 E0	8.1358 E-1
0.1	4.7268 E-1	2.3097 E-1	5.7880 E-1	4.7422 E-2	1.4152 E0	3.5337 E-1
0.3	3.0798 E-1	1.1511 E-1	5.6817 E-2	3.4796 E-3	1.8757 E-1	1.6349 E-1
0.7	2.4433 E-2	3.8429 E-3	7.6136 E-5	3.5004 E-6	1.0854 E-3	1.4013 E-2

Table 1. Reference results at $Q^2 = 100$ GeV^2 for the NLO evolution using the direct solution of eq. (1) (upper half), and the truncated analytic solution (5) (lower half). The initial conditions are specified in eqs. (6) and (7). The estimated numerical accuracy of these results is about 0.02%.

6 Summary

The results of seven programs for the NLO evolution of parton densities and structure functions have been compared. Differences due to terms of NNLO, truncated differently in the various implementations, turn out to be larger than anticipated. They can reach, e.g., about 6% at $x = 10^{-4}$ and $Q^2 = 100$ GeV^2. A full quantitative understanding of these differences has been achieved at an unprecedented level of accuracy for five of these codes. There the remaining numerical differences are on the level of $\pm 0.02\%$ at $Q^2 = 100$ GeV^2. Two sets of reference results, according to different theoretical prescriptions, have been provided for further high-precision checks of evolution programs.

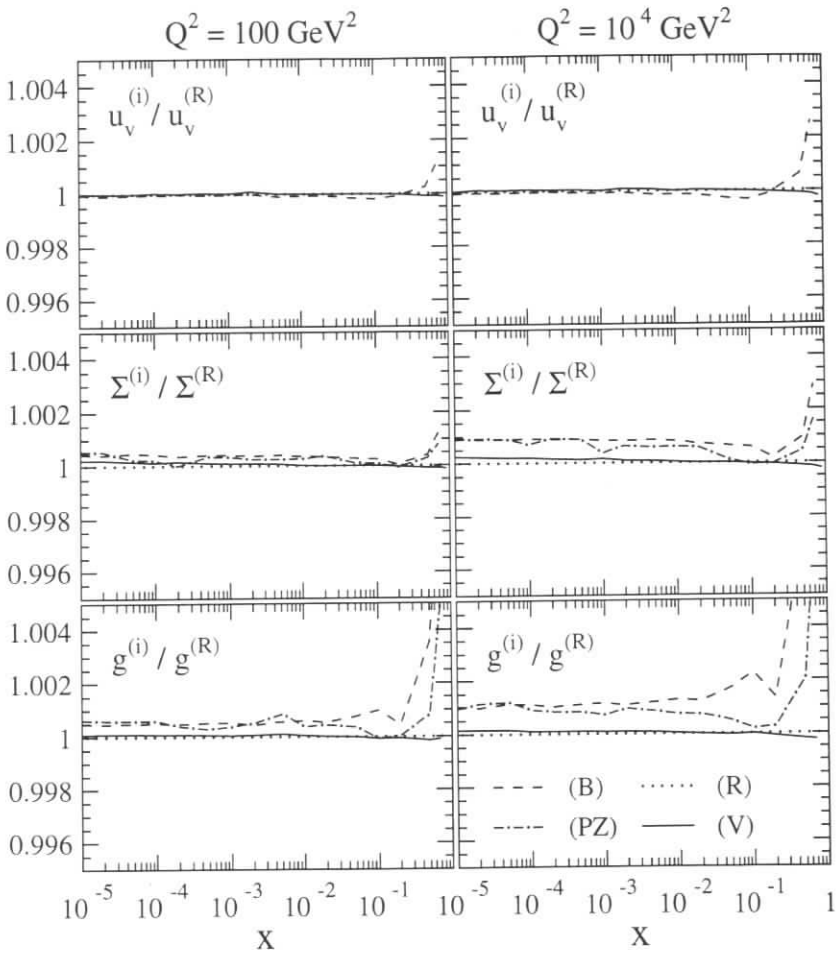

Figure 3: The remaining numerical x-dependent deviations on u_v, Σ and g at $Q^2 = 100$ and 10^4 GeV^2 between the programs of refs. [9, 10, 14, 15], after the differing theoretical assumptions have been corrected for, see the text. The results have been normalized to those of ref. [15].

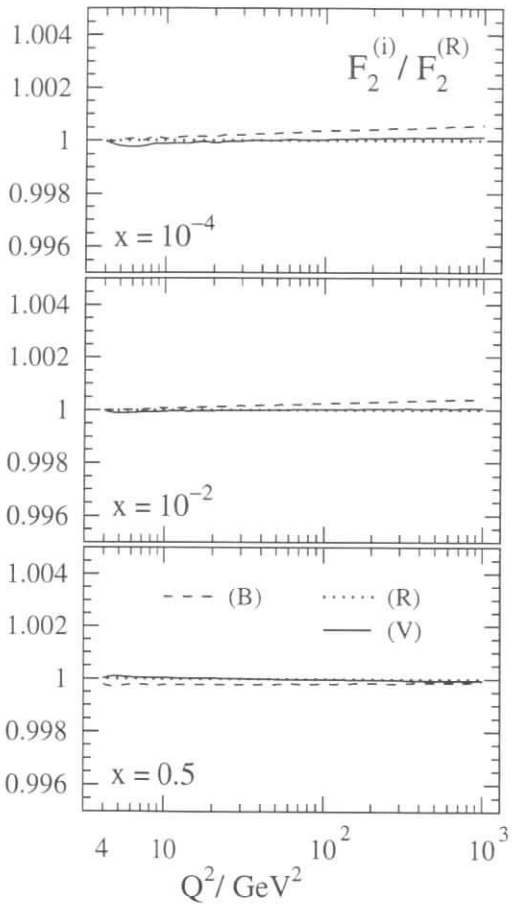

Figure 4: The residual relative offsets in the Q^2 evolution of F_2 between the programs of refs. [9, 14, 15], after removing the effects due to the different theoretical NLO prescriptions, for three typical values of x. As in all previous figures, the initial distributions are taken from eq. (7).

Acknowledgements :

We thank R.G. Roberts and W.K. Tung for providing the numerical results of the evolution of our test input with their programs. This work was supported on part by the EC Network 'Human Capital and Mobility' under contract No. CHRX-CT923-0004 and by the German Federal Ministry for Research and Technology (BMBF) under No. 05 7WZ91P (0).

References

[1] M. Botje, M. Klein, and C. Pascaud, these proceedings.

[2] see e.g. J. Blümlein, in: Proc. of the XXV International Symposium on Multiparticle Dynamics, Stara Lesna, Slovakia, 11–17 September, 1995, eds. D. Bruncko, L. Sandor, and J. Urban, (World Scientific, Singapore, 1996), hep-ph/9512272.

[3] W.K. Tung, Nucl. Phys. **B315** (1989) 378.

[4] A.C. Benvenuti et al., BCDMS collaboration, Phys. Lett. **B195** (1987) 97.

[5] W.L. van Neerven, these proceedings, and references therein.

[6] J. Blümlein, S. Riemersma, W.L. van Neerven, and A. Vogt, DESY 96–172, hep-ph/9609217, Proceedings of the Workshop 'QCD and QED in Higher Orders', Rheinsberg, Germany, April 1996, eds. J. Blümlein, F. Jegerlehner, and T. Riemann (Nucl. Phys. B (Proc. Suppl.) **51C**, 1996) p. 96.

[7] J. Blümlein, S. Riemersma, W.L. van Neerven, and A. Vogt, these proceedings.

[8] M. Virchaux and A. Ouraou, DPhPE 87–15;
M. Virchaux, Thèse, Université Paris-7 (1988);
A. Ourau, Thèse, Université Paris-11 (1988).

[9] M. Botje, QCDNUM15: A fast QCD evolution program, write-up in preparation.

[10] C. Pascaud and F. Zomer, H1 Note H1-11/94-404.

[11] M. Diemoz, F. Ferroni, E. Longo, and G. Martinelli , Z. Phys. **C39** (1988) 21.

[12] M. Glück, E. Reya, and A. Vogt, Z. Phys. **C48** (1990) 471.

[13] W. Furmanski and R. Petronzio, Z. Phys. **C11** (1982) 293.

[14] A. Vogt, unpublished.

[15] S. Riemersma, unpublished.

[16] R.G. Roberts, contributed to this workshop.

[17] W.K. Tung, contributed to this workshop.

[18] J. Blümlein and W.L. van Neerven, unpublished. For a short description, see Section 2.4 of ref. [6].

Future Precision Measurements of $F_2(x,Q^2)$, $\alpha_S(Q^2)$ and $xg(x,Q^2)$ at HERA

M. Botje[a], M. Klein[b], C. Pascaud[c]

[a] NIKHEF PO Box 41882, NL-1009 DB Amsterdam, Netherlands
[b] DESY-IfH Zeuthen, Platanenallee 6, D-15738 Zeuthen, Germany
[c] Universite de Paris Sud, LPTHE, F-91405 Orsay, France

Abstract: The results are presented of a study of the accuracy one may achieve at HERA in measuring the strong coupling constant α_s and the gluon distribution $xg(x,Q^2)$ using future data of the structure function $F_2(x,Q^2)$ which are estimated to be accurate at the few % level over the full accessible kinematic region down to $x \simeq 10^{-5}$ and up to $Q^2 \simeq 50000$ GeV^2. The analysis includes simulated proton and deuteron data, and the effect of combining HERA data with fixed target data is discussed.

1 Introduction

Deep inelastic scattering is the ideal place to investigate the quark-gluon interaction. Previous fixed target experiments have lead to very precise tests of Quantum Chromodynamics in the kinematic range of larger $x \geq 0.005$ and lower $Q^2 \leq 300$ GeV^2. The first few years of experimentation at HERA extended this range to very low $x \simeq 0.0001$ and large $Q^2 \simeq 3000$ GeV^2 leading to remarkable results in the investigation of deep inelastic scattering [1, 2] including rather accurate measurements already of the proton structure function $F_2(x,Q^2)$. In this study an attempt has been made to estimate the accuracy of future measurements of F_2 at HERA and their possible impact on precision mesurements of the strong coupling constant $\alpha_s(Q^2)$ and the gluon distribution $xg(x,Q^2)$. The measurement of these quantities is a key task at HERA. Both can be determined in a number of different processes as deep inelastic jet production, charm and J/ψ production and with future measurements of the longitudinal structure function. The measurement of F_2, however, is expected to be the most precise way to determine α_s and xg from the scaling violations of F_2. Those are most prominent at very low x due to quark pair production from the gluon field and weaker at large $x \geq 0.1$ due to gluon bremsstrahlung. Both processes, and their NLO corrections, will be accessible with future high statistics data at HERA which is hoped to deliver a final luminosity figure near to $\mathcal{L} \simeq 1$ fb^{-1} during the next 8 years of operation.

The QCD analysis of the past and present F_2 structure function data lead to remarkable results already, more than listed here:

- A rather precise determination of $\alpha_s(Q^2)$ with an experimental error of 0.003 at $Q^2 = M_Z^2$ was performed using the SLAC and the BCDMS structure function data [3].
- Both H1 [4, 5] and ZEUS [6, 7] have determined the gluon distribution with an about 15% accuracy at $Q^2 = 20$ GeV^2 and $x \simeq 10^{-4}$ by using different sets of fixed target data [8, 9, 10] combined with the HERA results.
- The HERA deep inelastic structure function data have a big impact on global analyses and the determination of parton distributions [11].

The analysis presented in this paper will show that HERA will allow to reach the 1% level of determining α_s and xg. This represents a challenge to the theoretical understanding of deep inelastic scattering in perturbative QCD in the low x and low $Q^2 \sim M_p^2$ region. A precision measurement of the strong coupling constant will represent an important constraint to unified theories. As such it represents one fundamental reason to perform an extended long term programme of experimentation at HERA.

This paper is organized as follows. Section 2 presents the assumptions and the results of the simulation of F_2 structure function data. Section 3 contains the outline of the QCD analysis procedure and error treatment required for the analysis. The results of a detailed study of the α_s measurement accuracy are given in section 4. Similarly the determination of the gluon distribution is presented in section 5. A brief summary is given in section 6.

2 Accuracy of Future HERA Structure Function Data

Recent measurements of the proton structure function $F_2(x,Q^2)$ by the H1 and ZEUS collaborations [4, 6], based on data taken in 1994 with an integrated luminosity $\mathcal{L}$ of about 3 pb^{-1}, have reached a systematic error level of about 4-5% in the bulk region of the data, $10 \leq Q^2 \leq 100$ GeV^2. Exploratory measurements of the very low Q^2 region with about 15-20% accuracy were presented by H1 with 1995 shifted vertex data [12] and by ZEUS using a rear calorimeter installed near the beam pipe in backward direction [13]. Based on the experience of these analyses a study has been made in order to estimate what might be the ultimate accuracy of F_2 measurements at HERA. This is a difficult task: on one hand one can rather easily extrapolate the present knowledge of systematic errors and also calculate rather straightforward the effect of residual miscalibrations on the cross section measurement. On the other hand there will always be local, detector dependent effects in addition and, furthermore, one can not simulate the results to be expected from innovations of the structure function analyses. For example, it is likely that a low electron energy calibration, much below the kinematic peak, can be performed reconstructing the π_0 mass or, to give another one, the region of y below 0.01, which was considered to be not accessible due to calorimetric noise, may be accessed nevertheless by imposing a p_T balance constraint using the electron information. Therefore this simulation study may give valid estimates but the truth will be the result of data taking and analysis work over many years still to come.

For this analysis the following kinematic constraints have been imposed:

- $Q^2 \geq 1$ GeV^2 which may be the limit of applicability of the DGLAP evolution equations at low x [14];
- $\theta_e \leq 177^o$ which might be accessible with nominal energy running even after the luminosity upgrade;
- $y \leq 0.8$ a limit arising from large radiative corrections and a small scattered electron energy limit $E'_e \geq$ few GeV due to photoproduction background and electron identification limitations;
- $\theta_h \geq 8^o$, a hadron reconstruction limit imposed by the beam pipe which may differ somewhat finally.

A number of data sets was generated as summarized in table 1 and illustrated in fig.1. The maximum Q^2 of the data depends on the available luminosity and might reach values of up to 50000 GeV^2. The generation and systematic error calculation was performed with a numerical program written by one of us which was checked to be in good agreement with the Monte Carlo programs used for real data analyses.

number	nucleon	E_e	E_N	$\mathcal{L}/pb^{-1}$	Q^2_{min}	Q^2_{max}
I	proton	27.6	820	10	0.5	100
II	proton	27.6	820	1000	100	50000
III	proton	27.6	400	200	100	20000
IV	proton	15.0	820	10	0.5	100
V	deuteron	27.6	410	10	0.5	100
VI	deuteron	27.6	410	50	100	20000

Table 1: Summary of simulated data sets for this study, energy values are in GeV and Q^2 in GeV^2.

The following systematic error sources were considered in the analysis the effect of which is illustrated in fig.2:

- An electron energy calibration error of 0.5% in the backward region ($\theta_e \geq 160^o$) and 1% in the central barrel and forward region of the detectors.
- An electron polar angle uncertainty of 0.5 mrad backwards and 1 mrad in the central part of the detector ($\theta_e \leq 165^o$).
- A 2% uncertainty of the hadronic energy scale which is important at lower $y \leq 0.1$ where the kinematics cannot be determined solely with the electron variables E'_e and θ_e because of divergencies of the resolution $\propto 1/y$. The energy scales E'_e and E_h may be cross calibrated by comparing cross section mesurements in different parts of the detector [15] once there is high statistics available in the barrel part, and using the electron and track information in the detector.

- The photoproduction background may cause a 1-2% error at large $y \geq 0.5$ and for $Q^2 \leq 100$ GeV^2. This requires an about 10% control of its shape and normalization which can be envisaged with the electron taggers, the hadronic calorimeter sections and using tracking information in front of the calorimeters which suppresses the π_0 part of the contamination.
- Radiative corrections can be controled to 1%, perhaps 2% at highest $y \geq 0.7$, using the hadronic and electron information which overconstrains the kinematics. The Monte Carlo [16] and numerical calculations [17] are known to be in very good agreement. This F_2 simulation assumes the radiative corrections to be performed, including the electroweak part which at high y and Q^2 modifies the cross section at the $\sim 20\%$ level.
- Beam background and various efficiencies are assumed to introduce an overall error of 2%.
- A luminosity error of 1% is assumed.

These systematic errors are about one half of those presently reached in the high statistics domain of the F_2 measurements. If the kinematic dependence of the correlated systematic errors is sufficiently well known, it can be taken into account in QCD fits, see below. Note in this respect that the required luminosity is not simply given by the statistical errors per bin but rather by the statistics needed for detailed systematic studies. However there will always be residual local and higher order effects which we represent here by a random systematic error of 1%.

3 Analysis Procedure

The generated data were analysed using the H1 [18] and ZEUS [19] QCD fitting programs. Elsewhere in these proceedings both programs are shown to be in good agreement [20]. In order to simplify the analysis the data were replaced by the QCD model (see below) so that the fits immediately converged to the minimum $\chi^2 = 0$ and CPU time was effectively spent only on the calculation of the covariance matrix of the fitted parameters. The errors on the gluon distribution and on α_s are then obtained from standard error propagation.

3.1 QCD Model

The QCD prediction for the F_2 structure function can be written as

$$F_2^{QCD}(x,Q^2) = F_2^{uds}(x,Q^2) + F_2^c(x,Q^2), \tag{1}$$

where F_2^{uds} obeys the NLO QCD evolution equations for $f = 3$ light flavours and the charm contribution F_2^c is calculated according to [21]. The light flavour contribution in turn is decomposed into a singlet and a non-singlet part:

$$F_2^{uds}(x,Q^2) = F_2^S(x,Q^2) + F_2^{NS}(x,Q^2). \tag{2}$$

The singlet structure function is related to the singlet quark momentum distribution, $x\Sigma = \sum_f x(q_f + \bar{q}_f)$, which obeys an evolution equation coupled to the gluon distribution xg. The

main contribution to F_2^{NS} comes from the difference of up and down quarks and antiquarks: $x\Delta_{ud} = x(u+\bar{u}) - x(d+\bar{d})$. We remark here that Δ_{ud} is constrained by the difference $F_2^p - F_2^d$ of proton and deuteron structure functions.

At the input scale $Q_0^2 = 4$ GeV^2 the parton distributions were parametrised as

$$\begin{aligned} xG(x,Q_0^2) &= A_G x^{B_G}(1-x)^{C_G} \\ x\Sigma(x,Q_0^2) &= A_S x^{B_S}(1-x)^{C_S}(1+D_S x + E_S\sqrt{x}) \\ x\Delta_{ud}(x,Q_0^2) &= A_{NS} x^{B_{NS}}(1-x)^{C_{NS}}. \end{aligned} \tag{3}$$

The input parameters for the gluon and the singlet distributions were obtained from a fit to the simulated data whereas the non-singlet parameters and their uncertainties were taken from [7]. The input value of α_s was set to $\alpha_s(M_Z^2) = 0.113$ corresponding to $\Lambda^{(4)}_{\overline{\rm MS}} = 263$ MeV [3].

3.2 Definition of the χ^2 and Fit Procedure

The two fitting programs of H1 and ZEUS have been used in parallel and all important numbers were cross checked. The ZEUS program uses a step by step (à la Runge Kutta) procedure to solve the DGLAP evolution equations. The H1 program projects the DGLAP equations on a functional basis where they are solved exactly [18, 22]. Both programs use MINUIT to make the fitting. In addition the H1 program has the possibility to use an independent set of routines (called LSQFIT) which performs a least chisquare fit. In LSQFIT the χ^2 function to be minimised is recognized to be the sum of the square of deviations and the derivatives of the deviations are computed by finite differences. Both MINUIT and LSQFIT can compute the second order derivatives of the χ^2 with respect to the parameters: these may be used for the error computation as will be shown in the following.

The χ^2 is defined as

$$\chi^2 = \sum_i \left(\frac{F_i(p,s) - f_i}{\Delta f_i}\right)^2 + \sum_l (s_l)^2 \tag{4}$$

where F_i is the model prediction, f_i the measured F_2 value, Δf_i its statistical error and the sum runs over all data points (i). In addition to the set of parton distribution parameters $\{p\}$, including α_s, we have introduced the parameter set $\{s\}$ which takes into account the systematic errors of the measurements. The relation between the model prediction and the QCD prediction for F_2 is written as:

$$F_i(p,s) = F_i^{QCD}(p)\ \ (1 - \sum_l s_l \Delta_{li}^{syst}) \tag{5}$$

where Δ_{li}^{syst} is the relative systematic error on data point (i) belonging to the source (l). We assume that the parameters s_l are gaussian distributed with zero mean and unit variance so that the Δ_l correspond to a one standard deviation systematic error[1].

3.3 Systematic Error Evaluation

Given the χ^2 definition of the previous section there are essentially three methods to evaluate the systematic errors on the fitted parameters:

[1]Asymmetric errors can be taken into account by adding terms quadratic in s_l in eq. 5.

- Repeat the fit with several values of the systematics variables s_l, either chosen at random or giving to each variable in turn the value 1. The systematic errors are then obtained by adding all the deviations from the central value in quadrature.

- Leave the systematic parameters fixed to zero but propagate the errors on s_l (assumed to be 1) to the covariance matrix of the fitted parameters [23]. If the deviations are linear functions of the systematic variables it is easy to compute directly the errors from the second derivatives of the χ^2. Let us introduce the following matrices:

$$M = \sum_i \frac{\partial F_i}{\partial p}\frac{\partial F_i}{\partial p}\frac{1}{\Delta m_i^2} \approx 1/2\frac{\partial^2\chi^2}{\partial p \partial p} \tag{6}$$

$$C = \sum_i \frac{\partial F_i}{\partial p}\frac{\partial F_i}{\partial s}\frac{1}{\Delta m_i^2} \approx 1/2\frac{\partial^2\chi^2}{\partial p \partial s} \tag{7}$$

  $V^{stat} = M^{-1}$ is the $\{p\}$ statistical error matrix and C is the matrix which expresses statistical and systematic correlations. One can show that [23]

$$V^{syst} = M^{-1}CC^TM^{-1} \tag{8}$$

  is the $\{p\}$ systematic error matrix. The LSQFIT program determines these matrices and also the function error bands. For MINUIT a fit has to be performed where the systematic parameters are left free and the inverse of the resulting covariance matrix contains the matrices M and C. Reinverting M and using eq.(8) yields the statistical and systematic errors in case all systematic parameters are kept fixed.

- The $\chi^2 = \chi^2_{min} + 1$ method
  If the correlations between parameters are big and/or the dependence of the deviations with respect to the parameters is highly non–linear, it is more appropriate to compute the error on a specific parameter by considering an increase of the χ^2 by one, all the other parameters being optimised. Both MINUIT and LSQFIT can provide this calculation. This method has been used also to draw error bands with LSQFIT which is faster than the MINOS option of MINUIT. In this case the value of the function itself at some fixed x and Q^2 point is taken as a parameter. Then the equation say $G(x,Q^2) = G$ is used to eliminate the more sensitive parameter.

The three different methods and the two different programs have been compared in detail leading to consistent results. Fits were performed on data randomly offset both statistically *and* systematically. Taking as the error the r.m.s. of the fitted α_s values this appeared to be in agreement with the standard error calculation. This method gives the most reliable error estimate, but it is clearly too elaborate to be of practical use in a study like the one undertaken here.

3.4 Fitting the Systematics

If the kinematical dependence of a systematic error, like the $1/y$ behaviour of the electron energy scale uncertainty, is well known, a contribution, $\sum_l s_l^2$, can be added to the χ^2 and a fit can be performed determining an extended set of parameters $\{p, s\}$. The interest of such a procedure is obviously that here full knowledge of the experiment enters to improve the measurement

accuracy. Such a procedure was adopted in [3] to reduce the influence of the main experimental errors, the magnetic field calibration of the BCDMS spectrometer for example, on the value and error of α_s. The method to find the resulting errors is practically the same as for the statistical error treatment. LSQFIT and MINUIT deliver the complete error matrix which in the case of MINUIT is exactly the one used in method 2.

4 Results on α_s

4.1 Introduction

The data and the fitting procedures as described above were used to determine the expected error of $\alpha_s(M_Z^2)$, and of xg in the subsequent section. Three types of fits were performed:

- A - Fits to HERA proton data alone.
- B - Fits to HERA proton and deuteron data.
- C - Fits to HERA proton data with inclusion of fixed target data, in most of the cases those from SLAC [8] and BCDMS [9].

In the fits the systematic error parameters were left free. The input values $s_l = 0$ were always reproduced while the input errors $\Delta_{s_l} = 1$ were typically reduced by a factor of two. The correlation coefficients between the systematic error parameters were well below unity. In the following we denote the error on α_s from these fits by $\Delta\alpha_{fit}$. The statistical error ($\Delta\alpha_{stat}$) and the systematic error ($\Delta\alpha_{syst}$) for fixed systematic errors were calculated from the covariance matrix as described above.

4.2 α_s with HERA Data only

As a starting point of the investigation fits were made to HERA high energy proton data alone (sets I and II in table 1). The low Q^2 sample (set I) covers an x range of $1.4 \times 10^{-5} < x < 4.3 \times 10^{-2}$ whereas the high Q^2 sample (set II) covers $2.4 \times 10^{-3} < x < 0.65$. For the nominal fits integrated luminosities of 10 and 500 pb^{-1} were assumed for the low and the high Q^2 data set respectively.

The strong coupling constant and the parameters describing the input singlet (5 parameters) and gluon distributions (3 parameters) at $Q_0^2 = 4$ GeV^2 were left free in the fit. The gluon normalization was calculated by imposing the momentum sumrule. The non-singlet contribution to F_2 was kept fixed since it is not well constrained by proton data alone.

Besides α_s and the parton distribution parameters five systematic error parameters were introduced as described in section 3. In addition the assumed random systematic error was added in quadrature to the statistical error.

Recent analyses of ZEUS [7] and H1 [4] F_2 data have shown that perturbative QCD might be applicable down to $Q^2 \simeq 1$ GeV^2 at very low x, see also [14]. In figure 3a and table 2 the α_s error is given as a function of Q_c^2 which is the lowest Q^2 considered in the fit. The statistical error (which includes the 1% random systematic error) increases from $\Delta\alpha_{stat} = 0.0024$ to

0.0053 with increasing Q_c^2. When all systematic errors are fitted, $\Delta\alpha_{fit}$ is almost identical to the statistical error for $Q_c^2 = 1$ GeV^2 but increases more rapidly to 0.0075 at $Q_c^2 = 8$ GeV^2. When the systematics are not fitted, their contribution to $\Delta\alpha_s$ rises very strongly to about 0.012 above $Q_c^2 = 2$ GeV^2. The same tendency is observed when all the systematic errors are scaled down by a factor of two (figure 3b) though, as expected, the uncertainty of α_s is reduced almost by a factor of two.

To investigate the impact of the high Q^2 data on the result, the luminosity of dataset II was varied between $\mathcal{L} = 10$ and 1000 pb^{-1}. For a Q_c^2 cut of 1 GeV^2 the variation of the α_s errors with L is fairly modest as shown in figure 4a and table 2. However, the dependence on the high Q^2 luminosity becomes stronger if the Q_c^2 cut is raised. This is illustrated in figure 4b for $Q_c^2 = 3$ GeV^2. Here a factor of 10 increase in luminosity decreases the α_s errors by about 40%. On the other hand, increasing the luminosity of the low Q^2 sample (dataset I) from 10 to 50 pb^{-1} gave an insignificant improvement ($\approx 10\%$) on the uncertainty in α_s.

An improvement of the result is obtained if the lower energy data are included, sets III and IV in table 1. For example, for $Q_c^2 = 3$ GeV^2 the nominal data set yields an error of 0.0061, see table 2 while the inclusion of the lower energy data reduces that error to 0.0046, if in both cases the systematics is fitted.

As described above, the nonsinglet distribution is input to the fit of the proton data. Taking its uncertainty from the QCD analysis of [7] a contribution of about 0.004 is estimated to the uncertainty on α_s. However, when both proton and deuteron data are available the nonsinglet contribution is constrained by the difference $F_2^p - F_2^d$ and the 0.004 error gets eliminated. Therefore, a low and a high Q^2 deuteron data sample (set V and VI in table 1) with modest lumionosities were included in the fit. Apart from the highest Q^2 region these data have roughly the same kinematic coverage as the proton data.

In the combined proton and deuteron QCD fit the three parameters which describe the nonsinglet input distribution were left free. Furthermore one normalization parameter and five independent systematic parameters for the deuteron data were added. The resulting α_s errors are given in table 2 for a Q_c^2 cut of 3 GeV^2. It is seen that the error on α_s is reduced by about 25% compared to the corresponding fit on proton data only although the number of fit parameters had to be increased and the non-singlet distribution is as well fitted.

4.3 Inclusion of High x Fixed Target Experiment Data

The published QCD analysis [3] of SLAC and BCDMS proton and deuteron structure function data yielded an experimental error of 0.003 on $\alpha_s(M_Z^2)$. The natural question to be answered is whether the combination of the low x and high Q^2 HERA data with the fixed target experiment data can improve this result significantly.

As a first necessary step it was studied if our fits can reproduce the error quoted above. The following conditions were applied to mimic the analysis of [3] as closely as possible:

- A cut of $W^2 > 10$ GeV^2 was imposed to effectively remove the region at high x and low Q^2 dominated by higher twist effects.
- The parameters of the input singlet, gluon and nonsinglet distributions were left free except B_S and B_G which describe the low x behaviour of $x\Sigma$ and xG (the SLAC/BCDMS data extend only down to $x = 0.07$).

- One normalisation parameter was kept fixed (BCDMS deuteron) whereas those of the remaining three datasets were left free. In addition two systematic parameters for the BCDMS data were left free.
- No momentum sumrule was imposed.
- Being interested in the derived error only, the SLAC and BCDMS data were replaced by the model input.
- The quoted errors of ref [3] correspond to an increase of the χ^2 by 9 units which was taken into account in the estimate of the statistical errors.

The fit defined above on the SLAC/BCDMS data alone yielded as a result $\Delta\alpha_s = 0.0030$, exactly as published.

Using all high energy HERA proton data in addition the error on α_s was reduced to $\Delta\alpha_{fit} = 0.0016$ with $Q_c^2 = 3$ GeV^2. Adding the latest data of the NMC experiment with a preliminary treatment of the systematic errors of this measurement reduces this number to 0.0013. In table 2 results are given on $\Delta\alpha_s$ for various choices of the Q_c^2 cut, the size of the systematic errors and the luminosity of the high Q^2 data sample. It turns out that $\Delta\alpha_{fit}$ ranges from about 0.001 to 0.002 and is thus fairly insensitive to these choices. Compared to fits on HERA proton data alone, the error on α_s is much less sensitive as to whether the systematic parameters are left free or kept fixed and the dependence on the minimum Q^2 is less severe. With fixed systematic errors the combined statistical and systematic error ranges from $\Delta\alpha_s = 0.002$ to about 0.003.

4.4 Double Logarithmic Scaling and the Error of α_s

With high precision data the low x behaviour of F_2 will be much better understood. If the data further support the double logarithmic approximation [24] of the low x, large Q^2 behaviour of F_2, then a precision of α_s to 0.001 or even better can be reached with HERA data alone. Already with the present H1 data only, such an analysis [25] lead to a value of $\alpha_s(M_Z^2) = 0.113 \pm 0.002(stat) \pm 0.006(syst)$. The advantage of this approach is obvious as it likely requires only the low x data of HERA and depends on two scale parameters, Q_o^2, x_o, a normalization constant and α_s only. This is in contrast to the QCD analysis of HERA and fixed target data, considered here, which has to include the full parametrization of two nonsinglet, the singlet and the gluon distribution leading to typically 15 parameters to be simultaneously controled. Further theoretical understanding of the double scaling approach is necessary, however.

5 Determination of the Gluon Distribution

5.1 HERA Proton Data Only

The previous determinations of the gluon distribution from the scaling violation of F_2 at low x by H1 [4, 5] and ZEUS [6, 7] were performed combining the HERA results with fixed target data and treating α_s as an extra parameter. Since the scaling violations essentially are proportional to the product of $\alpha_s \cdot xg$, a large data range in x and Q^2 is required to disentangle these two basic quantities.

Fit	L(LQ)	L(HQ)	sfac	qmin	sigf	stat	syst	total
A	10	500	1.0	1.0	.0024	.0021	.0052	.0056
A	10	500	1.0	2.0	.0050	.0036	.0107	.0113
A	10	500	1.0	3.0	.0061	.0041	.0114	.0120
A	10	500	1.0	5.0	.0069	.0047	.0114	.0123
A	10	500	1.0	8.0	.0075	.0052	.0105	.0117
A	10	500	0.5	1.0	.0015	.0013	.0024	.0028
A	10	500	0.5	2.0	.0033	.0026	.0055	.0061
A	10	500	0.5	3.0	.0040	.0031	.0060	.0067
A	10	500	0.5	5.0	.0046	.0035	.0060	.0070
A	10	500	0.5	8.0	.0050	.0040	.0054	.0067
A	10	10	1.0	1.0	.0028	.0023	.0045	.0050
A	10	100	1.0	1.0	.0026	.0022	.0048	.0053
A	10	1000	1.0	1.0	.0023	.0020	.0053	.0057
A	10	10	1.0	3.0	.0096	.0080	.0126	.0149
A	10	100	1.0	3.0	.0073	.0055	.0123	.0134
A	10	1000	1.0	3.0	.0057	.0037	.0110	.0116
B	10	500	1.0	3.0	.0043	.0030	.0087	.0092
C	10	500	1.0	1.0	.0014	.0011	.0031	.0033
C	10	500	1.0	8.0	.0016	.0012	.0032	.0034
C	10	500	0.5	1.0	.0011	.0009	.0018	.0020
C	10	500	0.5	8.0	.0014	.0011	.0018	.0022
C	10	10	1.0	3.0	.0020	.0018	.0022	.0028
C	10	100	1.0	3.0	.0017	.0015	.0023	.0027
C	10	1000	1.0	3.0	.0015	.0011	.0030	.0032

Table 2: Errors on α_s for fits with HERA proton data only (A), proton and deuteron data (B) and combinations of simulated HERA proton data with fixed target experiment data (C) from SLAC and BCDMS, see text.

Fig.5 shows the result of a QCD fit to the simulated F_2 data, sets I and II in table 1, without fitting the systematics but determining xg and the singlet distribution $x\Sigma$. In this fit α_s was fixed considering an α_s uncertainty of 0.005 for the calculated gluon error. The inner dark error band is the statistical error while the total error is shown as the outer grey band for all Q^2 values. The error bands were drawn using the LSQFIT routines and the $\chi^2 = \chi^2_{min} + 1$ method. At $Q^2 = 20$ GeV^2 and $x = 0.0001$ the total error amounts to 11% somewhat better than the present result which included the fixed target experiments. If α_s is allowed to vary and the systematics is fitted as described in section 3 the gluon determination gets very accurate with an estimated error of 3% at the same x and Q^2 values. This is illustrated in figure 6.

5.2 HERA Proton and Deuteron Data

The consideration of deuteron data of $\mathcal{L} = 50$ pb^{-1} allowed finally to perform a complete fit of all distributions. In particular one has to notice that the non-singlet distributions are not well constrained with proton data only. In section 3 the up-down quark distribution difference was introduced as the non-singlet quantity to be determined assuming the strange distribution was fixed, see [7]. Generally there are two non-singlet distributions which may be written as $u^+ = u + \bar{u} - \Sigma/3$ and similarly d^+. The deuteron data allow to determine these distributions. Fig.7 shows the calculated accuracy of the u^+ distribution at $Q^2_o = 2$ GeV^2 from a complete fit to all distributions, α_s and with free systematic error parameters. This represents an interesting result as apparently the non-singlet distributions will be measurable with high accuracy down to very low x, and the predicted weak Q^2 dependence can be verified. The gluon belonging to this fit is determined with an error of only 1-2% at the x, Q^2 point chosen for comparison.

Further studies of the importance of HERA deuteron data are necessary. For example, this data will have an additional few % uncertainty due to shadowing corrections at low x which was neglected here. Constraints on the non-singlet distributions are available already from the fixed target deuteron data, but at higher x. A more thorough discussion of these aspects has been beyond the scope of this study. Independently of theoretical preassumptions, however, one may regard this data as important to measure the low x behaviour of the up-down quark distribution difference which requires modest luminosity only. With larger luminosity $\mathcal{L} \simeq 50$ pb^{-1} it will help to decompose the flavour contents of the nucleon as was discussed already ten years ago [26].

6 Summary

According to this analysis HERA will have an important impact on the measurement of α_s and the gluon distribution. A precision near 0.001 for $\alpha_s(M_Z^2)$ and of almost 1% for xg is in reach if

- F_2 measurements in the full HERA range will become available with systematic and statistical errors of a few % only,
- the systematic errors are thoroughly studied at the per cent level as functions of x and Q^2 such that their gross effects can be absorbed in the QCD analysis,

- and the HERA data can be combined reliably with the fixed target experiment results on F_2.

Such an accuracy represents a great challenge for the experimental programme at HERA. The HERA data should be complete, i.e. comprise a high luminosity data set with $\mathcal{L} \geq 300$ pb^{-1} and modest luminosity data sets: i) at lowered proton energy $\mathcal{L} \geq 50$ pb^{-1} to reach highest x, as close as possible to the fixed target data region, ii) at lowered electron beam energy $\mathcal{L} \geq 3$ pb^{-1} to cover the x dependence at smallest Q^2 and iii) possibly also deuteron data with $\mathcal{L} \simeq 50$ pb^{-1}. Note that no attempt was made to optimize these luminosity values, in particular, since the necessary level of systematic error control is competing with the requirements coming from simple statistical error considerations.

Completion of this programme also requires a major theoretical effort to calculate the 3-loop coefficient functions since the present theoretical uncertainty of α_s of ~ 0.005 [27] exceeds most of the estimated experimental α_s errors discussed in this study. It is obvious that a precision at the level of 0.002 for $\alpha_s(M_Z^2)$ will lead to a very precise study of its Q^2 dependence and resolve the question of the compatibility of the deep inelastic α_s values with those from e^+e^- scattering.

Acknowledgement We would like to thank J. Blümlein, Th. Naumann, S. Riemersma, A. Vogt and F. Zomer for interesting discussions on various aspects of this study.

References

[1] M. Klein, *Deep Inelastic Physics with H1*, Invited Talk at the International Conference on Deep Inelastic Scattering, Rome, 1996, Proceedings to be published.

[2] R. Yoshida, *Deep Inelastic Physics with ZEUS*, Invited Talk at the International Conference on Deep Inelastic Scattering, Rome, 1996, Proceedings, to be published.

[3] M. Virchaux and A. Milsztajn, Phys.Lett. **B 274** (1992) 221.

[4] H1 Collaboration, S. Aid et al., Nucl.Phys. **B 490** (1996) 3.

[5] H1 Collaboration, S. Aid et al., Phys.Lett. **B 354** (1995) 494.

[6] ZEUS Collaboration, M. Derrick et al., DESY 96-789 (1996).

[7] ZEUS Collaboration, M. Derrick et al., Phys.Lett. **B 345** (1995) 576.

[8] L.W. Whitlow et al., Phys.Lett. **B 282** (1992) 475.

[9] BCDMS Collaboration, A.C. Benvenuti et al., Phys.Lett. **B 223** (1989) 485; Phys.Lett. **B 237** (1990) 592.

[10] NMC Collaboration, P. Amaudruz et al., Phys. Lett. **B 295** (1992) 159.

[11] W.K. Tung, R.G. Roberts and A. Vogt, talks presented at the International Conference on Deep Inelastic Scattering, Rome, 1996, Proceedings, to be published.

[12] H1 Collaboration, *Measurement of F_2 at low Q^2*, paper presented at the IHEP Conference, Warsaw, 1996.

[13] ZEUS Collaboration, *Measurement of F_2 at low Q^2*, papers presented at the Rome DIS Conference and at the IHEP Conference, Warsaw, 1996.

[14] A.D. Martin, R.G. Roberts and W.J. Stirling, DTP 96/44, hep-ph 9606345 (1996).

[15] J. Blümlein and M. Klein, Nucl.Instr.Meth. **A 329** (1993) 112;

[16] A. Kwiatkowski, H. Spiesberger and H.-J. Möhring, Computer Phys. Comm. **69**(1992)155.

[17] A.Arbuzov et al., Comp.Phys.Comm. **94**(1996)128;

[18] C. Pascaud and F. Zomer LAL/94-42.

[19] M. Botje, QCDNUM15, writeup in preparation.

[20] J. Blümlein et al., these proceedings.

[21] S. Riemersma et al., Phys.Lett. **B 347** (1995) 143 and ref. cited therein.

[22] C. Pascaud and F. Zomer H1-09/94-376.

[23] C. Pascaud and F. Zomer LAL/95-05.

[24] A. DeRujula et al., Phys.Rev. **D10**(1974)1649
R. Ball and S. Forte, Phys. Lett. **B 335**(1994)77.

[25] A. DeRoeck, M. Klein and T. Naumann, DESY 96-063 (1996), Phys.Lett.B, to appear.

[26] J. Blümlein, M. Klein, Th. Naumann and T. Riemann, Proceedings of the 1987 Workshop on Physics at HERA, Vol. 1, ed. by R. Peccei, p.67.

[27] J. Blümlein, S. Riemersma, W.L. van Neerven and A. Vogt, these proceedings.

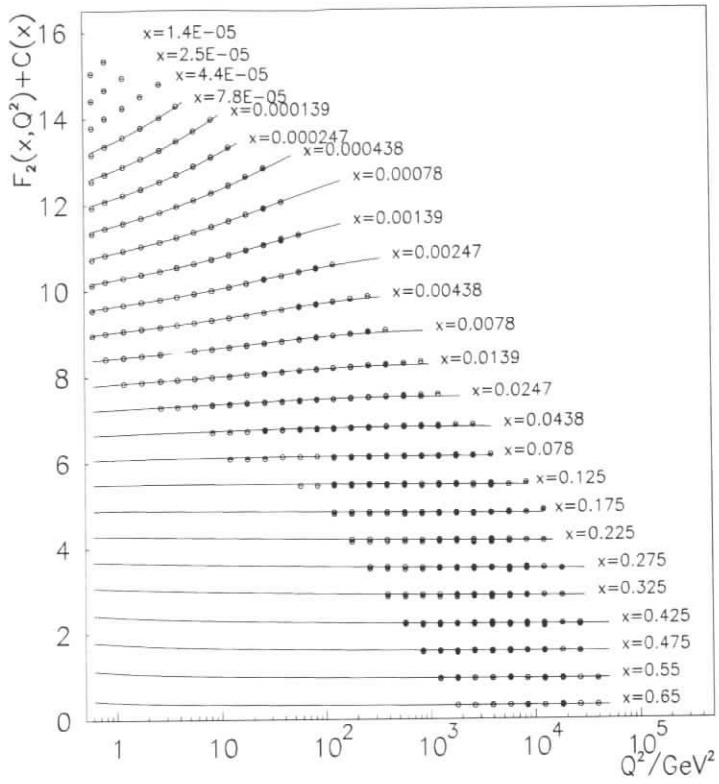

Figure 1: Simulated structure function data sets. The huge luminosity of 1 fb^{-1} will lead to precise data even at very high Q^2. For $Q^2 \geq 10000$ GeV^2 about 2000 events may be available. The largest bins shown are made with 20-50 events. With $\mathcal{L} = 10$ pb^{-1} for $Q^2 \geq 0.5$ GeV^2 about 10^7 events are occuring which will be prescaled at lowest Q^2. The curve represents a NLO QCD fit. The high x, low Q^2 region can not be accessed with HERA but is almost completely covered by the fixed target experiment data, not shown here.

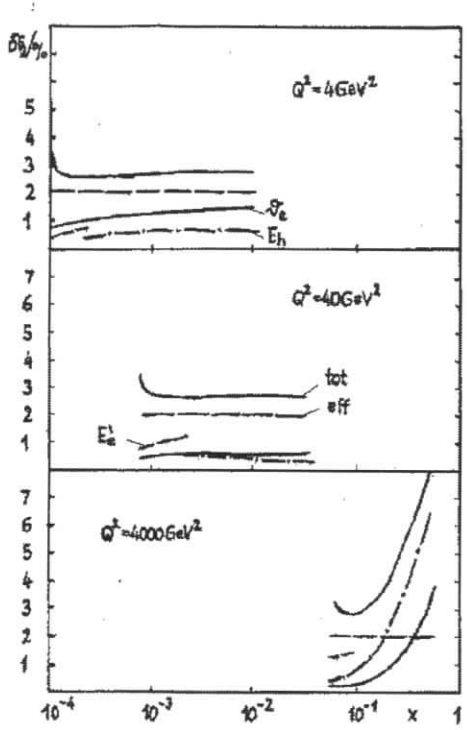

Figure 2: Estimated systematic errors of the F_2 measurement for different Q^2 as a function of x. Dashed line: effect of error on the scattered electron energy E'_e, dashed-dotted line: effect of error on the hadronic energy scale E_h, solid line: effect of error on the polar angle θ_e; long dashed line: 2% efficiency error. Not drawn are the effect of photoproduction background at high y and the radiative correction error. Both have been added to the other error sources which gives a total error drawn as the upper solid line. The authors apologize for the workshop style of this figure.

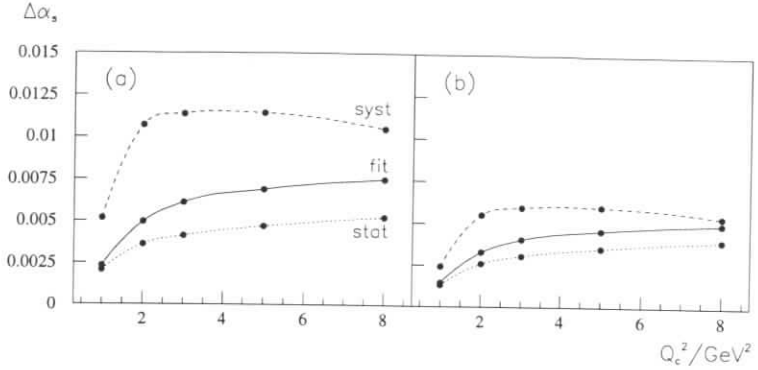

Figure 3: The error on $\alpha_s(M_Z^2)$ from fits to the HERA high energy proton data as a function of Q_c^2: (a) with full systematics included; (b) with systematics further reduced by a factor of two. The (dotted, solid, dashed) curves correspond to the errors ($\Delta\alpha_{stat}$, $\Delta\alpha_{fit}$, $\Delta\alpha_{syst}$) described in the text.

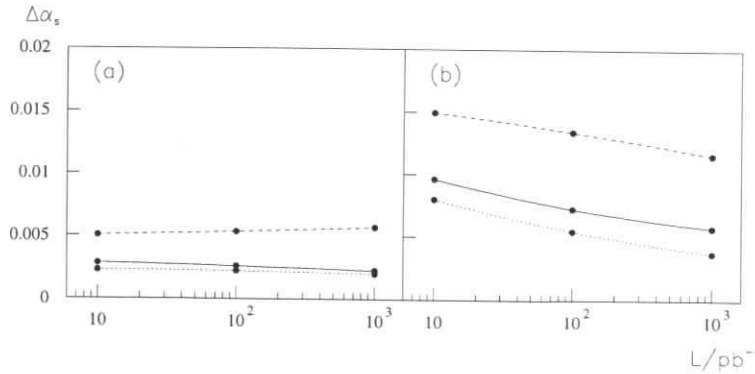

Figure 4: The error on $\alpha_s(M_Z^2)$ as a function of the luminosity of the high Q^2 sample: (a) for $Q_c^2 = 1$ GeV^2; (b) for $Q_c^2 = 3$ GeV^2. The (dotted, solid, dashed) curves correspond to the errors ($\Delta\alpha_{stat}$, $\Delta\alpha_{fit}$, $\Delta\alpha_{syst}$) described in the text.

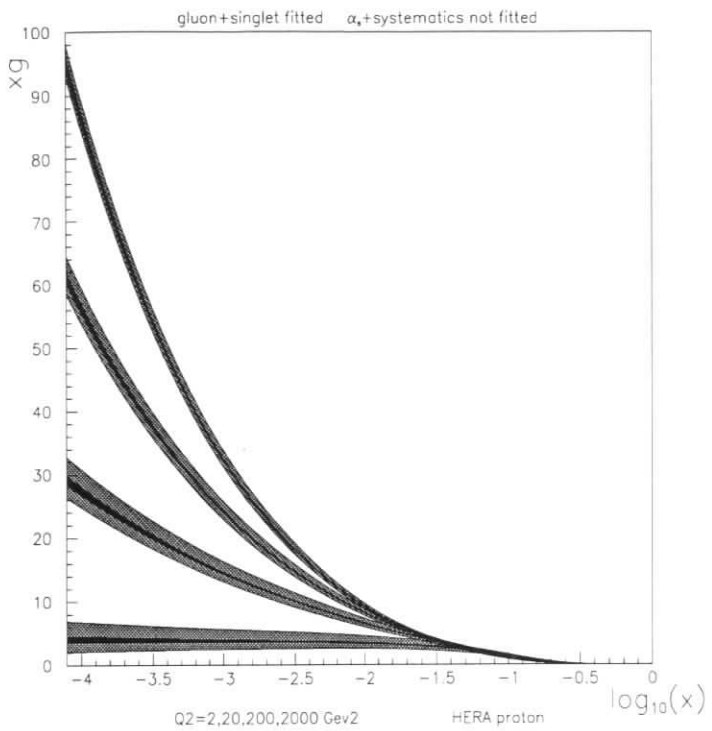

Figure 5: Determination of the gluon distribution using future F_2 data from electron-proton scattering with fixed systematic error parameters. The inner band is the statistical error. Note that for simplicity the gluon is shown outside the allowed region of $x \leq Q^2/10^5$.

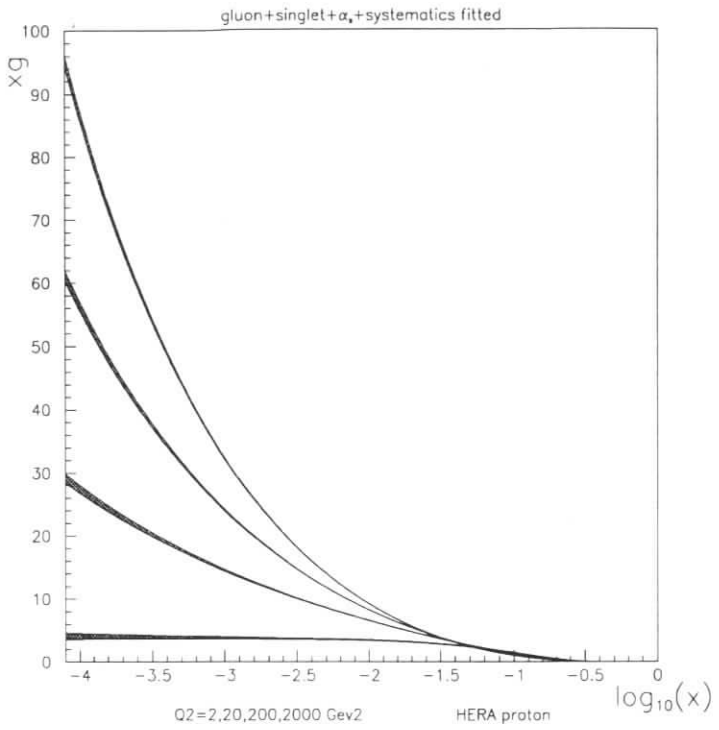

Figure 6: Determination of gluon distribution using future F_2 data from electron-proton scattering with fitted systematic error parameters. Note that for simplicity the gluon is shown also outside the allowed region of $x \leq Q^2/10^5$.

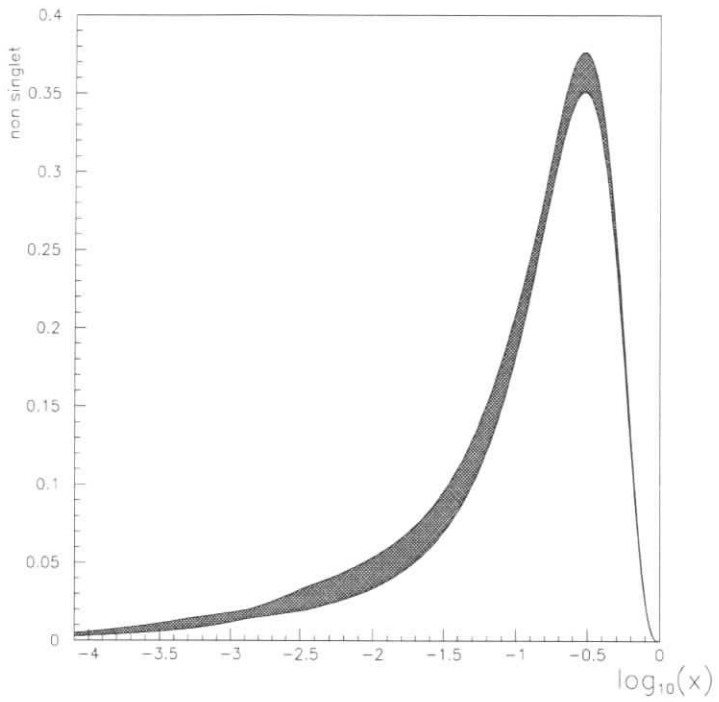

Figure 7: Determination of the non-singlet distribution $u^+ = u + \bar{u} - \Sigma/3$ from a QCD fit to the simulated proton and deuteron data (sets I,II and V,VI in table 1).

Theoretical Uncertainties in the Determination of α_s from F_2^p at HERA

J. Blümlein[a], S. Riemersma[a], W.L. van Neerven[b], and A. Vogt[c,d]

[a] DESY-Zeuthen, Platanenallee 6, D–15738 Zeuthen, Germany
[b] Instituut Lorentz, Rijksuniversiteit Leiden, PO Box 9506, 2300 RA Leiden, The Netherlands
[c] Deutsches Elektronen-Synchrotron DESY, Notkestraße 85, D–22603 Hamburg. Germany
[d] Institut für Theoretische Physik, Universität Würzburg, D–97074 Würzburg, Germany

Abstract: Uncertainties in the next-to-leading order evolution of deep–inelastic structure functions – arising from different prescriptions for truncating the perturbative series, and from the freedom the choose the renormalization and factorization scales – are briefly discussed, and their quantitative implications on α_s determinations from F_2^p at HERA are estimated.

1 Introduction

Deep–inelastic scattering (DIS), especially the proton structure function $F_2^p(x, Q^2)$, has been one of the classical tools for determining the strong coupling constant α_s. With the advent of HERA, the accessible kinematic range has been expanded to scales up to $Q^2 \approx 10^4$ GeV^2, and down to Bjorken-x values of $x \approx 10^{-4}$ in the deeply inelastic regime. Given a sufficient luminosity of HERA, this enhanced lever arm for measuring the scaling violations of F_2 can be used for obtaining improved α_s extractions from DIS.

For the anticipated experimental errors from such analyses, see refs. [1, 2]. In this contribution, we briefly summarize a recent study on present theoretical uncertainties pertaining the determination of α_S from F_2 scaling violations at HERA. For a detailed account the reader is referred to ref. [3].

2 QCD Evolution in Next-to-Leading Order

The complete understanding of the evolution of F_2 in perturbative QCD is currently limited to next-to-leading order (NLO). Generically, the evolution of the parton densities $f(x, M^2)$ at the fractional momentum x can be written as

$$\frac{\partial f(x, M^2)}{\partial \ln M^2} = \left[a_s(M^2)\, P^{(0)}(x) + a_s^2(M^2)\, P^{(1)}(x) + O(a_s^3)\right] \otimes f(x, M^2)\,, \qquad (1)$$

identifying M as the mass factorization scale and $a_s = \alpha_s/4\pi$. Here $\otimes$ stands for the Mellin convolution. The evolution equation (1) is understood to represent the non–singlet cases as

well as the coupled singlet quark and gluon evolutions. $P^{(0)}$ and $P^{(1)}$ denote the corresponding leading order (LO) and NLO splitting functions, respectively.

The second important ingredient is the scale dependence of α_s, governed by

$$\frac{\partial a_s(R^2)}{\partial \ln R^2} = -\beta_0 a_s^2(R^2) - \beta_1 a_s^3(R^2) + O(a_s^4)\,, \tag{2}$$

where R stands for the renormalization scale. Only the first two terms in the series, β_0 and β_1, are kept at NLO. As already indicated in eq. (1), we set $R = M$ in this section.

Beyond LO, the parton densities are not observables. To obtain the structure functions from the (anti-) quark and gluon densities, the latter have to be convoluted with the appropriate coefficient functions, e.g.

$$F_2(x,Q^2) = \sum_{i=q,g} c_{2,i}(x,Q^2) \otimes f_i(x,Q^2)\,. \tag{3}$$

Here we have additionally identified the factorization scale by putting $M^2 = Q^2$. The coefficient functions c_i are also treated as an expansion in a_s, according to

$$c_{2,i}(x,Q^2) = c_{2,i}^{(0)}\,\delta_{i,q}\,\delta(1-x) + a_s(Q^2)\,c_{2,i}^{(1)}(x) + O(a_s^2)\,. \tag{4}$$

This completes the ingredients required for a complete NLO calculation. For an overview of the concrete calculations of $P^{(l)}(x)$ and $c^{(l)}(x)$, see ref. [4].

We now turn back to the evolution equation (1). Two approaches to its solution, which differ in their treatment of terms beyond NLO, have been widely used. The first approach is to solve eq. (1) numerically in x-space, see for example refs. [5, 6, 7]. An important alternative, employed in refs. [8, 9], is to transform to Mellin-N space via

$$A_N \equiv \int_0^1 dx\, x^{N-1} A(x)\,. \tag{5}$$

The main virtue of this transformation is that the convolution is reduced to a simple product. Hence eq. (1) turns into a system of ordinary differential equations at fixed N, which allows for further analytical developments. After rewriting the evolution in terms of $a_s \equiv a_s(M^2)$ using eq. (2), and expanding the resulting r.h.s. in a power series in α_s, one arrives in NLO at

$$\frac{\partial f_N(a_s)}{\partial a_s} = -\frac{1}{\beta_0 a_s}\left[P_N^{(0)} + a_s\left(P_N^{(1)} - \frac{\beta_1}{\beta_0}P_N^{(0)}\right) + O(a_s^2)\right] f_N(a_s)\,. \tag{6}$$

Its solution can be written in a closed form for the non-singlet cases, with $a_0 \equiv a_s(M_0^2)$, as

$$f_N(a_s) = \left[1 - \frac{a_s - a_0}{\beta_0}\left(P_N^{(1)} - \frac{\beta_1}{\beta_0}P_N^{(0)}\right) + O(a_s^2)\right]\left(\frac{a_s}{a_0}\right)^{P_N^{(0)}/\beta_0} f_N(a_0)\,. \tag{7}$$

For the notationally more cumbersome singlet evolution, see refs. [8, 9]. From these analytic solutions, one can acquire the x-space results by one contour integral in the complex N-plane.

The truncation of the perturbative series at NLO in either eq. (1) [5, 6, 7] or eq. (6) [8, 9] leads to noticeably different evolutions, see refs. [3, 10]. Fitting the same data, in the HERA kinematical range for $Q^2 \geq 4$ GeV^2, with the two approaches leads to central values for $\alpha_s(M_Z^2)$ which differ by $\Delta\alpha_s(M_Z^2) \simeq 0.003$ [3]. This shift is very similar to the differences observed in earlier non-singlet fits with various programs to the large-x BCDMS data [11].

3 Renormalization and Factorization Scale Dependence

In the previous section, the condition $M^2 = R^2 = Q^2$ was imposed on the renormalization and factorization scales. In general, however, those scales can be chosen differently. The stability of the results against variations of R and M provides a measure of the quality of the perturbative approximation under consideration. For general choices of the scales, the NLO evolution equations for the parton densities read

$$\frac{\partial f(x;M^2,R^2)}{\partial \ln M^2} = a_s(R^2)\left[P^{(0)}(x) + a_s(R^2)P^{(1)}(x) + a_s(R^2)\beta_0 P^{(0)}(x)\ln\left(\frac{R^2}{M^2}\right)\right] \otimes f(x;M^2,R^2)\,. \tag{8}$$

This relation differs from eq. (1), where the parton densities are expressed as functions of one scale, only by terms beyond NLO.

In ref. [3] the scale-choice dependence of F_2 has been studied for two cases. The impact of varying the renormalization scale R has been considered for $M^2 = Q^2$. In this case, the structure function is given by

$$F_2(x,Q^2) = \sum_{i=q,g} f_i(x;Q^2,R^2) \otimes \left[c_{2,i}^{(0)}\,\delta_{i,q}\,\delta(1-x) + a_s(R^2)c_{2,i}^{(1)}(x)\right]. \tag{9}$$

The dependence on the factorization scale, on the other hand, has been investigated for $R^2 = M^2$. Then the parton densities obey eq. (1), and F_2 is determined via

$$F_2(x,Q^2) = \sum_{i,j=q,g}\left[c_{2,i}^{(0)}\,\delta_{i,q}\delta_{ij}\,\delta(1-x) + a_s(M^2)\left\{c_{2,i}^{(1)}(x)\,\delta_{ij} + P_{ij}^{(0)}(x)\ln\left(\frac{Q^2}{M^2}\right)\right\}\right] \otimes f_j(x,M^2)\,. \tag{10}$$

The uncertainty of $\alpha_s(M_Z^2)$, as determined in fits to future high-precision F_2 data from HERA, due to the arbitrariness of R and M has been estimated in the following way: a sample data set has been constructed for $R^2 = M^2 = Q^2$, using typical kinematic cuts, see fig. 3 of ref. [3]. Then one-parameter fits of $\alpha_s(M_Z^2)$ to these data have been performed, with R^2 and M^2 varied up and down up to factors of four in the manner described above. The resulting shifts from the assumed central value of $\alpha_s(M_Z^2) = 0.112$ are displayed in Table 1 for characteristic additional Q^2 cuts on the data.

Q^2 Cut (GeV^2)	$M^2 = Q^2/4$	$M^2 = Q^2/2$	$M^2 = 2Q^2$	$M^2 = 4Q^2$
4	–	–	−0.0068	−0.012
20	+0.0067	+0.0029	−0.0024	−0.0044
50	+0.0032	+0.0015	−0.0015	−0.0029
Q^2 Cut (GeV^2)	$R^2 = Q^2/4$	$R^2 = Q^2/2$	$R^2 = 2Q^2$	$R^2 = 4Q^2$
4	−0.0076	−0.0037	+0.0032	+0.0059
20	−0.0067	−0.0032	+0.0027	+0.0049
50	−0.0061	−0.0028	+0.0023	+0.0042

Table 1. Theoretical shifts on $\alpha_s(M_Z^2)$ from variations of the factorization scale M (upper part) and the renormalization scale R (lower part), for F_2 data in the HERA kinematic range. The reference data was generated for $\alpha_s(M_Z^2) = 0.112$ and imposing $M^2 = R^2 = Q^2$.

4 Summary

The theoretical uncertainties have been briefly outlined, which arise from the truncation of the (twist–2) perturbative series for the scaling violations of the structure function F_2 at NLO. Their effect on the value of $\alpha_s(M_Z^2)$ as extracted from data in the HERA regime has been investigated. An uncertainty of

$$\Delta\alpha_s(M_Z^2) = \left.\begin{matrix} +0.004 \\ -0.006 \end{matrix}\right|_R \left.\begin{matrix} -0.003 \\ +0.003 \end{matrix}\right|_M .$$

has been estimated originating in the freedom of choice of the renormalization scale R and the factorization scale M, if only data above $Q^2 = 50$ GeV^2 are taken into account. Different prescriptions for truncating the series at $M^2 = R^2 = Q^2$ lead to shifts of about $\Delta\alpha_s(M_Z^2) = 0.002$ under these conditions. Lower Q^2 cuts, as possibly experimentally desirable, lead to larger theoretical uncertainties. All these uncertainties can only be significantly reduced, if the analyses reach the next-to-next-leading order level. To achieve this goal, however, the extremely demanding calculation of the 3–loop splitting functions has to be carried out.

Acknowledgements : This work was supported on part by the EC Network 'Human Capital and Mobility' under contract No. CHRX–CT923–0004 and by the German Federal Ministry for Research and Technology (BMBF) under No. 05 7WZ91P (0).

References

[1] J. Blümlein, G. Ingelman, M. Klein, and R. Rückl, Z. Phys. **C45** (1990) 501, and references therein.

[2] M. Botje, M. Klein, and C. Pascaud, these proceedings.

[3] J. Blümlein, S. Riemersma, W.L. van Neerven, and A. Vogt, DESY 96–172, `hep-ph/9609217`, Proceedings of the Workshop 'QCD and QED in Higher Orders', Rheinsberg, Germany, April 1996, eds. J. Blümlein, F. Jegerlehner, and T. Riemann (Nucl. Phys. **B** (Proc. Suppl.) **51C**, 1996) p. 96.

[4] W.L. van Neerven, these proceedings, and references therein.

[5] M. Virchaux and A. Ouraou, DPhPE 87–15;
M. Virchaux, Thèse, Université Paris-7 (1988);
A. Ourau, Thèse, Université Paris-11 (1988).

[6] M. Botje, QCDNUM15: A fast QCD evolution Program, to appear.

[7] C. Pascaud and F. Zomer, H1 Note: `H1-11/94-404`.

[8] M. Diemoz, F. Ferroni, E. Longo, and G. Martinelli , Z. Phys. **C39** (1988) 21.

[9] M. Glück, E. Reya, and A. Vogt, Z. Phys. **C48** (1990) 471.

[10] J. Blümlein, M. Botje, C. Pascaud, S. Riemersma, W.L. van Neerven, A. Vogt, and F. Zomer, these proceedings.

[11] A.C. Benvenuti et al., BCDMS collaboration, Phys. Lett. **B195** (1987) 97.

Review of Higher Order QCD Corrections to Structure Functions

W.L. van Neerven[a]

[a] Instituut-Lorentz, University of Leiden, P.O. Box 9506, 2300 RA Leiden, The Netherlands

Abstract: A review is presented on all higher order QCD corrections to deep inelastic structure functions. The implications of these corrections for polarized and unpolarized deep inelastic lepton-hadron scattering will be discussed.

1 Introduction

The past twenty years have shown much progress in the field of perturbative calculations in strong interaction physics [1]. This in particular holds for the radiative corrections to the deep inelastic structure functions. Sometimes these corrections could be even extended up to third order in the strong coupling constant α_s. The structure functions we would like to discuss are measured in deep inelastic lepton-hadron scattering

$$l_1(k_1) + H(p) \rightarrow l_2(k_2) + "X" \tag{1}$$

where l_1, l_2 stand for the in- and outgoing leptons respectively. The hadron is denoted by H and "X" stands for any inclusive hadronic state. The relevant kinematical and scaling variables are defined by

$$q = k_1 - k_2 \qquad q^2 = -Q^2 > 0 \qquad x = \frac{Q^2}{2pq} \qquad y = \frac{pq}{pk_1} \tag{2}$$

with the boundaries

$$0 < y < 1 \qquad\qquad 0 < x \leq 1 \tag{3}$$

Reaction (1) proceeds via the exchange of one of the intermediate vector bosons V of the standard model which are represented by $V = \gamma, Z, W$. In the case of unpolarized scattering with $V = \gamma$ one can measure the structure functions $F_L(x, Q^2)$ (longitudinal) and $F_1(x, Q^2)$ (transverse) or the better known $F_2(x, Q^2)$ which is related to the former two via

$$F_2(x, Q^2) = 2x\, F_1(x, Q^2) + F_L(x, Q^2) \tag{4}$$

When $V = W$ or $V = Z$ one can in addition to F_1, F_2 and F_L also measure the structure function $F_3(x, Q^2)$ which is due to parity violation of the weak interactions. In the case the incoming

lepton and hadron are polarized one measures besides the structure functions F_i $(i = 1, 2, 3, L)$ also the spin structure functions denoted by $g_i(x, Q^2)$ $(i = 1, \cdots 5)$. At this moment, because of the low Q^2 available, reaction (1) is only dominated by the photon $(V = \gamma)$ so that one has data for $g_1(x, Q^2)$ (longitudinal spin) and $g_2(x, Q^2)$ (transverse spin) only. The measurement of the structure functions at large Q^2 gives us insight in the structure of the hadrons. According to the theory of quantum chromodynamics (QCD) the hadrons consist out of quarks and gluons where the latter are carriers of the strong force. When Q^2 gets large one can probe the light cone behaviour of the strong interactions which can be described by perturbation theory because the running coupling constant denoted by $\alpha_s(Q^2)$ is small. In particular perturbative QCD predicts the Q^2-evolution of the deep inelastic structure functions mentioned above. Unfortunately the theory is not at that stage that it enables us to predict the x-dependence so that one has to rely on parametrizations which are fitted to the data. A more detailed description of the structure functions is provided by the parton model which can be applied if one can neglect power corrections of the type $(1/Q^2)^p$ (higher twist effects). Here one asumes that in the Bjorken limit $(Q^2 \to \infty,\ x$ is fixed) the interaction between the hadron and lepton in process (1) proceeds via the partons (here the quarks and the gluons) of the hadron. If the scattering of the lepton with the partons becomes incoherent the structure function can be written as

$$\begin{aligned} F^{V,V'}(x,Q^2) &= \int_x^1 \frac{dz}{z}\left[\sum_{k=1}^{n_f}\left(v_k^{(V)}v_k^{(V')}+a_k^{(V)}a_k^{(V')}\right)\left\{\Sigma(\frac{x}{z},\mu^2)\,C_{i,q}^S(z,\frac{Q^2}{\mu^2})\right.\right. \\ &+ \left.\left. G\left(\frac{x}{z},\mu^2\right)C_{i,g}\left(z,\frac{Q^2}{\mu^2}\right)\right\}+\sum_{k=1}^{n_f}\left(v_k^{(V)}v_k^{(V')}+a_k^{(V)}a_k^{(V')}\right) \\ &\Delta_k\ \left(\frac{x}{z},\mu^2\right)C_{i,q}^{NS}\left(z,\frac{Q^2}{\mu^2}\right)\Big] \qquad i=1,2,L \end{aligned} \tag{5}$$

$$\begin{aligned} F_3^{V,V'}\left(x,Q^2\right) &= \int_x^1 \frac{dz}{z}\left[\sum_{k=1}^{n_f}\left(v_k^{(V)}a_k^{(V')}+a_k^{(V)}v_k^{(V')}\right)\right. \\ &V_k\ \left.\left(\frac{x}{z},\mu^2\right)C_{3,q}^{NS}\left(z,\frac{Q^2}{\mu^2}\right)\right] \end{aligned} \tag{6}$$

with similar expressions for the twist two contributions to the spin structure functions $g_1(x, Q^2)$ in which case we introduce the notations $\Delta\Sigma, \Delta G, \Delta C_{i,l}$ etc.. The vector- and axial-vector electroweak couplings of the standard model are given by $v_k^{(V)}$ and $a_k^{(V)}$ respectively with $V = \gamma, Z, W$ and $k = 1(u), 2(d), 3(s)$ .... . Further n_f denotes the number of light flavours and μ stands for the factorization/renormalization scale. The singlet (Σ) and non-singlet combinations of parton densities (Δ_k, V_k) are defined by

$$\Sigma\left(z,\mu^2\right) = \frac{1}{n_f}\sum_{k=1}^{n_f}\left(f_k\left(z,\mu^2\right)+f_{\bar{k}}\left(z,\mu^2\right)\right) \tag{7}$$

$$\Delta_k(z,\mu^2) = f_k(z,\mu^2)+f_{\bar{k}}(z,\mu^2)-\Sigma(z,\mu^2) \tag{8}$$

$$V_k(z,\mu^2) = f_k(z,\mu^2)-f_{\bar{k}}(z,\mu^2) \tag{9}$$

where $f_k, f_{\bar{k}}$ denote the quark and anti-quark densities of species k respectively. The gluon density is defined by $G(z, \mu^2)$. The same nomenclature holds for the coefficient functions

$C_{i,l}(l = q, g)$ which can also be distinguished in a singlet (S) and a non-singlet (NS) part. Like in the case of the structure functions the x-dependence of the parton densities cannot be determined by perturbative QCD and it has to be obtained by fitting the parton densities to the data. Fortunately these densities are process independent and they are therefore universal. This property is not changed after including QCD radiative corrections. It means that the same parton densities also show up in other so called hard processes like jet production in hadron-hadron collisions,direct photon production, heavy flavour production, Drell-Yan process etc. Another firm prediction of QCD is that the scale (μ) evolution of the parton densities is determined by the DGLAP [2] splitting functions P_{ij} $(i, j = q, \bar{q}, g)$ which can be calculated order by order in the strong coupling constant α_s. The perturbation series of P_{ij} gets the form

$$P_{kl} = a_s\,P_{kl}^{(0)} + a_s^2\,P_{kl}^{(1)} + a_s^3\,P_{kl}^{(2)} + \ldots \tag{10}$$

with $a_s = \alpha_s(\mu^2)/4\pi$. The splitting functions P_{ij} are related to the anomalous dimensions $\gamma_{ij}^{(n)}$ corresponding to twist two local operators $O_i^{\mu_1\cdots\mu_n}(x)$ of spin n via the Mellin transform

$$\gamma_{ij}^{(n)} = -\int_o^1 dz z^{n-1}\,P_{ij}(z) \tag{11}$$

These operators appear in the light cone expansion of the product of two electroweak currents which shows up in the calculation of the cross section of process (1)

$$J(x)\,J(0) \sim \sum_{n=0}^{\infty}\sum_k \tilde{C}_k^{(n)}\,(\mu^2x^2)\,x_{\mu_1}..x_{\mu_n}\,O_k^{\mu_1\cdots\mu_n}(0,\mu^2) \tag{12}$$

where $\tilde{C}_k^{(n)}$ (12) are the Fourier transforms of the coefficient functions $C_k^{(n)}$ (5),(6) $(k = q, g)$ in Minkowski space (x_μ). Like the splitting functions they are calculable order by order in α_s and the perturbation series takes the form

$$C_{i,k} = \delta_{kq} + a_s\,C_{i,k}^{(1)} + a_s^2\,C_{i,k}^{(2)} + a_s^3\,C_{i,k}^{(3)} + \ldots \tag{13}$$

with $i = 1, 2, 3, L$ and $k = q, g$. We will now review the higher order QCD corrections to the splitting functions and the coefficient functions which have been calculated till now.

2 Splitting Functions

The splitting functions are calculated by

1. $P_{ij}^{(0)}$ Gross and Wilczek (1974) [3]; Altarelli and Parisi (1977) [2].
2. $\Delta P_{ij}^{(0)}$ Sasaki (1975) [4]; Ahmed and Ross (1976) [5]; Altarelli and Parisi [2].
3. $P_{ij}^{(1)}$ Floratos, Ross, Sachrajda (1977) [6]; Gonzales-Arroyo, Lopez, Yndurain (1979) [7]; Floratos, kounnas, Lacaze (1981) [8]; Curci, Furmanski, Petronzio (1980) [9].

4. $\Delta P_{ij}^{(1)}$ Zijlstra and van Neerven (1993) [10]; Mertig and van Neerven (1995) [11]; Vogelsang (1995) [12].

Notice that till 1992 there was a discrepancy for $P_{gg}^{(1)}$ between the covariant gauge [6–8] and the lightlike axial gauge calculation [9] which was decided in favour of the latter by Hamberg and van Neerven who repeated the covariant gauge calculation in [12]. The DGLAP splitting functions satisfy some special relations. The most interesting one is the so called supersymmetric relation which holds in $\mathcal{N}=1$ supersymmetry [13]. Here the colour factors, which in $SU(N)$ are given by $C_F = (N^2-1)/2N$, $C_A = N$, $T_f = 1/2$ become $C_F = C_A = 2T_f = N$. The supersymmetric relation then reads

$$P_{qq}^{S,(k)} + P_{gq}^{(k)} - P_{qg}^{(k)} - P_{gg}^{(k)} = 0 \tag{14}$$

$$\Delta P_{qq}^{S,(k)} + \Delta P_{gq}^{(k)} - \Delta P_{qg}^{(k)} - \Delta P_{gg}^{(k)} = 0 \tag{15}$$

which is now confirmed up to first ($k=0$) and second ($k=1$) order in perturbation theory. The third order splitting functions $P_{ij}^{(2)}, \Delta P_{ij}^{(2)}$ are not known yet. However the first few moments $\gamma_{ij}^{(2),(n)}$ for $n = 2,4,6,8,10$ have been calculated by Larin, van Ritbergen, Vermaseren (1994) [14]. Besides exact calculations one has also determined the splitting functions and the anomalous dimensions in some special limits. Examples are the large n_f expansion carried out by Gracey (1994) [15]. Here one has computed the coefficients b_{21} and b_{31} in the perturbations series of the non-singlet anomalous dimension

$$\begin{aligned}\gamma_{qq}^{NS}\Big|_{n_f\to\infty} &= a_s^2\,[n_f\,C_F\,b_{21}] + a_s^3\,\Big[n_f^2\,C_F\,b_{31} \\ &+ n_f\,C_A\,C_F\,b_{32} + n_f\,C_F^2\,b_{33}\Big] + \ldots\end{aligned} \tag{16}$$

Further Catani and Hautmann (1993) [16] calculated the splitting functions $P_{ij}(x)$ in the limit $x \to 0$. The latter take the following form

$$P_{ij}^{(k)}(x)\Big|_{x\to 0} \sim \frac{ln^k x}{x} \to \gamma_{ij}^{(k),(n)}\Big|_{n\to 1} \sim \frac{1}{(n-1)^{k+1}} \tag{17}$$

The above expressions follow from the BFKL equation [17] and k_T-factorization [18]. Some results are listed below. The leading terms in $\gamma_{gg}^{(n)}$ are given by

$$\gamma_{gg}^{(n)}\Big|_{n\to 1} = \left[C_A\frac{a_s}{n-1}\right] + 2\zeta(3)\,\left[C_A\frac{a_s}{n-1}\right]^4 + 2\zeta(5)\,\left[C_A\frac{a_s}{n-1}\right]^6 \tag{18}$$

where $\zeta(n)$ denotes the Riemann zeta-function. Further we have in leading order $1/(n-1)$

$$\gamma_{gq}^{(n)}\Big|_{n\to 1} = \frac{C_F}{C_A}\,\gamma_{gg}^{(n)}\Big|_{n\to 1} \tag{19}$$

$$\begin{aligned}\gamma_{qg}^{(n)}\Big|_{n\to 1} &= a_s T_f \frac{1}{3}\left[1 + 1.67\left\{\frac{a_s}{n-1}\right\} + 1.56\left\{\frac{a_s}{n-1}\right\}^2\right. \\ &+ \left. 3.42\left\{\frac{a_s}{n-1}\right\}^3 + 5.51\left\{\frac{a_s}{n-1}\right\}^4 + \ldots\right]\end{aligned} \tag{20}$$

$$\gamma_{qq}^{S,(n)}\Big|_{n\to 1} = \frac{C_F}{C_A}\left[\gamma_{qg}^{(n)}\Big|_{n\to 1} - \frac{1}{3}\,a_s T_f\right] \tag{21}$$

Kirschner and Lipatov (1983) and Blümlein and Vogt (1996) have also determined the subleading terms in the splitting functions (anomalous dimensions). They behave like

$$P_{ij}^{(k)}(z)\Big|_{z\to 0} \sim ln^{2k} z \qquad \gamma_{ij}^{(k),(n)}\Big|_{n\to 0} \sim \frac{1}{n^{2k+1}} \tag{22}$$

The same logarithmic behaviour also shows up in ΔP_{ij} and $\Delta\,\gamma_{ij}^{(n)}$. In the latter case the expressions in (22) become the leading ones since the most singular terms in (17) decouple in the spin quantities. The expressions in (22) have been calculated for the spin case by Bartels, Ermolaev, Ryskin (1995) [20] and by Blümlein and Vogt (1996) [21] who also investigated the effect of these type of corrections on the spin structure function $g_1(x,Q^2)$. Finally the three-loop anomalous dimension $\Delta\gamma_{qq}^{S,(1)}$ is also known (see Chetyrkin,Kühn (1993) [22] and Larin (1993) [23]). It reads

$$\Delta\gamma_{qq}^{S,(1)} = a_s^2\,[-6n_f\,C_F] + a_s^3\left[\left(18C_F^2 - \frac{142}{3}C_A C_F\right)n_f + \frac{4}{3}\,n_f^2 C_F\right] \tag{23}$$

Notice that the second order coefficient was already determined by Kodaira (1980) [24].

3 Coefficient Functions

The higher order corrections to the coefficient functions are calculated by

1. $C_{i,q}^{(1)}$, $C_{i,g}^{(1)}$ $\quad i = 1,2,3,L$ — Bardeen, Buras, Muta, Duke (1978) [25], see also Altarelli (1980) [26].
2. $\Delta C_q^{(1)}$, $\Delta C_g^{(1)}$ — Kodaira et al. (1979) [27], see also Anselmino, Efremov, Leader (1995) [28]

Together with the splitting functions $P_{ij}^{(k)}$, $\Delta P_{ij}^{(k)}$ $(k=0,1)$ one is now able to make a complete next-to-leading (NLO) analysis of the structure functions $F_i(x,Q^2)$ $(i=1,2,3,L)$ and $g_1(x,Q^2)$. The second order contributions to the coefficient functions are also known

1. $C_{i,q}^{(2)}, C_{i,g}^{(2)}$ $\quad i = 1,2,3,L$ — Zijlstra and van Neerven (1991) [29]
2. $\Delta C_q^{(2)}, \Delta C_g^{(2)}$ — Zijlstra and van Neerven (1993) [10]

The first few moments of $C_{i,k}^{(2)}$ $(i=2,L;k=q,g)$ were calculated by Larin and Vermaseren (1991) [30] and they agree with Zijlstra and van Neerven [29]. The first moment of $\Delta C_q^{(2)}$ was checked by Larin (1993) [31] and it agrees with the result of Zijlstra and van Neerven [10]. The third order contributions to the coefficient functions are not known except for some few moments. They are given by

1. $C_{1,q}^{(3),(1)}$ (Bjorken sum rule) — Larin, Tkachov, Vermaseren (1991) [32];

2. $C_{3,q}^{(3),(1)}$ (Gross-Llewellyn Smith sum rule) — Larin and Vermaseren (1991) [33];

3. $\Delta C_{q}^{(3),(1)}$ (Bjorken sum rule) — Larin and Vermaseren (1991) [33];

4. $C_{i,q}^{(3),(n)}$ $(i = 2, L)$ $n = 2, 4, 6, 8$ — Larin, van Ritbergen, Vermaseren (1994) [14], (see also [34]).

Since the three-loop splitting functions $P_{ij}^{(2)}$, $\Delta P_{ij}^{(2)}$ are not known, except for a few moments, it is not possible to obtain a full next-to-next-to-leading order (NNLO) expression for the structure functions. However recently Kataev et al. (1996) [35] made a NNLO analysis of the structure functions $F_2(x, Q^2)$, $F_3(x, Q^2)$ (neutrino scattering) in the kinematical region $x > 0.1$ which is based on $\gamma_{qq}^{NS,(2),(n)}$ for $n = 2, 4, 6, 8, 10$ [14]. Like in the case of the DGLAP splitting functions Catani and Hautmann (1994) [16] also derived the small x-behaviour of the coefficient functions. At small x the latter behave like

$$C_{i,k}^{(l)}\Big|_{x\to 0} \sim \frac{ln^{l-2}x}{x} \qquad C_{i,k}^{(l),(n)}\Big|_{n\to 1} \sim \frac{1}{(n-1)^{l-1}} \qquad (l \geq 2) \tag{24}$$

[3mm] The ingredients of the derivation are again the BFKL equation [17] and k_T-factorizaton [18]. from [16] we infer the following Mellin-transformed coefficient functions.

$$\begin{aligned} C_{L,g}^{(n)}\Big|_{n\to 1} &= a_s T_f n_f \frac{2}{3}\left[1 - 0.33\left\{\frac{a_s}{n-1}\right\} + 2.13\left\{\frac{a_s}{n-1}\right\}^2\right. \\ &+ \left. 2.27\left\{\frac{a_s}{n-1}\right\}^3 + 0.43\left\{\frac{a_s}{n-1}\right\}^4 + ...\right] \end{aligned} \tag{25}$$

$$\begin{aligned} C_{2,g}^{(n)}\Big|_{n\to 1} &= a_s T_f n_f \frac{1}{3}\left[1 + 1.49\left\{\frac{a_s}{n-1}\right\} + 9.71\left\{\frac{a_s}{n-1}\right\}^2\right. \\ &+ \left. 16.43\left\{\frac{a_s}{n-1}\right\}^3 + 39.11\left\{\frac{a_s}{n-1}\right\}^4 + ...\right] \end{aligned} \tag{26}$$

$$C_{L,q}^{S,(n)}\Big|_{n\to 1} = \frac{C_F}{C_A}\left[C_{L,g}^{(n)}\Big|_{n\to 1} - \frac{2}{3} a_s n_f T_f\right] \tag{27}$$

$$C_{2,q}^{S,(n)}\Big|_{n\to 1} = \frac{C_F}{C_A}\left[C_{2,g}^{(n)}\Big|_{n\to 1} - \frac{1}{3} a_s n_f T_f\right] \tag{28}$$

The order α_s^2 coefficients were already obtained via the exact calculation performed by Zijlstra and van Neerven (1991) [29]. The subleading terms given by

$$C_{2,k}^{(l)}\Big|_{x\to 0} \sim \ln^{2l-1} x \qquad (l \geq 1) \tag{29}$$

were investigated by Blümlein and Vogt (1996) [21]. The most singular terms shown in (24) do not appear in the spin coefficient functions $\Delta C_k^{(l)}$ because the Lipatov pomeron decouples in

polarized lepton-hadron scattering. Therefore the most singular behaviour near $x = 0$ is given by (29) (see [10],[21]). Besides the logarithmical enhanced terms which are characteristic of the low x-regime we also find similar type of logarithms near $x = 1$. Their origin however is completely different from the one determining the small x-behaviour. The logarithmical enhanced terms near $x = 1$, which are actual distributions, originate from soft gluon radiation. They dominate the structure functions F_i and g_i near $x = 1$ because other production mechanisms are completely suppressed due to limited phase space. Following the work in [36] and [37] the DGLAP splitting functions and the coefficient functions behave near $x = 1$ like

$$P_{qq}^{NS,(k)} = \Delta P_{qq}^{NS,(k)} \sim \left(\frac{1}{1-x}\right)_+ \qquad P_{gg}^{(n)} = \Delta P_{gg}^{(k)} \sim \left(\frac{1}{1-x}\right)_+ \tag{30}$$

$$\Delta C_q^{NS,(k)} = C_{i,q}^{NS,(k)} \sim \left(\frac{\ln^{2k-1}(1-x)}{1-x}\right)_+ \qquad (l = 1, 2, 3) \tag{31}$$

Notice that the above corrections cannot be observed in the kinematical region ($x < 0.4$) accessible at HERA. Furthermore the behaviour in (30) is a conjecture (see [7]) which is confirmed by the existing calculations carried out up to order α_s^2.

4 Heavy Quark Coefficient Functions

The heavy quark coefficient functions have been calculated by

1. $C_{i,g}^{(1)}(x, Q^2, m^2)$ $(i = 2, L)$ — Witten (1976) [38];

2. $\Delta C_g^{(1)}(x, Q^2, m^2)$ — Vogelsang (1991) [39];

3. $C_{i,g}^{(2)}(x, Q^2, m^2)$, $C_{i,q}^{(2)}(x, Q^2, m^2)$ $(i = 2, L)$ — Laenen, Riemersma, Smith, van Neerven (1992) [40].

where m denotes the mass of the heavy quark. The second order heavy quark spin coefficient functions $\Delta C_g^{(2)}(x, Q^2, m^2)$ and $\Delta C_q^{(2)}(x, Q^2, m^2)$ are not known yet. Due to the presence of the heavy quark mass one was not able to give explicit analytical expressions for $C_{i,k}(i = 2, L; k = q, g)$. However for experimental and phenomenological use they were presented in the form of tables in a computer program [41]. Analytical expressions do exist when either $x \to 0$ or $Q^2 \gg m^2$. In the former case Catani, Ciafaloni and Hautmann [42] derived the general form

$$C_{i,k}^{(l)}\Big|_{x\to 0} \sim \frac{1}{x} \ln^{l-2}(x)\, f(Q^2, m^2) \qquad (l \geq 2,\ i = 2,\ L;\ k = q, g) \tag{32}$$

Like for the light parton coefficient functions (see (24)) the above expression is based on the BFKL equation [17] and k_T-factorization [18]. In second order Buza et al. (1996) [43] were able to present analytical formulae for the heavy quark coefficient functions in the asymptotic limit $Q^2 \gg m^2$. This derivation is based on the operator product expansion and mass factorization.

5 Phenomenology at low x

Since the calculation of the higher order corrections to the DGLAP splitting functions P_{ij} and the coefficient functions C_{ik} is very cumbersome various groups have tried to make an estimate of the NNLO corrections to structure functions in particular to $F_2(x,Q^2)$. The most of these estimates concerns the small x-behaviour. In [44] Ellis, Kunszt and Levin Hautman made a detailed study of the Q^2-evolution of F_2 using the small x-approximation for P_{ij} (17) and $C_{2,k}^{(2)}$ (24). Their results heavily depend on the set of parton densities used and the non leading small x-contributions to $P_{ij}^{(2)}$. The latter are e.g. needed to satisfy the momentum conservation sum rule condition. Large corrections appear when for $x \to 0$ the gluon density behaves like $xG(x,\mu^2) \to$ const. whereas they are small when the latter has the behaviour $xG(x,\mu^2) \to x^{-\lambda} (\lambda \sim 0.3 - 0.5$; Lipatov pomeron).
However other investigations reveal that the singular terms at $x = 0$, present in P_{ij} and $C_{i,k}$, do not dominate the radiatve corrections to $F_2(x,Q^2)$ near low x. This became apparent after the exact coefficient functions or DGLAP splitting functions were calculated.
In [45] Glück, Reya and Stratmann (1994) investigated the singular behaviour of the second order heavy quark coefficient functions (32) in electroproduction and they found that its effect on F_2 was small.
Similar work was done by Blümlein and Vogt (1996) [21] on the effect of the logarithmical terms (22),(29) on $g_1(x,Q^2)$ which contribution to the latter turned out to be negligable.
Finally we would like to illustrate the effect of the small x-terms, appearing in the coefficient functions $C_{2,k}^{(2)}$ and $C_{L,k}^{(2)}$, on the structure functions $F_2(x,Q^2)$ and $F_L(x,Q^2)$. For that purpose we compute the order α_s^2 contributions to F_2 and F_L. Let us introduce the following notations. When the exact expressions for the coefficient functions $C_{i,k}^{(2)}$ are adopted the order α_s^2 contributions to F_i will be called $\delta F_i^{(2),exact}$. If we replace the exact coefficient functions by their most singular part which is proportional to $1/x$ (see (24)) the order α_s^2 contributions to F_i are denoted by $\delta F_i^{(2),app}$. The results are listed in the table below. Further we have used the parton density sets MRS(D0) ($xG(x,\mu^2) \to const.$ for $x \to 0$) and MRS(D-) ($xG(x,\mu^2) \to x^{-\lambda}$ for $x \to 0$) [46]

	MRS(D0)			MRS(D-)		
x	F_2^{NLO}	$\delta F_2^{(2),exact}$	$\delta F_2^{(2),app}$	F_2^{NLO}	$\delta F_2^{(2),exact}$	$\delta F_2^{(2),app}$
10^{-3}	0.67	-0.069	0.088	0.99	-0.084	0.116
10^{-4}	0.82	-0.088	0.158	2.29	-0.226	0.349
10^{-5}	1.00	-0.092	0.251	5.99	-0.665	1.059
x	F_L^{NLO}	$\delta F_L^{(2),exact}$	$\delta F_L^{(2),app}$	F_L^{NLO}	$\delta F_L^{(2),exact}$	$\delta F_L^{(2),app}$
10^{-3}	0.149	-0.029	-0.040	0.263	0.008	-0.052
10^{-4}	0.210	-0.062	-0.071	0.780	0.031	-0.156
10^{-5}	0.281	-0.102	-0.113	2.370	0.105	-0.475

From the table above we infer that a steeply rising gluon density near $x = 0$ (MRS(D-)) leads to small corrections to F_2 and F_L. On the other hand if one has a flat gluon density (MRS(D0))

the corrections are much larger in particular for F_L. A similar observation was made for F_2 in [44]. However the most important observation is that the most singular part of the coefficient functions gives the wrong prediction for the order α_s^2 contributions to the structure functions except for F_L provided the set MRS(D0) is chosen. This means that the subleading terms are important and they cannot be neglected. Therefore our main conclusion is that only exact calculations provide us with the correct NNLO analysis of the structure functions. The asymptotic expressions obtained in the limits $x \to 0, x \to 1$ and $Q^2 \gg m^2$ can only serve as a check on the exact calculations of the DGLAP splitting functions and the coefficient functions.

Acknowledgement I would like to thank Mrs. Sabine Baer (DESY-Ifh Zeuthen, Germany) for putting the manuscript into LATEX.

References

[1] *QCD 20 years later*, Vol 1. eds. P.M. Zerwas and H.A. Kastrup, World Scientific, Singapore, 1992.

[2] V.N. Gribov and L.N. Lipatov, Sov. J. Nucl. Phys. 15 (1972) 675. G. Altarelli and G. Parisi, Nucl. Phys. B126 (1977) 298. Yu. L. Dokshitzer, Sov. Phys. JETP 46 (1977) 641.

[3] D.J. Gross and F. Wilczek , Phys. Rev. D9 (1974) 980.

[4] K. Sasaki, Progr. of Theor. Phys. 54 (1975) 1816.

[5] M.A. Ahmed and G.G. Ross , Nucl. Phys. B111 (1976) 441.

[6] E.G. Floratos, D.A. Ross and C.T. Sachrajda, Nucl. Phys. B129 (1977) 66; Erratum B139 (1978) 545; Nucl. Phys. B152 (1979) 493.

[7] A. Gonzales-Arroyo, C. Lopez and F.J. Yndurain, Nucl. Phys. B153 (1979) 161.
A. Gonzales-Arroyo and C. Lopez, Nucl. Phys. B166 (1980) 429.

[8] E.G. Floratos, C. Kounnas and R. Lacaze, Phys. Lett. B98 (1981) 89, 285;
Nucl. Phys. B192 (1981) 417.

[9] G. Curci, W. Furmanski and R. Petronzio, Nucl. Phys. B175 (1980) 27;
W. Furmanski and R. Petronzio, Phys. Lett. B97 (1980) 437; Z. Phys. C11 (1980) 293.

[10] E.B. Zijlstra and W.L. van Neerven, Nucl. Phys. B417 (1994) 61; Erratum B426 (1994) 245.

[11] R. Mertig and W.L. van Neerven, Z. Phys. C70 (1996) 637;
W. Vogelsang, Phys. Rev. D54 (1996) 2023, RAL-TR-96-020.

[12] R. Hamberg and W.L. van Neerven, Nucl. Phys. B379 (1992) 143.

[13] Yu. I. Dokshitzer, V.A. Khoze, A.H. Mueller and S.I. Troyan, *Basics of Perturbative QCD*, Series : Editions Frontieres 1991, Paris;
I. Antoniades and E.G. Floratos, Nucl. Phys. B191 (1981) 217.

[14] S.A. Larin, T. van Ritbergen, J.A.M. Vermaseren, Nucl. Phys. B427 (1994) 41;
S.A. Larin, P. Nogueira, T. van Ritbergen, J.A.M. Vermaseren, NIKHEF-96-010 (hep-ph/9605317).

[15] J.A. Gracey, Phys. Lett. B322 (1994) 141.

[16] S. Catani and F. Hautmann, Nucl. Phys. B427 (1994) 475.

[17] L.N. Lipatov, Sov. J. Nucl. Phys. 23 (1976) 338; E.A. Kuraev, L.N. Lipatov and V.S. Fadin, Sov. Phys. JETP 45 (1977) 199; Yu. Balitskii and L.N. Lipatov, Sov. J. Nucl. Phys. 28 (1978) 822.

[18] S. Catani, M. Ciafaloni and F. Hautmann, Phys. Lett. B242 (1990) 97;
Nucl. Phys. B366 (1991) 135;
J.C. Collins and R.K. Ellis, Nucl. Phys. B360 (1991) 3;
E.M. Levin, M.G. Ryskin, Yu.M. Shabel'skii and R.G. Shuvaev, Sov. J. Nucl. Phys. 53 (1991) 657.

[19] R. Kirschner and L.N. Lipatov, Nucl. Phys. B213 (1983) 122.

[20] J. Bartels, B.I. Ermolaev and M.G. Ryskin, Z. Phys. C70 (1996) 273; DESY-96-025.

[21] J. Blümlein and A. Vogt, Phys. Lett. B370 (1996) 149; Acta Phys. Pol. **27** (1996) 1309; DESY 96-050 (hep-ph/9606254), Phys. Lett. B in print;
J. Blümlein, S. Riemersma, and A. Vogt, DESY 96-131, `hep-ph/9608470`, Nucl. Phys. **B** (Proc. Suppl.) to appear.

[22] S.A. Larin, Phys. Lett. B303 (1993) 113.

[23] K.G. Chetyrkin and J.H. Kühn, Z. Phys. C60 (1993) 497.

[24] J. Kodaira, Nucl. Phys. B165 (1980) 129.

[25] W.A. Bardeen, A.J. Buras, D.W. Duke, T. Muta, Phys. Rev. D18 (1978) 3998.

[26] G. Altarelli, Phys. Rep. 81 (1982) 1.

[27] J. Kodaira, S. Matsuda, K. Sasaki and T. Kematsu, Nucl. Phys. B159 (1979) 99. J. Kodaira, S. Matsuda, T. Muta, T. Kematsu, K. Sasaki, Phys. Rev. D20 (1979) 627.

[28] M. Anselmino, A. Efremov and E. Leader, Phys. Rep. 261 (1995) 1.

[29] W.L. van Neerven and E.B. Zijlstra, Phys. Lett. B272 (1991) 127; E.B. Zijlstra and W.L. van Neerven, Phys. Lett. B273 (1991) 476; Nucl. Phys. B383 (1992) 525; Phys. Lett. B297 (1992) 377.

[30] S.A. Larin and J.A.M. Vermaseren, Z. Phys. C57 (1993) 93.

[31] S.A. Larin, Phys. Lett. B334 (1994) 192.

[32] S.A. Larin, F.V. Tkachov and J.A.M Vermaseren, Phys. Rev. Lett. 66 (1991) 862.

[33] S.A. Larin and J.A.M. Vermaseren, Phys. Lett. B259 (1991) 345.

[34] S.A. Larin, F.V. Tkachov and J.A.M. Vermaseren, Phys. Lett. B272 (1991) 121.

[35] A.L. Kataev, A.V. Kotikov, G. Parente, A.V. Sidorov, INR -09 19-16 (1996) (hep-ph/9605367).

[36] D. Amati, A. Bassetto, M. Ciafaloni, G. Marchesini and G. Veneziano, Nucl. Phys. B173 (1980) 429; W.R. Frazer and G. Rossi, Phys. Rev. D25 (1982) 843.

[37] W.L. van Neerven, Phys. Lett. B147 (1984) 175.

[38] E. Witten, Nucl. Phys. B104 (1976) 445.

[39] W. Vogelsang, Z. Phys. C50 (1991) 275.

[40] E. Laenen, S. Riemersma, J. Smith and W.L. van Neerven, Nucl. Phys. B392 (1993) 162.

[41] S. Riemersma, J. Smith, W.L. van Neerven, Phys. Lett. B347 (1995) 143.

[42] S. Catani, M. Ciafaloni and F. Hautmann,"Production of heavy flavours at high energies" in "Physics at HERA",Proceedings of the Workshop, Hamburg, Oct. 29-30, 1991.Editors W. Buchmüller and G. Ingelman, Vol. 2, p. 690.

[43] M. Buza, Y. Matiounine, J. Smith, R. Migneron, W.L. van Neerven, Nucl. Phys. B472 (1996) 611.

[44] R.K. Ellis, Z. Kunszt, E.M. Levin, Nucl. Phys. B420 (1994) 517; Erratum B433 (1995) 498.

[45] M. Glück, E. Reya and M. Stratmann, Nucl. Phys. B422 (1994) 37.

[46] A.D. Martin, R.G. Roberts and W.J. Stirling, Phys. Rev. D47 (1993) 867.

The next-to-next-to-leading QCD calculation of the moments of deep inelastic structure functions

S.A. Larin[ab], P. Nogueira[c1], T. van Ritbergen[a], J.A.M. Vermaseren[a]

[a] NIKHEF-H, P.O. Box 41882, 1009 DB, Amsterdam, The Netherlands
[b] Institute for Nuclear Research of the Russian Academy of Sciences, 60th October Anniversary Prospect 7a, Moscow 117312, Russia
[c] Instituto Superior Técnico, Edifício Ciência (Física) P-1096 Lisboa Codex, Portugal

Abstract: We present the calculation of the analytic next-to-next-to-leading perturbative QCD corrections in the leading twist approximation for the moments N=2,4,6,8 of the flavour singlet deep inelastic structure functions F_2 and F_L. We calculate the three-loop anomalous dimensions of the corresponding singlet operators and the three-loop coefficient functions of the structure functions F_L and F_2. In addition, we obtained the 10^{th} moment for the non-singlet structure functions in the same order of perturbative QCD.

1 Introduction

The calculation of the next-to-next-to-leading (NNL) QCD approximation for the structure functions F_2 and F_L of deep inelastic electron-nucleon scattering is important for the understanding of perturbative QCD and for an accurate comparison of perturbative QCD with experiment. To obtain the NNL approximation for these structure functions in the operator product expansion (OPE) formalism one needs the 3-loop anomalous dimensions of the operators, the 2-loop Wilson coefficient functions for F_2 and the 3-loop coefficient functions for F_L. At present, these structure functions are known in the next-to-leading approximation only, since the 3-loop anomalous dimensions and the 3-loop coefficient functions for F_L were not calculated yet.

The 1-loop anomalous dimensions were calculated in Ref. [1]. The complete 1-loop coefficient functions were obtained in Ref. [2] (see also the references therein). Anomalous dimensions in the 2-loop order were obtained in Refs. [3]-[6] and the 2-loop coefficient functions were calculated in Refs. [7]-[11]. In Ref. [12] we presented the NNL corrections of the *non-singlet* type in the leading twist approximation for the moments N=2,4,6,8 of the deep inelastic structure functions F_2 and F_L.

In the present contribution we describe the more recent calculation of the NNL QCD corrections to the *singlet* moments N=2,4,6,8 of both structure functions F_2 and F_L. To this end, we calculated the corresponding 3-loop anomalous dimensions and the 3-loop coefficient functions for the structure function F_L. In addition, we obtained the 3-loop coefficient functions for the

[1] Partially supported by Junta Nacional de Investigação Científica e Tecnológica, Lisbon

structure function F_2 (for N=2,4,6,8) and we obtained the N=10 *non-singlet* moments of F_2 and F_L. The calculations are done for the leading twist approximation for zero quark masses. The complete set of the results of our calculations can be found in Ref. [13] where further details and an analysis of the results are given.

2 The calculation

We need to calculate the hadronic part of the amplitude for unpolarized deep inelastic electron-nucleon scattering which is given by the hadronic tensor

$$\begin{aligned} W_{\mu\nu}(p,q) &= \frac{1}{4\pi}\int d^4z e^{iq\cdot z}\langle p,\mathrm{nucl}|J_\mu(z)J_\nu(0)|\ \mathrm{nucl},p\rangle \\ &= e_{\mu\nu}\frac{1}{2x}F_L(x,Q^2)+d_{\mu\nu}\frac{1}{2x}F_2(x,Q^2) \qquad (1)\\ e_{\mu\nu} &= \left(g_{\mu\nu}-\frac{q_\mu q_\nu}{q^2}\right) \\ d_{\mu\nu} &= \left(-g_{\mu\nu}-p_\mu p_\nu\frac{4x^2}{q^2}-(p_\mu q_\nu+p_\nu q_\mu)\frac{2x}{q^2}\right), \end{aligned}$$

where J_μ is the electromagnetic quark current, $x=Q^2/(2p\cdot q)$ is the Bjorken scaling variable $(0<x\leq 1)$, $Q^2=-q^2$ is the transferred momentum and $|\ \mathrm{nucl},p\rangle$ is the nucleon state with momentum p. Spin averaging is assumed. The longitudinal structure function F_L is related to the structure function F_1 by $F_L=F_2-2xF_1$.

As one approaches the Bjorken limit, $Q^2\to\infty$, x fixed, one can show that the integration region in Eq. (1) near the light cone $z^2\approx 0$ progressively dominates[14], due to increasingly rapid phase fluctuations of the term $e^{iq\cdot z}$ outside the light cone region (and presuming that the integrand $\langle p,\mathrm{nucl}|J_\mu(z)J_\nu(0)|\ \mathrm{nucl},p\rangle$ varies smoothly outside the light cone). Since we have to deal with this non-local limit $z^2\approx 0$, a formal operator product expansion in terms of local operators can only be applied together with the dispersion relation technique [15]. These techniques together provide a systematic way to study[2] the leading and non-leading contributions to the hadronic tensor.

The tensor $W_{\mu\nu}$ is, by application of the optical theorem, related to a scattering amplitude $T_{\mu\nu}$ which is a more convenient quantity for practical calculations since it has a time ordered product of currents to which standard perturbation theory applies ($T_{\mu\nu}$ is the amplitude for forward elastic photon–nucleon scattering)

$$W_{\mu\nu}(p,q)=\frac{1}{2\pi}\mathrm{Im}\,T_{\mu\nu}(p,q),\qquad T_{\mu\nu}(p,q)=i\int d^4z e^{iqz}\langle p,\mathrm{nucl}|T\left(J_\mu(z)J_\nu(0)\right)|\ \mathrm{nucl},p\rangle. \quad (2)$$

The operator product expansion in terms of local operators for a time ordered product of the two electromagnetic hadronic currents reads

$$i\int d^4z e^{iqz}T\left(J_{\nu_1}(z)J_{\nu_2}(0)\right)=$$

$$\sum_{N,j}\left(\frac{1}{Q^2}\right)^N\left[\left(g_{\nu_1\nu_2}-\frac{q_{\nu_1}q_{\nu_2}}{q^2}\right)q_{\mu_1}q_{\mu_2}C^j_{L,N}\left(\frac{Q^2}{\mu^2},a_s\right)-\left(g_{\nu_1\mu_1}g_{\nu_2\mu_2}q^2-g_{\nu_1\mu_1}q_{\nu_2}q_{\mu_2}\right.\right.$$

[2] For reviews see Refs. [16, 17, 18].

$$-g_{\nu_2\mu_2}q_{\nu_1}q_{\mu_1}+g_{\nu_1\nu_2}q_{\mu_1}q_{\mu_2})\,C^j_{2,N}(\frac{Q^2}{\mu^2},a_s)\Big]\,q_{\mu_3}...q_{\mu_N}O^{j,\{\mu_1,...,\mu_N\}}(0)+\text{ higher twists},$$

$$\text{j}=\alpha,\psi,\text{G} \qquad (3)$$

where everything is assumed to be renormalized (with μ being the renormalization scale). The use of the OPE in the short distance regime ($z \to 0$) differs from its use in the light cone region. In the former case the sum over spin-N extends to a finite value for a given approximation, while in the latter (the one we have to deal with) the sum over N extends to infinity. The sum over N runs over the standard set of the spin-N twist-2 irreducible (i.e. symmetrical and traceless in the indices $\mu_1,\cdots,\mu_N$) flavour non-singlet quark operators and the singlet quark and gluon operators:

$$O^{\alpha,\{\mu_1,\cdots,\mu_N\}} = \overline{\psi}\lambda^\alpha\gamma^{\{\mu_1}D^{\mu_2}\cdots D^{\mu_N\}}\psi, \quad \alpha=1,2,...,(n_f^2-1) \qquad (4)$$

$$O^{\psi,\{\mu_1,\cdots,\mu_N\}} = \overline{\psi}\gamma^{\{\mu_1}D^{\mu_2}\cdots D^{\mu_N\}}\psi, \qquad (5)$$

$$O^{G,\{\mu_1,\cdots,\mu_N\}} = G^{\{\mu\mu_1}D^{\mu_2}\cdots D^{\mu_{N-1}}G^{\mu_N\mu\}}. \qquad (6)$$

Here and in the following we denote the generators of the flavour group $SU(n_f)$ by λ^α, and the covariant derivative by D^{μ_i}; in addition, it is understood that the symmetrical and traceless part is taken with respect to the indices in curly brackets. The functions $C^j_{k,N}(Q^2/\mu^2,a_s)$ are the coefficient functions for the above operators. Since the coefficient functions $C^\alpha_{k,N}$ of non-singlet operators depend trivially on the number α (see e.g. Ref. [12]) we will use for them the standard notation $C^{ns}_{k,N}$. Here and throughout the whole contribution we use the notation

$$a_s=\frac{g^2}{16\pi^2}=\frac{\alpha_s}{4\pi} \qquad (7)$$

for the QCD strong coupling constant. The direct application of the OPE of Eq. (3) to the Green function $T_{\mu\nu}$ leads to a formal expansion for $T_{\mu\nu}$ in terms of the variable $q\cdot p/Q^2=1/(2x)$ i.e. an expansion for unphysical $x\to\infty$,

$$i\int d^4z e^{iqz}\langle p,\text{nucl}|T\,(J_\mu(z)J_\nu(0))\,|\,\text{nucl},p\rangle =$$

$$\sum_{N,j}(\frac{1}{2x})^N\left[\left(g_{\mu\nu}-\frac{q_\mu q_\nu}{q^2}\right)C^j_{L,N}\left(\frac{Q^2}{\mu^2},a_s\right)-\left(g_{\mu\nu}+p_\mu p_\nu\frac{4x^2}{q^2}\right.\right.$$

$$\left.\left.+(p_\mu q_\nu+p_\nu q_\mu)\frac{2x}{q^2}\right)C^j_{2,N}\left(\frac{Q^2}{\mu^2},a_s\right)\right]A^j_{\text{nucl},N}(m_n^2/\mu^2)+\text{ higher twists},$$

$$\text{j}=ns,\psi,\text{G} \qquad (8)$$

where the spin averaged matrix elements are defined as

$$\langle p,\text{nucl}|O^{j,\{\mu_1,...,\mu_N\}}|\text{nucl},p\rangle = p^{\{\mu_1}...p^{\mu_N\}}A^j_{\text{nucl},N}(m_n^2/\mu^2) \qquad (9)$$

and m_n is the nucleon mass.

To perform the proper analytic continuation of the representation Eq. (8) to the physical region $0<x\le 1$ one applies a dispersion relation in the complex x plane to the Green function $T_{\mu\nu}$. For electron-nucleon scattering where we have hermitian currents J^μ one finds that the

Mellin moments of the structure functions F_k are expressed through the parameters of the operator product expansion (3)

$$\frac{1+(-1)^N}{2}M_{k,N}\equiv\frac{1+(-1)^N}{2}\int_0^1 dx\,x^{N-2}F_k(x,Q^2)=\sum_{\text{i}=ns,\psi,G}C^i_{k,N}\left(\frac{Q^2}{\mu^2},a_s\right)A^i_{\text{nucl},N} \qquad (10)$$

Please note that the odd Mellin moments of F_k are not fixed by this equation. However, all moments in the complex N plane are fixed by analytic continuation from the even Mellin moments when all the even moments are known. This means that the structure functions in x-space, $0<x\le 1$, can be found by means of the inverse Mellin transformation when the (infinite set of) even moments are known.

The Q^2-dependence of the coefficient functions can be studied by the use of the renormalization group equations

$$\left[\mu^2\frac{\partial}{\partial\mu^2}+\beta(a_s(\mu^2))\frac{\partial}{\partial a_s(\mu^2)}\right]C^i_{k,N}\left(\frac{Q^2}{\mu^2},a_s(\mu^2)\right) = C^j_{k,N}\left(\frac{Q^2}{\mu^2},a_s(\mu^2)\right)\gamma^{ji}_N(a_s(\mu^2))$$

$$\text{, i,j}=\psi,\text{G} \qquad (11)$$

$$\left[\mu^2\frac{\partial}{\partial\mu^2}+\beta(a_s(\mu^2))\frac{\partial}{\partial a_s(\mu^2)}\right]C^{ns}_{k,N}\left(\frac{Q^2}{\mu^2},a_s(\mu^2)\right) = C^{ns}_{k,N}\left(\frac{Q^2}{\mu^2},a_s(\mu^2)\right)\gamma^{ns}_N(a_s(\mu^2)) \qquad (12)$$

where Eq. (11) represents the singlet sector where quark and gluon operators mix under renormalization, and Eq. (12) is the non-singlet equation. $\beta(a)$ is the beta-function that determines the renormalization scale dependence of the renormalized coupling constant. It is known at three loops [19] in the $\overline{\text{MS}}$ scheme

$$\begin{aligned}
\frac{\partial a_s}{\partial\ln\mu^2} &\equiv \beta(a_s)=-\beta_0a_s^2-\beta_1a_s^3-\beta_2a_s^4+O(a_s^5),\\
\beta_0 &= (\frac{11}{3}C_A-\frac{4}{3}T_Fn_f)\\
\beta_1 &= (\frac{34}{3}C_A^2-4C_FT_Fn_f-\frac{20}{3}C_AT_Fn_f)\\
\beta_2 &= (\frac{2857}{54}C_A^3+2C_F^2T_Fn_f-\frac{205}{9}C_FC_AT_Fn_f-\\
&\quad -\frac{1415}{27}C_A^2T_Fn_f+\frac{44}{9}C_FT_F^2n_f^2+\frac{158}{27}C_AT_F^2n_f^2)
\end{aligned} \qquad (13)$$

where $C_F=\frac{4}{3}$ and $C_A=3$ are the Casimir operators of the fundamental and adjoint representations of the colour group $SU(3)$, $T_F=\frac{1}{2}$ is the trace normalization of the fundamental representation and n_f is the number of (active) quark flavours. The anomalous dimensions $\gamma_N(a_s)$ determine the renormalization scale dependence of the operators, that is

$$\frac{d}{d\ln\mu^2}O_R^{j,\{\mu_1,...,\mu_N\}} \equiv -\gamma_N^{ji}(a_s)\,O_R^{i,\{\mu_1,...,\mu_N\}}, \qquad \text{i,j}=\psi,\text{G} \qquad (14)$$

$$\frac{d}{d\ln\mu^2}O_R^{ns,\{\mu_1,...,\mu_N\}} \equiv -\gamma_N^{ns}(a_s)\,O_R^{ns,\{\mu_1,...,\mu_N\}}. \qquad (15)$$

We define renormalized operators in terms of bare operators as $O_R=Z\,O_B$ and find

$$\frac{d}{d\ln\mu^2}O_R=\left(\frac{d}{d\ln\mu^2}Z\right)O_B=\left(\frac{d}{d\ln\mu^2}Z\right)Z^{-1}O_R \quad\Rightarrow\quad \gamma=-\left(\frac{d}{d\ln\mu^2}Z\right)Z^{-1} \qquad (16)$$

where it is understood that in the singlet case Z represents a matrix Z^{ij}. The renormalization group equations are solved in the standard form

$$C^{ns}_{k,N}\left(\frac{Q^2}{\mu^2}, a_s(\mu^2)\right) = C^{ns}_{k,N}(1, a_s(Q^2)) \times \exp\left(-\int_{a_s(\mu^2)}^{a_s(Q^2)} da'_s \frac{\gamma^{ns}_N(a'_s)}{\beta(a'_s)}\right) \qquad (17)$$

The solution for the singlet equations has a similar form but since one gets the exponential of a matrix of anomalous dimensions one has to define the exponential properly in the singlet case (i.e. a T-ordered exponential, see e.g. Ref. [20]). Here $a_s(Q^2) \equiv a_s(Q^2/\Lambda^2_{\overline{\rm MS}})$ is the renormalized (i.e. running) coupling constant at the renormalization scale Q^2 and $\Lambda_{\overline{\rm MS}}$ is the fundamental scale of QCD in the $\overline{\rm MS}$-scheme. In practice one may use the DGLAP evolution equations [21] for matrix elements of operators at the scale $\mu^2 = Q^2$ (i.e. Q^2-dependent parton distributions) instead of the renormalization group equations for the coefficient functions (for perturbative solutions of the DGLAP equations in moment space see e.g. Refs. [3, 22]).

We will now discuss the method [23] for the calculation of anomalous dimensions and coefficient functions in considerable detail as it applies to the singlet sector. Let us first elaborate on some details specific to the dimensional regularization[24] and the minimal subtraction scheme [25], and it's standard modification, the $\overline{\rm MS}$-scheme [2], which form a modern basis for multiloop calculations in QCD. We use the symbol a_s for the renormalized coupling constant and a_b for the bare coupling constant. Although renormalization constants Z contain poles in ε in D= $4 - 2\varepsilon$ dimensions, anomalous dimensions are finite as D$\to$ 4. This fact gives expressions for the higher poles of Z in terms of the first poles of Z. To see this we write Eq. (16) as

$$\gamma Z = -\left(\frac{d}{d\ln\mu^2} Z(a_s, \frac{1}{\varepsilon})\right) = -\left(\frac{\partial}{\partial a_s} Z\right) \frac{da_s}{d\ln\mu^2} = -\left(\frac{\partial}{\partial a_s} Z\right) [-\varepsilon a_s + \beta(a_s)] \qquad (18)$$

where $\beta(a_s)$ is the 4-dimensional beta function of Eq. (13) and $[-\varepsilon a + \beta(a)]$ is the beta function in $4 - 2\varepsilon$ dimensions. This latter function receives no higher order corrections in ε due to the form of renormalization factors in the minimal subtraction scheme. The factors Z^{ij} are calculated as series in a_s, and have the well known form

$$Z^{ij} = Z^{ij(0)} + Z^{ij(1)}(a_s)/\varepsilon + Z^{ij(2)}(a_s)/\varepsilon^2 + \cdots, \qquad i, j = \psi, G$$

with $Z^{\psi\psi(0)} = Z^{GG(0)} = 1$, $Z^{\psi G(0)} = Z^{G\psi(0)} = 0$. ¿From equation (18) and the form of the factors Z^{ij} it follows that the anomalous dimensions are expressed through the coefficients in front of the first poles of Z as

$$\gamma^{ij} = a_s\left(\frac{\partial}{\partial a_s} Z^{ij(1)}(a_s)\right) \qquad i, j = \psi, G \qquad (19)$$

where $Z^{ij(1)}(a_s)$ was defined as the order $1/\varepsilon$ part of Z^{ij}. The coefficients of higher poles in Z can then be expressed in terms of γ^{ij} by substituting the expression for γ^{ij} back into equation (18).

The operator product expansion of Eq. (3) is an operator statement and both the coefficient functions $C^i_{k,N}$ and the anomalous dimensions γ^{ij}_N of the operators are functions and do therefore not depend on the hadronic states of the Green function to which one wishes to apply the OPE. The information on the hadronic target is contained in the operator matrix elements A^i_N in Eq. (9) which are generally not calculable perturbatively. It is therefore standard to consider

simpler Green functions with quarks and gluons as external particles, instead of the physical nucleon states, in the calculation of coefficient functions and anomalous dimensions. In this case the Green functions can be calculated in perturbation theory as well as the operator matrix elements and the anomalous dimensions and coefficient functions can be extracted as will be shown below in detail.

Let us consider the following 4-point Green functions

$$T^{q\gamma q\gamma}_{\mu\nu}(p, q) = i \int d^4z e^{iqz} \langle p, \text{quark}|T\left(J_\mu(z) J_\nu(0)\right)| \text{ quark}, p\rangle \qquad (20)$$

$$T^{g\gamma g\gamma}_{\mu\nu}(p, q) = i \int d^4z e^{iqz} \langle p, \text{gluon}|T\left(J_\mu(z) J_\nu(0)\right)| \text{ gluon}, p\rangle \qquad (21)$$

where the label γ is used to indicate an external photon, q indicates an external quark and g an external gluon. Spin and colour averaging for the quark and gluon states is assumed. Analogously to the decomposition of the hadronic tensor $W_{\mu\nu}$ in terms of F_2 and F_L we decompose the Green functions $T_{\mu\nu}$ in terms of T_L and T_2. Applying the OPE to $T^{q\gamma q\gamma}$ and $T^{g\gamma g\gamma}$ we find the following equations for the renormalized Green functions

$$T^{q\gamma q\gamma}_k(p, q, a_s, \mu^2, \varepsilon) =$$
$$\sum_{N=2}^{\infty} \left(\frac{1}{2x}\right)^N \left[\left(C^{\psi}_{k,N}(a_s, \frac{Q^2}{\mu^2}, \varepsilon) Z^{\psi\psi}_N(a_s, \frac{1}{\varepsilon}) + C^G_{k,N}(a_s, \frac{Q^2}{\mu^2}, \varepsilon) Z^{G\psi}_N(a_s, \frac{1}{\varepsilon})\right) A^{\psi}_{\text{quark},N}(a_s, \frac{p^2}{\mu^2}, \varepsilon)\right.$$
$$\left. + \left(C^{\psi}_{k,N}(a_s, \frac{Q^2}{\mu^2}, \varepsilon) Z^{\psi G}_N(a_s, \frac{1}{\varepsilon}) + C^G_{k,N}(a_s, \frac{Q^2}{\mu^2}, \varepsilon) Z^{GG}_N(a_s, \frac{1}{\varepsilon})\right) A^{G}_{\text{quark},N}(a_s, \frac{p^2}{\mu^2}, \varepsilon)\right] + O(p^2) \quad (22)$$

$$T^{g\gamma g\gamma}_k(p, q, a_s, \mu^2, \varepsilon) =$$
$$\sum_{N=2}^{\infty} \left(\frac{1}{2x}\right)^N \left[\left(C^{\psi}_{k,N}(a_s, \frac{Q^2}{\mu^2}, \varepsilon) Z^{\psi G}_N(a_s, \frac{1}{\varepsilon}) + C^G_{k,N}(a_s, \frac{Q^2}{\mu^2}, \varepsilon) Z^{GG}_N(a_s, \frac{1}{\varepsilon})\right) A^{G}_{\text{gluon},N}(a_s, \frac{p^2}{\mu^2}, \varepsilon)\right.$$
$$\left. + \left(C^{\psi}_{k,N}(a_s, \frac{Q^2}{\mu^2}, \varepsilon) Z^{\psi\psi}_N(a_s, \frac{1}{\varepsilon}) + C^G_{k,N}(a_s, \frac{Q^2}{\mu^2}, \varepsilon) Z^{G\psi}_N(a_s, \frac{1}{\varepsilon})\right) A^{\psi}_{\text{gluon},N}(a_s, \frac{p^2}{\mu^2}, \varepsilon)\right] + O(p^2) \quad (23)$$

where k =2,L, $a_s \equiv a_s(\mu^2/\Lambda^2)$ and it is understood that the l.h.s. is renormalized by substituting the bare coupling constant in terms of the renormalized one,

$$a_b = a_s - \frac{\beta_0}{\varepsilon} a_s^2 + (\frac{\beta_0^2}{\varepsilon^2} - \frac{\beta_1}{2\varepsilon}) a_s^3 + O(a_s^4) \qquad (24)$$

The terms $O(p^2)$ in the r.h.s. of Eqs. (22) and (23) indicate higher twist contributions. The renomalization factors for the external quark and gluon lines are overall factors on both sides of the equations and are omited. The coefficient functions on the r.h.s are renormalized quantities. The matrix elements A^i_N are the matrix elements of *bare* operators and are defined as in Eq. (9) with the nucleon states replaced by the appropriate quark or gluon states.

It is known that the gauge invariant operators O^ψ and O^G mix under renormalization with unphysical operators (that are BRST variations of some operators or that vanish by the equations of motion) [18, 6, 26]. But physical matrix elements (i.e. on-shell matrix elements with physical polarizations) of such unphysical operators vanish. Since the method that is described below deals with physical matrix elements we omited the unphysical operators in Eqs. (22) and (23).

Starting from Eqs. (22) and (23), the anomalous dimensions and the coefficient functions are calculated using the method of projections of Ref. [23]. It reduces the calculation of (moments of) coefficient functions and anomalous dimensions to the calculation of diagrams of the propagator type instead of the 4-point diagrams that contribute to $T_{\mu\nu}$. This method relies heavily on the use of dimensional regularization and the minimal subtraction scheme and implicitly involves a considerable rearrangement of infrared and ultraviolet divergences.

The method consists of applying the following projection operator to both sides of Eqs. (22) and (23).

$$\mathcal{P}_N \equiv \left[\frac{q^{\{\mu_1} \cdots q^{\mu_N\}}}{N!} \frac{\partial^N}{\partial p^{\mu_1} \cdots \partial p^{\mu_N}} \right] \Bigg|_{p=0} \tag{25}$$

Here $q^{\{\mu_1} \cdots q^{\mu_N\}}$ is the harmonic (i.e. symmetrical and traceless) part of the tensor $q^{\mu_1} \cdots q^{\mu_N}$ (see next section). The operator $\mathcal{P}_N$ is applied to the integrands of all Feynman diagrams (nullifying p before taking the limit $\varepsilon \to 0$, to dimensionally regularize the infrared divergences as $p \to 0$ for individual diagrams). It is important to realize that this operation does not act on the renormalization constants Z_N^{ij} and the coefficient functions on the r.h.s. of Eqs. (22), (23). It does however act on the matrix elements A_N^i. The nullification of p has the effect that of all the diagrams that contribute to the perturbative expansion of A_N^i only the tree level terms (i.e. with no loops) survive since all diagrams containing loops become massless tadpole diagrams. Massless tadpole diagrams are put to zero in dimensional regularization. Furthermore, the N^{th} order differentiation in the operator $\mathcal{P}_N$ has the effect that $\mathcal{P}_N$ projects out only the N^{th} moment since of all the factors $1/(2x)^{N'}$ only $1/(2x)^N$ gives a non zero contribution after nullifying p. On the left hand side the effect of $\mathcal{P}_N$ is to effectively reduce the 4-point diagrams that contribute to $T_{\mu\nu}$ to 2-point diagrams (this follows from the nullification of the momentum p), which drastically simplifies the calculation. We apply the operator $\mathcal{P}_N$ after the tensor structures $2, L$ have been projected out because the operator $\mathcal{P}_N$ would mutilate the tensor structure of $T_{\mu\nu}$. In the projector $\mathcal{P}_N$ we use the harmonic tensor $q^{\{\mu_1} \cdots q^{\mu_N\}}$ to remove higher twist contributions (the $O(p^2)$ terms in Eqs. (22) and (23)) that after differentiation with respect to p^μ survive as terms proportional to the metric tensor.

After application of the projection operator $\mathcal{P}_N$ to Eqs. (22) and (23) we have

$$T_{k,N}^{\mathrm{q\gamma q\gamma}}\left(\frac{Q^2}{\mu^2}, a_s, \varepsilon\right) = \left(C_{k,N}^{\psi}\left(a_s, \frac{Q^2}{\mu^2}, \varepsilon\right) Z_N^{\psi\psi}\left(a_s, \frac{1}{\varepsilon}\right) + C_{k,N}^{G}\left(a_s, \frac{Q^2}{\mu^2}, \varepsilon\right) Z_N^{G\psi}\left(a_s, \frac{1}{\varepsilon}\right) \right) A_{\mathrm{quark},N}^{\psi,\mathrm{tree}}(\varepsilon) \tag{26}$$

$$T_{k,N}^{\mathrm{g\gamma g\gamma}}\left(\frac{Q^2}{\mu^2}, a_s, \varepsilon\right) = \left(C_{k,N}^{\psi}\left(a_s, \frac{Q^2}{\mu^2}, \varepsilon\right) Z_N^{\psi G}\left(a_s, \frac{1}{\varepsilon}\right) + C_{k,N}^{G}\left(a_s, \frac{Q^2}{\mu^2}, \varepsilon\right) Z_N^{GG}\left(a_s, \frac{1}{\varepsilon}\right) \right) A_{\mathrm{gluon},N}^{G,\mathrm{tree}}(\varepsilon) \tag{27}$$

where $k = 2, L$ and we defined

$$T_{k,N}\left(\frac{Q^2}{\mu^2}, a_s, \varepsilon\right) \equiv \frac{q^{\{\mu_1} \cdots q^{\mu_N\}}}{N!} \frac{\partial^N}{\partial p^{\mu_1} \cdots \partial p^{\mu_N}} T_k(p, q, a_s, \mu^2, \varepsilon) \Big|_{p=0} . \tag{28}$$

It should be understood that (26) and (27) represent a large coupled system of equations when both sides are expanded in powers of a_s and ε (i.e. C is expanded in positive powers of ε and Z is expanded in negative powers of ε).

After the calculation of $T^{\mathrm{q\gamma q\gamma}}$ and $T^{\mathrm{g\gamma g\gamma}}$ in the order a_s^3 and the determination of the tree level matrix elements $A_N^{j,\mathrm{tree}}$ one can solve Eqs. (26) and (27) simultaneously to obtain C_k^ψ, C_k^G, $Z^{\psi\psi}$ and $Z^{\psi G}$ in order a_s^3 but, unfortunately, $Z^{G\psi}$ and Z^{GG} only in the order a_s^2. This

limitation follows directly from the fact that C_k^ψ starts from the order a_s^0 but C_k^G starts from order a_s since the photon couples *directly* only to quarks. In solving the equations it is essential that all poles of the Z factors are fully expressed in terms of the anomalous dimensions as was discussed in the beginning of this section. Coefficient functions and operator matrix elements are finite as $\varepsilon \to 0$ but one must make sure that sufficiently high powers in ε are taken into account. For example, one should consider order ε^2 contributions for C_k^ψ at order a_s. We stress that by calculating only propagator type diagrams in the l.h.s. of Eqs. (26) and (27) we can get both renormalization constants of operators and coefficient functions.

To obtain $Z^{G\psi}$ and Z^{GG} in order a_s^3 we calculated two more unphysical Green functions $T^{\mathrm{q\phi q\phi}}$ and $T^{\mathrm{g\phi g\phi}}$, in which the photon is replaced by an external scalar particle ϕ that couples *directly* only to gluons. The vertices that describe the coupling between the external scalar field ϕ and the gluons follow from adding the simplest gauge invariant interaction term $\phi G_{\mu\nu}^a G_a^{\mu\nu}$ (where $G_{\mu\nu}^a$ is the QCD field strength tensor) to the QCD Lagrangian. For the Green functions $T^{\mathrm{q\phi q\phi}}$ and $T^{\mathrm{g\phi g\phi}}$ an OPE similar to (3) exists with the same operators but with different coefficient functions C_ϕ^G and C_ϕ^ψ, where C_ϕ^ψ starts from the order a_s and C_ϕ^G starts from the order a_s^0.

One can repeat the steps that led to Eqs. (26) and (27) for the Green function $T^{\mathrm{q\phi q\phi}}$ and $T^{\mathrm{g\phi g\phi}}$ but in addition, the external operators $G_{\mu\nu}^a G_a^{\mu\nu}$ have to be renormalized. After the calculation of $T_N^{\mathrm{q\phi q\phi}}$ and $T_N^{\mathrm{g\phi g\phi}}$ in the order a_s^3 one can obtain C_ϕ^G, C_ϕ^ψ, $Z^{G\psi}$ and Z^{GG} in the order a_s^3. Please note that the coefficients C_ϕ^G and C_ϕ^ψ are obtained as a byproduct and are not important for the physical process under consideration.

Summarizing, we apply the operator $\mathcal{P}_N$ for N=2,4,6,8 to 4 different Green functions, $T_k^{\mathrm{q\gamma q\gamma}}$, $T_k^{\mathrm{g\gamma g\gamma}}$, $T^{\mathrm{q\phi q\phi}}$ and $T^{\mathrm{g\phi g\phi}}$ and we sum over the physical spin polarizations of the external quarks and gluons. For the external quarks (in $T^{\mathrm{q\gamma q\gamma}}$ and $T^{\mathrm{q\phi q\phi}}$) the sum over the polarizations is performed by inserting the projection operator $\not{p}$ between the external quark legs and taking the trace over the strings of gamma matrices. For the external gluons (in $T_k^{\mathrm{g\gamma g\gamma}}$ and $T^{\mathrm{g\phi g\phi}}$) the sum over physical spins can be done by contracting the external gluon lines with $-g^{\alpha\beta} + (p^\alpha q^\beta + p^\beta q^\alpha)/p\cdot q - p^\alpha p^\beta q^2/(p\cdot q)^2$ in which the (on-shell) gluon has momentum p (with $p^2 = 0$). The presence of the extra powers of p poses considerable efficiency problems (the operator $\mathcal{P}_N$ will generate more than 3 times larger intermediate expressions as compared to the case of a simpler $g^{\alpha\beta}$ projection). Alternatively one may take the sum over physical gluon spins by contracting the external gluon lines with only $-g^{\alpha\beta}$ and adding external ghost contributions to the Green functions, $T_k^{\mathrm{h\gamma h\gamma}}$ to $T_k^{\mathrm{g\gamma g\gamma}}$ and $T^{\mathrm{h\phi h\phi}}$ to $T^{\mathrm{g\phi g\phi}}$, where the label h indicates an external ghost line. This procedure is identical to the standard use of ghost diagrams to remove unphysical polarizations of gluon propagators in the covariant gauge, and the ghost particle h is the same ghost that we use in closed loops. Although we now have to consider all diagrams that contribute to $T_k^{\mathrm{h\gamma h\gamma}}$ and $T^{\mathrm{h\phi h\phi}}$, and increase the total number of diagrams that we have to calculate, it still makes the computations more than a factor of 3 faster (since ghost diagrams are of a far simpler nature than gluon diagrams). We checked for the lowest moments that the two methods for taking the sum over the gluon spin polarizations gave the same results, but for the higher moments we only applied the ghost method.

The Feynman diagrams that we need to calculate are generated automatically with a special version of the diagram generator QGRAF[27]. The use of a Feynman diagram generator is very important since in total we need to calculate more than 10.000 3-loop diagrams for each value for the moment index N. For every class $\mathrm{q\gamma q\gamma}$, $\mathrm{q\phi q\phi}$ etc. the full set of diagrams is put into a single file using a dedicated database program MINOS that manages information about

thousands of diagrams and can be instructed to call other programs, giving them the proper information from a database file.

For the actual calculations we use programs written for the symbolic manipulation program FORM[28] to calculate colour factors for each diagram and bring the diagrams into a representation that explicitly contains information required at later steps in the calculation. For instance, this involves choosing automatically an optimal path (in most cases the shortest path) for the external momentum p to flow through each diagram (we are going to expand in p when the operator $\mathcal{P}_N$ is applied) and determining automatically the diagram's topology when p is nullified. This information, for all diagrams together, is kept in a single file and is accessible using MINOS. We instruct MINOS to run sequentially, one diagram at a time, a highly optimized FORM program that performs the explicit calculation i.e. it substitutes all the Feynman rules, it performs projections on the Lorentz structures of the Green functions, it Taylor-expands the diagram in the external momentum p (the depth of the expansion increases with the moment index N), it takes all the Dirac traces, contracts with the tensors $q^{\{\mu_1} \cdots q^{\mu_N\}}$ and finally calls the MINCER [29] integration package to perform the 3-loop scalar integrals of the massless propagator type (using the integration by parts algorithms published in Ref. [30]). The results together with some useful technical information about the calculation (such as the resources used) are again stored into a single file. MINOS will initiate the calculation of a next diagram as soon as the calculation of a previous diagram is completed without any need for human interference.

The complete set of the results of our calculations can be found in Ref. [13] where further details and an analysis of the results are given. The obtained 3-loop singlet anomalous dimensions and coefficient functions required the calculation of more than 10.000 3-loop diagrams. The calculation of these diagrams (for N=2,4,6,8) required more than the equivalent of 7500 hours on a 150 Mhz SGI Challenge workstation and at some instances 2 Gbyte of storage place for the intermediate stages in the calculation.

References

[1] D. Gross, F. Wilczek, Phys. Rev. D8 (1973) 3633; D9 (1974) 980.

[2] W.A. Bardeen, A.J. Buras, D.W. Duke, T. Muta, Phys. Rev. D 18 (1978) 3998.

[3] E.G. Floratos, D.A. Ross, C.T. Sachrajda, Nucl. Phys. B 129 (1977) 66, B 139 (1978) 545 (E); Nucl. Phys. B 152 (1979) 493.

[4] A. Gonzalez-Arroyo, C. Lopez, F.J. Yndurain, Nucl. Phys. B 153 (1979) 161;
A. Gonzalez-Arroyo, C. Lopez, Nucl. Phys. B 166 (1980) 429;
C. Lopez, F.J. Yndurain, Nucl. Phys. B 183 (1981) 157.

[5] W. Furmansky, R. Petronzio, Phys. Lett. B 97 (1980) 437;
G. Curci, W. Furmansky, R. Petronzio, Nucl. Phys. B 175 (1980) 27.

[6] R. Hamberg, W.L. van Neerven, Nucl. Phys. B 379 (1992) 143.

[7] D.W. Duke, J.D. Kimel, G.A. Sowell, Phys. Rev. D 25 (1982) 71;
A. Devoto, D.W. Duke, J.D. Kimel, G.A. Sowell, Phys. Rev. D 30 (1985) 541.

[8] D.I. Kazakov, A.B. Kotikov, Nucl. Phys. B 307 (1988) 721; Phys. Lett. B 291 (1992) 171.

[9] D.I. Kazakov, A.B. Kotikov, G. Parente, O.A. Sampayo J. Sanchez Guillen, Phys. Rev. Lett. 65 (1990) 1535; 65 (1990) 2921 (E).

[10] W.L. van Neerven, E. Zijlstra, Phys. Lett. B272 (1991) 127; Phys. Lett. B 273 (1991) 476; Nucl. Phys. B 383 (1992) 525.

[11] S.A. Larin, J.A.M. Vermaseren, Preprint NIKHEF-H/91-17 (Amsterdam, 1991); Z. Phys. C 57 (1993) 93.

[12] S.A. Larin, T. van Ritbergen, J.A.M. Vermaseren, Nucl. Phys. B 427 (1994) 41-52.

[13] S.A. Larin, P. Nogueira, T. van Ritbergen, J.A.M. Vermaseren, Preprint NIKHEF/96-010 (Amsterdam, 1996); hep-ph/9605317.

[14] B.L. Ioffe, Phys. Lett. 30B (1969), 123

[15] N. Christ, B. Hasslacher, A. Mueller, Phys. Rev. D6 (1972) 3543.

[16] A.J. Buras, Rev. Mod. Phys. 52 (1980) 199.

[17] E. Reya, Phys. Rep. 69 (1981) 195.

[18] J.C. Collins, Renormalization, Cambridge University Press, 1987.

[19] O.V. Tarasov, A.A. Vladimirov, A.Yu. Zharkov, Phys. Lett. B 93 (1980) 429;
S.A. Larin, J.A.M. Vermaseren, Phys. Lett. B 303 (1993) 334.

[20] M. Veltman, Diagrammatica, Cambridge University Press 1994, p. 44.

[21] G. Altarelli, G. Parisi, Nucl. Phys. B126 (1977) 298;
Yu. L. Dokshitzer, Sov. Phys. JETP 46 (1977) 641;
L.N. Lipatov, Sov. J. Nucl. Phys. 20 (1975) 94;
V.N. Gribov, L.N. Lipatov, Sov. J. Nucl. Phys. 15 (1972) 438, 675.

[22] R.K. Ellis, Z. Kunszt, E.M. Levin, Nucl. Phys. B 420 (1994) 517.

[23] S.G. Gorishny, S.A. Larin, F.V. Tkachov, Phys. Lett. B 124 (1983) 217;
S.G. Gorishny, S.A. Larin, Nucl. Phys. B 283 (1987) 452.

[24] G.'t Hooft, M. Veltman, Nucl. Phys. B 44 (1972) 189.

[25] G.'t Hooft, Nucl. Phys. B 61 (1973) 455.

[26] J. C. Collins, R.J. Scalise, Phys. Rev. D50 (1994) 4117;
B.W. Harris, J. Smith, Phys. Rev. D51 (1995) 4550.

[27] P. Nogueira, J. Comp. Phys. 105 (1993) 279.

[28] J.A.M. Vermaseren, Symbolic Manipulation with FORM, published by CAN (Computer Algebra Nederland), 1991.

[29] S.A. Larin, F.V. Tkachov, J.A.M. Vermaseren, Preprint NIKHEF-H/91-18 (Amsterdam, 1991).

[30] F.V. Tkachov, Phys. Lett. B100 (1981) 65; K.G. Chetyrkin, F.V. Tkachov, Nucl. Phys. B 192 (1981) 159; F.V. Tkachov, Teor. Mat. Fiz. 56 (1983) 350.

Future Measurement of the Longitudinal Proton Structure Function at HERA

L. Bauerdick[a], A. Glazov[b], M. Klein[b]
[a] DESY, Notkestraße 85, D-22607 Hamburg, Germany
[b] DESY-IfH Zeuthen, Platanenallee 6, D-15738 Zeuthen, Germany

Abstract: A study is presented of a possible future measurement of the longitudinal structure function $F_L(x, Q^2)$ with different proton beam energies at HERA.

1 Introduction

In the one-photon exchange approximation, the deep inelastic inclusive scattering (DIS) cross section is given by the expression

$$\frac{d\sigma}{dxdQ^2} = \frac{2\pi\alpha^2}{Q^4 x} \cdot [(2(1-y)+y^2)F_2(x,Q^2) - y^2 F_L(x,Q^2)]. \quad (1)$$

Here Q^2 is the squared four-momentum transfer, x is the Bjorken scaling variable and $y = Q^2/sx$ the inelasticity variable with $s = 4E_eE_p$ the centre of mass energy squared of the collision. The two form factors F_2 and F_L are related to the cross sections σ_T and σ_L of the scattering of transversely and longitudinally polarized virtual photons off protons. In the Quark Parton Model F_2 is the sum of quark and antiquark distributions in the proton weighted with the electric quark charges squared while F_L is predicted to be zero for spin 1/2 partons [1]. In Quantum Chromodynamics (QCD) F_L aquires a non zero value due to gluon radiation which is proportional to the strong coupling constant α_s [2] with possibly sizeable higher order corrections in QCD perturbation theory [3]. Measurements of F_L, expressed as the structure function ratio

$$R = \frac{F_L}{F_2 - F_L} = \frac{\sigma_L}{\sigma_T}, \quad (2)$$

were performed by various fixed target lepton-hadron scattering experiments at x values larger than 0.01 [4, 5].

A measurement of the longitudinal structure function at low x at HERA is important for a number of reasons:

- At lowest x the cross section measurement can not be uniquely interpreted as a determination of F_2 because the F_L contribution to the cross section becomes sizeable, see eq.1.

- A measurement of F_L and of F_2 represents an important test of QCD which uniquely describes the decomposition of the cross section into the F_2 and the F_L part based on a common set of parton distributions and NLO corrections [6]. In particular, the scaling violations of F_2 which at low x determine the gluon distribution are predicted to be in accord with F_L which is directly given by xg.
- The lowest Q^2 behaviour of F_2 is related to F_L or R: a hard input distribution leads to $R = 6.2\alpha_s(Q^2)/\pi$, independently of x while a soft distribution ,which implies approximate double logarithmic scaling of F_2, leads to a dependence of R on $\ln 1/x$ [7], see also [8].
- The F_L measurements are performed at lowest possible x where BFKL dynamics may show up. This may not affect F_2 in a sizeable way but may lead to F_L values predicted to be different by a factor of 2 from the standard DGLAP expectation [9].

The question is how precise one may hope to perform this measurement. This can be studied now more reliably than previously [10, 11] since the systematics of that measurement is better defined. This paper documents a study to measure F_L with a set of different proton beam energies. Similar conclusions were reached during this workshop in [12]. Data at lower electron beam energies E_e may be useful for systematic cross checks. Access to F_L with lowered electron energy, however, is even more complicated as about two times lower scattered electron energies have to be measured than with maximum E_e. Further information on R may be obtained from radiative events as originally proposed in [13].

2 Cross Section Measurement

A measurement of the longitudinal structure function requires to access the lowest possible scattered electron energies E'_e which approximately define y as $1 - E'_e/E_e$. The measurement accuracy improves with rising y like $1/y^2$, see eq.1. The kinematic range of the F_L measurement is a band in the Q^2, x plane of a y interval, between about 0.5 and 0.85, with a low Q^2 limit given by the maximum accepted polar angle of the scattered electron $\theta_e \simeq 177^\circ$ and a large Q^2 limit around 100 GeV^2. A measurement performed at several beam energy settings appropriately chosen permits to cover an x range at fixed Q^2 of about one order of magnitude. The smallest x values can be covered using highest energy data by the method introduced by H1 [14] which subtracts the F_2 contribution to the cross section assuming that F_2 is accurately described by NLO QCD.

The following sources of systematic errors of the high y cross section measurement were considered:

- The uncertainty of the scattered electron energy: using the kinematic peak and the π_0 mass reconstruction, the double angle method and Compton events one may assume a scale uncertainty of 0.5% which implies a cross section error of about 0.7% at high y.
- The polar angle measurement can be as accurate as 0.5 mrad, even independently of the event vertex reconstruction with hadron tracks, based on drift chambers and Silicon trackers. The resulting cross section uncertainty amounts to about 0.6%.

- The photoproduction background may cause an error of 2% which assumes a 10% control of the background. This should be possible using the electron tagger systems, the hadronic backward calorimeter sections and reducing the π_0 background part with tracking in front of calorimeters.
- At high y the radiative corrections are large [15] if the kinematics is reconstructed with the scattered electron. These get reduced due to possible track requirements or $E - p_z$ cuts which allows to study the effect of the radiative corrections. Moreover, with hadron calorimetry in backward direction one may use as well the hadronic final state to reconstruct the kinematics which then is much less affected by radiative effects. Altogether an uncertainty of 1% may remain.
- Various detector and analysis efficiencies give rise to an estimated uncertainty of 2%.
- At low E'_e the electron identification becomes difficult. For $E'_e \geq 6.5$ GeV an error of 1% has been achieved by the H1 Collaboration [14]. Refined cluster algorithms considering the highest energy cluster and the next high energy cluster can be employed and information on hadron deposition in the calorimeters be used. Here we assume an error of 1%.

Altogether it can be expected that a 3% cross section error is achievable owing to the large statistics envisaged for this measurement. This represents an improvement by a factor of 2 of the H1 result obtained at $y \simeq 0.7$ with data taken in 1994.

3 Longitudinal Proton Structure Function F_L

The estimated systematic cross section errors were converted into F_L measurement errors, see fig.1 (open points), which are typically 0.08 in absolute. At each Q^2 two or three rather precise F_L measurements can be obtained at different x for the set of energies considered. Some of the bins are accessed with more than one beam energy combination. The beam energies finally chosen should include smallest and largest possible proton beam energies because of the measurement accuracy and x range. An important parameter of the measurement accuracy is the minimum electron energy E'_e which was assumed to be 5 GeV. No use was made in the analysis of a possible reduction of the F_L errors by the cross calibration of the measurement results at low y where the sensitivity to F_L is negligible.

At lowest x information on F_L can be obtained using the F_2 subtraction method [14]. The result of a corresponding study for the highest beam energy is illustrated in fig.1 (closed points). The assumptions on the cross section error were those as described above. In the standard method two independent cross section measurements have to be combined. Here errors have to be considered from one data set only, i.e. those from the large and the low y region. These partially are compensating with the exception of the electron energy miscalibration. This, however, leads to a very distinguished departure of F_2 at low y from any possible QCD behaviour. Therefore it can be constrained further in the required QCD analysis of F_2 giving finally rise to an estimated 1.5% accuracy of the extrapolated F_2. Finally, the uncertainty of the QCD fit to F_2 and its extrapolation to high y were estimated to leave a residual 2% error of the subtracted F_2 cross section part.

The subtraction method can of course be applied to all data sets. The data at the present HERA energies have shown already that the QCD assumption on F_2 will be justified for the lower energy data since these are limited to relatively larger x, at fixed Q^2. The estimated F_L errors of the subtraction method and of the data comparison method are similar which should enable important systematic cross checks since the subtraction method depends on one energy data set only while the standard method uses at least two. These were not used here for any possible error reduction which would have been difficult to model.

4 Conclusions

A measurement of the longitudinal proton structure function can be performed at HERA with runs at ≥ 4 different proton energies with luminosities per beam of about 10 pb^{-1}. Such a dedicated measurement series is estimated to determine F_L for Q^2 values between about 4 and 100 GeV^2 with systematic errors of $\simeq 0.08$ for one order of magnitude in x at given Q^2. This accuracy is challenging but the measurement is of fundamental theoretical interest.

References

[1] C.G. Callan and D. Gross, Phys.Rev.Lett. **22**(1969)156;

[2] G.Altarelli and G.Martinelli, Phys.Lett.**B76**(1978)89;

[3] E.B. Zijlstra and W. van Neerven, Nucl.Phys. **B383**(1992)525;

[4] A.Bodek, Contribution to the Proceedings of the 4th International Conference on Deep Inelastic Scattering, Rome, April 1996, to appear, and references cited therein;

[5] A.Milstaijn, NMC Collaboration, Contribution to the Proceedings of the 4th International Conference on Deep Inelastic Scattering, Rome, April 1996, to appear;

[6] J. Blümlein and S. Riemersma, these proceedings;

[7] F.J. Yndurain, FTUAM 96-12(1996), Nucl.Phys.to be published;

[8] R.S. Thorne, these proceedings;

[9] R. Peschanski and G. Salam, these proceedings;

[10] J. Blümlein et al., Proc. HERA Workshop 1987, ed. by R. Peccei, Vol.1, p.67;

[11] A.M. Cooper-Sarkar et al; Proc. HERA Workshop 1987, ed. by R. Peccei, Vol.1, p.235 and Proc. HERA Workshop 1991, ed. by W. Buchmüller and G. Ingelman, Vol.1, p.155;

[12] H. Blaikley, M. Cooper-Sarkar and S. Dashu, Contribution to this workshop;

[13] M.W. Krasny, W. Placzek and H. Spiesberger, Proc. HERA Workshop 1991, ed. by W. Buchmüller and G. Ingelman, Vol.1, p.171;

[14] H1 Collaboration, *Determination of the Longitudinal Structure Function F_L at Low x at HERA*, Contributions to the Rome and Warsaw Conferences, 1996, to be published;

[15] D.Yu. Bardin et al., these proceedings;

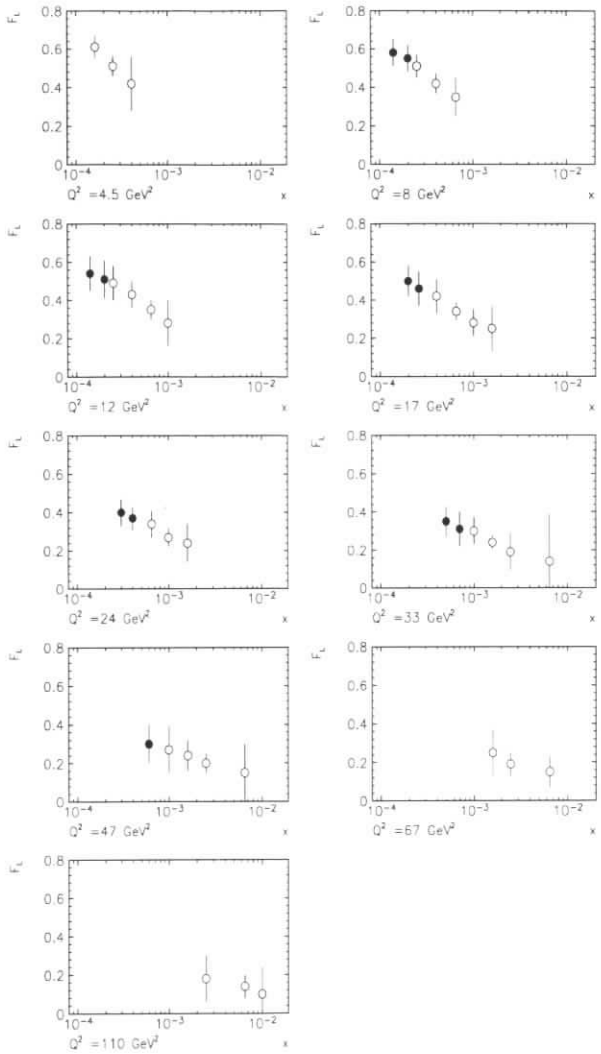

Figure 1: Estimated total accuracy of a measurement of the longitudinal structure function $F_L(x, Q^2)$ simulating data for an electron beam energy of 27.5 GeV and proton beam energies of 250, 350, 450 and 820 GeV with luminosities of 10 pb^{-1} per beam energy setting (open points). The closed points at lowest x represent the result of a simulation study using the method to determine F_L after subtraction of F_2. These points are based on the highest energy data set.

QCD corrections to $F_L(x, Q^2)$

Johannes Blümlein and Stephan Riemersma

DESY-Zeuthen, Platanenallee 6, D-15735 Zeuthen, Germany

Abstract: We perform a numerical study of the QCD corrections to the structure function $F_L(x, Q^2)$ in the HERA energy range. The K-factors are of $O(30\%)$ and larger in parts of the kinematic range. The relative corrections to $F_L^{c\bar{c}}$ turn out to be scale dependent and partially compensate contributions to the massless terms.

The longitudinal structure function in deep inelastic scattering, $F_L(x, Q^2)$, is one of the observables from which the gluon density can be unfolded. In leading order (LO) [1] it is given by

$$F_L^{ep}(x, Q^2) = \frac{\alpha_s(Q^2)}{\pi} \left\{ \frac{4}{3} c_{L,1}^q(x) \otimes F_2^{ep}(x, Q^2) + 2 \sum_q c_{L,1}^g(x, Q^2) \otimes [xG(x, Q^2)] \right\} \tag{1}$$

with

$$c_{L,1}^q(x) = x^2 \qquad c_{L,1}^g(x) = x^2(1-x), \tag{2}$$

and $\otimes$ denoting the Mellin convolution. Eq. (1) applies for light quark flavours. Due to the power behaviour of the coefficient functions $c_{L,1}^{q,g}(x)$, an approximate relation for the gluon density at small x

$$xG(x, Q^2) \simeq \frac{3}{5} \times 5.85 \left\{ \frac{3\pi}{4\alpha_s(Q^2)} F_L(0.4x, Q^2) - \frac{1}{2} F_2(0.8x, Q^2) \right\}, \tag{3}$$

has been used to derive a simple estimate for $xG(x, Q^2)$ in the past [2]. Heavy quark contributions and the next-to-leading order (NLO) QCD corrections complicate the unfolding of the gluon density using $F_L(x, Q^2)$ and have to be accounted for in terms of K-factors. In the present note, these contributions are studied numerically for the HERA energy range.

The NLO corrections for the case of light quark flavours were calculated in ref. [3] and the LO and NLO contributions for the heavy flavour terms were derived in refs. [4] and [5], respectively. While in LO the heavy flavour part of $F_L(x, M^2)$ is only due to $\gamma^* g$ fusion, in NLO also light quark terms contribute. Moreover, the choice of the factorization scale M^2 happens to affect $F_L^{Q\overline{Q}}(x, M^2)$ substantially.

Light flavour contributions

The leading order contributions to $F_L(x, Q^2)$ are shown in Figure 1 for $x \geq 10^{-4}$ and $10 \leq Q^2 \leq 500$ GeV^2. Here and in the following we refer to the CTEQ parametrizations [6] and assume $N_f = 4$. We also show the quarkonic contributions which are suppressed by one order of magnitude against the gluonic ones in the small x range. The ratio of the NLO/LO contributions

is depicted in figure 2. Under the above conditions, it exhibits a fixed point at $x \sim 0.03$. Below, the correction grows for rising Q^2 from $K = 0.9$ to 1 for $x = 10^{-4}$, $Q^2 \epsilon [10, 500]$ GeV^2. Above, its behaviour is reversed. The correction factor K rises for large values of x. For $x \sim 0.3$ it reaches e.g. 1.4 for $Q^2 = 10$ GeV^2. In NLO the quarkonic contributions are suppressed similarly as in the LO case at small x and contribute to F_L by 15% if only light flavours are assumed.

Heavy flavour contributions

The heavy flavour contributions to F_L are shown in figures 3 and 4, comparing the results for the choices of the factorization scale $M^2 = 4m_c^2$ and $M^2 = 4m_c^2 + Q^2$, with $m_c = 1.5$ GeV. Here we used again parametrization [6] for the description of the parton densities but referred to three light flavours only unlike the case in the previous section. The comparison of Figures 3a and 4a shows that the NLO corrections are by far less sensitive to the choice of the factorization scale than the LO results. Correspondingly the $K_{c\bar{c}}$–factors $F_L^{c\bar{c}}(NLO)/F_L^{c\bar{c}}(LO)$ are strongly scale dependent. Note that the ratios $K_{c\bar{c}}$ and K behave different and compensate each other partially. Thus the overall correction depends on the heavy-to-light flavour composition of $F_L(x, Q^2)$.

In summary we note that the NLO corrections to F_L are large. Partial compensation between different contributions can emerge. For an unfolding of the gluon density from $F_L(x, Q^2)$ the NLO corrections are indispensable.

References

[1] A. Zee, F. Wilczek, and S.B. Treiman, Phys. Rev. **D10** (1974) 2881.

[2] A. Cooper–Sarkar, G. Ingelman, K.R. Long, R.G. Roberts, and D.H. Saxon, Z. Phys. **C39** (1988) 281;
R.G. Roberts, The structure of the proton, (Cambridge, University Press, 1990).

[3] E. Zijlstra and W.L. van Neerven, Nucl. Phys. **B383** (1992) 525; S. Larin and J. Vermaseren, Z. Phys. **C57** (1993) 93.

[4] E. Witten, Nucl. Phys. **B104** (1976) 445.

[5] E. Laenen, S. Riemersma, J. Smith, and W.L. van Neerven, Phys. Lett. **B291** (1992) 325; Nucl. Phys. **B392** (1993) 162, 229.

[6] J. Botts, J. Morfin, J. Owens, J. Qiu, W. Tung, and H. Weerts, CTEQ collaboration, MSU–HEP 93/18 (1993).

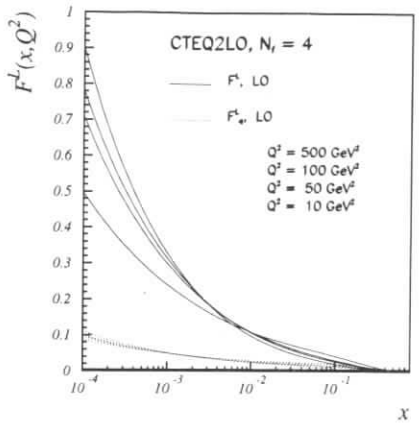

Figure 1 : Leading order contributions to $F_L(x, Q^2)$.

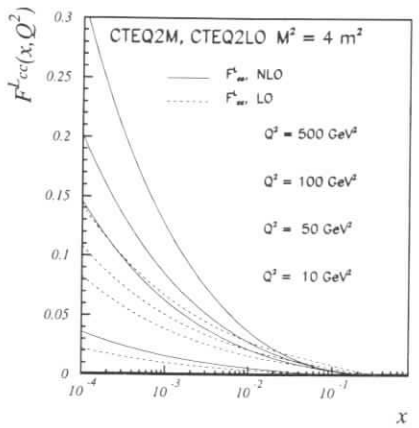

Figure 3a : LO and NLO $c\bar{c}$ contributions to $F_L(x, Q^2)$. The factorization scale is set to $M^2 = 4m_c^2$.

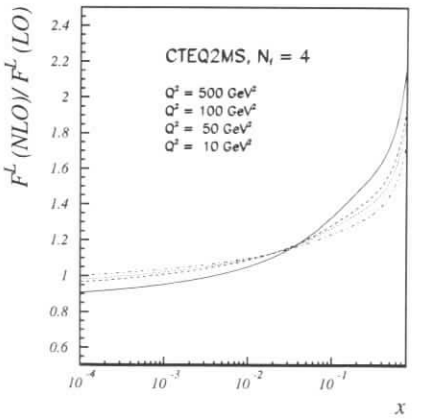

Figure 2 : The NLO correction factor for $F_L(x, Q^2)$ in the case of four light flavours.

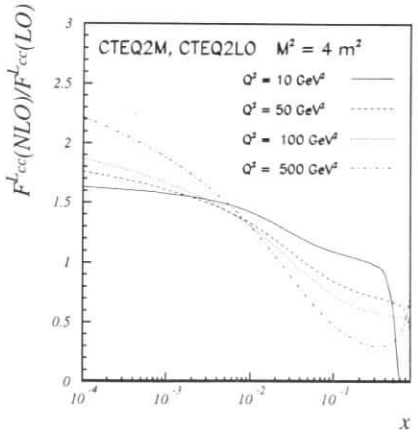

Figure 3b : Ratio of the NLO to LO $c\bar{c}$ contributions to $F_L(x, Q^2)$. The factorization scale is set to $M^2 = 4m_c^2$.

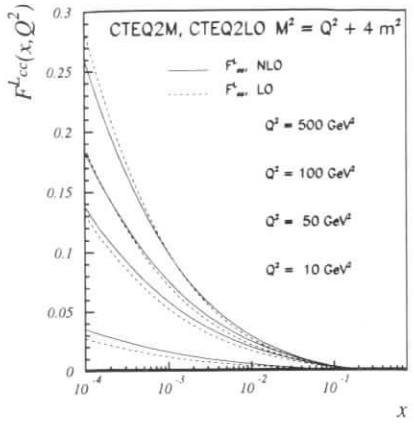

Figure 4a : Same as in Fig. 3a but for choosing the factorization scale $M^2 = 4m_c^2 + Q^2$.

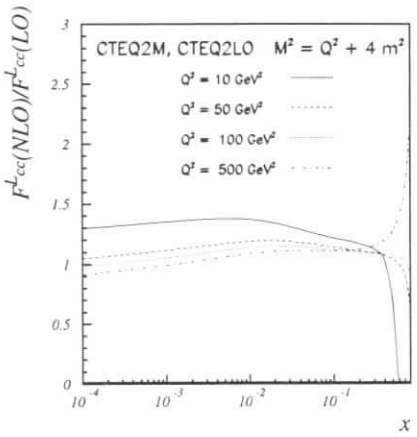

Figure 4b : Same as in Fig. 3b but for choosing the factorization scale $M^2 = 4m_c^2 + Q^2$.

IR-Renormalon Contribution to the Longitudinal Structure Function F_L

M. Meyer-Hermann[a], A. Schäfer[a], E. Stein[a]

[a] Institut für Theoretische Physik, J. W. Goethe-Universität, Postfach 11 19 32, D-60054 Frankfurt, Germany

Measurements of the ratio

$$R(x,Q^2) = \frac{\sigma_{\rm L}(x,Q^2)}{\sigma_{\rm T}(x,Q^2)} = \frac{F_2(x,Q^2)}{F_2(x,Q^2) - F_L(x,Q^2)} \left(1 + \frac{4M^2x^2}{Q^2}\right) - 1 \qquad (1)$$

which so far had only rather limited precision should improve substantially over the next years $F_L = F_2 - 2xF_1$. Phenomenological fits to the existing data suggest surprisingly large higher twist contributions. It would be interesting to get an estimate of the twist-4 part of F_L, which has been analyzed in the framework of operator product expansion. The corresponding matrix elements could not yet be evaluated, by relatively reliably methods like lattice gauge calculations or QCD sum rules. In this contribution we will derive an estimate for the nonsinglet part of the longitudinal structure function, denoted by F_L^{NS}, in the framework of the renormalon calculus [1].

The forward Compton-scattering-amplitude is calculated in the Borel-plane with an effective gluon propagator, taking only one gluon exchange into account. In the Landau gauge the effective gluon propagator resums arbitrary many quark loop insertions in the gluon line, which is an exact procedure in QED and reads in the Borel representation:

$$\mathcal{B}_{1/a_s}[a_s D^{ab}_{\mu\nu}(k)](u) \;=\; \delta^{ab} \frac{g_{\mu\nu} - \frac{k_\mu k_\nu}{k^2}}{k^2} \left(\frac{\mu^2 e^{-C}}{-k^2}\right)^{\beta_0 u} , \qquad (2)$$

$a_s = \alpha_s/(4\pi)$, C corrects for the renormalization scheme dependence and u is the Borel transformation parameter. In QCD the restriction to one gluon exchange is an exact procedure only in the large N_f-limit, where N_f is the number of quark-flavors. The next-to-leading N_f-order terms are approximated by naive-nonabelianization (NNA), which means to replace the one loop beta-function of QED by the QCD beta-function $\beta_0 = 11 - \frac{2}{3}N_f$ and corresponds to the replacement $N_f \to N_f - \frac{33}{2}$. The quality of this approximation has to be checked by comparing the NNA-perturbative-coefficients with the known exact ones.

The IR-renormalon-poles reflect the factorial growth of the perturbative series, which has to be interpreted as an asymptotic expansion. It has to be truncated after the minimal term, which determines the best accuracy one may achieve using perturbative expansion. As the Q^2 dependence of this ambiguity is power-like, it has been suggested to use it as an estimate of higher-twist contributions. Despite the fact that the conceptual basis for this approach is controversial, the procedure has given reasonable estimates [2, 3].

		Exact results	NNA approximants
$N=2$	$N_f=3$	$43.1254\,a_s^2+1386.59\,a_s^3$	$61.3333\,a_s^2+2168.\,a_s^3$
	$N_f=4$	$38.5822\,a_s^2+1032.7\,a_s^3$	$56.7901\,a_s^2+1858.71\,a_s^3$
$N=4$	$N_f=3$	$37.75\,a_s^2+1472.58\,a_s^3$	$46.08\,a_s^2+1984.51\,a_s^3$
	$N_f=4$	$34.3367\,a_s^2+1155.64\,a_s^3$	$42.6667\,a_s^2+1701.4\,a_s^3$
$N=6$	$N_f=3$	$32.9091\,a_s^2+1433.24\,a_s^3$	$36.3918\,a_s^2+1726.31\,a_s^3$
	$N_f=4$	$30.2134\,a_s^2+1152.07\,a_s^3$	$33.6961\,a_s^2+1480.03\,a_s^3$
$N=8$	$N_f=3$	$29.1822\,a_s^2+1373.83\,a_s^3$	$30.1249\,a_s^2+1519.45\,a_s^3$
	$N_f=4$	$26.9507\,a_s^2+1117.97\,a_s^3$	$27.8934\,a_s^2+1302.68\,a_s^3$

Table 1: *NNA approximants compared to the exact results [2].*

To obtain the NNA-approximated coefficient function $\tilde{C}_{L,N}(a_s)$ we have to calculate the first order a_s correction to the Compton scattering amplitude using the effective propagator (2). We get

$$\begin{aligned}\mathcal{B}[\tilde{C}_{L,N}(a_s)](s) &= C_F\left(\frac{\mu^2 e^{-C}}{Q^2}\right)^s \frac{8}{(2-s)(1-s)(1+s+N)}\frac{\Gamma(s+N)}{\Gamma(1+s)\Gamma(N)} \\ &= C_F\left(\frac{\mu^2 e^{-C}}{Q^2}\right)^s 8\frac{\Gamma(s+N)}{\Gamma(1+s)\Gamma(N)} \\ &\quad\times\left(\frac{1}{(2+N)(1-s)}-\frac{1}{(3+N)(2-s)}+\frac{1}{(2+N)(3+N)(1+s+N)}\right) \quad (3)\end{aligned}$$

Two IR-renormalons appear at $s=1$ and $s=2$ in the Borel-representation. The position of the UV-renormalon $s=-(1+N)$ depends on the moment N one is dealing with.

The NNA-approximated perturbative coefficients can be derived from (3) to all orders in a_s (setting the renormalization point to $\mu^2=Q^2$ and $C=-5/3$ for $\overline{\rm MS}$-scheme) and then be compared with the exact results derived by Larin et al. for the non singlet moments $N=2,\ 4,\ 6,\ 8$ (see table 1). In each order the leading N_f-term $N_f^{n-1}a_s^n$ agrees exactly, so that the result is exact for the first order a_s correction, which is not shown. The N_f-subleading terms are NNA approximated. It is interesting to observe that NNA is for higher moments a consistently better approximation than for lower ones. This is due to the fact that the most problematic property of NNA is to neglect multiple gluon emission. As such processes are important for small x we cannot expect our NNA structure functions to be correct in this region. Ever higher moments of the structure functions are less and less sensitive to their small-x behaviour and therefore the NNA should systematically improve.

As already mentioned the IR-renormalon poles in (3) reflect a factorial growth of the pertrubative series. This means that the perturbative expansion at best can be regarded as an asymptotic expansion. The general uncertainty in the perturbative prediction is then of the order of the minimal term in the expansion, which can be estimated either directly or by taking the imaginary part $\Im/\pi$ of the Borel transform. The leading IR-renormalon at $s=1$ gives rise to a Λ^2/Q^2 ambiguity for the asymptotic series. This uncertainty is easily transformed from the momentum-space to Bjorken-x:

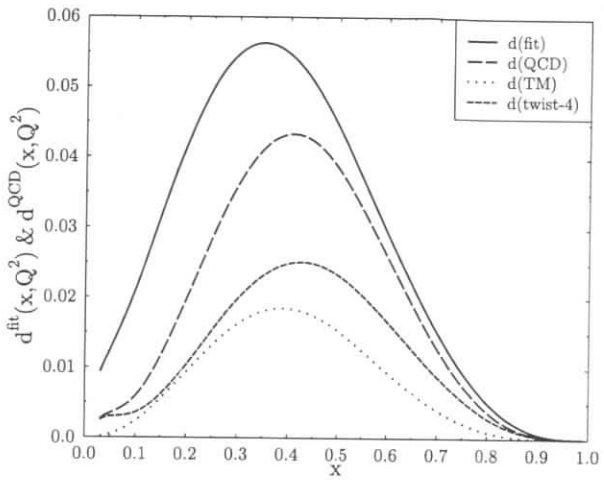

Figure 1: $\Lambda_{\overline{MS}}=250$ MeV, $Q^2=5$ GeV *and* $N_f=4$ *[2].*

$$F_L^{p-n}(x,Q^2)+\frac{4x^2M^2}{Q^2}F_2^{p-n}(x,Q^2)=4C_Fa_s(Q^2)\int_x^1\frac{dy}{y}\left(\frac{x}{y}\right)^2F_2^{p-n}(y,Q^2)+\mathcal{O}(a_s^2)$$
$$+4x^3\frac{M^2}{Q^2}\int_x^1\frac{dy}{y}F_2^{p-n}(y,Q^2)\pm\frac{8C_F}{\beta_0}\frac{\Lambda^2_{\overline{MS}}e^{5/3}}{Q^2}\left[F_2^{p-n}(x,Q^2)-2\int_x^1\frac{dy}{y}\left(\frac{x}{y}\right)^3F_2^{p-n}(y,Q^2)+\mathcal{O}(a_s)\right] \quad (4)$$

The first two terms are the standard convolution and the target mass correction respectively. The last term with undetermined sign is the calculated ambiguity, which we will use as an estimate of the twist-4 correction to F_L^{NS}.

In Figure 1 the experimental fit of the power corrections d^{fit} is compared with the QCD-calculation d^{QCD} (Eq. (4)) using an experimental fit for F_2, where we have shown target mass d^{TM} and twist-4 contribution $d^{twist-4}$ separately. We observe a rather large contribution coming from the IR renormalon estimate for the twist-4 part, which accounts for more than half of the discrepancy between the experimental fit and a prediction which takes into account the target mass correction only. In view of the fundamental objections concerning the used IR-renormalon method, the prediction of a large twist-4 contibution to F_L^{NS} in agreement with experimental results is a surprising success. It further supports the idea that, while the rigorous QCD calculations of higher twist contribution to F_L are not yet available, calculations like the one presented here may be used to predict the order of magnitude of power suppressed corrections.

References

[1] References may be found in [2, 3].

[2] E. Stein, M. Meyer-Hermann, L. Mankiewicz, A. Schäfer, Phys.Lett.B376 (1996) 177.

[3] M. Meyer-Hermann, M. Maul, L. Mankiewicz, E. Stein, A. Schäfer, *IR-Renormalon Contribution to the Polarized Structure Function* g_1, hep-ph/9605229, to appear in Phys.Lett.B.

The Heavy-Flavour Contribution to Proton Structure

K. Daum[a,b], S. Riemersma[c], B.W. Harris[d], E. Laenen[e], J. Smith[b,f]

[a] Rechenzentrum, Universität Wuppertal, Gaußstraße 20, D-42097 Wuppertal, Germany
[b] DESY, Notkestrasse 85, D-22603 Hamburg, Germany
[c] DESY-Zeuthen, Platanenallee 6 D-15738 Zeuthen, Germany
[d] Department of Physics, Florida State University, Tallahassee, Florida, 32306-3016, USA
[e] CERN Theory Division, CH-1211 Geneva 23, Switzerland
[f] Institute for Theoretical Physics, SUNY Stony Brook, NY 11794-3840, USA

Abstract: We present theoretical and experimental considerations pertaining to deeply inelastic heavy-flavour production. The various theoretical uncertainties in the cross section calculation are discussed. Cuts are imposed to determine the fraction of charm production accessible to the detectors. The production of charm at asymptotic Q^2 and bottom production are also covered. Experimental aspects include current charm production data analysis and prospects for future analyses including anticipated high precision and distinguishing photon-gluon fusion charm events from excitation from the charm parton density. The feasibility of measuring $F_2^{b\bar{b}}(x,Q^2)$ is investigated.

1 Introduction

Heavy-flavour production in deeply inelastic scattering (DIS) at HERA is now emerging as a very important means of studying proton structure. The ink is still drying on the first experimental reports of charm production from photon-mediated DIS at HERA [1, 2]. The next-to-leading order (NLO) calculations have also been published within the last four years. The inclusive calculation of the photon-mediated heavy-flavour structure functions $F_{2,L}^{\rm hq}(x,Q^2,m^2)$ [3], the inclusive single differential distribution $dF_{2,L}^{\rm hq}/dO$ [4] (O being the transverse momentum p_t of the heavy quark and the rapidity y), and the fully differential calculation [5] are now available for a complete NLO analysis of the photon-mediated heavy-flavour structure function.

In section 2, following a short review of the necessary formulae, we give event numbers for charm and bottom in bins of x and Q^2 and investigate the theoretical issues surrounding DIS heavy-flavour production. The primary sources of theoretical uncertainty include the imprecisely determined charm quark mass and renormalization and factorization scale dependences. Additional impediments to a clean extraction of the gluon density from heavy-flavour production include the effects of light-quark (u,d,s) initiated heavy-flavour production and the influence of the longitudinal heavy-flavour structure function $F_L^{\rm hq}(x,Q^2,m^2)$ upon the cross section results.

We investigate the effect of realistic cuts in p_t and pseudorapidity η on the cross section and determine acceptance probabilities as a function of x and Q^2. Charm production in the limit $Q^2 \gg m_c^2$ [6] is then discussed.

In section 3, we briefly summarize the analyses of charm production of the 1994 HERA data. These data allow for the determination of the source of the charm production, revealing the primary production mechanism at presently measured Q^2 values is photon-gluon fusion rather than stemming from the charm parton density. From the first measurement of the charm structure function $F_2^{c\bar{c}}$ at low x, the ratio $F_2^{c\bar{c}}/F_2$ is extracted.

Subsequently future experimental prospects are discussed. The current installation of the silicon vertex detectors at H1 will enable greater charm and bottom hadron detection efficiency. The anticipated luminosity of $500\,pb^{-1}$ will allow detailed studies of charm production dynamics. The transition from boson-gluon fusion of charm to excitation from the charm quark sea should become apparent as the accessible Q^2 grows. The predicted bottom quark production cross section will enable studies of $F_2^{b\bar{b}}/F_2^{c\bar{c}}$ as a function of x and Q^2 with reasonable precision.

2 Theoretical Aspects

2.1 Background

The reaction under study is

$$e^-(l) + P(p) \rightarrow e^-(l') + Q(p_1)(\bar{Q}(p_1)) + X\,, \tag{1}$$

where $P(p)$ is a proton with momentum p, $Q(p_1)(\bar{Q}(p_1))$ is a heavy (anti)-quark with momentum p_1 ($p_1^2 = m^2$) and X is any hadronic state allowed by quantum number conservation. The cross section may be expressed as

$$\frac{d^2\sigma}{dx\,dQ^2} = \frac{2\pi\alpha^2}{x\,Q^4}\left[(1+(1-y)^2)F_2^{\rm hq}(x,Q^2,m^2) - y^2 F_L^{\rm hq}(x,Q^2,m^2)\right]. \tag{2}$$

The inclusive structure functions $F_{2,L}^{\rm hq}$ were calculated to next-to-leading order (NLO) in Ref. [3]. The results can be written as

$$\begin{aligned} F_k(x,Q^2,m^2) &= \frac{Q^2\alpha_s(\mu^2)}{4\pi^2 m^2}\int_x^{z_{\rm max}}\frac{dz}{z}\left[e_H^2 f_g(\frac{x}{z},\mu^2)c_{k,g}^{(0)}\right] \\ &+ \frac{Q^2\alpha_s^2(\mu^2)}{\pi m^2}\int_x^{z_{\rm max}}\frac{dz}{z}\Big\{ e_H^2 f_g(\frac{x}{z},\mu^2)(c_{k,g}^{(1)} + \bar{c}_{k,g}^{(1)}\ln\frac{\mu^2}{m^2}) \\ &+ \sum_{i=q,\bar{q}}\left[e_H^2 f_i(\frac{x}{z},\mu^2)(c_{k,i}^{(1)} + \bar{c}_{k,i}^{(1)}\ln\frac{\mu^2}{m^2}) + e_{L,i}^2 f_i(\frac{x}{z},\mu^2)d_{k,i}^{(1)}\right]\Big\}, \end{aligned} \tag{3}$$

where $k = 2, L$ and the upper boundary on the integration is given by $z_{\rm max} = Q^2/(Q^2+4m^2)$. The functions $f_i(x,\mu^2), (i = g,q,\bar{q})$ denote the parton densities in the proton and μ stands for the mass factorization scale which has been set equal to the renormalization scale. The $c_{k,i}^{(l)}(\zeta,\xi)\,(i = g,q,\bar{q}; l = 0,1)$, $\bar{c}_{k,i}^{(l)}(\zeta,\xi)\,(i = g,q,\bar{q}; l = 1)$, and $d_{k,i}^{(l)}(\zeta,\xi)\,(i = q,\bar{q}; l = 1)$ are coefficient functions and are represented in the $\overline{\rm MS}$ scheme. They depend on the scaling variables ζ and ξ defined by

$$\zeta = \frac{s}{4m^2} - 1 \qquad \xi = \frac{Q^2}{m^2}\,. \tag{4}$$

where s is the square of the c.m. energy of the virtual photon-parton subprocess $Q^2(1-z)/z$. In Eq. (3) we distinguish between the coefficient functions with respect to their origin. The coefficient functions indicated by $c_{k,i}^{(l)}(\zeta,\xi), \bar{c}_{k,i}^{(l)}(\zeta,\xi)$ originate from the partonic subprocesses where the virtual photon is coupled to the heavy quark, whereas $d_{k,i}^{(l)}(\zeta,\xi)$ comes from the subprocess where the virtual photon interacts with the light quark. The former are multiplied by the charge squared of the heavy quark e_H^2, and the latter by the charge squared of the light quark e_L^2 respectively (both in units of e). Terms proportional to $e_H e_L$ integrate to zero for the inclusive structure functions. Furthermore we have isolated the factorization scale dependent logarithm $\ln(\mu^2/m^2)$.

We investigate the ability of heavy-flavour production to constrain the gluon density. The scale dependence and the poorly known charm quark mass are the largest contributors to the theoretical uncertainty. The effects of F_L^{hq} and the light-quark initiated contributions are discovered also to be important in the analysis. To aid the experimental analysis, the fully differential program [5] is used to apply a series of cuts to determine the percentage of events the detectors are likely to see in bins of x and Q^2. With the planned inclusion of silicon vertex detectors, the ability to see bottom events increases dramatically, motivating the presentation of results for the cross section and $F_2^{b\bar{b}}(x,Q^2,m_b^2)$. The transition of charm production from photon-gluon fusion to excitation from the charm parton density is something HERA is in a unique position to evaluate. For other phenomenological investigations, see [8, 9, 10].

2.2 Code Update

For this study we use an updated version of the code based upon [7]. The original code was based upon fitting the coefficient functions described in eq. (3) using a two-dimensional tabular array of points in ζ and ξ. The coefficient functions were generated via a linear interpolation between the calculated points. The linear interpolation was insufficiently accurate and required a more sophisticated interpolation procedure.

The present interpolation procedure is based upon a Lagrange three-point interpolation formula, see eq. 25.2.11 [11]. The results have been thoroughly compared with the original code in [3] and [5] and excellent agreement has been established.[1]

As a demonstration of the code, we present results for the Born $c_2^{(0)}(\zeta,\xi=1,10)$ in Fig. 1a and $c_{2,g}^{(1)}(\zeta,\xi=1,10)$ and $\bar{c}_{2,g}^{(1)}(\zeta,\xi=1,10)$ in Fig. 1b.

2.3 Scale and Parton Density Related Issues

For the subsequent studies we first construct a "data" set. The number of DIS charm events is calculated for an integrated luminosity of $500\,pb^{-1}$, using CTEQ3M [12] parton densities with $\Lambda_4 = 239$ MeV, $m_c = 1.5$ GeV, and $\mu^2 = Q^2 + 4m_c^2$. Unless otherwise mentioned, CTEQ3M is used for all results. The results in Fig. 2a. are produced for $1.8 < Q^2 < 1000$ GeV^2 and $10^{-4} < x < 1$ using four bins per decade for both Q^2 and x.

We also calculate the amount of bottom production events, which is greatly reduced due to the reduction of the charge factor by four as well as a significantly reduced phase space. The

[1] The code is available at http://www.ifh.de/theory/publist.html.

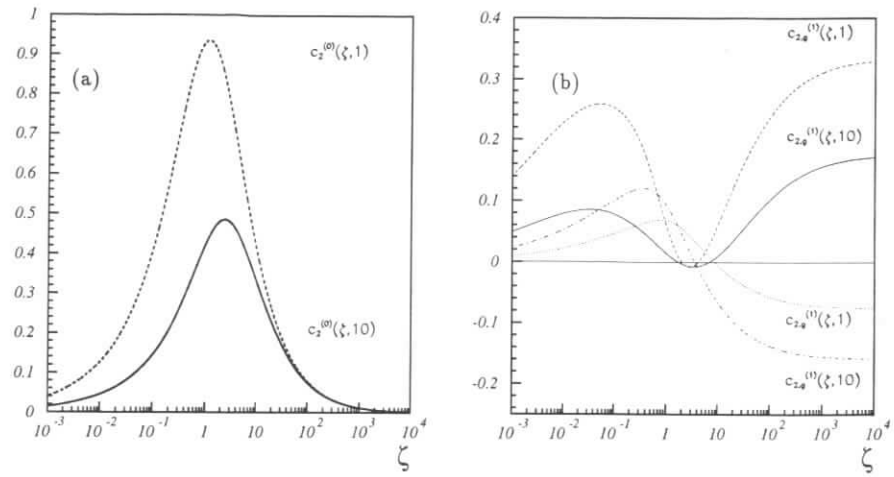

Figure 1: *(a) The Born coefficient function $c_2^{(0)}(\zeta,\xi)$, for $\xi = 1,10$ and (b)The NLO coefficient functions $c_{2,g}^{(1)}(\zeta,\xi)$, for $\xi = 1,10$ (upper curves at large ζ) and $\bar{c}_{2,g}^{(1)}(\zeta,\xi)$ for $\xi = 1,10$ (lower curves at large ζ).*

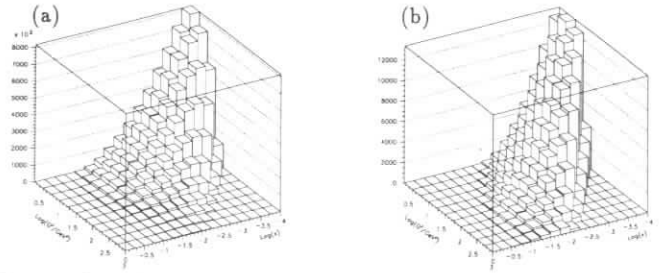

Figure 2: *Projected number of DIS events from (a) charm and (b) bottom production for an integrated luminosity of 500 pb^{-1} binned in x and Q^2 with no cuts applied.*

result is shown in Fig. 2b taking the same parameters as before except $m_b = 4.75$ GeV and $\mu^2 = Q^2 + m_b^2$. A discussion of the implications of this number of b events can be found in section 3.2.

The most important numerical sources of theoretical uncertainty in DIS heavy-flavour production are the factorization/renormalization scale dependence and the poorly known charm quark mass. Varying μ in Eq. (3) indicates the stability of the NLO result is against scale changes.

The "data" are peaked strongly at small x and Q^2. As Q^2 grows, the events become more evenly distributed in x. For small Q^2, the number of events N falls off as $x \to 1$. At larger Q^2, N rises, peaks at intermediate x, then drops.

Using the "data" set as a point of reference, we can investigate where in the kinematic region the effects of scale variation are most strongly felt. Keeping every other parameter fixed,

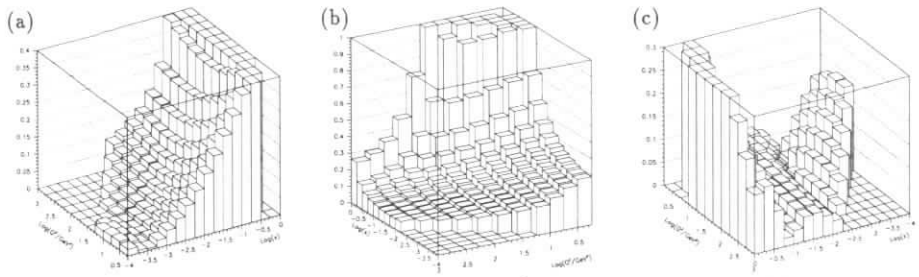

Figure 3: *The uncertainties in* $\sigma(ep \to c\bar{c}X)(x,Q^2)$*: (a)* Δ_μ*,(b)* Δ_{m_c}*, and (c)* $\Delta_{\rm glue}$*.*

we determine the number of events for $\mu^2 = 4m_c^2$ and $\mu^2 = 4(Q^2 + 4m_c^2)$. We investigate the quantity

$$\Delta_\mu(x,Q^2) \equiv \left| \frac{N(\mu^2 = 4m_c^2) - N(\mu^2 = 4(Q^2+4m_c^2))}{2N(\mu^2 = Q^2 + 4m_c^2)} \right|. \tag{5}$$

The results are displayed in Fig. 3a. Apart from the high-x region, which contains very few charm events, the scale dependence varies relatively little with Q^2. As $x \to 0$, we find the scale dependence disappearing. This behaviour bodes very well for a low-x extraction of the gluon density from charm events.

The charm quark mass uncertainty presents a stickier problem. A precise measurement of the charm mass is yet to be made. To develop a feeling for how much of an effect the uncertainty has, we calculated

$$\Delta_{m_c}(x,Q^2) \equiv \frac{N(m_c = 1.3\text{GeV}) - N(m_c = 1.7\text{GeV})}{2\,N(m_c = 1.5\text{GeV})}. \tag{6}$$

Very large effects are naturally found near threshould, but as Q^2 increases and x decreases, Δ_{m_c} approaches a value on the order of 0.1. Varying the charm mass from 1.3 to 1.7 GeV is a conservative estimate; the error induced by the uncertainty viewed in Fig. 3b. can be viewed as an upper bound.

A clear indication of the ability to extract the gluon density from charm production is whether one can distinguish the gluon densities from different available parton densities. We compare the cross section generated with CTEQ2MF[12] (with a flat gluon density as $x \to 0$) with GRV94HO[13] (with a steep gluon density as $x \to 0$). We define

$$\Delta_{\rm glue}(x,Q^2) \equiv \left| \frac{N_{\rm CTEQ2MF} - N_{\rm GRV94HO}}{2\,N_{\rm CTEQ3M}} \right| \tag{7}$$

and show the results in Fig. 3c.

Away from large x, $\Delta_{\rm glue}(x,Q^2)$ is flat as a function of Q^2. In the intermediate region in x, very little distinguishing power is observed. Beginning near $x = 10^{-3}$, a definite difference is seen. The analysis must seemingly extend to $x \lesssim 5 \cdot 10^{-4}$ to distinguish cleanly the gluon densities mentioned.

To summarize: While the scale dependence is well under control, the dominant source of uncertainty is clearly the charm quark mass, which has a strong influence on the cross section at low x and low Q^2. This region is exactly the region sensitive to the gluon density. This strong influence of m_c poses problems for a clean extraction of the gluon density at small x from inclusive measurements.

2.4 Smaller Contributions to the Cross Section: $F_L^{c\bar{c}}$ and Light-Quark Initiated Results

A clean extraction of the gluon density may be hindered by contributions of $F_L^{c\bar{c}}$ and light-quark initiated contributions to the cross section. We investigate the fractional F_L contribution to the cross section by investigating

$$C_{F_L} \equiv \left| \frac{\sigma_{tot} - \sigma_{F_2}}{\sigma_{tot}} \right|, \tag{8}$$

where σ_{F_2} represents the contribution to the cross section in Eq. (2) with F_L set to zero.

We find a sizeable contribution to the cross section at high y. This overlaps with the low Q^2 and low x region previously determined to be deemed the most suitable for a gluon density extraction. To do so, however, one must take into consideration $F_L^{c\bar{c}}$.

We investigate the light-quark initiated contribution by determining

$$C_{\rm lq} = \left| \frac{\sigma_{\rm lq}}{\sigma_{tot}} \right|. \tag{9}$$

The results are very nearly constant, amounting to a 5 – 8 % contribution except at large x, where the charm contribution does not appreciably contribute numerically.

Summarizing: the contributions to the cross section from $F_L^{c\bar{c}}$ are noticeable in the large y region, which overlaps with the small x and small Q^2 region, hindering the extraction of the gluon using only $F_2^{c\bar{c}}$. The light-quark initiated cross section contributes on the order of 5 % to the total cross section, and therefore cannot be totally neglected.

2.5 Cuts *vs.* No Cuts

With the fully differential code developed in [5], a series of cuts can be applied determining a more realistic expectation of charm events able to be detected.

The cuts imposed upon the data are

$$|\eta_c| \leq 1.5,\ p_t^c \geq 2\,\text{GeV}, \tag{10}$$

η_c being the pseudorapidity of the detected charm quark. We define the efficiency as the percentage of the cross section surviving the cuts relative to the the uncut cross section. Looking first at the low Q^2 range from 2 to 10 GeV^2 (σ_L), we present the cross section with and without the aforementioned cuts in the x bins outlined in Tab. 1. In the low x range, we observe an efficiency of 20 – 25 %, diminishing near threshould, the low efficiency mostly a result of the p_t cut.

In the intermediate Q^2 range (σ_I), from 10 to 100 GeV^2. We find the efficiency has risen considerably to the 30–40 % range where the cross section is peaked in intermediate x, with on the order of 20 % for the small x region.

In the high Q^2 range, from 100 to 1000 GeV^2 (σ_H), the efficiency continues to rise with Q^2, reaching 50–60 % in the high to intermediate x region and 30–40 % in the small x range.

The number of events falling within the imposed cuts mentioned in Eq. (10) is not overwhelmingly large, but a large enough sample should be accessible to gather significant statistics.

x_{min}	x_{max}	σ_L (nb)	$\sigma_{L,cuts}$ (nb)	σ_I (nb)	$\sigma_{I,cuts}$ (nb)	σ_H (nb)	$\sigma_{H,cuts}$ (nb)
0.10E-3	0.18E-3	4.39	1.06	0.33	0.06		
0.18E-3	0.32E-3	4.14	1.13	1.16	0.25		
0.32E-3	0.56E-3	3.60	0.96	1.73	0.48		
0.56E-3	0.10E-2	2.96	0.70	1.98	0.68		
0.10E-2	0.18E-2	2.32	0.40	1.91	0.77	0.040	0.012
0.18E-2	0.32E-2	1.74	0.17	1.62	0.70	0.12	0.049
0.32E-2	0.56E-2	1.25	0.04	1.27	0.50	0.16	0.089
0.56E-2	0.10E-1	0.85	0.002	0.94	0.28	0.16	0.096
0.10E-1	0.18E-1			0.66	0.11	0.13	0.076
0.018	0.32E-1			0.43	0.025	0.091	0.046
0.032	0.56E-1			0.26	0.014	0.057	0.017
0.56E-1	0.10E+0			0.13	0.000	0.032	0.003
0.10E+0	0.18E+0					0.014	0.000
0.18E+0	0.32E+0					0.041	0.000

Table 1: *Cross sections with and without the cuts mentioned in Eq. (10).*

2.6 Charm Production at Asymptotic Q^2

Near the threshould for charm production the deep inelastic structure functions F_i, $i = 2, L$, which include the contributions of the light partons u, d, s, and g and the charm quark with mass m_c are given by eq. (3).

Equation (3) gives an adequate prescription as long as the c.m. energy is not too far above the charm threshould, which implies that Q^2 is not too large compared to m_c^2. However, when we enter the asymptotic region $Q^2 \gg m_c^2$, the heavy quark coefficient functions behave like $\ln^i(m_c^2/\mu^2)\ln^j(Q^2/m_c^2)$ so that the higher order corrections can become large. At sufficiently large Q^2 the charm quark should be treated in the same way as the light partons were at smaller Q^2. The logarithmic behaviour of the coefficient functions is due to the collinear singularities which are regulated by m_c. Therefore when $Q^2 \gg m_c^2$, the charm quark behaves like a massless quark similar to the behaviour of the normal light quarks (u, d, and s) over the whole Q^2 range. Following the same procedure as has been used for the light partons, the mass singular (m_c -dependent) terms have to be factorized out of the heavy quark coefficient functions using the method of mass factorization. This leads to a redefinition of the parton densities and the heavy quark coefficient functions turn into the light parton analogues, wherein the number of light flavours is enhanced by one. The above procedure is called the variable flavour number scheme (VFNS) which is outlined in leading order in [14].

Since all coefficient functions are now available up to order α_s^2, this analysis can be extended to NLO to give a better description for the structure functions $F_i(x, Q^2)$ at large Q^2. A preprint is in preparation[15].

3 Experimental Aspects

3.1 Charm production

Results on charm production in deep inelastic ep scattering are available H1 and ZEUS based on a luminosity of approximately 3 pb^{-1} collected with each experiment at HERA in 1994. The H1 collaboration [1] has performed the tagging of heavy quark events by reconstructing $D^0/\overline{D}^0(1864)$ and $D^{*\pm}(2010)$ mesons, while the ZEUS collaboration [2] has given preliminary results for the inclusive $D^{*\pm}(2010)$ analysis. The number of currently observed events containing heavy quarks is only of the order of 100 to 200 charm mesons identified in any of the different analyses. Combining the D^0 and $D^{*\pm}$ analysis of H1 leads to a charm production cross section of

$$\sigma(ep \to ec\bar{c}X) = 17.4 \pm 1.6_{(stat.)} \pm 1.7_{(exp.syst.)} \pm 1.4_{(model)} \text{ nb} \qquad (11)$$

in the kinematic range 10 GeV^2 < Q^2 < 100 GeV^2 and $0.01 < y < 0.7$. This cross section is somewhat larger than predicted by the NLO calculations [3, 1].

H1 has also extracted information on the charm production mechanism in neutral current DIS at HERA from the distribution of $x_D = 2|\vec{P}^*_{D^0}|/W$, where $\vec{P}^*_{D^0}$ denotes the momentum of the D^0 in the $\gamma^* p$ system. This is found to agree well with the expectation from boson gluon fusion, but disagrees with the prediction from processes in which the charmed hadrons would originate directly from quarks in the proton. This analysis concludes that over 95% of charm production in neutral current ep DIS is due to boson-gluon fusion. This observation seems to be in contradiction to recent inclusive calculations of charm production in DIS [14], from which was concluded that for the kinematic range accessible in the current analyses at HERA charm quarks may already be considered as partons in the proton [10].

Finally, current charm production data allowes for a first glimpse at the charm contribution $F_2^{c\bar{c}}(x, Q^2)$ to the proton structure function at small x. Although the errors on the indivial data points are still large ($\mathcal{O}(20 - 30\%)$), clearly the charm contribution is important. Averaged over the kinematic range, a ratio $\left\langle F_2^{c\bar{c}}/F_2 \right\rangle = 0.237 \pm 0.021 \pm 0.041$ is obtained, which is one order of magnitude larger than at larger x.

In the following we give some estimates about the precision that may be expected at HERA for an integrated luminosity of 500 pb^{-1}. As an example the capabilities of the H1 detector [18] are considered. For heavy flavor physics an important new feature of the apparatus is the double layer silicon vertex detector (CST) [19] which will allow use of the apparent proper time of charm hadrons in selecting heavy flavor events. Other decay channels than $D^0 \to K^-\pi^+$ and $D^{*+} \to D^0\pi_s^+ \to K^-\pi^+\pi_s^+$ are already under investigation or will become accessible due to the CST.

Table 2 contains a list of decay modes which should be feasible for charm tagging in H1 in future by also including the CST. A total charm selection efficiency of 1% may be obtained. Compared to the present analysis this corresponds to an increase in the total selection efficiency of a factor 4 to 5. Although the new channels opened by the use of the CST corresponds only to 50% of this gain, the signal to background ratio will improve for all decay modes considerably. From the improved signal to background ratio, the improved effective number of events per luminosity $N_{eff} = (N_{signal}/\sigma_{stat})^2$ will increase by a factor of 6 to 8. Due to the cut in the impact parameter of the D^0 mesons, which is likely to be different in the D^0 and D^{*+} analyses, the events selected in the D^{*+} analyses will only partially overlap with the events selected in

Mode		$P(c \to D)$	$BR(D \to FS)$	ϵ_{tot}	$P \cdot BR \cdot \epsilon_{tot}$
$D^{*+} \to D^0\pi_s^+ \to K^-\pi^+\pi_s^+$	[1]	0.248	0.026	0.16	0.0010
$D^{*+} \to D^0\pi_s^+ \to K^-\pi^+\pi^0\pi_s^+$			0.096	0.04	0.0010
$D^{*+} \to D^0\pi_s^+ \to K^-3\pi\pi_s^+$			0.052	0.10	0.0013
$D^{*+} \to D^0\pi_s^+ \to K^0\pi^+\pi^-\pi_s^+$			0.013	0.20	0.0007
$D^{*+} \to D^0\pi_s^+ \to K^0\pi^+\pi^-\pi^0\pi_s^+$			0.024	0.08	0.0005
$D^{*+} \to D^0\pi_s^+ \to K^-\mu^+\nu_\mu\pi_s^+$			0.024	0.04	0.0002
$D^{*+} \to D^0\pi_s^+ \to K^-e^+\nu_e\pi_s^+$			0.024	0.04	0.0002
Sum D^{*+}		0.248	0.259		0.0049
$D^0 \to K^-\pi^+$	[1]	0.535	0.0383	0.06	0.0012
$D^0 \to K^0\pi^+\pi^-$			0.0186	0.06	0.0006
$D^0 \to K^-3\pi$	CST		0.075	0.04	0.0014
Sum D^0		0.535	0.132		0.0032
$D^+ \to K^0\pi^+$	CST	0.25	0.009	0.12	0.0003
$D^+ \to K^-\pi^+\pi^-$	CST		0.091	0.07	0.0016
$D^+ \to K^03\pi$	CST		0.07	0.07	0.0012
Sum D^+	CST	0.25	0.170		0.0031
Sum D					0.0097

Table 2: *Compilation of various decay channels of charm mesons accessible in H1. The channels marked by "CST" will be accessible only by using the silicon vertex detector. $BR(D \to FS)$ denotes the product of all branching ratios involved in the decay into the final state "FS". For the determination of the total charm tagging efficiency the correlations in the D^0 and D^{*+} analyses are taken into account.*

the corresponding D^0 analyses. Taking an integrated luminosity of 500 pb^{-1}, about 160,000 tagged charm events are expected for the kinematic range of the published H1 analysis. This has to be compared to the currently analyzed 250 events. We expect a gain of a factor of 1000 is expected for the statistical significance because of the increase in the effective number of events. In total, we expect to observe roughly 6,000 double-tag charm events in the range 1.7 GeV^2 $< Q^2 <$ 560 GeV^2 which would allow a study of the charm production dynamics in detail (see Ref. [10]).

Figure 4 shows the result of the hypothetical measurement of $F_2^{c\bar{c}}$ in the range 1.7 GeV^2 $< Q^2 <$ 560 GeV^2 for a luminosity of 500 pb^{-1} based on the gluon density determination from the NLO H1 fit to the inclusive F_2 data combining the statistics of the D meson decay modes summarized in Table 2 by assuming $m_c = 1.5$ GeV and $\mu^2 = Q^2 + 4m_c^2$. The contribution due to F_L and the light flavors are not included. Statistical and full errors are shown. The effect due to the uncertainty in m_c and μ is not included. For $Q^2 <$ 100 GeV^2 the precision of this measurement will be limited by the experimental systematic uncertainty.

A detailed analysis of the experimental systematic uncertainties in the determination of $F_2^{c\bar{c}}$ based on the current data is given in Ref. [1]. At present the total systematic error is approximately 20 %. It is dominated by the uncertainty in the assumptions made to extract the signal from the observed mass distributions. This will improve as soon as more data become available. Ultimately a systematic error of 10% is achievable, which will then be equally due to

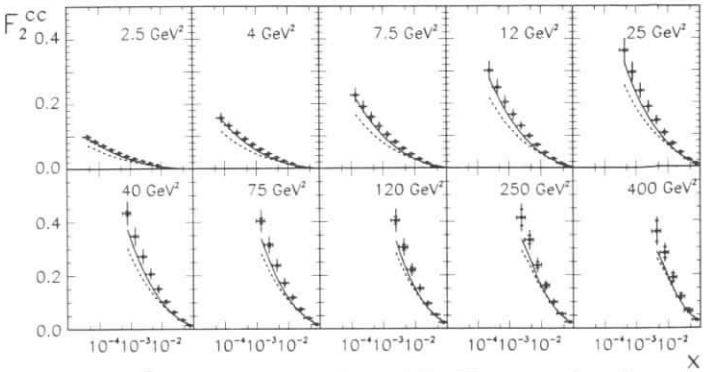

Figure 4: *Expected $F_2^{c\bar{c}}$ for a luminosity of 500 pb^{-1}. The points show the prediction from the gluon density determination by the NLO H1 fit to the inclusive F_2. The inner (outer) error represents the statistical and the total experimental error. The full (dashed) line gives the expectation from the NLO calculations based on GRV-HO [16] and MRSH [17] parton distributions using a charm quark mass of $m_c = 1.5$ GeV.*

detector and analysis related errors (7%) and to the knowledge of the fragmentation probability $P(c \to D)$ of a charm quark into a specific charm meson and their branching ratios (7%). The latter will not improve in the near future.

Figure 4 also shows the NLO predictions [3, 7] using the GRV-HO(1992) [16] and the MRSH [17] parameterization of the gluon density in the proton using $m_c = 1.5$ GeV and $\mu^2 = Q^2 + 4m_c^2$. For a given value of m_c the data will still allow a sensitive indirect determination of the gluon density even with the relatively large experimental systematic uncertainties. Due to the high statistics it will be possible to measure the charm production cross section up to $Q^2 \leq 1000$ GeV^2. Assuming charm tagging is performed for all decay modes listed in Tab. 2, the sensitivity limit for the inclusive measurements will already be reached at 50 pb^{-1} for $Q^2 \leq 100$ GeV^2, at which time the experimental systematic will dominate in this kinematic range.

As shown in the theory section, the measurement of $F_2^{c\bar{c}}$ is sensitive to the gluon density at large y. Unfortunately the $F_2^{c\bar{c}}$ measurement in this range is also very sensitive to the charm quark mass. Therefore it is not clear whether the measurement of $F_2^{c\bar{c}}$ alone will allow an extraction of the gluon density at small x. For the present data [1] it was concluded that the extraction of the gluon density from $F_2^{c\bar{c}}$ should be still feasible. The behavior for $Q^2 <$ 10 GeV^2 has not been studied yet. If it happens that $F_2^{c\bar{c}}$ does not provide an reliable indirect extraction of the gluon density because of the uncertainty in m_c, exclusive distributions of the identified charm hadrons have to be studied. As an example the result of the Monte Carlo study of the influence of m_c and the gluon density on the distribution $1/\sigma\ d\sigma/dx_D$ is shown in Fig. 5 for 6 GeV^2 $< Q^2 <$ 100 GeV^2 and the cuts of Eq. (10). Here $\Delta\ x_D$ is defined as

$$\Delta\ x_D = \frac{1/\sigma_i\ d\sigma_i/dx_D(x_D)}{1/\sigma_j\ d\sigma_j/dx_D(x_D)} \qquad (12)$$

where i, j denote the different values of the parameters, *i.e.* $m_c = 1.3$, 1.7 GeV and PDF=MRSH, GRV-HO(1992), respectively. The mass of the charm quark affects strongly

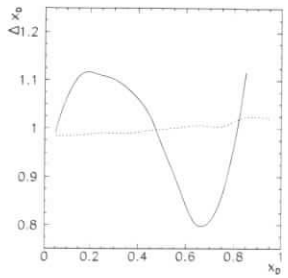

Figure 5: *Relative change Δx_D in the shape of the distribution $1/\sigma\ d\sigma/dx_D$ according to the LO Monte Carlo Simulation of the AROMA program for 6 $GeV^2 < Q^2 < 100\ GeV^2$ and the cuts of Eq. (10). The full line gives the change in the shape by changing m_c from 1.3 GeV to 1.7 GeV. The dashed line shows the influence of using the GRV-HO (1992) instead of the MRSH parameterization of the gluon density in the proton.*

the shape of the x_D distribution (full line) while there is only very little effect due to the choice of the parton density function (dashed line). A study of this distribution, for instance, should therefore disentangle the effect of the charm quark mass and the gluon density on $F_2^{c\bar{c}}$.

In section 2.5, the question when charm quarks should be treated as partons of the proton was discussed. The investigation of the x and Q^2 dependence of the exclusive measurement of $1/\sigma\ d\sigma/dx_D$ will allow a study of the origin of charm production as a function of the kinematic variables. At sufficiently large Q^2 it is expected that the charm quark behaves like a parton in the proton. This will result in a change of the x_D distribution from the boson gluon fusion dominated regime presently observed in the available data at $\langle Q^2 \rangle \approx 25\ \mathrm{GeV}^2$ to the sea quark dominated regime at large Q^2. If it becomes possible to control the μ and m_c dependence of charm production at large Q^2, the measurement of $F_2^{c\bar{c}}(x, Q^2, x_D)$ can determine $g(x, Q^2)$ and $c(x, Q^2)$ simultaneously. This study would certainly require a luminosity of 500 pb^{-1} to produce enough data at large Q^2.

3.2 Bottom Production

In the following the possibilities to measure $F_2^{b\bar{b}}(x, Q^2)$ at HERA are studied on the basis of the predictions for bottom production in section 2.3. Again the H1 detector is used as an example.

Compared to charm quark events the major experimental difference in bottom quark production is the relative long lifetime of the B mesons. With use of the CST, bottom events are selected by applying a cut in the impact parameter of tracks not fitting to the primary event vertex. The combinatorial background is negligible, while the charm production is a significant background source, because of the much larger cross section. Only the exclusive analysis of reconstructed D mesons will be discussed here. This method benefits from (a) the large branching ratios of B mesons into charm meson and (b) the relatively long visible lifetime observed in the decay chains. For a selection efficiency of 50% for the impact parameter cut, the contamination of charm events reduces by a factor of 12.5(2.8) for the $D^0(D^{\pm})$ analysis.

All decay modes summarized in Tab. 2 will also be accessible in this case. Due to the larger cut values in the impact parameter for the different decay modes, the combinatorial background

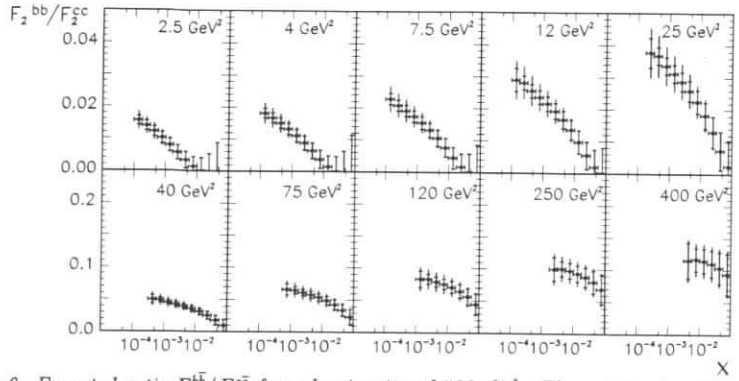

Figure 6: *Expected ratio $F_2^{b\bar{b}}/F_2^{c\bar{c}}$ for a luminosity of 500 pb^{-1}. The points show the predictions according to the calculations of section 2.1 and 2.6. The inner (outer) error represents the statistical and the total experimental error.*

is smaller. This will allow for softer cuts. Compared to charm production studies an increase in efficiency by a factor 3 is expected. A systematic error of 16% may be achieved, limited by the uncertainties in the branching fraction $BR(B \to DX)$.

Figure 6 shows the ratio of $F_2^{b\bar{b}}/F_2^{c\bar{c}}$ expected from this analysis where the charm production background is subtracted statistically. The errors refer to the statistical and the total experimental error. For a luminosity of 500 pb^{-1} will still be statistics limited. Integrated over the kinematic range a mean value of $F_2^{b\bar{b}}/F_2^{c\bar{c}} \approx 0.02$ is predicted.

4 Conclusions

In this paper, we have discussed DIS heavy-flavour production at HERA at NLO. The effect on the charm production cross section due to the uncertainties in the factorization/renormalization scale μ and the charm quark mass m_c has been studied as a function of x and Q^2. At small x and for $Q^2 < 300\ \mathrm{GeV}^2$ the predictions are found to be insensitive to μ while in this region the effect of m_c is found to be large. Unfortunately the sensitivity of $F_2^{c\bar{c}}(x, Q^2)$ to the gluon density at small x is also restricted to this kinematic region. It has been shown that the contribution of F_L has sizeable effects on the charm production cross section at large y. The contribution of light quarks to the cross section turned out to be of the order of 5%, nearly independent of x and Q^2. Results on bottom production have been presented.

The current experimental situation has been summarized. Based upon this knowledge, statistical and experimental systematic uncertainties for large luminosity have been estimated. Ultimately an accuracy of 10% in the overall normalization of the cross section may be achieved. In the kinematic range where the inclusive measurement $F_2^{c\bar{c}}(x, Q^2)$ is found to be sensitive to the gluon density, the error of the inclusive measurement will start to be systematics dominated with a luminosity of 50 pb^{-1}. It has been demonstrated that exclusive measurements of the charm mesons would disentangle the influence of m_c and the gluon density on the charm production cross section. An exploration of the kinematic plane, the extraction of the gluon density, as well as the question when the charm quark may be treated as a parton, will require a

luminosity of 500 pb^{-1}. Finally the ratio of $F_2^{b\bar{b}}/F_2^{c\bar{c}}(x,Q^2)$ has been investigated by performing an exclusive D meson analysis. With a luminosity of 500 pb^{-1} the predicted statistics is found to be sufficient to make a detailed study of the x and Q^2 dependence of this ratio.

Acknowledgments

S.R. thanks Jenny Ivarsson for her help making the figures.

References

[1] C. Adloff *et al.*, H1 Collaboration, DESY 96-138, accepted by Z. Phys. **C** (1996).

[2] ZEUS Collaboration, contributed paper to XXVIII Int. Conf. on HEP '96, Warsaw (1996).

[3] E. Laenen, S. Riemersma, J. Smith, and W.L. van Neerven, Nucl. Phys. **B392** (1993) 162.

[4] E. Laenen, S. Riemersma, J. Smith, and W.L. van Neerven, Nucl. Phys. **B392** (1993) 229.

[5] B.W. Harris and J. Smith, Nucl. Phys. **B452** (1995) 109; Phys. Lett. **353B** (1995) 535; B.W. Harris, talk A05057, presented at the American Physical Society, Division of Particles and Fields 1996 Meeting, Minneapolis, Minnesota, 10-15 August 1996, to appear in proceedings.

[6] M. Buza, Y. Matiounine, R. Migneron, J. Smith, and W.L. van Neerven, Nucl. Phys. **B472** (1996) 611.

[7] S. Riemersma, J. Smith, and W.L. van Neerven, Phys. Lett. **347B** (1995) 143.

[8] E. Laenen, S. Riemersma, J. Smith, and W.L. van Neerven, Phys. Letts. **291B** (1992) 325.

[9] A. Vogt, DESY 96-012, hep-ph/9601352

[10] E. Laenen, M. Buza, B.W. Harris, Y. Matiounine, R. Migneron, S. Riemersma, J. Smith, and W.L. van Neerven, these proceedings.

[11] Handbook of Mathematical Functions, eds. M. Abramowitz and I.E. Stegun, National Bureau of Standards, (1972) 879.

[12] H.L. Lai, J. Botts, J. Huston, J.G. Morfin, J.F. Owen, J.W. Qiu, W.K. Tung, and H. Weerts, Phys. Rev. **D51** (1995) 4763.

[13] M. Glück, E. Reya, and A. Vogt, Z. Phys. **C67** (1995) 433.

[14] M.A.G. Aivazis, F.I. Olness, and W-K. Tung, Phys. Rev. **D50** (1994) 3085; M.A.G. Aivazis, J.C. Collins, F.I. Olness, and W-K. Tung, Phys. Rev. **D50** (1994) 3102.

[15] M. Buza, Y. Matiounine, J. Smith and W.L. van Neerven, in preparation.

[16] M. Glück, E. Reya, and A. Vogt, Z. Phys. **C53** (1992) 127.

[17] P.N. Harriman, A.D. Martin, W.J. Stirling, and R.G. Roberts, Phys.Rev.**D42** (1990) 798.

[18] S. Aid et al., H1-Coll, DESY 96-01, accepted to Nucl. Inst. and Meth. (1996).

[19] W. Erdmann et al., Nucl. Inst. and Meth. **A372** (1996) 188.

The Charm–Strange Contribution to Charged–Current DIS Structure Functions

V. Barone[a], U. D'Alesio[a] and M. Genovese[b,1]

[a] Università di Torino and INFN, 10125 Torino, Italy
[b] Université Joseph Fourier and IN2P3-CNRS, 38026 Grenoble, France

Abstract: We review the present theoretical knowledge of the charm–strange contribution to charged–current DIS structure functions. In particular, the uncertainties arising from the choice of the factorization scale, of the massive QCD scheme, and of the parton fit are discussed.

1 Cross Sections

Charm production in charged–current (CC) deep inelastic scattering (DIS) is the best way to obtain information on the strange sea density [1], which is at present the most poorly known among the light–quark distributions. The strange distribution can also be obtained by properly combining fully inclusive CC cross sections. CC reactions are thus necessary in order to determine the strange sector and, in general, to reconstruct the whole flavor systematics.

The relevant subprocesses for charm excitation in CC DIS are (we consider only Cabibbo unsuppressed diagrams):

i) the $\mathcal{O}(\alpha_s^0)$ direct transition $W^+ s \to c$;

ii) the $\mathcal{O}(\alpha_s^1)$ W-gluon and W-quark fusion processes $W^+ g \to \bar{s}c$, $W^+ s \to gc$.

The CC DIS cross section reads

$$\frac{\mathrm{d}^2\sigma^{\pm}}{\mathrm{d}x\mathrm{d}y} = \frac{G^2 s}{4\pi(1+\frac{Q^2}{M_W^2})^2}\left[xy^2F_1 + (1-y-\frac{m_N^2 xy}{s})F_2 \mp (y-\frac{y^2}{2})xF_3\right], \qquad (1)$$

where the subscript $+$ $(-)$ denotes the reaction $e^+N \to \bar{\nu}X$ $(e^-N \to \nu X)$. If we restrict ourselves to charm excitation we get at order α_s^0 (for electron scattering)

$$\frac{\mathrm{d}^2\sigma_{cs}}{\mathrm{d}\xi\mathrm{d}y} = \frac{G^2 s}{4\pi(1+\frac{Q^2}{M_W^2})^2}\, 2\xi\, \bar{s}(\xi,Q^2)|V_{cs}|^2\left[(1-y)^2 + \frac{m_c^2}{s\xi}(1-y)\right], \qquad (2)$$

where the slow rescaling variable $\xi = x\,(1+m_c^2/Q^2)$ accounts for the finite mass of the charmed quark in the $Ws \to c$ transition. The cross section for positron scattering is obtained by the replacement $\bar{s} \to s$. The cross section (2) provides a direct measure of the strange sea density.

[1]Supported by EU Contract ERBFMBICT 950427.

However, at order α_s (often referred to, somehow improperly, as the next-to-leading order) formula (2) does not hold any longer because of the more complicated relation between structure functions and parton densities. The most important $\mathcal{O}(\alpha_s)$ contribution comes from the vector-boson–gluon fusion term which incorporates important dynamical effects (quark–mass threshold effects and large longitudinal contributions due to the non conservation of weak currents [2]).

2 Theoretical Uncertainties

The QCD analysis of the charm–strange structure function at order α_s is affected by theoretical uncertainties which have two sources: *i)* the choice of the massive QCD scheme; *ii)* the arbitrariness of the factorization scale. Besides these, there is a further uncertainty coming from the choice of the parton fit among those available on the market.

The most commonly used $\mathcal{O}(\alpha_s)$ schemes for massive quarks are the Fixed Flavor Scheme (FFS) [3] and the Variable Flavor Scheme (VFS) [4].

In the FFS, charm is treated as a heavy quark, in an absolute sense. There is no charm excitation term in the structure functions and the number of active flavors is $N_f = 3$. The collinear divergence $\log(Q^2/m_s^2)$ in the gluon fusion term is regularized at a scale μ^2. For the cs contribution to the F_2 structure function one explicitly has

$$\text{FFS}: \quad F_2^{cs}(x,Q^2) = 2\,\xi\, s(\xi,\mu^2) + \frac{\alpha_s(\mu^2)}{2\pi}\int_\xi^1 \frac{\mathrm{d}z}{z}\, 2\xi\,[C_2^g(z,\mu^2)\, g(\xi/z,\mu^2) + C_2^q(z,\mu^2)\, s(\xi/z,\mu^2)]\,, \tag{3}$$

where the Wilson coefficients C_2^g and C_2^q can be found in the literature [5].

In the VFS, charm is a "heavy" flavor for $\mu^2 < m_c^2$, and a partonic constituent of the nucleon for $\mu^2 > m_c^2$. Both the strange and the charm excitation terms appear and hence there are two subtractions in the Wilson coefficient, corresponding to the two singularities in the limits $m_s \to 0$ and $m_c^2/Q^2 \to 0$. The explicit expression is

$$\begin{aligned}\text{VFS}: \quad F_2^{cs}(x,Q^2) &= 2\,\xi\,[s(\xi,\mu^2) + c(x,\mu^2)] \\ &+ \frac{\alpha_s(\mu^2)}{2\pi}\int_\xi^1 \frac{\mathrm{d}z}{z}\, 2\xi\,[\hat{C}_2^g(z,\mu^2)\, g(\xi/z,\mu^2) + \hat{C}_2^q(z,\mu^2)\, s(\xi/z,\mu^2)]\,, \end{aligned} \tag{4}$$

where $\hat{C}_2^{g,q}$ denotes the doubly subtracted massive Wilson coefficients.

The factorization scale μ^2 is arbitrary and only an educated guess can be made on it. It is clear that a knowledge of the CC structure functions at order α_s^2, still lacking at present, would allow testing the perturbative stability of the various choices.

3 Results

We estimate now the theoretical uncertainties on F_2^{cs} and on the cs contribution to the DIS cross section.

In Fig. 1 we show the results of the calculation of F_2^{cs} and of

$$\tilde{\sigma}^{cs} \equiv K\,\frac{d\sigma^{cs}}{dx\,dy}\,, \qquad K^{-1} = \frac{G^2 s}{2\pi\,(1+Q^2/M_W^2)^2}\,|V_{cs}|^2\,[(1-y)^2 + \frac{m_c^2}{s\xi}\,(1-y)]\,, \tag{5}$$

at $Q^2 = 100$ GeV^2, for various NLO parton fits: MRS(A) [6], MRS(R$_1$) [7], CTEQ(4M) [8], GRV [9]. The scheme used is the FFS and the factorization scale is taken to be $\mu^2 = Q^2$. In the box on the right we also display $\xi s(\xi,Q^2)$, that is what $\tilde{\sigma}^{cs}$ reduces to at order α_s^0. Note that the CTEQ(4M) and MRS(R$_1$) curves nearly coincide whereas there is a non negligible difference between the two MRS fits and a larger discrepancy between MRS(R$_1$) and GRV. The global uncertainty due to the choice of the fit amounts to $\sim 30\%$ both for F_2^{cs} and for $\tilde{\sigma}^{cs}$.

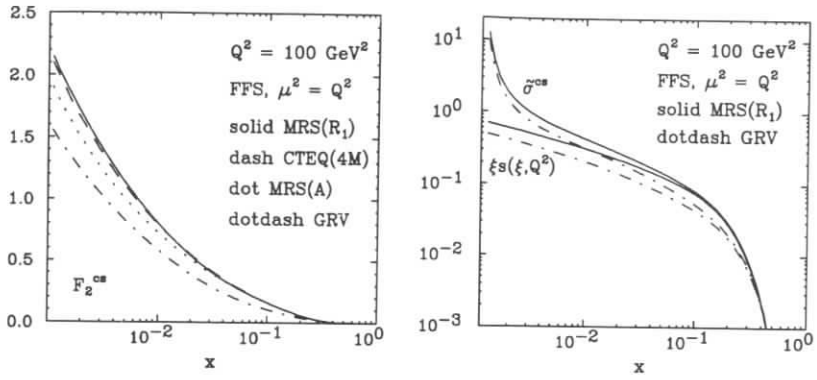

Figure 1: *F_2^{cs} and $\tilde{\sigma}^{cs}$ in the FFS for various parton fits.*

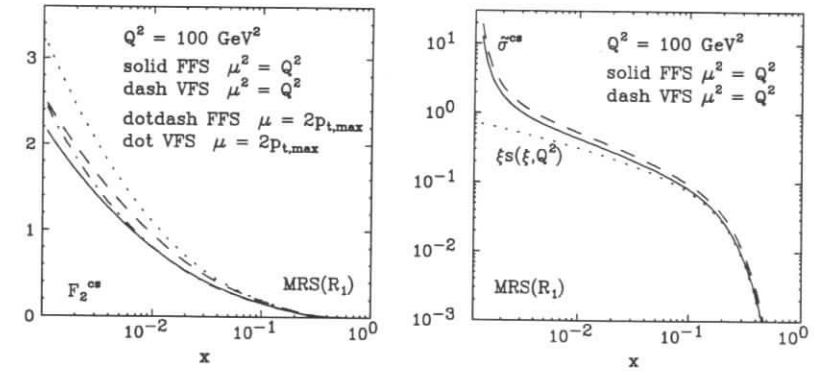

Figure 2: *F_2^{cs} and $\tilde{\sigma}^{cs}$ in the two schemes (FFS and VFS) and with two choices of the factorization scale.*

In Fig. 2, considering now only the MRS(R$_1$) parametrization, we illustrate the scheme dependence for two different factorization scales: $\mu^2 = Q^2$ and $\mu = 2p_{t,max}$, where p_t is the transverse momentum of the produced charmed quark. The difference between the FFS and the VFS results at $Q^2 = 100$ GeV^2 is again up to $\sim 30 - 40\%$ (attaining the largest value for $\mu = 2p_{t,max}$).

In Fig. 3 we show the situation at a higher physical scale, $Q^2 = 1000$ GeV^2. Notice that the difference between the two schemes is still relatively large whereas the choice $\mu = 2p_{t,max}$ gives curves (not displayed) which are indistinguishable from those corresponding to $\mu^2 = Q^2$.

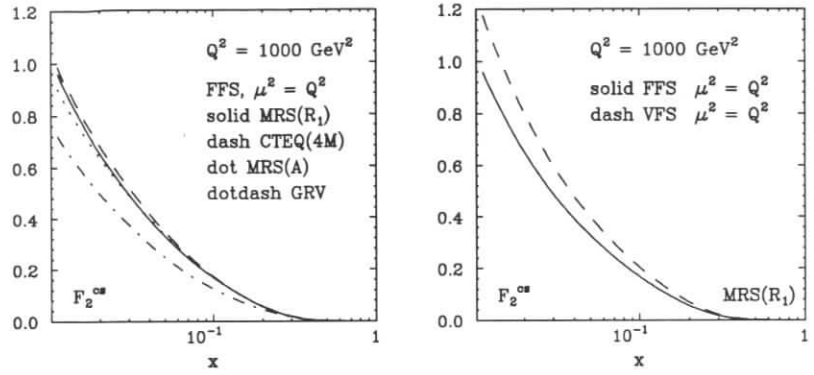

Figure 3: *Fit and scheme dependence of F_2^{cs} at $Q^2 = 1000$ GeV^2.*

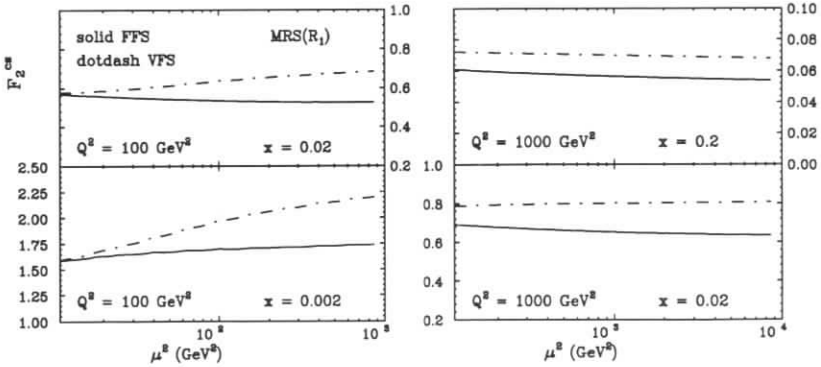

Figure 4: *Dependence of F_2^{cs} on the factorization scale in the two massive QCD schemes.*

In Fig. 4 we illustrate the dependence on the factorization scale. The parton fit used is the MRS(R$_1$) and the results of both schemes are presented for some kinematically accessible (x, Q^2) bins. It is clearly seen that when Q^2 is not very large the VFS is more unstable than the FFS. At very high Q^2 both the VFS and the FFS are not very sensitive to the factorization scale.

It is important for HERA to know also the expected uncertainties on the charm–strange contribution to the total cross section. These are presented in Table 1. It is interesting to notice that the main difference (~ 40 %) arises from the choice of the scheme.

σ_{tot}^{cs} (pb)	FFS/MRS(R$_1$)	FFS/GRV	VFS/MRS(R$_1$)
$\mu^2 = Q^2$	4.66	4.02	6.79
$\mu = 2p_{t,max}$	4.20	3.57	6.80

Table 1: *Total charm-strange cross-section for different parton fits, factorization scales and schemes in the kinematic region $Q^2 > 200$ GeV^2 and $x > 0.006$ ($\sqrt{s} \simeq 300$ GeV).*

4 Conclusions

The overall theoretical uncertainty on the charm–strange contribution to the charged–current structure functions is relatively large, being at least of order of 30 % in the typically accessible (x, Q^2) region. At not very high Q^2 the Fixed Flavor Scheme turns out to be preferable due to its greater stability. An order α_s^2 calculation is necessary to settle the problem of the scheme and factorization scale dependence. For the sake of consistency and for a safer analysis it would be important to use massive QCD evolution in the heavy–quark sector of the global fits. Possible HERA data on the charm–strange structure functions at large Q^2 would certainly be of the greatest utility.

References

[1] V. Barone *et al.*, Phys. Lett. B 317 (1993) 433; Phys. Lett. B 328 (1994) 143; Z. Phys. C 70 (1996) 83. V. Barone, U. D'Alesio and M. Genovese, Phys. Lett. B 357 (1995) 435. V. Barone and M. Genovese, Phys. Lett. B 379 (1996) 233.

[2] V. Barone *et al.*, Phys. Lett. B 268 (1991) 279; Phys. Lett. B 304 (1993) 176.

[3] M. Glück, E. Hoffmann and E. Reya, Z. Phys. **C13** (1982) 119; M. Glück, R.M. Godbole and E. Reya, Z. Phys. **C38** (1988) 441; M. Glück, E. Reya and M. Stratmann, Nucl. Phys. **B422** (1994) 37.

[4] M.A.G. Aivazis, J.C. Collins, F.I. Olness and W.-K. Tung, Phys. Rev. D 50 (1994) 3102. F.I. Olness and S.T. Riemersma, Phys. Rev. D 51 (1995) 4746.

[5] T. Gottschalk, Phys. Rev. D 23 (1981) 56.

[6] A.D. Martin, R.G. Roberts and W.J. Stirling, Phys. Rev. D 50 (1994) 6734.

[7] A.D. Martin, R.G. Roberts and W.J. Stirling, hep-ph/9606345.

[8] H.L. Lai *et al.* (CTEQ), hep-ph/9606399.

[9] M. Glück, E. Reya and A. Vogt, Z. Phys. C 67 (1995) 433.

$F_2(x,Q^2)$ and $F_L(x,Q^2)$ at Leading Order, in $\ln(1/x)$ as well as $\alpha_s(Q^2)$

R.S. Thorne

Rutherford Appleton Laboratory, Chilton, Didcot, OX11 0QX, UK

Abstract: We present a brief discussion of the full leading order, including $\ln(1/x)$ terms, renormalization group consistent calculation of structure functions. A fit to the available $F_2(x,Q^2)$ data is performed, and a prediction made for $F_L(x,Q^2)$. Comparison is made with two–loop results.

1 Introduction

Recent measurements of $F_2(x,Q^2)$ at HERA have provided data on a structure function at far lower values of x than any previous experiments, and show that there is a marked rise in $F_2(x,Q^2)$ at very small x down to rather low $Q^2(\sim 1.5GeV^2)$.[1, 2] These measurements have led to a great deal of interest in how one should best calculate structure functions, and in particular, whether one should include the leading $\ln(1/x)$ terms for a given power of α_s.

This presentation is a brief advertisement of the fact that the correct renormalization and factorization scheme independent expression for the structure functions naturally includes leading $\ln(1/x)$ terms, but leading in the expressions for the structure functions themselves, not in the unphysical (and hence factorization scheme dependent) anomalous dimensions and coefficient functions. Calculating the structure functions in this manner gives a vey good global fit to the data on $F_2(x,Q^2)$. Many more details of this are in a forthcoming paper.[3] As an example, let us consider an expression for a hypothetical physical quantity depending on the running coupling $\alpha_s(Q^2)$ and another variable N (N may be interpreted as the moment space variable), which can be expressed as

$$F(N,Q^2)=\sum_{m=1}^{\infty}\alpha_s^m(Q^2)\sum_{n=-m}^{\infty}a_{nm}N^n. \qquad (1)$$

In the standard loop expansion one includes all terms in the expression for $F(N,Q^2)$ up to a given m, and uses the m–loop coupling. Uncertainties in the expression for $F(N,Q^2)$ due to uncertainty in the definition of the coupling are then of order $\alpha_s^{m+1}(Q^2)$. However, any change in the defintion of the coupling $\alpha_s(Q^2)\rightarrow\alpha_s(Q^2)+\mathcal{O}(\alpha_s^2(Q^2))$, does not alter any of the terms of the form $(\alpha_s(Q^2)/N)^m$. Hence, each of these terms is renormalization scheme independent, and should be included in the leading order expression, which uses the one–loop coupling. (Also, since $F(N,Q^2)$ is a physical quantity, factorization scheme independence is guaranteed.) Terms $\sim\alpha_s(Q^2)(\alpha_s(Q^2)/N)^m$ are next–to–leading order, etc. When working with structure functions the details are rather more complicated, but the principle is the same. In essense, since the structure functions may be factorized into inputs at some starting scale Q_0^2, and the evolution to other scales Q^2, the expressions for both the input and the evolution should be

Table 1: Comparison of quality of fits for full leading order (including $\ln(1/x)$) terms, and two–loop fits, MRSR1 and MRSR2. For the LO(x) fit the HERA data is corrected for the low value of $F_L(x,Q^2)$ obtained using this method.

Experiment	# data	χ^2		
		R_1	R_2	LO(x)
H1 F_2^{ep}	193	158	149	121
ZEUS F_2^{ep}	204	326	308	257
BCDMS $F_2^{\mu p}$	174	265	320	200
NMC $F_2^{\mu p}$	129	155	147	147
NMC $F_2^{\mu d}$	129	139	129	142
NMC $F_2^{\mu n}/F_2^{\mu p}$	85	136	132	144
E665 $F_2^{\mu p}$	53	8	8	8
CCFR $F_2^{\nu N}$	66	41	56	49
CCFR $xF_3^{\nu N}$	66	51	47	64

the leading order, including leading $\alpha_s(Q^2)\ln(1/x)$ terms, expressions. (For more details see [3]) The full LO(x) (where we use the abbreviation LO(x) to mean leading order including leading $\alpha_s(Q^2)\ln(1/x)$ terms) expressions involve leading $\ln(1/x)$ terms which are in the form of Catani's factorization scheme independent anomalous dimensions.[4] These appear in the expressions for both the inputs and evolution, and give a theoretical prediction for the small x form of $F_2(x,Q_0^2)$ in terms of $F_L(x,Q_0^2)$ (or *vice versa*, of course).

2 Results

We obtain a good fit for $F_2(x,Q^2)$ data using the LO(x) scheme independent expression and the one–loop coupling constant with $\Lambda^{n_f=4}=90MeV$. Satisfying the theoretical relationship between the small x forms of $F_2(x,Q_0^2)$ and $F_L(x,Q_0^2)$, forces Q_0^2 to be roughly in the range $20-100GeV^2$ (with little sensitivity). Within this range the theoretical prediction for $F_L(x,Q_0^2)$ at very small x is in fact a little ($\sim$ 10-15 %) larger than that obtained from the best fit. Thus, the agreement is qualitatively fairly good. The discrepency may be, at least partially, due to the naive treatment of heavy quark thresholds in this fit, or is perhaps simply due the the fact that this is, after all, really only a leading order treatment. The LO(x) fit can be compared to pair of fits using the standard two–loop expressions[5] where R_1 allows $\Lambda_{\overline{MS}}^{n_f=4}$ to be free (giving $\Lambda_{\overline{MS}}^{n_f=4}=241MeV$) and R_2 fixes $\Lambda_{\overline{MS}}^{n_f=4}$ at the higher value of $344MeV$, forcing a better fit to the HERA data. The results are shown in table 1 (full references for the experimental data can be found in [5]). The full LO(x) scheme independent fit to the HERA data is markedly better than the two–loop fits, and this is combined with a much better fit to the BCDMS data. The fit to the rest of the data is similar in all three cases.

A stronger test of which of the two approaches (if either) is correct comes when the fit to $F_2(x,Q^2)$ is used to predict $F_L(x,Q^2)$. Predictions using the full LO(x) scheme independent expression (the prediction is different to that in [6] because in this previous treatment Q_0^2 was

too low to be consistent with the theoretical relationship between inputs) and one of the two–loop expressions are shown in fig. 1. (the two–loop curve corresponds to R_1: that for R_2 is very similar.) A direct measurement of $F_L(x, Q^2)$ at HERA will clearly help a great deal in determining whether the approach advocated in this paper is correct.

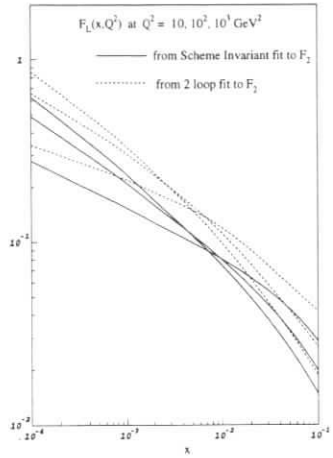

Figure 1: Comparison of predictions for $F_L(x, Q^2)$ using LO(x) fit and two–loop (MRSR1) fit.

Acknowledgments

I would like to thank R.G. Roberts for continual help during the period of this work and for the use of the MRS fit program.

References

[1] H1 collaboration: *Nucl. Phys.* B **470**, 3 (1996).

[2] ZEUS collaboration: M. Derrick *et al*, *Z. Phys.* C **69**, 607 (1996); preprint DESY 96-076 (1996), to be published in *Z. Phys.* C.

[3] R.S. Thorne, preprint RAL-TR-96-065 (to appear).

[4] S. Catani, talk presented at the UK Workshop on HERA Physics (Durham, September 1995), preprint DDF 248/4/96 (to appear); proceedings of International Workshop on Deep Inelastic Scattering and Related Phenomena, DIS 96, (Rome, April 1996).

[5] A.D. Martin, R.G. Roberts and W.J. Stirling, preprint DTP/96/44 or RAL-TR-96-037, to be published in *Phys. Lett.* B.

[6] R.S. Thorne, proceedings of International Workshop on Deep Inelastic Scattering and Related Phenomena, DIS 96, (Rome, April 1996).

The QCD dipole picture of small-x physics

R. Peschanski[a], G. P. Salam[b]

[a] CEA-Saclay, Service de Physique Théorique, F-91191 Gif-sur-Yvette Cedex, FRANCE
[b] Cavendish Laboratory, Cambridge University, Madingley Road, Cambridge CB3 0HE, UK

Abstract: The QCD dipole picture of BFKL dynamics provides an attractive theoretical approach to the study of the QCD (resummed) perturbative expansion of small-x physics and more generally to hard high-energy processes. We discuss applications to the phenomenology of proton structure functions in the HERA range and to the longstanding problem of unitarity corrections, and outline some specific predictions of the dipole picture.

1 Introduction

The dipole formulation [1, 2] is an approach to small-(Bjorken)x physics which for inclusive quantities can be shown [3] to be equivalent to the BFKL approach [4]. One starts with a $q\bar{q}$ state (onium), taken to be heavy enough to ensure the validity of perturbation theory. The main ingredients of the dipole picture of BFKL dynamics are the following

i) Choosing the quantisation in the infinite-momentum frame of the onium allows one to select the leading $\alpha \log 1/x$ terms of the QCD perturbative expansion of the onium wave-function.

ii) Changing the momentum representation into a mixed one $(\mathbf{b}, x)$, where $\mathbf{b}$ is the transverse coordinate, amounts to killing the contributions of the interference Feynman diagrams in the leading-log expansion. This results in a quasi-classical picture of the system of quarks and gluons in terms of probability distributions at the interaction time.

iii) Finally the $1/N_c$ limit leads to the emergence of a representation in terms of independent colourless dipoles, replacing the description in terms of soft, coloured gluons.

To illustrate these properties on a simple example, one constructs the component of the squared wave function that contains one soft gluon, as a function of the transverse positions $\mathbf{b}_0, \mathbf{b}_1$ (or impact parameter) of the onium quark and antiquark and $\mathbf{b}_2$ of the gluon, (see fig. 1). In the large-N_c limit, the original colour dipole of the onium state (of size b) effectively becomes two colour dipoles: one formed by qg (of size b_{02}) and the other by $g\bar{q}$ (of size b_{12}). So the addition of a gluon is equivalent to the branching of one dipole into two, and each of the produced dipoles can then branch independently — this leads to a cascade of dipoles developing when x becomes smaller and smaller, explaining the rise in the number of dipoles (or gluons) at small x.

To determine the gluon distribution, one must use some probe. One way is to measure the interaction cross section with a second onium. The evolution equation for the interaction cross-section (see fig. 1) of two $q\bar{q}$ states of sizes b and b' is

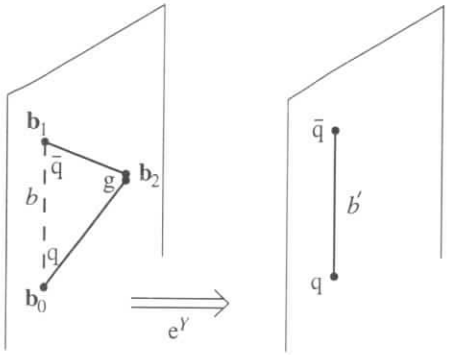

$$\frac{\mathrm{d}\sigma(b',b,Y)}{\mathrm{d}Y} = \frac{\alpha N_c}{2\pi^2}\int \frac{b^2\mathrm{d}^2\mathbf{b}_2}{b_{02}^2 b_{12}^2}[\sigma(b',b_{02},Y) + \sigma(b',b_{12},Y) - \sigma(b',b_{01},Y)], \quad (1)$$

where $Y \simeq \ln 1/x$ is known as the rapidity. The solution is

$$\sigma(b,b',Y) = \frac{8\pi\alpha^2 bb'}{\sqrt{\pi k Y}} \mathrm{e}^{(\alpha_{\mathbb{P}}-1)Y - \ln^2(b'/b)/kY} \quad (2)$$

with $(\alpha_{\mathbb{P}} - 1) = (4\ln 2)\alpha N_c/\pi$ and $k = \frac{\alpha N_c}{\pi} 14\zeta(3)$. Eq. (2) has some interesting features which deserve comment. First it reproduces exactly the high-energy ($\simeq$ small-x) behaviour associated with the BFKL "hard" Pomeron. Second, and more intriguing, a dependence appears on the scale-ratio b'/b between the two colliding onia. This is related to the property of BFKL dynamics that it "explores" a large region in the transverse-momentum plane, which is analogous to a classical diffusion mechanism.

Figure 1: *Onium-onium interaction at first order via the one-soft-gluon component of the onium wavefunction; under the effect of the Lorentz boost* e^Y*, the original* $\bar{q}q$ *configuration of size* b *gives rise to a soft gluon component, or in the* $N_c \to \infty$ *limit, to two dipoles of sizes* b_{02} *and* b_{12} *interacting with the other onium of size* b'.

2 Structure functions

The scale-ratio dependence obtained in formula (2) is of importance when considering another type of probe, a photon of virtuality Q^2, which corresponds on average[2] to a transverse size $1/Q$. In ref. [6], the (theoretical) process of deep-inelastic scattering on an onium state has been proposed to determine the origin of scaling violations of the structure function in the context of BFKL dynamics. Indeed from the viewpoint of the dipole picture, scaling violations are induced by a term analogous to the scale-ratio in eq. (2). One gets:

$$F_2^{onium} \propto \int \frac{d\gamma}{2i\pi}(bQ)^{2\gamma}\mathrm{e}^{\frac{\alpha N_c}{\pi}\chi(\gamma)\ln\frac{1}{x}} \propto bQ\; x^{-\left(\frac{4\alpha N_c \ln 2}{\pi}\right)} \frac{\exp\left(-\frac{1}{k\ln\frac{1}{x}}\ln^2(bQ)\right)}{\left(k\ln\frac{1}{x}\right)^{1/2}}, \quad (3)$$

where one uses the known BFKL analytic expression for the Mellin transform of the onium structure function, and $\chi(\gamma)$ is the corresponding kernel[4]. This expression leads to an interesting phenomenological extension to the proton structure functions, which has the property that it describes the scaling violations at small-x observed at HERA.

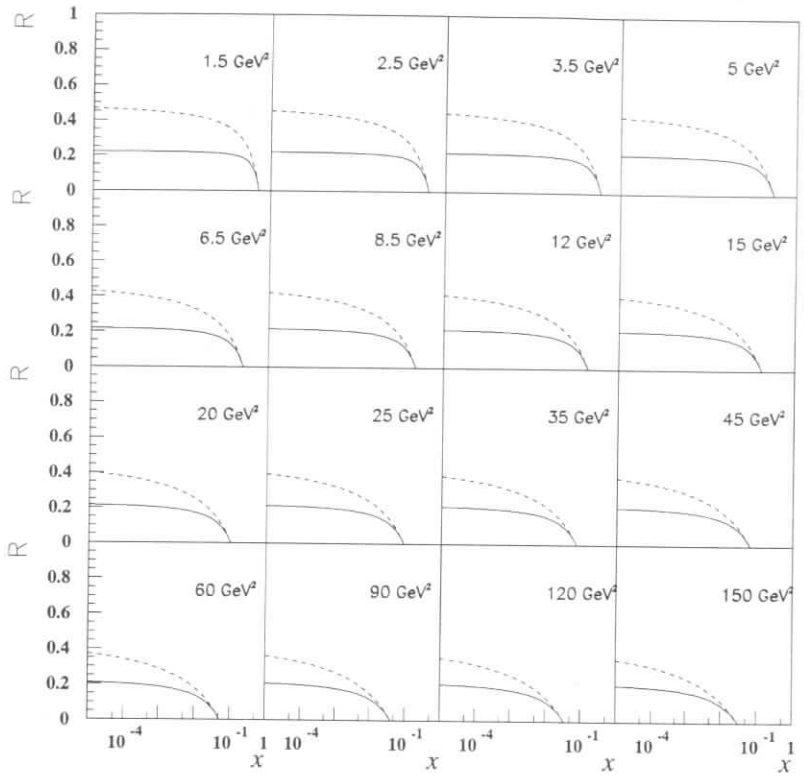

Figure 2: *Predictions for the ratio* $R \equiv F_L/F_T$ *in the dipole picture [6]. The full line describes the prediction based on a fit to* F_2 *data and, with the same parameters, a determination of the gluon structure function (not shown). The effect of the* $\ln\frac{1}{x}$ *resummation is seen by comparison with the one-loop approximation (dotted line). The prediction is significantly lower than the known DGLAP estimates, e.g. [8].*

Indeed, assuming k_T-factorisation properties[5] for high-energy scattering off a proton target, it is possible to extend the dipole model to deal with deep-inelastic scattering on a proton target[6]. Starting from formula (3), the Mellin integrand happens to be multiplied by $w(\gamma, b; Q_0)$ where w can be interpreted as the Mellin-transformed probability of finding a dipole of (small) transverse size b in the proton. $Q_0 >> b^{-1}$ is a typically non-perturbative proton scale. Noting that b is a small but arbitrary factorisation scale, the overall result has to be b-independent, provided it stays in the perturbative region. Hence, assuming renormalisation group properties to be valid[7], the b dependence of w has to match the $b^{-2\gamma}$ dependence in formula (3). One then writes

$$w(\gamma, b; Q_0) = w(\gamma)\ \ (bQ_0)^{2\gamma}\,. \tag{4}$$

This yields the final result[6]

$$\begin{pmatrix} F_T \\ F_L \\ F_G \end{pmatrix} = \frac{2\alpha N_c}{\pi} \int \frac{d\gamma}{2i\pi} \left(\frac{Q^2}{{Q_0}^2}\right)^{\gamma} e^{\frac{\alpha N_c}{\pi}\chi(\gamma)\ln(\frac{1}{x})} \begin{pmatrix} h_T \\ h_L \\ 1 \end{pmatrix} \frac{v(\gamma)}{\gamma} w(\gamma) \tag{5}$$

where $F_{T(L)}$ is the structure function corresponding to transverse(longitudinal) photons and F_G the gluon structure function. The known (resummed) coefficient functions $h_{T,L}(\gamma)$ are given in ref. [5], and the gluon-dipole coupling $v(\gamma)$ is derived in the second of refs. [6]. It is interesting that these formulae give a good fit of the HERA data on $F_2 = F_T + F_L$ in the small-x range and in a large domain of $Q^2 \leq 150\ GeV^2$. Moreover it leads to a gluon structure function in agreement with the H1 determination based on the next-leading order DGLAP evolution[8]. Note also that the ratios F_G/F_2 and $R \equiv F_L/F_T$ are independent of the non-perturbative function $w(\gamma)$. In relation to this a remark is in order for the future prospects of experimentation at HERA: As shown in fig.2, the predictions for R are rather low ($R < 2/9$) which appears to be in contradiction with the phenomenological estimate[8] based on the renormalisation group evolution for F_L. Indeed, as shown in fig. 2, the resummation of the leading $\alpha \log 1/x$ terms of the QCD perturbative expansion is crucial for obtaining the final prediction. This may give a hint for an experimental discrimination of DGLAP versus BFKL evolution equations which is difficult to achieve from the study of F_2 and F_G alone.

Another series of interesting phenomenological results apply to hard diffraction at HERA. The QCD dipole picture leads to two distinct dynamical components of diffraction by a virtual photon. One component, dominant at large diffractively produced masses, is analogous to the triple-(hard)Pomeron coupling and can be explicitly derived from the inelastic interaction of dipoles from both the photon and the proton sides [9]; A second component results from the *quasi-elastic* interaction of the primary dipole coupled to the photon to the proton target and is dominant at smaller diffractive masses [10]; The quantitative predictions from these two components are strongly correlated with the fits for F_2, giving a nice interrelation between the different aspects of deep-inelastic processes at HERA and the possibility to rely on perturbative QCD to get a coherent description for them.

3 Unitarity corrections

When the centre-of-mass energy becomes very high, the BFKL equation yields a scattering amplitude which violates the unitarity bound, or equivalently conservation of probability. The dipole formulation offers a well-defined way of alleviating the problem. One considers the scattering of two onia in the centre of mass frame. Schematically the scattering amplitude is just related to the probability that there will be an interaction between a parton in one onium and a parton in the other. The usual small-x growth of the cross section relies on the idea that the interaction cross section is proportional essentially to the product of the number of partons in each onium. This is only valid when the overall likelihood of an interaction is low. When there are many partons in each onium, multiple interactions become common[11], and

the interaction probability then depends on the details of how the partons are distributed in transverse position (for example if they are clumped together, then multiple interactions are much more likely than if they are uniformally spread out). These multiple-scattering corrections are equivalent to multiple t-channel pomeron exchange diagrams[1, 12].

To obtain the probabilities of different gluon distributions inside the onium, one can use OEDIPUS (Onium Evolution, Dipole Interaction and Perturbative Unitarisation Software) [13]. This simulates the small-x dipole branching producing random dipole configurations with the correct weights. It determines the interaction (both with and without multiple-scattering corrections) between pairs of these random configurations and then averages over the configurations. It is important that one averages over configurations only *after* taking into account multiple interactions — doing the averaging before taking into account the multiple interactions (the eikonal approximation) tends to wash out the correlations between gluons, and causes one to underestimate the point where corrections set in by up to two orders of magnitude in x.

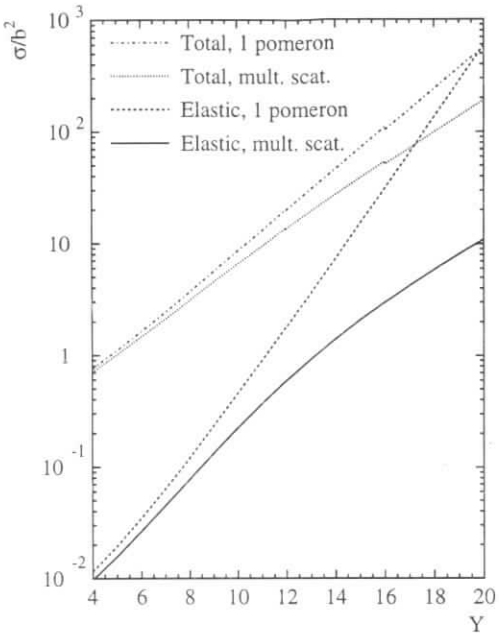

Figure 3: *The elastic and total cross sections for onium-onium scattering, as a function of rapidity, showing both the one-pomeron approximation and the results including multiple-scattering corrections.*

The results [12] are shown in figure 3. The rapidity Y corresponds roughly to $\ln 1/x$, and b is the onium size. The most striking point is that corrections to the total cross section set in very slowly, whereas the elastic cross section is subject to very strong modifications. The reason is that the total cross section is proportional to the integral over impact parameter, $\mathbf{r}$, of the amplitude $F(\mathbf{r})$, whereas the elastic cross section is proportional to the integral of the square of the amplitude:

$$\sigma_{\rm tot}(Y) = 2\int \mathrm{d}^2\mathbf{r}\, F(\mathbf{r}), \qquad \sigma_{\rm el}(Y) = \int \mathrm{d}^2\mathbf{r}\, |F(\mathbf{r})|^2. \tag{6}$$

Because of BFKL diffusion, for moderate $r = |\mathbf{r}|$ the leading dependence of the amplitude is $F(r) \sim 1/r^2$. Therefore the elastic cross section is dominated by small impact-parameters, where the amplitude is large and there are strong multiple-scattering corrections. The total cross section comes from a wide range of r, where the amplitude will on average be smaller, and so the corrections are less important. Effectively the total cross section carries on growing through an increase in area of interaction. More details can be found in [12]

Onium-onium scattering is a good theoretical laboratory because it ensures that it is safe to use perturbative QCD. For DIS one can expect two major qualitative differences: (a) infra-red effects will constrain the maximum size of the dipoles, limiting the growth of the total cross section, and altering the balance between total and elastic cross sections; (b) the presence of two different scales means that different kinds of dipole configurations will dominate the scattering, tending to reduce the multiple-interaction effects.

Acknowledgements

One of us (GPS) is grateful to B. R. Webber and A. H. Mueller for many helpful discussion and to the UK PPARC and the EU Programme "Human Capital and Mobility", Network "Physics at High Energy Colliders", contract CHRX-CT93-0357 (DG 12 COMA), for financial support. R.P. thanks A. Bialas, H. Navelet, Ch. Royon and S. Wallon for a fruitful collaboration.

References

[1] A. H. Mueller, Nucl. Phys. B 415 (1994) 373; A. H. Mueller and B. Patel, Nucl. Phys. B 425 (1994) 471; A. H. Mueller, Nucl. Phys. B 437 (1995) 107.

[2] N. N. Nikolaev and B. G. Zakharov, Zeit. f. Phys. C 64 (1994) 631; N. N. Nikolaev, B. G. Zakharov, and V. R. Zoller, JETP Lett. 59 (1994) 6.

[3] Z. Chen and A. H. Mueller, Nucl. Phys. B 451 (1995) 579.

[4] Ya. Ya. Balitskiĭ and L. N. Lipatov, Sov. J. Nucl. Phys. 28 (1978) 822; E. A. Kuraev, L. N. Lipatov, and V. S. Fadin, Sov. Phys. JETP 45 (1977) 199; L. N. Lipatov, Sov. Phys. JETP 63 (1986) 904.

[5] S. Catani, M. Ciafaloni and F. Hautmann, Phys. Lett. B 242 (1990) 97; Nucl. Phys. B 366 (1991) 135; J. C. Collins and R. K. Ellis, Nucl. Phys. B 360 (1991) 3; S. Catani and F. Hautmann, Phys. Lett. B 315 (1993) 157; Nucl. Phys. B 427 (1994) 475; see also E. M. Levin, M. G. Ryskin, Yu. M. Shabelski and A. G. Shuvaev, Sov. J. Nucl. Phys. 54 (1991) 867.

[6] H. Navelet, R. Peschanski and Ch. Royon, Phys. Lett. B 366 (1995) 329; H. Navelet, R. Peschanski, Ch. Royon and S. Wallon, hep-ph/9605389, submitted to Phys. Lett. B.

[7] A. De Rújula, S. Glashow, H. Politzer, S. Treiman, F. Wilczek, and A. Zee, Phys. Rev. D 10 1974 1649.

[8] H1 Coll., S. Aid et al., Nucl. Phys. B 470 (1996) 3.

[9] A. Bialas and R. Peschanski, Phys. Lett. B 378 (1996) 302.

[10] A. Bialas and R. Peschanski, hep-ph/9605298, to appear in Phys. Lett. B.

[11] L. V. Gribov, E. M. Levin and M. G. Ryskin, Phys. Rep. 100 (1983) 1.

[12] G. P. Salam, Nucl. Phys. B 449 (1995) 589; Nucl. Phys. B 461 (1996) 512; A. H. Mueller and G. P. Salam, preprint CU-TP-746, hep-ph/9605302, to appear in Nucl. Phys. B; Yu. Kovchegov, A. H. Mueller, and S. Wallon, in preparation.

[13] G. P. Salam, preprint Cavendish-HEP-95/07, hep-ph/9601220.

Gluon distributions from the CCFM equation.

P.J. Sutton

Department of Physics and Astronomy, University of Manchester, Brunswick Street, Manchester, M13 9PL, England.

Abstract: We solve a unified integral equation (the CCFM equation) for the gluon distribution of a proton in the small x regime. The equation generates a gluon with a steep $x^{-\lambda}$ behaviour, with $\lambda \sim 0.5$. We compare the solution with that of the double-leading-logarithm approximation to Altarelli-Parisi evolution and that of the BFKL equation.

1 Introduction

A theoretical framework which gives a unified treatment of both the DGLAP ($\ln(Q^2)$) and BFKL ($\ln(1/x)$) evolution has been provided by Catani, Ciafaloni, Fiorani and Marchesini [1]. It is based on the coherent radiation of gluons, which leads to an angular ordering of the gluons along a chain of multiple emissions. The CCFM equation is defined in terms of a scale (Q) dependent *unintegrated* gluon density $F(x, k_T^2, Q^2)$, which specifies the chance of finding a gluon with longitudinal momentum fraction x and transverse momentum of magnitude k_T.

$$F(x,k_T^2,Q^2) = F^0(x,k_T^2,Q^2) + \int_x^1 dz \int \frac{d^2q}{\pi q^2}\Theta(Q-zq)\Delta_S(Q,zq)\tilde{P}(z,q,k_T)F\left(\frac{x}{z},k_T'^2,q^2\right). \quad (1)$$

The inhomogeneous or "no-rung" contribution, F^0, may be regarded as the non-perturbative driving term. The function $\tilde{P}$ is the gluon-gluon splitting function

$$\tilde{P} = \overline{\alpha}_S\left[\frac{1}{1-z} + \Delta_R\frac{1}{z} - 2 + z(1-z)\right] \quad (2)$$

where $\overline{\alpha}_S \equiv 3\alpha_S/\pi$. The multiplicative factors Δ_S and Δ_R cancel the singularities manifest as $z \to 1$ and $z \to 0$ respectively. Their explicit form can be found in, for example, refs. [1, 2].

2 Numerical solution of the CCFM equation

In this contribution we are interested in the CCFM equation at small x. In this region we may simplify the equation (1) as follows [2]

$$F(x,k_T^2,Q^2) = F^0(x,k_T^2,Q^2) + \overline{\alpha}_S\int_x^1 \frac{dz}{z}\int \frac{d^2q}{\pi q^2}\Theta(Q-zq)\Delta_R(z,q,k_T)F\left(\frac{x}{z},(\boldsymbol{k}_T+\boldsymbol{q})^2,q^2\right) \quad (3)$$

We take the scale of the running coupling, α_s, to be k_T^2 and we choose F^0 such that it would generate a "flat" gluon, $xg \sim 3(1-x)^5$, in the absence of angular ordering and the Δ_R correction term [2]. With these choices we solve (3) by iteration from the starting distribution. Fig. 1 shows our solution in terms of the integrated gluon distribution, $xg(x, Q^2)$. Also shown are the corresponding solutions for the BFKL equation and the double-leading-logarithm (DLL) approximation to the DGLAP equations.

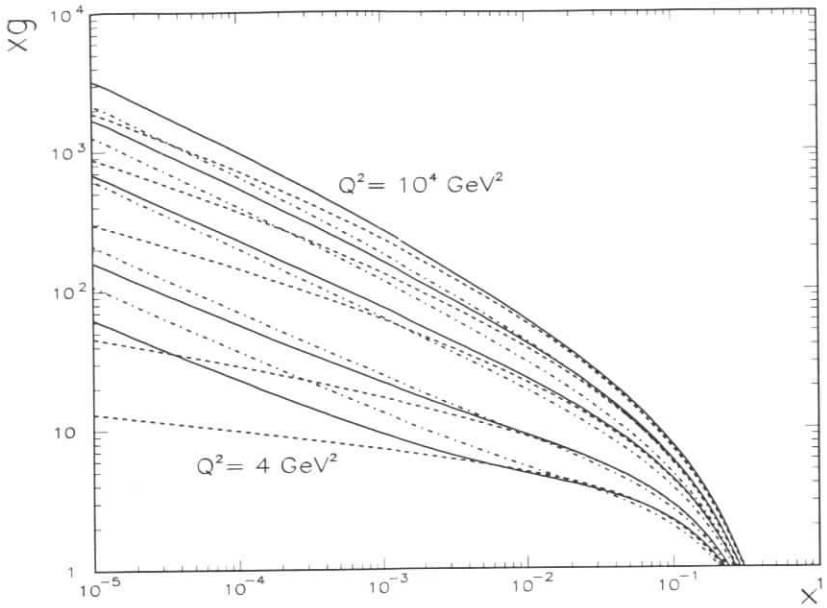

Figure 1: *The integrated gluon distribution xg versus x, obtained from the CCFM (continuous curves), BFKL (dot-dash curves) and the DLL (dashed curves) integral equations, for $Q^2 = 4, 10, 10^2, 10^3$ and 10^4 GeV^2. Our solutions are obtained from a "flat" gluon input [2]*

To quantify the increase in xg, we show in Fig. 2 the effective value of λ, defined by

$$xg(x, Q^2) = Ax^{-\lambda}. \tag{4}$$

For small x we see that the solutions converge to a typical $x^{-0.5}$ behaviour, approximately independent of Q^2, which is consistent with that obtained from the solution of the BFKL equation, although the onset of the $x^{-\lambda}$ form is more delayed for the CCFM solution.

The gluon distribution itself is, of course, not an observable. However, the behaviour of the gluon feeds through into physical quantities such as the structure functions. In deep inelastic scattering the virtual photon couples to the gluon via the $g \to q\bar{q}$ transition. We have therefore calculated the structure function F_2 from the unintegrated gluon distribution F using the k_T-factorization theorem. Details of this calculation can be found in ref. [3].

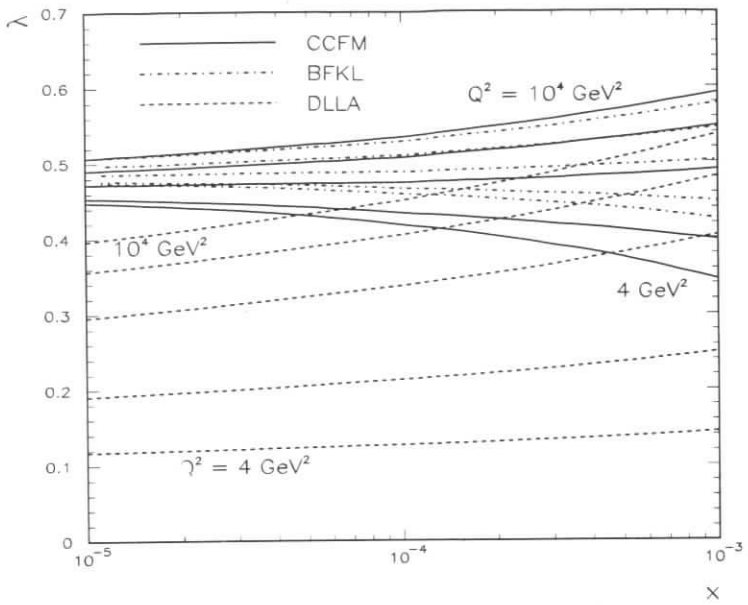

Figure 2: *The effective values of λ, defined by $xg = Ax^{-\lambda}$. The CCFM values (continuous curves) are compared with those obtained from the BFKL (dot-dashed curves) and DLL approximations (dashed curves). In each case we show curves corresponding to five different values of Q^2.*

3 Acknowledgements

I would like to thank Professors A.D. Martin and J. Kwieciński for their collaboration in the work discussed here.

References

[1] M. Ciafaloni, Nucl. Phys. **B296**, 49 (1988); S. Catani, F. Fiorani and G. Marchesini, Phys. Lett. **B234**, 339 (1990); Nucl. Phys. **B336**, 18 (1990);
G. Marchesini, in Proceedings of the Workshop "QCD at 200 TeV", Erice, Italy, 1990, edited by L. Cifarelli and Yu. L. Dokshitzer (Plenum Press, New York, 1992), p.183;
G. Marchesini, Nucl. Phys. **B445**, 49 (1995).

[2] J. Kwieciński, A. D. Martin and P. J. Sutton, Phys. Rev. **D52**, 1445 (1995).

[3] J. Kwieciński, A. D. Martin and P. J. Sutton, Phys. Rev. **D53**, 6094 (1996);
A. D. Martin, J. Kwieciński and P.J. Sutton, Durham preprint DTP/96/02, hep-ph/9602320, to be published in Z. Phys. C.

Experimental constraints on coefficients of α_S-expansion of Gottfried sum rule

A.V. Sidorov and M.V. Tokarev

Joint Institute for Nuclear Research, 141980 Dubna, Moscow Region, Russia

Abstract: The x- and Q^2-dependences of the Gottfried sum rule $S_G(x,Q^2)$ based on the experimental data on proton and deuteron structure functions are studied. For the first time, the coefficients c_1, c_2 of the expansion of $S_G(x,Q^2)$ in α_S/π up to second order are evaluated through the phenomenological analysis of NMC and H1 data. It is found that c_1 is negative while c_2 is positive. The obtained result is in disagreement with QCD predictions for these coefficients. We suggest measuring the low x-dependence of the F_2^D deuteron structure function at HERA in order to study the Q^2-dependence of the Gottfried sum rule.

1 Introduction

The experimental data on the proton and neutron structure functions (SF) are of great interest for verification of the theory of strong interaction, QCD. The relevant information can be used to extract the spin-dependent and spin-independent parton distributions, to estimate nonperturbative effects, to verify nucleon models and sum rules such as the Gottfried [1], Bjorken [2], Ellis-Jaffe [3], Gross-Llewellyn Smith [4] and Adler[5] ones.

New data on the deuteron SF F_2^D obtained at CERN, SLAC and Fermilab [6]-[9] stimulated great interest in theoretical studies of the deuteron structure.

The deuteron is an excellent neutron target and therefore the neutron structure functions F_2^n were usually extracted from the experimentally known proton and deuteron structure functions.

The extraction procedure of the neutron SF from deuteron and proton data is ambiguous and, therefore, the estimate of nuclear effects in the deuteron is extremely important not only to obtain new information on F_2^n but also to verify deuteron models and to perform a common QCD analysis of experimental data.

The Gottfried sum rule was verified by the NMC Collaboration [6] and the value of $S_G = 0.240 \pm 0.016$ was found to be below the parton model prediction. To study the sum rule in detail, the experimental data on the deuteron structure function F_2^D at low x and large Q^2 are necessary. Such measurements are possible to perform at HERA [10].

In the present paper, the phenomenological analysis of x and Q^2 dependences of the $S_G(x,Q^2)$ Gottfried sum rule is based on the NMC [7, 8], H1 [11] and ZEUS [12] parametrization of the proton structure function $F_2^p(x,Q^2)$. It is shown [13] that the available experimental data on

F_2^p and F_2^D allow one to estimate the α_S correction to $S_G(Q^2)$. The expansion coefficients of $S_G(Q^2)$ up to order $Q(\alpha^2)$ are estimated. It is found that the obtained results are in disagreement with the QCD predictions. To clarify the discrepancy, it was proposed to measure the $F_2^D(x,Q^2)$ deuteron structure function at low x and high Q^2 in order to extract precisely the coefficients of α_S-expansion of the Gottfried sum rule.

2 Deep-Inelastic Scattering on Deuteron

The cross section of deep-inelastic lepton-deuteron scattering in the one-photon approximation is expressed via the imaginary part of the forward scattering amplitude of the virtual photon or W-boson on the deuteron - $W_{\mu\nu}^D$. The latter is related to the deuteron spin-dependent - $g_{1,2}^D(\nu,Q^2)$ and spin-independent - $F_{1,2,3}^D(\nu,Q^2)$ structure functions as follows

$$W_{\mu\nu}^D = -(g_{\mu\nu} - q_\mu q_\nu/q^2)\cdot F_1^D + (p_\mu - q_\mu(pq)/q^2)(p_\nu - q_\nu(pq)/q^2)\cdot F_2^D/\nu$$
$$+i\epsilon_{\mu\nu\alpha\beta}q^\alpha\{s^\beta g_1^D/\nu + [s^\beta(qp) - p^\beta(sq)]M^{-1}g_2^D/\nu^2\} + i\epsilon_{\mu\nu\alpha\beta}\, q^\alpha p^\beta\cdot F_3^D/\nu. \quad (1)$$

Here q, p are momenta of the photon and deuteron; M is the deuteron mass; $\nu = (pq)$; the 4-vector s_α describes the deuteron spin. The symmetric part of the deuteron tensor $W_{\mu\nu}^D$ can be written as $W_{\mu\nu}^D = W_{\mu\nu}^{\alpha\beta}\cdot\rho_{\alpha\beta}^{(S)}$

$$W_{\mu\nu}^{\alpha\beta} = \int\frac{d^4k}{(2\pi)^4 i}\delta(m^2-k^2)\theta(k_0)\theta(p_+-k_+)\ Sp\{w_{\mu\nu}^N\cdot\bar\psi^\alpha(k_1)\cdot(m+\hat k)\cdot\psi^\beta(k_1)\}. \quad (2)$$

Here the θ-function and light-cone variables - $(k_\pm, k_\perp)$ are used. The tensor $\rho_{\alpha\beta}^{(S)}$ is the symmetric part of the deuteron polarization density matrix. The antisymmetric part of the deuteron tensor $W_{\mu\nu}^D$ is expressed in a form similar to (2). The procedure to construct the relativistic deuteron wave function (RDWF) ψ_α was proposed and RDWF was obtained in [14].

3 Deuteron and Neutron Structure Functions

The deuteron SF F_2^D in the light-cone variables is expressed as follows

$$F_2^D(\alpha,Q^2) = \int_\alpha^1 dx\ d^2k_\perp\ p(x,k_\perp)\cdot F_2^N(\alpha/x,Q^2). \quad (3)$$

The nucleon SF $F_2^N = (F_2^p + F_2^n)/2$ is defined by the proton and neutron ones. The function $p(x,k_\perp)$ describes the probability that the active nucleon carries away the fraction of the deuteron momentum $x = k_{1+}/p_+$ and the transverse momentum $k_\perp$ in the infinite momentum frame. It is expressed via the RDWF

$$p(x,k_\perp)\propto Sp\{\bar\psi^\alpha(k_1)\cdot(m+\hat k_1)\cdot\psi^\beta(k_1)\cdot\hat q/\nu\cdot\rho_{\alpha\beta}^{(S)}\}. \quad (4)$$

The nuclear effect in the deuteron is described by the ratio $R_F^{D/N} = F_2^D/F_2^N$. It was shown in [15] that the effect of relativistic Fermi motion grows with x and the ratio $R_F^{D/N}$ reaches 6% at $x\simeq 0.7$. The dependence of the ratio $R_F^{D/N}$ on x resembles the nuclear EMC effect and it is practically independent of Q^2. Using the universal behaviour of the ratio it is possible to extract the neutron SF F_2^n

$$F_2^n(x,Q^2) = 2 \cdot [R_F^{D/N}(x)]^{-1} \cdot F_2^D(x,Q^2) - F_2^p(x,Q^2). \quad (5)$$

We would like to note that for a reliable estimate of other contributions to F_2^D from nuclear effects such as nuclear shadowing, meson exchanges etc., the data at low x such as the E665 data [9] are required.

4 Gottfried Sum Rule

The extracted neutron SF can be used to verify the Gottfried sum rule [1]:

$$\int_0^1 [F_2^p(x) - F_2^n(x)]dx/x = 1/3. \quad (6)$$

The Gottfried integral as a function of x and Q^2 is defined as follows

$$S_G(x,Q^2) = \int_x^1 [F_2^p(y,Q^2) - F_2^n(y,Q^2)]dy/y. \quad (7)$$

To verify the sum rule, not only the x-dependence of SF's also Q^2-dependence in a wide kinematical range are necessary. The realistic comparison of the experimental results with theoretical predictions based on QCD is more argued at high Q^2.

As has been reported in [6], the value of S_G at $Q^2 = 4.0$ $(GeV/c)^2$ obtained from the measurements of F_2^D and F_2^p is considerably below the value of the naive quark-parton model equal to 1/3: $S_G = 0.240 \pm 0.016$. This result in the parton model is usually interpreted as the violation of the isospin symmetric sea. As will be shown later, the symmetry violation demonstrates the strong Q^2-dependence.

The QCD corrections of order $O(\alpha_s)$ [16] and $O(\alpha_s^2)$ [17] are estimated for the Gottfried sum rule in the case of flavor-symmetric sea $\bar{u} = \bar{d}$:

$$S_G(Q^2) = \frac{1}{3} \cdot (1 + \bar{c}_1 \cdot (\alpha_S/\pi) + \bar{c}_2 \cdot (\alpha_S/\pi)^2). \quad (8)$$

The coefficients $\bar{c}_1, \bar{c}_2$ are equal to 0.036, 0.72 for $n_f = 3$ and 0.038, 0.55 for $n_f = 4$, respectively. Thus, the coefficients $\bar{c}_1$, $\bar{c}_2$ are found to be positive and relatively small, and as mentioned in [17], the QCD corrections cannot explain the deviation of the theoretical prediction from the experimental result of the NMC collaboration without the assumption that the light quark sea is flavor asymmetric.

5 Procedure to Extract Neutron Structure Function

The method to extract $F_2^n(x,Q^2)$ from proton and deuteron experimental data was proposed and realized in [15].

The procedure includes the items: **1.** experimental data on the ratio $R_F^{D/p} = F_2^D/F_2^p$ and structure functions F_2^p, F_2^D; **2.** the relativistic deuteron model [14]; **3.** the choice of the parametrization of the F_2^n neutron structure function and the determination of free parameters to describe the ratio $R_F^{D/p} = F_2^D/F_2^p$; **4.** the comparison of the absolute values of the experimental and theoretical structure function $F_2^D(x,Q^2)$; **5.** the determination of the ratio

$R_F^{D/N} = F_2^D/F_2^N$ describing the nuclear effect in the deuteron; **6.** the extraction of the neutron structure function from experimental data using the formula

$$F_2^n(x,Q^2) = 2 \cdot [R_F^{D/N}]^{-1} \cdot F_2^D(x,Q^2) - F_2^p(x,Q^2). \quad (9)$$

In [15] the NMC data [6, 7] on the ratio $R_F^{D/p} = F_2^D/F_2^p$, F_2^p and the relativistic deuteron model were used to extract the neutron SF F_2^n. It was shown that the calculated results for ratio $R_F^{D/p}$ and $F_2^D(x,Q^2)$ are in good agreement with the available experimental data [6, 7, 18, 19].

Thus, the conclusion was made that the extraction procedure proposed for $F_2^n(x,Q^2)$ is self-consistent because it provides a good description of higher statistics experimental data on the ratio $R_F^{D/p}$ and F_2^D over a wide kinematic range of x and Q^2.

We would like to emphasize that the nuclear effect of Fermi motion was only used in [15]. The shadowing effect [20] should be also included into the procedure if the deuteron data in the low x- and Q^2- range are used (for example, E665 data). In that case, the factor $R^{D/N}$ should be corrected at low x.

6 Results and Discussion

Figure 1(a) shows the dependence of the Gottfried integral $S_G(x,Q^2)$ on x and Q^2. The parametrization of the proton structure function $F_2^p(x,Q^2)$ for H1 data is taken from [11]. It was shown in [13] that the x- and Q^2-dependences of $S_G(x,Q^2)$ for the parametrizations [7, 8] are similar to H1 one [11]. The NMC parametrization [7] was used in[15] for calculating the deuteron structure function $F_2^D(x,Q^2)$ and a good agreement with experimental data SLAC, BCDMS, NMC was obtained both for a low and high x range. It is assumed [15] that the ratio $f(x) = F_2^n(x,Q^2)/F_2^p(x,Q^2) \to 1$ as $x \to 0$. The parametrization of the $f(x)$ function was obtained and will be used later for the determination of the neutron SF from the H1 and ZEUS proton structure function parametrization.

We would like to note that there is the crossover point x_0 (in particular, $x_0 \sim 0.01$ for the H1 parametrization) separating two ranges: one - with decreasing $S_G(x,Q^2)$ and the other - with increasing $S_G(x,Q^2)$ with Q^2, respectively. A similar dependence of the $S_{GLS}(x,Q^2)$ Gross-Llewellyn Smith integral on Q^2 with the crossover point $x_0 = \simeq 10^{-2}$ is predicted in [21]. Note that the main part of the $S_G(x,Q^2)$ integral is given by integration over the interval of relatively large x ($10^{-2} < x < 1$.) and determines the first term in expansion (8).

Figure 1(b) shows the dependence of the derivative $dS_G(x,Q^2)/d\alpha_S$ on x and Q^2. The 3-loop perturbative QCD expression of α_S with $n_f = 4$ is used. The derivative grows up to $x \simeq 0.1 - 0.2$ then decreases and changes in sign for $Q^2 > 100$ GeV^2 for NMC and even for smaller Q^2 for H1 parametrization. It should be stressed that *the negative value of the derivative $dS_G(x,Q^2)/d\alpha_S$ is due to the small x contribution to the Gottfried integral.*

Figure 2 shows the dependence of $S_G(Q^2)$ on α_S/π at $x = 10^{-3}$ in (7). The α_S-dependence could be parametrized by the parabola:

$$S_G(Q^2) = S_0 \cdot (1 + c_1 \cdot (\alpha_S/\pi) + c_2 \cdot (\alpha_S/\pi)^2). \quad (10)$$

The values of S_0, c_1, c_2 are presented in Table 1. They could be considered as α_S corrections to the Gottfried sum rule. It was shown in [13] that the derivative $dS_G(Q^2)/d\alpha_S$ is negative at

$\alpha_S/\pi < 0.05$ for all parametrizations F_2^p, and the H1 curve crosses the NMC one in the range $Q^2 = 5 - 10$ $(GeV/c)^2$.

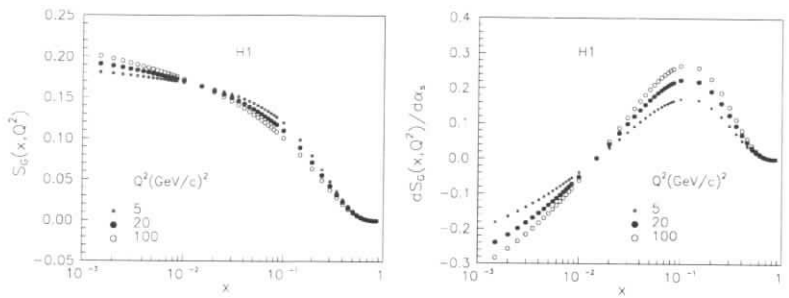

a) b)

Figure 1: *The Gottfried integral $S_G(x,Q^2)$ and the derivative $dS_G(x,Q^2)/d\alpha_S$ as a function of x and Q^2.*

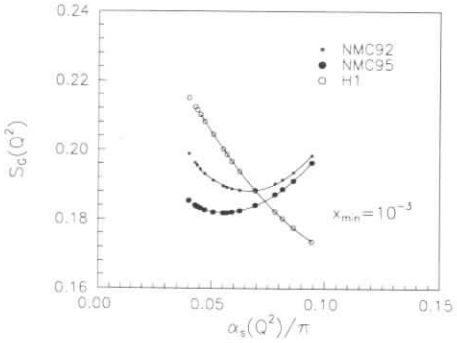

Figure 2: *The Gottfried integral $S_G(,Q^2)$ as a function of α_S at $x = 10^{-3}$. The lines present the paraboloic fit of $S_G(,Q^2)$ for different parameterisations F_2^p.*

Despite different kinematical regions of NMC and H1 experiments used for fits of experimental data one can see from Table 1 the reasonable quantitative and good qualitative agreement between the corresponding coefficients S_0, c_1, c_2 for parametrizations of the proton SF under consideration. Note that the F_2^p parametrization of H1 is combined with the data from NMC and BCDMS experiments and a smooth transition between different F_2^p data is obtained. The kinematic range covers almost four orders of magnitude in x and Q^2.

Table 1. The coefficients of the $S_G(Q^2)$ Gottfried integral expansion in α_S/π.

	S_0	c_1	c_1
NMC92 [7]	0.246	-7.06	53.2
NMC95 [8]	0.210	-4.87	44.2
H1 [11]	0.271	-6.04	23.7
average value	0.242± 0.21	-6.00± 0.74	40.4± 11.1

The average values for the coefficients r_i $(i = S_0, c_1, c_2)$ are calculated by $< r >= (\sum_i r_i)/n$ and $< \Delta r >= (\sum_i | < r > -r_i|)/n$ and presented in Table 1. The errors obtained could be considered as a crude estimation of systematic uncertainties.

It should be noted that the parametrization of the ZEUS data [12] for F_2^p provides qualitatively the same results: $S_0 = 0.383$, $c_1 = -12.9$ and $c_2 = 76.2$.

We would like to emphasize that the values of coefficients obtained from the phenomenological analysis of experimental data are essentially different from the theoretical QCD predictions for $\bar{c}_1$ and $\bar{c}_2$. The coefficient c_1 is found to be negative, in contrast to $\bar{c}_1$. Both c_1, c_2 are many times larger in the absolute value than $\bar{c}_1$, $\bar{c}_2$.

7 Conclusions

The analysis of Q^2-dependence of the Gottfried sum rule based on experimental data on the proton F_2^p and deuteron F_2^D structure functions in the framework of the covariant approach in the light-cone variables and relativistic deuteron model was performed:

- the procedure to extract the neutron SF $F_2^n(x,Q^2)$ is described and used to analyze the parametrizations of NMC, BCDMS, SLAC, H1, ZEUS data on F_2^D and F_2^p SF's
- the increase of the $S_G(Q^2)$ Gottfried sum rule for small $\alpha_S(Q^2)$ is a general feature for the NMC92, NMC95, H1 parametrizations. This behaviour is connected with the *negative value of the first order α_S correction* to the GSR
- it is shown that the results obtained for c_1 and c_2 are in disagreement with the calculation made in the framework of QCD assuming the flavour symmetry of sea quarks $(\bar{u} = \bar{d})$
- the measurements of the deuteron structure function F_2^D at HERA, extraction the neutron SF F_2^n and verification of the Q^2-dependence of $S_G(x,Q^2)$ at low x are necessary to determine the α_S-corrections to GSR more reliably.

8 Acknowledgement

The authors would like to thank Yu.A.Panebratsev for his support of our work. This work was partially supported by Grants of the Russian Foundation for Fundamental Research under No. 95-02-05061 and No. 96-02-18897. One of us (M.V.T.) are very grateful to R.Klanner and M.Klein for support to take part in the Workshop "Future at HERA".

References

[1] K. Gottfried, Phys. Rev. Lett. **18** (1967) 1174.

[2] J. Bjorken, Phys. Rev. **148** (1966) 1467.

[3] J. Ellis, R. Jaffe, Phys. Rev. **D9** (1974) 1444.

[4] D. J. Gross and C. H. Llewellyn Smith, Nucl. Phys. **B14** (1969) 337.

[5] S. L. Adler, Phys. Rev. **143** (1966) 1144.

[6] P. Amaudruz et al., Phys. Rev. Lett. **66** (1991) 2712;
M.Arneodo et al., Phys.Rev. **D50** (1994) R1.

[7] P. Amaudruz et al., Preprint CERN-PPE/92-124, 1992.

[8] M.Arneodo et al., Phys. Lett. **B364** (1995) 107;
Preprint CERN-PPE/95-138, 1995.

[9] M.R. Adams et al., Phys. Lett. **B309** (1993) 477.

[10] M.Düren, DESY HERMES-95-92, 1995.

[11] T.Ahmed et al., Nucl. Phys. B439 (1995) 471;
A.Aid et al., DESY 96-039, 1996.

[12] M.Derrick et al., Z.Phys. **C65** (1995) 379.

[13] A.V.Sidorov, M.V.Tokarev, JINR preprint E2-96-290, Dubna, 1996.

[14] M.A.Braun, M.V.Tokarev, Particles and Nuclei **22** (1991) 1237.

[15] M.A.Braun, M.V.Tokarev, Phys. Lett. **B320** (1994) 381.

[16] D.A. Ross, C.T. Sachrajda, Nucl. Phys. **B149** (1979) 497;
F.J.Yndurain, Quantum Chromodynamics (An Introduction to the Theory of Quarks and Gluons).- Berlin, Springer-Verlag (1983), 117.

[17] A.L.Kataev et al., Preprint INP-0919/96, Moscow, 1996 [hep-ph/9605367];
Submitted to Phys. Lett. **B**.

[18] L.Whitlow et al., Phys. Lett. **B282** (1992) 475.

[19] A.C. Benvenuti et al., Phys. Lett. **B223** (1989) 485;
A.C. Benvenuti et al., Phys.Lett. **B237** (1990) 592.

[20] B.Badelek, J.Kwieciński, Nucl. Phys. **B370** (1992) 278.

[21] A.V. Sidorov, M.V. Tokarev, Phys. Lett. **B358** (1995) 353.

Working Group on

Electroweak Physics

Conveners:

R. Cashmore (Oxford), E. Elsen (DESY),
B.A. Kniehl (MPI Munich), H. Spiesberger (DESY, MPI Munich)

Participants:

I. Akushevich (NC PHEP Minsk, Belarus), R. Beyer (DESY), F. Buesser (Hamburg), R. Cashmore (Oxford), A. Cooper-Sarkar (Oxford), F. Cornet (Granada), S. Dagan (Imp. College, Tel Aviv), O. Deppe (DESY), E. Elsen (DESY), J. Edmonds (Oxford), A. Fahr (Hamburg), J. Fleischer (Bielefeld), M. Flieser (MPI Munich), G. Grzelak (Warsaw), R. Graciani (Madrid), D. Haidt (DESY), J. Hart (RAL), H. Hessling (DESY), W. Hollik (Karlsruhe), A. Ilakovac (Zagreb), J. Illana (Granada), T. Ishii (Tokyo), U. Katz (Bonn), B. Kniehl (MPI Munich), S. Limentani (DESY), K. Long (Imp. College), M. Martinez (Madrid), N. McCubbin (RAL), J. Meyer (DESY), C. Nath (Oxford), V. Noyes (Oxford), J. Papavassiliou (Marseille), M. Pawlak (Warsaw), A. Pilaftsis (RAL), S. Riess (Hamburg), K. Rueter (MPI Munich), A. Schoening (DESY), J. Sedgbeer (Imp. College), H. Spiesberger (DESY, MPI Munich), B. Straub (DESY), R. Walczak (Oxford), D. Waters (Oxford), A. Whitfield (Imp. College), A. Zarnecki (DESY), F. Zetsche (DESY)

Electroweak Physics — Working Group Reports:

Electroweak Physics at HERA: Introduction and Summary

R. J. Cashmore[a], E. Elsen[b], B. A. Kniehl[cd], H. Spiesberger[c]

[a] Department of Physics, University of Oxford, 1 Keble Road, Oxford OX1 3NP, UK
[b] Deutsches Elektronen-Synchrotron DESY, Notkestraße 85, 22603 Hamburg, Germany
[c] Max-Planck-Institut für Physik (Werner-Heisenberg-Institut), Föhringer Ring 6, 80805 Munich, Germany
[d] Institut für Theoretische Physik, Ludwig-Maximilians-Universität, Theresienstraße 37, 80333 Munich, Germany

Abstract: A high luminosity upgrade of HERA will allow the measurement of standard model parameters and the neutral current couplings of quarks. These results will have to be consistent with other precision measurements or indicate traces of new physics. The analysis of W production will complement future results of LEP 2 and the Tevatron. We summarize the main results and conclusions obtained by the working group on *Electroweak Physics* concerning the potential of future experimentation at HERA.

1 Introduction

The DESY ep collider HERA is a unique place to explore the structure of the proton, in particular at low Bjorken x and large momentum transfer Q^2 and at the same time to probe the theory of electroweak interactions in the regime of large spacelike Q^2, extending previous measurements at fixed target experiments by more than two orders of magnitude. This is complementary to what can be accessed at LEP and hadron colliders in searches for deviations from the standard model (SM). In the 1987 [1] and 1991 [2] HERA workshop proceedings and elsewhere [3], comprehensive reviews on electroweak physics at HERA [4, 5] and the influence of radiative corrections [6, 7] have been published. In the meantime HERA has started and proved to work reliably. The detectors have shown to operate successfully and to be able to stand the special environment of an ep machine.

The experience collected in the first years of experimentation at HERA allowed us to consider in the present workshop in some detail experimental problems, like systematic uncertainties due to the energy scale, the luminosity measurement or the measurement of the polarization, as well as limited acceptance and efficiencies. In this respect, the contributions to this workshop go beyond earlier studies.

The principal goal of the present workshop, on *Future Physics at HERA*, is to explore the physics potential attainable by possible machine and detector upgrades with respect to the

various options under discussion: (i) high (1 TeV) versus design (820 GeV) proton energy; (ii) fixed-target versus collider mode; (iii) light or heavy nuclei versus protons; (iv) polarized versus unpolarized protons; (v) polarized versus unpolarized electrons and positrons; and (vi) high (1 fb^{-1}) versus design (250 pb^{-1}) luminosity. Working group 2 has analyzed these options and concentrated on the interesting cases for *Electroweak Physics*. In this introductory report, we shall summarize the main results obtained by the various subgroups and draw conclusions.

Prior to presenting an overview of the various subgroup activities and reporting the key results, we preselect from the upgrade options enumerated above those which will prove most useful for the study of electroweak physics at HERA, and argue why the residual options will have marginal advantage or even disadvantage. In order to suppress the impact of the (well-tested) electromagnetic interaction in neutral-current (NC) deep inelastic scattering and to gain sensitivity to the W-boson mass in charged-current (CC) deep inelastic scattering, large values of Q^2 and thus centre-of-mass energy $\sqrt{s}$ are required. Increasing the proton energy E_p by 22% while keeping the lepton energy E_e fixed, as in option (i), will only increase $\sqrt{s}$ by 10%, and will insignificantly improve the electroweak-physics potential. By the same token, the fixed-target mode of option (ii) will reduce the centre-of-mass energy to $\sqrt{s} = 7.6$ GeV, assuming the design lepton energy of $E_e = 30$ GeV, and will so render the study of electroweak physics much more difficult. Clearly, in order to perform precision tests of the electroweak theory, we will need as much luminosity per experimental setup as possible, so that option (vi) must receive high priority. Also, to disentangle the helicity structure of the weak NC and, in particular, to measure the vector and axial-vector couplings of quarks to the Z-boson, beams of longitudinally polarized electrons and positrons must be available with appropriate luminosities [8], as in option (v). On the other hand, options (iii) and (iv) are not useful for our purposes, since the structure functions of nuclei and polarized protons are at present poorly known, which would jeopardize electroweak precision tests. In addition, the total available luminosity would be distributed among too many different experimental setups and probably decreased due to the additional construction periods. In conclusion, options (v) and (vi) will be crucial for electroweak studies.

At HERA, investigations of electroweak physics may be classified according to two categories of processes: First, there is the more conventional measurement of inclusive deep inelastic scattering. Due to reasonably high cross sections, not only the measurement of total cross sections and their ratios, but also of differential cross sections, will allow us to envisage precision tests of the electroweak standard model. Experiments may be interpreted in terms of a measurement of the basic standard model parameters, e.g. the mass of the W boson, m_W, or the top-quark mass, m_t. The potential of HERA for this kind of analysis was investigated in Ref. [9] and is summarized in section 2.1. Confronting within the standard model measurements obtained at HERA with results from other experiments will constitute one important test of our present understanding of the electroweak interactions. Another type of test of the standard model is possible by measuring quantities which are not free parameters in the standard model Lagrangian and comparing the experimental results with corresponding theoretical predictions. In particular, the measurement of NC couplings of quarks is a test of this kind and was studied in Ref. [10] (section 2.2). More general quantities generalizing the standard model Lagrangian, like the ρ-parameter or the S, T, U parameters have been considered earlier in Ref. [3]. Finally, an analysis aiming to assess the sensitivity for additional heavy charged gauge bosons W' (section 2.4) starts to overlap with the activities of the working group *Beyond the Standard Model*.

The second class of processes with a potential to study electroweak physics comprises scattering processes into exclusive final states. The aim to measure processes like Higgs-boson production (see section 2.7), the production of b-quarks or, most interestingly, of W and Z bosons (section 2.5), and to compare corresponding experimental results with the predictions of the standard model is an experimental challenge by itself. In the latter case, in order to quantify the results of such measurements testing the validity of the standard model in the gauge sector, it has become customary to generalize the standard model Lagrangian by introducing non-standard, so-called anomalous, couplings. Eventually, the information obtained by studying these processes will be concentrated in statements about these anomalous 3-boson couplings, $\Delta\kappa_V$ and λ_V for WWV ($V = \gamma, Z$) and h_i^V for $Z\gamma V$.

Theoretical uncertainties due to an incomplete knowledge of the structure function input, as well as unknown higher-order QCD corrections and uncertainties in the scale of α_S, deserve particular attention since they could severely limit the usefulness of electroweak physics analyses of deep inelastic scattering [9, 11]. Each of the subgroups has therefore undertaken particular efforts to demonstrate that already with the present knowledge about structure functions sensible measurements can indeed be performed. With high luminosity available, future measurements at HERA are bound to improve the situation.

2 Summaries of the individual contributions

2.1 Electroweak precision tests

The most obvious question about the possible contribution of HERA for electroweak physics tests is to which extent the basic standard model parameters m_W, m_t and m_H can be constrained by precision measurements of deep inelastic scattering cross sections. From earlier work it is known that measurements at HERA without any additional input from other experiments are very similar to a measurement of G_μ, the μ decay constant, but at $\langle Q^2 \rangle = O(3000\,\mathrm{GeV}^2)$.

In the report of the subgroup on *Electroweak Precision Tests*, it is pointed out that, although an interpretation of deep inelastic scattering measurements in terms of either m_W or m_t results in rather large errors, HERA data will put a rather stringent constraint on the interrelation of these two parameters. Fig. 1 presents results for a measurement with 1000 pb^{-1} of data from polarized neutral and charged current electron proton scattering. The corresponding 2σ-contour is represented by the shaded ellipse. Projecting it onto the axes results in precisions of $\delta m_t = \pm 50\,\mathrm{GeV}$ and $\delta m_W = \pm 290\,\mathrm{MeV}$. These values are more than a factor of 2 better than what can be obtained from charged current scattering alone with the smaller luminosity of 250 pb^{-1} (see the large ellipse in the figure). Anticipating future direct high precision measurements of m_t and m_W, a comparison with these data will provide a stringent test of the standard model. One way to quantify the measurement is to combine HERA data on neutral and charged current data with a direct top mass measurement of $\pm 5\,\mathrm{GeV}$. Such a test yields $\delta m_W = \pm 60\,\mathrm{MeV}$. This scenario assumes a value of 1 % relative systematic uncertainty, which represents a serious experimental challenge. The figure also shows the relation between m_W and m_t following from the G_μ constraint. The upper full line is for a Higgs mass of $m_H = 100\,\mathrm{GeV}$, the lower dashed one for $m_H = 800\,\mathrm{GeV}$. Note that the confidence ellipses derived from HERA measurements are also obtained for a fixed Higgs mass value which was chosen to be 100 GeV. They would be shifted downwards much the same as the lines describing the G_μ constraint for

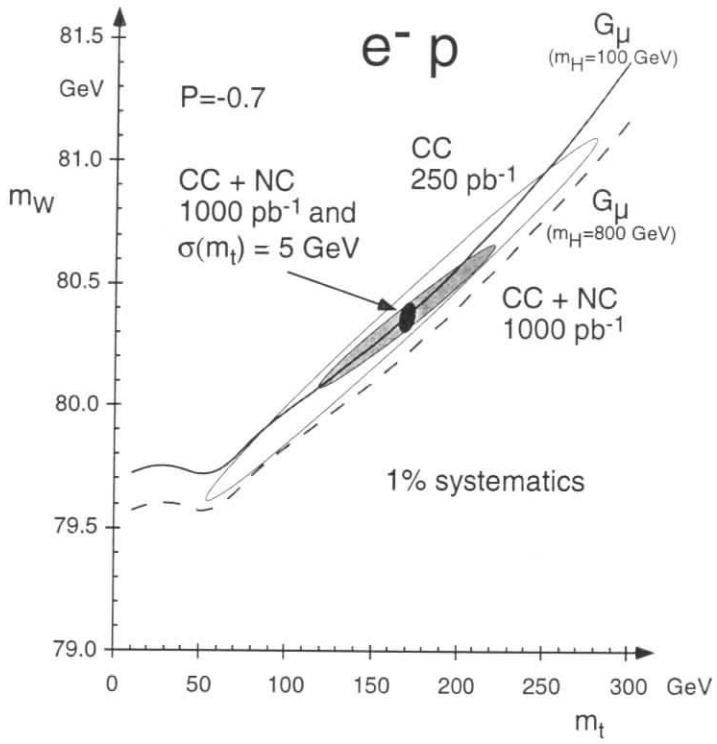

Figure 1: *1σ-confidence contours in the (m_W, m_t) plane from polarized electron scattering ($P = -0.7$), utilizing charged current scattering at HERA alone with an integrated luminosity of 250 pb^{-1} (large ellipse), neutral and charged current scattering at HERA with 1000 pb^{-1} (shaded ellipse), and the combination of the latter HERA measurements with a direct top mass measurement with precision $\sigma(m_t) = 5\,GeV$ (full ellipse). The m_W-m_t relation following from the G_μ-constraint is also shown for two values of m_H.*

a Higgs mass of $m_H = 800\,\mathrm{GeV}$. It is obvious from this figure that with such a high precision one would be able to constrain the allowed range of Higgs masses provided one has available a second precise measurement of the W boson mass.

Rather than taking into account a more or less well-motivated fixed size of experimental systematic errors, the *Electroweak Precision Tests* subgroup decided to investigate the dependence of the measurement error on m_W on the systematic uncertainty in a range up to conservative values of 5 %. Future experiments are expected to reduce this value of systematic uncertainty, as well as uncertainties from parton distribution functions, considerably.

Comparing different scenarios of beam setups (electrons versus positrons and degree of longitudinal polarization), it turned out that experiments with left-handed electrons alone would give the highest precision from both NC and CC scattering. This is essentially a consequence of the need to have as much data as possible and thus the process with the highest cross section is preferred.

2.2 NC couplings of quarks

Measurements of NC and CC cross sections with longitudinally polarized electrons and positrons would provide enough information to disentangle the neutral current couplings of the light u and d quarks. This is demonstrated in the contribution of the subgroup on *Measurement of NC Couplings*. The analyses are based on the NC and CC cross sections. In a scenario with $1000\,\mathrm{pb}^{-1}$ divided equally between the four charge/polarization combinations, all four u and d-type vector and axial-vector couplings can be measured with resulting fractional errors on a_u, v_u, a_d and v_d of 6 %, 13 %, 17 % and 17 %, respectively (see Fig. 2). Even higher precisions could be achieved by constraining two of the couplings to their standard model values. These results are comparable with the heavy quark couplings determined at LEP 1.

These studies are based on full Monte Carlo simulations taking into account the present knowledge of the ZEUS detector performance and the current analysis methods. Future upgrades to the detector and improvements in the understanding of calibration of existing detector components will serve to improve the precision of the measurements. In addition, a detailed investigation of uncertainties from parton distribution functions, entering into the analyses basically via ratios of u and d-type quark densities, and a comparison with the experimental errors have shown that this latter source of uncertainty will not be the limiting factor in determining NC couplings of quarks at HERA.

In the light of the intriguing R_b anomaly which has been presented by the four LEP experiments [12], the question was raised whether HERA would be able to provide complementary information. From earlier workshops it is known that the total rate of b-quark production is not at all small. However, the contribution due to photon-Z interference and pure Z-exchange is tiny (order 50 events for $100\,\mathrm{pb}^{-1}$) [13] and much too small to be helpful for electroweak physics.

2.3 W'

The potential of HERA for the discovery of additional heavy neutral or charged gauge bosons had been studied carefully in earlier workshops. In Ref. [14] it has been pointed out that

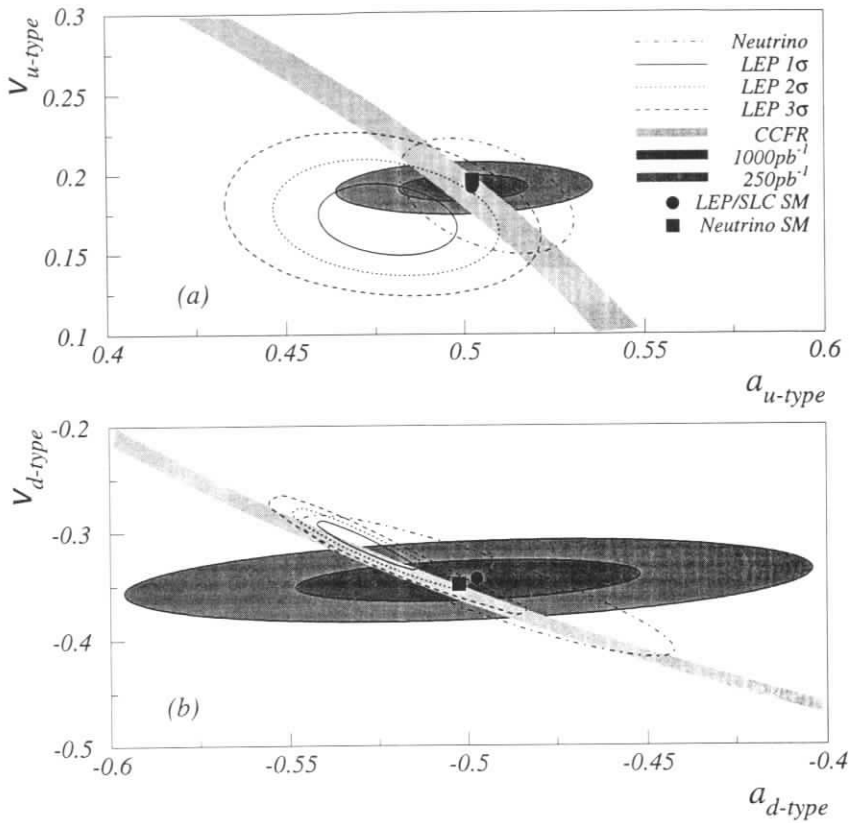

Figure 2: *Summary of measurements of u-type (a) and d-type (b) quark couplings to the Z^0. The results of a measurement at HERA are shown as the shaded ellipses. The outer ellipse shows the result which would be obtained with 250 pb^{-1} divided equally between the four lepton beam charge/polarization combinations, the inner ellipse shows the result which would be obtained with 1000 pb^{-1} equally divided. Fits for the couplings of the u (d) quarks were performed with the d (u) quark couplings fixed at their SM values. The open ellipse drawn with a dash-dotted line shows the one standard deviation (1σ) contour obtained in a fit of the four chiral couplings of the u and d quarks to a compilation of neutrino DIS data. The solid, dotted and dashed ellipses show the 1, 2 and 3 σ limits of the combined LEP/SLD results for the c and b quark couplings. The shaded band shows the result obtained by the CCFR collaboration from the ratio of NC and CC cross sections projected onto the quark coupling plane. In the case of the CCFR the couplings of the u (d) quarks are obtained with the d (u) quark couplings fixed at their SM values. SM coupling values including radiative corrections appropriate for comparison with e^+e^- (circle) and neutrino (square) measurements are also shown.*

charge and polarization asymmetries of NC cross sections are particularly suited for the search and the identification of a heavy Z' boson and exclusion limits for its mass have been given there. A model independent analysis, considering the 6-dimensional space of $Z'f\bar{f}$ couplings was performed in Ref. [15].

Similar discovery limits for a heavy charged boson W' can be derived by considering a possible deviation of the measured CC cross section from its standard model prediction assuming the existence of a heavy W'. A possible signal could show up in a comparison of the CC cross section at HERA with data at zero-momentum transfer, e.g. the μ-decay constant. The enhancement of the CC cross section with respect to the SM prediction in the presence of two charged W bosons is approximately given by

$$\frac{d\sigma(W+W')}{d\sigma_{SM}} = 1 + \frac{2x^2}{1+x^2\frac{m_W^2}{m_2^2}}\left(1-\frac{m_W^2}{m_2^2}\right)\frac{Q^2}{Q^2+m_2^2}, \qquad (1)$$

where $x = g_2/g_1$ is the ratio of the coupling constants of the two charged bosons. The mass of the lighter one has been identified with that of the standard model W, while the heavier one is denoted by m_2. The exclusion limits in the $(x,\ m_2)$ plane derived from the condition that the enhancement be larger than the statistical precision of the measurement of the CC cross section are shown in Fig. 3. Assuming equal coupling strengths, $g_2/g_1 = 1$, the resulting limits are $m_2 \lesssim 400$ GeV for positron scattering and $m_2 \lesssim 630$ GeV [16]. These mass limits do not supersede corresponding limits from the Tevatron and we have not considered them in further detail.

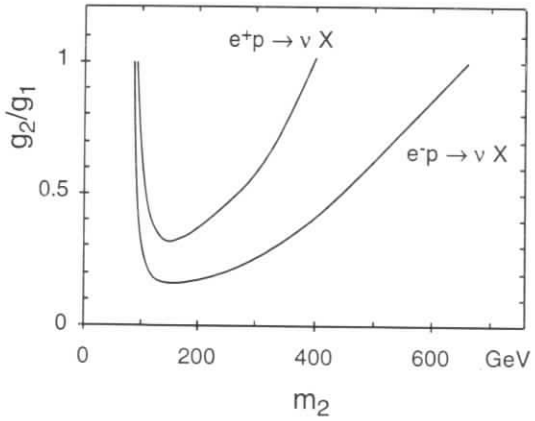

Figure 3: *95 % exclusion limits for a heavy W' in the $(g_2/g_1,\ m_2)$ plane.*

2.4 W production

The study of single W production offers the challenging opportunity to test the nonabelian structure of the standard model at HERA, in particular to search for deviations of the $WW\gamma$ couplings from its standard model values [17, 18]. In a new study of this process during the present workshop [19], a discussion of the event topology and kinematical cuts to optimize the event selection is presented. It is shown that HERA offers greater sensitivity to anomalous values of $\Delta\kappa_\gamma$ than λ_γ and therefore complements measurements made at the Tevatron and LEP 2 where the sensitivity to λ_V is greater. Since single W production at HERA is quite insensitive to anomalous WWZ couplings, unlike WW production at the Tevatron or LEP 2, measurements at HERA will be important to identify the nature of possible deviations, if they would be observed.

The sensitivity to anomalous $WW\gamma$ couplings has been studied for various integrated luminosities and at two center-of-mass energies. The resulting 95 % confidence level limits at $\sqrt{s} = 300$ GeV are given in Table 1. At $\sqrt{s} = 346$ GeV, the limits for $\int \mathcal{L}dt = 1000\,\mathrm{pb}^{-1}$ are $-0.27 < \Delta\kappa_\gamma < 0.26$ and $-1.26 < \lambda_\gamma < 1.28$. They are limited by statistical rather than systematic errors. For $\int \mathcal{L}dt = 1000\ \mathrm{pb}^{-1}$ the future sensitivity on anomalous values of $\Delta\kappa_\gamma$ which can be obtained at HERA is competitive with projected limits from $W\gamma$ production at the Tevatron (see Fig. 4). The bounds from LEP 2 shown in this figure are based on the auxiliary assumption that the WWZ and $WW\gamma$ couplings are not independent from each other (HISZ scenario) and can thus not be compared with the HERA results on equal footing.

$\int \mathcal{L}dt$	$\Delta\kappa_\gamma$	λ_γ
100 pb^{-1}	$-1.43 < \Delta\kappa_\gamma < 0.95$	$-2.93 < \lambda_\gamma < 2.94$
200 pb^{-1}	$-0.87 < \Delta\kappa_\gamma < 0.72$	$-2.46 < \lambda_\gamma < 2.47$
1000 pb^{-1}	$-0.38 < \Delta\kappa_\gamma < 0.38$	$-1.65 < \lambda_\gamma < 1.66$

Table 1: *95% CL limits derived for $WW\gamma$ couplings from the measurement of $\sigma(ep \to eWX)$ at HERA for the nominal center-of-mass energy of 300 GeV.*

2.5 Radiative NC scattering

Radiative deep inelastic scattering offers another possibility to study trilinear gauge boson couplings. Radiative CC scattering and its potential to probe the $WW\gamma$ couplings has been studied in Ref. [20]. As a new contribution to this workshop, Ref. [21] investigated whether $Z\gamma\gamma$ couplings can be tested in radiative NC scattering. Contributions due to $ZZ\gamma$ couplings are suppressed by two Z propagators. Since the rates are too small to exploit differential cross sections, estimates for bounds are obtained from total cross sections taking into account realistic cuts to improve the sensitivity to this source of new physics. HERA will explore these couplings in a different kinematic regime than at LEP 2, NLC or hadron colliders. However, it turns out that competitive bounds on these anomalous couplings cannot be achieved, even with the future luminosity upgrades.

2.6 SM Higgs-boson production

The prospects of producing light SM Higgs bosons at HERA under nominal conditions were discussed in the 1987 proceedings [22]. In the meantime, LEP has ruled out the mass range $M_H < 65.2$ GeV at the 95% confidence level [23]. An update of the 1987 analysis assessing the benefits from luminosity and proton energy upgrades may be found in Ref. [24]. W^+W^-

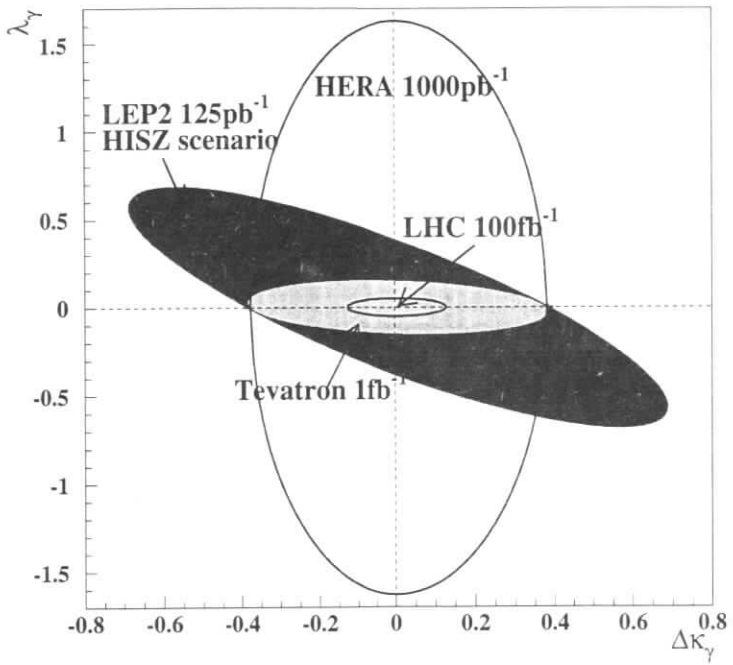

Figure 4: *Projected 95% confidence level sensitivity limits for $WW\gamma$ couplings determined from the single W production cross section at HERA and from $W\gamma$ production at the Tevatron and the LHC. The solid shading indicates the limits for the $WWV, V = \gamma, Z$ couplings from WW production at LEP 2 assuming the HISZ scenario.*

and ZZ fusion are by far the most copious sources of SM Higgs bosons at HERA. In the mass range 65 GeV $< M_H <$ 100 GeV, the Higgs boson decays with about 90% branching fraction to $b\bar{b}$ pairs, so that its visibility at HERA will suffer from severe intrinsic backgrounds due to continuum $b\bar{b}$ production. If such a Higgs boson exists, its production cross section at HERA will be below 6 (9) fb for E_p = 820 GeV (1 TeV). It is therefore unlikely that a signal can be established in the $b\bar{b}$ channel, even if the luminosity and/or proton energy are upgraded leaving this terrain to LEP 2.

3 Conclusions

The observation of the propagator effect due to W exchange was one of the first results from HERA at high Q^2 after decades of searching for deviations of the linearly rising cross section of the CC process. In the meantime, the finite mass of the W boson responsible for this effect, the propagator mass, has been measured with an accuracy of a few GeV at HERA. First candidate events for the direct production of the W boson have also been observed at HERA. In order to turn these observations into measurements of parameters and conclusive tests of the standard model electroweak sector the luminosity has to be increased tremendously. Luminosities of $1\,\mathrm{fb}^{-1}$ and polarized beams will make these measurements possible.

The cross section for the production of W bosons is the order of 1 pb so that it is an experimental challenge to establish the experimental signal and it is essential to consider all available decay channels. The study performed in this report shows that already with an integrated luminosity of $250\,\mathrm{pb}^{-1}$ deviations from the standard model couplings parametrized in terms of $\Delta\kappa_\gamma$ and λ_γ can be tested at a level which is comparable to present collider results.

While for W production neither lepton charge nor polarization is a prerequisite, the precision measurement with the charged current process profits especially from e^-p scattering due to the roughly threefold larger cross section as compared to e^+p scattering. For an analysis in terms of NC quark couplings it is indispensable to have available both charge states, while not necessarily with equal luminosity. To disentangle up- and down-type quark vector and axial-vector couplings beams have to be polarized. A proper choice of polarization would also render the NC data useful, and evidently enhance the significance of the CC data, for the precise determination of e.g. m_W or m_t.

The result of these measurements constitutes an important test of the standard model by comparing precision measurements of SM parameters obtained at HERA with those at other experiments. Differences appearing in such tests have always stimulated extensive research. The separation of the light up- and down-type quark couplings at HERA would complement the achievements of LEP in the heavy quark sector.

References

[1] *Proceedings of the HERA Workshop*, edited by R. D. Peccei, Hamburg, October 12–14, 1987.

[2] *Proceedings of the Workshop on Physics at HERA*, edited by W. Buchmüller and G. Ingelman, Hamburg, October 29–30, 1991.

[3] H. Spiesberger, in *Precision Tests of the Standard Model*, edited by P. Langacker (World Scientific, Singapore, 1995) p. 626.

[4] A. Bareiss et al., in Ref. [1], Vol. 2, p. 677.

[5] W. Buchmüller et al., in Ref. [2], Vol. 2, p. 917.

[6] D. Yu. Bardin et al., in Ref. [1], Vol. 2, p. 577.

[7] G. Kramer et al., in Ref. [2], Vol. 2, p. 785.

[8] F. Zetsche, in this working group report.

[9] R. Beyer et al., in this working group report.

[10] R. J. Cashmore et al., in this working group report.

[11] B. A. Kniehl, in this working group report.

[12] The LEP Collaborations ALEPH, DELPHI, L3, OPAL and the LEP Electroweak Working Group, CERN-PPE/95-172 (1995);
P. Renton, talk at the 17th International Symposium on Lepton-Photon Interactions, 10-15 August 1995, Beijing, China, OUNP-95-20 (1995);
A. Blondel, talk at the XXVIII International Conference on High Energy Physics, 25-31 July 1996, Warsaw, Poland.

[13] G. A. Schuler, Nucl. Phys. B299 (1988) 21.

[14] F. Cornet and R. Rückl, Phys. Lett. B184 (1987) 263;
F. Cornet and R. Rückl, in Ref. [1], Vol. 2, p. 771.

[15] P. Haberl, F. Schrempp, H.-U. Martyn and B. Schrempp, in Ref. [2], Vol. 2, p. 980;
H.-U. Martyn et al., in Ref. [2], Vol. 2, p. 987.

[16] D. Haidt, contribution to this working group.

[17] K. J. F. Gaemers and G. J. Gounaris, Z. Phys. C1 (1979) 259;
K. Hagiwara, R. D. Peccei, D. Zeppenfeld and K. Hikasa, Nucl. Phys. B282 (1987) 253.

[18] U. Baur and D. Zeppenfeld, Nucl. Phys. B325 (1989) 253;
U. Baur, J. A. M. Vermaseren and D. Zeppenfeld, Nucl. Phys. B375 (1992) 3.

[19] V. Noyes, in this working group report.

[20] T. Helbig and H. Spiesberger, in Ref. [2], Vol. 2, p. 973.

[21] F. Cornet, R. Graciani and J. I. Illana, in this working group report.

[22] K. J. F. Gaemers, R. M. Godbole and M. van der Horst, in Ref. [1], Vol. 2, p. 739.

[23] J.-F. Grivaz, in *Proceedings of the International Europhysics Conference on High Energy Physics*, Brussels, Belgium, July 27–August 2, 1995, to appear.

[24] B. A. Kniehl, in this working group report.

Electroweak Precision Tests With Deep Inelastic Scattering at HERA

R. Beyer[a], E. Elsen[a], S. Riess[b], H. Spiesberger[c], F. Zetsche[b]

[a] Deutsches Elektronen-Synchrotron DESY, Notkestrasse 85, D-22603 Hamburg, FRG
[b] II. Institut für Experimentelle Physik, Universität Hamburg, Luruper Chaussee 149, D-22761 Hamburg, FRG
[c] Max-Planck-Institut für Physik, Werner-Heisenberg-Institut, Föhringer Ring 6, D-80805 München, FRG

Abstract: We investigate the potential of deep inelastic lepton proton scattering with polarized electrons or positrons for precision tests of the electroweak standard model. We interpret the measurements of cross sections as a measurement of the electroweak parameters m_W and m_t, assuming that m_H is a fixed external parameter. As a main result we find that measurements with left-handed polarized electrons give the highest precision. Provided the top mass is known within ± 5GeV, HERA can measure the W boson mass with a precision of ± 55MeV from 1000 pb^{-1} of data from electron scattering with 70 % left-handed longitudinal polarization.

1 Introduction

Deep inelastic lepton nucleon scattering has always played an important rôle in understanding the interplay of electromagnetic, weak and strong interactions. In fact, weak neutral currents were first observed in deep inelastic scattering. Neutrino scattering has established the structure of the neutral current at low momentum transfer, Q^2, and, for a long period, provided the most precise value of the weak mixing angle [1]. It is therefore an important question whether experiments at HERA are able to provide further insight into the structure of the electroweak interaction. The hope that this question will have a positive answer is based on the fact that HERA is extending the measurements to much larger values of the momentum transfer and that beams with both electrons and positrons and with longitudinal polarization of up to 70 % [2] could be utilized at a future upgrade of the machine.

The electroweak theory based on $SU(2) \times U(1)$ gauge symmetry and the mechanism of spontaneous symmetry breaking (the Standard Model, SM) successfully describes the wealth of existing data on the electroweak interactions almost perfectly. After having fixed the basic free parameters of the standard model, it allows for the derivation of unambiguous predictions which can be compared to experimental data. In order to quantify the agreement or disagreement of theoretical predictions with experimental results it is often convenient to generalize the theory either by treating certain quantities as free parameters (e.g., the vector and axial-vector

couplings of leptons and quarks) or by introducing additional free parameters, for example anomalous three-boson couplings. Experimental results interpreted as measurements of these free parameters can then be confronted with the predictions of the standard model. Another possibility is to interpret experimental data as measurements of the basic standard model parameters, i.e., the mass of the W boson, m_W, or the top-quark mass, m_t, for example. A test of the theory is then possible by comparing results obtained in different experiments. It is the aim of this article to investigate whether HERA can contribute to this strategy of testing the standard model. A companion contribution to these proceedings prefers the first way of testing the standard model by investigating the question to what extent experiments at HERA would be able to measure the neutral current vector and axial-vector couplings of quarks [3].

In the following we shortly describe the predictions of the standard model for deep inelastic lepton proton scattering, taking into account $O(\alpha)$ electroweak radiative corrections. We will describe in detail the analysis strategy and the observables we suggest to use for precision measurements at HERA. Finally, we discuss the quality of HERA experiments in terms of the precision of the W boson mass that can be achieved with high luminosity.

The standard model has 5 independent free parameters (α, m_Z, m_W, m_H, m_t, apart from fermion masses other than the top-quark mass and CKM matrix elements) which are essentially not constrained by theory. Since present day's experimental observables depend only logarithmically on the Higgs mass m_H (via loop corrections), it is legitimate to perform analyses of data with fixed m_H and study variations of its value separately. Therefore we have to consider 4 independent parameters and meaningful tests of the theory can be performed only by combining the experimental measurements of more than 4 observables. Evidently the very precise measurements of the finestructure constant α and the Z boson mass m_Z can be taken from experiment. Any additional measurement will then put a constraint on the remaining two parameters m_W and m_t. Two additional measurements are needed to determine both m_W and m_t.

In analyses of the LEP data it is suggestive to reduce the number of free parameters to one (plus one for the Higgs mass) by taking into account the constraint from the precise measurement of the μ-decay constant, G_μ, which is unexplored at LEP. Thus it was possible to obtain an indirect determination of the top-quark mass from Z-peak observables. Former analyses of the electroweak physics potential of HERA [4, 5, 6] adopted a strategy similar to that used at LEP and attempted to combine HERA data with the G_μ constraint, i.e. only variations with m_W were considered and m_t was determined from m_W with the help of G_μ. Owing to the fact that at HERA most of the data are still obtained at relatively small Q^2, the constraint resulting from these data on the parameters of the standard model is not very different from the G_μ constraint. As a consequence, these former analyses usually predicted rather large uncertainties for measurements of m_W, of the order of 600 MeV. In the present work, however, we will adopt a different approach and choose to combine HERA data not with the G_μ constraint, but rather with independent information on the value of the top-quark mass. By the time when HERA has collected enough luminosity to allow for precision analyses, the top-quark mass will be known from experiments at Tevatron and the LHC with a precision of a few GeV. Since this direct constraint on one of the standard model parameters is very different from the G_μ constraint, a combination of HERA data with a direct m_t measurement allows to obtain an indirect m_W measurement with a reasonably small uncertainty. Comparing the results from such an analysis with other experiments (indirect determinations of m_W from LEP 1 precision measurements, or direct measurements of m_W at LEP 2 or hadron colliders, for

example) will provide constraints that simultaneously have to be fulfilled within the standard model.

2 Precise Standard Model Predictions for HERA

2.1 Lowest-Order Cross Sections

We study deep inelastic scattering of electrons or positrons off protons

$$e(l) + p(p) \to e'(l') + X(p_X), \tag{1}$$

with $e' = e$ for neutral current scattering (NC) and $e' = \nu_e$ for charged current scattering (CC). The particle momenta are given in parentheses. A useful set of kinematic variables to describe the process (1) is given by

$$Q^2 = -(l - l')^2, \quad s = (l + p)^2, \quad x = \frac{Q^2}{2p \cdot (l - l')}, \quad y = \frac{Q^2}{xs}. \tag{2}$$

In the region of large x and Q^2 where the contribution of the longitudinal structure function F_L and proton mass effects can be neglected, the differential cross section for the neutral current process for left-handed (L) and right-handed (R) polarized electrons is given by

$$\frac{d^2\sigma^{NC}}{dx\,dQ^2}(e^-_{L,R}) = \frac{2\pi\alpha^2}{xQ^4}\left[\left(1 + (1-y)^2\right) F_2^{L,R} + \left(1 - (1-y)^2\right) x F_3^{L,R}\right]. \tag{3}$$

For positron scattering one has to replace $F_3^{L,R} \to -F_3^{R,L}$ and cross sections for beams with an arbitrary degree of longitudinal polarization P can be obtained by calculating the appropriate average of the cross sections for left- and right-handed leptons. The structure functions are derived in the quark-parton model from basic 4-fermion scattering cross sections:

$$\begin{aligned} F_2^{L,R} &= \sum_q [xq(x,Q^2) + x\bar{q}(x,Q^2)] \cdot A_q^{L,R}, \\ xF_3^{L,R} &= \sum_q [xq(x,Q^2) - x\bar{q}(x,Q^2)] \cdot B_q^{L,R}. \end{aligned} \tag{4}$$

They contain the quark (q) and anti-quark ($\bar{q}$) distribution functions as well as coupling constants and propagators corresponding to photon and Z-boson exchange ($L = +, R = -$):

$$\begin{aligned} A_q^{L,R} &= Q_q^2 + 2Q_eQ_q(v_e \pm a_e)v_q\chi_Z + (v_e \pm a_e)^2(v_q^2 + a_q^2)(\chi_Z)^2, \\ B_q^{L,R} &= \pm 2Q_eQ_q(v_e \pm a_e)a_q\chi_Z \pm 2(v_e \pm a_e)^2 v_q a_q (\chi_Z)^2, \end{aligned} \tag{5}$$

with

$$\chi_Z = \frac{1}{4s_W^2 c_W^2}\frac{Q^2}{Q^2 + M_Z^2}. \tag{6}$$

In Eq. (3), also Higgs-boson exchange is neglected because of the small couplings to light fermions. By using Q^2 dependent parton distribution functions, QCD corrections in the leading-logarithmic approximation are included.

The parametrization of the lowest-order cross section in terms of vector and axial-vector coupling constants $v_{e,q}$, $a_{e,q}$ is quite general and applies to any model where a vector boson with v and a couplings is exchanged together with the photon. In the standard model, the couplings of the fermions to the bosons are given by the electric charge (in units of e) for the photon exchange and, for the Z-boson exchange, by ($f = e, q$)

$$\begin{aligned} a_f &= I_3^f, \\ v_f &= I_3^f - 2Q_f \sin^2\theta_W \end{aligned} \tag{7}$$

where Q_f and I_3^f denote the charge and the third component of the weak isospin of the fermion f. In the standard model with an arbitrary Higgs sector, the mixing angle is related to the vector boson masses by

$$\sin^2\theta_W = 1 - \frac{m_W^2}{\rho_0 m_Z^2}. \tag{8}$$

In the following we restrict ourselves to the minimal model with $\rho_0 = 1$ at the tree level and use as abbreviation

$$s_W^2 = 1 - \frac{m_W^2}{m_Z^2}. \tag{9}$$

In a similar way one can write for the charged current differential cross section

$$\frac{d^2\sigma^{CC}}{dx\,dQ^2}(e^-) = (1-P)\frac{\pi\alpha^2}{4s_W^4}\cdot\frac{1}{(Q^2+M_W^2)^2}\left[u + c + (1-y)^2(\bar{d}+\bar{s})\right], \tag{10}$$

with P denoting the degree of left-handed longitudinal polarization ($P = -1$ for left-handed electrons, $P = 1$ for right-handed electrons). For positron scattering one has to replace $u + c \to \bar{u} + \bar{c}$ and $\bar{d} + \bar{s} \to d + s$ and adjust the sign of P.

2.2 Higher-Order Corrections

A study of the sensitivity to electroweak parameters must be based on cross section formulae which incorporate their dependence on m_W, m_t, etc. as precisely as possible. It is, however, not necessary to include all kinds of corrections if these do not affect the electroweak parameter dependence. This is the case for the purely photonic (QED) corrections and for some parts of QCD corrections.

QED corrections are large and unavoidable, in particular for NC scattering at small x and large y. They constitute a well-understood (thus 'uninteresting') part of physics which has to be separated from genuine electroweak effects. Careful comparisons of different calculations during the HERA workshop in 1991 have shown good agreement at the permille level between results for the first order corrections obtained by various authors [7]. Also corrections of higher than one-loop order are known in the leading logarithmic approximation so that we can be confident that QED corrections can be taken into account in the analysis of experimental data at a level of precision that does not introduce severe uncertainties. Moreover, explicit calculations show that QED corrections do not change the sensitivity on electroweak parameters. An example is shown in Fig. 1 where the m_W dependence of the ratio R_+ of CC to NC cross sections for positron scattering at a fixed value of the momentum transfer Q^2 is compared for calculations without and including QED corrections. The corrections are large, of the order of 10 %, in

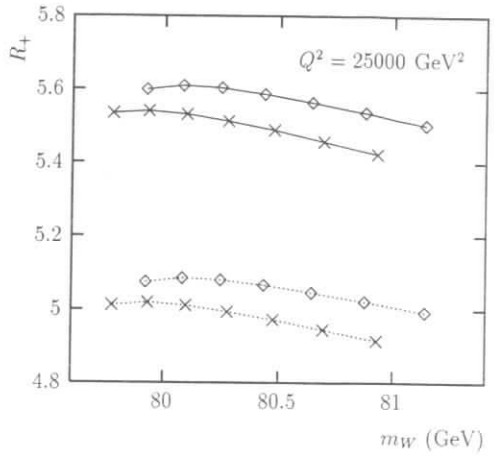

Figure 1: *The ratio R_+ of CC to NC cross sections $d\sigma/dQ^2$ for positron scattering at fixed $Q^2 = 25000$ GeV^2 with (full lines) and without (dashed lines) QED corrections. The curves with diamonds are for $m_H = 100$ GeV, those with crosses for $m_H = 800$ GeV. m_t has been fixed by the G_μ constraint.*

particular much larger than the variation of the results with m_W or m_H. However, it is obvious that QED corrections do not affect the dependence on these standard model parameters, but simply shift the theoretical predictions.

Since we are dealing with small effects, as we will see below, it will be indispensable to take also QCD corrections into account in the analysis of HERA data. QCD corrections needed for precise predictions of DIS cross sections can be classified according to three sources: *i*) there are universal corrections modifying the relations among standard model parameters, entering via the corrections to the μ-decay constant G_μ (see Δr in the formulae below). We included the dominating two-loop contributions of order $O(\alpha\alpha_s)$ [9] corresponding to shifts of m_W in the order of 60 MeV. Contributions of order $O(\alpha\alpha_s^2)$ are known [8], but not included in our calculations. *ii*) Additional corrections of $O(\alpha\alpha_s)$ modify the x and Q^2 dependence of the electroweak form factors. These contributions are only partly known and probably small. *iii*) Finally, corrections due to real and virtual emission of gluons from quarks in the hard lepton-quark scattering subprocesses modify the way the structure functions are expressed in terms of parton densities. In the DIS scheme, these corrections of order $O(\alpha_s)$ enter via F_L and affect F_3 in NC scattering and the CC cross section. They are known in next-to-leading order for all structure functions [10] and up to next-to-next-to-leading order for the photon-exchange contribution in NC scattering [11].

The calculations of electroweak higher order corrections to deep inelastic scattering at HERA have been reviewed in [7] (see also references therein). They are performed in the on-shell scheme, where m_W and m_Z are treated symmetrically as basic parameters together with m_t and m_H (besides the fine structure constant α and other fermion masses). Amplitudes are functions of these basic parameters. The electroweak corrections are collected in form factors that change the amplitudes in a simple form: the dressed photon-exchange amplitude can be

written in the following way:

$$\mathcal{M}_\gamma = \frac{e^2}{1-\hat{\Pi}_f^\gamma(Q^2)} \cdot \frac{1}{Q^2} \cdot Q_e\gamma_\mu \otimes Q_f\gamma^\mu. \tag{11}$$

$\hat{\Pi}_f^\gamma$ is the fermionic part of the photon vacuum polarization. Writing it in the denominator resums the leading logarithmic corrections according to the renormalization group equation and the first factor in Eq. (11) constitutes the running fine structure constant. Bosonic contributions to the vacuum polarization have to be combined with vertex and box corrections and added separately.

The weak one-loop corrections to the Z-exchange amplitude $\mathcal{M}_Z$ for $eq \to eq$ can be expressed in terms of four weak form factors (ρ_{eq}, κ_e, κ_q, and κ_{eq}) in the following way, making use of dressed vector couplings [12, 13]:

$$\mathcal{M}_Z(\hat{s},Q^2) \sim \frac{1}{Q^2+m_Z^2}\left[\frac{\pi\alpha}{4s_W^2c_W^2}\frac{\rho_{eq}(\hat{s},Q^2)}{1-\Delta r}\right]\Big[I_3^eI_3^q\gamma_\mu\gamma_5\otimes\gamma_\mu\gamma_5 + \bar{v}_eI_3^q\gamma_\mu\otimes\gamma_\mu\gamma_5 + I_3^e\bar{v}_q\gamma_\mu\gamma_5\otimes\gamma^\mu + \bar{v}_{eq}\gamma_\mu\otimes\gamma^\mu\Big], \tag{12}$$

$$\bar{v}_f = I_3^f\left[1-4|Q_f|s_W^2\,\kappa_f(\hat{s},Q^2)\right], \quad f=e,q\,, \tag{13}$$

$$\bar{v}_{eq} = I_3^e\bar{v}_q + \bar{v}_eI_3^q - I_3^eI_3^q\left[1-16|Q_eQ_q|s_W^4\,\kappa_{eq}(\hat{s},Q^2)\right], \tag{14}$$

with $\hat{s}=xs$ and s_W^2 from Eq. (9). The normalization factor in square brackets can be related to the μ-decay constant (taking into account the radiative corrections to the μ-decay, $(1-\Delta r)^{-1}$), $[\cdots] = (G_\mu m_Z^2/2\sqrt{2})\cdot\rho_{eq}$, showing that ρ_{eq} denotes the ratio of the NC and CC coupling strengths in eq scattering. In the Born approximation, $\rho=\kappa=1$, $\Delta r=0$ and $\bar{v}_{eq}=v_ev_q$. The above parametrization has the form of a Born-like expression except that at the Born level there is no parallel for the coupling $\bar{v}_{eq}$. The axial-vector couplings can be kept in their form $a_f=I_3^f$ by absorbing corresponding vertex corrections into the normalization factor $\rho_{eq}=\rho_{eq}(\hat{s},Q^2)$ which receives also contributions from self energies. The form factors κ_f and κ_{eq} combined with s_W^2 give rise to effective mixing angles which depend through the κ's on the fermion species and on the kinematic variables. The form factors can be separated into a universal part independent of the fermion species and a non-universal remainder term. The universal parts contain the dependence on the masses of the top quark and the Higgs boson. The dominating contribution to them is proportional to m_t^2 and with

$$\Delta\rho = \frac{3\alpha}{16\pi s_W^2c_W^2}\frac{m_t^2}{m_Z^2} \tag{15}$$

one has to one-loop precision

$$\rho_{eq} = 1+\Delta\rho+\Delta\rho_{eq}^{rem}, \tag{16}$$

$$\kappa_f = 1+\frac{c_W^2}{s_W^2}\Delta\rho+\Delta\kappa_f^{rem}. \tag{17}$$

Additional details, in particular concerning the inclusion of higher than one-loop order terms which are taken into account in our application, are described in [14].

The W-exchange amplitude including higher-order contributions can be written in the following way:

$$\mathcal{M}_W(\hat{s},Q^2) = \frac{\pi\alpha}{8s_w^2}\frac{\rho_{eq}^W(\hat{s},Q^2)}{1-\Delta r}\frac{1}{Q^2+m_W^2}\gamma_\mu[1-\gamma_5]\otimes\gamma^\mu[1-\gamma_5]. \tag{18}$$

Differently from the neutral current, only a single form factor ρ_{eq}^W for each parton scattering process is required to accommodate the higher-order contributions. Rewriting the normalization of the W-exchange amplitude with the help of the μ-decay constant using $\pi\alpha/8s_W^2(1-\Delta r) = G_\mu m_W^2/4\sqrt{2}$ shows explicitly that the measurement of the CC cross section at low Q^2 is, in fact, a measurement of G_μ. In this form, weak loop corrections are very small since ρ_{eq}^W deviates from 1 typically by a few permille with very little dependence on m_t and m_H.

The above formulae are implemented in the FORTRAN code `eprc93.f` [14] which has been used for all our numerical evaluations. We stress that the formulae given here are sufficient to study the *sensitivity* on electroweak parameters, but not for the determination of their central values from real data since QED corrections are not, and QCD corrections only partly, included. These corrections will have a non-negligible effect on the predicted values of observables. Consequently, using measurements of these observables for a determination of m_W, for example, these corrections will also have a non-negligible effect on the central value of m_W. In this work, however, we are interested in a determination of the *sensitivity* of such a measurement expressed in terms of the precision Δm_W of the measurement. Since it is completely sufficient to know the sensitivity Δm_W with a relative precision of $O(10\,\%)$, higher than one-loop corrections are not relevant here.

3 Precision Measurements at HERA

3.1 Analysis Strategy

We consider the well measured α and m_Z as fixed parameters of the theory ($1/\alpha = 137.036\cdots$ and $m_Z = 91.1884\,\mathrm{GeV}$). The Higgs boson enters via loops, so that there is only a weak logarithmic dependence on m_H which allows us to treat m_H as an external parameter. The numerical results presented below refer to $m_H = 100\,\mathrm{GeV}$ and variations of m_H are discussed separately. Hence, as discussed in the introduction, we are left with m_t and m_W as free parameters which are to be determined by experiment. A precision measurement of any observable constrains the allowed region in the (m_W, m_t) plane and a test of the theory consists in comparing the overlap of regions obtained from different experiments.

A possible result of a measurement is sketched in Fig. 2. The details of the correlation depend on the standard model and the particular choice of observable, i.e. its dependence on the particular electroweak parameter. The dependence on the parameters of the theory is smooth so that a linearization of the theoretical dependence around the value of the measurement is justified. The confidence levels are chosen such that for a single parameter test, i.e. a projection onto one of the axes, the usual 1 parameter confidence level for $1\,\sigma$ is obtained. The correlation between the two parameters can be exploited: using the value of a future direct top mass determination (vertical lines in Fig. 2) from other experiments yields the smaller tilted (shaded) ellipse in Fig. 2. Projecting this ellipse onto the m_W axis results in a tightly constrained interval for values of m_W. In quantifying results of the studies we have chosen, for

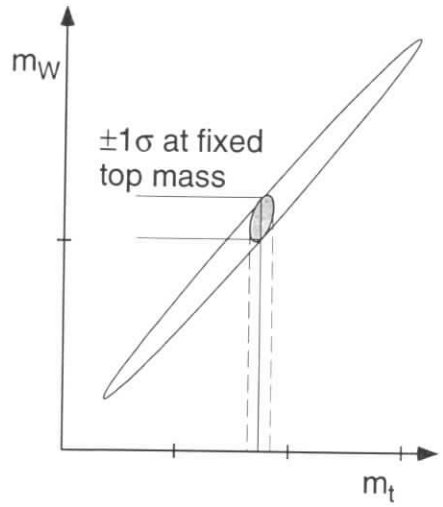

Figure 2: *Schematic view of the 1σ contour in the (m_W, m_t) plane, resulting from a measurement at HERA and its combination with a direct top-quark mass measurement (shaded ellipse)*

the sake of definiteness, to indicate the vertical extent of δm_W of the ellipse as the uncertainty of the W mass measurement. This corresponds to a scenario in which the top mass has been measured precisely elsewhere. In the end we shall indicate the extra uncertainty for a more realistic measurement of m_t for which we assume an uncertainty of 5 GeV[1].

The Higgs mass enters via one-loop contributions to the gauge boson self energies and modifies the interpretation of the measurement. Performing an analysis with different values for m_H leads to different contours (Fig. 3) which are shifted and have very similar slope.

3.2 Observables

We fix the beam energies at their nominal values $E_l = 27.5\,\text{GeV}$, $E_p = 820\,\text{GeV}$. All cross sections are evaluated with a cut on the transverse momentum of the scattered lepton (or missing transverse momentum) of $p_T \geq 15\,\text{GeV}$. For scattering with polarized leptons we assume a degree of longitudinal polarization of $|P| = 0.7$. In order to exploit the information contained in the shape of the Q^2 distribution, we take the cross sections to be measured in 5 bins of Q^2, equidistant in $\log Q^2$, with lower bin limits (225.6, 747.2, 2475, 8199, 27160) GeV^2, the last bin extending up to the kinematical limit $Q^2_{max} \approx s$. The SM predictions, depending on m_W and m_t, are obtained by integrating over the Q^2 intervals:

$$\sigma_i = \sigma_i(m_W, m_t) = \int_{Q^2_{i,min}}^{Q^2_{i,max}} dQ^2 \int dx \frac{d^2\sigma}{dx\, dQ^2}\,. \tag{19}$$

[1]Presently, the precision for m_t is already as small as 7 GeV [15].

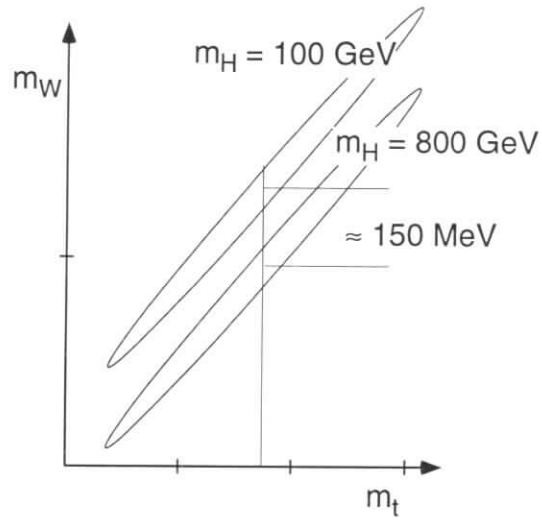

Figure 3: *The qualitative dependence of the 1σ confidence contour in the (m_W, m_t) plane from a measurement at HERA for two different values of the Higgs mass.*

The event numbers expected for an integrated luminosity of $\mathcal{L} = 1000\text{pb}^{-1}$ and $P = -0.7$ are shown in Fig. 4.

Future experiments measure cross sections σ_i^{exp} with errors $\Delta\sigma_i^{exp}$ for each Q^2 interval. To quantify the comparison of experimental data and theoretical predictions, we define a χ^2:

$$\chi^2 = \chi^2(m_W, m_t) = \sum_i \frac{(\sigma_i(m_W, m_t) - \sigma_i^{exp})^2}{(\Delta\sigma_i^{exp})^2}. \tag{20}$$

Lacking experimental data for the time being, we assume that the central value of the measurement coincides with the SM prediction for a set of reference values of the SM parameters. We choose

$$\sigma_i^{exp} = \sigma_i(m_W = 80.2\,\text{GeV}, m_t = 170\,\text{GeV}) \tag{21}$$

thus fixing the position of confidence regions in the (m_W, m_t) plane. Note again, that due to the weak dependence on the parameters the particular choice of reference values has a negligible influence on the following studies of sensitivity.

The precision of the measurement trivially improves with the statistical accuracy of the data,

$$\Delta\sigma_i^{stat} = \sqrt{\sigma_i^{exp}/\mathcal{L}}. \tag{22}$$

The systematic errors, $\Delta\sigma_i^{sys}$, encompass the uncertainties of the measurement (identification, efficiency, reconstruction of kinematics etc.) as well as uncertainties in the determination of the luminosity and the beam polarization. Hence, the $\Delta\sigma_i^{sys}$ will be correlated between different bins of Q^2 such as in the case of the luminosity and polarization measurement. Nevertheless,

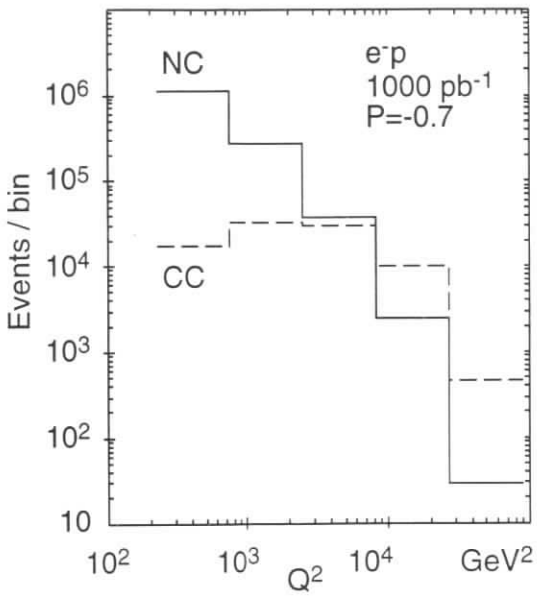

Figure 4: *Expected event numbers in the chosen Q^2 intervals for neutral (NC) and charged (CC) current e^-p cross sections at HERA for an integrated luminosity of 1000 pb^{-1} and longitudinal polarization $P = -0.7$.*

when quoting the dependence on the systematic error, we will assume a correlation coefficient $c = 0$ in most cases. However, we will also present a study on the transition from a result that is dominated by point-to-point errors $c = 0$ to a result that is dominated by overall normalization $c = 1$.

A precision of order 1 % has been achieved in present measurements of luminosity already and at high luminosity independent methods of measurements can be used for cross check. For the polarization measurement an accuracy of 2 % or better [2] is conceivable. (Note, that typically the polarization enters through a factor $(1+|P|)$ so that a precision of 2 % is adequate).

The largest experimental uncertainty arises from the incomplete knowledge of the absolute value of the calorimeter energy scale. The susceptibility to this uncertainty depends on the Q^2 variation of the cross section. Simplified, the photon propagator dominated NC cross section will be mostly affected in shape due to migration while the CC section will be predominantly affected in absolute normalization due to the lower Q^2 cut off. Typical experimental accuracies range around $1 - 2$ % for the reconstruction of the electron energy [16]. The hadronic energy measurement is presently considerably less certain [17]. However, the large statistics available from a high luminosity HERA will allow to impose considerable constraints on the reconstruction of the final state such that together with a good electron measurement a better precision at the level of per cent will be achieved. It will be important to cross check the CC channel with the more constrained data of the NC analysis.

Instead of fixing $\Delta\sigma_i^{sys}$ at some ad-hoc value, we will consider the dependence of the results on the relative systematic uncertainty $\epsilon = \Delta\sigma^{sys}/\sigma^{exp}$ ranging from 0 to 5 %. Since the theoretical uncertainties due to an imperfect knowledge of parton distribution functions can be absorbed in the $\Delta\sigma_i^{sys}$, the larger value of 5 % would become relevant if experimental measurements did not advance the precision beyond the present level, which is not expected. We consider the full range of variation.

The condition $\chi^2(m_W, m_t) = 1$ defines a 1σ-confidence region in the (m_W, m_t) plane. Since we are dealing with small variations of m_W and m_t, we assume that the parameter dependence can be linearly approximated. This simplifies the determination of confidence regions considerably. Our approach will become unreliable if these regions turn out to be large, corresponding to uncertainties for m_W of more than about 1 GeV.

3.3 Results

The results of the sensitivity studies are summarized in table 1. For two values of luminosity the sensitivity is shown for the different processes as a function of the systematic uncertainty ϵ. In the following discussion we compare the various options and will quote a value for the precision of the W mass measurement for a fixed value of the top mass as described above.

3.3.1 Charged vs. Neutral Current

Fig. 5 shows that a measurement of the charged current cross section for unpolarized electrons is superior to that of neutral current scattering. δm_W is of the order of 100 MeV and is only doubled when the relative systematic uncertainty is increased to 5 %. The neutral current measurement is worse by a factor of ≈ 3 and much more sensitive to systematic errors. Whereas for charged current scattering there is little improvement in precision for m_W when increasing

Electroweak Sensitivity for m_W								
	Charged Current				Neutral Current			
	e^-p		e^+p		e^-p		e^+p	
	$\mathcal{L}$ [pb^{-1}]		$\mathcal{L}$ [pb^{-1}]		$\mathcal{L}$ [pb^{-1}]		$\mathcal{L}$ [pb^{-1}]	
	250	1000	250	1000	250	1000	250	1000
ϵ [%]	δm_W [MeV] for $\|P\| = 0$							
0	68	34	101	51	223	112	363	181
1	80	53	111	68	347	237	699	526
2	105	84	136	101	475	364	1051	853
5	202	184	237	209	855	717	2032	1863
ϵ [%]	δm_W [MeV] for $\|P\| = 70\,\%$							
0	52	26	78	39	113	57	173	86
1	66	47	90	59	187	131	348	265
2	95	80	118	94	263	207	530	437
5	194	179	223	203	488	414	1048	973

Table 1: *The uncertainty δm_W in MeV for a given beam configuration and process as a function of the relative systematic uncertainty ϵ for fixed top mass. The sign of the longitudinal polarization is assumed to be chosen such that the cross sections are enhanced, i.e. $P = 0.7$ for e^+ and $P = -0.7$ for e^- beams.*

the luminosity from 250 pb^{-1} to 1000 pb^{-1}, there is an appreciable improvement for neutral current scattering.

3.3.2 Polarized vs. Unpolarized Lepton Beams

This trend persists for positron scattering and for polarized beams, as seen in Fig. 6 which shows the results for polarized electron scattering of degree of polarization $P = -0.7$. The gain in precision for m_W in this case is due to the increase of statistics (note that the charged current scattering cross section is proportional to $(1 - P)$). For a large systematic uncertainty, the gain in statistics is, of course, lost. This is in contrast to the case of neutral current scattering where polarization leads to a substantial increase of sensitivity even in the presence of large systematic uncertainties. This difference between NC and CC scattering is a consequence of the fact that for charged current scattering it is essentially the normalization of the cross section which determines m_W whereas in the neutral current case the shape of the Q^2 dependence contains the sensitivity. The influence of the weak interference terms can be enhanced by proper choice of polarization. Coarsely speaking, beams of $-70\,\%$ polarization are equivalent to a factor 4 larger integrated luminosity of unpolarized beams. Thus polarization is needed to render the NC data useful at all for precision measurements.

3.3.3 Electron vs. Positron Beams

Fig. 7 shows a comparison of the potential of unpolarized charged current electron and positron scattering. Positron scattering always yields a lower sensitivity than electron scattering simply

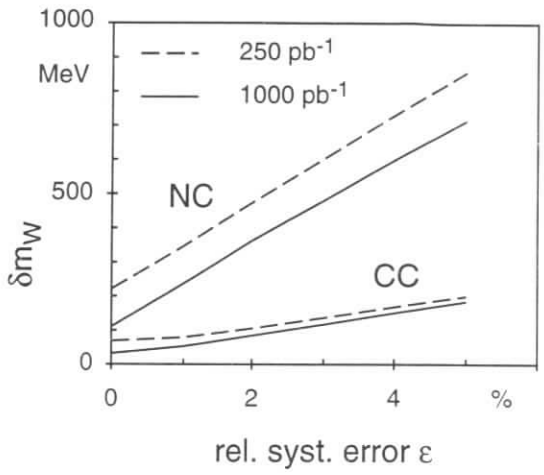

Figure 5: *Precision for m_W from measurements of the HERA NC and CC cross sections for unpolarized electrons at fixed top mass as a function of the relative systematic uncertainty ϵ.*

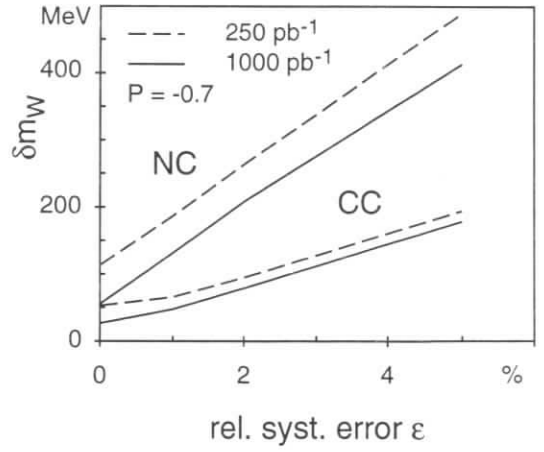

Figure 6: *Same as Fig. 5 for scattering with longitudinally polarized electrons of degree $P = -0.7$.*

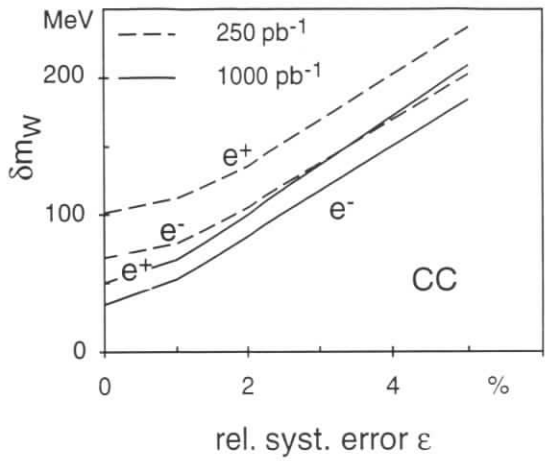

Figure 7: *Comparison of the precision for m_W from unpolarized electron and positron charged current scattering at HERA at fixed top mass.*

because of the smaller cross section. The same comparison for polarized neutral current scattering is made in Fig. 8. Again electron scattering is preferred since both the absolute values of δm_W as well as the sensitivity to systematic errors is more favourable in this case than for positron scattering.

3.3.4 Overall vs. Point-to-Point Error

Fig. 9 addresses the importance of the Q^2 dependence for an experimental determination of m_W. The sensitivity is depicted as a function of the correlation coefficient[2] c for the systematic error in the five chosen Q^2 bins (for the case of definiteness we have assumed a global value of the correlation coefficient c). A correlation coefficient of 0 describes a situation where the normalization of the cross section measurement has no systematic uncertainty, whereas a coefficient of 1 applies to an experiment where only normalization is affected by systematics. In turn, a coefficient of 0 ascribes the complete systematic error to relative uncertainties in different Q^2 bins and the value 1 for the correlation coefficient assumes no relative bin-to-bin uncertainties apart from statistical ones. The gently rising curve for the charged current measurement demonstrates that the normalization of the cross section measurement contains the information about the value of m_W. In this case, bin-to-bin uncertainties do not strongly increase the uncertainty δm_W provided the normalization can be well measured. In contrast to this, for neutral current scattering, uncertainties on the relative normalization result in a large

[2]If $\vec{\sigma} = \epsilon(\sigma_1^{exp}, \sigma_2^{exp} \cdots \sigma_5^{exp})$ describes the systematic uncertainties in the five Q^2 intervals the 5×5 variance matrix is calculated as $\mathbf{V} = \vec{\sigma}((1-c)\mathbf{I} + c\mathbf{1})\vec{\sigma}^T$. Here $\mathbf{I}$ and $\mathbf{1}$ refer to the unit matrix and the matrix containing ones in all positions respectively. The diagonal variance matrix of the statistical error has to be added.

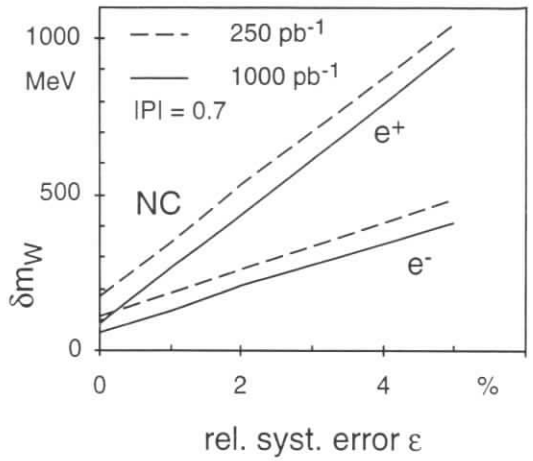

Figure 8: *Same as Fig. 7 for neutral current scattering of polarized electrons ($P = -0.7$) or positrons ($P = 0.7$).*

uncertainty for m_W and a good knowledge of the relative bin-to-bin normalization is essential for neutral current scattering to contribute significantly to an m_W determination. In the limit of vanishing point-to-point errors the NC measurement would compete or even be superior to the CC current measurement. The different dependence can thus be exploited in the interpretation of the experimental data in a favourable way.

3.3.5 The High Sensitivity Measurement at HERA

Finally, Fig. 10 indicates the result for a scenario with 1000 pb^{-1} of data from polarized neutral and charged current electron scattering. The corresponding 1σ-contour is represented by the shaded ellipse. Projecting it onto the axes results in precisions of $\delta m_t = \pm 50$ GeV and $\delta m_W = \pm 300$ MeV. These values are more than a factor of 2 better than what can be obtained from charged current scattering alone with the smaller luminosity of 250 pb^{-1} (see the large ellipse in the figure). Combining the neutral and charged current data from HERA with a realistic top mass uncertainty (assuming a value of ± 5 GeV) results in the small full ellipse in Fig. 10. The resulting precision on m_W is $\delta m_W = \pm 55$ MeV. This scenario assumes a 1 % relative systematic uncertainty, a serious experimental challenge. The accuracy decreases to $\delta m_W = \pm 81$ MeV for a systematic error of 2 %. With a very precise measurement of m_t the corresponding values are 45 and 75MeV respectively. The figure also shows the relation between m_W and m_t following from the G_μ constraint. The upper full line refers to a Higgs mass of $m_H = 100$ GeV, the lower dashed one to $m_H = 800$ GeV. Note that the confidence contours for the HERA measurements have to be associated with a fixed Higgs mass of 100 GeV. They have to be shifted downwards much the same as the lines describing the G_μ constraint for a Higgs

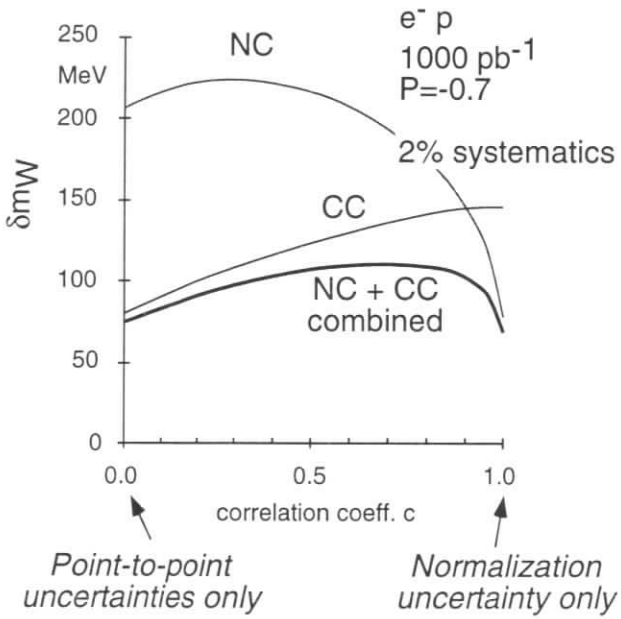

Figure 9: *Precision for m_W from neutral and charged current scattering of polarized electrons ($P = -0.7$) at fixed top mass as a function of the correlation coefficient c for the systematic error (see text). The overall systematic uncertainty for this example is assumed to be 2 %.*

mass of $m_H = 800$ GeV. It is obvious from this figure that with such precision one would be able to constrain the allowed range of Higgs masses in conjunction with independent measurements of both m_t and m_W.

3.4 Uncertainties from parton distributions

The DIS cross sections depend not only on electroweak parameters but also on QCD input given by parton densities and the strong coupling constant $\alpha_s(\Lambda_{QCD})$. A final analysis will have to determine all parameters simultaneously in a global fit to all DIS cross sections measured at HERA. The study of such a global fit is beyond the scope of the present work. The preceding discussions assumed that parton densities are a well-known independent input. Ignoring the possibility that electroweak parameters and QCD input might be correlated, we now address uncertainties of parton densities as an additional source of uncertainty for the precision of an m_W measurement. We have seen that the normalization of the CC cross section provides an important constraint to the measurement of m_W. Therefore we expect that uncertainties of the overall normalization of parton densities will have the largest impact on the precision of m_W.

Since no parton distribution functions exist which parametrize their errors, we are bound to study variations of the predictions for DIS cross sections obtained when using parametrizations given by different authors. A comparison of recent parton densities of GRV (94HO) [18], CTEQ (3D and 3M) [19] and MRS(H,A) [20] gives a variation in the CC cross section for left-handed electrons of up to 5pb. This can be interpreted as a contribution to the systematic uncertainty of about 5 %. Considering most recent parton densities which include 1994 HERA data (CTEQ3M and MRS(A')) yields already now only 2 % additional systematic uncertainty. It seems reasonable to expect that the uncertainties in our knowledge of the parton densities will further diminish with more data being available and that, consequently, the imperfect knowledge of parton densities will eventually not be the limiting source of uncertainties for the measurement of electroweak parameters.

An additional uncertainty is due to the error on α_s, viz. Λ_{QCD}. Since the extraction of parton densities from experimental data is usually performed for a fixed value of α_s, uncertainties on the latter induce uncertainties on the former. The effect on DIS cross sections can be studied using the parametrizations of MRS [21] which are given for a number of different values of Λ_{QCD}. Again concentrating on CC scattering, we observe an increase of the cross section by 0.7 pb (i.e., less than 1 %) when increasing α_s by 0.005. In addition, uncertainties on α_s would affect QCD corrections which modify the relation of structure functions to parton distributions. This direct effect is expected to be much smaller since QCD corrections themselves are small so that uncertainties oı α_s will not contribute much to the uncertainties of electroweak precision measurements.

4 Conclusions

Precise HERA measurements of the differential NC and CC cross sections complete the picture of successful tests of the Standard Model in the region of large space-like momentum transfers. This study has shown that, given sufficient luminosity, a test of the model to a level of accuracy hitherto only achieved at LEP 1 can be reached at HERA. Consistent values of m_W and m_t

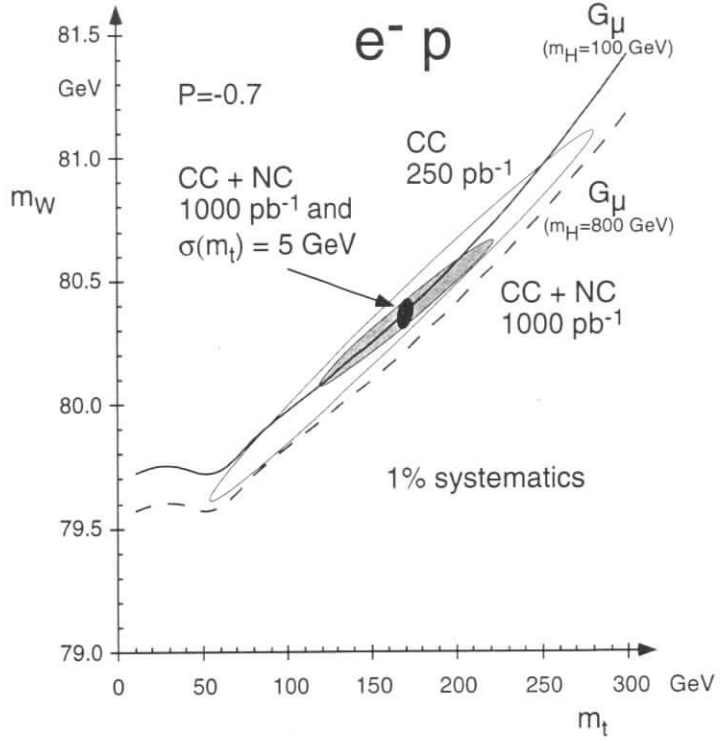

Figure 10: *1σ-confidence contours in the (m_W, m_t) plane from polarized electron scattering ($P = -0.7$), utilizing charged current scattering at HERA alone with an integrated luminosity of 250 pb^{-1} (large ellipse), neutral and charged current scattering at HERA with 1000 pb^{-1} (shaded ellipse), and the combination of the latter HERA measurements with a direct top mass measurement with precision $\sigma m_t = 5$ GeV (full ellipse). The m_W-m_t relation following from the G_μ constraint is also shown for two values of m_H.*

have to be obtained between the HERA measurements, the G_μ constraint and the direct mass measurements from colliders.

A luminosity of 250 pb^{-1} can be safely exploited at HERA for a given electroweak process. Admittedly, the uncertainty arising from the energy scale of the hadronic calorimeter imposes the largest experimental challenge. On the other hand sufficient NC data will be available to constrain the final state and hence the scale of the calorimeter energy. One can speculate that this uncertainty becomes dominating only well above the 250 pb^{-1} limit.

The most stringent tests can be performed with electrons rather than positrons. Both CC and NC cross sections are largest and the electroweak effects are enhanced for the latter. A scenario with nonzero longitudinal polarization will improve the sensitivity. In fact, NC data start to be useful once polarization is available which allows to enhance the γZ interference terms. Roughly speaking, a polarization of 70 % in the NC measurement is worth a factor 4 in luminosity.

In an optimistic scenario a value for m_W with an accuracy of 55 MeV can be extracted from each of the HERA experiments; this compares well with the projected precision from LEP 2 for all 4 LEP experiments combined.

Acknowledgement

We thank W. Hollik and D. Haidt for helpful discussions.

References

[1] D. Haidt, H. Pietschmann; Berlin, Springer (1988), Landolt-Boernstein. New Series, 1/10; G. L. Fogli and D. Haidt, Z. Phys. C40 (1988) 379.

[2] F. Zetsche, these proceedings.

[3] R. J. Cashmore et al., these proceedings.

[4] W. Hollik et al., in *HERA proceedings 1991* [22], Vol. 2, p. 923.

[5] V. Brisson et al., in *HERA proceedings 1991* [22], Vol. 2, p. 947.

[6] H. Spiesberger, in *Precision Tests of the Standard Model*, Advanced Series on Directions in High Energy Physics, World Scientific Publishing Co., Ed. P. Langacker, 1994.

[7] H. Spiesberger et al., in *HERA proceedings 1991* [22], Vol. 2, p. 798.

[8] L. Avdeev, J. Fleischer, S. Mikhailov and O. Tarasov, Phys. Lett. B336 (1994) 560; Err. Phys. Lett. B349 (1995) 597;
K. G. Chetyrkin, J. H. Kühn and M. Steinhauser, Phys. Lett. B351 (1995) 331.

[9] A. Djouadi and C. Verzegnassi, Phys. Lett. B195 (1987) 265.

[10] J. G. Körner, E. Mirkes and G. A. Schuler, Int. J. Mod. Phys. A4 (1989) 1781.

[11] E. B. Zijlstra and W. L. van Neerven, Nucl. Phys. B383 (1992) 525.

[12] D. Yu. Bardin, M. S. Bilenky, G. V. Mitselmakher, T. Riemann and M. Sachwitz, Z. Phys. C44 (1989) 493.

[13] D. Yu. Bardin, W. Hollik and T. Riemann, Z. Phys. C49 (1991) 485.

[14] H. Spiesberger, these proceedings.

[15] P. Tipton, *Top quark properties and their theoretical implications - Experimental aspects*, XXVIII International Conference on High Energy Physics, 25 - 31 July 1996, Warsaw, Poland.

[16] S. Aid et al., Nucl. Phys B470 (1996) 3.

[17] S. Aid et al., Phys. Lett B379 (1996) 319.

[18] M. Glück, E. Reya and A. Vogt, Z. Phys. C67 (1995) 433.

[19] H. H. Lai et al., CTEQ Collaboration, Phys. Rev. D51 (1995) 4763.

[20] A. D. Martin, R. G. Roberts and W. J. Stirling, Phys. Rev. D50 (1994) 6734.

[21] A. D. Martin, R. G. Roberts and W. J. Stirling, RAL-TR-95-013 (1995).

[22] W. Buchmüller and G. Ingelman, Eds., *Physics at HERA, Proceedings of the Workshop, Hamburg, Oct. 29 - 30, 1991*, Vol. 2 (Hamburg 1991).

Theoretical Uncertainties in Precision Electroweak Physics at HERA

Bernd A. Kniehl[ab]

[a] Max-Planck-Institut für Physik (Werner-Heisenberg-Institut), Föhringer Ring 6, 80805 Munich, Germany

[b] Institut für Theoretische Physik, Ludwig-Maximilians-Universität, Theresienstraße 37, 80333 Munich, Germany

Abstract: We assess the influence of those radiative corrections which are not presently included in the theoretical calculations underlying this study group report, and estimate the theoretical uncertainties from unknown higher orders.

The discussion of Ref. [1] focuses attention on the experimental uncertainties in the values of m_W and other electroweak observables extracted from the measurements of the cross sections of charged-current (CC) and neutral-current (NC) deep inelastic scattering (DIS) at HERA through the comparison with theoretical predictions. For the sake of estimating experimental sensitivities, it should be sufficient to compute the theoretical predictions with electroweak one-loop precision and to disregard the available QCD and higher-order electroweak corrections (see Section 2.2 of Ref. [1]). However, since, under favourable conditions, future measurements at HERA are aiming at experimental errors on m_W of order $\delta m_W = \pm 60$ MeV [1], which is considerably smaller than the shift due to the inclusion of the electroweak one-loop corrections, it is important to study by how much the extracted value of m_W is affected by the known QCD and higher-order electroweak corrections, and to estimate the residual uncertainty from theoretical sources.

In the case of the electroweak corrections, we may simplify this problem by studying the value of m_W predicted from the measured muon lifetime via Δr [2], i.e. the so-called G_μ constraint, since the dominant higher-order corrections coincide with those to the CC DIS cross section (see Fig. 9 of Ref. [1]), which is most important for the m_W determination at HERA (see Figs. 4 and 5 of Ref. [1]). The values of m_W derived through Δr to $\mathcal{O}(\alpha)$ in the electroweak on-shell scheme and the shifts due to the $\mathcal{O}(\alpha\alpha_s)$ [3], $\mathcal{O}(\alpha\alpha_s^2)$ [4], $\mathcal{O}(G_F^2 m_t^4)$ [5] and $\mathcal{O}(G_F^2 m_W^2 m_t^2)$ [6] corrections are listed in Table 1 for $m_t = (175 \pm 9)$ GeV and selected values of m_H [7]. We see that all higher-order corrections act in the same direction and typically reduce m_W by 100 MeV, to be contrasted with the envisaged experimental error $\delta m_W = \pm 60$ MeV [1]. It will therefore be crucial to implement these corrections in the theoretical predictions of Ref. [1] before one attempts to confront the latter with precision data on DIS to be collected with HERA or possible upgrades. In general, these corrections will shift, tilt and distort the ellipses shown in Figs. 1, 2 and 9 of Ref. [1].

The residual theoretical uncertainty in m_W is either due to experimental errors in the input parameters or to the corrections beyond present knowledge. From Table 1, we read off the errors

Table 1: m_W predicted for various values of m_t and m_H via Δr to one loop and shifts due to higher-order corrections. All masses are given in GeV.

m_t	m_H	m_W	δm_W			
		$\mathcal{O}(\alpha)$	$\mathcal{O}(\alpha\alpha_s)$	$\mathcal{O}(\alpha\alpha_s^2)$	$\mathcal{O}(G_F^2 m_t^4)$	$\mathcal{O}(G_F^2 m_W^2 m_t^2)$
166	100	80.420	−0.058	−0.011	−0.009	−0.011
	300	80.349	−0.058	−0.011	−0.015	−0.009
	800	80.273	−0.058	−0.011	−0.017	−0.006
175	100	80.485	−0.063	−0.012	−0.011	−0.013
	300	80.414	−0.063	−0.012	−0.017	−0.011
	800	80.338	−0.063	−0.012	−0.021	−0.007
184	100	80.553	−0.068	−0.013	−0.012	−0.015
	300	80.482	−0.068	−0.013	−0.021	−0.013
	800	80.406	−0.068	−0.013	−0.026	−0.008

$\delta m_W = {}^{+57}_{-54}$ MeV and ±76 MeV due to the variations $\delta m_t = \pm 9$GeV and $\delta m_H = {}^{+500}_{-200}$ GeV around the central values $m_t = 175$ GeV and $m_H = 300$ GeV, respectively. Furthermore, the errors in $\alpha_s(M_Z) = 0.117 \pm 0.006$ and the hadronic contribution $\Delta\alpha_{had} = 0.0280 \pm 0.007$ [8] to the running fine-structure constant lead to $\delta m_W = \pm 4$ MeV and ±13 MeV, respectively. The higher-order uncertainty may be estimated to be less than $\delta m_W = \pm 10$ MeV by considering the renormalization scheme and scale dependences of the presently known corrections [7, 9].

The next-to-leading order QCD corrections to NC and CC DIS are well under control [10], and in the case of the photon-exchange contribution to NC DIS even the next-to-next-to-leading-order QCD corrections are available [11]. As may be gleaned from Ref. [11], in the kinematic regime of interest here, the residual QCD uncertainty is likely to be smaller than the one from the parton distribution functions.

In conclusion, the extraction of electroweak parameters from future precision measurements of DIS at HERA will essentially be meaningless unless the presently known QCD and higher-order electroweak corrections will be included in the theoretical calculations. On the other hand, the residual uncertainty due to unknown higher-order corrections is estimated to be small against the envisaged [1] experimental accuracy.

References

[1] R. Beyer et al., in this working group report.

[2] A. Sirlin, Phys. Rev. D22 (1980) 971.

[3] A. Djouadi and C. Verzegnassi, Phys. Lett. B195 (1987) 265; B.A. Kniehl, Nucl. Phys. B347 (1990) 86.

[4] L. Avdeev, J. Fleischer, S. Mikhailov and O. Tarasov, Phys. Lett. B336 (1994) 560; (E) B349 (1995) 597; K.G. Chetyrkin, J.H. Kühn and M. Steinhauser, Phys. Lett. B351 (1995) 331.

[5] R. Barbieri, M. Beccaria, P. Ciafaloni, G. Curci and A. Viceré, Phys. Lett. B288 (1992) 95; (E) B313 (1993) 511; Nucl. Phys. B409 (1993) 105; J. Fleischer, O.V. Tarasov and F. Jegerlehner, Phys. Lett. B319 (1993) 249; Phys. Rev. D51 (1995) 3820.

[6] G. Degrassi, S. Fanchiotti and P. Gambino, Int. J. Mod. Phys. A10 (1995) 1337; G. Degrassi, S. Fanchiotti, F. Feruglio, P. Gambino and A. Vicini, Phys. Lett. B350 (1995) 75; G. Degrassi, P. Gambino and A. Vicini, Phys. Lett. B383 (1996) 219.

[7] B.A. Kniehl, Preprint FERMILAB-PUB-95/247-T, MPI/PhT/95-74 and hep-ph/9403386 (July 1995), to appear in Z. Phys. C.

[8] S. Eidelman and F. Jegerlehner, Z. Phys. C67 (1995) 585; H. Burkhardt and B. Pietrzyk, Phys. Lett. B356 (1995) 398.

[9] B.A. Kniehl and A. Sirlin, Nucl. Phys. B458 (1996) 35.

[10] J.G. Körner, E. Mirkes and G.A. Schuler, Int. J. Mod. Phys. A4 (1989) 1781.

[11] E.B. Zijlstra and W.L. van Neerven, Nucl. Phys. B383 (1992) 525.

Measurement of Weak Neutral Current Couplings of Quarks at HERA

R. J. Cashmore[a], S. Dagan[b†], O. Deppe[c], J. Edmonds[a], J. C. Hart[d], H. Heßling[c], K. R. Long[b], J. K. Sedgbeer[b], H. Spiesberger[e], R. Walczak[a], A. F. Whitfield[b], F. Zetsche[f]

[a] Department of Physics, University of Oxford, Oxford, UK.
[b] High Energy Physics Group, Imperial College, London, UK.
[c] Deutches Elektronen-Synchrotron DESY, Hamburg, Germany.
[d] Rutherford Appleton Laboratory, Chilton, Didcot, Oxon, UK.
[e] Max Planck Institut für Physik, München, Germany.
[f] Institut für Experimentalphysik, Universität Hamburg, Germany.
[†] On leave from Tel-Aviv University. Supported by a PPARC fellowship.

Abstract: We present methods to determine the Neutral Current (NC) axial and vector couplings of the quarks at HERA. Without beam polarisation, limits on deviations from the Standard Model (SM) value of the axial coupling of the up-type quark to the Z^0 may be obtained using ratios of NC cross sections to Charged Current (CC) cross sections. Assuming an electron (positron) beam polarisation of 70%, ratios of polarised NC and CC cross sections may be used to set limits on deviations of the up-type quark vector coupling from the SM value. We show that with an integrated luminosity of $1000\,\mathrm{pb}^{-1}$, divided equally between the left- and right-handed electron and positron beams, fractional errors on v_u, a_u, v_d and a_d of 13%, 6%, 17% and 17% may be obtained from a full fit, while if the d (u) quark couplings are held fixed while the u (d) quark couplings are allowed to vary then the errors on v_u (v_d) and a_u (a_d) are 4% (6%) and 4% (10%) respectively.

1 Introduction

The Standard Model of electroweak interactions (SM) has been experimentally verified in an extensive series of experiments over the last 25 years. Deep Inelastic Scattering (DIS) experiments with electron, muon and neutrino beams [1] have contributed to this success with measurements of the fundamental constants of the SM for space-like momentum transfer squared, Q^2, in the range $0 < Q^2 < 250$ GeV^2. The HERA experiments have already been able to extend the sensitivity of measurements of electroweak parameters in electron proton DIS to $Q^2 \sim 8000$ GeV^2 [2, 3, 4]. The high precision measurements of SM parameters made by the LEP and SLC collaborations have verified the SM at a time-like Q^2 of $M_{Z^0}^2 \approx 8100$ GeV^2. The mass of the top quark was predicted by combining the measurements of the Z^0 decay parameters with the mass of the W boson measured in $p\bar{p}$ annihilation at the Fermilab Tevatron [5]. The recent discovery of the top quark [6] at the predicted mass is a remarkable success for the SM.

The axial, a_f, and vector, v_f, couplings of the fermions to the Z^0 are defined by

$$a_f = I_3^f \quad \text{and} \quad v_f = I_3^f - 2e_f \sin^2\theta_W \tag{1}$$

where I_3^f is the third component of isospin for the fermion of flavour f and electric charge e_f. θ_W is the weak mixing angle which is defined by the ratio of the charged and neutral weak gauge boson masses, $\cos\theta_W = M_W/M_{Z^0}$. The LEP and SLC measurements of the partial width for Z^0 decay to $c\bar{c}$ and $b\bar{b}$ may be combined with forward-backward and polarisation asymmetries to yield measurements of the b and c quark couplings [7]. The results are shown in figure 1. The ratio of neutral current (NC) to charged current (CC) cross sections, R_ν, for neutrino DIS may be used to extract the couplings of the up-type and d-type quarks. The results of an analysis of a compilation of measurements of R_ν [8] are also shown in figure 1 together with the couplings determined from a measurement of R_ν made by the CCFR collaboration [9]. Note that in the case of the CCFR results the couplings of the u (d) quarks are obtained with the d (u) quark couplings fixed at their SM values. It is interesting to note that the b quark couplings obtained by combining the published LEP and SLC results are 3.7 standard deviations from the SM value [5, 7]. Recently new measurements of the partial width for Z^0 decay to $b\bar{b}$ have been reported. These measurements indicate that the coupling of the b quark to the Z^0 is shifted closer to the SM expectation [10].

The two HERA collider experiments, ZEUS and H1, have collected data corresponding to ~ 10 pb^{-1} per experiment over the period 1992-1995. An upgrade to the HERA machine is now proposed which will provide each of the HERA experiments with an integrated luminosity of up to 1000 pb^{-1} over its remaining period of operation. The availability of a longitudinally polarised lepton beam greatly enhances the HERA potential to make precise studies of electroweak physics. At the experimental interaction points in HERA spin rotators will be installed which can turn the naturally transversely polarised lepton beam into a longitudinally polarised beam. Currently polarisation values of 60 % have been routinely achieved and it is expected that 70% longitudinal polarisation for future running should be attainable [11]. The purpose of this article is to determine the precision with which the HERA experiments will be able to measure the NC couplings of the light quarks to the Z^0.

In the following section we show how measurements of the inclusive DIS cross sections at HERA are sensitive to the couplings and how experimental observables may be used to provide limits on, or measurements of, their values. Radiative corrections are also discussed. In

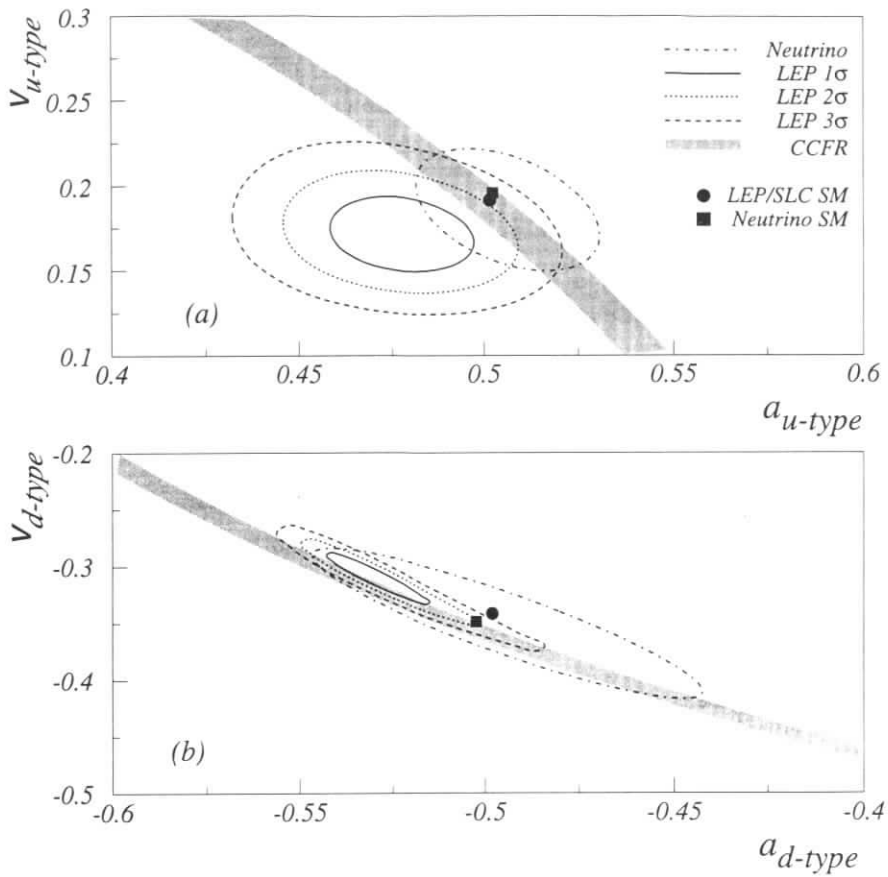

Figure 1: *Summary of measurements of u-type (a) and d-type (b) quark couplings to the Z^0. The dash-dotted ellipse shows the one standard deviation (1σ) contour obtained in a fit of the four chiral couplings of the u and d quarks to a compilation of neutrino DIS data. The solid, dotted and dashed ellipses show the 1, 2 and 3 σ limits of the combined LEP/SLC results for the c and b quark couplings as reported before the 1996 summer conferences [7]. The shaded band shows the result obtained by the CCFR collaboration from the ratio of NC and CC cross sections projected onto the quark coupling plane. In the case of the CCFR result the couplings of the u (d) quarks are obtained with the d (u) quark couplings fixed at their SM values. From equation 1 the Born level SM values of a_u, v_u, a_d, v_d are 0.5, 0.19, -0.5 and -0.35 respectively. For the LEP/SLC results radiative corrections (see section 2.3) modify the SM predictions to the values indicated by the circle. Different radiative corrections for neutrino data give the SM prediction shown as a square.*

section 3 we give a brief overview of the experimental issues involved in such a measurement and discuss event reconstruction, simulation and binning and we touch upon the various experimental sources of systematic error which will be important when analysing forthcoming data. Systematic errors arising from uncertainties in our current knowledge of parton density functions are discussed in section 4. Using samples of fully reconstructed Monte Carlo data, two complementary analyses, presented in section 5 and section 6, provide quantitative estimates of the potential to measure both the axial and the vector couplings of the light quarks at HERA. The results are compared to existing measurements from other experiments.

2 Formalism

2.1 Kinematics

Lowest order Feynman diagrams for lepton nucleon DIS are shown in figure 2. The neutral current process, which is mediated by the exchange of a photon or Z^0, is shown in figure 2a and the charged current process, where the exchanged boson is a $W^{\pm}$, is shown in figure 2b. The scattering may be described in terms of the Lorentz invariant quantities Q^2, x and y. $-Q^2$ is the square of the momentum transferred to the hadronic system. In the frame where the incoming proton has infinite momentum, x is the fraction of the proton's momentum carried by the struck quark. The quantity y is related to the scattering angle θ^* in the lepton-quark centre of mass system by $y = \sin^2(\theta^*/2)$. At a given lepton-proton centre of mass energy, $\sqrt{s}$, the combination of any two of the three variables, Q^2, x and y fully describes the inclusive DIS process.

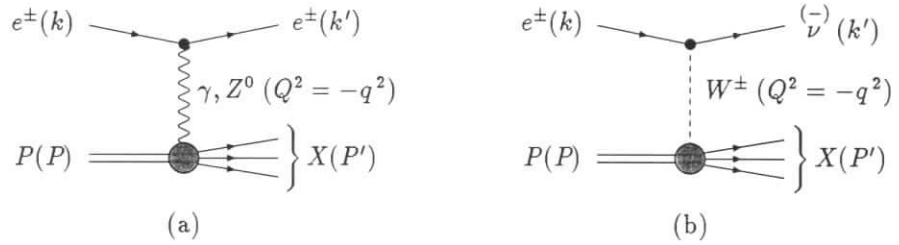

Figure 2: *Kinematics of deep inelastic scattering. a) Neutral Current DIS. b) Charged Current DIS. The four momenta are indicated in parentheses.*

2.2 Cross Section Formulæ

The neutral current cross section for polarised leptons scattering off unpolarised protons may be written

$$\left.\frac{d^2\sigma^{\pm}}{dxdQ^2}\right|_{NC} = \frac{2\pi\alpha^2}{xQ^4}\left[H_0^{\pm} + \mathcal{P}H_{\mathcal{P}}^{\pm}\right], \qquad (2)$$

where $\mathcal{P}$ denotes the lepton beam polarisation and is defined by

$$\mathcal{P} = \frac{N_R - N_L}{N_R + N_L}. \tag{3}$$

N_R and N_L are the number of right-handed and left-handed leptons in the beam respectively. $H_0^\pm$ contains the unpolarised structure functions. The extraction of the NC couplings of the quarks requires the measurement of DIS cross sections at high Q^2. For large Q^2 the longitudinal structure function, F_L, may be neglected so that $H_0^\pm$ may be written:

$$H_0^\pm = Y_+ F_2^0 \mp Y_- x F_3^0, \tag{4}$$

where the factors $Y_\pm = \left(1 \pm (1-y)^2\right)$ give the angular dependence of the cross section in the lepton-quark centre of mass system and F_2^0 and F_3^0 are the usual DIS structure functions given by:

$$F_2^0 = \sum_q x\,(q + \bar{q})\,A_q^0 \quad ; \quad xF_3^0 = \sum_q x\,(q - \bar{q})\,B_q^0 \tag{5}$$

where $q = q(x, Q^2)$ are the parton distribution functions (PDFs) and A_q^0 and B_q^0 are given by

$$A_q^0 = e_q^2 - 2e_q v_q v_e \chi_Z + \left(v_q^2 + a_q^2\right)\left(v_e^2 + a_e^2\right)\chi_Z^2 \quad ; \quad B_q^0 = -2e_q a_q a_e \chi_Z + 4 v_q a_q v_e a_e \chi_Z^2. \tag{6}$$

In the following we shall be considering deviations from the SM in which the vector and axial couplings of quarks are replaced by

$$v_q = v_q^{SM} + \delta v_q \quad ; \quad a_q = a_q^{SM} + \delta a_q. \tag{7}$$

Deviations of the electron couplings will not be considered here. At lowest order, the SM vector, v_q^{SM}, and axial, a_q^{SM}, couplings of the quarks to the Z^0 are given by equation 1. The variable

$$\chi_Z = \left[\frac{\sqrt{2} G_\mu M_{Z^0}^2}{4\pi\alpha}\right]\left(\frac{Q^2}{M_{Z^0}^2 + Q^2}\right) \tag{8}$$

is proportional to the ratio of the Z^0 and photon propagators. The numerical factor in square brackets is required to complete the SM neutral current couplings when v_q^{SM} and a_q^{SM} are defined as in equation 1. This choice of normalization factor is suited to a scheme where input parameters (the mass of the W boson, M_W, and thus also $\sin^2\theta_W$ and the NC couplings) are fixed using the constraint obtained from the experimental determination of the muon decay constant, G_μ [12] since it reduces the numerical size of electroweak one-loop corrections. Terms which are linear in χ_Z arise from γ/Z^0 interference while those which are quadratic in χ_Z are due to Z^0 exchange.

The effect of a finite lepton beam polarisation on the cross section given in equation 2 is contained in the functions $H_\mathcal{P}^\pm$ which, for high Q^2, where the longitudinal structure function may be neglected, may be written

$$H_\mathcal{P}^\pm = Y_+ F_2^\mathcal{P} \mp Y_- x F_3^\mathcal{P}. \tag{9}$$

The structure functions $F_2^\mathcal{P}$ and $xF_3^\mathcal{P}$ are given by

$$F_2^\mathcal{P} = \sum_q x\,(q + \bar{q})\,A_q^\mathcal{P} \quad ; \quad xF_3^\mathcal{P} = \sum_q x\,(q - \bar{q})\,B_q^\mathcal{P}, \tag{10}$$

where $A_q^\mathcal{P}$ and $B_q^\mathcal{P}$ are given by

$$A_q^\mathcal{P} = 2e_q v_q a_e \chi_Z - 2\left(v_q^2 + a_q^2\right) v_e a_e \chi_Z^2 \quad ; \quad B_q^\mathcal{P} = 2e_q a_q v_e \chi_Z - 2 v_q a_q \left(v_e^2 + a_e^2\right)\chi_Z^2. \tag{11}$$

The cross section for the charged current process depicted in figure 2b with an incident positron beam is given by

$$\left.\frac{d^2\sigma^+}{dx dQ^2}\right|_{CC} = [1 + \mathcal{P}]\,\frac{G_\mu^2}{2\pi}\left[\frac{M_W^2}{Q^2 + M_W^2}\right]^2 \left\{\bar{u} + \bar{c} + (1-y)^2\,(d + s + b)\right\}, \tag{12}$$

whilst for an electron beam the cross section is given by

$$\left.\frac{d^2\sigma^-}{dx dQ^2}\right|_{CC} = [1 - \mathcal{P}]\,\frac{G_\mu^2}{2\pi}\left[\frac{M_W^2}{Q^2 + M_W^2}\right]^2 \left\{u + c + (1-y)^2\left(\bar{d} + \bar{s} + \bar{b}\right)\right\}. \tag{13}$$

In equations 12 and 13 u, d etc. refer to the universal PDFs with an obvious notation.

2.3 Definition of Couplings and Radiative Corrections

The formulæ presented so far are Born level expressions and have to be improved to include radiative corrections. Part of the radiative corrections lead to a modification of gauge boson coupling constants. Therefore a clear understanding of them is needed before one can aim at an interpretation of measurements in terms of NC couplings.

A first class of radiative corrections is due to contributions where the process is accompanied by the emission of a bremsstrahlung photon [13]. This part has to be combined with virtual photonic corrections in order to obtain an infrared finite result. In practice, these QED corrections are broken down into four classes of events: non-radiative (NR) events, events with initial or final state radiation (ISR and FSR) and Compton (C) events. Radiation of a photon from the struck quark can safely be neglected at HERA. Radiative corrections of this first class do not change the structure of the NC cross section formulæ and may be written in the form

$$\frac{d^2\sigma^\pm}{dx dQ^2} = \frac{2\pi\alpha^2}{xQ^4}\left\{Y_+ R_2^0 F_2^0 \mp Y_- R_3^0 x F_3^0 + \mathcal{P}\left[Y_+ R_2^\mathcal{P} F_2^\mathcal{P} \mp Y_- R_3^\mathcal{P} x F_3^\mathcal{P}\right]\right\}. \tag{14}$$

The correction factors R_i^k depend on the kinematic variables x and Q^2 and result from the integration of radiator functions over the phase space of the emitted bremsstrahlung photon. It is essential that here the kinematic variables are the true ones, i.e. those which are determined from the hadronic final state. Otherwise, QED radiative corrections would involve an integration of structure functions over the true x and Q^2 and this would introduce a dependence of the correction factors on both the parton distributions and the NC couplings. Depending on kinematic cuts, these corrections may reach the level of 10 % and have to be taken into account before a sensible analysis in terms of NC couplings can be performed.

A second class of corrections receives contributions from electroweak loop diagrams (see [14, 15] and references therein). Apart from a small non-Born-like term, these electroweak corrections can be absorbed into the definition of the vector and axial coupling constants of the fermions, f. Introducing form factors $\rho_{f,i}$ and $\kappa_{f,i}$, one usually defines effective NC couplings

$$a_f^{SM} = \sqrt{\rho_{f,i}}\,I_3^f \quad \text{and} \quad v_f^{SM} = \sqrt{\rho_{f,i}}\left(I_3^f - 2\kappa_{f,i} e_f \sin^2\theta_W\right). \tag{15}$$

The effective couplings depend on the kinematic variables, i.e. in DIS on x and on Q^2 and on the process under consideration (indicated by the index i). In particular, there are ρ's and κ's for each lepton-quark subprocess. Examples for numerical results have been given in [14]. Using the effective couplings of equation 15 in the cross section formulæ of the preceding subsection would mean that the dominating electroweak radiative corrections are taken into account.

Electroweak radiative corrections to the charged current process are simpler since they do not change the $(V-A)$-structure of the interaction and there is only one form factor $\rho_{f,i}^{CC}$ for each process which multiplies the CC amplitude. Of course, QED corrections have to be added as well.

The aim of the present work is to study the precision of measurements of the neutral current couplings. Anticipating that the precision will be not much better than 5 %, further simplifications are possible. First, the non-Born-like term can be neglected since its effect can reach the level of a percent only at very large Q^2. Second, in the interesting kinematic regime at HERA, the x and Q^2 dependence of the effective couplings introduces modifications which are again small compared to the expected precision of vector and axial vector couplings. Therefore, the analysis performed in this work can safely be based on the Born-level formulæ of the preceding section. Eventually, however, when comparing the results for NC couplings obtained from an analysis of true data one would have to take into account the complete radiative corrections in order not to interpret shifts of the NC couplings induced by radiative corrections seen in the data erroneously as a sign of new physics. In particular, the x and Q^2 dependence of effective couplings will become important as soon as the level of a 2 % precision would be reached.

We also assume that the deviations δv_q and δa_q of the couplings from their SM values do not depend on x or Q^2, although it is likely that new physics that could lead to modified NC couplings would give rise to momentum dependent form factors, not just to constant shifts. This approach is sufficient for performing a test of whether the measured NC couplings agree within measurement errors with the SM predictions. A more general ansatz would be interesting if measurements should find deviations from the SM predictions or if they would allow the determination of the NC couplings at the level of a percent or better. Finally, it should be kept in mind that QCD corrections will eventually have to be taken into account. In the DIS renormalisation scheme, they will modify the CC cross section and also F_3 and F_L in NC scattering. Numerically, QCD corrections are small except at very small x (which is irrelevant for our purposes) and for x close to 1 [16]. For our work it is important that not only corrections of $O(\alpha_S)$, but also of $O(\alpha_S^2)$ are known [17], so that additional theoretical uncertainties can be kept to a minimum.

2.4 Sensitivity of DIS to the NC Quark Couplings

The NC DIS cross section is composed of a sum of terms in which PDFs multiply functions of the quark couplings. A determination of the couplings, therefore, requires that the PDFs be known. The effect of Z^0 exchange is to cause the cross sections, $\sum_{L,R}^{\pm} = d^2\sigma/dxdQ^2(e_{L,R}^{\pm}p \to e_{L,R}^{\pm}X)$, to deviate from the one photon exchange cross section, $\sum_{em}$, at high Q^2. As an example figure 3 shows the contribution of Z^0 exchange to the cross sections $\sum_{L,R}^{\pm}$ as a function of Q^2 for $x = 0.2$. At $Q^2 = 10^4$ GeV^2 the effect of Z^0 exchange is to split $\sum_{L,R}^{\pm}$ from $\sum_{em}$ by up to a factor of 2 (see figure 3a). The object of the analyses presented in subsequent sections is to exploit these differences between the cross sections for different lepton beam charges and polarisations to

determine the couplings. For $Q^2 \lesssim 500$ GeV^2 the Z^0 contributes $\lesssim 5$ % to the cross section so that measurements of $\sum_{L,R}^{\pm}$ can be used to determine the PDFs for $Q^2 \lesssim 500$ GeV^2. The QCD evolution equations [18] can then be used to evolve the PDFs up to high Q^2. Uncertainties in the PDFs will tend to affect all the $\sum_{L,R}^{\pm}$ in the same way. Therefore differences between the $\sum_{L,R}^{\pm}$ will be relatively insensitive to uncertainties in the PDFs. Differences between the $\sum_{L,R}^{\pm}$ are proportional to particular combinations of couplings and PDFs and consequently the errors with which these combinations are measured scale with the errors on the differences.

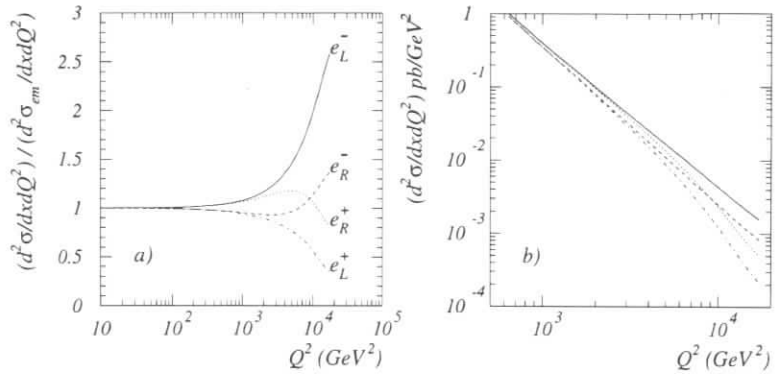

Figure 3: *Sensitivity to weak contributions of double differential NC cross sections as a function of Q^2 at $x = 0.2$. a) Ratio of Born level cross sections including weak terms with purely electromagnetic contributions. b) Absolute values of Born level NC cross sections.*

A first indication of the sensitivity of the structure functions to the neutral current couplings can be obtained by looking at the effect of simply setting one of them to zero. This is demonstrated in figure 4. Changing v_q from v_q^{SM} to zero while a_q is held fixed at a_q^{SM} lowers F_2^0 by $\sim 5\%$. With a_q set to zero while the vector couplings are held fixed at their SM values F_2^0 changes by $\sim -10\%$. In contrast, xF_3^0 shows little sensitivity to variation of v_q since the term in B_q^0 containing v_q is multiplied by v_e which is small ($v_e \approx -0.036$). xF_3^0 is strongly dependent on a_q since $B_q^0 \propto a_q$. A similar pattern emerges in the case of the polarised structure functions. $F_2^{\mathcal{P}}$ is relatively insensitive to a_q as the term in $A_q^{\mathcal{P}}$ containing a_q is multiplied by v_e. $F_2^{\mathcal{P}}$ changes by $\sim 20\%$ when v_q is set to zero while a_q is fixed at a_q^{SM}. $xF_3^{\mathcal{P}}$ is proportional to a_q and strongly sensitive to v_q.

The sensitivity of the structure functions to the couplings is summarised in table 1. Unpolarised DIS is sensitive to a_q mainly through xF_3^0. Polarised DIS shows strong sensitivity to a_q through xF_3^0 and $xF_3^{\mathcal{P}}$ and to v_q mainly through $xF_3^{\mathcal{P}}$.

In the following two subsections we identify specific ratios of NC and CC cross sections which can be utilised to perform quantitative tests of the structure of vector and axial couplings. Ratios of cross sections are preferred since to some extent a cancellation of systematic uncertainties can be expected. Moreover, by including CC cross sections which are independent of the neutral current couplings, one introduces a means of constraining the parton distribution functions, thus reducing the corresponding uncertainties.

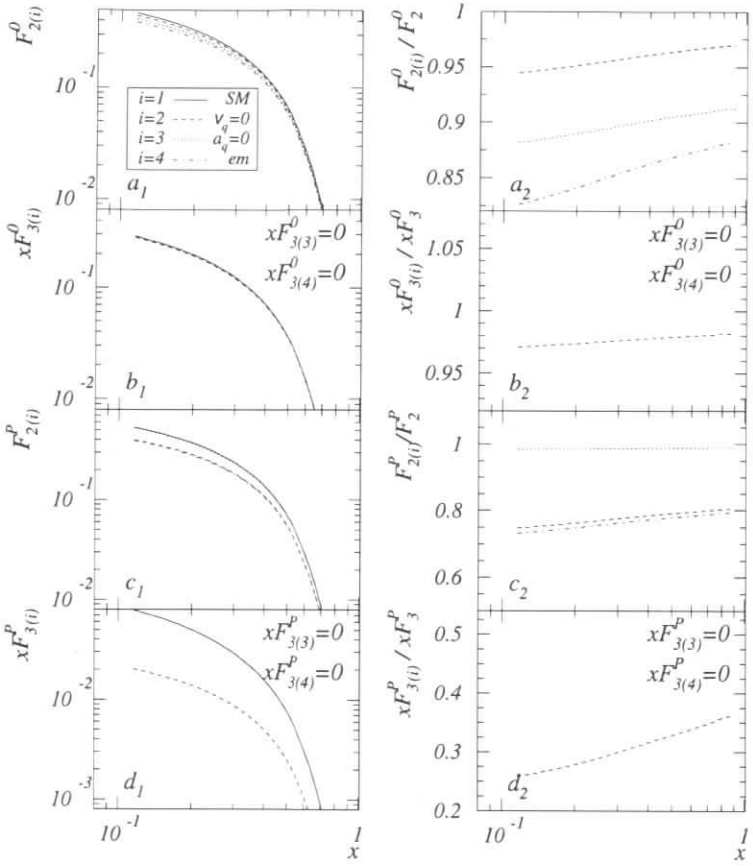

Figure 4: *Sensitivity of the NC DIS Structure Functions ($F_2^0, xF_3^0, F_2^{\mathcal{P}}, xF_3^{\mathcal{P}}$) to changes in the NC couplings (a_q, v_q) of the quarks. The structure functions are evaluated at $Q^2 = 10^4$ GeV^2 as a function of x using the MRSA parton distributions [19]. The label i is used to identify the values of the couplings used for the structure function evaluation in each plot. The axial and vector couplings both take their Standard Model values (a_q^{SM}, v_q^{SM}) when $i = 1$ with the results plotted as the solid lines. When $i = 2$, $v_q = 0$ and $a_q = a_q^{SM}$ and the results are plotted as the dashed lines. With $i = 3$ $a_q = 0$ and $v_q = v_q^{SM}$ and the results are plotted as the dotted lines. The pure electromagnetic (em) contribution to each structure function is obtained by setting $v_q = a_q = 0$, labelled $i = 4$ and plotted as the dash-dotted lines (where non-zero). The structure functions are shown in the subfigures labelled $a_1 - d_1$ while their ratios for $i = 2 - 4$ with the Standard Model values at $i = 1$, are shown in subfigures $a_2 - d_2$ respectively.*

$Q^2 = 10^4$ GeV^2	$v_q = 0$, $a_q = a_q^{SM}$	$v_q = v_q^{SM}$, $a_q = 0$
$1 - \frac{F_2^0(x,Q^2;v_q,a_q)}{F_2^0(x,Q^2)}$	~ 0.05	~ 0.12
$1 - \frac{xF_3^0(x,Q^2;v_q,a_q)}{xF_3^0(x,Q^2)}$	~ 0.03	1
$1 - \frac{F_2^{\mathcal{P}}(x,Q^2;v_q,a_q)}{F_2^{\mathcal{P}}(x,Q^2)}$	~ 0.2	~ 0.02
$1 - \frac{xF_3^{\mathcal{P}}(x,Q^2;v_q,a_q)}{xF_3^{\mathcal{P}}(x,Q^2)}$	~ 0.7	1

Table 1: *Summary of structure function sensitivity to neutral current couplings.*

2.5 Unpolarised Beams - Extraction of Axial Couplings

The structure function xF_3^0 is proportional to the axial couplings of the quarks so that the difference of the unpolarised electron and positron cross sections may be used to determine the axial couplings. The charged current cross sections, which are independent of the neutral current couplings, may be used to constrain the PDFs. The sum and difference of the charged current cross section for electrons and positrons may be written [20]

$$\overset{-+}{\underset{CC}{\Sigma^0}} = \left\{\frac{G_\mu^2}{2\pi x}\left[\frac{M_W^2}{M_W^2+Q^2}\right]^2\right\}^{-1}\left(\left.\frac{d^2\sigma^-}{dxdQ^2}\right|_{CC} + \left.\frac{d^2\sigma^+}{dxdQ^2}\right|_{CC}\right) = xU + (1-y)^2 xD \quad (16)$$

$$\overset{-+}{\underset{CC}{\Delta^0}} = \left\{\frac{G_\mu^2}{2\pi x}\left[\frac{M_W^2}{M_W^2+Q^2}\right]^2\right\}^{-1}\left(\left.\frac{d^2\sigma^-}{dxdQ^2}\right|_{CC} - \left.\frac{d^2\sigma^+}{dxdQ^2}\right|_{CC}\right) = xu_v - (1-y)^2 xd_v, \quad (17)$$

where

$$\begin{aligned} xU &= xu + x\bar{u} + xc + x\bar{c} & xD &= xd + x\bar{d} + xs + x\bar{s} + xb + x\bar{b} \\ xu_v &= xu - x\bar{u} + xc - x\bar{c} & xd_v &= xd - x\bar{d} + xs - x\bar{s} + xb - x\bar{b}. \end{aligned} \quad (18)$$

Similarly one may define sums and differences of the unpolarised neutral current cross sections as follows:

$$\begin{aligned} \overset{-+}{\underset{NC}{\Sigma^0}} &= \left[\frac{2\pi\alpha^2}{xQ^4}\right]^{-1}\left(\left.\frac{d^2\sigma^-}{dxdQ^2}\right|_{NC} + \left.\frac{d^2\sigma^+}{dxdQ^2}\right|_{NC}\right) = H_0^- + H_0^+ \quad (19) \\ &= 2Y_+ F_2^0 \qquad\qquad = 2Y_+\left[A_u^0 xU + A_d^0 xD\right] \end{aligned}$$

$$\begin{aligned} \overset{-+}{\underset{NC}{\Delta^0}} &= \left[\frac{2\pi\alpha^2}{xQ^4}\right]^{-1}\left(\left.\frac{d^2\sigma^-}{dxdQ^2}\right|_{NC} - \left.\frac{d^2\sigma^+}{dxdQ^2}\right|_{NC}\right) = H_0^- - H_0^+ \quad (20) \\ &= 2Y_- xF_3^0 \qquad\qquad = 2Y_-\left[B_u^0 xu_v + B_d^0 xd_v\right], \end{aligned}$$

where quark universality has been assumed (i.e. that $A_u^0 = A_c^0$, $A_d^0 = A_s^0 = A_b^0$, $B_u^0 = B_c^0$ and $B_d^0 = B_s^0 = B_b^0$). The assumption of quark universality has been made since it is consistent with present data. The ratio

$$R_\Delta^0 = \overset{-+}{\underset{NC}{\Delta^0}} \Big/ \overset{-+}{\underset{CC}{\Delta^0}} \tag{21}$$

is given by

$$R_\Delta^0 = \frac{2Y_- \left[B_u^0 + B_d^0 \frac{d_v}{u_v}\right]}{1-(1-y)^2\frac{d_v}{u_v}}. \tag{22}$$

Using equation 22 we may express the ratio R_Δ^0 in terms of deviations of axial couplings from the SM values so that

$$2\delta a_u - \delta a_d \frac{d_v}{u_v} + \delta\eta = a_d^{SM}\frac{d_v}{u_v} - 2a_u^{SM} - \frac{3R_\Delta^0\left(1-(1-y)^2\frac{d_v}{u_v}\right)}{4Y_-\chi_Z a_e} + \eta_{SM}. \tag{23}$$

The terms $\delta\eta$ and η_{SM} are given by

$$\begin{aligned} \eta_{SM} &= 6v_e\chi_Z\left[a_u^{SM}v_u^{SM} + a_d^{SM}v_d^{SM}\frac{d_v}{u_v}\right] \\ \delta\eta &= -6v_e\chi_Z\left[v_u^{SM}\delta a_u + v_d^{SM}\frac{d_v}{u_v}\delta a_d\right], \end{aligned} \tag{24}$$

where terms of second order in the deviations have been neglected.

The presence of the small electron vector coupling ($v_e \approx -0.036$) and the factor χ_Z ($\chi_Z = 0.67$ at $Q^2 = 10000$ GeV^2) in η_{SM} and $\delta\eta$ ensure that these terms give only a small contribution in equation 23. In the absence of deviations of the couplings from their SM values, the right-hand side of equation 23 should be zero. Thus, the measurement of the ratio in equation 21 can serve to constrain the axial couplings. Since only the ratio d_v/u_v of valence distributions enters, this way of utilising data to obtain NC couplings is particularly helpful when analysing the uncertainties coming from parton distribution functions.

2.6 Polarised Beams - Extraction of Vector Couplings

The structure function $F_2^{\mathcal{P}}$ is sensitive to the vector couplings of the quarks and so the latter may be extracted by taking sums and differences of polarised neutral current cross sections.

In the following the assumption is made that both electron and positron beams with right- and left-handed polarisation are available. In addition, the assumption is made that

$$\mathcal{P}_R = -\mathcal{P}_L = \mathcal{P},$$

where $\mathcal{P}_R$ and $\mathcal{P}_L$ are the degree of polarisation of the right- and left-handed beams respectively. Under these assumptions the sum of CC cross sections may be written

$$\overset{-+}{\underset{CC}{\sum^{\mathcal{P}}}} = \left\{\frac{G_\mu^2}{2\pi x}\left[\frac{M_W^2}{M_W^2+Q^2}\right]^2\right\}^{-1}\left(\frac{d^2\sigma^-}{dxdQ^2}\Big|_{CC}^{\mathcal{P}_L} + \frac{d^2\sigma^+}{dxdQ^2}\Big|_{CC}^{\mathcal{P}_R}\right) = (1+\mathcal{P})\left(xU + (1-y)^2 xD\right) \tag{25}$$

Note that the superscripts denote the charge of the lepton beam and are ordered such that the first superscript refers to the left-handed beam ($\mathcal{P}_L = -\mathcal{P}$) and the second to the right-handed beam ($\mathcal{P}_R = \mathcal{P}$).

In order to derive an expression for the vector couplings we consider the following two differences of NC cross sections

$$\overset{--}{\underset{NC}{\Delta^{\mathcal{P}}}} = \left[\frac{2\pi\alpha^2}{xQ^4}\right]^{-1}\left(\frac{d^2\sigma^-}{dxdQ^2}\Big|_{NC}^{\mathcal{P}_L} - \frac{d^2\sigma^-}{dxdQ^2}\Big|_{NC}^{\mathcal{P}_R}\right) = -2\mathcal{P}H_{\mathcal{P}}^- \tag{26}$$

$$\overset{++}{\underset{NC}{\Delta^{\mathcal{P}}}} = \left[\frac{2\pi\alpha^2}{xQ^4}\right]^{-1}\left(\frac{d^2\sigma^+}{dxdQ^2}\Big|_{NC}^{\mathcal{P}_L} - \frac{d^2\sigma^+}{dxdQ^2}\Big|_{NC}^{\mathcal{P}_R}\right) = -2\mathcal{P}H_{\mathcal{P}}^+ \tag{27}$$

Ignoring terms in v_e, equations 26 and 27 may be combined to give

$$2v_u xU - v_d xD = -\frac{3}{8}\frac{\overset{--}{\underset{NC}{\Delta^{\mathcal{P}}}} + \overset{++}{\underset{NC}{\Delta^{\mathcal{P}}}}}{\mathcal{P}Y_+ a_e\chi_Z}. \tag{28}$$

Dividing equation 28 by equation 25 and writing the vector couplings in terms of deviations from the SM values as in equation 7 gives

$$2\delta v_u - \delta v_d\frac{D}{U} = -\frac{3}{8}\frac{(1+\mathcal{P})}{\mathcal{P}}\left[\frac{\overset{--}{\underset{NC}{\Delta^{\mathcal{P}}}} + \overset{++}{\underset{NC}{\Delta^{\mathcal{P}}}}}{Y_+ a_e \overset{-+}{\underset{CC}{\sum^{\mathcal{P}}}}}\right]\left\{\frac{1+(1-y)^2\frac{D}{U}}{\chi_Z}\right\} - 2v_u^{SM} + v_d^{SM}\frac{D}{U}. \tag{29}$$

If the couplings take their SM values then the right-hand side of equation 29 should be zero. Thus the measurement of deviations of vector couplings from polarised cross sections receives uncertainties from parton distributions only via the ratio D/U.

3 Experimental considerations

The following section briefly describes the experimental techniques used in obtaining cross sections at high Q^2, highlighting the potential sources of systematic error.

Monte Carlo simulation

High luminosity Monte Carlo event samples for NC and CC DIS were generated using HERACLES which includes QED and electroweak radiative corrections [21] interfaced to LEPTO [22] via DJANGO6 [23]. The MRSA set of NLO PDF parametrisations was used, which is based on preliminary 1993 F_2 measurements by ZEUS and H1 as well as on recent data on W asymmetries from CDF and on Drell-Yan cross sections (see [19] and references therein). The hadronic final state was simulated using the colour-dipole model as implemented in ARIADNE [24] for the QCD cascade and JETSET [25] for the hadronization. Generated events were passed through the full ZEUS detector simulation and reconstruction chain.

Kinematic reconstruction and event selection

For CC DIS the Jacquet–Blondel (JB) method [26] may be used to reconstruct the kinematic variables using the measured missing transverse momentum, $\not{P}_t$, and the quantity $\delta = E - p_Z$, where E is the total energy and p_Z is the total longitudinal momentum. For NC DIS several reconstruction methods are available (see for example [27]). Unless otherwise stated the so called 'double angle' (DA) or 'electron' (EL) reconstruction methods are used for NC events as they have a significantly better precision and accuracy than the JB method.

Detailed descriptions of standard event selection cuts for the isolation of high Q^2 NC and CC DIS may be found in ZEUS publications [3, 28]. Here we shall summarise only the most important cuts. The NC selection is based upon the identification of the scattered lepton in the final state. The identification algorithm uses a neural network and is described in [29]. An electron (positron) of energy $E'_e > 10$ GeV detected in the calorimeter is required. Additionally a matching track, in the central tracking detector, between the primary event vertex and the electron energy deposit must be found. The value of δ is required to be within the range $35 < \delta < 65$ GeV. This cut, combined with an additional requirement that $y_{EL} < 0.95$, significantly reduces contamination from photoproduction events in data samples, where a fake scattered lepton is identified in the final state. For the selection of CC events the missing tranverse momentum carried by the final state (anti)neutrino motivates the main selection requirement: $\not{P}_t > 11$ GeV. A cut on the value of $y_{JB} < 0.8$ reduces contamination from NC events. Other cuts are used to remove backgrounds in the data originating mainly from photoproduction processes, cosmic rays and proton beam gas events [3].

The resolutions obtained for the reconstructed kinematic variables, Q^2_{JB}, y_{JB} and x_{JB} are 20%, 18% and 17% while those for Q^2_{DA}, y_{DA} and x_{DA} are typically 5%, 6% and 12% respectively.

Choice of Bins for Coupling Fit

In figure 5 migrations of the reconstructed values of y and Q^2 for NC events from their true values are shown for bins in the y, Q^2 plane. The decision to bin in y rather than x is motivated by a superior resolution in y and the event selection requirements. The tail of each arrow lies at the mean generated y and Q^2 of the events in the bin around it and the heads of the arrows are at the mean reconstructed y and Q^2 of the same events. For the electron and double angle methods the shifts are generally very small except at low y. For the Jacquet–Blondel method events are systematically shifted to lower Q^2 and slightly lower y values. This is a result of hadronic energy loss in the very forward region of the detector and inactive material. The contribution to the migrations coming from ISR and FSR is shown in the last subfigure. We remark that the migrations in the DA variables are somewhat smaller than those for the EL variables in the low y region where the effects of ISR are important.

NC/CC cross sections and acceptance

Using the MRSA PDF parametrisations [19], NC and CC cross section predictions for the y, Q^2 bins shown in figure 5 were computed using the EPRC program [30]. Weak radiative corrections, but no QED effects, to the Born level cross section are included in these predictions. The resulting integrated cross sections in each bin (in pb) are shown in figure 6. The subfigures $a-d$ show the NC polarised cross sections while subfigures e and f show the CC polarised cross sections for electron and positron beams. In all cases the incoming lepton beam polarisation is 100%.

The acceptance for NC events varies between 90% at $Q^2 \approx 1000$ GeV^2 and 60% at $Q^2 \approx 50000$ GeV^2 while that for CC events is approximately constant with Q^2 at around 85%. It is

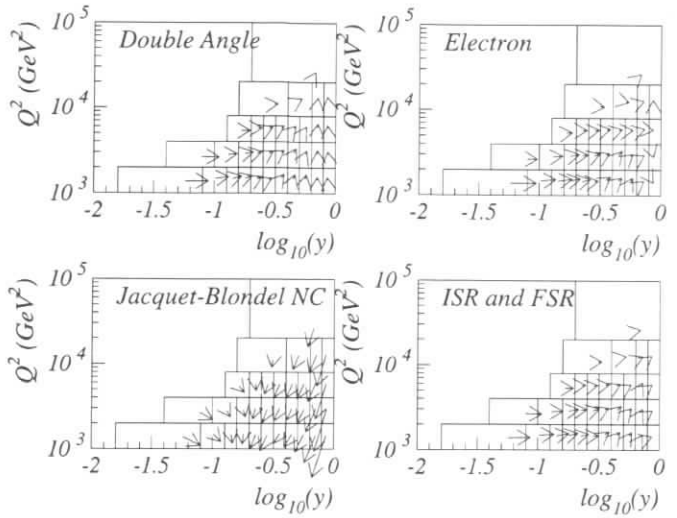

Figure 5: *Migrations in reconstructed variables.*

expected that the acceptance for NC events at very high Q^2 will increase in coming years as lepton identification techniques in the forward region of the detector are developed further.

3.1 Experimental sources of systematic error

The main sources of experimental systematic errors pertaining to cross section measurements are listed below. Based upon analyses of 1994 ZEUS data [3, 28], numerical estimates of errors are also given where appropriate. It is expected that further improvements to the ZEUS detector and the understanding of the data will reduce the systematic error contributions significantly for future running. In general the systematic errors are largest for the highest Q^2 and y regions of the accessible phase space.

Calorimeter Energy Scale

Uncertainties in the absolute energy scale of the ZEUS calorimeter provide the largest contribution to the systematic error for NC and CC high Q^2 cross section measurements. For CC cross section measurements a variation of $\pm 3\%$ in the energy scale gives rise to 5–30% systematic uncertainty on cross sections. For NC cross section measurements the use of the double angle reconstruction method greatly reduces the sensitivity to the absolute energy scale and the resulting uncertainty is at the level of 1–2% [28].

Contamination from photoproduction and other backgrounds

Conservative estimates of NC and CC cross section uncertainties arising from photoproduction background subtraction are $\sim 5\%$.

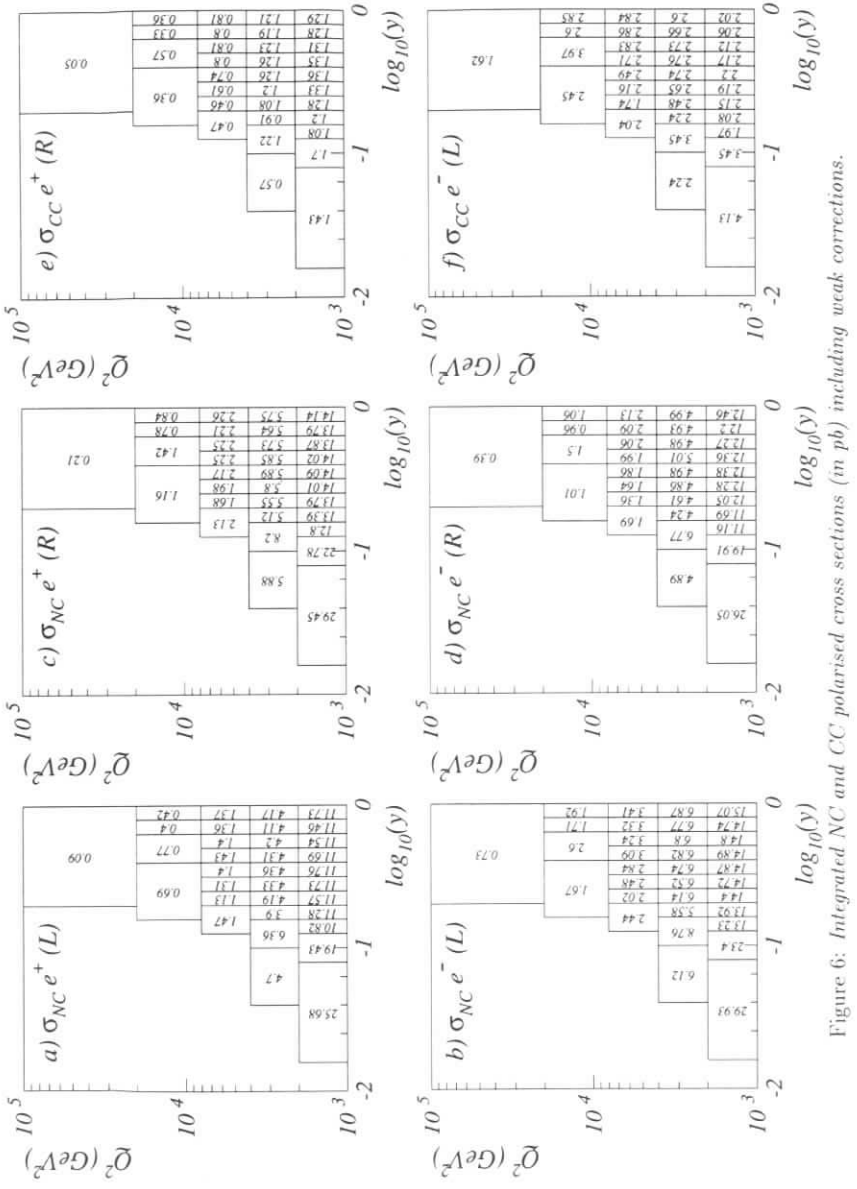

Figure 6: *Integrated NC and CC polarised cross sections (in pb) including weak corrections.*

Event selection cuts and reconstruction
Uncertainties arising from variations in the selection cuts are generally $\mathcal{O}(1-2)\%$.

Polarisation measurement
The uncertainty in the calibration of the polarisation scale is the most prominent systematic error of the polarisation measurement. The assumed scale can be checked experimentally. Preliminary results suggest that currently the polarisation scale is known to $\pm 3.2\,\%$ which, together with other minor sources of error, leads to a systematic error $\delta\mathcal{P}/\mathcal{P}_{\text{syst.}}$ of about 4 %. Further improvements of these values are expected and it seems to be feasible to reduce the systematic error of the polarisation measurement to 2 % or even below [11].

Luminosity Measurement
The uncertainty on the luminosity measurement is currently $\sim 1.5\%$.

With existing detectors and techniques it is possible to make precise measurements of the cross sections at high Q^2. With the proposed factor of 100 increase in luminosity we anticipate that the systematic errors can be reduced to the level of the statistical errors or better at high Q^2. In following figures and tables of results the quoted errors are statistical only unless stated otherwise.

4 Parton Distribution Functions

The NC and CC cross sections are not only dependent upon the SM couplings but also upon radiative corrections, PDFs, the polarisation and other electroweak parameters, namely the Z^0 and W boson masses. Radiative corrections for initial state, final state, vertex, propagator and box diagrams have all been calculated to at least first order and are known to better than 1.0% [21]. The expected accuracy of the polarisation has been discussed above and future precision measurements should allow the W mass to be measured at the per mille level [31]. The Z^0 mass is already very precisely measured. Here we consider the uncertainties on the PDFs.

There are many sets of parton density parametrisations available [32]. These parametrisations are obtained by global analyses of deep inelastic and related data from various experiments. High Q^2 data have not yet had great impact on these analyses and therefore the parton densities at high Q^2 are essentially determined from lower energy data through the QCD evolution equations[1]. Hence, both the fit to the lower energy data with associated errors, and the extrapolation, which, for example depends on the contribution of heavy quarks and on the QCD scale Λ, introduce uncertainties in the parton distributions. Parton density parametrisations are rarely, if ever, published with errors as a function of kinematic variables.

Some measure of the uncertainties on the PDFs at high Q^2 can be obtained from the differences between the parametrisations. This is not ideal since the universal use of the QCD evolution equations means that it is more likely to indicate similarities or differences in the form of the parametrisations. The PDFs compared here are MRSG, CTEQ3M and GRV94HO[2] [33, 34, 35]. These form a representative sample, with differing approaches in the parametrisation, which fit well the available data[3].

[1] Recent data on inclusive jet measurements at CDF and D0 have been used to obtain a new parametrisation CTEQ4HJ [37] which has, however, not been used in the present work.

[2] The GRV94HO version used here has only 3 active quark flavours; the heavy quarks are not present as partons in the Q^2 evolution.

[3] There now exist new global fits, MRSR [36] and CTEQ4M [37] which include the latest HERA data at low x. The parametrisations at high Q^2 have not altered significantly.

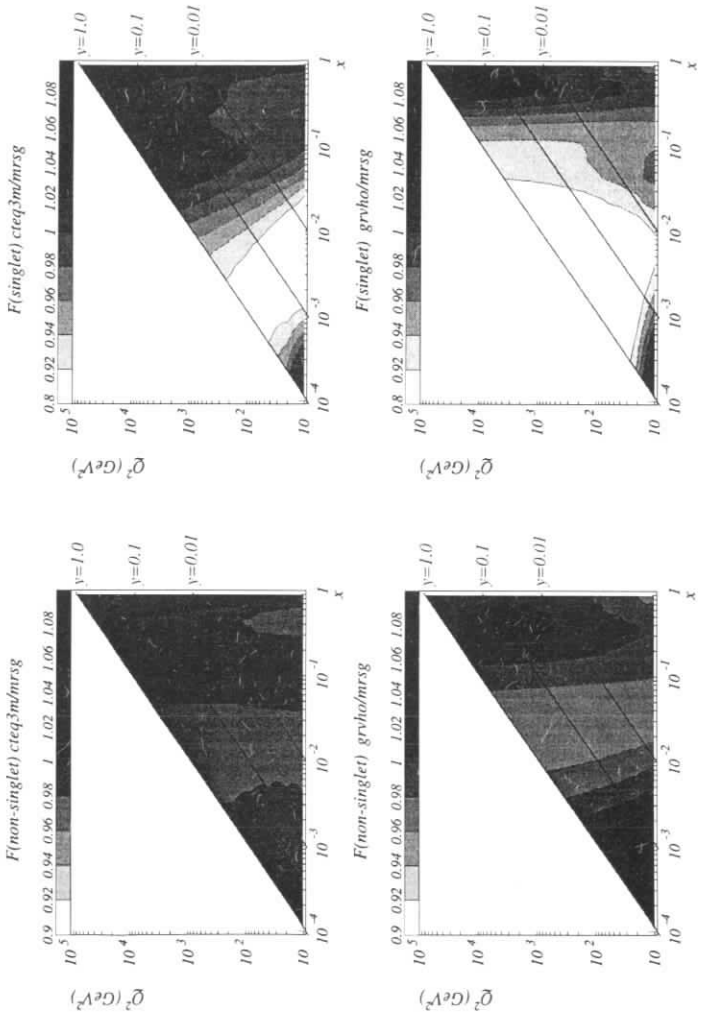

Figure 7: *Ratios of different PDF parametrisations for singlet and non-singlet structure functions over the HERA x, Q^2 plane. In the upper two figures the CTEQ3M and MRSG parametrisations are compared whilst the ratios of the GRV94HO and MRSG parametrisations are shown in the lower two figures. The spacing of the differently shaded bands is 2 percent as shown in the key for each figure.*

Figure 7 shows the ratios of various PDFs as contour plots in the (x, Q^2) plane. The singlet structure function, $F_S = x(U + D)$, and the non-singlet structure function, $F_{NS} = x(u_v + d_v)$, are shown for CTEQ3M and GRV94HO relative to MRSG. It can be seen that the differences are generally less than $\pm 5\%$ over the high Q^2 region ($\gtrsim$1000 GeV^2) except at very high x. The parton densities vanish as $x \to 1$, so that variations in the ratios here do not reflect significant variations in the PDFs themselves. Figure 8 shows the quantities d_v/u_v and D/U (which appear in equations 23 and 29) for different PDFs as a function of x for $Q^2 = 5000$ GeV^2. The variation with Q^2, at fixed x, is small ($\lesssim 5\,\%$). The ratios of d_v/u_v and D/U for different PDFs with respect to MRSG are also shown in figure 8. The difference from unity is generally less than 5% except at very high x.

The sensitivity to variation in α_s on the PDFs has been studied in [38]. In the high Q^2 HERA region a wide variation of α_s (from 0.105 to 0.125) leads to a variation in the structure function F_2 of less than $\pm 10\%$ except at very high x ($x \gtrsim 0.8$) where the variation is somewhat larger. This indicates the maximal possible variation in the PDFs due to parameter variation since the effects of varying α_s are larger than, for example, the effects of heavy quarks.

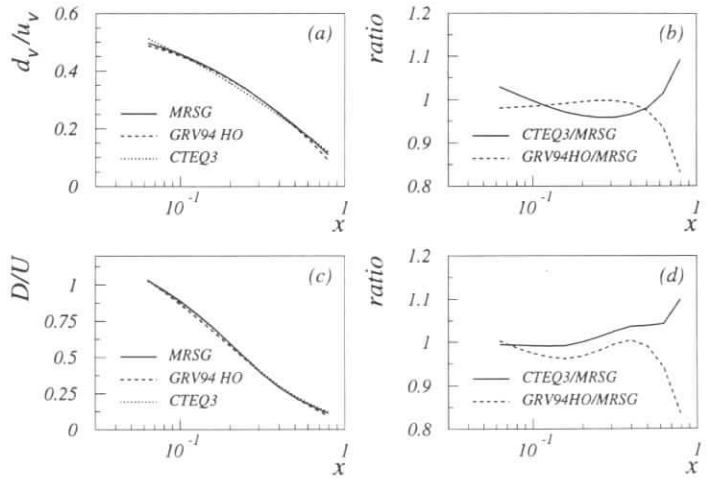

Figure 8: *Comparison of the structure function ratios d_v/u_v (a) and D/U (c) given by the CTEQ3M, GRV94HO and MRSG PDF parametrisations as functions of x at $Q^2 = 5000\ GeV^2$. Subfigures (b) and (d) show the ratios of d_v/u_v and D/U given by the CTEQ3M, GRV94HO parametrisations with respect to those of MRSG.*

Hence, it is estimated that the error introduced by the uncertainty in the PDFs to the total NC DIS cross-section at high Q^2 is $\lesssim 5\%$. Future measurements at HERA and elsewhere will increase the data available at high Q^2 allowing better PDF determinations and thereby reducing this source of uncertainty.

5 Limits on Light Quark Couplings

The estimates of limits on the deviations presented in this section are based on an analysis of Monte Carlo data samples for right- and left-handed electron and positron beams following the strategy of section 3. By considering the uncertainties in the cross sections and parton density ratios which enter the expressions 23 and 29, the accuracy of the couplings can be estimated. Since these equations involve ratios of combinations of differential cross sections some systematic errors will cancel.

Three bins at high Q^2 were used (see table 2). These bins were chosen such that the purity in each bin, i.e. the percentage of events reconstructed in the bin that were also generated in the same bin, was $\gtrsim$30%. The mean values of x and Q^2 were obtained from the generated events in each bin. The fractional statistical errors on the cross sections are obtained from the Monte Carlo and are shown in table 3 with the corresponding bin purities.

Bin	Bin Limits (GeV^2)	$< x >$	$< Q^2 >$
1	11000$< Q^2 <$20000	0.280	13957
2	7500$< Q^2 <$11000	0.232	8893
3	5000$< Q^2 <$7500	0.197	6010

Table 2: *Bin limits and mean values.*

Bin Number	% Errors(% Purity)					
	NC(e^-)		NC(e^+)		CC(e^-)	CC(e^+)
	LH	RH	LH	RH		
1	7.5 (73)	15.0 (72)	34.1 (46)	24.9 (43)	9.4 (41)	48.9 (56)
2	12.6 (51)	15.5 (53)	20.6 (49)	14.3 (43)	9.6 (40)	26.2 (33)
3	6.0 (61)	8.2 (57)	10.8 (66)	6.9 (67)	7.1 (41)	17.8 (32)

Table 3: *Bin purities and statistical errors on cross section measurements for a luminosity of* $62.5 pb^{-1}$ *per beam per polarisation.*

The deviations for the axial couplings were estimated from equation 23. The one standard deviation error on the right-hand side was calculated at each of the three bin centres using the cross section errors obtained from the Monte Carlo samples. The three bins were combined to give an overall estimated measurement error. The limits that this error imposes on possible deviations from the SM axial couplings, δa_d and δa_u, are shown in figure 9a. The outer (solid) lines correspond to a total luminosity of 250 pb^{-1} , the inner (dashed) lines correspond to 1000 pb^{-1} .

Limits on deviations of the vector couplings were obtained from equation 29. The limits on possible deviations from the SM vector couplings, δv_d and δv_u, are shown in figure 9b. The solid (dashed) lines correspond to a total luminosity of 250 pb^{-1} (1000 pb^{-1}), equally divided between the four possible lepton beam charge/polarisation states. The polarisation was taken to be 70%.

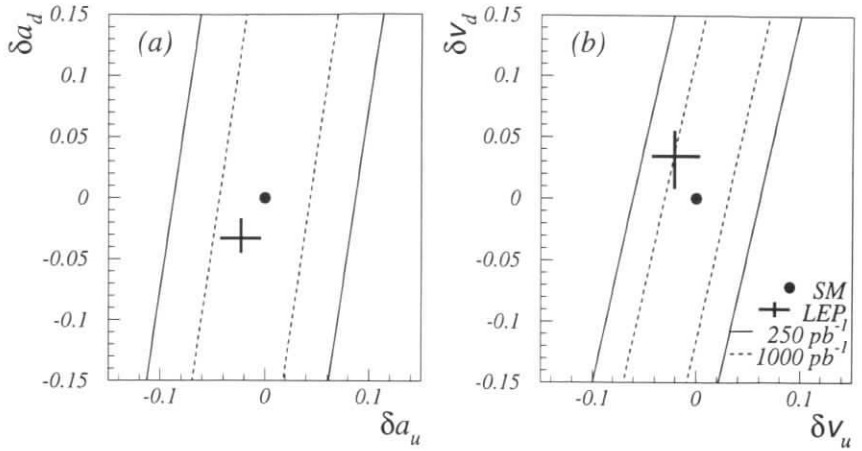

Figure 9: *Limits for a) axial coupling deviations and b) vector coupling deviations for 70% polarisation.*

The LEP points in figure 9 correspond to the values of the effective couplings (i.e. including weak radiative corrections) taken from [7] for the b and c quark couplings. The errors on the LEP points are simply projections onto the axes from the 68% confidence level correlation ellipses of vector versus axial coupling deviations for the b and c quarks.

Limits on deviations of the couplings, when all other deviations are zero, are shown in table 4. Results are shown for the case when the JB method is used for CC data, and the DA method is used for the NC data. Including additional errors of 10% on the PDF ratios, d_v/u_v and D/U, has no significant effect on the results. Furthermore, using a greater luminosity of electrons than positrons or *vice-versa* (given the same total luminosity) does not lead to any improvement.

Rec. Method	$\mathcal{L}$/beam per $\mathcal{P}$	Bin Number	Δa_u	Δa_d	Δv_u	Δv_d
DA (NC) & JB (CC)	62.5 pb^{-1}	1	0.12	0.72	0.12	0.59
		2	0.19	1.05	0.13	0.52
		3	0.17	0.88	0.082	0.28
		First 2 bins	0.10	0.61	0.090	0.39
		All 3 bins	0.087	0.50	0.061	0.23
DA(NC) & JB(CC)	250 pb^{-1}	1	0.060	0.36	0.062	0.29
		2	0.095	0.53	0.066	0.26
		3	0.085	0.44	0.041	0.14
		First 2 bins	0.051	0.30	0.045	0.20
		All 3 bins	0.044	0.25	0.031	0.12

Table 4: *Comparison of coupling deviations for two luminosities.*

6 Fit to Determine Light Quark Couplings

The most precise values for the couplings will be obtained by combining the data from all lepton beam charge/polarisation combinations in a fitting procedure. To determine the precision of such a fit the values of the quark couplings were estimated by minimising

$$\chi^2 = \sum_{i,s} \frac{[\mathcal{M}_i^s - \mathcal{E}_i^s(\mathbf{g})]^2}{\mathcal{E}_i^s(\mathbf{g})}, \qquad (30)$$

where i runs over the bins in the y, Q^2 plane (shown in figure 5) with $Q^2 > 1000$ GeV^2. s runs over the various charge and polarisation states of the beams (right- and left-handed electrons and positrons). $\mathcal{M}_i^s$ is the number of data events in bin i for polarisation state s. The expected number of events in bin i for a state s is given by $\mathcal{E}_i^s(\mathbf{g})$. $\mathcal{E}_i^s$ depends on the NC axial and vector couplings which are contained in the vector $\mathbf{g} = (v_u, a_u, v_d, a_d)$ through equations 6 and 11. As the fit is made to numbers of events measured in a particular set of bins the values of the $\mathcal{M}_i^s$ are statistically independent. The values of the $\mathcal{E}_i^s$ are derived from Monte Carlo simulation as described in section 3 so that detector acceptance, resolution and parameter biases are taken into account. The fitting procedure used was similar to that described in [39]. The MINUIT program [40] was used to minimise the χ^2 function with respect to the couplings.

The errors obtained on the couplings under two polarisation conditions are reported in table 5. With a total integrated luminosity of 1000 pb^{-1} divided equally between the four beam configurations, the fractional errors on v_u, a_u, v_d and a_d are 13%, 6%, 17% and 17% respectively. If the d quark couplings are held fixed while the u quark couplings are allowed to vary then the errors on v_u and a_u are 4% each. Holding the u quark couplings fixed and fitting for the d quark couplings gives errors of 6% for v_d and 10% for a_d. Changing the binning to that used in section 5, i.e. only three bins at high Q^2 (see table 2), results in greatly increased errors on all the couplings (a factor of 4 or greater). This indicates that the full structure in the kinematic plane must be input to the fit in order to obtain good accuracy in the couplings. Simulation of a perfect detector shows that the finite acceptance and resolution of our detector increases the errors on the coupling constants by about 15%.

Uncertainties in the PDFs have not been included. In section 4 it was shown that PDF errors are currently at the level of $\lesssim$5% and will be reduced further following analysis of forthcoming data from HERA and elsewhere. The cross sections are linear in the PDFs and the expected errors on the latter are comparable to or smaller than the statistical errors on the coupling measurements. Thus we anticipate that PDF uncertainties will not substantially increase the quoted errors.

The effect of beam polarisation on the errors is investigated in figure 10. The figure shows one standard deviation contours corresponding to a luminosity of 1000 pb^{-1} divided equally between the four charge/polarisation combinations, for fits in which the d (u) quark couplings are held fixed while the u (d) quark couplings are varied. The errors grow rapidly as the degree of polarisation is reduced. The error on v_u grows by a factor of ~ 6 when the polarisation, $\mathcal{P}$, is reduced from 0.7 to 0, while the errors on a_u, v_d and a_d grow by factors of $\sim 2, \sim 6$ and ~ 3 respectively. We see in particular that polarisation is essential in order to determine the vector couplings.

The sensitivity of the results to the way in which the total integrated luminosity is divided between the four beam charge/polarisation options is investigated in figure 11. This is done by,

$\sigma(v_u)$	$\sigma(a_u)$	$\sigma(v_d)$	$\sigma(a_d)$	$\sigma(v_u)$	$\sigma(a_u)$	$\sigma(v_d)$	$\sigma(a_d)$
$\mathcal{P} = 0.7$				$\mathcal{P} = 0$			
0.026	0.030	0.060	0.086	0.161	0.063	0.359	0.264
0.023	–	0.052	–	0.102	–	0.138	–
–	0.029	–	0.074	–	0.029	–	0.075
0.008	0.018	–	–	0.047	0.021	–	–
–	–	0.019	0.048	–	–	0.101	0.087
0.008	–	–	–	0.040	–	–	–
–	0.018	–	–	–	0.018	–	–
–	–	0.018	–	–	–	0.054	–
–	–	–	0.046	–	–	–	0.046

Table 5: *Precision of fit for coupling constants. The table shows the errors determined by the fitting procedure described in the text as a function of the beam polarisation $\mathcal{P}$ for a luminosity of 250 pb^{-1} per beam. The errors on the couplings, $\sigma(a_i)$ and $\sigma(v_i)$, are the square root of the diagonal elements of the relevant covariance matrix.*

in turn, varying the fraction of integrated luminosity devoted to a particular charge/polarisation combination from 1% to 97%, distributing the remaining luminosity equally between the other three to give the same total of 1000 pb^{-1} . A beam polarisation of 70 % is assumed. For each option the fractional error obtained, in a fit in which all couplings are allowed to vary, is plotted as a function of the fractional luminosity. It can be seen that there is generally no significant loss of precision when only three beams are used. Sharing the total integrated luminosity equally between only two of the four possible beams reduces the accuracy with which certain couplings are measured. Which couplings are affected depends on the pair of beams chosen, for example, using only right- and left-handed electron beams does not affect the measurement of v_u or v_d but greatly affects a_u and a_d. Therefore, more than two beam charge/polarisation combinations will be needed to measure all couplings to the best accuracy.

The precision with which the NC couplings of the quarks can be measured in a single ep collider experiment at HERA is summarised in figure 12. With 250 pb^{-1} divided equally between the four charge/polarisation combinations HERA can make a competitive measurement of the u quark couplings and provide a useful constraint on the value of the d quark couplings. With 1000 pb^{-1} equally divided both the axial and the vector couplings of the u and d quarks can be determined in a single experiment.

7 Conclusions

It has been shown that it will be possible to measure the NC couplings of the quarks in a single experiment at HERA. Ratios of NC and CC cross sections measured with unpolarised electron and positron beams can be used to determine the u quark axial coupling with a precision of 9 % (18 %) for a total luminosity of 1000 pb^{-1} (250 pb^{-1}). Polarised lepton beams allow the extraction of the vector coupling of the u quark from ratios of polarised NC and CC cross sections. With a polarisation of 70 % a precision of 15 % (30 %) can be achieved with 1000 pb^{-1} (250 pb^{-1}) divided equally between the four lepton beam charge/polarisation combinations.

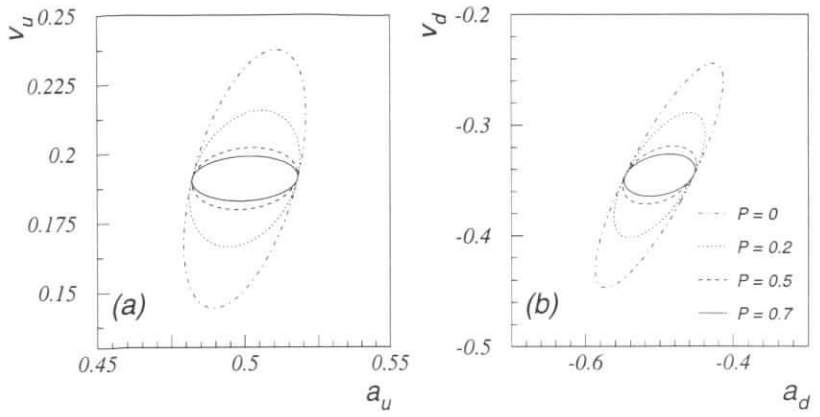

Figure 10: *Sensitivity of the errors on the quark couplings to beam polarisation, $\mathcal{P}$. One standard deviation contours for fits in which (a) the d quark couplings are held fixed while the u quark couplings are varied and (b) the u quark couplings are held fixed while the d quark couplings are varied.*

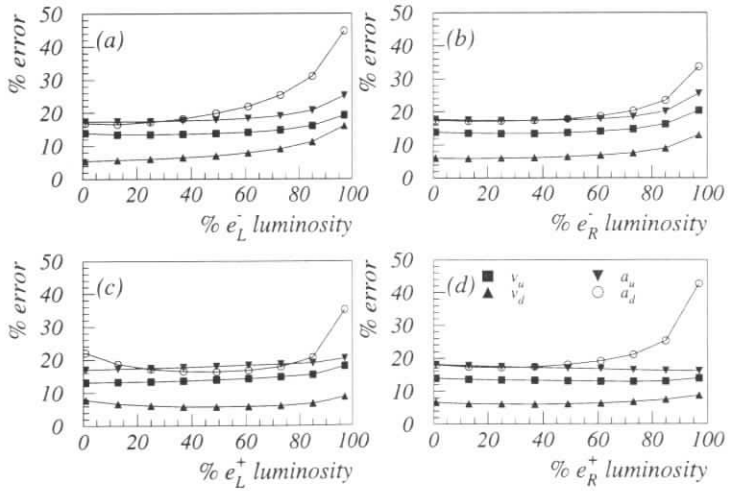

Figure 11: *Sensitivity of the errors on the coupling constants to the fractional luminosity carried by each of the four lepton beam charge/polarisation combinations.*

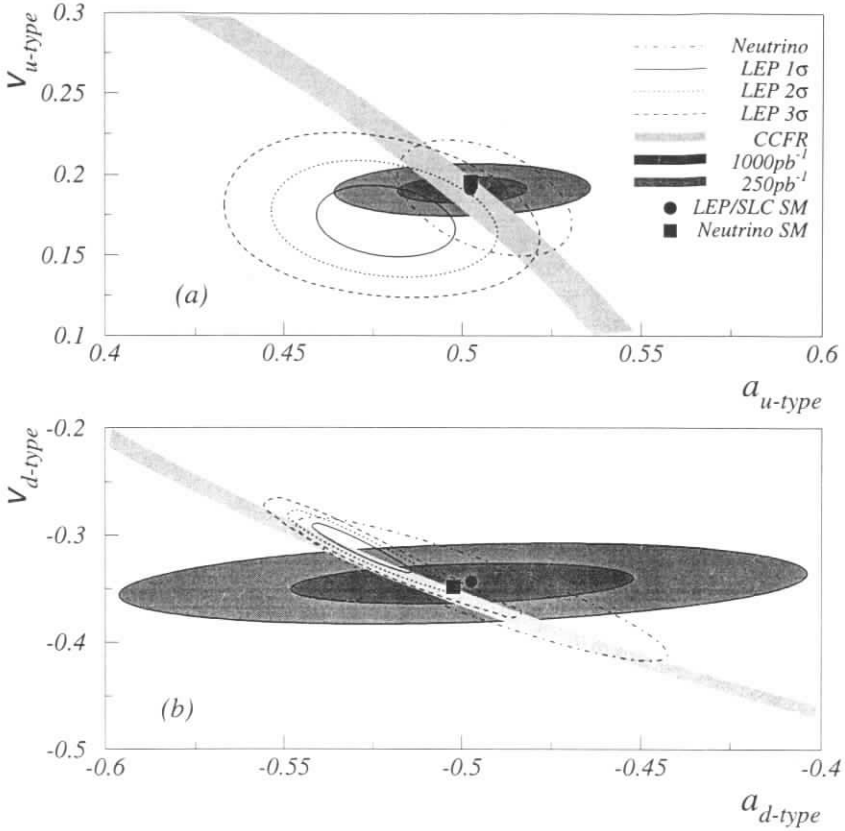

Figure 12: *Summary of measurements of u-type (a) and d-type (b) quark couplings to the Z^0. The results of a measurement at HERA are shown as the shaded ellipses. The outer ellipse shows the result which would be obtained with 250 pb^{-1} divided equally between the four lepton beam charge/polarisation combinations, the inner ellipse shows the result which would be obtained with 1000 pb^{-1} equally divided. Fits for the couplings of the u (d) quarks were performed with the d (u) quark couplings fixed at their SM values. The open ellipse drawn with a dash-dotted line shows the one standard deviation (1σ) contour obtained in a fit of the four chiral couplings of the u and d quarks to a compilation of neutrino DIS data. The solid, dotted and dashed ellipses show the 1, 2 and 3 σ limits of the combined LEP/SLD results for the c and b quark couplings. The shaded band shows the result obtained by the CCFR collaboration from the ratio of NC and CC cross sections projected onto the quark coupling plane. In the case of the CCFR the couplings of the u (d) quarks are obtained with the d (u) quark couplings fixed at their SM values. SM coupling values including radiative corrections appropriate for comparison with e^+e^- (circle) and neutrino (square) measurements are also shown.*

Measurements of the NC cross sections can be used in a fit to determine the NC couplings. A model independent fit, where all four couplings are allowed to vary, results in fractional errors on v_u, a_u, v_d and a_d of 13 %, 6 %, 17 % and 17 % respectively for $1000\,\mathrm{pb}^{-1}$ divided equally between the four charge/polarisation combinations. If the d (u) quark couplings are held fixed while the u (d) quark couplings are allowed to vary then the errors on v_u (v_d) and a_u (a_d) are 4 % (6 %) and 4 % (10 %) respectively. Using unpolarised beams the precision with which the vector (axial) couplings may be determined in such a fit is reduced by a factor of up to 6(2). Thus, the provision of polarised beams is essential for the measurement of the vector couplings. Also, in order to measure all four NC couplings with the best possible accuracy at least three of the four lepton beam charge/polarisation combinations will be required.

Uncertainties in the PDFs reduce the precision with which the couplings can be extracted. We estimate that the current uncertainty in the knowledge of the PDFs at high x and Q^2 is $\lesssim$5%. Hence, we anticipate that uncertainties in the PDFs will not be the limiting factor in determining the NC couplings of the quarks at HERA.

The analyses presented above were performed using a Monte Carlo simulation of the existing ZEUS detector and current analysis methods. Thus, upgrades to the detector and improvements in the understanding and calibration of existing detector components will serve to improve the precision of the measurements.

Acknowledgements

We thank the organisers of the DESY Workshop on Future Physics at HERA for their strong support and encouragement. It is a pleasure to thank P. Clarke, U. Katz, M. Kimber, A. Quadt and R. G. Roberts for valuable contributions and informative discussions.

References

[1] Lepton–Hadron Scattering, *Proceedings of the 19th SLAC Summer Institute on Particle Physics (1991)*, ed. J. Hawthorne, SLAC–398, 1992.

[2] ZEUS Collaboration, M. Derrick et al., Phys. Rev. Lett. **75** (1995) 1006-1011.

[3] ZEUS Collaboration, M. Derrick et al., *Study of Charged–Current ep Interactions at $Q^2 >$ 200 GeV^2 with the ZEUS detector at HERA*, DESY 96–104, accepted by Z. Phys.

[4] H1 Collaboration, T. Ahmed et al., Phys. Lett. **B379** (1996) 319.

[5] The LEP Collaborations and the LEP Electroweak Working Group, CERN–PPE 94–187, C94–07–20. Nov 1994, 36pp, Contributed to the 27th International Conference on High-Energy Physics - ICHEP 94, Glasgow, Scotland, UK, 20-27 Jul 1994; and CERN-PPE 95–172, Nov. 1995, 47 pp., Contributed to the *International Symposium on Lepton Photon Interactions*, 10-15th August 1995, Beijing, China.

[6] F. Abe et al., CDF Collaboration, Phys. Rev. Lett. **73** (1994) 225; Phys. Rev. **D50** (1994) 2966; Phys. Rev. Lett. **74** (1995) 2626;
S. Abachi et al., D0 Collaboration, Phys. Rev. Lett. **74** (1995) 2632.

[7] P. B. Renton, *Review of Experimental Results on Precision Tests of Electroweak Theories*, OUNP–95–20 (1995), 28pp., Invited talk at the *International Symposium on Lepton Photon Interactions (IHEP)*, Beijing, P.R. China, 10-15 Aug 1995.

[8] G. L. Fogli and D. Haidt, Z. Phys. **C40** 379–402 (1988).

[9] K. S. McFarland, *Electroweak Measurements from Neutrino-Nucleon Deeply Inelastic Scattering*, to be published in proceedings of the 28th Intl. Conf. on HEP, Warsaw, Poland, 25–31 July 1996.

[10] A. Blondel, *Experimental Status of Electroweak Interactions*, to be published in proceedings of the 28th Intl. Conf. on HEP, Warsaw, Poland, 25-31 July 1996.

[11] F. Zetsche, these proceedings.

[12] L. Montanet et al., Phys. Rev. **D50** (1994) 1173 and 1995 off-year partial update for the 1996 edition available on the PDG WWW pages (URL:http://pdg.lbl.gov/)

[13] H. Spiesberger et al., in *Physics at HERA, Proceedings of the Workshop, Hamburg, Oct. 29 - 30, 1991*, Eds. W. Buchmüller and G. Ingelman, Vol. 2, p. 798.

[14] W. Hollik et al., in *Physics at HERA, Proceedings of the Workshop, Hamburg, Oct. 29 - 30, 1991*, Eds. W. Buchmüller and G. Ingelman, Vol. 2, p. 923.

[15] H. Spiesberger, in *Precision Tests of the Standard Model*, Advanced Series on Directions in High Energy Physics, World Scientific Publishing Co., Ed. P. Langacker, 1994.

[16] J. G. Körner, E. Mirkes and G. A. Schuler, Int. J. Mod. Phys. **A4** (1989) 1781.

[17] E. B. Zijlstra and W. L. van Neerven, Nucl. Phys. **B383** (1992) 525.

[18] V. N. Gribov and L. N. Lipatov, Sov. Journ. Nucl. Phys. **15** (1975) 438, 765;
G. Altarelli and G. Parisi, Nucl. Phys. **B126** (1977) 298.

[19] A. D. Martin, R. G. Roberts, W. J.Stirling, Phys. Rev. **D50** (1994) 6734.

[20] G. Ingelman and R. Rückl, Phys. Lett. **B201** (1988) 369; G. Ingelman and R. Rückl, Z. Phys. **C44** (1989) 291-306.

[21] HERACLES 4.4: A. Kwiatkowski, H. Spiesberger and H. J. Möhring, Proc. 1991 Workshop on Physics at HERA, ed. W. Buchmüller and G. Ingelman (DESY, Hamburg, 1992), Vol. 3, p.1294.

[22] LEPTO 6.3: G.Ingelman, Proc. 1991 Workshop on Physics at HERA, ed. W.Buchmüller and G.Ingelman (DESY, Hamburg, 1992), Vol. 3, p.1366.

[23] DJANGO6: K. Charchuła, G. Schuler and H. Spiesberger, Comp. Phys. Commun. **81** (1994) 381.

[24] ARIADNE 4.06: L. Lönnblad, LU TP–89–10;
L. Lönnblad, Comp. Phys. Commun. **71**(1992)15.

[25] PYTHIA 5.7 and JETSET 7.4: T. Sjöstrand, CERN–TH 7112–93 (1994);
T. Sjöstrand, LU–TP–95–20 (1995).

[26] F. Jacquet and A. Blondel, Proceedings of the study for an *ep* facility for Europe, DESY 79–48 (1979) 391.

[27] S. Bentvelsen, J. Engelen, P. Kooijman, Proc. 1991 Workshop on Physics at HERA, ed. W. Buchmüller and G. Ingelman (DESY, Hamburg, 1992), Vol. 1, p.23.

[28] ZEUS Collaboration, M. Derrick et al., *Limits on New Physics from Neutral Current ep Deep Inelastic Scattering at High Q^2*, submitted to ICHEP 96, Warsaw, Poland (1996).

[29] H. Abramowicz, A. Caldwell, R. Sinkus, Nucl. Inst. Meth. **A365** (1995) 508.

[30] H. Spiesberger, *EPRC: A Program Package for Electroweak Physics at HERA*; these proceedings.

[31] G. Altarelli, T. Sjöstrand and F. Zwirner, eds., *Physics at LEP2*, Vol. 1, CERN 96-01.

[32] H. Plothow-Besch, *PDFLIB: Nucleon, Pion and Photon Parton Density Functions and Alpha-s Calculations*, User's Manual - Version 6.06, W5051 PDFLIB, 1995.03.15, CERN-PPE.

[33] A. D. Martin, W. J. Stirling and R. G. Roberts, Int. J. Mod. Phys. **A10** (1995) 2885.

[34] H. L. Lai et al., Phys. Rev. **D51** (1995) 4763.

[35] M. Glück, E. Reya and A. Vogt, Phys. Lett. **B306** (1993) 391.

[36] A. D. Martin, R. G. Roberts and W. J. Stirling, RAL-TR-96-037 and DTP/96/44 (1996).

[37] H. L. Lai et al., MSUHEP–60426 and CTEQ–604 (1996).

[38] A. D. Martin and W. J. Stirling, RAL-TR-95-013 (1995).

[39] G. Zech, *Comparing Statistical Data to Monte Carlo Simulation - Parameter Fitting and Unfolding*, DESY–95–113.

[40] MINUIT Function Minimisation, F. James and M. Roos, Comp. Phys. Commun. **10** (1975) 343, CERN library program D506; Nucl. Instr. Meth. **A340** (1994) 396.

Limits on $WW\gamma$ Couplings from Single W boson Production in ep Collisions

Valerie A. Noyes
Particle and Nuclear Physics Laboratory, Oxford University

Abstract: The cross section for the process ep $\rightarrow$ eWX at HERA can be used to measure the anomalous couplings $\Delta\kappa$ and λ in the three-boson vertex $WW\gamma$. A discussion of the event topology and kinematical cuts to optimise event selection is presented. The sensitivity to $\Delta\kappa$ and λ is studied for various values of integrated luminosity and in the scenarios where HERA provides a high degree of lepton polarisation, or is upgraded to higher centre-of-mass energy. With an integrated luminosity of 1000 pb^{-1}, HERA will be able to establish 95% confidence level limits of $-0.38 < \Delta\kappa < 0.38$ and $-1.65 < \lambda < 1.66$, the limits on $\Delta\kappa$ being competitive to projected future limits from other collider experiments.

1 Introduction

The most characteristic and fundamental signatures of the $SU(2) \times SU(1)$ gauge symmetry upon which the Standard Model (SM) is based are the couplings of the charged W boson to its neutral partners, the photon and the Z boson. The predicted interactions are described by the triple boson couplings $WW\gamma$ and WWZ. The gauge boson coupling strengths are strongly constrained by gauge invariance and are sensitive to deviations from the Standard Model. The self-couplings have not been measured with sufficient accuracy to rule out physics beyond the SM which may appear through the discovery of *anomalous* triple boson couplings. Consequently, measuring the $WW\gamma$ and WWZ couplings has become one of the main goals of experiments at LEP2 and the Tevatron where the sensitivity to the triple boson couplings can now be directly tested. An improvement in precision is expected at future collider experiments at the LHC and the Next Linear Collider [1].

This report concentrates on the ability to measure the anomalous couplings of the $WW\gamma$ vertex by measuring the cross section for single W production (ep$\rightarrow$eWX) at the HERA collider where positrons of energy 27.5 GeV collide head-on with protons of energy 820 GeV. The feasibility of measuring the $WW\gamma$ vertex via single W production at HERA has previously been studied by Baur et al. [2]. A complementary method to measure the $WW\gamma$ couplings in radiative charged current scattering events (ep$\rightarrow \nu\gamma X$) was studied at the last HERA workshop [3]. Since then, first measurements of the sensitivity to the $WW\gamma$ couplings at HERA have been presented by the H1 and ZEUS collaborations [4] using data corresponding an integrated luminosity of less than 10 pb^{-1}.

In this report, the sensitivity of the single W production cross section to anomalous $WW\gamma$ couplings is studied for various integrated luminosities, and for the first time, in the scenarios

where HERA is upgraded to a higher centre-of-mass energy, or provides a high degree of lepton polarisation.

Following a discussion in section 2 of the mechanisms in which single W events can be produced, the event characteristics are described in section 3. Given the small production cross section of ~ 1 pb, experimental cuts have been devised to optimise the signal-to-background ratio whilst maintaining a high acceptance for events in which a single W is produced. The effect anomalous $WW\gamma$ couplings have on the single W production cross section at HERA is introduced in section 4. Thereafter, in section 5, the resulting sensitivity to anomalous $WW\gamma$ couplings is derived for ep scattering and the limits are then compared to those derived in similar studies at other collider experiments [1]. Various integrated luminosities are studied at the nominal centre-of-mass energy, $\sqrt{s} = 300$ GeV and in the scenario where HERA runs with increased positron and proton beam energies of 30 GeV and 1 TeV respectively. The effect of running with a 70% polarised lepton beam is also considered.

2 The single W production process

The Standard Model predicts the production of W bosons at HERA via the two processes:

$$\text{ep} \rightarrow \text{e}WX, \quad \text{and} \tag{1}$$
$$\text{ep} \rightarrow \nu WX, \tag{2}$$

where X is the final hadronic state. As the cross section for νW production is an order of magnitude smaller than the that for eW production, this report concentrates on process 1.

At the parton level the reaction ep $\rightarrow$ eWX proceeds via the the Feynman diagrams shown in figures 1a-e. The triple boson vertex of interest enters via diagram 1c. The dominant contributions arise from the photon exchange graphs in figures 1a-c due to the t-channel pole induced by the photon propagator. The Z exchange diagrams in figures 1a-c are strongly suppressed by the large mass of the Z boson, hence ep $\rightarrow$ eWX is quite insensitive to anomalous WWZ couplings.

A commonly used way to measure the triple boson couplings and parameterise possible deviations from the Standard Model involves generalising the SM Lagrangian to allow for non-standard interactions. The most general $WW\gamma$ couplings which are consistent with Lorentz invariance and preserve electromagnetic gauge symmetry have been formulated and may be parametrised in terms of seven independent couplings [5]. Excluding C and P violating terms, two couplings remain, κ and λ. Within the Standard Model $\lambda = 0$ and $\kappa = 1$ and can be related to the magnetic dipole and electric quadrupole moments of the W. Deviations from the SM are expressed in terms of λ and $\Delta\kappa = \kappa - 1$.

The parton model process involves Feynman diagrams containing a u-channel pole which leads to quark mass singularities. The calculation of the cross section is therefore split into two contributions corresponding to two regions of phase space [6]:

$$\sigma = \sigma(|u| > u_{cut}) + \int^{u_{cut}} \frac{d\sigma}{d|u|} d|u| \tag{3}$$

where

$$u = (p_q - p_W)^2 \tag{4}$$

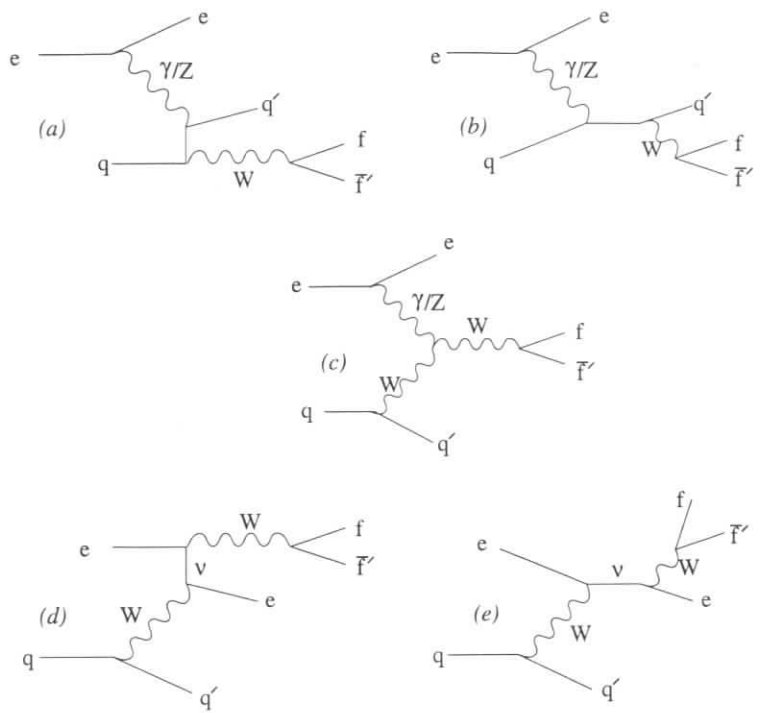

Figure 1: *Feynman diagrams for the parton level processes contributing to* ep $\rightarrow$ eWX *including the subsequent decay* $W \rightarrow f\bar{f}$. *Two additional diagrams which are required to preserve electromagnetic guage invariance and are included in the cross section calculation by Baur et al. are not shown.*

and p_q and p_W are the four momenta of the incoming quark and the final state W boson respectively. In the region where $|u| > u_{cut}$ the cross section is calculated perturbatively for the complete process $eq \rightarrow eWq', W \rightarrow f\bar{f}'$. In the second region, for small values of $|u| < u_{cut}$ figure 1a can be viewed as an almost on-shell photon which resolves into a quark-antiquark pair. The antiquark then annihilates with a quark in the proton to form a W boson. The on-shell photon structure functions together with the Weizsäcker-Williams approximation are used to calculate the cross section in this region. Although these individual contributions to the cross section vary strongly as a function of u_{cut}, the total cross section only varies by a few percent [6]. The Standard Model cross section for ep $\rightarrow$ eWX is ~ 1 pb, however can vary by $\sim 30\%$ depending on the choice of parton density parameterisations within the proton and photon. This variation is almost completely dominated by the choice of parton density parametrisations within the photon, and the scale at which they are evaluated as discussed in [6]. Despite this dependency, it is assumed that the photon structure function will have been precisely measured at HERA by the time this measurement becomes feasible.

3 Event selection and backgrounds

3.1 Signal Monte Carlo

The generator EPVEC written by Baur et al. [6] was used to generate signal Monte Carlo events with the value of u_{cut} set to 25 GeV^2. The proton and photon structure functions were parameterised by the HMRSB [7] and LAC2 [8] set of parton distribution functions respectively. The generator was interfaced to JETSET 7.3 [9] to simulate the fragmentation and hadronisation processes. The generated events were passed through the ZEUS detector simulation program which incorporates knowledge of the apparatus and trigger response based on previous running experience and test beam results. Events were generated in both of the regions described above and the samples were combined according to their cross sections.

3.2 Event Topology

Figure 2 shows generator level distributions of the energy, polar angle and transverse momentum of the scattered $e^{\pm}$, W decay products and struck quark. The polar angle, θ is measured with respect to the incoming proton direction. The scattered $e^{\pm}$ is typically lost in the rear beam-

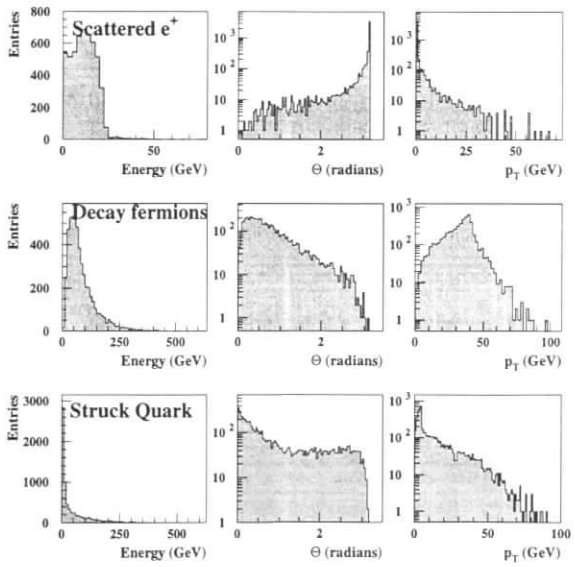

Figure 2: *Generator level distributions of the energy, polar angle and p_T spectrum of the scattered $e^{\pm}$, W decay products, and the struck quark in* $ep \to eWX$ *events.*

pipe, however, $\sim$ 35% of events have an $e^{\pm}$ tagged in the electron calorimeter of the ZEUS luminosity monitor. A similar tagging efficiency is obtained for the H1 electron tagger [10].

Due to the high mass of the W, its decay products are boosted in the forward (proton) direction and have high transverse momentum, peaked at 40 GeV. Figure 2 also shows that the current jet is typically in the forward direction. Although the transverse momentum of the current jet is generally low, the high p_T tail in the spectrum can be used to improve the signal-to-background ratio for the $W \to$ jets channel.

3.3 Background processes

This report concentrates on the $W \to e\nu$ and $W \to$ jets decay modes. The selection cuts applied are designed to provide a reasonable signal-to-background ratio whilst maintaining a relatively high acceptance for the signal events. Improvements to these cuts are to be expected as the integrated luminosity increases and a better understanding of the real data is accrued.

3.3.1 $W \to e\nu$ channel

The prominent signature of the leptonic decay process is a large missing transverse momentum together with an energetic forward $e^{\pm}$. Experimentally, electromagnetic clusters are identified using an algorithm based on the shower development within the calorimeter. The missing p_T is inferred from the imbalance of transverse momentum measured from the energy and topology of calorimeter cells.

Neutral and charged current deep inelastic scattering (DIS) events are the main sources of background to the signal. In neutral current DIS events where the energy from the current jet is not fully contained within the calorimeter, a transverse momentum imbalance will be measured together with the scattered $e^{\pm}$. In charged current events, π^0 decays may be mistaken for low energy $e^{\pm}$ by electron-finding algorithms which together with the high missing p_T produces a fake signal.

Monte Carlo samples of neutral and charged current DIS events were generated to devise selection cuts which would reduce this high-rate background. Two samples of neutral current DIS events were generated using LEPTO 6.1 [11] interfaced to HERACLES 4.4 [12] to include initial and final state photon radiation, and ARIADNE [13] to simulate the QCD cascade. The first sample, with $Q^2 > 3.3$ GeV^2, corresponded to an integrated luminosity of 0.78 pb^{-1}. The second sample comprised events selected with $Q^2 > 4$ GeV^2 and $\Sigma E_T > 40$ GeV, where the sum was taken over all stable final state particles. This high E_T event sample corresponded to $\int \mathcal{L} dt = 9.4$ pb^{-1}.

Charged current DIS events ($e^+p \to \nu X$) with $Q^2 > 10$ GeV^2 and corresponding to an integrated luminosity of 109.2 pb^{-1} were generated using the same programs. All events were passed through the ZEUS detector simulation.

The following selection criteria were applied and include cuts designed to reduce backgrounds associated with beam-gas interactions and cosmic rays which would be present in the real data as well as the DIS backgrounds.

- To reduce beam-induced background, cuts were applied on the z position of the interaction vertex reconstructed using charged tracks. Cosmic muons were rejected using algorithms based on calorimeter and tracking information.

- Charged current events with a fake electron were reduced by requiring an isolated electromagnetic cluster with energy greater than 10 GeV and a matched track.
- Neutral current background was reduced by requiring an isolated missing $p_T > 20$ GeV.

Table 1 details the cuts applied in the analysis together with the resulting cross section of signal and background after each cut. The cuts are effective at reducing the enormous rate of background events, providing a signal-to-background ratio of 1:7 and an acceptance for $W \to e\nu$ events of 66%. These selection cuts were also applied to signal events generated with anomalous couplings to investigate any dependency of the acceptance on $\Delta\kappa$ and λ. The variation in measured acceptance between $\Delta\kappa$=0 and $\Delta\kappa$=7 was found to be less than 2%.

Cut	Neutral current DIS High E_T σ (pb)	Neutral current DIS $Q^2 > 3.3\ GeV^2$ σ (pb)	Charged current DIS σ (pb)	Signal $B \cdot \sigma$ (pb)
None	2600	4.44×10^5	53.7	0.115
$\lvert z_{vtx}\rvert < 50$ cm	2360	3.15×10^5	42.4	0.10
Isolated $e^{\pm}$ with energy >10 GeV and matching track	1175	7.32×10^4	0.43	0.084
Isolated $\not{p}_T > 20$ GeV	0.21	0	0.33	0.074
Cosmic μ rejection	0.21	0	0.33	0.073
σ(pb)	**0.21**	**0**	**0.33**	**0.073**
% Acceptance	$< 10^{-2}$	negligible	0.6	66

Table 1: *Cuts applied to select the $W \to e\nu$ signal from the DIS background together with the cross section after each cut.*

By removing the isolated electromagnetic cluster requirement, the analysis could be readily extended to include the $W \to \mu\nu$ channel. With a similar event selection, H1 have observed an $e^+p \to \mu^+X$ event with a large missing p_T [14]. The kinematics of the event are consistent with single W production where the W subsequently decays to a $\mu\nu$ pair.

3.3.2 $W \to$ jets channel

The signature for the $W \to$ jets channel consists of two high p_T jets. As the scattered $e^{\pm}$ is typically undetected, photoproduction events with more than one high p_T jet become a significant background together with neutral current DIS.

Resolved and direct photoproduction events were generated using the HERWIG 5.8 [15] program where the minimum p_T for the hard scattering process was set to 5 GeV. The resolved photoproduction events were required to have $\Sigma E_T > 40$ GeV where the sum was taken over all stable final state particles and corresponded to an integrated luminosity of 6.94 pb^{-1}. A similar $\Sigma E_T > 30$ GeV cut was imposed on the $\int \mathcal{L}dt$=6.46 pb^{-1} sample of direct photoproduction events. The events were passed through the ZEUS detector simulation.

Table 2 compares the cross sections for the signal and the background processes after each stage of event selection. Without any cuts applied, the QCD background from neutral current

DIS and photoproduction is a factor ~ 7700 greater than the signal. The event selection was based on reconstructing high E_T jets from calorimeter information using the cone algorithm with a cone-radius of 0.7. The axis of the jets were required to have $\eta = -\ln(\tan(\theta/2) < 2.5$ to be far from the proton remnant direction. Although requiring at least two jets with $E_T > 12$ GeV reduces the background considerably, the signal is still swamped by the QCD background. By requiring a third similar jet and that the mass of any pair of jets to be within a range of 60 to 80 GeV/c^2 the signal-to-background ratio is reduced to 1:24 with an acceptance of 14% when the combinatorial background has been subtracted.

Cut	Photoproduction Resolved σ (pb)	Photoproduction Direct σ (pb)	Neutral current DIS $E_T > 40$ GeV σ (pb)	Signal $B \cdot \sigma$ (pb)
None	1535	1183	2600	0.694
Two jets	300	309	338	0.564
Three jets	5.62	2.63	1.23	0.132
Three jets, any pair with $60 < m_{ij} < 80$ GeV/c^2	1.153	0.773	0.335	0.096
% Acceptance	< 0.08	< 0.07	~ 0.01	13.8

Table 2: *Cuts applied to select the $W \to$ jets signal from the QCD background produced in neutral current DIS and photoproduction together with the cross section after each cut. The final cross section quoted with three jets, any two of which have combined mass between 60 and 80 GeV/c^2 has been corrected for the combinatorial background.*

The Monte Carlo programs have been used to estimate the background in a region of phase space which has not been thoroughly tested against real data. It is possible that further tuning of the Monte Carlo parameters will be required which may result in an optimised set of selection cuts which, in future, can considerably improve the signal-to-background ratio.

4 Anomalous $WW\gamma$ couplings

In generalising the Standard Model Lagrangian to allow for anomalous terms, the cross section can be written as a sum of the contributions from the SM, the anomalous couplings and an interference term:

$$\sigma_{\mathrm{TOT}} = \sigma_{\mathrm{SM}} + a\sigma_{\mathrm{Int}} + a^2\sigma_{\mathrm{An}} \tag{5}$$

where $a = \Delta\kappa, \lambda$, the deviation from the SM.

At HERA the sensitivity to the anomalous couplings in $ep \to eWX$ effectively stems from regions in phase space where the anomalous contributions to the cross section are considerably smaller than the SM. As a result, the interference effects between the SM amplitude and the anomalous contributions to the amplitude dominate over the squared non-standard terms. For large deviations from the SM cross section, the non-linear terms become important.

The interference effects, however, are significantly smaller for anomalous values of λ compared to non-standard values of κ once the sum over photon and W polarisations has been

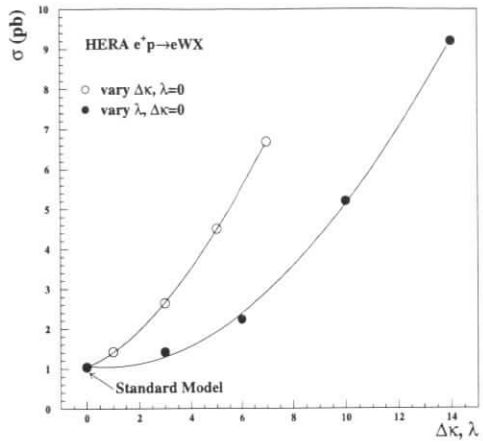

Figure 3: *Cross section for the reaction* $ep \rightarrow eWX$ *as a function of anomalous couplings* $\Delta\kappa = \kappa - 1$ *and* λ*, varying one coupling at a time. HERA offers greater sensitivity to anomalous values of* κ

taken into account [2]. Consequently, a large anomalous value of λ is required to produce a measurable effect at HERA, making $ep \rightarrow eWX$ more sensitive to anomalous values of κ than λ as shown in figure 3.

In the region of phase space where the cross section can be calculated perturbatively (see section 2) terms proportional to λ rise as the invariant mass of the γq system, $\sqrt{\hat{s}}$, increases. At the Tevatron, where higher values of $\sqrt{\hat{s}}$ can be obtained, the sensitivity to λ is greater than $\Delta\kappa$. A measurement of the $WW\gamma$ couplings at HERA will therefore complement results from the Tevatron.

5 Sensitivity to anomalous $WW\gamma$ couplings

The sensitivity to the $WW\gamma$ vertex which could be achieved from a measurement of $\sigma(ep \rightarrow eWX)$ at HERA was quantified by deriving those values of $\Delta\kappa$ and λ which would give rise to cross sections which deviated from the SM at the 95% confidence level (CL).

Using EPVEC, the cross section for single W production was calculated for various values of $\Delta\kappa$ and λ and also explored the effects of varying $\Delta\kappa$ and λ together. The resulting variation of the cross section with $\Delta\kappa$ and λ is shown in figure 4. No difference between incident positrons and electrons was observed for an unpolarised lepton beam. Several important features are noted in figure 4:

- $\sigma(\Delta\kappa)$ and $\sigma(\lambda)$ can be parameterised by a quadratic equation in order to determine the cross section at any $\Delta\kappa$ or λ;

- for fixed values of $\Delta\kappa$, $\sigma(-\lambda) = \sigma(+\lambda)$ illustrating that the interference effects between the Standard Model and the anomalous λ terms vanish as discussed in section 4;
- the cross section decreases for negative values of $\Delta\kappa$ indicating that the anomalous $\Delta\kappa$ terms interfere strongly with the SM terms; and
- there is an approximately constant difference between the the $\Delta\kappa$ variation at λ=0 and λ=2 indicating that $\Delta\kappa$ and λ are essentially uncorrelated at HERA using an unpolarised lepton beam.

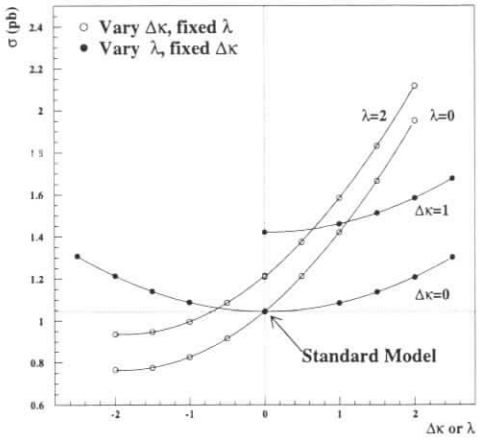

Figure 4: *Variation of* $\sigma(ep \rightarrow eWX)$ *as a function of* $\Delta\kappa$ *for fixed* λ*=0 and 2 (open circles) and as a function of* λ *for fixed* $\Delta\kappa$*=0 and 2.*

The acceptances for each of the W decay channels shown in table 3 were assumed, taking the systematic error on the acceptance to be 2% for $\int \mathcal{L}dt$ values of 100 pb^{-1} and 200 pb^{-1}. With the gain in event statistics at $\int \mathcal{L}dt$=1000 pb^{-1} an improvement in the systematic error to 1% was assumed. The uncertainty in the luminosity measurement was taken to be 2%. Combining all the decay channels gives an overall acceptance of 32.1 $\pm$ 1.4 (0.7)% for $\int \mathcal{L}dt$=100 and 200 pb^{-1} (1000 pb^{-1}).

Adding statistical and systematic errors in quadrature, the uncertainty on the cross section measurement is given by

$$\frac{\Delta\sigma}{\sigma} = \left(\frac{1}{N_W} + \left(\frac{\Delta\mathcal{L}}{\mathcal{L}} \right)^2 + \left(\frac{\Delta \text{Accep}}{\text{Accep}} \right)^2 \right)^{\frac{1}{2}} \qquad (6)$$

where N_W is the total number of single W events observed in all channels given their branching ratios and acceptances. This provides a lower limit to $\Delta\sigma$ as the error due to background subtraction has been assumed to be negligible here.

Channel	Acceptance	
$W \to e\nu$	65%	
$W \to \mu\nu$	65%	
$W \to \tau\nu$	40%	
$W \to$ jets	20%	
Combined channels	$32.1 \pm 1.4\%$	for 100, 200 pb^{-1}
	$\pm 0.7\%$	for 1000 pb^{-1}

Table 3: *Acceptance of each W decay channel used to derive 95% CL limits on the $\Delta\kappa$ and λ couplings. A systematic error of 2% (1%) on each acceptance is taken for $\int \mathcal{L}dt$ = 100 and* 200 pb^{-1}(1000 pb^{-1}).

From equation 6, the 95% CL limits can be derived and are shown in table 4 and figure 5. The limit on $\Delta\kappa$ is asymmetric for $\int \mathcal{L}dt$=100 pb^{-1} and 200 pb^{-1} due to the slow decrease of the cross section at values of $\Delta\kappa \lesssim -0.5$. Even with an integrated luminosity of 1000 pb^{-1} the sensitivity is limited by statistics rather than systematic errors.

The effect of changing the value of u_{cut} was investigated by lowering it to 10 GeV^2 within the EPVEC program and repeating the analysis. The limits changed by less than 1%.

Recalculating the limits using only the $W \to e\nu$ and $W \to \mu\nu$ channels, reduces the 95% CL sensitivity to $-0.54 < \Delta\kappa < 0.48$ and $-1.94 < \lambda < 1.97$ using an integrated luminosity of 1000 pb^{-1}.

$\int \mathcal{L}dt$	$\Delta\kappa$	λ
100 pb^{-1}	$-1.43 < \Delta\kappa < 0.95$	$-2.93 < \lambda < 2.94$
200 pb^{-1}	$-0.87 < \Delta\kappa < 0.72$	$-2.46 < \lambda < 2.47$
1000 pb^{-1}	$-0.38 < \Delta\kappa < 0.38$	$-1.65 < \lambda < 1.66$

Table 4: *95% CL limits derived for $WW\gamma$ couplings from measurement of $\sigma(ep \to eWX)$ at HERA.*

5.1 Comparison with other experiments

Figure 6 compares the 95% CL sensitivity limits HERA could achieve from $\int \mathcal{L}dt$=1 fb^{-1} of data to projected limits [1] from

- $e^+e^- \to W^+W^- \to l\nu jj$ where l = e or μ from an integrated luminosity of 125 pb^{-1} collected by the L3 experiment at LEP2 where $\sqrt{s}$ = 176 GeV;
- $p\bar{p} \to W\gamma \to e\nu\gamma$ production at the Tevatron for an integrated luminosity of 1 fb^{-1} at $\sqrt{s}$ = 2 TeV; and
- $pp \to W\gamma \to e\nu\gamma$ production at the LHC for an integrated luminosity of 100 fb^{-1} at $\sqrt{s}$ = 14 TeV.

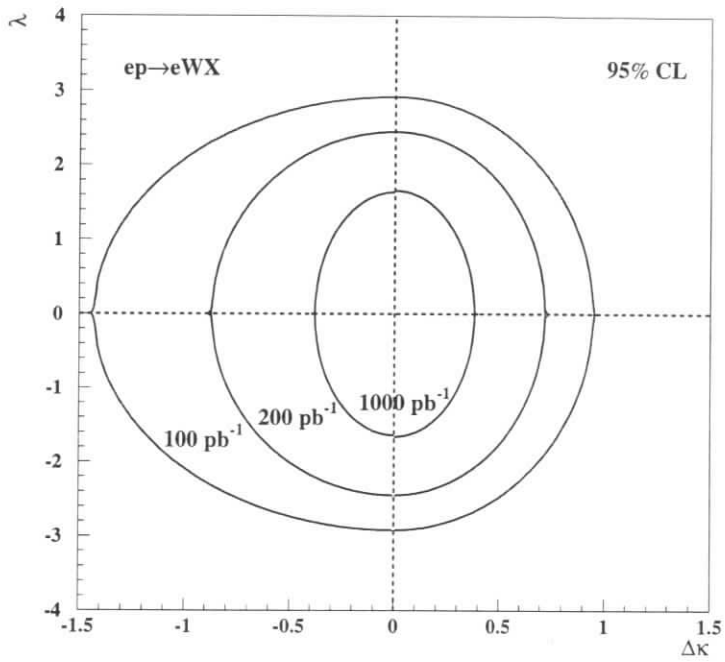

Figure 5: *Projected 95% confidence level sensitivity limits for $WW\gamma$ couplings from measurement of $\sigma(ep \to eWX)$ at HERA for integrated luminosities of 100* pb^{-1}, *200* pb^{-1}, *and 1* fb^{-1}.

In reference [1] the limits for LEP2 were calculated assuming an integrated luminosity of 500 pb^{-1} per experiment. As this was considered to be rather optimistic, the limits were recalculated for an integrated luminosity of 125 pb^{-1} per experiment by naively assuming that the limits given in [1] could be scaled by a factor of two.

The W^+W^- production process suffers from the drawback that both the $WW\gamma$ and WWZ couplings contribute and additional assumptions are often used to calculate the sensitivity to the $WWV(V = \gamma, Z)$ couplings. The limits from LEP2 in figure 6 have been calculated for the HISZ scenario [16] which relates $\Delta\kappa_\gamma$ and $\Delta\kappa_Z$ and equates λ_Z and λ_γ to reduce the number of anomalous couplings to two. $W\gamma$ production from which the Tevatron limits are derived, however, provides direct limits on the $WW\gamma$ couplings. When comparing the results between experiments, the strong correlation between $\Delta\kappa$ and λ at LEP2 should be taken into account. This correlation is smaller at the Tevatron and negligible at HERA when the lepton beam is unpolarised.

Figure 6 shows that the 95% CL limits on anomalous values of $\Delta\kappa$ which could be obtained from one HERA experiment with an integrated luminosity of 1000 pb^{-1} will be extremely competitive with those which may be achieved at LEP2 and the Tevatron after several years running. Limits from the LHC experiments for $\int \mathcal{L}dt = 100$ fb^{-1} are also included in figure 6 to indicate the sensitivity which could be achieved in the long term future.

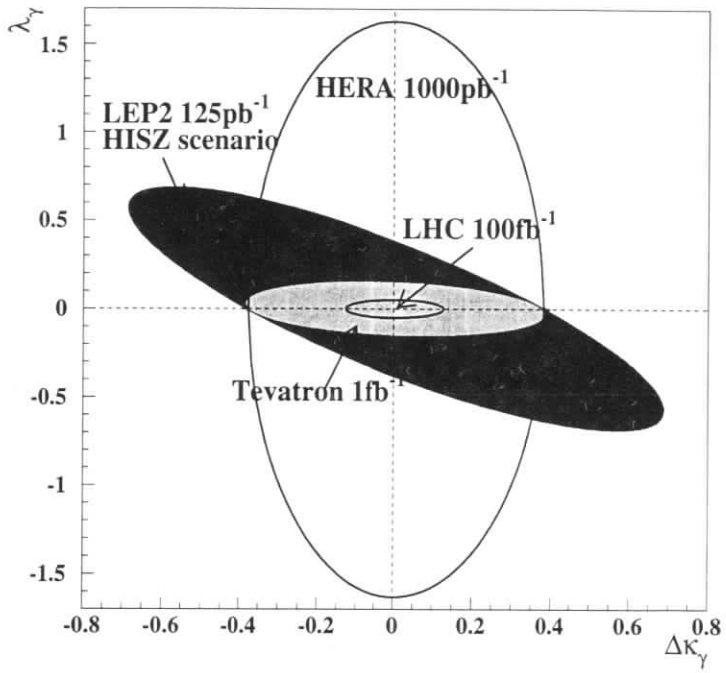

Figure 6: *Projected 95% confidence level sensitivity limits for $WW\gamma$ couplings determined from the single W production cross section at HERA and from $W\gamma$ production at the Tevatron and the LHC. The solid shading indicates the limits for the $WWV, V = \gamma, Z$ couplings from WW production at LEP2 assuming the HISZ scenario.*

5.2 Increased centre-of-mass energy

Given sufficient physics motivation, it is possible that HERA could be upgraded to collide a 30 GeV lepton beam with 1 TeV proton beam, increasing the centre-of-mass (cms) energy to $\sqrt{s} = 346$ GeV. The Standard Model cross section for $\sigma(\mathrm{ep} \to \mathrm{e}WX)$ increases from 1.043 pb

to 1.515 pb. Figure 7 compares $\sigma(\Delta\kappa, \lambda = 0)$ and $\sigma(\lambda, \Delta\kappa = 0)$ at the nominal and high cms energies. The higher cross section and steeper rise as a function of $\Delta\kappa$ or λ at $\sqrt{s} = 346$ GeV leads to a substantial improvement in the sensitivity to anomalous couplings as shown in table 5.

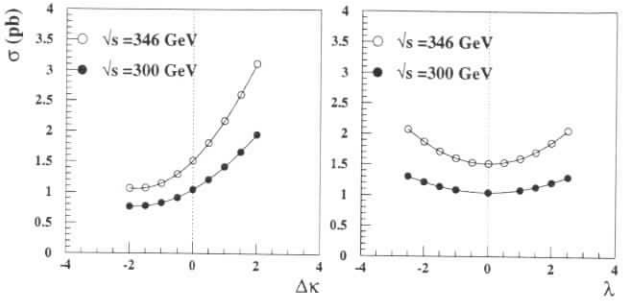

Figure 7: *Comparison of $\sigma(\Delta\kappa, \lambda = 0)$ and $\sigma(\lambda, \Delta\kappa = 0)$ for nominal and increased cms energies of 300* GeV *and 346* GeV.

$\sqrt{s} = 346$ GeV		
$\int \mathcal{L}dt$	$\Delta\kappa$	λ
100 pb^{-1}	$-0.84 < \Delta\kappa < 0.70$	$-2.20 < \lambda < 2.20$
200 pb^{-1}	$-0.59 < \Delta\kappa < 0.53$	$-1.87 < \lambda < 1.88$
1000 pb^{-1}	$-0.27 < \Delta\kappa < 0.26$	$-1.26 < \lambda < 1.27$

Table 5: *95% CL sensitivity limits derived from measurement of $\sigma(\mathrm{ep} \to \mathrm{e}WX)$ at HERA with a cms energy of 346* GeV.

5.3 Polarised lepton beam

Electroweak studies can be significantly expanded and improved if lepton polarisation can be achieved at HERA. The EPVEC Monte Carlo was used to investigate the effects using polarised $\mathrm{e}^\pm$ would have on the sensitivity to anomalous $WW\gamma$ couplings. Figure 8 compares $\sigma(\mathrm{e}^+\mathrm{p} \to \mathrm{e}^+WX)$ as a function of $\Delta\kappa$ and λ for different e^+ polarisations.

The Standard Model cross section increases from 1.043 pb when $P = 0$ to 1.199 when $P = +1$, a 100% left-handed positron beam[1]. This increase in cross section corresponds to the increase

[1] P is defined as $q_e \cdot \left(\frac{\sigma_L - \sigma_R}{\sigma_L + \sigma_R}\right)$, where q_e is the lepton charge.

expected when using unpolarised positrons and an anomalous coupling of $\Delta\kappa \sim 0.5$ i.e. is larger than the 95% CL limit on $\Delta\kappa$ found earlier. For the variation with $\Delta\kappa$ alone, figure 8 shows an approximately constant increase in cross section between $P = -1$ and $P = 0$, and $P = 0$ and $P = +1$. In contrast, the change in polarisation affects the shape of the cross sectional dependence on λ. For $P = 0$ the distribution is symmetric around its minimum at $\lambda = 0$. However for $P = +1 (P = -1)$ the minimum of the distribution is reached at $\lambda \sim +1 (\lambda \sim -0.5)$.

Moreover, figure 9 shows that when $P = +0.7$ the difference between the $\sigma(\Delta\kappa, \lambda = 0)$ and $\sigma(\Delta\kappa, \lambda = 2)$ curves, is not constant as in the case for an unpolarised lepton beam in figure 4. The $\Delta\kappa$ and λ couplings can therefore no longer be considered to be uncorrelated.

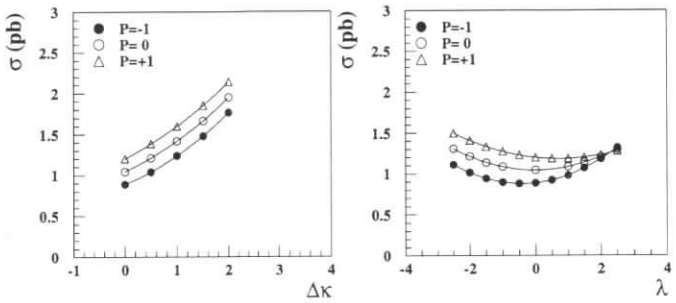

Figure 8: *Variation of* $\sigma(e^+p \to e^+WX)$ *with* $\Delta\kappa$ *(left) and* λ *(right) for polarised and unpolarised positrons.*

The dependency of the cross section on the lepton polarisation can be understood by considering the Weiszäcker-Williams approximation (WWA) given in equation 7 together with the helicity amplitudes given in reference [2] which depend on the helicities of the photon and W.

In the WWA the probability that a photon with helicity λ_γ is emitted from an electron with helicity $\sigma_e/2$ is given by

$$P_{\gamma/e}(z) = \frac{\alpha}{2\pi} \frac{(1 + \sigma_e\lambda_\gamma) + (1 - \sigma_e\lambda_\gamma)(1 - z)^2}{z} \ln\left(\frac{E_\gamma}{m_e}\right) \tag{7}$$

where $\alpha = e^2/4\pi$, E_γ is the photon energy and z is the fraction of the electron's momentum carried by the photon. For $\sigma_e\lambda_\gamma = -1$ ($\sigma_e\lambda_\gamma = +1$) the first (second) term in the numerator of equation 7 vanishes, giving

$$P_{\gamma/e} \sim \frac{1}{z} \quad \text{if } \lambda_\gamma = \sigma_e \tag{8}$$

$$P_{\gamma/e} \sim \frac{(1-z)^2}{z} \quad \text{if } \lambda_\gamma = -\sigma_e \tag{9}$$

Figure 1a illustrates that for a W to be produced at HERA, the cms energy of the γq system ($\sqrt{\hat{s}}$) must be larger than the mass of the W. This forces z to be large, and the photon is

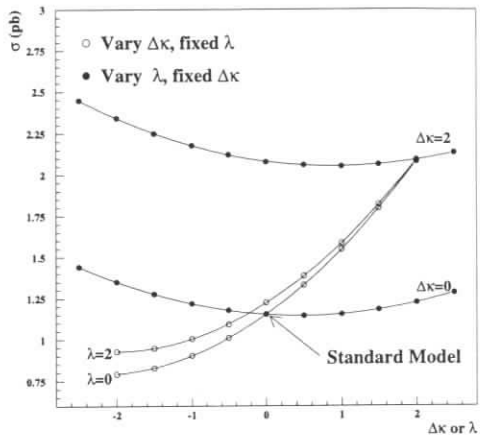

Figure 9: *Variation of* $\sigma(ep \to eWX)$ *with either* $\Delta\kappa$ *or* λ *using 70% polarised incident positrons.*

predominantly emitted with the same helicity as the incoming lepton which in turn favours certain helicity amplitudes in the cross section calculation.

At HERA it is expected that 70% polarisation can be achieved and that degree of polarisation will be known to an accuracy better than 5%. The SM cross sections for $e^{\pm}_{L,R}p \to eWX$ are shown in table 6. The difference in cross section between oppositely polarised positrons and electrons is less than 3% due to the suppression of the Z exchange and charged current diagrams in figure 1.

		σ (pb)
	e^+_L	1.153
$P = +0.7$	e^-_R	1.127
	e^+_R	0.933
$P = -0.7$	e^-_L	0.949

Table 6: *Standard Model cross sections for* $ep \to eWX$ *using 70% polarised positron and electron beams.*

The 95% CL limits on $\Delta\kappa$ and λ derived using $P = +0.7$ positrons and assuming that only one coupling departs from its SM value, are given in table 7 for various integrated luminosities. The results in table 7 indicate that the limits on $\Delta\kappa$ and λ do not improve substantially when measuring the couplings by this method.

Table 8 compares the 95% CL limits for left and right-handed polarised beams which could be achieved with $\int \mathcal{L}dt$=1000 pb^{-1}. Although the upper limit on λ improves for $P=-0.7$, the sensitivity to anomalous values of λ will not be competitive with those currently obtained at the Tevatron [17].

$\int \mathcal{L}dt$	$\Delta\kappa \quad \lambda = 0$	$\lambda \quad \Delta\kappa = 0$
100 pb^{-1}	$-1.17 < \Delta\kappa < 0.98$	$-2.91 < \lambda < 3.83$
200 pb^{-1}	$-0.80 < \Delta\kappa < 0.72$	$-2.39 < \lambda < 3.32$
1000 pb^{-1}	$-0.36 < \Delta\kappa < 0.35$	$-1.48 < \lambda < 2.41$

Table 7: *Limits derived on $\Delta\kappa$ and λ from measurement of $\sigma(e^+p \to eWX)$ at nominal HERA energies using a 70% polarised positron beam. Only one limit at a time is allowed to deviate from its Standard Model value.*

		$\Delta\kappa \quad \lambda = 0$	$\lambda \quad \Delta\kappa = 0$
$P=+0.7$	e^+_L	$-0.36 < \Delta\kappa < 0.35$	$-1.48 < \lambda < 2.41$
	e^-_R	$-0.36 < \Delta\kappa < 0.35$	$-1.51 < \lambda < 2.35$
$P=-0.7$	e^+_R	$-0.39 < \Delta\kappa < 0.35$	$-1.79 < \lambda < 1.21$
	e^-_L	$-0.39 < \Delta\kappa < 0.35$	$-1.84 < \lambda < 1.18$

Table 8: *Limits derived on $\Delta\kappa$ and λ from measurement of $\sigma(ep \to eWX)$ using 70% polarised electron and positron beams and an integrated luminosity of 1000 pb^{-1}. Only one limit at a time is allowed to deviate from its Standard Model value.*

6 Conclusions

The single W production cross section at HERA is sensitive to deviations of the $WW\gamma$ couplings from their Standard Model values. In particular, HERA offers greater sensitivity to anomalous values of $\Delta\kappa$ than λ and therefore complements measurements made at the Tevatron and LEP2 where the sensitivity to λ is greater. Furthermore, single W production is quite insensitive to anomalous WWZ couplings, unlike WW production at the Tevatron or LEP2. The sensitivity to anomalous $WW\gamma$ couplings has been studied for various integrated luminosities and at two centre-of-mass energies. With an integrated luminosity of 1000 pb^{-1} the 95% confidence level limits are: $-0.38 < \Delta\kappa < 0.38$ and $-1.65 < \lambda < 1.66$ at $\sqrt{s} = 300$ GeV; and $-0.27 < \Delta\kappa < 0.26$ and $-1.26 < \lambda < 1.27$ at $\sqrt{s} = 346$ GeV, and are limited by statistical rather than systematic errors. For $\int \mathcal{L}dt$=1000 pb^{-1} the future sensitivity on anomalous values of $\Delta\kappa$ which can be obtained at HERA are competitive with projected limits from $W\gamma$ production at the Tevatron.

Acknowledgements

I would like to thank the conveners of the Electroweak working group for many helpful discussions throughout the workshop and their critical reading of this report. I am grateful to D. Waters, G. Grzelak and A. Schöning whose work on W searches at ZEUS and H1 inspired the event selection used here, and to T. Ishii for interfacing the EPVEC Monte Carlo to JETSET and the ZEUS software environment.

References

[1] H. Aihara et. al. MAD/PH/871 and Fermilab-Pub-95/031, to be published in "Electroweak Symmetry Breaking and Beyond the Standard Model", eds. T. Barklow, S. Dawson, H. Haber and J. Siegrist.

[2] U. Baur and D. Zeppenfeld, Nucl. Phys. B325 (1989) 253 and references therein.

[3] T. Helbig and H. Spiesberger, Proc. 1991 Workshop on Physics at HERA, eds. W. Buchmüller, C. Ingelman, (DESY Hamburg 1992) Vol 2, p. 973.

[4] A. Schöning, Proc. Int. Symposium on Vector Boson Self-Interactions, (Los Angeles 1995), to be published.
A. Schöning, PhD thesis, University of Hamburg (1996).
ZEUS collaboration: M. Derrick et al., Proc. XXVIII Int. Conference on High Energy Physics, Warsaw (1996), to be published.

[5] K. Hagiwara et al., Phys. Rev. D48 (1990), 2113.

[6] U. Baur, J.A.M. Vermaseren and D. Zeppenfeld, Nucl. Phys. B375 (1992) 3.

[7] P.N. Harriman, A.D. Martin,R.G. Roberts, W.J. Stirling, Phys. Rev. D43 (1990) 798.

[8] H. Abramowicz, K. Charcuła and A. Levy, Phys. Lett B269 (1991) 458.

[9] T. Sjöstrand, CERN-TH-6488-92 (1992).

[10] Result presented by A-B. Fahr, December meeting of the Electroweak working group.

[11] G. Ingleman, Proc. 1991 Workshop on Physics at HERA, eds. W. Buchmüller, G. Ingelman, (DESY Hamburg 1992) Vol 3, p. 1366.

[12] A. Kwiatkowski, H. Spiesberger and H.J. Möhring, Proc. 1991 Workshop on Physics at HERA, eds. W. Buchmüller, G. Ingelman, (DESY Hamburg 1992) Vol 3, p. 1294.

[13] L. Lönnblad, Comp. Phys. Comm. 81 (1992) 15.

[14] H1 collaboration: T. Ahmed et al., DESY 94-248.

[15] B.R. Webber, Proc. 1991 Workshop on Physics at HERA, eds. W. Buchmüller, G. Ingelman, (DESY Hamburg 1992) Vol 3, p. 1363.

[16] K. Hagiwara, S. Ishihara, R. Szalapski and D. Zeppenfeld, Phys. Lett. B283 (1992) 353; and Phys. Rev. D48 (1993) 2182.

[17] D0 collaboration: S. Abachi et al., Phys. Rev. Lett. 75 (1995) 1034.
CDF collaboration: F. Abe et al., Phys. Rev. Lett, 75 (1995) 1017.

Bounds on the $Z\gamma\gamma$ couplings from HERA

F. Cornet[a], R. Graciani[b], J.I. Illana[a]

[a] Depto. de Física Teórica y del Cosmos, Universidad de Granada, E-18071 Granada, Spain
[b] Depto. de Física Teórica, Universidad Autónoma de Madrid, E-28049 Cantoblanco, Spain

Abstract: The possibility of testing trilinear neutral gauge boson couplings in radiative neutral current scattering at HERA is analyzed using a Monte Carlo program that includes the Standard Model at tree level and the anomalous vertices. Acceptance and isolation cuts are applied as well as optimized cuts to enhance the signal from new physics. The bounds on $Z\gamma\gamma$ couplings that can be achieved are not so stringent as present bounds, even for high luminosities, but probe a different kinematical region almost unsensitive to form factors.

1 Introduction

The precision data collected to date have confirmed the Standard Model to be a good description of physics below the electroweak scale [1]. Despite of its great success, there are many reasons to believe that some kind of new physics must exist. On the other hand, the non-abelian structure of the gauge boson self-couplings is still poorly tested and one of the most sensitive probes for new physics is provided by the trilinear gauge boson couplings (TGC) [2].

Many studies have been devoted to the $WW\gamma$ and WWZ couplings. At hadron colliders and e^+e^- colliders, the present bounds (Tevatron [3]) and prospects (LHC, LEP2 and NLC [2, 4]) are mostly based on diboson production (WW, $W\gamma$ and WZ). In ep collisions, HERA could provide further information analyzing single W production ($ep \to eWX$ [5]) and radiative charged current scattering ($ep \to \nu\gamma X$ [6]). There is also some literature on $WW\gamma$ couplings in W-pair production at future very high energy photon colliders (bremsstrahlung photons in peripheral heavy ion collisions [7] and Compton backscattered laser beams [8]).

Only recently, attention has been paid to the $Z\gamma Z$, $Z\gamma\gamma$ and ZZZ couplings. There is a detailed analysis of $Z\gamma V$ couplings ($V = \gamma, Z$) for hadron colliders in [9]. CDF [10] and DØ [11] have obtained bounds on the $Z\gamma Z$ and $Z\gamma\gamma$ anomalous couplings, while L3 has studied only the first ones [12]. Studies on the sensitivities to these vertices in future e^+e^- colliders, LEP2 [4] and NLC [13], have been performed during the last years. Some proposals have been made to probe these neutral boson gauge couplings at future photon colliders in $e\gamma \to Ze$ [14].

In this work we study the prospects for measuring the TGC in the process $ep \to e\gamma X$. In particular, we will concentrate on the $Z\gamma\gamma$ couplings, which can be more stringently bounded than the $Z\gamma Z$ ones for this process.

In Section 2, we present the TGC. The next section deals with the different contributions to the process $ep \to e\gamma X$ and the cuts and methods we have employed in our analysis. Section 4 contains our results for the Standard Model total cross section and distributions and the estimates of the sensitivity of these quantities to the presence of anomalous couplings. Finally, in the last section we present our conclusions.

2 Phenomenological parametrization of the neutral TGC

A convenient way to study deviations from the standard model predictions consists of considering the most general lagrangian compatible with Lorentz invariance, the electromagnetic U(1) gauge symmetry, and other possible gauge symmetries.

For the trilinear $Z\gamma V$ couplings ($V = \gamma, Z$) the most general vertex function invariant under Lorentz and electromagnetic gauge transformations can be described in terms of four independent dimensionless form factors [15], denoted by h_i^V, i=1,2,3,4:

$$\Gamma^{\alpha\beta\mu}_{Z\gamma V}(q_1,q_2,p) = \frac{f(V)}{M_Z^2}\{h_1^V(q_2^\mu g^{\alpha\beta} - q_2^\alpha g^{\mu\beta}) + \frac{h_2^V}{M_Z^2}p^\alpha(p\cdot q_2 g^{\mu\beta} - q_2^\mu p^\beta) + h_3^V \varepsilon^{\mu\alpha\beta\rho}q_{2_\rho} + \frac{h_4^V}{M_Z^2}p^\alpha \varepsilon^{\mu\beta\rho\sigma}p_\rho q_{2_\sigma}\}. \quad (1)$$

Terms proportional to p^μ, q_1^α and q_2^β are omitted as long as the scalar components of all three vector bosons can be neglected (whenever they couple to almost massless fermions) or they are zero (on-shell condition for Z or U(1) gauge boson character of the photon). The overall factor, $f(V)$, is $p^2 - q_1^2$ for $Z\gamma Z$ or p^2 for $Z\gamma\gamma$ and is a result of Bose symmetry and electromagnetic gauge invariance. These latter constraints reduce the familiar seven form factors of the most general WWV vertex to only these four for the $Z\gamma V$ vertex. There still remains a global factor that can be fixed, without loss of generality, to $g_{Z\gamma Z} = g_{Z\gamma\gamma} = e$. Combinations of $h_3^V(h_1^V)$ and $h_4^V(h_2^V)$ correspond to electric (magnetic) dipole and magnetic (electric) quadrupole transition moments in the static limit.

All the terms are C-odd. The terms proportional to h_1^V and h_2^V are CP-odd while the other two are CP-even. All the form factors are zero at tree level in the Standard Model. At the one-loop level, only the CP-conserving h_3^V and h_4^V are nonzero [16] but too small ($\mathcal{O}(\alpha/\pi)$) to lead to any observable effect at any present or planned experiment. However, larger effects might appear in theories or models beyond the Standard Model, for instance when the gauge bosons are composite objects [17].

This is a purely phenomenological, model independent parametrization. Tree-level unitarity restricts the $Z\gamma V$ to the Standard Model values at asympotically high energies [18]. This implies that the couplings h_i^V have to be described by form factors $h_i^V(q_1^2, q_2^2, p^2)$ which vanish when q_1^2, q_2^2 or p^2 become large. In hadron colliders, large values of $p^2 = \hat{s}$ come into play and the energy dependence has to be taken into account, including unknown dumping factors [9]. A scale dependence appears as an additional parameter (the scale of new physics, Λ). Alternatively, one could introduce a set of operators invariant under SU(2)×U(1) involving the gauge bosons and/or additional would-be-Goldstone bosons and the physical Higgs. Depending on the new physics dynamics, operators with dimension d could be generated at the scale Λ, with a strength which is generally suppressed by factors like $(M_W/\Lambda)^{d-4}$ or $(\sqrt{s}/\Lambda)^{d-4}$ [19]. It can be shown

that h_1^V and h_3^V receive contributions from operators of dimension ≥ 6 and h_2^V and h_4^V from operators of dimension ≥ 8. Unlike hadron colliders, in $ep \to e\gamma X$ at HERA energies, we can ignore the dependence of the form factors on the scale. On the other hand, the anomalous couplings are tested in a different kinematical region, which makes their study in this process complementary to the ones performed at hadron and lepton colliders.

3 The process $ep \to e\gamma X$

The process under study is $ep \to e\gamma X$, which is described in the parton model by the radiative neutral current electron-quark and electron-antiquark scattering,

$$e^- \overset{(-)}{q} \to e^- \overset{(-)}{q} \gamma. \quad (2)$$

There are eight Feynman diagrams contributing to this process in the Standard Model and three additional ones if one includes anomalous vertices: one extra diagram for the $Z\gamma Z$ vertex and two for the $Z\gamma\gamma$ vertex (Fig. 1).

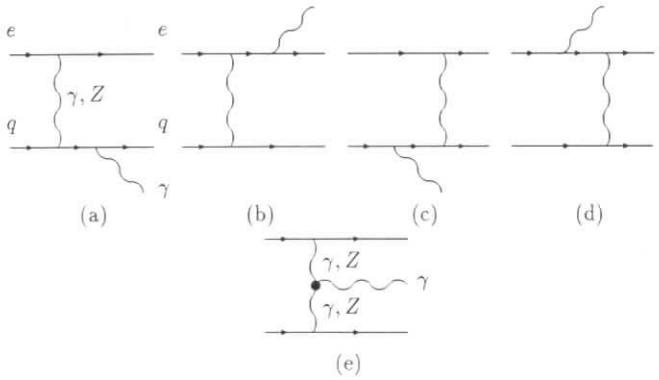

Figure 1: *Feynman diagrams for the process* $e^-q \to e^-q\gamma$.

Diagrams with γ exchanged in the t-channel are dominant. Nevertheless, we consider the whole set of diagrams in the calculation. On the other side, u-channel fermion exchange poles appear, in the limit of massless quarks and electrons (diagrams (c) and (d)). Since the anomalous diagrams (e) do not present such infrared or collinear singularities, it seems appropriate to avoid almost on-shell photons exchanged and fermion poles by cutting the transverse momenta of the final fermions (electron and jet) to enhance the signal from anomalous vertices. Due to the suppression factor coming from Z propagator, the anomalous diagrams are more sensitive to $Z\gamma\gamma$ than to $Z\gamma Z$ vertices. In the following we will focus our attention on the former.

The basic variables of the parton level process are five. A suitable choice is: E_γ (energy of the final photon), $\cos\theta_\gamma$, $\cos\theta_{q'}$ (cosines of the polar angles of the photon and the scattered quark

defined with respect to the proton direction), ϕ (the angle between the transverse momenta of the photon and the scattered quark in a plane perpendicular to the beam), and a trivial azimuthal angle that is integrated out (unpolarized beams). All the variables are referred to the laboratory frame. One needs an extra variable, the Bjorken-x, to connect the partonic process with the ep process. The phase space integration over these six variables is carried out by VEGAS [20] and has been cross-checked with the RAMBO subroutine [21].

We adopt two kinds of event cuts to constrain conveniently the phase space:

- *Acceptance and isolation* cuts. The former are to exclude phase space regions which are not accessible to the detector, because of angular or efficiency limitations:[1]

$$\begin{aligned} 8^\circ < \theta_e,\ \theta_\gamma,\ \theta_{\rm jet} < 172^\circ; \\ E_e,\ E_\gamma,\ p_{\rm T}^{\rm q'} > 10 \text{ GeV}. \end{aligned} \tag{3}$$

  The latter keep the final photon well separated from both the final electron and the jet:

$$\begin{aligned} \cos\langle\gamma, e\rangle < 0.9; \\ R > 1.5, \end{aligned} \tag{4}$$

  where $R \equiv \sqrt{\Delta\eta^2 + \phi^2}$ is the separation between the photon and the jet in the rapidity-azimuthal plane, and $\langle\gamma, e\rangle$ is the angle between the photon and the scattered electron.

- Cuts for *intrinsic background suppression*. They consist of strengthening some of the previous cuts or adding new ones to enhance the signal of the anomalous diagrams against the Standard Model background.

We have developed a Monte Carlo program for the simulation of the process $ep \to e\gamma X$ where X is the remnant of the proton plus one jet formed by the scattered quark of the subprocess (2). It includes the Standard Model helicitity amplitudes computed using the HELAS subroutines [22]. We added new code to account for the anomalous diagrams. The squares of these anomalous amplitudes have been cross-checked with their analytical expressions computed using FORM [23]. For the parton distribution functions, we employ both the set 1 of Duke-Owens' parametrizations [25] and the modified MRS(A) parametrizations [26], with the scale chosen to be the hadronic momentum transfer.

As inputs, we use the beam energies $E_e = 30$ GeV and $E_p = 820$ GeV, the Z mass $M_Z = 91.187$ GeV, the weak angle $\sin^2_W = 0.2315$ [24] and the fine structure constant $\alpha = 1/128$. A more correct choice would be the running fine structure constant with Q^2 as the argument. However, as we are interested in large Q^2 events, the value $\alpha(M_Z^2)$ is accurate enough for our purposes. We consider only the first and second generations of quarks, assumed to be massless.

We start by applying the cuts (3) and (4) and examining the contribution to a set of observables of the Standard Model and the anomalous diagrams, separately. Next, we select one observable such that, when a cut on it is performed, only Standard Model events are mostly eliminated. The procedure is repeated with this new cut built in. After several runs, adding new cuts, the ratio standard/anomalous cross sections is reduced and hence the sensitivity to anomalous couplings is improved.

[1]The threshold for the transverse momentum of the scattered quark ensures that its kinematics can be described in terms of a jet.

4 Results

4.1 Observables

The total cross section of $ep \to e\gamma X$ can be written as

$$\sigma = \sigma_{\rm SM} + \sum_i \tau_i \cdot h_i^\gamma + \sum_i \sigma_i \cdot (h_i^\gamma)^2 + \sigma_{12} \cdot h_1^\gamma h_2^\gamma + \sigma_{34} \cdot h_3^\gamma h_4^\gamma. \tag{5}$$

The forthcoming results are obtained using the MRS'95 parametrization of the parton densities[2] [26]. The linear terms of the P-violating couplings h_3^γ and h_4^γ are negligible, as they mostly arise from the interference of standard model diagrams with photon exchange (P-even) and anomalous P-odd diagrams ($\tau_3 \simeq \tau_4 \simeq 0$). Moreover, anomalous diagrams with different P do not interfere either. On the other hand, the quadratic terms proportional to $(h_1^\gamma)^2$ and $(h_3^\gamma)^2$ have identical expressions, and the same for h_2^γ and h_4^γ ($\sigma_1 = \sigma_3$, $\sigma_2 = \sigma_4$). Only the linear terms make their bounds different. The interference terms σ_{12} and σ_{34} are also identical.

We have analyzed the distributions of more than twenty observables in the laboratory frame, including the energies, transverse momenta and angular distributions of the jet, the photon and the final electron, as well as their spatial, polar and azimuthal separations. Also the bjorken-x, the leptonic and hadronic momenta transfer and other fractional energies are considered.

The process of intrinsic background suppression is illustrated by comparing Figures 2 and 3. For simplicity, only the most interesting variables are shown: the energy $E(\gamma)$ and transverse momentum $p_T(\gamma)$ of the photon; the angles between the photon and the scattered electron $\langle\gamma, e\rangle$, the photon and the jet $\langle\gamma, j\rangle$, and the scattered electron and the jet $\langle e, j\rangle$; and the leptonic momentum transfer $Q^2(e)$. In Fig. 2, these variables are plotted with only acceptance and isolation cuts implemented. All of them share the property of disposing of a range where any anomalous effect is negligible, whereas the contribution to the total SM cross section is large. The set of cuts listed below were added to reach eventually the distributions of Fig. 3:

- The main contribution to the Standard Model cross section comes from soft photons with very low transverse momentum. The following cuts suppress a 97% of these events, without hardly affecting the anomalous diagrams which, conversely, enfavour high energy photons:

$$\begin{aligned} E_\gamma > 30 \text{ GeV} \\ p_T^\gamma > 20 \text{ GeV} \end{aligned} \tag{6}$$

- Another remarkable feature of anomalous diagrams is the very different typical momentum transfers. Let's concentrate on the leptonic momentum transfer, $Q_e^2 = -(p'_e - p_e)^2$. The phase space enhances high Q_e^2, while the photon propagator of the Standard Model diagrams prefer low values (above the threshold for electron detectability, $Q_e^2 > 5.8$ GeV^2, with our required minimum energy and angle). On the contrary, the anomalous diagrams have always a Z propagator which introduces a suppression factor of the order of Q_e^2/M_Z^2 and makes irrelevant the Q_e^2 dependence, which is only determined by the phase space. As a consequence, the following cut looks appropriate,

$$Q_e^2 > 1000 \text{ GeV}^2 \tag{7}$$

[2]The values change $\sim 10\%$ when using the (old) Duke-Owens' structure functions.

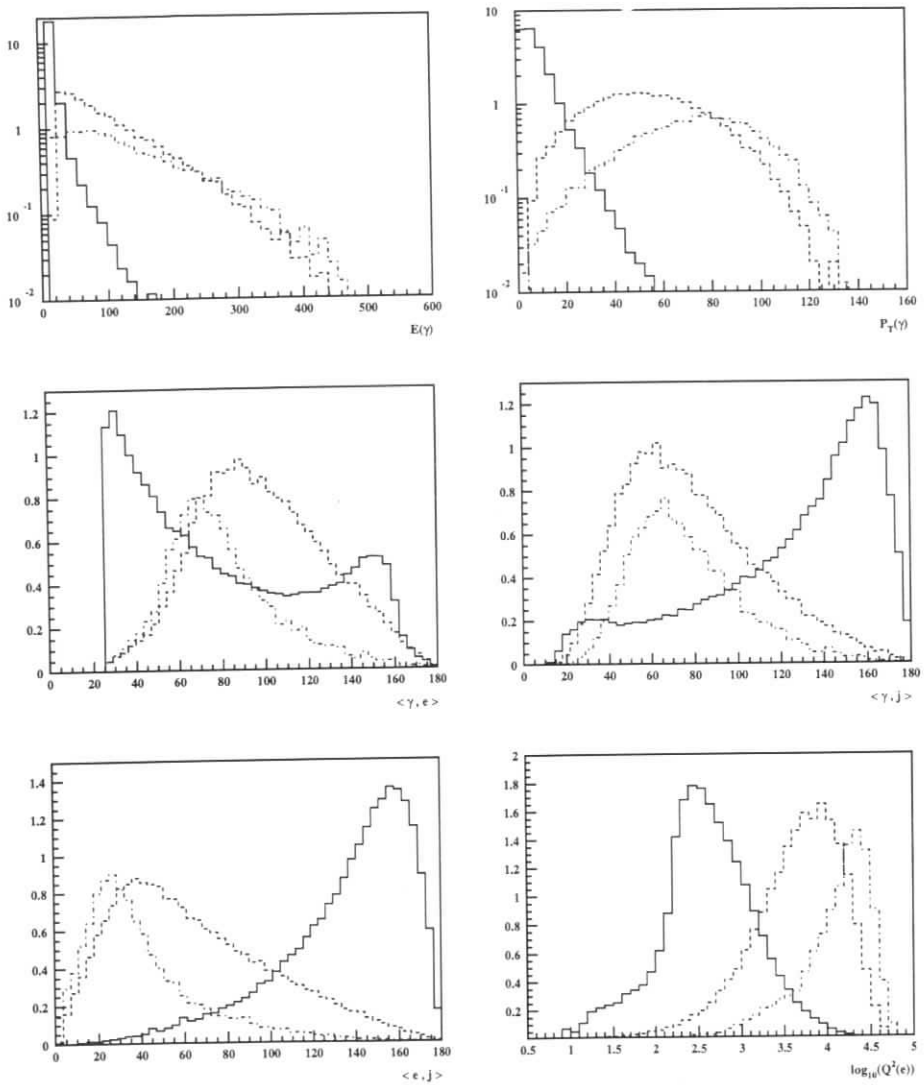

Figure 2: *Differential cross sections (pb) for the process* $ep \to e\gamma X$ *at HERA, with only acceptance and isolation cuts. The solid line is the Standard Model contribution and the dash (dot-dash) line correspond to 10000 times the* σ_1 *(*σ_2*) anomalous contributions.*

It is important to notice at this point why usual form factors for the anomalous couplings can be neglected at HERA. For our process, these form factors should be proportional to $1/(1 + Q^2/\Lambda^2)^n$. With the scale of new physics $\Lambda = 500$ GeV to 1 TeV, these factors can

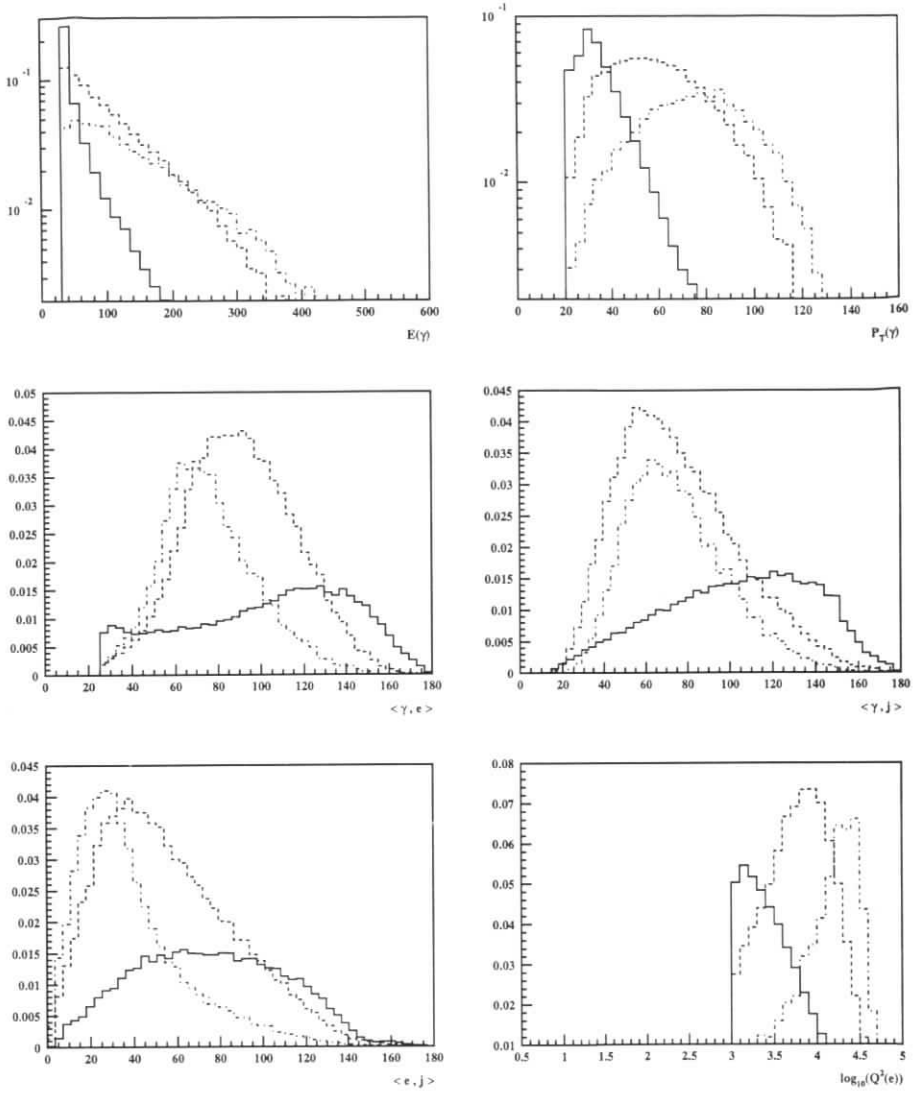

Figure 3: *Differential cross sections (pb) for the process* $ep \to e\gamma X$ *at HERA, after intrinsic background suppression. The solid line is the Standard Model contribution and the dash (dot-dash) line correspond to 500 times the* σ_1 *(*σ_2*) anomalous contributions.*

be taken to be one. This is not the case in lepton or hadron high energy colliders where the diboson production in the s-channel needs dumping factors $1/(1 + \hat{s}/\Lambda^2)^n$.

The total cross section for the Standard Model with acceptance and isolation cuts is $\sigma_{SM} = 21.38$ pb and is reduced to 0.37 pb when all the cuts are applied, while the quadratic contributions only change from $\sigma_1 = 2 \times 10^{-3}$ pb, $\sigma_2 = 1.12 \times 10^{-3}$ pb to $\sigma_1 = 1.58 \times 10^{-3}$ pb, $\sigma_2 = 1.05 \times 10^{-3}$ pb. The linear terms are of importance and change from $\tau_1 = 1.18 \times 10^{-2}$ pb, $\tau_2 = 1.27 \times 10^{-3}$ pb to $\tau_1 = 7.13 \times 10^{-3}$ pb, $\tau_2 = 1.26 \times 10^{-3}$ pb. Finally, the interference term $\sigma_{12} = 1.87 \times 10^{-3}$ pb changes to $\sigma_{12} = 1.71 \times 10^{-3}$ pb.

The typical Standard Model events consist of soft and low-p_T photons mostly backwards, tending to go in the same direction of the scattered electrons (part of them are emitted by the hadronic current in the forward direction), close to the required angular separation ($\sim 30^\circ$). The low-p_T jet goes opposite to both the photon and the scattered electron, also in the transverse plane. On the contrary, the anomalous events have not so soft and high-p_T photons, concentrated in the forward region as it the case for the scattered electron and the jet.

4.2 Sensitivity to anomalous couplings

In order to estimate the sensitivity to anomalous couplings, we consider the χ^2 function. One can define the χ^2, which is related to the likelihood function $\mathcal{L}$, as

$$\chi^2 \equiv -2 \ln \mathcal{L} = 2L \left(\sigma^{th} - \sigma^o + \sigma^o \ln \frac{\sigma^o}{\sigma^{th}} \right) \simeq L \frac{(\sigma^{th} - \sigma^o)^2}{\sigma^o}, \tag{8}$$

where $L = N^{th}/\sigma^{th} = N^o/\sigma^o$ is the integrated luminosity and N^{th} (N^o) is the number of theoretical (observed) events. The last line of (8) is a useful and familiar approximation, only valid when $| \sigma^{th} - \sigma^o | / \sigma^o \ll 1$. This function is a measure of the probability that statistical fluctuations can make undistinguisable the observed and the predicted number of events, that is the Standard Model prediction. The well known χ^2-CL curve allows us to determine the corresponding confidence level (CL). We establish bounds on the anomalous couplings by fixing a certain $\chi^2 = \delta^2$ and allowing for the h_i^γ values to vary, $N^o = N^o(h_i^\gamma)$. The parameter δ is often referred as the number of standard deviations or 'sigmas'. A 95% CL corresponds to almost two sigmas ($\delta = 1.96$). When $\sigma \simeq \sigma_{SM} + (h_i^\gamma)^2 \sigma_i$ (case of the CP-odd terms) and the anomalous contribution is small enough, the upper limits present some useful, approximate scaling properties, with the luminosity,

$$h_i^\gamma(L') \simeq \sqrt[4]{\frac{L}{L'}}\, h_i^\gamma(L). \tag{9}$$

A brief comment on the interpretation of the results is in order. As the cross section grows with h_i^γ, in the relevant range of values, the N^o upper limits can be regarded as the lowest number of measured events that would discard the Standard Model, or the largest values of h_i^γ that could be bounded if no effect is observed, with the given CL. This procedure approaches the method of upper limits for Poisson processes when the number of events is large ($\gtrsim 10$).

In Fig. 4 the sensitivities for different luminosities are shown. Unfortunately, HERA cannot compete with Tevatron, whose best bounds, reported by the DØ collaboration [11], are

$$\begin{aligned} |h_1^\gamma|,\ |h_3^\gamma| &< 1.9\ (3.1), \\ |h_2^\gamma|,\ |h_4^\gamma| &< 0.5\ (0.8). \end{aligned} \tag{10}$$

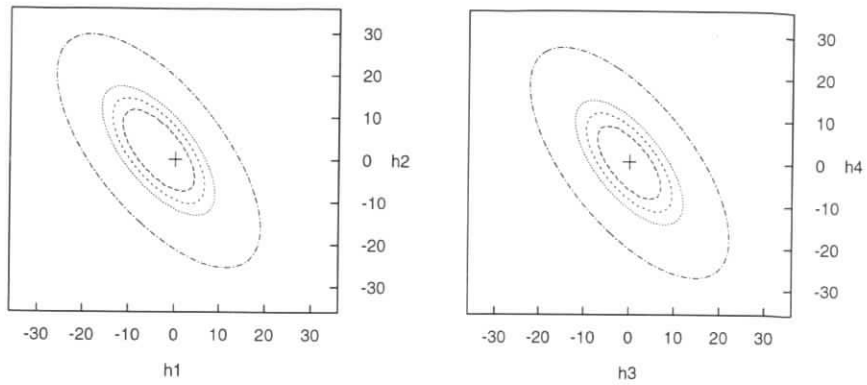

Figure 4: *Limit contours for $Z\gamma\gamma$ couplings at HERA with an integrated luminosity of 10, 100, 250, 1000 pb^{-1} and a 95% CL.*

HERA	10 pb^{-1}		100 pb^{-1}		250 pb^{-1}		1 fb^{-1}	
h_1^γ	-19.0	14.5	-11.5	7.0	-9.5	5.5	-8.0	3.5
	-26.0	19.5	-16.0	9.5	-14.0	7.0	-11.5	4.5
h_2^γ	-21.5	20.0	-12.0	10.0	- 9.5	8.0	-7.0	6.0
	-26.0	30.0	-13.0	18.0	-10.0	15.0	- 7.5	12.0
h_3^γ	-17.0	17.0	-9.0	9.0	-7.5	7.5	-5.5	5.5
	-22.5	22.5	-12.0	12.0	-10.0	10.0	-7.0	7.0
h_4^γ	-20.5	20.5	-11.0	11.0	-8.5	8.5	-6.0	6.0
	-27.5	27.5	-14.5	14.5	-12.0	12.0	-8.5	8.5

Table 1: *Axial and correlated limits for the $Z\gamma\gamma$ anomalous couplings at HERA with different integrated luminosities and 95% CL.*

For the first value it was assumed that only one anomalous coupling contributes ('axial limits') and for the second there are two couplings contributing ('correlated limits'). Our results are summarized in Table 1.

The origin of so poor results is the fact that, unlike diboson production at hadron or e^+e^- colliders, the anomalous diagrams of $ep \to e\gamma X$ have a Z propagator decreasing their effect. The process $ep \to eZX$ avoids this problem thanks to the absence of these propagators: the Standard Model cross section is similar to the anomalous one but, as a drawback, they are of the order of femtobarns.

5 Summary and conclusions

The radiative neutral current process $ep \to e\gamma X$ at HERA has been studied. Realistic cuts have been applied in order to observe a clean signal consisting of detectable and well separated electron, photon and jet.

The possibility of testing the trilinear neutral gauge boson couplings in this process has also been explored. The $Z\gamma Z$ couplings are very suppressed by two Z propagators. Only the $Z\gamma\gamma$ couplings have been considered. A Monte Carlo program has been developed to account for such anomalous vertex and further cuts have been implemented to improve the sensitivity to this source of new physics. Our estimates are based on total cross sections since the expected number of events is so small that a distribution analysis is not possible. The distributions just helped us to find the optimum cuts. Unfortunately, competitive bounds on these anomalous couplings cannot be achieved at HERA, even with the future luminosity upgrades.[3] As a counterpart, a different kinematical region is explored, in which the form factors can be neglected.

Acknowledgements

One of us (J.I.) would like to thank the Workshop organizers for financial support and very especially the electroweak working group conveners and the Group from Madrid at ZEUS for hospitality and useful conversations. This work has been partially supported by the CICYT and the European Commission under contract CHRX-CT-92-0004.

References

[1] D. Schaile: in *Proceedings of the 27th International Conference on High Energy Physics*, Glasgow, Scotland, 1994, edited by P.J. Bussey and I.G. Knowles (IOP, London, 1995), p. 27.

[2] H. Aihara et al.: FERMILAB-PUB-95/031, to be published in "Electroweak Symmetry Breaking and Beyond the Standard Model", eds. T. Barklow, S. Dawson, H. Haber and J. Seigrist.

[3] S.M. Errede: in *Proc. of the 27th International Conference on High Energy Physics*, Glasgow, Scotland, 1994, edited by P.J. Bussey and I.G. Knowles (IOP, London, 1995), p. 433.

[4] G. Gounaris, J.-L. Kneur and D. Zeppenfeld: in *Report of the Workshop on Physics at LEP2*, CERN 96-01, p. 525.

[5] V. Noyes et al.: in these Proceedings.

[6] T. Helbig and H. Spiesberger: *Nucl. Phys.* **B373** (1992) 73.

[7] F. Cornet and J.I. Illana: *Phys. Rev. Lett.* **67** (1991) 1705.

[3] We would like to apologize for the optimistic but incorrect results that were presented at the workshop due to a regrettable and unlucky mistake in our programs.

[8] F.T. Brandt et al.: *Phys. Rev.* **D50** (1994) 5591;
S.Y. Choi and F. Schrempp: in *Proc. of the Workshop on e^+e^- collisions at 500 GeV: The Physics Potential*, Munich, Annecy, Hamburg, 1991, edited by P. Zerwas, DESY 92-123B (Hamburg, 1992), p. 795.

[9] U. Baur and E.L. Berger: *Phys. Rev.* **D47** (1993) 4889.

[10] F. Abe et al.: *Phys. Rev. Lett.* **74** (1995) 1941.

[11] S. Abachi et al.: *Phys. Rev. Lett.* **75** (1995) 1028.

[12] M. Aciarri et al.: *Phys. Lett.* **B346** (1995) 190.

[13] F. Boudjema et al.: *Phys. Rev.* **D43** (1991) 3683;
F. Boudjema: in *Proc. of the Workshop on e^+e^- collisions at 500 GeV: The Physics Potential*, Munich, Annecy, Hamburg, 1991, edited by P. Zerwas, DESY 93-123B (Hamburg, 1993), p. 757.

[14] F. Cornet: in *Proc. of the Workshop on e^+e^- collisions at 500 GeV: The Physics Potential*, Munnich, Annecy, Hamburg, 1991, edited by P. Zerwas, DESY 93-123C (Hamburg, 1993), p. 229;
S.Y. Choi: *Z. Phys.* **C68** (1995) 163.

[15] K. Hagiwara et al.: *Nucl. Phys.* **B282** (1987) 253.

[16] A. Barroso et al: *Z. Phys.* **C28** (1985) 149.

[17] M. Suzuki: *Phys. Lett.* **B153** (1985) 289;
T.G. Rizzo and M.A. Samuel: *Phys. Rev.* **D35** (1987) 403.

[18] J.M. Cornwall, D.N. Levin and G. Tiktopoulos: *Phys. Rev. Lett.* **30** (1973) 1268; *Phys. Rev.* **D10** (1974) 1145;
C.H. Lewellyn Smith: *Phys. Lett.* **46B** (1971) 233.

[19] G.J. Gounaris, F.M. Renard and G. Tsirogoti: *Phys. Lett.* **B338** (1994) 51; *Phys. Lett.* **B350** (1995) 212.

[20] G.P. Lepage: *Jour. Comp. Phys.* **27** (1978) 192.

[21] S.D. Ellis, R. Kleiss and W.J. Stirling: *RAMBO* fortran subroutine for phase space generation.

[22] H. Murayama, I. Watanabe and K. Hagiwara: *HELAS: HELicity Amplitude Subroutines for Feynman Diagram Evaluations*, KEK Report 91-11, January 1992;
T. Stelzer and W.F. Long: *Comput. Phys. Commun.* **81** (1994) 357.

[23] J. Vermaseren: *FORM User's Guide*, Nikhef Amsterdam, 1990.

[24] Particle Data Group: *Phys. Rev.* **D54** (1996) 1.

[25] D.W. Duke, J.F. Owens: *Phys. Rev.* **D30** (1984) 45.

[26] A.D. Martin, R.G. Roberts, W.J. Stirling: *Phys. Rev.* **D51** (1995) 4756.

Standard-Model Higgs-Boson Production at HERA

Bernd A. Kniehl[ab]

[a] Max-Planck-Institut für Physik (Werner-Heisenberg-Institut), Föhringer Ring 6, 80805 Munich, Germany
[b] Institut für Theoretische Physik, Ludwig-Maximilians-Universität, Theresienstraße 37, 80333 Munich, Germany

Abstract: We assess the prospects of producing the Higgs boson of the minimal standard model at HERA and possible upgrades.

In this contribution, we discuss how the prospects of producing standard-model (SM) Higgs bosons at HERA may be ameliorated by upgrading the luminosity and/or proton energy. Higgs-boson search strategies in physics scenarios beyond the SM such as two-Higgs-doublet models are reported elsewhere in these proceedings [1]. At present, the experimental lower bound on the mass of the SM Higgs boson is $M_H = 65.2$ GeV at the 95% confidence level [2]. The discovery potential of LEP 2, with CM energy $\sqrt{s} = 192$ GeV and luminosity $L = 150$ pb^{-1} per experiment, will reach up to $M_H \approx 95$ GeV [3]. Roughly nine out of ten SM Higgs boson in the low mass range will decay into $b\bar{b}$ pairs [4], so that there will be a large irreducible background at HERA.

The possible production mechanisms of the SM Higgs boson at HERA under nominal conditions were already discussed in the 1987 proceedings [5]. W^+W^- and ZZ fusion, where the intermediate bosons are radiated from a quark inside the proton and from the lepton, are the most copious sources of SM Higgs bosons [6]. In the case of W^+W^- fusion, only four quark flavours contribute, namely $u, \bar{d}, \bar{s}, c$ for e^-p scattering and $\bar{u}, d, s, \bar{c}$ for e^+p scattering. In the mass range 65 GeV $< M_H <$ 100 GeV, the cross section of W^+W^- fusion in e^+p scattering is approximately four times smaller than the one in e^-p scattering. In the case of ZZ fusion, ten quark flavours $(u, \bar{u}, \ldots, b, \bar{b})$ are active, and the e^-p and e^+p cross sections are identical. The cross section of ZZ fusion is approximately eight times smaller than the e^-p cross section of W^+W^- fusion, due to propagator and coupling suppression. The contribution from NC DIS where a charm or bottom quark is hit inside the proton and radiates a Higgs boson is less than 10% of the ZZ-fusion cross section [5] and will be neglected in the following. In Fig. 1, the total cross sections of $e^-p \to H+X$ via W^+W^- and ZZ fusion and their sum are shown as a function of M_H, assuming $E_e = 30$ GeV and $E_p = 820$ GeV. The calculation is performed to lowest order using the CTEQ4L [7] parton density functions of the proton. The next-to-leading-order QCD corrections are known to be modest [8]. For $M_H > 65$ GeV, the combined cross section is below 6 fb, corresponding to less than 1.5 (6) signal events if $L = 250$ pb^{-1} (1 fb^{-1}). For 65 GeV $< M_H <$ 100 GeV, the combined cross section is increased by 48–74% if the proton energy is upgraded to be $E_p = 1$ TeV.

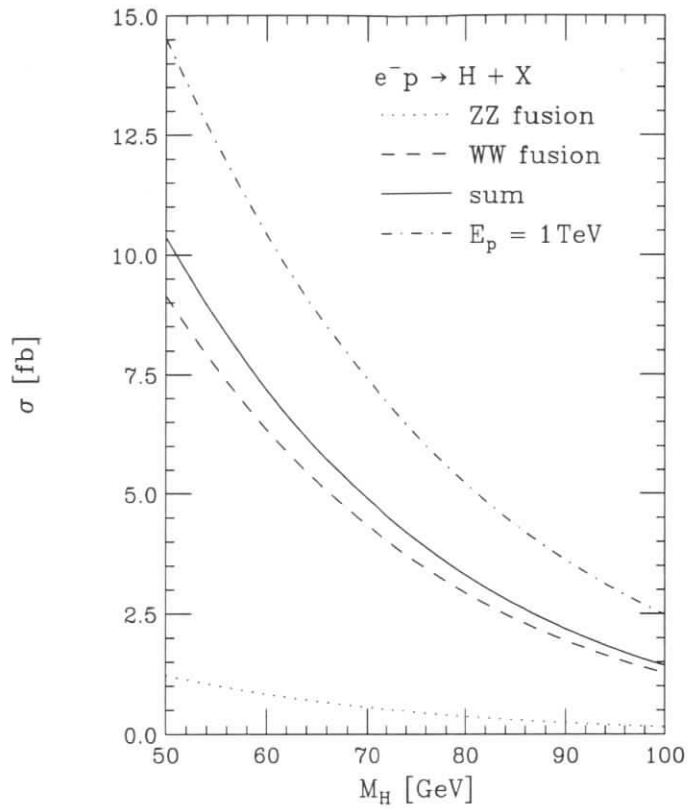

Figure 1: *Total cross sections of $e^-p \to H+X$ via W^+W^- and ZZ fusion and their sum under nominal HERA conditions. For comparison, the sum is also shown for $E_p = 1$ TeV.*

Alternative mechanisms of SM Higgs-boson production include: (i) $c\bar{c}$ or $b\bar{b}$ production via γg fusion with subsequent radiation of a Higgs boson off the heavy-quark line [9]; (ii) gg fusion (via a top-quark triangle) [10] where one of the gluons originates from a resolved quasi-real photon radiated off the incoming electron or positron; (iii) $\gamma\gamma$ fusion (via W-boson and top-quark loops) [11] with elastic [12] or inelastic [13] photon emission off the proton. In the kinematic regime of interest at HERA, the cross sections of these processes are more than two orders of magnitude smaller than the one of ZZ fusion [14].

In conclusion, should there be a low-mass SM Higgs boson, with 65 GeV $< M_H <$ 100 GeV, its production cross section at HERA will be below 6 (9) fb for $E_p = 820$ GeV (1 TeV). It is therefore unlikely that a signal can be established in the $b\bar{b}$ channel, even if the luminosity and/or proton energy are upgraded. As for SM Higgs production, there is no way how HERA can compete with LEP 2.

References

[1] M. Krawczyk, in the report by the working group on *Physics Beyond the Standard Model*; see also A.C. Bawa and M. Krawczyk, Phys. Lett. B357 (1995) 637.

[2] J.-F. Grivaz, in *Proceedings of the International Europhysics Conference on High Energy Physics*, Brussels, Belgium, July 27–August 2, 1995, to appear.

[3] M. Carena, P.M. Zerwas et al., in *Physics at LEP2*, edited by G. Altarelli, T. Sjostrand and F. Zwirner, CERN Yellow Report No. 96–01, Vol. 1 (February 1996) p. 351.

[4] E. Gross, B.A. Kniehl and G. Wolf, Z. Phys. C63 (1994) 417; C66 (1995) 321 (E); A. Djouadi, M. Spira and P.M. Zerwas, Z. Phys. C70 (1996) 427.

[5] K.J.F. Gaemers, R.M. Godbole and M. van der Horst, in *Proceedings of the HERA Workshop*, edited by R.D. Peccei, Hamburg, October 12–14, 1987, Vol. 2, p. 739.

[6] S. Midorikawa and M. Yoshimura, Nucl. Phys. B162 (1980) 365; Z. Hioki, S. Midorikawa and H. Nishiura, Prog. Theor. Phys. 69 (1983) 1484; D.A. Dicus and S.S.D. Willenbrock, Phys. Rev. D32 (1985) 1642; G. Altarelli, B. Mele and F. Pitolli, Nucl. Phys. B287 (1987) 205; B.A. Kniehl, Z. Phys. C55 (1992) 605.

[7] H.L. Lai, J. Huston, S. Kuhlmann, F. Olness, J. Owens, D. Soper, W.K. Tung and H. Weerts, MSU Report No. MSUHEP-60426, CTEQ-604 and hep-ph/9606399 (June 1996).

[8] J. Lindfors, Phys. Lett. 167B (1986) 471; T. Han, G. Valencia and S. Willenbrock, Phys. Rev. Lett. 69 (1992) 3274; J. Blümlein, G.J. van Oldenborgh and R. Rückl, Nucl. Phys. B395 (1993) 35.

[9] B. Grzadkowski, S. Pokorski and J. Rosiek, Phys. Lett. B272 (1991) 143; G.A. Leil and S. Moretti, Phys. Rev. D53 (1996) 163.

[10] H.M. Georgi, S.L. Glashow, M.E. Machacek and D.V. Nanopoulos, Phys. Rev. Lett. 40 (1978) 692.

[11] R. Bates and J.N. Ng, Phys. Rev. D33 (1986) 657; J.F. Gunion and H.E. Haber, Phys. Rev. D48 (1993) 5109.

[12] B.A. Kniehl, Phys. Lett. B254 (1991) 267.

[13] M. Glück, M. Stratmann and W. Vogelsang, Phys. Lett. B343 (1995) 399.

[14] M. Krawczyk, private communication.

Lepton Beam Polarisation at HERA

F. Zetsche

II. Institut für Experimentalphysik, Universität Hamburg, Germany

Abstract: Longitudinally polarised electron and positron beams enhance the physics potential of the HERA experiments considerably. In this report status and prospects of the production and the measurement of lepton beam polarisation at HERA will be summarised. Polarisation values of 70 % with relative uncertainties of 2 % seem to be feasable and match the requirements for physics measurements. The use of predominantly left and right handed electron beams to measure the polarisation deper dence of the charged current cross section, $\sigma(ep \to \nu X)$, is shortly discussed.

1 Introduction

The HERA electron storage ring is operated at a beam energy of 27.5 GeV with typical initial beam currents of 30–40 mA in about 180 bunches. In storage rings electrons become transversely polarised through the emission of synchrotron radiation which is known as the Sokolov-Ternov effect [1]. After the build-up (characteristic time is about 20 minutes at HERA) the polarisation asymptotically settles at an equilibrium value. The degree of polarisation which can be reached is governed by the strength of counteracting depolarising effects which strongly depend on the parameters of the storage ring. The theoretical maximum is 92.4 %. Longitudinal polarisation at an experimental interaction point in a straight section of the ring can then be achieved by the introduction of a pair of spin rotators. This means that the polarisation of the lepton beam is transverse around the ring except at the interaction points equipped with spin rotators. The presence of spin rotators reduces the theoretically achievable polarisation by about 3 % per pair [2]. Since 1994 one pair of spin rotators is installed around the East (HERMES) interaction point. Probably in the HERA shutdown 1997/98 the H1 and ZEUS interaction regions will also be equipped with spin rotators.

2 Measurement and Optimisation of Polarisation

The polarimeter at the HERA electron ring is located in the West Hall and measures the transverse polarisation of the lepton beam [3]. It employs the spin dependent Compton scattering of polarised laser light off the electrons. The most important components are a 10 W continuous argon ion laser and the associated laser beam optics, a calorimeter which measures energy and position of the Compton photons, and a fast data acquisition system. It is the difference in the Compton cross sections for left and right circularly polarised laser light which is exploited for

the electron polarisation measurement. It results in an azimuthal asymmetry of the backscattered photons which also depends on their energy. These quantities are measured with the help of the tungsten-scintillator sandwich calorimeter which is split in an upper and a lower half.

Transverse electron polarisation close to 70 % and longitudinal electron polarisation up to 65 % with one pair of spin rotators installed around the East (HERMES) interaction point has been produced in HERA during special polarisation runs [4, 5]. During 1995 when HERA routinely delivered polarised lepton beams the average asymptotic polarisation value was about 55 %.

With a systematic optimization of machine parameters one can hope to increase the degree of polarisation up to 70 % or even beyond for routine operation. Especially the promising technique of beam-based alignment for the quadrupole magnets has not fully been exploited yet. Since the spin matching procedure for the spin rotators has been proven to work excellently the insertion of two additional pairs of spin rotators for H1 and ZEUS should at most lead to a small decrease — if at all — of the degree of polarisation. Thus a polarisation value of 70 % can be considered a feasable number for physics measurements. This number applies to both electrons and positrons since there are no principal differences for polarisation build-up phenomena.

For typical beam conditions the relative statistical error of the polarisation measurement, $\delta P/P_{\text{stat.}}$, is well below 1 % when averaging the data for e.g. 15 minutes. The most important systematic error is the calibration of the polarisation scale. The assumed polarisation scale which initially was derived from Monte Carlo simulations has been verified within ± 5 % by various cross checks on the data. A direct determination of the polarisation scale is possible by measuring precisely the build-up of the polarisation at the beginning of a fill or after artificial depolarisation. The fitted characteristic rise time then fixes the expected asymptotic polarisation value and therefore the scale [6]. In principal this method is easy to apply. However in order to get meaningful and precise results one needs to have very stable and reproducable conditions for both the HERA machine and the polarimeter itself. Preliminary results from a limited number of rise time measurements suggest that at the moment the polarisation scale is known to ± 3.2 % [7] which leads together with other minor sources to a systematic error $\delta P/P_{\text{syst.}}$ of about 4 %.

Possible improvements on the determination of the polarisation scale are expected with a larger and more consistent set of risetime measurements to be done this year. With partial depolarisation of the beam it will be possible to better control the stability of machine and polarimeter. Further improvements can be done when the HERMES longitudinal polarimeter will be in operation. This polarimeter measures directly the longitudinal beam polarisation at the HERMES interaction point [8] and cross checks between both polarimeters become possible.

Compton polarimeters are also in operation at LEP and at SLC. After some years of operation for physics measurements at SLD the SLC polarimeter group has reached a relative systematic error $\delta P/P_{\text{syst.}}$ of less than 1 % [9]. The CERN group reports a substantially larger uncertainty on the polarisation scale, but no big effort has been made to reduce this value yet. Thus, with the technique of Compton polarimeters it seems possible to measure the beam polarisation of high energetic electron beams to a precision in the order of 1 %.

3 New Longitudinal Polarimeters

For the collider experiments H1 and ZEUS there exists an additional possibility to measure the longitudinal beam polarisation directly at their interaction point [10]: This scheme exploits the fact that bremsstrahlung from longitudinally polarised electrons is circularly polarised, the degree of polarisation depending on the relative energy transfer y from the electron to the photon. The task is to measure the circular polarisation of the bremsstrahlung photons, P_γ^C, and the quantity y. Then the longitudinal electron polarisation P_e^L can be deduced from

$$P_e^L = P_\gamma^C \frac{4(1-y)+3y^2}{y(4-y)}. \tag{1}$$

For large values of y it follows that $P_e^L \approx P_\gamma^C$. The measurement of P_γ^C is very demanding and involves special crystals for conversion of circular to linear photon polarisation and the subsequent absorption of the photons. The photon absorption depends strongly on the orientation of the crystal axis which must be varied during the measurement. The tagging of high y photons can be done with existing electron detectors close to the beam pipe.

It has been estimated that with this technique a precision of 2 % for the polarisation measurement can be achieved. Therefore this would be a nice cross check for the conventional polarisation measurement of the lepton beam.

4 Limits on Right Handed Charged Current Cross Section

An obvious measurement with polarised lepton beams concerns the polarisation dependence of the cross section for the charged current (CC) reaction, $\sigma(ep \to \nu X)$, which is governed by the exchange of W-bosons. In the standard model it is – for electrons – given by

$$\left.\frac{d^2\sigma}{dxdQ^2}\right|_{CC} = [1-P]\frac{G_\mu^2}{2\pi}\left[\frac{M_W^2}{Q^2+M_W^2}\right]^2 \left\{u + c + (1-y)^2\left(\bar{d}+\bar{s}+\bar{b}\right)\right\}. \tag{2}$$

For a definition of the variables refer to [11]. Here we are interested in the polarisation dependent factor $(1-P)$, where P is the degree of longitudinal polarisation and $P=-1$ denotes a fully left handed (i.e. negative helicity) electron beam. Since in the standard model only left handed weak charged currents exist the cross section vanishes for purely right handed electrons ($P=+1$).

A cross section measurement at electron polarisations of $P=-0.7,\ 0,\ +0.7$ could demonstrate the expected polarisation dependence and would give limits for the right handed charged current cross section ($P=+1$). In this study a cross section measurement for $Q^2 > 200\,\text{GeV}^2$ has been assumed with realistic detector acceptance and efficiency values as given in [12]. The possible outcome of such an experiment is given in figure 1. The insert shows the polarisation dependence of the cross section whereas the main plot shows the statistical precision of the extrapolation to the purely right handed charged current cross section at $P=+1$. Depending on the total luminosity and on the distribution to the three different polarisation states the statistical precision for experimental limits on the right handed CC cross section σ_R^{CC} vary between 0.3 % and 1 % of the left handed CC cross section σ_L^{CC}. Including systematic effects

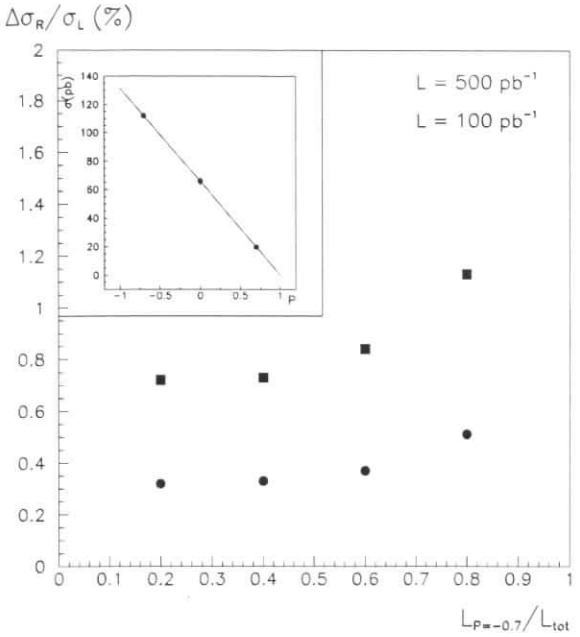

Figure 1: *Limit on the right handed CC cross section normalised to the left handed CC cross section as a function of the luminosity distribution to the different polarisation states ($P = -0.7,\ 0.7$). Shown are the limits based on statistics only for 2 different total luminosities. The insert shows the expected polarisation dependence of the CC cross section.*

(main contributions come from uncertainties in the background substraction for charged current reactions and knowledge of the polarisation scale) these numbers roughly double. At the end a cross section limit of $\sigma_R^{CC}/\sigma_L^{CC} < 0.02$ (95 % C. L.) assuming a total integrated luminosity of 500 pb^{-1} seems to be feasable.

A non-vanishing right handed CC cross section would signal the existence of a right handed W-boson, W_R, and upper limits for the right handed CC cross section can be converted to lower limits on the mass of such a hypothetical right handed W-boson. However these limits heavily depend on the models in which the W_R is incorporated. Some of these models have been already investigated in the Electroweak Working Group of the 1991 HERA Workshop. Rough lower limits for the mass of a hypothetical right handed W-boson of about 300 GeV can be inferred. This is much lower than limits placed recently from $p\bar{p}$ experiments at the Fermilab collider.

5 Conclusion

Currently HERA routinely delivers electron beam polarisation of 50–60 % which can be measured with an uncertainty of $\delta P/P = 4\,\%$. In the course of the year this precision is expected to improve to 2–3 % with the help of more calibration runs and cross checks with the HERMES longitudinal polarimeter. In the long run it may be possible to get close to a 1 % precision

as obtained at SLC. Longitudinal polarimeters for H1 and ZEUS can also be installed using existing luminosity detectors systems. The technique of these devices would be interesting in its own, but also their precision is likely to cope with the more conventional polarimeters. The measurement of the polarisation dependence of the charged current (CC) cross section can be extrapolated to an upper limit for the right handed CC cross section. A cross section limit of $\sigma_R^{CC}/\sigma_L^{CC} < 0.02$ (95 % C. L.) assuming a total integrated luminosity of 500 pb^{-1} seems to be feasable. Corresponing limits for the mass of a hypothetical right handed W-boson depend on the model considered and are of the order of 300 GeV.

References

[1] A. A. Sokolov and I. M. Ternov, Sov. Phys. Doklady **8** (1964) 1203.

[2] J. Buon and K. Steffen, *HERA Variable-Energy Mini Spin Rotator and Head-On ep Collision Scheme with Choice of Electron Helicity*, Nucl. Inst. and Meth. **A 245** (1986) 248.

[3] D. P. Barber et al., *The HERA Polarimeter and the First Observation of Electron Spin Polarization at HERA*, Nucl. Inst. and Meth. **A 329** (1993) 79.

[4] D. P. Barber et al., *High Spin Polarisation at the HERA Electron Storage Ring*, Nucl. Inst. and Meth. **A 338** (1994) 166.

[5] D. P. Barber et al., *The First Achievement of Longitudinal Spin Polarization in a High Energy Electron Storage Ring*, Phys. Lett. **B 343** (1995) 436.

[6] F. Zetsche, *Experience with the Fast Polarimeter at HERA*, Proc. of High Energy Spin Conference '94, Bloomington, Indiana, AIP Conference Proceedings 343, ed. K. J. Heller, S. L. Smith (1995).

[7] HERA Polarisation Group, *Interim Report on the Measurement of the Positron Beam Polarisation in 1995*, Internal Note (1996).

[8] HERMES Collaboration; W. Lorenzon et al., *A Proposal to DESY for a Longitudinal Electron Polarimeter at HERA-EAST Section*, (1995).

[9] C. Y. Prescott, *Physics Results with Polarized Electrons at SLAC*, SLAC-PUB-6998 (1996).

[10] K. Piotrzkowski, *Measurement of the Longitudinal Polarization of the HERA Electron Beam Using Crystals and the ZEUS Luminosity Monitor*, DESY 95-237 (1995), and references therein.

[11] R. Cashmore et al., in this working group report.

[12] ZEUS Collaboration; M. Derrick et al., *Study of Charged Current ep Interaction at $Q^2 > 200\ GeV^2$ with the ZEUS Detector at HERA*, DESY 96-104 (1996).

EPRC: A Program Package for Electroweak Physics at HERA

H. Spiesberger[1]

Max-Planck-Institut für Physik, Werner-Heisenberg-Institut, Föhringer Ring 6, D-80805 München, FRG

Abstract: I describe a collection of programs and subroutines for the calculation of cross sections for neutral and charged current deep inelastic lepton proton scattering at HERA including electroweak radiative corrections.

1 Introduction

The program package EPRC is the result of a development which started in 1986 with the calculation of the complete electroweak radiative corrections for deep inelastic electron proton scattering at HERA [1]. It was used during several workshops on HERA physics [2, 3] and continuously improved according to requests from many users. Major modifications have led to the development of the program `eprc93.f` which was used for the calculations published in [4]. Extensive use of this package also during the present workshop seems to justify the publication of a short description of it in these proceedings.

The purpose of EPRC is to assist in studies focussing on electroweak physics at HERA which do not require to rely on predictions which take into account QED and QCD higher-order effects in a most sophisticated way. Programs in EPRC either do not take into account purely photonic corrections or they take them into account in the leading logarithmic approximation. A separation of $O(\alpha)$ corrections into purely photonic and purely weak contributions is sensible for two reasons: First, QED corrections are very sensitive to kinematical cuts and details of the experimental selection criteria; therefore these corrections are usually applied directly to the data. Second, the cross section including purely weak corrections is sufficient to study the dependence on parameters of the electroweak standard model. Therefore the programs of EPRC have proved valuable tools in studying the sensitivity of deep inelastic scattering cross sections on standard model parameters and on neutral current couplings of quarks [5].

For a confrontation of experimental data with theoretical predictions, QED corrections are indispensable. The Monte Carlo event generator HERACLES [6] is a flexible tool which can be used for this purpose. Concerning the purely weak radiative corrections of order $O(\alpha)$, EPRC and HERACLES take into account the same physics; EPRC provides a few additional features with respect to higher-order corrections of order $O(\alpha^2)$. Studies of higher-order QCD effects can be performed with the help of DJANGO6 [7] which interfaces HERACLES to LEPTO [8]; moreover, there is a large number of special purpose programs suited for the investigation of QCD phenomena.

[1]e-mail: `hspiesb@mail.desy.de`

2 Standard Model Predictions for Deep Inelastic Scattering

2.1 Lowest Order Cross Sections

Deep inelastic scattering of electrons or positrons off protons

$$e(l) + p(p) \to e'(l') + X(p_X), \tag{1}$$

with $e' = e$ for neutral current scattering (NC) and $e' = \nu_e$ ($\bar{\nu}_e$) for charged current scattering (CC) (particle momenta are given in parentheses) is usually described by the following set of kinematic variables

$$Q^2 = -(l-l')^2, \quad s = (l+p)^2, \quad x = \frac{Q^2}{2p\cdot(l-l')}, \quad y = \frac{Q^2}{xs}. \tag{2}$$

In the region of large x and Q^2 where the contribution of the longitudinal structure function F_L and proton mass effects can be neglected, the differential cross section for the neutral current process for left-handed (L) and right-handed (R) polarized electrons is given by

$$\frac{d^2\sigma^{NC}}{dx\,dQ^2}(e^-_{L,R}) = \frac{2\pi\alpha^2}{xQ^4}\left[\left(1+(1-y)^2\right)F_2^{L,R} + \left(1-(1-y)^2\right)xF_3^{L,R}\right]. \tag{3}$$

For positron scattering one has to replace $F_3^{L,R} \to -F_3^{R,L}$ and cross sections for beams with an arbitrary degree of longitudinal polarization P can be obtained by calculating the appropriate average of the cross sections for left- and right-handed leptons. In the quark-parton model, the structure functions are expressed in terms of quark (q) and antiquark ($\bar{q}$) distribution functions:

$$\begin{aligned} F_2^{L,R} &= \sum_q [xq(x,Q^2) + x\bar{q}(x,Q^2)]\cdot A_q^{L,R}, \\ xF_3^{L,R} &= \sum_q [xq(x,Q^2) - x\bar{q}(x,Q^2)]\cdot B_q^{L,R}. \end{aligned} \tag{4}$$

By using Q^2-dependent parton distribution functions, QCD corrections are taken into account automatically in the leading-logarithmic approximation. The coefficients $A_q^{L,R}$ and $B_q^{L,R}$ contain coupling constants and propagators corresponding to photon and Z-boson exchange ($L \leftrightarrow +$, $R \leftrightarrow -$):

$$\begin{aligned} A_q^{L,R} &= Q_q^2 + 2Q_eQ_q(v_e \pm a_e)v_q\chi_Z + (v_e \pm a_e)^2(v_q^2+a_q^2)(\chi_Z)^2, \\ B_q^{L,R} &= \pm 2Q_eQ_q(v_e \pm a_e)a_q\chi_Z \pm 2(v_e \pm a_e)^2v_qa_q(\chi_Z)^2, \end{aligned} \tag{5}$$

with

$$\chi_Z = N_Z^{(0)}\frac{Q^2}{Q^2+m_Z^2} \tag{6}$$

and a normalization constant $N_Z^{(0)}$ which, in lowest order, can be expressed either with the help of the weak mixing angle or with the help of the μ decay constant, G_μ:

$$N_Z^{(0)} = \frac{1}{4s_W^2c_W^2} = \frac{\sqrt{2}G_\mu m_Z^2}{4\pi\alpha}. \tag{7}$$

In the standard model, the couplings of the fermions to the bosons are given by the electric charge (in units of e) for the photon exchange and, for the Z-boson exchange, by ($f = e, q$)

$$a_f = I_3^f, \qquad v_f = I_3^f - 2Q_f \sin^2\theta_W \tag{8}$$

where Q_f and I_3^f denote the charge and the third component of the weak isospin of the fermion f. In the standard model with a Higgs doublet, the mixing angle is related to the vector boson masses by

$$\sin^2\theta_W = s_W^2 = 1 - \frac{m_W^2}{m_Z^2}. \tag{9}$$

In a similar way one can write for the charged current differential cross section

$$\frac{d^2\sigma^{CC}}{dx\,dQ^2}(e^-) = (1-P)\pi\alpha^2\left(N_W^{(0)}\right)^2 \cdot \frac{1}{(Q^2+m_W^2)^2}\left[u + c + (1-y)^2(\bar{d}+\bar{s})\right], \tag{10}$$

with, to lowest order,

$$N_W^{(0)} = \frac{1}{2s_W^2} = \frac{G_\mu m_W^2}{\sqrt{2}\pi\alpha}, \tag{11}$$

and P denoting the degree of left-handed longitudinal polarization ($P = -1$ for left-handed electrons, $P = 1$ for right-handed electrons). For positron scattering one has to replace $u + c \to \bar{u} + \bar{c}$ and $\bar{d} + \bar{s} \to d + s$ and adjust the sign of P.

2.2 Higher-Order Corrections

Since the program package EPRC is devoted to studies of electroweak physics at HERA, we do not discuss QED corrections which are large and indispensable, in particular for NC scattering at small x and large y. Purely photonic corrections have been discussed extensively in [9] where the interested reader will also find short descriptions of and references to programs for their calculation. QCD corrections are also not discussed here. They should, of course, be included in order to obtain reliable predictions.

The calculations of higher-order electroweak corrections to deep inelastic scattering at HERA have been reviewed in [9, 10] (see also references therein). They are performed in the on-shell scheme, where the gauge boson masses m_W and m_Z are treated symmetrically as basic parameters together with the top quark mass m_t and the Higgs mass m_H (besides the fine structure constant α and other fermion masses). Amplitudes are functions of these basic parameters.

According to this scheme, a natural way to fix the standard model parameters is to choose values for m_W, m_Z, besides m_t and m_H. In view of the fact that there is a high precision measurement of the μ-decay constant G_μ, it is, however, useful and customary to consider the situation where a value for m_W is derived from G_μ after fixing the other mass parameters. Accordingly, the normalization of the Z and W exchange amplitudes can be expressed in different ways as indicated in Eqs. (7) and (11). When taking into account the generic higher-order corrections to these amplitudes, one has also to take into account higher-order corrections to the μ-decay constant when switching from one prescription to the other in order to be consistent.

The corrections are collected in form factors that change the amplitudes in a simple form: the dressed photon-exchange amplitude can be written in the following way:

$$\mathcal{M}_\gamma = \frac{e^2}{1 - \hat{\Pi}_f^\gamma(Q^2)} \cdot \frac{1}{Q^2} \cdot Q_e\gamma_\mu \otimes Q_f\gamma^\mu. \tag{12}$$

$\hat{\Pi}_f^\gamma$ is the fermionic part of the photon vacuum polarization. Writing it in the denominator resums the leading logarithmic corrections according to the renormalization group equation and the first factor in Eq. (12) constitutes the running fine structure constant $\alpha_{em}(Q^2)$. $\hat{\Pi}_f^\gamma$ contains hadronic contributions taken into account by using a parametrization derived from data on the total hadronic cross section in e^+e^- annihilation [11]. Bosonic contributions to the vacuum polarization have to be combined with vertex and box corrections and are added as a separate correction term.

The weak one-loop corrections to the Z-exchange amplitude, $\mathcal{M}_Z$, for $eq \to eq$ can be expressed in terms of four weak form factors (ρ_{eq}, κ_e, κ_q, and κ_{eq}) in the following way, making use of dressed vector couplings:

$$\mathcal{M}_Z(\hat{s}, t^2) \sim \frac{\pi\alpha}{Q^2+m_Z^2} N_Z^{(1)}\Big[I_3^e I_3^q \gamma_\mu\gamma_5 \otimes \gamma_\mu\gamma_5 + \bar{v}_e I_3^q \gamma_\mu \otimes \gamma_\mu\gamma_5 + I_3^e \bar{v}_q \gamma_\mu\gamma_5 \otimes \gamma^\mu + \bar{v}_{eq}\gamma_\mu \otimes \gamma^\mu\Big], \tag{13}$$

$$\bar{v}_f = I_3^f\left[1 - 4|Q_f|s_W^2\,\kappa_f(\hat{s}, Q^2)\right], \quad f = e, q, \tag{14}$$

$$\bar{v}_{eq} = I_3^e\bar{v}_q + \bar{v}_e I_3^q - I_3^e I_3^q\left[1 - 16|Q_eQ_q|s_W^4\,\kappa_{eq}(\hat{s}, Q^2)\right], \tag{15}$$

with $\hat{s} = xs$ and s_W^2 from Eq. (9). The normalization of the Z-exchange amplitude is modified at $O(\alpha)$ by a form factor $\rho_{eq}(\hat{s}, Q^2)$:

$$N_Z^{(1)} = \frac{\sqrt{2}G_\mu m_Z^2}{4\pi\alpha}\rho_{eq}(\hat{s}, Q^2) = \frac{1}{4s_W^2c_W^2}\frac{\rho_{eq}(\hat{s}, Q^2)}{1 - \Delta r}. \tag{16}$$

The second form of the normalization factor is used when m_W and m_Z (and thus s_W^2) is given as input. It follows when using the G_μ constraint with consistent inclusion of radiative corrections to the μ decay:

$$G_\mu = \frac{\pi\alpha}{\sqrt{2}s_W^2m_W^2}\frac{1}{1 - \Delta r(\alpha, m_W, m_Z, m_H, m_t)} \tag{17}$$

In the Born approximation, $\rho = \kappa = 1$, and $\bar{v}_{eq} = v_e v_q$. The above parametrization has the form of a Born-like expression except that at the Born level there is no parallel for the coupling $\bar{v}_{eq}$. The axial-vector couplings can be kept in their form $a_f = I_3^f$ by absorbing corresponding vertex corrections into the normalization factor $\rho_{eq} = \rho_{eq}(\hat{s}, Q^2)$ which receives also contributions from self energies. The form factors κ_f and κ_{eq} combined with s_W^2 give rise to effective mixing angles which depend through the κ's on the fermion species and on the kinematic variables. The form factors can be separated into a universal part independent of the fermion species and a non-universal remainder term. The universal parts contain the dependence on the masses of the top quark and the Higgs boson. The dominating contribution to them is proportional to m_t^2 and with

$$\Delta\rho = \frac{3\alpha}{16\pi s_W^2c_W^2}\frac{m_t^2}{m_Z^2} \tag{18}$$

one has to one-loop precision

$$\rho_{eq} = 1 + \Delta\rho + \Delta\rho_{eq}^{rem}, \tag{19}$$

$$\kappa_f = 1 + \frac{c_W^2}{s_W^2}\Delta\rho + \Delta\kappa_f^{rem}. \tag{20}$$

Resummation of higher-order terms can be performed by the replacements

$$\rho_{eq} \to \frac{1 + \Delta\rho_{eq}^{rem}}{1 - \Delta\bar{\rho}}, \tag{21}$$

$$\kappa_f \to (1 + \Delta\kappa_f^{rem})\left(1 + \frac{c_W^2}{s_W^2}\Delta\bar{\rho}\right), \tag{22}$$

$$\kappa_{eq} \to (1 + \Delta\kappa_{eq}^{rem})\left(1 + \frac{c_W^2}{s_W^2}\Delta\bar{\rho}\right)^2. \tag{23}$$

Here, $\Delta\bar{\rho}$ contains irreducible two-loop contributions and is defined by

$$\Delta\bar{\rho} = 3\,\frac{G_\mu m_t^2}{8\pi^2\sqrt{2}} \cdot \left[1 + \frac{G_\mu m_t^2}{8\pi^2\sqrt{2}} \cdot r_2\right] + \Delta\rho^{\alpha\alpha_s}. \tag{24}$$

In our calculation we use for r_2 the result of [12] with the full two-loop m_H-dependence. The leading correction of $\mathcal{O}(\alpha\alpha_s)$ is given by

$$\Delta\rho^{\alpha\alpha_s} = -\Delta\rho\frac{\alpha_s(m_t^2)}{\pi} \cdot \frac{2}{3}\left(\frac{\pi^2}{3} + 1\right) \tag{25}$$

with $\Delta\rho$ from Eq. (18). To $O(\alpha)$, $\Delta\bar{\rho}$ is equal to $\Delta\rho$. The remainder terms (index rem) are the one-loop expressions with the corresponding leading m_t^2 terms subtracted. More details and references to the original literature can be found in [10].

It should be stressed that the form factors are functions of the kinematic variables x and Q^2 and depend on the fermion species. The x-dependence is due to box diagram contributions which also lead to $\rho_{eq} \neq \rho_{e\bar{q}}$. Since the measurement of deep inelastic cross sections covers a large range of x and Q^2, this dependence which is as large as the constant m_t^2 terms cannot be neglected if a precision of few percent is needed (LEP1 measurements are, in contrast to this, performed at a fixed $Q^2 = -m_Z^2$).

The W-exchange amplitude including higher-order contributions can be written in the following way:

$$\mathcal{M}_W(\hat{s}, Q^2) = \frac{\pi\alpha}{4}\, N_W^{(1)} \frac{1}{Q^2 + m_W^2}\, \gamma_\mu[1 - \gamma_5] \otimes \gamma^\mu[1 - \gamma_5] \tag{26}$$

with

$$N_W^{(1)} = \frac{G_\mu m_W^2}{\sqrt{2}\pi\alpha}\, \rho_{eq}^W(\hat{s}, Q^2) = \frac{1}{2s_W^2}\frac{\rho_{eq}^W(\hat{s}, Q^2)}{1 - \Delta r}. \tag{27}$$

Differently from the neutral current, only a single form factor ρ_{eq}^W (or $\rho_{e\bar{q}}^W$) for each parton scattering process is required to accommodate the higher-order contributions. In the representation with fixed G_μ, the weak radiative corrections are very small with very little dependence on m_t and m_H and we have

$$\rho_{eq}^W \equiv (\rho_{eq}^W)^{rem} \tag{28}$$

which deviates from 1 typically by a few permille.

3 Description of program elements

This section gives an overview over the programs contained in the package EPRC. The recommended part of this library is the program contained in `eprc93.f` which allows the calculation of total cross sections and includes the complete electroweak loop corrections as described in the previous section. Other programs are designed for the calculation of Born cross sections, of purely weak corrections, or of leptonic QED corrections in the leading logarithmic approximation (LLA) of order $O(\alpha)$ or $O(\alpha^2)$ [13]. For the charged current process, the program `epcctot.f` contains an option to include soft photon exponentiation. In addition there are programs for deep inelastic scattering with polarized leptons and protons and for radiative charged current scattering.

The programs contained in this dataset are based on analytic calculations or on numerical integration methods which do not need too much CPU-time. Monte Carlo methods are only partly used for numerical integration, but no Monte Carlo event generator is contained in this dataset. The programs `epnctot.f` and `epcctot.f` contain the complete photonic corrections. Their use is, however, not particularly recommended since they provide results for the twofold differential cross sections only and need a rather large amount of CPU-time while not always giving results with high numerical precision. These programs call subroutines using `REAL*16` variables which is not supported on many existing computers.

Further helpful information can be found in the files `aacommon.doc` (definition of common blocks used in the programs), `aapdfs.doc` (convention for calls of parton distribution functions, see below) and `aalpar.doc` (conventions and recommendations for the steering parameters `LPAR`, see section 4). Future modifications and updates (after 28 July 1991) will be announced in the file `aaupdate.doc`. Additional files not mentioned in this description exist in the package, containing programs for specific test purposes. They should be used only by experienced users. Some of the programs have to be linked with the CERN library or the NAG library (for integration routines) as indicated by a corresponding comment in the files.

1.) Born cross sections

`epncborn.f`	Lowest order cross section $d^2\sigma/dxdy$ for deep inelastic neutral current electron (positron) proton scattering at HERA.
`epccborn.f`	Lowest order cross section $d^2\sigma/dxdy$ for deep inelastic charged current electron (positron) proton scattering at HERA.
`epncasym.f`	Lowest order results for the polarization and charge asymmetries in NC DIS ep scattering at HERA for twofold differential cross sections $d^2\sigma/dxdy$.

2.) Weak corrections and improved Born cross sections

`formff.f`	Program for the calculation of Δr, the (universal) effective weak mixing angle and the running fine structure constant $\alpha(Q^2)$.
`epncweak.f`	The improved Born cross section for neutral current scattering, including weak loop corrections and vacuum polarization.
`epccweak.f`	The improved Born cross section for charged current scattering, including weak loop corrections, vacuum polarization and some remnant parts of QED corrections.

`eprc93.f` Stand-alone version of a program to calculate neutral and charged current total cross sections and their ratio as well as polarization and charge asymmetries. This program includes the complete weak loop corrections, but QED corrections only in the leading logarithmic approximation. It allows the inclusion of non-standard contributions to the gauge boson self energies (S, T, U parameters, for details see [4]). Cuts on x, y, Q^2 and p_T, determined by the momentum of the scattered lepton, are possible. A sample output is stored in the file `eprc93.dat`.

`eprc93q.f` Same as `eprc93.f`, but for the single-differential cross section $d\sigma/dQ^2$.

`eprc93xy.f` Same as `eprc93.f`, but for twofold differential cross sections $d^2\sigma/dxdy$.

`zncvs.f` Contains subroutines for the calculation of the Born cross section, soft bremsstrahlung and electroweak virtual corrections. Contains also the initialization subroutine `SETPAR`.

`zccvs.f` Contains the additional subroutines for Born cross section, soft bremsstrahlung, and virtual corrections for the charged current process.

3.) Leading-log programs

`epncllas.f` Leptonic corrections of order $O(\alpha)$ in the leading logarithmic approximation including complete electroweak one-loop corrections.

`epccllas.f` The same for the charged current.

`epncllа2.f` Program for the calculation of leptonic corrections of order $O(\alpha^2)$ in the leading logarithmic approximation [13].

`zeplla.f` Routines for the calculation of leading logarithmic corrections (leptonic legs) to one- and two-loop order and the corrected cross sections for NC and CC scattering.

4.) Total cross sections including hard bremsstrahlung

`epnctot.f` The total electroweak corrections for the neutral current cross section.

`epcctot.f` The total electroweak corrections for the charged current cross section. Only for electron scattering, but with the option to exponentiate soft-photon corrections.

`znchbst.f16` Contains routines for the calculation of hard bremsstrahlung contributions to the total corrections in neutral current scattering. These routines are needed in `epnctot.f`.

`zcchbst.f16` Contains routines for the calculation of hard bremsstrahlung contributions to the total corrections in charged current scattering. These routines are needed in `epcctot.f`.

5.) Integrated cross sections

`zsigint.f` Routines for the calculation of integrated cross sections for NC and CC scattering. Integration can be performed over kinematical ranges defined with the help of upper and lower cuts on x, y, Q^2 and p_T (the transverse momentum of the electron). Virtual corrections and the leptonic leading logarithmic corrections can be included.

`zpdfint.f` Routine to obtain integrated parton distributions.

`zaxohs.f` The AXO library for integration and event sampling containing a modified version of the integration routine `VEGAS`. Used in programs for total cross sections which take into account hard bremsstrahlung corrections.

6.) Parton distribution functions

`zpver.f` Interface for calls to parton distribution functions. The conventions for codes of the various parametrizations are described in `aapdfs.doc`.

`zpystfu.f` Parton distribution functions from `PYTHIA` [14].

`zpdmrsh.f` Parton distributions from Martin, Roberts and Stirling, set H [15].

`zpdmrsa.f` Parton distributions from Martin, Roberts and Stirling, set A [16].

`zpdgrv.f` Parton distributions from Glück, Reya, and Vogt [17].

`zpdgrv94.f` Parton distributions from Glück, Reya, and Vogt, 1994 update [18].

`zpdcteq3.f` Parton distributions from the CTeq collaboration, version 3 [19].

7.) Polarized electron nucleon scattering

`epasyp.f` The cross section for neutral current scattering with polarized electrons and protons including the complete $O(\alpha)$ electroweak and QED corrections. Some sample results are stored in the file `epasyout.dat`.

`epasyn.f` The same for neutron scattering.

`zncvsa.f` The same as `zncvs.f` extended to include the case of longitudinal proton polarization. Called from `epasyp.f` and `epasyn.f`.

`znchbsta.f16` The same as `znchbst.f16` extended to include the case of longitudinal proton polarization. Called from `epasyp.f` and `epasyn.f`.

`zpverap.f` Polarized parton distribution functions (up and down only) for the calculation of deep inelastic electron proton scattering with polarized protons and electrons. Values are obtained by linear interpolation on a grid of 100 values of x, no Q^2 dependence. Values on the grid points are read from a dataset allocated to unit number 23. These data points are stored in the file `epasyp.dat`. The numbers are from a fit to EMC data (obtained from A. Schäfer).

`zpveran.f` The same for neutron scattering. Needs input from file `epasyn.dat`.

8.) Radiative charged current scattering

`epccrad.f` A program for the caluclation of the cross section for radiative charged current scattering $ep \to \nu\gamma X$ including leptonic and quarkonic radiation and its interference. A lower limit on the photon energy is required. The present version is for electron scattering only. A detailed description of the program can be found in the file `aaccrad.doc`.

4 Description of Steering Parameters in EPRC

Most of the steering parameters `LPAR(*)` can be used to study separate contributions to weak one-loop corrections and various options to treat higher-order contributions. They are not options which should be freely used, rather for some of them only one specific choice is recommended or even meaningful. They should be changed with care. If not stated explicitly, a value of 0 means that the given effect is not taken into account. More details and recommendations than given here can be found in the file `aalpar.doc`.

`LPAR(1)`: =1: include Born cross section;
=0: used to calculate only one-loop corrections in the NC cross section.

`LPAR(2)`: =1: include one-loop corrections in NC and CC cross sections;
=0: no one-loop corrections.

`LPAR(3)`: =1: some higher-order corrections are included (soft photon exponentiation in CC, QED corrections applied to improved Born for NC).

`LPAR(4)`: = 0, 1: use fixed m_W,
≥ 2: determine m_W from muon decay constant G_μ;
= 0: normalize cross sections with the help of s_W^2 from m_W,
≥ 1: normalize cross sections with the help of G_μ;
= 3: include Δr in normalization of Z-exchange in NC 'Born' cross section.

`LPAR(5)`: ≥ 1: Δr including one- and leading two-loop contributions;
≥ 2: Δr including corrections of order α_s.

`LPAR(6)`: code for the parametrization of parton densities, see `aapdfs.doc`.

`LPAR(7)`: > 0: include vacuum polarization:
= 1: from quark loops with effective quark masses;
= 2: hadronic part from Burkhard's parametrization (second reference of [11]);
= 3: hadronic part from Jegerlehner's parametrization (first reference of [11]).

`LPAR(8)`: > 0: include photon-Z-mixing.

`LPAR(9)`: > 0: include Z self energy.

`LPAR(10)`: > 0: include W self energy.

`LPAR(11)`: = 0: no QED corrections,
≥ 1: include QED corrections.

`LPAR(12)`: > 0: include leptonic QED corrections.

`LPAR(13)`: > 0: include quarkonic QED corrections.

`LPAR(14)`: > 0: include lepton-quark interference (QED).

`LPAR(15)`: > 0: include weak loops.

`LPAR(16)`: > 0: include weak box diagrams.

`LPAR(17)`: photon and/or Z-exchange in NC scattering:
= 0: photon and Z-exchange;
= 1: only photon exchange;
= 2: only photon-Z interference;
= 3: only Z-exchange.

`LPAR(18)`: = 0: no QED corrections (recommended);
= 1: including QED corrections in the leading logarithmic approximation.

`LPAR(19)`: definition of x and y in LLA QED corrections:
= 1: x and y defined from scattered lepton momentum;
= 2: x and y defined from hadronic final state;
= 3: y defined from hadronic final state, Q^2 from scattered electron, $x = Q^2/(ys)$ ('mixed' variables);
= 4: y and Q^2 from Jaquet-Blondel method.

`LPAR(20)`: = 0: parton distributions with Q^2 as argument;
= 1: use fixed external value for Q^2 as argument in parton distributions (given by `FIXQ2E`, for test purposes only).

Acknowledgment

I thank S. Dagan, U. Katz and S. Riess for reporting problems and solutions during the installation of the program package on Unix workstations.

References

[1] M. Böhm and H. Spiesberger, Nucl. Phys. B294 (1987) 1081;
M. Böhm and H. Spiesberger, Nucl. Phys. B304 (1988) 749;
H. Spiesberger, Nucl. Phys. B349 (1991) 109.

[2] R. D. Peccei, Ed., Proceedings of the HERA workshop, Vol. 2, Hamburg, Oct. 12 - 14, 1987.

[3] W. Buchmüller and G. Ingelman, Eds., *Physics at HERA, Proceedings of the Workshop, Hamburg, Oct. 29 - 30, 1991*, Vol. 2 (Hamburg 1991).

[4] H. Spiesberger, in *Precision Tests of the Standard Model*, Advanced Series on Directions in High Energy Physics, World Scientific Publishing Co., Ed. P. Langacker, 1994.

[5] R. J. Cashmore et al., these proceedings;
R. Beyer et al., these proceedings.

[6] A. Kwiatkowski, H.-J. Möhring and H. Spiesberger, *HERACLES. An Event Generator for ep Interactions at HERA Energies Including Radiative Processes, Version 4.0*, Comp. Phys. Commun. 69 (1992) 155; and *HERACLES, Version 4.5*, unpublished.

[7] K. Charchuła, G. A. Schuler and H. Spiesberger, *DJANGO6, Version 1.0*, Comp. Phys. Commun. 81 (1994) 381; and *DJANGO6, Version 2.3*, unpublished.

[8] G. Ingelman, A. Edin and J. Rathsman, *LEPTO 6.5*, DESY 96-057 (1996).

[9] H. Spiesberger et al., in *HERA proceedings 1991* [3], Vol. 2, p. 798.

[10] W. Hollik et al., in *HERA proceedings 1991* [3], Vol. 2, p. 923.

[11] F. Jegerlehner, DESY 96-121, to appear in the *Proceedings of the Workshop "QCD and QED in Higher Orders*, Rheinsberg, Germany, 1996, Nucl. Phys. B (Proc. Suppl.);
H. Burkhardt, F. Jegerlehner, G. Penso and C. Verzegnassi, Z. Phys. C43 (1989) 497.

[12] R. Barbieri et al., Phys. Lett. B288 (1992) 95.

[13] J. Kripfganz, H.-J. Möhring and H. Spiesberger, Z. Phys. C49 (1991) 501.

[14] T. Sjostrand, PYTHIA, Version 5.7, Comp. Phys. Commun. 82 (1994) 74; and CERN-TH.7112/93.

[15] A. D. Martin, R. G. Roberts and W. J. Stirling, Proc. *Workshop on Quantum Field Theoretical Aspects of HE Physics*, Kyffhäusser, Germany, Eds. B. Geyer and E.-M. Ilgenfritz, Leipzig (1993), p. 11.

[16] A. D. Martin, R. G. Roberts and W. J. Stirling, Phys. Rev. D50 (1994) 6734.

[17] M. Glück, E. Reya, A. Vogt, Z. Phys. C53 (1992) 127.

[18] M. Glück, E. Reya, A. Vogt, Z. Phys. C67 (1995) 433.

[19] H. H. Lai et al., CTEQ Collaboration, Phys. Rev. D51 (1995) 4763.

Working Group on

Beyond the Standard Model

Conveners:

H. Dreiner (Rutherford), H.-U. Martyn (Aachen),
S. Ritz (Columbia), D. Wyler (Zürich University)

Participants:

J. Blümlein (DESY-Zeuthen), E. Boos (DESY-Zeuthen), M. Corradi (Bologna), M. David (Saclay), J. Gilmore (OSU), D. Graudenz (CERN), P. Haberl (Heidelberg), M. Krawczyk (Warsaw), A. Kryukov (DESY-Zeuthen), K. Meier (Heidelberg), O. Nachtmann (Heidelberg), R. Peccei (UCLA), E. Perez (Saclay), P. Schleper (Heidelberg), Y. Sirois (Ecole Polytechnique), F. Sciulli (Columbia), D. Stevens (Heidelberg), B. Straub (Columbia), L. Wai (Columbia), S. Yang(Columbia), P. Zerwas (DESY), K. Zuber (Dortmund)

Beyond the Standard Model — Working Group Reports:

BEYOND THE STANDARD MODEL GROUP SUMMARY

H. Dreiner[a], H.-U. Martyn[b], S. Ritz[c], D. Wyler[d]

[a] *Rutherford Appleton Laboratory, Chilton, Didcot, Oxon, UK*
[b] *I. Physikalisches Institute, RWTH Aachen, Germany*
[c] *Columbia University, New York, N.Y., U.S.A.*
[d] *Universität Zürich, Zürich, Switzerland*

Abstract: We summarize the work done in the group. Of the various proposed HERA upgrades, the luminosity improvement is the most important for this physics. With an integrated luminosity of 1 fb^{-1}, collected by 2005, HERA can remain a competitive and potentially fruitful facility for new physics searches.

1 Summary Statement

The goal of the workshop was to work out the implications for physics with the proposed upgrades to HERA. Since, by construction, the Beyond the Standard Model group must study highly speculative topics (most, if not all, known extensions to the Standard Model are certainly wrong), we studied whether potentially interesting physics could be made more accessible by the upgrades.

Of the proposed upgrades, the luminosity enhancement is *a priori* the most important for this physics. Without substantially enlarging the data set in relatively short periods of time, exotic physics searches stall. In addition, the competition from other facilities, in particular LEP and the Tevatron, is stiff. The results of our studies indicate that a luminosity upgrade is essential if the HERA program is to remain interesting and competitive in this area.

Since we are going beyond the Standard Model, the topics we studied may be organized by *how* far beyond the Standard Model they lie, as follows.

1.1 Higgses

We start by revisiting searches for Higgs bosons. Standard Model Higgs physics has been deemed hopeless at HERA, mainly due to the small production cross-section[1]. (With an integrated luminosity of 1 fb^{-1}, HERA might actually produce a few Standard Model Higgs bosons in currently allowed mass ranges, but isolating these few events from the background still looks hopeless.) Plausible non-standard Higgs sectors offer more possibilities. Many models, including the minimal SUSY extension to the Standard Model, include two Higgs doublets, generating five physical particle degrees of freedom: two neutral scalars (H^0 and h^0), a neutral

pseudoscalar (A), and two charged scalars ($H^\pm$); and introducing two parameters that modify the couplings: a mixing angle for the neutral scalars (α) and the ratio of the vacuum expectation values for the two doublets ($\tan\beta$). In Minimal SUSY these parameters are constrained to regions that keep these light Higgses out of HERA's reach, when taking the LEP bounds into account. However, there is good reason to look anyway. The LEP program is steadily eating away the remaining allowed regions and, SUSY aside, non-minimal Higgs sectors have been proposed as mechanisms for a wide variety of phenomena, *e.g.*, electroweak CP violation, the suppression of strong CP violation, and neutrino mass generation. Such a search is well-motivated.

Maria Krawczyk has studied the phenomenology of a general two-doublet model. She found that there are regions of (α, β) that are not ruled out by LEP, even for very light Higgs massless of a few GeV. Such Higgses *can* be produced at HERA via photoproduction. The resolved process, $gg \to h$, results in a $b\bar{b}$ final state (or a $\tau^+\tau^-$ final state for very light h), while the direct process $\gamma g \to b\bar{b}h$ results in an enticing four-b final state (or a $b\bar{b}\tau^+\tau^-$ final state for very light h). The success of these searches will depend on how well the signals can be isolated from the backgrounds. Krawczyk and Ritz are producing[1] generators to study these processes. There may, after all, be a Higgs for HERA, in photoproduction.

1.2 Contact Interactions and Compositeness

Moving somewhat further beyond the Standard Model, the study of contact interactions provides a model-independent way to parametrize the sensitivity to new physics. Jason Gilmore has studied the sensitivity to $eeqq$ contact interactions, as well as to finite quark radii. He concludes that integrated luminosities of order 200-500 pb^{-1} in both e^-p and e^+p are necessary to probe distances shorter than $10^{-16}cm$ and contact interaction scales comparable to those accessible at the Tevatron.

1.3 Lepton Flavor Violation

With the relatively clean HERA environment, lepton flavor violating process can be probed in a straightforward and general manner: a high Q^2 DIS-like final state is sought with a μ or τ replacing the scattered lepton beam particle. There are already results from ZEUS[2] and H1[3]. Frank Sciulli and Songhoon Yang have extended their original analysis of leptoquarks with 2nd and 3rd generation couplings to the 1 fb^{-1} case, and show that HERA will have the world's best sensitivity to many types of these particles.

1.4 Heavy Neutral Leptons

Frank Sciulli and Larry Wai have studied an interesting case for HERA: a neutral right handed lepton with moderate mass may have escaped detection *if* it is more massive than the associated right-handed W_R boson. In that case, the W_R will decay only to a pair of jets with no missing momentum, and the existing experimental limits are not valid for W_R masses *below* 100 GeV. Again, high luminosities allow a significant discovery potential.

[1] Consult the web page for details.

1.5 Supersymmetry

Supersymmetry is the most widely studied extension of the Standard Model. Members of our group have focused on three distinct models of supersymmetry: (a) the minimal supersymmetric standard model (MSSM) with conserved R-parity and a gluino mass above the Tevatron bound of 140 GeV; (b) R-parity violation through the $LQ\bar{D}$[4] operator, and (c) the light gluino scenario where $M_{gluino} \lesssim 1GeV$.

1.5.1 R_p Conserving

In the MSSM we considered the two processes

$$e^- + q \rightarrow \tilde{e}^- + \tilde{q} \quad (1)$$
$$e^- + q \rightarrow \tilde{e}^- + \tilde{\chi}_1^0 + q \quad (2)$$

where $\tilde{\chi}_1^0$ is the lightest neutralino.

For the first process, studied by Peter Schleper, the present bounds from LEP1.3 are comparable to those from HERA[6]. The overall sensitivity with 500 pb^{-1} is comparable to LEP2. Therefore the sooner we obtain the upgrade the more likely HERA can remain in competition. Optimistically, if LEP2 discovers this process then HERA can also access this physics. Pessimistically, if one applies the model-dependent scalar quark bounds from the Tevatron then HERA is not competitive. The second process was investigated by Massimo Corradi. Unfortunately, LEP1.3 has already excluded the region of parameter space to which HERA can ever be sensitive[7] in this particular model.

1.5.2 R_p Violating

R-parity violation has several Yukawa couplings beyond those of the MSSM which violate either lepton number or baryon number. HERA is particularly sensitive to a subset of the lepton number-violating couplings, denoted $LQ\bar{D}$[4] since they lead to resonant scalar quark production:

$$e^- + q \rightarrow \tilde{q} \rightarrow q' + \tilde{\chi} \quad (3)$$

where $\tilde{\chi}$ represents a general gaugino (neutralino or chargino). This has been studied in much greater detail by Dreiner, Perez, and Sirois, extending the scalar squark decays to the entire supersymmetric spectrum. HERA remains the best machine for this process.

Previously, Dreiner and Morawitz studied the process[5]

$$e^- + q \rightarrow \tilde{e}^- + \tilde{q}, \quad (\tilde{q}, \tilde{e}) \rightarrow (q, e) + \tilde{\chi}_1^0. \quad (4)$$

HERA is sensitive to the case when the $\tilde{\chi}_1^0$ decays via lepton number-violating operators $L_3 Q \bar{D}$ or $L_3 Q \bar{E}$. These lead to tau-lepton final states. HERA is the best machine to test these operators.

1.5.3 Light Gluino

The exclusion of a light gluino with mass below 5-10 GeV is debated within the supersymmetry community. If a light gluino exists it should be copiously produced in photoproduction at HERA[8], and will likely hadronize as a long-lived, electrically neutral particle[9]. Marc David has studied the possibilities of detecting such processes using topologies of energy deposits in the H1 calorimeter.

For multi-jet processes in DIS involving a light gluino, Graudenz *et al.* confirm that extracting a signal from the very large QCD background would require more clever analyses than jet-angle variables alone.

It is worth noting that a recent reanalysis[10] of OPAL data may have closed the light gluino window definitively.

1.6 Other New Particles

With general scaling rules, Uli Martyn has extended previous workshop results and existing HERA results to the 1 fb^{-1} domain. Topics include exotic leptons, excited leptons, excited quarks, leptoquarks, leptogluons, new vector bosons, compositeness, and quark form factors. With an integrated luminosity of 1 fb^{-1}, HERA will remain an excellent facility to search for most of these extensions to the Standard Model.

We also have a contribution from Blümlein *et al.* explicitly considering scalar and vector leptoquark pair production. The advantage here is that leptoquark couplings to gauge particles are determined, in contrast to the more familiar single leptoquark production case where the Yukawa coupling is a free parameter. In this mode, HERA is likely to be most competitive, if at all, in searches for leptoquark pairs that decay to 3rd generation states (b, τ).

2 Conclusions

With a substantial luminosity upgrade HERA will continue to have good discovery potential for most of the topics we have studied. In addition to the amount of integrated luminosity, *when* that luminosity is delivered also matters. Table 1 shows luminosity profiles in different scenarios. The numbers represent only our best guesses, but they illustrate a point: as the annual integrated luminosity asymptotes, the time required to acquire substantially increased statistics grows. One figure of merit is the time to double the existing data sample. If HERA asymptotes to 35 pb^{-1}/y, it will be difficult to wait to accumulate even 250 pb^{-1}. By contrast, if the asymptotic value is 170-200 pb^{-1}/y, integrated delivered luminosities in the neighborhood of 1 fb^{-1} can be accumulated in a timely manner, with substantial new data sets each year to maintain an exciting program. Finally, since plans for the Tevatron indicate an integrated luminosity of 33 fb^{-1} by that same time, HERA must certainly upgrade to be of interest for physics beyond the Standard Model.

Year	Annual-35	Int	2yr ratio	Annual-170	Int	2yr ratio
1993	1	1		1	1	
1994	6	7		6	7	
1995	12	19	19	12	19	19
1996	15	34	4.9	15	34	4.9
1997	30	64	3.4	30	64	3.4
1998	35	99	2.9	50	114	3.4
1999	35	134	2.1	100	214	3.3
2000	35	**169**	1.7	125	339	3.0
2001	35	204	1.5	150	489	2.3
2002	35	239	1.4	170	659	1.9
2003	35	274	1.3	170	**829**	1.7
2004	35	309	1.3	170	999	1.5
2005	35	344	1.3	170	1169	1.4

Table 1: *Two versions of the future. Luminosity profiles for a machine that asymptotes to 35 pb^{-1}/y (first set of columns) and 170 pb^{-1}/y (second set of columns). In each group of columns, the first gives the delivered luminosity that year, the second gives the running total collected since turn-on, and the third gives the ratio of the running total of that year to that amount two years earlier. When this ratio falls below 2, we have failed to double our statistics within two years (see text). The running total at that point is given by the bold numbers for the two scenarios.*

References

[1] Proc. 'Physics at HERA', Eds. W. Buchmüller, G. Ingelman, DESY Hamburg 1992

[2] ZEUS Collaboration, DESY96-161, submitted to Z.Phys.C.

[3] H1 Collaboration, Phys.Lett. B369 (1996)173.

[4] J. Butterworth and H. Dreiner, Nucl. Phys. B397 (1993)3.

[5] H. Dreiner and P. Morawitz, Nucl. Phys. B428(1994)31.

[6] H1 Collaboration, Phys.Lett.B380(1996)461.

[7] P. Maettig, Plenary talk, 28^{th} ICHEP, Warsaw, Poland,July, 1996;
Aleph Coll., CERN-PPE/96-083, Delphi Coll., CERN-PPE/96-110,
L3 Coll., CERN-PPE/96-29, and Opal Coll., Phys Lett B 377 (1996) 181.

[8] S. Mrenna, http://sgi2.hep.anl.gov:8001/index.html, and links therein.

[9] Glennys R. Farrar, Phys.Rev.Lett.76(1996)4111, and references therein.

[10] Andre de Gouvea and Hitoshi Murayama, LBL-39030, Jun 1996, e-Print Archive: hep-ph/9606449.

Higgs search at HERA

Maria Krawczyk

Institute of Theoretical Physics,
Warsaw University, Hoża 69, 00 681 Warsaw, Poland

Abstract: Present data do not rule out a light neutral Higgs particle with mass below 40–50 GeV in the framework of 2HDM with $\tan\beta \sim$ 20-30. The promising possibility of searching for a light Higgs particle in such a scenario in photoproduction at HERA collider is discussed. For the MSSM there is only a very small chance to observe the Higgs sector, and only for limited mass range $\sim$ 45-50 GeV and with large $\tan\beta$.

1 Introduction

The possibilities of Higgs searches at the HERA collider have been studied in the first HERA Workshop in 1987 [1]. It was found that it 'is (almost) impossible' to observe the Standard Model (SM) Higgs. A similar conclusion for the SM scalar Higgs search at HERA, even with an upgraded luminosity and/or proton energy, can be found in the contribution to this Workshop [2].

Non-minimal Higgs boson production at HERA has also been investigated during the HERA Workshop'87 as well as in other papers [13, 14, 15]. It was found that photon-gluon fusion into $b\bar{b}h(A)$ may be an important production mechanism of Higgs bosons in the two Higgs doublet extension of the SM at HERA. Also other subprocesses with Higgs boson bremsstrahlung, namely those with the resolved photon in the initial state, are important at HERA [14]. Another production mechanism is gluon-gluon fusion via a quark loop, where the Higgs particle is produced in resonance. For large $\tan\beta$ and Higgs masses below 30 GeV this process dominates the production cross section over γg fusion [15].

According to LEP I data, Higgs bosons in the MSSM have to be heavier than 45 GeV, therefore their production rate at the HERA collider is rather small. For the mass of h and A equal to 45 GeV both the γg and the gg cross sections for $\tan\beta$=30 are $\sim$ 5 fb. When adding the similar contribution from WW fusion into h [2], one may expect 20-30 events to be produced at HERA with an integrated luminosity of 1 fb^{-1}.

The situation is quite different in the non-supersymmetric version of the two Higgs doublet extension of the SM (the so called general two Higgs doublet model - 2HDM) since in this model one light neutral Higgs boson with mass below 40-50 GeV may still exist, moreover with large coupling to τ and b -quark. In this case there is a good chance to study the Higgs sector at HERA, with one thousand events expected for a Higgs mass of 5 GeV and $\tan\beta$=30, assuming $\mathcal{L}_{ep}$=250 pb^{-1}.

Below we present the status of this model, *i.e.* , the 2HDM with a light Higgs boson, and in the next section we discuss the possibility to perform a Higgs boson search at HERA, focusing mainly on the gluon-gluon fusion production via a quark loop. Existing limits from LEP I for the coupling of a light neutral Higgs boson in the 2HDM are rather weak. Also present data on $(g-2)$ for the muon improve only slightly the limits on $\tan\beta$ for a Higgs mass below 2 GeV. Therefore it is extremely important to check if more stringent limits can be obtained from HERA measurements. The combined exclusion plot showing the potential of HERA measurement is presented in Sec.4. Sec.5 contains our conclusion.

2 Status of the 2HDM with a Light Neutral Higgs

The mechanism of spontaneous symmetry breaking proposed as the source of mass for the gauge and fermion fields in the SM leads to a neutral scalar particle, the minimal Higgs boson. According to the LEP I data, based on the Bjorken process $e^+e^- \to HZ^*$, it should be heavier than 66 GeV [3]. A possible extension of the SM is to include a second Higgs doublet to the symmetry breaking mechanism. In the two Higgs doublet models the observed Higgs sector is enlarged to five scalars: two neutral Higgs scalars (with masses M_H and M_h for the heavier and lighter particle, respectively), one neutral pseudoscalar (M_A), and a pair of charged Higgses ($M_{H^\pm}$). The neutral Higgs scalar couplings to quarks, charged leptons and gauge bosons are modified with respect to analogous couplings in SM by factors that depend on additional parameters: $\tan\beta$, which is the ratio of the vacuum expectation values of the Higgs doublets v_2/v_1, and the mixing angle in the neutral Higgs sector α. Also further new couplings appear, e.g. $Zh(H)A$ and ZH^+H^-.

In the following we will focus on the appealing version of the models with two doublets ("Model II") where one Higgs doublet with vacuum expectation value v_2 couples only to the "up" components of fermion doublets while the other one couples only to the "down" components [7]. (In particular, fermions couple to the pseudoscalar A with a strength proportional to $(\tan\beta)^{\pm 1}$ whereas the coupling of the fermions to the scalar h goes as $\pm(\sin\alpha/\cos\beta)^{\pm 1}$, where the sign $\pm$ corresponds to the isospin $\mp 1/2$ components). In such a model FCNC processes are absent and the ρ parameter retains its SM value at the tree level. Note that in such a scenario the large ratio $v_2/v_1 \sim m_{top}/m_b \gg 1$ is naturally expected.

The well known supersymmetric model (MSSM) belongs to this class. In the MSSM there are additional relations among the parameters required by supersymmetry, leaving only two free parameters (at the tree level) e.g. M_A and $\tan\beta$. In the general case, denoted 2HDM, masses and parameters α and β are not constrained. Therefore the same experimental data may lead to very distinct consequences depending on which version of the two Higgs doublet extension of the SM, supersymmetric or nonsupersymmetric, is considered.

2.1 Present constraints on the 2HDM from LEP I.

Important constraints on the parameters of the two Higgs doublet extensions of the SM were obtained in the precision measurements at LEP I. The current mass limit on the *charged* Higgs boson $M_{H^\pm}$=44 GeV was obtained at LEP I [6] from the process $Z \to H^+H^-$, which is independent of the parameters α and β. (Note that in the MSSM version one expects $M_{H^\pm} > M_W$). For the *neutral* Higgs particles h and A there are two main and complementary sources of

information at LEP I. One is the Bjorken process $Z \to Z^*h$ which constrains $g^2_{hZZ} \sim \sin^2(\alpha-\beta)$, for M_h below 50-60 GeV. The second process is $Z \to hA$, constraining $g^2_{ZhA} \sim \cos^2(\alpha-\beta)$ for $M_h + M_A \lesssim M_Z$. Results on $\sin^2(\alpha-\beta)$ and $\cos^2(\alpha-\beta)$ can be translated into limits on the neutral Higgs bosons masses M_h and M_A. In the MSSM, due to th additional relations among the parameters, the above data allow to draw limits for the masses of *individual* particles: $M_h \geq 45$ GeV for any $\tan\beta$ and $M_A \geq 45$ GeV for $\tan\beta \geq 1$ [5, 3]. In the general 2HDM the implications are quite different, here only the large portion of the (M_h,M_A) plane, where *both* masses are in the range between 0 and ~50 GeV, is excluded [4].

The third basic process to search for a neutral Higgs particle at LEP I is the Yukawa process, *i.e.* the bremsstrahlung production of a neutral Higgs boson $h(A)$ from a heavy fermion: $e^+e^- \to f\bar{f}h(A)$, where f means here b quark or τ lepton [22, 8, 9]. A new analysis of the Yukawa process by the ALEPH collaboration [10] led to an exclusion plot on $\tan\beta$ versus the pseudoscalar mass, M_A. (The analysis by the L3 collaboration is also in progress [11].). However, the obtained limits are rather weak allowing for the existence of a light A with mass below 10 GeV with $\tan\beta$ = 20-30, for M_A=40 GeV $\tan\beta$ till 100 is allowed! For the mass range above 10 GeV, similar exclusion limits should in principle hold also for a scalar h when replacing the coupling $\tan\beta \to \sin\alpha/\cos\beta$. However, one would expect larger differences in the lower mass region, where the production rate at the same value of coupling for the scalar is considerably larger than for the pseudoscalar. More stringent limits should be obtained there[9].

In the following we will study the 2HDM assuming that one light Higgs particle may exist. Moreover we will assume according to LEP I data the following mass relation between the lightest neutral Higgs particles: $M_h + M_A \gtrsim M_Z$. We specify the model further by choosing particular values for the parameters α and β within the present limits from LEP I. Since $\sin^2(\alpha-\beta)$ was found [4, 3] to be smaller than 0.1 for $10 \lesssim M_h \lesssim 50$ GeV, and even below 0.01 for a lighter scalar, we simply take $\alpha = \beta$. This leads to equal strengths of the coupling of fermions to scalars and pseudoscalars. Note that then the EW gauge boson couplings to the Higgs scalar h disappear [1]. For the scenario with large $\tan\beta \sim \mathcal{O}(m_t/m_b)$ a large enhancement in the coupling of both h and A bosons to the down-type quarks and leptons is expected.

Below we present how one obtains limits on the parameters of the 2HDM from current muon $(g-2)$ data [23], also the potential of the forthcoming E821 experiment [24] is discussed. (See Ref.[20] for details.)

2.2 Constraints on the 2HDM from $(g-2)_\mu$

The present experimental limit on $(g-2)$ for the muon, averaged over the sign of the muon electric charge, is given by [26]:

$$a_\mu^{exp} \equiv \frac{(g-2)_\mu}{2} = 1\ 165\ 923\ (8.4) \cdot 10^{-9}.$$

The quantity within parenthesis, σ_{exp}, refers to the uncertainty in the last digit.

The theoretical prediction of the SM for this quantity consists of the QED, hadronic and EW contributions:

$$a_\mu^{SM} = a_\mu^{QED} + a_\mu^{had} + a_\mu^{EW}.$$

[1] A does not couple to W and Z [7].

The recent SM calculations of a_μ are based on the QED results from [29], the hadronic contributions obtained in [34, 33, 31, 35, 36] and [37] and the EW results from [28, 27]. The uncertainties in these contributions differ among themselves considerably (see below and in Ref.[25, 28, 31, 20]). The main discrepancy is observed for the hadronic contribution, therefore we will here consider case A, based on Refs.[29, 30, 34, 33, 36, 28], with relatively small error in the hadronic part. It corresponds to : a_μ^{SM}=1 165 918.27 (0.76) $\cdot 10^{-9}$. (The results for case B (Refs. [30, 31, 37, 28]) with the 2 times larger error in the hadronic part is discussed in [28, 20].)

The room for new physics, like the 2HDM with a light scalar or a light pseudoscalar, is basically given by the difference between the experimental data and the theoretical SM prediction:[2] $a_\mu^{exp} - a_\mu^{SM} \equiv \delta a_\mu$. Below, the difference δa_μ for the considered case, A, is presented together with the error σ, obtained by adding the experimental and theoretical errors in quadrature (in 10^{-9}):

$$\delta a_\mu(\sigma) = 4.73(8.43) \quad \text{and} \quad \lim_{\pm}(95\%) : -13.46 \leq \delta a_\mu \leq 19.94$$

One can see that at the 1 σ level the difference δa_μ can be positive or negative. For the beyond the SM scenario where the contribution of only *one* sign is physically accessible (*i.e.* positive or negative δa_μ), the other sign being unphysical, the 95%C.L. limits should be calculated [26] separately for the positive and for the negative contributions ($lim_{\pm}(95\%)$ above).

The future accuracy of the $(g-2)_\mu$ experiments is expected to be $\sigma_{exp}^{new} \sim 0.4 \cdot 10^{-9}$ or better [24, 28]. One also expects an improvement in the calculation of the hadronic contribution [3] such that the total uncertainty will be basically due to the experimental error. Below we will assume that the accessible range for the beyond SM contribution will be smaller by a factor of 20 compared to the present ($lim_{\pm}95\%$) bounds. So, we consider the following option for future measurements (in 10^{-9}):

$$\lim_{\pm}{}^{new}(95\%) : -0.69 \leq \delta a_\mu^{new} \leq 1.00.$$

The difference δa_μ^{new} we now ascribe to the 2HDM contribution, so we take $\delta a_\mu = a_\mu^{(2HDM)}$ and $\delta a_\mu^{new} = a_\mu^{(2HDM)}$ for present and future $(g-2)_\mu$ data, respectively. We will consider two scenarios:

- *a)* pseudoscalar A is light
- *b)* scalar h is light.

Here we calculate the 2HDM contribution assuming for case a) $a_\mu^{(2HDM)}(M_A) = a_\mu^A(M_A)$, whereas for *b)* : $a_\mu^{(2HDM)}(M_h) = a_\mu^h(M_h)$. This simple approach is based on the LEP I mass limits for charged and neutral Higgs particles and differs from the full 2HDM predictions, studied in Ref.[20], significantly for a Higgs mass above about 30 GeV. Note that the contribution for the scenario *b)* is positive, whereas for the scenario *a)* it is negative.

The exclusion plots for $\tan\beta$ obtained from present $(g-2)_\mu$ data at 95%C.L. for a light h or A, go beyond those from LEP I for Higgs masses below 2 GeV. $\tan\beta \sim 15$ is still allowed for the mass of the Higgs particle as low as 1 GeV, above 2 GeV $\tan\beta$ is limited to 20. These results together with others will be presented later in Sec. 4.

[2] However in the calculation of a_μ^{EW} the (SM) Higgs scalar contribution is included (see discussion in [20]).

[3] An improvement in the ongoing experiments at low energy is expected as well.

It is worth pointing out the unique role of the forthcoming $(g-2)_\mu$ measurement in clarifying which scenario of the 2HDM is allowed: the model with a light scalar or with a light pseudoscalar. If the δa_μ^{new} is positive (negative) then the light pseudoscalar (scalar) is excluded. Further constraints on the coupling of the allowed light Higgs particle can be obtained from HERA, which is very well suited for this task.

3 Search for a Higgs particle at HERA

We now study the possibility of light neutral Higgs scalar and/or pseudoscalar production in a 2HDM at HERA [14, 15, 16]. We limit ourselves to the mass range above 5 GeV, in order to apply the LO approach. Next order results are in preparation [18], but we expect that even a K-factor $\sim$ 1.5-2 will not change the results drastically. The results obtained for 2HDM hold also for MSSM, provided the proper range of mass is considered, *i.e.* , above 45 GeV. The results relevant for SM can also be obtained from the 2HDM predictions for h production with $\tan\beta$=1.

Photon-gluon and gluon-gluon fusions in photoproduction at HERA are expected to be basic sources of a light Higgs bosons in 2HDM [15]. Note that the ZZ and WW fusions are not relevant since the pseudoscalar, A, does not couple to EW gauge bosons, and the scalar couplings, which are proportional to $\sin(\alpha-\beta)$, are put to zero by the assumed by us condition: $\alpha = \beta$. (Even if the upper experimental limits for $\sin(\alpha-\beta)$ are used (Sec. 2.1), light Higgs boson production in ZZ/WW fusion is still effectively suppressed.)

The total cross section for on-shell neutral Higgs boson production is calculated, along with the rates for the particular final states $\to \tau^+\tau^-$ or $b\bar{b}$. These decay channels are the most important since in 2HDM with large $\tan\beta$ h and A decay mainly to the heaviest available fermionic "down-type" states. (Details can be found elsewhere, *e.g.* , in [8, 17]).

3.1 Bremsstrahlung of the Higgs boson: $\gamma g \to b\bar{b}h(A)$ and other related processes.

At HERA, the production of neutral Higgs boson in a 2HDM via

$$\gamma g \to b\bar{b}h(A) \tag{1}$$

may be substantial [13, 15]. The total h cross section (integrated over the $b\bar{b}$ final state) is presented in Fig.1a. Note that this process also includes $\gamma b \to bh(A)$, as well the lowest order contributions due to the resolved photon, *i.e.*, $b\bar{b} \to h(A)$, $bg \to h(A)b$, etc. These subprocesses were studied in Ref. [14], in Fig.2a we present obtained results. Each of these processes needs an independent analysis of the background [18]. As this work is not yet completed, we will not use these processes for the derivation of the exclusion plot in Sec.4.

3.2 Gluon-gluon fusion via a quark loop

Higgs boson photoproduction in gluon-gluon fusion via a quark loop,

$$gg \to h(A), \tag{2}$$

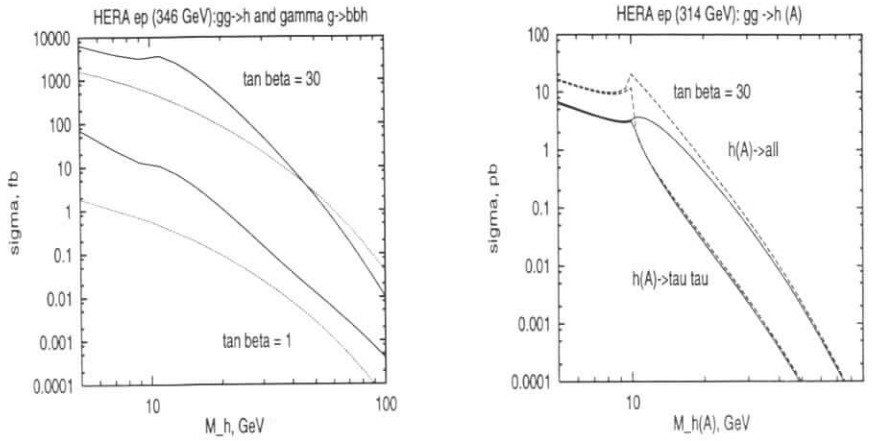

Figure 1: *a) The total cross section for h production at HERA with the upgraded energy. The gg fusion (solid lines) and γg fusion (dotted lines) are considered. The results for* $\tan\beta$ *=30 (upper curves) and the* $\tan\beta$*=1 (lower curves) are shown. GRV parametrizations were used for both the photon and the proton [18]. b) The cross sections for gg fusion for the nominal HERA energy (with* $\tan\beta$*=30). Total h (solid upper line) and A (dashed upper line) production cross-sections are shown, along with the results for the $\tau^+\tau^-$ final state (solid and dashed lower lines for h and A, respectively).*

can be even more significant [14, 15]. The results for HERA with upgraded energy are also presented in Fig. 1a. A comparison of (2) with γg fusion (1) shows that, for large $\tan\beta$ and for mass below $\sim$ 30 GeV, the gg fusion clearly dominates the total cross section. Note that the total gg cross section for $\tan\beta$=30 is large: $\sigma \sim 10^5$ fb for a Higgs mass of 5 GeV, falling to 5 fb at mass $\sim$ 45 GeV (where the σ_{gg} meets the $\sigma_{\gamma g}$).

A mass of 45 GeV corresponds to the lowest currently allowed mass for MSSM Higgs bosons. (Note that in MSSM, h and A tend to be degenerated in mass for large $\tan\beta$). Adding the contribution for $\tan\beta$=30 from processes (1) and (2) for both scalar and pseudoscalar as well as that due to WW fusion into h [2] which are of the same order, we estimate that HERA will produce 20-30 events of this sort with luminosity 1 fb^{-1}.

In Fig.1a the $\tan\beta$=1 case corresponds to the prediction for SM Higgs production in γg and gg fusion. Applying the current limit for the SM Higgs mass, $M_{Higgs} \geq 66$ GeV [3], we see how small the corresponding γg and gg cross sections are, more than three orders of magnitude smaller than the rate found in WW fusion into h [2].

Comparing the *scalar* production in Fig.1a with corresponding production in Fig.1b, in which the nominal HERA beam energy was used, we see an extremely weak dependence on beam energy for *scalar* production. In Fig.1b we also consider pseudoscalar production via gluon-gluon fusion (2) for $\tan\beta$=30. The total cross sections ($h(A) \rightarrow all$) and the cross sections for the $\tau^+\tau^-$ final state are shown. It is interesting to notice the large difference, in the mass range below 10 GeV, between scalar and pseudoscalar production seen both in the total cross section σ as well as in the $\sigma\cdot$Br($\rightarrow \tau^+\tau^-$). Note that the difference almost disappears for

the $\tau^+\tau^-$ cross section above the $b\bar{b}$ threshold.

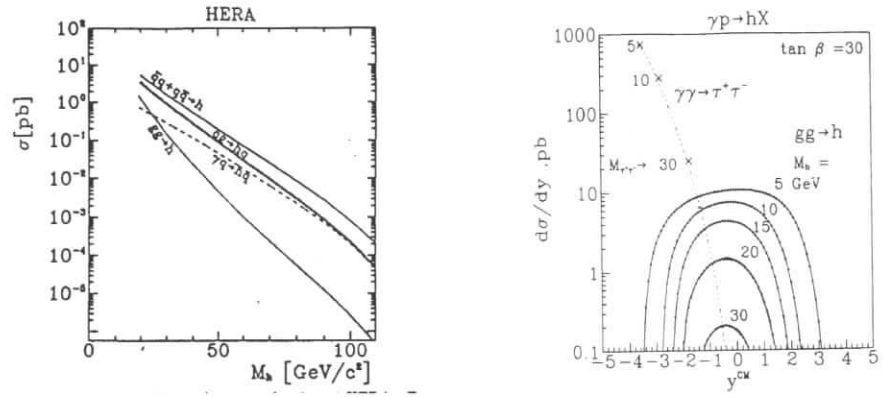

Figure 2: *In the γp CM system at $\sqrt{s_{\gamma p}}$ =170 GeV a) the cross section for scalar production in various subprocesses* ($\tan\beta$*=20, from Ref.[14]) and b) the rapidity distribution for $\tau^+\tau^-$ pair are presented. The background ($\gamma\gamma \rightarrow \tau^+\tau^-$) and the signal (the scalar Higgs boson contribution, integrated over ΔM_h=1 GeV) are shown (from Ref.[15]).*

For detection, it is useful to study the rapidity distribution $d\sigma/dy$ of the Higgs bosons in the γp centre of mass system. Note that $y = -\frac{1}{2} log \frac{E_h - p_h}{E_h + p_h} = -\frac{1}{2} log \frac{x_\gamma}{x_p}$, where $x_p(x_\gamma)$ are the ratio of the energy of the gluon to the energy of the proton and photon, respectively. The (almost) symmetric shape of the rapidity distribution found for the signal is extremely useful to reduce the background and to separate the $gg \rightarrow h(A)$ contribution, which we will discuss now for the $\tau^+\tau^-$ final state.

The main background in the mass range between $\tau^+\tau^-$ and $b\bar{b}$ thresholds is due to $\gamma\gamma \rightarrow \tau^+\tau^-$. In the region of negative rapidity $d\sigma/dy_{\tau^+\tau^-}$ is very large, *e.g.* ,for γp energy equal to 170 GeV the cross section $\sim$ 800 pb at the edge of phase space ($y_{\tau^+\tau^-} \sim -4$), and it then falls rapidly when $y_{\tau^+\tau^-}$ approaches 0. At the same time, the signal reaches at most 10 pb (for M_h=5 GeV). The results are shown in Fig.2b. The region of positive rapidity is *not* allowed kinematically for this process since here one photon interacts directly with $x_\gamma = 1$, and therefore $y_{\tau^+\tau^-} = -\frac{1}{2} log \frac{1}{x_p} \leq 0$. A significantly different topology found for $\gamma\gamma \rightarrow \tau^+\tau^-$ events than for the signal should allow a reduction of this background.

The other sources of background are $q\bar{q} \rightarrow \tau^+\tau^-$ processes (not shown here). These processes contribute to positive and negative rapidity $y_{\tau^+\tau^-}$, with a flat and relatively low cross-section (below 0.5 pb) in the central region.

Note that Higgs decaying into b-quarks has a much more severe background, and we will not discussed it here (see Ref.[14, 15]).

Assuming a luminosity $\mathcal{L}_{ep}$=250 pb^{-1}/y we predict that gg fusion will produce around one thousand events per annum for M_h = 5 GeV (and roughly 10 events for M_h = 30 GeV). A clear signature for the tagged case with a $\tau^+\tau^-$ final state at positive centre-of-mass rapidities

of the Higgs scalar should be seen, even for a Higgs mass above the $b\bar{b}$ threshold (more details can be found in Ref.[15]). For the pseudoscalar case even more events are expected in the mass region below 10 GeV.

To show the potential of HERA, the exclusion plot based on gg fusion via a quark loop with the $\tau^+\tau^-$ final state can be drawn. In this case, as we mentioned above, it is easy to find the part of phase space where the background is hopefully negligible. To calculate the 95% C.L. for allowed value of $\tan\beta$ we take into account signal events corresponding only to the positive rapidity region (in the γp CM system). The results for the ep luminosity $\mathcal{L}_{ep}$ =25 pb^{-1} and 500 pb^{-1} are presented in Fig. 3 and will be discused in the following section.

4 Exclusion plot for 2HDM

In Fig.3 the 95% C.L. exclusion curves for the $\tan\beta$ in the general 2HDM ("Model II") obtained by us for a light scalar (solid lines) and for a light pseudoscalar (dashed lines) are presented in mass range below 40 GeV. For comparison results from LEP I analysis presented recently by ALEPH collaboration for pseudoscalar [10] is also shown (dotted line). The region of $(\tan\beta, M_{h(A)})$ above curves is excluded.

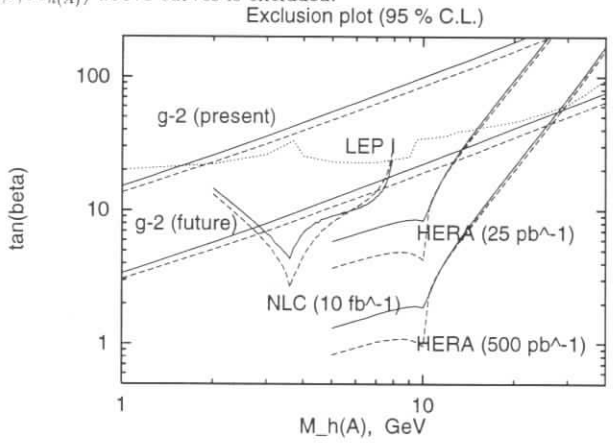

Figure 3: *The 95% C.L. exclusion plot for a light scalar(solid lines) or light pseudoscalar (dashed lines) in 2HDM. The limits derivable from present $(g-2)_\mu$ measurements and from existing LEP I results (pseudoscalar production in the Yukawa process) (dotted line) are shown. The possible exclusions from HERA (the gluon-gluon fusion via a quark loop with the $\tau^+\tau^-$ final state) for luminosity 25 pb^{-1} and 500 pb^{-1} as well from $\gamma\gamma \to \mu^+\mu^-$ at low energy NLC (10 fb^{-1}) are also presented (from [17]). Possible limits from future data for $(g-2)_\mu$ are also shown. The parameter space above the curves can be ruled out.*

Constraints on $\tan\beta$ were obtained from the existing $(g-2)_\mu$ data, including LEP I mass limits (Sec.2.2). We see that already the present $(g-2)_\mu$ data improve LEP I limits on $\tan\beta$ for $M_A \lesssim 2$ GeV. A similar situation should hold for a 2HDM with a light scalar, although here the Yukawa process may be more restrictive for $M_h \leq 10$ GeV [9].

The future improvement in the accuracy by a factor of 20 in the forthcoming $(g-2)_\mu$ experiment may lead to more stringent limits than provided by LEP I up to a mass of h or A equal to 30 GeV, if the mass difference between scalar and pseudoscalar is $\sim M_Z$, or to even higher mass for a larger mass difference [20]. Note, however, that there is some arbitrariness in the deriving the expected bounds for the δa_μ^{new}.

The search at HERA in the gluon-gluon fusion via a quark loop may lead to even more stringent limits (see Fig.3) for the mass range 5–15 (5–25) GeV, provided the luminosity will reach 25 (500) pb^{-1} and the efficiency for the $\tau^+\tau^-$ final state will be high enough [4]. The other production mechanisms, such as γg fusion and other subprocesses with the resolved photon, are expected to improve these limits further [14, 15, 18].

In the very low mass range, additional limits can be obtained from the low energy NL $\gamma\gamma$ collider with $\sqrt{s_{ee}}$=10 GeV. In Ref.[17] we found that the exclusion based on $\gamma\gamma$ fusion into Higgs, decaying into $\mu^+\mu^-$, may be very efficient. In Fig.3 the results corresponding to a luminosity 10 fb^{-1} are presented.

5 Conclusion

In the framework of 2HDM, a light neutral Higgs scalar or pseudoscalar in the mass range below 40-50 GeV is not ruled out by the present LEP I and $(g-2)_\mu$ data. The other low energy experiments cover only part of parameter space of 2HDM; some, such as the Wilczek process, have large theoretical uncertainties both due to the QCD and relativistic corrections([12, 7])(see also discussion in [15, 16]).

The role of the forthcoming $(g-2)_\mu$ measurement seems to be crucial in clarifying which scenario of 2HDM is allowed: with light scalar or with a light pseudoscalar. If the δa_μ^{new} is positive(negative) then the light pseudoscalar(scalar) is excluded. Then, further constraints on the coupling of the allowed light Higgs particle can be obtained from HERA, which is very well suited for this. The simple estimation performed at luminosity 500 pb $^{-1}$ for one particular production mechanism, namely gluon-gluon fusion, is already promising; adding more processes may further improve the situation significantly. The most important experimental handle is a good efficiency for the $\tau^+\tau^-$ channel.

All this suggests the large discovery/exclusion potential of HERA for the mass range 5–20 GeV [15]. It is unlikely that the LEP/LHC experiments will have a larger potential in such a mass region [14].

The very low mass region may also be studied at low energy NLC machines. We found that the exclusion based on $\gamma\gamma$ fusion into Higgs, decaying into $\mu^+\mu^-$, may be very efficient in probing the Higgs sector of 2HDM, even for luminosity 100 pb^{-1}. It is not clear however if these low energy options will come into operation.

Future experiments will clarify the status of the general 2HDM with a light neutral Higgs particle – the role of HERA in such a study may be very important.

By contrast, for the MSSM the potential of HERA even with luminosity 1 fb^{-1} is relatively poor, producing only 20-30 events of h and A, if the mass is in the 45-50 GeV range for $\tan\beta$=30.

[4] In this analysis the 100% efficiency has been assumed. If the efficiency will be 10 % the corresponding limits will be larger by factor 3.3 (a simple scaling) for fixed luminosity.

6 Acknowledgements

I would like to thank D. Choudhury and J.Żochowski for important contribution to this paper and B. Kniehl for fruitful discussions. I am grateful very much to P. Zerwas for very important suggestion and support. I am also grateful to H. Dreiner, S. Ritz and U. Katz for very importrant comments and suggestions.

References

[1] K. J. F. Gaemers et. al., in Proc. of the HERA Workshop, ed. R. D. Peccei, Hamburg, October 1987, Vol.2, p 739.

[2] B. Kniehl, contribution to this Proceedings (EW Working Group).

[3] P. Maettig, Plenary Talk at ICHEP96, Warsaw, July 1996.

[4] ALEPH Coll., D. Buskulic et al., *Z. Phys.* **C 62** (1994) 539;
DELPHI Collab., P. Abreu et al.,*Nucl. Phys.* **B 418** (1994) 403;
L3 Collab., M. Acciarri et al., *Z. Phys.* **C 62** (1994) 551; Note 1800 (1995);
OPAL Collab. R. Akers et al., *Z. Phys.* **C 61** (1994) 19.

[5] ALEPH Coll. Note EPS0415(1995);
L3 Coll. Note 1801(1995).

[6] A. Sopczak, talk at *IX Workshop on High Energy Physics, Moscow 1994*(hep-ph/9504300).

[7] J.F. Gunion et al., *The Higgs Hunter's Guide*, (Addison-Wesley,1990).

[8] J. Kalinowski and S. Pokorski, *Phys. Lett.* **B219** (1989) 116;
J. Kalinowski, N. P. Nilles,*Phys. Lett.* **B 255** (1991) 134;
A. Djouadi et al, *Phys. Lett.* **B259** (1990) 175.

[9] J. Kalinowski, M. Krawczyk, *Phys.Lett* **B361** (1995)66; *Acta Phys.Pol.* **B27** (1996) 961.

[10] ALEPH Coll. *Search for a light Higgs Boson in the Yukawa Process*, contr. to ICHEP96, PA13-027.

[11] A. Sopczak, private communication.

[12] Crystal Ball Collab., D. Antresyan et. al., *Phys. Lett.* **B251** (1990) 204;
CLEO Collab., R. Balest et al., CLEO 94-19;
P. Franzini et al., *Phys. Rev.***35** (1987) 2883.

[13] B. Grządkowski at al., *Phys. Lett.* **B272** (1991) 174

[14] A.C. Bawa and M. Krawczyk, Warsaw University IFT preprints 16/91 (and ERRATUM) and 16/92; in Proc. of XVI Kazimierz Meeting, May 1993, Poland, p. 83.

[15] A.C. Bawa and M. Krawczyk,*Phys. Lett* **B357** (1995) 637

[16] M. Krawczyk, Warsaw University IFT preprint IFT-95/20, in Proc. of XVIII Kazimierz Symposium (May 1995, Ames, USA); in Proc. of Moriond'96 (EW session), IFT preprint 96/15 (hep-ph/ 9607268); talk at ICHEP'96, (Warsaw, July 1996); IFT preprint 20/96, contr. to QS'96 Workshop. Minsk, May, 1996.

[17] D. Choudhury, M. Krawczyk, MPI-Pth/96-46, IFT 95/21, in *Proc. Workshop NLC*, 1995, p.69; preprint MPI-PTh/96-46, IFT 96/13 (hep-ph/9607271)- submitted to *Phys.Lett.* **B**.

[18] in preparation with D. Choudhury

[19] M. Glueck, E. Reya and A. Vogt, Phys. Rev. **D46** (1992) 1973; *Z. Phys.* **C53** (1991) 293.

[20] M. Krawczyk and J. Żochowski, *Constraining 2HDM by the present and future* $(g-2)_\mu$ *data* IFT 96-14 (hep-ph/9608321).

[21] M. Krawczyk and B.B. Levtchenko, *Two-photon mechanism production of the Higgs boson, SUSY particles, hadrons and lepton pairs in eA collision at HERA*, contr. to this Workshop; M. Krawczyk and J. Żochowski, *Two-photon coherent production of the light Higgs boson at LHC*- in preparation.

[22] E. Carlson, S. Glashow, U. Sarid, *Nucl.Phys.* **B309** (1988) 597

[23] J. Bailey et al., *Phys. Lett.* **68 B** (1977) 191;
F. J. M. Farley and E. Picasso, *Ann. Rev. Nucl. Sci.* **29** (1979) 243;
in *Quantum Electrodynamics*, ed. T. Kinoshita, (World Scientific, Singapore);
F. J. M. Farley, *Z. Phys.* **C56** (1992) S88.

[24] *Proposal for Brookhaven National Laboratory Experiment E821: A precision measurement of the muon* $g-2$ *value at the level of 0.35 ppm*, E. Benedict et al. (1986), co-spokesmen V. W. Hughes, W. M. Morse; B. L. Roberts; B. L. Roberts,*Z. Phys.* **C56** (1992) S101 and talk at ICHEP'96, July 1996, Warsaw, Poland.

[25] U.Chattopadhyay and P.Nath, *Phys. Rev.* **D53** (1996) 1648.

[26] Particle Data Group, *Phys. Rev.* **D50** (1994) 1173.

[27] T. V. Kukhto et al., *Nucl. Phys.* **B371** (1992) 567.

[28] A. Czarnecki et al., *Phys. Rev. Lett.* **76** (1996) 3267; *Phys. Rev.* **D52** (1995) R2619.

[29] T. Kinoshita et al., *Phys. Rev.* **D41** (1990) 593; E. de Rafael, *Phys. Lett.* **B322** (1994) 239;

[30] T. Kinoshita, *Phys. Rev. Lett.* **75** (1995) 523.

[31] S. Eidelman and F. Jegerlehner, *Z. Phys.* **C67** (1995) 585.

[32] F. Jegerlehner, in *Proc. of the Workshop "QCD and QED in Higher Orders", Rheinsberg, Germany, 1996* (hep-ph/9606484).

[33] T. Kinoshita and W. J. Marciano, in *Quantum Electrodynamics*, ed. by T. Kinoshita (World Scientific, Singapore, 1990), pp 419-478; T. Kinoshita et al, *Phys. Rev. Lett.* **31** (1985) 2108. T. Kinoshita,*Z. Phys.* **C56** (1992) S80.

[34] L. Martinovic and S. Dubnicka, *Phys. Rev.* **D42** (1990) 884.

[35] D. H. Brown and W. A. Worstell, *The lowest order hadronic contribution to the muon $g-2$ value with systematic error correlations*(hep-ph/9607319).

[36] J. Bijnens et al., *Phys. Rev. Lett.* **75** (1995) 1447;

[37] M. Hayakawa et al., *Phys. Rev. Lett.* **75** (1995) 790. DPNU-95-30,(hep-ph/9601310).

[38] W. A. Bardeen et al. *Nucl. Phys.* **B46** (1972) 315.

[39] H. E. Haber et al., *Nucl. Phys.* **B161** (1979) 493.

[40] J. Leveille, *Nucl. Phys.* **B137** (1978) 63.

Sensitivity of the ZEUS Experiment to Contact Interactions at High Integrated Luminosities

J. R. Gilmore

Dept. of Physics, The Ohio State University, 174 W. 18th Ave., Columbus, Ohio 43210 USA

Abstract: The sensitivity of the ZEUS experiment to $eeqq$ contact interactions in neutral current deep inelastic scattering has been studied for future integrated luminosities as high as 1000 pb^{-1}.

1 Introduction

The electron–proton collider HERA is an ideal place for the study of neutral current deep inelastic scattering (NC–DIS), and by making precise measurements of the cross section, the ZEUS experiment can potentially detect the effects of physics beyond the Standard Model (SM). Many new physics processes that occur at mass scales greater than $\sqrt{s}$ (*e.g.* compositeness, leptoquarks, and new heavy bosons) may be detected at ZEUS as a contact term which modifies the DIS cross section. A 'contact term' is a simple four–fermion interaction where the propagator mass is so much larger than the energy available that the propagator is contracted to a point. The most general chirally invariant expression for $eeqq$ contact interactions adds terms to the Lagrangian of the form [1] $L = \eta_{ss'}(e_s\gamma e_s)(q_{s'}\gamma q_{s'})$ where $\eta_{ss'} = \pm g^2/2\Lambda^2_{ss'\pm}$ is the parameter for the coupling between lepton helicity s and quark helicity s', Λ is the mass scale of the process and the $\pm$ sign denotes constructive or destructive interference. Using this modified Lagrangian, a simple technique for setting limits is presented which is complimentary to previously published methods [2].

Assuming unpolarized beams and neglecting radiative corrections, the NC–DIS differential cross section can be expressed as the sum of the proton structure functions F_2 and F_3, which in turn are functions of the parton momentum distributions and SM quark couplings [5]. The contact term then causes additional terms (Eqs. 2-5) in F_2 and F_3 proportional to $\eta_{ss'}Q^2$: [2]

$$\begin{aligned}
\frac{d^2\sigma(e^\pm p)}{dxdQ^2} &= \frac{2\pi\alpha^2}{xQ^4}\left[[1+(1-y)^2]F_2(x,Q^2) \mp [1-(1-y)^2]xF_3(x,Q^2)\right] \qquad (1)\\
F_2 &= \sum_{flavor}\left[xq(x,Q^2)+x\bar{q}(x,Q^2)\right]\frac{1}{2}\left[\left|V_f^L\right|^2+\left|V_f^R\right|^2+\left|A_f^L\right|^2+\left|A_f^R\right|^2\right]\\
xF_3 &= \sum_{flavor}\left[xq(x,Q^2)-x\bar{q}(x,Q^2)\right]\left[V_f^LA_f^L-V_f^RA_f^R\right]
\end{aligned}$$

$$V_f^L = e_f - (v_e + a_e)v_f P_Z + \frac{Q^2}{8\pi\alpha}(\eta_{LL} + \eta_{LR}) \quad (2)$$

$$V_f^R = e_f - (v_e - a_e)v_f P_Z + \frac{Q^2}{8\pi\alpha}(\eta_{RL} + \eta_{RR}) \quad (3)$$

$$A_f^L = -(v_e + a_e)a_f P_Z + \frac{Q^2}{8\pi\alpha}(\eta_{LL} - \eta_{LR}) \quad (4)$$

$$A_f^R = -(v_e - a_e)a_f P_Z + \frac{Q^2}{8\pi\alpha}(\eta_{RL} - \eta_{RR}) \quad (5)$$

$$P_z = \frac{1}{\sin^2\theta_W \cos^2\theta_W} \frac{Q^2}{Q^2 + M_Z^2}$$

$$v_i = \frac{1}{2}\, T_i^3 - q_i \sin^2\theta_W \qquad a_i = \frac{1}{2}\, T_i^3$$

where T_i^3 are the weak isospins ($+\frac{1}{2}$ for $i = u, \nu$, $-\frac{1}{2}$ for $i = d, e$) and q_i are the charges. At high Q^2, the contribution of the longitudinal structure function (F_L) to the cross section is very small, so it is ignored in this study.

The effect of the contact interaction on the cross section can be seen in Fig. 1, where the ratio of the differential cross section including a 1 TeV contact term to the SM only cross section for e^+p is shown as a function of Q^2. Since the valence quarks are the primary contributors at high Q^2, it is assumed that only the u and d quarks are involved in the contact interaction.

Additionally, if the quark has a finite size, then the cross section may be multiplied by a quark form factor. Assuming that the quark has charged constituents and that the electron is point-like, the cross section is modified to:

$$\left(\frac{d\sigma}{dQ^2}\right)_{FORM} = \left(\frac{d\sigma}{dQ^2}\right)_{NC} \left(1 - \frac{1}{6}R^2Q^2\right)^2$$

where R is the effective radius of the quark and the factor of 6 is chosen by convention [6].

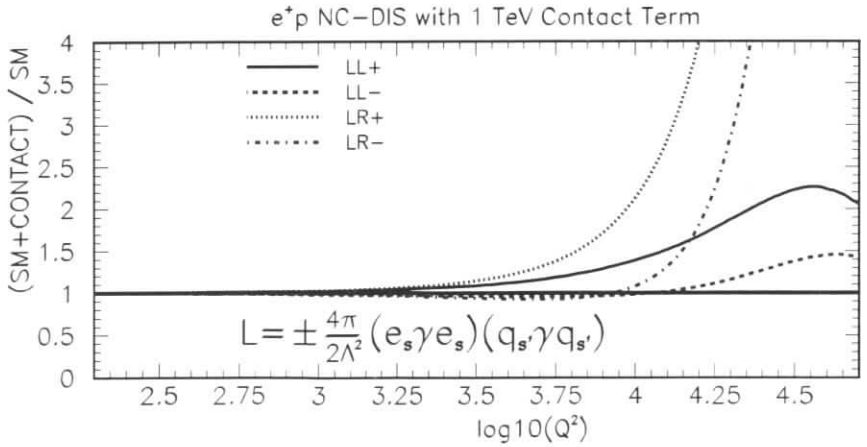

Figure 1: *Ratio of differential cross sections $\frac{d\sigma}{dQ^2}$(SM + CONTACT) to $\frac{d\sigma}{dQ^2}$(SM only) vs Q^2 calculated by integration of Eq. 1 over x for four different eeqq contact term couplings.*

2 Event Selection and Limits

The primary selection criteria for this analysis of the NC–DIS cross section are an isolated electron in the calorimeter with energy > 10 GeV, a matching track from the central tracking detector, and $Q^2 > 200$ GeV^2. Isolation and track matching requirements eliminate most of the photoproduction events with fake electrons, the primary background. Other requirements are energy and momentum conservation, $(E - P_z)$ and various non-ep background cuts (*e.g.* cosmic and halo muons, beam-gas). The effects of all cuts were studied using NC–DIS (Django [3]) and photoproduction (Herwig [4]) Monte Carlo. The efficiency with all cuts was found to be 80% and the background contamination less than 5%, decreasing for increasing Q^2. The 'double angle' method was used as an estimator for Q^2 because it is relatively insensitive to energy scale uncertainty. The overall systematic acceptance uncertainty is estimated to be 5%.

Both the contact term and the form factor have their strongest effect at high Q^2, so the simplest method to search for a signal is to look for an excess (or deficit) in the total number of events above some minimum Q^2 (Q^2_{MIN}), thus forming one bin in Q^2. The effect of a contact term or form factor has been simulated in this study by reweighting the DIS Monte Carlo event-by-event to the appropriate signal differential cross section, where the reweighting factor is $d\sigma(x,Q^2)_{SIGNAL}/d\sigma(x,Q^2)_{SM}$. The signal Monte Carlo is then used to determine the Q^2_{MIN} that maximizes the sensitivity to new physics.

A reduction in the SM cross section is expected in the presence of a quark form factor, so for setting limits it is necessary to define the *minimum* number of events N that are consistent with the number of observed events N_O with $Q^2 > Q^2_{MIN}$ at the 95% C.L. :

$$0.95 = \sum_{k=0}^{N_O} \epsilon^{-N} \frac{N^k}{k!}$$

This is just a modified version of the Poisson upper limit formulation [1], with the $1-\epsilon$ replaced by ϵ. Once N has been determined, R is varied until the number of events expected from the signal Monte Carlo matches N.

For the positive signal expected from contact interactions, Poisson statistics with background are used to determine the maximum number of signal events N that are consistent with N_b background events and N_O observed events with $Q^2 > Q^2_{MIN}$ at the 95% C.L. [1] Then Λ is varied until the number of events expected from the signal Monte Carlo equals N. Using this method and assuming that there is no significant deviation from the SM, the limits on the contact interaction mass scale Λ can be calculated for the eight lepton-quark couplings. The convention of setting $g^2 = 4\pi$ has been used [1] to determine the mass scale limits for integrated luminosities up to 1000 pb^{-1}. Four of the lepton-quark coupling limits are shown in Figs. 2a (e^-p) and 2b (e^+p). Similarly, the effective quark radius limits from the form factor analysis are plotted in Fig. 3.

In conclusion, it is clear from Figs. 2a and 2b that the e^-p measurement is particularly sensitive to the LL+ coupling while the e^+p measurement is most sensitive to the LR+ coupling. On the order of 500 pb^{-1} of each lepton species is neccessary to maintain limits that are competitive with $p\bar{p}$ experiments. Furthermore, if a signal is detected, the use of polarized beams may help to discern the chiral properties of the new interactions.

References

[1] Particle Data Group, *Phys. Rev.* D **54**, (1996).

[2] P. Haberl, *et al*, Proceedings *'Physics at HERA'*, eds. W. Buchmuller and G. Ingleman, 1133, DESY, Hamburg, 1992.

[3] DJANGO 1.0: G. Schuler and H. Spiesberger, *ibid.*, 1419.

[4] HERWIG 5.8: G. Marchesini *et al.*, Comput. Phys. Commun. **67**, 465 (1992).

[5] G. Ingelman and R. Rückl, *Phys. Lett.* B **201**, 369 (1988).

[6] G. Köpp, *et al.*, *Z. Phys.* C **65**, 545 (1995).

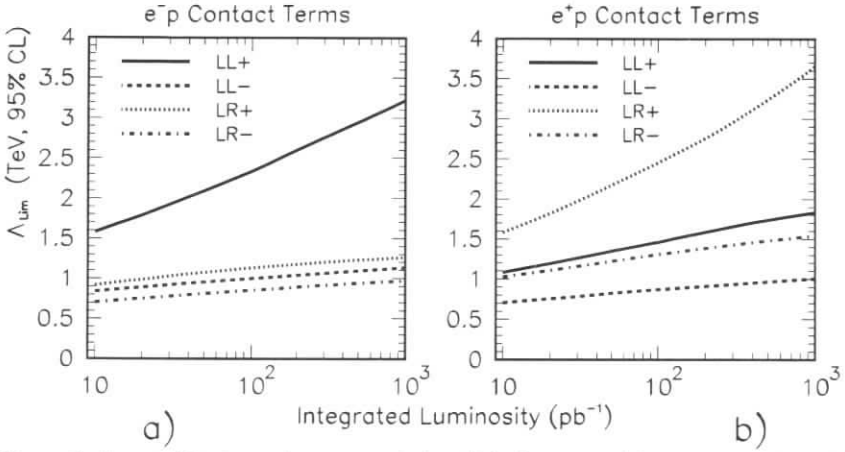

Figure 2: *Expected limits on the mass scale Λ with high integrated luminosities. Four different eeqq contact interaction couplings are shown using a) e^-p and b) e^+p Monte Carlo* [3].

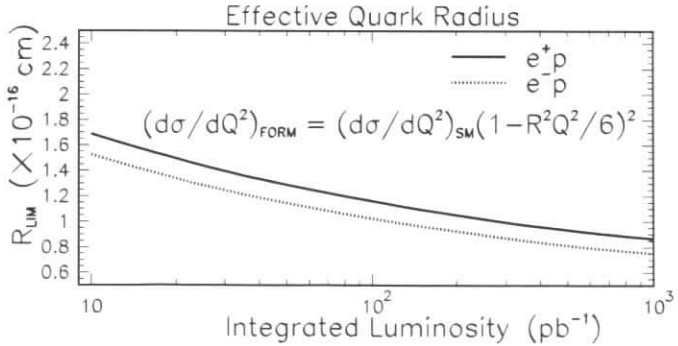

Figure 3: *Expected limits on the effective quark radius R with high integrated luminosities using e^-p (dotted line) and e^+p (solid line) Monte Carlo* [3].

Lepton Flavor Violation Searches

Frank Sciulli[a] and Songhoon Yang[b]

[a] Nevis Laboratory - Columbia University, Box 137, Irvington, NY 10533, USA
[b] California Institute of Technology, West Bridge 161-33, Pasadena, CA 91125, USA

Abstract: Experimental limits obtained at lower luminosities are extrapolated to estimate the range of parameter space available with a total luminosity of one inverse femtobarn. An additional order-of-magnitude beyond present coupling limits will be available to HERA experiments with this total exposure. For the case of electron to tau transitions, this will represent a substantial extension of explored parameter space and the most sensitive search for most of the mechanisms discussed.

1 Introduction

All known lepton interactions are consistent with the hypothesis of individual lepton number conservation. Indeed, this observation introduces into the standard model (SM) three globally conserved quantum numbers (L_e, L_μ, and L_τ) for (e^-, ν_e), (μ^-, ν_μ), and (τ^-, ν_τ), respectively. Discovery of lepton flavor violation (LFV) *in any form* will signal new physics. In many SM extensions, lepton flavor violating processes are thought to occur, but their rates must be suppressed to levels consistent with experimental upper bounds.

At the electron-proton collider, observation of the process

$$e + p \rightarrow l + X \tag{1}$$

where l represents a muon (μ) or tau (τ) would provide evidence for LFV. HERA provides a very sensitive instrument to seek examples of reaction (1). With present luminosities, such searches have been performed [1, 2] with little background. Even at very high luminosities, the spectacular signature of an isolated high transverse momentum muon or tau is expected to be nearly background free.

Though there are many limits [3] on flavor-violation from low energy experiments, the most sensitive of these relate to $e \leftrightarrow \mu$ transitions. In addition, the sensitivities apply only to specific generations, typically first and/or second, of quarks involved in the transition. However at HERA, $e \leftrightarrow \mu$ and $e \leftrightarrow \tau$ transitions can be sought for a wide range of quark flavors.

We described in this introductory section the motivations and capabilities for LFV searches at HERA. Specific mechanisms involving leptoquarks are discussed in section 2 to illustrate the sensitivity of HERA and other LFV search experiments. The search technique and existing results are outlined in section 3. From these low luminosity results, we extrapolate to the high luminosity sensitivities given in section 4. This report concludes with the future prospects of LFV searches.

2 Mechanisms

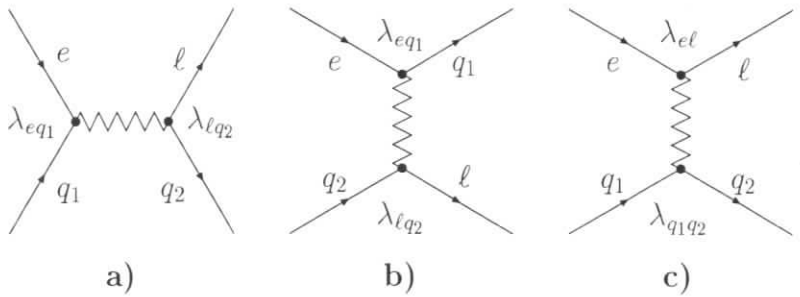

Figure 1: The (a) s–, (l) u–, and (c) t–channel Feynman diagrams for LFV. For the s–channel and u–channel diagrams, we denote the couplings as $\lambda_{\ell q}$, where the indices refer to the lepton and quark flavors.

Extensions of the SM typically introduce new particles and associated new couplings. The masses of new particles are assumed heavy enough and the couplings small enough so as not to effect well measured SM parameters, and not to significantly contribute through direct or virtual effects to unobserved SM forbidden processes, like $\mu \to e\gamma$ or the process (1).

For illustration, three specific mechanisms for lepton-flavor violation at HERA are shown in Figure 1. In the first two cases, leptoquarks (LQ), hypothesized bosons which provide direct connections between quark and lepton families, are responsible for the transition. The rate for the process in (1a) depends on the couplings from the initial state, λ_{eq_1}, and to the final state, λ_{lq_2}, and to the leptoquark mass, M_{LQ}. We use leptoquark mechanisms here to illustrate and compare the sensitivity to LFV from HERA with that of other experiments. It should be noted that two SUSY mechanisms producing LFV, involving non-conservation of R-parity, are equivalent to two specific leptoquark types [4].

The effective chiral LQ interaction Lagrangian with $SU(3) \otimes SU(2) \otimes U(1)$ symmetry [5] permits fourteen different types of leptoquarks with differing spin, weak isospin, and chirality. Given that reaction (1) could have either a μ or τ in the final state, that there are fourteen different leptoquark couplings, and that there are nine different combinations of quarks possible in the initial and final states, there are 252 different possible ways in which flavor-violation could be manifest in reaction (1) from leptoquark mechanisms alone.

3 Technique

In this report, we recall the sensitivity to LFV provided at HERA by ZEUS [2] with center of mass energy $\sqrt{s} = 300\ GeV$ using integrated luminosities of 0.84 pb^{-1} with e^-p and 2.94 pb^{-1} with e^+p, and indicate how this might be expected to improve for a scenario in which there exists 500 pb^{-1} for both e^-p and e^+p. For illustration, we indicate how the 95% confidence limits would improve for the situation in which no LFV were found.

The search in reference [2] involved specific cuts to identify isolated final state muons or taus (in all decay modes) with large transverse momenta. The search specifically required large missing transverse momentum *as observed in the calorimeter* to be greater than 12 GeV. No candidates survived all the selections, so that limits were obtained on the couplings and leptoquark masses.

The cross section for low LQ mass, $\sqrt{s} \gg M_{LQ}$ depends on the product $\lambda_{eq_1}\sqrt{B_{lq_2}}$ and on M_{LQ}. Here B_{lq_2} is the branching fraction into the observed final state. For high LQ mass, $\sqrt{s} \ll M_{LQ}$, the cross section depends on the single factor

$$\Psi = \left[\frac{\lambda_{eq_1}\lambda_{lq_2}}{{M_{LQ}}^2}\right] \tag{2}$$

As illustration of the low mass sensitivity, figure 2 shows the coupling limits versus leptoquark mass obtained to date for a few representative cases. Already with 3.8 pb^{-1} luminosity, HERA has probed leptoquark coupling strengths as small as $10^{-3}\alpha_{em}$, where α_{em} is the fine-structure constant. The HERA limits at low mass are better in all cases shown in figure 2 for any leptons involved with third generation quarks and for any quarks involved in $e \to \tau$ transitions. As we show below, all such limits will extend down by about an order-of-magnitude with the full 1 fb^{-1} luminosity.

4 High Luminosity

The high LQ mass limits for the parameter Ψ (with $M_{LQ} = 100\,GeV$) are given in tables 2-5. Here tables 2 and 3 apply for $e \leftrightarrow \mu$ transitions with LQ fermion numbers two and zero, respectively. Tables 4 and 5 apply for $e \leftrightarrow \tau$ transitions. The asterisk indicates cases in which the top quark must be involved. The four elements listed in each table entry are defined in table 1.

Process which defined previous best limit
Previous best limit for Ψ
Best limit from ZEUS with 3.8 pb^{-1}
Best limit expected with 1 fb^{-1}

Table 1: Items listed in each box of the subsequent tables.

The best limit to be expected in the 1 fb^{-1} case is obtained using the calculated efficiencies and backgrounds after optimizing the cut on missing transverse momentum. This was obtained after recognizing that the largest backgrounds are expected from processes involving $\gamma + \gamma \to \mu + \mu$ and $\gamma + \gamma \to \tau + \tau$. Monte Carlo calculations indicate that these backgrounds will remain small if the cut on missing transverse momentum is raised, for high luminosity, from 12 GeV to 25 GeV. The background cross section with this cut is estimated to be approximately 18 fb.

Though additional selections might lower this cross-section, we have not attempted to optimize to this level of detail.

In tables 2-5, we indicate by bold-face those cases in which the existing HERA limit (third entry) supersedes the previous best limit. We also indicate by bold face those cases in which the expected high luminosity limit will supersede the previous best limit.

Note that, for the $e \leftrightarrow \mu$ cases in tables 2-3, there are ten cases in which the present ZEUS limits supersede previous best limits, though in most cases these are only marginally better. (In three cases, the new limit is significantly better.) In all cases, we expect the integrated luminosity of 1 fb^{-1} to explore approximately an order of magnitude further of coupling parameter space.

For the $e \leftrightarrow \tau$ cases in tables 4-5, by contrast, there are twenty-three instances in which HERA is already exploring new parameter space. With a luminosity of 1 fb^{-1}, HERA should have become the principal instrument in such searches. Tables 4-5 indicate that over half the spaces will have been explored best at HERA. Of the remaining spaces, many involve transitions requiring participation by third generation up quarks (top), shown as asterisks.[1]

5 Conclusion

Soon after the discovery of the muon more than a half century ago, searches for lepton flavor violation began with the expected $\mu \rightarrow e\gamma$ decay mode. In addition to this classic process, other LFV reactions have been extensively sought. In the meantime, the number of LFV possibilities has increased with the discovery of the tau lepton. New opportunities for testing lepton flavor conservation have arisen using high energy colliders, like the ones for HERA described in this report.

Many models are severely restricted by the present experimental constraints on LFV, but some ideas, like the left-right symmetric models [6], predict LFV to be close to the observable range. The next generation of high-sensitivity experiments seeking forbidden kaon decay and muon transitions should be carried out. But direct LFV searches at HERA explore transitions which may not be visible in other ways.

In summary, HERA already is an important tool in the search for lepton flavor violation. A sensitive search for muons and taus in the final state is feasible at the highest luminosities. We anticipate that the most sensitive and broadest searches for $e \leftrightarrow \tau$ will be obtained using HERA.

References

[1] H1 Collaboration: S. Aid *et al*, Phys. Lett. **B369** (1996) 173.

[2] ZEUS Collaboration: M. Derrick *et al*, DESY **96-161** (1996), Submitted to Z. Phys.

[3] S. Davidson, D. Bailey, and B. Campbell, Z. Phys. **C61** (1994) 613.

[4] J. Butterworth *et al*, Nucl. Phys. **B397** (1993) 3.

[5] W. Buchmüller *et al*, Phys. Lett. **B191** (1987) 442.

[6] R. Mohapatra, Prog. Part. Nucl. Phys. **31** (1993) 39.

[1] Low energy experiments have little sensitivity here. Measurements of top decays at the Tevatron may be the instrument of choice. HERA has some sensitivity since the center of mass energy is above top threshold. For example, at $M_{LQ} = 200\ GeV$, a HERA sensitivity involving up quark to top quark transitions with Ψ as small as 0.8 might be visible.

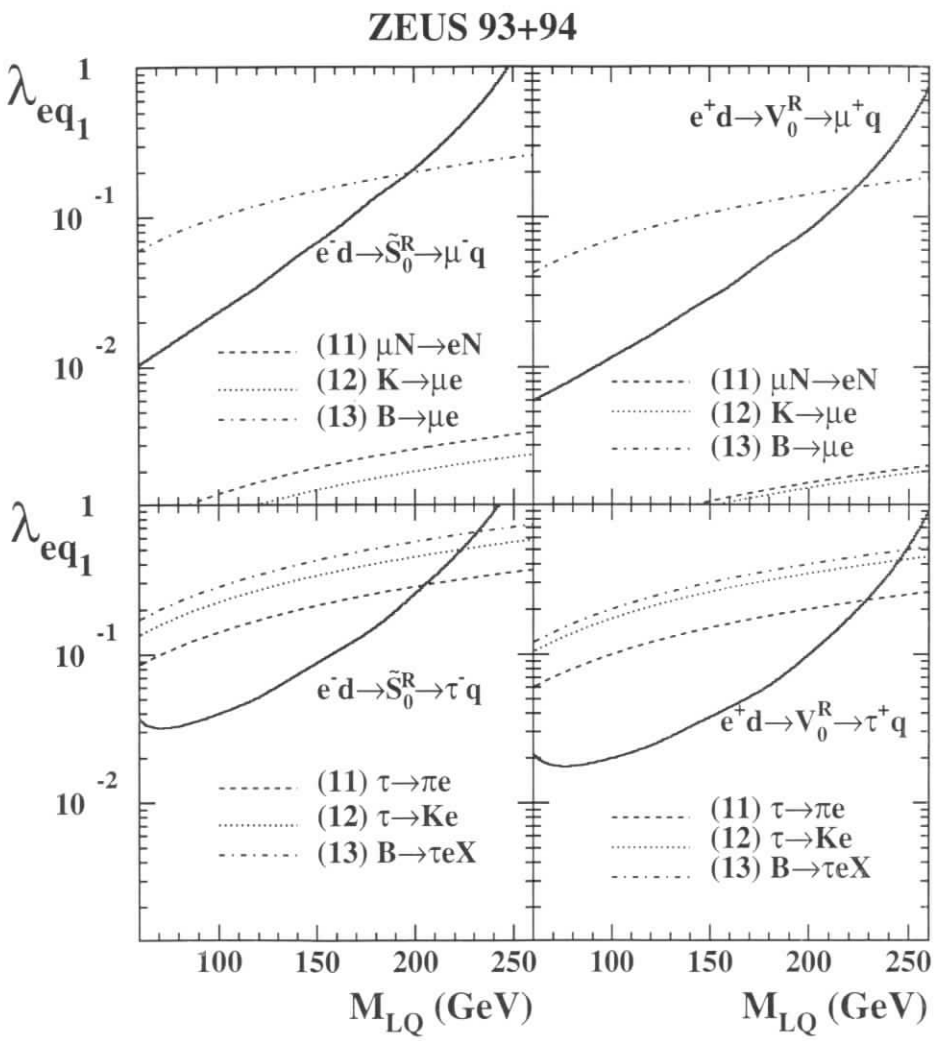

Figure 2: The 95% CL upper limits on λ_{eq_1} *vs.* leptoquark mass M_{LQ}, for selected LQ species which decay to ℓq, where $\ell = \mu$ (above) or τ (below), assuming $B_{\ell q_2} = 0.5$. The solid curves are ZEUS results [2], the various broken curves show existing limits [3]. Paired numbers in parentheses indicate the generations of the quarks which couple to e and ℓ respectively.

$e \to \mu$ $F = 2$							
$(q_1 q_2)$	S_0^L $e^- u$ $\nu\ d$	S_0^R $e^- u$	$\tilde{S}_0^R$ $e^- d$	S_1^L $e^-(u+\sqrt{2}d)$ $\nu\ (\sqrt{2}u+d)$	$V_{1/2}^L$ $e^- d$ $\nu\ d$	$V_{1/2}^R$ $e^-(u+d)$	$\tilde{V}_{1/2}^L$ $e^- u$ $\nu\ u$
(11)	$\mu N \to eN$ 2×10^{-6} 0.09 0.009	$\mu N \to eN$ 2×10^{-6} 0.09 0.009	$\mu N \to eN$ 2×10^{-6} 0.12 0.012	$\mu N \to eN$ 5×10^{-7} 0.05 0.005	$\mu N \to eN$ 7×10^{-7} 0.05 0.006	$\mu N \to eN$ 4×10^{-7} 0.03 0.004	$\mu N \to eN$ 7×10^{-7} 0.04 0.005
(12)	$K \to \pi\bar{\nu}\nu$ 2×10^{-5} 0.12 0.010	$D \to \mu\bar{e}$ 0.14 **0.12** **0.010**	$K \to \mu\bar{e}$ 10^{-6} 0.14 0.013	$K \to \mu\bar{e}$ 6×10^{-7} 0.06 0.005	$K \to \mu\bar{e}$ 6×10^{-7} 0.09 0.009	$K \to \mu\bar{e}$ 6×10^{-7} 0.06 0.006	$D \to \mu\bar{e}$ 0.07 0.08 **0.008**
(13)	V_{ub} 0.004 0.101	*	$B \to \mu\bar{e}$ 0.01 0.15 0.013	V_{ub} 0.004 0.07 0.007	$B \to \mu\bar{e}$ 0.005 0.10 0.010	$B \to \mu\bar{e}$ 0.005 0.10 0.010	*
(21)	$K \to \pi\bar{\nu}\nu$ 2×10^{-5} 0.12 0.016	$D \to \mu\bar{e}$ 0.14 **0.12** **0.016**	$K \to \mu\bar{e}$ 10^{-6} 0.14 0.018	$K \to \mu\bar{e}$ 6×10^{-7} 0.06 0.008	$K \to \mu\bar{e}$ 6×10^{-7} 0.05 0.007	$K \to \mu\bar{e}$ 6×10^{-7} 0.03 0.004	$D \to \mu\bar{e}$ 0.07 **0.04** **0.005**
(22)	$\mu \to e\gamma$ 2×10^{-4} 0.24 0.029	$\mu \to e\gamma$ 2×10^{-4} 0.24 0.029	$\mu \to e\gamma$ 8×10^{-5} 0.20 0.024	$\mu \to e\gamma$ 4×10^{-5} 0.09 0.011	$\mu \to e\gamma$ 0.15 **0.10** **0.012**	$\mu \to e\gamma$ 6×10^{-3} 0.08 0.009	$\mu \to e\gamma$ 6×10^{-3} 0.13 0.015
(23)	$B \to \ell\nu X$ 0.04	*	$B \to \mu eK$ 6×10^{-3} 0.21 0.026	$B \to \mu eK$ 3×10^{-3} 0.11 0.013	$B \to \mu eK$ 3×10^{-3} 0.13 0.016	$B \to \mu eK$ 3×10^{-3} 0.13 0.016	*
(31)	V_{ub} 0.004	*	$B \to \mu\bar{e}$ 0.01 0.16 0.020	V_{ub} 0.004 0.08 0.010	$B \to \mu\bar{e}$ 0.005 0.05 0.007	$B \to \mu\bar{e}$ 0.005 0.05 0.007	*
(32)	$B \to \ell\nu X$ 0.04	*	$B \to \mu eK$ 6×10^{-3} 0.26 0.031	$B \to \mu eK$ 3×10^{-3} 0.13 0.016	$B \to \mu eK$ 3×10^{-3} 0.11 0.013	$B \to \mu eK$ 3×10^{-3} 0.11 0.013	*
(33)		*	$\mu \to e\gamma$ 8×10^{-5} 0.29 0.036	$\mu \to e\gamma$ 4×10^{-5} 0.14 0.018	$\mu \to e\gamma$ 0.01 0.15 0.018	$\mu \to e\gamma$ 0.01 0.15 0.018	*

Table 2: Limits on flavor violation for the lepton transitions and leptoquark fermion number indicated in the first row of the table. The entries in each box are described in table 1.

$e \to \mu$ $F = 0$							
$(q_1 q_2)$	$S^L_{1/2}$ $e^- \bar{u}$ $\nu \bar{u}$	$S^R_{1/2}$ $e^-(\bar{u}+\bar{d})$	$\tilde{S}^L_{1/2}$ $e^- \bar{d}$ $\nu \bar{d}$	V^L_0 $e^- \bar{d}$ $\nu \bar{u}$	V^R_0 $e^- \bar{d}$	$\tilde{V}^R_0$ $e^- \bar{u}$	V^L_1 $e^-(\sqrt{2}\bar{u}+\bar{d})$ $\nu(\bar{u}+\sqrt{2}\bar{d})$
(11)	$\mu N \to eN$ 2×10^{-6} 0.07 0.009	$\mu N \to eN$ 7×10^{-7} 0.06 0.007	$\mu N \to eN$ 2×10^{-6} 0.10 0.012	$\mu N \to eN$ 7×10^{-7} 0.06 0.006	$\mu N \to eN$ 7×10^{-7} 0.06 0.006	$\mu N \to eN$ 7×10^{-7} 0.04 0.005	$\mu N \to eN$ 3×10^{-7} 0.02 0.002
(12)	$D \to \mu\bar{e}$ 0.14 **0.08** **0.010**	$K \to \mu\bar{e}$ 10^{-6} 0.06 0.008	$K \to \mu\bar{e}$ 10^{-6} 0.10 0.013	$K \to \mu\bar{e}$ 6×10^{-7} 0.07 0.009	$K \to \mu\bar{e}$ 6×10^{-7} 0.07 0.009	$D \to \mu\bar{e}$ 0.07 **0.06** **0.008**	$K \to \mu\bar{e}$ 6×10^{-7} 0.03 0.004
(13)	*	$B \to \mu\bar{e}$ 0.01 0.11 0.013	$B \to \mu\bar{e}$ 0.01 0.11 0.013	V_{bu} 0.002 0.08 0.010	$B \to \mu\bar{e}$ 0.005 0.08 0.010	*	V_{bu} 0.002 0.08 0.009
(21)	$D \to \mu\bar{e}$ 0.14 0.17 **0.016**	$K \to \mu\bar{e}$ 10^{-6} 0.12 0.012	$K \to \mu\bar{e}$ 10^{-6} 0.17 0.018	$K \to \mu\bar{e}$ 6×10^{-7} 0.07 0.007	$K \to \mu\bar{e}$ 6×10^{-7} 0.07 0.007	$D \to \mu\bar{e}$ 0.07 **0.06** **0.005**	$K \to \mu\bar{e}$ 6×10^{-7} 0.03 0.002
(22)	$\mu \to e\gamma$ 5×10^{-5} 0.24 0.029	$\mu \to e\gamma$ 5×10^{-5} 0.16 0.018	**0.20** **0.024**	$\mu \to e\gamma$ 0.07 0.10 **0.012**	$\mu \to e\gamma$ 0.07 0.10 **0.012**	$\mu \to e\gamma$ 9×10^{-3} 0.13 0.015	$\mu \to e\gamma$ 5×10^{-3} 0.05 0.006
(23)	*	$B \to \bar{\mu}eK$ 6×10^{-3} 0.21 0.026	$B \to \bar{\mu}eK$ 6×10^{-3} 0.21 0.026	$B \to \bar{\mu}eK$ 3×10^{-3} 0.13 0.016	$B \to \bar{\mu}eK$ 3×10^{-3} 0.13 0.016	*	$B \to \bar{\mu}eK$ 3×10^{-3} 0.13 0.016
(31)	*	$B \to \mu\bar{e}$ 0.01 0.20 0.020	$B \to \mu\bar{e}$ 0.01 0.20 0.020	V_{bu} 0.002 0.07 0.007	$B \to \mu\bar{e}$ 0.005 0.07 0.007	*	V_{bu} 0.002 0.07 0.006
(32)	*	$B \to \bar{\mu}eK$ 6×10^{-3} 0.26 0.031	$B \to \bar{\mu}eK$ 6×10^{-3} 0.26 0.031	$B \to \bar{\mu}eK$ 3×10^{-3} 0.11 0.013	$B \to \bar{\mu}eK$ 3×10^{-3} 0.11 0.013	*	$B \to \bar{\mu}eK$ 3×10^{-3} 0.11 0.013
(33)	*	**0.29** **0.036**	**0.29** **0.036**	$\mu \to e\gamma$ 0.001 0.15 0.018	$\mu \to e\gamma$ 0.001 0.15 0.018	*	$\mu \to e\gamma$ 0.001 0.15 0.018

Table 3: Limits on flavor violation for the lepton transitions and leptoquark fermion number indicated in the first row of the table. The entries in each box are described in table 1.

$e \to \tau$ $F = 2$							
$(q_1 q_2)$	S^L_0 $e^- u$ νd	S^R_0 $e^- u$	$\tilde{S}^R_0$ $e^- d$	S^L_1 $e^-(u+\sqrt{2}d)$ $\nu(\sqrt{2}u+d)$	$V^L_{1/2}$ $e^- d$ νd	$V^R_{1/2}$ $e^-(u+d)$	$\tilde{V}^L_{1/2}$ $e^- u$ νu
(11)	G_F 0.003 0.15 0.014	$\tau \to \pi e$ 0.02 0.15 **0.014**	$\tau \to \pi e$ 0.02 0.23 0.021	G_F 0.003 0.09 0.008	$\tau \to \pi e$ 0.01 0.09 0.011	$\tau \to \pi e$ 0.005 0.05 0.006	$\tau \to \pi e$ 0.01 0.06 **0.007**
(12)	$K \to \pi\bar{\nu}\nu$ 2×10^{-5} 0.20 0.016	**0.20** **0.016**	$\tau \to Ke$ 0.05 0.27 **0.024**	$K \to \pi\bar{\nu}\nu$ 2×10^{-5} 0.11 0.010	$K \to \pi\bar{\nu}\nu$ 10^{-5} 0.19 0.017	$\tau \to Ke$ 0.03 0.13 **0.010**	**0.16** **0.013**
(13)	V_{bu} 0.004	*	$B \to \tau\bar{e}X$ 0.08 0.28 **0.025**	V_{bu} 0.004 0.14 0.012	$B \to \tau\bar{e}X$ 0.04 0.23 **0.020**	$B \to \tau\bar{e}X$ 0.04 0.23 **0.020**	*
(21)	$K \to \pi\bar{\nu}\nu$ 2×10^{-5} 0.22 0.026	**0.22** **0.026**	$\tau \to Ke$ 0.05 0.31 **0.035**	$K \to \pi\bar{\nu}\nu$ 2×10^{-5} 0.12 0.014	$K \to \pi\bar{\nu}\nu$ 10^{-5} 0.09 0.012	$\tau \to Ke$ 0.03 0.05 **0.007**	**0.06** **0.008**
(22)	$\tau \to e\gamma$ 0.5 0.60 **0.071**	$\tau \to e\gamma$ 0.5 0.60 **0.071**	$\tau \to e\gamma$ 0.3 0.48 **0.050**	$\tau \to e\gamma$ 0.1 0.22 **0.024**	**0.25** **0.025**	**0.19** **0.021**	**0.31** **0.036**
(23)	$B \to \ell\nu X$ 0.04	*	$B \to \tau\bar{e}X$ 0.08 0.50 **0.056**	$B \to \ell\nu X$ 0.04 0.25 **0.028**	$B \to \tau\bar{e}X$ 0.04 0.33 **0.037**	$B \to \tau\bar{e}X$ 0.04 0.33 **0.037**	*
(31)	$B \to \ell\nu X$ 0.04	*	$B \to \tau\bar{e}X$ 0.08 0.34 **0.040**	$B \to \ell\nu X$ 0.04 0.17 **0.020**	$B \to \tau\bar{e}X$ 0.04 0.10 **0.012**	$B \to \tau\bar{e}X$ 0.04 0.10 **0.012**	*
(32)	$B \to \ell\nu X$ 0.04	*	$B \to \tau\bar{e}X$ 0.08 0.65 **0.073**	$B \to \ell\nu X$ 0.04 0.32 **0.037**	$B \to \tau\bar{e}X$ 0.04 0.26 **0.028**	$B \to \tau\bar{e}X$ 0.04 0.26 **0.028**	*
(33)	*	*	$\tau \to e\gamma$ 0.3 0.72 **0.092**	$\tau \to e\gamma$ 0.1 0.36 **0.046**	**0.38** **0.046**	**0.38** **0.046**	*

Table 4: Limits on flavor violation for the lepton transitions and leptoquark fermion number indicated in the first row of the table. The entries in each box are described in table 1.

$e \to \tau$					$F = 0$		
$(q_1 q_2)$	$S_{1/2}^L$ $e^- \bar{u}$ $\nu\ \bar{u}$	$S_{1/2}^R$ $e^-(\bar{u}+\bar{d})$	$\tilde{S}_{1/2}^L$ $e^- \bar{d}$ $\nu\ \bar{d}$	V_0^L $e^- \bar{d}$ $\nu\ \bar{u}$	V_0^R $e^- \bar{d}$	$\tilde{V}_0^R$ $e^- \bar{u}$	V_1^L $e^-(\sqrt{2}\bar{u}+\bar{d})$ $\nu\ (\bar{u}+\sqrt{2}d)$
(11)	$\tau \to \pi e$ 0.02 0.11 **0.014**	$\tau \to \pi e$ 0.01 0.09 **0.007**	$\tau \to \pi e$ 0.02 0.18 0.021	G_F 0.002 0.11 0.011	$\tau \to \pi e$ 0.01 0.11 0.011	$\tau \to \pi e$ 0.01 0.07 **0.007**	G_F 0.002 0.04 0.003
(12)		$\tau \to Ke$ 0.05 0.10 **0.008**	$K \to \pi\bar{\nu}\nu$ 2×10^{-5} 0.18 0.024	$\tau \to Ke$ 0.03 0.15 **0.017**	$\tau \to Ke$ 0.03 0.15 **0.017**	 **0.10** **0.013**	$K \to \pi\bar{\nu}\nu$ 5×10^{-6} 0.05 0.006
(13)	 * 	$B \to \tau\bar{e}X$ 0.08 0.18 **0.013**	$B \to \tau\bar{e}X$ 0.08 0.18 **0.025**	$B \to \ell\nu X$ 0.02 0.16 **0.020**	$B \to \tau\bar{e}X$ 0.04 0.16 **0.020**	 * 	$B \to \ell\nu X$ 0.02 0.16 **0.019**
(21)	 **0.34** **0.026**	$\tau \to Ke$ 0.05 0.26 **0.012**	$K \to \pi\bar{\nu}\nu$ 2×10^{-5} 0.39 0.035	$\tau \to Ke$ 0.03 0.14 **0.012**	$\tau \to Ke$ 0.03 0.14 **0.012**	 **0.10** **0.008**	$K \to \pi\bar{\nu}\nu$ 5×10^{-6} 0.05 0.004
(22)	$\tau \to e\gamma$ 0.2 0.60 **0.071**	$\tau \to e\gamma$ 0.2 0.37 **0.018**	 **0.48** **0.050**	 **0.25** **0.025**	 **0.25** **0.025**	 **0.31** **0.036**	 **0.13** **0.015**
(23)	 * 	$B \to \tau\bar{e}X$ 0.08 0.50 **0.026**	$B \to \tau\bar{e}X$ 0.08 0.50 **0.026**	$B \to \ell\nu X$ 0.02 0.33 0.056	$B \to \tau\bar{e}X$ 0.04 0.33 **0.037**	 * 	$B \to \ell\nu X$ 0.02 0.33 0.037
(31)	 * 	$B \to \tau\bar{e}X$ 0.08 0.47 **0.020**	$B \to \tau\bar{e}X$ 0.08 0.47 **0.040**	V_{bu} 0.002 0.15 0.012	$B \to \tau\bar{e}X$ 0.04 0.15 **0.012**	 * 	V_{bu} 0.002 0.15 0.011
(32)	 * 	$B \to \tau\bar{e}X$ 0.08 0.65 **0.031**	$B \to \tau\bar{e}X$ 0.08 0.65 **0.073**	$B \to \ell\nu X$ 0.02 0.26 0.028	$B \to \tau\bar{e}X$ 0.04 0.26 **0.028**	 * 	$B \to \ell\nu X$ 0.02 0.26 0.028
(33)	 * 	 **0.72** **0.036**	 **0.72** **0.092**	$\tau \to e\gamma$ 3.4 **0.38** **0.046**	$\tau \to e\gamma$ 3.4 **0.38** **0.046**	 * 	 **0.38** **0.046**

Table 5: Limits on flavor violation for the lepton transitions and leptoquark fermion number indicated in the first row of the table. The entries in each box are described in table 1.

Heavy Neutral Lepton Searches

Frank Sciulli[a] and Lawrence Wai[b]

[a] Nevis Laboratory - Columbia University, Box 137, Irvington, NY 10533, USA
[b] University of Washington, VTL, Physics Dept, Box 351560, Seattle, WA 98195-1560, USA

Abstract: Neutral right-handed leptons associated with the electron may have avoided detection, if nature has appropriately designed the right-handed sector. A search at HERA for these particles with the modest luminosities available to now have permitted some exclusion limits. Much of the parameter space available in the allowed region will be examined when HERA provides much higher luminosity.

1 Introduction

The Standard Model (SM) contains a lepton sector with nearly massless neutrinos in a left-handed doublet with the left-handed electron. The right-handed electron sits alone. This ugly lack of symmetry makes one wonder whether there is more to learn. Though detection of the right-handed sector may lay beyond our present capabilities, it is just possible that we have not seen it because we have not yet searched in the right place. One picture which would treat the left- and right-handed sectors more symmetrically involves the replacement

$$\begin{pmatrix} \nu_e \\ e_L^- \end{pmatrix}, e_R^- \longrightarrow \begin{pmatrix} \nu_e \\ e_L^- \end{pmatrix}, \begin{pmatrix} N_e \\ e_R^- \end{pmatrix}$$

where N_e is a right-handed coupled partner of the electron neutrino. This might occur, for example, in conjunction with a more symmetrized version of the SM electroweak sector

$$SU(2)_L \otimes U(1) \longrightarrow SU(2)_L \otimes SU(2)_R \otimes U(1)$$

in which a right-handed charged boson, W_R, carries the right-handed weak force with coupling, g_R. In this case, the replacement for the equation

$$\frac{1}{e^2} = \frac{1}{g_L^2} + \frac{1}{g'^2} \longrightarrow \frac{1}{e^2} = \frac{1}{g_L^2} + \frac{1}{g_R^2} + \frac{1}{g'^2}$$

leads to the following lower limit [1] on the right-handed coupling:

$$g_R > 0.55\, g_L$$

2 Discussion

There are stringent indirect limits on such scenarios [2], particularly from the observed value for the $K_L - K_S$ mass difference, as well as direct limits [3] on the mass of a right-handed boson, W_R. However, we find that there are scenarios involving relatively low mass N_e and W_R in which existing limits do not provide strong constraints. In particular, this is the case for the following assumptions:

1. There is little or no mixing between N_e and ν_e (or between W_L and W_R).
2. The Cabibbo-Kobayashi-Moskawa (CKM) matrix characterizing the right-handed sector is nearly diagonal in comparison with that of the left-handed sector.
3. The mass for the W_R is less than about $100\,GeV$.
4. The mass for the N_e is greater than that for the W_R.

We note that under assumptions (1) and (4), the only decay mode available to the right-handed boson is

$$W_R \rightarrow jet + jet$$

and the existing direct experimental limits [3] for such right-handed bosons do not extend below masses of $100\,GeV$. Furthermore, indirect limits on the W_R mass from the $K_L - K_S$ mass difference with assumption (2) are significantly less stringent and depend strongly on assumptions about the mass (or effective mass) of the up quark. For these reasons, we conclude that existing limits could be avoided under the circumstances described by the four assumptions listed above.

3 HERA Search

We have searched [4] in HERA data using integrated luminosities of 0.84 pb^{-1} with e^-p and 2.94 pb^{-1} with e^+p for processes of the following type:

$$e^{\pm} + p \rightarrow N + X$$

followed by the decays

$$N_e \rightarrow e + W_R$$
$$W_R \rightarrow jet + jet$$

The properties of such events include the following:

1. high transverse energy (E_t);
2. presence of a final state electron ($e^{\pm}$);
3. at least three jets with large transverse momenta (p_T);
4. two jets which form the W_R and hence have invariant mass, M_W; and
5. two jets and the electron form the N_e and hence have invariant mass, M_N.

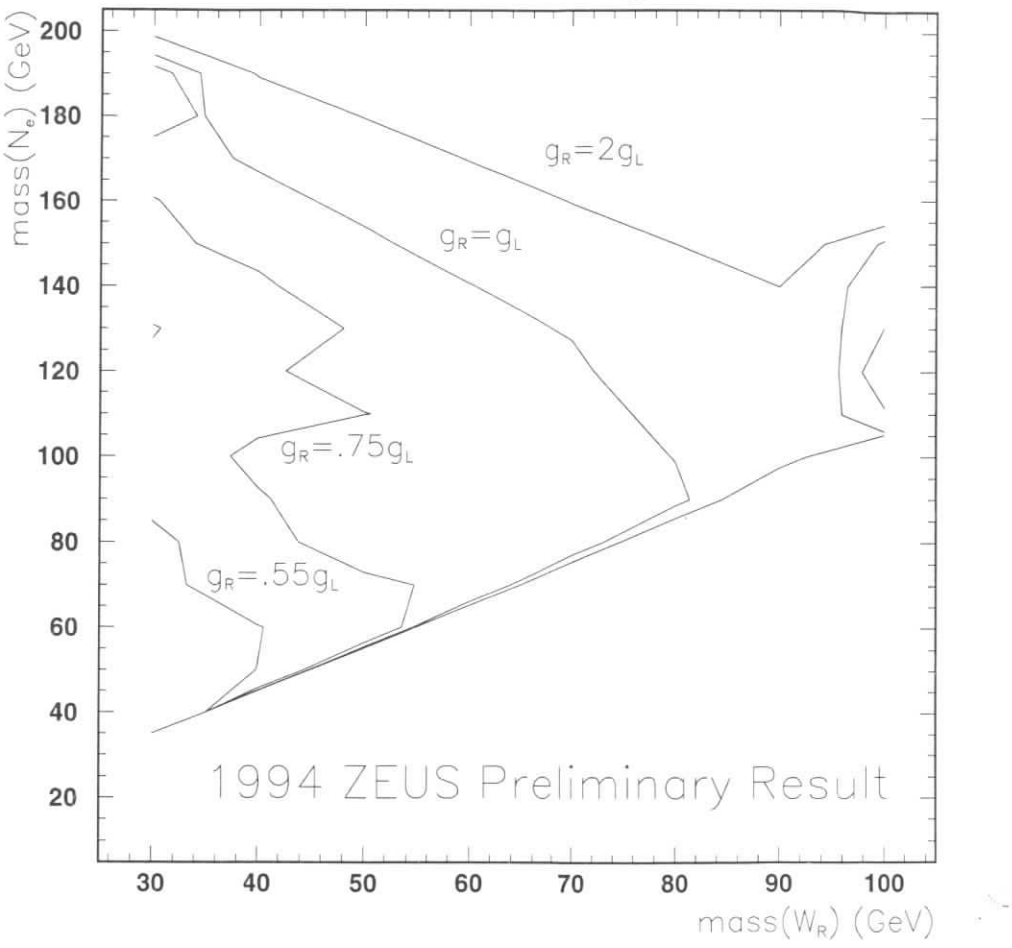

Figure 1: Limits on the mass of N_e versus the mass of W_R for various assumptions regarding the coupling, g_R. The area to the left of the curve is forbidden from existing HERA data.

Selection criteria based on the properties 1 - 3 provided a sample of ninety-five events, in agreement with background expectations from neutral current deep-inelastic data. The criteria 4 -5 led us to look in bins of M_W and M_N for excessive numbers of events. No excess was seen beyond what might be expected from statistical fluctuations in the background. Though the search provided no strong evidence for the existence of these right handed particles, the data permitted limits on the masses M_W and M_N for various assumptions about the RH weak coupling, g_R. Exclusion contours are shown in figure 1, where the regions to the left of the contours are excluded subject to the assumption shown for g_R. Note that a substantial fraction of the plane is excluded for $g_R \geq 2\,g_L$, and a smaller though significant fraction is excluded for $g_R \geq g_L$. Very little of the plane is excluded for $g_R \geq 0.55\,g_L$.

4 Future Searches

Figure 2 shows the expectations for exclusion limits expected for an accumulated luminosity of 1 fb^{-1}, split evenly between operation with electron and positron beams. Note that for such searches, operation with electron beam provides more sensitivity. With this accumulated luminosity, the electron running will permit discovery of right-handed N_e and W_R over a large fraction of the available parameter space, even with the coupling at the lowest permitted value.

We conclude that the running at HERA with a large accumulated luminosity (≈ 1 fb^{-1}) will permit discovery of a right-handed sector which has thus far been avoided, if nature has put one there. Otherwise, the high luminosity should permit us to rule out such a scenario.

References

[1] M. Cvetic, P. Langacker, and B. Kayser, Phys. Rev. Lett. **68** (1992) 2871.

[2] P. Langacker and U. Sankar, Phys. Rev. **D40** (1989) 1569.

[3] UA2 Collaboration: J. Alitti et al, Z. Phys. **C49** (1991) 17;
UA2 Collaboration: J. Alitti et al, Nucl. Phys. **B400** (1993) 3.

[4] F. Sciulli, B. Straub, and L. Wai, "Search for an $\mathcal{O}(100\ GeV)$ Mass Right-Handed Electron Neutrino with the 1993 and 1994 ZEUS Data", ZEUS note 95-140 (1995).
Lawrence Wai, "Search for an $\mathcal{O}(100\ GeV)$ Mass Right-Handed Electron Neutrino at the HERA Electron-Proton Collider Using the ZEUS Detector", PhD thesis Columbia University (1995).

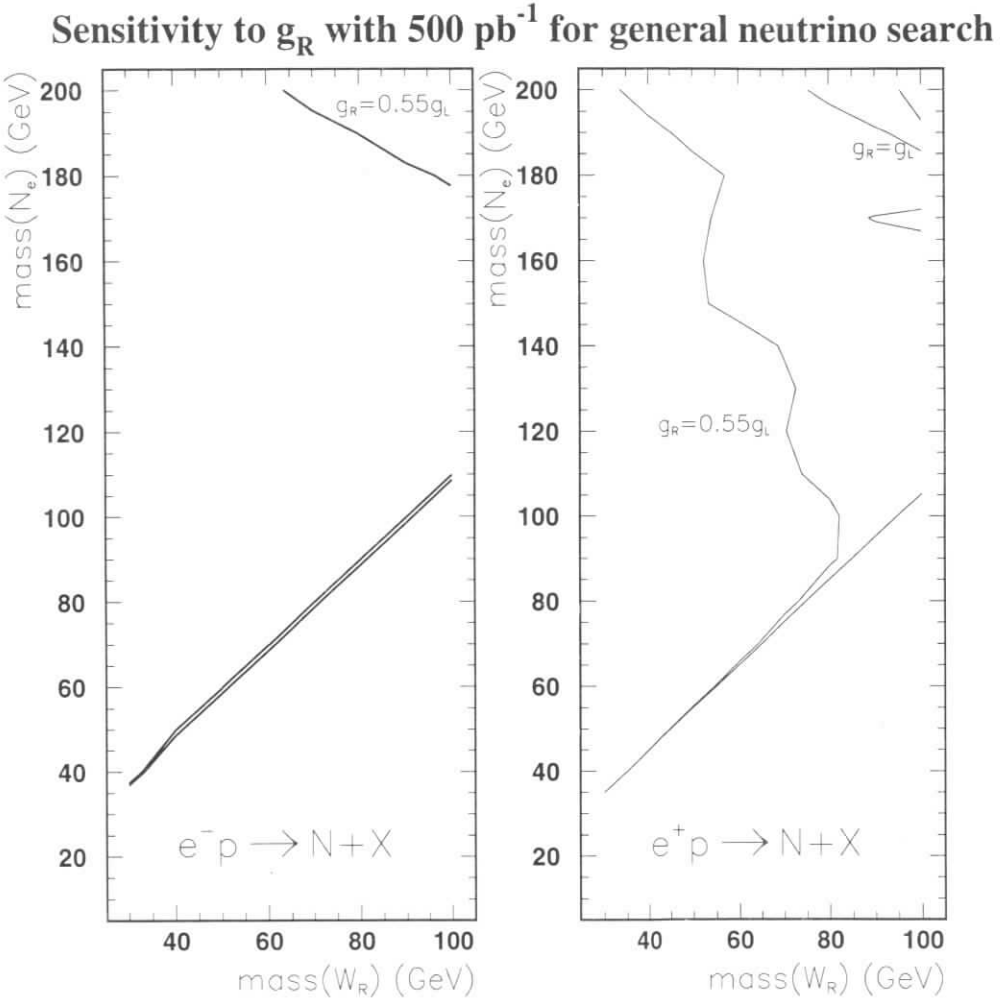

Figure 2: Limits on the mass of N_e versus the mass of W_R for various assumptions regarding the coupling, g_R, expected for luminosities of 500 fb^{-1} for e^-p (left figure) and e^+p (right figure).

Searches for Minimal Supersymmetry at HERA

Peter Schleper

Physikalisches Institut, Universität Heidelberg
and
CERN-PPE, Geneva
Peter.Schleper@cern.ch

Abstract: The potential for the discovery of particles predicted by the minimal supersymmetric standard model in a future, high luminosity run of HERA is investigated. For the most promising process of selectron and squark production, the kinematic analysis shows that a supersymmetric signal can be found free of background from standard model processes. If however no signal would be found, selectrons and squarks can be excluded up to $(M_{\tilde{e}}+M_{\tilde{q}})/2 \lesssim 100$ GeV for a large part of the SUSY parameter space. This number assumes that an integrated luminosity of 250 pb^{-1} will be collected by both experiments and that the experimental results are combined. This search is in many aspects complementary to the potential yield at LEP II and the TEVATRON.

1 Introduction

Supersymmetry (SUSY) is presently considered to be the most promising candidate for an extension of the standard model (SM). While there is strong theoretical motivation for the existence of this new fundamental symmetry of nature, there is as yet no convincing experimental evidence for the new particles predicted. For an introduction to the SUSY particle spectrum and the corresponding literature see [1].

In the following the discussion is restricted to the minimal supersymmetric standard model (MSSM), which is defined by having minimal particle content in addition to the SM and minimal additional interactions, i.e. it will be assumed that R-parity [1] is conserved. It is generally assumed that the lightest SUSY particle (LSP) is the lightest neutralino χ_1^0. R-parity conservation implies that the LSP is stable and that SUSY particles can only be produced in pairs. Since the initial state at an ep collider, namely $e+q$ or $e+g$, does not easily allow for pair productions of new particles, the search for minimal SUSY at HERA is limited to only very few processes:

- $eq \to \tilde{e}\tilde{q}$. This is the most promising channel and will be analysed here (see Fig. 1). A similar analysis using the presently available data of H1 was published in [2]. The same process, however with the assumption that R-parity is broken, was analysed in [3].
- $eq \to \tilde{\nu}\tilde{q}'$. Experimentally this process has a less distinct signature, and an irreducible background from charged current events.

- $eq \to eq\tilde{g}\tilde{g}$ for light gluinos. This channel is difficult to distinguish from SM multi-jet events as discussed in [4].
- $eq \to \tilde{e}\chi_1^0 q$. This channel has a rather small cross section and does not allow a discovery [5].

Any SUSY search depends in detail on the numerous new parameters of the MSSM, or on theoretical assumptions for relations between these parameters. In the following, two different scenarios will be evaluated:

MSSM with no additional constraints: For this analysis, the relevant free parameters of this model are the gaugino mass parameters M_1 and M_2, the parameters of the Higgs sector $\tan\beta$ and μ, and the sfermion masses of $\tilde{f}_L, \tilde{f}_R$, where f stands for e, ν_e, u, d, s, c.

MSSM with constraints from GUT models: Here only one common scalar mass m_0 and one common gaugino mass $m_{1/2}$ are relevant together with $\tan\beta$ and $sign(\mu)$. The assumptions motivated by GUT models are used to derive all other masses via renormalisation group equations (RGE), which results in strong correlations between the masses of SUSY particles.

For the general discussion of kinematics, cross sections etc. the unconstrained model will be used. For the sake of simplicity all numerical results are derived assuming equal masses for the partners of left and right handed fermions. Also the squark masses of the first two generations are assumed to be equal. Further, all calculations are done with a value of $M_1 = (5/3)\tan^2\theta_W\ M_2$ where θ_W is the weak mixing angle. This is in fact motivated by GUT models. Relaxing these assumptions will not modify the main conclusions, as will be discussed. In section 7 the constrained model is treated. It will always be assumed that gluinos are heavier than squarks.

The most promising SUSY process at HERA is the interchange of a supersymmetric neutralino between the beam electron and a quark of the proton as shown in Fig. 1. The

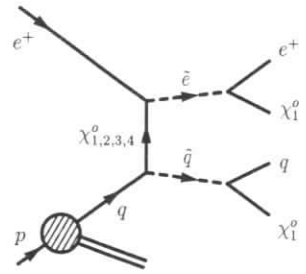

Figure 1: *Feynman diagram for selectron - squark production via neutralino exchange and the subsequent decays into the lightest supersymmetric particle LSP.*

final state consists of a selectron and a squark. These sfermions decay into their SM

partners and gauginos. The signature of the process is therefore an electron, a jet and 2 gauginos. In the experimentally most favourable case, these gauginos are χ_1^0's. They leave the apparatus undetected and therefore can be tagged by requiring missing energy and momentum. Depending in detail on which part of the MSSM parameter space is investigated, decays into other gauginos are possible or even dominant. These are much more difficult to detect and will not be considered at this stage. In any case it is crucial to take the full dependence on the MSSM parameters into account for the interpretation of the experimental results.

2 The event generator HERASUSY

For the determination of numerical results an event generator (HERASUSY) was written. This generator was also applied for the analysis in [2]. The program makes use of the ISASUSY package [7] for the investigation of the SUSY parameter space. In the context of HERASUSY, the ISASUSY package is mainly used to calculate from the basic SUSY parameters the mass eigenstates of neutralinos and the branching ratios of sfermions into gauginos. For the evaluation of the constrained MSSM, the routines ISASUGRA from the ISASUSY package are applied. These allow to calculate from the parameters $m_0, m_{1/2}$ etc. the low energy SUSY masses and couplings by making use of the second order RGEs.

From the results of ISASUSY or ISASUGRA, the couplings between neutralinos and sfermions are determined, which enter in the cross section calculation. The differential cross section for the neutralino exchange diagrams and their interference was derived in [6]. This calculation includes the full dependence on the free parameters of the unconstrained MSSM. The integration of this cross section and random generation of events in x and Q^2 is done using the programs BASES and SPRING. The results on the total cross section are found to be in reasonable agreement with those in [6].

Routines for the kinematics of sfermion decays into fermions and the χ_1^0 are added. The whole package is interfaced to PYTHIA [8] in order to allow for parton showers and fragmentation. The output of PYTHIA is available in a format suitable for simulations with the standard, GEANT–based detector simulation of the H1 detector, which was applied for all distributions shown.

In order to allow a detailed investigation of the MSSM parameter space the package can be steered such that loops on the MSSM parameters, constrained or unconstrained, are performed. For each new set of parameters the cross section is calculated and events are generated, if desired.

The program is available on request from the author.

3 Cross Section and Branching Ratios

The sensitivity of the HERA experiments depends on the cross section for $\tilde{e}$-$\tilde{q}$ production, the branching ratios into different gauginos and how well the corresponding signals can be detected. Each of these ingredients depends in a non-trivial way on the basic SUSY parameters as defined in section 1.

Concerning the cross section, the exchange of neutralinos in the t-channel is completely analogous to deep inelastic scattering (DIS) in the SM, where γ and Z^0 are exchanged. The main difference is that potentially very heavy particles have to be produced. This means first of all, that the invariant mass of the incident electron and quark has to be larger than the kinematic threshold for $\tilde{e}$-$\tilde{q}$ production,

$$(e + xp)^2 = x\,s > (M_{\tilde{e}} + M_{\tilde{q}})^2, \tag{1}$$

where x denotes the momentum fraction of the quark in the proton and e and p denote the 4-vectors of the beam particles. Due to the steep fall of the quark distribution function towards large x this determines the main dependence of the cross section on the SUSY parameters. Also the 4-momentum transfer Q^2 between the beam electron and the $\tilde{e}$ has to be larger than

$$Q^2 > \frac{1}{2}\left\{xs - M_{\tilde{e}}^2 - M_{\tilde{q}}^2 - \sqrt{\left(xs - M_{\tilde{e}}^2 - M_{\tilde{q}}^2\right)^2 - 4M_{\tilde{e}}^2 M_{\tilde{q}}^2}\right\}. \tag{2}$$

In this supersymmetric process four neutralinos $\chi^0_{1,2,3,4}$ can be exchanged. Their amplitudes interfere, similar to the interference of γ and Z^0 in standard DIS processes. The relative contribution of the $\chi^0_{1,2,3,4}$ depends on the strength of their couplings to fermions and on the neutralino masses. Because the neutralinos are the mass eigenstates of a mixing matrix of $\tilde{\gamma}$, $\tilde{Z}$ and neutral higgsinos, their couplings are derived from the parameters entering this mixing matrix. If a neutralino has a strong higgsino component (i.e. $M_2 << |\mu|$), it couples only extremely weakly to the electron and the light quarks in the proton. In this case this neutralino does not contribute significantly to the cross section. In the other cases, when the $\tilde{\gamma}$ or $\tilde{Z}$ components are large (for $\mu << -M_2$ or $\mu >> M_2$), the couplings are of the same magnitude as for the γ or Z^0.

The dependence of the χ_1^0 and $\chi_1^\pm$ masses on the MSSM parameters is shown in Fig. 2. For a given set of parameters the LSP is considerably lighter than the lightest chargino.

The neutralino masses $m_{1,2,3,4}$ for $\chi^0_{1,2,3,4}$ enter in the propagator term of the cross section in the form

$$\sigma \sim \sum_{i,j=1}^{4} \frac{C_{ij}}{(Q^2 + m_i^2)(Q^2 + m_j^2)} \tag{3}$$

where the interference between the four exchange diagrams is already taken into account. C_{ij} denotes products of the couplings of neutralino i and j to fermions as discussed above. Due to the potentially large mass differences the most important contribution is expected from the lightest supersymmetric particle, the LSP. If however the LSP is higgsino like, the χ_2^0 will most often give the largest contribution. In this case the cross section is very much reduced since the leading part of the propagator sum in the equation above is much smaller, and often too small for a measurement.

Also the branching ratios of the $\tilde{e}$ and $\tilde{q}$ depend on the neutralino couplings and masses. In the simplest case, the $\tilde{e}$ and $\tilde{q}$ decay only into the χ_1^0 and e, q, respectively. This is the case when the χ_1^0 is lighter than $\tilde{e}$ and $\tilde{q}$, and all other gauginos are heavier such that decays into them are kinematically forbidden. If also other gauginos, first of all χ_2^0 and $\chi_1^\pm$, are light enough (and not higgsino–like), then decays into these particles will generally contribute considerably, and the branching ratios into the χ_1^0 are correspondingly reduced.

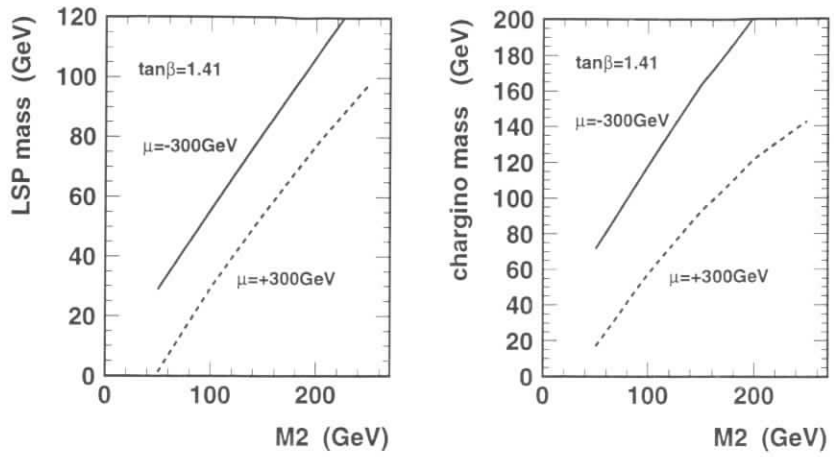

Figure 2: *Masses for the lightest neutralino (LSP) and the light chargino $\chi_1^\pm$ in dependence of other MSSM parameters.*

Experimentally, the two decay modes of sfermions, $\tilde{f} \to f\chi_1^0$ and $\tilde{f} \to f\chi$ (where $\chi = \chi_{1,2,3,4}^0, \chi_{1,2}^\pm$) have very different characteristics. The χ_1^0 is absolutely stable in the MSSM, because it is the lightest SUSY particle, and cannot be measured in the detector. The signature of an χ_1^0 is therefore missing energy or momentum. This is the gold plated signature for supersymmetry, for which searches have been performed at all colliders.

The other gauginos undergo decays into matter fermions and lighter gauginos, $\chi_m \to f\bar{f}'\chi_n$, where $f\bar{f}'$ are pairs of matter fermions and $\chi_{m,n} = \chi_{1,2,3,4}^0, \chi_{1,2}^\pm$ with $M_{\chi_m} > M_{\chi_n}$. In fact a cascade of decays to lighter and lighter gauginos occurs with the χ_1^0 as the final particle. This leads to multi-fermion final states, which are generally more difficult to identify than the direct decay $\tilde{f} \to f\chi_1^0$. Also the momentum of the χ_1^0's from cascade decays are smaller than from the direct decay, which leads to less striking signals.

In the analysis presented here, and also in the published analysis of H1 [2], cascade decay modes have been taken into account as a change of the branching ratio $BR(\tilde{f} \to f\chi_1^0)$, but have not been searched for directly.

In Fig. 3 the cross section for $\tilde{e}$-$\tilde{q}$ production times the branching ratios $BR(\tilde{e} \to e\chi_1^0)$ $BR(\tilde{q} \to q\chi_1^0)$ is shown, as obtained from HERASUSY. Given is the dependence on the sum of the $\tilde{e}$ and $\tilde{q}$ masses, $(M_{\tilde{e}} + M_{\tilde{q}})/2$, which reflects the kinematic threshold for this process. Beside phase space effects and branching ratios, the slope of the curves is mainly driven by the drop of the quark density functions in the proton towards large x. For the value of the higgsino mass parameter μ two extreme cases are shown. For $\mu = -500$ GeV the χ_1^0 is $\tilde{\gamma}$–like and for $\mu = +500$ GeV it is $\tilde{Z}$–like. The cross sections are not very different and range from about 1pb at $(M_{\tilde{e}} + M_{\tilde{q}})/2 \approx 60$ GeV to about 0.01pb for $(M_{\tilde{e}} + M_{\tilde{q}})/2 \approx 100$ GeV. The cross sections have been obtained for $\tan\beta = 1.41$ as an example for a low value for $\tan\beta$, $M_2 = 100$ GeV and $M_1 = 50$ GeV. These values lead to $M_{\chi_1^0} = 55$ GeV (30 GeV) and $M_{\chi_2^\pm} = 117$ GeV (55 GeV) for $\mu = -300$ GeV (+300 GeV),

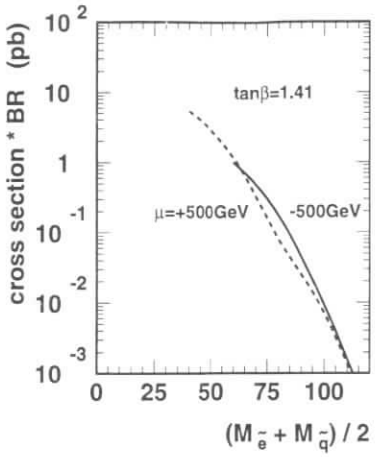

Figure 3: *Cross section times branching ratios for selectron-squark production and subsequent decays into the χ_1^0 at HERA.*

respectively. For the envisaged integrated luminosity of up to 500 pb^{-1}, these are still reasonable cross sections.

4 Background Rejection

The most important background processes are those which either lead to electron candidates or to neutrinos, since these would fake the unmeasured χ_1^0's, namely DIS neutral and charged current events and W decays into $e\nu$. The following cuts are suitable to reject these backgrounds, and illustrated in Fig. 4:

- The polar angle θ_e of the electron should be in the range $20^o < \theta_e < 130^o$, where the upper bound is used to reduce the NC background. The lower bound ensures that the charged track of the electron is measured in the central tracking detector. This requirement is used mainly to reject CC events with radiative γ's, which cannot be rejected otherwise and would have led to an irreducible background of 29 expected events for 500 pb^{-1} after all cuts.
- The quark polar angle θ_q as predicted by the measured electron must be larger than 20^o in order to avoid large missing transverse momentum $P_{T,miss}$ induced by leakage in the beam pipe. This is the most important contribution to $P_{T,miss}$ in neutral current events as shown in Fig. 4 a), where at small θ_q a tail towards positive values of the net transverse momentum of the event parallel to the electron indicates a loss of hadronic energy.
- The $E - P_z$ value of the entire event has to be below 30 GeV. For $\tilde{e}$-$\tilde{q}$ events this small value (when compared to the nominal value of twice the electron beam energy) is due to the unmeasured χ_1^0's. For NC events this means that only events with hard initial state radiation remain as background.

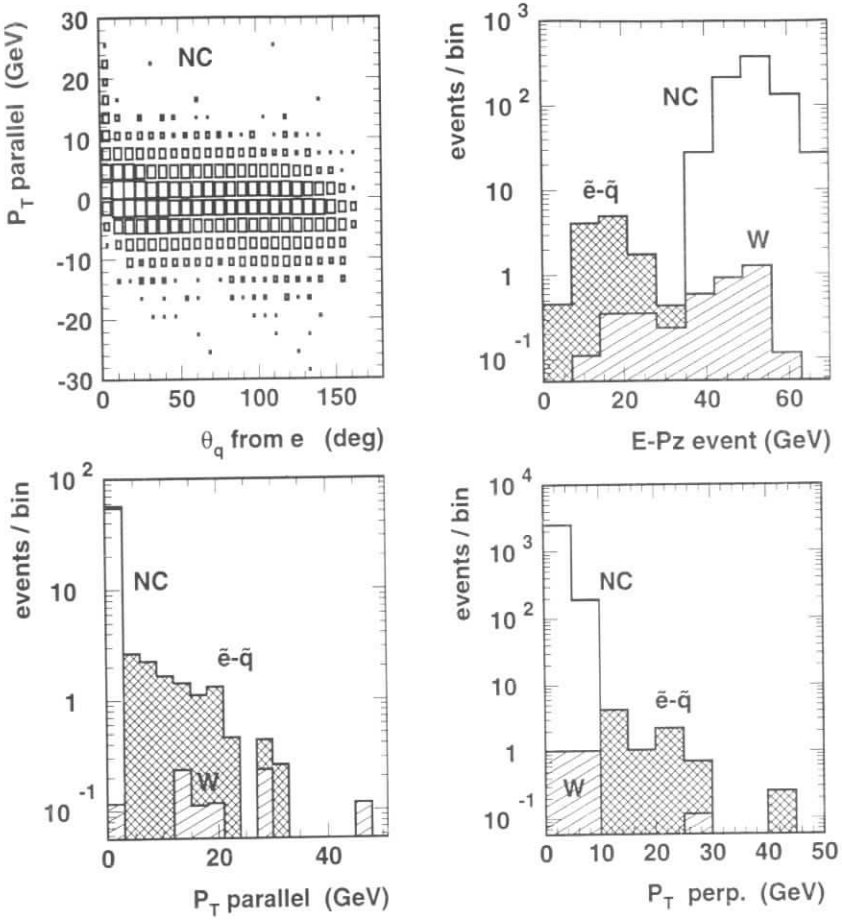

Figure 4: *Kinematic quantities from monte carlo event samples used for the $\tilde{e}$-$\tilde{q}$ search: a) Component of the event P_T vector parallel to the electron versus the quark polar angle calculated from the electron for neutral current events (NC). The size of the boxes is proportional to the logarithm of the number of events. b) E-Pz distribution for W events with decays into $e + \nu$, and added to this the contribution from NC and $\tilde{e}$-$\tilde{q}$ events ($M_{\tilde{e}} = M_{\tilde{q}} = 80$ GeV, $M_{\chi_1^0} = 60$ GeV). c) and d) Distributions of the event P_T vector parallel and perpendicular to the electron for the same monte carlo events. All distributions are normalised to a luminosity of 500* pb^{-1}.

- The $P_{T,miss}$ vector components perpendicular (parallel) to the electron momentum direction has to exceed 7 (3) GeV. These small values are necessary for a good efficiency for the signal. However they impose a major challenge for the understanding of the detector calibration and of tails in the experimental resolution for $P_{T,miss}$. In the published analysis [2] similar cuts were used and turned out to be feasible.
- The electron energy has to be smaller than 40 GeV. This suppresses W decays by about a factor 2, while for small mass differences between χ_1^0 and $\tilde{e}$,$\tilde{q}$ the efficiency loss is marginal.

In Fig. 4 b,c,d), the distributions for $E - Pz$ and the $P_{T,miss}$ vector components parallel and perpendicular to the electron directions are shown after full detector simulation. All cuts mentioned above have been applied, with the exception of the cut on the quantity which is shown in the figure. The background from W decays into $e\nu$ is given as a hatched histogram. Added on this is the NC contribution (open hist.) and the expected signal for $\tilde{e}$-$\tilde{q}$ production (crossed hist.). All distributions are normalised to an integrated luminosity of 500 pb^{-1}. For the SUSY signal, $\tilde{e}$ and $\tilde{q}$ masses of 80 GeV and a $\tilde{\gamma}$-like χ_1^0 with a mass of 60 GeV were chosen as an example. The cross section in this case is $\approx$ 0.1pb, which means that for the achieved efficiency of 22% more than 10 candidate events are expected. The huge NC background falls rapidly for the quantities shown and is completely suppressed by the cuts. In all distributions the signal is easily recognised. The only remaining background origins from W production and amounts to 0.16 events for W^+ and W^- together. This good suppression is here mainly achieved by the cut on the perpendicular component of P_T, and to a lesser extend also due to the cuts on electron energy and angle.

The efficiency of this search depends on the visible energy of the decay products of $\tilde{e}$-$\tilde{q}$, which can be parameterised as a function of the mass differences $M_{\tilde{e}} - M_{\chi_1^0}$ and $M_{\tilde{q}} - M_{\chi_1^0}$ (for details see [2]). They range from 20 to 25% for $M_{\tilde{e},\tilde{q}} - M_{\chi_1^0} > 15$ GeV. At smaller mass differences the efficiency drops rapidly and reaches 5% (1%) for mass differences of 10 GeV (5 GeV). The dependence on all other MSSM parameters is very weak in comparison, since these do not influence the final state kinematics significantly. The systematic errors due to the knowledge of the parton density functions, energy calibration and background estimation modify the final results typically by less than 2 GeV. This does not include theoretical uncertainties in the cross section calculation due to higher order effects.

In conclusion a signal for $\tilde{e}$-$\tilde{q}$ production could be found basically without background contamination, as long as the mass difference between $\tilde{e}$ and χ_1^0 and also $\tilde{q}$ and χ_1^0 is larger than $\approx$ 15 GeV.

5 Results for the unconstrained MSSM

For the derivation of possible bounds, a systematic survey of the MSSM parameter space was performed. Within the unconstrained MSSM described in section 1, the parameters $M_{\tilde{e}}$, $M_{\tilde{q}}$, and M_2 were varied independently within the bounds $45 < M_{\tilde{e}}, M_{\tilde{q}} < 160$ GeV and $0 < M_2 < 200$ GeV. This was done for values of μ of -300 and +300 GeV, corresponding to a $\tilde{\gamma}$-dominated and $\tilde{Z}$-dominated χ_1^0. As argued in section 3, a higgsino-dominated χ_1^0 is not accessible at HERA. The values chosen for $\tan\beta$ are 1.41 and 35. For other

MSSM parameters see section 1. The results for $\tan\beta$ =1.41 and μ=-300 GeV are presented in Fig. 5. Shown is the excluded region of $(M_{\tilde{e}} + M_{\tilde{q}})/2$ versus the gaugino mass

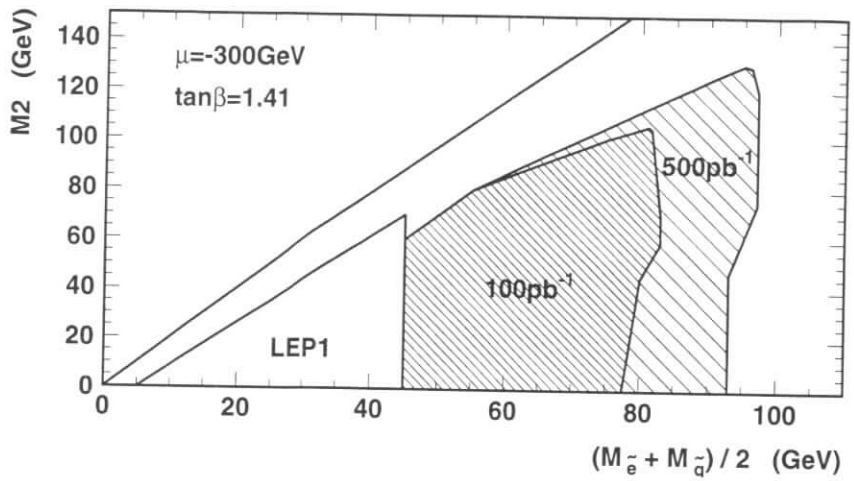

Figure 5: *Exclusion limits from HERA for $\tilde{e}$-$\tilde{q}$ production. Shown are areas which could be excluded at 95% CL for an integrated luminosity of 100* pb^{-1} *and 500* pb^{-1}. *Also shown is the region excluded by LEP 1.*

parameter M_2. The hatched areas correspond to an integrated luminosity of 100 pb^{-1} respectively 500 pb^{-1} of both experiments together , assuming that no candidates are found. The highest masses accessible are 130 GeV for M_2, and up to 100 GeV for $(M_{\tilde{e}} + M_{\tilde{q}})/2$. The shape of the excluded domain can be understood as follows:

The diagonal line is the limit where the χ_1^0 has the same mass as the $\tilde{e}$ or $\tilde{q}$. The region very close to this line cannot be explored because for small mass differences, the remaining energy for the final state e and q of the decays $\tilde{e} \to e\chi_1^0$ and $\tilde{q} \to q\chi_1^0$ becomes too small. Also the cross section is smaller for large χ_1^0 masses.

The maximum range for $(M_{\tilde{e}} + M_{\tilde{q}})/2$ is limited by the available energy in the initial eq system. The drop of the quark density function towards large x (roughly $\sim (1-x)^3$) is compensated by an increase of the integrated luminosity. It should be noted that the highest energy reached in the figure, namely $M_{\tilde{e}} + M_{\tilde{q}} \approx 190$ GeV, is still considerably below the maximum possible reach of $\sqrt{s} = 300$ GeV. Therefore an even higher luminosity than 500 pb^{-1} is certainly desirable.

At small values of the gaugino mass parameter M_2 the sensitivity for $(M_{\tilde{e}} + M_{\tilde{q}})/2$ is slightly reduced because also decays into other gauginos start to become allowed kinematically.

Parameter Dependence In [2] it has been shown that the dependence on μ is negligible if the higgsino–component of the χ_1^0 is small. The result therefore applies as long as $\mu \lesssim M_2$. A higgsino–like χ_1^0 is not accessible at HERA. For a $\tilde{Z}$–like χ_1^0 the bounds on $M_{\tilde{e},\tilde{q}}$

are about 10 GeV higher than shown in Fig. 5 (see however the discussion of the bounds from LEP2 below).

The choice of $\tan\beta$ influences only very little the cross section and the values chosen here are preferred theoretically and close to those obtained from global fits of SUSY parameters to data [9]. For $\tan\beta$ =35, the bound on M_2 is about 10 GeV higher than for $\tan\beta$ =1.41.

M_1 was related here to M_2 only because this allows a straight forward comparison with LEP2 results. For a $\tilde{\gamma}$–like χ_1^0, the limits depend however more directly on the χ_1^0 mass, because this enters in the propagator term of the cross section and the efficiency. The dependence on M_1 and M_2 is to first approximation given only indirectly through this dependence on the χ_1^0 mass, and can be deduced from Fig. 2 and Fig. 5. Therefore the relation $M_1 = (5/3)\tan^2\theta_W\, M_2$ can be relaxed without a major change of the result, as long as the χ_1^0 mass remains constant and the χ_1^0 is $\tilde{\gamma}$–like. Also the other neutralinos have to be heavy enough so that their contribution to the cross section is small. This means that M_2 could be much higher than actually shown in Fig. 5.

The assumption was made that the SUSY partners of left and right handed fermions have the same mass. If this is not the case the cross section would be reduced. In the extreme case that for example both $\tilde{e}_L$ and $\tilde{q}_L$ are much heavier than $\tilde{e}_R$ and $\tilde{q}_R$, the cross section would be reduced by more than a factor two, as can be verified from [6]. Fig. 3 shows that this would lead to mass bounds about 5 GeV (at most 10 GeV) lower than the ones displayed in Fig. 5.

6 Comparison with LEP and TEVATRON

At the time when the HERA experiments will have achieved the luminosities shown in Fig. 5, the LEP2 collider will presumably run at $\approx$ 190 GeV, and the main injector at the TEVATRON is expected to deliver a luminosity of 1000 pb^{-1} per year. The searches at both colliders will be close to their maximum reach when the HERA upgrade becomes effective.

Chargino Searches at LEP2: A mass of the $\chi_1^\pm$ close to $E_{\rm cms}$ /2=95 GeV can be tested [10]. For a $\tilde{\gamma}$–like χ_1^0 ($\mu = -300$ GeV), this corresponds to M_2 =75 GeV as can be seen from Fig. 2. The HERA sensitivity is much better in comparison and reaches up to 130 GeV. In addition the LEP2 bounds will be weaker if the $\tilde{\nu}$ mass is small. In contrast, for a $\tilde{Z}$–like χ_1^0 the LEP2 bound of M_2 =155 GeV is stronger than the HERA bound.

$\tilde{e}$ and $\tilde{q}$ searches at LEP2: Also here, mass limits close to the kinematic boundary for pair production can be achieved provided the integrated luminosity is high enough [10]. The resulting bound is therefore almost identical to the one reachable at HERA. In case of a discovery the combination of the results will allow important checks because the production mechanisms depend in a different way on the MSSM parameters.

$\tilde{q}$ searches at the TEVATRON: Already now the TEVATRON experiments have set limits for $\tilde{q}$ masses of several hundred GeV, which however depend on the values assumed for the χ_1^0 and gluino masses and on theoretical assumptions [11]. The HERA results in contrast are independent of the $\tilde{g}$ mass.

- In [11] no bounds on $M_{\tilde{q}}$ could be set within the *constrained* MSSM for $M_{\tilde{g}} \gtrsim 500$ GeV. This is partially due to the inclusion of cascade decays, to the connection of $M_{\tilde{g}}$ to $M_{\chi_1^0}$ in GUT models, and to a reduced sensitivity if $M_{\chi_1^0}$ is close to $M_{\tilde{q}}$.

  This result cannot be translated directly into the different theoretical assumptions made in this paper, because the masses of gauginos, the squark branching ratios and the significance of the $P_{T,miss}$ signal from χ_1^0's differ considerably.

- In [11] high bounds on $M_{\tilde{q}}$ were set within the *unconstrained* MSSM independently of the gluino mass, however only for $M_{\chi_1^0} < 15$ GeV and assuming that there are no cascade decays. The HERA bounds in comparison extend up to about $M_{\chi_1^0}$ =60 GeV.

The TEVATRON certainly has a larger potential for $\tilde{q}$ searches than HERA. On the other hand also the QCD background is much larger. This means that the HERA results will only be competitive in that part of the parameter space where the mass difference between $\tilde{q}$ and χ_1^0 is very small. In this case the jets from squark decays into the χ_1^0 have rather low energies and also the missing P_T signal is degraded. This signature is probably much more difficult to find at the TEVATRON than the $e + q + P_{T,miss}$ signal at HERA. For example this analysis uses a $P_{T,miss}$ threshold of less than 10 GeV, and is sensitive to mass differences as small as 20 GeV.

In conclusion, the HERA results will be competitive to those from LEP for a $\tilde{\gamma}$–like χ_1^0. In comparison to TEVATRON the only gap, if existing, would be for a χ_1^0 mass close to the $\tilde{q}$ mass.

7 Results for the Constrained Supersymmetric Model

Using the procedure described in section 2 the cross section for $\tilde{e}$–$\tilde{q}$ production was evaluated for many combinations of m_0 and $m_{1/2}$, positive and negative μ and $\tan\beta$ =1.41 and 35. Only those parameter sets were accepted which obey constraints from the measurement of the Z^0 width, from grand unification and electroweak symmetry breaking. In comparison to Fig. 3 only small differences were found due to the mass splittings in the fermion sector. However, as expected, the limits for $M_{\chi_1^0}$ and $M_{\tilde{q}}$ as shown in Fig. 5 also lead to limits on the gluino mass, since these quantities are related to each other via the RGEs. In comparison to the TEVATRON bounds [11] obtained already now with the same theoretical assumptions, the gluino mass limits obtained for HERA were found to be smaller for all parameter combinations tested. From this it is concluded that HERA also with high luminosity can not improve on present bounds for this model.

8 Detector Modifications for High Luminosity Runs

The envisaged upgrade of HERA implies severe changes to the detectors, the most important being that new magnets are inserted very close to the vertex. These will not disturb the central track measurements, but in front of the calorimeters and at polar angles below 80mrad, a large amount of material will be added. The expected effects for new particle searches are the following:

- The acceptance for particles at low angles is reduced. For the production of heavy new particles this could cause problems because these are always boosted into the forward direction due to the large mismatch between the beam energies at HERA. As it is shown however in Fig. 6 this turns out to be no problem. For a heavy

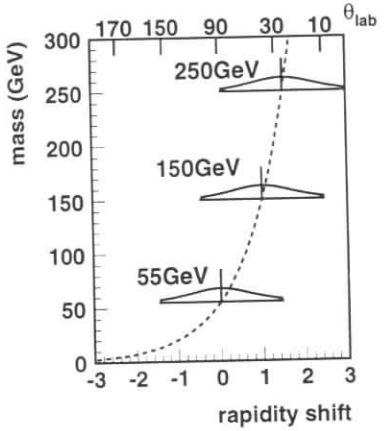

Figure 6: *Mean rapidity boost for decay products of heavy particles (dashed line). Overlayed are for three different masses the rapidity distributions of decay products, assuming an isotropic 2-body decay.*

particle A of mass M_A produced via $ep \to AX$, the rapidity boost δy depends only logarithmically on M_A

$$\delta y = \ln \frac{M_A}{2E_{e,beam}} \tag{4}$$

where $E_{e,beam}$ is the electron beam energy. This function is shown in figure Fig. 6 as a dashed line, and gives a maximum rapidity boost of 1.7. The decay products of this particle A are typically centred in 1 unit of pseudorapidity around this value as is shown in Fig. 6 for three different masses for a scalar particle A. The decay products therefore are not outside the acceptance of the detector. In the case of $\tilde{e}$-$\tilde{q}$ production, M_A corresponds to the invariant mass of the $\tilde{e}$-$\tilde{q}$ system.

- For H1 the loss of acceptance will mainly influence the analysis of the forward PLUG calorimeter, which was used in [2] as a veto against energy losses close to the beam pipe. In this analysis, the cut on PLUG energies could be avoided by cutting much stronger on other quantities (θ_q). This lead to a loss of efficiency by almost a

factor 2. However one should note that a reduced efficiency was anyhow expected because at much higher luminosities more and different background ($W \to e\nu$) is expected and naturally requires stronger cuts. In fact the cuts were not tuned to avoid dependencies on the forward region of the apparatus, but evolved that way naturally because the W background is strongly forward peaked.

- More uncertain is the effect of secondary interactions of particles at low angles, which hit the inner part of the magnet and produce particles at larger polar angles. Because particles at low angles tend to have very high energies at HERA, the shower products will also be highly energetic and might carry considerable transverse momentum. The net effect will be an increased energy flow for polar angles much larger than 80mrad, which could considerably disturb the measurements. At present it is not known how large the effects will be on average, and more important here, to what extend tails in the $P_{T,miss}$ distribution would be induced. If this turns out to be the case, then such secondary interactions must be tagged in order to maintain the present situation of an almost background free signal.

In conclusion, there is no direct loss of acceptance for new particle searches. It remains however to be proven that the tails of the $P_{T,miss}$ distributions from SM processes can be controlled. In any case, one should not use a reduced detector performance for new particles searches as an argument against a luminosity upgrade. In contrast, only a major increase of the luminosity, far beyond 100 pb^{-1} per experiment, allows also for the future the possibility of discoveries at HERA.

9 Summary

The process $eq \to \tilde{e}\tilde{q} \to e\chi_1^0 q\chi_1^0$ was found to yield a very clean signal for Supersymmetry at HERA. With simple kinematic cuts on missing momenta and angular distributions the background from Standard Model processes can be reduced down to 0.16 events expected events from $W \to e\nu$ for an integrated luminosity of 500 pb^{-1}. It is argued that these results are also realistic for a detector setup with magnets close to the interaction vertex.

For a photino like χ_1^0, masses up to $(M_{\tilde{e}} + M_{\tilde{q}})/2 \lesssim 100$ GeV can be explored for $M_{\chi_1^0} \lesssim 75$ GeV with only minor dependences on other parameters of the MSSM. No assumptions on constraints from GUT models are made here. Similar values for $M_{\tilde{e},\tilde{q}}$ can be reached in a high luminosity run at LEP2, however with different dependences on the parameters of the MSSM. Results from the Tevatron experiments exclude much larger squark masses. These bounds are however at present not valid for large gluino masses or heavy χ_1^0's, and have been derived with different theoretical assumptions. It seems plausible that also in the future a gap for HERA might remain in case the χ_1^0 mass is close to the squark mass.

It has to be emphasised that the HERA results are only limited by statistics, and that either with an increase of the integrated luminosity or, even more favourable, with an increase of the beam energies, this search could carry on to even higher masses.

Acknowledgment

I would like to thank Herbi Dreiner for his careful reading of the manuscript as well as for his stimulation during the workshop.

References

[1] H.P.Nilles, Phys. Rep. **110** (1984) 1.
H.Haber and G.Kane, Phys. Rep. **C117** (1985) 75.
G.G.Ross, *Grand Unified Theories*, Benjamin Cummings (1985).
for a recent review see H. Baer et. al.,
FSU-HEP-950401, hep-ph/953479, and references therein.

[2] H1 Collaboration, S. Aid et al., Phys. Lett. B380 (1996) 461.

[3] H. Dreiner, P. Morawitz, Nucl. Phys. B428 (1994) 31.

[4] D. Graudenz, K. Meier, O. Nachtmann, D. Stevens, K. Zuber, these proceedings.
M. David, these proceedings.

[5] M. Corradi, these proceedings.

[6] J. Bartels, W. Hollik, Z. Phys. C39 (1988) 433.

[7] H. Baer, F. Paige, S. Protopopescu and X. Tata, Proceedings of the workshop on Physics at Current Accelerators and Supercolliders, ed. J. Hewett, A. White and D. Zeppenfeld, Argonne National Laboratory (1993).

[8] T. Sjöstrand, Comp. Phys. Comm. **82** (1994) 74.

[9] W. de Boer, Prog. Part. Nucl. Phys. **33** (1994) 201-302.

[10] Proceedings of the workshop on 'Physics at LEP 2', ed. G. Altarelli, T. Sjöstrand and F. Zwirner, Geneva 1996.

[11] CDF Collaboration, F. Abe et al., Phys. Rev. Lett. **69** (1992) 3439.
D0 Collaboration, S. Abachi et al., Phys. Rev. Lett. **75** (1995) 618.
CDF Collaboration, F. Abe et al., Phys. Rev. Lett. **76** (1996) 2006.

Associated production of selectron neutralino pairs

M. Corradi[a]

[a] Universitá di Bologna and INFN Bologna, Via Irnerio 46, Bologna, Italy

Abstract: A Monte Carlo study of the process $ep \to \tilde{e}\chi_1^0 X$ has been performed, including detector simulation and background estimate. Exclusion plots in the $m_{\chi_1^0}$ versus $m_{\tilde{e}}$ plane are provided for different values of integrated luminosity.

1 Introduction

Most of SUSY GUT models predict squarks heavier than sleptons. No-scale supergravity models [1], (that have been the object of renewed interest [2]), predict a ratio $m_{\tilde{q}}/m_{\tilde{e}_R} \gtrsim 3$. In these models, the process $ep \to \tilde{e}\tilde{q}$ has a small cross section or is beyond the accessible region of HERA, given the exisiting LEP1 (sleptons) and TEVATRON (squarks) lower mass bounds. Therefore the associated production of slepton gaugino pairs becomes the most important process for the production of (R_p conserving) SUSY particles [3, 4]

$$e^{\pm}p \to \tilde{e}^{\pm}\chi_i^0, X \qquad (1)$$

$$e^{\pm}p \to \tilde{\nu}\chi_i^{\pm}X. \qquad (2)$$

Assuming that χ_1^0 is the LSP and that the selectron decays to $\chi_1^0 e$, the signature for process

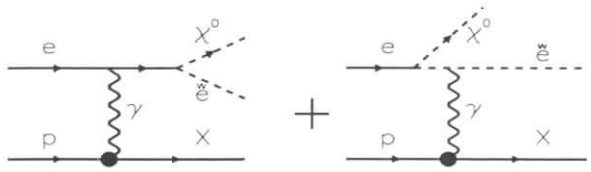

Figure 1: *Relevant graphs for selectron neutralino production.*

(1) is an electron (from selectron decay) and missing P_t (from the two neutralinos). Moreover, the fact that a very low mass neutralino is not yet excluded by other experiments (at least for low $\tan\beta$) makes this channel interesting at HERA. Process (2) may have an higher cross section for some set of SUSY parameters, but it produces various final states, due to different chargino and sneutrino decay channels, some of them leading to jets and missing p_t, not easy to distinguish from Standard Model backgrounds. Only the selectron neutralino production channel (1) is considered in this note.

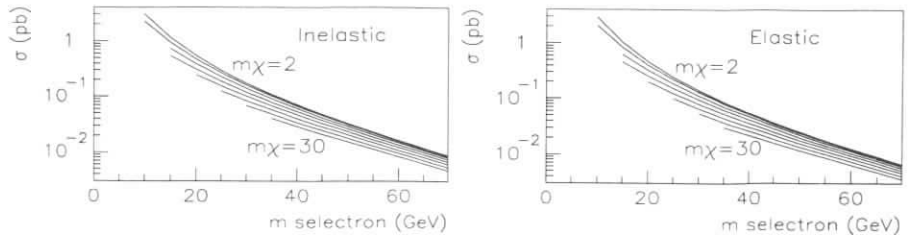

Figure 2: *$ep \to \tilde{e}\chi_1^0 X$ cross section for the elastic and inelastic process as a function of selectron mass in the pure photino limit. Each curve is for a different value of the $m_{\chi_1^0}$ in 4 GeV steps.*

2 Production Cross Section and MC Generator

The relevant Feynman diagrams for process (1) are shown in fig.1. The pair of SUSY particles is produced at the electron vertex. The hadronic final state X can be an elastically scattered proton or an higher mass system.

A monte carlo generator (PYSUS [1]) has been used to evaluate the cross section and to generate events. It is based on a cross section factorized into a photon flux times a parton cross section: $\sigma_{ep\to\tilde{e}\chi_1^0} = \int_{z_{min}}^1 dz f_{\gamma/p}(z)\sigma_{\gamma e\to\tilde{e}\chi_1^0}(sz)$ [4, 5, 6]. The parton ($e\gamma \to \tilde{e}\chi_1^0$) cross section is taken from [4]. In the elastic case, the modified Weizsäcker-Williams approximation [7] is used for the photon flux. In the inelastic case, the photon flux is convoluted from GRV92 parton densities: $f_{\gamma/p}(z) = \sum_i \int_{x_{min}}^1 dx/x \int_{Q^2_{min}}^{Q^2_{max}} dQ^2/Q^2 f_{\gamma/q}(z/x)q_i(x,Q^2)$. The Q^2_{min} cutoff is set to 1 GeV^2, in order to reproduce the inelastic cross section given in ref [6]. Figure 1 shows the cross

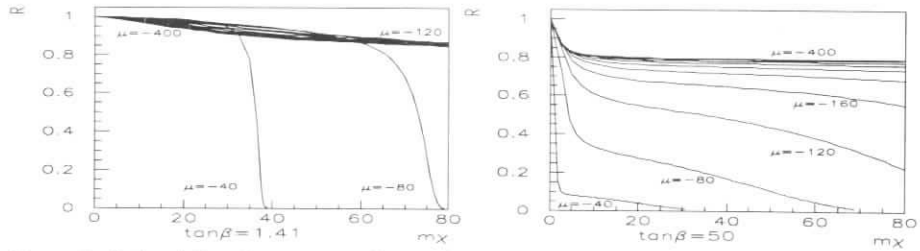

Figure 3: *Ratio of the selectron neutralino to the pure photino cross section (fig. 1) for* $\tan\beta = 1.41$ *(left) and* $\tan\beta = 50$ *(right), as a function of the* χ_1^0 *mass. The lines are from* $\mu = -400$ *to* $\mu = -40$ *in steps of 40.*

section for (left) inelastic and (right) elastic process, as a function of the selectron and neutralino mass. In this plot, the right and left handed selectron are assumed to be mass degenerate and the neutralino to be a pure photino ($\tilde{\gamma}$). Since the value of the $e\chi_1^0\tilde{e}$ coupling constant depends on the neutralino mixing matrix, in the MSSM the total cross section is a function of the parameters $\tan\beta$, μ and M_1. The dependence on these parameters can be included in the normalization factor $R(\mu, \tan\beta, m_{\chi_1^0}) = \sigma_{\tilde{e}\chi_1^0}(m_{\tilde{e}}, m_{\chi_1^0}, \tan\beta, \mu)/\sigma_{\tilde{e}\tilde{\gamma}}(m_{\tilde{e}}, m_{\tilde{\gamma}})$ shown in fig. 3. R is close to 1 in the gaugino region ($|\mu| >> M_1$).

[1] Contact the author for the code and documentation on PYSUS MC generator: `corradi@vxdesy.desy.de`

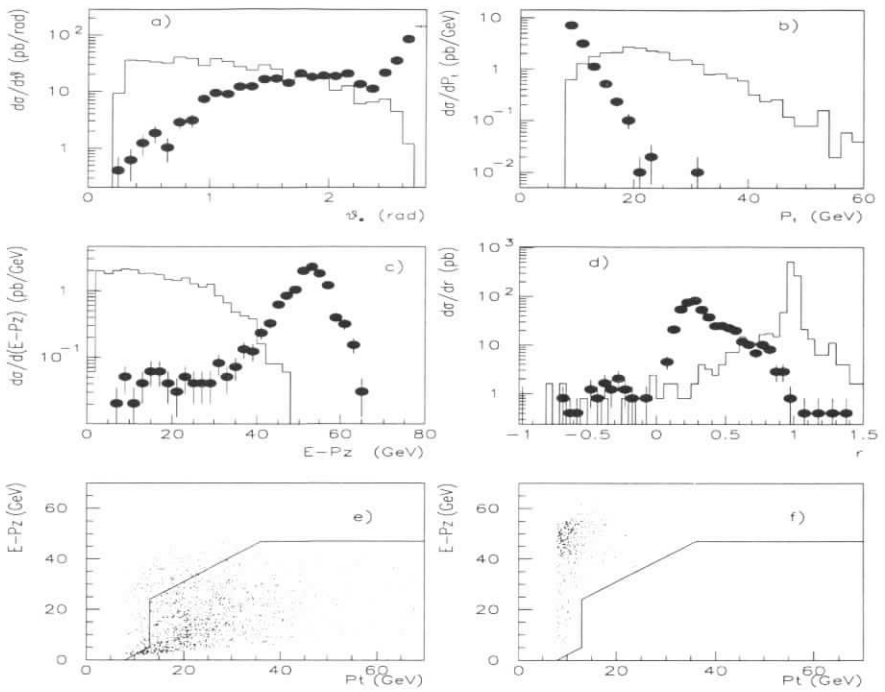

Figure 4: *Detector level distributions for SM background (dots) and for SUSY events ($m_{\tilde{e}} = 40$, $m_{\chi_1^0} = 5$) (line) with arbitrary normalization: a) electron polar angle after cuts 1-3; b) missing P_t, c) $E - P_z$ and d) $r = \mathbf{p}_t^e \cdot \mathbf{p}_t / |p_t|^2$ after cuts 1-4; e) distribution in the $E - P_z$ versus missing P_t plane for SUSY and f) for 48.8 pb^{-1} of NC DIS after cuts 1-5. The line shows the cut adopted in the inelastic selection.*

3 Selection Efficiency and Backgrounds

MC samples of $ep \to \tilde{e}\chi_1^0 X$ and SM backgrounds have been produced and passed through the ZEUS detector simulation. A selection procedure based on the following requests was adopted (see fig. 4 a-d):

1) An isolated electromagnetic cluster in the calorimeter identified as an electron and matching a track of the correct charge from the central tracking detector;
2) missing transverse momentum $P_t > 8$ GeV;
3) standard cuts to remove cosmic muons and beam-gas interactions;
4) polar angle of the electron $\theta_{el} < 2.5 rad$;
5) A cut on the variable $r = \mathbf{p}_t \cdot \mathbf{p}_t^{el} / |\mathbf{p}_t|^2 > 0.4$ (where -$\mathbf{p}_t$ is the missing P_t vector and $\mathbf{p}_t^{el}$ is the electron transverse momentum vector) (fig. 4 d).

$m_{\tilde{e}}$ (GeV)	m_{χ} (GeV)	Elastic process a) ϵ (%)	Elastic process b) ϵ (%)	Inelstic process a) ϵ (%)	Inelstic process b) ϵ (%)
20	5	16	42	16	8
40	5	55	71	44	15
40	25	31	55	28	13
40	35	1	5	2	2
60	5	59	66	51	17
60	25	59	65	51	20

Table 1: *Efficiencies for elastic and inelastic process. a) inelastic selection, b) elastic selection. Obtained from selectron neutralino MC samples of 1000 events each.*

At this point two different selections are made:
a) The inelastic selection, based on a cut in the missing P_t vs $E - P_z$ plane along the line shown in fig. 4 e-f.
b) The elastic selection, obtained by the request of no energy deposit in the calorimeter other than the electron.

Table 1 shows the selection efficiency ϵ for different MC samples. The efficiency depends on the electron p_t spectrum, and therefore on $\Delta m = m_{\tilde{e}} - m_{\chi_1^0}$.

Process	MC Generator	Lumi (pb^{-1})	Inelastic b (fb)	Elastic b (fb)
NC DIS	Herwig, Lepto, Ariadne $Q^2 > 100$	48.8	0	0
CC DIS	Lepto $Q^2 > 100$	490	0	0
$c\bar{c}$	Pythia $P_t^{miss} > 8$	50	0	0
$b\bar{b}$	Pythia $P_t^{miss} > 8$	64	0	0
$\gamma\gamma$ elast.	Lpair $P_t^e > 5$	1910	0	0.5
$\gamma\gamma$ inelast.	Lpair $P_t^e > 5$	782	0	1.3
W^+ DIS	Epvec	10000	17.9	0
W^+ resolved	Epvec	10000	12.3	1.0
Z0 DIS	Epvec	14300	1.5	.07
Z0 quasi-elast.	Epvec	27000	1.3	0
Z0 resolved	Epvec	15600	0	0
Z0 elastic	Epvec	20000	2.4	2.8
TOTAL			35.4	5.7

Table 2: *SM backgrounds. The table shows the process, the MC generator and the generator level cuts, the MC luminosity used and the background rate (i.e. the number of surviving events normalized to 1000 pb^{-1}) for the inelastic and elastic selection.*

The following background processes have been considered: NC DIS, CC DIS, heavy quark production, $\gamma\gamma$ interaction and vector boson production. The MC equivalent luminosity and

the rate of surviving events b are given in table 2. The inelastic selection is affected by an high background from W production ($ep \to WeX, W \to e\nu$, with the scattered electron undetected). The background for the elastic selection is lower. It comes mainly from elastic Z production ($ep \to epZ^0$, $Z^0 \to \nu\bar{\nu}$) and from the $\gamma\gamma \to e^+e^-$ process. The main uncertainty on the background comes from the limited MC statistics for NC DIS and heavy quarks.

In the elastic $ep \to \tilde{e}\chi_1^0 p$ selection, 20 to 30% of the events have the elastically scattered proton detected by the Leading Proton Spectrometer (LPS). The proton momentum $\mathbf{p}'$ measured in the LPS can be used to reconstruct kinematical variables such as the center of mass energy $W_{\gamma e} = m_{\tilde{e}\chi_1^0}$ (fig. 5 a) and the missing mass $m^2_{\chi_1^0\chi_1^0} = (\mathbf{p} + \mathbf{e} - \mathbf{p}' - \mathbf{e}')^2$ (fig. 5 b), allowing a measurement of the mass of SUSY particles. Moreover the background from elastic Z0 events can be removed by a cut on $m_{\chi_1^0\chi_1^0}$.

4 Search Reach

Given an expected integrated luminosity L and assuming a number of detected events equal to the expected background $n_0 = \mu_B = bL$, a 90% CL upper limit on the signal events $N^{90\%}$ can be set [8]. This limit can be transformed in an exclusion plot on $m_{\tilde{e}}$ and $m_{\chi_1^0}$, excluding the mass sets that satisfy $\sigma(m_{\tilde{e}}, m_{\chi_1^0})\epsilon L > N^{90\%}$.

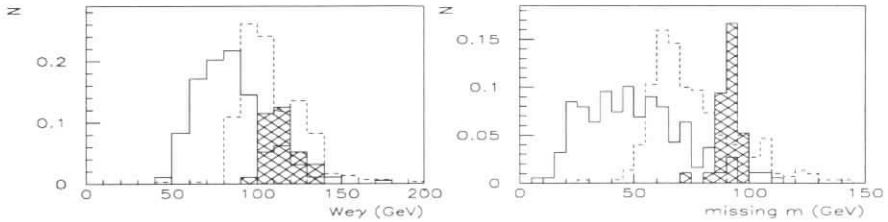

Figure 5: *Distributions of kinematical quantities reconstructed from the elastically scattered proton detected in the LPS. a) The center of mass $W_{\gamma e} = m_{\tilde{e}\chi_1^0}$ mass and b) the missing mass $m_{\chi_1^0\chi_1^0}$. The filled histogram is elastic Z0 background, the full line is $m_{\tilde{e}} = 40$, $m_{\chi_1^0} = 5$ and the dashed line is $m_{\tilde{e}} = 60$, $m_{\chi_1^0} = 25$. Note that $m_{\tilde{e}} + m_{\chi_1^0} = \min(W_{\gamma e})$ and $2m_{\chi_1^0} = \min(m_{\chi_1^0\chi_1^0})$*

Figure 6 a-b) shows the contours of the 90% CL excluded region for different luminosities for $\chi_1^0 = \tilde{\gamma}$ and $m_{\tilde{e}_R} = m_{\tilde{e}_L}$. Figure 6 c-d) shows the 90% CL excluded regions with a luminosity of 1000 pb^{-1} in the MSSM, assuming the relation $\frac{M_1}{M_2} = \frac{5}{3}\sin\theta_w$. Since the selectron can decay also to chargino and to the second neutralino, the branching ratio $\tilde{e} \to e\chi_1^0$ (evaluated with the ISASUSY[9] code) has been taken into account. The dash-dotted line is the limit for the process $e^-p \to \tilde{e}_R^-\chi_1^0 X$, i.e. the case of the left handed selectron heavyer than right handed. The shaded area shows the region excluded by LEP1 and LEP1.5. [10]. The elastic selection is the more promising: with a luminosity $\sim 1 fb^{-1}$ existing limits can be substantially improved.

Acknowledgments

I wish to thank R.Nania, M.Basile and I.Gialas for their unvaluable suggestions and A.Zichichi for having initiated and stimulated these studies.

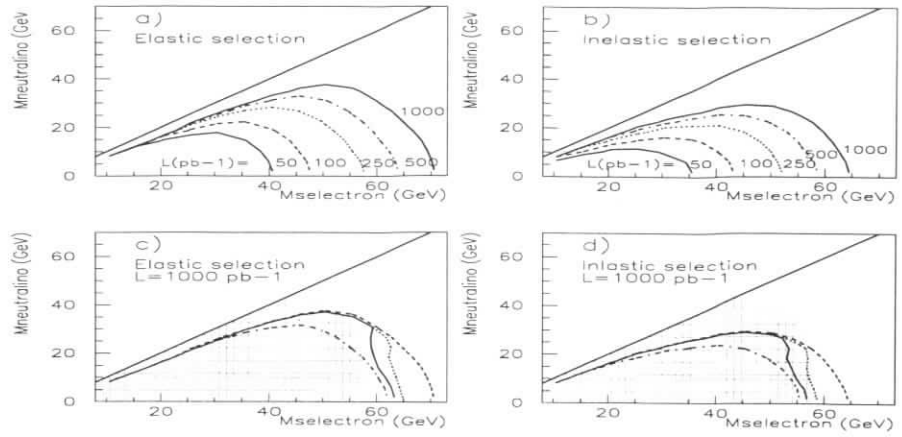

Figure 6: *Contours of the regions excluded at 90% CL in the plane $m_{\chi_1^0}$ vs $m_{\tilde{e}}$ for the elastic (a,c) and the inelastic (b,d) selection. a,b) for various values of the integrated luminosity in the pure photino case. c,d) for fixed luminosity (1 fb^{-1}) and different values of the MSSM parameters:* $\tan\beta = 1.41$, $\mu = -50$ *(dashed line);* $\tan\beta = 1.41$, $\mu = -500$ *(dotted line);* $\tan\beta = 35$, $\mu = -500$ *(solid line);* $m_{\tilde{e}_L} >> m_{\tilde{e}_R}$ *(dash-dotted line). The hatched area is excluded by LEP.*

References

[1] A.Lahanas and D.V.Nanopoulos, Phys Rep. 145(1987) 1 and references therein;

[2] J.L.Lopez, D.V.Nanopoulos and A.Zichichi, PRD 49(1994)343, Int. J. Mod. Phys. A 10(1995)4241, PRD 52(1995)4178, and PRD 53(1996)5253; J.Lopez and D.V.Nanopoulos, PRL 76(1996)1566, hep-ph/9412332 (int. J. Mod. Phys. A) , hep-ph/9607220; J.L.Lopez, D.V.Nanopoulos and K. Yuan, Nucl. Phys. B399(1993)654;

[3] J.Lopez *et al.* CERN-TH.7401/94;

[4] J.L.Lopez, D.V.Nanopoulos, X. Wang and A.Zichichi, PRD 48(1993)4029.

[5] P.Salati, J.Wallet PLB 122(1983)397; G.Altarelli, *et al.* Nucl. Phys. B262(1985)204; M.Drees, D.Zeppenfeld PRD 39(1989)2536;

[6] H.Tsutsui *et al.* PLB245(1990)663;

[7] B.A.Kniehl PLB 254(1991)267;

[8] L.Montanet *et al.* (PDG) Review of Particle Properties, PRD 54(1996) equation 28.40;

[9] H.Baer *et al.* in *Physics at Current Accelerators and Supercolliders*, J. Hewett *et al.* editors, (Argonne N.L. 1993);

[10] Decamp *et al.* (ALEPH coll.) Phys.Rep. 216(1992)253; Adriani *et al.* (L3 coll.) Phys.Rep. 236(1993)1; ALEPH coll. CERN PPE 96-10;

R-Parity Violating Supersymmetry at HERA

E. Perez[a], Y. Sirois[b]
[a] CEN-Saclay, DSM/DAPNIA/SPP, Gif-sur-Yvette, France
[b] LPNHE Ecole Polytechnique, IN2P3-CNRS, Palaiseau, France

H. Dreiner
Rutherford Appleton Laboratory, Chilton, Didcot, Oxon, United Kingdom

Abstract: The phenomenology and prospects for a discovery of R-parity violating Supersymmetry at HERA is reviewed. Emphasis is put on the direct resonant production of squarks by electron-quark fusion and *all possible* subsequent decay modes of the squarks are considered. In particular, the full consequences of the mixing in the supersymmetric gaugino-higgsino sector are taken into account. A rich phenomenology emerges for HERA which offers a unique sensitivity to new R-parity violating couplings and good discriminating power against free parameters of the theory.

1 Introduction

Supersymmetry (SUSY) which fundamentally links fermions and bosons is likely to be chosen as an essential property of a true theory beyond the Standard Model (SM). Among the most compelling arguments for a SUSY world are the fact that local supersymmetric transformations are fundamentally related to generators of space-time translation (hence necessarily incorporates gravity) [1], the possibility to "explain" the hierarchy between the electroweak mass scale and the Grand Unification or Planck mass scale, and the stability of a softly broken SUSY which "naturally" avoids the arbitrary fine tuning of the parameters which is necessary in the SM [2].

A natural framework for SUSY searches is provided by the Minimal Supersymmetric extension of the Standard Model (MSSM) [3] which has predictive power within a finite and well defined set of free parameters and has neither been proven nor falsified by experimental observations. The latter is a non-trivial status given the remarkable precision tests of the SM at the LEP collider over the recent years. It might have to do with the fact that quantum corrections due to the sparticles which otherwise respect all gauge symmetries of the SM tend to be small rendering indirect observations difficult. It is in addition possible that direct searches for particles of the minimal field representation offered by the MSSM have at least partly failed because they were looking at the wrong phenomenology.

The most general Yukawa couplings in a supersymmetric theory which is gauge invariant and minimal in terms of field content can be written [4] in the compact formalism of the

superpotential as $W_{SUSY} = W_{MSSM} + W_{\not R_p}$. The W_{MSSM} contains terms which are responsible for the Yukawa couplings of the Higgs fields to ordinary fermions. The $W_{\not R_p}$ is given by:

$$W_{\not R_p} = \lambda_{ijk} L_i L_j \bar{E}_k + \lambda'_{ijk} L_i Q_j \bar{D}_k + \lambda''_{ijk} \bar{U}_i \bar{D}_j \bar{D}_k \qquad (1)$$

where ijk are generation indices of the superfields L, Q, E, D and U. The L and Q are left-handed doublets while $\bar{E}$, $\bar{D}$ and $\bar{U}$ are right-handed singlet superfields for charged leptons, down and up-type quarks, respectively. The λ and λ' terms induce lepton number violation while the λ'' terms induce baryon number violation. In the strict MSSM framework, one imposes that the SUSY theory be also minimal in terms of allowed couplings and all $W_{\not R_p}$ terms are avoided by imposing a strict conservation of the R-parity defined as $R_p = (-1)^{3B+L+2S} = 1$ (for particles) $= -1$ (for sparticles), where S denotes the spin, B the baryon number and L the lepton number. Imposing this discrete symmetry is a somewhat *ad hoc* prescription. Another viable [5] and less restrictive discrete symmetry is the B-parity which imposes only baryon number conservation (i.e. $\lambda'' = 0$). Vanishing λ'' couplings is sufficient to avoid unacceptable $n - \bar{n}$ oscillations and fast proton decay. Moreover from the cosmological point of view, the observed matter/antimatter asymmetry imposes much more severe constraints on λ'' than on λ or λ' [6]. Finally, B-parity is favoured over R-parity conservation in a large class of superstring inspired models [5]. It is also interesting to note that the λ and λ' terms in (1) which have no equivalent in the SM arise in a fundamental way from the fact that $SU(2)$-doublet lepton superfields have the same gauge quantum numbers as the Higgs supermultiplets.

The ep collider HERA which provides both leptonic and baryonic quantum numbers in the initial state is ideally suited for $\not R_p$ searches. This was realized long ago and was first investigated theoretically in the context of the previous HERA Workshop [7] which motivated early experimental searches [8]. The cases $\lambda' \neq 0$ which could lead to resonant production of squarks via e-q fusion offers of course the most exciting prospects. Recent investigations [9, 10, 11] have shown that a new and rich phenomenology (different for e^- and e^+ beams) emerges when considering the full complexity of the mixing in the gaugino-higgsino sector of the theory. This is studied in more details in this contribution in view of future high luminosity runs at HERA.

The case of associated $\tilde{e}$-$\tilde{q}$ production at HERA followed by the $\not R_p$-decay of the sfermions has already been studied in detail and also in view of high luminosity runs at HERA in [12]. Via this process one can probe significantly smaller Yukawa couplings than via the resonant production but only at smaller sfermion masses.

2 Phenomenology of $\not R_p$ SUSY

2.1 Modelling and Free Parameters

The $\lambda'_{ijk} L_i Q_j \bar{D}_k$ terms in the $\not R_p$ extension of the MSSM correspond in expanded field notation to the Lagrangian

$$\begin{aligned} \mathcal{L}_{L_i Q_j \bar{D}_k} &= \lambda'_{ijk} \left[-\tilde{e}^i_L u^j_L \bar{d}^k_R - e^i_L \tilde{u}^j_L \bar{d}^k_R - (\bar{e}^i_L)^c u^j_L \tilde{d}^{k*}_R \right. \\ &\quad \left. + \tilde{\nu}^i_L d^j_L \bar{d}^k_R + \nu_L \tilde{d}^j_L \bar{d}^k_R + (\bar{\nu}^i_L)^c d^j_L \tilde{d}^{k*}_R \right] + \text{h.c.} \end{aligned} \qquad (2)$$

where the superscripts ^{c} denote the charge conjugate spinors and the * the complex conjugate of scalar fields. Among the 27 possible λ'_{ijk} couplings, the cases $i = 1$ can lead to direct squark resonant production and are thus of special interest at HERA. These cases are studied first in this paper assuming conservatively that one of the λ' dominates.

The masses of the scalar quarks and scalar leptons, bosonic sparticle partners of the SM fermions, are treated here as free parameters. In the gaugino-higgsino sector, there are four neutralinos χ_i^0 $(i = 1 \ldots 4)$ which are mixed states of the photino $\tilde{\gamma}$, the zino $\tilde{Z}$ and the supersymmetric partners $\tilde{H}_1^0$ and $\tilde{H}_2^0$ of the two neutral Higgs fields. Two charginos $\chi_j^{\pm}$ $(j = 1, 2)$ are mixed states of the winos $\tilde{W}^{\pm}$ and of the SUSY partners of the charged Higgs fields. The masses and couplings of the χ^0 and $\chi^{\pm}$ are calculated in terms of the MSSM basic parameters :

- M_1 and M_2, the $U(1)$ and $SU(2)$ soft-breaking gaugino mass terms;
- μ, the Higgs mixing parameter;
- $\tan\beta$, the ratio of the vacuum expectation values of the two neutral Higgs fields.

The number of free parameters is reduced by assuming a relation at the Grand Unification (GUT) scale between M_1 and M_2 (see Appendix for detail). No other GUT relations are used and in particular the gluino ($\tilde{g}$) mass is left free.

We moreover consider the following simplifying assumptions :

- all squarks (except the stop) are quasi-degenerate in mass;
- the lightest supersymmetric particle (LSP) is the lightest neutralino χ_1^0;
- gluinos are heavier than the squarks such that decays $\tilde{q} \to q + \tilde{g}$ are kinematically forbidden.

It should be made clear that there are no compelling cosmological constraints in $\not{R}_p$ models which impose that the LSP be neutral and colourless. Other possible choices for the LSP (e.g. $\tilde{g}$ or $\chi^{\pm}$) would not significantly change the search and analysis strategy and will only be briefly discussed. In $\not{R}_p$ models, in contrast to the strict MSSM, the LSP is generally unstable. This leads to event topologies which differ strongly from the characteristic "missing energy" signal due to LSP's escaping detection in the MSSM. Hence, except for exclusion limits derived from indirect searches (e.g. from the intrinsic width of the Z^0), the mass constraints obtained in the MSSM framework do not apply directly in $\not{R}_p$ models. The search for $\not{R}_p$ squarks is "complementary" (hence mandatory) to that performed in the strict MSSM framework.

2.2 Squark Production

The resonant squark production mode through direct e-q fusion is illustrated in Fig. 1 for $\lambda'_{111} \neq 0$. By gauge symmetry, only $\tilde{u}_L$-like or $\tilde{d}_R$-like squarks (or their charge conjugates) can be produced in ep collisions. The production of "left" squarks (i.e. supersymmetric partners of left-handed quarks) is the dominating process if HERA delivers positrons, since the fusion occurs via a d valence quark. On the contrary, with electrons in the initial state, mainly "right" squarks are produced. This dichotomy has important consequences since "left" and

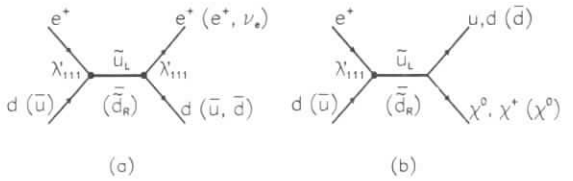

Figure 1: *$\not{R}_p$ resonant production of $\tilde{u}_L$ or $\tilde{d}_R$ squarks in e^+p collisions with subsequent (a) $\not{R}_p$ decay or (b) gauge decay involving a (generally) unstable gaugino-higgsino (χ^0 or χ^+).*

"right" squarks have different allowed or dominant decay modes as will be seen in the following sections. In particular, new exotic final state topologies might have sizeable contributions in e^+p collisions.

HERA offers a high sensitivity to any of the nine λ'_{1jk} couplings, in contrast to most indirect processes. The production processes allowed for each λ'_{1jk} are listed in Table 1 for an e^+ beam. Squark production via λ'_{1j1} is especially interesting in e^+p collisions as it involves a valence d quark, whilst λ'_{11k} are best probed with an e^- beam since squark production then involves a valence u quark.

Figure 2 shows the production cross-sections via λ'_{111} for $\tilde{u}_L$ and $\bar{\tilde{d}}_R$, and for $\tilde{c}_L$ via λ'_{121}, each plotted for coupling values of $\lambda' = 0.1$. In the narrow width approximation, these cross-sections are simply expressed as

$$\sigma_{\tilde{q}} = \frac{\pi}{4s}\lambda'^2 q'(\frac{M^2}{s}) \qquad (3)$$

where $\sqrt{s} = \sqrt{4E_e^0 E_p^0} \simeq 300$ GeV is the energy available in the CM frame for incident beam energies of $E_e^0 = 27.5$ GeV and $E_p^0 = 820$ GeV, and $q'(x)$ is the probability to find the relevant quark (e.g. the d for $\tilde{u}_L$ or $\tilde{c}_L$ and the $\bar{u}$ for $\bar{\tilde{d}}_R$) with momentum fraction $x = M^2/s \simeq M_{\tilde{q}}^2/s$ in

λ'_{1jk}	Production processes	
111	$e^+ + \bar{u} \to \bar{\tilde{d}}_R$	$e^+ + d \to \tilde{u}_L$
112	$e^+ + \bar{u} \to \bar{\tilde{s}}_R$	$e^+ + s \to \tilde{u}_L$
113	$e^+ + \bar{u} \to \bar{\tilde{b}}_R$	$e^+ + b \to \tilde{u}_L$
121	$e^+ + \bar{c} \to \bar{\tilde{d}}_R$	$e^+ + d \to \tilde{c}_L$
122	$e^+ + \bar{c} \to \bar{\tilde{s}}_R$	$e^+ + s \to \tilde{c}_L$
123	$e^+ + \bar{c} \to \bar{\tilde{b}}_R$	$e^+ + b \to \tilde{c}_L$
131	$e^+ + \bar{t} \to \bar{\tilde{d}}_R$	$e^+ + d \to \tilde{t}_L$
132	$e^+ + \bar{t} \to \bar{\tilde{s}}_R$	$e^+ + s \to \tilde{t}_L$
133	$e^+ + \bar{t} \to \bar{\tilde{b}}_R$	$e^+ + b \to \tilde{t}_L$

Table 1: *Squark production processes at HERA (e^+ beam) via a R-parity violating λ'_{1jk} coupling.*

the proton. Hence the production cross-section approximately scales in λ'^2. The full kinematic domain can be probed at HERA for couplings weaker than the electromagnetic coupling (i.e. $\lambda^2/4\pi < \alpha_{em}$) given an integrated luminosity of $\simeq 500\text{pb}^{-1}$.

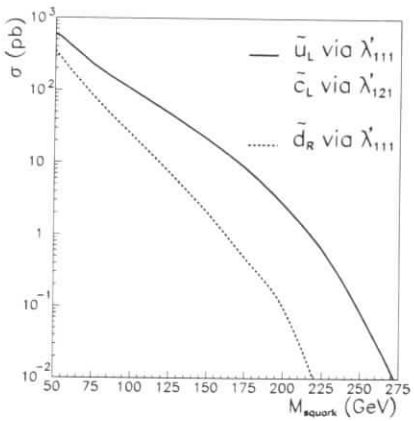

Figure 2: *Squark production cross-sections in e^+p collisions for a coupling $\lambda'_{1j1} = 0.1$.*

2.3 Squark Decays

The squarks decay either via their Yukawa coupling into ordinary matter fermions, or in a first step via their gauge coupling into a quark and a neutralino χ_i^0 ($i = 1 \ldots 4$) or a chargino χ_j^+ ($j = 1,2$). The former modes are henceforward called "squark $\not{R}_p$ decays" and the latter "squark gauge decays".

$\not{R}_p$ decays of squarks:
In cases where both production and decay occurs through a λ'_{1jk} coupling (e.g. Fig. 1a for $\lambda'_{111} \neq 0$), the squarks behave as scalar leptoquarks [13, 14]. For $\lambda'_{111} \neq 0$, the $\bar{d}_R$ resembles on event-by-event the $\bar{S}^0$ leptoquark and decays in either $e^+ + \bar{u}$ or $\nu_e + \bar{d}$ while the $\tilde{u}_L$ resembles the $\tilde{\bar{S}}_{1/2}$ and only decays into $e^+\bar{d}$. The partial decay width reads :

$$\Gamma_{\tilde{q}\to\not{R}_p} = \Gamma_{\tilde{u}_L\to e^+\bar{d}} = \Gamma_{\tilde{d}_R\to e^+\bar{u}} = \Gamma_{\tilde{d}_R\to\nu\bar{d}} = \frac{1}{16\pi}\lambda'^2_{111} M_{\tilde{q}} \qquad (4)$$

so that squark $\not{R}_p$ decays will mainly contribute at high mass for large Yukawa coupling values λ'. Hence, the final state signatures consist of a lepton and a jet and are, event-by-event, indistinguishable from the SM neutral (NC) and charged current (CC) deep inelastic scattering (DIS).

Gauge decays of squarks:
The MSSM Lagrangian contains terms coupling a sfermion to an ordinary fermion and a gaugino-higgsino. The partial widths for squark gauge decays depend on MSSM parameters via the composition of the neutralinos or charginos.

Both $\tilde{q}_L$ and $\tilde{q}_R$ squarks can decay via $\tilde{q} \to q\chi_i^0$. The partial width of the $\tilde{q} \to q\chi_i^0$ decay is calculated to be

$$\Gamma_{\tilde{q}\to q+\chi_i^0} = \frac{1}{8\pi}(A^2 + B^2) M_{\tilde{q}} \left(1 - \frac{M^2_{\chi_i^0}}{M^2_{\tilde{q}}}\right)^2 \qquad (5)$$

where :

$$A = \frac{g M_q N_{i4}}{2 M_W \sin\beta} \quad , \quad B = e e_q N'_{i1} + g(0.5 - e_q \sin^2\theta_W)\frac{N'_{i2}}{\cos\theta_W}, \qquad (6)$$

and where N_{ij} (N'_{ij}) is the transport matrix which diagonalizes the neutralino mass matrix (see Appendix for detail) in the $\tilde{A} - \tilde{W}_3$ ($\tilde{\gamma} - \tilde{Z}$ basis). In practice, the χ_i^0 masses and the exact values of the "chiral" couplings A and B depend on the relative $\tilde{\gamma}$, $\tilde{Z}$ and $\tilde{H}$ components of the χ_i^0.

The dependence of the χ_i^0 mass on the μ parameter is shown in Fig. 3a for fixed M_2 and $\tan\beta$. The dominant component ($\tilde{\gamma}$, $\tilde{Z}$ or $\tilde{H}$) of the lightest state χ_1^0 is shown in Fig. 3b. More

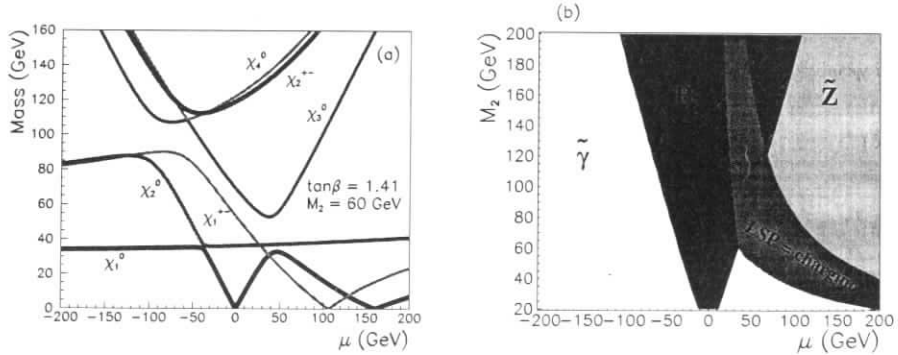

Figure 3: *(a) Physical masses of the χ_i^0 and $\chi_i^{\pm}$ as a function of μ for $\tan\beta = 1$ and $M_2 = 60$ GeV; (b) Main component of the LSP for $\tan\beta = 1$*

details on the way the nature (and masses) of the various neutralino states depend on the basic MSSM parameters M_2, μ and $\tan\beta$ can be found in the Appendix.

For a $\tilde{\gamma}$-like LSP, i.e. a χ_1^0 dominated by its photino component, the $\tilde{q}$ to $q + \tilde{\gamma}$ coupling is proportional to the q electric charge and the $\tilde{q}$ partial width reduces to

$$\Gamma_{\tilde{q}\to q+\tilde{\gamma}} = \frac{1}{8\pi} e^2 e_q^2 M_{\tilde{q}} \left(1 - \frac{M^2_{\tilde{\gamma}}}{M^2_{\tilde{q}}}\right)^2 . \qquad (7)$$

In such a case, more than 90% of the $\tilde{q} \to q\chi_i^0$ decays will involve the χ_1^0. A similar partial branching ratio holds for a $\tilde{H}$-like LSP with a relatively large $\tilde{Z}$ component (e.g. in the $\tilde{H}$ region close to the $\tilde{Z}$ region in Fig. 3b). For a $\tilde{Z}$-like LSP, this branching ratio reduces to $20\% < \mathcal{B} < 80\%$. Decays involving the LSP are negligible only in the $\tilde{H}$ domain extending to negative μ's adjacent to the $\tilde{\gamma}$ domain (Fig. 3b).

(Almost) only the $\tilde{q}_L$ are allowed by gauge symmetry to decay into $q'\chi_i^+$. This is because the $SU(2)_L$ symmetry which implies in the SM that the right handed fermions do not couple to the W boson also forbids a coupling of $\bar{\tilde{q}}_R$ to the $\bar{W}$. The $\bar{\tilde{q}}_R$ decays involving the chargino is only possible through the $\tilde{H}^+$ component of the χ^+ in which case the coupling is proportional to the q' mass. Hence the decay $\bar{\tilde{q}}_R \to q'\chi_i^+$ is strongly suppressed for a $\bar{\tilde{q}}_R$ of the first or second generation. The partial width of the $\tilde{q} \to q\chi_i^+$ decay is obtained from (5) with the interchange $M_{\chi_i^0} \to M_{\chi_i^+}$ and with :

$$A = \frac{gV_{i1}}{\sqrt{2}} \qquad B = \frac{-gM_{q'}U_{i2}}{2M_W \cos\beta} \; . \tag{8}$$

The regions of the M_2 vs μ plane where the $\tilde{u}$ decays involving a chargino dominate are shown in Fig. 4. In most of the parameter space, the $\tilde{u}_L$ squarks will mainly undergo a decay involving

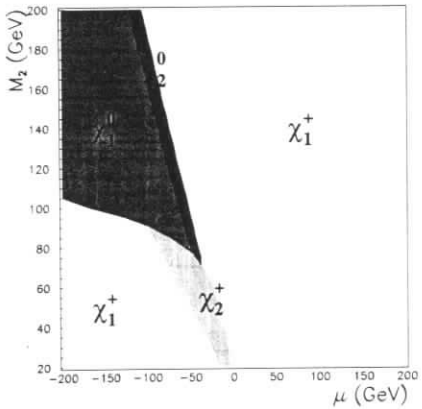

Figure 4: *Dominant gauge decay of a 150 GeV $\tilde{u}_L$ squark.*

a chargino if kinematically allowed. The mass dependence of the χ_i^+ states on the μ parameter is shown in Fig. 3a for fixed M_2 and $\tan\beta$.

2.4 Decays of the LSP

In $\not{R}_p$ SUSY models with $\lambda'_{1jk} \neq 0$, the LSP will undergo one of the following decays : $\chi_1^0 \to \nu\bar{d}_k d$, $\chi_1^0 \to e^+\bar{u}_j d_k$ or $\chi_1^0 \to e^- u_j \bar{d}_k$. Representative diagrams of such decays are given in Fig. 5. The relevant matrix elements for these decays can be found in [12]. They depend on the coupling λ', but also on the parameters M_2, μ and $\tan\beta$. This dependence is illustrated in Fig. 6a for the LSP decay $\chi_1^0 \to e^\pm q\bar{q}'$. Such decay modes are seen to be dominant ($63\% < \mathcal{B}_R < 88\%$) if the χ_1^0 is $\tilde{\gamma}$-like in which case both the "right" and the "wrong" sign lepton (compared to the incident beam) are equally probable. This leads to largely background free striking signatures for lepton number violation. The latter will dominate if the χ_1^0 is $\tilde{Z}$-like. A $\tilde{H}$-like χ_1^0 will most probably be long lived and escape detection since its coupling to fermion-sfermion pairs is proportional to the fermion mass [15]. This is illustrated in Fig. 6b, which shows the flight distance $c\tau_0$ of

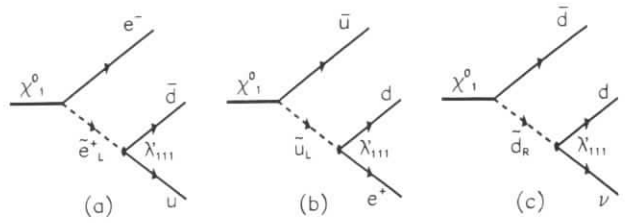

Figure 5: *Example diagrams of the LSP decays $\chi_1^0 \to lqq'$ involving a $\not{R}_p$ Yukawa coupling.*

the χ_1^0 in the plane (M_2, μ) for $\lambda' = 0.1$. The $c\tau_0$ exceeds 1 m in most of the $\tilde{H}$-like domain surrounding the singularity at $\mu = 0$ where $M_{\chi_1^0} = 0$ at tree level. Hence processes involving a higgsino-like χ_1^0 will be affected by an imbalance in transverse momenta.

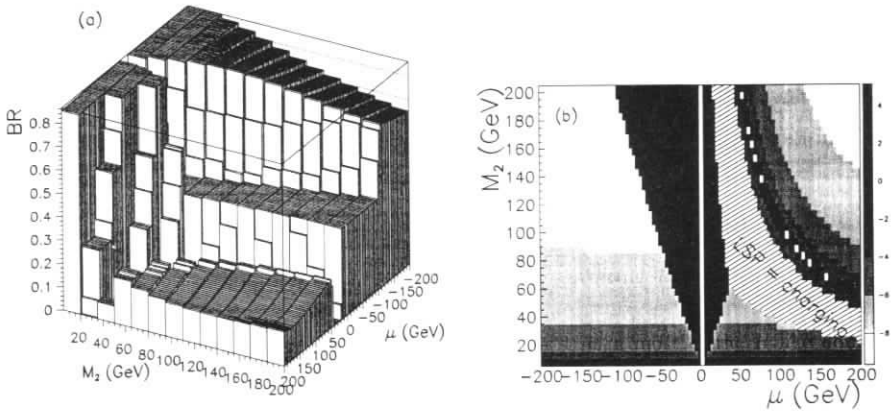

Figure 6: *(a) LSP (χ_1^0) decay branching ratio into charged leptons (i.e. $e^\pm + jets$), as a function of μ and M_2 for sfermion masses $M_{\tilde{f}} = 150$ GeV and $\tan\beta = 1$; (b) $\log c\tau_0$ (m) of the LSP with $\lambda' = 0.1$, the LSP mass is vanishingly small around $\mu = 0$ and along the ridge at large $\mu + M_2$.*

2.5 Decays of Charginos

R-parity conserved χ^+ decays into a χ^0 and two matter fermions, have been investigated in detail in [16], where the relevant matrix elements can be found. New decay modes of the χ^+ into $e^+ + d_j + \bar{d}_k$ or $\nu_e + u_j + \bar{d}_k$ are allowed by the $\not{R}_p$ couplings λ'_{1jk} as illustrated in Fig. 7.

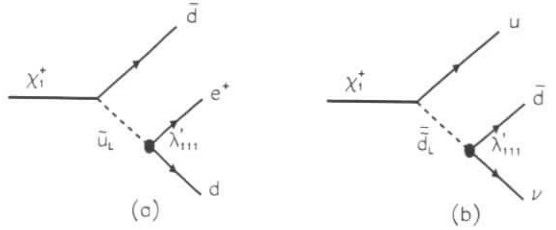

Figure 7: *Representative diagrams for the χ_1^+ decays $\chi_1^+ \to lqq'$ involving a $\not{R}_p$ Yukawa coupling.*

The branching ratio of the χ_1^+ into these $\not{R}_p$ modes is obtained using the partial widths calculated from the relevant matrix elements. Considering for instance the process $\chi^+ \to e^+ + d_j + \bar{d}_k$ (Fig. 7a) in the following notation $\chi_1^+(k) \to e^+(l) + \bar{d}(q_1) + d(q_2)$, and using Mandelstam variables $s = (q_1+q_2)^2 = (k-l)^2$, $t = (k-q_1)^2 = (l+q_2)^2$ and $u = (k-q_2)^2 = (l+q_1)^2$, the squared matrix element can be written as :

$$|\mathcal{M}|^2_{\not{R}_p} = 3g^2\lambda'^2_{111}|V_{11}|^2 \left(\frac{s(M_\chi^2 - s)}{|R(s)|^2} + \frac{t(M_\chi^2 - t)}{|D(t)|^2} - \mathcal{R}e\frac{I(s,t,u)}{R(s)D(t)} \right) \tag{9}$$

where the propagators R and D and the interference term I are :

$$R(s) = s - m^2_{\tilde{\nu}_L}, \tag{10}$$

$$D(t) = t - m^2_{\tilde{u}_L}, \tag{11}$$

$$I(s,t,u) = s(M_\chi^2 - s) - u(M_\chi^2 - u) + t(M_\chi^2 - t). \tag{12}$$

The matrix element corresponding to the process $\chi_1^+ \to \nu_e + u + \bar{d}$ (Fig. 7b) is deduced from the previous one with the following substitutions: $e \to \nu$, $\bar{d} \to u$, $d \to d$ and $|V_{11}|^2 \to |U_{11}|^2$. The corresponding partial width is obtained by integrating over phase space as :

$$\Gamma = \int_{s=0}^{s=M^2_{\chi_1}} \int_{t=0}^{t=M^2_{\chi_1}-s} \frac{1}{M^3_{\chi_1^+}} \frac{1}{256\pi^3} |\mathcal{M}|^2 ds dt \tag{13}$$

The $\not{R}_p$ decays of the χ_1^+ will mainly dominate over MSSM decays as soon as λ' is not too small, as can be seen in Fig. 8. For $\chi_1^0 \simeq \tilde{\gamma}$, $\not{R}_p$ decays of the chargino dominate over MSSM modes for coupling values above $\simeq 0.25$, which is typically HERA's sensitivity limit with current luminosity.

2.6 Classification of Final States

Taking into account the dependence on the nature of the χ_1^0, the possible decay chains of the $\tilde{u}_L$ and $\tilde{d}_R$ squarks can be classified into eight distinguishable event topologies listed in tables 2 and 3 and labelled S1 to S8. The S1 and S2 classes cover $\not{R}_p$ squark decays. The S3 and S4 classes are squark gauge decay topologies not accompanied by escaping transverse momenta

Figure 8: *$\not{R}_p$ chargino decay branching ratio as a function of λ'_{111} and μ, for $M_2 =$ 80 GeV, $\tan\beta = 1$ and sfermions masses = 150 GeV; the hatched domain corresponds to μ values for which $M(\chi_1^+) < M(\chi_1^0)$.*

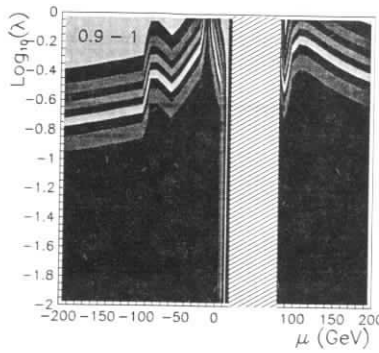

Channel	χ_1^0 nature	Decay processes	Signature
S1	$\tilde{\gamma},\tilde{Z},\tilde{H}$	$\tilde{q} \xrightarrow{\lambda'} e^+ \; q'$	High $P_\perp$ e^+ + 1 jet
S2	$\tilde{\gamma},\tilde{Z},\tilde{H}$ $\tilde{H}$	$\tilde{d}_R \xrightarrow{\lambda'} \nu_e \; \bar{d}$ $\tilde{q} \longrightarrow q \; \chi_1^0$	Missing $P_\perp$ + 1 jet
S3	$\tilde{\gamma},\tilde{Z}$ $\tilde{\gamma},\tilde{Z},\tilde{H}$ $\tilde{\gamma},\tilde{Z}$	$\tilde{q} \longrightarrow q \; \chi_1^0 \xhookrightarrow{\lambda'} e^+\bar{q}'q''$ $\tilde{u}_L \longrightarrow d \; \chi_1^+ \xhookrightarrow{\lambda'} e^+ d\bar{d}$ $\tilde{u}_L \longrightarrow d \; \chi_1^+ \hookrightarrow W^+\chi_1^0 \begin{cases} \xhookrightarrow{\lambda'} e^+\bar{q}'q'' \\ \hookrightarrow q\;\bar{q}' \end{cases}$	High $P_\perp$ e^+ + multiple jets
S4	$\tilde{\gamma},\tilde{Z}$ $\tilde{\gamma},\tilde{Z}$	$\tilde{q} \longrightarrow q \; \chi_1^0 \xhookrightarrow{\lambda'} e^-\bar{q}'q''$ $\tilde{u}_L \longrightarrow d \; \chi_1^+ \hookrightarrow W^+\chi_1^0 \begin{cases} \xhookrightarrow{\lambda'} e^-\bar{q}'q'' \\ \hookrightarrow q\;\bar{q}' \end{cases}$	High $P_\perp$ e^- (i.e. wrong sign lepton) + multiple jets

Table 2: *Squark decays in $\not{R}_p$ SUSY classified per distinguishable event topologies (PART I). The dominant component of the χ_1^0 for which a given decay chain is relevant is given in the second column. The list of processes contributing to a given event topology is here representative but not exhaustive.*

Channel	χ_1^0 nature	Decay processes	Signature
S5	$\tilde{\gamma},\tilde{Z}$	$\tilde{q} \longrightarrow q\ \chi_1^0$, $\chi_1^0 \hookrightarrow^{\lambda'} \nu\bar{q}'q'$	Missing $P_\perp$ + multiple jets
	$\tilde{\gamma},\tilde{Z}$	$\tilde{u}_L \longrightarrow d\ \chi_1^+$, $\chi_1^+ \hookrightarrow W^+\chi_1^0$, $W^+ \hookrightarrow^{\lambda'} \nu\bar{q}'q'$ or $W^+ \hookrightarrow q\ \bar{q}'$	
	$\tilde{\gamma},\tilde{Z},\tilde{H}$	$\tilde{u}_L \longrightarrow d\ \chi_1^+$, $\chi_1^+ \hookrightarrow^{\lambda'} \nu u\bar{d}$	
	$\tilde{H}$	$\tilde{u}_L \longrightarrow d\ \chi_1^+$, $\chi_1^+ \hookrightarrow W^+\chi_1^0$, $W^+ \hookrightarrow q\ \bar{q}'$	
S6	$\tilde{H}$	$\tilde{u}_L \longrightarrow d\ \chi_1^+$, $\chi_1^+ \hookrightarrow W^+\chi_1^0$, $W^+ \hookrightarrow l^+\ \nu$	High $P_\perp$ e^+ or μ^+ + missing $P_\perp$ + 1 jet
S7	$\tilde{\gamma},\tilde{Z}$	$\tilde{u}_L \longrightarrow d\ \chi_1^+$, $\chi_1^+ \hookrightarrow W^+\chi_1^0$, $W^+ \hookrightarrow^{\lambda'} e^\pm\bar{q}'q''$ or $W^+ \hookrightarrow l^+\ \nu$	High $P_\perp$ $e^\pm$ + high $P_\perp$ e^+ or μ^+ + missing $P_\perp$ + multiple jets
S8	$\tilde{\gamma},\tilde{Z}$	$\tilde{u}_L \longrightarrow d\ \chi_1^+$, $\chi_1^+ \hookrightarrow W^+\chi_1^0$, $W^+ \hookrightarrow^{\lambda'} \nu\bar{q}'q'$ or $W^+ \hookrightarrow l^+\ \nu$	High $P_\perp$ e^+ or μ^+ + missing $P_\perp$ + multiple jets

Table 3: *Squark decays in $\not{R}_p$ SUSY classified per distinguishable event topologies (Part II). As in table 2, the list of processes given here is not exhaustive, e.g. the gauge decays $\chi_1^+ \to \chi_1^0 l^+\nu$ and $\chi_1^+ \to \chi_1^0 q\bar{q}'$ may also proceed via a virtual sfermion.*

$\not{P}_\perp$, while those with large $\not{P}_\perp$ are covered by classes S5 to S8. A set of event selection cuts has been developed and discussed in detail in [8, 11].

For S1 and S3 (or S4), the DIS NC background is strongly suppressed by requiring a high $P_\perp$ $e^\pm$ found at high y_e, where $y_e = 1/2(1+\cos\theta_e^*)$ and θ_e^* is the electron angle in the $e-q$ CM frame. The uniform decay of the scalar particle in the CM frame leads to a flat y_e spectrum for S1 and one shifted towards largest y_e for S3. This is in contrast to the $1/y_e^2$ spectrum expected for the DIS NC background at fixed quark momentum fraction x. For S3 the H1 analysis [11] has been improved [17], using θ^*'s computed for the scattered electron and for the highest $P_\perp$ jet found in the azimuthal hemisphere opposite to the electron, and cutting on $\sum y = y_e + y_{jet}$ as shown in Fig. 9. Good signal detection efficiencies are obtained in each of these classes, reaching $\sim 70\%$ for S1 and up to $\sim 60\%$ depending on $M_{\chi_1^0}$ for S3.

The S4 topology with a wrong sign lepton in the final state is quasi-background free. Event candidates in classes S2 and S5 to S8 have a large $\not{P}_\perp$. Classes S2 and S5 suffer from DIS CC background and from tails of photoproduction background. The S6 to S8 topologies have one

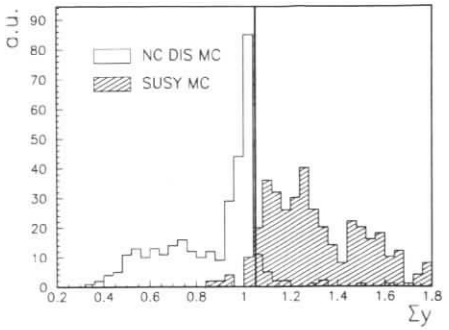

Figure 9: *Distribution of the variable Σy for neutral current DIS processes, and for a simulation of 75 GeV squarks undergoing gauge decays involving 20 GeV neutralinos; the vertical line is the cut used in the H1 analysis [17].*

or many leptons in the final states and are thus quasi-background free. Typical signal detection efficiencies [11] reach $\sim 30\% \to 80\%$ in these channels.

The relative contributions of the squark $\not{R}_p$ and gauge decays are shown in Fig. 10a. Gauge decays are seen to dominate through most of the accessible mass range. Only large Yukawa couplings can be probed at largest masses and thence $\not{R}_p$ decays dominate. The shape of the curves in Fig. 10a is only distorted at lowish mass (e.g. $M_{\tilde{q}} \lesssim 75$ GeV) when convoluting with signal detection efficiencies. The measurement of the relative branching ratio in $S3$ and $S4$ in case of a discovery, could be used to constrain the χ_1^0 LSP nature in the MSSM parameter space as seen in Fig. 10b.

It is interesting to note that the final state classification discussed here should not be

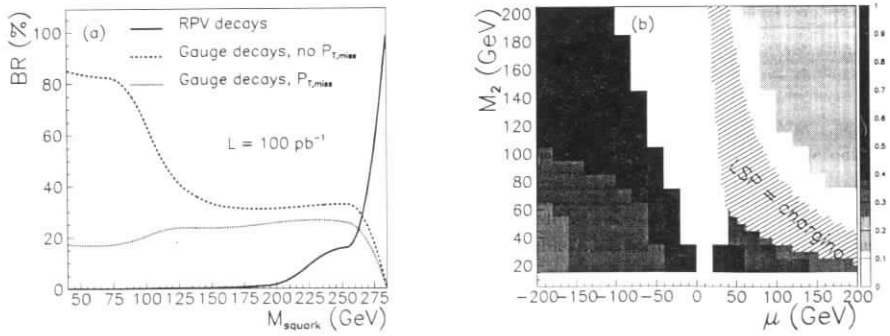

Figure 10: *(a) Squark decay branching ratio as a function of squark mass integrated over three distinct set of event topologies for $\tan\beta = 1$ and $M_{\tilde{\gamma}} = 40$ GeV. (b) Ratio $\mathcal{B}_{S4}/\mathcal{B}_{S3}$ of the squark "gauge" decay branching ratios without $\not{P}_\perp$ involving the like (S3) and unlike (S4) sign lepton viewed in the M_2 versus μ plane; the plot is obtained for $M_{\tilde{q}} = 150$ GeV at the expected limit of λ' coupling sensitivity for an integrated HERA luminosity of 100 pb^{-1}.*

dramatically affected when relaxing the hypothesis of section 2.1, e.g. in models where the $\tilde{g}$ are lighter than the $\tilde{q}$, or where the LSP is the χ_1^+.

Assuming $M_{\tilde{g}} < M_{\tilde{q}}$, the decay $\tilde{q} \to q + \tilde{g}$ will generally dominate. If the $\tilde{g}$ is the LSP, the $\tilde{q}$ decay will be followed by the $\not{R}_p$ decay $\tilde{g} \to q + q' + e^{\pm}$ or $\tilde{g} \to q + \bar{q} + \nu$. In such a case, possible final states contain several jets and either one electron or $\not{P}_\perp$. These topologies correspond to channels S3 and S5, previously considered. If $M_{\tilde{q}} > M_{\tilde{g}}$, with the LSP being the lightest neutralino, the $\tilde{g}$ arising from squark decay will undergo $\tilde{g} \to q + \tilde{q}$, the latter squark being off-shell. Possible final states are similar to those listed above, but more jets would be expected. Assuming now that the LSP is the χ_1^+ (see the relevant MSSM parameters in Fig. 3b), a new event topology would only emerge for a relatively stable χ_1^+ which could behave as a "heavy muon". However, the time of flight of the χ_1^+, obtained from the integration (13) over phase space, reads as :

$$\tau = \frac{4\pi}{g^2} \frac{1}{|V_{11}|^2} \frac{1}{\lambda'^2} (8 \times 64\pi^2) \left(\frac{M_{\tilde{q}}}{M_{\chi_1^+}} \right)^4 \frac{1}{M_{\chi_1^+}} \tag{14}$$

which numerically leads to :

$$\tau = (2.5 \cdot 10^{-15} s) \left(\frac{5.10^{-3}}{\lambda'} \right)^2 \frac{1}{|V_{11}|^2} \left(\frac{100 \text{ GeV}}{M_{\chi_1^+}} \right)^5 \left(\frac{M_{\tilde{f}}}{150 \text{ GeV}} \right)^4 . \tag{15}$$

From this formula one obtains that the relevant parameter space for the χ_1^+ to decay outside the detector ($\gtrsim$ 1m), is already excluded from the intrinsic Z^0 width measurement at CERN [18].

3 Results for the Mass-Coupling Reach of HERA

In the absence of a significant deviation from the SM expectations, exclusion limits for the Yukawa couplings λ'_{1jk} as a function of mass can be derived, showing the domain HERA could probe in the near future. Results are shown for λ'_{1j1} in Fig. 11 at 95% confidence level (CL), for integrated luminosities $L = 100\text{pb}^{-1}$ and $L = 500\text{pb}^{-1}$. These have been obtained assuming a 40 GeV $\tilde{\gamma}$-like χ_1^0, and combining all contributing channels. For $\mathcal{L} = 500\text{pb}^{-1}$, the existence of first generation squarks with $\not{R}_p$ Yukawa coupling λ'_{1j1} could be excluded for masses up to $\sim$ 270 GeV for coupling strengths $\lambda'^2_{111}/4\pi \gtrsim \alpha_{em}$.

From the analysis of the λ'_{1j1} case involving the $\bar{d}_R$ and $\tilde{u}_L$ squarks, limits can be deduced on the λ'_{1jk} by folding in the proper parton densities. Such limits are given in Table 4 at $M_{\tilde{q}} = 150$ GeV and for an integrated luminosity of 500pb^{-1}. Also quoted in this table are the most severe existing indirect limits for each of these couplings. The most stringent concern couplings λ'_{1jk} with $j = k$ and come either from the non-observation of neutrinoless double-beta decay ($j = k = 1$) or from constaints on the ν_e mass ($j = k = 2, 3$). The limit from $\beta\beta0\nu$ decay depends on the gluino mass and is given here for $M_{\tilde{g}} = 500$ GeV.

By the time HERA reaches high luminosity running conditions, new direct limits (or a discovery !) from other colliders will have further constrained the possible squark masses and SUSY parameters. In e^+e^- collisions, the direct squark pair production process does not violate R-parity and LEP2 should directly probe squark masses up to $\sqrt{s}/2$, i.e. $\simeq$ 90 GeV. In $p\bar{p}$ collisions, squarks can be produced in pair or in association with gluinos. No complete analysis in the $\not{R}_p$-SUSY framework has been performed yet with existing TEVATRON data.

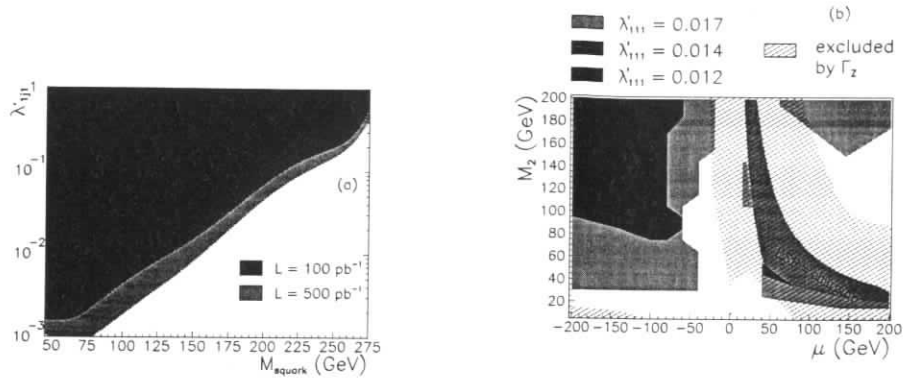

Figure 11: *(a) Exclusion upper limits at 95% CL on the λ'_{1j1} coupling as a function of squark mass which could be reached with e^+p collisions at HERA ($\sqrt{s} \sim 300$ GeV) for integrated luminosities of $L = 100$ pb^{-1} (dark shaded area) and 500 pb^{-1} (shaded); (b) Regions of the M_2 versus μ plane excluded for $L = 100$ pb^{-1} and for couplings λ'_{1j1} equal or smaller to the exclusion upper limit at $M_{\tilde{q}} = 150$ GeV.*

Table 4: *Exclusion upper limits at 95% CL on the coupling λ'_{1jk} for $M_{\tilde{q}} = 150$ GeV and $M_{\chi_1^0} = 40$ GeV together with best existing indirect limits. The indirect limits have been scaled from those found in the cited references to $M_{\tilde{q}} = 150$ GeV and 95% CL.*

	HERA sensitivity		Indirect limits	
	$\tilde{\gamma}$-like χ_1^0	Z-like χ_1^0	Value [Ref.]	Nature of the process
λ'_{111}	0.008	0.023	0.003 [19]	$\beta\beta0\nu$ decay
λ'_{112}	0.020	0.057	0.05 [20]	CC-universality
λ'_{113}	0.026	0.072	0.05 [20]	CC-universality
λ'_{121}	0.008	0.023	0.5 [21]	$D^+ \to K$ decays
λ'_{122}	0.027	0.077	0.04 [22]	ν_e-mass
λ'_{123}	0.043	0.012	0.5 [21]	$D^+ \to K$ decays
λ'_{131}	0.007	0.024	0.77 [23]	R_e^{exp}
λ'_{132}	0.027	0.091	0.77 [23]	R_e^{exp}
λ'_{133}	0.068	0.230	0.0015 [22]	ν_e-mass

Nevertheless, $\tilde{q}$ decay topologies similar to those described here have been explored by D0 [24] and CDF [25] in scalar leptoquark or MSSM searches. From these and from di-lepton data [26], one can infer that the range 200 $\to$ 300 GeV of $\not{R}_p$-SUSY squark masses will most probably be not fully excluded by TEVATRON data for an integrated luminosity of ~ 100 pb^{-1}, thus leaving open a discovery window at HERA in the hypothesis $M_{\tilde{g}} \gg M_{\tilde{q}}$.

If the presence of two simultaneously non-vanishing Yukawa couplings (e.g. λ'_{1jk} and λ'_{ijk} with $i \neq 1$), resonant $\tilde{q}$ production at HERA can be directly followed by a lepton flavor violation (LFV) decay leading to μ + jet or τ + jet signatures. Relevant analysis with existing data have

been performed by the H1 [13] and ZEUS [27] collaborations and limits comparable to the best existing indirect LFV limits have been derived in the context of R_p-SUSY for a pure $\tilde{\gamma}$ like LSP. A new range of possible coupling products could be probed with increasing luminosity [28].

4 Summary and Conclusions

The HERA potential for R-parity violating supersymmetry searches was studied. Direct resonant production of squarks through nine new Yukawa couplings λ'_{1jk} is possible up to the kinematical limit of ~ 300 GeV.

Supersymmetric partners $\tilde{q}_L$ of left handed u-like squarks are produced preferentially in e^+p collisions and most favourably via λ'_{1j1}. In contrast, e^-p collisions mainly produce partners $\tilde{q}_R$ of right-handed d-like quarks and most favourably via λ'_{11k}. Squark decays via a λ' coupling into $l + q$ final states dominate only at largest accessible masses, while elsewhere squarks undergo mainly gauge decays into a quark and a gaugino-higgsino. The $\tilde{q}_R$ decays involve a neutralino χ^0 while $\tilde{q}_L$ decays dominantly proceed via a chargino χ^+ in a large portion of the MSSM parameter space. The χ's, including the LSP, are generally unstable and their decay chain involves the λ'_{1jk} coupling.

In total, eight classes of event topologies are identified for R-parity and gauge decays of squarks, with single or multi-leptons final states accompanied or not by missing transverse momenta. A good experimental sensitivity is expected in each of these classes. Thus, for an integrated luminosity of 500 pb^{-1}, squarks can be searched for Yukawa couplings smaller than the electromagnetic coupling up to masses of $\lesssim 270$ GeV, almost independently of the specific choice of MSSM parameter values. Coupling values below the most stringent indirect limits can be probed at $M_{\tilde{q}} = 150$ GeV for seven out of the nine possible λ'_{1jk} couplings.

References

[1] For reviews on Supergravity see
P. Van Nieuwenhuizen, Phys. Rep. 68 (1981) 189 or H.P. Nilles, Phys. Rep. 110 (1984) 1 and references therein.

[2] The "hierarchy" and "naturalness" problems are reviewed in
L.E. Ibáñez and G.G. Ross, Perspectives on Higgs Physics, G. Kane (Editor) World Scientific (1993) and references therein.

[3] For a phenomenological review see for instance
H.E. Haber and G.L. Kane, Phys. Rep. 117 (1985) 75.

[4] L.J. Hall and M. Suzuki, Nucl. Phys. B231 (1984) 419; S. Dawson, Nucl. Phys. B261 (1985) 297; S. Dimopoulos and L.J. Hall, Phys. Lett. B207 (1987)210.

[5] L.E. Ibáñez and G.G. Ross, Nucl. Phys. B368 (1992) 3.

[6] A. Nelson and S. Barr, Phys. Lett. B246 (1990) 141; H. Dreiner and G.G. Ross, Nucl. Phys. B410 (1993) 188.

[7] J. Butterworth and H. Dreiner, Proceedings of the Workshop Physics at HERA, W. Buchmüller, G. Ingelman (Editors), DESY Hamburg (October 1991) p1079; Idem, Nucl. Phys. B397 (1993) 3.

[8] H1 Collaboration, T. Ahmed et al., Z. Phys. C64 (1994) 545.

[9] E. Perez and Y. Sirois, Proceedings of the International Workshop on Supersymmetry and Unification of Fundamental Interactions, Editions Frontières, I. Antoniadis and H. Videau (Editors), Palaiseau, France (May 1995) p21; Y. Sirois, Proceedings of the 4th International Conference on Supersymmetries in Physics, R. Mohapatra (Editor) College Park, Maryland, USA (May 1996).

[10] E. Perez, "Recherche de Particules en Supersymétrie Violant la R-parité dans H1 à HERA", Thèse de Doctorat, DAPNIA/SPP report 96-1008 (in French).

[11] H1 Collaboration, S. Aid et al., Z. Phys. C71 (1996) 211.

[12] H. Dreiner, P. Morawitz, Nucl. Phys. B428(1994) 31.

[13] H1 Collaboration, S. Aid et al., Phys. Lett. B369 (1996) 173.

[14] W. Buchmüller, R. Rückl and D. Wyler, Phys. Lett. B191 (1987) 442.

[15] J.F. Gunion, H.E. Haber, Nucl. Phys. B272 (1986) 1.

[16] A. Bartl, H. Fraas, W. Majerotto and B. Mosslächer, Z. Phys. C55 (1992) 257.

[17] E. Perez, on behalf of H1 and ZEUS Collaborations, to be published in the proceedings of the XXVIIIth International Conference on High Energy Physics, World Scientific (Editor), Warsaw (25-31 July 1996).

[18] ALEPH Collaboration, D. Buskulic et al., Phys. Lett. B349 (1995) 238.

[19] M. Hirsch, H.V. Klapdor-Kleingrothaus, S.G. Kovalenko, Phys. Rev. Lett. 75 (1995) 17.

[20] V. Barger, G.F. Giudice, T. Han, Phys. Rev. D40 (1989) 2987.

[21] G. Bhattacharyya, D. Choudhury, Mod. Phys. Lett. A10 (1995) 1699.

[22] R. Godbole, P. Roy, X. Tata, Nucl. Phys. B401 (1993) 67.; S. Dimopoulos, L.J. Hall, Phys. Lett. B207 (1987) 210.

[23] G. Bhattacharyya, J. Ellis, K. Sridhar, Mod. Phys. Lett. A10 (1995) 1583.

[24] D0 Collaboration, S. Abachi et al., Phys. Rev. Lett. 75 (1995) 618.

[25] CDF Collaboration, F. Abe et al., Phys. Rev. Lett. 75 (1995) 613.

[26] M. Guchait, D.P. Roy, Phys. Rev. D54 (1996) 3276; H. Dreiner, M. Guchait and D.P. Roy, Phys. Rev. D49 (1994) 3270.

[27] ZEUS Collaboration, M. Derrick et al., Preprint DESY-96-161 (Aug. 1996), 38 pp.

[28] F. Sciulli and S. Yang, Contribution to this Workshop.

Appendix: Gaugino-higgsino mixing

Detailed expressions (and conventions) used for the mass mixing in the gaugino-higgsino sector are presented here for completeness.

Neutralino mass mixing:
Mass terms of the Lagrangian describing $SU(2)_L \times U(1)_Y$ neutral gauginos and higgsinos can be written as :

$$\mathcal{L}_m = -1/2(\psi_i^0)^T Y^{ij} \psi_j^0 + h.c. \tag{16}$$

where the neutralino mass matrix in the basis $\psi_i^0 = (-i\tilde{A}, -i\tilde{W}_3, \tilde{H}_1^0, \tilde{H}_2^0)$ is given by :

$$Y = \begin{pmatrix} M_1 & 0 & -m_Z \sin\theta_W \cos\beta & m_Z \sin\theta_W \sin\beta \\ 0 & M_2 & m_Z \sin\theta_W \cos\beta & -m_Z \cos\theta_W \sin\beta \\ -m_Z \sin\theta_W \cos\beta & m_Z \cos\theta_W \cos\beta & 0 & -\mu \\ m_Z \sin\theta_W \sin\beta & -m_Z \cos\theta_W \sin\beta & -\mu & 0 \end{pmatrix} \tag{17}$$

The number of free MSSM parameters is reduced by using a GUT inspired relation between soft-breaking terms M_1 and M_2, $M_1 = \frac{5}{3}\tan^2\theta_W M_2$.

Neutralinos correspond to the mass eigenstates and are defined as $\chi_i^0 = N^{ij}\psi_j^0$, with N_{ij} being the unitary matrix which diagonalize Y. Finally, we make use of the matrix N', which diagonalizes the neutralino mass matrix expressed in the basis $(\tilde{\gamma}, \tilde{Z})$ instead of $(\tilde{A}, \tilde{W}_3)$: $N'_{j1} = N_{j1}\cos\theta_W + N_{j2}\sin\theta_W$, $N'_{j2} = -N_{j1}\sin\theta_W + N_{j2}\cos\theta_W$, $N'_{j3} = N_{j3}$ and $N'_{j4} = N_{j4}$.

Chargino mass mixing:
The Lagrangian mass terms for winos and charged higgsinos are written as :

$$\mathcal{L}_m = -\frac{1}{2}(\psi^+, \psi^-) \begin{pmatrix} 0 & X^T \\ X & 0 \end{pmatrix} \begin{pmatrix} \psi^+ \\ \psi^- \end{pmatrix} + \text{h.c} \tag{18}$$

where :

$$X = \begin{pmatrix} M_2 & m_W\sqrt{2}\sin\beta \\ m_W\sqrt{2}\cos\beta & \mu \end{pmatrix} \tag{19}$$

and $\psi_j^+ = (-i\tilde{W}^+, \tilde{H}_2^+)$, $\psi_j^- = (-i\tilde{W}^-, \tilde{H}_1^-)$. This mass matrix is diagonalized using two $(2,2)$ unitary matrices U and V [16] : $\chi_i^+ = V^{ij}\psi_j^+$ and $\chi_i^- = U^{ij}\psi_j^-$. Masses for these eigenstates are easily derived from the above X matrix :

$$\begin{aligned} M^2_{1,2} \;=\; & \tfrac{1}{2}(M_2^2 + \mu^2 + 2m_W^2 \\ & \mp [(M_2^2 - \mu^2)^2 + 4m_W^4\cos^2 2\beta \\ & + 4m_W^2(M_2^2 + \mu^2 + 2M_2\mu\sin 2\beta)]^{1/2} \end{aligned} \tag{20}$$

Direct Search for Light Gluinos at HERA

M. David
CEA DSM/DAPNIA CE-Saclay, Gif-sur-Yvette,France

Abstract Using Monte Carlo simulations for signal and background it is shown that direct detection of light and almost stable gluinos ($M_{\tilde{g}} < O(10)\,GeV$) might be possible at HERA using anomalous calorimetric events.

1 Introduction

As explained in the summary of the BSM working group the gluino ($\tilde{g}$) is the supersymmetric partner of the gluon (g). According to the boson-fermion symmetry of supersymmetry (SUSY); the gluino is an electrically neutral, colored octet Majorana fermion. The existence of a light gluino $M_{\tilde{g}} < O(10)\,GeV$ is not experimentaly excluded [1,2], eventhough it is not widely considered. In addition, the determination of the strong coupling constant $\alpha_S(Q)$ derived from the processes at low Q, e.g. in fixed target deep inelastic scattering (DIS), are systematically slightly lower than those coming from high Q processes, e.g. at LEP, when they are compared to the running predicted by QCD [3]. This slight discrepancy could be, in part, due to the existence of a light gluino [4]. On the theoretical side there exist arguments that favor the presence of light gluinos: There is a class of minimal supersymmetric standard models (MSSM) with R conservation that imply light gluinos, these models are "without dimension-3 operators" and they solve economicaly some cosmological problems and the SUSY-CP problem [5].

The preceeding arguments both theoretical and experimental show that the possible existence of a light gluino deserves more work: As its indirect effects are very small, e.g. on the structure function of the nucleon even when measured in high energy DIS at HERA [6], one attempts here to to work out a method for a direct search of the final state gluino.

2 Production of Gluinos at HERA

Many authors have computed gluino production in pp and $p\bar{p}$ interactions [7], there are very few results for ep interactions . Productions that happen through gluon bremsstrahlung starting from the quark line and followed by g$\rightarrow \tilde{g}\,\tilde{g}$ have been computed [8] but unfortunately, even for light gluinos, the yield is very small with $\sigma(ep \rightarrow e\tilde{g}\tilde{g}X)/\sigma(ep \rightarrow eX)$ of the order of 10^{-3}. The production of $\tilde{g}\tilde{g}$ pairs (R-parity is conserved) will be more important with the photoproduction part of the ep interaction (at $Q^2 \hat{=} 0$). In particular the so called "resolved" photoproduction where the γ behaves as an 1^- hadron, should lead to higher yields.

In hadroproduction estimates have been made [9] using the fact that the production of a gluino pair should be similar to the production of a $c\bar{c}$ pair

$$\sigma(ep \to e\tilde{g}\tilde{g}X) \doteq C(Mc/M\tilde{g})^7 \sigma(ep \to ec\bar{c}X). \quad (1)$$

The constant C takes into account the difference in the color factor for $\tilde{g}\tilde{g}$ versus $c\bar{c}$. At the energy of HERA σ(ep→ec$\bar{c}$X) has been mesured and is of the order of $500\,nb$. This estimate leads to cross-sections that are quite large; for example at $M_{\tilde{g}} = 3\,GeV$ one gets $\sigma(ep \to e\tilde{g}\tilde{g}X) \doteq 45\,nb$. The corresponding value for $p\bar{p}$ can be found in [7] and is, also for $\sqrt{s} = 300\,GeV$ and $M_{\tilde{g}} = 3\,GeV$, of the order of $40\,\mu b$. This can be crudly converted to an ep interaction if one notices that

$$\sigma(ep \to X) \doteq \frac{1}{10}\sigma(\gamma p \to X) \quad (2)$$

$$\sigma(\gamma p \to X)/\sigma(pp \to X) \doteq \sigma_{TOT}(\gamma p)/\sigma_{TOT}(pp) \quad (3)$$

This leads to a value of $20\,nb$ for $\sigma(ep \to e\tilde{g}\tilde{g}X)$. More accurate estimates can hopefully be obtained with an existing PYTHIA + JETSET simulation of $ep \to e\tilde{g}\tilde{g}X$ done by S. Mrenna [10]. The PYTHIA parameters are choosen to simulate this reaction through resolved photoproduction. The content of the electron into photons is taken into account and the hadronic content of the photon into quarks and gluons is also considered. With quarks and gluons from the proton, $q\bar{q}$ and gg subprocesses are simulated that lead to $\tilde{g}\tilde{g}$. The cross section formula used for these subprocesses are those of [7]. Except for these modifications, PYTHIA JETSET is set to the default and is similar to the one used in H1 for photoproduction of jets by resolved photons (MSTP(12)=1).

In Fig. 1 one can see the variation of $\sigma(ep \to e\tilde{g}\tilde{g}X)$ given by this simulation versus $M_{\tilde{g}}$, the two preceding estimates at $M_{\tilde{g}} = 3\,GeV$ are also shown to be in agreement with PYTHIA. One must remark that among both contributions; gg→ $\tilde{g}\tilde{g}$ and $q\bar{q} \to \tilde{g}\tilde{g}$, the first one is dominant, consequently the results do not depend much on the squark mass that appears in the t channel of the subprocess $q\bar{q} \to \tilde{g}\tilde{g}$. Another remark is that no intrinsic gluino is considered in the structure function of the proton. These intrinsic gluinos could lead to other subprocesses for gluino production (i.e. g$\tilde{g}$ →g$\tilde{g}$). According to [6] gluinos could carry about 5 to 10 % of the proton momentum, so represent 10 to 20 % of the gluons. But including gluinos in the proton corresponds to a decrease of the gluon part used for the production of $\tilde{g}\tilde{g}$ pairs. One assumes that altogether the total yield does not change.

3 Gluino Lifetimes and Gluino Hadronisation

The most likely decay of the gluino is through its coupling to squark-antiquark. For a light gluino the squark is virtual and decays to a quark-photino pair. The lifetime for the decay $\tilde{g} \to q\bar{q}\tilde{\gamma}$ is

$$\tau_{\tilde{g}} \doteq 10^{-19} s(M_{\tilde{q}})^4/(M_{\tilde{g}})^5; \quad (4)$$

with masses in GeV. Another possibility would be the decay of the gluino through its coupling to a gluon and a goldstino; this occurs for global SUSY theories and the only change for the lifetime is that in the above formula one has to replace $M_{\tilde{q}}$ by $\Lambda_{SUSY}/10$. Λ_{SUSY} being the scale of the SUSY breaking.

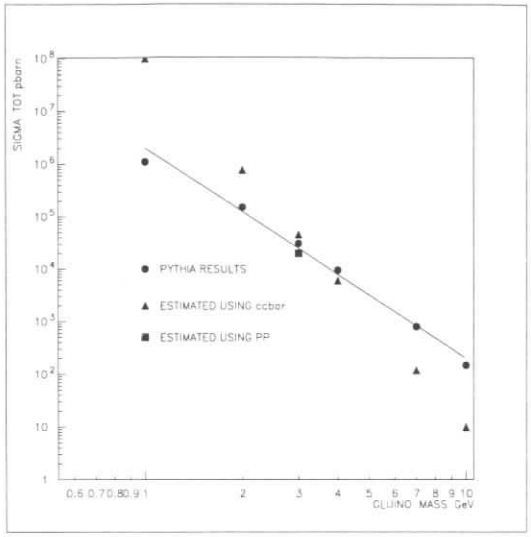

Figure 1: *Total cross section for $ep \to e\tilde{g}\tilde{g}$ at HERA versus the gluino mass.*

For most masses ($M_{\tilde{g}}$, $M_{\tilde{q}}$) the lifetime is long enough so that the gluino has time to bind with gluons or $q\bar{q}$ pairs before decay. Because of the strong octet binding forces the binding to the gluon is the most likely and leads to the production of an electrically neutral, color singlet hadron. This hadron is a $g\tilde{g}$ complex and is often denoted R^0 hadron [5]. This R^0 is built rather fast at the very beginning of the hadronisation, so that its kinematics are very close to the one of the gluino at the parton level. The mass and the lifetime of the R^0 are also not very different of the one of the gluino, as argued by G. Farrar [5]. The R^0 interacts hadronically in the calorimeter and its energy is degraded in the hadronic shower. When the gluino decays, the noninteracting photino (goldstino) produced in the decay gives a small missing transverse energy signal; in contrast to a heavy gluino with a short life time that decays before the calorimeter and therefore without energy degradation.

4 Detection of Gluino Pairs, Simulation and Efficiency

In the above phenomenological scenario a pair of light gluinos is produced and these gluinos may live long enough to strike the calorimeter. In the hadronization these gluinos are dressed as a R^0 hadron; i.e. a neutral hadron that behaves somewhat like a neutron or a K^0_L. A possible signature of their presence is to look for a pair of clusters in the calorimeter which have the following characteristics

1. The clusters must have no link to a charged track (neutral cluster).

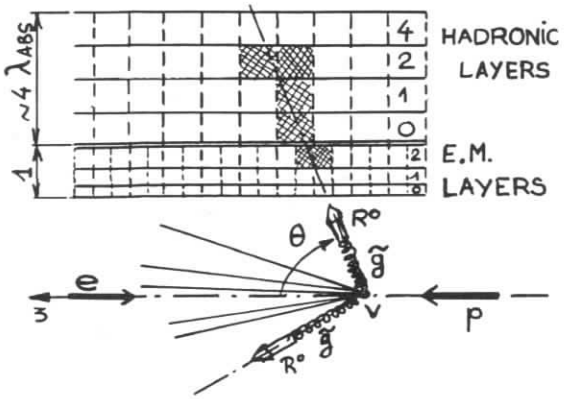

Figure 2: *Description of a late neutral hadronic cluster (LNHC) in the calorimeter.*

2. They must be of the hadronic type. In order to enforce this for a neutral hadron one asks for a cluster with a late start, i.e. not starting in the first electro-magnetic layers of the calorimeter as described in Fig 2. Such clusters are called late neutral hadronic clusters (LNHC).
3. The clusters must be somehow opposite in P_T, i.e. back to back in the (r, ϕ) plane.
4. A weak isolation condition could be imposed, because the R^0 hadron should be very leading in this scenarios: $(R_{iso}(\eta, \phi) > 0.5)$.
5. For a good dectection efficiency of a hadronic cluster one asks that $T_{R^0} \doteq E_{\tilde{g}} - M_{\tilde{g}} > 4GeV$. and $10^0 < \theta_{\tilde{g}} < 130^0$.
6. Not be of unphysical background origin (see next paragraph).

These cuts have been applied to events simulated with the supersymmetric PYTHIA of S. Mrenna [10]. In addition to what is described in paragraph 2, a crude hadronisation of the gluino is implemented, i.e. the gluino after the parton level is treated as a gluon in the showering and in the later string fragmentation. In order to represent the R^0 hadron one uses the gluino at the parton level, as in this model the R^0 is built early in the hadronization, this is a reasonnable asumption. Alternatively the leading particle of the "gluino jet" could be used to represent the R^0 hadron.

Results of this simulation for a gluino mass of 2 GeV are presented in Fig 3a to 3d. The efficiency of the above selection versus the gluino mass is presented in Fig 4. One must remark that lifetime effects are not treated at this level and also although the efficiency is low, the correponding quite large cross-section leads nevertheless to a significant number of events.

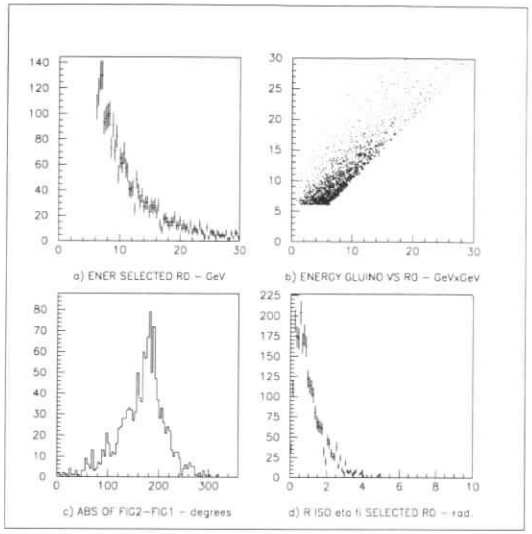

Figure 3: *a) Energy distribution of the gluinos. b) Correlation $E_{\tilde{g}}versus E_{leading} \doteq E_{R^0}$. c) Absolute value of $\Delta\phi$ in the transverse plane for the gluino pair. d) Isolation: Minimal distance in (η, ϕ) plane between the leading particle of the gluino jet and neighbouring particles of more than $3\,GeV$.*

5 Backgrounds

As already mentioned conventional hadrons with long enough lifetime (i.e. K^0_L, neutron and antineutron) can also interact in the calorimeter where they produce LNHC. This represents a physical background, but one must also take into accout some artifacts due to imperfections of the detector that lead to unphysical background.

- A) Unphysical Background

1. If the tracker for some reason is inefficient for a given charged hadron, the cluster of the corresponding particle is not linked to a charged track and if in addition the calorimeter does not record the beginning of the shower (at the beginning of the shower the charged particle behaves as a m.i.p.). Then one is left exactly with a late neutral hadronic cluster. This can be even more frequent if the clustering program cuts the cluster in two parts with one necessarily late.
2. The gammas, that are abundantly produced through π^0 decays, lead normally to clusters of the electromagnetic type. They can nevertheless represent a very severe background when they are emited in the "cracks" of the E.M. calorimeter because in this case they start their showering late in the hadonic part of the calorimeter. The only way to get rid of this background is by means of a cut in ϕ and z that eliminates

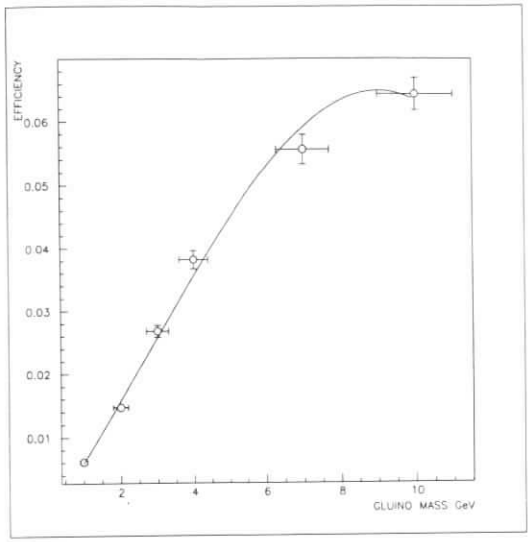

Figure 4: *Efficiency of gluino pairs selection versus the gluino mass with the cuts described in paragraph 4.*

the crack region of the E.M. calorimeter from the acceptance. In the following this cut is always done.

- B) Physical Background.

  In order to study this background due to K_L^0, n (neutron) and $\bar{n}$ (antineutron) production, one has used the standard H1 simulation for tagged photoproduction. This is a full PYTHIA5.6 simulation of resolved and direct processes for the H1 detector. The Monte-Carlo luminosities used are $372\,nb^{-1}$ for resolved γp and $7440\,nb^{-1}$ for direct γp. In addition to the tagging conditions, events are selected to have

$$0.3 < y < 0.7, \quad Q^2 < 0.01\,GeV^2 \tag{5}$$

$$E_{perp}^{tot} > 25\,GeV, \quad P_T^{miss} < 15\,GeV \tag{6}$$

  The LNHC are selected with the cuts described in paragraph 4 and for the pseudorapidity (η) range defined by $-1.3 < \eta < 1.3$. In these conditions one finds that

  1. It is mostly resolved photoproduction that counts

$$(K_L^0 + n)_{direct}/(K_L^0 + n)_{resolved} = 0.05. \tag{7}$$

  2. K_L^0 are as frequent as neutrons or antineutrons but even with both contributions added this represents only 2 events out of 1000 events with the cuts defined above.

  3. LNHC due to artifacts are more numerous than the physical one, they amount to 5 out of 1000 events.
  4. K_L^0 and neutrons are linked to a late cluster in the calorimeter. One can see that if one makes a histogram of the distance of closest approach (DCA) between the line of flight of the K_L^0 and the clusters. This shows a clear peak for $DCA < 20.cm$.
  5. The purity of the detection improves with an higher energy cut. The ratio of the physical LNHC to all LNHC is 0.3 at $E_{cut} = 4\,GeV$ and 0.6 at $E_{cut} = 7\,GeV$.

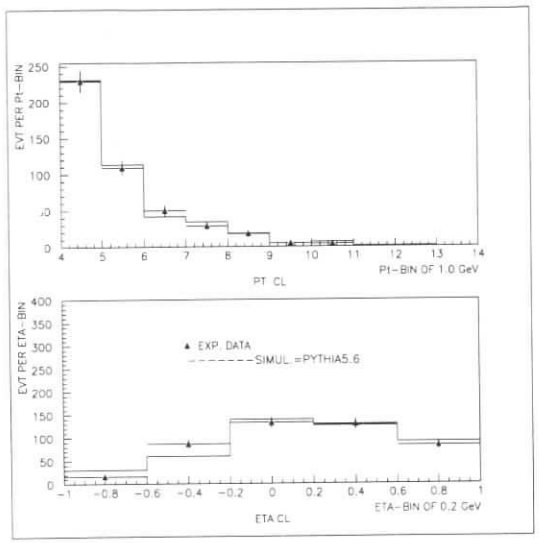

Figure 5: *Comparison Data-PYTHIA Simulation for η and P_T distributions.*

The simulation agrees fairly well with the data as it can be seen in Fig.5 where the distributions in η and P_T are compared between experimental data and simulation. This Monte-Carlo study of the background and the comparison to the data show that it is possible to understand both physical and unphysical backgrounds . It shows also that there is no anomalous production of LNHC.

6 Derivation of Limits

The fact that one finds no anomalous production of LNHC is an argument against the light gluino hypothesis, but one can be more specific on this question. One has seen in paragraph 4 that a better way to sign the presence of such gluinos was to ask for 2 LNHC approximately back to back. If one does so for the tagged events in the 1994 data ($\mathcal{L}_{94} = 3.3pb^{-1}$) one is left with no candidate. The same cuts as above are used with the following additionnal

cuts; $E_{\gamma TAG} < 1\,GeV$ and timing cuts again cosmics and halo-muons. The same result is also obtained for the corresponding PYTHIA simulation. The calculated number of events for a given hypothesis on $M_{\tilde{g}}$ and $M_{\tilde{q}}$ is

$$N_{cal} = \mathcal{L}\epsilon_{geo}\epsilon_{decay}\sigma_{\tilde{g}\tilde{g}} \tag{8}$$

where $\mathcal{L}$ is the integrated luminosity, $\sigma_{\tilde{g}\tilde{g}}$ is the cross-section given in paragraph 2, ϵ_{geo} is the efficiency described in paragraph 4, ϵ_{decay} is the efficiency factor resulting from the finite life time of the gluinos. Both gluinos produced must live long enough to interact with the calorimeter and are weighted by a term $e^{-d/\lambda}$; d is the distance before the calorimeter on the line of flight of the gluino and λ is the decay length connected to $\tau_{\tilde{g}}$ seen in paragraph 3. This term gives a dependence on both $M_{\tilde{g}}$ and $M_{\tilde{q}}$ and combining this with the above null values leads to regions of gluino and squark mass that are excluded at 90 % CL. These limits are computed under the hypothesis of an integrated luminosity of $45\,pb^{-1}$ and are presented on Fig.6, under these conditions they could about close the gap between UA1 results and neutral particle searches.

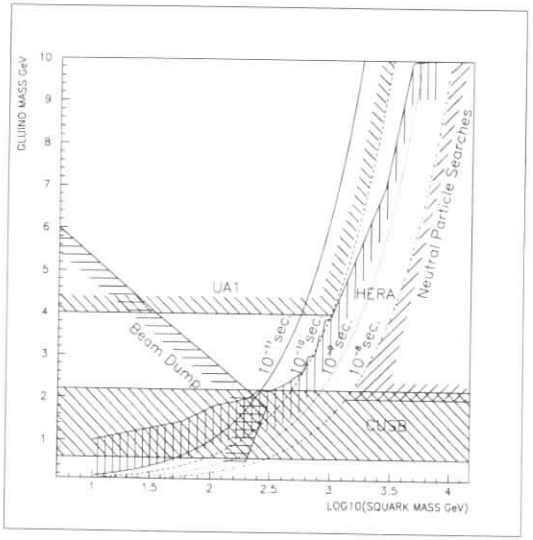

Figure 6: *Limits on the gluino mass as a function of the squark mass(excluded regions at 90 % CL are on the hatched side of the limits). Neutral stable particle searches is ref. [11], CUSB is ref. [12], Beam dump is ref. [13]; HERA is the possible HERA reach (see text) and curves of equal gluino lifetime are also shown (see paragraph 3).*

7 Conclusion

We have recalled the controversy about whether light gluinos (less than 10 GeV) are ruled out or not. Although the detection efficiency for pair production of light gluinos is small, we have

shown that the cross-section at HERA is large enough to allow an improvement of the limits on the gluino mass, as soon as one has at hand an integrated luminosity of 45 pb^{-1} obtained with stable conditions. A Monte Carlo study of the background and a comparison to the present H1 data has also shown that there is in the HERA data no anomalous production of late neutral cluster that could be a signal for such light gluinos.

8 Acknowledgements

I am grateful to S. Mrenna for introducing me to his SUSY PYTHIA and to its use for gluinos production [10] and also to G. Cozzika and G. Villet for carefull readings.

References

[1] UA1 Collaboration, C. Albajar et al., Phys. Lett. 198B (1987) 261.

[2] G.R. Farrar, Phys. Rev. 51D (1995) 3904.

[3] S. Bethke, Proc. of the XXX^{th} of Moriond (QCD) (1995) 213.

[4] J. Ellis et al., Phys. Lett. 305B (1993) 375.

[5] G.R. Farrar and P. Fayet, Phys. Lett. 76B (1978) 575.
G.R. Farrar, hep-ph/9504295

[6] R. Rueckl and A. Vogt, Z. Phys. 64C (1994) 431.

[7] S. Dawson et al., Phys. Rev. 31D (1985) 1581.
P.R. Harrison et al., Nucl. Phys. 213B (1982) 223.

[8] A. Campbell et al., Nucl. Phys. 198B (1982) 1.
R. Munoz-Tapia, Phys. Rev. 52D (1995) 3894.

[9] NA3 Collaboration, J. Badier et al., Z. Phys. 31C (1986) 21.
CHARM Collaboration, F. Bergsma et al., Phys. Lett. 121B (1983) 429.

[10] PYTHIA 5.6, H.U. Bengtsson and T. Sjoestrand, Comp. Phys. Comm. 46 (1987) 43.
JETSET 7.3, T. Sjoestrand and M. Bengtsson, Comp. Phys. Comm. 43 (1987) 367.
S. Mrenna, http://sgi2.hep.ane.gov:8001/index.html

[11] H.R. Gustafson et al., Phys. Rev. Lett. 37 (1976) 474.

[12] CUSB Collaboration, P.M. Tuts et al., Phys. Lett. 186B (1987) 233

[13] BEBC Collaboration, A.M. Cooper-Sarkar et al., Phys. Lett. 160B (1985) 212.

Light, Long-Lived Gluinos in DIS at HERA

D. Graudenz[a], K. Meier[b], O. Nachtmann[c], D. Stevens[b], K. Zuber[d]

[a] Theoretical Physics Division, CERN, CH–1211 Geneva 23
[b] Institut für Hochenergiephysik, Universität Heidelberg, D–69120 Heidelberg
[c] Institut für Theoretische Physik, Universität Heidelberg, D–69120 Heidelberg
[d] Lehrstuhl für exp. Physik IV, Universität Dortmund, D–40227 Dortmund

Abstract: A method of searching for gluinos in (3+1) jet events in deep inelastic scattering (DIS) at HERA is presented. Event shape variables that are sensitive to gluino production and the dependence of cross-sections on x and Q^2 are investigated. A parton-level Monte Carlo study for events with $Q^2 > 4$ GeV^2 shows that although standard QCD and gluino producing processes behave differently, the small size of the gluino cross-section makes a search for gluinos using this method impossible, given the present prospects for luminosity ($500\,\mathrm{pb}^{-1}$) at HERA.

1 Introduction

The supersymmetric partner of the gluon, the spin 1/2 gluino ($\tilde{g}$), is predicted by supersymmetric extensions of the Standard Model [1]. Gluino searches have placed limits on the mass $m_{\tilde{g}}$, and lifetime $\tau_{\tilde{g}}$, of the gluino, but it is not clear that a light, long-lived gluino has been experimentally excluded [2]. Like the gluon, a long-lived gluino would be a strongly interacting particle, which fragments and could be detected as a jet in multijet events. Unlike the gluon, the gluino has spin 1/2, causing gluino and gluon events to exhibit different event shapes. Rather than seeking to identify individual gluino events, a search could detect gluino production by means of an event shape distribution for a large number of events. OPAL performed such a search [3], but the results were inconclusive [4].

This paper discusses whether such a search for gluinos is possible in DIS at HERA. We first examine the dependence of gluino production on the kinematic variables x and Q^2 and discuss in which regions of phase space the gluino cross-section would be expected to be larger than its average. We then examine the distributions of three topological variables which are sensitive to the presence of gluino production. Finally, we study whether an experimental search at HERA would be able to detect gluino production using this method.

Electronic mail addresses:
Dirk.Graudenz@cern.ch, meierk@ihep.uni-heidelberg.de,
O.Nachtmann@thphys.uni-heidelberg.de, stevens@ihep.uni-heidelberg.de, Kai.Zuber@cern.ch

2 Gluino and (3+1) Jet Production at HERA

Gluino production at HERA would occur to leading order in α_s^2, producing 3 jets in the detector, plus the proton remnant jet, which partly disappears into the beam pipe. The absolute DIS cross-section is not constant with respect to the kinematic variables x, Q^2. Due to the photon propagator in Fig. 1(a), there is a strong Q^2 dependence in the DIS differential cross-section, while the structure functions $F_2(x,Q^2)$ and $F_1(x,Q^2)$ grow rapidly with decreasing x [5]. Thus, the DIS cross-section is largest at small Q^2 and small x. The relative contributions of the various

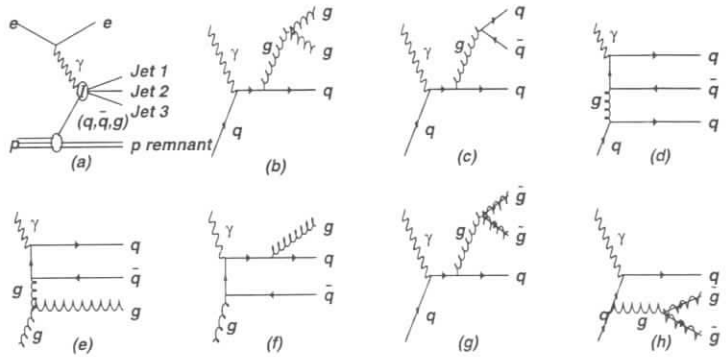

Figure 1: *(a) Generic diagram of (3+1) jet production at HERA. The vertex* I *represents a subprocess generating any of the final states: (b) qgg, (c) direct $qq\bar{q}$, (d) t-channel $qq\bar{q}$, (e) direct $q\bar{q}g$, (f) t-channel $q\bar{q}g$, (g), (h) gluino production by initial and final state gluon radiation.*

subprocesses are also dependent on x and Q^2. In Figs. 1(g) and (h), one sees that gluino production occurs only in quark-initiated events. Among the standard QCD backgrounds (Figs. 1(b)-(f)), however, there are gluon-initiated final states, such as $q\bar{q}g$ (Figs. 1(e),(f)). Because quark parton densities diminish with respect to the gluon density as x decreases, we expect the ratio of gluino events to standard QCD events to be more favourable at large x.

Figures 2(a) and (b) show the x and Q^2 dependence of the differential subprocess cross-sections and the total (3+1) jet cross-section. The deep inelastic (3+1) jet cross-section decreases with increasing x and Q^2, but the proportion of gluino events increases with increasing x. Thus, two competing factors play a role when deciding in which area of x and Q^2 space to conduct a search. A discussion of tradeoffs between statistics and signal-to-background ratio appears in Section 4.

To simulate (3+1) jet events to order α_s^2, we have used the parton-level Monte Carlo program PROJET [6] using the GRV parton densities [7]. PROJET contains the standard contributions to the (3+1) jet cross-section as well as the leading order matrix elements for gluino production in DIS. In order to avoid infra-red singularities in the cross-section due to collinear gluon radiation, PROJET uses the modified JADE jet algorithm which defines jets according to a parameter y_{cut}, requiring for each jet pair i,j that $m_{ij}^2 \geq y_{cut} W^2$. This algorithm also includes a reconstructed beam jet to account for longitudinal momentum which is partly lost into the beam pipe. To account for detector acceptance, we have required that the polar angle of the

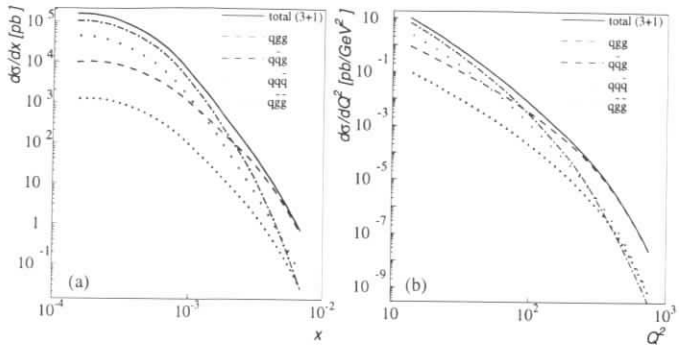

Figure 2: *Differential cross-sections of (3+1) jet QCD processes and of gluino production with respect to (a) x and (b) Q^2.*

outgoing detector jets and the outgoing electron be between 4° and 173°, an angular acceptance typical for the HERA detectors. This corresponds to a range of $4\,\mathrm{GeV}^2 < Q^2 < 8 \times 10^4\,\mathrm{GeV}^2$.

Because the goal of this study is to determine whether a search for gluinos in DIS at HERA is possible at all, we make three optimistic assumptions in our calculation:

(1) All calculations are made with $y_{cut} = 0.01$. Although at $y_{cut} = 0.01$ the calculation is theoretically well defined, when analysing data it is often desirable to increase y_{cut} to decrease the influence of detector resolution and hadronisation on the jet definition. This would result in a decrease in the total (3+1) jet cross-section and a reduction of statistics.

(2) We use a parton-level Monte Carlo prediction. Directly examining the behaviour of final-state partons ignores hadronization effects and the difficulties of reconstructing original parton momenta from energy deposited in a detector. This will cause any effects of gluino production in this study to appear more clearly than they would in practice.

(3) We assume $m_{\tilde{g}} = 0$. Supersymmetric theories require a gluino mass larger than several hundred MeV [8]. Due to reductions in phase space, the gluino cross-section decreases as $m_{\tilde{g}}$ increases [9]. Our choice of $m_{\tilde{g}} = 0$ means we will be considering a cross-section which is slightly larger than what would be seen in reality.

3 Topological Signatures

We studied three event shape variables that differentiate standard QCD from QCD with gluinos:

1. η_{struck} : The pseudorapidity of the struck quark. Unlike standard QCD processes, gluino events must be quark initiated in leading order. Because of the relatively high quark densities at larger x, we expect the struck quark in a gluino event to carry a larger fraction of the proton's momentum. Thus, we expect that for gluino events, the pseudorapidity of the struck quark ($-\ln(\tan^{-1}(\theta_{struck}/2))$) is generally larger than in standard QCD events, i.e. the struck quark in a gluino event is more inclined to exit the event vertex in the proton direction.

To identify the struck quark jet we reconstruct the event in the Breit frame where the virtual photon is antiparallel to the struck quark and has twice its momentum (i.e. $-p_{\gamma^*} = 2p_{struck}$). In this frame we identify the highest-energy jet with the jet formed by the struck quark. Figure 3(a) shows the predicted distribution of η_{struck} for gluino events and for the standard QCD background. As expected, more gluino events are at larger η_{struck}.

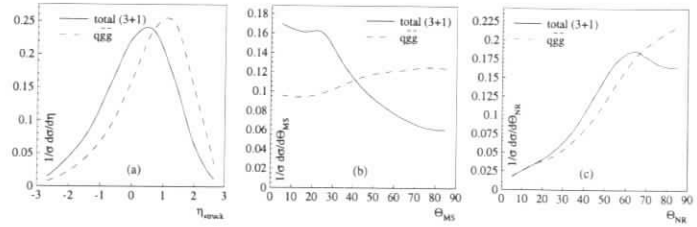

Figure 3: *Normalized differential cross-section with respect to the event shape variables (a) η_{struck}, (b) θ_{MS}, and (c) θ_{NR}. In each figure the distributions for standard QCD events and for events with gluino production are shown.*

2. θ_{MS} : The Muñoz-Tapia-Stirling angle. In the gluino producing diagrams, Figs. 1(g) and (h), the virtual photon always interacts directly with the parton from the proton. For the $q\bar{q}q$ and $q\bar{q}g$ final states, there are also diagrams in which the interaction between the photon and the proton proceeds by t-channel gluon exchange. Muñoz-Tapia and Stirling have defined an angle θ_{MS} which is sensitive to the presence of this exchange in photoproduction at HERA [10]; θ_{MS} is the angle between the plane formed by the highest-p_T jet and the proton beam and the plane formed by the two other jets. We have applied this angle to DIS.

In photoproduction, an electron radiates a photon along its direction of motion. When this photon interacts with a beam proton travelling antiparallel to the electron direction, the resulting event has very little transverse momentum and is boosted parallel to the beam axis. In DIS, the direction of momentum transfer need not be parallel to the beam axis. Therefore, when applying θ_{MS} to HERA DIS events, we first transform the event into the centre-of-mass frame of the virtual photon and the struck quark, where the angle θ_{MS} is defined. As prescribed in Ref. [10], we place a cut of $|\eta_{struck}| < 1$ in this system. Although η_{struck} is peaked far in the forward direction in the laboratory frame, in the centre-of-mass frame the η_{struck} is peaked at 0, and consequently this cut results in only a small loss of statistics.

Fig. 3(b) shows the differential cross-section as a function of θ_{MS} for gluino and standard QCD processes. Just as in photoproduction, θ_{MS} is (in principle) capable of differentiating between gluino and standard QCD events in DIS.

3. θ_{NR} : The Nachtmann-Reiter angle. The Nachtmann-Reiter angle θ_{NR} was conceived as a means of detecting the existence of the non-Abelian gluon self-coupling in QCD [11]. The angle's sensitivity to the spin of the particles produced at the secondary vertex of a radiated gluon also allows it to test for the production of spin-1/2 gluinos.

Originally, the Nachtmann-Reiter angle was defined for the case of e^+e^- annihilation as the angle between suitable directions formed from the two highest energy jets and the two lowest energy jets. We have defined θ_{NR} at HERA to be the angle between the struck quark jet and the two lower energy jets in the rest frame of the two lower energy jets. Similar angular momentum conservation and γ_5 invariance arguments apply as in the e^+e^- case.

The differential cross-section as a function of θ_{NR} is shown in Fig. 3(c). We see that for the gluino events it exhibits the same $\sin^2\theta_{NR}$ behaviour that is predicted for a virtual gluon splitting into two fermions [11]. For standard QCD events, the distribution is qualitatively different.

4 Search Strategies

To determine whether gluinos could be detected at HERA we pursued two different search strategies. First we investigated whether an experiment would be able to extract a gluino signal from a standard QCD background by imposing cuts based on the angular distributions mentioned above. Second we determined whether a χ^2 fit of the angular distributions of standard QCD plus gluino production to the angular distributions of standard QCD would be able to distinguish between the two distributions. For each method we investigated whether the result could be improved by looking in a favourable region of x and Q^2.

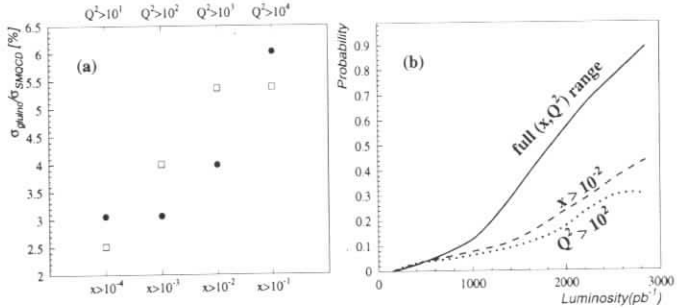

Figure 4: *(a) Signal-to-background ratio (in per cent) after event shape cuts for different regions of x (dots) and Q^2 (squares). (b) Probability that an experiment would be able to distinguish between QCD and gluino production at a 95% confidence level as a function of the available luminosity.*

The cuts made in an attempt to extract a gluino signal from the standard QCD background were derived from the distributions in Fig. 3. Our cuts are chosen to be at the point where the normalized distribution curves intersect: $\theta_{MS} \geq 50$, $\theta_{NR} \geq 70$, $\eta_{struck} \geq 1.0$. We computed the signal-to-background ratios for several values of cuts on x and Q^2. Although we vary the kinematic region where we evaluate our cuts, qualitatively the distributions change very little, and we impose the same cuts regardless of the kinematic region considered.

Figure 4(a) shows the gluino cross-section in the considered region in proportion to the standard QCD cross-section. Although the signal-to-background ratio has been improved from 1% (Fig. 2) to 6%, the uncertainties in the absolute cross-sections of QCD related processes are over 20%. Even with an unlimited statistical sample, this method would not succeed.

A χ^2 fit of the calculated signal-plus-background event shape distributions to the calculated background distribution would avoid the uncertainties inherent in the absolute cross-sections.

We divided our Monte Carlo sample into 5 bins in each of the variables η_{struck}, θ_{MS}, and θ_{NR}. Using a random number generator we simulated the statistical errors that would be seen in an experimental data sample containing QCD and gluino production events. For each value of the luminosity considered, we simulated 10000 experiments, and performed a χ^2 fit of the calculated signal ($\tilde{g}$) plus background (QCD) event shape distributions to the distribution from the calculated background (QCD).

The probability that an experiment performed would be able to distinguish standard QCD processes from standard QCD plus gluino production at a 95% confidence level is shown in Fig. 4(b). The current estimate of the lifetime integrated luminosity of HERA, $500\,\mathrm{pb}^{-1}$, is far too low to allow a search for gluinos at HERA by the above method.

5 Conclusion

We have investigated the effects of gluino production on three event shape variables that are in principle capable of differentiating between events with and without gluinos in (3+1) jet events in DIS at HERA. We have also studied the x and Q^2 dependence of the gluino production mechanism and the standard QCD subprocess mechanisms. Because the total gluino cross-section is small compared to the competing QCD background, it will not be possible using the angular distributions to determine whether or not gluinos are being produced at HERA.

Acknowledgements

O.N. wishes to thank U. Ellwanger and M. Rausch de Traubenberg for discussions.

References

[1] H. Haber and G. Kane, Phys. Rep. **117** (1985) 75.

[2] G. Farrar, Phys. Rev. **D51** (1995) 3904.

[3] OPAL Collaboration, Z. Phys. **C49** (1991) 49.

[4] R.G. Roberts and W.J. Stirling, Phys. Lett. **B313**, (1993) 453.

[5] H1 Collaboration, Nucl. Phys. **B470** (1996) 3;
ZEUS Collaboration, preprint DESY 96-076 (1996).

[6] D. Graudenz, Comput. Phys. Commun. **92** (1995) 65.

[7] M. Glück, E. Reya and A. Vogt, Z. Phys. **C67** (1995) 433.

[8] R. Barbieri, L. Girardello and A. Masiero, Phys. Lett. **127B** (1983) 429.

[9] R. Muñoz-Tapia and W.J. Stirling, Phys. Rev. **D49** (1994) 3763.

[10] R. Muñoz-Tapia and W.J. Stirling, Phys. Rev. **D52** (1995) 3894.

[11] O. Nachtmann and A. Reiter, Z. Phys. **C16** (1982) 45.

Perspectives on New Phenomena

Hans–Ulrich Martyn

I. Physikalisches Institut, RWTH Aachen, Germany

Abstract A compilation of searches for new phenomena at HERA is presented. Reviewed are direct searches of new fermions and leptoquarks and indirect signatures of compositeness, leptoquarks and new heavy neutral vector bosons mediated through contact interactions.

1 Introduction

This article reviews the perspectives to discover new phenomena beyond the Standard Model at the future upgraded HERA $e\,p$ collider. Direct formation of new particles, *e.g.* heavy fermions or leptoquarks, typically occur as s-channel resonance and would lead to a spectacular mass peak at $M_X = \sqrt{x\,s} \lesssim 300$ GeV. A considerably larger mass range can be explored through the study of effects from new *virtual* particle exchange or contact interactions. All details and formulae on the underlying model assumptions can be found in the Proceedings *Physics at HERA* of the previous 1991 workshop [1].

The present status of searches for heavy fermions, leptoquarks and contact interactions at HERA is reviewed, labeled as HERA '95, *i.e.* including 1995 data with typical luminosities of $\mathcal{L} = 5 \div 10$ pb^{-1} (H1 and ZEUS publications or contributions to ICHEP 96, Warsaw). Comparing the achieved results with the projections of ref. [1], it turns out that these Monte Carlo analyses are quite realistic. It is therefore appropriate to extrapolate the expected sensitivity on masses and couplings with increasing luminosity by simple scaling laws. Only in few cases new Monte Carlo studies were necessary. Direct searches are assumed to scale as $\propto \mathcal{L}^{1/2}$, while the sensitivity of indirect searches increases like $\propto \mathcal{L}^{1/4}$. Expectations for $\mathcal{L} = 250$ pb^{-1} are labeled HERA 250, those for $\mathcal{L} = 1000$ pb^{-1} as HERA 1000.

Results from other colliders or experiments are included, taking the values compiled by the Particle Data Group [2]. No attempt is made to give a complete list of references.

2 New Fermions

2.1 Exotic Leptons

Searches for exotic leptons $L = E,\ N$ have so far not being carried out at HERA [1] due to the limited luminosity. Mixing angles to ordinary leptons are expected to be smaller than $\mathcal{O}(10^{-1})$.

[1] Recently ZEUS [3] searched for right-handed electron neutrinos decaying into a relatively light right-handed W boson, $N_R \to e\,W_R$

The coupling parameters $\zeta = \zeta_L$ or ζ_R (left or right handed leptons) should be close to the values of the mixing angles. The neutral and charged current Lagrangians are

$$\mathcal{L}^{NC} = \frac{e}{4\,\sin\theta_W\,\cos\theta_W}\left[\zeta_L^E\,\bar{e}\,\gamma_\mu\,(1-\gamma_5)\,E + \zeta_R^E\,\bar{e}\,\gamma_\mu\,(1+\gamma_5)\,E\right]\,Z^\mu + h.c.\,, \tag{1}$$

$$\mathcal{L}^{CC} = \frac{e}{2\sqrt{2}\,\sin\theta_W}\left[\zeta_L^N\,\bar{e}\,\gamma_\mu\,(1-\gamma_5)\,N + \zeta_R^N\,\bar{e}\,\gamma_\mu\,(1+\gamma_5)\,N\right]\,W^\mu + h.c.\,, \tag{2}$$

$$\Gamma_{L\to Z\,l} \simeq \frac{G_F}{16\sqrt{2}\,\pi}\,\zeta^2\,M_L^3\,, \qquad \Gamma_{L\to W\,l} \simeq \frac{G_F}{8\sqrt{2}\,\pi}\,\zeta^2\,M_L^3\,. \tag{3}$$

The cross section for heavy lepton production at HERA can be parametrized as

$$\sigma(e\,p\to L\,X) \simeq c\,\zeta^2\left(\frac{M_L}{100\ \text{GeV}}\right)^{-b}\ \text{pb}\,, \tag{4}$$

with the coefficients

$$c(N_L) = 15\,,\quad c(N_R) = 10\,,\quad b(N_L \text{ or } N_R) = 4.5\,,$$
$$c(E_L) = 2.5\,,\quad c(E_R) = 1.5\,,\quad b(E_L \text{ or } E_R) = 3.5\,.$$

heavy lepton	HERA 250 M_L [GeV]	HERA 1000 M_L [GeV]
N_L	130	170
N_R	115	160
E_L	60	110
E_R	50	90

Table 1: Accessible heavy lepton masses ($N_{evt}^{obs} \geq 20$) for couplings $\zeta^2 = 0.02$ and a detection efficiency $\epsilon = 0.5$

Experiments at e^+e^- colliders can exclude heavy lepton masses up to $M_L \lesssim \sqrt{s}/2$.

Conclusion HERA is an excellent place to search for exotic leptons E and N.

2.2 Excited Leptons

The cross section for excited lepton l^* production in narrow width approximation is

$$\sigma(e\,p\to l^*\,X) = \frac{4\,\pi^2}{s}\,(2\,J+1)\,\frac{\Gamma_{l^*}}{M_{l^*}}\,\mathcal{B}\,f_{\gamma/p}(M_{l^*}^2/s)\,, \tag{5}$$

$$\Gamma_{l^*} \simeq \alpha\,M_{l^*}^3\,\frac{c_{V\,l^*\,l}^2}{\Lambda^2}\,. \tag{6}$$

The decay into an ordinary lepton l and vector boson V, branching ratio $\mathcal{B}(l^*\to l\,V)$, occurs via magnetic coupling $-i\,\frac{e}{\Lambda}\,\sigma_{\mu\nu}\,q^\nu\,(1-\gamma_5)\,c_{V\,l^*\,l}$. $f_{\gamma/p}(x)$ is the photon density in the proton.

LEP experiments can exclude excited leptons up to masses $M_{l^*} \lesssim \sqrt{s}/2$ for pair production and $M_{l^*} \lesssim \sqrt{s}$ for single production, assuming $\mathcal{B}(l^*\to l\,\gamma) = 1$ and electroweak couplings to the photon (λ_γ) or Z (λ_Z) exchange. The relation between the couplings is $\lambda/M_{l^*} = \sqrt{2}\,c_{V\,l^*\,l}/\Lambda$.

	HERA '95	
$e^* \to e\,\gamma$	$\sigma \lesssim 0.8\ (2)$ pb	$M \gtrsim 100\ (50)$ GeV
$e^* \to \nu\,W,\ e\,Z$	$\sigma \lesssim 2$ pb	$M \gtrsim 110$ GeV
$\nu^* \to \nu\,\gamma$	$\sigma \lesssim 1$ pb	$M \gtrsim 50$ GeV
$\nu^* \to e\,W,\ \nu\,Z$	$\sigma \lesssim 2.5$ pb	$M \gtrsim 125$ GeV

Table 2: Upper limits (95% *cl*) on the cross section for excited lepton production

	HERA '95	HERA 250	HERA 1000
M_{l^*} [GeV]	$c\,\mathcal{B}^{1/2}/\Lambda$ [GeV]$^{-1}$	$c\,\mathcal{B}^{1/2}/\Lambda$ [GeV]$^{-1}$	$c\,\mathcal{B}^{1/2}/\Lambda$ [GeV]$^{-1}$
$e^* \to e\,\gamma$			
100	$1 \cdot 10^{-3}$	$2 \cdot 10^{-4}$	$1 \cdot 10^{-4}$
150	$1.2 \cdot 10^{-3}$	$2 \cdot 10^{-4}$	$1 \cdot 10^{-4}$
200	$2.5 \cdot 10^{-3}$	$5 \cdot 10^{-4}$	$2.5 \cdot 10^{-4}$
250	$1 \cdot 10^{-2}$	$2 \cdot 10^{-3}$	$1 \cdot 10^{-3}$
$\nu^* \to \nu\,\gamma$			
100	$8 \cdot 10^{-3}$	$1.5 \cdot 10^{-3}$	$8 \cdot 10^{-4}$
150	$1 \cdot 10^{-2}$	$2 \cdot 10^{-3}$	$1 \cdot 10^{-3}$
200	$2.5 \cdot 10^{-2}$	$5 \cdot 10^{-3}$	$2.5 \cdot 10^{-3}$

Table 3: Upper limits (95% *cl*) on couplings $c\,\mathcal{B}^{1/2}/\Lambda$ as a function of the excited lepton mass

Conclusion HERA is an excellent place to search for excited electrons and neutrinos. The sensitivity to couplings $c\,\mathcal{B}^{1/2}/\Lambda$ can be increased by an order of magnitude.

References HERA data: H1 Collaboration [4], ZEUS Collaboration [5]

2.3 Leptogluons

The cross section for leptogluon LG production in narrow width approximation is

$$\sigma(e\,p \to LG\,X) = \frac{2\,\pi^2\,\alpha_s}{s}\left(\frac{M_{LG}}{\Lambda}\right)^2 g(M_{LG}^2/s)\,, \tag{7}$$

$$\Gamma_{LG} = \frac{\alpha_s}{4}\frac{M_{LQ}^3}{\Lambda^2}\,, \tag{8}$$

where $g(x)$ is the gluon density in the proton.

Conclusion HERA has a rich potential to search for leptogluons. Scale parameters Λ of more than one order of magnitude larger can be probed.

References HERA data: H1 Collaboration [6]

	HERA '95	HERA 250	HERA 1000
M_{LG} [GeV]	Λ [TeV]	Λ [TeV]	Λ [TeV]
50	5	125	250
100	3	65	125
150	1.2	30	65
200	0.5	25	50
250	0.2	6	15
280	0.1	1.5	3

Table 4: Lower limits (95% *cl*) on the scale parameter Λ as a function of the leptogluon mass

2.4 Excited Quarks

At HERA excited quark q^* production proceeds via electroweak couplings $\gamma\,q \to q^*$. The cross section for excited quark production can be written analogous to the excited fermion case including a convolution of the photon densities in the electron $f_{\gamma/e}$

$$\sigma(e\,p \to q^*\,X) = \frac{4\,\pi^2}{s}\,(2\,J+1)\,\frac{\Gamma_{q^*}}{M_{q^*}}\,\mathcal{B}\,f_{\gamma/e}\,f_{q/p}(M_{q^*}^2/s)\,, \tag{9}$$

$$\Gamma_{q^*} \simeq \alpha\,M_{q^*}^3\,\frac{c_{V\,q^*l}^2}{\Lambda^2}\,. \tag{10}$$

The actual upper limit on the cross section for q^* production (HERA '95 data at 95% *cl*) is

$$\sigma(e\,p \to q^*\,X)\cdot\mathcal{B}(q^* \to q\,\gamma) \lesssim 2\text{ pb} \qquad \text{for } M_{q^*} \gtrsim 100\text{ GeV}\,.$$

	HERA '95	HERA 250	HERA 1000
M_{q^*} [GeV]	$c\,\mathcal{B}^{1/2}/\Lambda$ [GeV]$^{-1}$	$c\,\mathcal{B}^{1/2}/\Lambda$ [GeV]$^{-1}$	$c\,\mathcal{B}^{1/2}/\Lambda$ [GeV]$^{-1}$
100	$1 \cdot 10^{-3}$	$2 \cdot 10^{-4}$	$1 \cdot 10^{-4}$
150	$1.2 \cdot 10^{-3}$	$2.5 \cdot 10^{-4}$	$1.2 \cdot 10^{-4}$
200	$3 \cdot 10^{-3}$	$6 \cdot 10^{-4}$	$3 \cdot 10^{-4}$
250	$2 \cdot 10^{-2}$	$4 \cdot 10^{-3}$	$2 \cdot 10^{-3}$

Table 5: Upper limits (95% *cl*) on couplings $c\,\mathcal{B}^{1/2}/\Lambda$ as a function of the excited quark mass

LEP experiments can exclude excited quarks up to masses $M_{q^*} \lesssim \sqrt{s}/2$ for pair production and $M_{q^*} \lesssim \sqrt{s}$ for single production. At the TEVATRON excited quark production proceeds via QCD couplings $g\,q \to q^*$, yielding $M_{q^*} > 540$ GeV.

Conclusion HERA is superior to LEP in the search for excited quarks q^*. The mass limit from $\bar{p}\,p$ experiments, giving complementary information on the $g\,q$ coupling, cannot be reached.

References HERA data: H1 Collaboration [4], ZEUS Collaboration [5]

3 Leptoquarks

Leptoquarks LQ are colour triplet bosons of spin 0 (7 scalars S) or 1 (7 vectors V), carrying lepton and baryon number and fractional electric charge.

The cross section for leptoquark production in narrow width approximation is

$$\sigma(e\,p \to LQ\,X) \;=\; \frac{\pi}{4\,s}\,\lambda^2\,(J+1)\,q(M_{LQ}^2/s)\;, \tag{11}$$

$$\Gamma_S \;=\; \frac{\lambda^2}{16\,\pi}\,M_{LQ}\;, \qquad \Gamma_V \;=\; \frac{\lambda^2}{24\,\pi}\,M_{LQ}\;, \tag{12}$$

where $q(x)$ denotes the quark densities in the proton.

There may exist 252 additional flavour changing leptoquarks (2 lepton flavours l, 3×3 initial and final quark generations i, j, couplings $\lambda^2 = \lambda_{ei}\,\lambda_{lj}$) with a production cross section

$$\sigma(e\,p \to LQ\,X) \;=\; \frac{s}{16\,\pi}\left(\frac{\lambda_{ei}\,\lambda_{lj}}{M_{LQ}^2}\right)^2 \int dx\,dy\,x\,q_i(x) \begin{cases} \frac{1}{2} & s\text{-channel } S \\ \frac{1}{2}\,(1-y)^2 & u\text{-channel } S \\ 2\,(1-y)^2 & s\text{-channel } V \\ 2 & u\text{-channel } V \end{cases} \tag{13}$$

Leptoquarks of the first generation with masses ranging from 215 GeV to 275 GeV are already excluded by present HERA data for couplings larger than the electromagnetic scale $\lambda > \sqrt{4\,\pi\,\alpha} = 0.3$. Masses of up to 250 GeV are excluded for couplings with leptons of the second and third generation larger than $\lambda > 0.3$.

Complementary information can be obtained from electron and positron beams. For the extrapolation to high luminosities an equal share of $e^\pm$ beams is assumed.

M_{LQ} [GeV]	HERA '95	HERA 250	HERA 1000
scalars			
100	$1.5\cdot10^{-2}$	$2\cdot10^{-3}$	$1\cdot10^{-3}$
150	$2.5\cdot10^{-2}$	$4\cdot10^{-3}$	$2\cdot10^{-3}$
200	$7\cdot10^{-2}$	$1\cdot10^{-2}$	$5\cdot10^{-3}$
250	$2.5\cdot10^{-1}$	$4\cdot10^{-2}$	$2\cdot10^{-2}$
vectors			
100	$1.5\cdot10^{-2}$	$2\cdot10^{-3}$	$1\cdot10^{-3}$
150	$2.5\cdot10^{-2}$	$4\cdot10^{-3}$	$2\cdot10^{-3}$
200	$5\cdot10^{-2}$	$8\cdot10^{-3}$	$4\cdot10^{-3}$
250	$2\cdot10^{-1}$	$3\cdot10^{-2}$	$1.5\cdot10^{-2}$

Table 6: Upper limits (95% *cl*) on first generation leptoquark couplings λ_{11}. Values of individual leptoquarks may differ by a factor of 2

In $\bar{p}\,p$ collisions leptoquarks are produced in pairs, thus their production does not depend on the coupling λ. However, the derived mass limits depend on the assumed decay branching ratio $\mathcal{B}(LQ \to l + jet)$.

M_{LQ} [GeV]	HERA '95	HERA 250	HERA 1000
scalar $S^L_{1/2}$			
100	$5\cdot10^{-3}$	$1.5\cdot10^{-3}$	$8\cdot10^{-4}$
150	$1\cdot10^{-2}$	$3\cdot10^{-3}$	$1.5\cdot10^{-3}$
200	$2.5\cdot10^{-2}$	$8\cdot10^{-3}$	$4\cdot10^{-3}$
225	$5\cdot10^{-2}$	$1.5\cdot10^{-2}$	$8\cdot10^{-3}$
vector $\tilde{V}_0^R$			
100	$3\cdot10^{-3}$	$1\cdot10^{-3}$	$5\cdot10^{-4}$
150	$7\cdot10^{-2}$	$2.5\cdot10^{-3}$	$1.2\cdot10^{-3}$
200	$1.5\cdot10^{-2}$	$5\cdot10^{-3}$	$2.5\cdot10^{-3}$
225	$3\cdot10^{-2}$	$1\cdot10^{-2}$	$5\cdot10^{-3}$

Table 7: Upper limits (95% *cl*) on second generation leptoquark couplings λ_{22}. Values for other leptoquarks may be up to a factor of 4 worse

	$\mathcal{B} = 1.0$ M_{LQ} [GeV]	$\mathcal{B} = 0.5$ M_{LQ} [GeV]
first generation		
scalars (CDF)	113	80
scalars (D0)	129	116
second generation		
scalars (CDF)	131	96
scalars (D0)	119	97
third generation		
scalars (CDF [9])	94	—

Table 8: Lower mass limits (95% *cl*) on first, second and third (preliminary) generation scalar leptoquarks from $\bar{p}\,p$ experiments, decay branching ratio $\mathcal{B}(LQ \to l + jet)$.

Conclusion HERA remains competitive in the search for leptoquarks, in particular for leptoquarks with lepton flavour violating couplings, although the mass limits from $\bar{p}\,p$ experiments may increase in the future. The limits on coupling strengths λ can be improved by an order of magnitude.

References HERA data: H1 Collaboration [7], ZEUS Collaboration [8]

4 Contact Interactions $(\bar{e}e)\,(\bar{q}q)$

New currents or bosons may produce indirect effects through *interference* of a *virtual* particle exchange with the γ and Z fields of the Standard Model. For a sufficiently heavy particle X with mass $M_X \gg \sqrt{s}$ and coupling strength $g_{X\to i,f}$ (i, $f = L$, R fermion helicities) new contact terms arise from contracting the particle propagators to an effective four-fermion pointlike interaction. The effective couplings η_{if} carry dimension [mass^{-2}]. The expected signatures are deviations from the Standard Model predictions at high Q^2, being either positive or negative.

The neutral current Lagrangian for deep inelastic scattering $e\,p \to e\;hadrons$ gets an additional term

$$\mathcal{L}^{NC}_{\text{contact}} = \sum_{q=u,d} \{\eta^q_{LL}\,(\bar{e}_L\gamma_\mu e_L)(\bar{q}_L\gamma^\mu q_L) + \eta^q_{LR}\,(\bar{e}_L\gamma_\mu e_L)(\bar{q}_R\gamma^\mu q_R) + \eta^q_{RL}\,(\bar{e}_R\gamma_\mu e_R)(\bar{q}_L\gamma^\mu q_L) + \eta^q_{RR}\,(\bar{e}_R\gamma_\mu e_R)(\bar{q}_R\gamma^\mu q_R)\}\ , \tag{14}$$

$$\eta^q_{if} \equiv \frac{g_{X\to i}\,g_{X\to f}}{M_X^2}\ . \tag{15}$$

Only vectorial Lorentz structures need to be considered. Scalar and tensor terms, involving helicity flip amplitudes proportional to a small fermion mass, are strongly suppressed at HERA.

Specific models, *e.g.* compositeness, leptoquarks or new gauge bosons Z', can be uniquely described in terms of the completely general *eight* coupling coefficients η^q_{ij}. This concept can be extended to charged current phenomena, but contact interactions in charged currents have not been considered in this workshop.

Note that contact interactions depend only on the ratio g_X/M_X and the sensitivity rises with the center of mass energy and luminosity as $\propto (s\cdot\mathcal{L})^{1/4}$.

Contrary to the opinion of several authors polarized leptons do not help in discovering new contact interaction phenomena. Polarization might only be useful, once a discrepancy with the Standard Model has been observed.

4.1 Compositeness Scales

In the Standard Model the fundamental particles – leptons, quarks and gauge bosons – are assumed to be pointlike. In extended models it is conceivable that leptons and quarks have a substructure. If they have common constituents a possible $e\,q$ compositeness can be characterized by a compositeness scale parameter Λ and a coupling strength g

$$\eta^q_{if} \equiv \pm\frac{g^2}{\Lambda^{\pm\,2}_{if}}\ ,$$

where i, j are helicity indices L, R and the signs indicate positive and negative interference with the Standard Model currents. The coupling strength is conventionally chosen as $g^2/4\,\pi = 1$.

Conclusion HERA is and will continue to be competitive with experiments at other colliders in the search for $e\,q$ compositeness. Compositeness scales Λ up to 8 TeV can be reached depending on the chiral structure and sign of interference.

References HERA data: H1 Collaboration [10], ZEUS Collaboration [11]

			HERA '95	HERA 250	HERA 1000	CDF		OPAL [12]	
Λ^+_{LL}	Λ^+_{RR}	[TeV]	$1.7 \div 2.3$	5.1	8.0	1.7	—	2.4	1.9
Λ^-_{LL}	Λ^-_{RR}	[TeV]	1.0	3.5	4.1	2.2	—	1.7	2.2
Λ^+_{LR}	Λ^+_{RL}	[TeV]	$2.1 \div 2.5$	5.1	6.3			2.0	1.6
Λ^-_{LR}	Λ^-_{RL}	[TeV]	$1.2 \div 1.4$	2.1	4.5			2.0	2.5

Table 9: Lower limits (95% *cl*) on $e\,q$ compositeness scale parameters $\Lambda^\pm$ for chiralities LL, LR, RL and RR, assuming $g^2/4\,\pi = 1$. $\bar{p}\,p$ experiments use Drell-Yan production, in e^+e^- annihilation 5 quark flavours contribute

4.2 Form Factors and Quark Radii

An alternative method to study fermion substructures is to assign a finite size of radius R to the leptons and/or quarks. A convenient parametrisation is to introduce 'classical' form factors $f(Q^2)$ at the gauge boson–fermion vertices [13]. A finite extension of a lepton or quark is expected to diminish the Standard Model cross section at high Q^2

$$\frac{d\sigma}{dQ^2} = \frac{d\sigma^{SM}}{dQ^2}\,f_e^2(Q^2)\,f_q^2(Q^2)\ , \tag{16}$$

$$f(Q^2) = 1 - \frac{1}{6}\,R^2\,Q^2\ . \tag{17}$$

Note that this concept does not imply interference effects as discussed in the previous section.

The HERA data are analyzed in terms of a single form factor for the light u and d quarks, since the pointlike nature of the electron is already established down to much smaller distances in e^+e^- and $(g-2)_e$ experiments.

	HERA '95	HERA 250	HERA 1000	$Z \to q\,\bar{q}$	$Z \to f\,\bar{f}$
R_q [cm]	$1.4 \div 2.6\cdot 10^{-16}$	$0.6\cdot 10^{-16}$	$0.4\cdot 10^{-16}$	$1.2\cdot 10^{-16}$	$0.2\cdot 10^{-16}$

Table 10: Upper limits at 95% *confidence level* on quark radii. Z decays are for 5 quark flavours, the last column assumes lepton quark universality

Conclusion HERA is and will continue to be competitive with other colliders in the search for quark form factors or quark radii R_q down to distance of a few 10^{-17} cm.

References HERA data: H1 collaboration [10], ZEUS collaboration [11]

4.3 Leptoquarks

The direct search for leptoquarks can be complemented by contact interaction analyses, extending the accessible mass range beyond the HERA center of mass energy. Each leptoquark

is specified by a set of coupling coefficients

$$\eta^q_{if} \;=\; c^q_{if}\left(\frac{\lambda}{M_{LQ}}\right)^2 ,$$

where the constants c^q_{if} are given by the model. *Note* that such a contact term analysis is only sensitive to the ratio coupling over mass and the resulting coupling limits may only be extrapolated to lower leptoquark masses $M_{LQ} \gtrsim \sqrt{s}$.

Contact interaction analyses at HERA have been carried out for the first, second and third leptoquark generation. In general one obtains more stringent bounds for vectors than for scalars. The access to various leptoquark types cannot be simply guessed on the basis of the quark densities in the proton. This naive expectation is spoiled by interference effects and by the fact that not all coefficients η^q_{if} contribute with the same weight and in addition to the s channel amplitudes of direct production the contact interaction ansatz implicitly contains the crossed t and u channel diagrams. The extrapolation to high luminosities assumes an equal share of $e^\pm$ beams.

Other indirect limits on leptoquarks come primarily from low energy data, using information from meson decays and atomic parity violation experiments. The bounds on M_{LQ}/λ derived by different authors differ by factors up to ~ 1.5 in either direction [14], reflecting the model dependent assumptions.

Conclusion Contact interactions provide a powerful tool to search for high mass leptoquark signals, thus complementing direct searches. With a substantial increase in luminosity HERA will be competitive with the results on M_{LQ}/λ of low energy experiments.

References HERA data: H1 Collaboration [10], ZEUS Collaboration [8]

4.4 New Neutral Vector Bosons

New heavy neutral vector bosons Z' appear as extensions of the electroweak $SU(2)_L \times U(1)_Y$ Standard Model. The mass eigenstates Z^0_1, Z^0_2 mix to give the physical masses of Z and Z'

$$Z \;=\; \cos\theta\, Z^0_1 + \sin\theta\, Z^0_2 \,, \tag{18}$$

$$Z' \;=\; -\sin\theta\, Z^0_1 + \cos\theta\, Z^0_2 \,. \tag{19}$$

Popular models include:

- Standard Model couplings Z'_{SM}
  used as a reference for comparing different accelerators
- Left-right symmetric extension of the Standard Model Z_{LR}
  $SU(2)_L \times SU(2)_R \times U(1)_{B-L}$ $(g_L = g_R = g)$
- Gauge models of string inspired grand unifying E_6 theories Z_β
  $SU(2)_L \times U(1)_Y \times U(1)$

$$Z^0_2 \equiv Z_\beta \;=\; \cos\beta\, Z_\chi + \sin\beta\, Z_\psi \,, \tag{20}$$

$$Z_\eta \;=\; \frac{1}{4} Z_\chi + \frac{\sqrt{15}}{4} Z_\psi \,.$$

leptoquark	F	coupling to u quark	coupling to d quark	HERA '95 M_{LQ}/λ	HERA 250 M_{LQ}/λ	HERA 1000 M_{LQ}/λ
S_0^L	2	$\eta^u_{LL} = -\frac{1}{2}\,(\lambda/M_{LQ})^2$			0.93	1.03
S_0^R	2	$\eta^u_{RR} = -\frac{1}{2}\,(\lambda/M_{LQ})^2$			0.85	0.92
$\tilde{S}_0^R$	2		$\eta^d_{RR} = -\frac{1}{2}\,(\lambda/M_{LQ})^2$	0.35	0.71	1.19
$S_{1/2}^L$	0	$\eta^u_{LR} = -\frac{1}{2}\,(\lambda/M_{LQ})^2$			0.62	1.05
$S_{1/2}^R$	0	$\eta^u_{RL} = -\frac{1}{2}\,(\lambda/M_{LQ})^2$	$\eta^d_{RL} = -\frac{1}{2}\,(\lambda/M_{LQ})^2$		0.48	0.87
$\tilde{S}_{1/2}^L$	0		$\eta^d_{LR} = -\frac{1}{2}\,(\lambda/M_{LQ})^2$	0.36	0.73	1.07
S_1^L	2	$\eta^u_{LL} = -\frac{1}{2}\,(\lambda/M_{LQ})^2$	$\eta^d_{LL} = -1\,(\lambda/M_{LQ})^2$	0.34	0.48	0.60
V_0^L	0		$\eta^d_{LL} = +1\,(\lambda/M_{LQ})^2$		0.78	0.83
V_0^R	0		$\eta^d_{RR} = +1\,(\lambda/M_{LQ})^2$		0.55	0.58
$\tilde{V}_0^R$	0	$\eta^u_{RR} = +1\,(\lambda/M_{LQ})^2$		0.76	1.70	2.78
$V_{1/2}^L$	2		$\eta^d_{LR} = +1\,(\lambda/M_{LQ})^2$	0.30	0.41	0.47
$V_{1/2}^R$	2	$\eta^u_{RL} = +1\,(\lambda/M_{LQ})^2$	$\eta^d_{RL} = +1\,(\lambda/M_{LQ})^2$	0.71	1.43	1.83
$\tilde{V}_{1/2}^L$	2	$\eta^u_{LR} = +1\,(\lambda/M_{LQ})^2$		0.80	1.71	2.27
V_1^L	0	$\eta^u_{LL} = +2\,(\lambda/M_{LQ})^2$	$\eta^d_{LL} = +1\,(\lambda/M_{LQ})^2$	1.02	2.34	3.74

Table 11: Accessible lower bounds (95% *cl*) on M_{LQ}/λ [TeV] for first generation leptoquarks from contact interactions

model	HERA 250 M [GeV]	HERA 1000 M [GeV]	$p\bar{p}$ search M [GeV]	electroweak fit M [GeV]
Z'_{SM} (e^-)	460	650	505	779
Z_{LR} (e^-)	260	370	445	389
Z_χ (e^+)	235	340	425	321
Z_ψ $(e^\pm)$	95	135	415	160
Z_η (e^-)	145	200	440	182

Table 12: Lower mass limits (95% *cl*) on additional Z' bosons, indicated is the most sensitive lepton polarity at HERA

Conclusion HERA cannot compete with the direct Z' searches from $\bar{p}p$ collisions.

References

[1] Proceedings *Physics at HERA*, Hamburg (1991), eds. W. Buchmüller and G. Ingelmann, volume 2.

[2] Particle Data Group, Phys. Rev. D54 (1996) 1.

[3] ZEUS Collaboration, paper pa12-011, contribution to ICHEP 96, Warsaw.

[4] H1 Collaboration, T. Ahmed et al., Phys. Lett. B340 (1994) 205; paper pa07-083, contribution to ICHEP 96, Warsaw.

[5] ZEUS Collaboration, M. Derrick et al., Z. Phys. C65 (1995) 627; paper pa11-020, contribution to ICHEP 96, Warsaw.

[6] H1 Collaboration, I. Abt et al., Nucl. Phys. B396 (1993) 3.

[7] H1 Collaboration, S. Aid et al., Phys. Lett. B369 (1996) 173.

[8] ZEUS Collaboration, M. Derrick et al., Phys. Lett. B306 (1993) 173; paper pa11-019, contribution to ICHEP 96, Warsaw.

[9] CDF Collaboration, paper pa13-025, contribution to ICHEP 96, Warsaw.

[10] H1 Collaboration, S. Aid et al., Phys. Lett. B353 (1995) 578.

[11] ZEUS Collaboration, paper pa04-036, contribution to ICHEP 96, Warsaw.

[12] OPAL Collaboration, paper pa13-012, contribution to ICHEP 96, Warsaw.

[13] G. Köpp et al., Z. Phys. C65 (1995) 545.

[14] M. Leurer, Phys. Rev. D49 (1994) 333 and Phys. Rev. D50 (1994) 536; S. Davidson, D. Baily and B.A. Campbell, Z. Phys. C61 (1994) 613.

Leptoquark Pair Production at HERA

Johannes Blümlein[a], Edward Boos[a,b], and Alexander Kryukov[a,b]

[a] DESY-Zeuthen, Platanenallee 6, D-15735 Zeuthen, Germany

[b] Institute of Nuclear Physics, Moscow State University, RU-119899 Moscow, Russia

Abstract: The scalar and vector leptoquark pair production cross sections for deep inelastic ep scattering are calculated. Estimates are presented for the search potential at HERA.

1 Introduction

In many extensions of the Standard Model bosonic states carrying both lepton and quark quantum numbers, so–called leptoquarks, are contained. Leptoquarks may exist in the mass range reached by high energy colliders if their couplings are B and L conserving. A general classification of these states was given in ref. [1] demanding also non–derivative and family diagonal couplings. In most of the scenarios the fermionic leptoquark couplings are not predicted. Moreover, a detailed analysis of low energy data [2] showed that the these leptoquark couplings are small in the mass range up to $O(1\ \mathrm{TeV})$. Thus processes depending on the fermionic couplings can not be used to obtain rigorous mass bounds for these states.

On the other hand, the couplings of the leptoquarks to the electroweak gauge bosons and gluons are determined by the respective gauge symmetries. In the case of scalar leptoquarks the couplings are thus completely predicted. For vector leptoquarks additionally anomalous couplings may contribute. Due to the small fermionic couplings the pair production cross sections depend only on the bosonic couplings and mass limits may be derived directly.

In the present paper a brief account is given on results obtained in refs. [3, 4] and estimates are presented for the search potential in the HERA energy range.

2 The Pair Production Cross Sections

The integral leptoquark pair production cross sections in deep inelastic ep collisions are described by

$$\sigma_{S,V}^{ep,tot} = \sigma_{S,V}^{ep,dir} + \sigma_{S,V}^{ep,res}, \tag{1}$$

containing a direct and a resolved photon contribution which are given by

$$\sigma_{S,V}^{ep,dir} = \int_{y_{min}}^{y_{max}} dy \int_{x_{min}}^{x_{max}} dx \phi_{\gamma/e}(y) G_p(x,\mu^2) \hat{\sigma}_{S,V}^{dir}(\hat{s}, M_\Phi) \theta(\hat{s} - 4M_\Phi^2), \tag{2}$$

and

$$\sigma^{ep,res}_{S,V}(s,M_\Phi) = \int_{y_{min}}^{y_{max}} dy \int_{4M_\Phi^2/Sy}^1 dz \int_{4M_\Phi^2/Syz}^1 dx \phi_{\gamma/e}(y)\theta(\hat{s}-4M_\Phi^2) \times \left\{ \sum_{f=1}^{N_f} \left[q_f^\gamma(z,\mu_1)\overline{q}_f^p(x,\mu_2) + \overline{q}_f^\gamma(z,\mu_1) q_f^p(x,\mu_2) \right] \hat{\sigma}^q_{S,V}(\hat{s},M_\Phi) + G^\gamma(z,\mu_1) G^p(x,\mu_2) \hat{\sigma}^g_{S,V}(\hat{s},M_\Phi) \right\}, \quad (3)$$

respectively. Here $\phi_{\gamma/e}$ denotes the Weizsäcker–Williams distribution and M_Φ is the leptoquark mass. q_f^γ and $G^{p(\gamma)}$ are the quark and gluon distributions in the photon and proton, respectively, $\hat{s} = Sxy$, and μ_1 and μ_2 denote the factorization scales.

The subsystem scattering cross sections $\hat{\sigma}^{q,g}_{S,V}(\hat{s},M_\Phi)$ were calculated in [3] for the direct process and in [4] for the resolved processes, both for scalar and vector leptoquarks. There also the differential scattering cross were derived. In the case of vector leptoquarks the scattering cross sections were calculated accounting both for anomalous photon κ_A, λ_A, and gluon couplings, κ_G, λ_G. These contributions are understood in an effective description being valid in the threshold range, i.e. for $S \sim 4M_\Phi^2$. Due to the anomalous couplings the pair production cross sections for vector leptoquarks obtain as well unitarity violating pieces which however are assumed to never become large. It is hardly possible in general, to provide a correct high energy description in a model-independent way, as intended in the present paper focussing on the threshold range only. This, instead, requests to consider a specific scenario accounting also for the details of the respective pattern of symmetry breaking.

For all details of the calculation we refer to refs. [3] and [4].

3 Numerical Results

In figures 1 and 2 the integrated scattering cross sections for a series of scalar and vector leptoquarks are shown in dependence of the leptoquark mass and charges. For the vector leptoquarks different choices of anomalous couplings are also considered. For simplicity we identified $\kappa_A = \kappa_G$ and $\lambda_A = \lambda_G$. It is interesting to note that not the Yang–Mills type couplings, $\kappa = \lambda = 0$, but the so–called minimal couplings, $\kappa = 1, \lambda = 0$, result in the smallest cross section. In further experimental studies it might be interesting to vary even all the four anomalous couplings independently. As seen in figures 1 and 2 the integral cross sections behave about like

$$\sigma^{S,V}_{tot}(M_\Phi) \sim A \exp(-BM_\phi). \quad (4)$$

This relation can be used to obtain an estimate of the respective search limits which can be reached at a given integrated luminosity, $\mathcal{L}$.

For $\mathcal{L} = 100$ pb^{-1} and $\sqrt{s} = 314$ GeV the search limits for charge $|Q_\Phi| = 5/3$ scalar leptoquarks ranges up to 60 (45) GeV and for vector leptoquarks up to 70 (55) GeV, given a signal sample of 10 (100) events, respectively.

For most of the channels the experiments at LEP 1 have excluded leptoquarks with masses below $M_Z/2$. At present the most stringent mass bound for both scalar [5] and vector leptoquarks[1] decaying into the fermions of the first and second family come from TEVATRON and exclude the range $M_\Phi \lesssim 90$ GeV. For some leptoquark types the range $M_\Phi \lesssim 130$ GeV is excluded [5]. No bounds were yet derived for 3rd generation leptoquarks, e.g. those decaying as $\Phi_{S,V} \to b\,\tau$, etc., in the TEVATRON analyses. Due to the lower background rates, an investigation of particularly this channel may be more suited to ep or e^+e^- collisions than for proton collisions.

[1] Studies considering also anomalous leptoquark couplings were not performed yet.

References

[1] W. Buchmüller, R. Rückl, and D. Wyler, Phys. Lett. **B191** (1987) 442.

[2] M. Leurer, Phys. Rev. Lett. **71** (1993) 1324; Phys. Rev. **D49** (1994) 333; Phys. Rev. **D50** (1994) 536;
S. Davidson, D. Bailey, and B.A. Campbell, Z. Phys. **C61** (1994) 613.

[3] J. Blümlein, E. Boos, and A. Pukhov, Mod. Phys. Lett. **A9** (1994) 3007.

[4] J. Blümlein, E. Boos, and A. Kryukov, DESY 96–174.

[5] F. Abe et al., CDF collaboration, Phys. Rev. **D48** (1993) R3939; Phys. Rev. Lett. **75** (1995) 1012;
S. Abachi et al., D0 collaboration, Phys. Rev. Lett. **72** (1994) 965; **75** (1995) 3618.

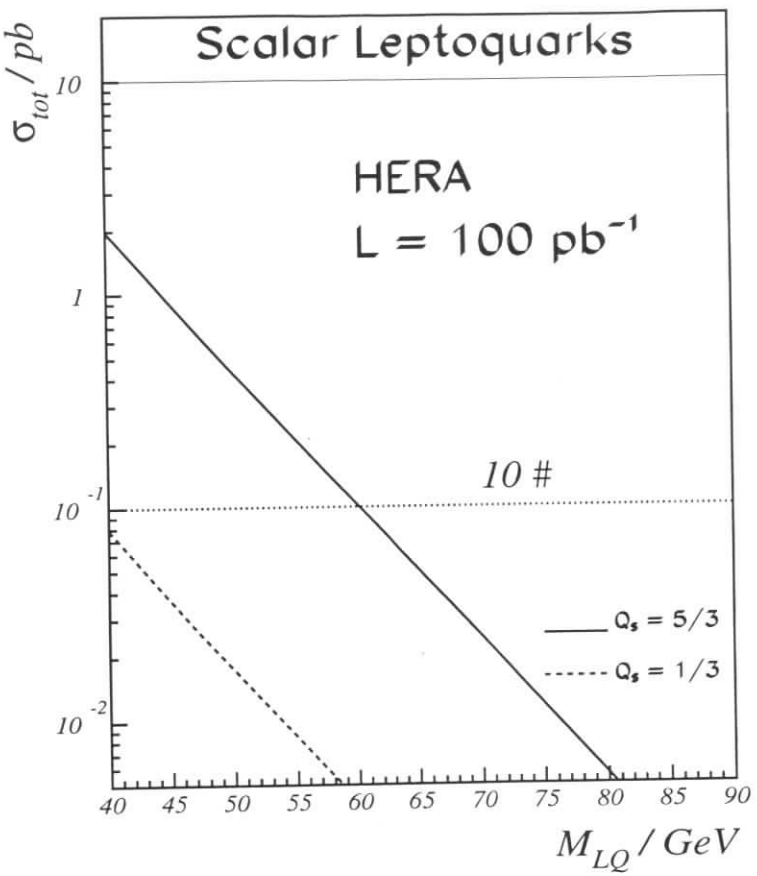

Figure 1: Integrated cross sections for scalar leptoquark pair production at HERA, $\sqrt{S} = 314$ GeV. Full line: σ_{tot} for $|Q_\Phi| = 5/3$; dotted line: σ_{dir} for $|Q_\Phi| = 5/3$; dashed line: σ_{tot} for $|Q_\Phi| = 1/3$; dash–dotted line: σ_{dir} for $|Q_\Phi| = 1/3$.

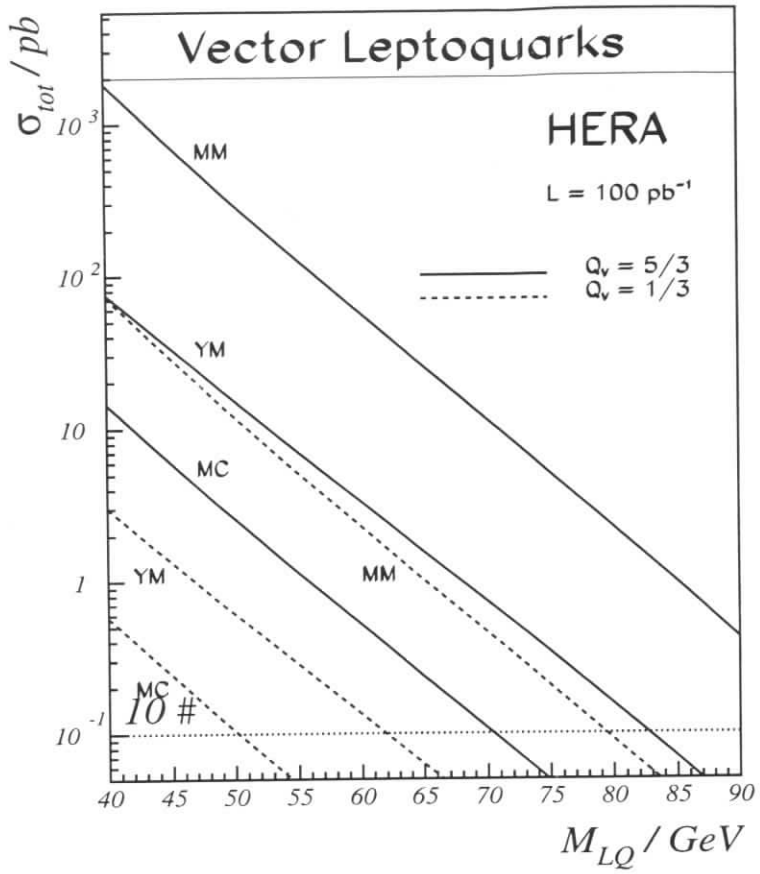

Figure 2: Integrated cross sections $\sigma_{tot} = \sigma_{dir} + \sigma_{res}$ for vector leptoquark pair production at HERA, $\sqrt{S} = 314$ GeV. Upper full line: $|Q_\Phi| = 5/3, \kappa_{A,G} = \lambda_{A,G} = -1$ (MM5); Upper dashed line: $|Q_\Phi| = 5/3, \kappa_{A,G} = \lambda_{A,G} = 0$ (YM5); Upper dotted line: $|Q_\Phi| = 5/3, \kappa_{A,G} = 1, \lambda_{A,G} = 0$ (MC5). The corresponding lower lines are those for $|Q_\Phi = 1/3$.

Working Group on

Heavy Quark Production and Decay

Conveners:

A. Ali (DESY), R. Eichler (ETH Zürich), S. Frixione (ETH Zürich),
U. Karshon (Weizmann), H. Schröder (DESY)

Participants:

G. Abbiendi (Padova), H. Albrecht (DESY), A. Ali (DESY), J. Appel (FNAL), S. Baranov, S. Barsuk (ITEP Moscow), I. Belyaev (ITEP Moscow), P. Ball (CERN), V. Braun (Nordita), S. Brodsky (SLAC), A. Bruni (Bologna), J.M. Butterworth (University College), M. Caccari (DESY), C. Coldewey (Weizmann), N. Coppola (Padova), K. Daum (Wuppertal), M. Danilov (ITEP Moscow) R. Eichler (Zürich), Y. Eisenberg (Weizmann), J.P. Fernández (Madrid), R. Fleischer (Karlsruhe), S. Frixione (ETH Zürich), M. Geerts (Bonn), P. Göttlicher (DESY), C. Grab (Zürich), R. Graciani (Madrid), L. Handoko (Hiroshima), J.M. Hernández (Madrid), G. Hiller (DESY), C. Hilton (Manchester), K. Höpfner (CERN), D. Hoffmann (DESY), V. Hudgson (Birmingham), G. Iacobucci (Bologna), G. Ingelman (DESY), J. Ivarsson (Lund), R. Kagan (ITEP Moscow), U. Karshon (Weizmann), J. Köhne (MPI Munich), M. Krämer (DESY), P. Kreuzer (UCLA), M. Kuze (INS Tokyo), E. Laenen (CERN), L. Lamberti (Torino), M. Lindström (Lund), D. London (Montreal), U. Marconi (Bologna), T. Mannel (Karlsruhe), R. Mahn (DESY/Rostock), S. Mari (DESY-Zeuthen), J. McFall (Oxford), A. Meyer (Hamburg), R. Mizuk (ITEP Moscow), T. Morozumi (Hiroshima), B. Naroska (Hamburg), E. Paul (Bonn), M. Paulini (LBL), D. Pitzl (Zürich), D. Ressing (DESY), R. Rückl (Würzburg), R. Rylko (Brunel), F. Saadi-Lüdemann (DESY), T. Schober (IFH Zeuthen), T. Sloan (Lancaster), G. Schmidt (DESY), H. Schröder (DESY), G. Schuler (CERN), F. Sefkow (DESY), C.H. Shepherd-Themistocleous (DESY), J. Stamm (Bonn), J.P. Sutton (Birmingham), J. Thom (Hamburg), H. Tiecke (Nikhef), K. Tsamariudaki (DESY), G. Tsipolitis (Zürich), M. Vänttinen (Nordita), B. Waugh (Manchester), A. Wegner (MPI Munich), Yu. Zaitsev (ITEP Moscow), A. Zoccoli (Bologna), N. Zotov (Moscow)

Heavy Quark Production and Decay — Working Group Reports:

Introductory remarks

A. Ali[a], R. Eichler[b], S. Frixione[b], U. Karshon[c] H. Schröder[a]

[a] Deutsches Elektronen-Synchrotron DESY, Notkestrasse 85, D-22603 Hamburg, FRG
[b] ETH-Zürich, Hönggerberg, CH-8093 Zürich, Switzerland
[c] Weizmann Inst. of Science, 76100 Rehovot, Israel.

Heavy quark physics is an active part of the current research at HERA. With the projected luminosity of 250 $(pb)^{-1}$, many detailed aspects of charm physics (production and decay) will be studied. The aim of the HERA-B experiment is to measure CP violation in B decays and determine the CKM matrix elements essential for a quantitative test of the standard model. In addition, estimated charm hadron cross section at HERA-B will make it competitive with other concurrent facilities elsewhere. The anticipated high luminosity would allow both HERA-B and HERA(ep) to gain sensitivities in searches for new phenomena, such as mixing, CP violation and rare decays in the charm sector, which go significantly beyond those of the existing experiments. In addition, an increase in the proton beam energy will greatly help the B-physics programme of HERA-B.

The work done in the Heavy Quark Physics working group divided itself naturally into two distinct parts, namely production and decays of heavy quarks. Consequently, we summarize these parts separately in two summaries. These summaries and overview, together with the individual contributions, are listed below. In addition, a large number of invited talks was given during the workshop. They are discussed in the summaries. We would like to thank all the participants, in particular the speakers, who contributed to the proceedings.

- Heavy Flavour Production
  R. Eichler (ETH Zürich), S. Frixione (ETH Zürich)
- Heavy Flavour Decays - Introduction and Summary
  A. Ali (DESY), H. Schröder (DESY)
- Rare D Meson Decays at HERA
  C. Grab (ETH Zürich)
- $D^0 - \overline{D}^0$ mixing at the ep-collider HERA
  G. Tsipolitis (ETH Zürich)
- Deep-inelastic Production of Heavy Quarks
  E. Laenen (CERN) et. al.
- High p_T Charm Photoproduction
  G. Abbiendi (DESY), J.M. Butterworth (Imperial College), R. Graciani (Madrid)
- Prospects for heavy flavour photoproduction at HERA
  S. Frixione (ETH Zürich)

- Future Perspectives of Quarkonium Physics at HERA
  M. Cacciari (DESY), M.Krämer (DESY)
- CP Violation and Flavour Mixing in the Standard Model - 1996 Update
  A. Ali (DESY), D. London(Montreal)
- Rare B decays in the Standard Model
  A. Ali (DESY)
- The partial reconstruction of $B^0 \to \chi_{c1} K_S^0$, $B^0 \to \psi' K_S^0$ and $B^0 \to J/\psi K^{*0}$
  R. Misuk (ITEP Moscow)
- Pion tag of B meson flavour at HERA-B
  C.H.Shepherd-Themistocleous (DESY)
- Low p_t lepton tag at the HERA-B experiment
  R. Misuk (ITEP Moscow)
- Trigger for Radiative B Decays at the HERA-B experiment
  F. Saadi-Lüdemann (DESY)
- Accuracy of $B^0 - \overline{B}^0$ mixing and B^0 lifetime measurements at HERA-B
  P. Kreuzer (UCLA)
- On the Study of $B\overline{B}$ Correlations at HERA-B
  R. Rylko (Brunel)

Heavy Flavour Production

R. Eichler, S. Frixione

ETH-Zürich, CH 8093 Zürich, Switzerland

Abstract: We discuss the impact of the planned upgrades of the HERA collider on the study of open heavy flavour and quarkonium production. New experimental techniques in charm physics are presented.

1 Introduction

The *ep* collider HERA offers new opportunities to study the production mechanism of heavy quarks and to test the predictions of the underlying theory. In the following, we will deal with the processes

$$e + p \longrightarrow Q + \overline{Q} + X, \quad (1)$$
$$\gamma + p \longrightarrow Q + \overline{Q} + X, \quad (2)$$
$$\gamma + p \longrightarrow \left(Q\overline{Q}\right) + X, \quad (3)$$

where $\left(Q\overline{Q}\right)$ indicates a generic heavy quarkonium state, like J/ψ. The dominant contribution to the $Q\overline{Q}$ cross section is due to those events in which the virtuality of the photon exchanged between the electron and the proton is very small. In this case, the electron can be considered to be equivalent to a beam of on-shell photons, whose distribution in energy (Weizsäcker-Williams function [1]) can be calculated in QED. The underlying production mechanism is therefore a photoproduction one (eqs. (2) and (3)), which has been studied extensively in fixed-target experiments. At HERA, the available center-of-mass energy is about one order of magnitude larger than at fixed-target facilities; this energy regime is totally unexplored in photoproduction, and several new features have to be taken into proper account. In particular, the large contribution of the resolved photon component introduces in the theoretical predictions a source of uncertainty which is totally negligible at fixed-target energies.

A complementary way of studying heavy flavour production at HERA is to retain only those events characterized by a large photon virtuality (eq. (1)). Although the total rates are much smaller than the photoproduction ones, the resolved component is completely eliminated and more reliable theoretical and experimental results can be obtained. Also, the dependence of the data upon the photon virtuality can be used as a further test of QCD predictions.

2 Theoretical summary

Fully exclusive, next-to-leading order perturbative QCD calculations [2, 3, 4] are now available for the processes of eqs. (1) and (2). In the framework of the factorization theorem of ref. [5], a next-to-leading order calculation for the direct color-singlet photoproduction of quarkonium has been presented in ref. [6]. Other contributions to the production of quarkonium, like the resolved photoproduction and the direct color-octet photoproduction, which are potentially

relevant in kinematical regions accessible at HERA, have been considered at the leading order in ref. [7].

In spite of these substantial progresses in understanding the production mechanism, the (fixed-order perturbative) results may become unreliable in certain kinematical regions, due to the appearance of potentially large logarithms which spoil the convergence of the perturbative expansion. In this case, a resummation to all orders of these large logarithms has to be performed.

When the available center-of-mass energy $\sqrt{S}$ gets large, the effective expansion parameter of the perturbative series becomes $\alpha_s \log(S/m_Q^2)$. The problem of resumming these terms (*small-x effects*) has been tackled by several authors [8], mainly in the context of b production in hadronic collisions. Specific studies for HERA [9] lead to the conclusion that the total photoproduction rates can be increased by the resummation of the $\log(S/m_Q^2)$ terms by a factor smaller than or equal to 40% (45%) with respect to the next-to-leading order prediction for the direct (resolved) contribution in charm production. In the case of bottom, the effect is much milder, being always smaller than 10%.

The transverse momentum distribution is in principle affected by the presence of $\log(p_T/m_Q)$ terms. These logarithms can be resummed by observing that, at high p_T, the heavy-quark mass is negligible, and by using perturbative fragmentation functions [10]. Remarkably enough, the fixed-order and the resummed results agree in a very wide range in p_T for charm production (in the HERA energy range, the contribution of the resummation of this kind of logarithms is expected to be negligible for bottom production); the effect of the resummation might be visible only for p_T larger than 50 GeV.

Finally, multiple soft gluon emission makes the perturbative expansion unreliable close to the threshold or to the borders of the phase space, like for example the regions $p_T^{Q\bar{Q}} \simeq 0$ and $\Delta\phi^{Q\bar{Q}} \simeq \pi$. This problem has not been directly dealt with during the workshop, but a lot of theoretical work has recently been performed [11]. The resummation of soft gluons would be of great help in order to have a reliable prediction for J/ψ production at $p_T \simeq 0$; also, threshold effects are important for b production at HERA-B.

2.1 Quarkonium Photoproduction

Quarkonium photoproduction has been dealt with in ref. [12]. The benchmark process is in this case the production of J/ψ. With suitable cuts, typically $p_T > 1$ GeV and $z < 0.9$, where

$$z = \frac{k(p) \cdot k(J/\psi)}{k(p) \cdot k(\gamma)}, \quad (4)$$

the dominant contribution to the cross section is due to the direct color-singlet production of J/ψ; this cross section has been calculated at next-to-leading order in QCD [6]. The radiative corrections turn out to be sizeable in the HERA energy range, being of the same order of the leading-order contribution. The total rate is of the order of tens of nb, and a first comparison with data [13] has already been performed. Although there is a good agreement as far as the shape of (z and p_T) distributions is concerned, the theoretical predictions appear to slightly undershoot the data for the total cross section; this can be adjusted by properly tuning the input parameters of the calculation, since the normalization is affected by large uncertainties.

With a larger integrated luminosity, a more significant comparison will be possible, eventually helping in constraining the input parameters.

The luminosity upgrade is mandatory in order to assess the importance of the J/ψ production mechanisms neglected so far, namely the direct color-octet contribution and the resolved contribution. The former has been considered in refs. [7, 12] at the leading order in QCD. It has to be stressed that this contribution can not be calculated from first principles, and relies upon fits to Tevatron data on color-octet J/ψ production. The comparison with HERA data can therefore be regarded as a test of the underlying factorization picture [5]. Using the result of ref. [7], the color-octet contribution appears to be dominant over the color-singlet one in the large-z region; the first HERA data do not support this behaviour. Nevertheless, since both the data and the theoretical calculations need some refinement, no definite conclusion can be drawn at present. The resolved J/ψ production is expected to be dominant at very low-z values, being enhanced by the color-octet terms. Since the total rate is $\mathcal{O}(1\ nb)$ in that region, large integrated luminosity is needed to study this problem.

To further investigate the interplay between color-singlet and color-octet contributions, other possibilities were taken into account in ref. [12]. For example, the photoproduction cross section of χ should be dominated by color-octet terms; the total rate is however suppressed by two orders of magnitude with respect to the one of J/ψ, and therefore large luminosity is required. The $J/\psi+\gamma$ production has a very distinctive signature to color-octet contribution in the large-z region [14], but the cross section is very small ($\mathcal{O}(10\ pb)$). Finally, large luminosity is necessary also in order to investigate J/ψ production for $p_T > 10$ GeV, where the dominant contribution is expected to be due to charm fragmentation (the total rate is at most $\mathcal{O}(1\ pb)$).

2.2 Open Heavy Flavour Production

Several aspects of the deep-inelastic production of heavy flavours at HERA have been studied during the workshop. The work of ref. [15] basically falls into three parts. To begin with, the authors present a study of the heavy quark inclusive structure function $F_2(x, Q^2, m^2)$, its sensitivity to the input parameters of the calculation, and the size of the QCD corrections. The full next-to-leading order theoretical prediction [3, 4] suffers from a fairly little uncertainty, and the radiative corrections are not too large. The structure function is on the other hand significantly sensitive to the small-x behaviour of the gluon density in the proton. Therefore, it is concluded that F_2 in charm production is an excellent probe to infer the gluon density in the proton at small x.

Next, the exclusive properties of the final state are investigated, since they allow a deeper understanding of the dynamics of the production process with respect to the inclusive structure function. The next-to-leading order corrections to F_k, $k = 2, L$, in a fully differential form have been recently calculated [4] using the subtraction method. The results were incorporated in a Monte-Carlo style program which allows one to study correlations in the laboratory frame. The authors of ref. [15] present some single-inclusive distributions and compare them with preliminary ZEUS data [16]. In general, the data follow the shape of the theoretical curves, but lie above them. This behaviour is consistent with the recent analysis by H1 [17] that, using a single-inclusive quantity, showed that the charm production mechanism is boson-gluon fusion, and not a consequence of charm quarks in the sea. Correlations between charm and anticharm are also presented. Clearly, all these issues will be further clarified as soon as data with better statistics will be available; a large integrated luminosity is highly desirable.

Finally, the authors of ref. [15] deal with the fact that, at truly large Q^2, a charm quark should be described as a light quark, i.e. as a constituent parton of the proton, whereas at Q^2 of order of m^2 it can only be produced through boson-gluon fusion (see ref. [18] for a detailed discussion). It is shown that, surprisingly, already at Q^2 of order 20-30 GeV^2, the asymptotic next-to-leading order formula (large Q^2) for the inclusive structure function differs from the exact result for a factor of 5% or less, indicating that at these not so large Q^2 values the charm quark behaves already very much like a parton. Since, as mentioned before, the boson-gluon fusion almost correctly accounts for experimental results on single-inclusive distributions, this points out that the scale at which the charm quark can be regarded as a parton actually depends upon the physical observables considered.

Open heavy flavour photoproduction has been considered in ref. [19]. With an integrated luminosity of 1000 pb^{-1}, next-to-leading order QCD predicts about 10^9 (10^6) charm (bottom) particles produced in ep collisions (Weizsäcker-Williams approximation). Therefore, taking into account the experimental efficiencies, the number of reconstructed particles will be comparable to or larger than the one obtainable by the fixed-target hadroproduction experiments of the new generation at Fermilab. This will provide the HERA experiments with the possibility of performing studies of charm and bottom physics at an excellent level of accuracy. In this respect, it is extremely interesting to compare the results at HERA with the results of fixed-target photoproduction experiments, which have a center-of-mass energy of about one order of magnitude smaller. In charm physics, high luminosity will allow to consider exclusive quantities, like correlations, which constitute the most stringent test for the underlying theoretical picture. One may also adopt a different point of view, namely to look at charm production as a useful tool to constrain the input parameters entering the calculations, like for example the quark mass. To this end, it is mandatory to have data with large statistics. The capability of HERA of producing bottom quarks is also very promising. In particular, the comparison of the QCD prediction for the p_T spectrum of bottom (which has been shown in ref. [20] to be only marginally affected by the uncertainties on the input parameters of the calculation) with the data could be of great help in understanding the origin of the discrepancy observed at the Tevatron for the same quantity.

2.3 Production at HERA-B

The study of the production mechanism of heavy flavours at HERA-B might prove to be extremely useful. The data on bottom production at fixed target have low statistics, and have been mainly obtained in πN collisions (only very recently, the first measurement of the total $b\bar{b}$ rate in pN collisions has been presented). A study of distributions would be interesting in order to test the QCD description of bottom quark production at low center-of-mass energies. In charm physics, the results of fixed-target experiments at CERN and Fermilab still leave plenty of open questions (see ref. [21] and references therein). In particular, new measurements may help in understanding the importance and the nature of non-perturbative contributions to charm cross section. The hypothesis of the intrinsic charm in the proton could be tested as well.

2.4 Determination of the Gluon Density in the Proton using Charm Data

The possibility has been considered of using charm data to constrain (or to measure) the gluon density in the proton, both in the unpolarized and the polarized case. Photoproduction of charm is in principle an ideal tool in order to perform this measurement, since the gluon density enters the cross section already at the leading order, and in a simpler way with respect to hadroproduction processes. It has been shown in ref. [22] that the use of correlations between the charm and the anticharm can give a direct measure of the unpolarized gluon density in the proton in a fairly large range in x ($10^{-3} \div 10^{-1}$), since the contribution of the resolved component can be suitably suppressed. Being necessary to reconstruct both the charm and the anticharm for this kind of measurements, a very large integrated luminosity is required. The measurement of the polarized gluon density in the proton has been considered in refs. [23, 24] (see also ref. [25]), in view of the possibility for HERA to operate in the polarized mode. The conclusion has been reached [23] that charm photoproduction data can be used to constrain this quantity, if an integrated luminosity of at least 100 pb^{-1} will be achieved.

2.5 Intrinsic Charm

The possibility of detecting signals due to intrinsic charm in the proton has been discussed during the workshop by G. Ingelman. An intrinsic charm contribution has been suggested long time ago [26] to explain an excess of data from fixed-target experiments with respect to theoretical predictions in the large-x_F region. Recently, this problem has been tackled in ref. [27], dealing directly with ep collisions at HERA. It turns out that the intrinsic charm contribution is non-negligible only in the very forward region, and can not be detected with the present experimental configuration; an upgrade in the very forward region would be necessary.

3 Heavy Quark Production Cross Sections and Reconstruction Efficiencies

In this section we give measured cross sections and expected reconstruction efficiencies for charmed mesons. As an example the capabilities of the H1 detector [28] are given. The effect of a double layer silicon vertex detector [29] is investigated.

The charm production cross section has been measured by both collaborations H1 and ZEUS [30, 31] and is close to one microbarn. The value for photoproduction ($Q^2 < 0.01$ GeV^2) amounts to [30]

$$\sigma(ep \to c\bar{c}X) = 941 \pm 160^{+142}_{-120}\ nb.$$

The first error is the statistical and the second the systematic error dominated by the extrapolation uncertainty to the unmeasured phase space. This rather large cross section makes HERA an ideal place for charm physics.

The b cross section has not been measured yet. An estimate [32] $\sigma(ep \to b\bar{b}X) = 6 \pm 2\ nb$ is of similar magnitude as on the Z^0- or the Υ-resonance and much lower than at hadron colliders.

The reconstruction of charm uses the central tracking chambers with an angular coverage of $-1.5 < \eta < 1.5$. The decay chain

$$ep \to D^* X \to D^0 \pi_s \to (K^-\pi^+)\pi_s$$

yields a signal to background ratio of 1:1 for the mass difference $\Delta M = M(K^-\pi^+\pi^+) - M(K^-\pi^+)$ with a cut on the transverse momentum of $p_T(D^*) > 2.5\ GeV$. A total efficiency in photoproduction of trigger, acceptance, branching fraction, and reconstruction of charmed events via D^*-tagging of 10^{-4} has been achieved (table 1). This is only a tiny fraction of the total cross section. The yield can be enlarged by summing other decay channels of the D meson. A similar signal to background ratio can be achieved with the reconstruction of

$$D^0 \to K^-\pi^+\ (3.83\%),\ K^0\pi^+\pi^-\ (5.4\%),\ K^-\pi^+\pi^+\pi^-\ (7.5\%),\ K^-\mu^+\nu\ (3.23\%).$$

This is an improvement of a factor of 5 over the single $K^-\pi^+$ channel.

Besides the branching fractions into a specific decay channel the biggest event loss (order of magnitude) comes from the transverse momentum cut of the D^* which is necessary to reduce the combinatorial background. This can be partially compensated with the help of a vertex detector.

3.1 Charm Reconstruction with the H1 Vertex Detector

The main effect of a vertex detector is the assignment of charged particle tracks to a secondary vertex which results in a much improved signal to background ratio S/N, but with a corresponding loss of acceptance.

This can be seen in figure 1a (from ref. [33]), where this ratio S/N is plotted versus the separation d/σ of primary and secondary vertex, with d the distance and σ its error. No lower momentum cut for the D^* was applied. The track finding efficiency of the slow pion in the $D^* \to D^0\pi_s$ decay is non zero only above $p_T(\pi_s)$=120 MeV which implies an indirect transverse momentum cutoff for the D^* meson of about 1 GeV.

The signal to background grows rapidly with the vertex separation and reaches values above one for $d/\sigma > 2-2.5$. At the same time we observe a loss of the signal by a factor two compared to no vertex cut (see figure 1b). Therefore the net gain is not very large.

But with the vertex cut even more decay channels are reconstructable. The D^0 mesons can be found directly without the detour via the D^*. This gains a factor of more than two. Also the D^+ decays into $K^-\pi^+\pi^+$(9.1%), $K^0\pi^+\pi^+\pi^-$ (7%), and $K^0\pi^+$ (2.8%) will be possible. Therefore the net gain with a vertex detector to fully reconstruct charmed final states is a factor 5-10.

A vertex detector is also useful for tagging charm by looking for secondary vertices inside jets. A study [34] has been performed where two or more jets with $E_T^{jet} \geq 6\ GeV$, $|\eta^{jet}| < 2$, Q^2 <4 GeV^2, and 135 GeV < $W_{\gamma p}$ < 270 GeV were selected. The efficiency using very loose cuts (at least one track with an impact parameter displaced by d/σ >2) is 37% for charm and 17% for bottom with S/N=0.9 and also here the gain from a vertex detector is significant (order of magnitude).

Tables 1 and 2 summarize the efficiencies. For an integrated luminosity of 300 pb^{-1} we expect therefore of order 10^6 fully reconstructed D^0 and $D^\pm$ mesons with a S/N$\geq$1.

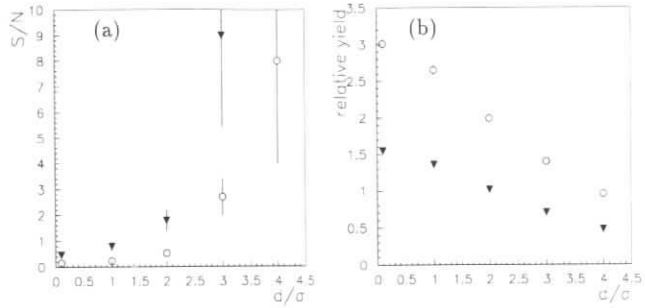

Figure 1: *a): Signal to background ratio S/N of the D^* signal versus the vertex separation d normalized to its error σ for a transverse momentum cutoff of 1 GeV (open circles) and 2 GeV (closed triangles) of the D^*. (b): Yield of the D^* signal with $p_T(D^*) > 1$ GeV (open circles) and > 2 GeV (closed triangles) respectively relative to a momentum cutoff of $p_T(D^*) > 2.5$ GeV.*

3.2 Charm-Anticharm Correlations

For many applications and QCD studies the two-particle inclusive distribution is of interest. We investigated the probability to fully reconstruct two charmed particles in H1.

The acceptance that both charm quarks fall inside the acceptance of the tracking system ($|\eta| < 1.5$, $p_T > 1$ GeV) is 3%. Using all the above decay channels and a vertex detector we can reach a double tagging efficiency of order 2.5×10^{-5}, which translates into 7000 charm pairs for 300 pb^{-1}. Without a vertex detector this number will be an order of magnitude less.

If we do not require the full reconstruction of both charmed mesons, but ask only for one reconstructed D meson plus a lepton of momentum $p_T > 1.5$ GeV which does not come from the primary vertex, we reach similar efficiencies as above, therefore doubling the number of double charm tags. Relaxing the quality of the double tagged events even more one would ask for one fully reconstructed charmed meson and a well separated jet. Efficiencies depend very much on chosen cuts and no numbers are given here.

4 Summary and Comparison with other Machines

At HERA, a rich physics program can be achieved with an integrated luminosity $\mathcal{L} = 300$ pb^{-1}. The inclusive properties of open charm photo- and electroproduction can be studied at an excellent level of accuracy. The next-to-leading order QCD predictions for the direct color-singlet photoproduction of J/ψ can be thoroughly tested. Correlations between charm and anticharm, open bottom production, resolved and direct color-octet quarkonium photoproduction could be studied with $\mathcal{L} = 300$ pb^{-1} as well, although larger luminosity would allow a more significant

no vertex detector	acceptance $p_T > 2.5$ GeV	reconstr. efficiency	$c \to D^* \to D^0\pi$	D^0 decay mode	total efficiency
$D^0 \to K^-\pi^+$	0.03	0.5	0.18	0.038	$1\ 10^{-4}$
$D^0 \to K^-\pi^+\pi^+\pi^-$				0.075	
$D^0 \to K^-\mu^+\nu$				0.032	
$D^0 \to K^0\pi^+\pi^- \to 4\pi$				0.019	
sum (D^0)	0.03	0.5	0.18	0.164	$4\ 10^{-4}$
with vertex detector	acceptance $p_T > 1.0$ GeV $d/\sigma > 2.3$	reconstr. efficiency	$c \to D^0/D^+$	D^0/D^+ decay mode	total efficiency
$D^0 \to K^-\pi^+$	0.05	0.3	0.55	0.038	$3\ 10^{-4}$
$D^0 \to K^-\pi^+\pi^+\pi^-$				0.075	
$D^0 \to K^-\mu^+\nu$				0.032	
$D^0 \to K^0\pi^+\pi^- \to 4\pi$				0.019	
sum (D^0)	0.05	0.3	0.55	0.164	$1\ 10^{-3}$
$D^+ \to K^0\pi^+ \to 3\pi$	0.05	0.3	0.21	0.019	$6\ 10^{-5}$
$D^+ \to K^-\pi^+\pi^+$				0.091	
$D^+ \to K^0\pi^+\pi^+\pi^- \to 5\pi$				0.024	
sum ($D^\pm$)	0.05	0.3	0.21	0.134	$4\ 10^{-4}$
sum (all D-mesons)					$2\ 10^{-3}$

Table 1: *Summary of various reconstruction efficiencies for D^0 mesons in photoproduction with and without a vertex detector. Charged particles have been confined to $|\eta| < 1.5$, and a vertex separation of $d/\sigma > 2.3$ has been assumed for the lower example with a vertex detector. Acceptance and reconstruction efficiencies depend on details of cuts and only rough numbers using cuts similar to ref. [30] are given.*

tagging method	charm-tagging	bottom-tagging
D^*-meson	0.014	0.09
identified muon	0.073	0.20
non-vertex track, $d/\sigma > 3$	0.10	0.33
non-vertex track, $d/\sigma > 2$	0.37	0.17

Table 2: *Summary of charm and bottom tagging efficiency inside jets with $E_T^{jet} \geq 6$ GeV, $|\eta^{jet}| < 2$, $Q^2 < 4$ GeV^2, and 135 GeV $< W_{\gamma p} <$ 270 GeV. Non-vertex track means a track with an impact parameter d larger than 2 resp. 3 times its error σ (from ref. [34]).*

comparison between theory and experiments. Charm correlations can be exploited in order to measure the gluon density in the proton. In polarized ep collisions, charm data are useful to constrain the *polarized* gluon density in the proton. Very large luminosity is mandatory in order to study the production of χ, $J/\psi + \gamma$ and to investigate the charm fragmentation into J/ψ. Intrinsic charm signals are not detectable without upgrading the detectors in the very forward region. A vertex detector is essential to reach a high tagging efficiency for open charm and should be taken into account in the design of the luminosity upgrade program.

A figure of merit of the potential for charm physics is the total number of reconstructed open charmed particles. The biggest competition comes from fixed target experiments at Fermilab. A program to reach 10^6 reconstructed open charm is in place which corresponds to 300 pb^{-1} at HERA. Progress beyond 10^6 will depend on commitment to the physics and a potential to get 10^8 at Fermilab is enticing [35].

Acknowledgements: One of the authors (S.F.) wishes to thank the Swiss National Foundation for financial support.

References

[1] C. F. Weizsäcker, *Z. Phys.* **88**(1934)612;
E. J. Williams, *Phys. Rev.* **45**(1934)729.

[2] R. K. Ellis and P. Nason, *Nucl. Phys.* **B312**(1989)551;
J. Smith and W. L. van Neerven, *Nucl. Phys.* **B374**(1992)36;
S. Frixione, M. Mangano, P. Nason and G. Ridolfi, *Nucl. Phys.* **B412**(1994)225;
P. Nason, S. Dawson and R. K. Ellis, *Nucl. Phys.* **B303**(1988)607; **B327**(1988)49;
W. Beenakker et al., *Phys. Rev.* **D40**(1989)54; *Nucl. Phys.* **B351**(1991)507;
M. Mangano, P. Nason and G. Ridolfi, *Nucl. Phys.* **B373**(1992)295.

[3] E. Laenen, S. Riemersma, J. Smith and W. L. van Neerven, *Nucl. Phys.* **B392**(1993)162; *Phys. Lett.* **B291**(1992)325.

[4] B. W. Harris and J. Smith, *Nucl. Phys.* **B452**(1995)109; *Phys. Lett.* **B353**(1995)535.

[5] G. T. Bodwin, E. Braaten and G. P. Lepage, *Phys. Rev.* **D51**(1995)1125.

[6] M. Krämer, J. Zunft, J. Steegborn and P.M. Zerwas, *Phys. Lett.* **B348**(1995)657;
M. Krämer, *Nucl. Phys.* **B459**(1996)3.

[7] M. Cacciari and M. Krämer, *Phys. Rev. Lett.* **76**(1996)4128;
J. Amundson, S. Fleming and I. Maksymyk, UTTG-10-95, hep-ph/9601298;
P. Ko, J. Lee and H. S. Song, SNUTP-95-116, hep-ph/9602223.

[8] R. K. Ellis and D. A. Ross, *Nucl. Phys.* **B345**(1990)79;
S. Catani and L. Trentadue, *Nucl. Phys.* **B327**(1989)323;
S. Catani, M. Ciafaloni and F. Hautmann, *Phys. Lett.* **B242**(1990)97;
J. C. Collins and R. K. Ellis, *Nucl. Phys.* **B360**(1991)3.

[9] S. Catani, M. Ciafaloni and F. Hautmann, in *Proceedings of the Workshop: "Physics at HERA"*, eds. W. Buchmüller and G. Ingelman, DESY, Hamburg, 1992;
S. Frixione, M. Mangano, P. Nason and G. Ridolfi, *Phys. Lett.* **B348**(1995)633;
V. A. Saleev, N. P. Zotov, hep-ph/9505279 (May 1995).

[10] M. Cacciari and M. Greco, *Z. Phys.* **C69**(1996)459.

[11] E. Laenen, J. Smith and W. L. van Neerven, *Nucl. Phys.* **B369**(1992)543; *Phys. Lett.* **B321**(1994)254;
E. L. Berger and H. Contopanagos, *Phys. Lett.* **B361**(1995)115;
Phys. Rev. **D54**(1996)3085;
S. Catani, M. Mangano, P. Nason and L. Trentadue, CERN-TH/96-86, hep-ph/9604351;
N. Kidonakis and G. Sterman, ITP-SB-96-7, hep-ph/9604234;
E. L. Berger and R. Meng, *Phys. Rev.* **D49**(1994)3248.

[12] M. Cacciari and M. Krämer, these proceedings.

[13] S. Aid et al., H1 Coll., *Nucl. Phys.* **B472**(1996)3;
ZEUS Coll., pa-02-47, *XXVIII Int. Conf. on HEP*, Warsaw (1996).

[14] M. Cacciari, M. Greco and M. Krämer, DESY-96-147, in preparation.

[15] E. Laenen et al., these proceedings.

[16] ZEUS Coll., *XXVIII Int. Conf. on HEP*, Warsaw (1996).

[17] C. Adloff et al., H1 Coll., DESY-96-138, hep-ex/9607012, to appear in *Z. Phys.* C.

[18] S. Riemersma and F. I. Olness, *Phys. Rev.* **D51**(1995)4746;
M. A. G. Aivazis et al., *Phys. Rev.* **D50**(1995)3085; *Phys. Rev.* **D50**(1995)3102;
M. Buza et al., *Nucl. Phys.* **B472**(1996)611.

[19] S. Frixione, these proceedings.

[20] S. Frixione, P. Nason and G. Ridolfi, *Nucl. Phys.* **454**(1995)3.

[21] S. Frixione, M. Mangano, P. Nason and G. Ridolfi, *Nucl. Phys.* **B431**(1994)453.

[22] S. Frixione, M. Mangano, P. Nason and G. Ridolfi, *Phys. Lett.* **B308**(1993)137.

[23] S. Frixione and G. Ridolfi, hep-ph/9605209, to appear in *Phys. Lett.* **B**.

[24] M. Stratmann and W. Vogelsang, DO-TH-96/10, RAL-TR-96-033, hep-ph/9605330.

[25] M. Glück and E. Reya, *Z. Phys.* **C39**(1988)569;
M. Glück, E. Reya and W. Vogelsang, *Nucl. Phys.* **B351**(1991)579;
W. Vogelsang, in *Proceedings of the Workshop: "Physics at HERA"*, eds. W. Buchmüller and G. Ingelman, DESY, Hamburg, 1992.

[26] B. L. Combridge, *Nucl. Phys.* **B151**(1979)429;
S. J. Brodsky et al., *Phys. Lett.* **B93**(1980)451.

[27] G. Ingelman and M. Thunman, TSL/ISV-96-0137, hep-ph/9604289.

[28] S. Aid et al., H1 Coll., DESY 96-01, accepted by *Nucl. Instr. & Meth.* (1996).

[29] W. Erdmann et al., *Nucl. Instr. & Meth.* **A372**(1996)188.

[30] S. Aid et al., H1 Coll., *Nucl. Phys.* **B472**(1996)32.

[31] M. Derrick et al., ZEUS Coll., *Phys. Lett.* **B349**(1995)225.

[32] R. Eichler and Z. Kunszt, *Nucl. Phys.* **B308**(1988)791;
S. Frixione, M. Mangano, P. Nason and G. Ridolfi, *Phys. Lett.* **B348**(1995)633.

[33] S. Prell, Dissertation (1996), DESY FH1-96-02.

[34] G. Abbiendi, J.M. Butterworth and R. Graciani, these proceedings.

[35] J. A. Appel, contribution to this workshop.

Heavy Flavour Decays - Introduction and Summary

A. Ali[a] and H.Schröder[a]

[a] Deutsches Elektronen-Synchrotron DESY, Notkestrasse 85, D-22603 Hamburg, FRG

Abstract: We review some selected topics in the decays of heavy flavours, beauty and charm, which are of principal interest at HERA-B and HERA. The topics in B physics include: an update on the quark mixing matrix and CP violating phases, issues bearing on an improved resolution on the CP-violating phase $\Delta(\sin 2\beta)$, prospects of measuring radiative and semileptonic rare B decays, the B_s^0 - $\overline{B_s^0}$ mixing ratio x_s, improved measurements of the B_d^0 - $\overline{B_d^0}$ mixing ratio x_d and the B-hadron lifetimes, in particular $\tau(\Lambda_b)$. In the charm sector, we have focussed on rare decays and D^0- $\overline{D^0}$ mixing, whose measurements will signal physics beyond the standard model.

1 Introduction

The origin of CP violation, even 32 years after its discovery by Christenson et al. in neutral K decays [1], remains a puzzle. So far the ratio ϵ_K is the only precisely determined CP violating quantity in particle physics [2]. In the standard model (SM), the couplings of the charged vector bosons $W^{\pm}$ with the quark-antiquark pairs are complex, which for three generations lead to a complex phase in the quark mixing matrix - the Cabibbo-Kobayashi-Maskawa (CKM) matrix [3]. The quantity ϵ_K in the SM measures essentially this complex phase. However, this hypothesis remains to be tested by independent measurements of other CP-violating quantities. In neutral B-meson decays, the angles in the CKM-unitarity triangle shown in Fig. 1 are characteristic measures of CP violation, as the CP violating asymmetries in the decay rates of a B-hadron into specific modes and their CP-conjugates can be related to these angles. The primary aim of the HERA-B experiment is to measure the CP-violating asymmetry in B decays related to the phase $\sin(2\beta)$.

A related and equally important goal of the HERA-B physics programme is to quantitatively test the unitarity of the CKM matrix, in which apart from the improved measurements of the matrix elements $|V_{cb}|$ and $|V_{ub}|$, the matrix element $|V_{td}|$ plays a central role (see Fig. 1). This matrix element can, in principle, be determined in a number of B and K decays [4, 5]. At HERA-B, this would require either measuring the mass difference between the two eigenstates of the B_s^0-$\overline{B_s^0}$ system, ΔM_s, (equivalently the ratio of the mass difference to the averaged decay width $x_s = \Delta M_s/\Gamma_s$), which can then be compared with the already well-measured quantity

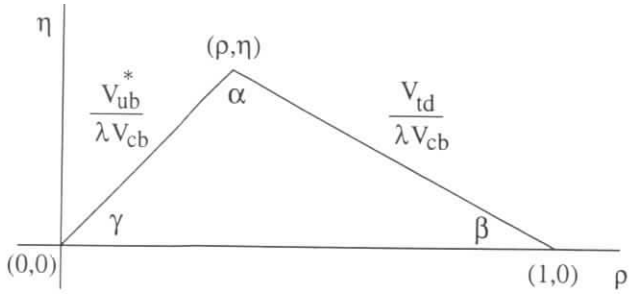

Figure 1: The unitarity triangle. The angles α, β and γ can be measured via CP violation in the B system.

ΔM_d [6] to extract the ratio $|V_{td}|/|V_{ts}|$, or the branching ratios of at least one of the CKM-suppressed rare decays, such as $B^0 \to \rho^0 + \gamma$, which would yield $|V_{td}|/|V_{cb}|$. These measurements are also very challenging; apart from efficient triggers and good vertex resolution, both high luminosity and higher proton beam energy will be big assets here. The unitarity of the CKM matrix will, of course, be very precisely tested by the measurements of all three angles in the unitarity triangle shown in Fig. 1. This, however, is an ambitious programme, which may or may not materialize in three years of HERA-B running and may require a post-HERA-B facility such as the LHC. Hence, in this workshop, we have concentrated on $\sin(2\beta)$, x_s, and rare B decays.

Concerning charm physics at HERA and HERA-B, which will undoubtedly contribute to our understanding of the dynamics of heavy flavour production in QCD (reviewed here by Eichler and Frixione [7]), the principal interest is in attaining improved experimental sensitivities in searches for rare decays, D^0 - $\overline{D^0}$ mixing and CP violation. As opposed to the FCNC phenomena in B decays, SM predicts tiny FCNC decay rates, mixing frequency, and CP asymmetries in the charm sector. This reflects the observed pattern of quark masses and mixings and the built-in GIM-mechanism [8] in the SM. Long-distance (LD) effects may increase some of the transition rates but these enhancements in all realistic estimates remain modest; FCNC-related phenomena in the charm sector remain unmeasurable in SM for all practical purposes. Hence, finding a positive signal in any of the rare decays such as $D^0 \to \ell^+\ell^-$, $D^0 \to \gamma\gamma$, D^0 - $\overline{D^0}$ mixing or CP violation in any charmed hadron decay mode will unambiguously signal physics beyond the SM. As argued quantitatively in these proceedings by Grab [9] and Tsipolitis [10], counting rate is the decisive parameter in such searches and an increase in HERA-luminosity will be very welcome in the ep mode. At HERA-B, the anticipated charmed hadron production rate is already very high. Here, one has to develop an efficient trigger to make use of this high yield and do competitive physics.

2 Flavour Mixings and CP Violation in the SM and at HERA-B

The profile of the CKM matrix [3] is updated by Ali and London in [11]. In particular, they focussed on the CKM unitarity triangle and CP asymmetries in B decays, which are the principal objects of interest in experiments at present and forthcoming B facilities, in particular HERA-B.

2.1 Present profile of the CKM unitarity triangle

In updating the CKM matrix elements the Wolfenstein parametrization [12] has been used which follows from the observation that the elements of this matrix exhibit a hierarchy in terms of λ, the Cabibbo angle. In this parametrization the CKM matrix can be written approximately as

$$V_{CKM} \simeq \begin{pmatrix} 1-\frac{1}{2}\lambda^2 & \lambda & A\lambda^3(\rho - i\eta) \\ -\lambda(1+iA^2\lambda^4\eta) & 1-\frac{1}{2}\lambda^2 & A\lambda^2 \\ A\lambda^3(1-\rho-i\eta) & -A\lambda^2 & 1 \end{pmatrix} . \tag{1}$$

The allowed region in ρ-η space can be displayed quite elegantly using the so-called unitarity triangle. The unitarity of the CKM matrix leads to the following relation:

$$V_{ud}V_{ub}^* + V_{cd}V_{cb}^* + V_{td}V_{tb}^* = 0 . \tag{2}$$

Using the form of the CKM matrix in Eq. 1, this can be recast as

$$\frac{V_{ub}^*}{\lambda V_{cb}} + \frac{V_{td}}{\lambda V_{cb}} = 1 , \tag{3}$$

which is a triangle relation in the complex plane (i.e. ρ-η space), illustrated in Fig. 1. Thus, allowed values of ρ and η translate into allowed shapes of the unitarity triangle.

The present status of the CKM-Wolfenstein parameters λ and A is as follows [2, 6]:

$$\begin{aligned} |V_{us}| &= \lambda = 0.2205 \pm 0.0018 , \\ |V_{cb}| &= 0.0393 \pm 0.0028 \implies A = 0.81 \pm 0.058 , \end{aligned} \tag{4}$$

The other two parameters ρ and η (the all important complex phase) are determined at present through the measurements of $|V_{ub}|/|V_{cb}|$, ΔM_d, the B_d^0-$\overline{B_d^0}$-mixing induced mass difference, and $|\epsilon_K|$, the CP-violating parameter in K decays. The present experimental input can be summarized as [11]:

$$\begin{aligned} \sqrt{\rho^2+\eta^2} &= 0.363 \pm 0.073 \quad (\text{from } |V_{ub}/V_{cb}| = 0.08 \pm 20\%), \\ (f_{B_d}\sqrt{\hat{B}_{B_d}}/1\text{ GeV})\sqrt{(1-\rho)^2+\eta^2} &= 0.202 \pm 0.017 \quad (\text{from } \Delta M_d = 0.464 \pm 0.018\ (ps)^{-1}), \\ \hat{B}_K\eta[0.93 + (2.08 \pm 0.34)(1-\rho)] &= (0.79 \pm 0.11) \quad (\text{from } |\epsilon_K| = (2.280 \pm 0.013) \times 10^{-3}) \end{aligned} \tag{5}$$

The errors of the last two lines include the small experimental errors on ΔM_d (3.9%) and $|\epsilon_K|$ (0.6%), as well as the larger errors on m_t^2 (11%) and A^2 (14%). In [11], two types of CKM fits have been considered.

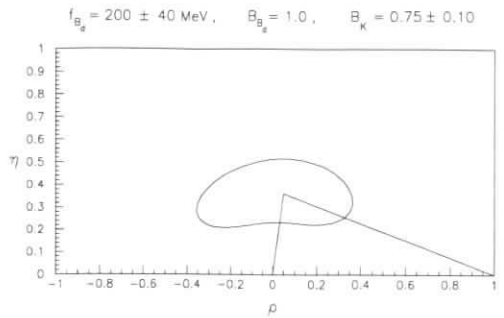

Figure 2: Allowed region in ρ-η space, from a simultaneous fit to both the experimental and theoretical quantities given in eqs. (4) and (5). The theoretical errors are treated as Gaussian for this fit. The solid line represents the region with $\chi^2 = \chi^2_{min} + 6$ corresponding to the 95% C.L. region. The triangle shows the best fit. (From [11].)

- Fit 1: the "experimental fit." Here, only the experimentally measured numbers are used as inputs to the fit with Gaussian errors; the coupling constants $f_{B_d}\sqrt{\hat{B}_{B_d}}$ and $\hat{B}_K$ are given fixed values.
- Fit 2: the "combined fit." Here, both the experimental and theoretical numbers (indicated on Fig. 2) are used as inputs assuming Gaussian errors for the theoretical quantities.

These two methods provide very similar results and we focus here on the "combined fit" (Fit 2), which is shown in terms of the allowed CKM triangle in Fig. 2. As is clear from this figure, the allowed region is still rather large at present. However, present data and theory do restrict the parameters ρ and η to lie in the following range:

$$\begin{aligned} 0.20 \;&\leq\; \eta \leq 0.52, \\ -0.35 \;&\leq\; \rho \leq 0.35\ . \end{aligned} \tag{6}$$

The preferred values obtained from the "combined fit" are

$$(\rho, \eta) = (0.05, 0.36) \quad (\text{with } \chi^2 = 6.6 \times 10^{-3})\ , \tag{7}$$

which gives rise to an almost right-angled unitarity triangle, with the angle γ being close to 90 degrees.

2.2 CP Violation in the B System

It is expected in the SM that the B system will exhibit large CP-violating effects, characterized by nonzero values of the angles α, β and γ in the unitarity triangle (Fig. 1). The most promising method to measure CP violation is to look for an asymmetry between $\Gamma(B^0 \to f)$ and

$\Gamma(\overline{B^0} \to f)$, where f is a CP eigenstate. If only one weak amplitude contributes to the decay, the CKM phases can be extracted cleanly (i.e. with no hadronic uncertainties). Thus, $\sin 2\alpha$, $\sin 2\beta$ and $\sin 2\gamma$ can in principle be measured in $(\overline{B^0} \to \pi^+\pi^-$, $(\overline{B^0} \to J/\psi K_s$ and $(\overline{B_s} \to \rho K_s$, respectively. Penguin diagrams will, in general, introduce some hadronic uncertainty into an otherwise clean measurement of the CKM phases. In the case of $(\overline{B^0} \to J/\psi K_s$, the penguins do not cause any problems, since the weak phase of the penguin is the same as that of the tree contribution. Thus, the CP asymmetry in this decay still measures $\sin 2\beta$. This augers well as measuring this asymmetry is the primary goal of the HERA-B experiment.

For $(\overline{B^0} \to \pi^+\pi^-$, however, although the penguin is expected to be small with respect to the tree diagram, it will still introduce a theoretical uncertainty into the extraction of α. This uncertainty can, in principle, be removed by the use of an isospin analysis, which requires the measurement of the rates for $B^+ \to \pi^+\pi^0$, $B^0 \to \pi^+\pi^-$ and $B^0 \to \pi^0\pi^0$, as well as their CP-conjugate counterparts. Help will come here from e^+e^- experiments which are the only ones which can measure the $B^0 \to \pi^0\pi^0$ mode. Still, this isospin program is ambitious experimentally. If it cannot be carried out, the error induced on $\sin 2\alpha$ is of order $|P/T|$, where P (T) represents the penguin (tree) diagram. The ratio $|P/T|$ is difficult to estimate since it is dominated by hadronic physics. It is $(\overline{B_s} \to \rho K_S$ which is most affected by penguins. In fact, the penguin contribution is probably larger in this process than the tree contribution. Other methods to measure γ have been devised, not involving CP-eigenstate final states, and are reviewed in [11].

The CP-violating asymmetries, parametrized by $\sin 2\alpha$, $\sin 2\beta$ and and $\sin^2\gamma$, can be expressed straightforwardly in terms of the CKM parameters ρ and η. The 95% C.L. constraints on ρ and η found previously can be used to predict the ranges of $\sin 2\alpha$, $\sin 2\beta$ and $\sin^2\gamma$ allowed in the standard model. The ranges for the CP-violating rate asymmetries are determined at 95% C.L. to be [11]:

$$\begin{aligned} -0.90 \leq \sin 2\alpha \leq 1.0\ , \\ 0.32 \leq \sin 2\beta \leq 0.94\ , \\ 0.34 \leq \sin^2\gamma \leq 1.0\ . \end{aligned} \tag{8}$$

It is assumed that the angle β is measured in $(\overline{B^0} \to J/\psi K_s$, and an extra minus sign due to the CP of the final state has been included. Since the CP asymmetries all depend on ρ and η, these ranges for $\sin 2\alpha$, $\sin 2\beta$ and $\sin^2\gamma$ are correlated. The correlation in ($\sin 2\alpha$ - $\sin 2\beta$) is shown in Fig. 3. Finally, in the SM the relation $\alpha + \beta + \gamma = \pi$ is satisfied. However, note that the allowed range for β is rather small. Thus, there is a strong correlation between α and γ [11].

It is seen from this figure that the smallest value of $\sin 2\beta$ occurs in a small region of parameter space around $\sin 2\alpha \simeq 0.8$-0.9. Excluding this small tail, one expects the integrated CP-asymmetry in $(\overline{B^0} \to J/\psi K_S$ to be at least 20% (i.e., $\sin 2\beta > 0.4$), with the central value estimated as $A(J/\psi K_s) = (30 \pm 7)\%$ [11]. Less satisfactory at present is the prediction for the asymmetry related to $\sin 2\alpha$, for which practically all values are allowed by the fits, including the one $\sin 2\alpha = 0$. If the preferred solution of nature is in the vicinity of $\sin(2\alpha) = 0$, it is improbable that the asymmetry related to this quantity will ever be measured. However, even

if $\sin(2\alpha)$ is not measured at HERA-B, a measurement of $\sin(2\beta)$ and a demonstration that $\sin(2\alpha) \ll \sin(2\beta)$ will lead to non-trivial constraints on the unitarity triangle. Such a scenario will also rule out the so-called superweak theory of CP violation [13], in which case one has the relation $\sin(2\alpha) = \sin(2\beta)$.

Returning to the CP-asymmetry in the decay $(\overline{B^0} \to J/\psi K_s$, we recall that the time dependent asymmetry is given by

$$\frac{n(t) - \overline{n}(t)}{n(t) + \overline{n}(t)} = D \sin 2\beta \sin xt \,,$$

where $n(t)$ and $\overline{n}(t)$ are the time dependent rates for the decay of a B^0 ($\overline{B}^0$) to decay into $J/\psi K_s$. D is a dilution factor which accounts for imperfect tagging.

The accuracy on $\sin 2\beta$ is given by

$$\Delta \sin 2\beta \propto \frac{1}{P} \frac{1}{\sqrt{N_{B^0}}}$$

where $P = D\sqrt{\epsilon_{tag}}$ is the tagging power, ϵ_{tag} the efficiency to get a tag of the B^0 meson and N_{B^0} the number of reconstructed B^0 mesons. A potential enlargement in the CP reach of HERA-B could be achieved by an increase in the proton energy at HERA and thus an increase in the rate of produced B^0 mesons. This scenario, which would substantially improve the Signal/Background ratio for B physics at HERA-B, is, however, somewhat unlikely. A reduction of the error on $\sin 2\beta$ could however come from reconstructing other B^0 decays which also measure $\sin 2\beta$. This was studied at this workshop for the decays $(\overline{B^0} \to \chi_c K^0$ by Misuk and Belyaev and for $(\overline{B^0} \to J/\psi K^{*0}$ by Barsuk [14]. These studies showed that one could expect a gain in statistics of about 20% including both these decays and the favourite mode $B \to J/\psi K_s$.

An increase in the tagging power P and thus a smaller error on $\sin 2\beta$ could also come from new tagging techniques. For this purpose the decay $B^{**+} \to \pi^+ B^0$ was studied by Kagan and Shepherd-Themistocleous in the HERA-B environment [15]. This tagging is particularly useful because it is not spoiled by $B\overline{B}$ mixing. The analysis gave promising results with a tagging power of $P = 0.21$ compared to the tagging with primary leptons which yielded $P = 0.17$. Misuk investigated the possibility to tag the flavour of the B mesons by using cascade leptons from the decay chain $B \to D \to \ell^{\pm}$ and obtained for this tagging method a tagging power of $P = 0.08$ [16]. In summary, these studies undertaken to increase the sensitivity of the HERA-B experiment for $\sin 2\beta$ showed that a gain in the statistical power of about 30% is possible.

2.3 ΔM_s (and x_s) and the Unitarity Triangle

Mixing in the B_s^0-$\overline{B_s^0}$ system is quite similar to that in the B_d^0-$\overline{B_d^0}$ system in the SM in which the B_s^0-$\overline{B_s^0}$ and B_d^0-$\overline{B_d^0}$ box diagrams are dominated by t-quark exchange. Using the fact that $|V_{cb}| = |V_{ts}|$ (Eq. 1), it is clear that one of the sides of the unitarity triangle, $|V_{td}/\lambda V_{cb}|$, can be obtained from the ratio of ΔM_d and ΔM_s,

$$\frac{\Delta M_s}{\Delta M_d} = \frac{\hat{\eta}_{B_s} M_{B_s} \left(f_{B_s}^2 \hat{B}_{B_s}\right)}{\hat{\eta}_{B_d} M_{B_d} \left(f_{B_d}^2 \hat{B}_{B_d}\right)} \left|\frac{V_{ts}}{V_{td}}\right|^2 . \tag{9}$$

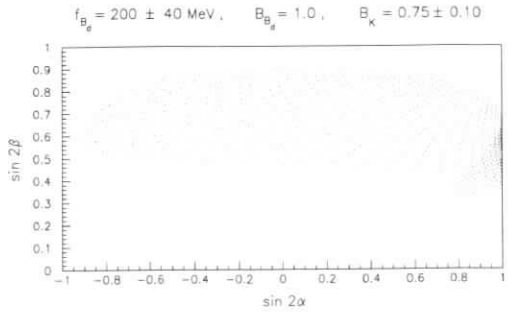

Figure 3: Allowed region of the CP-violating quantities $\sin 2\alpha$ and $\sin 2\beta$ resulting from the "combined fit" of the data for the ranges for $f_{B_d}\sqrt{\hat{B}_{B_d}}$ and $\hat{B}_K$ given in the text. (From [11].)

Here $\hat{\eta}_{B_s} = \hat{\eta}_{B_d} = 0.55$ is the perturbative QCD correction factor [17]. The only real uncertainty (apart from the CKM matrix element ratio which we would like to determine) is the ratio of hadronic matrix elements $f_{B_s}^2 \hat{B}_{B_s}/f_{B_d}^2 \hat{B}_{B_d}$. Using the determination of A given earlier, $\tau(B_s) = 1.52 \pm 0.07$ ps, and $\overline{m_t} = 165 \pm 9$ GeV, one gets

$$\begin{aligned} \Delta M_s &= (12.8 \pm 2.1) \frac{f_{B_s}^2 \hat{B}_{B_s}}{(230 \text{ MeV})^2} \, (ps)^{-1} \,, \\ x_s &= (19.5 \pm 3.3) \frac{f_{B_s}^2 \hat{B}_{B_s}}{(230 \text{ MeV})^2} \,. \end{aligned} \tag{10}$$

The choice $f_{B_s}\sqrt{\hat{B}_{B_s}} = 230$ MeV corresponds to the central value given by the lattice-QCD estimates, and with this the fits in [11] give $x_s \simeq 20$ as the preferred value in the SM. Allowing the coefficient to vary by $\pm 2\sigma$, and taking the central value for $f_{B_s}\sqrt{\hat{B}_{B_s}}$, this gives

$$\begin{aligned} 12.9 &\leq x_s \leq 26.1 \,, \\ 8.6 \; (ps)^{-1} &\leq \Delta M_s \leq 17.0 \; (ps)^{-1} \,. \end{aligned} \tag{11}$$

It is difficult to ascribe a confidence level to this range due to the dependence on the unknown coupling constant factor. All one can say is that the standard model predicts large values for ΔM_s (and hence x_s). The present experimental limit from the combined fit of the ALEPH [18] and OPAL experiments $\Delta M_s > 9.2$ $(ps)^{-1}$ [6] is better than the lower bound on this quantity obtained from the CKM fits given above. In particular, the LEP-bound, expressed as $\Delta M_s/\Delta M_d > 19.0$, removes the (otherwise allowed) large-negative-ρ region, leaving the reduced parameter space ($-0.25 \leq \rho \leq 0.35$, $0.25 \leq \eta \leq 0.52$) as the presently allowed one [11]. In terms of the ratio $|V_{td}|/|V_{ts}|$, this implies $|V_{td}|/|V_{ts}| < 0.29$, to be compared with the central value from the CKM fits $|V_{td}|/|V_{ts}| = 0.24$ [11]. The constraints on the unitarity triangle from ΔM_s will become more pronounced with improved data. With the present HERA-B detector, one expects to reach a sensitivity $x_s \simeq 17$ (or $\Delta M_s \simeq 11$ ps^{-1}) combining various B_s reconstruction

and tagging techniques and data for three years [19]. This overlaps with the x_s-range expected in the SM, though it is somewhat on the lower side. To completely cover the estimated x_s-range in eq. (11), one must strive to increase the experimental sensitivity to $x_s = 26$.

3 Rare B Decays in the SM and at HERA-B

The FCNC B decay with the largest branching ratio in the SM, $B \to X_s + \gamma$, has been observed by the CLEO collaboration [20] through the measurement of the photon energy spectrum in the high E_γ-region. This was preceded by the observation of the exclusive decay $B \to K^* + \gamma$ by the same collaboration [21]. The present measurements give [22]: $\mathcal{B}(B \to X_s + \gamma) = (2.32 \pm 0.57 \pm 0.35) \times 10^{-4}$ and $\mathcal{B}(B \to K^* + \gamma) = (4.2 \pm 0.8 \pm 0.6) \times 10^{-5}$, yielding an exclusive-to-inclusive ratio: $R_{K^*} = \Gamma(B \to K^* + \gamma)/\Gamma(B \to X_s + \gamma) = (18.1 \pm 6.8)\%$. In the SM the decay rates determine the ratio of the CKM matrix elements $|V_{ts}|/|V_{cb}|$ and the quantity R_{K^*} provides information on the decay form factor in $B \to K^* + \gamma$. It is important to undertake independent measurements of the above-mentioned decays and related processes elsewhere.

A Monte Carlo study by Saadi-Lüdemann described in these proceedings [23] shows that the large-p_T photons emerging from the decays $B \to K^* + \gamma$ can, in principle, be distinguished from the background events at HERA-B, which range out earlier in p_T. Only slight modifications to the present HERA-B trigger scheme are necessary. This argument also holds for the photons from the inclusive decay $B \to X_s + \gamma$, as the photon p_T-spectrum is rather hard and the additional requirement of a large-p_T charged track accompanying the energetic photon will be fulfilled by these decays. Since b-quark fragments include typically 20% of the time a B_s^0 meson or a b baryon (henceforth generically called Λ_b), the FCNC rare decays of the B_s^0 meson and Λ_b baryon will be new and valuable additions to this field which cannot be studied at e^+e^- threshold machines, optimized to operate at the $\Upsilon(4S)$ resonance. The approximate equality of the inclusive radiative branching ratios for the decays $B^\pm \to X_s^\pm + \gamma$, $B_d^0 \to X_s^0 + \gamma$, $B_s^0 \to X_{(s\bar{s})}^0 + \gamma$ and $\Lambda_b \to (\Lambda + X) + \gamma$ will test the hypothesis that these decays are indeed dominated by short-distance physics. Given conducive triggers, HERA-B has the potential of contributing significantly to the field of rare B decays. Here, we summarize some representative examples which can be studied at HERA-B, given the present and planned triggers and assuming that 10^9 $b\bar{b}$ pairs will be produced in three years of data taking at HERA-B.

3.1 Inclusive decay rates $B \to X_s + \gamma$ and $B \to X_d + \gamma$

The leading contribution to $b \to s + \gamma$ arises at one-loop from the so-called penguin diagrams. With the help of the unitarity of the CKM matrix, the decay matrix element in the lowest order can be written as:

$$\mathcal{M}(b \to s\ + \gamma) = \frac{G_F}{\sqrt{2}} \frac{e}{2\pi^2} \lambda_t \left(F_2(x_t) - F_2(x_c)\right) q^\mu \epsilon^\nu \bar{s} \sigma_{\mu\nu} (m_b R\ +\ m_s L) b\ . \qquad (12)$$

where $x_i = m_i^2/m_W^2$, and q_μ and ϵ_μ are, respectively, the photon four-momentum and polarization vector, and $\lambda_t = V_{tb} V_{ts}^*$. The (modified) Inami-Lim function $F_2(x_i)$ derived from the (1-loop) penguin diagrams [24] can be seen in [4]. The measurement of the branching ratio for $B \to X_s + \gamma$ can be readily interpreted in terms of the CKM-matrix element product $\lambda_t/|V_{cb}|$ or equivalently $|V_{ts}|/|V_{cb}|$. For a quantitative determination of $|V_{ts}|/|V_{cb}|$, however, QCD radiative corrections have to be included and the contribution of the so-called long-distance effects estimated. This has been reviewed in [4], yielding:

$$\mathcal{B}(B \to X_s + \gamma) = (3.20 \pm 0.58) \times 10^{-4}, \qquad (13)$$

which is compatible with the present measurement $\mathcal{B}(B \to X_s + \gamma) = (2.32 \pm 0.67) \times 10^{-4}$ [20]. Expressed in terms of the CKM matrix element ratio, one gets [4]

$$\frac{|V_{ts}|}{|V_{cb}|} = 0.85 \pm 0.12(\text{expt}) \pm 0.10(\text{th}), \qquad (14)$$

which is within errors consistent with unity, as expected from the unitarity of the CKM matrix.

Since the masses and lifetimes of the $B^\pm$, B_d^0, and B_s^0 mesons are very similar, the branching ratio quoted above holds (within minor differences) for all three B mesons. The branching ratio for the Λ_b-baryon will be reduced by the ratio of the lifetimes. One estimates,

$$\begin{aligned} \mathcal{B}(\Lambda_b \to (\Lambda + X)\gamma) &= \mathcal{B}(B_d \to X_s \gamma) \left[\frac{\tau(B_d)}{\tau(\Lambda_b)}\right] \\ &= (2.5 \pm 0.6) \times 10^{-4}\ , \end{aligned} \qquad (15)$$

where we have used $\tau(B_d)/\tau(\Lambda_b) = 0.78 \pm 0.04$ [25].

The theoretical interest in studying the (CKM-suppressed) inclusive radiative decays $B \to X_d + \gamma$ lies in the first place in the possibility of determining the parameters of the CKM matrix. With that goal in view, one of the relevant quantities in the decays $B \to X_d + \gamma$ is the end-point photon energy spectrum which has to be measured requiring that the hadronic system X_d recoiling against the photon does not contain strange hadrons, so as to suppress the large-E_γ photons from the decay $B \to X_s + \gamma$. This requires, in particular, a good K/π-separation. Assuming that this is feasible, one can determine from the ratio of the decay rates $\mathcal{B}(B \to X_d + \gamma)/\mathcal{B}(B \to X_s + \gamma)$ the CKM-Wolfenstein parameters ρ and η. To get an estimate of the inclusive branching ratio at present, the CKM parameters ρ and η have to be constrained from the unitarity fits discussed above. Taking the preferred values of the fitted CKM parameters from eq. (7), one gets [26, 27]

$$\mathcal{B}(B \to X_d + \gamma) = 1.63 \times 10^{-5}, \qquad (16)$$

whereas $\mathcal{B}(B \to X_d + \gamma) = 8.0 \times 10^{-6}$ and 2.8×10^{-5} for the other two extremes $\rho = 0.35$, $\eta = 0.50$ and $\rho = -\eta = -0.25$, respectively. Therefore, one expects $O(10^4)$ $B \to X_d + \gamma$ events at HERA-B, which taking into account an estimated trigger and reconstruction efficiency of 1% would yield $O(10^2)$ reconstructed B decays of this kind. However, one will have to suppress the background from the dominant $B \to X_s + \gamma$ decays which requires further study.

3.2 $\mathcal{B}(B \to V + \gamma)$ and constraints on the CKM parameters

Exclusive radiative B decays $B \to V+\gamma$, with $V = K^*, \rho, \omega$, are also potentially very interesting from the point of view of determining the CKM parameters [29]. The extraction of these parameters would, however, involve a trustworthy estimate of the SD- and LD-contributions in the decay amplitudes.

The SD-contribution in the exclusive decays $(B^\pm, B^0) \to (K^{*\pm}, K^{*0}) + \gamma$, $(B^\pm, B^0) \to (\rho^\pm, \rho^0) + \gamma$, $B^0 \to \omega + \gamma$ and the corresponding B_s decays, $B_s \to \phi + \gamma$, and $B_s \to K^{*0} + \gamma$, involve the magnetic moment operators [4]. The transition form factors governing these decays can be generically defined as:

$$\langle V, \lambda | \frac{1}{2} \bar{\psi} \sigma_{\mu\nu} q^\nu b | B \rangle = i \epsilon_{\mu\nu\rho\sigma} e_\nu^{(\lambda)} p_B^\rho p_V^\sigma F_S^{B \to V}(0). \tag{17}$$

Here V is a vector meson with the polarization vector $e^{(\lambda)}$, $V = \rho, \omega, K^*$ or ϕ; B is a generic B-meson $B^\pm$, B^0 or B_s, and ψ stands for the field of a light u, d or s quark. The vectors p_B, p_V and $q = p_B - p_V$ correspond to the 4-momenta of the initial B-meson and the outgoing vector meson and photon, respectively. Keeping only the SD-contribution leads to obvious relations among the exclusive decay rates,

$$\frac{\Gamma((B^\pm, B^0) \to (\rho^\pm, \rho^0) + \gamma)}{\Gamma((B^\pm, B^0) \to (K^{*\pm}, K^{*0}) + \gamma)} \simeq \kappa_{u,d} \left[\frac{|V_{td}|}{|V_{ts}|} \right]^2 , \tag{18}$$

where $\kappa_i \equiv [F_S(B_i \to \rho\gamma)/F_S(B_i \to K^*\gamma)]^2 \Phi_{u,d}$ and $\Phi_{u,d}$ is a phase-space factor which in all cases is close to 1. Likewise, using the SD-contribution and isospin symmetry yields

$$\Gamma(B^\pm \to \rho^\pm \gamma) = 2\,\Gamma(B^0 \to \rho^0 \gamma) = 2\,\Gamma(B^0 \to \omega\gamma)\,. \tag{19}$$

If the SD-amplitudes were the only contributions, the measurements of the CKM-suppressed radiative decays $(B^\pm, B^0) \to (\rho^\pm, \rho^0) + \gamma$, $B^0 \to \omega + \gamma$ and $B_s^0 \to K^{*0} + \gamma$ could be used in conjunction with the decays $(B^\pm, B^0) \to (K^{*\pm}, K^{*0}) + \gamma$ to determine one of the sides of the unitarity triangle. The present experimental upper limits on the CKM ratio $|V_{td}|/|V_{ts}|$ from radiative B decays are indeed based on this assumption. The present limits on some of the decay modes are reviewed in [4], which yield at 90% C.L.[22]:

$$\left| \frac{V_{td}}{V_{ts}} \right| \leq 0.45 - 0.56\,, \tag{20}$$

depending on the models used for the $SU(3)$ breaking effects in the form factors. The estimated range for this ratio is $0.15 \leq |V_{td}|/|V_{ts}| \leq 0.29$, which implies that an improvement of a factor of 3 - 10 in the experimental sensitivity would result in measurements of several CKM-suppressed radiative decay modes.

The possibility of significant LD-contributions in radiative B decays from the light quark intermediate states has been raised in a number of papers. The LD-contributions in $B \to V + \gamma$ are induced by the matrix elements of the four-Fermion operators (see [4] for definitions and references). Their amplitudes necessarily involve other CKM matrix elements and hence the

simple factorization of the decay rates in terms of the CKM factors involving $|V_{td}|$ and $|V_{ts}|$ no longer holds thereby invalidating the relations (18) and (19) given above. The modified relations have been worked out in [30, 31]. Combining the estimates for the LD- and SD-form factors in [31] and [29], respectively, and restricting the Wolfenstein parameters in the range $-0.25 \leq \rho \leq 0.35$ and $0.2 \leq \eta \leq 0.5$, as discussed above, the following estimates for the absolute branching ratios have been given in [4]:

$$\begin{aligned} \mathcal{B}(B^\pm \to \rho^\pm \gamma) &= (1.5 \pm 1.1) \times 10^{-6}\,, \\ \mathcal{B}(B^0 \to \rho\gamma) &\simeq \mathcal{B}(B^0 \to \omega\gamma) = (0.65 \pm 0.35) \times 10^{-6}\,, \end{aligned} \tag{21}$$

where we have used the experimental value for the branching ratio $\mathcal{B}(B \to K^* + \gamma)$ [21], adding the errors in quadrature. The large error reflects the poor knowledge of the CKM matrix elements and hence experimental determination of these branching ratios will put rather stringent constraints on the Wolfenstein parameters, in particular ρ.

In addition to studying the radiative penguin decays of the $B^\pm$ and B^0 mesons discussed above, HERA-B will be in a position to study the corresponding decays of the B_s^0 meson and Λ_b baryon, such as $B_s^0 \to \phi + \gamma$ and $\Lambda_b \to \Lambda + \gamma$, which have not been measured so far. We list below the branching ratios in a number of interesting decay modes calculated in the QCD sum rule approach in [29].

$$\begin{aligned} \mathcal{B}(B_s \to \phi\gamma) &\simeq \mathcal{B}(B_d \to K^*\gamma) = (4.2 \pm 2.0) \times 10^{-5}\,, \\ \frac{\mathcal{B}(B_s \to K^*\gamma)}{\mathcal{B}(B_d \to K^*\gamma)} &\simeq (0.36 \pm 0.14) \frac{|V_{td}|^2}{|V_{ts}|^2} \\ &\Longrightarrow \mathcal{B}(B_s \to K^*\gamma) = (0.75 \pm 0.5) \times 10^{-6}\,. \end{aligned} \tag{22}$$

The branching ratio for the radiative decay $\Lambda_b \to \Lambda\gamma$ can be calculated in terms of the exclusive-to-inclusive function $R_\Lambda \equiv \Gamma(\Lambda_b \to \Lambda + \gamma)/\Gamma(\Lambda_b \to (\Lambda + X) + \gamma)$, analogous to the ratio R_{K^*}, defined for the B meson decays earlier. This would then give:

$$\mathcal{B}(\Lambda_b \to \Lambda\gamma) = R_\Lambda \mathcal{B}(\Lambda_b \to (\Lambda + X)\gamma) = (3.8 \pm 1.5) \times 10^{-5}\,, \tag{23}$$

where we have used the SM estimate $\mathcal{B}(B_d \to X_s\gamma) = (3.2 \pm 0.6) \times 10^{-4}$ [4], assumed $R_\Lambda = R_{K^*}$, with $R_{K^*} = 0.15 \pm 0.05$ [29] and $\tau(B_d)/\tau(\Lambda_b) = 0.78 \pm 0.04$ [25]. We note that a much smaller branching ratio has been calculated in [28]. The CKM-suppressed decay $\Lambda_b^0 \to n + \gamma$ is related to the decay $\Lambda_b^0 \to \Lambda + \gamma$ by the CKM ratio $|V_{td}|/|V_{ts}|^2$ in the $SU(3)$ limit. Using the central value $|V_{td}|/|V_{ts}|^2 = 0.058$, this gives $\mathcal{B}(\Lambda_b \to n + \gamma) = (2.2 \pm 1.0) \times 10^{-6}$. Estimated counting rates for several of the exclusive decay modes in the HERA-B experimental environment are given in these proceedings [23], taking into account the trigger and reconstruction efficiency. They range between $O(10^2)$ for the CKM-allowed decays and $O(10)$ for the CKM-suppressed decays.

3.3 Inclusive rare decays $B \to X_s \ell^+ \ell^-$ in the SM

The decays $B \to X_s \ell^+ \ell^-$, with $\ell = e, \mu, \tau$, provide a more sensitive search strategy for finding new physics in rare B decays than for example the decay $B \to X_s \gamma$, which constrains the

magnitude of the effective Wilson coefficient of the magnetic moment operator, C_7^{eff}. The sign of C_7^{eff} (which is negative in the SM but in general depends on the underlying physics) is not determined by the measurement of $\mathcal{B}(B \to X_s + \gamma)$ alone. It is known (see for example [32]) that in supersymmetric (SUSY) models, both the negative and positive signs are allowed as one scans over the allowed SUSY parameter space. We recall that the $B \to X_s \ell^+ \ell^-$ amplitude in the standard model (as well as in SUSY and multi-Higgs models) has two additional terms, arising from the two FCNC four-Fermi operators. Calling their coefficients C_9 and C_{10}, it has been argued in [32] that the signs and magnitudes of all three coefficients C_7^{eff}, C_9 and C_{10} can, in principle, be determined from the decays $B \to X_s + \gamma$ and $B \to X_s \ell^+ \ell^-$.

The differential decay rate in the dilepton invariant mass in $B \to X_s \ell^+ \ell^-$ can be expressed in terms of the semileptonic branching ratio $\mathcal{B}_{sl}$,

$$\begin{aligned} \frac{\mathrm{d}\mathcal{B}(\hat{s})}{\mathrm{d}\hat{s}} &= \mathcal{B}_{sl} \frac{\alpha^2}{4\pi^2} \frac{\lambda_t^2}{|V_{cb}|^2} \frac{1}{f(\hat{m}_c)\kappa(\hat{m}_c)} u(\hat{s}) \Big[\left(|C_9^{eff}(\hat{s})|^2 + C_{10}^2 \right) \alpha_1(\hat{s}, \hat{m}_s) \\ &\quad + \frac{4}{\hat{s}} (C_7^{eff})^2 \alpha_2(\hat{s}, \hat{m}_s) + 12 \alpha_3(\hat{s}, \hat{m}_s) C_7^{eff} \Re(C_9^{eff}(\hat{s})) \Big], \end{aligned} \tag{24}$$

with $\hat{s} = s/m_b^2$, $u(\hat{s}) = \sqrt{[\hat{s} - (1+\hat{m}_s)^2][\hat{s} - (1-\hat{m}_s)^2]}$, $\hat{m}_i = m_i^2/m_b^2$, and the functions $f(\hat{m}_c)$, $\kappa(\hat{m}_c)$, and α_i can be seen in [4]. Here $\Re(C_7^{eff})$ represents the real part of C_7^{eff}. A useful quantity is the differential FB asymmetry in the c.m.s. of the dilepton defined in refs. [33]:

$$\frac{d\mathcal{A}(\hat{s})}{d\hat{s}} = \int_0^1 \frac{d\mathcal{B}}{dz} - \int_0^{-1} \frac{d\mathcal{B}}{dz}, \tag{25}$$

where $z = \cos\theta$, which can be expressed as:

$$\frac{\mathrm{d}\mathcal{A}(\hat{s})}{\mathrm{d}\hat{s}} = -\mathcal{B}_{sl} \frac{3\alpha^2}{4\pi^2} \frac{1}{f(\hat{m}_c)} u^2(\hat{s}) C_{10} \left[\hat{s} \Re(C_9^{eff}(\hat{s})) + 2 C_7^{eff} (1 + \hat{m}_s^2) \right]. \tag{26}$$

The Wilson coefficients C_7^{eff}, C_9^{eff} and C_{10} appearing in the above equations can be determined from data by solving the partial branching ratio $\mathcal{B}(\Delta\hat{s})$ and partial FB asymmetry $\mathcal{A}(\Delta\hat{s})$, where $\Delta\hat{s}$ defines an interval in the dilepton invariant mass [32]. From the experimental point of view, the normalized FB-asymmetry, which is defined as

$$\frac{dA(\hat{s})}{d\hat{s}} = \frac{\int_0^1 \frac{d\mathcal{B}}{dz} - \int_0^{-1} \frac{d\mathcal{B}}{dz}}{\int_0^1 \frac{d\mathcal{B}}{dz} + \int_0^{-1} \frac{d\mathcal{B}}{dz}}, \tag{27}$$

is a more useful quantity. Following branching ratios for the SD-piece have been estimated in [34]:

$$\begin{aligned} \mathcal{B}(B \to X_s e^+ e^-) &= (8.4 \pm 2.2) \times 10^{-6}, \\ \mathcal{B}(B \to X_s \mu^+ \mu^-) &= (5.7 \pm 1.2) \times 10^{-6}, \\ \mathcal{B}(B \to X_s \tau^+ \tau^-) &= (2.6 \pm 0.5) \times 10^{-7}. \end{aligned} \tag{28}$$

The present best upper limit is $\mathcal{B}(B \to X_s \mu^+ \mu^-) < 3.6 \times 10^{-5}$ at (90% C.L.) by the D0 collaboration [35], and there are no useful limits on the other two decay modes. To get the

physical decay rates and distributions, one has to include the LD-contributions (which are dominated by the J/ψ and ψ' resonances) and the hadronic wave function effects. These aspects have been recently studied in [34], using the Fermi motion model [36] which depends on two parameters p_F (the b-quark kinetic energy) and m_q (the spectator quark mass in $B = \bar{b}q$). We show here the resulting invariant dilepton mass spectrum in Fig. 4, from which it is obvious that only in the dilepton mass region far away from the resonances is there a hope of extracting the Wilson coefficients governing the short-distance physics. The region below the J/ψ resonance is well suited for that purpose for HERA-B as the dilepton invariant mass distribution here is dominated by the SD-piece. The prerequisite for measurements at HERA-B is a lower dilepton

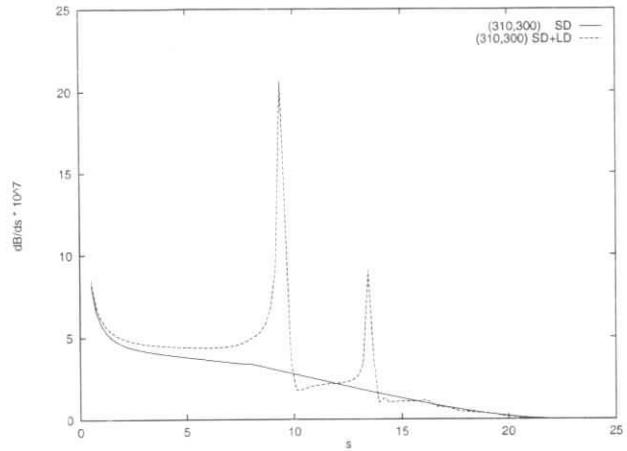

Figure 4: Differential branching ratio $d\mathcal{B}/ds$ for $B \to X_s \ell^+ \ell^-$ calculated in the SM using the next-to-leading order QCD corrections and Fermi motion effect (solid curve), and including the LD-contributions (dashed curve). The Fermi motion model parameters (p_F, m_q) are displayed in the figure. (From [34].)

mass trigger than is the case now which is optimized at the J/ψ mass, otherwise the SD-piece in $B \to X_s \mu^+ \mu^-$ will be harder to extract. Including the LD-contributions, following branching ratio has been estimated for the dilepton mass range 2.10 GeV^2 $\leq s \leq$ 2.90 GeV^2 in [34]:

$$\mathcal{B}(B \to X_s \mu^+ \mu^-) = (1.3 \pm 0.3) \times 10^{-6}, \tag{29}$$

with $\mathcal{B}(B \to X_s e^+ e^-) \simeq \mathcal{B}(B \to X_s \mu^+ \mu^-)$. The normalized FB-asymmetry is estimated to be in the range 10% - 27%. These branching ratios and the FB asymmetry are expected to be measured within the next several years at HERA-B with few tens of events [23] and other forthcoming B facilities. In the high invariant mass region, the short-distance contribution dominates. However, the rates are down by roughly an order of magnitude compared to the region below the J/ψ-mass. Estimates of the branching ratios are of $O(10^{-7})$, which should be accessible at the LHC.

In conclusion, the semileptonic FCNC decays $B \to X_s \ell^+ \ell^-$ (and the related exclusive decays) will provide very precise tests of the SM in flavour physics. They may also reveal new

physics beyond the SM. The MSSM model is a good case study where measurable deviations from the SM are anticipated are anticipated and worked out [32, 37].

3.4 Other topics in B physics

With large samples of B hadrons available, also other precision measurements involving B decays are feasible at HERA-B, e.g. precise determination of $|V_{cb}|$, B-hadron lifetimes and the B_d^0 - $\overline{B_d^0}$ mixing ratio x_d. Present measurements of $|V_{cb}|$ are at $\pm 7\%$ [6], and the lifetimes of the specific B hadrons are (all in ps): $\tau(B^{\pm}) = 1.65 \pm 0.04$, $\tau(B_d^0) = 1.55 \pm 0.04$, $\tau(B_s^0) = 1.52 \pm 0.07$ and $\tau(\Lambda_b) = 1.21 \pm 0.06$ [25]. Theoretical estimates based on the QCD-improved parton model predict almost equal lifetimes of the charged ($B^{\pm}$) and neutral (B_d^0, B_s^0) mesons and the Λ_b baryons. Power corrections will split these lifetimes but only moderately. There exists a mild embarrassment for present theoretical estimates in that the ratio $\tau(\Lambda_b)/\tau(B_d) = 0.78 \pm 0.04$ is significantly lower than unity (expected to be > 0.9 in most estimates). To check these models, lifetime have to be measured very accurately, in particular of the Λ_b and B_s^0. Of some theoretical interest is also the lifetime difference between the two mass eigenstates $\Delta\Gamma(B_{s,1} - B_{s,2})$, which is expected to be $O(15\%)$ [39]. Kreuzer showed that lifetime measurements at one to two percent level are feasible for the $B^{\pm}$ and the neutral B^0 mesons, and at $\pm 5\%$ for Λ_b and B_s^0 at HERA-B [38]. Another interest lies in the precise determination of Δm_d, [38]. Although the combined LEP and ARGUS/CLEO measurements have reached an accuracy of a few percent with $\Delta M_d = 0.464 \pm 0.018$ $(ps)^{-1}$ [6], HERA-B would be able to contribute to these measurement with comparable errors and very different systematic effects, as it was demonstrated by Kreuzer in this workshop.

The question of producing and detecting the mesons $B_c \equiv \bar{b}c$ (and its charge conjugate) at HERA-B and HERA(ep) was discussed by Baranov, Ivarsson, Mannel, and Rückl at this workshop. This is an interesting object to study, as both the $\bar{b}$ and c quarks can decay independently and $O(5\%)$ decays would take place via the annihilation diagram. The decay products involve final states such as $J/\psi + (\pi, \rho, A_1, ...)$ and the semileptonic decays such as $J\psi\ell^+\nu_\ell$, which are measurable at HERA-B and HERA(ep). Unfortunately, the production cross sections are small at HERA in both the ep and pp modes. Typical estimates are: $\sigma(pp \to B_c\bar{c}bX) \simeq 10\ fb$ at the HERA-B energy $\sqrt{s} \simeq 40$ GeV, with the cross section in the vector meson (B_c^*) mode a factor 2 - 3 larger. This, for example for the $J/\psi\pi$ mode yields $\sigma(B_cX) \cdot \mathcal{B}(J/\psi\pi) = O(10^{-2}) fb$, putting its detection beyond the integrated HERA-B luminosity. At HERA(ep), the production cross section is estimated as $\sigma(ep \to B_c\bar{c}bX) \simeq 1\ pb$, making it well nigh impossible to detect the B_c-meson even with an integrated luminosity of 250 $(pb)^{-1}$.

4 Rare Decays, D^0 - $\overline{D^0}$ Mixing and CP Violation

As discussed by Eichler and Frixione in these proceedings, the measured charm hadron photoproduction cross section at HERA is close to one microbarn. At present, a total efficiency of 10^{-4} of charmed hadron reconstruction via D^*-tagging has been achieved at HERA, which is expected to go up to $O(10^{-3})$ by adding various useful decay modes of D^0 and having the benefit of a vertex detector. With an integrated luminosity of 250 $(pb)^{-1}$, and including the

$D^{\pm}$ mesons, this could yield up to 10^6 reconstructed $D^0(\overline{D^0})$ and $D^{\pm}$ events with a $S/N \geq 1$. At HERA-B, the charmed hadron production cross section is estimated as $O(10\ \mu b)$/Nucleon, consistent with the fixed target experiments [40], leading to $O(10^{12})$ charmed hadrons produced in three years of data taking. No detailed study of the charmed hadron reconstruction efficiency has been undertaken at HERA-B. Hence, it is difficult to be quantitative. However, the method of D^*-tagging coupled with vertex resolution studied in the context of HERA will be useful at HERA-B as well. With an (assumed) overall reconstruction efficiency of $O(10^{-5})$ at HERA-B, this would lead to $O(10^7)$ reconstructed charmed events. As reviewed by Jeff Appel during this workshop, fixed target experiments (in particular E791 and E687) have already reconstructed in excess of 10^5 charmed hadrons. A programme to reach $O(10^6)$ charmed hadrons in fixed target experiments in USA is already in place. There are enticing proposals to get to $O(10^8)$ (or even 10^9) charmed hadrons, though the time scale for beyond 10^6 is difficult to predict. It is clear that both HERA and HERA-B have formidable tasks ahead in matching the current and planned performances in the charmed hadron sector.

The current interest in the charm sector lies in doing what has become to be known as "the high impact physics". This means searches for rare decays, D^0 - $\overline{D^0}$ mixing and CP violation. Some of the rare D decays were studied during the previous HERA workshop [41]. An updated study of $D^0 \to \mu^+\mu^-$ has been undertaken by Grab during this workshop [9], with the conclusions that with an integrated luminosity of 250 $(pb)^{-1}$ at HERA, a sensitivity of 2.5×10^{-6} will be reached in this channel. The present upper limit on this decay mode is 7.6×10^{-6} [2]. This implies a factor of 3 improved sensitivity at HERA. The sensitivity in the other leptonic modes $D^0 \to e^+e^-$, $D^0 \to \mu^{\pm}e^{\mp}$ and the semileptonic decays $D^0 \to \rho^0 e^+e^-$, $\rho^0\mu^+\mu^-$, as well as the analogous charged decays $D^{\pm} \to \pi^{\pm}e^+e^-$, $D^{\pm} \to \pi^{\pm}\mu^+\mu^-$ was studied during the previous HERA workshop and can be seen there. In the meanwhile, upper limits on several of these decay modes have moved up significantly [2], leaving a reduced window for searches at HERA.

Finally, we note that both mixing and CP violation in the charm sector are too small to be measured, if the SM is the only source of such transitions. Typically in the SM, one has the following scenario [42]:

$$\frac{\Delta M_D}{\Gamma_D} \simeq O(10^{-5}), \quad \frac{\Delta\Gamma_D}{\Delta M_D} \ll 1, \tag{30}$$

with the CP-violating quantity $Im(\Delta M_d/\Gamma_D)$ negligible. The feature $\Delta\Gamma_D/\Delta M_D \ll 1$ will hold in all extensions of the SM, as the decay rates are determined essentially by the tree diagrams and one does not anticipate large enhancements here. However, in a number of extensions of the SM, the quantity $\Delta M_D/\Gamma_D$ may receive additional contributions pushing it close to its present upper limit [43]. In addition, in some theoretical scenarios, one has $Im(\Delta M_d/\Gamma_D) \simeq Re(\Delta M_d/\Gamma_D)$, implying also measurable CP-violation. This could manifest itself in the differences in the time-dependent and time-integrated rates, leading to CP violating asymmetries in $D^0(t) \to f$ and $\overline{D^0}(t) \to \bar{f}$, where f and $\bar{f}$ are CP-conjugate states. Examples of such extensions are: SUSY models with quark-squark alignment, in which case there are additional contributions to ΔM_D from box diagrams with gluinos and squarks [44], models with a fourth quark generation in which ΔM_D gets new contributions from the W and b' intermediate states [45], models with an $SU(2)$-singlet left-handed up-type quark u'_L, inducing tree-level FCNC couplings, for example in the form of a $Zu\bar{c}$ coupling [46] with implications for the unitarity of the quark mixing matrix, multiscalar models with natural flavour conservation

[47], in which ΔM_D gets new contributions from box diagrams with intermediate charged Higgs $H^{\pm}$ and quarks. Finally, leptoquark models with light scalar leptoquarks [48] may also lead to a large value for ΔM_D; with leptoquark couplings $F_{\ell c} F_{\ell u} \geq 10^{-3}$ and leptoquark masses $M_{LQ} \leq 2$ TeV, new contributions could be of the order of the present experimental bounds [49].

The present limit on D^0 - $\overline{D^0}$ mixing can be expressed in terms of the quantity $r_D \equiv (\Delta M_D/\Gamma_D)^2/[2+(\Delta M_D/\Gamma_D)^2]$. The decay modes of interest here are $D^0 \to K^+\pi^-$ and $D^0 \to K^+\pi^-\pi^+\pi^-$, which can be reached both via a doubly suppressed Cabibbo (DSC) decay and D^0 - $\overline{D^0}$ mixing. Decay time information is therefore required to distinguish the two mechanisms. The present experimental limit is somewhat porous, namely at 90% C.L. one has $r_D \leq 5.0 \times 10^{-3}$ in each of the two decay modes from the E691 experiment [2], assuming no interference between the DSC- and mixing-amplitudes. As pointed out in [49], taking into account this interference the upper limit is degraded, and one gets instead $r_D < 0.019$ from the $K^+\pi^-$ mode and $r_D \leq 0.007$ from the $K^+\pi^-\pi^+\pi^-$ mode [2]. A monte carlo study to estimate the mixing reach at HERA(ep) has been done by Tsipolitis [10], with the conclusions that a factor of 5 improvement in r_D is conceivable, given the assumed luminosity and vertex resolution.

In the workshop, also experimental developments were discussed. Jeff Appel (FNAL) gave an overview of the physics program at Fermilab in the next years with respect to heavy quark physics. Manfred Paulini (LBL) reported on the achievements of CDF and Kerstin Höpfner (CERN) presented a novel, radiation-hard vertex detector using scintillation fibres.

References

[1] J.H. Christenson, J.W. Cronin, V.L. Fitch, and R. Turlay, Phys. Rev. Lett. **13** (1964) 138.

[2] R.M. Barnett et al. (Particle Data Group), Phys. Rev. **D54** (1996) 1.

[3] N. Cabibbo, Phys. Rev. Lett. **10** (1963) 531; M. Kobayashi and K. Maskawa, Prog. Theor. Phys. **49** (1973) 652.

[4] A. Ali, preprint DESY 96-106 [hep-ph/9606324]; to appear in the Proceedings of the XX International Nathiagali Conference on Physics and Contemporary Needs, Bhurban, Pakistan, June 24-July 13, 1995 (Nova Science Publishers, New York, 1996); and in these proceedings.

[5] G. Buchalla, A.J. Buras, and M.E. Lautenbacher, Preprint MPI-Ph/95-104 [hep-ph/9512380]; A.J. Buras, preprint TUM-HEP-255/96 [hep-ph/9609324].

[6] L. Gibbons (CLEO Collaboration), Invited talk at the International Conference on High Energy Physics, Warsaw, ICHEP96 (1996). 6505.

[7] R. Eichler and S. Frixione, companion summary report, these proceedings.

[8] S. Glashow, J. Iliopoulos and L. Maiani, Phys. Rev. **D2** (1970) 1285.

[9] C. Grab, these proceedings.

[10] G. Tsipolitis, these proceedings.

[11] A. Ali and D. London, preprint DESY 96-140, UdeM-GPP-TH-96-45, [hep-ph/9607392], to appear in the *Proc. of QCD Euroconference 96*, Montpellier, July 4-12, 1996; and in these proceedings.

[12] L. Wolfenstein, Phys. Rev. Lett. **51** (1983) 1945.

[13] L. Wolfenstein, Phys. Rev. Lett. **13** (1964) 562.

[14] R.Misuk (HERA-B Collaboration), these proceedings.

[15] C.Shepherd-Themistocleous (HERA-B Collaboration), these proceedings.

[16] R.Misuk (HERA-B Collaboration), these proceedings.

[17] A.J. Buras, M. Jamin and P.H. Weisz, Nucl. Phys. **B347** (1990) 491.

[18] "Combined limit on the B_s^0 oscillation frequency", contributed paper by the ALEPH collaboration to the International Conference on High Energy Physics, Warsaw, ICHEP96 PA08-020 (1996).

[19] J. Thom (HERA-B Collaboration), to be published.

[20] M.S. Alam et al. (CLEO Collaboration), Phys. Rev. Lett. **74** (1995) 2885.

[21] R. Ammar et al. (CLEO Collaboration), Phys. Rev. Lett. **71** (1993) 674.

[22] R. Ammar et al. (CLEO Collaboration), contributed paper to the International Conference on High Energy Physics, Warsaw, 25 - 31 July 1996, CLEO CONF 96-05.

[23] F. Saadi-Lüdemann (HERA-B Collaboration), these proceedings.

[24] T. Inami and C.S. Lim, Prog. Theor. Phys. **65** (1981) 297.

[25] J. Richman, Invited talk at the International Conference on High Energy Physics, Warsaw, ICHEP96 (1996).

[26] A. Ali and C. Greub , Phys. Lett. **B287** (1992) 191.

[27] A. Ali, H.M. Asatrian, and C. Greub, to be published.

[28] P. Singer and D.-X. Zhang, Phys. Lett. **B383** (1996) 351; H.-Y. Cheng and B. Tseng, Phys. Rev. **D53** (1996) 1457.

[29] A. Ali, V.M. Braun and H. Simma, Z. Phys. **C63** (1994) 437.

[30] A. Khodzhamirian, G. Stoll, and D. Wyler, Phys. Lett. **B358** (1995) 129.

[31] A. Ali and V.M. Braun, Phys. Lett. **B359** (1995) 223.

[32] A. Ali, G. F. Giudice and T. Mannel, Z. Phys. **C67** (1995) 417.

[33] A. Ali, T. Mannel and T. Morozumi, Phys. Lett. **B273** (1991) 505.

[34] A.Ali, G. Hiller, L.T. Handoko, and T. Morozumi, (to be published).

[35] S. Abachi et al. (D0 Collaboration), contributed paper to the International Conference on High Energy Physics, Warsaw, ICHEP96 (1996).

[36] A. Ali and E. Pietarinen, Nucl. Phys. **B154** (1979) 519; G. Altarelli et al., Nucl. Phys. **B208** (1982) 365.

[37] P. Cho, M. Misiak, and D. Wyler, Phys. Rev. **D54** (1996) 3329.

[38] P.Kreuzer (HERA-B Collaboration), these proceedings

[39] M. Beneke, G. Buchalla, I. Dunietz, preprint SLAC-PUB-7165 (1996) [hep-ph/9605259].

[40] J.A. Appel, in Proc. of XXVII Int. Conf. on High Energy Physics, Glasgow, 20 - 27 July 1994 (IOP Publishing, 1995); eds.: P.G. Bussey and I.P. Knowles.

[41] S. Egli et al., in Physics at HERA, Vol. 2 (1992) 770, eds.: W. Buchmüller and G. Ingelman.

[42] J.F. Donoghue et al., Phys. Rev. **D33** (1986) 179; H. Georgi, Phys. Lett. **B297** (1992) 353; T. Ohl, G. Ricciardi and E.H. Simmons, Nucl. Phys. **403** (1993) 605. See also L. Wolfenstein, Phys. Lett. **B164** (1985) 170.

[43] For a recent review, see J.L. Hewett, T. Takeuchi and S. Thomas, preprint SLAC-PUB-7088 (1996), [hep-ph/9603391].

[44] Y. Nir and N. Seiberg, Phys. Lett. **B309** (1993) 337; M. Leurer, Y. Nir and N. Seiberg, Nucl. Phys. **B420** (1994) 468.

[45] K.S. Babu, X.-G. He, X.-Q. Li and S. Pakvasa, Phys. Lett. **B205** (1988) 540.

[46] G.C. Branco, P.A. Parada and M.N. Rebelo, Phys. Rev. D52 (1995) 4217.

[47] L.F. Abbott, P. Sikivie and M.B. Wise, Phys. Rev. **D21** (1980) 1393; V. Barger, J.L. Hewett and R.J.N. Phillips, Phys. Rev. **D41** (1990) 3421; Y. Grossman, Nucl. Phys. **B246** (1994) 355.

[48] W. Buchmüller and D. Wyler, Phys. Lett. **B177** (1986) 377; S. Davidson, D. Bailey and B.A. Campbell, Z. Phys. **C61** (1994) 613; M. Leurer, Phys. Rev. Lett. **71** (1993) 1324; Phys. Rev. **D48** (1994) 333.

[49] G. Blaylock, A. Seiden and Y. Nir, Phys. Lett. **B355** (1995) 555.

Rare D Meson Decays at HERA

Christoph Grab*

* Institute for Particle Physics, ETH Zürich, CH-8093 Zürich

Abstract: A status report on the prospects of measuring rare decays of charmed mesons at HERA is given. Based on actual experience with measuring charm at HERA, the sensitivity on limits of rare decays is estimated.

1 Why should we study rare charm decays?

At HERA recent measurements of the charm production cross section in ep collisions at an energy $\sqrt{s_{ep}} \approx 300$ GeV yielded a value of about 1μb [1]. For an integrated luminosity of 250 pb^{-1}, one expects therefore about $25 \cdot 10^7$ produced $c\bar{c}$ pairs, mainly through the boson-gluon fusion process. This corresponds to a total of about $30 \cdot 10^7$ neutral D^o, $10 \cdot 10^7$ charged $D^{\pm}$, some $5 \cdot 10^7$ D_S, and about $5 \cdot 10^7$ charmed baryons. A sizable fraction of this large number of D's is accessible via decays within a HERA detector, and thus should be used to improve substantially our knowledge on charmed particles.

There are several physics issues of great interest. This report will cover however only aspects related to the decay of charmed mesons in rare decay channels, and in this sense provides an update of the discussion presented in an earlier workshop on HERA physics [2]. In the following we shall discuss these aspects, and point out the theoretical expectations. Based on experiences made at HERA with charm studies, we shall present an estimate on the sensitivity for the detailed case study of the search for the rare decay $D^0 \to \mu^+\mu^-$. Other challenging aspects such as the production mechanism and detailed comparisons with QCD calculations, or the use of charmed particles in the extraction of proton and photon parton densities, will not be covered here.

Possibly the most competitive future source of D-mesons is the proposed tau-charm factory. The continuing efforts at Fermilab (photoproduction and hadroproduction experiments), at CERN (LEP) and at Cornell(CESR), which are presently providing the highest sensitivities, are compared with the situation at HERA. In addition, all these different approaches provide useful and complementary information on various properties in the charm system.

2 Decay processes of interest

2.1 Leading decays

The charm quark is the only heavy quark besides the b quark and can be used to test the heavy quark symmetry [3] by measuring form factors or decay constants. Hence, the D-meson containing a charmed quark is heavy as well and disintegrates through a large number of decay channels. The leading decays $c \to s + q\bar{q}$ or $c \to s + \bar{l}\nu$ occur with branching ratios of order a few % and allow studies of QCD mechanisms in a transition range between high and very low energies.

Although experimentally very challenging, the search for the purely leptonic decays $D^{\pm} \to \mu^{\pm}\nu$ and an improved measurement of $D_S^{\pm} \to \mu^{\pm}\nu$ should be eagerly pursued further, since these decays offer direct access to the meson decay constants f_D and f_{D_S}, quantities that can possibly be calculated accurately by lattice gauge theory methods [4],[5].

2.2 Singly Cabibbo suppressed decays (SCSD)

Decays suppressed by a factor $\sin\theta_C$, the socalled singly Cabibbo suppressed decays (SCSD), are of the form $c \to du\bar{d}$ or $c \to s\bar{s}u$. Examples of SCSD, such as $D \to \pi\pi$ or $K\bar{K}$ have been observed at a level of 10^{-3} branching ratio (1.5 and 4.3 $\cdot 10^{-3}$, respectively) [6]. They provide information about the CKM-matrix, and also are background processes to be worried about in the search for rare decays.

2.3 Doubly Cabibbo suppressed decays and $D^0 \longleftrightarrow \bar{D}^0$ mixing

Doubly Cabibbo suppressed decays (DCSD) of the form $c \to d\bar{s}u$ have not been observed up to now[6], with the exception of the mode $BR(D^0 \to K^+\pi^-)$ that has a branching ratio of $(2.9 \pm 1.4) \cdot 10^{-4}$. The existing upper bounds are at the level of a few 10^{-4}, with branching ratios expected at the level of 10^{-5}. These DCSD are particularly interesting from the QCD-point of view, and quite a few predictions have been made[7]. DCSD also act as one of the main background processes to the $D^0 \leftrightarrow \bar{D}^0$ mixing and therefore must be well understood, before the problem of mixing itself can be successfully attacked.

As in the neutral Kaon and B-meson system, mixing between the D^0 and the $\bar{D}^0$ is expected to occur (with $\Delta C = 2$). The main contribution is expected due to long distance effects, estimated to be as large as about $r_D \sim 5 \cdot 10^{-3}$ [8], while the standard box diagram yields $r_D \sim 10^{-5}$ [9]. Here r_D is the mixing parameter $r_D \simeq (1/2) \cdot (\Delta M/\Gamma)^2$, with contributions by the DCSD neglected. Recall that the DCSD poses a serious background source in case only the time-integrated spectra are studied. The two sources can however be better separated, if the decay time dependence of the events is recorded separately (see e.g. [10]). More details on the prospect of measuring mixing at HERA are given in [11].

2.4 Flavour Changing Neutral Currents (FCNC)

An important feature of the standard model is that *flavour changing neutral currents (FCNC with $\Delta C = 1$)* only occur at the one loop level in the SM *i.e.* through short distance contributions, such as e.g. in penguin and box diagrams as shown in figs.1 and 2. These are transitions of the form $s \to d + N$ or $c \to u + N$, where N is a non-hadronic neutral state such as γ or $l\bar{l}$, and give rise to the decays $D \to \rho\gamma$, $D^0 \to \mu^+\mu^-$, $D^+ \to \pi^+\mu^+\mu^-$ etc. Although the relevant couplings are the same as those of leading decays, their rates are very small as they are suppressed by the GIM mechanism [12] and the unfavourable quark masses within the loops. The SM-prediction for the branching ratios are of order 10^{-9} for $D^0 \to Xl^+l^-$ and of $O(10^{-15})$ for $D^0 \to l^+l^-$, due to additional helicity suppression. A summary of the expected branching ratios obtained from calculations of the loop integrals ([13], [7], [2], [14]) using also the QCD-short distance corrections available [15] is given in table 1.

However, FCNC are sensitive to new, heavy particles in the loops, and above all, to new physics in general.

In addition to these short distance loop diagrams, there are contributions from long distance effects, which might be even larger by several orders of magnitude[14]. To mention are photon pole amplitudes (γ-pole) and vector meson dominance (VMD) induced processes. The γ-pole model (see fig.3) in essence is a W-exchange decay with a virtual photon radiating from one of the quark lines. The behaviour of the amplitude depends on the spin state of the final state particle (vector V or pseudoscalar P). The dilepton mass distribution for $D \to Vl^+l^-$ modes peaks at zero (small Q^2) since the photon prefers to be nearly real. On the other hand, the pole amplitude for $D \to Pl^+l^-$ decays vanishes for small dilepton masses because $D \to P\gamma$ is forbidden by angular momentum conservation. The VMD model (see fig.3b) proceeds through the decay $D \to XV^0 \to Xl^+l^-$. The intermediate vector meson V^0 (ρ, ω, ϕ) mixes with a virtual photon which then couples to the lepton pair. The dilepton mass spectrum therefore will exhibit poles at the corresponding vector meson masses due to real V^0 mesons decaying.

Observation of FCNC processes at rates that exceed the long distance contributions hence opens a window into physics beyond the standard model. Possible scenarios include leptoquarks or heavy neutral leptons with sizable couplings to e and μ.

A measurement of such long distance contributions in the charm sector is inherently of interest, as it can be used to estimate similar effects in the bottom sector [16], e.g. for the decay $b \to s\gamma$, which was seen at the level of $2.3 \cdot 10^{-4}$. A separation of short and long range contributions would allow e.g. a determination of $|V_{td}/V_{ts}|$ from the ratio $BR(B \to \rho\gamma)/BR(B \to K^*\gamma)$ and bears as such a very high potential.

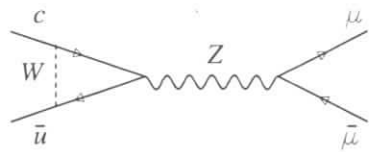

Figure 1: *Example of an FCNC process in the standard model at the loop level:* $D^0 \to \mu^+\mu^-$.

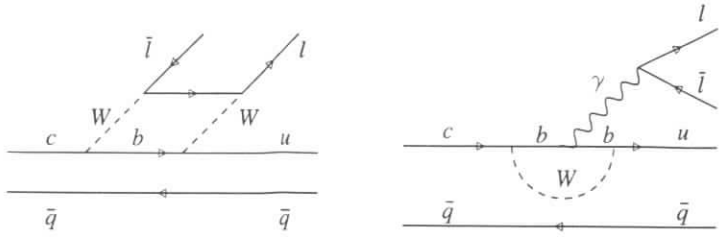

Figure 2: *FCNC processes: short range contributions due to box diagrams (a) or penguin diagrams (b).*

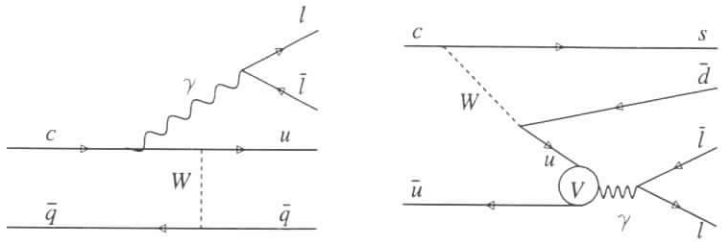

Figure 3: *FCNC processes : long range contributions due to γ-pole amplitude (a) and vector meson dominance (b).*

2.5 Forbidden decays

Decays which are not allowed to all orders in the standard model, the *forbidden* decays, are exciting signals of new physics. Without claim of completeness, we shall list here some of the more important ones:

- Lepton number (L) or lepton family (LF) number violation (LFNV) in decays such as $D^0 \to \mu e$, $D^0 \to \tau e$. It should be strongly emphasized that decays of D-mesons test couplings complementary to those effective in K- or B-meson decays. Furthermore, the charmed quark is the only possible charge 2/3 quark which allows detailed investigations of unusual couplings. These are often predicted to occur in models with i) technicolour [17]; ii) compositeness [18]; iii) leptoquarks [19] [20]; (see e.g. fig.4a and b); this can include among others non-SU(5) symmetric flavour-dependent couplings (u to $l^{\pm}$, and d to ν), which would forbid decays of the sort $K_L \to \mu\mu$, μe, while still allowing for charm decays; iv) massive neutrinos (at the loop level) in an extended standard model; v) superstring inspired phenomenological models e.g. MSSM models with a Higgs doublet; vi) scalar exchange particles that would manifest themselves e.g. in decays of the form $D^0 \to \nu\bar{\nu}$.

Decay mode	Expected branching ratio
$c \to u\gamma$	$10^{-15} - 10^{-14}$
$D \to \rho\gamma$	10^{-7}
$D \to \gamma\gamma$	10^{-10}
$c \to ull$	$5 \cdot 10^{-8}$
$D^+ \to \pi^+e^+e^-$	10^{-8}
$D^0 \to \mu^+\mu^-$	10^{-19}

Table 1: Expectations for branching ratios of loop processes based on SM calculations, hereby assuming the BR of both $D \to \rho\rho$ and $D \to \rho\pi$ to be below 10^{-3}.

- Further models feature *horizontal* interactions, mediated by particles connecting u and c or d and s quarks (see e.g. fig.4a). They appear with similar signatures as the doubly Cabibbo suppressed decays.
- Baryon number violating decays, such as $D^0 \to pe^-$ or $D^+ \to ne^-$. They are presumably very much suppressed, although they are not directly related to proton decay.
- The decay $D \to \pi\gamma$ is absolutely forbidden by gauge invariance and is listed here only for completeness.

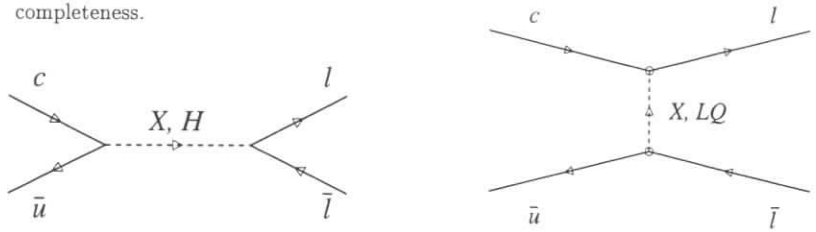

Figure 4: *FCNC processes or LFNV decays, mediated by the exchange of a scalar particle X or a particle H mediating "horizontal interactions", or a leptoquark LQ.*

The clean leptonic decays make it possible to search for leptoquarks. If they do not couple also to quark-(anti)quark pairs, they cannot cause proton decay but yield decays such as $K \to \bar{l}_1 l_2$ or $D \to \bar{l}_1 l_2$. In the case of scalar leptoquarks there is no helicity suppression and consequently the experimental sensitivity to such decays is enhanced. Let us emphasize here again, that decays of D-mesons are complementary to those of Kaons, since they probe different leptoquark types. To estimate the sensitivity we write the effective four-fermion coupling as (g^2_{eff}/M^2_{LQ}), and obtain

$$\frac{(M_{LQ} \ / \ 1.8\ TeV)}{g_{eff}} \geq \sqrt[4]{\frac{10^{-5}}{BR(D^0 \to \mu^+\mu^-)}}. \qquad (1)$$

Here g_{eff} is an effective coupling and includes possible mixing effects. Similarly, the decays $D^+ \to e^+\nu$, $D^+ \to \pi^+e^+e^-$ can be used to set bounds on M_{LQ}. With the expected sensitivity, one can probe heavy exchange particles with masses in the 1 (TeV/g_{eff}) range.

Any theory attempting to explain the hadron-lepton symmetry or the "generation" aspects of the standard model will give rise to new phenomena connected to the issues mentioned here. Background problems make it quite difficult to search for signs of them at high energies; therefore precision experiments at low energies (like the highly successful μ-, π- or K-decay experiments) are very suitable to probe for any non-standard phenomena.

3 Sensitivity estimate for HERA

In this section we present an estimate on the sensitivity to detect the decay mode $D^0 \rightarrow \mu^+\mu^-$. As was pointed out earlier, this is among the cleanest manifestation of FCNC or LFNV processes [13]. We base the numbers on our experience gained in the analysis of the 1994 data, published in [1]. There the D-meson decay is measured in the decay mode $D^{*+} \rightarrow D^0\pi_s^+$; $D^0 \rightarrow K^-\pi^+$, exploiting the well established $D^{*+}(2010)$ tagging technique[21]. In analogy, we assume for the decay chain $D^{*+} \rightarrow D^0\pi_s^+; D^0 \rightarrow \mu^+\mu^-$, a similar resolution of $\sigma \approx 1.1$ MeV in the mass difference $\Delta M = M(\mu^+\mu^-\pi_s^+) - M(\mu^+\mu^-)$ as in [1]. In order to calculate a sensitivity for the $D^0 \rightarrow \mu^+\mu^-$decay branching fraction we make the following assumptions:

i) luminosity $L = 250\ pb^{-1}$; ii) cross section $\sigma(ep \rightarrow c\bar{c}X)\ |_{\sqrt{s}_{ep}\approx 300; Q^2<0.01} = 940\ nb$; iii) reconstruction efficiency $\epsilon_{reconstruction} = 0.5$; iv) trigger efficiency $\epsilon_{trigger} = 0.6$; this is based on electron-tagged events, and hence applies to photoproduction processes only. v) The geometrical acceptance A has been properly calculated by means of Monte Carlo simulation for both decay modes $D^0 \rightarrow K^-\pi^+$ and $D^0 \rightarrow \mu^+\mu^-$ for a rapidity interval of $|\ \eta\ | < 1.5$. For the parton density functions the GRV parametrizations were employed, and the charm quark mass was assumed to be $m_c = 1.5$. We obtained
$A = 6\%$ for $p_T(D^*) > 2.5$ (for $K^-\pi^+$)
$A = 18\%$ for $p_T(D^*) > 1.5$ (for $K^-\pi^+$)
$A = 21\%$ for $p_T(D^*) > 1.5$ (for $\mu^+\mu^-$)

A direct comparison with the measured decays $N_{K\pi}$ into $K^-\pi^+$ [1] then yields the expected number of events $N_{\mu\mu}$ and determines the branching ratio to

$$BR(D^0 \rightarrow \mu^+\mu^-) = BR(D^0 \rightarrow K^-\pi^+) \cdot \frac{N_{\mu\mu}}{L_{\mu\mu}} \cdot \frac{L_{K\pi}}{N_{K\pi}} \cdot \frac{A(p_T > 2.5)}{A(p_T > 1.5)}$$

Taking the numbers from [1] $N_{K\pi} = 119$ corresponding to an integrated luminosity of $L_{K\pi} = 2.77\ pb^{-1}$, one obtains

$$\boxed{BR(D^0 \rightarrow \mu^+\mu^-) = 1.1 \cdot 10^{-6} \cdot N_{\mu\mu}}$$

In the case of *NO* events observed, an upper limit on the branching ratio calculated by means of Poisson statistics ($N_{\mu\mu} = 2.3$), yields a value of $BR(D^0 \rightarrow \mu^+\mu^-) < 2.5 \cdot 10^{-6}$ at 90% c.l.

In the case of an observation of a handful events e.g. of $O(N_{\mu\mu} \approx 10)$, one obtains $BR(D^0 \rightarrow \mu^+\mu^-) \approx 10^{-5}$. This can be turned into an estimate for the mass of a potential leptoquark mediating this decay according to eqn.1, and yields a value of $M_{LQ}/g_{eff} \approx 1.8$ TeV.

4 Background considerations

4.1 Background sources and rejection methods

The most prominent sources of background originate from i) genuine leptons from semileptonic B- and D-decays, and decay muons from K, π decaying in the detector; ii) misidentified hadrons, *i.e.* π, K, from other decays, notably leading decays and SCSD; and iii) combinatorial background from light quark processes.

The background can be considerably suppressed by applying various combinations of the following techniques:

Mode	BR (90% C.L.)	Interest	Reference
$\frac{\tau=(D^0\rightarrow\mu^+X)}{(D^0\rightarrow\mu^-X)}$	$1.2 * 10^{-2}$	$\Delta C = 2$, Mix	BCDMS 85
	$5.6 * 10^{-3}$	$\Delta C = 2$, Mix	E615 86
$\frac{(D^0\rightarrow\bar{D}^0\rightarrow K^+\pi^-)}{(D^0\rightarrow K^+\pi^-+K^-\pi^+)}$	$4 * 10^{-2}$	$\Delta C = 2$, Mix	HRS 86
	$= 0.01^*$	$\Delta C = 2$, Mix	MarkIII 86
	$1.4 * 10^{-2}$	$\Delta C = 2$, Mix	ARGUS 87
	$3.7 * 10^{-3}$	$\Delta C = 2$, Mix	E691 88
$D^0 \rightarrow \mu^+\mu^-$	$7.0 * 10^{-5}$	FCNC	ARGUS 88
$D^0 \rightarrow \mu^+\mu^-$	$3.4 * 10^{-5}$	FCNC	CLEO 96
$D^0 \rightarrow \mu^+\mu^-$	$1.1 * 10^{-5}$	FCNC	E615 86
$D^0 \rightarrow e^+e^-$	$1.3 * 10^{-4}$	FCNC	MarkIII 88
$D^0 \rightarrow e^+e^-$	$1.3 * 10^{-5}$	FCNC	CLEO 96
$D^0 \rightarrow \mu^\pm e^\mp$	$1.2 * 10^{-4}$	FCNC, LF	MarkIII 87
$D^0 \rightarrow \mu^\pm e^\mp$	$1.0 * 10^{-4}$	FCNC, LF	ARGUS 88
$D^0 \rightarrow \mu^\pm e^\mp$	$(1.9 * 10^{-5})$	FCNC, LF	CLEO 96
$D^0 \rightarrow \bar{K}^0e^+e^-$	$1.7 * 10^{-3}$		MarkIII 88
$D^0 \rightarrow \bar{K}^0e^+e^-/\mu^+\mu^-/\mu^\pm e^\mp$	$1.1/6.7/1. * 10^{-4}$	FCNC, LF	CLEO 96
$D^0 \rightarrow \bar{K}^{*0}e^+e^-/\mu^+\mu^-/\mu^\pm e^\mp$	$1.4/11.8/1. * 10^{-4}$	FCNC, LF	CLEO 96
$D^0 \rightarrow \pi^0e^+e^-/\mu^+\mu^-/\mu^\pm e^\mp$	$0.5/5.4/.9 * 10^{-4}$	FCNC, LF	CLEO 96
$D^0 \rightarrow \eta e^+e^-/\mu^+\mu^-/\mu^\pm e^\mp$	$1.1/5.3/1. * 10^{-4}$	FCNC, LF	CLEO 96
$D^0 \rightarrow \rho^0e^+e^-/\mu^+\mu^-/\mu^\pm e^\mp$	$1./4.9/0.5 * 10^{-4}$	FCNC, LF	CLEO 96
$D^0 \rightarrow \omega e^+e^-/\mu^+\mu^-/\mu^\pm e^\mp$	$1.8/8.3/1.2 * 10^{-4}$	FCNC, LF	CLEO 96
$D^0 \rightarrow \phi e^+e^-/\mu^+\mu^-/\mu^\pm e^\mp$	$5.2/4.1/0.4 * 10^{-4}$	FCNC, LF	CLEO 96
$D^0 \rightarrow K^+\pi^-\pi^+\pi^-$	< 0.0015	DC	CLEO 94
$D^0 \rightarrow K^+\pi^-\pi^+\pi^-$	< 0.0015	DC	E691 88
$D^0 \rightarrow K^+\pi^-$	$= 0.00029$	DC	CLEO 94
$D^0 \rightarrow K^+\pi^-$	< 0.0006	DC	E691 88

Table 2: Experimental limits at 90% c.l. on rare D^0-meson decays (except where indicated by =). Here L, LF, FCNC, DC and Mix denote lepton number and lepton family number violation, flavour changing neutral currents, doubly Cabibbo suppressed decays and mixing, respectively.

- D^*-tagging technique [21]:
  A tight window on the mass difference ΔM is the most powerful criterium.

- Tight kinematical constraints ([22],[2]):
  Misidentification of hadronic D^0 2-body decays such as $D^0 \rightarrow K^-\pi^+(3.8\%$ BR), $D^0 \rightarrow \pi^+\pi^-(0.1\%$ BR) and $D^0 \rightarrow K^+K^-(0.5\%$ BR) are suppressed by more than an order of magnitude by a combination of tight windows on both ΔM and M_D^{inv}. Final states containing Kaons can be very efficiently discriminated, because the reflected M^{inv} is sufficiently separated from the true signal peak. However, this is not true for a pion-muon or pion-electron misidentification. The separation is slightly better between $D^0 \rightarrow e^+e^-$ and $D^0 \rightarrow \pi^+\pi^-$.

- Vertex separation requirements for secondary vertices:

Background from light quark production, and of muons from K- and π- decays within the detector are further rejected by exploiting the information of secondary vertices (e.g. decay length separation, pointing back to primary vertex etc.).

- Lepton identification (example H1) :
  Electron identification is possible by using dE/dx measurements in the drift chambers, the shower shape analysis in the calorimeter (and possibly the transition radiators information). Muons are identified with the instrumented iron equipped with limited streamer tubes, with the forward muon system, and in combination with the calorimeter information. The momentum has to be above $\sim$ 1.5 to 2 GeV/c to allow the μ to reach the instrumented iron. Thus, the decay $D^0 \to \mu^+\mu^-$ suffers from background contributions by the SCSD mode $D^0 \to \pi^+\pi^-$, albeit with a known $BR = 1.6 \cdot 10^{-3}$; here μ-identification helps extremely well. An example of background suppression using the particle ID has been shown in ref.[2], where a suppression factor of order $O(100)$ has been achieved.

- Particle ordering methods exploit the fact that the decay products of the charmed mesons tend to be the *leading* particles in the event (see e.g. [23]). In the case of observed jets, the charmed mesons are expected to carry a large fraction of the jet energy.

- Event variables such as e.g. the total transverse energy $E_{transverse}$ tend to reflect the difference in event topology between heavy and light quark production processes, and hence lend themselves for suppression of light quark background.

4.2 Additional experimental considerations

- Further possibilities to enhance overall statistics are the usage of inclusive decays (no tagging), where the gain in statistics is expected to be about $\frac{N(allD^0)}{N(D^0 from D^*)} = 0.61/0.21 \approx 3$, however on the the cost of higher background contributions.

- In the decays $D^0 \to ee$ or $D^0 \to \mu e$ one expects factors of 2 to 5 times better background rejection efficiency.

- Trigger : A point to mention separately is the trigger. To be able to measure a BR at the level of 10^{-5}, the event filtering process has to start at earliest possible stage. This should happen preferably at the first level of the hardware trigger, because it will not be feasible to store some 10^{+7} events on permanent storage to dig out the few rare decay candidates. This point, however, has up to now not yet been thoroughly studied, let alone been implemented at the hardware trigger level.

5 Status of sensitivity in rare charm decays

Some of the current experimental upper limits at 90% c.l. on the branching ratios of rare D decays are summarised in tables 2 and 3 according to [6].

Taking the two-body decay $D^0 \to \mu^+\mu^-$ to be the sample case, a comparison of the achievable sensitivity on the upper limit on branching fraction $B_{D^0 \to \mu^+\mu^-}$ at 90% c.l. is summarized in table 4 for different experiments, assuming that NO signal events are being detected (see

Mode	BR (90% C.L.)	Interest	Reference
$D^+ \to \pi^+e^+e^-$	$6.6 * 10^{-5}$	FCNC	E791 96
$D^+ \to \pi^+\mu^+\mu^-$	$1.8 * 10^{-5}$	FCNC	E791 96
$D^+ \to \pi^+\mu^+e^-$	$3.3 * 10^{-3}$	LF	MarkII 90
$D^+ \to \pi^+\mu^-e^+$	$3.3 * 10^{-3}$	LF	MarkII 90
$D^+ \to \pi^-e^+e^+$	$4.8 * 10^{-3}$	L	MarkII 90
$D^+ \to \pi^-\mu^+\mu^+$	$2.2 * 10^{-4}$	L	E653 95
$D^+ \to \pi^-\mu^+e^+$	$3.7 * 10^{-3}$	L+LF	MarkII 90
$D^+ \to Kll$	similar	L+LF	MarkII 90
$c \to X\mu^+\mu^-$	$1.8 * 10^{-2}$	FCNC	CLEO 88
$c \to Xe^+e^-$	$2.2 * 10^{-3}$	FCNC	CLEO 88
$c \to X\mu^+e^-$	$3.7 * 10^{-3}$	FCNC	CLEO 88
$D^+ \to \phi K^+$	$1.3 * 10^{-4}$	DC	E687 95
$D^+ \to K^+\pi^+\pi^-$	$= 6.5 * 10^{-4}$	DC	E687 95
$D^+ \to K^+K^+K^-$	$1.5 * 10^{-4}$	DC	E687 95
$D^+ \to \mu^+\nu_\mu$	$7.2 * 10^{-4}$	f_D	MarkIII 88
$D_S \to \pi^-\mu^+\mu^+$	$4.3 * 10^{-4}$	L	E653 95
$D_S \to K^-\mu^+\mu^+$	$5.9 * 10^{-4}$	L	E653 95
$D_S \to \mu^+\nu_\mu$	$= 9 * 10^{-4}$	$f_{D_S} = 430$	BES 95

Table 3: Selection of experimental limits at 90% c.l. on rare D^+- and D_s-meson decays[6] (except where indicated by =).

[24] and [6]). Note that the sensitivity reachable at HERA is compatible with the other facilities, provided the above assumed luminosity is actually delivered. This does not hold for a proposed τ-charm factory, which - if ever built and performing as designed - would exceed all other facilities by at least two orders of magnitude ([25]).

The status of competing experiments at other facilities is the following :

- SLAC : e^+e^- experiments : Mark-III, MARK-II, DELCO : stopped.

- CERN : fixed target experiments : ACCMOR, E615, BCDMS, CCFRC : stopped.
  LEP-experiments : previously ran at the Z^0-peak; now they continue with increased $\sqrt{s}$, but at a *reduced* σ for such processes;

- Fermilab (FNAL) : the photoproduction experiments E691/TPS and hadroproduction experiments E791 and E653 are stopped, with some analyses being finished based on about $O(10^5)$ reconstructed events. In the near future highly competitive results are to be expected from the γp experiments E687 and its successor E831 (FOCUS), based on an statistics of about $O(10^5)$ and an estimated 10^6 reconstructed charm events, respectively. But also the hadroproduction experiment E781 (SELEX) is anticipated to reconstruct some 10^6 charm events within a few years.

- DESY : ARGUS e^+e^- : stopped, final papers emerging now.
  HERA-B : With a very high cross section of $\sigma(pN \to c\bar{c}) \approx 30\mu$b at $\sqrt{s} = 39$ GeV and an extremely high luminosity, a total of up to 10^{12} $c\bar{c}$-events may be produced. Although

	SPEAR	BEPC	E691	LEP	$\tau - cF$	CLEO	HERA
σ_{cc} (nb)	5.8	8.6	500	4.5	5.8	1.3	$\sigma_{ep} = 940$
$L(pb^{-1})$	9.6	30	0.5	150	10^4	3850	250
N_D	$6 * 10^4$	$3 * 10^5$	$2.5 * 10^5$	10^6	$6 * 10^7$	$5 * 10^6$	$2.4 * 10^8$
$\epsilon \cdot A$	0.4	0.5	0.25	0.05	0.5	0.1	0.06
N_{BGND}	O(0)	O(1)	O(10)	O(10)	O(1)	O(1)	S/N≈1
$\frac{\sigma_{charm}}{\sigma_{total}}$	1	0.4	0.01	0.1	1	0.1	0.1
$B_{D^0 \to \mu^+\mu^-}$	$1.2 * 10^{-4}$	$2 * 10^{-5}$	$4 * 10^{-5}$	$5 * 10^{-5}$	$5 * 10^{-8}$	$3.4 * 10^{-5}$	$2.5 * 10^{-6}$

Table 4: Comparison of estimated sensitivity to the sample decay mode $D^0 \to \mu^+\mu^-$ for different facilities or experiments.

no detailed studies exist so far, a sensitivity of order 10^{-5} to 10^{-7} might be expected, depending on the background rates.

- CESR : CLEO is continuing steadily to collect data, and above all is the present leader in sensitivity for many processes (see table 2).
- BEPC : BES has collected data at $\sqrt{s} = 4.03$ GeV (and 4.14 GeV), and is continuing to do so; BES will become competitive as soon as enough statistics is available, because the background conditions are very favourable.
- τ-charm factory : The prospects for a facility being built in China (Beijing) are uncertain. If realized, this is going to be the most sensitive place to search for rare charm decays. Both, kinematical constraints (e.g. running at the $\psi''(3700)$) and the missing background from non-charm induced processes will enhance its capabilities.

6 Summary

D-meson decays offer a rich spectrum of interesting physics; their rare decays may provide information on new physics, which is complementary to the knowledge stemming from K-meson and B-decays. With the prospect of order a few times 10^8 produced charmed mesons per year, HERA has the potential to contribute substantially to this field. Further competitive results can be anticipated from the fixed target experiments at Fermilab or from a possible τ-charm factory.

For the rare decay $D^0 \to \mu^+\mu^-$investigated here we expect at least an order of magnitude improvement in sensitivity over current results (see table given above) for a total integrated luminosity of $\int Ldt = 250$ pb^{-1}, the limitation here being statistical. An extrapolation to even higher luminosity is rather difficult without a very detailed numerical simulation, because at some (yet unknown) level the background processes will become the main limiting factor for the sensitivity, rendering sheer statistics useless. For this, a good tracking resolution, excellent particle identification (e, μ, π, K, p) and a high resolution for secondary vertices is required to keep the systematics under control, and either to unambigously identify a signal of new physics, or to reach the ultimate limit in sensitivity.

References

[1] S. Aid *et al.*, H1 collab., DESY 96-055, submitted to Nucl. Phys. 1996; M. Derrick *et al.*, ZEUS collab., Phys. Lett. B349, (1995), 225.

[2] Proc. 'Physics at HERA', Eds. W. Buchmüller, G. Ingelman, DESY 1992, p. 770.

[3] N. Isgur and M. Wise, Phys.Lett. **B**232, (1989) 113; ibid **B**237, (1990) 527; M. Wise Nucl.Phys. **A**527, (1991) 209; M. Neubert, V. Rieckert, B. Stech and A. Xu, Heidelberg Uni. preprint HD-THEP-91-28, 1991.

[4] C. Alexandrou *et al.*, Phys.Lett. **B**256, (1991) 60;
and G. Martinelli in Proc. of LP-HEP conf. Geneva, 1991.

[5] H. Wittig, Preprint DESY 96-110, 1996.

[6] Review of Particle Properties; Phys. Rev. **D**54, (1996) 1.

[7] I. Bigi, F. Gabbiani and A. Masiero, Z. Phys. **A**48, (1990) 633; I. I. Bigi in SLAC report 343, 1989; ibid UND-HEP-88-01, (1988); UND-HEP-89-01, (1989).

[8] L. Wolfenstein, Phys. Lett. **B**164, (1985) 170.

[9] L. L. Chau, Phys. Rep. 95, (1983) 1.

[10] J. C. Anjos *et al.*, Phys. Rev. Lett. 60, (1988) 1239.

[11] G. Tsipolitis, these proceedings.

[12] S. Glashow, J. Iliopoulos and L. Maiani, Phys. Rev. D**2**, (1970) 1285.

[13] R. S. Willey in Proc. of τ-charm factory workshop, SLAC report. 343, 1989, p.196.

[14] A. J. Schwartz, Mod. Phys. Lett. A8, (1993) 967; J. L. Hewett, SLAC-PUB-95-6821.

[15] see e.g. G. Cella *et al.*, Phys. Lett. **B**258, (1991) 212.
and B. Grinstein *et al.*, Phys. Lett. **B**202, (1988) 138.

[16] E. Golowich and S. Pakvasa, Phys. Rev. D**51**, (1995) 1215.

[17] A. Masiero *et al.*, Phys. Lett. **B**115, (1982) 229.

[18] W. Buchmüller, Proc. of Schladming School 1985, p.517.

[19] W. Buchmüller, D. Wyler, Phys. Lett. **B**177, (1986) 377.

[20] B. A. Campbell *et al.*, Int. J. Mod. Phys. A2, (1987) 831.

[21] G. J. Feldman *et al.*, Phys. Rev. Lett. 38, (1977) 1313.

[22] C. Grab in Proc. of Rare Decay Symposium, Vancouver, Dec. 1988; World Scient. 1989.

[23] S. Aid *et al.*, H1 collab., DESY 96-138, submitted to Z. f. Phys.

[24] C. Grab in Proc. of Int. Europhys. conf. on HEP, EPS Vol.1, p.349, 1987.

[25] R. H. Schindler in Proc. of τ-charm factory workshop, Stanford, SLAC report. 343, 1989.

$D^0 - \bar{D}^0$ mixing at the ep-collider HERA

Georgios Tsipolitis[a]

[a] ETH-Zürich, CH 8093 Zürich, Switzerland

Abstract: The sensitivity to $D^0 - \bar{D}^0$ mixing at the ep-collider HERA is evaluated. It is found that with an integrated luminosity of about 600 pb^{-1}, a limit for the $D^0 - \bar{D}^0$ mixing which is more than a factor 5 better than the existing limits can be reached. Furthermore, it can establish a more accurate measurement of the Doubly Cabbibo Suppressed Decays.

1 Introduction

It is known in particle physics that mixing between a neutral P^0 meson and its CP-conjugate state $\bar{P}^0$ can occur. Up to now mixing has been observed only in the kaon and B-meson system and is expected to be present at the D-meson system as well.

One can characterize $D^0\bar{D}^0$ mixing in terms of two dimensionless variables: $x = \delta m/\Gamma_+$ and $y = \Gamma_-/\Gamma_+$, where the quantities $\Gamma_\pm$ and δm are defined by $\Gamma_\pm = (\Gamma_1 \pm \Gamma_2)/2$ and $\delta m = m_2 - m_1$ with m_i, Γ_i $(i = 1, 2)$ being the masses and decay rates of the two CP eigenstates. One usually defines the parameter r as

$$r \equiv \frac{\int_0^\infty \mathcal{P}(D^0 \to \bar{D}^0; t)dt}{\int_0^\infty \mathcal{P}(D^0 \to D^0; t)dt} = \frac{N_{mixed\ evts}}{N_{unmixed\ evts}}$$

with $\int_0^\infty \mathcal{P}(\mathcal{X}; t)dt$ being the probability that the process $\mathcal{X}$ occurs. Assuming a small mixing, i.e. $\delta m, \Gamma_- \ll \Gamma_+$ we have $r = (x^2 + y^2)/2$. Mixing can be caused either by $x \neq 0$ (meaning that the mixing is genuinly caused by the $D^0 - \bar{D}^0$ transition) or by $y \neq 0$ (meaning that the mixing is caused by the fact that the fast decaying component quickly disappears, leaving the slow decaying component which is a mixture of D^0 and $\bar{D}^0$).

There are big uncertainties on the theoretical estimates of r. The predicted rate of the $D^0\bar{D}^0$ mixing in the Standard Model is $r < 10^{-7}$ [1]. However, long distance effects expect r to be of the order of 10^{-4}[2]. r can be measured experimentally by measuring the ratio

$$r = \frac{N(D^0 \to \bar{D}^0 \to X)}{N(D^0 \to X)}.$$

At HERA, the charm production cross section in ep collisions at an energy of $\sqrt{s} \sim 300GeV$, was found to be about 1 μb [3]. This corresponds to about 10^8 $c\bar{c}$ pairs produced per 100 pb^{-1} collected luminosity. A more detailed report on the production and the expected number of

events for the different decay channels can be found in the article of R. Eichler and S. Frixione in these proceedings.

In this report an attempt is made to evaluate the sensitivity to measure $D^0\bar{D}^0$ mixing at a high luminosity HERA run. A Monte Carlo simulation of the H1 detector [4] equipped with a silicon vertex detector [5] was used. The events were generated with AROMA 2.1 [6] and the study corresponds to an integrated luminosity of about 600 pb^{-1}.

2 $D^0 - \bar{D}^0$ Mixing Studies with H1

The possibility of a mixing signal is studied by looking at the decay chain[1] $D^{*+} \to D^0\pi_s^+$. The charge of the charm quark in the D^0 at production is tagged through the slow pion, π_s, of the decay $D^{*+} \to D^0\pi_s^+$. Two ways of tagging the charge of the charm quark in the D^0 at the time of its decay are used. In the first, the decay $D^0 \to K^+\mu^-\nu$ is used, where the charge of the lepton is identified and in the second the decay $D^0 \to K^+\pi^-$ where the charge of the kaon is taken. The first decay mode is free of Double Cabibbo Suppressed Decays (DCSD). One would measure the ratio

$$r = \frac{D^{*+} \to D^0\pi_s^+ \to \bar{D}^0\pi_s^+ \to (K^+\ell^-\nu)\pi_s^+}{D^{*+} \to D^0\pi_s^+ \to (K^-\ell^+\nu)\pi_s^+}.$$

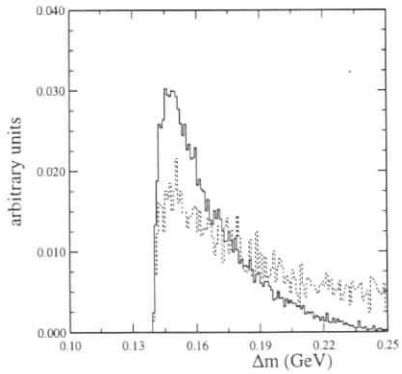

Figure 1: Monte Carlo simulation of mass difference $M(K\mu\pi_s) - M(K\mu)$ for the correct π_s assignment (full histogram) and the π_s from the wrong D^* decay (dashed histogram). The two histograms are normalized to the same number of events.

The Monte Carlo simulation has shown that an irreducible background of order 5% comes from events with two D*-mesons produced in the same event. The slow pion π_s^+ from the D^{*+} decay

[1] Henceforth, charge conjugate states are always implicitly included.

can be combined with a $\bar{D}^0$ from the D^{*-} decay. This is illustrated in Figure 1, where the mass difference $\Delta M = M(K\mu\pi_s) - M(K\mu)$ is ploted for the correct π_s assignment (full histogram) and the π_s from the wrong D^* decay (dashed histogram). Both histograms are normalized to the same number of events. The background clearly peaks at the same place as the signal and we consider this background as very difficult to subtract on a statistical basis. This background is absent in pion-production of charm on a nucleon, where single charmed mesons are produced [7]. An attempt was made to get information about the charge of the second charm in the event by requiring an additional lepton in the event. This way one could use the charge of the two leptons to tag a possible mixed event. The tag of the second lepton reduces the statistics considerably and the range of R_{mix} that can be reached is not competitive.

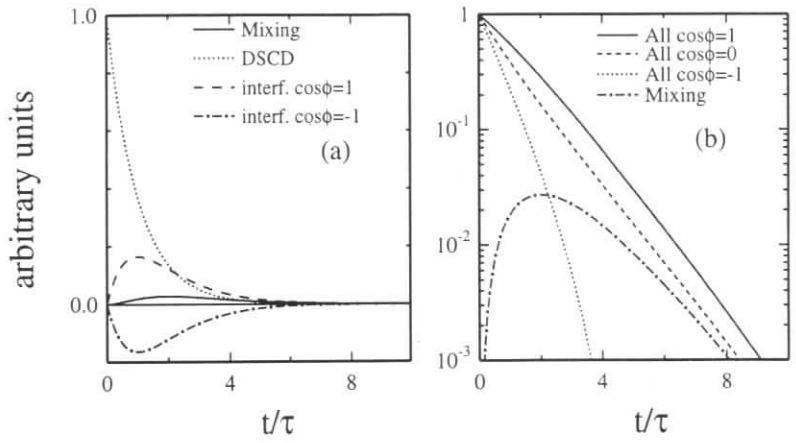

Figure 2: (a) The expected distributions for the DSCD term, the mixing term and the interference term for $\cos\phi = -1, 1$ contributing to $R(t)$ assuming $R_{DCSD} = 1$ and $R_{mix} = 0.1 \cdot R_{DCSD}$. (b) The expected distributions for $R(t)$ for $\cos\phi = -1, 0, 1$ assuming $R_{DCSD} = 1$ and $R_{mix} = 0.1 \cdot R_{DCSD}$.

The second method measures the time dependence of the ratio

$$R(t) = \frac{D^{*+} \to D^0\pi_s^+ \to (K^+\pi^-)\pi_s^+}{D^{*+} \to D^0\pi_s^+ \to (K^-\pi^+)\pi_s^+},$$

where $D^{*+} \to D^0\pi_s^+ \to (K^-\pi^+)\pi_s^+$ is the Cabbibo allowed decay and $D^{*+} \to D^0\pi_s^+ \to (K^+\pi^-)\pi_s^+$ is the sum of the decays with $D^0\bar{D}^0$ mixing and the DCS decays. One also expects interference between the DCSD and the decays through $D^0\bar{D}^0$ mixing. Therefore $R(t)$ can be written as :

$$R(t/\tau) \propto (R_{DCSD}(1 + \sqrt{2\alpha}\frac{t}{\tau}\cos\phi + \frac{1}{2}R_{mix}(\frac{t}{\tau})^2)e^{-\frac{t}{\tau}})$$

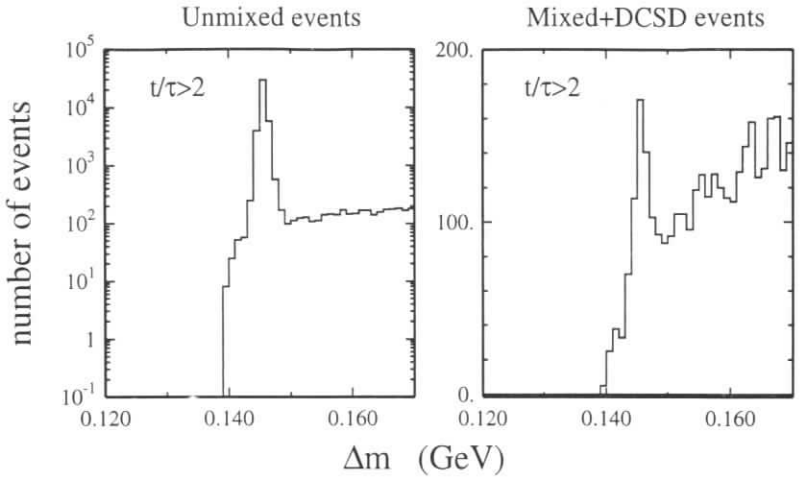

Figure 3: Monte Carlo simulation of mass difference $\Delta m = M(K\pi\pi_s) - M(K\pi)$ for 600 pb^{-1} and $t/\tau > 2$. Left plot: unmixed events; right plot: a rate of DCSD of $5 \cdot 10^{-3}$ and a mixing of $r = 10^{-3}$ without interference was assumed.

where $R_i = (D^0 \to K^+\pi^-)_i/(D^0 \to K^-\pi^+)$ with $(i = mix, DCSD)$, $\alpha = R_{mix}/R_{DCSD}$ and ϕ is the interference angle.

For the analysis the following selection criteria are imposed: 2 tracks with opposite charge and $p_t > 0.3$ GeV/c fitted to a common vertex with probability greater than 5%. For each of these track pairs both the $K\pi$ and πK hypothesis are assumed. The invariant mass of the two track system is required to be between 1.819 and 1.909 GeV/c^2. To suppress the double misidentification background if the $M_{K\pi}$ is in the range 1.819 and 1.909 the $M_{\pi K}$ is required to be outside this range and vice versa. In addition the angle θ^* between the K and the direction of flight of the D^0 candidate has to be $-0.6 < \cos\theta^* < 0.6$. Furthermore, an additional track with $p_t > 0.150$ GeV/c originating from the main vertex is required and is assumed to be the π_s of the D^* decay. The p_t of the $K\pi\pi_s$ system has to be greater than 1.5 GeV/c.

Without any information on the decay length only the integral of $R(t)$ can be measured. This has been already done by the CLEO collaboration and found to be $\int R(t)dt = (7.7\pm3.5)\cdot10^{-3}$[8]. Taking this number one would expect a sample of 380 ± 175 events in the decay $D^{*+} \to D^0\pi_s^+ \to (K^+\pi^-)\pi_s^+$ with the above mentioned cuts and an integrated luminosity of about 600 pb^{-1}. Figure 2 shows the expected distributions for $R(t)$ as a function of t/τ for three different hypothesis for the interference angle as well as the individual contributions to the $R(t)$ of R_{DCSD}, R_{mix} and their interference term. With τ being the lifetime of the D^0 meson. It is clear that the mixing term peaks at $t/\tau \approx 2$. If one studies the evolution of the number of observed events as a function of t/τ the maximum information on the composition of the

observed signal can be obtained.

In Figure 3 the result of a MC simulation is shown. The background shape can be accurately estimated by fitting simultaneously the $\Delta M = M(K\pi\pi_s) - M(K\pi)$ distributions for both the $K^-\pi^+$ and $K^+\pi^-$.

In Figure 4 the number of fitted events as a function of the decay time t/τ is shown. The open points give the total event number for an integrated luminosity of 600 pb^{-1} for three different phase angles of the interference term between DCSD and mixing.

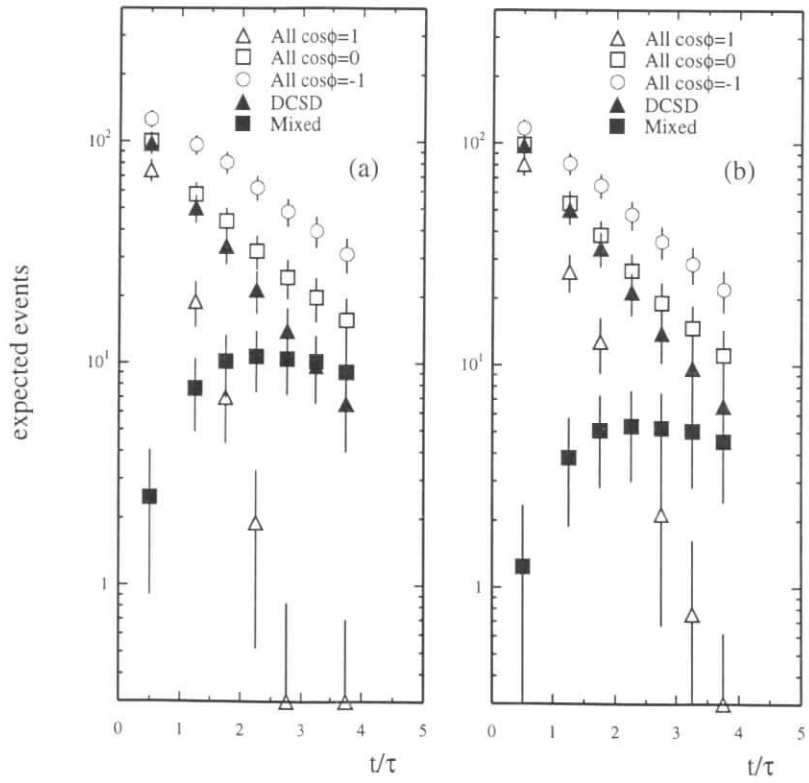

Figure 4: Simulated number of expected events for 600 pb^{-1}. A rate of DCSD of $5 \cdot 10^{-3}$ and a mixing of $r = 10^{-3}$ (a) and $r = 5 \cdot 10^{-4}$ (b) was assumed.

From this figure, it is concluded that a mixing ratio, R_{mix}, less than 10^{-3} can be achieved with HERA, which is more than a factor 5 better than the existing limit of $5{\cdot}10^{-3}$ [7, 9]. Furthermore, the DCSD can be studied with high accuracy.

References

[1] See, for example, A. Datta and D. Kumbhakar, *Z. Phys.* **C27**(1985)515; J.F. Donoghue *et al.*, *Phys. Rev.* **D33**(1986)179;T.Ohl, G.Ricciardi and E.H. Simmons, *Nucl. Phys.* **B403**(1993)605.

[2] See, for example, K.S.Babu *et al.*, pl B20588540; L.Hall and S.Weinberg, *Phys. Rev.* **D48**(1993)979; E.Ma, Mod. Phys. Lett. **A3**(1988)319; A.Datta, *Phys. Lett.* **B154**(1985)287.

[3] H1-Collaboration, S. Aid *et al.*,*Nucl. Phys.* **B472**(1996)32.

[4] H1-Collaboration, S. Aid *et al.*, DESY 96-01, accepted by *Nucl. Instr. & Meth.* (1996).

[5] W. Erdmann *et al.*, *Nucl. Instr. & Meth.* **A372**(1996)188.

[6] G.Ingelman, J.Rathsman and G.A.Schuler, DESY 96-058

[7] E791 Collaboration, E.M. Aitala *et al.*, Fermilab-PUB-96/109E, and hep-ex/9606016.

[8] CLEO Collaboration, D. Cinabro *et al.*, *Phys. Rev. Lett.* **72**(1994)1406.

[9] E615 Collaboration, J.C. Anjos *et al.*, *Phys. Rev. Lett.* **60**(1988)1239; W.C. Louis et al., *Phys. Rev. Lett.* **56**(1986)1027;
E791 Collaboration, E.M.Aitala *et al.*, hep-ex/9608018.

Deep-inelastic Production of Heavy Quarks

E. Laenen[a], M. Buza[b], B.W. Harris[c], Y. Matiounine[d], R. Migneron[e], S. Riemersma[f], J. Smith[d], W.L. van Neerven[g]

[a] CERN Theory Division, CH-1211 Geneva 23, Switzerland
[b] NIKHEF, PO Box 41882, NL-1009 DB Amsterdam, The Netherlands
[c] Physics Department, Florida State University, Tallahassee, FL 32306-3016, USA
[d] Institute for Theoretical Physics, SUNY Stony Brook, NY 11794, USA
[e] Dept. of Applied Math., University of Western Ontario, London, Ontario, N6A 5B9, Canada
[f] DESY IfH-Zeuthen, Platanenallee 6, D-15735 Zeuthen, Germany
[g] Instituut Lorentz, University of Leiden, PO Box 9506, NL-2300 RA Leiden, The Netherlands

Abstract: Deep-inelastic production of heavy quarks at HERA, especially charm, is an excellent signal to measure the gluon distribution in the proton at small x values. By measuring various differential distributions of the heavy quarks this reaction permits additional more incisive QCD analyses due to the many scales present. Furthermore, the relatively small mass of the charm quark, compared to the typical momentum transfer Q, allows one to study whether and when to treat this quark as a parton. This reaction therefore sheds light on some of the most fundamental aspects of perturbative QCD. We discuss the above issues and review the feasibility of their experimental investigation in the light of a large integrated luminosity.

1 Introduction

Since the previous HERA workshop in 1991 significant progress has been made on the theoretical side in understanding the production of heavy quarks in electron proton collisions. Improvements in available experimental techniques and particularly the expected increase in luminosity amply justify this effort. In general the progress consists of the calculation of all $O(\alpha_s)$ corrections to the processes of interest, thus improving the accuracy of the theoretical predictions both in shape and normalization. At the time of the previous workshop the only NLO calculations available were for the case of inclusive photoproduction [1]. In the meantime NLO calculations have also been performed for inclusive electroproduction [2, 3, 4], and both have been extended to the fully differential cases [5, 6, 7]. Therefore, meaningful and extensive comparisons between theory and data can now be made. In what follows we review how the deeply inelastic electroproduction process allows us to explore, in detail, three areas of perturbative QCD in particular.

We first discuss the inclusive case, via the structure function $F_2(x, Q^2, m^2)$. We show that this structure function for the case of charm suffers from only very modest theoretical uncertainty, that its NLO corrections are not too large, and that it is sensitive to the shape of the small-x gluon density. Next we treat single particle differential distributions in the charm kinematical variables, and also charm-anticharm correlations. Because many distributions can be studied, many QCD tests can be performed. Examples are tests of the production mechanism (boson-gluon fusion), studies of gluon radiation patterns, and dependence on scales such as deep-inelastic momentum transfer Q, the heavy quark mass m (with enough luminosity one can detect a sizable sample of bottom quarks), the transverse momentum of the charm quark, etc. Finally, in the last subsection, we review the theoretical status of the boson-gluon fusion description of charm production at small and very large Q. In essence, it involves answering the question: when is charm a parton?

2 Structure Functions and Gluon Density

This subsection has some overlap with the more detailed review on heavy flavour structure functions in the structure function section. Here we only present the most salient features. The reaction under study is

$$e^-(p_e) + P(p) \to e^-(p'_e) + Q(p_1)(\bar{Q}(p_1)) + X\,, \tag{1}$$

where $P(p)$ is a proton with momentum p, $Q(p_1)(\bar{Q}(p_1))$ is a heavy (anti)-quark with momentum p_1 ($p_1^2 = m^2$) and X is any hadronic state allowed. Its cross section may be expressed as

$$\frac{d^2\sigma}{dx dQ^2} = \frac{2\pi\alpha^2}{x\,Q^4}\left[(1+(1-y)^2)F_2(x,Q^2,m^2) - y^2 F_L(x,Q^2,m^2)\right]\,, \tag{2}$$

where

$$q = p_e - p'_e\,, \qquad Q^2 = -q^2\,, \qquad x = \frac{Q^2}{2p\cdot q}\,, \qquad y = \frac{p\cdot q}{p\cdot p_e}\,. \tag{3}$$

The inclusive structure functions F_2 and F_L were calculated to next-to-leading order (NLO) in Ref. [2]. The results can be written as

$$\begin{aligned} F_k(x,Q^2,m^2) \;=\; & \frac{Q^2\alpha_s}{4\pi^2 m^2}\int_x^{z_{\max}}\frac{dz}{z}\left[e_H^2 f_g(\frac{x}{z},\mu^2)c_{k,g}^{(0)}\right] \\ & + \frac{Q^2\alpha_s^2}{\pi m^2}\int_x^{z_{\max}}\frac{dz}{z}\Big[e_H^2 f_g(\frac{x}{z},\mu^2)(c_{k,g}^{(1)} + \bar{c}_{k,g}^{(1)}\ln\frac{\mu^2}{m^2}) \\ & + \sum_{i=q,\bar{q}}\left[e_H^2\, f_i(\frac{x}{z},\mu^2)(c_{k,i}^{(1)} + \bar{c}_{k,i}^{(1)}\ln\frac{\mu^2}{m^2}) + e_{L,i}^2 f_i(\frac{x}{z},\mu^2)d_{k,i}^{(1)}\right]\Big]\,, \end{aligned} \tag{4}$$

where $k = 2, L$ and the upper boundary on the integration is given by $z_{\max} = Q^2/(Q^2 + 4m^2)$. The functions $f_i(x,\mu^2)\,,(i = g,q,\bar{q})$ denote the parton densities in the proton and μ stands for the mass factorization scale, which has been put equal to the renormalization scale. The $c_{k,i}^{(l)}(\eta,\xi)\,,\bar{c}_{k,i}^{(l)}(\eta,\xi)\,,(i = g\,,q\,,\bar{q}\,;l = 0,1)$ and $d_{k,i}^{(l)}(\eta,\xi)$, $(i = q\,,\bar{q}\,;l = 0,1)$ are coefficient functions and are represented in the $\overline{\rm MS}$ scheme. They depend on the scaling variables η and ξ defined by

$$\eta = \frac{s}{4m^2} - 1 \qquad \xi = \frac{Q^2}{m^2}\,. \tag{5}$$

where s is the square of the c.m. energy of the virtual photon-parton subprocess which implies that in (4) $z = Q^2/(Q^2+s)$. In eq. (4) we distinguished between the coefficient functions with respect to their origin. The coefficient functions indicated by $c^{(l)}_{k,i}(\eta,\xi), \bar{c}^{(l)}_{k,i}(\eta,\xi)$ originate from the partonic subprocesses where the virtual photon is coupled to the heavy quark, whereas the quantity $d^{(l)}_{k,i}(\eta,\xi)$ comes from the subprocess where the virtual photon interacts with the light quark. Hence the former are multiplied by the charge squared of the heavy quark e_H^2, and the latter by the charge squared of the light quark e_L^2 respectively (both in units of e). Terms proportional to $e_H e_L$ integrate to zero for the inclusive structure functions. Furthermore we have isolated the factorization scale dependent logarithm $\ln(\mu^2/m^2)$. A fast program using fits to the coefficient functions [8] is available.

The first thing to note about eq. (4) is that the lowest order term contains only the gluon density. Light quark densities only come in at next order, and this is the reason $F_2(x,Q^2,m^2)$ is promising as a gluon probe. To judge its use as such, we must examine some of the characteristics of this observable. These are: the size of the $O(\alpha_s)$ corrections, the scale dependence, the mass dependence, its sensitivity to different gluon densities, and the relative size of the light quark contribution. These are the issues we investigate in this subsection. We take the charm mass 1.5 GeV, the bottom mass 5 GeV, the factorization scale equal to $\sqrt{Q^2+m^2}$ and choose at NLO the CTEQ4M [9] set of parton densities, with a two-loop running coupling constant for five flavors and $\Lambda = 202$ MeV, and at LO the corresponding CTEQ4L set, with a one-loop running coupling with five flavors and $\Lambda = 181$ MeV. In Fig. 1 we display $F_2(x,Q^2,m^2)$ vs. x

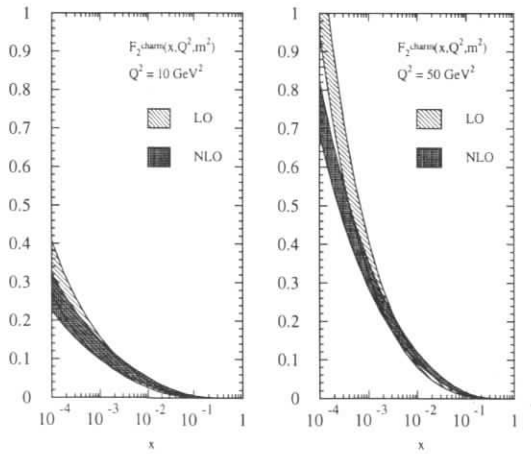

Figure 1: *$F_2(x,Q^2,m^2)$ vs. x at LO and NLO for two values of Q^2. The shaded areas indicate the uncertainty due to varying the charm mass from 1.3 to 1.7 GeV.*

for two values of Q^2 at LO and NLO. The scale dependence is much reduced by including the NLO corrections (when varying μ from 2 to 1/2 times the default choice, the structure function varies from, at LO, at most 20% and 13% at $Q^2 = 10$ and 50 GeV^2 respectively, to at most 5%

and 3% at NLO), but the dominant uncertainty is due to the charm mass and stays roughly constant, amounting at NLO maximally to about 16% for $Q^2 = 10$ GeV^2 and 10% for $Q^2 = 50$ GeV^2. The feature that the LO result is mostly larger than the NLO ones is due to the use of LO parton densities and one-loop α_s, and scale choice. Had we used NLO densities and a two-loop α_s, or chosen the scale μ equal to m, the LO result would have been below the NLO result. In the first case the size of the corrections is then about 40% at the central values at $Q^2 = 10$ GeV^2, and 25% at $Q^2 = 50$ GeV^2, and in the second case, at small x, about 20% and 30% respectively. In the next figure, Fig. 2, we show for the same values of Q^2 an important

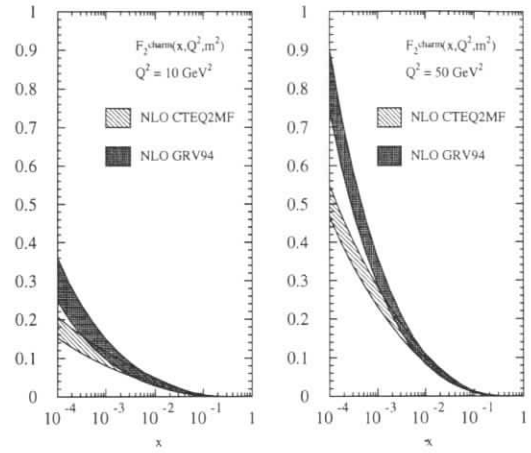

Figure 2: *$F_2(x,Q^2,m^2)$ vs. x at NLO for two choices of parton densities. The shaded areas again indicate the uncertainty due to varying the charm mass from 1.3 to 1.7 GeV.*

property, namely the sensitivity of the NLO F_2 to different parton density parametrizations. In this case we compare the CTEQ2MF set [10], whose gluon density stays quite flat when x becomes small, and the GRV94 set [11], which has a steeply rising gluon density. One sees that the difference is visible in the structure function. Finally we remark that the contribution of light quarks to the charm structure function is typically less than 5%. The bottom quark structure function is suppressed by electric charge and phase space effects and amounts to less than 2% (5%) at $Q^2 = 10\,(50)$ GeV^2 of the charm structure function. Previous investigations of the scale and parton density dependence of F_2 using the same NLO computer codes are available in [12] and [13].

We conclude that $F_2(x,Q^2,m^2)$ for charm production is an excellent probe to infer the gluon density in the proton at small x. The NLO theoretical prediction suffers from fairly little uncertainty, and the QCD corrections are not too large. See the section on structure functions in these proceedings for many more details, where also a comparison with (preliminary) data is shown. Therefore in view of a large integrated luminosity, a theoretically well-behaved observable, and promising initial experimental studies [14, 15] a precise measurement at HERA

of the gluon density should be possible.

3 Single Particle Distributions and Heavy Quark Correlations

In this subsection we leave the fully inclusive case and examine in more detail the structure of the final state of the reaction

$$e^-(p_e) + P(p) \to e^-(p'_e) + Q(p_1) + \bar{Q}(p_2) + X\,. \tag{6}$$

By studying various differential distributions of the heavy quarks we can learn more about the dynamics of the production process than from the structure function alone.

Single particle distributions $dF_2(x, Q^2, m^2, v)/dv$, where v is the transverse momentum p_T or rapidity y of the charm quark, were presented in NLO in [4] for various choices of x and Q^2. The LO distributions differed significantly from the NLO ones, so that the effect of $O(\alpha_s)$ corrections on such distributions cannot be described by a simple K-factor.

The $O(\alpha_s)$ corrections to $F_k(x, Q^2, m^2)$ in a fully differential form were calculated in Ref. [6] using the subtraction method. Recently [7], these fully differential structure functions were incorporated in a Monte-Carlo style program resulting in the $O(\alpha_s)$ corrections for reaction (6). The program for the full cross section, generated according to Eq. (2), allows one to study correlations in the lab frame. The phase space integration is done numerically. Therefore, it is possible to implement experimental cuts. It furthermore allows the use of a Peterson type fragmentation function. For details about the calculational techniques we refer to Ref. [6, 7]. Here we show mainly results.

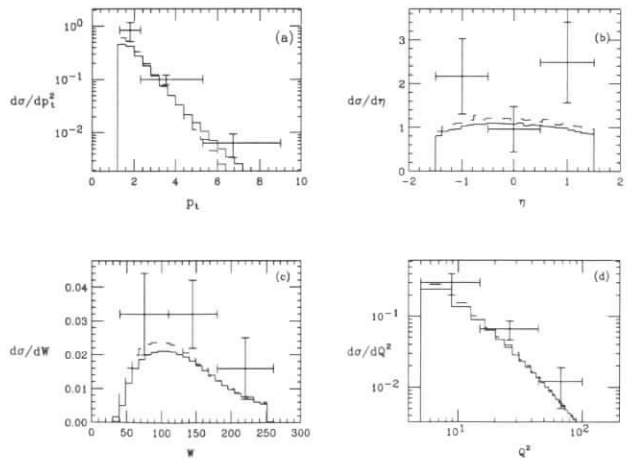

Figure 3: *Differential cross sections and ZEUS data.*

Shown in Fig. 3 are various distributions $d\sigma/dv$ for the reaction (6), where the heavy (anti)quark has fragmented into a D^* meson, with v representing (a) the D^* transverse momentum $p_T^{D^*}$ (b) its pseudorapidity η^{D^*} (c) the hadronic final state invariant mass W (d) Q^2 for the kinematic range 5 GeV^2 $< Q^2 <$ 100 GeV^2, $0 < y < 0.7$, 1.3 GeV $< p_T^{D^*} <$ 9GeV and $|\eta^{D^*}| < 1.5$. The data are from a recent ZEUS analysis [15]. The NLO theory curves have been produced by using the GRV [11] parton density set, with Peterson fragmentation [16]. The dashed line is for $\mu = 2m$, $m = 1.35$ GeV and $\epsilon = 0.035$, whereas the solid line is for $\mu = 2\sqrt{Q^2 + 4m^2}$, $m = 1.65$ GeV and $\epsilon = 0.06$. From Fig. 3 and studies in Ref. [14] it is clear that a wide range of studies can be and are being performed already at the single particle inclusive level. Preliminary conclusions [14, 15] are that the data follow the shape of the NLO predictions quite well, but lie above the theory curves. The H1 collaboration [14] has recently shown clearly from the $d\ln\sigma/dx_D$ distribution that the charm production mechanism is indeed boson-gluon fusion, (after earlier indications from the EMC collaboration [17]) as opposed to one where the charm quark is taken from the sea. Here $x_D = 2|\vec{p}_{D^*}|/W$ in the γ^*P c.m. frame

Next we examine a few charm-anticharm correlations. At the experimental level such correlations are more difficult to measure since it requires the identification of both heavy quarks in the final state. However, with the expected large luminosity that both ZEUS and H1 will collect, such studies are likely to be done. As an example we show in Fig. 4 the p_T distribution of the pair, $p_T^{c\bar{c}}$, and the distribution in their azimuthal angle difference, $\Delta\phi^{c\bar{c}}$ in the γ^*P c.m. frame for a particular choice of x and Q^2. For these figures we used the MRSA′ densities [18]. Both distributions are a measure of the recoiling gluon jet.

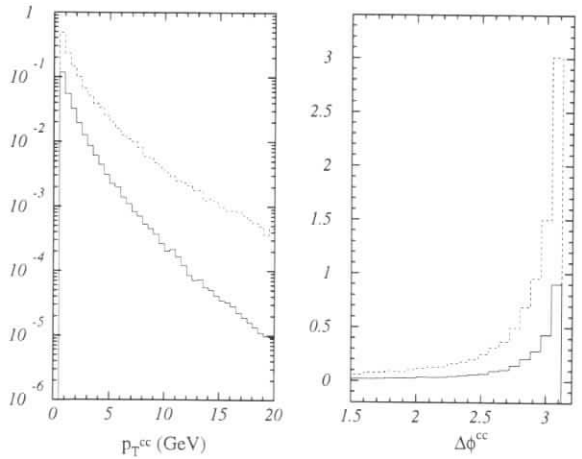

Figure 4: *Differential distributions* $dF_2(x, Q^2, m^2, p_{c\bar{c}})/dp_T^{c\bar{c}}$ *and* $dF_2(x, Q^2, m^2, p_{c\bar{c}})/d\Delta\phi^{c\bar{c}}$ *at* $x = 0.001$ *and* $Q^2 = 10$ *GeV*^{2} *(solid) and 100 GeV*^{2} *(dashed).*

In summary, differential distributions of deep-inelastic heavy quark production offer a rich variety of studies of the QCD production mechanism. Fruitful experimental studies, even with

low statistics, have been done [14, 15], and with a large integrated luminosity we therefore fully expect many more. We finally point out that besides a LO shower Monte Carlo program [19], now also a NLO program is available for producing differential distributions.

4 When is Charm a Parton?

We return to the inclusive case to ask the fundamental question in the title. The question can be more accurately phrased as follows: intuitively one expects that at truly large Q^2 the charm quark should be described as a light quark, i.e. as a constituent parton of the proton, whereas at small Q^2 (of order m^2) the boson-gluon fusion mechanism, in which the charm quark can only be excited by a hard scattering, is the correct description. This has been demonstrated recently by H1 [14] and ZEUS in [15]. In this subsection we examine where the transition between the two pictures occurs.

At LO this issue was investigated in [20]. A picture that consistently combines both descriptions, the so-called variable flavor number scheme, is presented and worked out to LO in [21]. Here we exhibit where the transition occurs at NLO [22]. In other words we will locate the onset of the large Q^2 asymptotic region, where the exact partonic coefficient functions of [2] are dominated by large logarithms $\ln(Q^2/m^2)$. These logarithms are controlled by the renormalization group, and, when resummed, effectively constitute the charm parton density. Here we however restrict ourselves to the onset of the asymptotics. Let us be somewhat more precise. In (4) we can rewrite e.g. all terms proportional to e_H^2 as

$$x\int_x^{zmax}\frac{dz}{z}\Big\{\Sigma(\frac{x}{z},\mu^2)H_{i,q}(z,\frac{Q^2}{m^2},\frac{m^2}{\mu^2})+G(\frac{x}{z},\mu^2)H_{i,g}(z,\frac{Q^2}{m^2},\frac{m^2}{\mu^2})\Big\} \tag{7}$$

where $G(x,\mu^2)$ is the gluon density and $\Sigma(x,\mu^2)=\sum_{i=q,\bar{q}}f_i(x,\mu^2)$ is the singlet combination of quark densities. In the asymptotic regime one may write

$$H_{i,j}^{(k)}(z,\frac{Q^2}{m^2},\frac{m^2}{\mu^2})=\sum_{l=0}^{k}a_{i,j}^{(k)}(z,\frac{m^2}{\mu^2})\ln^l\frac{Q^2}{m^2}\,. \tag{8}$$

The effort lies in determining the coefficients $a_{i,j}^{(k)}$. Similar expressions hold for the other coefficients in (4). Taking the limit of the coefficients in [2] is extremely complicated. Rather, a trick [22] was used, exploiting the close relationship of the $\ln(Q^2/m^2)$ logarithms with collinear (mass) singularities. The ingredients are the massless two-loop coefficient functions of [23] and certain two-loop operator matrix elements. The trick, dubbed "inverse mass factorization", essentially amounts to reinserting into the IR safe massless coefficient functions the collinear singularities represented by the logarithms $\ln(Q^2/m^2)$. See [22] for details.

There is another advantage to obtaining the asymptotic expresssions. The terms in eq. (4) proportional to e_L^2 have been integrated and full analytical expressions for them exist [22], but in the other terms in eq. (4) two integrals still need to be done numerically. Therefore in the large Q^2 region the asymptotic formula is able to give the same results much faster, as the latter formula needs no numerical integrations.

In Fig. 5 we show the ratio of the asymptotic to exact expressions for $F_2(x,Q^2,m^2)$ for the case of charm as a function of Q^2 for four different x values. Here the GRV [11] parton density

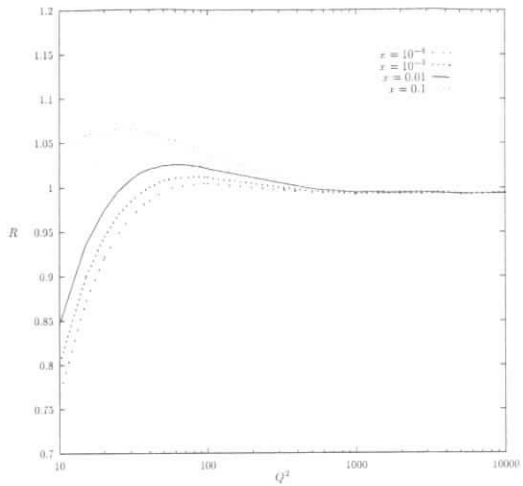

Figure 5: *Ratio of the asymptotic to exact expressions for $F_2(x,Q^2,m^2)$ for the case of charm.*

set was used, for three light flavors. We see that, surprisingly, already at Q^2 of order 20-30 GeV^2 the asymptotic formula is practically identical to the exact result, indicating that at these not so large Q^2 values, and for the inclusive structure function, the charm quark behaves already very much like a parton. This is in apparent contradiction with the findings [14], mentioned in the previous subsection, that the production mechanism is boson-gluon fusion, and illustrates that, interestingly, the question in the title can have a different answer for inclusive quantities than for differential distributions having multiple scales.

We finally note that with the results shown in this subsection also the first important step is made for extending the variable flavour number scheme to NLO.

5 Conclusions

In the above we have reviewed the many interesting facets of deep-inelastic production of heavy quarks. The possibility of selecting the heavy quarks among the final state particles affords a window into the heart of the scattering process, and allows tests and measurements of some of the most fundamental aspects of perturbative QCD: the direct determination of the gluon density, many and varied studies of the heavy quark production dynamics, and insight into how and when a heavy quark becomes a parton.

References

[1] R.K. Ellis and P. Nason, Nucl. Phys. **B**312 (1989) 551; J. Smith and W.L. van Neerven, Nucl. Phys. **B**374 (1992) 36.

[2] E. Laenen, S. Riemersma, J. Smith and W.L. van Neerven, Nucl. Phys. **B**392 (1993) 162.

[3] E. Laenen, S. Riemersma, J. Smith and W.L. van Neerven, Phys. Lett. **B**291 (1992) 325.

[4] E. Laenen, S. Riemersma, J. Smith and W.L. van Neerven, Nucl. Phys. **B**392 (1993) 229.

[5] S. Frixione, M. Mangano, P. Nason and G. Ridolfi, Nucl. Phys. **B**412 (1994) 225.

[6] B.W. Harris and J. Smith, Nucl. Phys. **B**452 (1995) 109; Phys. Lett. **B**353 (1995) 535.

[7] B.W. Harris, talk A05057, presented at American Physical Society, Division of Particles and Fields 1996 Meeting, Minneapolis, Minnesota, 10-15 August 1996, to appear in proceedings.

[8] S. Riemersma, J. Smith and W.L. van Neerven, Phys. Lett. **B**347 (1995) 143.

[9] H.L. Lai et al.(CTEQ Collab.), preprint MSUHEP-60426, CTEQ-604, hep-ph/9606399.

[10] H.L. Lai et al.(CTEQ Collab.), Phys. Rev. **D**51 (1995) 4763.

[11] M. Glück, E. Reya and A. Vogt, Z. Phys. **C**67 (1995) 433.

[12] A. Vogt, DESY-96-012.

[13] M. Glück, E. Reya and M. Stratmann, Nucl. Phys. **B**422 (1994) 37.

[14] C. Adloff et al. (H1 Collab.), DESY 96-138, hep-ex/9607012.

[15] ZEUS Collab., XXVIII Int. Conf. on HEP, Warsaw (1996).

[16] C. Peterson, D. Schlatter, I. Schmitt and P. Zerwas, Phys. Rev. **D**27 (1983) 105.

[17] J.J. Aubert et al. (EMC Collab.), Nucl. Phys. **B**213 (1983) 31.

[18] A. Martin, R. Roberts and W.J. Stirling, Phys. Rev. **D**51 (1995) 4756.

[19] G. Ingelman, J. Rathsman and G.A. Schuler, DESY 96-058, hep-ph/9605285.

[20] S. Riemersma and F.I. Olness, Phys. Rev. **D**51 (1995) 4746.

[21] M.A.G. Aivazis, F.I. Olness, and W.-K. Tung, Phys. Rev. **D**50 (1995) 3085; M.A.G. Aivazis, J.C. Collins, F.I. Olness, and W.-K. Tung, Phys. Rev. **D**50 (1995) 3102.

[22] M. Buza, Y. Matiounine, R. Migneron, J. Smith and W.L. van Neerven, Nucl. Phys. **B**472 (1996) 611; M. Buza, Y. Matiounine, J. Smith and W.L. van Neerven, preprint in preparation.

[23] E. Zijlstra and W.L. van Neerven, Phys. Lett. **B**272 (1991) 127 ; Nucl. Phys. **B**383 (1992) 525.

High p_T Charm Photoproduction

G. Abbiendi[a] J. M. Butterworth[b], R. Graciani[c]

[a] Deutsches Elektronen-Synchrotron DESY, Hamburg, Germany
[b] Dept. of Physics and Astronomy, University College London, London, UK.
[c] Universidad Autonoma de Madrid, Spain.

Abstract: The expected rates for charm-tagged jet photoproduction are evaluated for a number of tagging procedures, and some of the physics potential is discussed. Charm in jets is tagged using D^*'s, μ's, or tracks from secondary vertices which might be identified in a microvertex detector. We find high expected event rates, leading to the possibility of placing strong constraints on the kinematics of charm production and on the gluon content of the proton and the charm content of the photon.

1 Introduction

At HERA energies interactions between almost real photons (of virtuality $P^2 \approx 0$) and protons can produce jets of high transverse energy (E_T^{jet}). A significant fraction of these jets are expected to arise from charmed quarks. The presence of a 'hard' energy scale means that perturbative QCD calculations of event properties can be confronted with experiment, and hence the data have the potential to test QCD and to constrain the structures of the colliding particles.

At leading order (LO) two processes are responsible for jet production. The photon may interact directly with a parton in the proton or it may first resolve into a hadronic state. In the first case all of the photon's energy participates in the interaction with a parton in the proton. In the second case the photon acts as a source of partons which then scatter off partons in the proton. Examples of charm production in these processes are shown in Fig. 1.

The possibility of experimentally separating samples of direct and resolved photon events was demonstrated in [1], and in [2] a definition of resolved and direct photoproduction was introduced which is both calculable to all orders and measurable. This definition is based upon the variable

$$x_\gamma^{OBS} = \frac{\sum_{jets} E_T^{jet} e^{-\eta^{jet}}}{2yE_e}, \qquad (1)$$

where the sum runs over the two jets of highest E_T^{jet}. x_γ^{OBS} is thus the fraction of the photon's energy participating in the production of the two highest E_T^{jet} jets. This variable is used to define cross sections in both data and theoretical calculations. High x_γ^{OBS} events are identified as direct, and low x_γ^{OBS} events as resolved photoproduction.

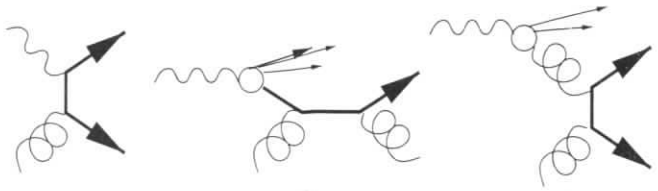

a) b) c)

Figure 1: *Examples of charm photoproduction at HERA: a) Direct; photon-gluon fusion, b) Resolved; single excitation of charm in the photon, c) Resolved; gluon-gluon fusion. The charm and anticharm quarks are indicated by the bold lines.*

Charm-tagged jet cross sections have several advantages over untagged jet cross sections. Knowledge of the nature of the outgoing parton reduces the number of contributing subprocesses and thus simplifies calculations and the possible extraction of parton densities, including the charm content of the photon and the gluon content of the proton. Detailed studies of the dynamics of charm production should provide a stringent test of the QCD calculations. In addition, in the case that charm decays are fully reconstructed, the outgoing momenta provide an alternative to calculating the event kinematics from jet momenta, which could provide a useful *model independent* examination of the uncertainties coming from non-perturbative fragmentation effects.

Here we briefly examine the event rates and distributions obtainable with high luminosities using the three charm tagging methods described below. We use the HERWIG 5.8 [3] Monte Carlo simulation, including multiparton interactions [4], along with simple cuts and smearing to mimic the expected gross features of detector effects. We define our starting sample by running the k_T jet algorithm [5] on the final state particles of HERWIG (after the decay of charmed particles) and demanding at least two jets with transverse energy $E_T^{jet} > 6$GeV and absolute pseudorapidity $|\eta^{jet}| < 2$. In addition we demand $P^2 < 4\text{GeV}^2$ and 135 GeV $< W_{\gamma p} <$ 270 GeV. This is a kinematic region in which dijet cross sections have already been measured at HERA [2].

According to HERWIG, the total cross section for heavy flavour (b or c) jets in this kinematic region is 1900 pb^{-1} (1000 pb^{-1}) for direct (resolved) photoproduction, using the GRV94 LO proton parton distribution set [6] and the GRV LO photon parton distribution set [7].

There is some evidence [2, 8] that these LO calculations may underestimate the cross section, particularly the resolved cross section, by a factor of around two. On the other hand, the dominant LO subprocess for resolved charm production is predicted to be excitation of charm from the photon. This expectation is not fully reliable: the charm content in the photon is presently overestimated in the available parton distribution sets as they assume only massless quarks. If quark masses are included one would expect the resolved charm cross section to be considerably *smaller* than the number we are quoting here. Its measurement will be an important topic in its own right.

2 Charm tagging methods

2.1 D^* tagging method

Currently, the reconstruction of D^* is the only method used to tag open charm by the HERA experiments in published data [9]. D^* are tagged by reconstructing the D^0 produced in the decay $D^{*\pm} \to D^0 + \pi^\pm$ and the mass difference $\Delta(M)$ between the D^* and the D^0.

The overall tagging efficiency for the D^* method is given in table 1, along with the expected number of events after an integrated luminosity of 250 pb^{-1}. For this study we have demanded a D^* with $p_T > 1.5$ GeV and $|\eta| < 2$, and assumed that for these D^* the efficiency of reconstruction is 50%. The decay channels used are $D^* \to D^0 + \pi \to (K + \pi) + \pi$ and $D^* \to D^0 + \pi \to (K + \pi\pi\pi) + \pi$. A signal/background ratio of around 2 is estimated, although this (as well as the D^* reconstruction efficiency) will depend upon the understanding of the detectors and cuts eventually achieved in the real analysis, which cannot be simulated here.

2.2 μ tagging method

The capability of the μ tagging method has been evaluated using a complete simulation of the ZEUS detector [10] based on the GEANT package [11]. The method itself develops previous work [12] in which a measurement of the total charm photoproduction cross section was obtained in the range $60 < W < 275$ GeV. Muons are tagged requiring a match between a track in the ZEUS central tracking detector pointing to the interaction region and a reconstructed segment in the inner muon detectors (which lie about one metre away, outside the uranium calorimeter).

The position and the direction of the reconstructed segment are used to determine the displacements and deflection angles of its projections on two orthogonal planes with respect to the extrapolated track. These quantities are distributed according primarily to the multiple Coulomb scattering within the calorimeter. In comparison the measurement errors are negligible and have not been taken into account. With this approximation and a simple model accounting for the ionization energy loss of the muon through the calorimeter, a χ^2 has been defined from the four variables. The cut on the χ^2 has been chosen to keep 90% of the events with a reconstructed true muon in large Monte Carlo charm samples and checked in selected data samples. The results are contained in table 1.

2.3 Tagging using secondary vertices

If a high resolution microvertex detector is installed close to the interaction region, the tagging of charm by looking for secondary vertices inside jets becomes practical. For this study we have simulated three example methods ('A', very tight cuts and 'B', looser cuts and 'C', very loose cuts) as follows:

- Look at all stable charged tracks which have transverse momentum $p_T(\text{track}) > 500$ MeV and $|\eta(\text{track})| < 2$ and which lie within $\delta R = \sqrt{(\delta\phi)^2 + (\delta\eta)^2} < 1.0$ of the centre of either of the two jets, and

Tagging Method	Direct			Resolved		
	Efficiency	N(events)	Sig./Bkgd	Efficiency	N(events)	Sig./Bkgd
D^*	1.4%	6500 (9% b)	≈ 2	0.7%	1700 (4% b)	≈ 1
μ	7.3%	34000 (20% b)	2.0	3.4%	8400 (10% b)	0.3
Vertex A	2.3%	11000 (63% b)	76	1.0%	2500 (34% b)	8
Vertex B	10%	47000 (33% b)	3.4	6.0%	15000 (17% b)	0.5
Vertex C	37%	170000 (17% b)	0.9	32%	79000 (6% b)	0.2

Table 1: *Estimated tagging efficiencies, signal to background ratio and total numbers of expected signal events for various tagging methods after an integrated luminosity of 250 pb^{-1}. The efficiencies given are the ratios of good events which are tagged to all good events. 'Good events' are ep $\rightarrow$ 2 or more jets with $E_T^{jet} \geq 6$ GeV, $|\eta^{jet}| < 2$, for virtualities of the exchanged photon less than 4 GeV^2 in the range 135 GeV $< W_{\gamma p} <$ 270 GeV and where one or more of the outgoing partons from the hard subprocess was a charm or beauty quark. The fraction of the signal events which are from b quarks is also given.*

- Assume a (Gaussian) impact parameter resolution for these tracks of 180 μm in XY and Z independent of momentum and angle. This corresponds to the design value of the H1 vertex detector [13] for tracks with momentum 500 MeV at 90°.
- Demand at least two tracks which have impact parameters displaced by 3σ (condition A) or one track with an impact parameter displaced by 3σ (condition B) or 2σ (condition C) from the primary vertex.

The results are given in table 1. We note that an enriched sample of b quarks could be obtained by using very tight tagging conditions in a microvertex detector.

3 Physics Potential and Conclusions

High luminosity running at HERA will provide large samples of jets containing heavy quarks. These jets can be identified using muons or D^* with efficiencies of a few percent and signal-to-background ratios of around 2. In addition there is the possibility of identifying the electron channel for semi-leptonic decays, which we have not considered here but which could be very effective at these high transverse energies. The presence of a high resolution vertex detector would enormously enrich the tagging possibilities, allowing improved signal-to-noise ratios and/or improved efficiencies (up to around 35%) depending upon the details of the cuts and reconstruction. Combining the tagging methods we have studied here can be expected to give still more flexibility in the experimental selection and cross section measurement.

With the samples of several tens of thousands of charm-tagged jets thus obtainable, jet cross sections can be measured over a wide kinematic range. For the signal events selected by the vertex method B, various distributions are shown in Fig.2. From the x_γ^{OBS} distribution (Fig.2a) we see that the resolved photon component, whilst suppressed relative to the direct component compared to the untagged case [2], is significant. This component is largely due to the charm content in the GRV photon parton distribution set. Measurement of this cross section can be expected to constrain the charm content of the resolved photon and the implementation of the $\gamma \rightarrow c\bar{c}$ splitting in the perturbative evolution. The boson gluon fusion diagram dominates

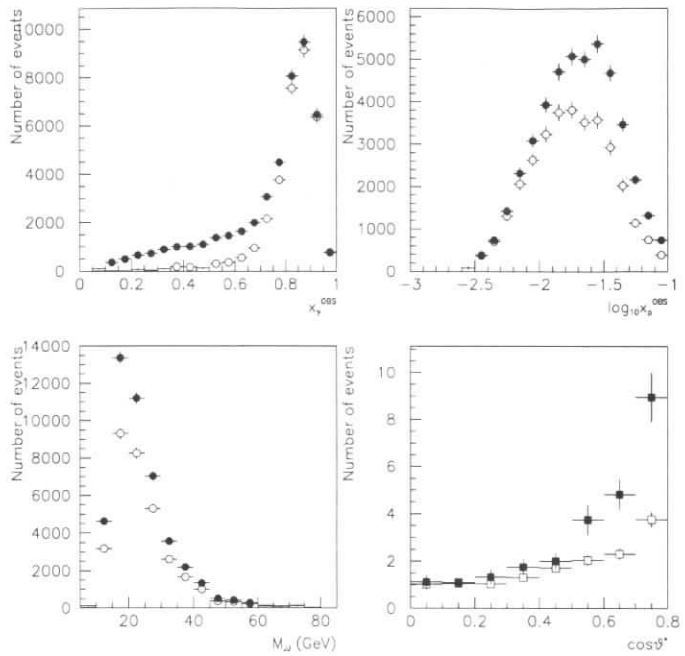

Figure 2: *a) x_γ^{OBS}, b) x_p^{OBS}, c) M_{JJ}, and d) $\cos\theta^*$. In a), b) and c), clear circles are the LO direct only, solid dots are the full sample. The normalisation is to 250 pb^{-1}. In d) the solid squares are the $x_\gamma^{OBS} < 0.75$ sample and the clear squares are the $x_\gamma^{OBS} > 0.75$ sample. Both samples are normalised to one at $|\cos\theta^*| = 0$ and the error bars have been scaled to correspond to the statistical uncertainty expected after 250 pb^{-1}.*

for the high-x_γ^{OBS} range and this cross section is sensitive to the gluon content of the proton in the range $0.003 < x_p^{OBS} < 0.1$, where $x_p^{OBS} = \frac{\sum_{jets} E_T^{jet} e^{\eta^{jet}}}{2E_p}$ is the fraction of the proton's energy manifest in the two highest E_T^{jet} jets (Fig.2b). The M_{JJ} distribution is shown in Fig.2c, where $M_{JJ} = \sqrt{2E_T^{jet1} E_T^{jet2}[\cosh(\eta^{jet1} - \eta^{jet2}) - \cos(\phi^{jet1} - \phi^{jet2})]}$ is the dijet invariant mass. For $M_{JJ} > 23$ GeV the dijet angular distribution [14] $|\cos\theta^*| = |\tanh(\frac{\eta^{jet1} - \eta^{jet2}}{2})|$ is unbiased by the E_T^{jet} cut. As shown in Fig.2d the angular distributions of high and low x_γ^{OBS} should differ strongly, due to the underlying bosonic (gluon) or fermionic (quark) exchange processes [14]. The measurement of such a distribution should confirm that the dominant charm production process in direct photoproduction was photon-gluon fusion. In addition it will determine whether excitation of charm from the incoming particles or gluon-gluon fusion is the dominant production mechanism in resolved photoproduction.

Acknowledgements

It is a pleasure to thank U. Karshon, D. Pitzl, A. Prinias, S. Limentani and the members and conveners of the working group for discussions and encouragement.

References

[1] ZEUS Collab., M. Derrick et al., Phys. Lett. B322 (1994) 287.

[2] ZEUS Collab., M. Derrick et al., Phys. Lett. B348 (1995) 665.

[3] G. Marchesini et al., Comp. Phys. Comm. 67 (1992) 465.
`http://surya11.cern.ch/users/seymour/herwig/`

[4] J. M. Butterworth and J. R. Forshaw, J. Phys. G19 (1993) 1657;
J. M. Butterworth, J. R. Forshaw and M. H. Seymour, CERN-TH-95-82, to appear in Zeit. f. Phys. C.

[5] S. Catani, Yu.L. Dokshitzer, M.H. Seymour and B.R. Webber, Nucl.Phys.B406(1993)187.
S.D. Ellis and D.E. Soper, Phys.Rev.D48(1993)3160.
`http://surya11.cern.ch/users/seymour/ktclus/`

[6] M. Glück, E. Reya and A. Vogt, Z. Phys. C67 (1995) 433.

[7] M. Glück, E. Reya and A. Vogt, Phys. Rev. D46 (1992) 1973.

[8] R. Graciani, for the ZEUS Collab., Rome DIS'96.
U. Karshon, for the ZEUS Collab., QCD'96, Montpellier.

[9] H1 Collab., C. Adloff et al., DESY 96-138, hep-ex/9607012
H1 Collab., S. Aid et al., DESY 96-055, hep-ex/9604005
ZEUS Collab., M. Derrick et al., Phys. Lett. B 349 (1995) 225.

[10] ZEUS Collab., The ZEUS Detector, Status Report (1993).
`http://www-zeus.desy.de/bluebook/bluebook.html`

[11] `http://wwwcn.cern.ch/asdoc/geant_html3/geantall.html`

[12] G.Abbiendi, Tesi di Dottorato (1995) Padova University and ZEUS internal note 95-027.

[13] H1 Collab., Technical Proposal to build Silicon Tracking Detectors for H1, DESY-PRC 92/01.

[14] ZEUS Collab., M. Derrick et al., DESY 96-094, hep-ex/9605009; to appear in Phys. Lett. B.

Prospects for heavy flavour photoproduction at HERA

Stefano Frixione

Theoretical Physics, ETH, Zürich, Switzerland

Abstract: I discuss few selected topics in heavy flavour photoproduction at HERA which require large integrated luminosity in order to be experimentally investigated. I present phenomenological predictions for bottom production. As a possible application of measurements involving double-tagged charm events, I outline a method for the direct measurement of the gluon density in the proton. The possibility of using charm data in polarized electron-proton collisions to constrain the polarized gluon density in the proton is also discussed.

Charm quarks are copiously produced at HERA. Total cross sections in photoproduction have been measured [1, 2], and appear to be in reasonable agreement with next-to-leading order QCD calculations [3, 4, 5, 6]. Recently, the first results on single-inclusive distributions have been presented [2]. Although in substantial agreement with experiments, the theory displays the tendency to undershoot the data. On the other hand, preliminary results by the ZEUS collaboration [7] show sizeable discrepancies in the comparison with next-to-leading order QCD, especially in the pseudorapidity distribution.

The limited statistics of the data prevents from any definite conclusion on the capability of fixed-order QCD calculations to correctly describe charm photoproduction at the large center-of-mass energies available at HERA. It has to be pointed out that the resummation of logarithms which in certain regions of the phase space may grow large and spoil the convergence of the perturbative expansion, can not improve the comparison between theory and experiments (see ref. [8] and references therein). The luminosity upgrade of the HERA collider will allow to increase the statistics of present measurements, and to perform new ones. The underlying theoretical picture will therefore face a severe test. Detailed phenomenological predictions for total rates and single-inclusive distributions of charm quarks in photoproduction at HERA have been available for some time [9, 10, 11]. In the following, I will deal with quantities whose measurement has not yet been performed.

1 Bottom production

Due to the higher value of the quark mass, perturbative QCD predictions for bottom production are more reliable than those for charm. In monochromatic photon-proton collisions, the pointlike component has an uncertainty of a factor of 2 if all the parameters are varied *together* in the direction that makes the cross section larger or smaller. At $\sqrt{S_{\gamma p}} = 100$ GeV, the lower and upper limits of the pointlike component are 16 nb and 35 nb respectively, while at $\sqrt{S_{\gamma p}} = 280$ GeV we get 41 nb and 101 nb [10]. The hadronic component has larger uncertainties, but much smaller than for charm, since in bottom production the small-x region is probed to a lesser extent than in charm production, and the sensitivity of the result to the photon densities is therefore milder; we get an uncertainty of a factor of 3 (to be compared with a factor of 10 in the case of charm). The hadronic component can still be the dominant

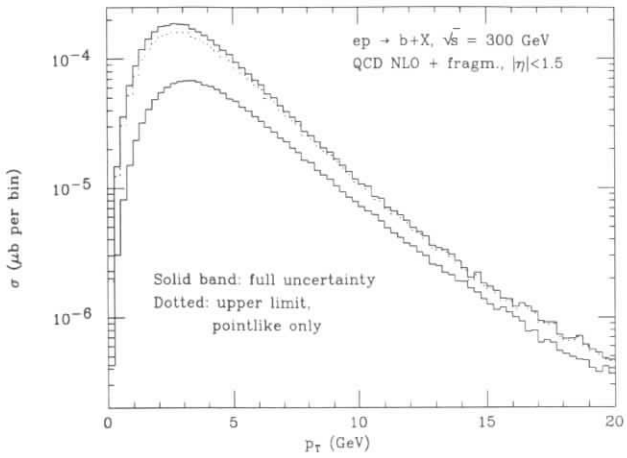

Figure 1: *Full uncertainty on the transverse momentum distribution for bottom electroproduction (Weizsäcker-Williams approximation) with Peterson fragmentation and a pseudorapidity cut.*

contribution to the photoproduction cross section, if the gluon in the photon is as soft as the LAC1 parameterization suggests.

The bottom rates are about a factor of 200 smaller than the charm ones. To perform a statistically significant study of bottom production, the luminosity upgrade at HERA is necessary. In any case, it is very likely that a comparison with the theory could only be done by considering the electroproduction (in the Weizsäcker-Williams approximation) process. In this case the sensitivity of the theoretical predictions to the input parameters is sizeably reduced, and a reliable comparison between theory and data can be performed. For example, in electroproduction the hadronic component contribution to the total cross section is at most 75% of the pointlike contribution, even if the LAC1 set is used. The most interesting results are however obtained when considering more exclusive quantities, like single-inclusive distributions [4, 11]. In particular, as shown in fig. 1, the transverse momentum of the bottom quark at HERA can be predicted by perturbative QCD quite accurately. It is clear that even with the LAC1 set the hadronic component affects the prediction only marginally; this fact is basically a consequence of the applied pseudorapidity cut. Figure 1 can therefore be regarded as a reliable prediction of QCD for the p_T spectrum of B mesons at HERA. The comparison of this prediction with the data would be extremely useful in light of the status of the comparison between theory and data for b production at the Tevatron.

2 The gluon density in the proton

As discussed in ref. [8], the experimental efficiency for double-tagged charm events is quite low, and in order to study fully-exclusive quantities, like the correlations between the charm and

the anticharm, a large integrated luminosity is mandatory. The comparison between theoretical predictions and experimental results for correlations constitutes the most stringent test for the underlying theory, and it is therefore extremely interesting for a complete understanding of the production mechanism of heavy flavours. However, at present it is not particularly useful to present detailed predictions for double-differential distributions, since data will not be available for a long time. In the following, I will therefore concentrate on a possible application of measurements involving double-tagged charm events, namely the determination of the gluon density in the proton ($f_g^{(p)}$).

At present, no *direct* measurement of $f_g^{(p)}$ has been performed. In principle, this quantity could be determined by investigating the exclusive properties of hard scattering processes initiated by gluons. In practice, this procedure is quite difficult; the data on direct photon production and on inclusive jet production, which depends upon $f_g^{(p)}$ already at the leading order in QCD, are not as statistically significant as DIS data are (DIS data allow a direct and accurate determination of the quark densities). Direct photon and inclusive jet data are used to constrain, in complementary regions of x and Q^2, the gluon density. Furthermore, in a next-to-leading order QCD evolution, $f_g^{(p)}$ affects the quark densities through the Altarelli-Parisi equations, and therefore has an impact on the description of DIS data on $F_2(x, Q^2)$ (for a detailed presentation of the determination of parton densities from a global QCD analysis, see for example refs. [12, 13]).

A direct measurement of the gluon density is therefore highly desirable. In ref. [14] it was argued that charm production in high energy ep collisions may help to solve this problem. To proceed explicitly, I begin by writing the heavy-quark cross section at the leading order in the following form

$$\frac{d\sigma^{(0)}}{dy_{Q\overline{Q}}\, dM^2_{Q\overline{Q}}} = x_g \frac{d\sigma^{(0)}}{dx_g\, dM^2_{Q\overline{Q}}} = \frac{1}{E^2}\, f_\gamma^{(e)}(x_\gamma, \mu_0^2) f_g^{(p)}(x_g, \mu_F^2) \hat{\sigma}^{(0)}_{\gamma g}(M^2_{Q\overline{Q}}), \tag{1}$$

where $M_{Q\overline{Q}}$ is the invariant mass of the heavy-quark pair, and $y_{Q\overline{Q}}$ is the rapidity of the pair in the electron-proton center-of-mass frame (I choose positive rapidities in the direction of the incoming proton). $E = \sqrt{S}$ is the electron-proton center-of-mass energy, and

$$x_\gamma = \frac{M_{Q\overline{Q}}}{E} \exp(-y_{Q\overline{Q}}), \tag{2}$$

$$x_g = \frac{M_{Q\overline{Q}}}{E} \exp(y_{Q\overline{Q}}). \tag{3}$$

The function $f_\gamma^{(e)}$ is the Weizsäcker-Williams function [15] (for a discussion on its use in production processes involving heavy particles, see ref. [16]); the explicit expression for the leading-order cross section $\hat{\sigma}^{(0)}_{\gamma g}$ can be found in ref. [3]. The factorization and renormalization scales (μ_F and μ_R) are set equal to $2\mu_0$ and μ_0 respectively, where μ_0 is a reference scale; when studying correlations, it is customary to choose [5]

$$\mu_0 = \sqrt{(p_T^2 + \bar{p}_T^2)/2 + m^2}, \tag{4}$$

where p_T and $\bar{p}_T$ are the transverse momenta of the heavy quark and of the heavy antiquark respectively.

Assuming that the left-hand side of eq. (1) is identified with the data, the equation can be inverted, and we can get a first determination of $f_g^{(p)}$:

$$f_g^{(0)}(x_g,\mu_F^2) = x_g \frac{d\sigma^{\rm data}}{dx_g\, dM^2_{Q\bar{Q}}} \frac{E^2}{f_\gamma^{(e)}(x_\gamma,\mu_0^2)\hat{\sigma}^{(0)}_{\gamma g}(M^2_{Q\bar{Q}})}. \tag{5}$$

The inclusion of radiative corrections does not pose any problem. I write the full cross section as

$$x_g \frac{d\sigma}{dx_g\, dM^2_{Q\bar{Q}}} = \frac{1}{E^2}\, f_\gamma^{(e)}(x_\gamma,\mu_0^2) f_g^{(p)}(x_g,\mu_F^2)\hat{\sigma}^{(0)}_{\gamma g}(M^2_{Q\bar{Q}}) + \Delta(f_g^{(p)}, x_g, M^2_{Q\bar{Q}}), \tag{6}$$

where Δ represents all the radiative effects. In Δ I have also indicated explicitly the functional dependence upon the gluon density in the proton. The light quarks, which enter at the next-to-leading order via the $\gamma q \to q Q \bar{Q}$ process, give a small contribution (less than 5% for all values of x_g and $M_{Q\bar{Q}}$ considered here). I now write $f_g^{(p)}$ as

$$f_g^{(p)}(x,\mu_F^2) = f_g^{(0)}(x,\mu_F^2) + f_g^{(1)}(x,\mu_F^2), \tag{7}$$

where the second term is the next-to-leading order correction, and plug it back into eq. (6). Then

$$f_g^{(1)}(x_g,\mu_F^2) = -\frac{E^2\Delta(f_g^{(0)}, x_g, M^2_{Q\bar{Q}})}{f_\gamma^{(e)}(x_\gamma,\mu_0^2)\ \hat{\sigma}^{(0)}_{\gamma g}(M^2_{Q\bar{Q}})}. \tag{8}$$

I have neglected the $f_g^{(1)}$ piece contained in the Δ term, the corresponding contribution being of order $\alpha_{\rm em}\alpha_s^3$. It could also be easily incorporated by iterating eq. (8), using the full gluon density in the right-hand side.

The charm cross section receives a large contribution from the hadronic component, which was neglected in the above derivation. In order to extract the gluon density in the proton with the method previously outlined, we have to consider only those kinematical regions where the hadronic component is suppressed by the dynamics. I study this possibility in figure 2, where I present the next-to-leading order QCD predictions for the variable x_g, defined in eq. (3), in electron-proton collisions at $\sqrt{S} = 314$ GeV. The partonic densities in the proton are given by the MRSG set, while both the LAC1 and GRV-HO sets for the photon are considered, in order to account for the uncertainty affecting the gluon density in the photon. Figs. 2(a)-2(c) show the effect of applying a cut on the invariant mass of the pair. Even in the case of the smallest invariant-mass cut, there is a region of small x_g where the hadronic component is negligible with respect to the pointlike one. When the invariant-mass cut is increased, the hadronic component can be seen to decrease faster than the pointlike one. This is due to the fact that, for large invariant masses of the pair, the production process of the hadronic component is suppressed by the small value of the gluon density in the photon at large x. By pushing the invariant-mass cut to 20 GeV, it turns out that the pointlike component is dominant over the hadronic one for x_g values as large as 10^{-1}. The conclusion can be drawn that the theoretical uncertainties affecting the charm cross section, in the range $10^{-3} < x_g < 10^{-1}$, are small enough to allow for a determination of the gluon density in the proton by using invariant-mass cuts to suppress the hadronic component. In a more realistic configuration, like the present one of the detectors at HERA, additional cuts are applied to the data. Fig. 2(d) shows the effect on the x_g distribution due to a small-p_T and a pseudorapidity cut, applied to both the charm and the anticharm. In this case, even without an invariant-mass cut, the pointlike component is dominant in the whole kinematically accessible range. Taking into account experimental efficiencies [8], a statistically significant measurement of the gluon density requires an integrated luminosity of at least 250 pb^{-1}.

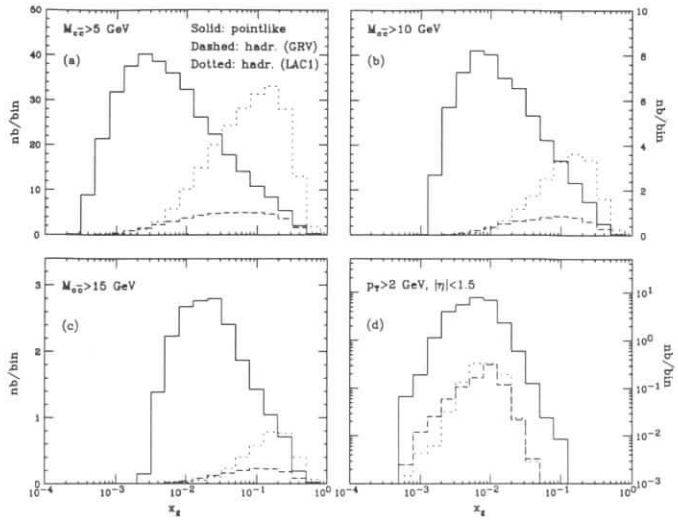

Figure 2: *x_g distribution in ep collisions (Weizsäcker-Williams approximation) at HERA, for $m_c = 1.5$ GeV. The proton parton density set adopted is MRSG.*

3 Polarized *ep* collisions

It is conceivable that in the future the HERA collider will be operated in a polarized mode. The heavy flavour cross section in polarized *ep* scattering is dependent already at the leading order in QCD upon the polarized gluon density in the proton, $\Delta g^{(p)}$. Therefore, data on charm production could be used to directly measure $\Delta g^{(p)}$, as previously shown for the unpolarized case. In practice, the situation for the polarized scattering is much more complicated. First of all, a full next-to-leading order calculation is not available for the partonic processes relevant for polarized heavy flavour production. Furthermore, there is no experimental information on the partonic densities in the polarized photon. It is reasonable, however, to think that charm production at the HERA collider in the polarized mode can help in constraining the polarized gluon density in the proton. This possibility was first suggested in ref. [17], and recently reconsidered in refs. [18, 19].

The next-to-leading and higher order corrections to the polarized cross section are expected to be sizeable, therefore casting doubts on the phenomenological relevance of leading-order predictions. To overcome this problem, one possibility is to present predictions [18] for the ratio $\Delta\sigma/\sigma$ (asymmetry), where σ is the unpolarized cross section and

$$\Delta\sigma = \frac{1}{2}\left(\sigma^{\uparrow\uparrow} - \sigma^{\uparrow\downarrow}\right). \tag{9}$$

Here $\sigma^{\uparrow\uparrow}$ and $\sigma^{\uparrow\downarrow}$ are the cross sections for $c\bar{c}$ production with parallel and antiparallel polarizations of the incoming particles respectively. One might expect that the effect of the radiative

corrections approximately cancels in the ratio. It has to be stressed that, for consistency reasons, the unpolarized cross section σ appearing in the asymmetry must be calculated at the leading order, as the polarized one.

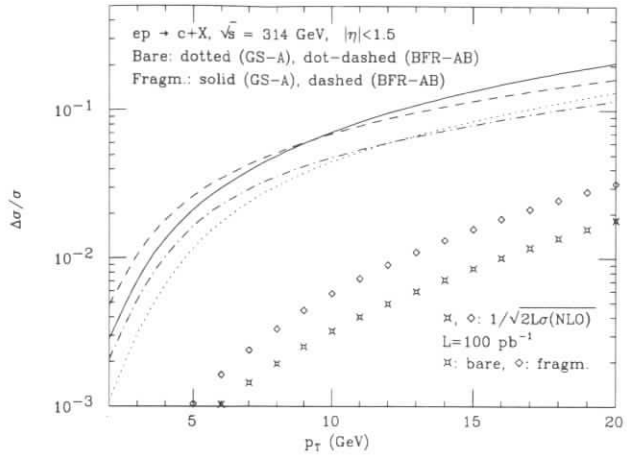

Figure 3: *Asymmetry cross section versus transverse momentum in polarized ep collisions (Weizsäcker-Williams approximation) at $\sqrt{S} = 314$ GeV. The minimum observable asymmetry, computed at next-to-leading order, is also displayed.*

The next-to-leading order value of σ can then be used to estimate the sensitivity of the experiment. A rough estimate of the minimum value of the asymmetry observable at HERA can be obtained by requiring the difference between the numbers of events with parallel and antiparallel polarizations of the initial state particles to be larger than the statistical error on the total number of observed events. This gives

$$\left[\frac{\Delta\sigma}{\sigma}\right]_{min} \simeq \frac{1}{\sqrt{2\sigma\mathcal{L}\epsilon}}, \tag{10}$$

where $\mathcal{L}$ is the integrated luminosity and the factor ϵ accounts for the experimental efficiency for charm identification and for the fact that the initial beams are not completely polarized. This procedure can be applied to total cross sections, as well as to differential distributions; in this case, the values of σ and $\Delta\sigma$ have to be interpreted as *cross sections per bin* in the relevant kinematical variable.

In ref. [18] it was shown that total cross section asymmetries for the pointlike component are quite small in absolute value, and can be measured only if ϵ is equal or larger than 1% (0.1%), assuming $\mathcal{L} = 100$ pb^{-1} (1000 pb^{-1}). Therefore, even with a vertex detector (see ref. [8]), it appears to be unlikely that this kind of measurements will be performed at HERA. Furthermore, in ref. [19] a rough estimate of the hadronic contribution to the polarized cross section has been given, assuming polarized parton densities in the photon to be identical to

zero or to the unpolarized densities to get a lower and an upper bound on the cross section. It was found that a non-negligible contamination of the pointlike result might indeed come from the hadronic process. The situation clearly improves when considering more exclusive quantities; in ref. [18] it was found that at moderate p_T values the asymmetry for the pointlike component can be rather large, well above the minimum observable value (in this region, the experimental efficiency is sizeable [8]); this is shown in fig. 3. In ref. [19] it was argued that the hadronic component should have a negligible impact in this case. I conclude that, with an integrated luminosity of 100 pb^{-1}, charm data in high-energy polarized *ep* collisions will help in the determination of the polarized gluon density in the proton. In order to distinguish among different parameterizations for $\Delta g^{(p)}$, a larger luminosity is likely to be needed.

4 Conclusions

I have discussed few selected topics in heavy flavour physics which will become of practical interest at HERA after that the planned upgrades of the machine will be carried out. With an integrated luminosity $\mathcal{L} = 100$ pb^{-1}, about 10^5 bottom quarks are predicted by QCD to be produced in *ep* collisions at $\sqrt{S} = 300$ GeV. If the experimental efficiency for B-meson identification will be large enough, this will provide with the possibility of a detailed study of the bottom production mechanism, and of an interesting comparison with the results at the Tevatron. In order to study charm-anticharm correlations, $\mathcal{L}$ must be equal to or larger than 250 pb^{-1}. As a possible application of measurements involving double-tagged charm events, I presented a method for the direct measurement of the gluon density in the proton. Charm data in polarized *ep* collisions could also be used to constrain the *polarized* gluon density in the proton. In this case, an integrated luminosity of at least 100 pb^{-1} is required.

Acknowledgements: The financial support by the Swiss National Foundation is acknowledged.

References

[1] M. Derrick et al., ZEUS Coll., *Phys. Lett.* **B349**(1995)225.

[2] S. Aid et al., H1 Coll., *Nucl. Phys.* **B472**(1996)32.

[3] R. K. Ellis and P. Nason, *Nucl. Phys.* **B312**(1989)551.

[4] J. Smith and W. L. van Neerven, *Nucl. Phys.* **B374**(1992)36.

[5] S. Frixione, M. Mangano, P. Nason and G. Ridolfi, *Nucl. Phys.* **B412**(1994)225.

[6] P. Nason, S. Dawson and R. K. Ellis, *Nucl. Phys.* **B303**(1988)607; **B327**(1988)49;
W. Beenakker et al., *Phys. Rev.* **D40**(1989)54; *Nucl. Phys.* **B351**(1991)507;
M. Mangano, P. Nason and G. Ridolfi, *Nucl. Phys.* **B373**(1992)295.

[7] ZEUS Coll., paper pa05-051, submitted to the ICHEP96 Conference in Warsaw.

[8] R. Eichler and S. Frixione, these proceedings.

[9] S. Riemersma, J. Smith and W. L. van Neerven, *Phys. Lett.* **B282**(1992)171.

[10] S. Frixione, M. Mangano, P. Nason and G. Ridolfi, *Phys. Lett.* **B348**(1995)633.

[11] S. Frixione, P. Nason and G. Ridolfi, *Nucl. Phys.* **B454**(1995)3.

[12] A.D. Martin, R.G. Roberts and W.J. Stirling, *Phys. Rev.* **D50**(1994)6734.

[13] H. L. Lai et al., MSUHEP-60426, CTEQ-604, `hep-ph/9606399`.

[14] S. Frixione, M. Mangano, P. Nason and G. Ridolfi, *Phys. Lett.* **B308**(1993)137.

[15] C. F. Weizsäcker, *Z. Phys.* **88**(1934)612;
E. J. Williams, *Phys. Rev.* **45**(1934)729.

[16] V. M. Budnev et al., *Phys. Rep.* **C15**(1974)181;
H. A. Olsen, *Phys. Rev.* **D19**(1979)100;
A. C. Bawa and W. J. Stirling, *J. Phys.* **G15** (1989)1339;
S. Catani, M. Ciafaloni and F. Hautmann, *Nucl. Phys.* **B366**(1991)135;
S. Frixione, M. Mangano, P. Nason and G. Ridolfi, *Phys. Lett.* **B319**(1993)339.

[17] M. Glück and E. Reya, *Z. Phys.* **C39**(1988)569;
M. Glück, E. Reya and W. Vogelsang, *Nucl. Phys.* **B351**(1991)579;
W. Vogelsang, in *Physics at HERA*, Proc. of the Workshop, Vol. 1, eds. W. Buchmüller and G. Ingelman (1991).

[18] S. Frixione, and G. Ridolfi, `hep-ph/9605209`, to appear in *Phys. Lett.* **B**.

[19] M. Stratmann and W. Vogelsang, DO-TH-96/10, RAL-TR-96-033, `hep-ph/9605330`.

Future Perspectives of Quarkonium Physics at HERA

Matteo Cacciari and Michael Krämer

Deutsches Elektronen-Synchrotron DESY, D-22607 Hamburg, FRG

Abstract: We work out and review prospects for future quarkonium physics at HERA. We focus on the impact of color-octet contributions and discuss how measurements at HERA can be used to test the picture of quarkonium production as developed in the context of the NRQCD factorization approach.

1 Introduction

The production of heavy quarkonium states in high energy collisions provides an important tool to study the interplay between perturbative and nonperturbative QCD dynamics. Quarkonium production in deep inelastic scattering and photon-proton collisions at HERA has been analysed at some length in the context of the previous HERA workshops (see e.g. ref.[1]). However, most of the previous studies have been carried out within the color-singlet model (CSM) [2] or the color-evaporation model [3]. Only recently, a rigorous theoretical framework for treating quarkonium production and decays has been developed in ref.[4]. The factorization approach is based on the use of non-relativistic QCD (NRQCD) [5] to separate the short-distance parts from the long-distance matrix elements and explicitly takes into account the complete structure of the quarkonium Fock space. This formalism implies that so-called color-octet processes, in which the heavy-quark antiquark pair is produced at short distances in a color-octet state and subsequently evolves nonperturbatively into a physical quarkonium, should contribute to the cross section. According to the factorization formalism, the inclusive cross section for the production of a quarkonium state H can be expressed as a sum of terms, each of which factors into a short-distance coefficient and a long-distance matrix element:

$$\mathrm{d}\sigma(ep \to H + X) = \sum_n \mathrm{d}\hat{\sigma}(ep \to Q\overline{Q}\,[n] + X)\,\langle \mathcal{O}^H\,[n]\rangle\,. \tag{1}$$

Here, $\mathrm{d}\hat{\sigma}$ denotes the short-distance cross section for producing an on-shell $Q\overline{Q}$-pair in a color, spin and angular-momentum state labelled by n. The NRQCD vev matrix elements $\langle \mathcal{O}^H\,[n]\rangle$ give the probability for a $Q\overline{Q}$-pair in the state n to form the quarkonium state H. The relative importance of the various terms in (1) can be estimated by using NRQCD velocity scaling rules [6]. For $v \to 0$ (v being the average velocity of the heavy quark in the quarkonium rest frame) each of the NRQCD matrix elements scales with a definite power of v and the general expression (1) can be organized into an expansion in powers of v^2.

It has recently been argued in refs.[7, 8] that quarkonium production in hadronic collisions at the Tevatron can be accounted for by including color-octet processes and by adjusting the unknown long-distance color-octet matrix elements to fit the data. In order to establish the

phenomenological significance of the color-octet mechanism it is however necessary to identify color-octet contributions in different production processes.[1] In this report we will focus our discussion on the prospects of extracting information on the color-octet processes from the measurements of inelastic quarkonium production at HERA. Elastic/diffractive mechanisms will be discussed elsewhere [10]. We shall briefly review the impact of color-octet contributions and higher-order QCD corrections on the cross section for J/ψ photoproduction and compare the theoretical predictions with recent experimental data. In this context we will also comment on the possibility of measuring the gluon distribution in the proton from J/ψ photoproduction. The high-statistics data to be expected in the future at HERA will allow for a detailed comparison of the theoretical predictions with experimental data not only for J/ψ photoproduction, but also for various other channels and final states, like photoproduction of ψ', Υ and χ states, associated $J/\psi + \gamma$ production, fragmentation and resolved-photon contributions as well as deep inelastic J/ψ production. We will discuss how these reactions can be used to constrain the color-octet matrix elements and test the picture of quarkonium production as developed in the context of the NRQCD factorization approach.

2 J/ψ photoproduction

Quarkonium production in high energy ep collisions at HERA is dominated by photoproduction events where the electron is scattered by a small angle producing photons of almost zero virtuality. The measurements at HERA provide information on the dynamics of quarkonium photoproduction in a wide kinematical region, 30 GeV $\lesssim \sqrt{s_{\gamma p}} \lesssim$ 200 GeV, corresponding to initial photon energies in a fixed-target experiment of 450 GeV $\lesssim E_\gamma \lesssim$ 20,000 GeV. The production of J/ψ particles in photon-proton collisions proceeds predominantly through photon-gluon fusion. Elastic/diffractive mechanisms can be eliminated by measuring the J/ψ energy spectrum, described by the scaling variable $z = p \cdot k_\psi \,/\, p \cdot k_\gamma$, with $p, k_{\psi,\gamma}$ being the momenta of the proton and J/ψ, γ particles, respectively. In the proton rest frame, z is the ratio of the J/ψ to γ energy, $z = E_\psi / E_\gamma$. For elastic/diffractive events z is close to one; a clean sample of inelastic events can be obtained in the range $z \lesssim 0.9$.

For J/ψ production and at leading order in v^2, the general factorization formula (1) reduces to the standard expression of the color-singlet model [2]. The short-distance cross section is given by the subprocess

$$\gamma + g \to c\bar{c}\,[^3S_1, \underline{1}] + g \tag{2}$$

with $c\bar{c}$ in a color-singlet state (denoted by $\underline{1}$), zero relative velocity, and spin/angular-momentum quantum numbers $^{2S+1}L_J = {}^3S_1$. Relativistic corrections due to the motion of the charm quarks in the J/ψ bound state enhance the large-z region, but can be neglected in the inelastic domain [11]. The calculation of the higher-order perturbative QCD corrections to the short-distance process (2) has been performed in refs.[12, 13]. Inclusion of the NLO corrections reduces the scale dependence of the theoretical prediction and increases the color-singlet cross section by more than 50%, depending in detail on the photon-proton energy and the choice of parameters [13].

[1] Quarkonium production via color-octet states has also been studied in e^+e^- annihilation and Z decays, for hadronic collisions in the energy range of fixed-target experiments and in B decays [9].

Color-octet configurations are produced at leading order in α_s through the $2 \to 1$ parton processes [14, 15, 16]

$$\begin{aligned} \gamma + g &\to c\bar{c}\,[^1S_0, \underline{8}] \\ \gamma + g &\to c\bar{c}\,[^3P_{0,2}, \underline{8}]\,. \end{aligned} \tag{3}$$

Due to kinematical constraints, the leading color-octet terms will only contribute to the upper endpoint of the J/ψ energy spectrum, $z \approx 1$ and $p_T \approx 0$, p_T being the J/ψ transverse momentum. It has, however, been argued in ref.[17] that sizable higher-twist effects are expected to contribute in the region $p_T \lesssim 1$ GeV, which cause the breakdown of the factorization formula (1). Moreover, diffractive production mechanisms which cannot be calculated within perturbative QCD might contaminate the region $z \approx 1$ and make it difficult to extract precise information on the color-octet processes.

It is therefore more appropriate to study J/ψ photoproduction in the inelastic region $z \leq 0.9$ and $p_T \geq 1$ GeV where no diffractive channels contribute and where the general factorization formula (1) and perturbative QCD calculations should be applicable. Color-octet configurations which contribute to inelastic J/ψ photoproduction are produced through the subprocesses [14, 16]

$$\begin{aligned} \gamma + g &\to c\bar{c}\,[^1S_0, \underline{8}] + g \\ \gamma + g &\to c\bar{c}\,[^3S_1, \underline{8}] + g \\ \gamma + g &\to c\bar{c}\,[^3P_{0,1,2}, \underline{8}] + g\,. \end{aligned} \tag{4}$$

Light-quark initiated contributions are strongly suppressed at HERA energies and can safely be neglected. Adopting NRQCD matrix elements consistent with those extracted from the fits to prompt J/ψ data at the Tevatron [8] (see Table 1) one finds that color-octet and color-singlet contributions to the inelastic cross section are predicted to be of comparable size [14, 16].

$\langle \mathcal{O}^{J/\psi}\,[^3S_1, \underline{1}] \rangle$	1.16 GeV^3	$m_c^3 v^3$
$\langle \mathcal{O}^{J/\psi}\,[^1S_0, \underline{8}] \rangle$	10^{-2} GeV^3	$m_c^3 v^7$
$\langle \mathcal{O}^{J/\psi}\,[^3S_1, \underline{8}] \rangle$	10^{-2} GeV^3	$m_c^3 v^7$
$\langle \mathcal{O}^{J/\psi}\,[^3P_0, \underline{8}] \rangle / m_c^2$	10^{-2} GeV^3	$m_c^3 v^7$

Table 1: Values of the NRQCD matrix elements used in the numerical analysis, with the velocity and mass scaling. v is the velocity of the heavy quark in the quarkonium rest frame. For charmonium it holds $v^2 \simeq 0.25$.

However, taking into account the uncertainty due to the value of the charm quark mass and the strong coupling, the significance of color-octet contributions can not easily be deduced from the analysis of the absolute J/ψ production rates. A distinctive signal for color-octet processes should, however, be visible in the J/ψ energy distribution $d\sigma/dz$ shown in fig.1 [8]. Since the shape of the distribution is insensitive to higher-order QCD corrections or to the uncertainty induced by the choice for m_c and α_s, the analysis of the J/ψ energy spectrum $d\sigma/dz$ should provide a clean test for the underlying production mechanism. From fig.1 we can conclude that the shape predicted by the color-octet contributions is not supported by the experimental data and that the J/ψ energy spectrum is adequately accounted for by the color-singlet channel.

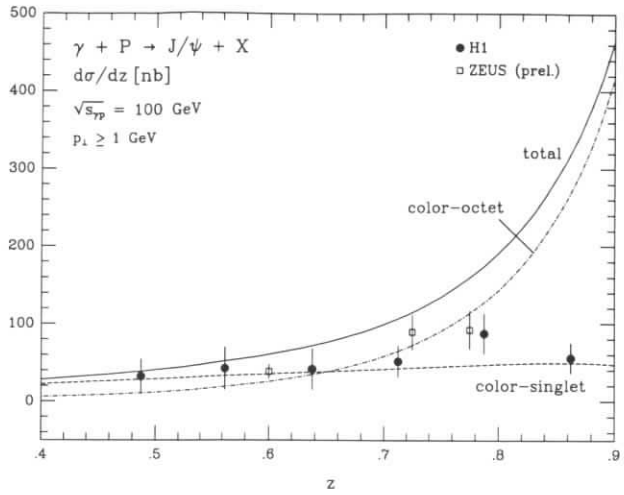

Figure 1: Color-singlet and color-octet contributions to the J/ψ energy distribution $d\sigma/dz$ at the photon-proton centre of mass energy $\sqrt{s_{\gamma p}} = 100$ GeV integrated in the range $p_T \geq 1$ GeV [14]. Experimental data from [18, 19].

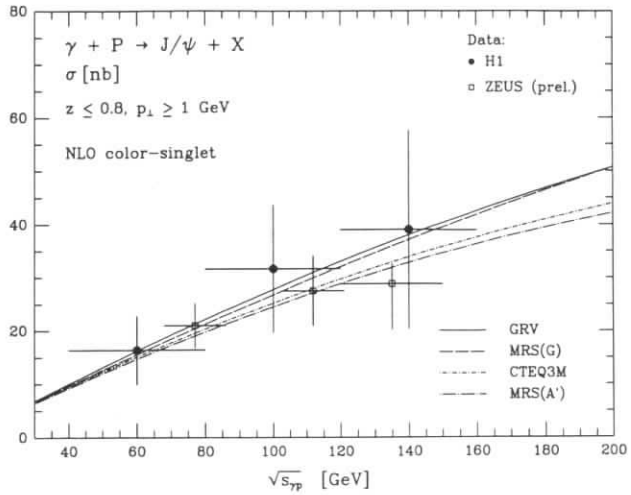

Figure 2: NLO color-singlet prediction for the total inelastic J/ψ photoproduction cross section as a function of the photon-proton energy for different parametrizations [20] of the parton distribution in the proton [13]. Experimental data from [18, 19].

This is however not to be considered as a failure of the factorization approach, since also other analyses (see for instance the last item of ref. [9]) have pointed out that the fits to the Tevatron data may have returned slightly too large values for the matrix elements. With higher statistics data it will be possible to extract more detailed information on the color-octet matrix elements, in particular from the analysis of the J/ψ energy distribution in the inelastic region.

The impact of higher-order QCD corrections on total cross sections and differential distributions has been studied thoroughly for the color-singlet channel in ref.[13]. A detailed analysis of the spectra in the high energy range at HERA shows that the perturbative calculation is not well-behaved in the limit $p_T \to 0$, where p_T is the transverse momentum of the J/ψ. No reliable prediction can be made in this singular boundary region without resummation of large logarithmic corrections caused by multiple gluon emission. If the small p_T region is excluded from the analysis, experimental results on differential distributions and total cross sections are well accounted for by the color-singlet channel alone, including NLO QCD corrections, see e.g. fig.2. However, since the average momentum fraction of the partons is shifted to larger values when excluding the small-p_T region, the sensitivity of the prediction to the small-x behaviour of the gluon distribution is not very distinctive. A detailed analysis reveals that the size of the QCD corrections increases when adopting parton densities with flatter gluons. The sensitivity to different gluon distributions is thus reduced in next-to-leading order as compared to the leading-order result, in particular when choosing a small charm mass and a large value for the strong coupling. Parametrizations with extremely flat gluons like MRS(D0') [21] are clearly disfavoured by the recent HERA measurements of the proton structure function [22] and do not allow for a reliable prediction in the high energy region. For the parameters adopted in

fig.2, the MRS(D0') distribution leads to next-to-leading order results not very different from those obtained with the MRS(A') parametrization. The corresponding K-factors are however uncomfortably large, $K \sim 4$, casting doubts on the reliability of the perturbative expansion as obtained by using flat gluon distributions. If parton distributions with steep gluon densities are adopted, the next-to-leading order cross section is well-behaved and gives an adequate description of the experimental data, as demonstrated in fig.2.

The cross section for the production of ψ' particles has been measured by several photo- and hadroproduction experiments [23] to be suppressed by a factor ~ 0.25 compared to J/ψ production. This result is consistent with naive estimates obtained within the color-singlet model where one assumes that the effective charm masses in the short distance amplitudes scale like the corresponding ψ' and J/ψ masses [2]. Within the NRQCD factorization approach it is however conceptually preferred to express the short-distance coefficients in terms of the charm quark mass rather than the quarkonium mass, yielding $\sigma(\psi')/\sigma(J/\psi) \sim 0.5$ for color-singlet dominated production channels. Relativistic corrections and color-octet contributions are expected to affect the ratio $\sigma(\psi')/\sigma(J/\psi)$, but no quantitative prediction can be made with the present experimental and theoretical information.

Bottomonium production is a particular interesting subject to be studied at HERA. The larger value of the bottom quark mass makes the perturbative QCD predictions of the short-distance cross section more reliable than for charm production. Moreover, the derivation of the factorization formula eq.(1) relies on the fact that the momentum scales which govern the bound state dynamics are well separated: $(m_Q v^2)^2 \ll (m_Q v)^2 \ll m_Q^2$. This assumption is

reasonably good for charmonium (where $v^2 \sim 0.3$) but very good for bottomonium (where $v^2 \sim 0.1$). Thus, the theoretical predictions for bottomonium production should be much more reliable than those for charmonium. The production rates for Υ bound states are, however, suppressed, compared with J/ψ states, by a factor of about 300 at HERA, a consequence of the smaller bottom electric charge and the phase space reduction by the large b mass.

3 J/ψ production via fragmentation

At sufficiently large transverse momentum p_T, quarkonia production is dominated by fragmentation, the production of a parton with large p_T which subsequently decays into the quarkonium state and other partons [24]. While the fragmentation contributions are of higher order in α_s compared to direct quarkonia production in fusion processes, they are enhanced by powers p_T^2/m_c^2 and can thus overtake the fusion contribution at $p_T \gg m_c$. It has in fact been argued that quarkonium production at large p_T in hadronic collisions at the Tevatron can be accounted for by including gluon fragmentation into color-octet states [7].

The fragmentation contribution to the differential cross section for producing a quarkonium state H at large p_T can be written in the factorized form

$$\mathrm{d}\sigma(\gamma + p \to H + X) = \sum_i \int_0^1 \mathrm{d}\zeta \, \mathrm{d}\hat{\sigma}(\gamma + p \to i + X) \, D_{i\to H}(\zeta) \tag{5}$$

where $\mathrm{d}\hat{\sigma}$ is the differential cross section for producing a parton of type i with momentum p_T/ζ. The fragmentation function $D_{i\to H}$ gives the probability that a jet initiated by parton i contains a hadron H carrying a fraction ζ of the parton momentum. According to the NRQCD factorization formalism, fragmentation functions for charmonium have the general form

$$D_{i\to H}(\zeta, \mu) = \sum_n d_{i\to c\bar{c}[n]X}(\zeta, \mu) \, \langle \mathcal{O}^H[n] \rangle \tag{6}$$

analogous to eq.(1). The function $d_{i\to c\bar{c}[n]X}$ gives the probability for the parton i to form a jet that includes a $c\bar{c}$ pair in the state labelled by n. It can be calculated at an initial scale $\mu \sim m_c$ as a perturbative expansion in $\alpha_s(m_c)$ [24, 25] and be evolved up to higher scales $\mu \sim p_T$ by using the Altarelli-Parisi evolution equations.

A quantitative analysis of the fragmentation contributions to J/ψ photoproduction at HERA has been performed in ref.[26] (see also ref.[27] for an earlier analysis within the color-singlet model). The authors have considered the fragmentation of gluons and charm quarks produced at leading order via the Compton- and Bethe-Heitler processes, $\gamma + q \to q + g$ and $\gamma + g \to c + \bar{c}$, respectively. It appears that at large transverse momenta, $p_T \gtrsim 10$ GeV, color-singlet charm quark fragmentation dominates over the photon-gluon fusion process while gluon-fragmentation is suppressed by an order of magnitude over the whole range of p_T, see fig.3 [26]. Color-octet contributions to the gluon fragmentation function considerably enhance the large-z region, but have no strong effect in the inelastic domain $z \lesssim 0.9$. Thus, the information that will be obtained from large p_T production of J/ψ particles at HERA can be used to study the charm quark fragmentation mechanism and is complementary to the analyses performed at the Tevatron where the large p_T region is dominated by gluon fragmentation. However, since the cross section for J/ψ photoproduction at $p_T \gtrsim 10$ GeV is at the most $\mathcal{O}(1pb)$, a large luminosity is required to probe fragmentation contributions to quarkonium production at HERA.

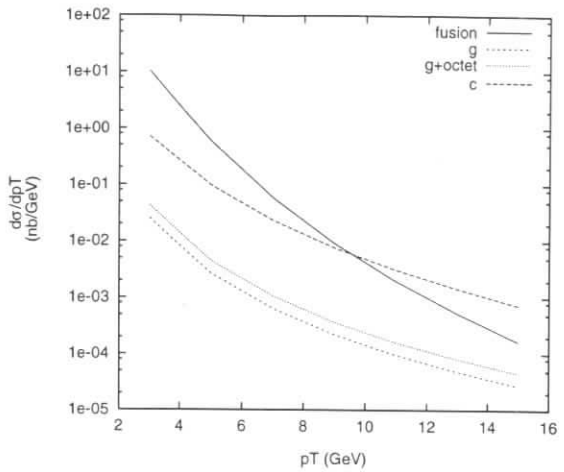

Figure 3: Transverse momentum distribution $\mathrm{d}\sigma/\mathrm{d}p_\perp$ for J/ψ photoproduction at the photon-proton centre of mass energy $\nu = 100$ GeV. The solid line represents the (leading-order) fusion contribution and the dashed-dotted line the charm quark fragmentation contribution. The dotted and dashed lines represent the gluon fragmentation contributions with and without a color-octet component for the S state. The cut on the inelasticity parameter z is $0.1 < z < 0.9$. From Ref.[26].

4 Resolved photon contributions

The photoproduction of a J/ψ particle can also take place via a so called resolved photon interaction, where the photon couples through one of its hadronic components. For J/ψ production within the color-singlet model the process goes like:

$$\gamma p \to g_\gamma + g_p \to c\bar{c}[^3S_1, \underline{1}] + g \to J/\psi + g \tag{7}$$

meaning that the gluon coming from the photon fuses with the one coming from the proton to give a $^3S_1$ color-singlet $c\bar{c}$ pair which subsequently hadronizes into a J/ψ. This process has been extensively analyzed in the past (see for instance [1]) and found to contribute to the overall cross section only marginally everywhere but in the low-z region. More contributions, coming from production and radiative decay of χ states, are also expected to be present. These terms also probe the quark content of the photon. They are expected to be of comparable size with the J/ψ production process (7) described above (see [1] for a survey of these and other resolved production mechanisms).

Within the factorization approach, however, more channels have to be considered, where the J/ψ production goes via color-octet $c\bar{c}$ pairs. Namely, the following processes contribute:

$$g_\gamma + g_p \to c\bar{c}[^1S_0, \underline{8}] + g$$

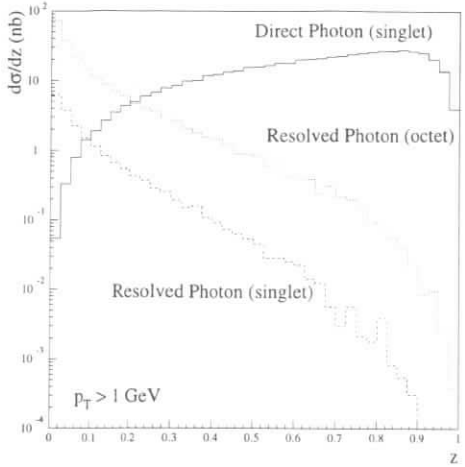

Figure 4: Comparison of the inelasticity distributions for direct (singlet) and resolved (singlet and octet) J/ψ photoproduction.

$$g_\gamma + g_p \to c\bar{c}[^3S_1, \underline{8}] + g$$
$$g_\gamma + g_p \to c\bar{c}[^3P_J, \underline{8}] + g\,.$$

They are in every respect analogous to the ones which have been argued to greatly increase the J/ψ production in $p\bar{p}$ collisions at the Tevatron. They must therefore be carefully considered here to understand whether or not they change the picture established by the CSM.

Using the matrix elements squared evaluated in ref.[8] and the choice of nonperturbative parameters displayed in Table 1 we can calculate the cross sections and compare them with the CSM ones. The results are shown in Table 2, with a minimum p_T cut needed to screen the collinear singularity present in the $^1S_0$ and ^3P_J channels.

Channel		$\sigma_{\gamma p}$ (nb) $\sqrt{s} = 100$ GeV $p_T > 1$ GeV
Direct	$^3S_1, \underline{1}$	13.68
Resolved	$^3S_1, \underline{1}$	.48
	$^1S_0, \underline{8}$	.79
	$^3S_1, \underline{8}$	.34
	$^3P_0, \underline{8}$	1.61
	$^3P_1, \underline{8}$	.50
	$^3P_2, \underline{8}$	2.06

Table 2: Results for the total cross sections (in nb).

These results make clear that the color-octet channels could provide a non-negligible increment of the overall J/ψ photoproduction cross section. It's therefore worth studying in more detail which regions of phase space will be mostly affected. A close look to the differential distributions of experimental interest shows that the behaviour of the color-octet contributions to the resolved channels is similar to that of the color-singlet one. Namely, it is only visible in the low-z region. Fig.4 shows the z distribution for the direct photon color-singlet channel (full line) compared with the old CSM resolved photon contribution (dashed line) and the new resolved photon color-octet one (dotted line). The resolved contributions can be seen to be enhanced by the color-octet terms, but the qualitative picture of them being visible only in the low-z region remains unchanged.

5 χ photoproduction

For the production of S-wave quarkonia, like J/ψ, ψ' or Υ, the factorization approach coincides with the color-singlet model in the nonrelativistic limit $v \to 0$. In the case of χ bound states, however, color-singlet and color-octet mechanisms contribute at the same order in v to annihilation rates and production cross sections and must therefore both be included for a consistent calculation [28]. The production of χ states plays a peculiar role in photon-hadron collisions. Unlikely what happens in hadron-hadron collisions, were χs are copiously produced by gg, gq and $q\bar{q}$ interactions, the process

$$\gamma + g \to c\bar{c}[^3P_J, \underline{1}] + g \tag{8}$$

namely the production of a color-singlet $c\bar{c}$ pair with the χ quantum numbers, happens to be forbidden at leading order in α_s. This is due to the color factor of the two gluons having to be symmetric in order to produce a color-singlet states. The gluons could therefore be replaced by two colorless photons, and the process $\chi \to \gamma\gamma\gamma$ is know to be forbidden by the request of charge conjugation invariance.

To have χ production initiated by a direct photon we must therefore either go to higher orders within the CSM, adding one gluon to the leading order diagram, or consider color-octet mediated channels.

Within the factorization approach, indeed, χ production can still take place at the leading $\mathcal{O}(\alpha\alpha_s^2)$, provided it is a color-octet $^3S_1$ charm pair which is produced in the hard interaction and subsequently hadronizes into a physical χ particle. The following two processes contribute:

$$\gamma + g \to c\bar{c}[^3S_1, \underline{8}] + g$$
$$\gamma + q(\bar{q}) \to c\bar{c}[^3S_1, \underline{8}] + q(\bar{q})$$

The first of these two reaction is by far the dominant one in the HERA energy range and at low transverse momentum. Within the spirit of the factorization approach, the cross section is given by the same short distance cross section evaluated for color-octet J/ψ photoproduction (see eq.(1) and the second process of eq.(4)), times the appropriate matrix elements $\langle \mathcal{O}^{\chi_J}[^3S_1, \underline{8}] \rangle$. These matrix elements have also been fitted to the Tevatron data in [7, 8], and found to be of order 10^{-2} GeV^3. Using, for the sake of simplicity, $\langle \mathcal{O}^{\chi_0}[^3S_1, \underline{8}] \rangle = 10^{-2}$ GeV^3 and the relation

$$\langle \mathcal{O}^{\chi_J}[^3S_1, \underline{8}] \rangle = (2J+1) \langle \mathcal{O}^{\chi_0}[^3S_1, \underline{8}] \rangle \tag{9}$$

we find

$$\sum_J \sigma(\gamma p \to \chi_J) = 9\langle \mathcal{O}^{\chi_0}[^3S_1, \underline{8}]\rangle \times 0.9 \text{ nb GeV}^{-3} \simeq 80 \text{ pb} \tag{10}$$

at $\sqrt{s} = 100$ GeV and with a minimum p_T cut of 3 GeV.

It is worth noticing here a pretty large discrepancy with the result of ref.[29]. Despite using a nonperturbative matrix element about a factor of two smaller than ours, it finds $\sigma(\gamma p \to \chi_1) = 0.13$ nb, which is about a factor of five larger than our result.

6 Associated $J/\psi + \gamma$ production

A particularly distinctive experimental probe of the relevance of color-octet contributions in quarkonia production can be the observation of the exclusive process given by the associated production of a J/ψ and a photon [30][2]:

$$\gamma p \to J/\psi + \gamma \tag{11}$$

Within the CSM this process can only undergo via the resolved photon channel, since at least two gluons must couple to the heavy quark line to produce a color-singlet $c\bar{c}$ pair:

$$\gamma p \to g_\gamma + g_p \to c\bar{c}[^3S_1, \underline{1}] + \gamma \to J/\psi + \gamma \tag{12}$$

A big suppression of the cross section, and the characteristic z distribution typical of resolved photon processes, peaked at low z, can therefore be expected.

Within the factorization approach, on the other hand, other $c\bar{c}$ states can contribute and, in particular, the reaction can now proceed also via a direct photon channel. Indeed, the following processes are now possible:

Direct photon (fig.5a):

$$\begin{aligned} &\gamma + g_p \to c\bar{c}[^1S_0, \underline{8}] + \gamma \\ &\gamma + g_p \to c\bar{c}[^3S_1, \underline{8}] + \gamma \\ &\gamma + g_p \to c\bar{c}[^3P_J, \underline{8}] + \gamma \end{aligned}$$

Resolved photon (fig.5b):

$$\begin{aligned} &g_\gamma + g_p \to c\bar{c}[^1S_0, \underline{8}] + \gamma \\ &g_\gamma + g_p \to c\bar{c}[^3S_1, \underline{1}] + \gamma \qquad \text{(Standard CSM process)} \\ &g_\gamma + g_p \to c\bar{c}[^3S_1, \underline{8}] + \gamma \\ &g_\gamma + g_p \to c\bar{c}[^3P_J, \underline{8}] + \gamma \end{aligned}$$

Though the nonperturbative matrix elements which mediate the hadronization of the color-octet $c\bar{c}$ pairs to a J/ψ are suppressed with respect to the color-singlet one (see Table 1), we can however still expect the two following features:

[2]see also ref.[31] for an analysis within the color-evaporation model.

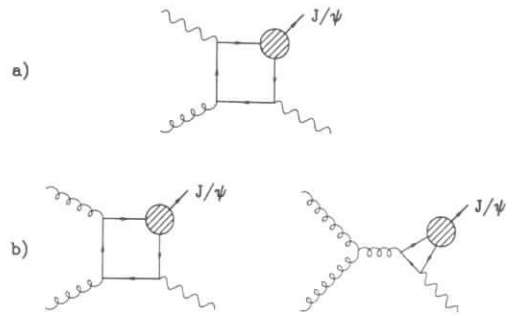

Figure 5: Diagrams contributing within the factorization approach to J/ψ + photon associated production in direct (a) and resolved (b) photon collisions. In (b) the right diagram contributes to $^1S_0$ and ^3P_J states production only.

i) the production of color-octet states via a direct process - rather than a resolved one - will at least partially compensate for the smaller matrix elements. We should therefore expect an increase in the overall cross section;

ii) the z distribution of the J/ψ, will be more peaked towards one. This is again due to the presence of a direct photon coupling as opposed to the resolved one, where the g_γ only carries part of the photon energy into the reaction.

These (and especially the second one) are the reasons why we expect this process to be a sensitive probe to color-octet components.

Channel		$\sigma_{\gamma p}(pb)$ $\sqrt{s} = 100$ GeV $p_T > 1$ GeV
Direct	$^1S_0, \underline{8}$	–
	$^3S_1, \underline{8}$	7.67
	$^3P_J, \underline{8}$	–
Resolved	$^1S_0, \underline{8}$	.35
	$^3S_1, \underline{1}$	16.70
	$^3S_1, \underline{8}$	.27
	$^3P_0, \underline{8}$	1.03
	$^3P_1, \underline{8}$	.14
	$^3P_2, \underline{8}$	.97

Table 3: Results for the total cross sections of $J/\psi + \gamma$ photoproduction (in pb). At leading-order, the $^1S_0$ and ^3P_J direct contributions vanish identically.

The total cross sections (with a minimum p_T cut of 1 GeV) are shown in Table 3 for γp collisions at a cm energy of 100 GeV (see ref. [30] for more details). The bulk of the cross section

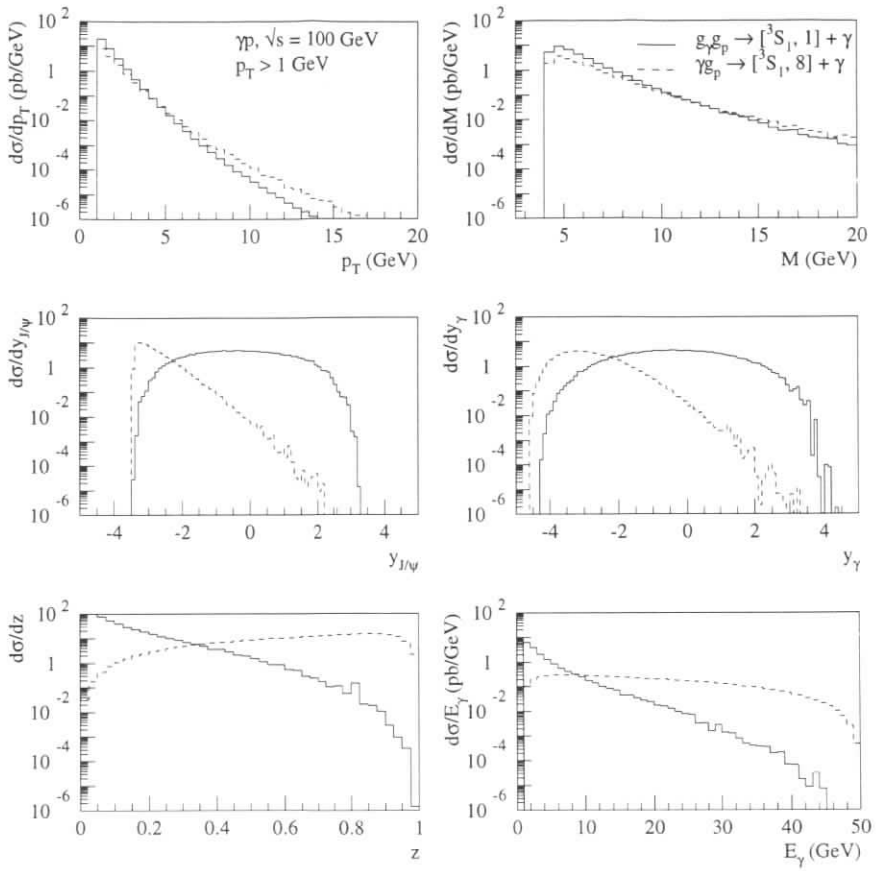

Figure 6: Differential distributions in γp collision at $\sqrt{s} = 100$ GeV. A minimum p_T cut of 1 GeV is applied.

can be seen to come from the standard CSM channel $gg \to c\bar{c}[^3S_1, \underline{1}] + \gamma$. However, the direct channel gives a non negligible contribution, amounting to about 25% of the overall cross section of ~ 27 pb. This increase is however far too small to be reliably used to assess the presence of the color-octet terms, given the smallness of this cross section (in the picobarn region) and the large theoretical uncertainties involved (like the charm mass, the strong coupling and the nonperturbative matrix elements values).

On the other hand, the study of the differential distributions can make easier to disentangle the color-octet contributions from the standard color-singlet one.

We therefore show in fig.6 the differential distributions related to the total γp cross sections

at $\sqrt{s} = 100$ GeV with a minimum p_T cut of 1 GeV, presented in Table 3. The distributions due to $[^3S_1,\underline{1}]$ production in resolved photon collision (continuous line) and to $[^3S_1,\underline{8}]$ production in direct photon collision (dashed line) only are shown. The distributions due to the other color-octet processes do indeed present the same features as the ones of $[^3S_1,\underline{1}]$, being also produced in resolved photon interactions, but are suppressed in magnitude, as can be seen from Table 3. Their inclusion would therefore not change the picture we are going to discuss.

Fig.6 compares the result of the CSM with that due to the production of a color-octet $^3S_1$ state in direct photon collision, fig.5a, as predicted by the factorization approach. As expected, the effect of the direct photon coupling can easily be seen in at least some of the plots. While the p_T of the J/ψ and the invariant mass distribution of the J/ψ-γ pair are pretty similar for the two processes, the z, rapidity and photon energy distributions do indeed show a strikingly different behaviour.

Recalling that we put ourselves in the so-called "HERA-frame", with the photon (or the electron) traveling in the direction of negative rapidities, we notice how the direct photon coupling favours the production of the quarkonium and of the photon in the negative rapidities region. This contrasts the case of resolved photon production of color-singlet $^3S_1$ states, which are uniformly produced around the central region.

As for the z distribution, the resolved photon process predicts a decrease of the cross section going towards the high-z region. The direct photon process does on the other hand predict the opposite behaviour: the cross section now increases going towards $z = 1$. The small dip in the last few bins is due to the minimum p_T cut.

Similarly to the z distribution behaves the photon energy one, which is predicted to be much harder in direct photon processes.

These distributions (which were also checked to be robust with respect to a higher p_T cut, so as to be sure of the absence of p_T^{min} effects) could already be good experimental discriminators: observation of a substantial fraction of $J/\psi + \gamma$ events in the high z region would provide good evidence for the presence of color-octet contributions to the overall cross section.

7 J/ψ production in deep inelastic scattering

Leptoproduction of quarkonium states has been extensively studied in the framework of the color-singlet model [2]. Though the color-singlet contribution can explain inelastic leptoproduction of J/ψ it can not explain the total cross section. Thus, in order to arrive at a complete description of J/ψ leptoproduction, the color-octet contributions to the J/ψ production rate have been calculated in ref.[32]. The authors obtain the following expression for the differential subprocess cross section:

$$\begin{aligned} Q^2 \frac{d\hat{\sigma}}{dQ^2}(eg \to eJ/\psi) \;=\; & \frac{2\pi^2 e_c^2 \alpha_s \alpha^2}{m_c \hat{s}} \int \frac{dy}{y^2} \Bigg\{ \frac{1+(1-y)^2}{y} \\ & \times \left[y \langle \mathcal{O}^{J/\psi}[^1S_0, \underline{8}] \rangle + \frac{\langle \mathcal{O}^{J/\psi}[^3P_0, \underline{8}] \rangle}{m_c^2} \frac{3Q^2 + 7(2m_c)^2}{\hat{s}} \right] \\ & - \frac{\langle \mathcal{O}^{J/\psi}[^3P_0, \underline{8}] \rangle}{m_c^2} \frac{8(2m_c)^2 Q^2}{\hat{s}^3} \Bigg\} \delta\left(\hat{s}y - (4m_c^2 + Q^2)\right) , \end{aligned} \tag{13}$$

where $\sqrt{\hat{s}}$ is the subprocess center-of-mass energy, Q^2 is the negative invariant mass of the photon, and y is the momentum fraction of the J/ψ relative to the incoming electron. To obtain the cross section one convolutes the expression given in eq.(13) with the gluon distribution function. The hadronization of the $c\bar{c}$ pair, produced initially in a color-octet state with spin/angular-momentum quantum numbers $^{2S+1}L_J$, into a J/ψ bound state is parametrized by the NRQCD matrix elements $\langle \mathcal{O}^{J/\psi}[^1S_0, \underline{8}]\rangle$ and $\langle \mathcal{O}^{J/\psi}[^3P_0, \underline{8}]\rangle$. Note that it is precisely the matrix elements appearing in eq.(13) that are at the heart of the discrepancy between the CDF measurement and the photoproduction results.

There is an important point regarding the differential cross section presented in eq.(13). In principle this result is valid for all values of Q^2, however, there are corrections due to higher twist terms that have been neglected in the derivation of the factored form of the cross section. These higher twist terms are suppressed by powers of m_c^2/Q^2, and will, therefore, vanish for $Q^2 \gg m_c^2$. Thus it is necessary to compare the theoretical results presented in eq.(13) to experimental data in the large Q^2 regime. In the limit where $\hat{s}, Q^2 \gg m_c^2$, eq.(13) reduces to

$$\lim_{\hat{s},Q^2 \gg m_c^2} Q^2 \frac{d\hat{\sigma}}{dQ^2}(eg \to eJ/\psi) \longrightarrow \frac{2\pi^2 e_c^2 \alpha_s \alpha^2}{m_c \hat{s}} \int dy \frac{1+(1-y)^2}{y^2} \times \left\{ \langle \mathcal{O}^{J/\psi}[^1S_0, \underline{8}]\rangle + 3\frac{\langle \mathcal{O}^{J/\psi}[^3P_0, \underline{8}]\rangle}{m_c^2} \right\} \delta(y - \frac{Q^2}{\hat{s}}) \,. \tag{14}$$

Note that for large Q^2 the linear combination $\langle \mathcal{O}^{J/\psi}[^1S_0, \underline{8}]\rangle + 3\langle \mathcal{O}^{J/\psi}[^3P_0, \underline{8}]\rangle/m_c^2$ is determined. This is precisely the linear combination of NRQCD matrix elements that is measured at CDF. Therefore J/ψ leptoproduction can provide an independent means of determining this linear combination of NRQCD matrix elements in a manner different from the CDF measurement.

Currently there exists experimental data on the production of J/ψ in μN collisions [33], however, the values of Q^2 probed in this experiment are too low to be in the asymptotic region, and the error on the experimental measurements are too large to allow for an accurate determination of the color-octet matrix elements. The high-statistics measurements to be expected in the future at HERA could definitely help to improve the situation and to constrain the color-octet matrix elements.

8 Conclusion

We have worked out and reviewed the impact of color-octet contributions on quarkonium production in photon-proton collisions and deep-inelastic scattering at HERA. Photoproduction of J/ψ, ψ', Υ and χ states, associated $J/\psi + \gamma$ production, fragmentation and resolved-photon contributions as well as deep inelastic J/ψ production have been discussed. We have shown how these reactions can be used to constrain the color-octet matrix elements and test the picture of quarkonium production as developed in the context of the NRQCD factorization approach.

Acknowledgements

Numerous and fruitful conversations with Mario Greco are gratefully acknowledged. Section 7 was prepared in collaboration with Sean Fleming. We are grateful to him and to Rohini Godbole and K. Sridhar for providing Figure 3 at short notice.

References

[1] H. Jung, G.A. Schuler and J. Terrón, Proc. 'Physics at HERA', Eds. W. Buchmüller, G. Ingelman, DESY, Hamburg, 1992 and Int. J. Mod. Phys. A7 (1992) 7955; A. Ali, Proceedings, 'XXI International Meeting on Fundamental Physics', Madrid, 1993.

[2] E.L. Berger and D. Jones, Phys. Rev. **D23** (1981) 1521; R. Baier and R. Rückl, Phys. Lett. **102B** (1981) 364; J.G. Körner, J. Cleymans, M. Kuroda and G.J. Gounaris, Nucl. Phys. **B204** (1982) 6; R. Baier and R. Rückl, Nucl. Phys. **B208** (1982) 381, *ibid.* B218 (1983) 289, Z. Phys. **C19** (1983) 251; for a recent review see also G.A. Schuler, CERN-TH.7170/94 (hep-ph/9403387).

[3] H. Fritzsch, Phys. Lett. **B67** (1977) 217; H. Fritzsch and K.H. Streng, Phys. Lett. **B72** (1978) 385; M. Glück, J.F. Owens and E. Reya, Phys. Rev. **D17** (1978) 2324; for a recent work see J.F. Amundson, O.J.P. Eboli, E.M. Gregores and F. Halzen, MADPH-96-942 (hep-ph/9605295).

[4] G.T. Bodwin, E. Braaten and G.P. Lepage, Phys. Rev. **D51** (1995) 1125.

[5] W.E. Caswell and G.P. Lepage, Phys. Lett. **B167** (1986) 437.

[6] G.P. Lepage, L. Magnea, C. Nakhleh, U. Magnea and K. Hornbostel, Phys. Rev. **D46** (1992) 4052.

[7] E. Braaten and S. Fleming, Phys. Rev. Lett. **74** (1995) 3327; M. Cacciari, M. Greco, M.L. Mangano and A. Petrelli, Phys. Lett. **B356** (1995) 560.

[8] P. Cho and A.K. Leibovich, Phys. Rev. **D53** (1996) 150 and *ibid.* **53** (1996) 6203.

[9] E. Braaten and Y.-Q. Chen, Phys. Rev. Lett. **76** (1996) 730; K. Cheung, W.-Y. Keung and T.C. Yuan, Phys. Rev. Lett. **76** (1996) 877; P. Cho, Phys. Lett. **B368** (1996) 171; W.-K. Tang and M. Vänttinen, Phys. Rev. **D53** (1996) 4851 and NORDITA-96-18-P (hep-ph/9603266); S. Fleming and I. Maksymyk, Phys. Rev. **D54** (1996) 3608; S. Gupta and K. Sridhar, TIFR-TH-96-04 (hep-ph/9601349); M. Beneke and I.Z. Rothstein, Phys. Rev. **D54** (1996) 2005; P. Ko, J. Lee and H.S. Song, Phys. Rev. **D53** (1996) 1409; S. Fleming, O.F. Hernández, I. Maksymyk, H. Nadeau, MADPH-96-953 (hep-ph/9608413).

[10] W. Koepf, P.V. Landshoff, E.M. Levin and N.N. Nikolaev, Proc. 'Future Physics at HERA', Eds. A. de Roeck, G. Ingelman and R. Klanner, DESY, Hamburg, 1996 and references therein.

[11] W.Y. Keung and I.J. Muzinich, Phys. Rev. **D27** (1983) 1518; H. Jung, D. Krücker, C. Greub and D. Wyler, Z. Phys. **C60** (1993) 721; H. Khan and P. Hoodbhoy Phys. Lett. **B382** (1996) 189.

[12] M. Krämer, J. Zunft, J. Steegborn and P.M. Zerwas, Phys. Lett. **B348** (1995) 657.

[13] M. Krämer, Nucl. Phys. **B459** (1996) 3.

[14] M. Cacciari and M. Krämer, Phys. Rev. Lett. **76** (1996) 4128.

[15] J. Amundson, S. Fleming and I. Maksymyk, UTTG-10-95 (hep-ph/9601298).

[16] P. Ko, J. Lee and H.S. Song, SNUTP-95-116 (hep-ph/9602223).

[17] E. Braaten, S. Fleming and T.C. Yuan, OHSTPY-HEP-T-96-001 (hep-ph/9602374), E. Braaten and Y.-Q. Chen, Phys. Rev. **D54** (1996) 3216.

[18] S. Aid et al. [H1 Collab.], Nucl. Phys. **B472** (1996) 3.

[19] M. Derrick et al. [ZEUS Collab.], presented by L. Stanco at the International Workshop on Deep Inelastic Scattering, Rome, April 1996.

[20] M. Glück, E. Reya and A. Vogt, Z. Phys. **C67** (1995) 433; A.D. Martin, G. Roberts and W.J. Stirling, Phys. Lett. **B354** (1995) 155; H.L. Lai, J. Botts, J. Huston, J.G. Morfin, J.F. Owens, J.W. Qiu, W.K. Tung and H. Weerts, Phys. Rev. **D51** (1995) 4763.

[21] A.D. Martin, R.G. Roberts and W.J. Stirling, Phys. Lett. **B306** (1993) 145.

[22] M. Derrick et al. [ZEUS Collaboration], Phys. Lett. **B345** (1995) 576; S. Aid et al. [H1 Collaboration], Phys. Lett. **B354** (1995) 494.

[23] For a compilation of data see G.A. Schuler in [2].

[24] E. Braaten and T.C. Yuan, prl71931673; M. Cacciari and M. Greco, Phys. Rev. Lett. **73** (1994) 1586; E. Braaten, M.A. Doncheski, S. Fleming and M.L. Mangano, Phys. Lett. **B333** (1994) 548; D.P. Roy and K. Sridhar, Phys. Lett. **B339** (1994) 141.

[25] E. Braaten and T.C. Yuan, Phys. Rev. **D50** (1994) 3176; Y.Q. Chen, Phys. Rev. **D48** (1993) 5181; T.C. Yuan, Phys. Rev. **D50** (1994) 5664.

[26] R. Godbole, D.P. Roy and K. Sridhar, Phys. Lett. **B373** (1996) 328.

[27] V.A. Saleev, Mod. Phys. Lett. **A9** (1994) 1083.

[28] G.T. Bodwin, E. Braaten and G.P. Lepage, Phys. Rev. **D46** (1992) R1914.

[29] J.P. Ma, Nucl. Phys. **B460** (1996) 109.

[30] M. Cacciari, M. Greco and M. Krämer, DESY 96-147.

[31] C.S. Kim and E. Reya, Phys. Lett. **B300** (1993) 298.

[32] S. Fleming, I. Maksymyk and T. Mehen, talk presented at the workshop 'Quarkonium Physics', Chicago, USA, June 13-15, 1996 and publication in preparation.

[33] J.J. Aubert et al., Nucl. Phys. **B213** (1983) 1, Z. Phys. **C56** (1992) 21; D. Allasia et al., Phys. Lett. **B258** (1991) 493.

CP Violation and Flavour Mixing in the Standard Model – 1996 Update

A. Ali[a], D. London[b]

[a] Deutsches Elektronen-Synchrotron DESY, Notkestrasse 85, D-22603 Hamburg, FRG
[b] Laboratoire de physique nucléaire, Université de Montréal, C.P. 6128, succ. centre-ville, Montréal, QC, Canada H3C 3J7.

Abstract: We have recently reviewed and updated the constraints on the parameters of the quark flavour mixing matrix V_{CKM} in the standard model. A summary of the main results is given here, emphasizing the features relevant for HERA-B. These include the standard model predictions for the B_s^0-$\overline{B_s^0}$ mixing parameter x_s (or, equivalently, ΔM_s) and the quantities $\sin 2\alpha$, $\sin 2\beta$ and $\sin^2\gamma$, which characterize CP asymmetries in B-decays.

1 An Update of the CKM Matrix

We have recently revised and updated the profile of the Cabibbo-Kobayashi-Maskawa (CKM) matrix [1] in Ref. [2]. Our main focus is on the CKM unitarity triangle and CP asymmetries in B decays, which are the principal objects of interest in experiments at present and forthcoming B facilities. In performing this update, we have included the improvements reported in a number of measurements of the lifetime, mixing ratio, and the CKM matrix elements $|V_{cb}|$ and $|V_{ub}/V_{cb}|$ from B decays, as well as the top quark mass, $|\epsilon|$, and progress in theoretical calculations involving a number of perturbative and non-perturbative aspects of QCD. We summarize the input and those results which have a direct bearing on the physics of HERA-B. For details and references, we refer to [2].

In updating the CKM matrix elements, we make use of the Wolfenstein parametrization [3], which follows from the observation that the elements of this matrix exhibit a hierarchy in terms of λ, the Cabibbo angle. In this parametrization the CKM matrix can be written approximately as

$$V_{CKM} \simeq \begin{pmatrix} 1-\frac{1}{2}\lambda^2 & \lambda & A\lambda^3(\rho-i\eta) \\ -\lambda(1+iA^2\lambda^4\eta) & 1-\frac{1}{2}\lambda^2 & A\lambda^2 \\ A\lambda^3(1-\rho-i\eta) & -A\lambda^2 & 1 \end{pmatrix} . \qquad (1)$$

We shall discuss those quantities which constrain these CKM parameters, pointing out the significant input in the determination of λ, A, ρ and η.

- $|V_{us}|$: We recall that $|V_{us}|$ has been extracted with good accuracy from $K \to \pi e \nu$ and hyperon decays [4] to be

$$|V_{us}| = \lambda = 0.2205 \pm 0.0018 \ . \tag{2}$$

This agrees quite well with the determination of $V_{ud} \simeq 1 - \frac{1}{2}\lambda^2$ from β-decay [4],

$$|V_{ud}| = 0.9736 \pm 0.0010 \ . \tag{3}$$

- $|V_{cb}|$: The determination of $|V_{cb}|$ from inclusive and exclusive B decays has been reviewed earlier in a number of studies [5, 6, 7, 8]. Here, we shall concentrate on the exclusive decay $B \to D^* \ell \nu_\ell$ analyzed in the context of heavy quark effective theory (HQET) [9], as this method seems to have been scrutinized in great detail. This gives [2]:

$$|V_{cb}| = 0.0393 \pm 0.0028 \ , \tag{4}$$

yielding

$$A = 0.81 \pm 0.058 \ . \tag{5}$$

- $|V_{ub}/V_{cb}|$: The knowledge of the CKM matrix element ratio $|V_{ub}/V_{cb}|$ is based on the analysis of the end-point lepton energy spectrum in semileptonic decays $B \to X_u \ell \nu_\ell$ and the measurement of the exclusive semileptonic decays $B \to (\pi, \rho) \ell \nu_\ell$ reported by the CLEO collaboration [8]. Present measurements in both the inclusive and exclusive modes are compatible with [10]:

$$\left|\frac{V_{ub}}{V_{cb}}\right| = 0.08 \pm 20\% \ . \tag{6}$$

This gives

$$\sqrt{\rho^2 + \eta^2} = 0.363 \pm 0.073 \ . \tag{7}$$

- $|\epsilon|, \hat{B}_K$, and constraints on ρ and η: The experimental value of $|\epsilon|$ is [4]:

$$|\epsilon| = (2.280 \pm 0.013) \times 10^{-3} \ . \tag{8}$$

Theoretically, $|\epsilon|$ is essentially proportional to the imaginary part of the box diagram for K^0-$\overline{K^0}$ mixing and is given by [11]

$$|\epsilon| = \frac{G_F^2 f_K^2 M_K M_W^2}{6\sqrt{2}\pi^2 \Delta M_K} \hat{B}_K \left(A^2 \lambda^6 \eta\right) \left(y_c \left\{\hat{\eta}_{ct} f_3(y_c, y_t) - \hat{\eta}_{cc}\right\} + \hat{\eta}_{tt} y_t f_2(y_t) A^2 \lambda^4 (1 - \rho)\right), \tag{9}$$

where $y_i \equiv m_i^2/M_W^2$, and the functions f_2 and f_3 can be found in Ref. [5]. Here, the $\hat{\eta}_i$ are QCD correction factors, calculated at next-to-leading order in [12] ($\hat{\eta}_{cc}$), [13] ($\hat{\eta}_{tt}$) and [14] ($\hat{\eta}_{ct}$). The theoretical uncertainty in the expression for $|\epsilon|$ is in the renormalization-scale independent parameter $\hat{B}_K$, which represents our ignorance of the hadronic matrix element $\langle K^0 | (\bar{d}\gamma^\mu(1-\gamma_5)s)^2 | \overline{K^0} \rangle$. Recent calculations of $\hat{B}_K$ using lattice QCD methods and the $1/N_c$ approach are summarized in [2], which gives

$$\hat{B}_K = 0.75 \pm 0.10. \tag{10}$$

- $\Delta M_d, f_{B_d}^2 \hat{B}_{B_d}$, and constraints on ρ and η: The present world average for ΔM_d is $\Delta M_d = 0.464 \pm 0.018 \ (ps)^{-1}$ [10] . The mass difference ΔM_d is calculated from the B_d^0-$\overline{B_d^0}$ box diagram. Unlike the kaon system, where the contributions of both the c- and the t-quarks in the loop are important, this diagram is dominated by t-quark exchange:

$$\Delta M_d = \frac{G_F^2}{6\pi^2} M_W^2 M_B \left(f_{B_d}^2 \hat{B}_{B_d}\right) \hat{\eta}_B y_t f_2(y_t) |V_{td}^* V_{tb}|^2 \ , \tag{11}$$

where, using Eq. 1, $|V_{td}^* V_{tb}|^2 = A^2 \lambda^6 [(1-\rho)^2 + \eta^2]$. Here, $\hat{\eta}_B$ is the QCD correction. In the fits presented in [2] we used the value $\hat{\eta}_B = 0.55$, calculated in the $\overline{MS}$ scheme, following Ref. [13]. Consistency requires that the top quark mass be rescaled from its pole (mass) value of $m_t = 175 \pm 9$ GeV to the value $\overline{m_t}(m_t(pole)) = 165 \pm 9$ GeV in the $\overline{MS}$ scheme.

For the B system, the hadronic uncertainty is given by $f_{B_d}^2 \hat{B}_{B_d}$, analogous to $\hat{B}_K$ in the kaon system, except that in this case f_{B_d} has not been measured. In our fits in [2], we have taken

$$f_{B_d} \sqrt{\hat{B}_{B_d}} = 200 \pm 40 \text{ MeV} \ , \tag{12}$$

which is compatible with the results from both lattice-QCD and QCD sum rules for this quantity.

For the CKM fits, the present experimental input can be summarized as follows:

$$\begin{aligned} \sqrt{\rho^2 + \eta^2} &= 0.363 \pm 0.073 \quad \text{(from } |V_{ub}/V_{cb}|\text{)}, \\ (f_{B_d}\sqrt{\hat{B}_{B_d}}/1 \text{ GeV}) \sqrt{(1-\rho)^2 + \eta^2} &= 0.202 \pm 0.017 \quad \text{(from } \Delta M_d\text{)}, \\ \hat{B}_K \eta [0.93 + (2.08 \pm 0.34)(1-\rho)] &= (0.79 \pm 0.11) \quad \text{(from } |\epsilon|\text{)}, \end{aligned} \tag{13}$$

The errors of the last two lines include the small experimental errors on ΔM_d (3.6%) and $|\epsilon|$ (0.6%), as well as the larger errors on m_t^2 (11%) and A^2 (14%). Adding all these errors in quadrature, one finds that the total experimental errors involved in $|V_{ub}/V_{cb}|$, ΔM_d and $|\epsilon|$ are about 20%, 8% and 16%, respectively. The theoretical error on $f_{B_d}\sqrt{\hat{B}_{B_d}}$ is about 20% and on $\hat{B}_K$ about 13%. Thus, one sees that the present theoretical and experimental errors are not terribly different.

We have considered two types of fits in Ref. [2]. In Fit 1, we assume particular fixed values for the theoretical hadronic quantities. The allowed ranges for the CKM parameters are derived from the (Gaussian) errors on experimental measurements only. In Fit 2, we assign a central value plus an error (treated as Gaussian) to the theoretical quantities. In the resulting fits, we combine the experimental and theoretical errors in quadrature. For both fits we calculate the allowed region in CKM parameter space at 95% C.L.

We have also estimated in [2] the SM prediction for the B_s^0-$\overline{B_s^0}$ mixing parameter, ΔM_s and x_s. The experimental lower limits on these quantities have steadily increased, thanks to the experiments at LEP [16, 17] and more recently also from SLC. These limits have now started to be significant for the allowed CKM parameter space. We show how the improved ALEPH limit of $\Delta M_s > 7.8 \ (\text{ps})^{-1}$ leading to $\Delta M_s/\Delta M_d > 16.0$ (95% C.L.) [15, 17] constrains the CKM parameter space. We have presented in [2] the allowed ranges for the CP-violating phases that

Parameter	Value
λ	0.2205
$\lvert V_{cb}\rvert$	0.0393 ± 0.0028
$\lvert V_{ub}/V_{cb}\rvert$	0.08 ± 0.016
$\lvert\epsilon\rvert$	$(2.280 \pm 0.013) \times 10^{-3}$
ΔM_d	$(0.464 \pm 0.018)\ (ps)^{-1}$
$\tau(B_d)$	$(1.52 \pm 0.05)\ (ps)$
$\overline{m_t}(m_t(pole))$	(165 ± 9) GeV
$\hat{\eta}_B$	0.55
$\hat{\eta}_{cc}$	1.38
$\hat{\eta}_{ct}$	0.47
$\hat{\eta}_{tt}$	0.57
$\hat{B}_K$	0.75 ± 0.1
$f_{B_d}\sqrt{\hat{B}_{B_d}}$	200 ± 40 MeV

Table 1: Parameters used in the CKM fits. Values of the hadronic quantities $\hat{B}_K$ and $f_{B_d}\sqrt{\hat{B}_{B_d}}$ shown are motivated by lattice QCD results, QCD sum rules and chiral perturbation theory. In Fit 1, specific values of these hadronic quantities are chosen, while in Fit 2, they are allowed to vary over the given ranges.

will be measured in B decays, characterized by $\sin 2\beta$, $\sin 2\alpha$ and $\sin^2\gamma$. These can be measured directly through rate asymmetries in the decays $\overset{(-)}{B_d} \to J/\psi K_S$, $\overset{(-)}{B_d} \to \pi^+\pi^-$, and $\overset{(-)}{B_s} \to D_s^{\pm}K^{\mp}$ (or $B^{\pm} \to \overset{(-)}{D}\, K^{\pm}$), respectively. We also show the allowed correlated domains for two of the CP asymmetries ($\sin 2\alpha, \sin 2\beta$).

This contribution is organized as follows. In Section 2, we summarize the results of our updated fits for the CKM parameters [2] in terms of the allowed domains of the unitarity triangle, which are displayed in several figures and tables. In Section 3, we discuss the impact of the recent lower limit on the ratio $\Delta M_s/\Delta M_d$ reported by the ALEPH collaboration on the CKM parameters and estimate the expected range of the mixing ratio x_s and ΔM_s in the SM based on our fits. In Section 4 we discuss the predictions for the CP asymmetries in the neutral B meson sector and calculate the correlations for the CP-violating asymmetries proportional to $\sin 2\alpha$, $\sin 2\beta$ and $\sin^2\gamma$. Section 5 contains a summary and an outlook for improving the profile of the CKM unitarity triangle.

2 The Unitarity Triangle

The allowed region in ρ-η space can be displayed quite elegantly using the so-called unitarity triangle. The unitarity of the CKM matrix leads to the following relation:

$$V_{ud}V_{ub}^* + V_{cd}V_{cb}^* + V_{td}V_{tb}^* = 0\ . \tag{14}$$

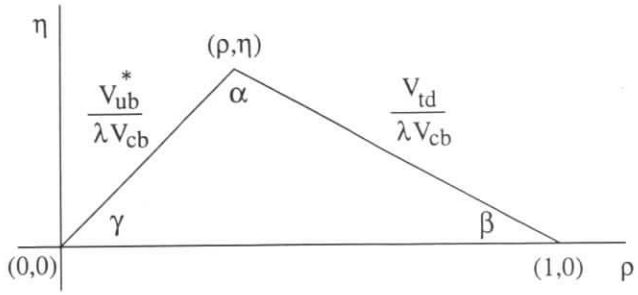

Figure 1: The unitarity triangle. The angles α, β and γ can be measured via CP violation in the B system.

Using the form of the CKM matrix in Eq. 1, this can be recast as

$$\frac{V_{ub}^*}{\lambda V_{cb}} + \frac{V_{td}}{\lambda V_{cb}} = 1\ , \tag{15}$$

which is a triangle relation in the complex plane (i.e. ρ-η space), illustrated in Fig. 1. Thus, allowed values of ρ and η translate into allowed shapes of the unitarity triangle.

In order to find the allowed unitarity triangles, the computer program MINUIT is used to fit the CKM parameters A, ρ and η to the experimental values of $|V_{cb}|$, $|V_{ub}/V_{cb}|$, $|\epsilon|$ and x_d. Since λ is very well measured, we have fixed it to its central value given above. As discussed in the introduction, two types of fits have been presented in [2]. We first discuss the "experimental fit" (Fit 1). The goal here is to restrict the allowed range of the parameters (ρ, η) for given values of the coupling constants $f_{B_d}\sqrt{\hat{B}_{B_d}}$ and $\hat{B}_K$. For each value of $\hat{B}_K$ and $f_{B_d}\sqrt{\hat{B}_{B_d}}$, the CKM parameters A, ρ and η are fit to the experimental numbers given in Table 1 and the χ^2 is calculated.

First, we fix $\hat{B}_K = 0.75$, and vary $f_{B_d}\sqrt{\hat{B}_{B_d}}$ in the range 130 MeV to 240 MeV. The resulting χ^2_{min} values were calculated together with the best-fit values of the CKM parameters (ρ, η), which can be seen in [2]. The fits are presented as an allowed region in ρ-η space at 95% C.L. ($\chi^2 = \chi^2_{min} + 6.0$). The results are shown in Fig. 2. As we pass from Fig. 2 (top left) to Fig. 2 (bottom right), the unitarity triangles represented by these graphs become more and more obtuse, which leads us to the conclusion that our quantitative knowledge of the unitarity triangle is at present not very solid. This is seen more clearly in the results of Fit 2. So, unless our knowledge of hadronic matrix elements improves considerably, measurements of $|\epsilon|$ and x_d, no matter how precise, will not help much in further constraining the unitarity triangle. This is why measurements of CP-violating rate asymmetries in the B system are so important [19, 20]. Being largely independent of theoretical uncertainties, they will allow us to accurately pin down the unitarity triangle.

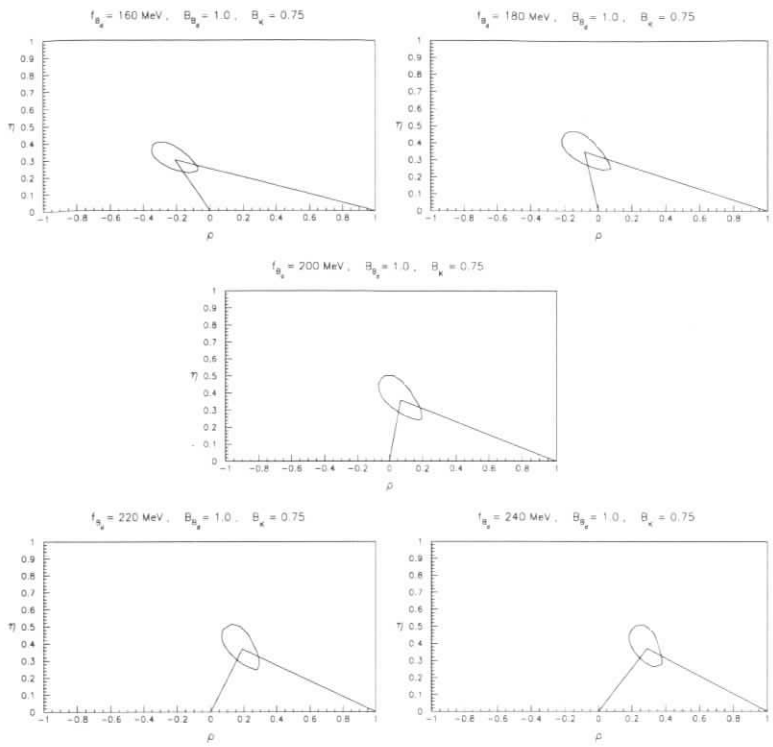

Figure 2: Allowed region in ρ-η space, from a fit to the experimental values given in Table 1. We have fixed $\hat{B}_K = 0.75$ and vary the coupling constant product $f_{B_d}\sqrt{\hat{B}_{B_d}}$ as indicated on the figures. The solid line represents the region with $\chi^2 = \chi^2_{min} + 6$ corresponding to the 95% C.L. region. The triangles show the best fit.

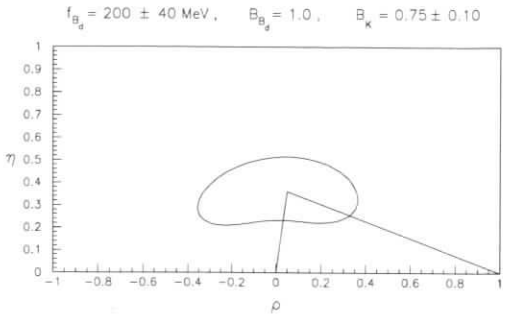

Figure 3: Allowed region in ρ-η space, from a simultaneous fit to both the experimental and theoretical quantities given in Table 1. The theoretical errors are treated as Gaussian for this fit. The solid line represents the region with $\chi^2 = \chi^2_{min} + 6$ corresponding to the 95% C.L. region. The triangle shows the best fit.

We now discuss the "combined fit" (Fit 2). Since the coupling constants are not known and the best we have are estimates given in the ranges in Eqs. (10) and (12), a reasonable profile of the unitarity triangle at present can be obtained by letting the coupling constants vary in these ranges. The resulting CKM triangle region is shown in Fig. 3. As is clear from this figure, the allowed region is still rather large at present. However, present data and theory do restrict the parameters ρ and η to lie in the following range:

$$\begin{aligned} 0.20 \le \eta \le 0.52, \\ -0.35 \le \rho \le 0.35\ . \end{aligned} \tag{16}$$

The preferred values obtained from the "combined fit" are

$$(\rho, \eta) = (0.05, 0.36) \quad (\text{with } \chi^2 = 6.6 \times 10^{-3})\ , \tag{17}$$

which gives rise to an almost right-angled unitarity triangle, with the angle γ being close to 90 degrees. However, as we quantify below, the allowed ranges of the CP violating angles α, β, and γ estimated at the 95% C.L. are still quite large, though correlated.

Finally, to check that our combined fit (Fit 2) is not introducing a significant theoretical bias in estimating the profile of the unitarity triangle, we have also determined the allowed parameter space in the ρ–η plane by overlaying the individual constraints following from the experimental measurements of $|V_{ub}/V_{cb}|$, $|\epsilon|$, and ΔM_d given in Eqs. (13). In doing this, we took the central experimental value for the ratio $|V_{ub}/V_{cb}|$, and varied the experimental error by $\pm 2\sigma$, which is then a common feature with Fit 2. For $|\epsilon|$ and ΔM_d, we varied the experimental errors by $\pm 1\sigma$ and varied the theoretical input $\hat{B}_K$ in the range $0.65 \le \hat{B}_K \le 0.85$ and $f_{B_d}\sqrt{\hat{B}_{B_d}}$ in the range 160 MeV $\le f_{B_d}\sqrt{\hat{B}_{B_d}} \le 240$ MeV. The resulting allowed domain in the ρ–η plane is shown in Fig. 4 together with the (95%) C.L. contours allowed by our Fit 2. This plot shows that one gets essentially the same allowed region using the two techniques, reflecting the fact

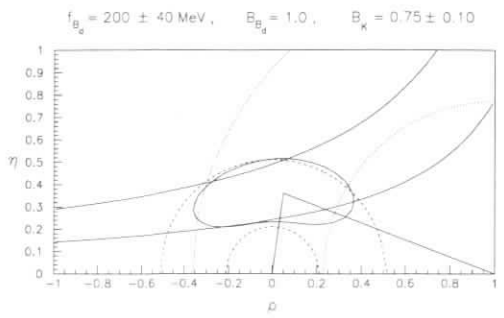

Figure 4: Allowed region in ρ-η space obtained by overlaying the individual constraints following from $|V_{ub}/V_{cb}|$ (with $\pm 2\sigma$ error) (dashed curves), $|\epsilon|$ (solid curves), and ΔM_d (dotted curves) [both with $\pm 1\sigma$ errors given in Eqs. (13)], and varying $\hat{B}_K$ in the range $0.65 \leq \hat{B}_K \leq 0.85$ and $f_{B_d}\sqrt{\hat{B}_{B_d}}$ in the range 160 MeV $\leq f_{B_d}\sqrt{\hat{B}_{B_d}} \leq 240$ MeV. The 95% C.L. contour from Fig. 3 resulting from a simultaneous fit to both the experimental and theoretical quantities in Table 1 is also shown ("haggis"-type curve). The triangle shows the best fit.

that the experimental and theoretical errors at present are very similar. In view of this, we shall now show only results from our Fit 2.

3 ΔM_s (and x_s) and the Unitarity Triangle

Mixing in the B_s^0-$\overline{B_s^0}$ system is quite similar to that in the B_d^0-$\overline{B_d^0}$ system. The B_s^0-$\overline{B_s^0}$ box diagram is again dominated by t-quark exchange, and the mass difference between the mass eigenstates ΔM_s is given by a formula analogous to that of Eq. (11):

$$\Delta M_s = \frac{G_F^2}{6\pi^2} M_W^2 M_{B_s} \left(f_{B_s}^2 \hat{B}_{B_s}\right) \hat{\eta}_B y_t f_2(y_t) |V_{ts}^* V_{tb}|^2 \ . \tag{18}$$

Using the fact that $|V_{cb}| = |V_{ts}|$ (Eq. 1), it is clear that one of the sides of the unitarity triangle, $|V_{td}/\lambda V_{cb}|$, can be obtained from the ratio of ΔM_d and ΔM_s,

$$\frac{\Delta M_s}{\Delta M_d} = \frac{\hat{\eta}_{B_s} M_{B_s} \left(f_{B_s}^2 \hat{B}_{B_s}\right)}{\hat{\eta}_{B_d} M_{B_d} \left(f_{B_d}^2 \hat{B}_{B_d}\right)} \left|\frac{V_{ts}}{V_{td}}\right|^2 \ . \tag{19}$$

All dependence on the t-quark mass drops out, leaving the square of the ratio of CKM matrix elements, multiplied by a factor which reflects $SU(3)_{\text{flavour}}$ breaking effects. The only real uncertainty in this factor is the ratio of hadronic matrix elements. Whether or not x_s can be used to help constrain the unitarity triangle will depend crucially on the theoretical status of the ratio $f_{B_s}^2 \hat{B}_{B_s}/f_{B_d}^2 \hat{B}_{B_d}$. In what follows, we will take $\xi_s \equiv (f_{B_s}\sqrt{\hat{B}_{B_s}})/(f_{B_d}\sqrt{\hat{B}_{B_d}}) = (1.15 \pm 0.05)$,

consistent with both lattice-QCD [21] and QCD sum rules [22]. (The SU(3)-breaking factor in $\Delta M_s/\Delta M_d$ is ξ_s^2.)

The mass and lifetime of the B_s meson have now been measured at LEP and Tevatron and their present values are $M_{B_s} = 5369.3 \pm 2.0$ MeV and $\tau(B_s) = 1.52 \pm 0.07$ ps [23]. The QCD correction factor $\hat{\eta}_{B_s}$ is equal to its B_d counterpart, i.e. $\hat{\eta}_{B_s} = 0.55$. The main uncertainty in ΔM_s (or, equivalently, x_s) is now $f_{B_s}^2 \hat{B}_{B_s}$. Using the determination of A given previously, $\tau_{B_s} = 1.52 \pm 0.07$ (ps) and $\overline{m_t} = 165 \pm 9$ GeV, we obtain [2]:

$$\Delta M_s = (12.8 \pm 2.1) \frac{f_{B_s}^2 \hat{B}_{B_s}}{(230 \text{ MeV})^2} \ (ps)^{-1} \ ,$$
$$x_s = (19.5 \pm 3.3) \frac{f_{B_s}^2 \hat{B}_{B_s}}{(230 \text{ MeV})^2} \ . \tag{20}$$

The choice $f_{B_s}\sqrt{\hat{B}_{B_s}} = 230$ MeV corresponds to the central value given by the lattice-QCD estimates, and with this our fits give $x_s \simeq 20$ as the preferred value in the SM. Allowing the coefficient to vary by $\pm 2\sigma$, and taking the central value for $f_{B_s}\sqrt{\hat{B}_{B_s}}$, this gives

$$12.9 \leq x_s \leq 26.1 \ ,$$
$$8.6 \ (ps)^{-1} \leq \Delta M_s \leq 17.0 \ (ps)^{-1} \ . \tag{21}$$

It is difficult to ascribe a confidence level to this range due to the dependence on the unknown coupling constant factor. All one can say is that the standard model predicts large values for ΔM_s (and hence x_s), which are somewhat above the present experimental limit $\Delta M_s > 9.2 \ (ps)^{-1}$ [10, 17].

Summarizing the discussion on x_s, we note that the lattice-QCD-inspired estimate $f_{B_s}\sqrt{\hat{B}_{B_s}} \simeq 230$ MeV and the CKM fit predict that x_s lies between 13 and 26, with a central value around 20. All of these values scale as $(f_{B_s}\sqrt{\hat{B}_{B_s}}/230 \text{ MeV})^2$. The present constraints from the lower bound on ΔM_s on the CKM parameters are now competitive with those from fits to other data. In particular, the LEP-bound $\Delta M_s/\Delta M_d > 19.0$ removes the large-negative-ρ region, leaving the reduced range $[-0.25 \leq \rho \leq 0.35, \ 0.25 \leq \eta \leq 0.52]$ as the allowed one [2]. This is shown in Fig. 5. The constraints on the unitarity triangle from ΔM_s will become more pronounced with improved data. At HERA-B, one expects to reach a sensitivity $x_s \simeq 17$ (or $\Delta M_s \simeq 11 \ ps^{-1}$) combining various tagging techniques and data for three years [18]. Of course, an actual measurement of ΔM_s (equivalently x_s) would be very helpful in further constraining the CKM parameter space.

4 CP Violation in the B System

It is expected that the B system will exhibit large CP-violating effects, characterized by nonzero values of the angles α, β and γ in the unitarity triangle (Fig. 1) [19]. The most promising method to measure CP violation is to look for an asymmetry between $\Gamma(B^0 \to f)$ and $\Gamma(\overline{B^0} \to f)$, where f is a CP eigenstate. If only one weak amplitude contributes to the decay, the CKM phases

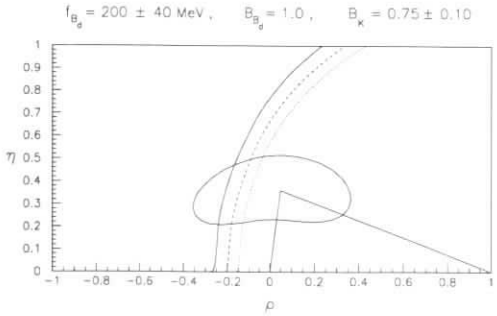

Figure 5: Further constraints in ρ-η space from the LEP bound $\Delta M_s/\Delta M_d > 19.0$. The bounds are presented for 3 choices of the SU(3)-breaking parameter: $\xi_s^2 = 1.21$ (dotted line), 1.32 (dashed line) and 1.44 (solid line). In all cases, the region to the left of the curve is ruled out.

can be extracted cleanly (i.e. with no hadronic uncertainties). Thus, $\sin 2\alpha$ and $\sin 2\beta$ can in principle be measured in $(\overline{B_d}) \to \pi^+\pi^-$ and $(\overline{B_d}) \to J/\psi K_S$, respectively. Penguin diagrams [24] may introduce some hadronic uncertainty into the measurement of $\sin 2\alpha$, but this can be removed via an isospin analysis [25]. For the measurement of the angle γ, two other methods have been devised, not involving CP-eigenstate final states. The CP asymmetry in the decay $(\overline{B_s}) \to D_s^{\pm} K^{\mp}$ can be used to extract $\sin^2\gamma$ [26]. Similarly, the CP asymmetry in $B^{\pm} \to D^0_{CP} K^{\pm}$ also measures $\sin^2\gamma$ [27]. Here, D^0_{CP} is a D^0 or $\overline{D^0}$ which is identified in a CP-eigenstate mode (e.g. $\pi^+\pi^-$, K^+K^-, ...).

These CP-violating asymmetries can be expressed straightforwardly in terms of the CKM parameters ρ and η. The 95% C.L. constraints on ρ and η found previously can be used to predict the ranges of $\sin 2\alpha$, $\sin 2\beta$ and $\sin^2\gamma$ allowed in the standard model. The allowed ranges which correspond to each of the figures in Fig. 2, obtained from Fit 1, are found in Table 2. In this table we have assumed that the angle β is measured in $(\overline{B_d}) \to J/\Psi K_S$, and have therefore included the extra minus sign due to the CP of the final state.

Since the CP asymmetries all depend on ρ and η, the ranges for $\sin 2\alpha$, $\sin 2\beta$ and $\sin^2\gamma$ shown in Table 2 are correlated. That is, not all values in the ranges are allowed simultaneously. We illustrate this in Fig. 6, corresponding to the "combined fit" (Fit 2), by showing the region in $\sin 2\alpha$-$\sin 2\beta$ space allowed by the data. From this figure one sees that the smallest value of $\sin 2\beta$ occurs in a small region of parameter space around $\sin 2\alpha \simeq 0.8$-0.9. Excluding this small tail, one expects the CP-asymmetry in $(\overline{B_d}) \to J/\Psi K_S$ to be at least 20% (i.e., $\sin 2\beta > 0.4$).

5 Summary and Outlook

We summarize our results:

$f_{B_d}\sqrt{\hat{B}_{B_d}}$ (MeV)	$\sin 2\alpha$	$\sin 2\beta$	$\sin^2\gamma$
160	0.86 – 1.0	0.38 – 0.58	0.47 – 0.92
180	−0.05 – 1.0	0.47 – 0.71	0.77 – 1.0
200	−0.69 – 0.90	0.53 – 0.81	0.61 – 1.0
220	−0.85 – 0.61	0.60 – 0.89	0.44 – 0.98
240	−0.90 – 0.32	0.67 – 0.94	0.34 – 0.86

Table 2: The allowed ranges for the CP asymmetries $\sin 2\alpha$, $\sin 2\beta$ and $\sin^2\gamma$, corresponding to the constraints on ρ and η shown in Fig. 2. Values of the coupling constant $f_{B_d}\sqrt{\hat{B}_{B_d}}$ are stated. We fix $\hat{B}_K = 0.75$. The range for $\sin 2\beta$ includes an additional minus sign due to the CP of the final state $J/\Psi K_S$.

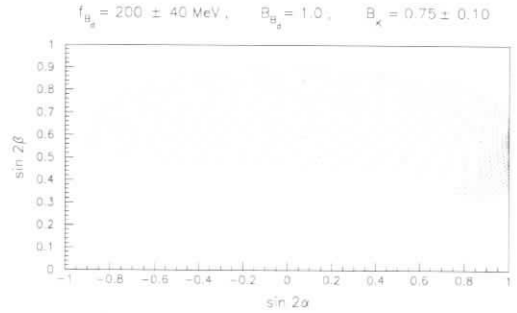

Figure 6: Allowed region of the CP-violating quantities $\sin 2\alpha$ and $\sin 2\beta$ resulting from the "combined fit" of the data for the ranges for $f_{B_d}\sqrt{\hat{B}_{B_d}}$ and $\hat{B}_K$ given in the text.

(i) We have presented an update of the CKM unitarity triangle using the theoretical and experimental improvements in the following quantities: $|\epsilon|$, $|V_{cb}|$, $|V_{ub}/V_{cb}|$, ΔM_d, $\tau(B_d)$, $\overline{m_t}$. The fits can be used to exclude extreme values of the pseudoscalar coupling constants, with the range 130 MeV $< f_{B_d}\sqrt{\hat{B}_{B_d}} <$ 250 MeV still allowed for $\hat{B}_K = 0.75$, although the fits at the two boundary values of $f_{B_d}\sqrt{\hat{B}_{B_d}}$ are poor.

(ii) The newest experimental and theoretical numbers restrict the allowed CKM unitarity triangle in the (ρ, η)-space. However, the present uncertainties are still large – despite the new, more accurate experimental data, our knowledge of the unitarity triangle is still deficient. This underscores the importance of measuring CP-violating rate asymmetries in the B system. Such asymmetries are largely independent of theoretical hadronic uncertainties, so that their measurement will allow us to accurately pin down the parameters of the CKM matrix. It may be possible to measure the parameter f_{B_d}, using isospin symmetry, via the charged-current decay $B_u^{\pm} \to \tau^{\pm}\nu_{\tau}$. Along the same lines, the prospects for measuring (f_{B_d}, f_{B_s}) in the FCNC leptonic and photonic decays of B_d^0 and B_s^0 hadrons, $(B_d^0, B_s^0) \to \mu^+\mu^-, (B_d^0, B_s^0) \to \gamma\gamma$ in future B physics facilities are not entirely dismal [28].

(iii) We have determined bounds on the ratio $|V_{td}/V_{ts}|$ from our fits. For 130 MeV $\leq f_{B_d}\sqrt{\hat{B}_{B_d}} \leq$ 250 MeV, i.e. in the entire allowed domain, at 95 % C.L. we find [2]

$$0.15 \leq \left|\frac{V_{td}}{V_{ts}}\right| \leq 0.34 \ . \tag{22}$$

The upper bound from this analysis is more restrictive than the current experimental upper limit following from the CKM-suppressed radiative penguin decays $BR(B \to \omega + \gamma)$ and $BR(B \to \rho + \gamma)$, which at present yield at 90% C.L. [29]

$$\left|\frac{V_{td}}{V_{ts}}\right| \leq 0.64 - 0.75 \ , \tag{23}$$

depending on the model used for the SU(3)-breaking in the relevant form factors [30]. Long-distance effects in the decay $B^{\pm} \to \rho^{\pm} + \gamma$ may introduce theoretical uncertainties comparable to those in the SU(3)-breaking part but the corresponding effects in the decays $B^0 \to (\rho^0, \omega) + \gamma$ are expected to be very small [31]. As emphasized in [28], we expect some of the CKM-suppressed radiative rare B decays will be measured at HERA-B and at the B factories, thereby making an essential input to the CKM unitarity physics.

(iv) Using the measured value of m_t, we find [2]:

$$x_s = (19.5 \pm 3.3)\,\frac{f_{B_s}^2 \hat{B}_{B_s}}{(230\ \text{MeV})^2} \ . \tag{24}$$

Taking $f_{B_s}\sqrt{\hat{B}_{B_s}} = 230$ (the central value of lattice-QCD estimates), and allowing the coefficient to vary by $\pm 2\sigma$, this gives

$$12.9 \leq x_s \leq 26.1 \ . \tag{25}$$

We conclude that the SM predicts large values for x_s, which lie above the ALEPH 95% C.L. lower limit of $x_s > 12.0$. Measurements of the B_s^0 - $\overline{B_s^0}$ oscillation frequency up to $x_s = 17$ are feasible at HERA-B, which lies inside the predicted range for this quantity given above.

(v) The ranges for the CP-violating rate asymmetries parametrized by $\sin 2\alpha$, $\sin 2\beta$ and and $\sin^2\gamma$ are determined at 95% C.L. to be [2]

$$\begin{aligned} -0.90 \leq \sin 2\alpha \leq 1.0 \ , \\ 0.32 \leq \sin 2\beta \leq 0.94 \ , \\ 0.34 \leq \sin^2\gamma \leq 1.0 \ . \end{aligned} \tag{26}$$

Barring a small range in $\sin 2\alpha$, we expect $\sin 2\beta > 0.4$, with the central value around $\sin 2\beta = 0.63$, implying a CP-violating asymmetry $\mathcal{A}(J/\psi K_S) \simeq 30\%$, which augurs well for HERA-B and the B factories.

References

[1] N. Cabibbo, Phys. Rev. Lett. **10** (1963) 531; M. Kobayashi and K. Maskawa, Prog. Theor. Phys. **49** (1973) 652.

[2] A. Ali and D. London, preprint DESY 96-140, UdeM-GPP-TH-96-45, [hep-ph/9607392], to appear in the *Proc. of QCD Euroconference 96*, Montpellier, July 4-12, 1996.

[3] L. Wolfenstein, Phys. Rev. Lett. **51** (1983) 1945.

[4] R.M. Barnett et al. (Particle Data Group), Phys. Rev. **D54** (1996) 1.

[5] A. Ali and D. London, *Z. Phys.*, C65 (1995) 431, preprint DESY 95-148, UdeM-GPP-TH-95-32 [hep-ph/9508272], to appear in the *Proc. of the 6th Int. Symp. on Heavy Flavour Physics*, Pisa, June 6-9, 1995.

[6] M. Neubert, Preprint CERN-TH/95-107 [hep-ph/9505238].

[7] M. Shifman, Preprint TPI-MINN-95/15-T [hep-ph/9505289].

[8] T. Skwarnicki, preprint [hep-ph/9512395], to appear in the *Proc. of the 17th Int. Symp. on Lepton Photon Interactions*, Beijing, P.R. China, August 1995.

[9] N. Isgur and M.B. Wise, *Phys. Lett.*, B232 (1989) 113; 237 (1990) 527.

[10] L. Gibbons (CLEO Collaboration), Invited talk at the International Conference on High Energy Physics, Warsaw, ICHEP96 (1996). These results have been kindly communicated to us by Lawrence Gibbons for performing the CKM fits.

[11] A.J. Buras, W. Slominski, and H. Steger, Nucl. Phys. **B238** (1984) 529; *ibid.* **B245** (1984) 369.

[12] S. Herrlich and U. Nierste, Nucl. Phys. **B419** (1994) 292.

[13] A.J. Buras, M. Jamin and P.H. Weisz, Nucl. Phys. **B347** (1990) 491.

[14] S. Herrlich and U. Nierste, Phys. Rev. **D52** (1995) 6505.

[15] C. Zeitnitz, invited talk at the 4th International Workshop on B-Physics at Hadron Machines (BEAUTY 96), Rome, 17-21 June, 1996, and private communication.

[16] Sau Lan Wu, preprint WISC-EX-96-343 [hep-ex/9602003], to appear in the *Proc. of the 17th Int. Symp. on Lepton and Photon Interactions*, Beijing, P.R. China, August 1995.

[17] "Combined limit on the B_s^0 oscillation frequency", contributed paper by the ALEPH collaboration to the International Conference on High Energy Physics, Warsaw, ICHEP96 PA08-020 (1996).

[18] J. Thom (HERA-B Collaboration), to be published.

[19] For reviews, see, for example, Y. Nir and H.R. Quinn, in *B Decays*, edited by S. Stone (World Scientific, Singapore, 1992) 362; I. Dunietz, *ibid* 393.

[20] R. Aleksan, B. Kayser, and D. London, Phys. Rev. Lett. **B73** (1994) 18.

[21] H. Wittig, Invited talk presented at the III German-Russian Workshop on Heavy Quark Physics, Dubna, Russia, 20-22 May, 1996, [hep-ph/9606371].

[22] S. Narison, Phys. Lett. **B322** (1994) 247; S. Narison and A. Pivovarov, *ibid* **B327** (1994) 341.

[23] J. Richman, plenary talk at the International Conference on High Energy Physics, Warsaw, ICHEP96 (1996).

[24] D. London and R. Peccei, Phys. Lett. **B223** (1989) 257; B. Grinstein, Phys. Lett. **B229** (1989) 280; M. Gronau, Phys. Rev. Lett. **63** (1989) 1451, Phys. Lett. **B300** (1993) 163.

[25] M. Gronau and D. London, Phys. Rev. Lett. **65** (1990) 3381.

[26] R. Aleksan, I. Dunietz, and B. Kayser, Z. Phys. **C54** (1992) 653.

[27] M. Gronau and D. Wyler, Phys. Lett. **B265** (1991) 172. See also M. Gronau and D. London, Phys. Lett. **B253** (1991) 483; I. Dunietz, Phys. Lett. **B270** (1991) 75.

[28] A. Ali, preprint DESY 96-106 [hep-ph/9606324]; to appear in the Proceedings of the XX International Nathiagali Conference on Physics and Contemporary Needs, Bhurban, Pakistan, June 24-July 13, 1995 (Nova Science Publishers, New York, 1996).

[29] M. Ahtanas et al. (CLEO Collaboration), CLEO CONF 94-2 (1994).

[30] A. Ali, V.M. Braun and H. Simma, Z. Phys. **C63** (1994) 437; J.M. Soares, Phys. Rev. **D49** (1994) 283; S. Narison, Phys. Lett. **B327** (1994) 354.

[31] A. Ali and V.M. Braun, Phys. Lett. **B359** (1995) 223; A. Khodzhamirian, G. Stoll, and D. Wyler, Phys. Lett. **B358** (1995) 129.

Rare B Decays in the Standard Model

A. Ali[a]

[a] Deutsches Elektronen-Synchrotron DESY, Notkestrasse 85, D-22603 Hamburg, FRG.

Abstract: We discuss the electromagnetic-penguin-dominated radiative B decays $B \to X_s + \gamma$, $B^{\pm(0)} \to K^{*\pm(0)} + \gamma$, $B_s \to \phi + \gamma$ and $\Lambda_b \to \Lambda + \gamma$ in the context of the standard model (SM) and their Cabibbo-Kobayashi-Maskawa (CKM)-suppressed counterparts, $B \to X_d + \gamma$, $B^{\pm} \to \rho^{\pm} + \gamma$, $B^0 \to (\rho^0, \omega) + \gamma$, $B_s \to K^{*0} + \gamma$, and $\Lambda \to n + \gamma$, using QCD sum rules for the exclusive decays. The importance of these decays in determining the parameters of the CKM matrix [1] is emphasized. The semileptonic decays $B \to X_s \ell^+ \ell^-$ are also discussed in the context of the SM and their role in determining the Wilson coefficients of the effective theory is stressed. Comparison with the existing measurements are made and SM-based predictions for a large number of rare B decays are presented.

1 Estimates of $\mathcal{B}(B \to X_s + \gamma)$ and $|V_{ts}|$ in the Standard Model

The Standard Model (SM) of particle physics does not admit Flavour-changing-neutral-current (FCNC) transitions in the Born approximation. However, they are induced through the exchange of $W^{\pm}$ bosons in loop diagrams. The short-distance contribution in rare decays is dominated by the (virtual) top quark contribution. Hence the decay characteristics provide quantitative information on the top quark mass and the Cabibbo-Kobayashi-Maskawa (CKM) matrix elements V_{ti}; $i = d, s, b$ [1]. We shall discuss representative examples from several such transitions involving B decays, starting with the decay $B \to X_s + \gamma$, which has been measured by CLEO [2]. This was preceded by the measurement of the exclusive decay $B \to K^* + \gamma$ by the same collaboration [3]. The present measurements give [4]:

$$\mathcal{B}(B \to X_s + \gamma) = (2.32 \pm 0.57 \pm 0.35) \times 10^{-4} \,, \tag{1}$$

$$\mathcal{B}(B \to K^* + \gamma) = (4.2 \pm 0.8 \pm 0.6) \times 10^{-5} \,, \tag{2}$$

yielding an exclusive-to-inclusive ratio:

$$R_{K^*} = \frac{\Gamma(B \to K^* + \gamma)}{\Gamma(B \to X_s + \gamma)} = (18.1 \pm 6.8)\% \,. \tag{3}$$

These decay rates determine the ratio of the CKM matrix elements $|V_{ts}|/|V_{cb}|$ and the quantity R_{K^*} provides information on the decay form factor in $B \to K^* + \gamma$. In what follows we take up these points briefly.

The leading contribution to $b \to s+\gamma$ arises at one-loop from the so-called penguin diagrams. With the help of the unitarity of the CKM matrix, the decay matrix element in the lowest order can be written as:

$$\mathcal{M}(b \to s\ +\gamma) = \frac{G_F}{\sqrt{2}} \frac{e}{2\pi^2} \lambda_t \left(F_2(x_t) - F_2(x_c)\right) q^\mu \epsilon^\nu \bar{s} \sigma_{\mu\nu} (m_b R\ +\ m_s L) b\ . \tag{4}$$

where $x_i = m_i^2/m_W^2$, and q_μ and ϵ_μ are, respectively, the photon four-momentum and polarization vector. The GIM mechanism [5] is manifest in this amplitude and the CKM-matrix element dependence is factorized in $\lambda_t \equiv V_{tb} V_{ts}^*$. The (modified) Inami-Lim function $F_2(x_i)$ derived from the (1-loop) penguin diagrams is given by [6]:

$$F_2(x) = \frac{x}{24(x-1)^4} \left[6x(3x-2)\log x - (x-1)(8x^2+5x-7)\right]. \tag{5}$$

The measurement of the branching ratio for $B \to X_s + \gamma$ can be readily interpreted in terms of the CKM-matrix element product $\lambda_t/|V_{cb}|$ or equivalently $|V_{ts}|/|V_{cb}|$. For a quantitative determination of $|V_{ts}|/|V_{cb}|$, however, QCD radiative corrections have to be computed and the contribution of the so-called long-distance effects estimated.

The appropriate framework to incorporate QCD corrections is that of an effective theory obtained by integrating out the heavy degrees of freedom, which in the present context are the top quark and $W^\pm$ bosons. The operator basis depends on the underlying theory and for the SM one has (keeping operators up to dimension 6),

$$\mathcal{H}_{eff}(b \to s+\gamma) = -\frac{4G_F}{\sqrt{2}} V_{ts}^* V_{tb} \sum_{i=1}^{8} C_i(\mu) \mathcal{O}_i(\mu), \tag{6}$$

where the operator basis, the "matching conditions" $C_i(m_W)$, and the solutions of the renormalization group equations $C_i(\mu)$ can be seen in ref. [7]. The perturbative QCD corrections to the decay rate $\Gamma(B \to X_s + \gamma)$ have two distinct contributions:

- Corrections to the Wilson coefficients $C_i(\mu)$, calculated with the help of the renormalization group equation, whose solution requires the knowledge of the anomalous dimension matrix in a given order in α_s.
- Corrections to the matrix elements of the operators $\mathcal{O}_i$ entering through the effective Hamiltonian at the scale $\mu = O(m_b)$.

The anomalous dimension matrix is needed in order to sum up large logarithms, i.e., terms like $\alpha_s^n(m_W)\log^m(m_b/M)$, where $M = m_t$ or m_W and $m \le n$ (with $n = 0, 1, 2, \ldots$). At present only the leading logarithmic corrections ($m = n$) have been calculated systematically and checked by several independent groups in the complete basis given in Eq. (6) [8]. First calculations of the NLO corrections to the anomalous dimension matrix have been recently reported by Misiak [9] and are found to be small. Next-to-leading order corrections to the matrix elements are now available completely. They are of two kinds:

- QCD Bremsstrahlung corrections $b \to s\gamma + g$, which are needed both to cancel the infrared divergences in the decay rate for $B \to X_s + \gamma$ and in obtaining a non-trivial QCD contribution to the photon energy spectrum in the inclusive decay $B \to X_s + \gamma$.

- Next-to-leading order virtual corrections to the matrix elements in the decay $b \to s + \gamma$.

The Bremsstrahlung corrections were calculated in [10, 11] in the truncated basis and last year also in the complete operator basis [12, 13]. The higher order matching conditions, i.e., $C_i(m_W)$, are known up to the desired accuracy, i.e., up to $O(\alpha_s(M_W))$ terms [14]. The next-to-leading order virtual corrections have also been calculated [15]. They reduce the scale-dependence of the inclusive decay width. The branching ratio $\mathcal{B}(B \to X_s + \gamma)$ can be expressed in terms of the semileptonic decay branching ratio

$$\mathcal{B}(B \to X_s\gamma) = \left[\frac{\Gamma(B \to \gamma + X_s)}{\Gamma_{SL}}\right]^{th} \mathcal{B}(B \to X\ell\nu_\ell) \quad , \tag{7}$$

where the leading-order QCD corrected expression for Γ_{SL} can be seen in [7]. The leading order $(1/m_b)$ power corrections in the heavy quark expansion are identical in the inclusive decay rates for $B \to X_s + \gamma$ and $B \to X\ell\nu_\ell$, entering in the numerator and denominator in the square bracket, respectively, and hence drop out [16, 17].

In Ref. [7], the present theoretical errors on the branching ratio $\mathcal{B}(B \to X_s\gamma)$ are discussed, yielding:

$$\mathcal{B}(B \to X_s + \gamma) = (3.20 \pm 0.30 \pm 0.38 \pm 0.32) \times 10^{-4} \tag{8}$$

where the first error comes from the combined effect of Δm_t and $\Delta\mu$ (the scale dependence), the second error arises from the extrinsic sources (such as $\Delta(m_b)$, $\Delta(BR_{SL})$), and the third error is an estimate ($\pm 10\%$) of the NLO anomalous dimension piece in C_7^{eff}, the coefficient of the magnetic moment operator. Combining the theoretical errors in quadrature gives [7]:

$$\mathcal{B}(B \to X_s + \gamma) = (3.20 \pm 0.58) \times 10^{-4}, \tag{9}$$

which is compatible with the present measurement $\mathcal{B}(B \to X_s + \gamma) = (2.32 \pm 0.67) \times 10^{-4}$ [2]. Expressed in terms of the CKM matrix element ratio, one gets

$$\frac{|V_{ts}|}{|V_{cb}|} = 0.85 \pm 0.12(\text{expt}) \pm 0.10(\text{th}), \tag{10}$$

which is within errors consistent with unity, as expected from the unitarity of the CKM matrix.

In order to get the complete amplitude for $B \to X_s + \gamma$ one has to include also the effects of the long-distance (LD) contributions, which arise from the matrix elements of the four-quark operators in $\mathcal{H}_{eff}$, $\langle X_s\gamma|\mathcal{O}_i|B\rangle$. For the exclusive radiative decays $B \to (\rho, \omega) + \gamma$, these contributions have been calculated using QCD sum rules [18, 19] and we shall discuss them later. Concerning the inclusive decays $B \to X_s + \gamma$, one has at present little choice other than invoking phenomenological models to estimate the LD-amplitude. They have been used in a number of papers [20], which typically give $\mathcal{M}(B \to X_s + \gamma)^{\text{LD}}/\mathcal{M}(B \to X_s + \gamma)^{\text{SD}} \le O(0.1)$, based on which we shall ignore the LD-effects in the decays $B \to X_s + \gamma$ (likewise, in $B \to K^* + \gamma$).

2 Inclusive radiative decays $B \to X_d + \gamma$

The theoretical interest in studying the (CKM-suppressed) inclusive radiative decays $B \to X_d+\gamma$ lies in the first place in the possibility of determining the parameters of the CKM matrix. We shall use the Wolfenstein parametrization [21], in which case the matrix is determined in terms of the four parameters $A, \lambda = \sin\theta_C$, ρ and η. Since A and λ are well determined, and ρ and η are bounded from present measurements (in particular, from B_d^0 - $\overline{B_d^0}$ frequency x_d and $|\epsilon|$, the CP violation parameter in K decays) [22, 23], we shall concentrate on the improved determination of the last two parameters from radiative B decays. With that goal in view, one of the relevant quantities in the decays $B \to X_d + \gamma$ is the end-point photon energy spectrum, which has to be measured requiring that the hadronic system X_d recoiling against the photon does not contain strange hadrons to suppress the large-E_γ photons from the decay $B \to X_s+\gamma$. Assuming that this is feasible, one can determine from the ratio of the decay rates $\mathcal{B}(B \to X_d+\gamma)/\mathcal{B}(B \to X_s+\gamma)$ the CKM-Wolfenstein parameters ρ and η. This measurement was first proposed in [11], where the photon energy spectra were also worked out.

In close analogy with the $B \to X_s+\gamma$ case discussed earlier, the complete set of dimension-6 operators relevant for the processes $b \to d\gamma$ and $b \to d\gamma g$ can be written as:

$$\mathcal{H}_{eff}(b \to d) = -\frac{4G_F}{\sqrt{2}}\,\xi_t \sum_{j=1}^{8} C_j(\mu)\,\hat{O}_j(\mu), \tag{11}$$

where $\xi_j = V_{jb}V_{jd}^*$ for $j = t, c, u$. The operators $\hat{O}_j$, $j = 1,2$, have implicit in them CKM factors. In the Wolfenstein parametrization [21], one can express these factors as :

$$\xi_u = A\,\lambda^3(\rho - i\eta), \quad \xi_c = -A\,\lambda^3, \quad \xi_t = -\xi_u - \xi_c. \tag{12}$$

We note that all three CKM-angle-dependent quantities ξ_j are of the same order of magnitude, $O(\lambda^3)$. This aspect can be taken into account by defining the operators $\hat{O}_1$ and $\hat{O}_2$ entering in $\mathcal{H}_{eff}(b \to d)$ as follows [11]:

$$\begin{aligned}
\hat{O}_1 &= -\frac{\xi_c}{\xi_t}(\bar{c}_{L\beta}\gamma^\mu b_{L\alpha})(\bar{d}_{L\alpha}\gamma_\mu c_{L\beta}) - \frac{\xi_u}{\xi_t}(\bar{u}_{L\beta}\gamma^\mu b_{L\alpha})(\bar{d}_{L\alpha}\gamma_\mu u_{L\beta}),\\
\hat{O}_2 &= -\frac{\xi_c}{\xi_t}(\bar{c}_{L\alpha}\gamma^\mu b_{L\alpha})(\bar{d}_{L\beta}\gamma_\mu c_{L\beta}) - \frac{\xi_u}{\xi_t}(\bar{u}_{L\alpha}\gamma^\mu b_{L\alpha})(\bar{d}_{L\beta}\gamma_\mu u_{L\beta}),
\end{aligned} \tag{13}$$

with the rest of the operators ($\hat{O}_j$; $j = 3...8$) defined like their counterparts O_j in $\mathcal{H}_{eff}(b \to s)$, with the obvious replacement $s \to d$. With this choice, the matching conditions $C_j(m_W)$ and the solutions of the RG equations yielding $C_j(\mu)$ become identical for the two operator bases O_j and $\hat{O}_j$. The essential difference between $\Gamma(B \to X_s + \gamma)$ and $\Gamma(B \to X_d + \gamma)$ lies in the matrix elements of the first two operators O_1 and O_2 (in $\mathcal{H}_{eff}(b \to s)$) and $\hat{O}_1$ and $\hat{O}_2$ (in $\mathcal{H}_{eff}(b \to d)$). The branching ratio $\mathcal{B}(B \to X_d + \gamma)$ in the SM can be written as:

$$\mathcal{B}(B \to X_d + \gamma) = D_1\lambda^2\{(1-\rho)^2 + \eta^2 - (1-\rho)D_2 - \eta D_3 + D_4\}, \tag{14}$$

where the functions D_i depend on the parameters m_t, m_b, m_c, μ, as well as the others we discussed in the context of $\mathcal{B}(B \to X_s + \gamma)$. These functions were first calculated in [11]

in the leading logarithmic approximation. Recently, these estimates have been improved in [24], making use of the NLO calculations in [15]. For the central values of these parameters ($m_t = 175$ GeV, $m_b = 4.8$ GeV, $m_c/m_b = 0.29$, $\mu = 5$ GeV, and $\alpha_s(m_b) = 0.212$), one gets $D_1 = 4.5 \times 10^{-4}$, $D_2 = 0.30$, $D_3 = 0.23$, and $D_4 = 0.06$ [24]. To get an estimate of the inclusive branching ratio, the CKM parameters ρ and η have to be constrained from the unitarity fits. Present data and theory restrict the parameters ρ and η to lie in the following range (at 95% C.L.) [22]:

$$\begin{aligned}
0.25 \le \eta \le 0.52,\\
-0.35 \le \rho \le 0.35\ ,
\end{aligned} \tag{15}$$

which, on using the current lower bound from LEP on the B_s^0 - $\overline{B_s^0}$ mass difference $\Delta M_s > 9.2$ $(\mathrm{ps})^{(-1)}$ [25], is reduced to $-0.14 \le \rho \le 0.35$ using $\xi_s = 1.1$ where ξ_s is the $SU(3)$-breaking parameter $\xi_s = f_{B_s}\hat{B}_{B_s}/f_{B_d}\hat{B}_{B_d}$. The preferred CKM-fit values are

$$(\rho, \eta) = (0.05, 0.36) \quad (\text{with } \chi^2 = 6.6 \times 10^{-3})\ , \tag{16}$$

Taking the preferred values of the fitted CKM parameters one gets [24]

$$\mathcal{B}(B \to X_d + \gamma) = 1.63 \times 10^{-5}, \tag{17}$$

whereas $\mathcal{B}(B \to X_d + \gamma) = 8.0 \times 10^{-6}$ and 2.8×10^{-5} for the other two extremes $\rho = 0.35$, $\eta = 0.50$ and $\rho = -\eta = -0.25$, respectively. In conclusion, we note that the functional dependence of $\mathcal{B}(B \to X_d+\gamma)$ on the Wolfenstein parameters (ρ, η) is mathematically different than that of ΔM_s. However, qualitatively they are very similar. From the experimental point of view, the situation $\rho < 0$ is favourable for both the measurements as in this case one expects (relatively) smaller values for ΔM_s and larger values for the branching ratio $\mathcal{B}(B \to X_d + \gamma)$, as compared to the $\rho > 0$ case which would yield larger ΔM_s and smaller $\mathcal{B}(B \to X_d + \gamma)$.

2.1 $\mathcal{B}(B \to V + \gamma)$ and constraints on the CKM parameters

Exclusive radiative B decays $B \to V+\gamma$, with $V = K^*, \rho, \omega$, are also potentially very interesting from the point of view of determining the CKM parameters [26]. The extraction of these parameters would, however, involve a trustworthy estimate of the SD- and LD-contributions in the decay amplitudes.

The SD-contribution in the exclusive decays $(B^\pm, B^0) \to (K^{*\pm}, K^{*0}) + \gamma$, $(B^\pm, B^0) \to (\rho^\pm, \rho^0) + \gamma$, $B^0 \to \omega + \gamma$ and the corresponding B_s decays, $B_s \to \phi + \gamma$, and $B_s \to K^{*0} + \gamma$, involve the magnetic moment operator $\mathcal{O}_7$ and the related one obtained by the obvious change $s \to d$, $\hat{O}_7$. The transition form factors governing these decays can be generically defined as:

$$\langle V, \lambda|\frac{1}{2}\bar{\psi}\sigma_{\mu\nu}q^\nu b|B\rangle = i\epsilon_{\mu\nu\rho\sigma}e_\nu^{(\lambda)}p_B^\rho p_V^\sigma F_S^{B\to V}(0). \tag{18}$$

Here V is a vector meson with the polarization vector $e^{(\lambda)}$, $V = \rho, \omega, K^*$ or ϕ; B is a generic B-meson $B^\pm, B^0$ or B_s, and ψ stands for the field of a light u, d or s quark. The vectors p_B, p_V

and $q = p_B - p_V$ correspond to the 4-momenta of the initial B-meson and the outgoing vector meson and photon, respectively. Keeping only the SD-contribution leads to obvious relations among the exclusive decay rates, exemplified here by the decay rates for $(B^\pm, B^0) \to (\rho^\pm, \rho^0) + \gamma$ and $(B^\pm, B^0) \to (K^{*\pm}, K^{*0}) + \gamma$:

$$\frac{\Gamma((B^\pm, B^0) \to (\rho^\pm, \rho^0) + \gamma)}{\Gamma((B^\pm, B^0) \to (K^{*\pm}, K^{*0}) + \gamma)} = \frac{|\xi_t|^2}{|\lambda_t|^2} \frac{|F_S^{B\to\rho}(0)|^2}{|F_S^{B\to K^*}(0)|^2} \Phi_{u,d} \simeq \kappa_{u,d} \left[\frac{|V_{td}|}{|V_{ts}|}\right]^2 , \tag{19}$$

where $\Phi_{u,d}$ is a phase-space factor which in all cases is close to 1 and $\kappa_i \equiv [F_S(B_i \to \rho\gamma)/F_S(B_i \to K^*\gamma)]^2$. The transition form factors F_S are model dependent. Estimates of F_S in the QCD sum rule approach in the normalization of Eq. (18) range between $F_S(B \to K^*\gamma) = 0.31$ (Narison in [27]) to $F_S(B \to K^*\gamma) = 0.37$ (Ball in [27]), with a typical error of $\pm 15\%$, and hence are all consistent with each other. This, for example, gives $R_{K^*} = 0.16 \pm 0.05$, using the result from [26], which is in good agreement with data. The ratios of the form factors, i.e. κ_i, should therefore be reliably calculable as they depend essentially only on the SU(3)-breaking effects.

If the SD-amplitudes were the only contributions, the measurements of the CKM-suppressed radiative decays $(B^\pm, B^0) \to (\rho^\pm, \rho^0) + \gamma$, $B^0 \to \omega + \gamma$ and $B_s \to K^* + \gamma$ could be used in conjunction with the decays $(B^\pm, B^0) \to (K^{*\pm}, K^{*0}) + \gamma$ to determine the CKM parameters. The present experimental upper limits on the CKM ratio $|V_{td}|/|V_{ts}|$ from radiative B decays are indeed based on this assumption. The 90% C.L. limits on some of the decay modes are given in Table 1, which yield at 90% C.L.[4]:

$$\left|\frac{V_{td}}{V_{ts}}\right| \leq 0.45 - 0.56 , \tag{20}$$

depending on the models used for the $SU(3)$ breaking effects in the form factors [26, 27].

The possibility of significant LD-contributions in radiative B decays from the light quark intermediate states has been raised in a number of papers [20]. Their amplitudes necessarily involve other CKM matrix elements and hence the simple factorization of the decay rates in terms of the CKM factors involving $|V_{td}|$ and $|V_{ts}|$ no longer holds thereby invalidating the relation (19) given above. As we already discussed, the LD-contributions are small in the exclusive decays $B \to K^* + \gamma$ and so this issue hinges sensitively upon the LD-contributions in the CKM-suppressed charged and neutral exclusive B-decays, $B^\pm \to \rho^\pm\gamma$ and $B \to (\rho^0, \omega)\gamma$.

The LD-contributions in $B \to V + \gamma$ are induced by the matrix elements of the four-Fermion operators $\hat{O}_1$ and $\hat{O}_2$ (likewise O_1 and O_2). Estimates of these contributions require non-perturbative methods. This problem has been investigated in [18, 19] using a technique [28] which treats the photon emission from the light quarks in a theoretically consistent and model-independent way. This has been combined with the light-cone QCD sum rule approach to calculate both the SD and LD — parity conserving and parity violating — amplitudes in the decays $(B^\pm, B^0) \to (\rho^\pm, \rho/\omega) + \gamma$. To illustrate this, we concentrate on the $B^\pm$ decays, $B^\pm \to \rho^\pm + \gamma$ and take up the neutral B decays $B^0 \to \rho(\omega) + \gamma$ at the end. The LD-amplitude of the four-Fermion operators $\hat{O}_1$, $\hat{O}_2$ is dominated by the contribution of the weak annihilation of valence quarks in the B meson and it is color-allowed for the decays of charged $B^\pm$ mesons. Using factorization, the LD-amplitude in the decay $B^\pm \to \rho^\pm + \gamma$ can be written in terms of

the form factors F_1^L and F_2^L,

$$\mathcal{A}_{long} = -\frac{e\,G_F}{\sqrt{2}} V_{ub}V_{ud}^* \left(C_2 + \frac{1}{N_c}C_1\right) m_\rho \varepsilon_\mu^{(\gamma)} \varepsilon_\nu^{(\rho)} \times \left\{ -i\left[g^{\mu\nu}(q\cdot p) - p^\mu q^\nu\right] \cdot 2F_1^L(q^2) + \epsilon^{\mu\nu\alpha\beta} p_\alpha q_\beta \cdot 2F_2^L(q^2)\right\} . \tag{21}$$

Again, one has to invoke a model to calculate the form factors. Estimates from the light-cone QCD sum rules give [19]:

$$F_1^L/F_S = 0.0125 \pm 0.0010 , \quad F_2^L/F_S = 0.0155 \pm 0.0010 , \tag{22}$$

where the errors correspond to the variation of the Borel parameter in the QCD sum rules. Including other possible uncertainties, one expects an accuracy of the ratios in (22) of order 20%. The parity-conserving and parity-violating amplitudes turn out to be numerically close to each other in the QCD sum rule appraoch, $F_1^L \simeq F_2^L \equiv F_L$, hence the ratio of the LD- and the SD- contributions reduces to a number [19]

$$\mathcal{A}_{long}/\mathcal{A}_{short} = R_{L/S}^{B^\pm\to\rho^\pm\gamma} \cdot \frac{V_{ub}V_{ud}^*}{V_{tb}V_{td}^*} . \tag{23}$$

Using $C_2 = 1.10$, $C_1 = -0.235$, $C_7^{eff} = -0.306$ from Ref. [7] (corresponding to the scale $\mu = 5$ GeV) gives:

$$R_{L/S}^{B^\pm\to\rho^\pm\gamma} \equiv \frac{4\pi^2 m_\rho (C_2 + C_1/N_c)}{m_b C_7^{eff}} \cdot \frac{F_L^{B^\pm\to\rho^\pm\gamma}}{F_S^{B^\pm\to\rho^\pm\gamma}} = -0.30 \pm 0.07 , \tag{24}$$

which is not small. To get a ball-park estimate of the ratio $\mathcal{A}_{long}/\mathcal{A}_{short}$, we take the central value from the CKM fits, yielding $|V_{ub}|/|V_{td}| \simeq 0.33$ [22],

$$|\mathcal{A}_{long}/\mathcal{A}_{short}|^{B^\pm\to\rho^\pm\gamma} = |R_{L/S}^{B^\pm\to\rho^\pm\gamma}| \frac{|V_{ub}V_{ud}|}{|V_{td}V_{tb}|} \simeq 10\% . \tag{25}$$

Thus, the CKM factors suppress the LD-contributions.

The analogous LD-contributions to the neutral B decays $B^0 \to \rho\gamma$ and $B^0 \to \omega\gamma$ are expected to be much smaller, a point that has also been noted in the context of the VMD and quark model based estimates [20]. The corresponding form factors for the decays $B^0 \to \rho^0(\omega)\gamma$ are obtained from the ones for the decay $B^\pm \to \rho^\pm\gamma$ discussed above by the replacement of the light quark charges $e_u \to e_d$, which gives the factor $-1/2$; in addition, and more importantly, the LD-contribution to the neutral B decays is colour-suppressed, which reflects itself through the replacement of the factor a_1 by a_2. This yields for the ratio

$$\frac{R_{L/S}^{B^0\to\rho\gamma}}{R_{L/S}^{B^\pm\to\rho^\pm\gamma}} = \frac{e_d a_2}{e_u a_1} \simeq -0.13 \pm 0.05, \tag{26}$$

where the numbers are based on using $a_2/a_1 = 0.27 \pm 0.10$ [29]. This would then yield at most $R_{L/S}^{B^0\to\rho\gamma} \simeq R_{L/S}^{B^0\to\omega\gamma} = 0.05$, which in turn gives

$$\frac{\mathcal{A}_{long}^{B^0\to\rho\gamma}}{\mathcal{A}_{short}^{B^0\to\rho\gamma}} \leq 0.02. \tag{27}$$

Even if this underestimates the LD-contribution by a factor 2, due to the approximations made in [18, 19], one can safely neglect the LD-contribution in the neutral B-meson radiative decays.

Restricting to the colour-allowed LD-contributions, the relations, which obtains ignoring such contributions (and isospin invariance),

$$\Gamma(B^{\pm} \to \rho^{\pm}\gamma) = 2\,\Gamma(B^0 \to \rho^0\gamma) = 2\,\Gamma(B^0 \to \omega\gamma)\,, \tag{28}$$

get modified to

$$\frac{\Gamma(B^{\pm} \to \rho^{\pm}\gamma)}{2\Gamma(B^0 \to \rho\gamma)} = \frac{\Gamma(B^{\pm} \to \rho^{\pm}\gamma)}{2\Gamma(B^0 \to \omega\gamma)} = \left|1 + R_{L/S}^{B^{\pm}\to\rho^{\pm}\gamma}\frac{V_{ub}V_{ud}^*}{V_{tb}V_{td}^*}\right|^2 =$$
$$= 1 + 2\cdot R_{L/S}V_{ud}\frac{\rho(1-\rho)-\eta^2}{(1-\rho)^2+\eta^2} + (R_{L/S})^2V_{ud}^2\frac{\rho^2+\eta^2}{(1-\rho)^2+\eta^2}\,. \tag{29}$$

where $R_{L/S} \equiv R_{L/S}^{B^{\pm}\to\rho^{\pm}\gamma}$. The ratio $\Gamma(B^{\pm} \to \rho^{\pm}\gamma)/2\Gamma(B^0 \to \rho\gamma)(= \Gamma(B^{\pm} \to \rho^{\pm}\gamma)/2\Gamma(B^0 \to \omega\gamma))$ is shown in Fig. 1 as a function of the parameter ρ, with $\eta = 0.2,\ 0.3$ and 0.4. This suggests that a measurement of this ratio would constrain the Wolfenstein parameters (ρ, η), with the dependence on ρ more marked than on η. In particular, a negative value of ρ leads to a constructive interference in $B^{\pm} \to \rho^{\pm}\gamma$ decays, while large positive values of ρ give a destructive interference.

The ratio of the CKM-suppressed and CKM-allowed decay rates for charged B mesons gets modified due to the LD contributions. Following [20], we ignore the LD-contributions in $\Gamma(B \to K^{*}\gamma)$. The ratio of the decay rates in question can therefore be written as:

$$\frac{\Gamma(B^{\pm} \to \rho^{\pm}\gamma)}{\Gamma(B^{\pm} \to K^{*\pm}\gamma)} = \kappa_u\lambda^2[(1-\rho)^2+\eta^2]$$
$$\times\left\{1 + 2\cdot R_{L/S}V_{ud}\frac{\rho(1-\rho)-\eta^2}{(1-\rho)^2+\eta^2} + (R_{L/S})^2V_{ud}^2\frac{\rho^2+\eta^2}{(1-\rho)^2+\eta^2}\right\}, \tag{30}$$

Using the central value from the estimates of the ratio of the form factors squared $\kappa_u = 0.59 \pm 0.08$ [26], we show the ratio (30) in Fig. 2 as a function of ρ for $\eta = 0.2, 0.3$, and 0.4. It is seen that the dependence of this ratio is rather weak on η but it depends on ρ rather sensitively. The effect of the LD-contributions is modest but not negligible, introducing an uncertainty comparable to the $\sim 15\%$ uncertainty in the overall normalization due to the $SU(3)$-breaking effects in the quantity κ_u.

Neutral B-meson radiative decays are less-prone to the LD-effects, as argued above, and hence one expects that to a good approximation the ratio of the decay rates for neutral B meson obtained in the approximation of SD-dominance remains valid [26]:

$$\frac{\Gamma(B^0 \to \rho^0\gamma, \omega\gamma)}{\Gamma(B \to K^{*}\gamma)} = \kappa_d\lambda^2[(1-\rho)^2+\eta^2]\,, \tag{31}$$

where this relation holds for each of the two decay modes separately.

Finally, combining the estimates for the LD- and SD-form factors in [19] and [26], respectively, and restricting the Wolfenstein parameters in the range $-0.25 \le \rho \le 0.35$ and

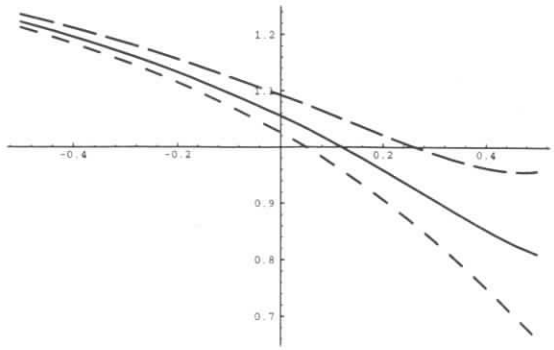

Figure 1: Ratio of the neutral and charged B-decay rates $\Gamma(B^{\pm} \to \rho^{\pm}\gamma)/2\Gamma(B^0 \to \rho\gamma)$ as a function of the Wolfenstein parameter ρ, with $\eta = 0.2$ (short-dashed curve), $\eta = 0.3$ (solid curve), and $\eta = 0.4$ (long-dashed curve). (Figure taken from [19].)

$0.2 \le \eta \le 0.4$, as suggested by the CKM-fits [22], we give the following ranges for the absolute branching ratios:

$$\mathcal{B}(B^{\pm} \to \rho^{\pm}\gamma) = (1.5 \pm 1.1) \times 10^{-6}\,,$$
$$\mathcal{B}(B^0 \to \rho\gamma) \simeq \mathcal{B}(B^0 \to \omega\gamma) = (0.65 \pm 0.35) \times 10^{-6}\,, \tag{32}$$

where we have used the experimental value for the branching ratio $\mathcal{B}(B \to K^{*} + \gamma)$ [3], adding the errors in quadrature. The large error reflects the poor knowledge of the CKM matrix elements and hence experimental determination of these branching ratios will put rather stringent constraints on the Wolfenstein parameter ρ.

In addition to studying the radiative penguin decays of the $B^{\pm}$ and B^0 mesons discussed above, hadron machines such as HERA-B will be in a position to study the corresponding decays of the B_s^0 meson and Λ_b baryon, such as $B_s^0 \to \phi + \gamma$ and $\Lambda_b \to \Lambda + \gamma$, which have not been measured so far. We list below the branching ratios in a number of interesting decay modes calculated in the QCD sum rule approach in [26].

$$\mathcal{B}(B_s \to \phi\gamma) = \mathcal{B}(B^0 \to K^{*0}\gamma) = (4.2 \pm 2.0) \times 10^{-5}\,,$$
$$\frac{\mathcal{B}(B_s \to K^{*}\gamma)}{\mathcal{B}(B^0 \to K^{*0}\gamma)} \simeq (0.36 \pm 0.14)\left|\frac{V_{td}}{V_{ts}}\right|^2$$
$$\Longrightarrow \mathcal{B}(B_s \to K^{*}\gamma) = (0.75 \pm 0.5) \times 10^{-6}\,. \tag{33}$$

The branching ratio for the radiative decay $\Lambda_b \to \Lambda\gamma$ can be estimated as follows. Assuming the electromagnetic penguin dominance, one expects $\Gamma(\Lambda_b \to Y_s + \gamma) \simeq \Gamma(B \to X_s + \gamma)$, where

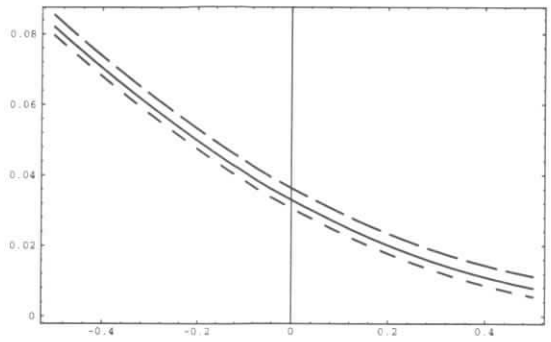

Figure 2: Ratio of the CKM-suppressed and CKM-allowed radiative B-decay rates $\Gamma(B^{\pm} \to \rho^{\pm}\gamma)/\Gamma(B \to K^{*}\gamma)$ (with $B = B^{\pm}$ or B^0) as a function of the Wolfenstein parameter ρ, a) with $\eta = 0.2$ (short-dashed curve), $\eta = 0.3$ (solid curve), and $\eta = 0.4$ (long-dashed curve). (Figure taken from [19].)

Y_s represents a baryonic system having an overall net strangeness quantum number. The exclusive decay rate can be calculated in terms of the exclusive-to-inclusive function $R_\Lambda \equiv \Gamma(\Lambda_b \to \Lambda + \gamma)/\Gamma(\Lambda_b \to Y_s + \gamma)$, analogous to the ratio R_{K^*}, defined for the B meson decays earlier. This would then give:

$$\begin{aligned} \mathcal{B}(\Lambda_b \to \Lambda\gamma) &= R_\Lambda \mathcal{B}(\Lambda_b \to Y_s\gamma) \simeq R_{K^*}\mathcal{B}(B_d \to X_s\gamma)\left[\frac{\tau(B_d)}{\tau(\Lambda_b)}\right] \\ &= (3.8 \pm 1.5) \times 10^{-5} \ , \end{aligned} \tag{34}$$

where we have used the SM estimate $\mathcal{B}(B_d \to X_s\gamma) = (3.2 \pm 0.6) \times 10^{-4}$ [7], assumed $R_\Lambda = R_{K^*}$, with $R_{K^*} = 0.15 \pm 0.05$ [26] and $\tau(B_d)/\tau(\Lambda_b) = 0.78 \pm 0.04$ [30]. The CKM-suppressed decay $\Lambda_b^0 \to n + \gamma$ is related to the decay $\Lambda_b^0 \to \Lambda + \gamma$ by the CKM ratio $|V_{td}|/|V_{ts}|^2$ in the $SU(3)$ limit. Using the central value $|V_{td}|/|V_{ts}|^2 = 0.058$, this gives $\mathcal{B}(\Lambda_b \to n + \gamma) = (2.2 \pm 1.0) \times 10^{-6}$. The estimated branching ratios in a number of inclusive and exclusive radiative B decay modes are given in Table 1, where we have also listed the branching ratios for $B_s \to \gamma\gamma$ and $B_d \to \gamma\gamma$.

2.2 Inclusive rare decays $B \to X_s\ell^+\ell^-$ in the SM

The decays $B \to X_s\ell^+\ell^-$, with $\ell = e, \mu, \tau$, provide a more sensitive search strategy for finding new physics in rare B decays than for example the decay $B \to X_s\gamma$, which constrains

the magnitude of C_7^{eff}. The sign of C_7^{eff}, which depends on the underlying physics, is not determined by the measurement of $\mathcal{B}(B \to X_s + \gamma)$. This sign, which in our convention is negative in the SM, is in general model dependent. It is known (see for example [31]) that in supersymmetric (SUSY) models, both the negative and positive signs are allowed as one scans over the allowed SUSY parameter space. The determination of the sign of C_7^{eff} is an important matter as this will impose further constraints on the parameters of many models. We recall that for low dilepton masses, the differential decay rate for $B \to X_s\ell^+\ell^-$ is dominated by the contribution of the virtual photon to the charged lepton pair, which in turn depends on the effective Wilson coefficient C_7^{eff}. However, as is well known, the $B \to X_s\ell^+\ell^-$ amplitude in the standard model has two additional terms, arising from the two FCNC four-Fermi operators, [1] which are not constrained by the $B \to X_s + \gamma$ data. Calling their coefficients C_9 and C_{10}, it has been argued in [31] that the signs and magnitudes of all three coefficients C_7^{eff}, C_9 and C_{10} can, in principle, be determined from the decays $B \to X_s + \gamma$ and $B \to X_s\ell^+\ell^-$.

The SM-based rates for the decay $b \to s\ell^+\ell^-$, calculated in the free quark decay approximation, have been known in the LO approximation for some time [32]. The LO calculations have the unpleasant feature that the decay distributions and rates are scheme-dependent. The required NLO calculation is in the meanwhile available, which reduces the scheme-dependence of the LO effects in these decays [33]. In addition, long-distance (LD) effects, which are expected to be very important in the decay $B \to X_s\ell^+\ell^-$ [34], have also been estimated from data on the assumption that they arise dominantly due to the charmonium resonances J/ψ and ψ' through the decay chains $B \to X_s J/\psi(\psi', ...) \to X_s\ell^+\ell^-$. The effect of these resonances persists even far away from the resonant masses deforming the short-distance based distributions appreciably [34]. Likewise, the leading $(1/m_b^2)$ power corrections to the partonic decay rate and the dilepton invariant mass distribution have been calculated with the help of the operator product expansion in the effective heavy quark theory [35]. The results of [35] have, however, not been confirmed in a recent independent calculation [36], which finds that the power corrections in the branching ratio $\mathcal{B}(B \to X_s\ell^+\ell^-)$ are negligible. Moreover, the end-point dilepton invariant mass spectrum is not calculable in the heavy quark expansion and will have to be modelled. In what follows, we shall ignore the power corrections.

The amplitude for $B \to X_s\ell^+\ell^-$ is calculated in the effective theory approach, which we have discussed earlier, by extending the operator basis of the effective Hamiltonian introduced in Eq. (6):

$$\mathcal{H}_{eff}(b \to s + \gamma; b \to s + \ell^+\ell^-) = \mathcal{H}_{eff}(b \to s + \gamma) - \frac{4G_F}{\sqrt{2}} V_{ts}^* V_{tb} \left[C_9\mathcal{O}_9 + C_{10}\mathcal{O}_{10}\right], \tag{35}$$

where the two additional operators are:

$$\begin{aligned} \mathcal{O}_9 &= \frac{\alpha}{4\pi}\bar{s}_\alpha\gamma^\mu P_L b_\alpha \bar{\ell}\gamma_\mu\ell, \\ \mathcal{O}_{10} &= \frac{\alpha}{4\pi}\bar{s}_\alpha\gamma^\mu P_L b_\alpha \bar{\ell}\gamma_\mu\gamma_5\ell \ . \end{aligned} \tag{36}$$

[1] This also holds for a large class of models such as MSSM and the two-Higgs doublet models but not for all SM-extensions. In LR symmetric models, for example, there are additional FCNC four-Fermi operators involved [37].

The analytic expressions for $C_9(m_W)$ and $C_{10}(m_W)$ can be seen in [33] and will not be given here. We recall that the coefficient C_9 in LO is scheme-dependent. However, this is compensated by an additional scheme-dependent part in the (one loop) matrix element of $\mathcal{O}_9$. We call the sum C_9^{eff}, which is scheme-independent and enters in the physical decay amplitude given below,

$$\mathcal{M}(b \to s + \ell^+\ell^-) = \frac{4G_F}{\sqrt{2}} V_{ts}^* V_{tb} \frac{\alpha}{\pi} \times \left[C_9^{eff} \bar{s}\gamma^\mu P_L b \bar{\ell}\gamma_\mu \ell + C_{10} \bar{s}\gamma^\mu P_L b \bar{\ell}\gamma_\mu\gamma_5 \ell - 2C_7^{eff} \bar{s} i\sigma_{\mu\nu} \frac{q^\nu}{q^2} (m_b P_R + m_s P_L) b \bar{\ell}\gamma^\mu \ell \right], \tag{37}$$

with

$$C_9^{eff}(\hat{s}) \equiv C_9 \eta(\hat{s}) + Y(\hat{s}). \tag{38}$$

The function $Y(\hat{s})$ is the one-loop matrix element of $\mathcal{O}_9$ and can be seen in literature [33, 7]. The differential decay rates in $B \to X_s \ell^+\ell^-$ (ignoring lepton masses) are,

$$\frac{d\mathcal{B}(\hat{s})}{d\hat{s}} = \mathcal{B}_{sl} \frac{\alpha^2}{4\pi^2} \frac{\lambda_t^2}{|V_{cb}|^2} \frac{1}{f(\hat{m}_c)\kappa(\hat{m}_c)} u(\hat{s}) \left[\left(|C_9^{eff}(\hat{s})|^2 + C_{10}^2 \right) \alpha_1(\hat{s}, \hat{m}_s) + \frac{4}{\hat{s}} (C_7^{eff})^2 \alpha_2(\hat{s}, \hat{m}_s) + 12\alpha_3(\hat{s}, \hat{m}_s) C_7^{eff} \Re(C_9^{eff}(\hat{s})) \right], \tag{39}$$

with $u(\hat{s}) = \sqrt{[\hat{s} - (1+\hat{m}_s)^2][\hat{s} - (1-\hat{m}_s)^2]}$, $f(z) = 1 - 8z^2 + 8z^6 - z^8 - 24z^4 \ln z$, $\kappa(z) = 1 - 2\alpha_s(\mu)/3\pi \left[(\pi^2 - 31/4)(1-z)^2 + 3/2 \right]$, and

$$\alpha_1(\hat{s}, \hat{m}_s) = -2\hat{s}^2 + \hat{s}(1+\hat{m}_s^2) + (1-\hat{m}_s^2)^2, \tag{40}$$

$$\alpha_2(\hat{s}, \hat{m}_s) = -(1+\hat{m}_s^2)\hat{s}^2 - (1 + 14\hat{m}_s^2 + \hat{m}_s^4)\hat{s} + 2(1+\hat{m}_s^2)(1-\hat{m}_s^2)^2, \tag{41}$$

$$\alpha_3(\hat{s}, \hat{m}_s) = (1-\hat{m}_s^2)^2 - (1+\hat{m}_s^2)\hat{s}. \tag{42}$$

Here $\Re(C_7^{eff})$ represents the real part of C_7^{eff}. A useful quantity is the differential FB asymmetry in the c.m.s. of the dilepton defined in refs. [38]:

$$\frac{d\mathcal{A}(\hat{s})}{d\hat{s}} = \int_0^1 \frac{d\mathcal{B}}{dz} - \int_0^{-1} \frac{d\mathcal{B}}{dz}, \tag{43}$$

where $z = \cos\theta$, which can be expressed as:

$$\frac{d\mathcal{A}(\hat{s})}{d\hat{s}} = -\mathcal{B}_{sl} \frac{3\alpha^2}{4\pi^2} \frac{1}{f(\hat{m}_c)} u^2(\hat{s}) C_{10} \left[\hat{s}\Re(C_9^{eff}(\hat{s})) + 2C_7^{eff}(1+\hat{m}_s^2) \right]. \tag{44}$$

The Wilson coefficients C_7^{eff}, C_9^{eff} and C_{10} appearing in the above equations can be determined from data by solving the partial branching ratio $\mathcal{B}(\Delta\hat{s})$ and partial FB asymmetry $\mathcal{A}(\Delta\hat{s})$, where $\Delta\hat{s}$ defines an interval in the dilepton invariant mass [31].

There are other quantities which one can measure in the decays $B \to X_s \ell^+\ell^-$ to disentangle the underlying dynamics. We mention here the longitudinal polarization of the lepton in $B \to X_s \ell^+\ell^-$, in particular in $B \to X_s \tau^+\tau^-$, proposed by Hewett [39]. In a recent paper, Krüger and

Sehgal [40] have stressed that complementary information is contained in the two orthogonal components of polarization (P_T, the component in the decay plane, and P_N, the component normal to the decay plane), both of which are proportional to m_ℓ/m_b, and therefore significant for the $\tau^+\tau^-$ channel. A third quantity, called energy asymmetry, proposed by Cho, Misiak and Wyler [41], defined as

$$\mathcal{A} = \frac{N(E_{\ell^-} > E_{\ell^+}) - N(E_{\ell^+} > E_{\ell^-})}{N(E_{\ell^-} > E_{\ell^+}) + N(E_{\ell^+} > E_{\ell^-})}, \tag{45}$$

where $N(E_{\ell^-} > E_{\ell^+})$ denotes the number of lepton pairs where ℓ^+ is more energetic than ℓ^- in the B-rest frame, is, however, not an independent measure, as it is directly proportional to the FB asymmetry discussed above. The relation is [36]:

$$\int \mathcal{A}(\hat{s}) = \mathcal{B} \times A\,. \tag{46}$$

This is easy to notice if one writes the Mandelstam variable $u(\hat{s})$ in the dilepton c.m. and the B-hadron rest systems.

Next, we discuss the effects of LD contributions in the processes $B \to X_s \ell^+\ell^-$. Note that the LD contributions due to the vector mesons such as J/ψ and ψ', as well as the continuum $c\bar{c}$ contribution already discussed, appear as an effective $(\bar{s}_L\gamma_\mu b_L)(\bar{\ell}\gamma^\mu\ell)$ interaction term only, i.e. in the operator $\mathcal{O}_9$. This implies that the LD-contributions should change C_9 effectively, C_7 as discussed earlier is dominated by the SD-contribution, and C_{10} has no LD-contribution. In accordance with this, the function $Y(\hat{s})$ is replaced by,

$$Y(\hat{s}) \to Y'(\hat{s}) \equiv Y(\hat{s}) + Y_{\rm res}(\hat{s}), \tag{47}$$

where $Y_{\rm res}(\hat{s})$ is given as [38],

$$Y_{\rm res}(\hat{s}) = \frac{3}{\alpha^2} \kappa \left(3C_1 + C_2 + 3C_3 + C_4 + 3C_5 + C_6 \right) \sum_{V_i = J/\psi, \psi', \ldots} \frac{\pi\Gamma(V_i \to l^+l^-) M_{V_i}}{M_{V_i}^2 - \hat{s}m_b^2 - iM_{V_i}\Gamma_{V_i}}, \tag{48}$$

where κ is a fudge factor, which appears due to the inadequacy of the factorization framework in describing data on $B \to J/\psi X_s$. Here we use $\kappa\left(3C_1 + C_2 + 3C_3 + C_4 + 3C_5 + C_6\right) = +0.88$ for the numerical calculation, which reproduces (in average) the measured branching ratios for $B \to J/\psi X_s$ and $B \to \psi' X_s$, after the contributions from the χ_c states have been subtracted. The long-distance effects lead to significant interference effects in the dilepton invariant mass distribution and the FB asymmetry in $B \to X_s \ell^+\ell^-$ shown in Figs. 3 and 4, respectively. This can be used to test the SM, as the signs of the Wilson coefficients in general are model dependent.

Taking into account the spread in the values of the input parameters, μ, Λ, m_t, and $\mathcal{B}_{SL}$ discussed in the previous section in the context of $\mathcal{B}(B \to X_s + \gamma)$, we estimate the following branching ratios for the SD-piece only (i.e., from the intermediate top quark contribution only) [36]:

$$\begin{aligned} \mathcal{B}(B \to X_s e^+e^-) &= (8.4 \pm 2.2) \times 10^{-6}, \\ \mathcal{B}(B \to X_s \mu^+\mu^-) &= (5.7 \pm 1.2) \times 10^{-6}, \\ \mathcal{B}(B \to X_s \tau^+\tau^-) &= (2.6 \pm 0.5) \times 10^{-7}, \end{aligned} \tag{49}$$

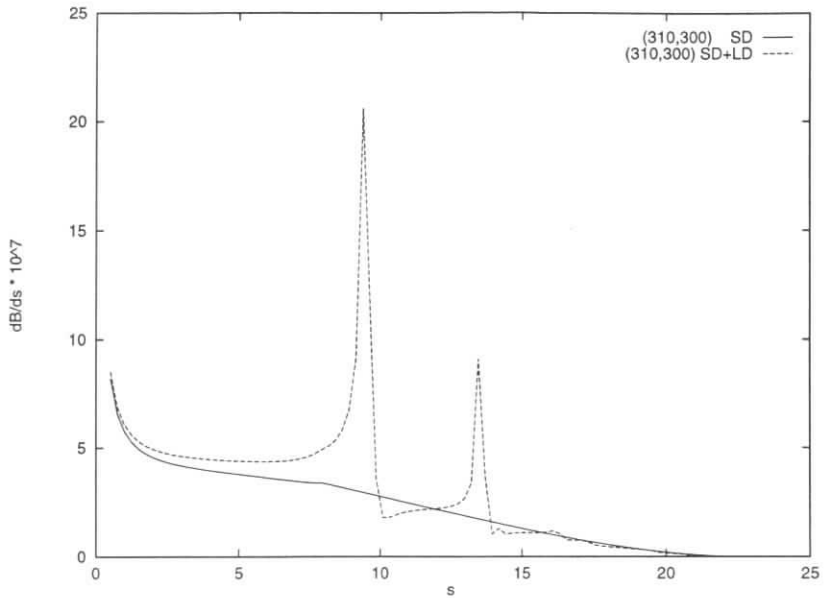

Figure 3: Differential branching ratio $d\mathcal{B}/ds$ for $B \to X_s\ell^+\ell^-$ calculated in the SM using the next-to-leading order QCD corrections and Fermi motion effect (solid curve), and including the LD-contributions (dashed curve). The Fermi motion model parameters (P_F, m_q) are displayed in the figure. (Figure taken from [36].)

where theoretical errors and the error on $\mathcal{B}_{SL}$ have been added in quadrature. The present experimental limit for the inclusive branching ratio in $B \to X_s\ell^+\ell^-$ is actually still the one set by the UA1 collaboration some time ago [42], namely $\mathcal{B}(B \to X_s\mu^+\mu^-) > 5.0 \times 10^{-5}$. As far as we know, there are no interesting limits on the other two modes, involving $X_se^+e^-$ and $X_s\tau^+\tau^-$.

It is obvious from Fig. 3 that only in the dilepton mass region far away from the resonances is there a hope of extracting the Wilson coefficients governing the short-distance physics. The region below the J/ψ resonance is well suited for that purpose as the dilepton invariant mass distribution here is dominated by the SD-piece. Including the LD-contributions, following branching ratio has been estimated for the dilepton mass range 2.1 GeV$^2 \leq s \leq$ 2.9 GeV^2 in [36]:

$$\mathcal{B}(B \to X_s\mu^+\mu^-) = (1.3 \pm 0.3) \times 10^{-6}, \tag{50}$$

with $\mathcal{B}(B \to X_se^+e^-) \simeq \mathcal{B}(B \to X_s\mu^+\mu^-)$. The FB-asymmetry is estimated to be in the range 10% - 27%, as can be seen in Fig. 4. These branching ratios and the FB asymmetry are expected to be measured within the next several years at BABAR, BELLE, CLEO, CDF, D0, and HERA-B. In the high invariant mass region, the short-distance contribution dominates. However, the rates are down by roughly an order of magnitude compared to the region below the J/ψ-mass. Estimates of the branching ratios are of $O(10^{-7})$, which should be accessible at the LHC.

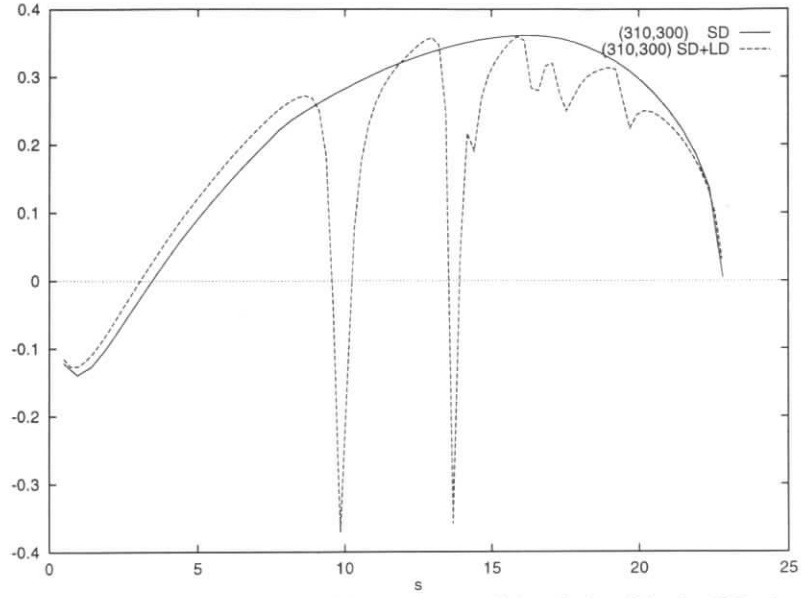

Figure 4: Normalized FB asymmetry $\mathcal{A}(s)$ for $B \to X_s\ell^+\ell^-$ calculated in the SM using the next-to-leading order QCD corrections and Fermi motion effect (solid curve), and including the LD-contributions (dashed curve). The Fermi motion model parameters (P_F, m_q) are displayed in the figure. (Figure taken from [36].)

The experimental limits on the decay rates of the exclusive decays $B \to (K, K^*)\ell^+\ell^-$ [29, 43], while arguably closer to the SM-based estimates, can only be interpreted in specific models of form factors, which hinders somewhat their transcription in terms of the information on the underlying Wilson coefficients. However, many of these form factors can be related to the known ones using ideas from heavy quark effective theory augmented with QCD sum rule estimates in studying the heavy to light form factors in B decays. We will not take up such exclusive decays, important as they are, and content ourselves with presenting the expected branching ratios for some of the experimentally interesting decay modes. Using the exclusive-to-inclusive ratios $R_{K\ell\ell} \equiv \Gamma(B \to K\ell^+\ell^-)/\Gamma(B \to X_s\ell^+\ell^-) = 0.07 \pm 0.02$ and $R_{K^*\ell\ell} \equiv \Gamma(B \to K^*\ell^+\ell^-)/\Gamma(B \to X_s\ell^+\ell^-) = 0.27 \pm 0.0.07$, which were estimated in [45], the results are presented in Table 1.

In conclusion, the semileptonic FCNC decays $B \to X_s\ell^+\ell^-$ (and also the exclusive decays) will provide very precise tests of the SM, as they will determine the signs and magnitudes of the three Wilson coefficients, C_7, C_9^{eff} and C_{10}. This, perhaps, may also reveal physics beyond-the-SM if it is associated with not too high a scale. The MSSM model is a good case study where measurable deviations from the SM are anticipated and worked out [31, 41].

Decay Modes	$\mathcal{B}$(SM)	Measurements and Upper Limits (90% C.L.)
$(B^\pm, B^0) \to X_s\gamma$	$(3.2 \pm 0.58) \times 10^{-4}$	$(2.32 \pm 0.67) \times 10^{-4}$ CLEO [2]
$(B^\pm, B^0) \to K^*\gamma$	$(4.0 \pm 2.0) \times 10^{-5}$	$(4.2 \pm 0.8 \pm 0.6) \times 10^{-5}$ CLEO [4]
$(B^\pm, B^0) \to X_d\gamma$	$(1.6 \pm 1.2) \times 10^{-5}$	–
$B^\pm \to \rho^\pm + \gamma$	$(1.5 \pm 1.1) \times 10^{-6}$	$< 1.1 \times 10^{-5}$ CLEO [4]
$B^0 \to \rho^0 + \gamma$	$(0.65 \pm 0.35) \times 10^{-6}$	$< 3.9 \times 10^{-5}$ CLEO [4]
$B^0 \to \omega + \gamma$	$(0.65 \pm 0.35) \times 10^{-6}$	$< 1.3 \times 10^{-5}$ CLEO [4]
$B_s \to \phi + \gamma$	$(4.2 \pm 2.0) \times 10^{-5}$	–
$B_s \to K^* + \gamma$	$(0.8 \pm 0.5) \times 10^{-6}$	–
$\Lambda_b \to \Lambda + \gamma$	$(3.8 \pm 1.5) \times 10^{-5}$	–
$\Lambda_b \to n + \gamma$	$(2.2 \pm 1.0) \times 10^{-6}$	–
$(B_d, B_u) \to X_s e^+ e^-$	$(8.4 \pm 2.2) \times 10^{-6}$	–
$(B_d, B_u) \to X_d e^+ e^-$	$(4.9 \pm 2.9) \times 10^{-7}$	–
$(B_d, B_u) \to X_s \mu^+ \mu^-$	$(5.7 \pm 1.2) \times 10^{-6}$	$< 3.6 \times 10^{-5}$ D0 [47]
$(B_d, B_u) \to X_d \mu^+ \mu^-$	$(3.3 \pm 1.9) \times 10^{-7}$	–
$(B_d, B_u) \to X_s \tau^+ \tau^-$	$(2.6 \pm 0.5) \times 10^{-7}$	–
$(B_d, B_u) \to X_d \tau^+ \tau^-$	$(1.5 \pm 0.8) \times 10^{-8}$	–
$(B_d, B_u) \to K e^+ e^-$	$(5.9 \pm 2.3) \times 10^{-7}$	$< 1.2 \times 10^{-5}$ CLEO [43]
$(B_d, B_u) \to K \mu^+ \mu^-$	$(4.0 \pm 1.5) \times 10^{-7}$	$< 0.9 \times 10^{-5}$ CLEO [43]
$(B_d, B_u) \to K \mu^+ \mu^-$	$(4.0 \pm 1.5) \times 10^{-7}$	$< 0.9 \times 10^{-5}$ CLEO [43]
$(B_d, B_u) \to K^* e^+ e^-$	$(2.3 \pm 0.9) \times 10^{-6}$	$< 1.6 \times 10^{-5}$ CLEO [43]
$(B_d, B_u) \to K^* \mu^+ \mu^-$	$(1.5 \pm 0.6) \times 10^{-6}$	$< 2.5 \times 10^{-5}$ CDF [44]
$B_s \to \gamma\gamma$	$(3.0 \pm 1.0) \times 10^{-7}$	$< 1.1 \times 10^{-4}$ L3 [48]
$B_d \to \gamma\gamma$	$(1.2 \pm 0.8) \times 10^{-8}$	$< 3.8 \times 10^{-5}$ L3 [48]
$B_s \to \tau^+ \tau^-$	$(7.4 \pm 1.9) \times 10^{-7}$	–
$B_d \to \tau^+ \tau^-$	$(3.1 \pm 1.9) \times 10^{-8}$	–
$B_s \to \mu^+ \mu^-$	$(3.5 \pm 1.0) \times 10^{-9}$	$< 8.4 \times 10^{-6}$ CDF [44]
$B_d \to \mu^+ \mu^-$	$(1.5 \pm 0.9) \times 10^{-10}$	$< 1.6 \times 10^{-6}$ CDF [44]
$B_s \to e^+ e^-$	$(8.0 \pm 3.5) \times 10^{-14}$	–
$B_d \to e^+ e^-$	$(3.4 \pm 2.3) \times 10^{-15}$	–

Table 1: Estimates of the branching fractions for FCNC B-decays in the standard model taking into account the uncertainties in the input parameters as discussed in [7]. The entries in the second column correspond to the short-distance contributions only except for the radiative decays $B^\pm \to \rho^\pm + \gamma$ and $B^0 \to (\rho^0, \omega) + \gamma$, where long-distance effects have also been included. For the two-body branching ratios, we have used $f_{B_d} = 200$ MeV and $f_{B_s}/f_{B_d} = 1.16$. Experimental measurements and upper limits are also listed. (Updated from [7].)

3 Acknowledgements

I would like to thank Hrachia Asatrian, Patricia Ball, Vladimir Braun, Christoph Greub, L. Handoko, Gudrun Hiller, Alexander Khodzhamirian, and Tak Morozumi for helpful discussions and input.

References

[1] N. Cabibbo, Phys. Rev. Lett. **10** (1963) 531;
M. Kobayashi and K. Maskawa, Prog. Theor. Phys. **49** (1973) 652.

[2] M.S. Alam et al. (CLEO Collaboration), Phys. Rev. Lett. **74** (1995) 2885.

[3] R. Ammar et al. (CLEO Collaboration), Phys. Rev. Lett. **71** (1993) 674.

[4] R. Ammar et al. (CLEO Collaboration), contributed paper to the International Conference on High Energy Physics, Warsaw, 25 - 31 July 1996, CLEO CONF 96-05.

[5] S.L. Glashow, J. Iliopoulos and L. Maiani, Phys. Rev. **D2** (1970) 1285.

[6] T. Inami and C.S. Lim, Prog. Theor. Phys. **65** (1981) 297.

[7] A. Ali, preprint DESY 96-106 [hep-ph/9606324]; to appear in the Proceedings of the XX International Nathiagali Conference on Physics and Contemporary Needs, Bhurban, Pakistan, June 24-July 13, 1995 (Nova Science Publishers, New York, 1996).

[8] M. Ciuchini et al., Phys. Lett. **B316** (1993) 127; Nucl. Phys. **B415** (1994) 403;
G. Cella et al., Phys. Lett. **B325** (1994) 227;
M. Misiak, Nucl. Phys. **B393** (1993) 23; [E. **B439** (1995) 461].

[9] M. Misiak, contribution to the International Conference on High Energy Physics, Warsaw, 25 - 31 July 1996.

[10] A. Ali and C. Greub, Z. Phys. **C49** (1991) 431; Phys. Lett. **B259** (1991) 182; Z. Phys. **C60** (1993) 433.

[11] A. Ali and C. Greub , Phys. Lett. **B287** (1992) 191.

[12] A. Ali and C. Greub, Phys. Lett. **B361** (1995) 146.

[13] N. Pott, preprint TUM-T31-93/95 [hep-ph/9512252].

[14] K. Adel and Y.-p. Yao, Phys. Rev. **D49** (1994) 4945.

[15] C. Greub, T. Hurth and D. Wyler, preprints SLAC-PUB-96-7113, ZU-TH/2/1996 [hep-ph/9602281] and SLAC-PUB-96-7144 [hep-ph-9603404].

[16] J. Chay, H. Georgi and B. Grinstein, Phys. Lett. **B247** (1990) 399.

[17] I. Bigi, N. Uraltsev and A. Vainshtein, Phys. Lett. **B293** (1992) 430; [E: **B297** (1993) 477]; B. Blok and M. Shifman, Nucl. Phys. **B399** (1993) 441, *ibid.* 459;
I. Bigi et al., Phys. Rev. Lett. **71** (1993) 496 and in:
Proc. of the Annual Meeting of the Division of Particles and Fields of the APS, Batavia, Illinois, 1992, edited by C. Albright et al. (World Scientific, Singapore), 610.

[18] A. Khodzhamirian, G. Stoll, and D. Wyler, Phys. Lett. **B358** (1995) 129.

[19] A. Ali and V.M. Braun, Phys. Lett. **B359** (1995) 223.

[20] D. Atwood, B. Blok, and A. Soni, preprint TECHNION-PH-94-11 (1994) [hep-ph-9408373]; H.-Y. Cheng, preprint IP-ASTP-23-94 [hep-ph-9411330] (1994); J.M. Soares, Phys. Rev. **D53** (1996) 241; J. Milana, Phys. Rev. **D53** (1996) 1403; G. Eilam, A. Ioannissian, and R.R. Mendel, preprint TECHNION-PH-95-4 [hep-ph-9505222]; G. Ricciardi, Phys. Lett. **B355** (1995) 313; N.G. Deshpande, X.-G. He, and J. Trampetic, Phys. Lett. **B367** (1996) 362; E. Golowich and S. Pakvasa, Phys. Rev. **D51**, 1215 (1995).

[21] L. Wolfenstein, Phys. Rev. Lett. **51** (1983)

[22] A. Ali and D. London, preprint DESY 96-140, UdeM-GPP-TH-96-45, [hep-ph/9607392], to appear in the *Proc. of QCD Euroconference 96*, Montpellier, July 4-12, 1996.

[23] R.M. Barnett et al. (Particle Data Group), Phys. Rev. **D54** (1996) 1.

[24] A. Ali, H.M. Asatrian, and C. Greub, to be published.

[25] L. Gibbons, Plenary talk at the International Conference on High Energy Physics, Warsaw, ICHEP96 (1996).

[26] A. Ali, V.M. Braun and H. Simma, Z. Phys. **C63** (1994) 437.

[27] P. Ball, TU-München Report TUM-T31-43/93 (1993); P. Colangelo et al., Phys. Lett. **B317** (1993) 183; S. Narison, Phys. Lett. **B327** (1994) 354; J. M. Soares, Phys. Rev. **D49** (1994) 283.

[28] I.I. Balitsky, V.M. Braun, and A.V. Kolesnichenko, Nucl. Phys. **312** (1989) 509.

[29] T.E. Browder and K. Honscheid, Prog. Part. Nucl. Phys. **35** (1995) 81.

[30] J. Richman, Plenary talk at the International Conference on High Energy Physics, Warsaw, ICHEP96 (1996).

[31] A. Ali, G. F. Giudice and T. Mannel, Z. Phys. **C67** (1995) 417.

[32] S. Bertolini, F. Borzumati and A. Masiero, Phys. Rev. Lett. **59** (1987) 180; R. Grigjanis et al., Phys. Lett. **B213** (1988) 355; B. Grinstein, R. Springer, and M.B. Wise, Phys. Lett. **202** (1988) 138; Nucl Phys. **B339** (1990) 269; G. Cella et al., Phys. Lett. **B248** (1990) 181.

[33] M. Misiak in ref. [8]; A.J. Buras and M. Münz, Phys. Rev. **D52** (1995) 186.

[34] C. S. Lim, T. Morozumi and A. I. Sanda, Phys. Lett. **218** (1989) 343; N. G. Deshpande, J. Trampetic and K. Panose, Phys. Rev. **D39** (1989) 1461; P. J. O'Donnell and H. K. K. Tung, Phys. Rev. **D43** (1991) R2067; N. Paver and Riazuddin, Phys. Rev. **D45** (1992) 978.

[35] A. F. Falk, M. Luke and M. J. Savage, Phys. Rev. **D49** (1994) 3367.

[36] A.Ali, G. Hiller, L.T. Handoko, and T. Morozumi, (to be published).

[37] K. Fujikawa and A. Yamada, Phys. Rev. **D49** (1994) 5890; P. Cho and M. Misiak, Phys. Rev. **D49** (1994) 5894.

[38] A. Ali, T. Mannel and T. Morozumi, Phys. Lett. **B273** (1991) 505.

[39] J. Hewett, Phys. Rev. **D53** (1996) 4964.

[40] F. Krüger and L.M. Sehgal, preprint PITHA 96/4 [hep-ph/9603237].

[41] P. Cho, M. Misiak, and D. Wyler, preprint ZU-TH 24/95, CALT-68-2028 [hep-ph/9601360].

[42] C. Albajar et al. (UA1), Phys. Lett. **B262** (1991) 163.

[43] T. Skwarnicki, preprint [hep-ph/9512395], to appear in: Proc. of the 17th Int. Symp. on Lepton Photon Interactions, Beijing, P.R. China, August 1995.

[44] CDF Collaboration, Fermilab Conf. 95/201-E(1995).

[45] A. Ali, C. Greub and T. Mannel, DESY Report 93-016 (1993), and in *B*-Physics Working Group Report, ECFA Workshop on a European *B*-Meson Factory, ECFA 93/151, DESY 93-053 (1993), edited by R. Aleksan and A. Ali.

[46] G.-L. Lin, J. Liu, and Y.-P. Yao, Phys. Rev. **D42** (1990) 2314; H. Simma and D. Wyler, Nucl. Phys. **B344** (1990) 283; S. Herrlich and J. Kalinowski, Nucl. Phys. **381** (1992) 501; T.M. Aliev and G. Turan, Phys. Rev. **D48** (1993) 1176; G.G. Devidze, G.R. Jibuti, and A.G. Liparteliani, preprint HEP Institute, Univ. of Tbilisi (revised version) (1995).

[47] S. Abachi et al. (D0 Collaboration), contributed paper to the International Conference on High Energy Physics, Warsaw, ICHEP96 (1996).

[48] L3 Collaboration, contributed paper to the EPS Conference, (EPS-0093-2) Brussels, 1995.

The partial reconstruction of $B^0 \to \chi_{c1} K^0_S$, $B^0 \to \psi' K^0_S$ and $B^0 \to J/\psi K^{*0}$ decays at the HERA-B experiment

R. Mizuk [1]

Inst. of Theoretical and Experimental Physics, B. Cheremushk. 25, 127259 Moscow, RUSSIA

Abstract: The possibility of partial reconstruction of additional $\mathcal{CP}$ channels at the HERA-B experiment is considered. The resulting error in $\sin 2\beta$ is estimated.

1 Introduction

The decays $B^0 \to J/\psi K^0_S$ and $B^0 \to \pi^+\pi^-$ determine the $\mathcal{CP}$ reach of the HERA-B experiment [1, 2]. Some more $\mathcal{CP}$ channels are automatically included into the main trigger. The use of these additional $\mathcal{CP}$ channels can effectively enhance the statistics coming from the main channels. Besides, if $\mathcal{CP}$ violation is observed in more than one channel, the reliability of the obtained result becomes larger. Among the additional $\mathcal{CP}$ channels are:

$$\begin{array}{lll} B^0 \to \chi_{c1} K^0_S \to (J/\psi\gamma) K^0_S & & (a) \\ B^0 \to \psi' K^0_S \to (J/\psi X^0) K^0_S & (X^0 \text{ is mainly } \pi^0\pi^0) & (b) \\ B^0 \to J/\psi K^{*0} \to J/\psi (K^0_S \pi^0) & & (c) \end{array}$$

The longitudinal polarization has been measured to dominate in the latter decay [3], thus resulting in a $\mathcal{CP}$ eigenstate. This mode is especially important, since the predicted $\mathcal{CP}$ parity of the final state is opposite in sign to that of $J/\psi K^0_S$ mode and possible systematic biases can be revealed. The neutral particles in the final state can not be detected with high efficiency. Another approach is to reconstruct these channels partially as it is described below.

2 Method

In a two-body decay the direction of mother particle and the momentum of one of the daughters determine the kinematics of the decay if masses of all particles are known. This fact is used to reconstruct the kinematics of the decays $B^0 \to J/\psi K^0_S X$, where X - undetected particle(s). The J/ψ and K^0_S are regarded as one daughter particle and undetected particle(s) are regarded as the other one. Measured values are the B^0 meson flight direction (known from the reconstruction of B^0 meson production and decay vertices) and the J/ψ and K^0_S momenta. The method of partial reconstruction is described in more detail in [4]. The found energy-momentum of X can be used

[1] Partially supported by INTAS Foundation with grant 94-3819

to calculate the invariant masses of $J/\psi X$ and $K^0_S X$. The peaks at χ_{c1} and ψ' masses in $J/\psi X$ invariant mass distribution would be the signatures of **(a)** and **(b)** decays correspondingly. The peak at K^{*0} mass in $K^0_S X$ invariant mass distribution would be the signature of **(c)** decay.

The mass of X is set to zero, when the invariant mass of $J/\psi X$ is calculated (the error in $m_{J/\psi X}$ due to substitution $m_{\pi^0\pi^0}$ by zero is negligible) and to m_{π^0} when the invariant mass of $K^0_S X$ is calculated.

The decay kinematics is known with two-fold ambiguity (this fact is considered in [1] for the similar partial reconstruction of semileptonic B decays). The invariant masses are calculated for both solutions and their average is taken as a final value.

Simulation shows that the maximal value of θ (where θ is the angle between the B^0 meson flight direction and the $J/\psi K^0_S$ momentum): $\theta_{\max} \sim 5 \cdot 10^{-3}$, is comparable with the accuracy in θ due to finite vertex resolution: $\delta\theta \sim 3 \cdot 10^{-3}$. Therefore the measured value of θ is often outside the kinematically allowed region and the solutions exist only in about one half of cases.

3 Monte Carlo Simulation

For simulation we use the `PYTHIA 5.6` [5] event generator for $b\bar{b}$ events and `FRITIOF 7.0` [6] for minimum bias events. To reproduce HERA-B experimental conditions we generate 1 $b\bar{b}$ event with 4 Poisson distributed minimum bias events for every interaction of bunch of protons with target. J/ψ vertex is smeared with the nominal detector resolution [2] $\sigma_x = \sigma_y = 25\mu$m, $\sigma_z = 500\mu$m. The B production vertex is smeared with $\sigma_x = \sigma_y = \sigma_z = 10\mu$m.

Branching ratios of B decays to charmonium for signal and background processes are listed in Table 1. Only a few decay modes are measured experimentally (shown in **bold**) [7]. For

	J/ψ	ψ'	χ_{c1}	χ_{c2}
K^0	**0.94 (+)**	0.69 (+)	1.0 (+)	0.29 (-)
K^{*0}	**1.6 (-)**	1.18 (-)	1.7 (-)	0.49
$K^0\pi^0$	1.0	0.27	0.23	0.31
$K^+\pi^-$	**1.0**	0.27	0.23	0.31
$K^0\pi^0\pi^0$	1.2	0.33	0.29	0.37
$K^0\pi^+\pi^-$	1.2	0.33	0.29	0.37
$K^+\pi^-\pi^0$	1.2	0.33	0.29	0.37
anything	**8.0**	**3.4**	**4.0**	**2.5**

Table 1: *Branching ratios of* B^0 *decays to charmonium (in* 10^{-3}*). Measured values are shown in* **bold**. *The channels, which result in* $J/\psi K^0_S X$ *final states with positive* $\mathcal{CP}$ *parity are marked with* (+)*, with negative* - (-).

some channels isotopic relations can be used:

$$\begin{array}{lcl} \mathcal{B}(B^0 \to \chi_{c1} K^0) & = & \mathcal{B}(B^+ \to \chi_{c1} K^+) \\ \mathcal{B}(B^0 \to \psi' K^0) & = & \mathcal{B}(B^+ \to \psi' K^+) \\ \mathcal{B}(B^0 \to J/\psi K^0\pi^0) & = & \mathcal{B}(B^0 \to J/\psi K^+\pi^-) \\ \mathcal{B}(B^0 \to J/\psi K\pi\pi) & = & \mathcal{B}(B^+ \to J/\psi K^+\pi^+\pi^-) \end{array}$$

In order to compare with $B^0 \to J/\psi K^0_S$ decay, the trigger and reconstruction efficiencies determined for this decay were used.

The $J/\psi\,X$ mass peaks of $\chi_{c1}K^0_S$ and $\psi' K^0_S$ decay modes overlap (see Figure 1). However the final states are predicted to have the same $\mathcal{CP}$ parity and both channels can be combined for $\mathcal{CP}$ violation studies.

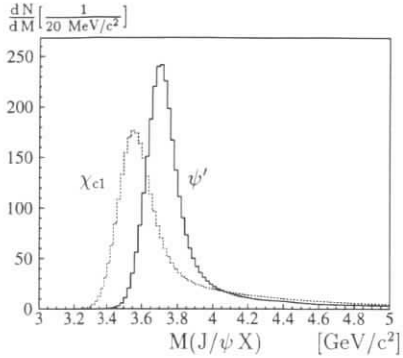

Figure 1: $J/\psi\,X$ *mass distribution of* $\chi_{c1}K^0_S$ *and* $\psi' K^0_S$ *decay modes.*

The main sources of background both for the decays **(a)**, **(b)** and **(c)** are:
1) J/ψ and K^0_S from $B^0 \to J/\psi K^0_S X$ decays, in which the final states have a $\mathcal{CP}$ parity opposite in sign to that of signal. This source of background dilutes strongly the observable $\mathcal{CP}$ asymmetry. For $(\chi_{c1},\,\psi')K^0_S$ signal such background modes are $(J/\psi,\,\chi_{c1},\,\psi')K^{*0}$ (we assume, that in $(\chi_{c1},\psi')K^{*0}$ modes longitudinally polarized helicity state dominates, like in $J/\psi K^{*0}$ mode). For the $J/\psi K^{*0}$ signal such background modes are $(\chi_{c1},\,\psi')K^0_S$.
2) J/ψ and K^0_S from $B^0 \to J/\psi K^0_S X$ decays, in which the final states have the same $\mathcal{CP}$ parity as the signal. For $J/\psi K^{*0}$ signal such background modes are $(\chi_{c1},\,\psi')K^{*0}$.
3) J/ψ and K^0_S from $B \to J/\psi K^0_S X$ decays, which does not result in a $\mathcal{CP}$ eigenstate.
4) J/ψ and accidental K^0_S. It is considered, that only J/ψ and K^0_S originating from the same target wire contribute to this source of background.
The background from direct J/ψ and accidental K^0_S is strongly suppressed by the cut on minimal B meson flight distance of 4 mm.

In the $J/\psi K^{*0}$ mode the expected distribution in $\theta_{K^{*0}}$ (where $\theta_{K^{*0}}$ is the angle between K^{*0} direction in B^0 meson rest frame and K^0_S direction in K^{*0} rest frame) is $d\Gamma_L/d\cos\theta_{K^*} = \frac{3}{2}\cos^2\theta_{K^*}$ [3]. The background with positive sign of $\mathcal{CP}$ parity is concentrated in the region of negative $\cos\theta_{K^{*0}}$ (see Figure 2). Therefore, the cut $\cos\theta_{K^{*0}} > 0.4$ is applied.

In the signal decay modes no hadron tracks originate from the B^0 decay vertex. The background from B decays with additional hadrons from the B decay vertex can be suppressed. The event is rejected if there is at least one track near the B decay vertex and far from interaction vertices. The cut in distance from a track to vertices is at the level $2.5\,\sigma_{\rm imp.par.}$ ($\sigma_{\rm imp.par.} = 25\mu{\rm m} \oplus 30\mu{\rm m}/p_t$ - nominal impact parameter resolution for a given track). Only tracks with transverse momentum $p_t > 0.3{\rm GeV/c}$ are regarded. The efficiency of this cut is 85%, while the background is suppressed by a factor of three.

The $J/\psi\,X$ and $K^0_S X$ mass distributions expected after one year of HERA-B operation, are shown in Figure 3. The accuracy in $\sin 2\beta$ using the combined $B^0 \to \chi_{c1}K^0_S \to (J/\psi\gamma)K^0_S$ and

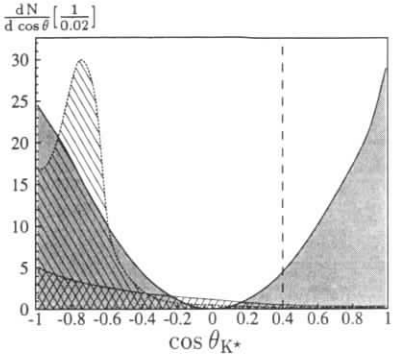

Figure 2: $\cos\theta_{K^*}$ *distributions. The contribution of* $J/\psi K^{*0}$ *signal is represented by the grey area. The contribution of background with positive sign of* $\mathcal{CP}$ *parity – by the area, hatched with the slope to the left, the contribution of background with negative sign of* $\mathcal{CP}$ *parity – by the area, hatched with the slope to the right.*

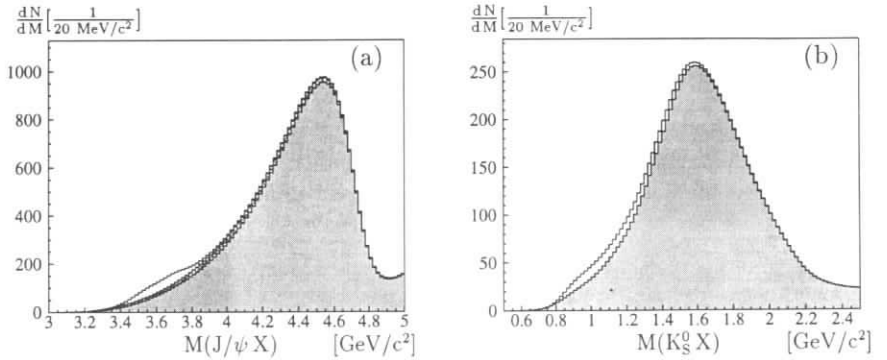

Figure 3: *Invariant mass distribution of* $J/\psi\,X$ (a) *and* $K^0_S X$ (b) *expected after one year of operation of HERA-B. The open histogram represents the contribution of the signal. The hatched histogram* (a) *represents the contribution of the background with negative* $\mathcal{CP}$ *parity. Gray histogram represents contribution of background of B decays which do not lead to a* $\mathcal{CP}$ *eigenstate. In the case of* $K^0_S X$ *mass the background from* $\mathcal{CP}$ *eigenstates is strongly suppressed by the cut on* $\cos\theta_{K^{*0}}$.

$B^0 \to \psi' K^0_S \to (J/\psi X^0)K^0_S$ channels is $\delta\sin 2\beta \sim 0.5$, using $B^0 \to J/\psi K^{*0} \to J/\psi(K^0_S\pi^0)$ channel – $\delta\sin 2\beta \sim 0.6$ (the $J/\psi K^0_S$ mode is used for normalization - $\delta\sin 2\beta = 0.13$ for about 1400 signal events without a background; the event numbers and background conditions for the decays under analysis are taken into account). The error of background subtraction is not included here. The values of errors depend strongly on the accuracy in the measurement of vertex coordinates. 10% improvement in vertex resolution gives 5% improvement in $\delta\sin 2\beta$.

The simulation can be checked with data sample. We expect about 800 fully reconstructed $B^+ \to \psi' K^+ \to (J/\psi\pi^+\pi^-)K^+$ decays per year, 3000 $B^0 \to J/\psi K^+\pi^-$ decays and 3000

$B^+ \to J/\psi K^+\pi^+\pi^-$ decays. Comparison of partially reconstructed events $B^0 \to \psi' K^0_S$ followed by $\psi' \to J/\psi\pi^+\pi^-$ with full reconstruction allows the determination of the systematic errors coming from the method described. Thus after normalization of any decay under study to the $\psi' \to J/\psi X$ the systematic errors due to method uncertainties mainly cancel. The shape, normalization and efficiency are determined directly from the data.

4 Summary

The accuracy in $\sin 2\beta$ using combined $B^0 \to \chi_{c1} K^0_S \to (J/\psi\gamma)K^0_S$ and $B^0 \to \psi' K^0_S \to (J/\psi X^0)K^0_S$ channels is $\delta \sin 2\beta \sim 0.5$, and using $B^0 \to J/\psi K^{*0} \to J/\psi(K^0_S\pi^0)$ channel is $\delta \sin 2\beta \sim 0.6$. The latter channel is especially important, since it is predicted to carry $\mathcal{CP}$ parity opposite in sign to that of "gold-plated" $J/\psi K^0_S$ mode and possible systematic biases can be revealed. About 10% effective enhancement of $J/\psi K^0_S$ mode statistics can be expected. The errors can be reduced by the improvements in vertex resolution.

The statistics of all three additional channels can be combined and then the error is $\delta \sin 2\beta \sim 0.4$. Since $\sin 2\beta$ is expected to be about 0.6, an independent measurement of $\mathcal{CP}$ violation with these modes seems to be possible after 4 years of HERA-B operation.

References

[1] T.Lohse *et al.*, (HERA-*B* Collaboration), *An Experiment to Study $\mathcal{CP}$ Violation in the B System Using an Internal Target at the HERA Proton Ring*, Proposal, **DESY-PRC 94/02**, (1994).

[2] E.Hartouni *et al.*, (HERA-*B* Collaboration), *An Experiment to Study $\mathcal{CP}$ Violation in the B System Using an Internal Target at the HERA Proton Ring*, Design Report, **DESY-PRC 95/01**, (1995).

[3] H. Albrecht *et al.*, (ARGUS Collaboration), Phys. Lett. **B 340** (1994) 217;
K.E. Ohl (CDF Collaboration), FNAL preprint **FERMILAB-CONF-94/127-E**;
M.S. Alam *et al.*, (CLEO Collaboration), Phys. Rev. **D50** (1994) 43.

[4] R. Mizyuk, ITEP preprint **96-17**.

[5] T.S. Sjöstrand, **CERN-TH-6488-92** (1992).

[6] B. Anderson, G. Gustafson and Hong Pi, Z. Phys. **C57** (1993) 485.

[7] Particle Data Group: Review of Particle Properties, Phys. Rev. **D50** (1994);
R. Balest *et al.*, (CLEO Collaboration), Phys. Rev. **D52** (1995) 2661.

Pion tag of B meson flavour at HERA-B

C.H.Shepherd-Themistocleous[a]

[a] Deutsches Elektronen-Synchrotron DESY, Notkestrasse 85, D-22603 Hamburg, FRG

Abstract: The high rate of P–wave B mesons, recently measured at LEP, enables their use for tagging the flavour of neutral B mesons at HERA–B. A tagging power of 0.21 is found. This power is comparable to that of the conventional techniques.

1 Introduction

The study of $\mathcal{CP}$ violation at HERA-B requires the tagging of the initial flavour of a neutral B meson. It has been suggested that pions produced in b fragmentation may provide such a tag [1]. This type of tag has the advantage that no information from the $\overline{B}$ hadron containing the associated b quark is required. The presence of narrow resonant states of b and light quarks decaying into $B^0\pi$ would enhance the performance of such a tagging method. A further advantage is that good particle identification, as in the case of the kaon tag, is not a requirement for this tag.

Recent results from LEP [2] experiments have demonstrated the existence of, at least, the two predicted narrow P-wave B resonances[1]. It has also been established that pions both from B^{**} resonances and those that do not come from the decay of a B^{**} (refered to as non-resonant pions here) provide useful flavour tags. When a B^0 meson, which contains a d quark, is formed it implies that a $\overline{d}$ will exist nearby in phase space. If this $\overline{d}$ gives rise to a pion then it can only be a π^+ or a π^0. These are the pions that can provide a flavour tag when no B^{**} resonance exists in the event.

2 Modelling

A Monte Carlo simulation that does not include any detector simulation[2] was used. In a comparison of generator level simulation and OPAL data it was found that the purity and efficiency of the tags agreed very well. This implies that the physics and not detector effects are of paramount importance and therefore the use of a generator level simulation for this study at HERA-B is probably reasonable.

[1] a general P-wave B resonance is denoted B^{**} here

[2] Refered to as generator level simulation hereafter.

To retain any correlation there might be between pion charge and B flavour in the case where the B meson has not come from a B** only the PYTHIA 5.7 generator was used.[3] The mean multiplicity for a Bπ invariant mass is 2.0 for PYTHIA alone and 2.4 for PYTHIA+FRITIOF.

The parameters used for the P-wave B mesons are given in the table below. They are essentially taken from reference [3]

B**	Mass (GeV)	Width (MeV)	Decay mode
B_2^+ $P_2(3/2)$	5.77	24	$B^{(*)}\pi^+$; $(B^{(*)}\pi^+\pi^0)$[4]
B_1 $P_1(3/2)$	5.76	20	$B^*\pi^+$
B_1^* $P_1(1/2)$	5.67	100	$B^*\pi^+$
B_0^* $P_0(1/2)$	5.67	100	$B\pi^+$

[4]Branching fraction 30%.

There are no experimental measurements of the fractions of the different B** that are produced. The extremes of equal fractions and fractions proportional to 2J+1 (where J is the spin of the B meson) are considered. The purities and efficiencies are not found to be strong functions of B** species therefore the particular choice for this study is not very important.

3 Pion Tags

In all of the following only pions known to have come from the primary vertex are considered. Various kinematic variables were examined. Some of the more successful tagging variables are listed here. The tagging pion was chosen to be the one with the

- maximum cosine of the helicity angle (cosα). That is the angle between the Bπ direction in the laboratory frame and the pion direction in the Bπ centre of mass frame.
- maximum value of the π momentum projected along the B direction (P_ℓ).
- minimum value of the π momentum transverse to the B direction (P_t).
- minimum angle between the B and the π in the laboratory frame.
- value of the invariant mass closest to some particular value (X). The best choice of this value depends upon the masses of the B**, their decay modes and their relative fractions.

Monte Carlo simulation samples with and without P-wave B mesons were studied separately. The purities obtained using these various tags on event samples where all the events contain one particular B** are shown in table 2. The energy of the B in the event is always required to be greater than 40 GeV and pions are only considered if their energy is above 1 GeV.

As can be seen from the table when an invariant mass cut is applied there are no great differences between the tags shown (where the mass tag with the optimum value of X is considered) with the exception of the mass tag for B_1, which is somewhat better than the rest. When no invariant mass cut is applied the mass tag gives the best performance. It should

[3]The standard procedure for the HERA-B environment is to use PYTHIA to generate B hadrons; to keep these particles and then to generate the "rest" of the event with a beam momentum of the original minus that of the B hadrons using FRITIOF. Using this procedure however removes any correlation there might be between pion charge and B flavour in the case where the B meson has not come from a B**.

be noted however that the performance of this tag depends on the value of X used. Since mass measurements do not yet exist for the various P-wave B mesons the estimates of the purities given here may prove to be inaccurate. The performances of the alternative tags do not depend significantly on the actual masses of the B** and are therefore likely to be more reliable. If, for example, the differences between the masses of the B** are found to be larger than expected the performance of the mass tag will be degraded. A further caution with regard to the mass tag is that if the mass difference between the charged and neutral B** is large then simple use of $B^+\pi^-$ correlations to calibrate (or optimise) the performance of the tag for a particular value of X will be incorrect. Cuts in a variety of variables were investigated, but no improvement in the purity was found.

The branching ratio of b quarks to B** is only of the order of 30%. The performance of a pion tag in events that do not contain a B** is therefore important to the ultimate performance of a pion tag of B flavour. The performance of the various tags on Monte Carlo simulation samples that do not contain any P-wave B mesons is given is table 2. Since only the PYTHIA generator was used and no effects due to the interactions of pions with nuclear material are considered it is probable that the numbers presented here are better than can be expected in the data. The purities found for the various tags can again be seen to be similar but are quite low. It is likely therefore that non-resonant pions will not provide a very useful tag at HERA-B. There may still however be a small effect due to the average number of pions with the correct sign being slightly larger than the average number with the wrong sign. This effect is a consequence of the fact that the light quark partner of the one that was used in forming the B meson will combine with another quark and if this forms a charged pion it will have the correct tagging sign. All other fragmentation pion production will be charge symmetric. All pions in an event are considered so that if a B^0 $\overline{B^0}$ pair is produced the two tagging pions in the event are of opposite charge. If however the other B meson produced is a charged one then the two tagging pions will be of the same charge. This then is the origin of the average number of pions with the correct tagging sign being greater than the average number with the wrong sign.

4 Tagging Powers

The tag quality is characterised by two quantities: the dilution factor D, which determines the observed asymmetry, given the actual one: $A_{CP}^{obs} = D \times A_{CP}$, and the tagging power P, to which the error of the asymmetry measurement is inversely proportional: $\sigma_{A_{CP}} = 1/(P \times \sqrt{N_{B^0}})$. The tagging power is given by $D \times \sqrt{(\text{efficiency})}$. The results are quoted in terms of purity where $D = 2(\text{purity}) - 1 \equiv 1 - 2(\text{mistag fraction})$.

The average of the LEP experimental values gives a fraction of B^0 from B** of $29 \pm 4\%$. A value of 30% is used for the results quoted here. Using a mass cut of $M_{B\pi} < 5.8$ gives a tagging power of 0.18 for the cosα tag and 0.19 for the mass tag. Removing the mass cut improves the tagging power of the mass tag to 0.21. This is because the purity stays almost constant whilest the efficiency increases. The tagging power of the cosα tag decreases to 0.12 when the mass cut is removed. A pion tag is likely therefore to be at least as good as the lepton tag reported on in the HERA-B proposal [4] and possibly better.

Assuming isospin invariance this tag can be studied in data using charged Bπ correlations to determine the best tagging variable and to determine the the efficiency and purity. Given a

B^{**}	Tagging Variable										
	cosα		$\lvert M_{B\pi} - X \rvert$					P_ℓ		$\theta_{B\pi}$	
		$M_{B\pi}$<5.8		$M_{B\pi}$<5.8					$M_{B\pi}$<5.8		$M_{B\pi}$<5.8
			X=5.72	X=5.72	X=5.70	X=5.68	X=5.66				
B_2^*	0.56	0.68	0.68	0.70	0.66	0.64	0.63	0.54	0.69	0.57	0.67
B_1	0.55	0.65	0.76	0.78	0.75	0.71	0.66	0.53	0.68	0.55	0.63
B_1^*	0.57	0.68	0.66	0.68	0.68	0.69	0.71	0.54	0.68	0.58	0.67
B_0^*	0.56	0.68	0.69	0.71	0.70	0.71	0.72	0.54	0.70	0.57	0.67

Table 1: Values of purities for pion tags for B flavour where the B comes from a B^{**}. The efficiencies are 99% for no mass cut and 90% for an invariant mass cut of $M_{B\pi}< 5.8$. The B energy is required to be above 40 GeV and only pions with an energy above 1 GeV are considered.

Tagging Variable	Purity	
		$M_{B\pi}< 5.8$
cosα	0.55	0.55
P_ℓ	0.56	0.55
$\theta_{B\pi}$	0.56	0.56
$\lvert M_{B\pi} - X \rvert$		
$X = 5.65$	0.57	0.56
$X = 5.70$	0.57	0.56
$X = 5.75$	0.55	0.56

Table 2: Values of purities for pion tags of B flavour where the B does not come from a B^{**}. The efficiency is 97% for no mass cut and 74% for an invariant mass cut of $M_{B\pi}< 5.8$. The B energy is required to be above 40 GeV and only pions with an energy above 1 GeV are considered.

good determination of B^0 mixing, the decay $B^0 \to J/\psi K^*$, where the flavour of the decaying B^0 can be determined from the K^* decay, provides a good channel in which to study tagging because of its similarity to the $J/\psi K_S^0$ channel. The difficulties of simulating the behaviour of the non-resonant pion tag would be overcome in this way.

It may be possible to improve this type of tag by combining some of the tagging variables mentioned. The correlations of the various tagging variables mentioned were investigated [5] and all tags were found to be quite highly correlated. The least correlated tags appear to be the angular ($\theta_{B\pi}$) tag and the mass ($M_{B\pi}$) tag. A simple combination of these results does not however provide an improvement of the tag. The use of a neural net which could be trained on the data, by using charged $B\pi$ correlations may help.

5 Conclusion

The observation of P-wave mesons at LEP [2] has suggested that using pion charge to tag the flavour of neutral B mesons is possible.[5] Using a simple generator level Monte Carlo simulation of HERA-B conditions has suggested that this type of tag will work reasonably well and be at least as good a the lepton tag described in the HERA-B proposal. This tag also does not use information from the other B in the event and is therefore complimentary to the three tags discussed in the proposal.

[5] In a recent conference contribution [6] CDF reports on their observation of B-π flavour charge correlations.

References

[1] M. Gronau, A. Nippe, and J. L. Rosner, Phys. Rev. **D 47**, (1993) 1988.

[2] OPAL Collaboration, R. Akers et al., Z. Phys **C66** (1995) 19.
Delphi Collaboration P. Abreu et al., Phys. Lett. **B345** (1995) 598.
Aleph Collaboration, D. Buskulic et al., Zeit. Phys.**C69** (1996) 393.
Aleph Collaboration, D. Buskulic et al., Resonant Structure and Flavor-tagging in the $B\pi$ System Using Fully Reconstructed B Decays. Contribution of International Conference on High Energy Physics, Brussels, Belgium. 27 July - 2 August, 1995.

[3] E. J. Eichten, C. T. Hill, and C. Quigg, Phys. Rev. Lett. **71** (1993) 4116.

[4] T.Lohse et al., (HERA–B Collaboration), *An Experiment to Study CP Violation in the B System Using an Internal Target at the HERA Proton Ring*, Proposal, **DESY-PRC 94/02** (1994);

[5] C.H. Shepherd-Themistocleous, HERA-B 96-109, Hera-b internal note. *A study of the feasibility of a pion tag of B meson flavour at HERA-B.*

[6] Observation of $\pi - B$ meson Charge-flavor Correlations and Measurement of Time Dependent $B^0\overline{B}^0$ Mixing in $p\bar{p}$ Collisions. Paper contributed to ICHEP96 conference, Warsaw, Poland. ICHEP96/pa08-032.

Low p_t lepton tag at the HERA-B experiment

R. Mizuk [1]

Inst. of Theoretical and Experimental Physics, B. Cheremushk. 25, 127259 Moscow, Russia

Abstract: The low p_t lepton tag is proposed for the HERA-B experiment. The tagging efficiency, dilution and the statistical power are expected to be 14%,0.21 and 0.08 correspondingly.

To measure mixing-induced $\mathcal{CP}$ asymmetries in B mesons, the initial flavor of the neutral B meson under study has to be determined. Several tagging techniques are expected to be used in the HERA-B experiment: high p_t lepton tag, charged kaon tag, secondary vertex charge tag [1, 2, 3] and tag with B** decays [4]. The idea of the soft "wrong-sign" (with respect to the sign of primary leptons from B-decays) lepton tag of the B meson flavor belongs to BaBar Collaboration [5] and can also be effectively used in the HERA-B experiment. The transverse momentum spectrum of the "wrong-sign" leptons (mainly cascade leptons from $\bar{b} \to \bar{c} \to \ell^- \nu X$ decay chain) and the "right-sign" leptons (mainly from $\bar{b} \to \ell^+ \nu X$) taking into account the mixing of the b-hadrons which accompany the neutral B meson to be tagged are shown in Figure 1(a). The significant excess of the "wrong-sign" leptons over the "right-sign" leptons in the low transverse momentum region can be effectively used as a tool for B flavour tagging.

The estimation of the characteristics of the low p_t lepton tag was performed at the level of Monte Carlo event generators. The `PYTHIA 5.6` [6] and `FRITIOF 7.0` [7] generators were combined [1] to generate events with $b\bar{b}$ pairs. The momentum of the tagging candidate was required to exceed 5 GeV/c, which is close to the minimal momentum where the reliable lepton identification at HERA-B is possible. The transverse momentum of the candidates was deemed to be less than 0.5 GeV/c.

The numbers of lepton and hadron tag candidates satisfying these requirements per event are listed in Table 1. The corresponding momentum spectra are shown in Figure 1(b).

For the estimation of the total misidentification probability for hadrons to be detected as leptons the information from Muon system [8], Electromagnetic Calorimeter (ECAL) and Ring Imaging Čerenkov Counter (RICH) can be used (see Figure 2). The μ-π, e-π, e-K and μ-K separation capabilities with the aid of the RICH Detector were recalculated from the π-K separation studied in detail in [2]. The results of the Neural Network Analysis of ECAL information were used. The misidentification probabilities were convoluted with the hadron momentum spectra to obtain the numbers of fake leptons (see Table 2).

Particles from the main vertex will be additionally suppressed by the vertex cut. Three values of the suppression factor α have been considered in this work: 1.0, 0.5 and 0.1. The statistical powers for low p_t μ-tag and low p_t e-tag are correspondingly $P_\mu = \{0.060,\ 0.064,\ 0.067\}$ and $P_e = \{0.047,\ 0.051,\ 0.056\}$. Since the e and μ tagging efficiencies are small, the combined statistical power can be estimated as $P_{\mu+e} = \{0.075,\ 0.080,\ 0.087\}$. The characteristics of the low p_t and high p_t lepton tags are compared in Table 3. Also, neglecting the probability to have in the event both the high p_t and low p_t lepton tags, the combined statistical power can be roughly estimated to be 0.19. This is equivalent (taking into account the difference in the dilution factors) to the effective enhancement of the high p_t lepton tag statistics by about 22%.

In summary, the low p_t lepton tag was proposed for the HERA-B experiment and its characteristics were estimated. The statistical power was found to be 0.08.

[1] Partially supported by INTAS Foundation with grant 94-3819

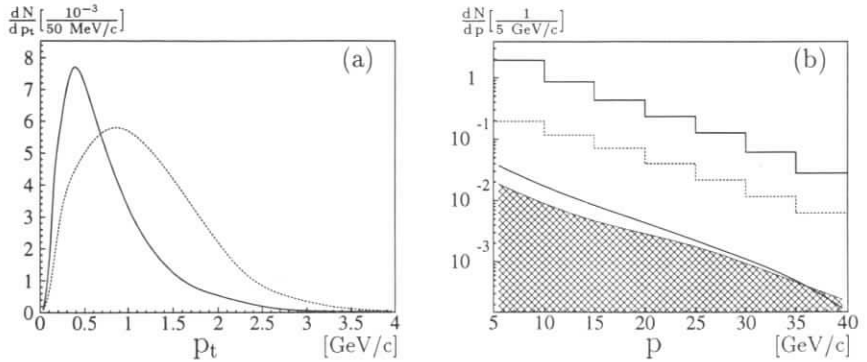

Figure 1: (a) *The transverse momentum spectra of "wrong-sign" (solid line) and "right-sign" (dashed line) leptons* ($p > 5$ GeV/c). (b) *The momentum spectra of pions (solid histogram), kaons (dashed histogram), "wrong-sign" (solid line) and "right-sign" (hatched area) leptons* ($p_t < 0.5$ GeV/c). *The normalization corresponds to one* $B^0 \to J/\psi K^0_S$ *decay to be tagged. Regarded are tracks in the geometrical acceptance only.*

Table 1: *The numbers of lepton and hadron tag candidates per event. "−" stands for the "wrong-sign" and "+" stands for the "right-sign" leptons. Main vertex* (MVx) *is a* B *production vertex and tracks from secondary vertices* (SVx) *are the tracks which can not be assigned to the main vertex, placed on the target wire.*

	μ			e			π		K	
	SVx		MVx	SVx		MVx	SVx	MVx	SVx	MVx
	−	+		−	+					
production	0.11	0.13	-	0.16	0.18	0.17	5.0	12.0	0.73	1.1
acceptance	0.10	0.12	-	0.14	0.15	0.10	4.1	7.0	0.62	0.75
$p > 5$ GeV/c	0.074	0.10	-	0.083	0.11	0.016	2.6	3.8	0.58	0.51
$p_t < 0.5$ GeV/c	0.028	0.013	-	0.032	0.018	0.013	1.4	2.3	0.21	0.25

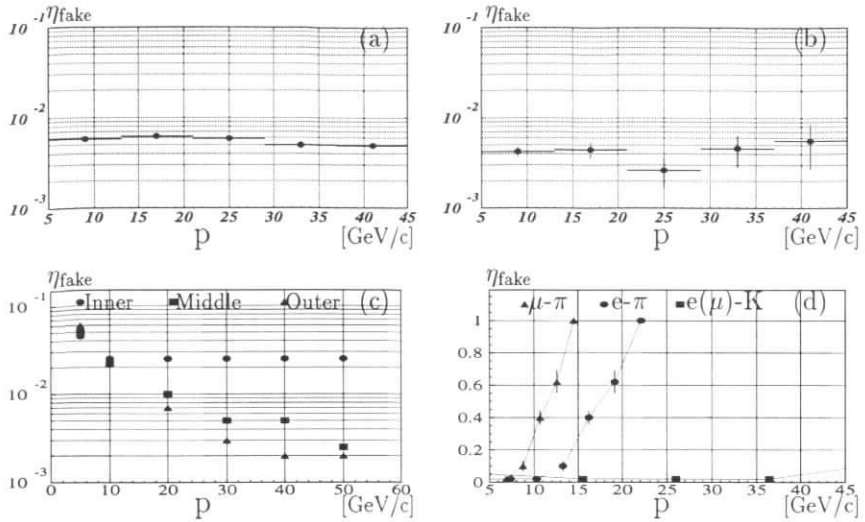

Figure 2: *The total (sum of the punch-through and decays-in-flight) fake rate of* μ-π (a) *and* μ-K (b) *separation with Muon System and Tracker.* (c) *The fake rates for* e-*hadron separation with ECAL: Inner, Middle and Outer parts.* (d) *The fake rates for* μ-π, e-π, e-K *and* μ-K *separation with RICH. The lepton identification efficiency is as high as 95%.*

Table 2: *The numbers of tagging fake leptons per event.*

	SVx	MVx
μ-π	$7.7 \cdot 10^{-3}$	$12.7 \cdot 10^{-3}$
μ-K	$1.5 \cdot 10^{-4}$	$1.8 \cdot 10^{-4}$
e-π	$9.9 \cdot 10^{-3}$	$16.3 \cdot 10^{-3}$

Table 3: *Tagging efficiency, dilution factor and statistical power for low* p_t *lepton tag* ($\alpha = 0.5$) *and for high* p_t *lepton tag.*

	ε [%]	D	P
Low p_t leptons ($\alpha = 0.5$)	14	0.21	0.08
High p_t leptons	16	0.43	0.17

References

[1] H. Albrecht *et al.*, (HERA-*B* Collaboration), *An Experiment to Study* $\mathcal{CP}$ *Violation in the* B *System Using an Internal Target at the HERA Proton Ring*, Letter of Intent, **DESY-PRC 92/04** (1992).

[2] T.Lohse *et al.*, (HERA-*B* Collaboration), *An Experiment to Study* $\mathcal{CP}$ *Violation in the* B *System Using an Internal Target at the HERA Proton Ring*, Proposal, **DESY-PRC 94/02** (1994).

[3] E. Hartouni *et al.*, (HERA-*B* Collaboration), *An Experiment to Study* $\mathcal{CP}$ *Violation in the* B *System Using an Internal Target at the HERA Proton Ring*, Design Report, **DESY-PRC 95/01** (1995).

[4] R. Kagan and C.H. Shepherd-Themistocleuos, B-*flavor tagging with* B** *decays*, Contribution to the International Workshop "Future Physics at HERA",DESY (1995-1996).

[5] D. Boutigny *et al.*, (BaBar Collaboration), *Letter of Intent for the Study of* $\mathcal{CP}$ *Violation and Heavy Flavor Physics at PEP-II*, **SLAC-0443** (1994).

[6] H.-U. Bengtsson and T.S. Sjöstrand, *The Lund Monte Carlo for Hadronic Processes:* `PYTHIA` *Version* 4.8, Computer Physics Commun. **46** (1987) 43;
T.S. Sjöstrand, `PYTHIA 5.6` *and* `JETSET 7.3`: *Physics and Manual*, **CERN-TH-6488-92** (1992).

[7] B. Anderson, G. Gustafson and Hong Pi, *The* `FRITIOF` *Model for Very High-Energy Hadronic Collisions*, Z. Phys. **C57** (1993) 485.

[8] M. Titov, *Muon Identification and Background Studies at the HERA-B Experiment*, ITEP 1996-24.

Trigger for Radiative B Decays at the HERA-B experiment.

F. Saadi-Lüdemann.

Deutsches Elektronen-Synchrotron DESY,Notkestrasse 85, D-22603 Hamburg.

Abstract: We have studied the possibility to extend the HERA-B trigger to accept events of type $B \longrightarrow X\gamma$. An interesting aspect of the measurement of the radiative B decays branching fractions is the extraction of the ratio $|V_{td}|/|V_{ts}|$ which gives a constraint on one side of the unitarity triangle. This trigger will also allow to search for B_s and Λ_b radiative decays.

1 Introduction

The evidence for Penguin decays (Figure. 1) has been seen by the CLEO collaboration [1]. They have observed the decays $B^0 \to K^*(892)\gamma$ and $B^- \to K^*(892)^-\gamma$ in a data sample of $1.39 \cdot 10^6\, B\bar{B}$ events with an average branching ratio of $(4.5 \pm 1.5 \pm 0.9) \cdot 10^{-5}$. With the additional measurement of the decay $B^0 \to \rho^0\gamma$ one can extract the ratio $|V_{td}|/|V_{ts}|$ [2] providing a constraint on the unitarity triangle [3] and allowing precision tests of the Standard Model. This ratio is also given by the measurement of the mixing parameters x_d and x_s. But if x_s is too high its measurement within HERA-B will be technically limited by the vertex detector resolution.

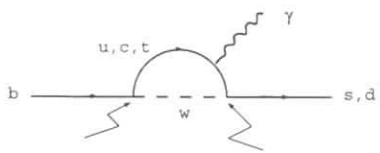

Figure 1: *Penguin diagram*

In HERA-B we expect a production of more than 10^8 $b\bar{b}$ pairs/year and hence thousands of radiative B decays. Some of the predicted radiative B decay modes which can be reconstructed in HERA-B are summarized in Table 1 where we show the theoretical predictions for the corresponding branching ratios [4] and the number of produced events per year. The decays $B_s \to \phi\gamma$ (which can be reconstructed in the decay mode $\phi \to K^+K^-$) and $\Lambda_b \to \Lambda\gamma$ are

Decay modes	BR	Decays/year
$B_d \to K^*\gamma$	$(4.5 \pm 1.75) \cdot 10^{-5}$	14500
$B_d \to X_s\gamma$	$(3.2 \pm 0.58) \cdot 10^{-4}$	103000
$B_d \to \rho^0\gamma$	$(0.85 \pm 0.6) \cdot 10^{-6}$	270
$B_d \to X_d\gamma$	$(1.0 \pm 0.8) \cdot 10^{-5}$	3220
$B_s \to \phi\gamma$	$(4.8 \pm 1.5) \cdot 10^{-5}$	2850
$\Lambda_b \to \Lambda\gamma$	$(3.8 \pm 1.5) \cdot 10^{-5}$	1040

Table 1: *Theoretical branching ratios [4] and expected produced radiative B decays assuming* $3.7 \cdot 10^8$ *produced* $b\bar{b}$ *pairs/year and the production probabilities* $\overset{(-)}{B}_d : \overset{(-)}{B}_s : \overset{(-)}{\Lambda}_b = 0.87{:}0.16{:}0.074$ *(the probabilities include a factor 2 due to pair production). Note that for* $B^0 \to K^*(892)\gamma$ *the experimentally measured branching ratio is used.*

very interesting to measure in HERA-B since they can not be measured by e^+e^- B factories at $\Upsilon(4S)$.

The originally proposed HERA-B first level trigger system based on charged track finding is very selective and does not accept this kind of events. In this paper we will present an extension of the first level trigger with a reasonable signal efficiency and a low background rate. This study is based on the channel $B^0 \to K^*(892)\gamma$ where $K^{*0} \to K^+\pi^-$.

2 Signatures of the decay $B^0 \to K^*(892)\gamma$

Due to the high background interaction rate in the HERA-B environment ($\sigma_{b\bar{b}}/\sigma_{inel} \approx 10^{-6}$) the first level trigger system has to reject background events by a factor better than 200 while keeping the signal efficiency high. To achieve such high background rejection one need a very good signature for the signal.

In this section we will look for such a signature for the decay chain $B^0 \to \gamma K^{*0}(892) \to K^+\pi^-$ using Monte Carlo events without detector simulation. HERA-B Monte Carlo event generation is based on PYTHIA for heavy flavor production and FRITIOF for nuclear interactions. The pN interaction center of mass energy is 40 GeV. One event is a mixture of several single pN interactions. The number of interactions n_i per event is generated according to a Poisson distribution with $n_i = 5$ as mean value.

Fig. 2 shows momentum and transverse momentum distributions of photons from radiative B decays and photons from background events. The transverse momentum $P_\perp$ [1] of photons from B's is in average large and this fact represents a good signature. Also the decay products of K^* carry a valuable information in their transverse momentum.

3 Hard photon trigger

We will briefly describe the general concept of the First Level Trigger FLT of the HERA-B experiment (for details see [5] [6]). The basic task of the HERA-B first level trigger is to

[1] In this note $P_\perp$ is defined with respect to the beam axis.

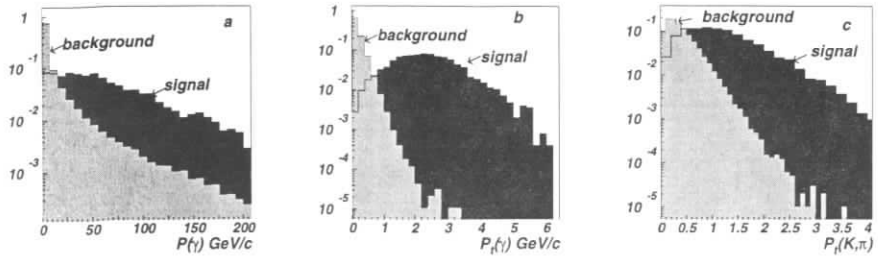

Figure 2: *a)Momentum and b) transverse momentum distributions for photons from* $B^0 \to K^*(892)\gamma$ *and from background. c)Transverse momentum of decay products of the* K^* *and charged tracks from background. The plots are drawn at arbitrary scale.*

accept events with lepton pairs (e^+e^-, $\mu^+\mu^-$) that originate from the decay of a J/ψ meson and events with charged hadrons pairs that originate from a B meson decay. In addition it should allow triggers based on any combination of leptons and charged hardrons with given type, charge, momentum, transverse momentum and mass. Thus the original FLT design does not accept photons. To trigger on photons we will use the electromagnetic calorimeter (ECAL) pretrigger. The photon clusters fortunately satisfy the electron pretrigger thresholds. The new high $P_\perp$threshold and a flag for photon triggers are implemented in the ECAL pretrigger processors. The second step is to allow the photon candidates to pass all the track finding steps without requiring found hits. This condition is implemented in the redesigned FLT processors. The hard photon trigger is combined with the high $P_\perp$hadron trigger (see [5]) used to trigger on the K^* decay products.

4 FLT simulation and results

Using a full Geant simulation of the HERA-B detector and the FLT simulation software L1SIMU, we generated 10000 background events and 3000 signal events. Each signal event involves one decay $B^0 \to K^*\gamma$. Figure 3 presents the efficiencies and the rejection factor as a function of the $P_\perp$ cut.

The rejection factor using only the photon information i.e. requiring an ECAL cluster with $E_\perp > 3.0\,GeV/c$ is better than 300 but it is not a sufficient requirement which can be used by the higher level triggers to reject further background. Hence we have used the High $P_\perp$trigger as additional requirement. The high $P_\perp$trigger efficiency is shown in Figure 3.

Requiring a photon with $P_\perp > 3.GeV/c$ and a high $P_\perp$track with $P_\perp > 1.5\,GeV/c$, the FLT efficiency for $B^0 \to K^*(892)\gamma$ is 10% and the background rejection factor is better than 500. It is possible to increase the rejection factor requiring neutral clusters (i.e. no track is matched to the ECAL photon pretrigger). But to keep the FLT efficiency as high as possible, this requirement can be used together with a refit of the high $P_\perp$tracks and cuts on their impact parameters in the higher level triggers.

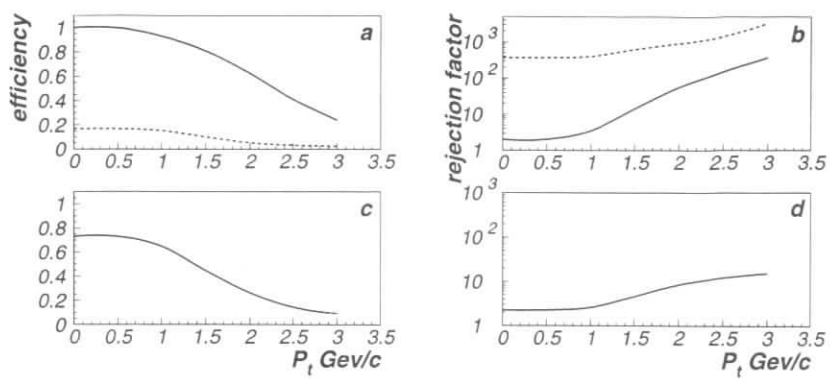

Figure 3: *FLT signal efficiency and background rejection factor as functions of transverse momentum cut: a-b) solid line: cut on* $P_\perp$ *of photon, dashed line: cut on* $P_\perp$ *of the photon and at least one high* $P_\perp$ *track, c-d) cut on high* $P_\perp$ *trigger tracks only.*

5 Semileptonic FCNC B-decays $B \to Xl^+l^-$

The semileptonic FCNC B-decays $B \to Xl^+l^-$ are of great interest for precision tests of the SM and may probe physics beyond the SM as discussed in [4] [7]. The forward backward asymmetry of the dileptons in their center of mass system as calculated in [4] is proportional only to the Z and W^+W^- exchange diagrams. Thus this observable is sensitive to any enhancement due to non standard effect. Experimentally the measurement of the short distance contribution is interesting if we are in a regime where the dilepton invariant mass is far below the J/ψ and ψ' resonances. For the HERA-B experiment the most critical step is to accept this kind of events at the first level trigger. The actual lower cut on the dilepton invariant mass is 2.75 GeV/c^2. Hence the mass window for the measurement of the decays $B \to Xl^+l^-$ below the J/ψ mass is quite tight and the expected reconstruction efficiency of these channels is lower than 2%. With the expected branching fractions $Br(B \to X_s e^+e^-) = (8.4 \pm 2.2) \cdot 10^{-6}$ and $Br(B \to X_s\mu^+\mu^-) = (5.7 \pm 1.3) \cdot 10^{-6}$ [4] and after collecting a few 10^9 B mesons the detection of the discussed channels could be possible with few tens of events. Since the HERA-B trigger is flexible one will investigate the possibility to increase the trigger efficiency of these channels based on high $P_\perp$mixed tracks trigger.

6 Conclusion

We have extended the HERA-B First Level Trigger scheme to accept radiative B decay events. The achieved FLT efficiency is better than 10% for the studied channel $B^0 \to K^*(892)\gamma$ and behaves accordingly for similar radiative B decays. Assuming $3.7 \cdot 10^8$ produced $b\bar{b}$ pairs/year,

we expect about 1000 events/year of the studied channel passing the FLT trigger and about 100 events after full reconstruction. This redesigned trigger enriches the HERA-B physics program by opening the possibility to extract the ratio $|V_{td}|/|V_{ts}|$ via the measurement of $\mathrm{Br}(B \to K^*\gamma)$ and $\mathrm{Br}(B \to \rho\gamma)$ which provides a constraint on the unitarity triangle. It will also allow to search for observation of B_s and Λ_b radiative decays.

References

[1] R. Ammar et al. Phys. Rev. Lett. **71**, 674 (1993).

[2] A. Ali and D. London, CP Violation and Flavour Mixing in the Standard Model- 1996 Update **DESY 96-140**.

[3] A. Ali and D. London, these proceedings, Figure 1.

[4] A. Ali, *B* Decays, Flavour Mixing and CP Violation in the Standard Model **DESY 96-106**.

[5] H. Albrecht et al., (HERA-B collaboration), *An Experiment to Study CP Violation in the B System Using an Internal Target at the Hera Proton Ring*, **DESY-PRC 95/01**

[6] H. D. Schulz, Nucl. Phys. **B** (Proc. Suppl.) 44(1995) 441-447

[7] A. Ali, Rare *B* Decays in the Standard Model, these proceedings.

Accuracy of B^0-$\bar{B}^0$ mixing and B^0 lifetime measurements at Hera-*B*

Peter Kreuzer

University of California, Los Angeles, USA

Abstract

This article presents an estimate of the expected accuracy Hera-*B* should reach in the measurement of time-dependent oscillations of neutral B^0 mesons. The full reconstruction of about 3700 $B^0 \to J/\psi K^{*0} \to l^+l^-K\pi$ events per year, together with lepton, kaon and charge tagging should allow the determination of Δm_d with a relative error of about 4.0% after two Hera-*B* running years. A similar estimate for the B^0 meson lifetime measurement accuracy yields a relative error on the B^0 proper lifetime of about 1.5%. Both results will improve the existing world averages.

1 Introduction

The accurate determination of Standard Model parameters is presently one of the main issues in high energy physics. The mixing factor Δm_d which characterizes B^0 oscillations is coupled to the CKM-parameter $|V_{td}|^2$. Hence the accuracy of $|V_{td}|$ is related to the error of a Δm_d measurement. The most sensitive measurements of Δm_d are obtained through time dependent studies. If one neglects the effects of CP non-conservation and the decay rate difference $\Delta\Gamma_d$ between the "long-lived" and "short-lived" B^0 under study, the probabilities for a B^0 meson with a given initial flavor (B or $\bar{B}$)[1] to decay with the same flavor (unmixed) or to undergo mixing before it decays are given by the following distributions:

$$P_u(t) = \frac{\Gamma}{2} e^{-\Gamma t}\left[1 + \cos(\Delta m_d\, t)\right] \quad (1)$$

$$P_m(t) = \frac{\Gamma}{2} e^{-\Gamma t}\left[1 - \cos(\Delta m_d\, t)\right] \quad (2)$$

The $B^0 \to J/\psi K^{*0} \to l^+l^-K\pi$ decay mode is a good choice for mixing measurements at Hera-*B* because it can be triggered with the J/ψ-trigger used for the "golden channel" $B^0 \to J/\psi K_S \to l^+l^-\pi^+\pi^-$.

The time-dependent observation of B oscillations requires the determination of

(a) the proper time of the B meson decay

(b) the production (B or $\bar{B}$) and decay (B or $\bar{B}$) flavors of the B meson

If the B decays can be fully reconstructed, the effect of the energy (or momentum) resolution on the decay time resolution is negligible and the main contribution to the decay time resolution

[1] For convenience, B is now used for B^0 .

is the decay length resolution. At Hera-B , the vertex resolution in the silicon vertex detector should reach $\sigma_z \approx 500\mu m$ and the expected boost of the B meson is $\gamma\beta \approx 20$. Therefore, the decay time resolution can be computed as :

$$\frac{\sigma_t}{t} = \frac{\sigma_z}{\gamma\beta \cdot c\tau} = 5.5\,\% \tag{3}$$

This resolution will only have a little influence on the accuracy of a B^0 - $\bar{B}^0$ mixing measurement, because σ_t is very small compared to $\frac{1}{\Delta m_d}$.

The b flavour at the B decay is given by the reconstruction of the decay. The determination of the production flavor of the B meson requires flavor-tagging of the "second B" in the event. As tagging is never perfect, one has to account for dilution effects such as mixing of the tagging B, wrong charged particles or wrong tags due to particle misidentification. The tagging efficiencies from the Hera-B proposal [1] for lepton, kaon and charge tags are presented in Table 1.

Table 1: *Tagging efficiencies and dilution factors*

TAG	Lepton	Kaon	Charge
Efficiencies:			
ϵ (tag found)	16.1 %	46.0 %	96.4 %
ϵ_c (correct)	11.5 %	31.3 %	56.0 %
ϵ_w (wrong)	4.6 %	14.7 %	40.4 %
Dilution:			
$D = \frac{\epsilon_c - \epsilon_w}{\epsilon}$	0.43	0.36	0.16

The determination of Δm_d is achieved through the fit of a measured mixing assymetry function. The main factor affecting the statistical accuracy of Δm_d is the number of reconstructible B decays per Hera-B running year in a given channel. An estimate of this number for the $B^0 \to J/\psi\, K^{*0} \to l^+l^- K\pi$ channel is presented in section 2. In section 3, the simulation of the mixing analysis is described and the results on the estimated Δm_d accuracy are given. Finally, a similar estimate on the B^0 lifetime measurement accuracy is presented.

Similar measurements have been achieved at the various LEP experiments. However, none of them are based on fully reconstructed B events, which leads to a substantial increase of systematic errors from lifetimes and fractions of individual B hadron species, as well as from the parametrization of the b fragmentation function.

2 Signal-reconstruction efficiency

The only difference between the $B^0 \to J/\psi\, K^{*0} \to l^+l^- K\pi$ decay channel and the Hera-B "golden channel" is the $K^{*0} \to K\pi$ decay versus the $K_S \to \pi^+\pi^-$ decay. Therefore, all the trigger and reconstruction efficiencies [1] except the K^{*0} reconstruction efficiency are the same in the two channels[2]. A summary of all the factors used in the signal-reconstruction efficiency estimation is given in Table 2.

The K^{*0} reconstruction efficiency is estimated separately. It mainly depends on the kaon identification capability of the RICH detector. This is simulated using the momentum-dependent

[2]This is a conservative choice. One expects better B reconstruction efficiency in the $J/\psi\, K^{*0}$ channel, since the B forms a 4-track decay vertex.

Table 2: $B^0 \to J/\psi\, K^{*0} \to l^+l^- K\pi$ *reconstruction efficiency*

	$J/\psi \to \mu^+\mu^-$	$J/\psi \to e^+e^-$
Branching ratios	$5.056 \cdot 10^{-5}$	$5.056 \cdot 10^{-5}$
Trigger	0.637	0.325
Lepton tracking	0.837	0.757
K^{*0} **reconstruction**	0.540	0.540
J/ψ **and B reconstr.**	0.941	0.679
Decay kinematics	0.799	0.799
Secondary vertex	0.690	0.690
Overall efficiency	$\mathbf{7.552 \cdot 10^{-6}}$	$\mathbf{2.514 \cdot 10^{-6}}$

kaon detection efficiency curve [1] shown in Figure 1; the probability to identify a kaon with less than 35 GeV is set to 90% and for higher momenta it drops according to a Gaussian distribution. A 5% probability to misidentify a pion as a kaon is also assumed. The thresholds for pions (3.5 GeV), kaons (12.5 GeV) and protons (23.4 GeV) correspond to the lower bound of 20 detected photons. If a kaon doesn't make sufficient light, identification is made by excluding pions. The resulting overall kaon detection efficiency is $\epsilon_K = 72\,\%$. Considering geometrical acceptances for kaons and pions (88 % each) and a 10 % probability for kaons to decay before the RICH detector, one obtains a K^{*0} reconstruction efficiency of 54 %.

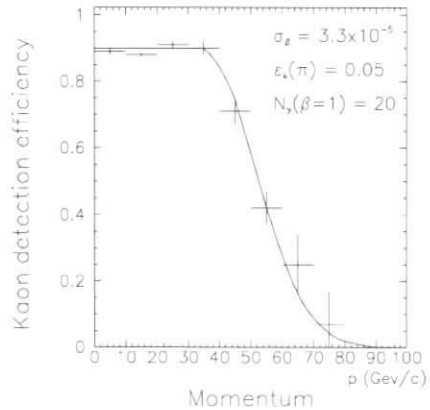

Figure 1: *Momentum dependence of the kaon detection efficiency for a fixed pion fake rate of* $\epsilon_K(\pi) = 5\,\%$. *The number of detected photons was set to the pessimistic case of 20. Above 35 GeV, the points where fitted with a Gaussian distribution.*

The number of estimated reconstructible B decays per year is extracted from Table 2;

the overall efficiency for the electron and muon channels together is $\epsilon_{RECO} = 9.948 \cdot 10^{-6}$. At Hera-$B$, one running year is expected to produce about $3.7 \cdot 10^8$ $b\bar{b}$ pairs, therefore the corresponding number of reconstructible $B^0 \to J/\psi\, K^{*0} \to l^+l^- K\pi$ decays is

$$N_{\mathrm{B}^0} \approx \mathbf{3700\ events/\ year}$$

3 Accuracy of a Δm_d measurement

This study is achieved using a fast Monte-Carlo simulation. For every decay, a decay time is generated and smeared with the resolution given in (3). The "candidate" is then mixed according to equations (1) and (2) and the tagging efficiencies from Table 1 are introduced. The proposed mixing asymmetry measurement for a given time-bin (t) is the difference between the number of mixed ($n_m(t)$) and unmixed ($n_u(t)$) "candidates" divided by the sum. Using equations (1) and (2) one can easily show that

$$A(t) = \frac{n_m(t) - n_u(t)}{n_m(t) + n_u(t)} = -\, D_T \cos(\Delta m_d\, t) \tag{4}$$

where D_T is the overall tagging dilution factor due to wrong tags[3]. The result of the simulation and the fit using A(t) are shown in Figure 2. The relative error on Δm_d extracted from the fit

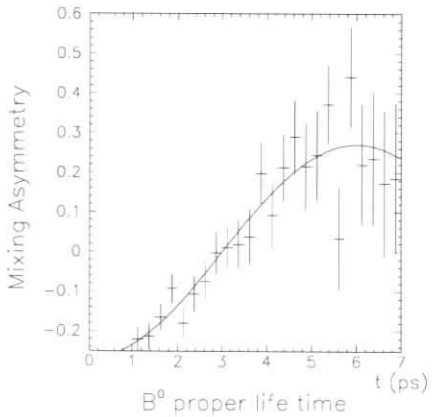

Figure 2: *Asymmetry distribution fitted with* $A(t) = -\, D_T \cos(\Delta m_d\, t)$ *for an input of 7400 events (2 Hera-B running years). The decay length cut corresponds to* $t_0 \geq (0.7) \cdot \tau_{B^0}$. *The extracted values from the fit are* $\Delta m_d = 0.5219\, ps^{-1}$ *and* $\delta(\Delta m_d) = 0.02081\, ps^{-1}$.

[3]The overall dilution factor D_T is a combination of dilution factors from the various taggs. Their individual contribution given in Table 1 is included in the Monte-Carlo simulation, but D_T is left as a free parameter in the fit to extract Δm_d.

for 1 Hera-B running year (3700 reconstructed B events) is

$$\frac{\delta(\Delta m_d)}{\Delta m_d} = \frac{0.02689}{0.5252} \approx \mathbf{5.5\,\%} \tag{5}$$

After two running years (7400 reconstructed B events), this relative error decreases to **4.0 %**. The actual world average [2] has a higher relative error ($\frac{\delta(\Delta m_d)}{\Delta m_d} \approx \frac{0.031}{0.474} = 6.5\,\%$).

It is important to note that no background effects have been included in the present simulation. Nevertheless, the expected capability of Hera-B to fully reconstruct B^0 decay's should limit the systematic errors compared to LEP results.

4 Accuracy of a B^0 lifetime measurement

The HQE model predicts small lifetime differences between charged and neutral B mesons: $\frac{\tau_{B^-}}{\tau_{B^0}} = 1 + 0.05 \cdot \frac{f_B^2}{(200MeV)^2}$. Precise lifetime measurements are necessary to check this model. In order to estimate how accurately Hera-B can measure the lifetime τ_{B^0} in the $B^0 \to J/\psi\, K^{*0} \to l^+l^- K\pi$ channel, a similar simulation to the mixing study is used. In this case, no tagging is required, and the lifetime is extracted from an exponential fit to the decay-time distribution (Figure 3). The obtained accuracy after two Hera-B running years is

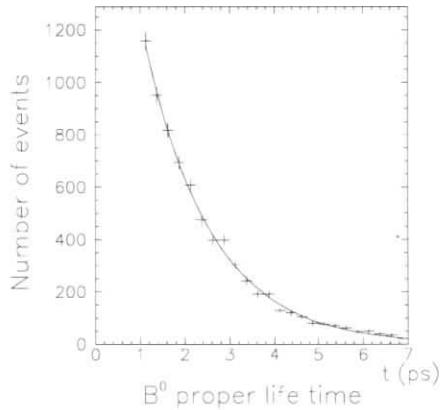

Figure 3: *Lifetime distribution fitted with an exponential for an input of 7400 events. The extracted values from the fit are* $\tau_{B^0} = 1.48522\, ps$ *and* $\delta(\tau_{B^0}) = 0.02246\, ps$.

$$\frac{\delta(\tau_{B^0})}{\tau_{B^0}} \approx \mathbf{1.5\,\%} \tag{6}$$

Again, no background effects have been included in this simulation. In comparison, the existing world average [2] on τ_{B^0} is given with an accuracy of ($\frac{\delta(\tau_{B^0})}{\tau_{B^0}} \approx \frac{0.06}{1.56} = 3.8\%$).

5 Conclusion

The simulation has shown that Hera-B will be able to measure accurately both Δm_d and τ_{B^0} (4.0% and 1.5% accuracy respectively after 2 running years) using the $B^0 \to J/\psi K^{*0} \to l^+l^- K\pi$ decay mode. The accuracy estimates indicate an improvement of the existing world averages. Mixing studies in additional channels like semi-leptonic decays could further enhance the statistics and therefore improve the measurement accuracy.

6 References

[1] The Hera-B collaboration, Proposal, DESY-PRC 94/02, May 1994;
[2] R.M. Barnett et al. (Particle Data Group), Phys. Rev. D54, 1 (1996).

On the Study of $B\bar{B}$ Correlations at HERA-B

R. Rylko[a]

[a] Department of Physics, Brunel, The University of West London, Uxbridge UB8 3PH, UK

Abstract: We analyze the possibility of studying the heavy flavour hadroproduction properties at the HERA-B experiment. In addition to the high statistics single inclusive B spectra measurements, the measurement of the $B\bar{B}$ meson correlations is considered. The techniques of momentum estimators, widely used in the charm sector, are demonstrated to be useful for the $B\bar{B}$ correlation studies at HERA-B. The kinematic limits for the precision of the momentum estimator within which the pair spectra can be measured are determined. The errors are weakly dependent on the topology of the multibody B meson decay.

1 Introduction

Although the flagship goal of the HERA-B experiment is to study the CP violation in the B system, there should be quite an interesting data sample available for studies of production properties of heavy hadrons. Here we report on a study of possibilities for measurements of various heavy hadron production properties with an emphasis on the measurements of the distribution of pairs. We concentrate on beauty hadrons, as the momentum estimators were already demonstrated to be a useful tool in the charm sector. First, we briefly review the existing experimental results on the fixed target hadroproduction of heavy hadron pairs (mostly for the charm sector) and we briefly discuss the momentum estimator techniques used. Next, we find the lower boundaries for the systematic errors for the distributions of pairs when the momentum estimator is used in the kinematic situation of HERA-B. This is illustrated for a typical B decay channel. The major systematic effect on the momentum estimator coming from the secondary vertex resolution is also evaluated. Finally, the errors of the momentum estimator are studied for a wide range of B decays classified topologically.

2 Single inclusive B production

With a heavy hadron sample of the order of 10^5 B mesons per year [1] the HERA-B will be a very competitive experiment for the study of properties of the single inclusive production. Although the QCD calculations of the single inclusive heavy hadron production have been performed some time ago [2], the next-to-leading order (NLO) QCD calculations [3] must be supplemented by various soft phenomena [4] in order to give predictions that agree with the experimental data. There are two sources of theoretical uncertainties: the choice of the heavy

quark masses, the renormalization and factorization scales etc., which are input for the NLO QCD calculations, as well as the parameters of the nonperturbative models which supplement them. Thus, the resulting total cross-section for the bottom production at HERA-B energies is predicted only within a range of 6-17 nb. The single inclusive Feynman-x and the transverse momentum spectra are predicted with similar uncertainties [4].

On phenomenological grounds, the high statistics sample of B mesons may be used to answer questions concerning the x_F and p_T spectra for heavy hadrons. Namely, several experiments (see e.g. [5] and references cited therein) report non-vanishing x_F^0, the center of Feynman-x distribution

$$\frac{d\sigma}{dx_F} \sim (1 - |x_F - x_F^0|)^n \,. \qquad (1)$$

This offset, although predicted by the theory, is experimentally demonstrated only within one standard deviation. Another problem is the shape (of the tail) of the p_T spectrum. While the $e^{-b_2 p_T^2}$ form is used for most of the data, some collaborations find the simple exponential form $e^{-b_1 p_T}$ better describes the data, particularly in the high p_T region (see e.g. [5]).

3 Current results $B\bar{B}$ correlations

The perturbative and nonperturbative input parameters produce considerable uncertainties for the predictions of the single inclusive heavy hadron production. The distributions of heavy hadron pairs seems to be even more sensitive to the choice of those parameters. In addition, some nontrivial effects for distributions of pairs, absent in the leading order QCD (where the heavy hadron pair is produced back-to-back), arise entirely as the NLO or the nonperturbative effects. Thus, the distributions of heavy hadron pairs, although more difficult from experimental point of view, are an excellent place to study the effects of higher order QCD and nonperturbative contributions.

The kinematic variables commonly used to study the hadroproduction of heavy hadron pairs may be divided into two groups

- the angular variables, e.g.
  - azimuthal angle difference $\Delta\phi = |\phi_1 - \phi_2|$,
  - *pseudo*rapidity difference $\Delta\eta = |\eta_1 - \eta_2|$;
- the momentum variables, e.g.
  - the Feynman-x of a pair x_F^{pair},
  - the effective mass of the pair M_{eff},
  - the transverse momentum of the pair $p^2_{sum\ T} = (\vec{p}_{1T} + \vec{p}_{2T})^2$,
  - the rapidity difference $y_{diff} = |y_1 - y_2|$.

A majority of data comes from the fixed target hadroproduction of charmed pairs. The only result for bottom is based on 9 pairs (not fully reconstructed). The results are collected in Table 1. In all these studies momentum estimators have been used.

experiment	No. of pairs	$< p^2_{sum\ T} >$ [GeV^2]	$< M_{eff} >$ [GeV]	$< y_{diff} >$ [1]	$< \Delta\phi >$ [^{o}]
E653 p-em. 800 GeV [6]	35	-	$5.56^{+0.21}_{-0.37}$	$1.21^{+0.10}_{-0.13}$	107.1 ± 9.6
WA75 π^-−em. 350 GeV [7]	177	$2.0^{+0.50}_{-0.33}$	$4.59^{+0.14}_{-0.09}$	0.80 ± 0.05	109.2 ± 4.0
WA92 π^-−Cu 350 GeV [8]	475	1.90 ± 0.17	5.02 ± 0.16	-	102.4 ± 3.6
NA32 π^-−Cu 230 GeV [9, 10]	557	1.98 ± 0.11	4.45 ± 0.03	0.54 ± 0.02	109.2 ± 2.4
E653 π^--em. 600 GeV [11]	9 $B\bar{B}$	5.0 ± 2.5	-	-	147.3 ± 19

Table 1: *Experimental results for the heavy hadron momentum correlations. The first four are the results for the charm pairs, the last one is for the beauty pairs.*

4 Momentum estimators

To study the distributions of angular variables of the heavy hadrons one needs to know the flight directions of both hadrons. This is achieved from the precisely determined primary and secondary vertices. It is enough that one (or even none) of the hadrons is fully reconstructed.

In order to study the momentum correlations, one needs to know the momenta of both heavy hadrons[1]. There are various techniques used for the estimation of the momentum of decaying heavy hadrons. They are based on the precise measurement of the position of the primary and secondary vertex and the measurement of the charged decay products' momenta. The kinematic techniques described below are often supplemented by Monte Carlo information. There are two popular approaches:

- estimator EQ, the problem may be solved exactly with three inputs: the heavy hadron flight vector, the visible decay products' momenta and the effective mass of the invisible decay products.
- estimator ET, relies on the assumption that the invisible decay products' momentum, in the rest frame of the heavy hadron, is perpendicular to its flight vector. Then the corresponding boost from the rest frame may be found to match the laboratory visible momentum.

The estimator EQ gives the exact answer, which is ambiguous. Then either the most probable solution (as suggested by MC or the ET estimator) or just the average of the two solutions may be used. For this estimator one needs to know the effective mass of the invisible decay products. This is simple when the invisible decay product is e.g. one π^0, neutrino or a narrow state decaying into neutrals. But in a case of e.g. nonresonant $\pi^0\pi^0$ in the final state, the necessary estimates of the invisible effective mass and the experimental uncertainties of the

[1] There is an alternative approach to study the correlations of heavy hadron pairs in a case of experiment like HERA-B [12]. In this report we concentrate on the momentum estimator approach.

measured quantities needed for the exact solution, limit the applicability of this estimator to a small class of events.

The ET estimator is simple to apply and works well for multibody final states [2]. It has been used for studies of the single inclusive distributions by the E653 collaboration [13], and the charm hadron momentum correlations in the E653 [6], WA75 [7], WA92 [8] and NA32 [9] data.

5 HERA-B and $B\bar{B}$ correlations

According to expectations [1], the HERA-B experiment should collect a sample of about 10^5 $B\bar{B}$ events per year. The advantage of the design of the experiment is that one of the B hadrons in each event will be fully reconstructed. The other B hadron will decay into any decay mode. The momentum estimator ET has typically a sizable error, however, the estimated momentum of the other B will be added to the well measured, fully reconstructed B. Thus, the relative error of the momentum of the $B\bar{B}$ pair will be roughly halved. The results of the simulation [14], with HERA-B parameters and x_F and p_T acceptances [1], for the $B\bar{B}$ pairs with one of the B mesons fully reconstructed and the other decaying into $B^- \to D^{*+}(2010)\pi^-\pi^-\pi^0 \to (K^-\pi^+\pi^0)\pi^+\pi^-\pi^-\pi^0$ chain (D^0 decay products are in the brackets and both π^0s are unmeasured) are shown in Fig.1. The resolution of the momentum estimator for the laboratory momentum of the single B meson is 18 %, while for the laboratory momentum of the pair p_{lab}^{pair} is 9.1%. This results in the errors for the pair variables[3] Δx_F^{pair}=0.027, $\Delta p^2_{sum\ T}$=1.3 GeV^2, ΔM_{eff}= 0.34 GeV and Δy_{diff}=0.16.

The quoted errors of the pair variables are the lower limits, determined by the production and the decay kinematics, when the momentum estimator ET is used. One of the most important sources of additional systematics is the secondary vertex resolution[4]. To use the momentum estimator, only the flight vector direction, and not e.g. the decay length, must be known. The longitudinal resolution has a little influence on the flight vector direction. This is further reduced if the decay length cut is applied. Indeed, the simulation with the secondary vertex resolution $\sigma_z = 500\mu m$ and $\sigma_x = \sigma_y = 25\mu m$ [1] results in small changes of the momentum estimator errors for the pair Feynman-x, Δx_F^{pair}=0.028, and for the rapidity difference, Δy_{diff}=0.17, once the cut[5] of 3 mm on the decay length is applied. The effect is stronger for the transverse momentum $\Delta p^2_{sum\ T}$=1.8 GeV^2 and the effective mass ΔM_{eff}= 0.38 GeV.

[2] In practical applications, in order to reduce the error of the estimator, the measured distributions are cut at the very tail (with a typical loss of a few percent of events). A strong improvement for the momentum estimator comes from the application of the cut on the transverse momentum of the visible decay products with respect to the flight vector. This cut, however, has much stronger influence on the statistics. For the following studies of the errors of the momentum estimator we do not optimize the selection cuts, thus keeping more than 90% of events.

[3] The B mesons in the $B\bar{B}$ pair are uncorrelated, thus giving the averages $< p^2_{sum\ T} >$=10.3 GeV^2 and $< M_{eff} >$=11.8 GeV.

[4] The primary vertex resolution at HERA-B is of the order of 10μm [1] and is neglected here.

[5] The mean flight path of the B meson at HERA-B energies is of the order of 9 mm.

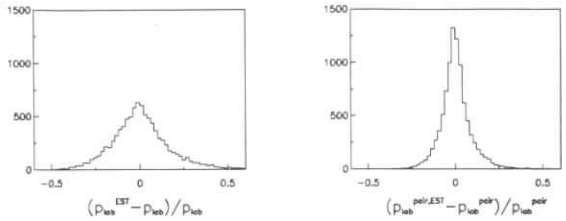

Figure 1: *The relative difference of the estimated and the true laboratory momentum for the single B meson (left) and for the $B\bar{B}$ pair (right). One of the B mesons in the pair decays into $B^- \to D^{*+}(2010)\pi^-\pi^-\pi^0 \to (K^-\pi^+\pi^0)\pi^+\pi^-\pi^-\pi^0$ with both π^0s being unmeasured. The other B meson is fully reconstructed.*

6 Topological approach

As shown in the previous section, the ET momentum estimator is adequate within a typical error of ~10% for the laboratory momentum of the $B\bar{B}$ pair. The studied decay channel has the branching ratio of (1.5±0.7)% [15] only. On the other hand, the inclusive branching ratios for B mesons are $B \to D^+X = (26 \pm 4)\%$ and $B \to D^0X = (54 \pm 6)\%$ [15]. As the B mesons decay in a large number of channels with small branching ratios, in any practical approach, one needs to identify the decay vertex of the other B hadron and all tracks which belong to this vertex. Exact knowledge of the decay channel and the decay chain is not necessary for the momentum estimator ET to be applied. The dependence on the decay chain for the decays with the same number of tracks emerging from the secondary vertex is week (see Table 2). In addition, the vertex missing mass may be used to estimate the number of missing neutrals. The events may be classified topologically and their systematics studied for the whole class of events.

7 Conclusions

We show that the HERA-B experiment will provide an excellent opportunity to study the heavy quark hadroproduction and the perturbative and nonperturbative contributions to this process. It should resolve long standing problems of the single inclusive heavy hadron production like the shape of the Feynman-x and p_T distributions. The heavy hadron pair distributions are also worth studying at HERA-B. Firstly, there should be a large $B\bar{B}$ sample for the study of angular correlations (comparing with current results). In addition, the study of the $B\bar{B}$ momentum correlations, although difficult, is possible with the use of momentum estimators. Approximately a few percent of $B\bar{B}$ events, with the first B meson fully reconstructed and the

decay mode	Δp_{lab}^{pair} [%]	Δx_F^{pair}	$\Delta p^2_{sum\ T}$ [GeV^2]	ΔM_{eff} [GeV]	Δy_{diff}
$(K\pi)\pi\pi\pi^0\pi^0$	8.1	0.023	1.2	0.30	0.14
$(K\pi\pi^0)\pi\pi\pi^0$	11.1	0.034	1.4	0.43	0.20
$(K\pi\pi^0\pi^0)\pi\pi$	10.9	0.033	1.4	0.43	0.19
$(K\pi\pi)\pi\pi\pi^0\pi^0$	7.5	0.021	1.2	0.28	0.13
$(K\pi\pi\pi^0)\pi\pi\pi^0$	9.1	0.027	1.3	0.34	0.16
$(K\pi\pi\pi^0\pi^0)\pi\pi$	9.2	0.027	1.3	0.35	0.16

Table 2: *Errors of the momentum estimator ET for various classes of the B decaying into the $D^{(*)} + (n\pi)$ channels. In brackets are the decay products of the $D^{(*)}$. The π^0s are not being measured. The other B meson in the event is fully reconstructed.*

second B meson partially reconstructed, could be used, compared with $\ll 10^{-3}$, when both B mesons are required to be fully reconstructed. The kinematic limits on the resolutions of the momentum estimator are of the order of 8-12% for the laboratory momentum of the $B\bar{B}$ pair, resulting in the resolutions

- 0.02-0.04 for the x_F^{pair} distribution,
- 1.2-1.4 GeV^2 for the $p^2_{sum\ T}$ distribution (with the average $< p^2_{sum\ T} >$=10.3 GeV^2),
- 0.3-0.5 GeV for the M_{eff} distribution (with the average $< M_{eff} >$=11.8 GeV),
- 0.15-0.20 for the y_{diff} distribution.

The source of the main systematic error, namely the effects of the secondary vertex resolution, are under control once the cut on the secondary vertex separation of 2-3 mm is applied.

Acknowledgements

I want to thank the workshop organizers for financial support. My thanks also to Dr. R. Eichler and Dr. A. Hasan for reading the manuscript and their helpful remarks.

References

[1] HERA-B collaboration, E.Hartouni et al., Technical Design Report, DESY-PRC 95/01.

[2] P.Nason, S.Dawson and R.K.Ellis, Nucl. Phys. **B303**(1988)607, **B327**(1988)49; W.Beenakker et al., Phys. Rev. **D40**(1989)54, Nucl. Phys. **B351**(1991)507.

[3] M.Mangano, P.Nason and G.Ridolfi, Nucl. Phys. **B373**(1992)295, Nucl. Phys. **B405**(1993)507.

[4] S.Frixione, M.Mangano, P.Nason, G.Ridolfi, Nucl.Phys. **B431**(1994)453.

[5] J.A.Appel, Annu. Rev. Nucl. Part. Sci. **42**(1992)367.

[6] E653 collaboration, K.Kodama et al., Phys. Lett. **B263**(1991)579.

[7] WA75 collaboration, S.Aoki et al., Phys. Lett. **B209**(1988)113, Prog. Theor. Phys. **87**(1992)1315.

[8] BEATRICE (WA92) collaboration, M.Adamovich et al., Phys. Lett. **B348**(1995)256.

[9] K.Rybicki, R.Rylko, Phys. Lett. **B353**(1995)547.

[10] ACCMOR collaboration, S.Barlag et al., Phys. Lett. **B302**(1993)112.

[11] E653 collaboration, K.Kodama et al., Phys. Lett. **B303**(1993)359.

[12] R.Rylko, *work in progress.*

[13] E653 collaboration, K.Kodama et al., Phys. Lett. **B263**(1991)573.

[14] R.Rylko, DECEST, a package for vertex based momentum estimation and Monte Carlo study of its errors, manual, 1995 (*unpublished*).

[15] Particle Data Group, L.Montanet et al., Review of Particle Properties, Phys. Rev. **D50** No 11, part II (1994).

Working Group on

Jets and High-$E_\perp$ Phenomena

Conveners:

M. Erdmann (Heidelberg), D. Graudenz (CERN, Geneva),
L. Lönnblad (NORDITA, Copenhagen), K. Tokushuku (INS, Tokyo)

Participants:

P. Aurenche (ENSLAPP, Annecy), A. Bamberger (Freiburg), J. Binnewies (Hamburg), L. Bourhis (Paris), J. Bromley (Glasgow), N. Brook (Glasgow), A. Buniatian (Antwerpen), P. Bussey (Glasgow), J. Butterworth (University College London), T. Carli (MPI, Munich), S. Catani (INFN, Florence), J. Chýla (Prague), J. Cvach (Prague), A. Edin (Uppsala), S. Eisenhardt (Freiburg), R. Engel (Leipzig), M. Erdmann (Heidelberg), L. Feld (Bonn), M. Fontannaz (Orsay), I. Gialas (Bologna), M. Gibbs (Liverpool), D. Graudenz (CERN, Geneva), T. Greenshaw (Liverpool), G. Grindhammer (MPI, Munich), J.P. Guillet (ENSLAPP, Annecy), G. Gustafson (Lund), T. Haas (DESY, Hamburg), Th. Hadig (Aachen), M. Hampel (Aachen), J. Hartmann (McGill), M. Hayes (Bristol), H. Hessling (DESY, Hamburg), Ch. Hoeger (DESY, Hamburg), G. Ingelman (DESY, Hamburg & Uppsala), H. Kharraziha (Lund), M. Klasen (Hamburg), B.A. Kniehl (MPI, Munich), G. Kramer (Hamburg), M. Kuhlen (MPI, Munich), A. Lebedev (Moscow), B. Levtchenko (Moscow), G. Lobo (Paris), L. Lonnblad (NORDITA, Copenhagen), S. Magill (Argonne), D. Milstead (Liverpool), E. Mirkes (Karlsruhe), R. Mohr (MPI, Munich), B. Musgrave (Argonne), Ch. Niedzballa (Aachen), E. Pilon (Orsay), H. Raach (Freiburg), K. Rabbertz (Aachen), J. Rameš (Prague), J. Rathsman (Uppsala), A. Ringwald (DESY, Hamburg), M. Riveline (McGill), K. Rosenbauer (Aachen), F. Schrempp (DESY, Hamburg), M. Seymour (CERN, Geneva), A. Shumilin (Moscow), L. Sinclair (Glasgow), E. Strickland (Glasgow), M. Sutton (University College London), K. Tokushuku (INS, Tokyo), Th. Trefzger (Munich), J. Vazdik (Moscow), A. Vogt (Wuerzburg), R. Waugh (Glasgow), S. Wölfle (Freiburg), D. Zeppenfeld (Wisconsin),

Jets and High-$E_\perp$ Phenomena

Martin Erdmann[a], Dirk Graudenz[b], Leif Lönnblad[c], Katsuo Tokushuku[d]

[a] Physikalisches Institut, Universität Heidelberg, Philosophenweg 12, D-69120 Heidelberg, FRG
[b] CERN, Theory Divison, CH-1211 Genève 23, Switzerland
[c] NORDITA, Blegdamsvej 17, DK-2100 Copenhagen Ø, Denmark
[d] Institute for Nuclear Study, University of Tokyo, Tanashi, Tokyo 188, Japan

Abstract: The working group on jets and high-$E_\perp$ phenomena studied subjects ranging from next-to-leading order (NLO) corrections in deeply inelastic scattering (DIS) and photoproduction with the corresponding determinations of physical quantities, to the physics of instanton-induced processes, where a novel non-perturbative manifestation of QCD could be observed. Other centres of interest were the physics of the forward direction, the tuning of event generators and the development of a new generator which includes a consistent treatment of the small- and large-x QCD evolution. The recommendations of the working group concerning detector upgrades and machine luminosity are summarized.

Introduction

The physics of hadronic final states is currently one of the main interests at HERA. To mention only a few points, the study of jets has led to a determination of the strong coupling constant and of the gluon density, and the investigation of the hadronic activity in the forward direction has improved our understanding of parton radiation in the initial state. Concurrently with these phenomenology issues, there was the development of tools such as next-to-leading order Monte Carlo programs for jet production and event generators modelling the hadronic final state. The goal of the working group was to study the future prospects of the physics of jets and high-$E_\perp$ phenomena in the light of the two different improvements of an increased machine luminosity (of the order of $\int \mathcal{L} dt = 250 - 1000\,\mathrm{pb}^{-1}$) and improved detectors in the forward direction. Because of the wide range of subjects, the working group was organized in four subgroups:

- **Deeply Inelastic Scattering.** The subjects considered in this subgroup were the study of QCD-instanton-induced processes, the calculation of jet cross-sections in NLO and the extraction of the strong coupling constant and the gluon density via hadronic final states. A particular emphasis has been the study of the statistical and systematic errors for large luminosity. One project studied the semi-DIS region, defined by events with $p_\perp \gg Q \gg \Lambda_{\mathrm{QCD}}$, and the prospects of the determination of the virtual photon structure function.

Electronic mail addresses:
erdmann@dice2.desy.de, Dirk.Graudenz@cern.ch, leif@nordita.dk, toku@vxdesy.desy.de

- **QCD Evolution and the Forward Region.** This subgroup studied the prospects of measuring in deeply inelastic scattering the QCD evolution in the initial state. Several small groups searched for relevant observables in order to (a) distinguish the QCD evolution schemes of DGLAP and BFKL, (b) detect instanton formation, and (c) establish 'hot spots' in the proton. Also studied were detector upgrades in the outgoing proton direction which concern the results of this working group and the working group on *Diffractive Hard Scattering*. All results from the two working groups which are related to a detector upgrade in the forward direction are summarized in a separate report [9].

- **Photoproduction.** Two projects considered the calculation of the NLO corrections to jet cross-sections, where in one of the projects the matching of theoretical and experimental jet cross-sections has been studied in detail. The measurement of the gluon density of the photon by means of the rapidity distribution of charged particles has been studied. Two projects considered the effects of colour coherence and of rapidity gaps between jets, respectively, and one project studied prompt photon, Drell–Yan and Bethe–Heitler processes.

- **Event Generators and Tuning.** In this subgroup, a standardized framework (HZTOOL) for the comparison of experimental data and generator predictions has been developed and used to tune existing generators. Another project considered the implementation of the linked dipole chain model in a Monte Carlo program interfaced to ARIADNE.

The outline of this working group summary is as follows. The next section introduces the notation. In the following four sections the activities of the subgroups are summarized. A concluding section then gives the final recommendations of the working group concerning detector upgrades and machine luminosity.

Notation

The momenta of the incident and outgoing electron[1] and of the incident proton are denoted by l, l' and P, respectively. In deeply inelastic scattering, the electron phase space is parametrized by the Bjorken variable[2] $x_B = Q^2/2Pq$ and by $y = Pq/Pl$, where $q = l - l'$ is the (space-like) momentum of the exchanged virtual photon, and $Q^2 = -q^2$ is the square of the photon virtuality. In this way Q represents the energy scale of the scattering and x_B may be interpreted, in the case of lowest-order QCD sub-processes, as the momentum fraction of the proton carried by the scattered parton. For some processes such as heavy-flavour production or the photoproduction of large transverse energy jets the energy scale is not determined by the photon virtuality. In these cases the photon virtuality may be denoted by P (not to be confused with the proton momentum), where for photoproduction, $P^2 \approx 0$.

Because of the hadronic component of a real photon, the parton densities $f_{i/\gamma}(x_\gamma, \mu^2)$ of the photon have to be introduced for photoproduction. Here x_γ denotes the momentum fraction of the photon carried by the parton i. More commonly used is the experimentally observed quantity $x_\gamma^{\rm OBS} \equiv (E_{\perp 1} e^{-\eta_1} + E_{\perp 2} e^{-\eta_2})/2yE_l$ derived from the two jets with the highest $E_\perp$.

[1] We use the term "electron" as synonymous to "positron". Charged-current processes and Z^0 exchange have not been studied in the working group.

[2] The variable x_B is sometimes also denoted by x.

The convention of placing the proton along the positive z-axis in the laboratory frame, and the virtual photon along the positive z-axis in the hadronic centre of mass and Breit frames is used throughout. For jet rates in DIS the "(n+1)" counting convention is used, where the "+1" refers to the proton remnant jet.

References to contributions printed in these proceedings are made by quoting the *author names*, printed in italics.

Deeply Inelastic Scattering

The subgroup on deeply inelastic scattering had three main focuses: QCD instantons, the calculation of next-to-leading-order jet cross-sections, and the determination of the strong coupling constant $\alpha_s(\mu_r^2)$ and the gluon density $g(x, \mu_f^2)$ from hadronic final states. Deeply inelastic scattering is defined by a photon virtuality much larger than the fundamental QCD scale parameter, $Q \gg \Lambda_{\rm QCD}$. The presence of this large scale allows the calculation of infrared-safe quantities in perturbative QCD. A possible approach to the inclusion of hadronization effects in an analysis is to take them into account by data unfolding or by the inclusion of correction factors based on a comparison of the hadron level and the parton level by means of event generators.

QCD Instantons. QCD instantons give rise to helicity-violating non-perturbative processes, whose experimental discovery would clearly be of basic significance. *M. Gibbs, T. Greenshaw, D. Milstead, A. Ringwald and F. Schrempp* considered the discovery potential for these processes at HERA by studying the characteristics of the hadronic final state. Because the processes are flavour-democratic, strange particles would be produced in abundance. In addition, a suitably defined event-shape variable might help to discriminate the QCD-instanton-induced processes from standard QCD background. Despite large uncertainties in the first (preliminary) estimates of the cross-section, HERA offers a distinct discovery window for these spectacular processes, notably with a substantial luminosity upgrade.

NLO Corrections. The calculation of jet cross-sections in NLO was considered in two projects. *E. Mirkes and D. Zeppenfeld* have calculated the (2+1) jet cross-section by means of the phase space slicing method, employing helicity amplitudes and the technique of universal crossing functions. *S. Catani and M. Seymour* used the subtraction method, where the subtraction term in the collinear and soft regions is obtained by means of the recently developed dipole formalism. Because the Monte Carlo program based on the latter calculation has been finished only recently, a numerical comparison of the two different approaches has not yet been done.

The Strong Coupling Constant. The future prospects of the determination of α_s via the (2+1) jet rate has been considered by *Th. Hadig, Ch. Niedzballa, K. Rabbertz and K. Rosenbauer*. They studied the dependence of statistical and systematic errors in dependence of the available luminosity. It turns out that the energy scale error of the detector is the dominant experimental systematic error. Assuming this error to be 2%, a total error of ± 0.007 can be achieved for $\alpha_s(M_Z^2)$ with $\int \mathcal{L} dt = 250\,{\rm pb}^{-1}$, which is to be compared with the present error of the world average of $\alpha_s(M_Z^2)$ of ± 0.006. A further increase of the luminosity might lead to a reduction of the energy scale error and thus to a further improvement of the error. The effect of additional acceptance cuts to reduce the systematic error has also been studied. In particular, a cut in the jet transverse momentum seems to be promising. The systematic error induced by the dependence of parton densities on $\Lambda_{\rm QCD}$ has been estimated by *J. Chýla and*

J. Rameš by considering the relative importance of α_s in the matrix element and in the evolution of the parton densities. At moderately large Q^2, where the present α_s measurements have been done, the former is dominant. It would be desirable to find a way to consistently include this dependence at smaller Q^2, where the data sample is much larger. An α_s measurement by means of scaling violations of fragmentation functions has been studied by *D. Graudenz*. Here a large systematic error is induced by the choice of parton densities. This error can be reduced by going to large values of Q^2. Because of the rapid fall-off of the cross-sections, a large luminosity is required. It turns out that the measurement would not be competitive concerning the size of the error (the effect being only logarithmic in the factorization scale), but might be an interesting complementary measurement at HERA.

The Gluon Density. The photon–gluon fusion process, giving rise to (2+1) jets in the final state, can be exploited for a measurement of the gluon density. *G. Lobo* has studied the prospects for a combined global fit of F_2 and jet rates. By including the jet rate data, the error at large $x \gtrsim 0.03$ can be reduced considerably. The global approach also allows a combined fit of the quark and gluon densities. The direct measurement of $g(x)$ by means of the Mellin transform method has been studied by *D. Graudenz, M. Hampel and A. Vogt*. Here the quark densities are assumed to be input distributions; the momentum sum rule is taken care of by means of the normalization of $g(x)$. An increased luminosity of the order of $250\,\mathrm{pb}^{-1}$ may allow the reduction of the error band by a factor of two, compared to the present integrated luminosity of $3\,\mathrm{pb}^{-1}$.

The Semi-DIS Region. *J. Chýla and J. Cvach* have studied the prospects of a measurement of the virtual photon structure function by looking at DIS events with some additional hard scale $p_\perp \gg Q \gg \Lambda_{\mathrm{QCD}}$, and conclude that an integrated luminosity of $50\,\mathrm{pb}^{-1}$ is sufficient for a measurement that allows for a discrimination between various models, assuming the virtual photon structure functions suppression is x-independent. To measure the x-dependence of the virtual photon structure functions, an integrated luminosity at least 10 times higher would be necessary.

Except for the analysis in the semi-DIS region, all projects in this subgroup related to the extraction of physical quantities as well as the QCD instanton study strongly favour a substantial luminosity increase, whereas a detector upgrade in the forward direction is not required. The α_s analysis shows that above an integrated luminosity of about $250\,\mathrm{pb}^{-1}$ the systematic errors will eventually dominate over the statistical ones. A similar situation can be expected in the case of the direct determination of the gluon density via jets. It should be kept in mind, however, that the energy scale error, and thus the systematic error of the extracted physical quantities, also depends on the available integrated luminosity, since high-$p_\perp$ jets are required to calibrate the detector [1].

QCD Evolution and the Forward Region

The leading question of the 'forward physics' group was: how can we understand the QCD evolution of the initial state? Compared to the interpretation of inclusive measurements of the proton structure function F_2, exclusive measurements in the forward direction (outgoing proton) are sensitive to the explicit details of the evolution between the proton and the photon–quark vertex.

Today's conventional description of the evolution of a single parton are the DGLAP evolution equations. These equations resum terms of the form $(\alpha_s \ln Q^2)^n$. At small fractional parton momenta x, contributions of the form $(\alpha_s \ln(1/x))^n$, not described by the DGLAP equations, become important. It is, however, still debated at which values of x this will be the case. HERA offers the opportunity to settle this question empirically, for instance by testing predictions of the BFKL type against those of DGLAP evolution. Apart from these perturbatively calculated effects, also non-perturbative effects, such as instanton formation, are expected to contribute to the parton evolution. Beyond single parton evolution, multi-parton evolution effects are expected which could exhibit inhomogeneous regions in the proton, e.g. regions of high parton density ('hot spots'). Their detection would imply a significant step forward in our understanding of the proton.

It is essential to find observables which reflect the evolution of the partons from the proton to the γq vertex:

a) Indirect access is given by a measurement of kinematical variables of the final-state proton which can, in the case of a hard scattering process, be described by models where the proton initially lost partons during the scattering and finally received partons for the colour neutralization process (*I. Gialas, J. Hartmann; A. Edin, G. Ingelman and J. Rathsman*).

b) Direct measurements of the parton evolution require observables which involve high transverse momenta in order to suppress the influence of non-perturbative effects (*A. Edin, G. Ingelman and J. Rathsman*). Single charged particle spectra can distinguish at high transverse momenta different scenarios of QCD evolution (*M. Kuhlen*). In a similar way, jet cross-sections can be used to study parton evolution in the forward direction (*T. Haas and M. Riveline; J. Bartels, A. De Roeck and M. Wüsthoff*). In a related project (*E. Mirkes, D. Zeppenfeld*) it has been found that the measured forward jet cross section at small x_B [2] is not described by a fixed-order NLO calculation. However, it can be explained by a LO calculation amended with a BFKL ladder in the initial state [3]. A different class of observables are shape variables which can, in principle, resolve short range effects at sufficiently large transverse momenta (*H. Heßling*).

Detector upgrades in the direction of the outgoing proton will give essential improvements in all the direct measurements of parton evolution (*M. Kuhlen; A. Bamberger, S. Eisenhardt, H. Heßling, H. Raach and S. Wölfle*). The extension of the ZEUS detector by a PLUG calorimeter which enlarges the rapidity coverage by 1.6 units, was studied in detail (*A. Bamberger et al.*).

A high luminosity upgrade of the HERA machine, as proposed by the working group *HERA Optics and Layout of Interaction Region*, will signal the end of the physics described in this section. Before such upgrade, data corresponding to a luminosity of order $100\,\mathrm{pb}^{-1}$ should be collected in order to ensure that the HERA project may contribute significantly to the understanding of QCD evolution.

Photoproduction

A further, important field of testing perturbative QCD is the study of photoproduction processes with large transverse energy in the hadronic final state. Here one of the goals is to

obtain new information on the partonic structure of the photon and the proton. Whereas F_2^γ measurements in e^+e^- collider experiments constrain the quark distribution in the photon, the gluon distribution is largely unknown. In the region where x_γ is close to zero or unity, even the quark distribution is not well constrained at present. In this workshop, three different final states were considered to study the structure of the photon and proton: jets, inclusive hadronic particle distributions, direct photons and lepton pairs.

Jets. *J. Butterworth, L. Feld, M. Klasen and G. Kramer* have made a detailed comparison in order to match the definition of jets in experimental and theoretical studies. It is shown that one can match jets of NLO calculations to various experimental jet definitions by tuning a parameter R_{sep}. The matching is better when the $E_\perp$ of jets becomes larger. Smearing effects from hadronization are smaller at high $E_\perp$ as well. By selecting high-$E_\perp$ jets in a good detector acceptance region ($E_\perp^{jet} \geq 30\,\mathrm{GeV}$ and $\eta^{jet} < 2$), one can test the photon and proton structure in the high-x region provided a large integrated luminosity ($\geq 250\,\mathrm{pb}^{-1}$) is available. *P. Aurenche, L. Bourhis, M. Fontannaz and J.Ph. Guillet* have developed a Monte Carlo program describing the 2- and 3-jet photoproduction in NLO. These jet cross-sections can be extracted from the generated events using a cone algorithm together with desired experimental cuts.

Inclusive Particle Production. *J. Binnewies, M. Erdmann, B. Kniehl and G. Kramer* have demonstrated that inclusive differential rapidity cross-sections of charged particles with large transverse momenta are sensitive to the gluon distribution of the photon, at low x_γ. Assuming that the gluon fragmentation function will be better known from LEP data on the longitudinal polarized cross-sections, the extraction of the NLO gluon distribution in the photon can be done with a precision of the order 10% using an integrated luminosity of $100\,\mathrm{pb}^{-1}$.

Prompt Photon and Lepton Pair Production. With a high integrated luminosity, it is possible to study the quark distribution of the photon using processes which are suppressed by the fine structure constant α relative to the dominant di-jet production, but with the advantage of a very clean environment. Processes with non-hadronic particles directly coming from the hard scattering process is an example of this. *P. Bussey* estimated the event rates with a high-$p_\perp$ photon (prompt photon). One can obtain sufficient data to determine the quark distributions in the photon at the 5–10% level with an integrated luminosity of $1000\,\mathrm{pb}^{-1}$. *B. Levtchenko and A. Shumilin* studied Drell–Yan process. It is important to separate Drell–Yan lepton pairs from the pairs that come from the Bethe–Heitler process, which has a much larger cross-section. Kinematical cuts for this separation are proposed.

There are two studies on event topology of high-$p_\perp$ photoproduction, on the colour coherence effect and on colour-singlet exchange.

Colour Coherence. *L. Sinclair and E. Strickland* studied the effect of colour coherence in multi-jet events. In order to obtain a large sample of multi-jet events it is necessary to have high luminosity. However, it turned out that a large acceptance in the forward region is also important. The luminosity upgrade at the expense of reducing the forward region acceptance is not worthwhile for this study. By extending the detector coverage up to 4 in pseudorapidity, the effect could be more pronounced. *A. Lebedev and J. Vazdik* studied the process-dependence of colour coherence. Particle flows in the inter-jet region are sensitive to the effect.

Colour-Singlet Exchange. *J. Butterworth, M. Hayes, M. Seymour and L. Sinclair* studied events with a rapidity gap between jets. The colour-singlet exchange appears here at a scale where perturbative QCD calculations give reliable predictions. Such data therefore give access to the origin of the so-called hard Pomeron. It is shown that with a larger detector coverage in

the forward region one can obtain an unambiguous signature for the colour-singlet exchange. The luminosity requirement is of the order of $100\,\mathrm{pb}^{-1}$.

Event Generators and Tuning

The importance of theoretically well-founded event generators which give a good description of data cannot be emphasised enough. The situation at HERA in this respect has not been very satisfactory, especially when comparing to the extraordinary success of event generators at LEP [4]. This can be exemplified in DIS where all available generators have had great problems with describing fairly simple distributions, such as the $E_\perp$-flow [5].

This is not surprising considering the extra complications introduced at HERA which are not present in e^+e^- annihilation. In photoproduction there is the problem that the photon sometimes behaves as a point-like object and sometimes as a resolvable hadron. In the latter case, multiple interactions may occur, giving rise to an underlying event. Also, in photoproduction as well as in DIS, there is the problem of initial-state QCD evolution and how to handle it, especially in the small-x region, and in relation with the fragmentation of the proton remnant.

During the course of this workshop, the situation has much improved. Both for DIS and photoproduction, the available generators have been developed and the agreement with data is now at a level where a tuning of the parameters is meaningful. Two closely related projects have been working with the tuning of event generators. One of them *(J. Bromley, N. Brook, A. Buniatian, T. Carli, G. Grindhammer, M. Hayes, M. Kuhlen, L. Lönnblad and R. Mohr)* developed a library of FORTRAN routines called HZTOOL for easy comparison of event generators with published data. The other *(N. Brook, T. Carli, R. Mohr, M. Sutton and R.G. Waugh)* used this library to perform a first tuning of the DIS generators ARIADNE [6], HERWIG [7] and LEPTO [8]. A few of the measured distribution were selected, from which a global χ^2 was constructed to measure the quality of the fits. For all three programs the χ^2 was much improved by the tuning. The final numbers presented were $\chi^2 = 0.81$, 1.85 and 1.36 per degree of freedom for ARIADNE, HERWIG and LEPTO, respectively.

One new generator has been developed by *G. Gustafson, H. Kharraziha and L. Lönnblad.* It implements the Linked Dipole Chain model, which is a reformulation on the CCFM evolution equations based on the colour dipole picture. Here a careful division between initial and final state emissions results in a model well suited for an event generator implementation. This is the first complete generator where QCD coherence is correctly taken into account in the small-x region and where DGLAP and BFKL dynamics both are reproduced in the relevant limits. The preliminary comparison with data presented here looks promising.

Summary of Recommendations

The recommendations of the working group concerning a detector upgrade in the forward direction and an upgrade of the luminosity, as summarized in Table 1, are not unambiguous, because the two options are conflicting. The physics involving processes with large transverse momenta of final state jets would benefit substantially from a luminosity upgrade. This would allow the study of processes at large Q^2, thus increasing, for instance, the lever arm for a measurement of the *running* coupling constant $\alpha_s(Q^2)$. A larger data sample would also permit the application

of strict acceptance cuts to bias the sample towards a phase region where perturbative QCD is applicable unambiguously, i.e. without taking into account large hadronization or resummation effects. It would moreover allow a reduction of the energy scale error, which has a direct impact on the extraction of physical quantities.

On the other hand, HERA offers a unique opportunity to study the QCD evolution and the physics of the forward direction in a comparably clean environment. The results of the working group show that most studies in this phase space region would already benefit from an increase of the detector acceptance by one unit of rapidity, with a total integrated luminosity requirement of the order of $100\,\mathrm{pb}^{-1}$. However, the proposed high luminosity upgrade of the HERA machine would to a large extent make such studies impossible. In a separate report by members from both the *Jets and High-$E_\perp$ Phenomena* and *Diffractive Hard Scattering* working groups, the cases for a forward detector upgrade are summarized [9], strongly recommending that a luminosity upgrade should at least be postponed to allow for more studies of forward physics.

In conclusion: the physics of jets and high-$E_\perp$ phenomena will continue to be a very interesting topic at HERA. Both options for the future of HERA, a substantial luminosity increase and a forward detector upgrade, which have been studied in the working group, would mean new physics opportunities. It is worth while to consider running HERA for two or three years with a total integrated luminosity of $100\,\mathrm{pb}^{-1}$, to allow for the instrumentation of and measurement in the forward direction, and then moving to the luminosity upgrade, which is definitely required for precise QCD studies at large transverse momenta.

References

[1] J. Gayler, private communication.

[2] H1 Collaboration, A. Aid et al., *Phys. Lett.* **B356** (1995) 118.

[3] J. Bartels, V. Del Duca, A. De Roeck, D. Graudenz, M. Wüsthoff, DESY 96-036 (1996), [hep-ph/9604272].

[4] I.G. Knowles et al., *QCD Event Generators*, in Proc. LEP2 workshop, CERN report 96-01, Eds. G. Altarelli, T. Sjöstrand and F. Zwirner.

[5] H1 Collaboration, I. Abt et al., *Phys. Lett.* **B356** (1995) 118.

[6] L. Lönnblad, *Comput. Phys. Commun.* **71** (1992) 15.

[7] G. Marchesini et al., *Comput. Phys. Commun.* **67** (1992) 465.

[8] G. Ingelman, in Proc. HERA workshop, Eds. W. Buchmüller and G. Ingelman, Hamburg (1991) vol. 3, 1366.

[9] H. Abramowicz, L. Lönnblad et al., *The Physics Case for a Forward Detector Upgrade*, these proceedings.

Jets and High-$E_\perp$ Measurements[1,2]		Competition[3]	$\int \mathcal{L}dt$ [pb^{-1}][4]	Luminosity Upgrade[5]	Detector Upgrade[6]
DIS	Instanton ($K, \mu, E_\perp$)		1000	yes	
	α_s (particles, jets)	e^+e^-	250	–	
	gluon in proton (jets)	$\bar{p}p$	250	–	
	QCD evolution (jets)		30	no	ZEUS plug
	(particles)		100	no	very forward H1 tracker
	(shape variables)		>10	no	ZEUS plug
	proton fragm. (LPS)		>10	–	
$\gamma p \leftrightarrow$ *DIS*	quark in γ^* (2 jets)	quark at LEPII	50/500	no	H1 VLQ
	gluon in γ^* (2 jets)	none			
γp	gluon in γ ($d\sigma^{\mathrm{particle}}/d\eta$)	(charm at LEPII)	100	–	
	quark in γ (prompt γ)	quark at LEPII	1000	yes	
	(Drell-Yan)		1000	yes	
	(high-$E_\perp$ jets)		250	–	
	hard Pomeron ($\Delta\eta_{\mathrm{gap}}^{\mathrm{jets}}$)	($\bar{p}p$)	100	no	ZEUS plug
	colour coherence (jets)	e^+e^-, $\bar{p}p$	250	no	ZEUS plug

Table 1: Future HERA measurements recommended by the *Jets and High-$E_\perp$ Phenomena* working group; the columns show
1) process type: deeply inelastic scattering (DIS), photoproduction (γp),
2) physics topic (experimental method); LPS stands for the leading proton spectrometer,
3) (possible) competition from other laboratories,
4) required luminosity in pb^{-1},
5) statement on the luminosity upgrade *including acceptance losses in the current detectors*,
6) a detector upgrade which would significantly improve the results. (VLQ = very low Q^2 tagger)

Search Strategies for Instanton-Induced Processes at HERA

M. Gibbs[a], T. Greenshaw[a], D. Milstead[a], A. Ringwald[b], F. Schrempp[b]

[a] Oliver Lodge Laboratory, University of Liverpool, Liverpool L69 3BX, UK
[b] Deutsches Elektronen-Synchrotron DESY, Notkestrasse 85, D-22603 Hamburg, FRG

Abstract: We study the discovery potential for QCD-instanton induced events at HERA. A significant enhancement of the signal compared to the perturbative QCD background may be achieved by merging searches for an excess in strangeness production and multiplicity with information on the expected event shape. While first (preliminary) estimates of the production rates for instanton-induced events are surprisingly large, an upgrade in luminosity appears to be most important, in view of the inherent theoretical uncertainties in the estimates.

1 Introduction

Instantons [1] are known to represent tunnelling transitions in non-abelian gauge theories between degenerate vacua of different topology. These transitions induce processes which are *forbidden* in perturbation theory, but have to exist in general [2] due to Adler-Bell-Jackiw anomalies. The experimental discovery of such a novel, non-perturbative manifestation of non-abelian gauge theories would clearly be of basic significance.

Searches for instanton-induced processes have received new impulses during recent years: It was shown [3] that the natural exponential suppression of these tunnelling rates, $\propto \exp(-4\pi/\alpha)$, may be overcome at *high energies*. Furthermore, deep inelastic scattering (DIS) at HERA offers a unique window [4, 5, 6, 7] to experimentally detect processes induced by *QCD-instantons*. Here, a theoretical estimate of the corresponding production rates also appears feasible [4, 7, 8], since a well defined instanton contribution in the regime of small QCD gauge coupling may be isolated on account of the photon virtuality Q^2.

In this brief report we concentrate on improved search strategies for instanton-induced events at HERA. The main idea is to merge searches for an excess in strangeness production and multiplicity with information on the expected event *shape* (Sect. 3). Our results are based on the instanton Monte-Carlo generator [6, 9] QCDINS 1.3.

While first (preliminary) estimates of the production rates for instanton-induced events at HERA [7, 8] are surprisingly large (Sect. 2), an upgrade in luminosity appears to be most important, in view of the inherent theoretical uncertainties in the estimates.

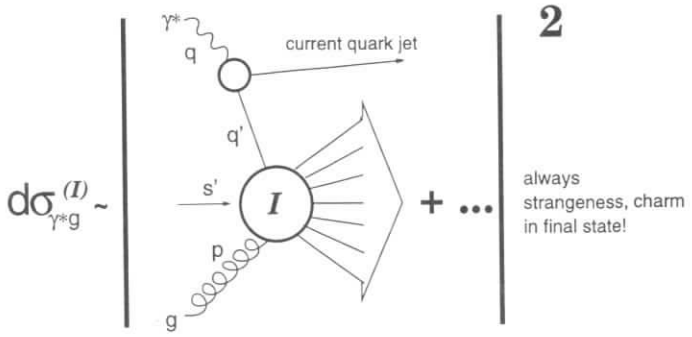

Figure 1: *Instanton-induced contribution to the cross-section of $\gamma^* g$ scattering exhibiting the structure of an I-induced subprocess, denoted by "I".*

2 Instanton-Induced Cross-Sections

The instanton (I) contribution to hadronic observables (e.g. cross-sections) is described in terms of a standard convolution of corresponding partonic observables with parton densities [5, 7, 8]. Therefore, let us confine our theoretical discussion to the partonic level. The generic structure of the I-contribution to the (dominating) $\gamma^* g$ cross-section $d\sigma^{(I)}_{\gamma^* g}(x, Q^2, \ldots)$ is displayed in Fig. 1. The apparent structure of an I-subprocess with cross-section $d\sigma^{(I)}_{q^* g}$ is due to the fact that the virtual photon only couples to instantons via their quark content.

A standard evaluation [10] of the I-contribution to the total $q^* g$ cross-section leads to the result [8]

$$\sigma^{(I)}_{q^* g}(x', Q'^2) \simeq \frac{\Sigma(x')}{Q'^2} \left(\frac{4\pi}{\alpha_s(\mu(Q'))}\right)^{21/2} \exp\left[-\frac{4\pi}{\alpha_s(\mu(Q'))} F(x')\right] , \qquad (1)$$

where primed variables such as $Q'^2 = -q'^2$ and $x' = Q'^2/(s' + Q'^2) \geq x \geq x_{\rm Bj}$ always refer to the I-subprocess. The running scale $\mu(Q')$ in α_s, satisfying $\mu(Q') = \kappa Q' \alpha_s(Q')/(4\pi)$ with $\kappa = \mathcal{O}(1)$, plays the rôle of an effective renormalization scale. The x' dependence resides in the functions $\Sigma(x')$ and the so-called "holy-grail" function $F(x') \leq 1$, which are both known as low-energy expansions in $s'/Q'^2 = (1-x')/x' \ll 1$ within conventional I-perturbation theory. Their form implies a rapid growth of $\sigma^{(I)}_{q^* g}$ for decreasing x'. Unfortunately, in the phenomenologically most relevant region of small x', the perturbative expressions are of little help and we have to resort to some extrapolation based on a suitable resummation technique.

An appropriate approach to resumming instanton perturbation theory is the $I\bar{I}$-valley approximation [11, 10] which we have adopted. It amounts to the identification of the holy-grail function with the known $I\bar{I}$-valley action. It appears reasonable to trust this method down to $x' = 0.2$, where $F(0.2) \equiv S_{I\bar{I}-\rm valley}(0.2) \simeq 1/2$, a value sometimes advocated [12] as the lower bound for the holy-grail function. An important phenomenological/experimental task will be to make sure (e.g. via kinematical cuts on the final state) that x' does not become too small.

Note the following important feature of $\sigma^{(I)}_{q^* g}$ as a function of Q'^2: The Q'^2 dependences from the high inverse power of α_s and the exponential in Eq. (1) compete to produce a strong peak

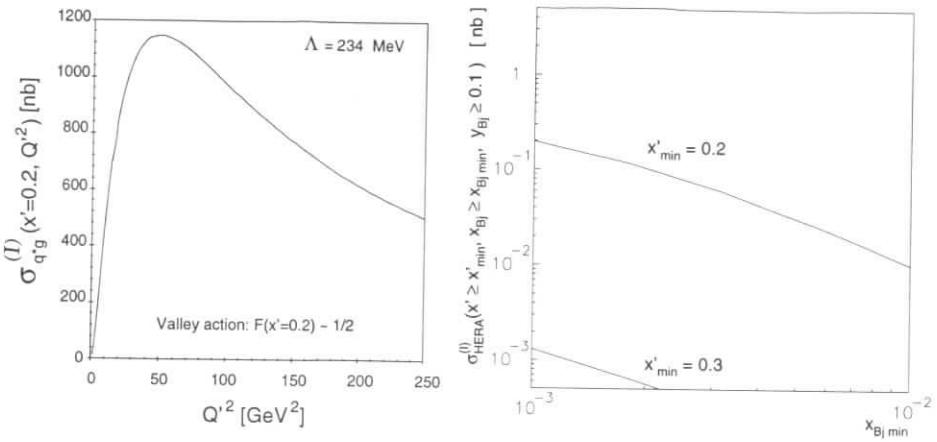

Figure 2: *Left: Q'^2 dependence of the total cross-section, $\sigma^{(I)}_{q^*g}(x', Q'^2)$, for fixed $x' = 0.2$. Right: I-induced total cross-section for HERA (preliminary) with various cuts.*

far away from the IR region, e.g. $Q'_{\rm peak}(x' = 0.2) \approx 31\,\Lambda$. This implies that in the Bjorken limit $\sigma^{(I)}_{\gamma^* g}(x, Q^2)$ is dominated by this peak, since it involves an integration over Q'^2. This strongly peaked structure also feeds through into the invariant-mass distribution ($\sqrt{s'}$) of the I-subprocess, via $s' \simeq Q'^2(1/x'_{\rm min} - 1)$, an important feature for the search strategies to be discussed below.

In Fig. 2 (right) we present the resulting I-induced total cross section for HERA for two values (0.2, 0.3) of the lower x' cut (c.f. discussion above), as a function of the minimal Bjorken x considered. It is surprisingly large. So far, only the (dominating) gluon contribution has been taken into account. The inherent uncertainties associated with the renormalization/factorization scale dependences may be considerable and are presently being investigated. Therefore, the results in Fig. 2 are still to be considered preliminary.

3 Search Strategy

The typical I-induced event (Fig. 3) from the Monte-Carlo generator [9] QCDINS 1.3, illustrates most of the important features characteristic for the underlying instanton mechanism: A current-quark jet along with a densely populated hadronic "band" of width $\triangle\eta = \pm 0.9$ in the $(\eta_{\rm lab}, \phi_{\rm lab})$-plane [5]. The band reflects the *isotropy* in the I-rest system. The total $E_T = \mathcal{O}(20)$ GeV is large as well as the multiplicity, $N_{\rm band} = \mathcal{O}(25)$. Finally, there is a characteristic flavour flow: All (light) flavours are democratically represented [2] in the final state. Therefore, strongly enhanced rates of K^0's and μ's (from strange and charm decays) represent crucial signatures for I-induced events.

The search strategy proposed here relies upon two characteristics of the hadronic final state in I-induced DIS, namely:

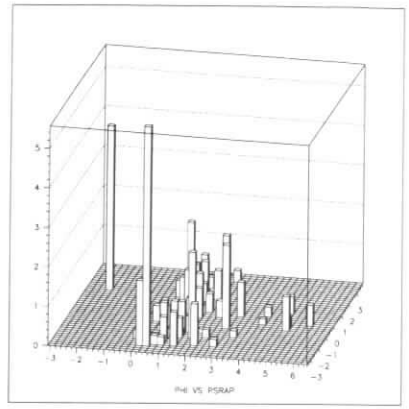

Figure 3: *Lego plot $(\eta_{\rm lab}, \phi_{\rm lab}, E_T[\text{GeV}])$ of a typical I-induced event in the HERA-lab system at $x_{\rm Bj} = 10^{-3}$.*

1. The event shape, which is determined by the isotropic production [5] of large numbers of partons and hence hadrons, in the I-subprocess rest frame.

2. The democratic production of all kinematically allowed quark flavours.

The former allows an experimental estimate of $\sqrt{s'}$ to be made. In a frame in which the virtual photon (γ^*) and the proton (P) are collinear, such as the $\gamma^* P$ centre-of-mass frame, it is easy to show that $\sqrt{s'}/2 = E_{out} = \sum_n^N |\vec{p}_n \cdot \hat{i}|$, where the E_n are the energies of the N final state hadrons (assumed massless) and $\hat{i}$ is a unit vector normal to the $\gamma^* P$ direction, $\hat{k}$, chosen such that the sum is minimised. Large values of E_{out} occur in I-induced events, whereas in (1+1) or (2+1) jet DIS events (where the +1 refers to the proton remnant) E_{out} only receives contributions due to the k_T spread of the jets. In addition, in $(1+1)$ jet events E_{in} is small, where $E_{in} = \sum_n^N |\vec{p}_n \cdot \hat{j}|$ with $\hat{i} = \hat{j} \times \hat{k}$. Events with $(2+1)$ jets have $E_{out} << E_{in}$, whereas $E_{out} \lesssim E_{in}$ for I-induced events (isotropy). The separation obtainable using E_{out} and E_{in} between events arising from higher order QCD processes, leading to the production of three or more jets, and I-induced events can be enhanced by calculating E'_{out} and E'_{in} using only hadrons in a limited range of pseudorapidity, close to the pseudorapidity at which the transverse energy is maximal. This modification is effective as the isotropic distribution of energy in the I-subprocess centre-of-mass leads to a peaked E_{out} distribution in the $\gamma^* P$ frame, with a full-width half-maximum $\sim$ 1.5 units of pseudorapidity, whereas the jets produced in higher-order QCD processes may be spread over a large pseudorapidity range. The power of an I-induced event selection based upon event shape is illustrated in Fig. 4 as is the correlation between the I-subprocess centre-of-mass energy and $2E_{out}$. The values of E_{out} and E_{in} were calculated using hadrons within 1.5 units of pseudorapidity of the mean E_T weighted pseudorapidity. The QCDINS 1.3 Monte Carlo was used to simulate the I-induced events and standard DIS was simulated using HERWIG [13]. Nominal HERA detector acceptance cuts were applied, but no allowance was made for finite detector resolution. The separation illustrated in the figure is thus better than that obtainable using the HERA detectors.

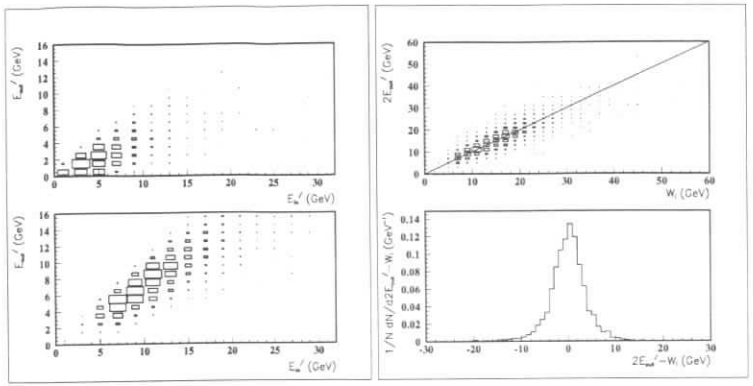

Figure 4: *Left: Distribution of I-induced (lower plot) and standard DIS events in the* (E'_{in}, E'_{out}) *plane with logarithmic z scale for the kinematic region* $0.001 < x < 0.01$, $0.1 < y < 0.6$ *and* $20 < Q^2 < 70\ GeV^2$. *Right: Correlation between* $2E_{out}$ *and the I-subprocess centre-of-mass energy,* $W' = \sqrt{s'}$.

The production of large numbers of partons in the *I*-subprocess also leads to large charged particle multiplicities in the hadronic final state (c.f. Fig. 3). This is of particular interest for an instanton search if the HERA detectors can extend their multiplicity measurements to include the region covered by the forward trackers.

The second characteristic of *I*-induced DIS events, their flavour democracy, has been used by the H1 collaboration in a recent study of strange particle production in DIS [14]. Instanton-induced events contain more strange particles than standard DIS events. The H1 measurements showed no evidence for anomalous K^0 production and hence it was possible to place an upper limit of 0.9 nb on the cross-section for *I*-induced DIS.

A second feature associated with the flavour democracy of *I*-induced events is the large number of muons they contain. These result largely from the decay of charmed particles. Unfortunately their energies are rather low, the transverse momenta of the muons in the laboratory frame is typically less than 1.5 GeV, and hence their detection is a challenging task for the experimenters.

4 Conclusions

The cross-section for instanton-induced processes in DIS at HERA is surprisingly large. Current cross-section estimates do, however, contain large uncertainties. The isotropy of the hadron production in the instanton subprocess rest frame and the democratic flavour production make a search for instanton-induced events using event shape, multiplicity and particle identification a feasible proposition. Given the uncertainties in the cross-section estimates, of highest priority for this search is the total luminosity available. Upgrades to the tracking in the forward region of the HERA detectors could improve their sensitivity to instanton-induced events, but little is gained by upgrades to the calorimetry in the forward direction.

References

[1] A. Belavin, A. Polyakov, A. Schwarz and Yu. Tyupkin, *Phys. Lett.* B **59** (1975) 85.

[2] G. 't Hooft, *Phys. Rev. Lett.* **37** (1976) 8; *Phys. Rev.* D **14** (1976) 3432; *Phys. Rev.* D **18** (1978) 2199 (Erratum).

[3] A. Ringwald, *Nucl. Phys.* B **330** (1990) 1;
O. Espinosa, *Nucl. Phys.* B **343** (1990) 310.

[4] I. Balitsky and V. Braun, *Phys. Lett.* B **314** (1993) 237.

[5] A. Ringwald and F. Schrempp, DESY 94-197, hep-ph/9411217, in: "Quarks '94", Proc. Eighth Int. Seminar, Vladimir, Russia, May 11-18, 1994, eds. D. Gigoriev et al., pp. 170-193.

[6] M. Gibbs, A. Ringwald and F. Schrempp, DESY 95-119, hep-ph/9506392, in: Proc. Workshop on Deep Inelastic Scattering and QCD, Paris, France, April 24-28, 1995, eds. J.-F. Laporte and Y. Sirois, pp. 341-344.

[7] A. Ringwald and F. Schrempp, DESY 96-125, hep-ph/9607238, to appear in: Proc. Workshop DIS96 on Deep Inelastic Scattering and Related Phenomena, Rome, Italy, April 15-19, 1996.

[8] S. Moch, A. Ringwald and F. Schrempp, to be published.

[9] M. Gibbs, A. Ringwald and F. Schrempp, to be published.

[10] V.V. Khoze and A. Ringwald, *Phys. Lett.* B **259** (1991) 106;
I. Balitsky and V. Braun, *Phys. Rev.* D **47** (1993) 1879.

[11] A. Yung, *Nucl. Phys.* B **297** (1988) 47.

[12] V. Zakharov, *Nucl. Phys.* B **353** (1991) 683;
M. Maggiore and M. Shifman, *Nucl. Phys.* B **365** (1991) 161; *Nucl. Phys.* B **371** (1991) 177;

[13] M. Seymour, Comp. Phys. Comm. **67** (1993) 465.

[14] H1 Collaboration, S. Aid et al., DESY 96-122 (1996).

Jet Production in Deep Inelastic Scattering at Next-to-Leading Order

Erwin Mirkes[a] and Dieter Zeppenfeld[b]

[a]Institut für Theoretische Teilchenphysik, Universität Karlsruhe, D-76128 Karlsruhe, Germany
[b]Department of Physics, University of Wisconsin, Madison, WI 53706, USA

Abstract: NLO corrections to jet cross sections in DIS at HERA are studied, with particular emphasis on the two jet final state. High jet transverse momenta are a good criterion for the applicability of fixed order perturbation theory. A "natural" scale choice is the average k_T^B of the jets in the Breit frame, which suggest analyzing the data in different $< k_T^B >$ intervalls.

An important topic to be studied at HERA is the production of multi-jet events in DIS, where the expected good event statistics [1] allows for precision tests of QCD [2]. Such tests require next-to-leading order (NLO) QCD corrections. Full NLO corrections for one and two-jet production cross sections and distributions are now available and implemented in the fully differential $ep \to n$ jets event generator MEPJET [3], which allows to analyze arbitrary jet definition schemes and general cuts in terms of parton 4-momenta. A variety of topics can be studied with these tools. They include: a) The determination of $\alpha_s(\mu_R)$ from dijet production over a range of scales, μ_R, b) The measurement of the gluon density in the proton (via $\gamma g \to q\bar{q}$), c) Associated forward jet production in the low x regime as a signal of BFKL dynamics [4].

The effects of NLO corrections and recombination scheme dependences on the 2-jet cross section were discussed in Refs. [3, 5, 6] already for four different jet algorithms (cone, k_T, JADE, W) . While these effects are small in the cone and k_T schemes, very large corrections can appear in the W-scheme or the modified JADE scheme, which was introduced for DIS in Ref. [7].

At leading order (LO) the W and the JADE scheme are equivalent. The NLO cross sections in the two schemes, however, can differ by almost a factor of two [3, 5], depending on the recombination scheme and on the definition of the jet resolution mass ($(M_{ij}^2 = (p_i + p_j)^2$ in the W scheme versus $M_{ij}^2 = 2E_iE_j(1 - \cos\theta_{ij})$ defined in the lab frame in the JADE scheme). Trefzger and Rosenbauer [2] find similarly large differences in the experimental jet cross sections (which are in good agreement with MEPJET predictions[1]), when the data are processed with exactly the same jet resolution mass and recombination prescription as used in the theoretical calculation. The large differences between and within the JADE and W schemes are caused by sizable single jet masses (compared to their energy), predominantly for jets in the central part of the detector. Such single jet mass effects first appear in a NLO calculation where a jet may be composed of two partons. *Clearly, theoretical calculations must be matched to experimental definitions and such potentially large single jet mass effects must be taken into account.*

[1]The two jet rate in the W scheme (with E recombination) and in the JADE scheme for corrected ZEUS data are $18.6 \pm 0.7\%$ and $8.6 \pm 0.5\%$, respectively. The corresponding NLO predictions from MEPJET for the same kinematics and the same jet definitions are 17.9% and 8.6 % (see T. Trefzger [2]).

Previous programs [8, 9] were limited to a W type algorithm[2] and are not flexible enough to take into account the effects of single jet masses or differences between recombination schemes. In addition, approximations were made to the matrix elements in these programs which are not valid in large regions of phase space [3]. These problems are reflected in inconsistent values for $\alpha_s(M_Z^2)$ [ranging, for example, from 0.114 to 0.127 in the H1 analysis [1], (see K. Rosenbauer [2])], when these programs are used to analyze the data with different recombination schemes. Because of these problems, the older programs cannot be used for precision studies at NLO in their present form [10]. In order to reduce theoretical errors, previous analyses [1] should be repeated with MEPJET or a similar flexible Monte Carlo program [11]. A first reanalysis, with MEPJET, of H1 data by K. Rosenbauer yields a markedly lower central value, $\alpha_s(M_Z^2) = 0.112$, which is *independent* of the recombination scheme (used in both data and theory), and the $\alpha_s(\mu_R^2)$ extracted from different kinematical bins follows nicely the expectation from the renormalization group equation. A similar reanalysis of the ZEUS data has already been performed by T. Trefzger, also with MEPJET.

Single jet mass effects and recombination scheme dependences are fairly small in the cone and k_T schemes [3] which, therefore, appear better suited for precision QCD tests. In the following, we concentrate on these two and the E recombination scheme. A first issue which must be addressed is the dependence of the NLO 2-jet cross section on the renormalization scale, μ_R, and the factorization scale, μ_F. The chosen scale should be characteristic for the QCD portion of the process at hand. For dijet invariant masses, m_{jj}, below Q we are in the DIS limit and Q is expected to be the relevant scale. For large dijet invariant masses, however, $m_{jj} \gg Q$, the situation is more like in dijet production at hadron colliders and the jet transverse momenta set the physical scale of the process. A variable which interpolates between these two limits is the sum of jet k_Ts in the Breit frame [6], $\sum_j k_T^B(j)$. Here, $(k_T^B(j))^2$ is defined by $2\,E_j^2(1 - \cos\theta_{jP})$, where the subscripts j and P denote the jet and proton, respectively. $\sum_j k_T^B(j)$ approaches Q in the parton limit and it corresponds to the sum of jet transverse momenta, p_T^B, (with respect to the γ^*-proton direction) when the photon virtuality becomes negligible. We use this "natural" scale for multi-jet production in DIS in the following.

A good measure of the improvement of a NLO over a LO prediction is provided by the residual scale dependence of the cross section. As an example we use the k_T algorithm (implemented in the Breit frame) as described in Ref. [12]. One finds very similar results for the cone scheme. Kinematical cuts are imposed on the final state lepton and jets to closely model the H1 event selection [13]. More specifically, we require $10\ \text{GeV}^2 < Q^2 < 10000\ \text{GeV}^2$, $0.01 < y < 1$, $0.0001 < x < 1$, and an energy cut of $E(l') > 10$ GeV and a cut on the pseudo-rapidity $\eta = -\ln\tan(\theta/2)$ of the scattered lepton. This η cut is Q^2 dependent: $-2.794 < \eta(l') < -1.735$ for $Q^2 < 100\ \text{GeV}^2$ and $-1.317 < \eta(l') < 2.436$ for $Q^2 > 100\ \text{GeV}^2$. In addition, we require $-1.154 < \eta(j) < 2.436$. The hard scattering scale, E_T^2, in the k_T algorithm is fixed to $40\ \text{GeV}^2$ and $y_{cut} = 1$ is the resolution parameter for resolving the macro-jets.

Fig. 1a shows the scale dependence of the dijet cross section in LO and NLO for the k_T scheme. The LO (NLO) results are based on the LO (NLO) parton distributions of GRV [14]

[2]DISJET [9] and PROJET [8] are largely based on the fact that the calculation of the jet resolution mass squared, M_{ij}^2, can be done in a lorentz invariant way, as in the W scheme. Only in LO does this agree with the JADE definition, defined in the lab frame.

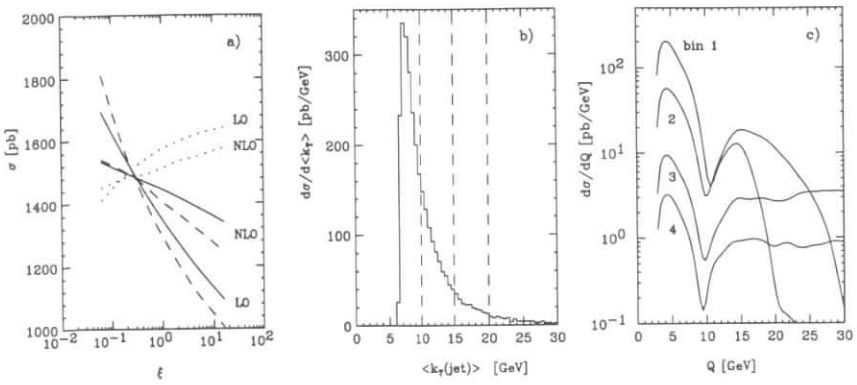

Figure 1: a) Dependence of the two-jet exclusive cross section in the k_T scheme on the scale factor ξ. The solid curves are for $\mu_R^2 = \mu_F^2 = \xi\ (\sum_i\ k_T^B(i))^2$, while for the dashed (dotted) curves only $\xi_R = \xi\ (\xi_F = \xi)$ is varied but $\xi_F = 1/4\ (\xi_R = 1/4)$ is fixed. Results are shown for the LO and NLO calculations. b) NLO $< k_T^B >$ distribution for the two-jet exclusive cross section. c) NLO Q distribution for the four bins in b).

together with the one-loop (two-loop) formula with five flavors for the strong coupling constant. The scale factors ξ are defined via

$$\mu_R^2 = \xi_R\ (\sum_i\ k_T^B(i))^2\,, \qquad \mu_F^2 = \xi_F\ (\sum_i\ k_T^B(i))^2\,. \tag{1}$$

The LO variation by a factor 1.55 is reduced to a 11% variation at NLO when both scales are varied simultaneously over the plotted range (solid curves). Also shown is the $\xi = \xi_R$ dependence of LO and NLO cross sections at fixed $\xi_F = 1/4$ (dashed curves) and the $\xi = \xi_F$ dependence of LO and NLO cross sections at fixed $\xi_R = 1/4$ (dotted curves). The NLO corrections substantially reduce the renormalization and factorization scale dependence. If not stated otherwise, we fix the scale factors to $\xi = \xi_R = \xi_F = 1/4$ in the following discussion.

Let us denote the average k_T^B of the (two) jets in the Breit frame by

$$< k_T^B >= \frac{1}{2}\ (\sum_{j=1,2}\ k_T^B(j)). \tag{2}$$

Fig. 1b shows the $< k_T^B >$ distribution for the NLO 2-jet exclusive cross section in the k_T scheme. We divide the distribution into four $< k_T^B >$ bins (suggesting a separate determination of $\alpha_s(< k_T^B >^2)$ for each). The dependence of the NLO cross section on the scale factor, ξ, is shown in Table 1 for individual bins, and is typically below $\pm 5\%$. These fairly small theoretical uncertainties in the k_T algorithm are due to the relatively high value of the hard scattering scale, $E_T^2 > 40\ \mathrm{GeV}^2$ (or roughly equivalent cuts of $p_T^{jab}, p_T^B \gtrsim 5$ GeV on the jets in the cone scheme). Thus a precise measurement of $\alpha_s(< k_T^B >^2)$ should be possible.

The Q distributions for the NLO exclusive dijet cross section for these four bins in Fig. 1c show that even events with very large $< k_T^B >$ are dominated by the small Q^2 region. (The dips in the Q distribution around $Q = 10$ GeV are a consequence of the rapidity cuts on the

Table 1: NLO (LO) 2-jet exlusive cross sections in pb for the four $< k_T^B >$ bins and their sum. Results are shown for three different choices of the scale factor $\xi = \xi_R = \xi_F$.

	$\xi = 1$	$\xi = 1/4$	$\xi = 1/16$
bin 1: 5 GeV $< < k_T^B > <$ 10 GeV	881 (821)	900 (907)	934 (999)
bin 2: 10 GeV $< < k_T^B > <$ 15 GeV	396 (357)	415 (403)	433 (461)
bin 3: 15 GeV $< < k_T^B > <$ 20 GeV	105 (102)	107 (118)	106 (137)
bin 4: 20 GeV $< < k_T^B >$	63 (68)	64 (80)	57 (95)
sum of bins	1445 (1348)	1486 (1508)	1530 (1692)

scattered lepton, see above). Thus there is a qualitative difference betwen scale choices tied to $< k_T^B >$ versus scales related to Q. One finds that μ_R^2, $\mu_F^2 = \xi Q^2$ gives a much larger ξ dependence for dijet events at NLO than the ones exhibited in Fig. 1a [3]. This is the reason why scales tied to k_T^B are better suited for QCD analyses of multijet events in DIS.

References

[1] H1 Collaboration, Phys. Lett. **B346** (1995) 415;
ZEUS Collaboration, Phys. Lett. **B363** (1995) 201.

[2] K. Rosenbauer, talk presented at the DIS 96 workshop in Rome;
T. Trefzger, talk presented at the DIS 96 workshop in Rome.

[3] E. Mirkes and D. Zeppenfeld, Phys. Lett. **B380** (1996) 105, [hep-ph/9511448].

[4] E. Mirkes and D. Zeppenfeld, these proceedings;
For more details, see MADPH-96-957, TTP96-38, [hep-ph/9609231].

[5] E. Mirkes and D. Zeppenfeld, Acta Phys. Pol. **B27** (1996) 1393, [hep-ph/9604281].

[6] E. Mirkes and D. Zeppenfeld, In the proceedings of the "QCD and QED in Higher Orders" 1996 Zeuthen Workshop on Elementary Particle Theory, April 22-26, (1996), [hep-ph/9606332]; see also [hep-ph/9608201].

[7] J.G. Körner, E. Mirkes and G. Schuler, Int. J. Mod. Phys. **A4** (1989) 1781;
T. Brodkorb, J.G. Körner, E. Mirkes, and G. Schuler, Z. Phys. **C44** (1989) 415.

[8] D. Graudenz, Comp. Phys. Commun. **92** (1995) 65; Phys. Rev. **D49** (1994) 3291.

[9] T. Brodkorb and E. Mirkes, Z. Phys. **C66** (1995) 141, [hep-ph/9402362, hep-ph/9404287];
T. Brodkorb and J.G. Körner, Z. Phys. **C54** (1992) 519.

[10] D. Kosower, talk presented at the DIS 96 workshop in Rome.

[11] S. Catani and M. Seymour, these proceedings.

[12] S. Catani, Y.L. Dokshitzer and B.R. Webber, Phys. Lett. **B285** (1992) 291.

[13] We thank Ch. Niedzballa, K. Rabbertz and K. Rosenbauer for this information.

[14] M. Glück, E. Reya and A. Vogt, Z. Phys. **C67** (1995) 433.

NLO QCD calculations in DIS at HERA based on the dipole formalism

S. Catani[a], M.H. Seymour[b]

[a] I.N.F.N., Sezione di Firenze, and Dipartimento di Fisica, Università di Firenze, Largo E. Fermi 2, I-50125 Florence, Italy
[b] Theory Division, CERN, CH-1211 Geneva 23, Switzerland

Abstract: We briefly describe a new general algorithm for carrying out QCD calculations to next-to-leading order in perturbation theory. The algorithm can be used for computing arbitrary jet cross sections in arbitrary processes and can be straightforwardly implemented in general-purpose Monte Carlo programs. We show numerical results for the specific case of jet cross sections in deep inelastic scattering at HERA energies.

1 Introduction

In order to make quantitative predictions in perturbative QCD, it is essential to work to (at least) next-to-leading order (NLO). However, this is far from straightforward because for all but the simplest quantities, the necessary phase-space integrals are too difficult to do analytically, making numerical methods essential. But the individual integrals are divergent, and only after they have been regularized and combined is the result finite. The usual prescription, dimensional regularization, involves working in a fractional number of dimensions, making analytical methods essential.

To avoid this dilemma, one must somehow set up the calculation such that the singular parts can be treated analytically, while the full complexity of the integrals can be treated numerically. Efficient techniques have been set up to do this, at least to NLO, during the last few years.

A new general algorithm was recently presented [1], which can be used to compute arbitrary jet cross sections in arbitrary processes. It is based on two key ingredients: the *subtraction method* for cancelling the divergences between different contributions; and the *dipole factorization theorems* for the universal (process-independent) analytical treatment of individual divergent terms. These are sufficient to write a general-purpose Monte Carlo program in which any jet quantity can be calculated simply by making the appropriate histogram in a user routine.

In this contribution we give a brief summary of these two ingredients (more details and references to other general methods can be found in Refs. [1]–[3]) and show numerical results for the specific case of jets in deep-inelastic lepton-hadron scattering (DIS) at HERA energies.

A Monte Carlo program for jet calculations in DIS based on a different method [4] is presented in Ref. [5]. Previous calculations [6, 7] were limited to a specific jet definition and used approximated methods.

2 The Dipole Formalism

2.1 The subtraction method

Considering the case of DIS (full details for other processes are given in Ref. [1]), the general structure of a QCD cross section in NLO is:

$$\sigma = \sum_a f_a \times (\sigma_a^{LO} + \sigma_a^{NLO}) \tag{1}$$

where the symbol $\times$ denotes the convolution with the density f_a of the parton a in the incoming hadron and the leading-order (LO) cross section σ_a^{LO} is obtained by integrating the fully exclusive Born cross section $d\sigma_a^B$ over the phase space for the corresponding jet quantity. We suppose that this LO calculation involves m final-state partons, and write:

$$\sigma_a^{LO} = \int_m d\sigma_a^B \,. \tag{2}$$

At NLO, we receive contributions from real and virtual processes (we assume that the ultraviolet divergences of the virtual term are already renormalized) and from a collinear counterterm that is necessary to define the scale-dependent parton densities:

$$\sigma_a^{NLO} = \int_{m+1} d\sigma_a^R + \int_m \left[d\sigma_a^V + d\sigma_a^C\right] \,. \tag{3}$$

As is well known, each of these is separately divergent, although their sum is finite. These divergences are regulated by working in $d = 4 - 2\epsilon$ dimensions, where they are replaced by singularities in $1/\epsilon$. Their cancellation only becomes manifest once the separate phase space integrals have been performed.

The essence of the subtraction method [8] is to use the *exact* identity

$$\sigma_a^{NLO} = \int_{m+1} \left[d\sigma_a^R - d\sigma_a^A\right] + \int_{m+1} d\sigma_a^A + \int_m \left[d\sigma_a^V + d\sigma_a^C\right] \,, \tag{4}$$

which is obtained by subtracting and adding back the 'approximate' (or 'fake') cross section contribution $d\sigma_a^A$, which has to fulfil two main properties. Firstly, it must exactly match the singular behaviour (in d dimensions) of $d\sigma_a^R$ itself. Thus it acts as a *local* counterterm for $d\sigma_a^R$ and one can safely perform the limit $\epsilon \to 0$ under the integral sign in the first term on the right-hand side of Eq. (4). Secondly, $d\sigma_a^A$ must be analytically integrable (in d dimensions) over the one-parton subspace leading to the divergences. Thus we can rewrite the integral in the last term of Eq. (4), to obtain

$$\sigma_a^{NLO} = \int_{m+1} \left[\left(d\sigma_a^R\right)_{\epsilon=0} - \left(d\sigma_a^A\right)_{\epsilon=0}\right] + \int_m \left[d\sigma_a^V + d\sigma_a^C + \int_1 d\sigma_a^A\right]_{\epsilon=0} \,. \tag{5}$$

Performing the analytic integration $\int_1 d\sigma_a^A$, one obtains ϵ-pole contributions that can be combined with those in $d\sigma_a^V$ and $d\sigma_a^C$, thus cancelling all the divergences. Equation (5) can be easily implemented in a 'partonic Monte Carlo' program that generates appropriately weighted partonic events with $m+1$ final-state partons and events with m partons.

2.2 Dipole factorization and universal subtraction term

The fake cross section $d\sigma_a^A$ can be constructed in a fully process-independent way, by using the factorizing properties of gauge theories. Specifically, in the soft and collinear limits, which give rise to the divergences, the factorization theorems can be used to write the cross section as the contraction of the Born cross section with universal soft and collinear factors (provided that colour and spin correlations are retained). However, these theorems are only valid in the exactly singular limits, and great care should be used in extrapolating them away from these limits. In particular, a careful treatment of momentum conservation is required. Care has also to be taken in order to avoid double counting the soft and collinear divergences in their overlapping region (e.g. when a gluon is both soft and collinear to another parton). The use of the dipole factorization theorem introduced in Ref. [2] allows one to overcome these difficulties in a straightforward way.

The dipole factorization formulae relate the singular behaviour of $\mathcal{M}_{m+1}$, the tree-level matrix element with $m+1$ partons, to $\mathcal{M}_m$. They have the following symbolic structure:

$$|\mathcal{M}_{m+1}(p_1,...,p_{m+1})|^2 = |\mathcal{M}_m(\tilde{p}_1,...,\tilde{p}_m)|^2 \otimes \boldsymbol{V}_{ij} + \dots \quad . \tag{6}$$

The dots on the right-hand side stand for contributions that are not singular when $p_i \cdot p_j \to 0$. The dipole splitting functions $\boldsymbol{V}_{ij}$ are universal (process-independent) singular factors that depend on the momenta and quantum numbers of the m partons in the tree-level matrix element $|\mathcal{M}_m|^2$. Colour and helicity correlations are denoted by the symbol $\otimes$. The set $\tilde{p}_1,...,\tilde{p}_m$ of modified momenta on the right-hand side of Eq. (6) is defined starting from the original $m+1$ parton momenta in such a way that the m partons in $|\mathcal{M}_m|^2$ are physical, that is, they are on-shell and energy-momentum conservation is implemented exactly. The detailed expressions for these parton momenta and for the dipole splitting functions are given in Ref. [1].

Equation (6) provides a *single* formula that approximates the real matrix element $|\mathcal{M}_{m+1}|^2$ for an arbitrary process, in *all* of its singular limits. These limits are approached smoothly, avoiding double counting of overlapping soft and collinear singularities. Furthermore, the precise definition of the m modified momenta allows an *exact* factorization of the $m+1$-parton phase space, so that the universal dipole splitting function can be integrated once and for all.

This factorization, which is valid for the total phase space, is not sufficient to provide a universal fake cross section however, as its phase space should depend on the particular jet observable being considered. The fact that the m parton momenta are physical provides a simple way to implement this dependence. We construct $d\sigma_a^A$ by adding the dipole contributions on the right-hand side of Eq. (6) and for each contribution we calculate the jet observable not from the original $m+1$ parton momenta, but from the corresponding m parton momenta, $\tilde{p}_1,...,\tilde{p}_m$. Since these are fixed during the analytical integration, it can be performed without any knowledge of the jet observable.

3 Final Results

Refering to Eq. (5), the final procedure is then straightforward. The calculation of any jet quantity to NLO consists of an $m+1$-parton integral and an m-parton integral. These can be performed separately using standard Monte Carlo methods.

For the $m+1$-parton integral, a phase-space point is generated and the corresponding real matrix element in $d\sigma_a^R$ is calculated. These are passed to a user routine, which can analyse the

event in any way and histogram any quantities of interest. Next, for each dipole term (there are at most 10 of them in the calculation of (2+1)-jet observables in DIS) in $d\sigma_a^A$, the set of m parton momenta is derived from the same phase-space point and the corresponding dipole contribution is calculated. These are also given to the user routine. They are such that for any singular $m+1$-parton configuration, one or more of the m-parton configurations becomes indistinguishable from it, so that they fall in the same bin of any histogram. Simultaneously, the real matrix element and dipole term will have equal and opposite weights, so that the total contribution to that histogram bin is finite. Thus the first integral of Eq. (5) is finite.

The m-parton integral in Eq. (5) has a simpler structure: it is identical to the LO integration in Eq. (2), but with the Born term replaced by the finite sum of the virtual matrix element in $d\sigma_a^V$, the collinear counterterm $d\sigma_a^C$ and the analytical integral of the dipole contributions in $d\sigma_a^A$ (to be precise, the second term on the right-hand side of Eq. (5) involves an additional one-dimensional convolution [1], which is a finite remainder that is left after the cancellation of the singularities in $d\sigma_a^C$).

Note that our algorithm does not require the convolution with the parton densities f_a to be made during Monte Carlo integration. One is free to choose either to calculate the hadron-level cross section in Eq. (1), thus including the convolution, or the parton-level cross section $\sigma_a = \sigma_a^{LO} + \sigma_a^{NLO}$ as a function of the partonic momentum fraction. The latter can then be convoluted with the parton densities after Monte Carlo integration. This can be extremely useful in many respects. For instance, one can produce cross sections with a wide variety of parton densities, or study the scheme- and scale-dependence of the results without having to reintegrate for each new scheme or scale.

For the specific case of jet observables in DIS, we have implemented the algorithm as a Monte Carlo program, which can be obtained from `http://surya11.cern.ch/users/seymour/nlo/`. The program uses the matrix elements evaluated by the Leiden group [9]. In Fig. 1a we show as an example the differential jet rate as a function of jet resolution parameter, f_{cut}, using the $k_\perp$ jet algorithm [10]. We see that the NLO corrections are generally small and positive, except at very small f_{cut} (where large logarithmic terms, $-\alpha_s \log^2 f_{cut}$ arise at each higher order). In Fig. 1b, we show the variation of the jet rate at a fixed f_{cut} with factorization and renormalization scales. The scale dependence is considerably smaller at NLO.

4 Conclusion

The subtraction method provides an *exact* way to calculate arbitrary quantities in a given process using a general purpose Monte Carlo program. The dipole formalism provides a way to construct such a program from process-independent components. Recent applications have included jets in DIS.

We have constructed a Monte Carlo program that can be used to carry out NLO QCD calculations for any infrared- and collinear-safe observable (jet cross sections using different jet algorithms, event shapes, energy correlations and so forth) in $(2+1)$-jet configurations in DIS. Possible applications to future physics at HERA include determinations of the strong coupling constant $\alpha_S(Q)$ and extraction of the parton densities. More details of the program, and its results, will be given elsewhere.

Acknowledgments. This research is supported in part by EEC Programme *Human Capital and Mobility*, Network *Physics at High Energy Colliders*, contract CHRX-CT93-0357 (DG 12

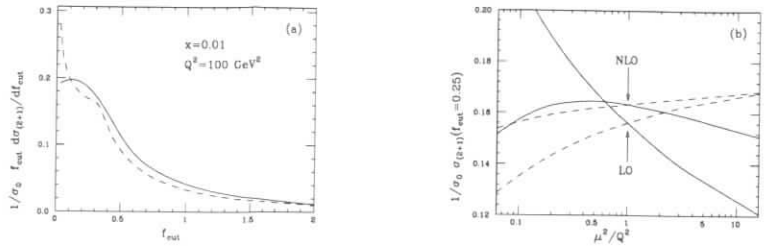

Figure 1: Jet cross sections in ep collisions at HERA energies ($\sqrt{s}$ = 300 GeV). (a) The distribution of resolution parameter f_{cut} at which DIS events are resolved into $(2+1)$ jets according to the $k_\perp$ jet algorithm. Curves are LO (dashed) and NLO (solid) using factorization and renormalization scales equal to Q^2, and the MRS D$-'$ distribution functions. Both curves are normalized to the LO cross section. (b) The rate of events with exactly $(2+1)$ jets at f_{cut} = 0.25 with variation of renormalization (solid) and factorization (dashed) scales. Normalization is again the LO cross section with fixed factorization scale.

COMA). We wish to thank P.J. Rijken and W.L. van Neerven for having provided the matrix elements for us.

References

[1] S. Catani and M.H. Seymour, preprint CERN-TH/96-29 (hep-ph/9605323).

[2] S. Catani and M.H. Seymour, Phys. Lett. 378B (1996) 287.

[3] S. Catani and M.H. Seymour, preprint CERN-TH/96-181 (hep-ph/9607318), preprint CERN-TH/96-239 (hep-ph/9609237).

[4] W.T. Giele, E.W.N. Glover and D.A. Kosower, Nucl. Phys. B403 (1993) 633.

[5] E. Mirkes and D. Zeppenfeld, Phys. Lett. 380B (1996) 205, preprint TTP-96-30 (hep-ph/9608201) and in these Proceedings.

[6] D. Graudenz, Phys. Rev. D 49 (1994) 3291, Comp. Phys. Commun. 92 (1995) 65.

[7] T. Brodkorb and E. Mirkes, preprint MAD-PH-821 (hep-ph/9404287).

[8] R.K. Ellis, D.A. Ross and A.E. Terrano, Nucl. Phys. B178 (1981) 421; Z. Kunszt and P. Nason, in 'Z Physics at LEP 1', CERN 89-08, vol. 1, p. 373; Z. Kunszt and D.E. Soper, Phys. Rev. D 46 (1992) 192.

[9] E.B. Zijlstra and W.L. van Neerven , Nucl. Phys. B383 (1992) 525.

[10] S. Catani, Yu.L. Dokshitzer and B.R. Webber, Phys. Lett. 285B (1992) 291, Phys. Lett. 322B (1994) 263; B.R. Webber, J. Phys. G19 (1993) 1567; S. Catani, Yu.L. Dokshitzer, M.H. Seymour and B.R. Webber, Nucl. Phys. B406 (1993) 187.

Prospects of a Determination of α_S from Jet Rates

Th. Hadig, Ch. Niedzballa, K. Rabbertz, K. Rosenbauer

I. Physikalisches Institut der RWTH Aachen
Sommerfeldstr. 28, D-52056 Aachen, Germany

Abstract: Prospects of the direct determination of the running strong coupling constant $\alpha_S(Q^2)$[1] based on jet rates in deep inelastic ep-scattering at HERA for a future integrated H1-luminosity up to 1000 pb^{-1} will be presented. After a few introductory remarks on the basic method the error treatment in the present α_S analysis will be briefly reviewed [1, 2, 3]. Subsequently the impact of an enlarged luminosity on the errors of α_S in the three investigated Q^2 bins and at the scale equal to the mass squared of the Z^0-boson, M_Z^2, is estimated.

1 Introduction

The physics of jets in deep inelastic scattering is a promising subject at HERA. Considering the current discrepancy between α_S measurements from fixed target deep inelastic scattering experiments, $\alpha_S(M_Z^2) = 0.112 \pm 0.002(\text{stat.} \oplus \text{sys.}) \pm 0.004$ (scale uncert.) [4], and for example hadronic event shapes in the experiments at the SLC and LEP colliders, $\alpha_S(M_Z^2) = 0.122 \pm 0.007$ [4], HERA can contribute to a better understanding. Therefore a very precise measurement of $\alpha_S(M_Z^2)$ is aimed at to draw a conclusion by HERA.

The error discussion on $\alpha_S(Q^2)$ presented here is based on an extraction of the running strong coupling constant essentially following the strategy of the previous measurement [5]. The fractional (2+1)-jet rate $R_{2+1}(Q^2, y_c) = \frac{\sigma_{2+1}(Q^2, y_c)}{\sigma_{\text{tot}}(Q^2)} = f(\alpha_S(Q^2))$ is chosen to explore the running of $\alpha_S(Q^2)$ [6], where $\sigma_{\text{tot}}(Q^2)$ represents the sum of the (1+1)- and (2+1)-jet cross sections. The resolution criterion of the applied modified JADE [9] jet algorithm[2] is $y_{ij} = 2E_iE_j(1-\cos\theta_{ij})/W^2 > y_c$, with the resolution parameter y_c set to 0.02 in this analysis. Here W^2 denotes the invariant mass squared of the total hadronic final state. Since the proton remnant, which can only partially be observed in the detector, is included in the clustered objects, the algorithm takes into account a pseudo-particle representing the missing longitudinal momentum in the measured events. Then R_{2+1} is obtained by dividing the number of events with two current jets observed in the final acceptance region, N_{2+1}, by N_{tot}, the number of events with one or two jets in this region. Using a full event generator like LEPTO 6.3 [10], these measured jet rates at the detector level are corrected to the parton level. Here they can be compared with NLO, i.e. up to $\mathcal{O}(\alpha_S^2)$, QCD predictions, which are available in the PROJET and MEPJET Monte Carlo integration programs [7, 8]. Based on the independent α_S measurements in bins of Q^2 with their statistical errors a fit to the renormalization group equation (RGE) is performed as discussed in [5]. Afterwards a value for $\alpha_S(M_Z^2)$ is evaluated.

[1] In the study presented here, the renormalization and factorization scales μ_r^2 and μ_f^2 are identified with Q^2, the absolute four-momentum transfer squared between the in- and outgoing electron.

[2] Two objects i and j are recombined to a new one k by taking the sum of the four-momentum-vectors: $p_k = p_i + p_j$.

2 On the error determination

The present analysis is based on data taken in 1994 with the H1-detector corresponding to an integrated luminosity of $\mathcal{L} = 2.74$ pb^{-1}. A range of 150 GeV^2 $< Q^2 <$ 4000 GeV^2 was selected, where the (2+1)-jet cross section is dominated by quark initiated processes and the corresponding parton densities are well known.

The use of PROJET as in earlier analyses [1, 5] results in $\alpha_S(M_Z^2) = 0.124 \pm 0.006(\text{stat.}) \pm 0.008(\text{sys.})$ [2, 3], which, in view of theoretical discrepancies when PROJET is replaced by MEPJET, cannot be taken as a measured value of α_S. For the purpose of this study the explicit value of $\alpha_S(M_Z^2)$ can be considered as arbitrary and only the determined errors are of interest. The event selection requirements are: $W^2 > 5000$ GeV^2, $E_e > 11$ GeV, $10° < \theta_e < 150°$, and $y_e < 0.7$. To suppress higher order QCD effects a jet acceptance cut of $10° < \theta_{jet} < 145°$ is applied and in addition, for (2+1)-jet events, $z_p > 0.1$. In the CMS of the hard subprocess z_p is defined by the smaller (with respect to the incoming parton) polar angle θ^*_{jet} of the two current jets: $z_p = \frac{1}{2}(1 - \cos\theta^*_{jet})$.

The systematic experimental and theoretical error on $\alpha_S(M_Z^2)$ was estimated by analyzing different scenarios taking into account possible correlations between the error sources. For this task the cuts relevant for the jet analysis were varied around their central values as defined above. The error includes uncertainties due to detector effects, y_c, acceptance cuts, QCD models, hadronization effects, parton densities (and the Λ_{QCD} used therein), μ_r and μ_f. The final systematic experimental (± 0.006) and theoretical error (± 0.006) was taken from the maximum spread of the fit results of all the corresponding scenarios investigated. Their quadratic sum is taken as the total systematic error.

As errors on the measured values of $\alpha_S(Q^2)$ in the three Q^2 bins the spread of all values of the different cut scenarios belonging to each Q^2 bin is considered as the systematic error. The total systematic error on $\alpha_S(Q^2)$ is given in the same way as described above. This procedure assumes that errors in the different Q^2 bins are uncorrelated and gives an upper estimate of the true systematic error. The statistical and total systematic error are summed in quadrature to give the total error.

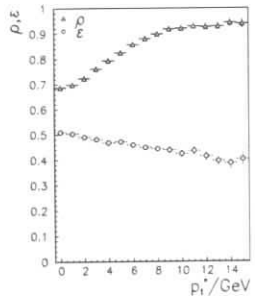

$p_t^* > 0$ GeV	N_1	N_2
N^1	75.74%	9.66%
N^2	4.57%	10.03%

$p_t^* > 15$ GeV	N_1	N_2
N^1	98.20%	1.04%
N^2	0.05%	0.71%

Figure 1: *Purity $\rho = N_2^2/(N_2^2 + N_1^2)$ and efficiency $\varepsilon = N_2^2/(N_2^2 + N_2^1)$ of the jet classification after kinematical cuts in dependence of a p_t^* cut, where N_n^m denotes the number of simulated events which are classified as $(n+1)$-jet events at the parton level and as $(m+1)$-jet events at the detector level. In addition, the correlation matrices for $p_t^* > 0$ GeV and $p_t^* > 15$ GeV are explicitly given.*

3 Error estimate for increased luminosity

The systematic experimental error in the present analysis is dominated by the error due to the hadronic energy scale (4% uncertainty). Therefore a realistic hadronic energy scale uncertainty of 2% [11] is assumed for the estimation of the future experimental error. The systematic theoretical error is dominated by parton shower effects and hadronization parameters/models estimated with LEPTO and HERWIG [12]. At higher luminosity it is possible to reduce this error by a cut on the transverse momentum p_t^* of the two current jets in the hadronic centre-of-mass system, because the jets become narrower with increasing p_t^*. Besides a p_t^* cut improves the purity of the jet classification as shown in Fig. 1. In order to estimate the effects of different p_t^* cuts on the error, the parton and hadron levels are studied explicitly for different parton shower and hadronization parameters in LEPTO while the correction factor from the hadron to the detector level is taken over from the present analysis. Here the theoretical cross sections are calculated with MEPJET. It is assumed that the behavior of the uncertainty due to HERWIG tends to be similar to that of the LEPTO parameters.

The resulting error estimations are summarized in the tables 1 and 2. In addition, Fig. 2 compares the errors of the present analysis [2, 3] and the error estimations for an integrated luminosity of $\mathcal{L} = 250$ pb^{-1} (with and without a cut $p_t^* > 15$ GeV) with measurements by other experiments.

4 Conclusion

To achieve a precision measurement of $\alpha_S(M_Z^2)$ and to prove the running of the strong coupling constant according to the RGE at HERA high luminosity is needed. In that case the systematic uncertainties can be reduced significantly and the errors can be expected to reach a magnitude comparable to the error of the present world average.

Luminosities above 250 pb^{-1} might allow a better understanding of the hadronic energy scale than assumed here, possibly leading to a decrease in the systematic experimental error. For very high luminosity it might even be feasible to use a higher p_t^* cut in order to reduce the systematic uncertainties and migrations in the jet classification further.

	$\mathcal{L} = 2.74$ pb^{-1}			$\mathcal{L} = 250$ pb^{-1}			$\mathcal{L} = 1000$ pb^{-1}		
	stat	sys	tot	stat	sys	tot	stat	sys	tot
$p_t^* > 0$ GeV	0.006	0.008	0.010	0.0006	0.007	0.007	0.0003	0.007	0.007
$p_t^* > 10$ GeV				0.0008	0.006	0.006	0.0004	0.006	0.006
$p_t^* > 15$ GeV				0.0013	$^{+0.004}_{-0.005}$	$^{+0.004}_{-0.005}$	0.0007	$^{+0.004}_{-0.005}$	$^{+0.004}_{-0.005}$

Table 1: *The statistical, systematic and total errors on $\alpha_S(M_Z^2)$ in the present analysis and for an increased luminosity for several p_t^* cuts.*

Q^2 range	$\mathcal{L} = 2.74$ pb^{-1}				$\mathcal{L} = 250$ pb^{-1}			$\mathcal{L} = 1000$ pb^{-1}		
[GeV^2]	$\alpha_S(Q^2)$	stat	sys	tot	stat	sys	tot	stat	sys	tot
150-300	0.202	0.020	$^{+0.027}_{-0.035}$	$^{+0.034}_{-0.040}$	0.002	$^{+0.027}_{-0.035}$	$^{+0.027}_{-0.035}$	0.001	$^{+0.027}_{-0.035}$	$^{+0.027}_{-0.035}$
300-700	0.149	0.016	$^{+0.032}_{-0.012}$	$^{+0.036}_{-0.020}$	0.002	$^{+0.032}_{-0.006}$	$^{+0.032}_{-0.006}$	0.001	$^{+0.032}_{-0.006}$	$^{+0.032}_{-0.006}$
700-4000	0.137	0.018	$^{+0.013}_{-0.021}$	$^{+0.022}_{-0.028}$	0.002	$^{+0.010}_{-0.021}$	$^{+0.010}_{-0.021}$	0.001	$^{+0.010}_{-0.021}$	$^{+0.010}_{-0.021}$
150-300	0.202				0.003	$^{+0.026}_{-0.033}$	$^{+0.026}_{-0.033}$	0.001	$^{+0.026}_{-0.033}$	$^{+0.026}_{-0.033}$
300-700	0.149				0.002	$^{+0.031}_{-0.005}$	$^{+0.031}_{-0.005}$	0.001	$^{+0.031}_{-0.005}$	$^{+0.031}_{-0.005}$
700-4000	0.137				0.003	$^{+0.010}_{-0.021}$	$^{+0.010}_{-0.021}$	0.001	$^{+0.010}_{-0.021}$	$^{+0.010}_{-0.021}$
150-300	0.202				0.004	$^{+0.025}_{-0.032}$	$^{+0.025}_{-0.032}$	0.002	$^{+0.025}_{-0.032}$	$^{+0.025}_{-0.032}$
300-700	0.149				0.004	$^{+0.030}_{-0.004}$	$^{+0.030}_{-0.006}$	0.002	$^{+0.030}_{-0.004}$	$^{+0.030}_{-0.004}$
700-4000	0.137				0.004	$^{+0.008}_{-0.020}$	$^{+0.009}_{-0.020}$	0.002	$^{+0.008}_{-0.020}$	$^{+0.008}_{-0.020}$

Table 2: *The statistical, systematic and total errors on $\alpha_S(Q^2)$ in the three Q^2 bins in the present analysis and for an increased luminosity without (first part) and with a p_t^* cut (> 10 GeV: second part; > 15 GeV: third part). For the scenarios at high luminosity studied here the total error is dominated by systematics.*

Acknowledgments

This work was supported in part by the Bundesministerium für Bildung und Forschung and the Deutsche Forschungsgemeinschaft. It is a pleasure to thank S. Bethke for making the α_S summary plots available to us.

References

[1] H1 Collaboration, "Determination of the Strong Coupling Constant α_S in Deep Inelastic *ep* Scattering at HERA", paper EPS-0485 submitted to the 1995 Europhysics Conference, Brussels, Belgium.

[2] M. Jaffré, on behalf the H1 and ZEUS collaborations, "Recent results on physics with jets at HERA", talk given at Les Recontres de Physique de la Vallée d'Aoste, La Thuile, Italy, March 3-9 1996.

[3] K. Rosenbauer, on behalf of the H1 collaboration, "Determination of α_S", talk given at the Workshop on Deep Inelastic Scattering and Related Phenomena (DIS 96), Rome, Italy, Apr. 15-19 1996.

[4] Particle Data Group, L. Montanet et al., Phys. Rev. **D54** (1996) 1–720.

[5] H1 Collaboration, T. Ahmed et al., Phys. Lett. **B346** (1995) 415.

[6] R. Nisius, PhD thesis, Aachen, PITHA 94/21 (1994).

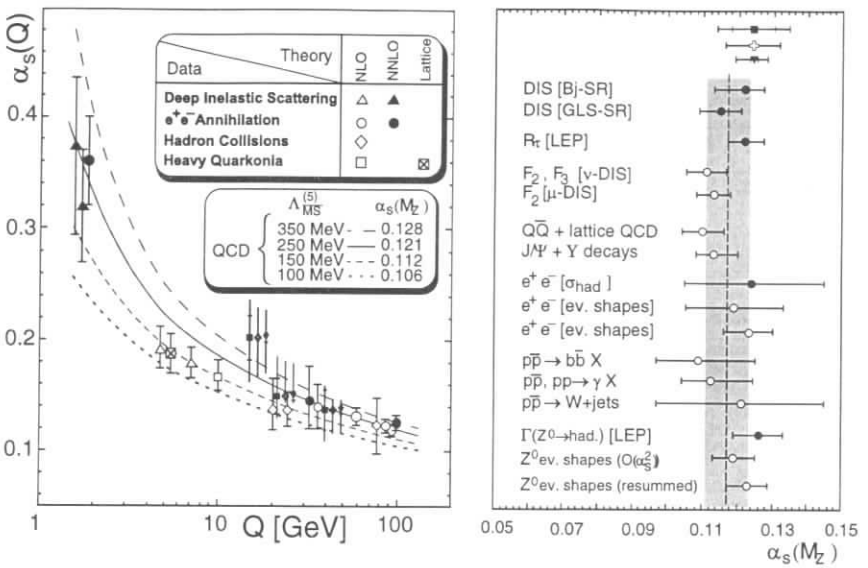

Figure 2: *Errors on the $\alpha_S(Q^2)$ (left plot) in the three different Q^2 bins for the present H1-analysis (■) (the inner error bar corresponds to the statistical error and the full error bar to the total error) and error estimates for an integrated luminosity of $\mathcal{L} = 250$ pb^{-1} without (+) and with (▾) a cut $p_t^* > 15$ GeV in comparison to α_S measurements by other experiments [13]. The plot on the right hand side shows a comparison for the derived/expected $\alpha_S(M_Z^2)$ errors. The shaded area represents the world average of $\alpha_S(M_Z^2) = 0.118 \pm 0.005$ [13].*

[7] D. Graudenz, Comput. Phys. Commun. 92 (1995) 65.

[8] E. Mirkes and D. Zeppenfeld, Phys. Lett. **B380** (1996) 105.

[9] JADE Collaboration, W. Bartel et al., Z. Phys. **C33** (1986) 23;
D. Graudenz and N. Magnussen, in: Proc. Workshop 'Physics at HERA', DESY, Hamburg, Vol. 1 (1991) 261, and references therein.

[10] G. Ingelman, LEPTO version 6.3, unpublished program manual; see also: LEPTO 6.1, in: Proc. Workshop 'Physics at HERA', DESY, Hamburg, Vol. 3 (1991) 1366.

[11] H1 Collaboration, Technical Proposal for the H1-Detector, (1986).

[12] B.R. Webber, HERWIG version 5.8, unpublished program manual; see also: HERWIG 5.4, in: Proc. Workshop 'Physics at HERA', DESY, Hamburg, Vol. 3 (1991) 1354.

[13] S. Bethke, Proceedings of the XXXIth Rencontres des Moriond 1995, to be published.

On a Consistent Determination of α_s from Jet Rates in DIS

J. Chýla[a+], J. Rameš[a+]

[a] Institute of Physics, Na Slovance 2, Prague 8, 18040, Czech Republic
[+] Supported by grant No. A1010602 of the Grant Agency of the Academy of Sciences of CR

Abstract: For a theoretically consistent determination of α_s from jet rates in deep inelastic scattering the dependence on α_s of parton distribution functions is in principle as important as that of hard scattering cross-sections. For the kinematical region accessible at HERA we investigate in detail the numerical importance of these two sources of the α_s dependence of jet rates.

As QCD enters the stage of a truly quantitative theory, great emphasis is put on a precise determination of its basic parameter α_s, or equivalently $\Lambda_{\overline{\rm MS}}$, using different sorts of hard scattering processes in a broad range of kinematical conditions. The production of jets in DIS at HERA offers a possibility to investigate the running of $\alpha_s(\mu)$ in a single experiment. Recently both the H1 [1] and ZEUS [2] Collaborations have reported evidence for the running of $\alpha_s(\mu)$ obtained from the measurement of the quantity

$$R_{2+1}(Q^2) \equiv \frac{\sigma_{2+1}(Q^2)}{\sigma_{1+1}(Q^2)+\sigma_{2+1}(Q^2)}, \tag{1}$$

where σ_{k+1}, the cross-section for the production of k hard and one proton remnant jet, is given as

$$\sigma_{k+1}(Q^2, y_c, \Lambda) \equiv \sum_i \int_0^1 {\rm d}x f_i(x, M, \Lambda) C_{k+1,i}(Q, M, x, y_c, \Lambda). \tag{2}$$

In eq. (2), $f_i(x, M)$ denote parton distribution functions (PDF) of the proton evaluated at the factorization scale M, the sum runs over all parton species i, and

$$C_{2+1,i}(Q, M, x, y_c, \Lambda) = a(\mu/\Lambda)\left[c^{(1)}_{2+1,i}(x, y_c) + a(\mu/\Lambda)c^{(2)}_{2+1,i}(Q/M, x, y_c)\right], \tag{3}$$

$$C_{1+1,i}(Q, M, x, y_c, \Lambda) = c^{(0)}_{1+1,i}(Q, x) + a(\mu/\Lambda)c^{(1)}_{1+1,i}(Q/M, x, y_c). \tag{4}$$

Using PROJET 4.1 [3] with the JADE jet algorithm and $y_c = 0.02$, the H1 Collaboration has obtained the following result $\alpha_s(M_Z, \overline{\rm MS})$

$$\alpha_s(M_Z, \overline{\rm MS}) = 0.123 \pm 0.012({\rm stat.}) \pm 0.008({\rm syst.}). \tag{5}$$

In Ref. [1] $\alpha_s(\mu, \overline{\rm MS})$ (or, equivalently, $\Lambda_{\overline{\rm MS}}$) was considered as a free parameter in the parton-level hard-scattering cross-sections $C_{k+1,i}$ but not in the parton distribution functions (PDF), for which the MRSH set was used. Theoretical consistency of this procedure has been frequently questioned. In Ref. [4] we have shown that the variation of Λ in PDF changes the ratio R_{2+1} by the same order as the variation of Λ in parton level cross-sections C_{k+1} and **must** therefore in

principle be taken into account. We have also investigated the *numerical* importance of varying $\Lambda_{\overline{\rm MS}}$ in the PDF and in particular addressed the question under which conditions neglecting $\Lambda_{\overline{\rm MS}}$ in the PDF is *numerically* a good approximation for determining α_s from (1) at HERA. The main results are presented below. For details see Ref. [4].

In Ref. [4] we have developed a procedure for varying $\Lambda_{\overline{\rm MS}}$ in PDF while keeping certain parameters specifying the initial conditions for the GLAP evolution equations fixed. It should be emphasized that this procedure *does not* use fixed boundary conditions at a finite initial M_0. It exploits in a crucial way the parametrization of the solutions of GLAP equations by means of the evolution distance

$$s \equiv \ln\left(\frac{\ln(M/\Lambda)}{\ln(M_0/\Lambda)}\right) \doteq \ln\left(\frac{\alpha_s(M_0/\Lambda)}{\alpha_s(M/\Lambda)}\right). \tag{6}$$

In our studies we have used several of the GRV parametrizations [5]. All the results reported below were obtained using the PROJET 4.1 generator [3]. To quantify the dependence of R_{2+1} on Λ separately in hard scattering cross-sections and PDF we considered it as a function of Q^2, y_c and two independent Λ-parameters, denoted as $\Lambda^{\rm hsc}$ and $\Lambda^{\rm pdf}$, respectively, and defined

$$V(Q^2, y_c, r, s) \equiv \frac{R_{2+1}(Q^2, y_c, \Lambda^{\rm pdf} = s, \Lambda^{\rm hsc} = r)}{R_{2+1}(Q^2, y_c, \Lambda^{\rm pdf} = r, \Lambda^{\rm hsc} = s)}. \tag{7}$$

Considered as a function of s for fixed r, eq. (7) quantifies the relative importance of varying Λ in the PDF (described by R_{2+1} in the numerator) and in hard scattering cross-sections (described by R_{2+1} in the denominator). To a good approximation, eq. (7) is a linear function of s for any fixed Q^2, y_c, r. We therefore fitted $V(Q^2, y_c, r, s)$ by a linear function of s and defined

$$W(Q^2, y_c, r) \equiv \frac{{\rm d}V^{fit}(Q^2, y_c, r, s)}{{\rm d}s}, \tag{8}$$

which, by construction, is an s-independent function of Q^2, y_c and r. Positive W means that the variation of Λ in the PDF is more important than that in the hard scattering cross-sections, while for negative W the situation is opposite. The simulations were done at both the leading and next-to-leading order and for 12 values of Q^2 (equidistant in $\ln Q^2$ between 5 and 10^4 GeV^2), 5 values of $\Lambda^{\rm pdf}$ or $\Lambda^{\rm hsc}$ (equal to 0.1, 0.2, 0.3, 0.4 and 0.5 GeV), 3 values of $y_c = 0.01, 0.02, 0.04$ and two options concerning cuts on final jets (with no cuts as well as with the cuts as used in Ref. [1]). The main results are displayed in Figs. 1,2 and summarized below:

1. For Q^2 below about 40 GeV^2 the variation of Λ is more important in the PDF than in the hard-scattering cross-sections, while above 40 GeV^2 the situation is reversed.
2. Above $Q^2 \approx 10^3$ GeV^2 the variation of Λ in PDF becomes negligible.
3. The preceding conclusions depend only weakly on y_c.
4. the "cross-over" point Q^2_{cr}, where $W(Q^2_{cr}, y_c, r) = 0$, is at higher values of $Q^2_{cr} \sim 50 - 200$ GeV^2 and depends more sensitively on y_c, than at the NLO,
5. the relative importance of varying Λ in PDF is larger at the LO,
6. the difference between the LO and NLO results increases with increasing y_c.
7. the H1 cuts result in a significant reduction of the sensitivity to $\Lambda_{\overline{\rm MS}}$ in PDF in low Q^2.

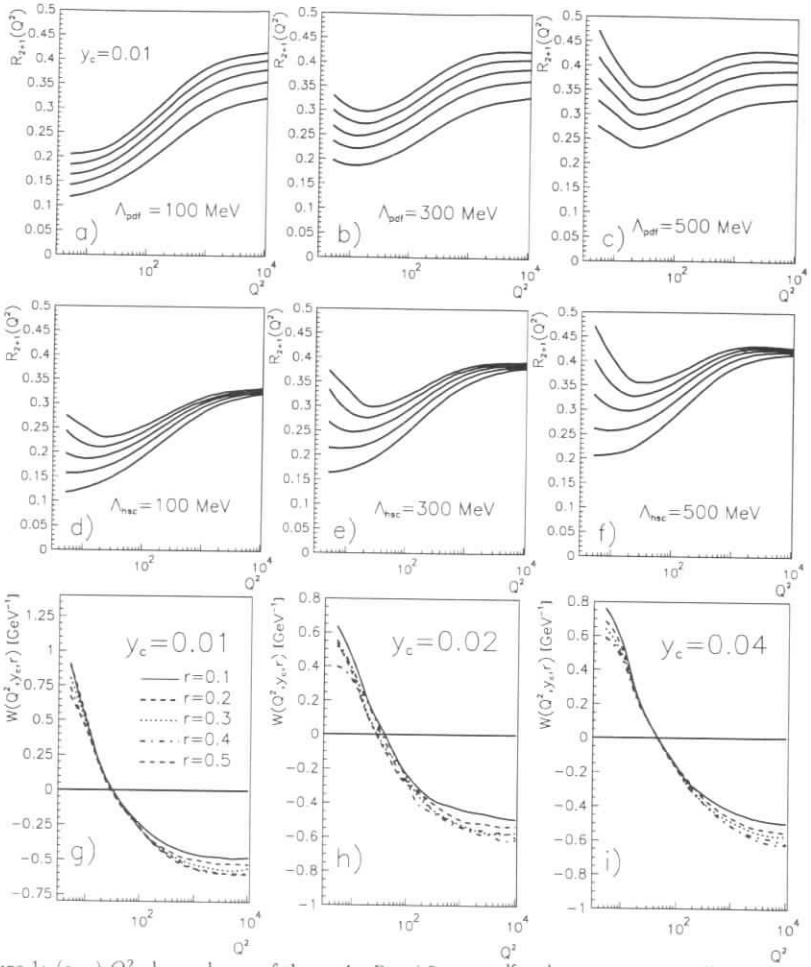

Figure 1: (a–c) Q^2–dependence of the ratio $R_{2+1}(Q, y_c, \Lambda^{\rm pdf}, \Lambda^{\rm hsc})$ for fixed $\Lambda^{\rm pdf} = 0.1, 0.3, 0.5$ GeV and five values of $\Lambda^{\rm hsc} = 0.1, 0.2, 0.3, 0.4, 0, 5$ GeV. (d–f) The role of $\Lambda^{\rm pdf}$ and $\Lambda^{\rm hsc}$ is reversed. No cuts were applied in evaluating R_{2+1} and $y_c = 0.01$. In all plots the curves are ordered from below according to increasing $\Lambda^{\rm hsc}$ (in a–c) or $\Lambda^{\rm pdf}$ (in d–f). (g-i): The quantity $W(Q^2, y_c, r)$ as a function of Q^2 for five values of r (given in GeV) and $y_c = 0.01, 0.02, 0.04$. All curves correspond to the case of no cuts.

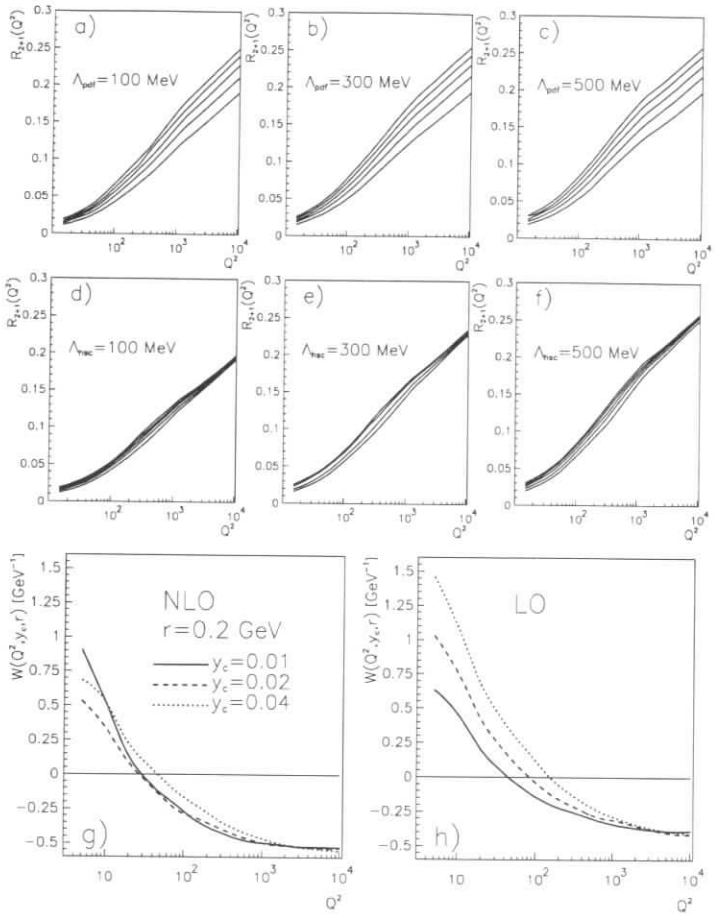

Figure 2: (a–f): The same as in Fig. 1a–f but for the H1 acceptance cuts. (g–h): Q^2–dependence of $W(Q^2, y_c, r = 0.2)$ for three values of y_c at the NLO (g) and LO (h) and no cuts.

References

[1] H1 Collab., T. Ahmed et al., Phys. Lett. **B 309** (1995) 415.

[2] ZEUS Collab., M. Derrick et al., Phys. Lett. **B 363** (1995) 201.

[3] D. Graudenz, Comput. Phys. Commun. **92** (1995) 65.

[4] J. Chýla, J. Rameš, PRA-HEP/96-01, hep-ph/9604265.

[5] M. Glück, E. Reya and A. Vogt, Z. Phys. **C 67** (1995) 433.

Prospects for a Measurement of α_s via Scaling Violations of Fragmentation Functions in Deeply Inelastic Scattering

Dirk Graudenz[a*†]

[a] Theoretical Physics Division, CERN, 1211 Geneva 23, Switzerland

Abstract: The prospects for a determination of the strong coupling constant α_s via scaling violations of fragmentation functions in deeply inelastic scattering are studied. The statistical error in the case of an integrated luminosity of $250\,\mathrm{pb}^{-1}$, and the theoretical errors due to the various parton density parametrizations and to the factorization scale dependence are estimated.

1 Introduction

The strong coupling constant α_s has been measured at HERA by means of the (2+1) jet rate [1]. This particular process has the advantage that α_s is, up to higher order corrections, directly proportional to the ratio of the measured cross-sections. Another route to a determination of α_s is given by scaling violations of phenomenological distribution functions. Perturbative QCD predicts the scale evolution of these quantities by means of renormalization group equations [2,3]. As a consequence, again up to higher order corrections and resummation effects, the experimentally measurable quantities (the structure functions, and the fragmentation functions, which depend on factorization scale and scheme) are (symbolically) of the form $A + B\,\alpha_s \ln \mu^2$. Here μ is the factorization scale, which is to be identified, in deeply inelastic scattering, with a scale of the order of the photon virtuality Q, for lack of other hard scales related to the leading-order process. The distribution functions contain a μ-independent term A, and the α_s dependence is only logarithmic in the factorization scale. The scaling violations are therefore expected to be small, and will require large luminosity to be statistically significant. An α_s determination via scaling violations has the advantage that, in principle, no explicit model assumptions such as specific fragmentation models go into the measurement. In the case of scaling violations of structure functions[1] a completely inclusive quantity is measured, and the theoretical basis, namely the operator product expansion, is very transparent and can be derived rigorously from light cone dominance. In the case of one-particle-inclusive processes, where the operator product expansion is not available, the factorization theorem of perturbative QCD (see, for example, Ref. [4] and references therein) allows the separation of the hard scattering process from the non-perturbative fragmentation process. The one-particle-inclusive cross-section is a convolution of a mass-factorized parton-level scattering cross-section, a parton density and a fragmentation function: $\sigma = \sigma_{\mathrm{hard}} \otimes f \otimes D$. A possible strategy for an α_s measurement at HERA is to perform a combined multiparameter fit of fragmentation functions and of the strong coupling constant to the x_F-distribution $\rho(x_F) = (\mathrm{d}\sigma/\mathrm{d}x_F)/\sigma_{\mathrm{tot}}$ (or to any other distribution sensitive to the fragmentation functions) of charged hadrons at two different scales Q. Here the variable x_F is defined to be $2h_L/W$, where h_L is the longitudinal momentum fraction of the observed charged hadron in the direction of the virtual photon in the hadronic centre-of-mass frame[2], and W is the total hadronic final state energy. In leading order, x_F is the momentum fraction of the final state current quark carried by the observed hadron. The total cross-section is denoted by σ_{tot}. The strong coupling constant enters the expression for ρ in three places: (a) as an expansion parameter in the next-to-leading order expression for σ_{hard}, and in the renormalization group equations of (b) the fragmentation functions and (c) the parton densities. The parton densities are an input to the analysis. Since they are obtained by a global fit, where a specific value of α_s is used, it is necessary to include this dependence as well as the variation due to the different parametrizations into the systematic error[3]. The next-to-leading-order one-particle-inclusive cross-section has been calculated in Ref. [6]. For our study, we use a recent recalculation and numerical implementation described in Ref. [7]. A comparison of the theoretical x_F-distribution with experimental data from the H1 and ZEUS Collaborations [8] has been done in Ref. [9]. It turns out that the theoretical description of the experimental data is quite satisfactory. The next-to-leading order result is always within one standard deviation of the experimental data points except for those at very large x_F, where the currently available fragmentation function parametrizations are not well constrained by e^+e^- data.

In the next section, we describe the estimate of the various errors[4] of the value of α_s. We also discuss the sensitivity to the strong coupling constant of various ranges in x_F. The paper closes with a short summary and conclusions.

2 Error Estimates

To get a quantitative estimate of the dependence of the scale evolution of fragmentation functions on the employed value of α_s, we fix the fragmentation functions at a scale of $\mu_0 = 2\,\mathrm{GeV}$ as the leading-order parametrization of Ref. [10]. We then evolve this input with two different values for $\Lambda^{(4)}_{\mathrm{QCD}}$ of 0.1 GeV {a} and 0.2 GeV {b}. The corresponding x_F-distributions $\rho^{\{a\}}$ and $\rho^{\{b\}}$ are determined for these two sets of fragmentation functions. We now assume that the x_F-distributions ρ are measured in two different bins i, j of the factorization scale Q. The ratios $\lambda^{\{ij\}} = \rho^{\{i\}}/\rho^{\{j\}}$ for an arbitrary coupling constant α_s (taken at the mass of the Z boson) are expanded in a power series in α_s, where only the linear term is kept:

$$\lambda^{\{ij\}} = \lambda^{\{aij\}} + \frac{\lambda^{\{bij\}} - \lambda^{\{aij\}}}{\alpha_s^{\{b\}} - \alpha_s^{\{a\}}} \left(\alpha_s - \alpha_s^{\{a\}}\right). \qquad (1)$$

*Electronic mail address: Dirk.Graudenz@cern.ch

†WWW URL: http://wwwcn.cern.ch/~graudenz/index.html

[1] See, for example, the contributions of the working group on structure functions.

[2] It might be possible to reduce the dependence on the parton densities and on the not yet well understood physics of the forward direction by performing an analysis in the Breit frame. I thank N. Brook and T. Doyle for remarks concerning this issue.

[3] Alternatively, parton density parametrizations with varying values of the strong coupling constant [5] can be employed.

[4] We do not consider experimental systematic errors.

Based on this formula, a quantitative estimate of the statistical error of α_s is possible. Moreover, by varying $\lambda^{(ij)}$, for example by using various parton density distributions or by modifying the factorization scale, the impact of systematic effects can be studied.

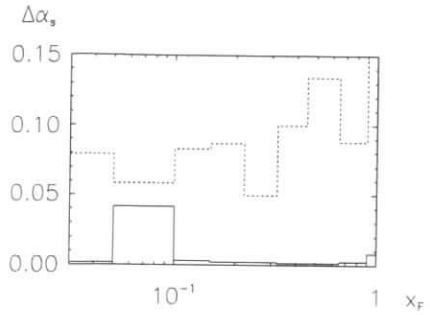

Figure 1: *Statistical errors of α_s for the individual x_F-bins, for the Q-bins* {1}, {2} [——] *and* {2}, {3} [- - -].

To be more specific, we assume the phase space cuts and x_F-bins of the ZEUS analysis, except for the range in the photon virtuality Q, where we consider three bins: [3.16, 12.6] GeV {1}, [12.6, 100] GeV {2} and [100, 150] GeV {3}. To obtain explicit numerical values, we use the CTEQ 3L parametrization [11] for the parton densities (for simplicity, we work in leading order). The integrated luminosity is assumed to be 250 pb^{-1}. Under the assumption of Gaussian statistical errors we arrive at a statistical error of $\alpha_s(M_Z^2)$ of $\Delta\alpha_s^{\mathrm{stat}} = \pm 0.0007$ for an analysis based on bins {1} and {2} and of ± 0.027 for an analysis based on bins {2} and {3}. The individual errors of α_s for the various x_F-bins are shown in Fig. 1. The large error around $x_F \sim 0.08$ for the large-Q bins comes from the fact that the evolution of the fragmentation functions around this value of the momentum fraction is quite small (for smaller values, the fragmentation functions increase with increasing factorization scale, and for larger values, they decrease). The sensitivity of the cross-section to a variation of α_s is largest at large x_F, but this region also suffers from small statistics of the data sample. It turns out that the full x_F-range is about equally important.

As briefly mentioned already in the introduction, an input parton density has to be chosen. To estimate the size of this effect, we determine the spread of the results for $\alpha_s(M_Z^2)$ depending on the next-to-leading-order parton densities from Refs. [11, 12]. For the bins {1} and {2}, the spread is $\Delta\alpha_s^{\mathrm{PDF}} = \pm 0.017$, and for the bins {2} and {3}, it is ± 0.005. Future global fits of parton densities including improved HERA data should reduce this systematic uncertainty.

Perturbative QCD allows for some freedom in the choice of the factorization scale μ of the fragmentation functions $D(z, \mu^2)$. This brings out the inherent uncertainty in the theoretical prediction, and can be interpreted as an effect of unknown higher order contributions. To obtain an estimate of this uncertainty, the ratios λ are determined for the three choices $Q/2$, Q and $2Q$ of this scale. The change of cross-section has for consequence a variation in the extracted $\alpha_s(M_Z^2)$ value of $\Delta\alpha_s^{\mathrm{scale}} = \pm 0.013$ and ± 0.011 for the combinations of the bins {1}, {2} and {2}, {3}, respectively.

3 Summary and Conclusions

We have studied the prospects of a measurement of the strong coupling constant in deeply inelastic scattering at HERA by means of scaling violations of fragmentation functions. The combinations of the obtained values for $\Delta\alpha_s^{\mathrm{stat}}$, $\Delta\alpha_s^{\mathrm{PDF}}$ and $\Delta\alpha_s^{\mathrm{scale}}$ are large compared with the present error $\Delta\alpha_s = 0.006$ of the world average. It is therefore likely that a measurement of this kind will not be competitive, concerning the size of the error. Nevertheless, it is worth doing as an independent quantitative test of QCD and, more important, because it complements the other (potential) HERA measurements based on (2+1) jet rates and scaling violations of structure functions.

Acknowledgements

I wish to thank Ch. Berger, N. Brook, T. Doyle, M. Kuhlen and N. Pavel for discussions, H. Spiesberger for comments on the manuscript, and J. Binnewies for clarifying remarks concerning the parametrizations of Ref. [10]. This work was supported in part by a Habilitandenstipendium of the Deutsche Forschungsgemeinschaft.

References

[1] T. Ahmed et al. (H1 Collaboration), Phys. Lett. B346 (1995) 415; M. Derrick et al. (ZEUS Collaboration), Phys. Lett. B363 (1995) 201.

[2] G. Altarelli and G. Parisi, Nucl. Phys. B126 (1977) 298.

[3] R. Baier and K. Fey, Z. Phys. C2 (1979) 339.

[4] J.C. Collins, D.E. Soper and G. Sterman, in: *Perturbative Quantum Chromodynamics*, ed. A.H. Mueller (World Scientific, Singapore, 1989).

[5] A. Vogt, Phys. Lett. B354 (1995) 145; A.D. Martin, W.J. Stirling and R.G. Roberts, Rutherford Appleton Lab. preprint RAL-TR-95-013 (June 1995).

[6] G. Altarelli, R.K. Ellis, G. Martinelli and S.Y. Pi, Nucl. Phys. B160 (1979) 301.

[7] D. Graudenz, *Heavy-Quark Production in the Target Fragmentation Region*, preprint CERN-TH/96-52, in preparation.

[8] I. Abt et al. (H1 Collaboration) Z. Phys. C63 (1994) 377; M. Derrick et al. (ZEUS Collaboration), Z. Phys. C70 (1996) 1.

[9] D. Graudenz, *Charged-Meson Production and Scaling Violations of Fragmentation Functions in Deeply Inelastic Scattering at HERA*, preprint CERN-TH/96-155 (June 1996).

[10] J. Binnewies, B.A. Kniehl and G. Kramer, Z. Phys. C65 (1995) 471; Phys. Rev. D52 (1995) 4947.

[11] CTEQ Collaboration, Phys. Rev. D51 (1995) 4763.

[12] M. Glück, E. Reya and A. Vogt, Z. Phys. C67 (1995) 433; A.D. Martin, R.G. Roberts and W.J. Stirling, Phys. Rev. D51 (1995) 4756.

Extraction of the Gluon Density from F_2 and Jet Rates

G. Lobo

Laboratoire de l'Accélérateur Linéaire, IN2P3-CNRS et Université de Paris-Sud,
F-91405 Orsay Cédex, France.

Abstract: An extraction method of the gluon density in leading order from a global fit to F_2 and jet rates is presented. Prospects are studied for an integrated luminosity of 250 pb^{-1} and 1000 pb^{-1}. This study is particularly focused on the gluon error band behavior. Only statistical errors are taken into account.

Introduction

Up to now the usual way to extract the gluon density from DIS events was mainly by the study of scaling violations of structure functions. With HERA experiments one has the opportunity to measure the hadronic final states [1, 2, 3, 4]. Given this, new methods are possible, for example the (2+1) jet cross-section measurement (or the jet rate R_{2+1}) as a physical observable to extract the gluon density [5, 6].

The advantage of using the (2+1) jet cross-section ($\sigma_{(2+1)}$) comes from the fact that the latter is directly dependent on the gluon density and this gluon-induced part is expected to dominate in the HERA kinematical range. So far all methods using $\sigma_{(2+1)}$ or R_{2+1} treat the quark-induced part of the cross-section by fixing the quark densities. Such a hypothesis does not necessarily change the result itself, but surely the error treatment, since quark densities are coupled to the gluon via the DGLAP [7] equations. In order to avoid this problem, one should use a measured quantity which can give strong constraints on the quark densities, e.g. an F_2 measurement. In this way, we can have a correct treatment of the gluon density, taking in account correlations between quarks and gluons.

1 Method and jet cross-section computation

Basically, the method is a global QCD fit as usually made in DIS. The differences comes from incorporating R_{2+1}. The problem is to compute the time-consuming $\chi^2_{R_{(2+1)}}$ many times. Already in leading order (LO) each term of the (2+1) jet cross-section is a convolution of a parton density with hard matrix elements [8]. These integrations are time consuming and a straightforward calculation is not really suited best for a fit program. In next-to-leading order (NLO) [9, 12, 11] this problem becomes much more important, and the existing programs [10, 11] cannot be used without modifications. One way to overcome this has been proposed in Ref. [13] by use of the Mellin transform. Here we develop a procedure using cubic spline interpolation. We illustrate this method with the BGF term of the cross-section:

$$\sigma_g \sim \int d\xi C_q(\xi, x, Q^2, y_{cut}) \xi g(\xi, Q^2). \tag{1}$$

First, we define a network $\{\xi_1, \ldots, \xi_{N_z}\}$ in ξ. Then we define a set of basis functions $\phi_i(\xi)$ such that the $\phi_i(\xi)$ are continuous and $\phi_i(\xi_k) = \delta_{ik}$. If we interpolate the $\phi_i(\xi)$'s with cubic splines, then we can expand

$$\xi g(\xi, Q^2) = \sum_{i=1}^{N_z} \xi_i g(\xi_i, Q^2) \phi_i(\xi). \tag{2}$$

With such an expansion Eq. (1) becomes :

$$\sigma_g \sim \sum_{i=1}^{N_z} \xi_i g(\xi_i, Q^2) \int d\xi C_q(\xi, x, Q^2, y_{cut}) \phi_i(\xi). \tag{3}$$

Now we can compute all integrals since they are not affected by the parton densities changes in the fit. We calculate them before the χ^2 minimization procedure. At each step of the fit we only have to perform a vector product instead of a integral.

It is very easy to extend this procedure to NLO. In LO the analytical results from [8] have been used, but in NLO this cannot be done so easily, one has to use theoretical programs [10, 11]. The best suited program for this job is the DISENT [12] program since it allows to have only the coefficient functions and convolute them with any arbitrary function.

2 Choice of the data points

The "data points" which we use were extracted as follows. We choose a binnning in x with two samples of low and high Q^2. This binning corresponds to reasonable statistics for 1994 luminosity (2.5 pb^{-1}). Considering this binning we compute the jet rate R_{2+1} using parton densities obtained *from the fit to F_2 1994 data.* The justification of such a procedure comes from the fact that no real difference was seen from the gluon obtained from F_2 fit alone and the combined F_2 &R_{2+1} fit. The statistical errors are computed according to the desired luminosity. We used two jet definitions :

- mJADE [14]
  - $m_{ij} > y_{cut} W^2$ ($y_{cut} = 0.02$)
- k_t [15]
  - $d_{ip} > y_{cut} Q^2$
  - $d_{ij} > y_{cut} Q^2$ ($y_{cut} = 0.5$)

The data points used are shown in Fig. 1.

3 Fit with F_2 and R_{2+1}

Using F_2 and R_{2+1} to fit the gluon density, we expect to include the maximum information about parton densities. Figure 2 shows the gluon error bands for three kinds of fits: F_2 only, F_2 and R_{2+1}^{mJADE}, F_2 and $R_{2+1}^{k_t}$; with errors computed on the basis of 1994 statistics. While there is no improvement with mJADE one can see a small improvement with k_t. We hope that this improvement increases with luminosity. These results are not surprising considering the fact that for mJADE we have $\xi \gtrsim y_{\text{cut}}$ whereas for k_t we have $\xi \gtrsim x/y_{\text{cut}}$. Adding the fact that we have much more statistics at low x for k_t, we could have expected such an improvement.

Now if we use the k_t and take statistical errors corresponding to $250\,pb^{-1}$ and $1000\,pb^{-1}$ (Fig. 4), we see that we have a real improvement at medium and high x. We could also have expected this result since the bulk of the statistics for the jet rates corresponds to this region of ξ. Going to $1000\,pb^{-1}$ does not improve the result substantially.

4 Conclusions

This study shows that running HERA can substantially improve the precision on gluon density knowledge. The gain is not so important at low x but it seems that at high x we can learn something. Of course, to be complete this study should be redone in NLO, and maybe we can have new information about gluon and not only increase the precision.

Acknowledgments

I would like to thank C. Pascaud and F. Zomer for their moral and technical support. I would like to thank also S. Catani and M. Seymour for useful discussions. Special thanks to D. Graudenz for his constructive remarks.

References

[1] A.D. Martin, W.J. Stirling, R.G. Roberts, Phys. Lett. **B252** (1990) 653.

[2] CTEQ Collaboration: J. Botts *et al.*, Phys. Lett. **B304** (1993) 159.

[3] H1 Collaboration: DESY preprint 96-039.

[4] ZEUS Collaboration: Phys. Lett. **B345** (1995) 576.

[5] H1 collaboration: S. Aid *et al.*, Nucl. Phys. **B449** (1995) 3.

[6] D. Graudenz, M. Hampel, A. Vogt, these Proceedings.

[7] V.N. Gribov and L.N. Lipatov, Sov. Journ. Nucl. Phys. **15** (1972) 438 and 675;
G. Altarelli and G. Parisi, Nucl. Phys. **B126** (1977) 297;
Yu.L.Dokshitzer, Sov. Phys. JETP **46** (1977) 641.

[8] J.G. Körner, E. Mirkes, G.A. Schuler, Int. J. Mod. Phys. **A4** (1989) 1781.

[9] D. Graudenz, Phys. Rev. **D49** (1994) 3291.

[10] D. Graudenz, Comput. Phys. Commun. **92** (1995) 65.

[11] E. Mirkes, D. Zeppenfeld, Phys. Lett. **B380** (1996) 205.

[12] S. Catani, M.H. Seymour, Phys. Lett. **B378** (1996) 287;
S. Catani, M.H. Seymour, CERN preprint, CERN-TH-96-029.

[13] D. Graudenz, M. Hampel, A. Vogt, C. Berger, Z. Phys. **C70** (1996) 77.

[14] D. Graudenz, N. Magnussen, in: Proceedings of the HERA Workshop 1991, DESY (eds. W. Buchmüller, G. Ingelman).

[15] S. Catani, Yu.L. Dokshitser, Phys. Lett. **B285** (1992) 291.

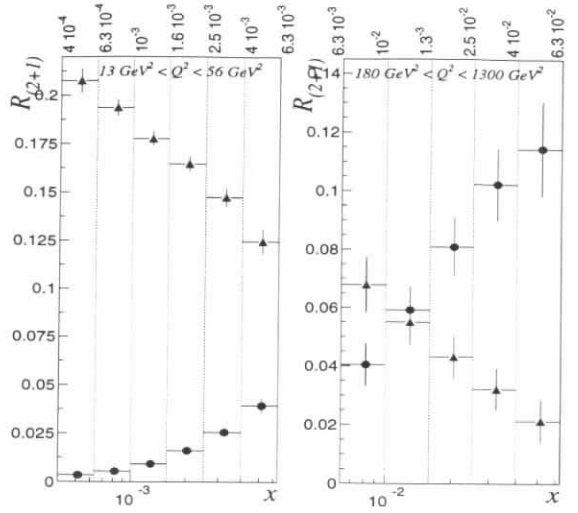

Figure 1: *$R_{(2+1)}$ "data points" used for this study as a function of x. The circles represent the jet rate obtained with the mJADE algorithm. The triangles represent the jet rate for the k_t algorithm. The first plot is the low Q^2 sample ($13\ GeV^2 < Q^2 < 56\ GeV^2$), the second is the high Q^2 sample ($180\ GeV^2 < Q^2 < 1300\ GeV^2$).*

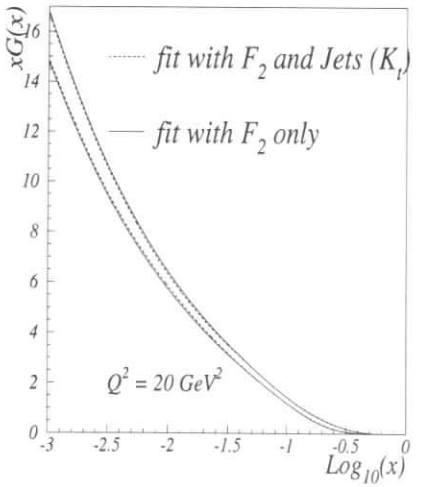

Figure 2: *Gluon errors bands from a fit to F_2 only (full line) and from a fit to F_2 and R_{2+1} (k_t algorithm) (dotted line) (The fit with the mJADE algorithm lies exactly on the full line).*

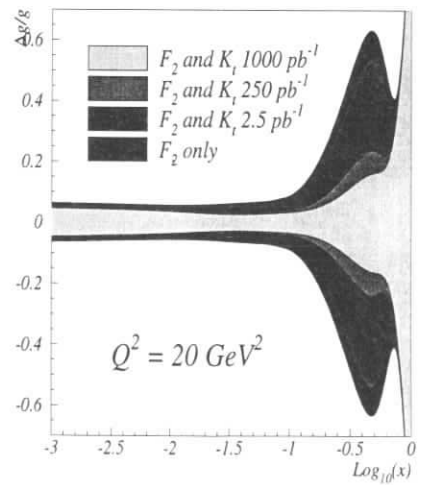

Figure 3 : *Relative gluon error bands, obtained from various fits to F_2 and R_{2+1} for three sets of luminosity: 2.5 pb^{-1} (dark grey), 250 pb^{-1} (grey) and 1000 pb^{-1} (light grey). The black area is a fit to F_2 only.*

The Extraction of the Gluon Density from Jet Production in Deeply Inelastic Scattering

D. Graudenz[a], M. Hampel[b], A. Vogt[c]

[a] Theoretical Physics Division, CERN, CH–1211 Geneva 23, Switzerland
[b] I. Physikalisches Institut, RWTH Aachen, D–52056 Aachen, Germany
[c] Institut für Theoretische Physik, Universität Würzburg, D–97074 Würzburg, Germany

Abstract: The prospects of a direct extraction of the proton's gluon density in next-to-leading order via jet rates in deeply inelastic scattering are studied. The employed method is based on the Mellin transform, and can be applied, in principle, to all infra-red-safe observables of hadronic final states. We investigate the dependence of the error band on the extracted gluon distribution on the statistical and systematic error of the data.

1 Introduction

The extraction of the proton's gluon density over a wide kinematical range is one of the central issues at HERA. This distribution is important for phenomenological applications at pp-colliders, as well as at small x, $x \lesssim 0.005$ say, for studies related to parton dynamics, since higher-order terms of the type $[\alpha_s \ln(1/x)]^k$ in the perturbative expansion may become important here. At HERA, this region is mainly covered by the scaling violations and (with increasing luminosity) more directly by the charm content of the structure function F_2. The classical gluon constraint at larger x ($x > 0.01$), direct photon production in pp collisions, is plagued by sizeable theoretical uncertainties, see Ref. [1]. It is therefore desirable to have a direct determination of the gluon density from HERA also at $x \gtrsim 0.01$, complementing the observables so far employed in global fits (see, for example, Ref. [2]).

Experimental analyses of hadronic final states use very complicated sets of cuts. The theoretical predictions for the employed infra-red-safe observables are in general obtained by means of time-consuming Monte-Carlo integrations of parton cross-sections. This is contrary to the case of DIS structure functions, for example, where the convolution kernels can be given in a compact analytical form. Parametrizations of the gluon density involve some free parameters — for a decent description at, say, a scale of a few GeV^2 at least $3-4$ parameters are necessary [1, 2] — so that a fitting procedure with a large number of iterations is unavoidable. This leads to the problem of the repeated evaluation of the theoretical cross-section for various gluon density parametrizations. It turns out that the direct method is not easily feasible due to its

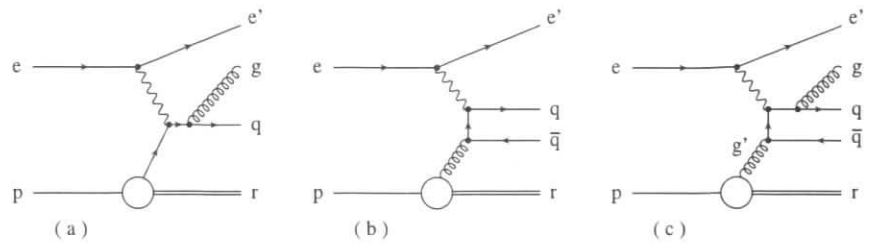

Figure 1: *Generic Feynman diagrams for the leading-order processes of QCD Compton scattering (a) and photon–gluon fusion (b), and an example for a diagram corresponding to a next-to-leading order real correction (c).*

prohibitive need of computer time. A method based on the Mellin transform technique[1] to circumvent this problem has been presented in Ref. [3]. It allows the rapidly repeated evaluation of the convolution of a cross-section and a parton density, even if the cross-section is not of the Mellin-factorizing form. In fact, this is always the case when acceptance cuts are applied, even for "factorizing" jet definition schemes [4].

Jet observables are particularly suitable for the extraction of the gluon density. The reason for this is that the lowest-order gluon-induced subprocess is the photon–gluon fusion process (Fig. 1b), which can give rise to (2+1) jet final states. The cross-section of the competing quark-initiated "QCD Compton"-subprocess (Fig. 1a) is either small (at small x) or well-known (at large x). Hence it can be determined theoretically and then subtracted from the experimental cross-sections. In leading-order QCD, the momentum fraction of the incident parton can be reconstructed from the final-state jet momenta, and therefore a direct unfolding of the gluon density is possible [5]. This procedure does no longer work beyond leading order, where the mass-factorized hard scattering cross-section is a distribution (in the mathematical sense) to be convoluted with the parton densities.

For general factorization schemes, the parton-level cross-section contains subtractions, thus "the momentum fraction of the incident gluon" in a naive probabilistic interpretation no longer makes sense. The physical origin of this phenomenon is initial-state radiation (see Fig. 1c; in this example, the antiquark $\bar{q}$ is assumed to be radiated into the forward direction, giving a contribution to the hard process of Fig. 1a). The separation of the calculable short-distance subprocess from the long-distance physics of the proton state (whose onset appears in the form of collinear and soft divergences of matrix elements) requires the renormalization of the parton densities. A change of the factorization scheme amounts to a redefinition of both the hard scattering cross-section as well as of the parton densities — in other words, the notion of an

[1] The Mellin transform $F_n = \int_0^1 \mathrm{d}x\, x^{n-1} F(x)$ maps a convolution $\sigma(x_B) = \int_{x_B}^1 (\mathrm{d}\xi/\xi) f(\xi)\, \sigma^p(x_B/\xi)$ of a parton density f and a parton-level cross-section σ^p into the product $\sigma_n = f_n\, \sigma_n^p$ of the respective moments. For a specific set of acceptance cuts, the time-consuming Monte Carlo calculation of the moments σ_n^p has to be done only once. The cross-section σ can be evaluated repeatedly for varying parton densities by means of an inverse Mellin transform. A restriction of the method is that the factorization scale in every bin of analyzed data is assumed to be constant. However, owing to scale-compensating terms in the parton-level cross-section, the procedure is always accurate to the order of perturbation theory for which the cross section is calculated. For details, in particular on how to treat the non-factorizable case, see Ref. [3].

"incident parton" becomes a factorization-scheme dependent concept — such that, to all orders, observable quantities are unaffected. For general factorization schemes, the determination of the gluon density has to rely on a fitting method.

2 Two Scenarios at HERA

In this section, we present the explicit results for a study based on jet rates in the modified JADE jet definition scheme [6] with a jet cut parameter of $y_{cut} = 0.02$. We use the PROJET next-to-leading-order Monte-Carlo program [7] with the matrix elements from Ref. [8]. The program is applied in a phase space region (jets in the very forward direction are excluded) where the approximations made in the calculation underlying PROJET should be justified. In Fig. 2a the error bands for a typical statistical-, systematic- and theoretical-error scenario are shown. The employed acceptance cuts are discussed in Ref. [9]. A luminosity of about $3\,\mathrm{pb}^{-1}$ has been assumed. The inner shaded region shows the statistical plus experimental systematic errors, added in quadrature. The outer shaded region displays the total error, obtained by subsequently adding the theoretical error quadratically, including a scale variation in the range of $[Q/2, 2Q]$. Only the region with $x > y_{cut}$ is covered by data[2], but the extrapolation to smaller x exhibits a reasonable behaviour of the gluon density parametrization.

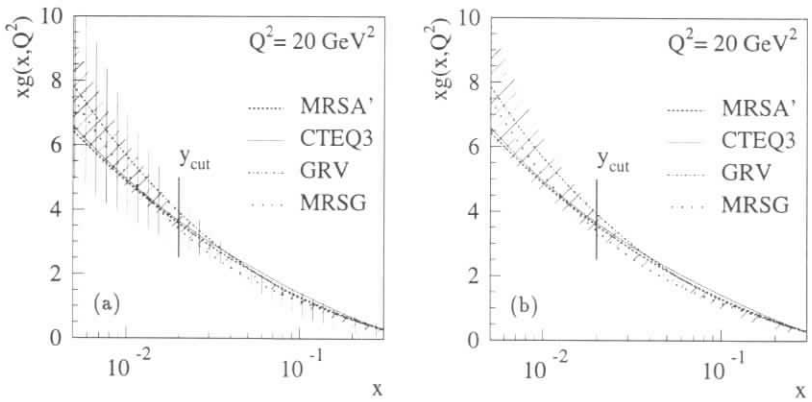

Figure 2: *Fit result on the proton's gluon density with typical error bands for statistical, systematic (and theoretical) errors added in quadrature compared with recent parametrizations* [2]. *(a) for 1994 HERA luminosity, (b) high-luminosity scenario. For details see the text.*

In Fig. 2b it is assumed that, owing to a much higher luminosity (of the order of $250\,\mathrm{pb}^{-1}$), the systematic error can be halved by much tighter cuts leaving the same statistical error in the sample, and that the progress in the understanding of theoretical uncertainty will allow for neglecting its influence against the remaining experimental error. Under these assumptions the error is reduced dramatically, enabling a discrimination between different present-day parton parametrizations [2]. It should be noted that the spread of these parametrizations does not represent the real uncertainty on the gluon distribution, due to the use of similar data samples and theoretical assumptions. This emphasizes the discriminating power and constraining effect of a DIS jet data sample at HERA with much reduced systematic error in the region $0.01 < x < 0.1$.

[2]The use of the modified JADE algorithm restricts the accessible range in the gluon momentum fraction to values larger than the jet cut, because the invariant mass of the outgoing hadronic system is constrained. It is possible to extend this range by using other jet algorithms, such as the cone or the k_T schemes.

3 Summary and Conclusions

We have studied the prospects of a direct determination of the proton's gluon density via jet rates in deeply inelastic scattering at HERA. The application of the Mellin transform method [3] allows for an efficient fitting procedure with several parameters, the input data of the fit being the jet rates in bins of Q^2. We have illustrated that high luminosity at HERA and, consequently, smaller systematic errors owing to tight acceptance cuts, can permit a useful constraint of the gluon density, complementary to (and finally includible in) global fits. Forthcoming high-statistics runs of HERA will also allow for a binning in other variables more closely related to the (unobservable) momentum fraction of the gluon, which should have a direct impact on the quality of the fit.

Acknowledgements

This work was supported in part by the German Federal Ministry for Research and Technology (BMBF) under contract No. 05 7WZ91P (0). M. Hampel gratefully acknowledges support by the Studienstiftung des deutschen Volkes.

References

[1] W. Vogelsang and A. Vogt, Nucl. Phys. B453 (1995) 334.

[2] A. Martin, R. Roberts and W.J. Stirling, Phys. Lett. B354 (1995) 155;
M. Glück, E. Reya and A. Vogt, Z. Phys. C67 (1995) 433;
H.L. Lai et al., CTEQ Collaboration, Phys. Rev. D51 (1995) 4763.

[3] D. Graudenz, M. Hampel, A. Vogt and Ch. Berger, Z. Phys. C70 (1996) 77.

[4] S. Catani, Y.L. Dokshitzer and B.R. Webber, Phys. Lett. B285 (1992) 291;
B.R. Webber, J. Phys. G19 (1993) 1567.

[5] H1 Collaboration, S. Aid et al., Nucl. Phys. B449 (1995) 3.

[6] D. Graudenz and N. Magnussen, Proceedings of the 1991 HERA Workshop, eds. W. Buchmüller and G. Ingelman (DESY, Hamburg, 1991), p. 261.

[7] D. Graudenz, Comput. Phys. Commun. 92 (1995) 65.

[8] D. Graudenz, Phys. Lett. B256 (1991) 518; Phys. Rev. D49 (1994) 3291.

[9] M. Hampel, Ph.D. thesis (1996), in preparation.

Virtual Photon Structure from Jet Production at HERA

J. Chýla[a*], J. Cvach[a*]

[a] Institute of Physics, Na Slovance 2, Prague 8, 18040, Czech Republic
* Supported by grants No. A1010619 and A1010602 of the GA of the Academy of Sciences of CR

Abstract: The feasibility of measuring parton distribution functions of of virtual photons via the jet production at HERA is investigated.

Production of jets in ep collisions at HERA offers one of the ways of studying the structure of the virtual photon. Due to the fact that this structure needs time to develop, parton distribution functions (PDF) $f_i(x, P^2, Q^2)$ of the virtual photon, probed at the hard scattering scale Q, are expected to be decreasing functions of the magnitude P^2 of its virtuality. As P^2 approaches Q^2 from below $f_q(x, P^2, Q^2)$ should approach parton model formula

$$f_i^{\rm PM}(x, P^2, Q^2) \equiv \frac{3\alpha}{2\pi}\left[x^2 + (1-x)^2\right] \ln\frac{Q^2}{P^2}. \qquad (1)$$

The transition of the quark distribution functions of the real photon to the form (1) is so far not calculable but there are models which interpolate between $f_q^{\rm real}$ and (1). Measurement of the PDF of the virtual photon would provide valuable new information on the properties of parton interactions at short distances. In ref. [3] this transition is parametrized as follows

$$f_q(x, Q^2, P^2) = f_q^{\rm real}(x, Q^2) L(Q^2, P^2, \omega), \quad L \equiv \frac{[\ln(Q^2+\omega^2)/(P^2+\omega^2)]}{[\ln(Q^2+\omega^2)/(\omega^2)]}, \qquad (2)$$

while in analogous relation for the gluon L is replaced by L^2. The parameter ω determines the value of P^2 above which the suppression factor L becomes significant. Small ω means strong suppression already for weekly off-mass shell photons, while $\omega \to \infty$ corresponds to no suppression at all. The suppression formula (2) is implemented, for instance, in the recent versions of HERWIG MC generator. Because of a different x behaviour of PDF of the real photon and parton model formula (1), ω must in general be a function of x. As, however, in our simulations $P^2 \ll Q^2 \approx 4(p_T^{\rm jet})^2 \geq 100$ GeV^2 we considered ω as x independent.

Jet production at HERA for general values of P^2 and $p_T^{\rm jet}$ is a two-scale problem, where it is thus not obvious what to take for the relevant har-scattering scale Q^2 in $f_i(x, P^2, Q^2)$: P^2 or p_T^2 of the produced jets, or some combinations thereof? In this study we stayed in the region $\Lambda_{\rm QCD} \ll P^2 \ll p_T^2$ and therefore assumed $Q^2 = \kappa p_T^2$ with the proportionality factor of the order of unity. To make the experimental procedure of jet finding well-defined and ensure the applicability of perturbative QCD, we furthemore required $p_T^{\rm jet} \geq p_T^{\rm min} = 5$ GeV, $P^2 \leq 10$ GeV^2. As in this region dynamics of the jet production is close to that of the real photoproduction, all our further considerations were carried out in the γ^*p CMS. To study the P^2 dependence

we split the region $P^2 \leq 10$ GeV^2 into eight intervals: $(0, 0.1)$ ("photoproduction"), $(0.1, 0.2)$, $(0.2, 0.5)$, $(0.5, 1)$, $(1, 2)$, $(2, 5)$, $(5, 10)$ GeV^2, each with roughly the same number of events. To guarantee good electron identification, the cut on $0.2 \leq y \leq 0.7$ was imposed in all simulations.

Our simulations were guided by recent preliminary H1 and ZEUS data on virtual photon structure [1, 2]. The results presented here are based on HERWIG 5.8d MC generator and standard cone jet finder with $R = 1$. To estimate the dependence of the results on the strength of the virtual photon suppression factor the simulations were performed for three values of $\omega = 0.1, 1.0, 3.0$. We addressed the following questions:

a) How to isolate the contribution of the resolved photon, which depend on $f_i(x, P^2, Q^2)$ and thus in principle allow its measurement, from direct photon one?
b) What are the ensuing requirements on the detector and experimental procedure?
c) What is the required luminosity upgrade to get a reasonable statistics?

Most of the current attempts at separating resolved from direct photon contributions to jet cross-sections are based on the fact that for the latter the distribution of the variable

$$x_\gamma \equiv \frac{E_T^{(1)}\exp(-\eta^{(1)}) + E_T^{(2)}\exp(-\eta^{(2)})}{2E_\gamma}, \qquad (3)$$

where $\eta^{(j)}$ and $E_T^{(j)}$ correspond to two jets with highest transverse energies, peaks at a value close to unity, while for the resolved component the spectrum peaks at low x and drops rapidly as $x_\gamma \to 1$. In parton model x_γ is interpreted as a fraction of the photon momentum carried by the parton or photon participating in the hard collision with a parton from the proton. In the direct channel and for two final state massless partons $x_\gamma = 1$ identically. Taking into account nonzero P^2 leads to slightly modified formula for x_γ but we sticked to (3) as in realistic QCD-based MC simulations there are other, more important, effects that lead to the smearing of the x_γ distribution. To see which of them is most important we compared, in both direct and resolved channels, our MC results for a) two final massless partons with no parton showers, b) two final partons after they acquire nonzero virtuality, c) jets formed out of final state on mass-shell partons and finally d) realistic hadron jets. It turns out that the most dramatic effect of the smearing, due mainly to hadronization, occurs for the x_γ distribution: instead of a pronounced peak for $x_\gamma = 1$ we get much wider and less pronounced structure peaked at about $x_\gamma = 0.85$, as shown in Fig.1a. Its position and shape is essentially independent of P^2.

To measure the parton structure of the virtual photon requires a suitable signature to separate resolved and direct components. The best candidate remains, even after the smearing shown in Fig. 1a, the x_γ distribution. The resolved component can be enhanced by imposing cuts on other variables. The most effective would be a cut on the pseudorapidity $\eta > 0$, illustrated in Fig. 1b. Unfortunately, in this region there are problems with the separation of hard jets from the proton remnant one. Both experiments [1, 2] therefore restrict their jets to the region $\eta < -0.5$. Another, but less effective way of enhancing the resolved component exploits the fact that the $|\Delta\eta|$ distribution is broader for the resolved component. In some simulations we therefore imposed also the cut $|\Delta\eta| > 1$.

To assess the feasibility of measuring PDF of the virtual photon at HERA and to get some idea of what the theoretical predictions look like, we show in Fig.2 for three values of the suppression parameter $\omega = 0.1, 1, 3$ our MC results for the x_γ distribution. We see that the direct component of the virtual photon gives rise to a peak at about $x_\gamma = 0.85$, while the resolved one, wherefrom the virtual photon PDF would be determined, is dominant below

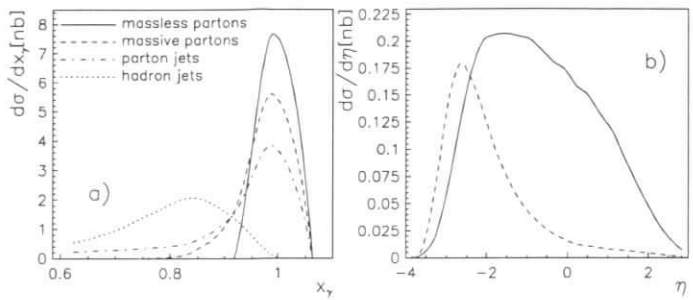

Figure 1: a) Distributions of x_γ in direct channel for $2 < P^2 < 5$ GeV^2, taking into account various smearing effects. b) The η distributions of jets with $E_T > 5$ GeV in direct (dashed curve) and resolved (solid curve) channels.

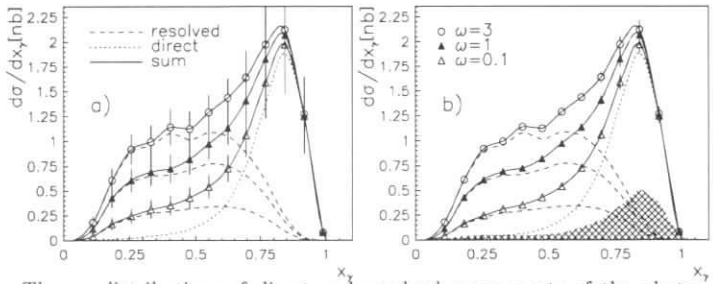

Figure 2: The x_γ distributions of direct and resolved components of the photon and their sum for three values of ω and jets with $\eta < -0.5$. Superimposed are present (a) as well as anticipated future (b) statistical error bars. The hatched in b) area shows systematic error due to 3% uncertainty in jet energy measurement.

$x_\gamma \approx 0.5$. The cross–over point, where the two contributions are equal depends on ω and P^2 but lies around $x_\gamma^{cr} = 0.75$. The peak of the direct photon contribution at $x_\gamma = 0.85$ is reflected in the η distribution (not shown) as the dominance of the direct component in the low η region around $\eta \approx -3$. The error bars superimposed in Fig. 2a on the MC results characterize the present statistical errors, while those in Fig. 2b indicate the effect of increasing the present luminosity by a factor of 50 to 50 pb^{-1}. This increase would allow rather detailed study of P^2 dependence of overall suppression factor. To measure the x_γ dependence of the virtual photon PDF would, however, require still significantly higher luminosity.

The crudest measure of the resolved photon contribution to jet cross–sections is the ratio $R \equiv \sigma^{\text{resolved}}/\sigma^{\text{direct}}$. It depends, beside ω, sensitively on $p_T^{\min}$ and also on cuts on η. We consider $p_T^{\min} = 5$ GeV as is the minimal reasonable lower cut–off on p_T^{jet}. Increasing $p_T^{\min}$ would significantly improve the possibility of separating direct and resolved components but, on the other hand, lower the statistics. In Fig. 3 we plot the ratio R as a function of P^2 for three

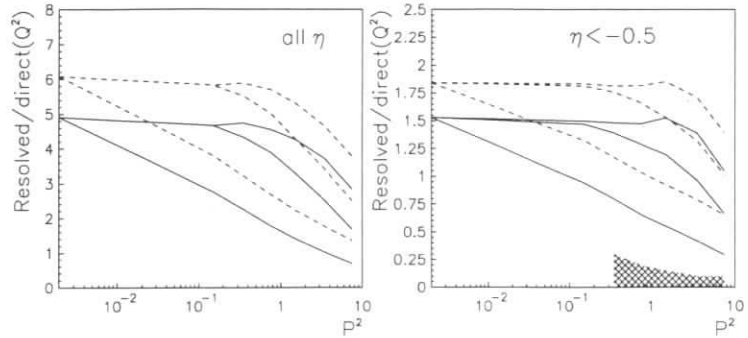

Figure 3: P^2 dependence of the ratio $R \equiv \sigma^{\text{resolved}}/\sigma^{\text{direct}}$. The hatched area shows the systematic error due to 3% uncertainty in jet energy measurement. Solid lines correspond to R as given by generator, the dashed ones to the method based on the x_{cr} cut–off described in the text. The triplets of solid and dashed curves correspond from above to $\omega = 3, 1, 0.1$.

values of ω. The solid curves correspond to R evaluated from the knowledge, available in MC generators, of separate contributions of direct and resolved channels. In real experiments at HERA we may attempt to separate them using the cut on x_γ, defining the resolved contribution by the condition $x_\gamma \leq x_\gamma^{\text{crit}} = 0.75$ and complementarily for the direct one. The corresponding results for R are shown as dashed curves in Fig. 3.

Conclusions:

- Higher luminosity is clearly a precondition to serious studies of virtual photon structure.
- Kinematical region of positive η in hadronic CMS and large $\mid \Delta\eta \mid$ can further enhance the contribution of the resolved component.
- Direct photon component should be observable at about $x_\gamma \doteq 0.85$.
- Generator dependence should be investigated.

References

[1] T. Ebert (H1 Collab.): Talk at the DIS96 Workshop, Rome 1996

[2] Foudas (ZEUS Collab.): Talk at the DIS96 Workshop, Rome 1996

[3] J. Drees, R. Godbole: Phys. Rev. **D50** (1994), 3124

Access to the NLO Gluon Distribution of the Photon

J. Binnewies[a], M. Erdmann[b], B.A. Kniehl[c], G. Kramer[a]

a II.Inst. f. Th. Physik, Universität Hamburg, Luruper Chaussee 149, D-22761 Hamburg, FRG
b Physikalisches Institut, Universität Heidelberg, Philosophenweg 12, D-69120 Heidelberg, FRG
c Max-Planck-Institut für Physik, Föhringer Ring 6, D-80805 München, FRG

Abstract: Inclusive differential rapidity cross sections of charged particles with large transverse momenta are sensitive to the parton content of the photon. We discuss the accuracy of a future measurement and the uncertainties of the different input distributions required for the next-to-leading order (NLO) QCD calculations.

1 Motivation and Method

The fluctuations of photons into quark-anti-quark pairs have been studied in deep inelastic electron-photon scattering ($e\gamma$ DIS) at e^+e^- colliders [1]. The subsequent radiation of gluons from the quark or anti-quark has been analyzed in resolved photon-proton scattering at the ep collider HERA. Here the first measurement of the gluon distribution in the photon was carried through using two-jet events and a leading order (LO) QCD analysis [2]. However, sizable error bars resulted from the uncertainties in the corrections of the underlying event energy effects.

In this contribution we suggest a measurement of the inclusive differential rapidity cross sections $d\sigma/d\eta$ of charged particles in γp scattering in the range $-1.5 < \eta < 2.5$. By comparison with a next-to-leading (NLO) QCD calculation, the gluon distribution of the photon can be extracted at NLO. The transverse momenta of these hadrons should be sufficiently large in order to a) minimize the influence of underlying event effects which cannot be calculated in NLO QCD, and b) have the scale in a regime where perturbative QCD calculations give reliable results.
On the other hand, p_t should not be much larger, since the sensitivity to the gluon component in the photon decreases with increasing p_t. Our choice of $p_t > 4$GeV satisfies both requirements.

The rapidity of the particles is to some extent correlated with the incoming fractional energy $x_\gamma = E_{parton}/E_\gamma$ of the parton from the photon side. In LO QCD, x_γ can be reconstructed from the two final state partons using $x_\gamma = p_t\,(e^{-\eta_1} + e^{-\eta_2})/(2E_\gamma)$. Here we have predominantly one high-p_t particle per event with $p_t \approx 4$ GeV, carrying a rapidity η and reflecting the direction of one of the final state partons. With $\eta \propto \ln x_\gamma$, the rapidity distribution is sensitive to the parton distribution functions (PDF's) of the photon with a lower limit around $x_\gamma = 0.01$.

2 Measurement

The inclusive differential rapidity cross section for charged particles has been measured before [3]. Events were used where the scattered electron is tagged in the electron detector of the luminosity system. The statistical uncertainty from an integrated luminosity of 1 pb^{-1} was however too large at $p_t > 4$ GeV for a sufficiently precise measurement. A future measurement using 100 pb^{-1} will result in a statistical uncertainty of order 1%. The dominant systematic error is an overall uncertainty in the luminosity measurement which is currently of order 1−2%.

The rapidity interval of the previous measurements was $|\eta| < 1.5$. In future measurements it should be extended to the positive rapidity region as far as possible (forward trackers reach $\eta = 2.5$) to also cover the region of small x_γ.

In order to control the scaling violation, the differential cross section need to be measured in bins of p_t between $4 < p_t < 12$ GeV. $d\sigma/d\eta$ is expected to exhibit not only a decrease in the rate, but also a strong change in the shape of the distribution. The statistical error will be of order 5% in the highest anticipated bin $10 < p_t < 12$ GeV, which is still tolerable.

3 Prediction in NLO QCD

The NLO QCD calculation of the charged particle cross sections requires five ingredients. These are the splitting function $f_{\gamma/e}$, the PDF's for the photon and the proton ($f_{i/\gamma}$ and $f_{j/p}$), the fragmentation functions (FF's) $D_{h/k}$, and the hard scattering cross section $d\hat{\sigma}_{ij\to k}/d\eta$:

$$\frac{d\sigma^h}{d\eta} = \sum_{ijk=1}^{4} \int dy dx_\gamma dx_p dz\, f_{\gamma/e}(y,Q^2)\, f_{i/\gamma}(x_\gamma, M_i^2)\, f_{j/p}(x_p, M_i^2)\, \frac{d\hat{\sigma}_{ij\to k}}{d\eta}(\mu^2, M_i^2, M_h^2)\, D_{h/k}(z, M_h^2).$$

Here y denotes the scaled photon energy, x_p the fractional energy of the parton entering the hard scattering process from the proton side, z is the energy carried by the hadron relative to the energy of the scattered parton, Q^2 the virtuality of the photon, and μ, M_i, M_h the renormalization, factorization, and fragmentation scales. In the following the uncertainties in the different contributions are discussed. They are partly shown in Fig. 1:

$f_{\gamma/e}$: The Equivalent Photon Approximation for events where the scattered electron is measured at small scattering angles is precise to the percent level.

$f_{i/\gamma}$: (Fig.1a) The quark distributions in the photon $f_{q/\gamma}$ have been measured in $e\gamma$ DIS with an accuracy of $\approx 30\%$ in the relevant kinematic region [1]. With the upcoming measurements at the LEP2 collider the precision in $f_{q/\gamma}$ will improve to the level of a few percent [4]. The gluon distribution in the photon $f_{g/\gamma}$ has so far the largest uncertainty and is expected to contribute up to 50% to the cross section.

$f_{j/p}$: (Fig.1b) The uncertainties in the PDF's of the proton currently contribute < 10% to the uncertainty in the cross section calculation. This error will be reduced with new HERA data and analysis.

$d\hat{\sigma}/d\eta$: (Fig.1c) The NLO QCD parton cross sections have been calculated for direct and resolved photoproduction processes [6]. The dependence of the calculation on the renormalization, factorization and fragmentation scales has been studied in multiples ξ of the hadron transverse momenta p_t. With the requirement $p_t > 4$ GeV the scale dependence of the calculation does not show a point of minimal sensitivity. We employ the method of fastest apparant convergence, which yields a scale of $\xi = 1/\sqrt{2}$. Variations of this scale choice between $0.5 < \xi < 1$ result in an overall shift of the cross section, but not in a sizeable change of its shape.

$D_{h/k}$: (Fig.1d) The quark FF's $D_{h/q}$ have been determined from e^+e^- data with an accuracy of a few percent [7]. The gluon FF $D_{h/g}$ currently has a relatively large uncertainty. The gluon FF is expected to increase by about 45%, when $\mathcal{O}(\alpha_S^2)$ corrections to the cross section are included in the analysis [8]. With new LEP data on the longitudinal polarized cross sections, the uncertainty in $D_{h/g}$ will be reduced to below 10%.

Therefore, in 1997 the expected uncertainty in the theoretical calculation – apart from the gluon contribution of the photon $f_{g/\gamma}$ – is expected to be at the level of 10%. Comparisons of precise cross section measurements with the NLO calculations will then allow the extraction of $f_{g/\gamma}$ for a fixed choice of the scale.

4 Summary

A measurement of the inclusive rapidity cross section for charged particles with $p_t > 4$ GeV will have an accuracy of order few percent using an integrated luminosity of 100 pb^{-1}. The uncertainty of a corresponding NLO QCD calculation due to the input PDF's (except for the gluon in the photon) and the FF's is expected to be at the level of 10% in 1997. The comparison between the measurement and the calculation at a fixed scale will then allow the extraction of the NLO gluon distribution in the photon with a precision of order 10%.

References

[1] Ch. Berger and W. Wagner, Phys. Rep. 146 (1987) 1; H. Kolanoski and P. Zerwas, DESY-87-175 (1987), 'High Energy Electron-Positron Physics', Ed. A. Ali and P. Söding, Singapore: World Scientific (1988); T. Sjöstrand, J.K. Storrow, A. Vogt, LU-TP-96-5 (1996), to appear in 'Durham Workshop on HERA Physics', Durham, (1995)

[2] H1 Collab., T. Ahmed *et al.*, Nucl. Phys. B445 (1995) 195

[3] H1 Collab., I. Abt *et al.*, Phys. Lett. B328 (1994) 176; W. Hoprich, diploma thesis, Heidelberg (1995)

[4] P. Aurenche, G.A. Schuler *et al.*, in 'Physics at LEP2', eds. G. Altarelli, T. Sjöstrand and F. Zwirner, CERN (yellow report) 96-01, p.291

[5] M. Glück, E. Reya and A. Vogt, Phys. Rev. D46 (1992) 1973

[6] B.A. Kniehl and G. Kramer, Z. Phys. C62 (1994) 53

[7] J. Binnewies, B.A. Kniehl and G. Kramer, Phys. Rev. D52 (1995) 4947

[8] P.J. Rijken and W.L. van Neerven, hep-ph 9604436 (1996); J. Binnewies, in preparation

[9] L.E. Gordon and J.K. Storrow, Z. Phys. C56 (1992) 307

[10] P. Aurenche, J.P. Guillet and M. Fontannaz, Phys. Lett. B338 (1994) 98

[11] M. Glück, E. Reya and A. Vogt, Z. Phys. C53 (1992) 127

[12] H.L. Lai, J. Botts, J. Huston, J.G. Morfin, J.F. Owens, J.W. Qiu, W.K. Tung, and H. Weerts, Phys. Rev. D51 (1995) 4763

[13] A.D. Martin, W.J. Stirling, and R.G. Roberts, Phys. Lett. B354 (1995) 155

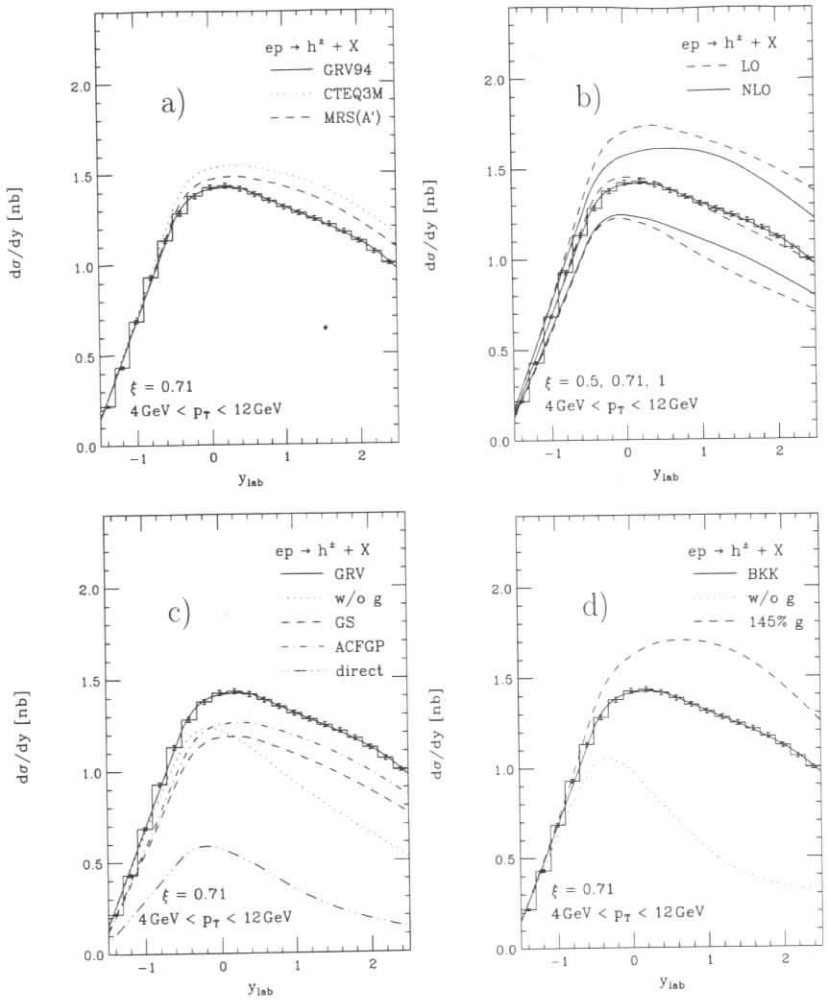

Figure 1: The inclusive differential rapidity cross section for charged particles with $4 < p_t < 12$ GeV, $-1.5 < \eta < 2.5$ is shown for events with photon energy $0.3 < y < 0.7$ and virtualities $Q^2 < 0.01$ GeV^2. The symbols represent a possible measurement with statistical errors corresponding to an integrated luminosity of 100 pb^{-1}.
a) $f_{i/p}$: the full (dotted) [dashed] curve gives the NLO QCD calculations using the proton PDF of GRV [11] (CTEQ3M [12]) [MRS(A') [13]].
b) The scale dependence of a LO (dashed) and NLO (full) QCD calculation is shown as function of $\xi = \mu/p_t$.
c) $f_{i/\gamma}$: the full (dashed) [dot-dashed] curve gives the NLO QCD calculations using the photon PDF's of GRV [5] (GS [9]) [ACFGP [10]]. The double-dot-dashed curve is the direct γ component, the dotted curve shows the contribution resulting from the direct γ and the quark distribution of the photon (using GRV).
d) $D_{h/k}$: contribution of the quark FF $D_{h/q}$ (dotted) and total (quark+gluon) FF (full) are shown [7]. The dashed curve corresponds to a 45% rise in $D_{h/g}$, as expected for an updated analysis.

Matching Experimental and Theoretical Jet Definitions for Photoproduction at HERA

J.M. Butterworth[a], L. Feld[b], M. Klasen[c], G. Kramer[c]

[a] University College London, Physics and Astronomy Dept., London, U.K.
[b] Physikalisches Institut der Universität Bonn, Bonn, FRG
[c] II. Institut für Theoretische Physik, Universität Hamburg, Hamburg, FRG

Abstract: Predictions from a new next-to-leading order (NLO) calculation for direct and resolved photoproduction of one and two jets are compared to simulated HERA data. We propose a method to match experimental and theoretical jet definitions and observe a reduced dependence on jet definitions and hadronization corrections at larger transverse energies. From the irreducible uncertainty, we estimate the maximum benefit that can be obtained from increased luminosity to constrain the structure of the photon and the proton.

1 Introduction

Hard scattering of real photons off partons can be reliably predicted by perturbative QCD. The first NLO QCD calculation for complete (direct and resolved) photoproduction of one and two jets was completed recently [1]. It is based on the phase space slicing method and uses an invariant mass cut to integrate soft and collinear singularities analytically. The program has successfully been tested with an older existing program in single jet production [2]. In order to be able to compare these theoretical cross sections to experimental data in photoproduction of jets from the ep collider HERA [3, 4], the soft interaction links between initial and final state partons and hadrons have to be under control. Therefore it is only possible to extract new information on the parton densities in the proton and the photon if the jet definitions in the measurement and in the theoretical prediction match. In this paper we propose a method to achieve this for various jet algorithms. The experimental cross sections are simulated for 1994 HERA conditions, where electrons of energy $E_e = 27.5$ GeV collided with protons of energy $E_p = 820$ GeV, using HERWIG 5.8 [5].

2 Jet Definitions

According to the standardization of cone jet algorithms at the Snowmass meeting in 1990 [6], calorimeter cells or partons i are included in a jet, if they have a distance of

$$R_i = \sqrt{(\eta_i - \eta_J)^2 + (\phi_i - \phi_J)^2} \leq R \qquad (1)$$

from the jet center and a distance of

$$R_{ij} = \sqrt{(\eta_i - \eta_j)^2 + (\phi_i - \phi_j)^2} \leq \frac{E_{T_i} + E_{T_j}}{\max(E_{T_i}, E_{T_j})} R \tag{2}$$

from each other. Here, $\eta = -\ln[\tan(\theta/2)]$ is the pseudorapidity related to the polar angle θ, and ϕ is the azimuthal angle. If two partons have equal transverse energy they may be separated from each other by as much as $2R$. As parton j does then not lie inside a cone of radius R around parton i and vice versa, one might with some justification also count the two partons separately. If one wants to study only the highest-E_T jet, this "double counting" must be excluded. The definition of an initiating cluster before a cone is introduced ("seed-finding") is not fixed by the Snowmass convention, and different approaches are possible. The ZEUS collaboration at HERA uses two different cone algorithms: EUCELL takes the calorimeter cells in a window in $\eta - \phi$ space as seeds to find a cone with the highest E_T. The cells in this cone are then removed, and the search is continued. On the other hand, PUCELL was adapted from CDF and starts with single calorimeter cells. It then iterates cones around each of them, until the set of enclosed cells is stable. In this case it may happen that two stable jets overlap. If the overlapping transverse energy amounts to a large fraction of the jets, they are merged, otherwise the overlapping energy is split. In addition, we simulate the same cross sections with the k_T algorithm KTCLUS [7, 8], where particles are combined if their distance

$$d_{ij} = \min(E_{T_i}, E_{T_j})^2 R_{ij}^2 \tag{3}$$

is small. As the same recombination scheme is used, the results are quite similar to the PUCELL results. In the following we choose $R = 1$ throughout. Partonic jets with a large distance of two contributing partons are hard to find because of the missing seed in the jet center. This is especially true for the PUCELL algorithm, which does not perform a preclustering and does indeed find smaller cross sections and different hadronization corrections than the less affected EUCELL algorithm. We propose to model this theoretically by introducing an additional parameter $R_{\rm sep}$ to restrict the distance of two partons from each other [9]. This modifies eq. (2) to

$$R_{ij} \leq \min\left[\frac{E_{T_i} + E_{T_j}}{\max(E_{T_i}, E_{T_j})} R, R_{\rm sep}\right]. \tag{4}$$

The meaningful range of $R_{\rm sep}$ is between 1 and 2. For two partons of similar or equal transverse energies E_T, $R_{\rm sep}$ is the limiting parameter, whereas it is the parton-jet distance R for two partons with large E_T imbalance. On a NLO three parton final state we find that $R_{\rm sep} = 1.5...2$ for EUCELL and $R_{\rm sep} \simeq 1$ for PUCELL and KTCLUS.

3 Results

In figure 1, we show the dijet cross section $\mathrm{d}\sigma/\mathrm{d}\overline{\eta}$ with $E_T > 6$ GeV and $\Delta\eta = (\eta_1 - \eta_2) \in [-0.5, 0.5]$ for a) direct and b) resolved photoproduction as a function of the average pseudorapidity of the two observed jets $\overline{\eta} = (\eta_1 + \eta_2)/2$. The photon distribution in the electron is taken from the Weizsäcker-Williams approximation with maximum virtuality of $Q^2_{\rm max} = 4$ GeV^2 and longitudinal momentum fraction $y \in [0.2, 0.8]$. The direct and resolved regions are defined by $x_\gamma^{\rm OBS} > 0.75$ and $x_\gamma^{\rm OBS} \in [0.3, 0.75]$, where the sum in $x_\gamma^{\rm OBS} = \frac{\sum_i E_{T_i} e^{-\eta_i}}{2yE_e}$ runs over the two jets

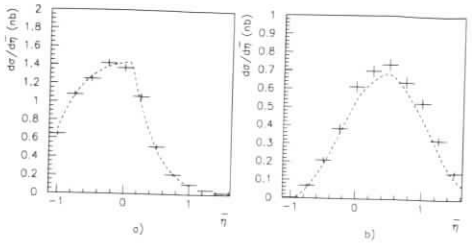

Figure 1: *Demonstration of compatibility of the HERWIG Monte Carlo generator on matrix element level (histograms) and the leading-order (LO) perturbative QCD prediction (curves) for a) direct and b) resolved dijet cross sections* $\mathrm{d}\sigma/\mathrm{d}\overline{\eta}$.

with largest E_T. In both regions, direct and resolved contributions are added because only their sum is physically meaningful. We demonstrate the compatibility of the two tools used in this study comparing the HERWIG Monte Carlo generator on LO matrix element level and the LO perturbative QCD prediction. We use the CTEQ3L proton and the GRV$_\gamma$(LO) photon structure functions. It was not possible to calculate α_s in 1-loop approximation in HERWIG, so we took the (inconsistent) choice of the 2-loop formula for α_s with $\Lambda^{(4)}_{\rm QCD} = 177$ MeV for this part in the calculation as well. The scales in HERWIG could also not be changed from $\mu^2 = M_\gamma^2 = M_p^2 = 2stu/(s^2 + t^2 + u^2)$, but the effect with respect to using E_T^2 as in the calculation is very small. After these adjustments, HERWIG agrees with the LO QCD prediction.

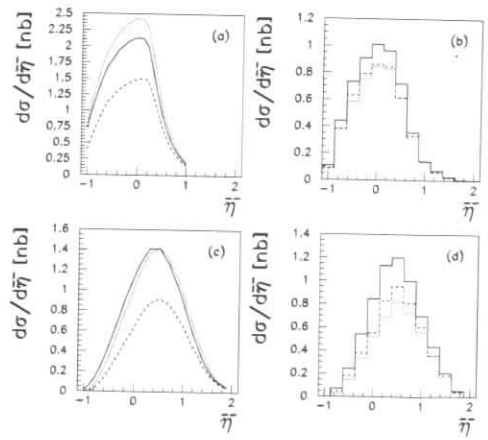

Figure 2: *NLO (left) and HERWIG (right) predictions for direct (top) and resolved (bottom) dijet cross sections* $\mathrm{d}\sigma/\mathrm{d}\overline{\eta}$. *We compare jet double counting (dotted), no* $R_{\rm sep}$ *(full), and* $R_{\rm sep} = 1$ *(dashed) curves with EUCELL (full), PUCELL (dashed), and* k_T *(dotted) histograms.*

Figure 2 shows the same cross section for different jet algorithms. We compare our new NLO calculation with jet double counting, without jet double counting, and with $R_{sep} = 1$ to simulated data from HERWIG with the EUCELL, PUCELL, and KTCLUS algorithms run on the final state particles. In the calculation, we now use a NLO set of input parameters, i.e. CTEQ3M proton, GRV$_\gamma$(HO) photon structure functions, and 2-loop α_s with $\Lambda^{(4)}_{\overline{\rm QCD}} = 239$ MeV. For the Monte Carlo, we now take HERWIG including parton showers and hadronization. Due to the different parameters used in the NLO calculation and in HERWIG, we do not expect the overall normalization of HERWIG and NLO QCD to agree. However, the relative changes between no R_{sep} (equivalent to $R_{sep} = 2$) and $R_{sep} = 1$ on the theoretical side and EUCELL and PUCELL or KTCLUS on the experimental side show the expected similar behaviour, so that the R_{sep} parameter is well suited to match theoretical and experimental jet definitions. Jet double counting does not correspond to an experimental situation and is only shown to illustrate its effect on the theory.

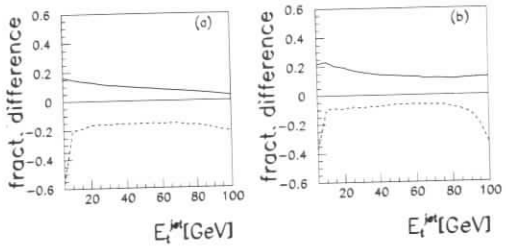

Figure 3: *E_T-dependence of the Snowmass jet definition uncertainties for a) direct and b) resolved dijet cross sections $d\sigma/dE_T$. We demonstrate the effects of jet double counting (full curves) and setting $R_{sep} = 1$ (dashed curves) compared to no double counting with $R_{sep} = 2$.*

The E_T-dependence of the Snowmass jet definition uncertainties is shown in figure 3 for the a) direct and b) resolved dijet cross sections $d\sigma/dE_T$, where we integrated over the complete $\overline{\eta}$ range and over $\Delta\eta \in [-0.5, 0.5]$. The fractional difference of jet double counting from no double counting amounts to $\sim 20\%$ at 5 GeV and decreases continuously towards larger E_T. Including the parameter $R_{sep} = 1$ lowers the cross sections by as much as $\sim 40\%$ at 5 GeV, but its influence drops rapidly and gives a constant difference of about 20% (direct) and 10% (resolved) almost over the whole E_T-range. Only at the boundary of phase space at very large E_T, the fractional difference increases again. Thus, one should match the jet definitions at small and large E_T even more carefully.

The E_T-dependence of the hadronization corrections is shown in figure 4 for the a) direct and b) resolved dijet cross sections $d\sigma/dE_T$. We integrated again over the complete $\overline{\eta}$ range and over $\Delta\eta \in [-0.5, 0.5]$. At low transverse energies of $E_T \simeq 5$ GeV, the hadronization corrections amount to $\sim 20\%$ - a comparable effect to the theoretical uncertainties discussed before. They decrease very nicely towards larger E_T and vanish at 30 to 40 GeV to establish the correspondence between partonic and hadronic jets there. The error bars are due to limited statistics

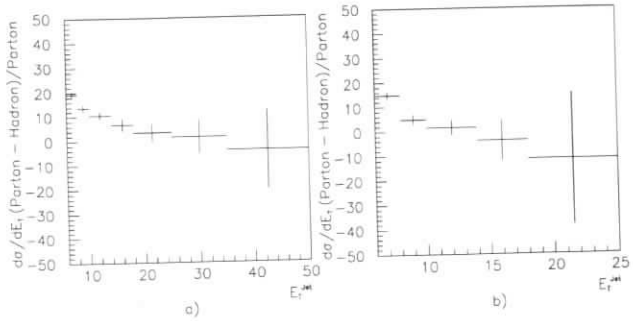

Figure 4: *E_T-dependence of hadronization corrections for a) direct and b) resolved dijet cross sections $d\sigma/dE_T$.*

and could be drastically reduced with more computer time.

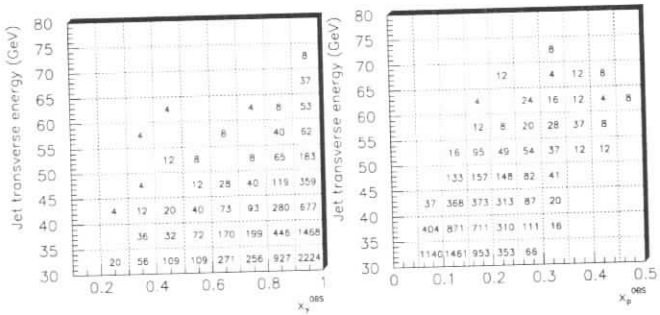

Figure 5: *Number of events produced at an increased HERA luminosity of 250 pb^{-1} as a function of x_γ^{OBS} (left), x_p^{OBS} (right), and transverse jet energy E_T.*

Finally, we estimate the benefit that can be obtained from an increased HERA luminosity of 250 pb^{-1} to constrain the photon and the proton parton densities. Figure 5 gives the number of jets produced as a function of x_γ^{OBS} (left), x_p^{OBS} (right), and transverse jet energy E_T, where the bin sizes reflect the approximate expected experimental resolution. The cuts applied to the dijet cross section are $y \in [0.2, 0.9]$, $E_T > 30$ GeV, and $\eta < 2$. If we require at least 100 events, where statistical and systematic errors start to be of comparable size, jets with transverse energies up to 55 GeV can be measured, where the jet double counting uncertainties and hadronization corrections are very much reduced. We can still test the photon structure at large E_T in the region of $x_\gamma^{OBS} = 0.4-1$ and the proton structure in the region $x_p^{OBS} = 0.05-0.3$.

4 Conclusions

Constraining the proton and photon structure functions in photoproduction of jets at HERA requires a good understanding of the jets in experiment and in theory. We used a new NLO calculation and simulated HERA data to match different experimental jet definitions (EUCELL, PUCELL, and KTCLUS) with theory predictions with different values for the $R_{\rm sep}$ parameter. At larger transverse energies, the uncertainties from different theoretical jet definitions and hadronization corrections are reduced. These regions can be studied if the HERA luminosity is increased to 250 pb^{-1}, thus providing valuable information on the proton and photon structure functions over large x ranges.

References

[1] M. Klasen, G. Kramer, to be published.

[2] M. Klasen, G. Kramer, S.G. Salesch, Z. Phys. **C68** (1995) 113.

[3] M. Derrick et al., ZEUS collaboration, Phys. Lett. **B348** (1995) 665.

[4] S. Aid et al., H1 collaboration, Z. Phys. **C70** (1996) 17.

[5] G. Marchesini et al., Comp. Phys. Comm. **67** (1992) 465.

[6] J.E. Huth et al., Proc. of the 1990 DPF Summer Study on High Energy Physics, Snowmass, Colorado, edited by E.L. Berger, World Scientific, Singapore (1992) 134.

[7] S. Catani, Yu.L. Dokshitzer, M.H. Seymour and B.R. Webber, Nucl. Phys. **B406** (1993) 187.

[8] S.D. Ellis, D.E. Soper, Phys. Rev. **D48** (1993) 3160.

[9] S.D. Ellis, Z. Kunszt, D.E. Soper, Phys. Rev. Lett. **69** (1992) 3615.

Colour Coherence in Photon Induced Reactions

A. Lebedev[a], L. Sinclair[b], E. Strickland[b], J. Vazdik[a].

[a] P.N.Lebedev Physical Institute, Academy of Sciences of Russia, Leninsky Prospect 53, 117924 Moscow, Russia

[b] Department of Physics and Astronomy, Glasgow University, G12 8QQ Glasgow, Scotland, U.K.

Abstract: Colour coherence in hard photoproduction is considered using the Monte Carlo event generators PYTHIA and HERWIG. Significant effects in the parton shower are found using multijet observables for direct and resolved photon induced reactions. The particle flow in the interjet region of direct processes shows a strong influence of string fragmentation effects.

1 Introduction

Colour coherence is an intrinsic property of QCD. Its observation is important in the study of strong interactions and in the search for deviations from the Standard Model [1]. It is interesting to look for colour coherence effects in hard photoproduction processes at the ep-collider HERA where large momentum transfers can be achieved and both direct (Fig. 1(a)) and resolved (Fig. 1(b)) photon induced events occur. In Section 2 multijet observables are studied which

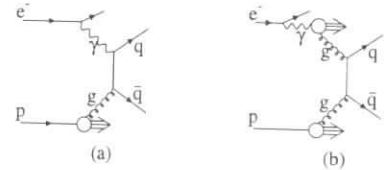

Figure 1: *Examples of (a) direct and (b) resolved photoproduction*

reveal coherence at the parton shower level for both direct and resolved photoproduction. In Section 3 consideration of the particle flow in direct photoproduction shows colour coherence effects at the fragmentation stage of hadron production.

2 Multijet observables

The effects of colour coherence on the emission pattern of jets in e^+e^- collisions are well known and intuitive. However in hadron–hadron collisions the large number of possible colour flows involved in jet production complicates the identification of variables sensitive to coherence.

Here, radiation patterns in γp collisions are studied by considering events where soft radiation is hard enough to form a jet. This reduces the effect of secondary interactions in resolved photoproduction.

The effects arising from different implementations of coherence were studied using 500 pb^{-1} of events generated with PYTHIA 5.7 [2] and HERWIG 5.8 [3]. Direct and resolved events were generated separately and combined according to their cross sections. Events were generated with a minimum p_T of 20 GeV using the GRV proton and photon structure functions [4]. Two event samples were generated using PYTHIA: the PYTHIA Coherent sample and the PYTHIA Incoherent sample which was obtained by switching off the coherence in the parton shower and the initial-final state coherence. HERWIG represents an alternate implementation of coherent processes. Jets of particles were found using the KTCLUS [5] algorithm in covariant p_T mode with radius equal to 1. Three jet events with at least two jets of transverse energy (E_t^{jet}) satisfying $E_t^{jet} > 30$ GeV and a third jet of $E_t^{jet} > 3$ GeV were selected. The jets are ordered by E_t^{jet} decreasing and referred to as "first", "second" and "third" jet acccordingly in the following. Two scenarios were considered, one to reflect the acceptance in jet pseudorapidity (η^{jet}) of the present ZEUS detector, $|\eta^{jet}| < 2.5$, and one to show the possibilities with an extended acceptance, $|\eta^{jet}| < 4$. In addition the events satisfied $0.2 < y < 0.85$ and $P^2 < 4$ GeV^2, where P^2 is the negative of the four-momentum squared of the photon.

An overall drop in cross section is observed between incoherent and coherent event samples. For example, with a luminosity of 250 pb^{-1} and the standard detector acceptance, $|\eta^{jet}| < 2.5$, 2600 multijet events are predicted by PYTHIA Incoherent, 1728 by PYTHIA Coherent and 1665 events by HERWIG. For comparison in the extended acceptance scenario, $|\eta^{jet}| < 4$, 3012 multijet events are predicted by HERWIG.

The angular distribution of the third jet is also affected. Following [6] the angle α is defined as the azimuthal angle of the third jet about the second jet in the $\eta - \varphi$ plane. Here, however, we use centre-of-mass (c.m.) variables so $\alpha = \arctan(\Delta H/|\Delta\varphi|)$ where $\Delta H = \mathrm{sign}(\eta_2^{cm})(\eta_3 - \eta_2)$ and $\eta_2^{cm} = \eta_2 - 1/2(\eta_2 - \eta_1)$ and $\Delta\varphi = \varphi_3 - \varphi_2$. η_1, η_2 and η_3 refer to the pseudorapidities in the lab frame of the first, second and third jets respectively and positive η is in the direction of the incoming proton. $\Delta\varphi$ is the difference in azimuth (φ) between the second and third jets (in radians). The definition of α is illustrated for a typical event geometry in Fig. 2(c). The distribution of α as shown in Fig. 2(a) is broader for coherent events. This is consistent

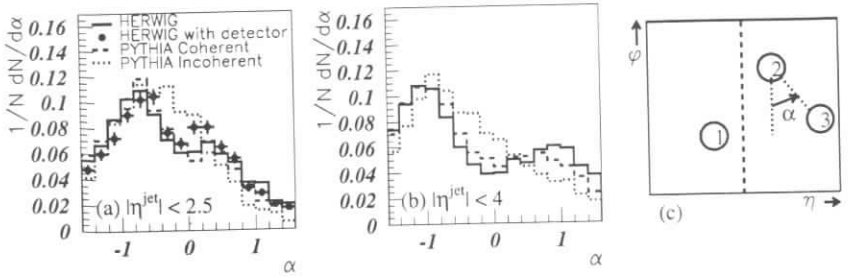

Figure 2: *α distributions (a) with the present acceptance and (b) with extended acceptance. (c) illustrates the definition of α for a typical event geometry. Jets are ordered by E_t^{jet} decreasing.*

with our understanding that for coherent processes radiation is generally suppressed in regions far from the directions of the incoming coloured partons. In addition, reducing the bias on the distribution by increasing the acceptance from $|\eta^{jet}| < 2.5$ to $|\eta^{jet}| < 4$ produces a more pronounced depletion in the central region for coherent events (Fig. 2(b)).

Canonical detector effects were simulated by smearing the HERWIG jet quantities with Gaussian distributions of varying widths. A resolution of 20% (10%) was used to smear the E_t^{jet} of jets with $E_t^{jet} < 10$ GeV ($E_t^{jet} \geq 10$ GeV). The width of the difference between generated and detected values of η^{jet} and φ^{jet} was taken to be 0.1. As shown in Fig. 2(a) such detector effects should not seriously hinder the measurement of α distributions.

The coherent emission of soft radiation does not have a strong effect on the jet profiles of the first and second jets. For instance, in Fig. 3(a) the transverse energy profile of the second jet is shown. This is the distribution of $\delta\eta_2 = \eta^{part} - \eta_2$, where η^{part} is the η of a particle within

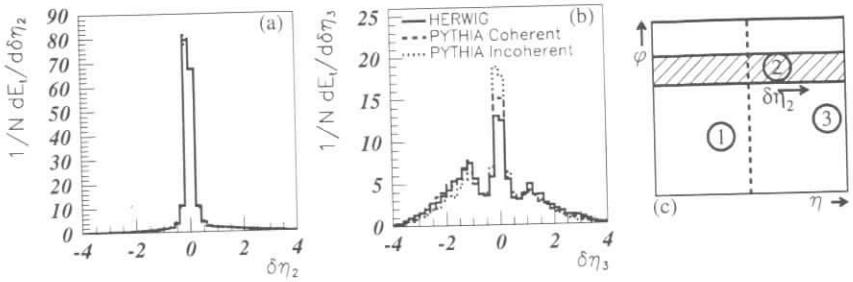

Figure 3: *Jet profiles for (a) the second and (b) the third highest E_t^{jet} jets for the extended acceptance scenario. The definition of the jet profile is illustrated in (c) for the second jet.*

one radian of φ of the jet centre, weighted by the transverse energy of the particle, as illustrated in Fig. 3(c). For this the extended acceptance scenario particles are considered with absolute η up to 5. The profile of the third jet is shown in Fig. 3(b). The occurrence of two peaks outside the jet core is due to partial overlap in φ of the first or second jet. A strong effect of coherence is apparent; it leads to less energy in the core of the third jet.

One of the anticipated effects of colour coherence is that radiation from an incoming parton should be inhibited in regions far from the initial partons direction. Therefore in direct photoproduction events, where the single coloured parton in the initial state has positive η, the coherent emission pattern should be at relatively higher η than the incoherent emission. We have selected a subsample of events which is enriched in direct photon events by requiring $x_\gamma > 0.8$ where $x_\gamma = (\sum_{jets} E_t^{jet} e^{-\eta^{jet}})/(2E_\gamma)$. The sum runs only over the two highest E_T^{jet} jets and E_γ is the energy of the incoming photon. The η of the third jet in the c.m. frame, $\eta_3^{cm} = \eta_3 - 1/2(\eta_2 - \eta_1)$, is shown for this selection in Fig. 4(a). The expected effective enhancement of radiation at large η_3^{cm} can clearly be seen.

Resolved events, with incoming coloured partons from both the γ and p directions, should show an effective enhancement of radiation in coherent processes both at higher positive and at more negative pseudorapidities in comparison to incoherent emission. This effect is evident as shown in Fig. 4(b). Note that the extended acceptance scenario must be employed in order to see the relative enhancement of radiation at high η in resolved events.

To summarize this section, a high integrated luminosity ($\sim 250\mathrm{pb}^{-1}$) is desirable in order to accumulate statistics in multijet events at high E_t^{jet}. However luminosity upgrades which involve a significant reduction of forward acceptance are not worthwhile for this study. They destroy the sensitivity to colour coherence without significantly improving the statistical uncertainty.

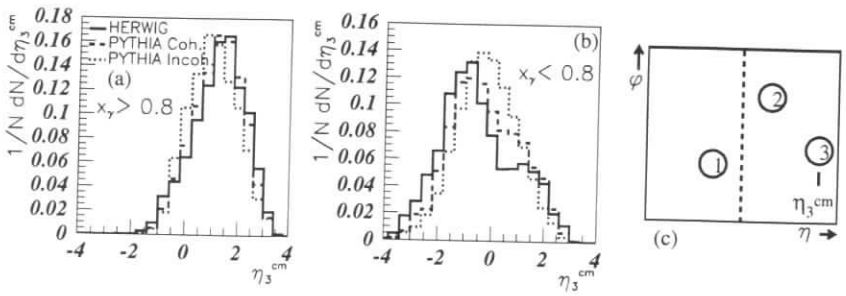

Figure 4: η_3^{cm} *distributions separated by an* x_γ *cut of* 0.8 *into (a) direct and (b) resolved samples for the extended acceptance scenario of* $|\eta^{jet}| < 4$. *In (c) the definition of* η_3^{cm} *is illustrated.*

3 Interjet string effects in direct photoprocesses

Colour coherence effects which lead to a change in particle flow N distributions in the interjet region should be rather pronounced in the direct photon induced processes such as QED Compton on quark (QEDC), QCD Compton (QCDC) and Photon Gluon Fusion (PGF). These distributions are considered here using the PYTHIA [2] generator with string (SF) or independent parton fragmentation (IF) into hadrons. Using SF is equivalent to taking into account the coherence effects at the hadronization phase of event generation. The flow N depends on the string topology and colour antennae which are different for the three direct processes as shown in Fig. 5(left).

The calculation at the generator level was done using the GRV proton structure function [4] and minimum p_T equal to 2.0 GeV. The H1 detector simulation was taken into account as well. A jet-cone algorithm [7] with radius equal to 1 was used for the selection of two jets and gamma-jet events with $E_t^{jet\,or\,\gamma} > 3$ GeV and jet (or final γ) emission angles $25 - 155^o$. This procedure corresponds to the selection of mainly direct processes. The calculated flow of charged particles with $p_t > 0.2$ GeV emitted at angles of less than 20^o to the reaction plane is shown in Fig. 5(right) as a function of the scale angle Ω. Ω is defined [8] as the ratio of the particle angle θ_h to the angle between partons. $\Omega = 0$ corresponds to the direction of the initial state photon; $\Omega = 1$ – the final state quark; $\Omega = -1$ – the final state γ, gluon or antiquark for QEDC, QCDC or PGF respectively; $\Omega = -2$ or 2 – the proton remnant.

It is seen that in the scale angle region between 1 and 2 (region II in Fig. 5) SF (solid histogram, generator level) and IF (dashed histogram, generator level) give different predictions for N. SF taking into account colour forces leads to a suppression of particle flow which is especially strong for QCDC process. The H1 detector simulation (dark circles, SF) weakly distorts the generator level N distribution except for directions close to remnant proton emission where detector acceptance is rather low. Thus colour coherence effects can be observed at the detector level.

It is interesting to consider ratios of particle flows N for different processes since the ratio is less sensitive to experimental errors. The ratios $R = N(QCDC)/N(QEDC)$, $R^* = N(QCDC)/N(PGF)$ are shown in Fig. 6. Fig. 6 displays more clearly the role of colour coherence which leads to drag effects in particle distributions. It is seen that for the case of SF the suppression in N for QCDC is more pronounced than for QEDC and PGF. At $\Omega = 1.7$ the suppression reaches a factor of ~ 3. It has been found that misidentification of quark and

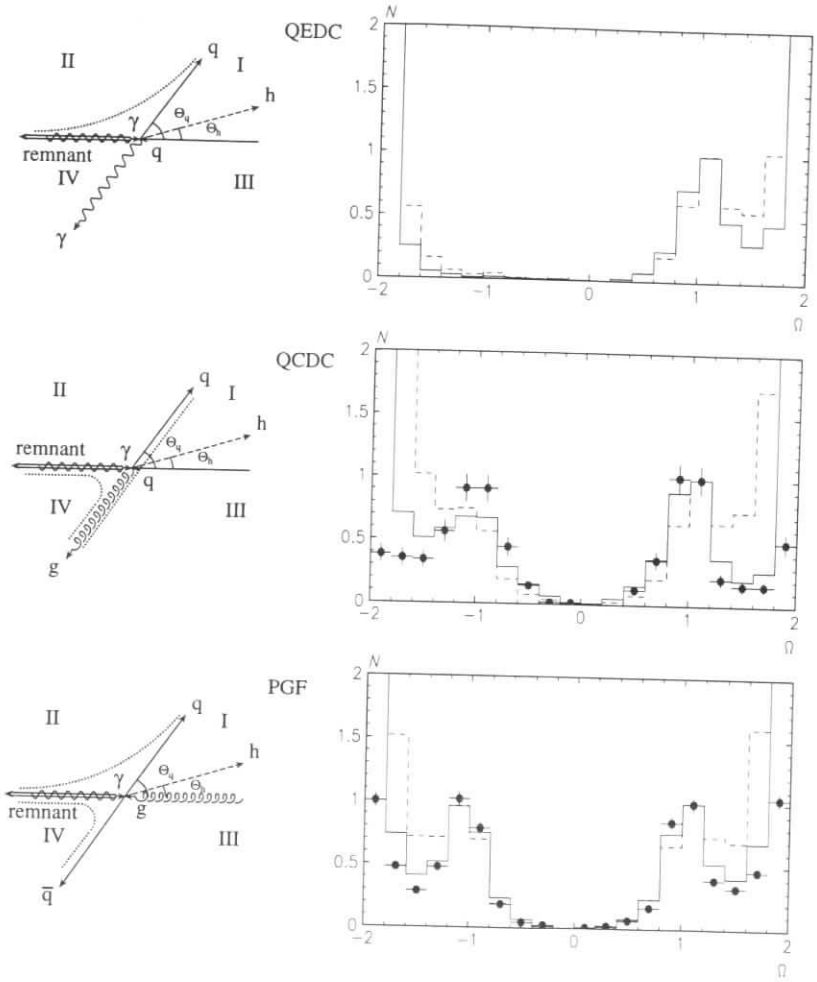

Figure 5: *Left: Topology of direct photoproduction processes in the* $\gamma -$ *parton c.m. frame. The double line is the proton remnant, dotted - strings.* θ_q *and* θ_h *are quark and hadron emission angles. Right: Charged particle flow* N *normalized to 1 at the quark emission angle vs the scale angle* Ω. *Solid line - generator level SF, dashed line - generator level IF, dark circle - H1 simulation SF. In the regions I - IV* Ω *is changing within the limits:* $0 \le \Omega \le 1$ *(I),* $1 \le \Omega \le 2$ *(II),* $-1 \le \Omega \le 0$ *(III),* $-2 \le \Omega \le -1$ *(IV).*

gluon jets for QCDC does not change this conclusion.

To observe colour coherence at the fragmentation stage of hadron production in direct processes it is necessary to distinguish these processes from resolved photoproduction and to

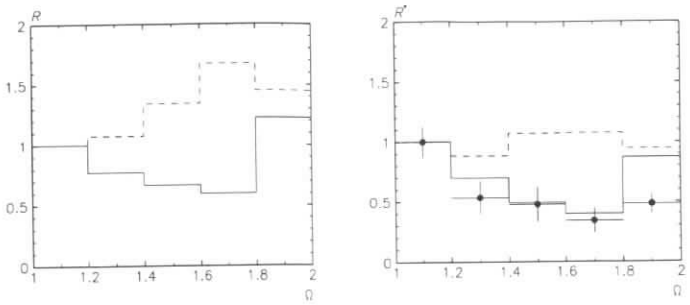

Figure 6: *Ratios R and R^* in the scale angle region $1 < \Omega < 2$. Notations are as in Fig. 5.*

separate QEDC, QCDC and PGF from each other. The jet selection procedure used here enriches the data sample with direct processes. Further enrichment can be achieved by going to larger $E_t^{\text{jet or }\gamma}$ and by choosing events with x_γ close to 1. Since the direct processes cross section is low we expect ~ 230 QEDC events at the detector level for an integrated luminosity of ~ 100 pb^{-1}. So higher luminosity is needed to study interjet coherence.

4 Conclusions

The observation of colour coherence in photoproduction processes is an important challenge, particularly given the unique opportunity at HERA to study direct as well as resolved photon induced reactions. Since the cross sections of multijet events or of prompt photon reactions are small high luminosity ep-collisions are necessary for their study. 250 pb^{-1} would appear to be barely sufficient for these studies; however in upgrading to 1000 pb^{-1} it is essential that the forward acceptance should not be reduced.

References

[1] Yu.L.Dokshitzer, V.A.Khoze, A.H.Mueller and S.I.Troyan, *Basics of Perturbative QCD*, ed. Tran Than Van (Editions Frontières, Gif/Yvette, 1991).

[2] H-U.Bengtsson and T.Sjöstrand, *Computer Phys.Comm.* **46**, 43 (1987); T. Sjöstrand, M.Bengtsson, *Computer Phys.Comm.*, **43**, 367 (1987).

[3] G.Marchesini and B.Webber, *Nucl. Phys. B* **286**, 461 (1988).

[4] M.Gluck, E.Reya, A.Vogt, *Z.Phys. C* **53**, 127 (1992); *Phys. Rev. D* **46**, 1973 (1992).

[5] S.Catani, Yu.L.Dokshitzer, M.H.Seymour and B.R.Webber, *Nucl.Phys. B***406**, 187 (1993).

[6] F.Abe et al, CDF Collaboration, *Phys. Rev. D***50**, 5562 (1994).

[7] J.E.Huth et al, *Fermilab-Conf-90/249-E* (1990).

[8] V.A.Khoze, A.I.Lebedev, J.A.Vazdik, *Mod.Phys.Lett. A* **9**, 1665 (1994).

Rapidity Gaps Between Jets

J. M. Butterworth[a], M. E. Hayes[b], M. H. Seymour[c], L. E. Sinclair[d]

[a] University College London, Physics and Astronomy Dept., London, UK
[b] H.H. Wills Physics Laboratory, University of Bristol, Bristol, UK
[c] TH Division, CERN, CH-1211 Genève 23, Switzerland
[d] Dept. of Physics and Astronomy, University of Glasgow, Glasgow, UK

Abstract: An excess of events with a rapidity gap between jets, over what would be expected from non-diffractive processes, has been observed at HERA. A process based on a perturbative QCD calculation of colour singlet exchange has been added to HERWIG. With this addition, HERWIG is able to describe the number of events with a gap between jets over the number without a gap. This gap fraction is predicted to rise at large rapidity intervals between jets which would only be visible if the detector coverage were increased.

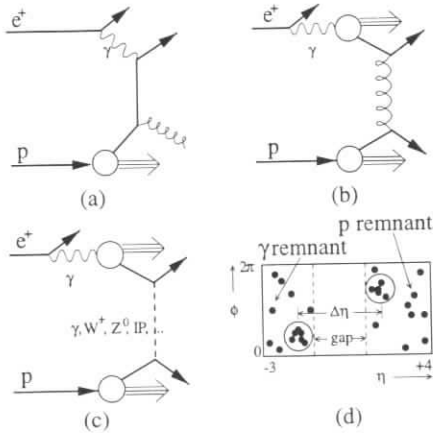

Figure 1: *Feynman diagrams of processes involved. (a) and (b) are examples of the direct and resolved contributions in photoproduction. (c) is the colour singlet exchange. (d) is the representation of how an individual event would appear in η–ϕ space.*

At HERA the incoming electron is accompanied by a cloud of photons. The spectrum of photon virtuality, P^2, is dominated by almost-real photons and, provided P^2 is prevented from being too large, the incoming photon can be regarded as real and the types of event it

participates in are classified as photoproduction events. We use the usual experimental cut of $P^2 < 4GeV^2$. If the event contains one or more jets it is assumed to have a hard interaction and is then perturbatively calculable in QCD; hence it is referred to as a hard photoproduction event. Here we will refer only to these kinds of events. These can be of two main types: direct and resolved photoproduction, shown in figures 1(a) and (b). In the direct case the whole photon interacts with a parton in the proton. In the resolved case the photon 'resolves' into partons, one of which then interacts with a parton from the proton. If the transverse momentum exchanged is high enough, outgoing partons give rise to 'jets' of particles in the detector.

In most cases of parton-parton scattering a coloured object is exchanged (e.g. fig. 1(b)) with an associated colour flow between the outgoing partons and the remnant particles. This can be modelled by a colour string which is stretched across the central rapidity interval. This string then fragments into particles which occupy the region between the two jets. However it is also possible for the exchanged object to be a colour singlet (fig. 1(c)). In this case the colour strings connect each outgoing parton with the remnant jet closest to it in rapidity. This leads to a suppression of particle production in the rapidity region between the two jets. It was first observed at $p\bar{p}$ colliders [1] and subsequently measured at HERA [5].

The presence of high E_T jets in these events guarantees a high value of $\hat{t}$ and assures us of the applicability of perturbative QCD, $-\hat{t}/\Lambda^2_{QCD} \gg 1$ ($\hat{s}$ is the centre of mass energy and $\hat{t}$ the invariant momentum transfer squared of the parton system). In addition, the pseudorapidity interval between the jets, $\Delta\eta$, reflects the separation in rapidity of the outgoing partons, y. Therefore at large $\Delta\eta$ we have $y \simeq \ln(-\hat{s}/\hat{t})$ and $-\hat{s}/\hat{t} \gg 1$. Gluon exchange in the $\hat{t}$-channel increases with $1/\hat{t}^2$. However because a gluon is a coloured object, a rapidity gap does not normally result. Two gluon exchange, which may be in a colour singlet state, can give rise to a rapidity gap. Gluons exchanged between this $\hat{t}$–channel gluon pair can further enhance the cross section such that it rises faster than $1/\hat{t}^2$ at small $\hat{t}$. These gluons can be summed using the BFKL equation [2], to give

$$\frac{\mathrm{d}\sigma(\mathrm{qq} \to \mathrm{qq})}{\mathrm{d}\hat{t}} = (\alpha_s C_F)^4 \frac{\pi^3}{4\hat{t}^2} \frac{\exp(2\omega_0 y)}{[\frac{7}{2}\alpha_s C_A \zeta(3) y]^3},$$

as derived in ref. [3] ($C_F = 4/3$, $C_A = N_c = 3$, $\zeta(3) \simeq 1.202$ is the Riemann zeta function and $\omega_0 = \frac{C_A \alpha_s}{\pi} 4 \ln 2$). The approximations made in deriving this formula mean that the correct scale to use in α_s cannot be determined, and does not even need to be the same in each case. We use $\alpha_s(-\hat{t})$ in the prefactor, $\alpha_s = 0.25$ in the denominator and $\omega_0 = 0.3$ (which have been installed as HERWIG defaults).

The package HzTool [4] was used to generate the Monte Carlo and to compare to the original analysis [5] on ZEUS 1994 data. This facilitated the comparison of the data to the Monte Carlo generated. HERWIG 5.8d [6] was upgraded to include the QCD calculation [3] described above. About 2.6pb^{-1} (the 1994 ZEUS luminosity) of events were then generated. A cone-based jet finding algorithm was run on this sample. Events were required to have at least two jets of $E_T^{jet} > 6$ GeV with pseudorapidity satisfying $\eta_{jet} < 2.5$. Denoting by η_1 and η_2 the pseudorapidities of the two highest E_T jets, the events were required to satisfy in addition $|\frac{\eta_1+\eta_2}{2}| < 0.75$ and $\Delta\eta = \eta_1 - \eta_2 > 2$. Events with no particle with transverse energy greater than 300 MeV between the two jets were then classified as 'gap' events. The characteristic signature of these events is illustrated in fig. 1(d).

The selected sample exhibits an exponential decay in transverse momentum (fig. 2(a)) and a bias towards high x_γ^{OBS} (fig. 2(b)). x_γ^{OBS} is the fraction of momentum of the photon that participates in the interaction as calculated from the observed jets. The differential cross section as a function of $\Delta\eta$ is also shown (fig. 2(c)). The gap fraction (fig. 2(d)) is the number of events with a gap divided by the total number of dijet events. It levels off at around 60%. Although a fraction of 100% might be expected, many gap events are lost by such factors as the final state particles escaping the bounds defined by the jet cone and hence filling the gap.

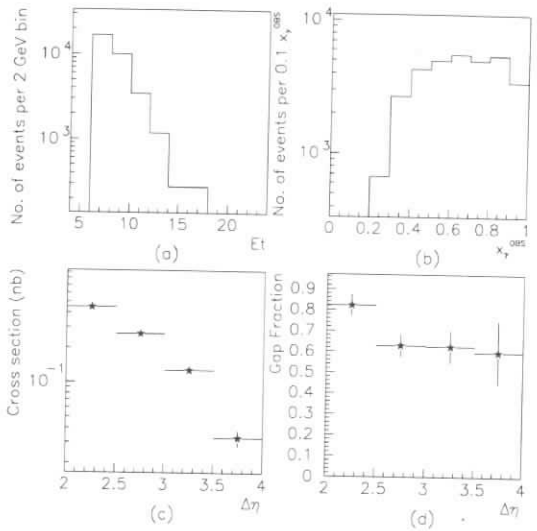

Figure 2: *The QCD colour singlet process by itself. (a) shows the spectrum of the jet E_T used in the sample. (b) shows the x_γ^{OBS} distribution of the sample. (c) shows the cross section of the sample as producd by HERWIG, in bins of $\Delta\eta$ (the interval between jets). (d) shows the fraction of events with a gap over the total number of dijet events.*

HERWIG 5.8d was then used to produce 'standard' direct and resolved photoproduction events and these were added to the sample of 'colour singlet' events. The cross section for the dijet sample without the requirement for a jet was tuned to the ZEUS 1994 data. This was then held fixed as the 'colour singlet' sample normalization was adjusted to fit the gap fraction graph. An overall normalization factor of 30 for the 'colour singlet' sample was found necessary to describe the data. This factor is allowed due to theoretical uncertainties in the value of α_s as mentioned above. PYTHIA 5.7 [7] was then used to produce 'standard' events, as a comparison.

Both Monte Carlos are compared to the data (fig. 3(a)). As can be seen from the last two bins, PYTHIA, which does not include colour singlet exchange fails to describe the data. However HERWIG, with the new QCD process, provides a good description. Also included is the standard HERWIG plot (HERWIG 5.8d) without the colour singlet sample. This emphasizes the dramatic effect, at high $\Delta\eta$ of the new process on the gap fraction.

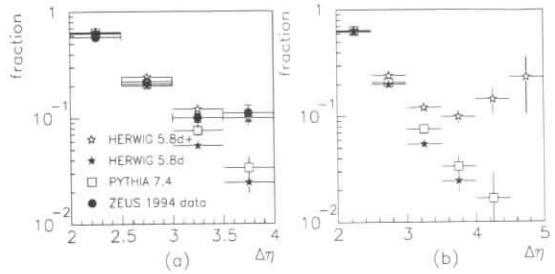

Figure 3: *Gap fractions as produced by PYTHIA and HERWIG (with the colour singlet interaction denoted by 5.8d+). (a) is for a standard detector, and the ZEUS 1994 data has been superimposed. (b) is for an extended coverage detector.*

Using this model the Monte Carlo was used to simulate an extended detector. The extended detector coverage was simulated by changing the η_{jet} cut to $\eta_{jet} < 3.5$. With the extended detector clear evidence for the colour singlet exchange for $\Delta\eta > 4.0$ is seen (fig. 3(b)). Figure 3 also shows a characteristic rise in the gap fraction. The gap fraction of the process by itself is 60%. The diffractive cross section falls less rapidly as $\Delta\eta$ increases than does the 'background' non-diffractive cross section. Thus at large $\Delta\eta$ we expect the gap fraction to rise towards 60%. Hence given an increased detector acceptance, we can see a clear signal for this kind of event.

The extended HERWIG was also used to simulate increased luminosity with the current detector coverage. Although increased statistics would allow different bins of E_T of the jets and of x_γ^{OBS} no such striking signal of the colour singlet exchange would be seen. So we conclude in favour of the extended detector coverage.

References

[1] D0 Collaboration, S. Abachi et al., Phys. Rev. Lett. 72 (1994) 2332;
CDF Collaboration, F. Abe et al, Phys. Rev. Lett. 74 (1995) 855.

[2] E.A. Kuraev, L.N. Lipatov and V.S. Fadin, Sov. Phys. JETP 44 (1976) 443;
L.V. Gribov, E.M. Levin and M.G. Ryskin, Phys. Rep. 100 (1983) 1.

[3] A.H. Mueller and W.-K. Tang, Phys. Lett. B 284 (1992) 123-126.

[4] The HzTool program and documentation can be obtained from
`http://dice2.desy.de/~h01rtc/hztool.html`.
See also these proceedings for further details.

[5] ZEUS Collaboration, M. Derrick et al, Phys. Lett. B 369 (1996) 55-68.

[6] HERWIG 5.8; G. Marchesini, B.R. Webber, G. Abbiendi, I.G. Knowles, M.H. Seymour and L. Stanco, Comp. Phys. Commun. 67 (1992) 465.

[7] H.-U. Bengtsson and T. Sjöstrand, Comp. Phys. Comm. 46 (1987) 43;
T. Sjöstrand, CERN-TH.6488/92 (1992).

Dijet cross section in photoproduction at HERA

P. Aurenche[a], L. Bourhis[b], M. Fontannaz[b], J. Ph. Guillet[a]

[a] Laboratoire de Physique Théorique ENSLAPP[1] - Groupe d'Annecy, LAPP, IN2P3-CNRS, B.P. 110, F-74941 Annecy-le-Vieux Cedex, France
[b] Laboratoire de Physique Théorique et Hautes Energies[2], Université de Paris XI, bâtiment 211, F-91405 Orsay Cedex, France

Abstract: We have built a Monte Carlo program describing the photoproduction of 2 and 3 jets at HERA. With desired cuts and cone algorithms, any cross section can be extracted from the generated events. We study the effect on the cross section of Higher Order QCD corrections.

1 Introduction

The importance of the photoproduction of jets at HERA arises from the possibility of probing the hadronic structure of the photon in a way complementary to the usual studies of the deep inelastic photon structure function. In the latter case, one can reach the very small-x domain of the parton densities in the photon and, in particular, directly measure the quark distributions whereas the gluon distribution is constrained by the evolution equations. On the contrary, in photoproduction reactions one directly probes the gluon density in the photon assuming the parton distributions in the proton are known from elsewhere. A simultaneous study of both processes should then lead to a precise determination of the photon structure very much in the same way as it does in purely hadronic reactions.

In the QCD-improved parton model, the jet cross sections are given by convolutions of the parton distribution functions with the hard subprocess cross sections. The more exclusive the cross section, the less numerous the convolutions, since the internal variables are more constrained by the final jet kinematics. For instance the dijet cross section, as a function of the transverse momentum $p_\perp$ and the jet rapidities η_3 and η_4, is given by a product if the subprocess is a $2 \to 2$ reaction [1] (Leading Logarithm approximation)

$$\frac{d\sigma}{dp_\perp^2 d\eta_3 d\eta_4} = \sum_{a,b} x_e\ F_e^a(x_e)\ x_p\ F_p^b(x_p) \frac{d\sigma}{dt}(ab \to p_3 p_4)\ , \qquad (1)$$

$d\sigma/dt$ is the $a + b \to p_3 + p_4$ cross section, and $F_e^a(F_p^b)$ the parton distributions in the electron (proton). The direct contribution corresponds to $a = \gamma$ and F_e^γ is the Weizsäcker-Williams

[1] URA 14-36 du CNRS, associée à l'Ecole Normale Supérieure de Lyon, et au Laboratoire d'Annecy-le-Vieux de Physique des Particules.
[2] Laboratoire associé au CNRS - URA 0063.

formula. In the resolved case, F_e^a is given by a convolution of F_e^γ with the parton distribution in the photon

$$F_e^a(x_e) = \int_0^1 dz\ dx_\gamma\ F_e^\gamma(z)\ F_\gamma^a(x_\gamma)\ \delta(x_\gamma z - x_e) \tag{2}$$

with $x_e = \frac{p_\perp(e^{-\eta_3}+e^{-\eta_4})}{2E_e}$ (E_e is the incident electron energy in the LAB frame). If the photon energy (zE_e) is known (for instance, by tagging the outgoing electron), we can write

$$\frac{d\sigma}{dx_\gamma} = \sum_{a,b} x_\gamma\ F_\gamma^a(x_\gamma) \int_0^1 dz\ dp_\perp^2 d\eta_3 d\eta_4\ \delta\left(x_\gamma - \frac{p_\perp\,(e^{-\eta_3}+e^{-\eta_4})}{2zE_e}\right)\ F_e^\gamma(z)\ x_p\ F_p^b(x_p)\frac{d\sigma}{dt}\ . \tag{3}$$

Thus the dijet cross section written as a function of x_γ is proportional to the parton distribution in the photon $F_\gamma^a(x_\gamma)$.

Higher Order (HO) QCD corrections to the LL expression (3) blur the simple kinematics of formulae (1) to (3). There are contributions with three jets in the final state, and we can no longer fix x_γ, because the third jet is not observed. However we can follow the strategy of the ZEUS collaboration [2] which defines the variable

$$x_\gamma^{obs} = \left(p_{3\perp}e^{-\eta_3} + p_{4\perp}e^{-\eta_4}\right)/2E_\gamma \tag{4}$$

and observe the dijet cross section $d\sigma/dx_\gamma^{obs}$. However this definition of x_γ^{obs} constrains the phase space integration too much. An inclusive dijet cross section can only be a function of $p_\perp$, η_3 and η_4; the transverse momentum of the second jet cannot be observed without spoiling IR compensation between the virtual and real HO cross section. We therefore propose the infrared safe definition

$$x_\gamma^{LL} = p_{3\perp}\left(e^{-\eta_3} + e^{-\eta_4}\right)/2E_\gamma\ . \tag{5}$$

In the LL approximation, x_γ^{LL} is equal to x_γ (note that x_γ^{LL} can be larger than one at NLO); it is important to check how much the HO corrections change this simple picture, and if the determination of $F_\gamma^a(x_\gamma)$ from $d\sigma/dx_\gamma^{LL}$ remains accurate.

2 HO QCD corrections to the dijet cross section

HO corrections to the $2 \to 2$ processes involve virtual corrections to these processes and $2 \to 3$ real contributions. We perform these corrections by using a Maple [3] program originally written [4] in order to study dihadron production. The final three body phase-space, with parton of momenta p_3, p_4 and p_5, is divided into an initial collinear region with $p_{5\perp} \le p_{5\perp}^{min}$, in a final collinear region with d_{35} or $d_{45} \le R_c$ ($d_{ij} = (\Delta\varphi_{ij}^2 + \Delta\eta_{ij}^2)^{\frac{1}{2}}$) and in a 3-body region (without collinear and/or IR singularity). The collinear contribution are analytically calculated and the IR singularities are cancelled by the virtual contributions. The remaining collinear singularities are absorbed in the distribution functions. The collinear contributions contain large logarithms $\log^2 p_{5\perp}^{min}$ and $\log p_{5\perp}^{min} \log R_c$ of the unphysical cut-offs $p_{5\perp}^{min}$ and R_c which are cancelled by the 3-body contributions.

A Monte Carlo program [5] generates (with a weight equal to one) quasi $2 \to 2$ events (according to the collinear and virtual contributions) and $2 \to 3$ events. Then we perform histograms [6] of these events for any cross section we may want with any cone algorithm (with a physical cone radius $R > R_c$). We have checked this method by comparing the single inclusive

jet cross section with a full analytical calculation [7]. In fig. 1 we see that agreement is quite good [8]. The Monte Carlo method leads to a dispersion of the predictions at large $p_\perp$ where the cross section is small. This effect can be corrected by slicing the $p_\perp$ range and generating events in each slice independently. We have also checked that the results in fig. 1 are independent of $p_{5\perp}^{min}$ and R_c. The values used in fig. 1 are $p_{5\perp}^{min} = 0.5$ GeV, $R_c = 0.1$ and $R = 1$.

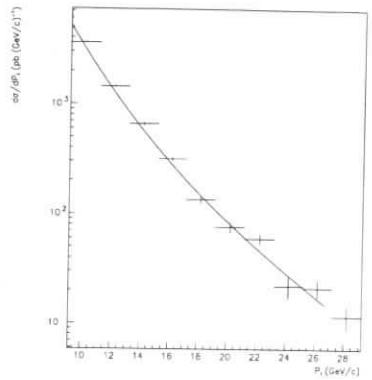

Figure 1: *Single jet inclusive cross section as a function of $p_\perp$. Comparison of the Monte Carlo results with those of ref. [7] (full line).*

3 Results for $d\sigma/dx_\gamma^{LL}$

In order to obtain $d\sigma/dx_\gamma^{LL}$, we histogram the Monte Carlo events with constraint (5) and cuts $p_{3,4\perp} \ge 9.2$ GeV and $-1 \le \eta_{3,4} \le 2$. The radius of the cone is $R = 1$. The scales used are $\mu_{renormalisation} = M_{factorisation} = p_\perp$ and the distribution functions are those of the ABFOW collaboration [9] and AFG collaboration [10]. The direct and resolved contributions are shown in fig. 2 and fig. 3. Note however that the splitting in direct and resolved parts is factorization scheme dependent and so is not physical at NLO.

The Born term leads to a peak at $x_\gamma^{LL} = 1$ in fig. 2 with $d\sigma^{born}/dx_\gamma^{LL} = 36232$ pb (with a resolution $\Delta x_\gamma^{LL} = 0.08$). It corresponds to the delta function which appears in (3) when $F_\gamma^a(x_\gamma) = \delta(1 - x_\gamma)$. When HO corrections are included, the height of the peak is decreased and we obtain the histogram of fig. 2. In fig. 3 we show the LL and NLO contributions of the resolved part. In the LL case, we still use NLO distribution functions and the shape of the spectrum is proportional to $F_\gamma^a(x_\gamma^{LL})$. With our choice of parameters, the HO corrections appear to be large. Obviously, changing the value of R, Δx_γ^{LL}, the cuts on η_3, η_4, $\cdots$ will affect the relative weight of HO corrections [11].

In conclusion, a quantitative determination of $F_\gamma^a(x_\gamma)$ from the dijet cross section should be possible.

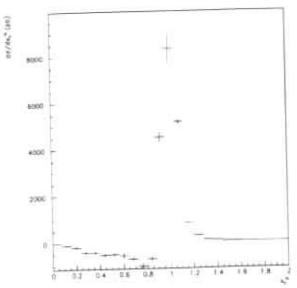

Figure 2: *Total contributions of the direct term.*

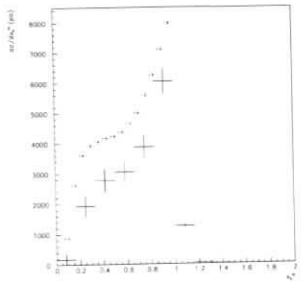

Figure 3: *LL (dashed) and total (full) contributions of the resolved part.*

4 Conclusion

We have built a Monte Carlo program, at NLO, describing the photoproduction of 2 and 3 jets at HERA. With desired experimental cuts and jet algorithms, any cross section can be extracted from the generated events.

References

[1] M. Klasen and G. Kramer, Preprint DESY 95-226, Phys. Lett. **B366** (1996) 385.

[2] M. Derrick et al., ZEUS collaboration, Phys. Lett. **B348** (1995) 665.

[3] B. W. Char et al., Maple V Language Reference Manual, Springer Verlag.

[4] P. Chiappetta, R. Fergani and J. Ph. Guillet, Z. Phys. **C69** (1996) 443.

[5] A new version of the Multidimensional Integration and Event Generation Package, BASES/SPRING, S. Kawabata, National Laboratory for High Energy Physics, Tsukuba.

[6] HBOOK Reference Manual, Applications Software Group, Computing and Network Division, CERN.

[7] P. Aurenche, M. Fontannaz and J. Ph. Guillet, Phys. Lett. **B338** (1994) 98.

[8] In comparing the jet cross sections, we notice an error in ref. [7]. A factor 2 has been introduced in the convolution of the Weizsäcker-Williams formula with the parton distributions in the photon. Therefore the resolved contribution of [7] is too high by a factor 2.

[9] ABFOW collaboration, Phys. Rev. **D39** (1989) 3275.

[10] P. Aurenche, M. Fontannaz and J. Ph. Guillet, Z. Phys. **C64** (1994) 62.

[11] P. Aurenche, L. Bourhis, M. Fontannaz and J. Ph. Guillet, work in progress.

Prompt photon, Drell-Yan and Bethe-Heitler processes in hard photoproduction

P. J. Bussey[a], B. Levtchenko[b] and A. Shumilin[b]

[a] Department of Physics and Astronomy, University of Glasgow, Glasgow G12 8QQ, UK
[b] Institute of Nuclear Physics, Moscow State University, 119899 Moscow, Russia

Abstract: We present prospects and requirements for the study of hard photon processes which generate high p_T photons in the final state, and processes which generate Drell-Yan lepton pairs.

1 Introduction

The ZEUS and H1 experiments at HERA have published a variety of studies on hard processes in quasi-real photoproduction. In lowest order (LO) QCD, an incoming photon (or parton from the photon) interacts with a parton from the proton, and two outgoing high p_T partons emerge in the final state, which can then hadronise to give rise to two observable jets. Two major classes of LO process are defined: direct, in which the entire photon interacts in the QCD subprocess, and resolved, in which the photon is a source of partons one of which interacts. A major objective is to determine the parton densities in the photon and the proton, the latter complementing the many measurements which have been made in DIS processes.

A problem concerning measurements of this type concerns the effects of final state QCD radiation, or higher order QCD effects in general. These are reduced if we can measure processes in which the emerging particles from the QCD subprocess are not themselves subject to QCD effects. Two classes of process which have been used in this way in hadron collisions are those in which high-p_T photons are produced, i.e. so-called "prompt" photons, and those in which quark-antiquark annihilation gives rise a pair of leptons, known as Drell-Yan processes. Fig. 1 illustrates the different types of process. In "dijet" processes, both final state particles in the basic diagram are quarks or gluons, while the others involve a photon or a pair of leptons.

In $p\bar{p}$ collisions at Fermilab, prompt photon processes provide a way to study the gluon content of the proton [1, 2]. At HERA, the accessible kinematic range restricts the main sensitivity to the quark content of the photon [3–6], together with the quark and gluon contents of the proton. The particular virtue of prompt photon processes is that the observed final-state photon emerges from the QCD process directly, without the intermediate hadronisation that accompanies the observation of a quark or gluon through the means of a final state jet. This, together with the availability of NLO calculations [7, 5], makes such processes attractive in providing the prospect of a relatively clean technique for studying QCD. On the other hand, the cross sections are substantially lower than those of dijet processes.

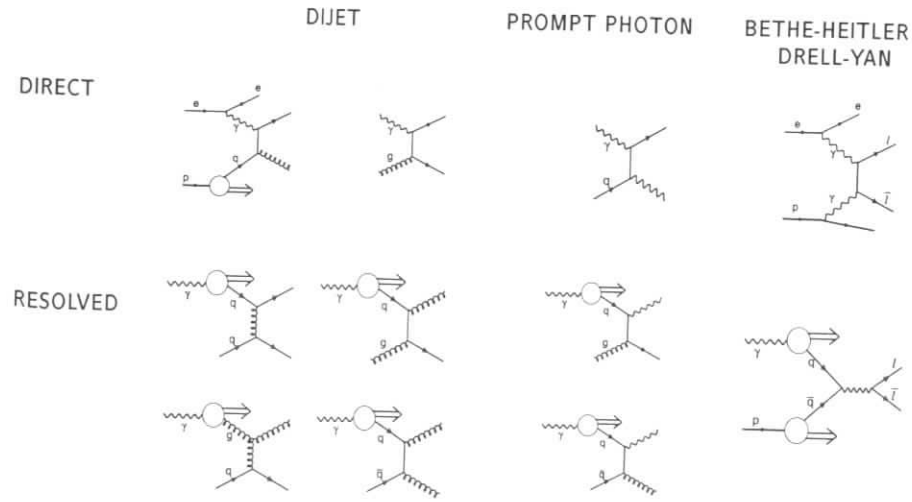

Figure 1: *Main LO diagrams for direct dijet and prompt photon processes in hard photoproduction, and examples for resolved processes. Diagrams for Bethe-Heitler and LO Drell-Yan processes are also shown. Broad arrows represent photon or photon remnants.*

Drell-Yan (DY) processes in photoproduction are by definition resolved at LO. There is no exactly parallel class of direct events, but a background comes from Bethe-Heitler (BH, "photon-photon") processes, as illustrated in Fig. 1. (A further BH diagram, not shown, has an inelastic excitation of the proton at the lower vertex.) Both BH photons interact in a direct way in producing the lepton pair. Direct-resolved and resolved-resolved photon photon interactions can also occur and give hadronic final states. A higher order "direct" DY diagram can also be drawn in which the photon remnant is replaced by a high-p_T $\bar{q}$ or q [8].

The study of lepton pair production through DY processes is of interest because it can provide a further alternative way to measure the parton densities of the photon and the proton, testing perturbative QCD and the determination of the running coupling constant. It is also an important background process for other production mechanisms of lepton pairs, such as J/Ψ and Υ decays. The twist-two chirality violating proton structure function $h_1(x)$ can be measured in the DY reaction when both beam and target are transversely polarized. In the framework of the nuclear program at HERA the DY reaction will allow investigation of the violation of charge symmetry in the valence quark distributions of the nucleon at large x, and tests of $SU(2)$-flavour symmetry breaking.

In 1971 Jaffe [9] suggested that the photon structure function could be determined through the DY process in photoproduction experiments. Since then, several other authors have studied lepton pair production theoretically using the QCD formalism at kinematic conditions at fixed target experiments [10], as well as ep colliders such as HERA [11]. Much attention was paid to find proper kinematic variables and to determine a kinematic region where the major contribution from the DY leptons would not be dominated by the background processes. All

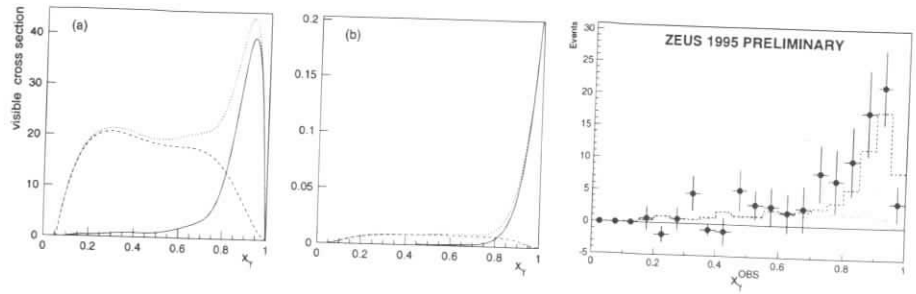

Figure 2: *Distributions of x_γ [6] for (a) dijet events, (b) prompt photon events as observed in an idealised HERA detector. Solid curve = direct contribution; dashed curve = resolved; dots = total. (c) Preliminary ZEUS results [15]: dashes = resolved + direct, dots = resolved.*

of them, however, reached the not very comforting conclusion that, because of the overwhelming Bethe-Heitler background, photoproduction of lepton pairs from a proton target is not an adequate way of measuring the photon structure function through the DY effect.

The planned HERA upgrade, however, will increase the integrated luminosity by two orders of magnitude and allow stricter selection criteria to separate the processes of interest. The conclusion of [11] for HERA was based on a comparison of inclusive spectra (p_T and rapidity), calculated for 4π geometry without taking into account the acceptances of the H1 or ZEUS detectors. One should therefore make an effort to analyse the Drell-Yan and background processes using a more precise approach to the experimental conditions. Results presented below show that it is possible to find kinematic criteria under which the Bethe-Heitler background is totally suppressed.

2 Prompt photon processes

The quantity x_γ is defined as the fraction of the photon energy taking part in the hard QCD subprocess, and is a powerful tool in characterising high energy photoproduction processes [13, 14]. For direct processes its value is by definition unity. Experimentally, its distribution is expected to differ markedly between dijet processes and prompt photon processes. An "observed" value of x_γ may be evaluated, using the definitions of [13] and [6], as $\sum_{jets}(E-p_Z)/\sum_{event}(E-p_Z)$, summing over particles (or calorimeter cells) in the jets (or the jet plus the photon) and in the whole event, for dijet events or prompt photon events as appropriate.

Figure 2 shows the difference between the distributions of the "observed" value of x_γ between dijet events and events with a prompt photon and an accompanying high-E_T jet, subject to the typical kinematic constraints of a HERA experiment. High E_T jets have been reconstructed ($E_T > 5$ GeV) from the four-vectors of HERWIG simulations of direct and resolved events, with jets and prompt photons (also $E_T > 5$ GeV) accepted in the pseudorapidity range $-1.5 \leq \eta \leq 1.7$. First experimental results from ZEUS have been reported at the Rome DIS 96 Workshop [15]. In round figures, an integrated luminosity of 6 pb^{-1} gives approximately 50 direct events with a prompt photon in the ZEUS barrel calorimeter and 30 resolved events, an accompanying jet also being observed.

The Direct Compton diagram gives a good measurement of the quark content of the proton, but an even more important aim is to measure the photon structure by means of the resolved events. With an integrated luminosity of 1000 pb^{-1} we may thus expect to record around 5000 resolved events and 7500 direct events with a prompt photon and a jet. This should suffice to give a reasonable measurement of the photon quark density and distinguish between present models which currently give cross sections differing among themselves by typically 10-20% [6]. Such measurements would be noticeably degraded if the total integrated luminosity were less, say, by a factor of 4. Use of photons detected in the rear calorimeter would give a small improvement, but not in the numbers of resolved events. To improve the resolved statistics we would require a better understanding of photon detection in the forward calorimeter. This is technically difficult, however, and its viability needs further study.

An alternative possibility would be to use inclusive prompt photon distributions. These [4] appear to give a better sensitivity to the photon structure, different models varying by as much as 40%. The inclusive cross section for prompt photons within a pseudorapidity range of $|\eta| \leq 1$ is given by [4] as 24-34 pb for the resolved contribution, with a similar figure for the direct. An integrated luminosity of 1000 pb^{-1} will then give around 30k events in each category, the gain coming by an avoidance of the need to detect the jet. However to take advantage of these statistics, it would still be necessary to distinguish somehow between direct and resolved events. One way to do this is to model the photon remnant in terms of energy detected (outside any high E_T jets) in the rear regions of the detector, with the aim of reconstructing x_γ approximately for each event. First investigations have been made [16] but the technique is clearly more difficult than if the outgoing jet is detected. For this reason, it seems necessary at present to aim for an x_γ measurement, for which the highest possible luminosity is required.

3 Drell-Yan and Bethe-Heitler processes

In our present analysis, e^+e^- and $\mu^+\mu^-$ production in ep collisions ($E_e = 26.7$ GeV, $E_p = 820$ GeV) was simulated by PYTHIA5.7 (for DY leptons) and LPAIR [17] (for BH leptons). This allows us easily to apply all the necessary cuts to account for detector resolution and detector geometry. The results presented here are correspond to the geometry of the ZEUS detector and are based on samples of $2 \cdot 10^4$ events (for DY pairs) and 10^5 events (BH pairs).

To study the effects of different selection criteria on the background suppression, cuts on the the polar angle θ_l and energy E_l of produced leptons were defined as follows: $1L_e \equiv 2.2° < \theta_e < 176.5°$; $1L_\mu \equiv 5° < \theta_\mu < 170°$; $2L_e \equiv 2.2° < \theta_{e^+}, \theta_{e^-} < 176.5°$; $2L_\mu \equiv 5° < \theta_{\mu^+}, \theta_{\mu^-} < 170°$; $1E \equiv E_l > 1$ GeV, $1E5 \equiv E_l > 5$ GeV, $2E \equiv E_{1,2} > 1$ GeV. These conditions correspond to lepton acceptances in the ZEUS detector. Two types of trigger were considered: a) "tagged", requiring the detection of the scattered electron ($5 < E_{e'} < 25$ GeV) at very small angles, thereby limiting Q^2 to less than 0.02 GeV^2, and b) "untagged", requiring the absence of a detected scattered electron in the main rear calorimeter ($Q^2 < 4$ GeV^2).

The total "untagged" and "tagged" cross sections for photoproduction of DY pairs with masses $M_{l^+l^-} > 1$ GeV were found to be 84 pb and 25 pb respectively.

Table 1 presents numbers of events with electron pairs passing the different combinations of cuts defined above. From the last column of the table it can be seen that the requirement of detecting at least one of the BH electrons in the calorimeter ($1L_e \otimes 1E$) dramatically reduces the number of BH events passing this cut. With simultaneous detection of both electrons ($2L_e \otimes 2E$)

TRIGGERS	PYTHIA $Q^2 < 4\,GeV^2$	PYTHIA $Q^2 < 0.02\,GeV^2$	PYTHIA $Q^2 < 0.02\,GeV^2$ $5\,GeV < E_{e'} < 25\,GeV$	LPAIR
No Cuts	20 000	20 000	7 125	10^5
1L	14 301	14 099	5 903	54 569
2L	12 475	12 248	3 974	44 649
1E	15 560	15 589	5 221	5 801
1E5	8 874	9 058	2 209	1 050
1L⊗1E	9 824	9 693	3 997	8
2L⊗2E	5 771	5 609	2 439	0

Table 1: *Numbers of events with photoproduction of an electron pair (PYTHIA 5.7 for DY and LPAIR for BH) under different trigger conditions.*

only about 12% of the DY electron pairs survive, but the BH background is totally eliminated. The ZEUS muon detector system has a smaller angular acceptance and so the number of DY muon pairs passing the $2L_\mu \otimes 2E$ cuts is 1548 events of 20 000.

Figure 3 illustrates these results and shows the (pseudo)-rapidity distributions of DY and BH leptons (i.e. electrons + muons) under different trigger conditions. The final plot summarizes the results of our analysis; at an integrated luminosity of 10 pb^{-1}, with the $2L \otimes 2E$ cuts in the ZEUS detector, about 40 events can be detected with DY electron pairs and 25 events with DY muon pairs. With an integrated luminosity of 1000 pb^{-1} these data samples will increase by two orders of magnitude, which should just be sufficient to enable the photon structure to be investigated.

A further feature which could be used to distinguish DY from BH events is the presence of a photon remnant. This can be quantified once again by evaluating x_γ (in terms of the two leptons instead of jets). The BH events will have $x_\gamma \approx 1$; x_γ must be evaluated in any case for

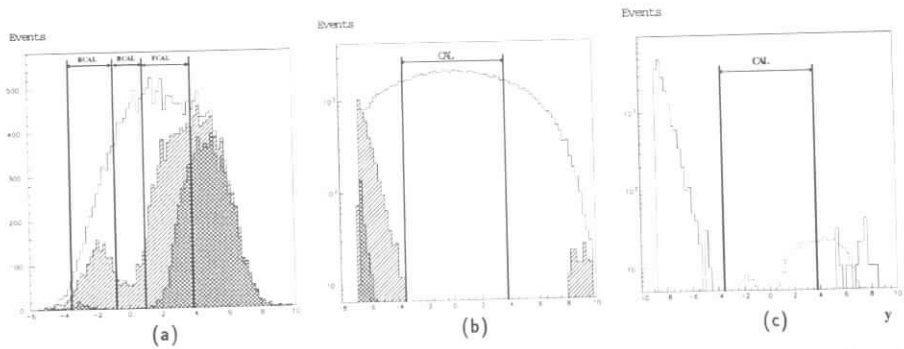

Figure 3: *Pseudo-rapidity distributions of (a) DY leptons for all events (open histogram), and the subsets with applied cuts 2E (shaded, light) and 2E5 (shaded, heavy), (b) BH leptons with the same cuts as above, (c) leptons passing the $2L \otimes 2E$ cuts with an integrated luminosity of 10 pb^{-1}. The solid and dashed histograms correspond to BH and DY leptons respectively. The acceptance of the ZEUS calorimeter is indicated.*

a study of the photon structure, and a cut to remove high x_γ events should help to remove the BH background and perhaps allow other conditions to be loosened. We have not had time to investigate this question further, but it is clear that a number of possibilities exist for studying DY pairs at HERA. All require the highest luminosities that can be obtained.

4 Conclusions

To study the photon structure through prompt photon and Drell-Yan processes will require the highest integrated luminosities that HERA can deliver. We support a full upgrade to an integrated luminosity of 1000 pb^{-1}.

References

[1] CDF Collaboration, F. Abe et al., Phys. Rev. Lett. **73** (1994) 2662; D0 Collaboration, S. Abachi et al., Fermilab-pub-96/072-E

[2] W. Vogelsang and A. Vogt, DESY 95-096 (1995)

[3] A. C. Bawa and W. J. Stirling, J. Phys. **G14** (1988) 1353; A. C. Bawa, M. Krawczyk and W. J. Stirling, Z. Phys. **C50** (1991) 293. A. C. Bawa and M. Krawczyk, Proc. Workshop *Physics at HERA,* eds. W. Buchmüller and G. Ingelman, DESY (1992) 579

[4] L. E. Gordon and J. K. Storrow, Z. Phys. **C63** (1994) 581

[5] L. E. Gordon and W. Vogelsang, Phys. Rev. **D50** (1994) 1901, **D52** (1995) 58

[6] P. J. Bussey in *Photon 95,* Sheffield, ed. D. J. Miller et al. (World Scientific, 1996)

[7] P. Aurenche et al., Z. Phys. **C56** (1992) 589

[8] We thank Dirk Graudenz for bringing this to our attention.

[9] R. L. Jaffe, Phys. Rev. **D4** (1971) 1507

[10] L. M. Jones et al., Phys. Rev. **D20** (1979) 2749;
J. Busenitz and J. D. Sullivan, Phys. Rev. **D24** (1981) 1794

[11] N. Arteaga-Romero, C. Carimalo and P. Kessler, Z. Phys. **C52** (1991) 289

[12] ZEUS Collaboration, M. Derrick et al., Z. Phys. **C65** (1995) 379

[13] ZEUS Collaboration, M. Derrick et al., Phys. Lett. **B322** (1994) 287

[14] ZEUS Collaboration, M. Derrick et al., Phys. Lett. **B348** (1995) 665

[15] ZEUS Collaboration, presented by P. J. Bussey, in proc. *DIS 96*, Rome, (World Scientific)

[16] ZEUS Collaboration, M. Derrick et al., Phys. Lett. **B354** (1995) 163

[17] S. P. Baranov et al., Proc. Workshop *Physics at HERA,* eds. W. Buchmüller and G. Ingelman, DESY (1992) 1478

QCD in the Forward Region

A. Edin[a], G. Ingelman[ab], J. Rathsman[a]

[a] Dept. of Radiation Sciences, Uppsala University, Box 535, S-751 21 Uppsala, Sweden
[b] Deutsches Elektronen-Synchrotron DESY, Notkestrasse 85, D-22603 Hamburg, FRG

Abstract: We illustrate how improved detection in the forward region can give further knowledge on important unsolved problems of QCD dynamics at small-x and confinement. The physics issues considered are QCD multiparton emission (GLAP, BFKL), proton remnant hadronization and diffractive interactions. The possibility to investigate the transition from diffractive to non-diffractive events and obtain a 'continuous' description of the interaction dynamics is emphasized.

QCD at small-x. The current strong interest in QCD at small-x is likely to remain for some years, given the complexity and importance of the problems involved. The observables considered first, e.g. the rise of F_2 and the large forward transverse energy flow, are presently too inclusive to give decisive results. The measured forward transverse energy flow [1] is consistent with BFKL [2] dynamics, but can also be understood in terms of GLAP evolution [3] combined with non-perturbative hadronization effects [4]. Therefore, one needs to consider other observables and extended coverage of the forward phase space region.

The following results are obtained from Monte Carlo (MC) event simulations in neutral current deep inelastic scattering (DIS) at HERA (27.5 GeV e on 820 GeV p) in the kinematic region $Q^2 > 7\ \mathrm{GeV}^2$, $x > 10^{-4}$, $0.05 < y < 0.7$ (unless otherwise stated).

Fig. 1a shows the mean transverse energy ($E_\perp$) flow in pseudorapidity from the conventional GLAP-based LEPTO 6.5 [5] MC together with the ARIADNE 4.08 [6] MC based on the colour dipole model (CDM). Although CDM is not based on BFKL, it has a similar non-ordering of

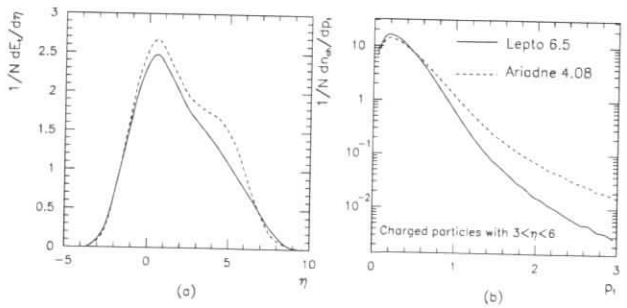

Figure 1: (a) Transverse energy flow in the laboratory system and (b) $p_\perp$ spectrum of charged particles with $3 < \eta < 6$ from LEPTO (solid) and ARIADNE (dashed).

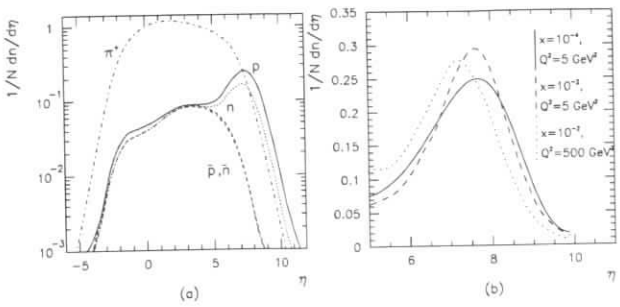

Figure 2: Pseudorapidity distributions in the laboratory frame from LEPTO for (a) various particle species and (b) protons at different fixed x and Q^2.

$p_\perp$ in the emissions, which combined with a low $p_\perp$-cutoff in the emissions gives a larger $E_\perp$ flow at large rapidities.

The present data only extend to $\eta \simeq 3$ and cannot demonstrate BFKL behaviour due to the uncertainties from hadronization effects. An extension of the detectable range would be helpful, but a decisive test may still be impossible using the transverse energy flow. The hadronization effects should not be so important for other less inclusive observables like the rate of forward jets or the tail of the $p_\perp$-distribution [7] of charged particles in a forward rapidity bin. This is illustrated in Fig. 1b, where emissions at high $p_\perp$ are suppressed for the GLAP-based model. Here, one should be more sensitive to few hard emissions in perturbative QCD rather than a cumulative effect from many soft particle emissions in the hadronization.

Proton remnant. Confinement and non-perturbative QCD are still major unsolved problems in particle physics. Related to this is the hadronization of the proton remnant. In MC models the remnant can be defined on the parton level as the proton 'minus' the parton that enters the hard scattering. Since the partons are not observable, the experimental definition of the remnant is not clear and cannot be made unambigously event-by-event, except in the case of large rapidity gaps (see below).

Fig. 2a shows pseudorapidity distributions of different particle species as obtained with LEPTO. This illustrates that a natural statistical definition of the remnant region is where $p - \bar{p} > 0$, i.e. at $\eta \gtrsim 5$. This is, however, model dependent given the uncertainties in how the remnant should be treated. This concerns, in particular, the case when the remnant is not a simple diquark, but a more complex parton system remaining when a sea quark or gluon interacted. The remnant can then have effects down to much more central rapidities [4]. These issues could be investigated by measuring very forward (anti)baryon spectra (see also Fig. 3d). The background of very forward charged pions (Fig. 2a) is quite large in the angular η-variable, but much less in terms of energy or momentum since the pions in general are much softer than the baryons (cf. Fig. 3d).

The variation of the proton spectrum with x and Q^2 shown in Fig. 2b is rather limited. This is expected as long as the remnant is considered a spectator relative to the hard scattering system. The leading proton spectrum is, therefore, not directly affected by the perturbative QCD radiation, which otherwise has substantial effects in the forward region as discussed above.

However, since the spectator system takes the remaining energy-momentum it is affected by the fraction going into the hard system and thereby indirectly by the QCD emissions. For the same x (dashed and the dotted lines in Fig. 2b) the proton spectrum is somewhat softer for larger Q^2. This allows more QCD radiation and thereby a larger momentum fraction for the parton from the proton and hence a softer proton spectrum.

Transition to diffraction. Although the observed rapidity gap events can be phenomenologically described in terms of Regge-based models of pomeron exchange, there are still theoretical problems in understanding the pomeron concept and its interaction mechanism. Moreover, the gap events are then described by one kind of model with no clear direct connection, or 'continuous' transition, to the models for normal DIS. The theoretical description should preferably contain both event types, and a smooth transition, within a common framework.

Recently introduced models [8,4] attempts to describe the rapidity gap events without using Regge or pomeron concepts. In the soft colour interaction (SCI) model [4], the main assumption is that the partons produced in the perturbative phase may exchange colour, through soft non-perturbative gluon exchange, with the colour field of the proton remnant. The hard scattering system may then become a colour singlet which is well separated from the colour singlet proton remnant system, i.e. a rapidity gap appears between them.

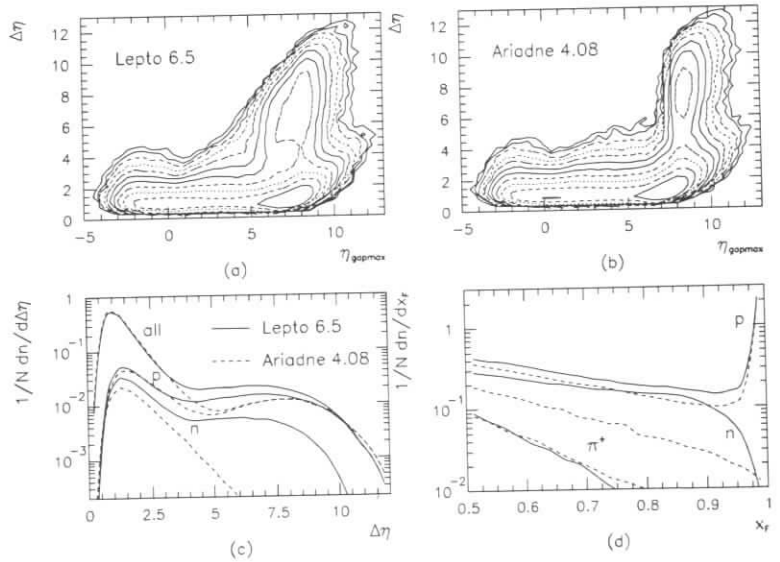

Figure 3: (a,b) Size ($\Delta\eta$) of the largest gap in each event versus the position of its upper edge (η_{gapmax}) with iso-lines showing changes by a factor two in the number of events per bin. (c) Distribution in $\Delta\eta$ for all events and those with a leading proton or neutron. (d) x_F-distribution for leading protons, neutrons and pions. Monte Carlo results from LEPTO (solid) with SCI and ARIADNE (dashed) representing models including pomeron exchange.

The position of the largest gap in the event is different in this model (Fig. 3a) as compared to a pomeron-based model (Fig. 3b). The latter gives a large rapidity gap by construction, as a kinematical consequence of a soft pomeron exchange, which gives a two-component structure in Fig. 3b when added to normal non-gap events. In the SCI model, on the other hand, gaps appear as random fluctuations and can be of arbitrary size, providing the smoother transition in Fig. 3a between smaller gaps at any rapidity and the large gaps ($\Delta\eta \gtrsim 4$) at very forward rapidities. The remainder system forward of the gap has a continuous mass spectrum, but for large gaps it is dominated by a proton (Fig. 3c) giving a characteristic diffractive peak (Fig. 3d). However, the continuum of higher mass states (see [4]) could describe proton dissociation, which in a Regge model must be added separately. Also leading neutrons emerge in the model as shown in Fig. 3cd, but give only a small contribution to the large-rapidity-gap events. This corresponds to pion exchange in Regge, which is not included in ARIADNE resulting in the exponential fall-off in Fig. 3c due to fluctuations in normal hadronization.

The development of a consistent theoretical description of both diffractive and normal DIS would benefit from measurements of these kinds of observables. In particular, dependences on the gap size, the properties of the forward system, leading particles and effective quantum number exchange over the gap etc. should then be considered.

Conclusions. Improved forward detection capabilities, both in coverage and quality (energy/momentum measurements and particle identification) would give new information of interest for several important physics issues:

- Novel perturbative QCD at small-x, e.g. BFKL dynamics may be observable through $E_\perp$ flow, jets or high-$p_\perp$ particles at very forward rapidities.
- Non-perturbative QCD and confinement, e.g. issues in connection with the hadronization of the proton remnant and its correlation with the hard interaction.
- The transition from diffractive to normal DIS events and a 'continuous' theoretical description of the interaction dynamics.

The forward rapidity region can be moved more into the detector by lowering the proton energy. With the lowest realistic beam energy of 300 GeV the forward region essentially moves about 1 unit of rapidity towards the center. Although this certainly helps to some extent, it does not give enough improved coverage for most of these issues. One should also realize that a limitation of the forward coverage, e.g. due to low-β insertions for increased luminosity, would essentially remove the discussed opportunities.

References

[1] T. Ahmed et al., H1 Collaboration, Phys. Lett. B356 (1995) 118
M. Derrick et al., ZEUS collaboration, Phys. Lett. B338 (1994) 483
[2] E.A. Kuraev, L.N. Lipatov, V.S. Fadin Sov. Phys. JETP 45 (1977) 199
Ya. Balitsky, L.N. Lipatov, Sov. J. Nucl. Phys. 28 (1978) 822
[3] V.N. Gribov, I.N. Lipatov, Sov. J. Nucl. Phys. 15 (1972) 438
G. Altarelli, G. Parisi, Nucl. Phys. B126 (1977) 298
[4] A. Edin, G. Ingelman, J. Rathsman, DESY 96-060, Z. Phys. C in press
[5] G. Ingelman, A. Edin, J. Rathsman, LEPTO 6.5, DESY 96-057
[6] L. Lönnblad, ARIADNE version 4, Comp. Phys. Comm. 71 (1992) 15
[7] M. Kuhlen, Phys. Lett. B382 (1996) 441
[8] W. Buchmüller, A. Hebeker, Phys. Lett. B355 (1995) 573
G. Ingelman, A. Edin, J. Rathsman, Phys. Lett. B366 (1996) 371

On Forward Jets and the Hot Spot Limit at HERA

H. Heßling

Abstract: A Monte Carlo study of forward jets in deep inelastic lepton–proton scattering at HERA is presented. The jets are identified with an extension of the JADE algorithm which differs from the JADE algorithm by jet mass terms.

A new variable for the transverse hadronic activity, $\kappa^2 = E(E - P_Z)$, is introduced and investigated in the "Hot Spot Limit", i.e. at high jet energies, high transverse jet momenta and low Bjorken–x (x_{Bj}). It is shown that a study of the shape of the κ–distribution allows to discriminate between the predictions of two Monte Carlo programs, which are based on a color dipol model and a parton shower model, respectively.

1 Introduction

Transverse energy flow measurements of H1 and ZEUS at small x_{Bj} seem to indicate that the DGLAP evolution of the parton densities [3] is underestimating the data [4]. It is expected that the BFKL evolution [8] which is applicable in the small Bjorken–x (x_{Bj}) region, is producing more transverse hadronic activity than the DGLAP evolution. However the transverse energy flow is not an infrared–safe observable, and it may turn out that the observed gap between the DGLAP evolution and the data is mostly due to hadronization effects, so that non–perturbative models, such as the Soft Color Interaction model [2], are able to explain the gap [12].

Jets of high energy and high transverse momentum, i.e. 'hard jets, at very low x_{Bj} are expected to be suited for a search for new QCD phenomena, such as Hot Spots [11]. Hot Spots are small regions in the proton where the parton densities are so large that parton recombination processes are more dominant than parton splitting processes, which are the dominating processes at high x_{Bj}. Experimental evidence for new QCD phenomena can be found by looking for discrepancies between the data and predictions of conventional theoretical approaches. Hot Spots, for example, are believed to suppress differential jet cross sections compared to standard approaches because of recombination processes of partons in the proton [11]. In Ref. [4] first measurements of the cross section of hard jets at low x_{Bj} were presented. The results seem to favour the BFKL evolution over the DGLAP evolution, however a firm conclusion could not be extracted from the data. Cross sections are difficult to measure. In this study we are looking for a different signature of new perturbative QCD phenomena. The idea is to take into account that the recombination processes could influence the hadronization of partons in such way that on the hadron level certain distributions of hard jets differ not only in the normalization but also in the shape from predictions of conventional Monte Carlo programs. Shapes are easier to measure than cross sections, i.e. a different possibility to find evidence for new QCD phenomena would be to find a jet variable which shows, for hard jets, significant discrepancies in the shape between the data and conventional Monte Carlo programs.

As a first step we identify in this work a jet variable which discriminates between two different Monte Carlo models: a MEPS model which is based on low order QCD matrix elements and parton showers [6], and a color dipol model (CDM) [9].

2 Extended JADE Algorithm

In Ref. [5] a jet clustering algorithm was deduced from a few conditions of general nature, such as energy–momentum conservation, Lorentz invariance and infrared safety[1]. The jet clustering is applied to a set of momenta $p_1, \ldots p_N$. First, the squared distance $d_{ij}^2 = (p_i+p_j)^2-(m_i+m_j)^2$is assigned to all pairs of momenta p_i and p_j, where $i < j \leq N$ and $m_i = \sqrt{p_i^2}$ is the mass of the i–th momentum. Secondly, the momenta p_i and p_j are recombined to the momentum $p_i + p_j$ (E–scheme), if d_{ij} is not only the smallest of all distances but also smaller than a reference distance $\sqrt{y_{\rm cut}}M_{\rm ref}$, where $M_{\rm ref}^2 = (p_1+p_2+\ldots)^2-(m_1+m_2+\ldots)^2$. $y_{\rm cut}$ is called jet resolution parameter and $M_{\rm ref}$ reference mass. The second step is iterated until all distances are larger than the reference distance. The final set of momenta defines the jets of the hadronic final state.

The proton remnant is identified as the jet with the smallest distance $d_{i\,\rm prot}$ to the momentum of the incoming proton. Within the set of the non–remnant jets, the jet with the smallest distance $d_{i\,\rm prot}$ to the incoming proton momentum is called the forward jet. We stress that this interpretation of the forward jet will be applied to each event, also to (1+1) jet events, despite the fact that because of kinematic constraints the current jet of (1+1) jet events may not be emitted into the region around the proton direction in the HERA laboratory frame.

The jet resolution parameter is set in the following to $y_{\rm cut} = 0.02$.[2]

3 Hot Spot Limit

Heisenberg's uncertainty relations suggest that subregions in the proton may be investigated, if the energy of forward jets with a high transverse momentum is increased.

The basic idea of the following analysis is to find a jet variable whose distribution has a shape which is not identical for the conventional Monte Carlo programs DJANGO6–MEPS[3] and DJANGO6–CDM[4], respectively, if the behavior of high transverse momentum jets ($p_T^2 \sim Q^2$) is studied in the limit of high energies and small $x_{\rm Bj}$

$$\xi = \frac{x_{\rm Bj}}{E_{jet1}/E_{\rm prot}} \to 0, \qquad (1)$$

where E_{jet1} is the energy of the forward jet. A study of this kind was suggested in the context of Hot Spots [11]. Therefore, the limit (1) will be called Hot Spot Limit in the following.

[1] A jet algorithm is infrared safe if it does not resolve infrared or collinear momenta.

[2] For the extended JADE algorithm it can be shown that at $y_{\rm cut} = 0.01$ and at high Q^2 (> 100 GeV^2) the next–to–leading order correction factors (K–factors) to the (2+1) jet cross sections in leading order are reasonably small ($K \sim 1.3$).

[3] DJANGO6–MEPS [1] is an interface between the Monte Carlo programs LEPTO [6] and HERACLES [13].

[4] DJANGO6–CDM [1] is an interface between the Monte Carlo programs ARIADNE [9] and HERACLES.

Jets in the Hot Spot Limit should be sensitive to perturbative (multi–parton) effects and only weakly influenced by non–perturbative hadronization effects since, on the one hand, in the Hot Spot Limit subregions in the proton should be probed and since, on the other hand, hadronization effects are long distance effects.

It is a non–trivial task to find a jet variable which is shape sensitive in the Hot Spot Limit, mainly because there is no information from theory available, as to how a shape sensitive jet observable should look like. For example, it turns out that the shape of the transverse momentum distributions of the forward jet does not change very much in the Hot Spot Limit.

Let us introduce the observable $\kappa^2 = E(E - P_Z)$, i.e. the energy weighted $E - P_Z$ of the forward jet. The qualitative agreement in the shape of the κ distribution between the Monte Carlo predictions is lost if $x_{\rm Bj}$ is decreased and the energy of the forward jet is increased at the same time (see Fig. 2, where the κ distribution is shown for the jet energies larger than 10, 15 and 20 GeV).

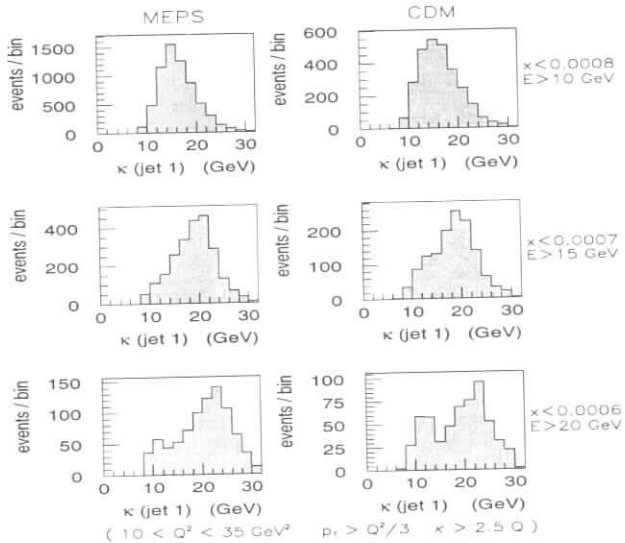

Figure 1: *Comparison of the Hot Spot Limit of the κ distribution on the ZEUS detector level using the Monte Carlo programs DJANGO6–MEPS and DJANGO6–CDM. (The kinematic range is limited to $13\,{\rm GeV}^2 < Q^2 < 35\,{\rm GeV}^2$. Moreover, it is required that the forward jet has a high transverse momentum, $p_T^2 > Q^2/3$, and a high "energy weighted $E - P_Z$", $\kappa > 2.5\,Q$. The distributions of the partons inside the proton are taken from the MRSD–' set [10].)*

It can be shown that the discrepancies with respect to the peak structure are stable against the experimental uncertainties in the hadronic energy scale, one of the most important experimental uncertainty. The contribution to the systematic error from the uncertainty in the leptonic energy scale is small. Moreover, it turns out that there is a (weak) correlation between

the generated and reconstructed events, indicating that the influence of the ZEUS detector on the κ distribution in the Hot Spot Limit can be unfolded. Thus, the ZEUS detector seems to be suitable to measure the κ distribution in the Hot Spot Limit.

Newer versions of ARIADNE and LEPTO were published, now with similar predictions for the forward energy flow. It can be shown, however, that the discrepancies found here are still present.

In summary, a measurement of the shape of the κ distribution of the forward jet in the Hot Spot Limit may lead to an improvement of the understanding of perturbative QCD.

We thank the organizers of the workshop "Future Physics at HERA" and the convenors of the working group "Jets and High E_T Phenomena" for their strong support.

References

[1] K. Charchuła, G. A. Schuler and H. Spiesberger, *DJANGO6*, version 1.1, Comp. Phys. Commun., **81** (1994) 381.

[2] A. Edin, G. Ingelman and J. Rathsman, Phys. Lett. **B 366** (1996) 371.

[3] V. N. Gribov and L. N. Lipatov, Sov. Journ. Nucl. Phys. **15** (1972) 438 and 675;
Y. L. Dokshitzer, Sov. Phys. JETP **46** (1975) 641;
G. Altarelli and G. Parisi, Nucl. Phys. **B 126** (1977) 297.

[4] H1 Collab., Phys. Lett. **B 356** (1995) 118;
ZEUS Collab., Phys. Lett. **B 338** (1994) 483.

[5] H. Heßling, DESY 95–069.

[6] G. Ingelman, *LEPTO*, version 6.1, Proceedings 'Physics at HERA', W. Buchmüller, G. Ingelman (eds.), DESY Hamburg 1992, vol. 3.

[7] G. Kramer, DESY 82–029 (1982), published in Proc. of the 13th Spring Symp. on High Energy Physics, Bad Schwandau/GDR (1982);
JADE Collab., W. Bartel et al., Phys. Lett. **B 119** (1982) 239;
JADE Collab., W. Bartel et al., Z. Phys. **C 33** (1986) 22;
JADE Collab., S. Bethke et al., Phys. Lett. **B 213** (1988) 235.

[8] L. N. Lipatov, Sov. J. Nucl. Phys. **23** (1976) 338;
E.A. Kuraev, L. N. Lipatov, V. S. Fadin, Sov. Phys. JETP **45** (1977) 199;
Y. Y. Balitskii, L. N. Lipatov, Sov. J. Nucl. Phys. **28** (1978) 822.

[9] L. Lönnblad, *ARIADNE*, version 4, Comput. Phys. Commun. 71 (1992) 15.

[10] A. D. Martin, W. J. Stirling and R. G. Roberts, Phys. Lett. B306 (1993) 145.

[11] A. H. Mueller and H. Navelet, Nucl. Phys. **B 282** (1987) 727;
A. H. Mueller, Nucl. Phys. B (Proc. Suppl.) **18 C** (1991) 125.

[12] N. Pavel, Workshop "DIS 96", Rome 1996.

[13] H. Spiesberger, *HERACLES*, version 4.4, unpublished program manual (1993); version 4.0 is described in A. Kwiatkowski, H.–J. Möhring and H. Spiesberger, Comp. Phys. Commun. **69** (1992) 155.

Fixed-Order QCD Backgrounds to BFKL Dynamics in Forward Jet Production

Erwin Mirkes[a] and Dieter Zeppenfeld[b]

[a]Institut für Theoretische Teilchenphysik, Universität Karlsruhe, D-76128 Karlsruhe, Germany
[b]Department of Physics, University of Wisconsin, Madison, WI 53706, USA

Abstract: The production of forward jets of transverse momentum $p_T(j) \approx Q$ and large momentum fraction $x_{jet} \gg x$ probes the onset of BFKL dynamics at HERA. A full $\mathcal{O}(\alpha_s^2)$ calculation of the inclusive forward jet cross section is presented and compared to the expected BFKL cross section.

Deep-inelastic scattering (DIS) at HERA provides an ideal place to probe strong interaction dynamics. One focus of interest has been the small Bjorken-x region, where one would like to distinguish BFKL evolution [1], which resums the leading $\alpha_s \ln 1/x$ terms, from the more traditional DGLAP evolution equation [2], which resums leading $\alpha_s \ln Q^2$ terms. Unfortunately, the measurement of $F_2(x, Q^2)$ in the HERA range is probably too inclusive to discriminate between the two [3].

A more sensitive test of BFKL dynamics at small x is expected from deep inelastic scattering with a measured forward jet (in the proton direction) and $p_T^2(j) \approx Q^2$ [4]. The idea is to study DIS events which contain an identified jet of longitudinal momentum fraction $x_{jet} = p_z(jet)/E_{proton}$ which is large compared to Bjorken x. When tagging a forward jet with $p_T(j) \approx Q$ this leaves little room for DGLAP evolution while the condition $x_{jet} \gg x$ leaves BFKL evolution active. This leads to an enhancement of the forward jet production cross section proportional to $(x_{jet}/x)^{\alpha_P - 1}$ over the DGLAP expectation.

A conventional fixed order QCD calculation up to $\mathcal{O}(\alpha_s^2)$ does not yet contain any BFKL resummation and must be considered a background for its detection; one must search for an enhancement in the forward jet production cross section above the expectation for two- and three-parton final states. In this contribution we perform a full next-to-leading order (NLO) analysis of this "fixed order" background. Such an analysis has become possible with the implementation of QCD radiative corrections to dijet production in DIS in a fully flexible Monte Carlo program, MEPJET [5].

Numerical results below will be presented both for leading order (LO) and NLO simulations. The LO 1-jet and 2-jet results employ the LO parton distributions of Glück, Reya and Vogt [6] together with the one-loop formula for the strong coupling constant. At $\mathcal{O}(\alpha_s^2)$ all cross sections are determined using the NLO GRV parton distribution functions $f(x_i, \mu_F^2)$ and the two loop formula for $\alpha_s(\mu_R^2)$. With this procedure the 2-jet inclusive rate at NLO is simply given as the

	with forward jet $p_T^B, p_T^{lab} > 4$ GeV	$k_T^B > 4$ GeV	without forward jet $p_T^B, p_T^{lab} > 4$ GeV
$\mathcal{O}(\alpha_s^0)$: 1 jet	0 pb	0 pb	8630 pb
$\mathcal{O}(\alpha_s)$: 2 jet	18.9 pb	22.4 pb	2120 pb
$\mathcal{O}(\alpha_s^2)$: 1 jet inclusive	100 pb	100 pb	
2 jet inclusive	83.8 pb	98.3 pb	2400 pb
2 jet exclusive	69.0 pb	66.8 pb	2190 pb
3 jet	14.8 pb	31.5 pb	210 pb

Table 1: Cross sections for n-jet events in DIS at HERA at order α_s^0, α_s, and α_s^2. The jet multiplicity includes the forward jet which, when required, must satisfy $p_T(j) > 5$ GeV and the cuts of Eqs. (1,2). The transverse momenta of additional (non-forward) jets must only exceed cuts of 4 GeV (first and third column). This requirement is replaced by the condition $k_T^B > 4$ GeV in the second column. No p_T^B cut is imposed in the 1-jet case at $\mathcal{O}(\alpha_s^0)$ and the factorization scale is fixed to Q.

sum of the NLO 2-jet and the LO 3-jet exclusive cross sections. The value of α_s is matched at the thresholds $\mu_R = m_q$ and the number of flavors is fixed to $n_f = 5$ throughout, *i.e.* gluons are allowed to split into five flavors of massless quarks.

Unless otherwise stated, both the renormalization and the factorization scales are tied to the sum of parton k_T's in the Breit frame, $\mu_R = \mu_F = \frac{1}{2}\sum_i k_T^B(i)$, where $(k_T^B(i))^2 = 2E_i^2(1-\cos\theta_{ip})$. Here θ_{ip} is the angle between the parton and proton directions in the Breit frame. $\sum_i k_T^B(i)$ constitutes a natural scale for jet production in DIS [7] because it interpolates between Q, in the naive parton model limit, and the sum of jet transverse momenta, when Q becomes negligible.

We are interested in events with a forward jet with $p_T(j) \approx Q$ and $x_{jet} \gg x$ and impose kinematical cuts which closely model the H1 selection[8] of such events. Jets are defined in the cone scheme (in the laboratory frame) with $\Delta R = 1$ and $|\eta| < 3.5$. Here $\eta = -\ln\tan(\theta/2)$ denotes the pseudorapidity of a jet. Unless noted otherwise, all jets must have transverse momenta of at least 4 GeV in both the laboratory and the Breit frames. Events are selected which contain a forward jet (denoted "j") in the pseudorapidity range $1.735 < \eta(j) < 2.9$ (corresponding to $6.3° < \theta(j) < 20°$) and with transverse momentum $p_T^{lab}(j) > 5$ GeV. This jet must satisfy

$$x_{jet} = p_z(j)/E_p > 0.05 , \quad (1)$$

$$0.5 < p_T^2(j)/Q^2 < 4 \quad (2)$$

in the laboratory frame. The condition $x_{jet} \gg x$ is satisfied by requiring $x < 0.004$. Additional selection cuts are $Q^2 > 8$ GeV^2, $0.1 < y < 1$, an energy cut of $E(l') > 11$ GeV on the scattered lepton, and a cut on its pseudorapidity of $-2.868 < \eta(l') < -1.735$ (corresponding to $160° < \theta(l') < 173.5°$). The energies of the incoming electron and proton are set to 27.5 GeV and 820 GeV, respectively.

Numerical results for the multi-jet cross sections with (or without) a forward jet are shown in Table 1. Without the requirement of a forward jet, the cross sections show the typical decrease with increasing jet multiplicity which is expected in a well-behaved QCD calculation. The 3-jet cross section in the last column constitutes only about 10% of the 2-jet cross section and both rates are sizable. The requirement of a forward jet with large longitudinal momentum fraction

($x_{jet} > 0.05$) and restricted transverse momentum ($0.5 < p_T^2(j)/Q^2 < 4$) severely restricts the available phase space. In particular one finds that the 1-jet cross section vanishes at LO, due to the contradicting $x < 0.004$ and $x_{jet} > 0.05$ requirements: this forward jet kinematics is impossible for one single massless parton in the final state.

Suppose now that we had performed a full $\mathcal{O}(\alpha_s^2)$ calculation of the DIS cross section, which would contain 3-parton final states at tree level, 1-loop corrections to 2-parton final states and 2-loop corrections to 1-parton final states. These 2-loop contributions would vanish identically, once $x \ll x_{jet}$ is imposed. The remaining 2-parton and 3-parton differential cross sections, however, and the cancellation of divergences between them, would be the same as those entering a calculation of 2-jet inclusive rates. These elements are already implemented in the MEPJET program which, therefore, can be used to determine the inclusive forward jet cross section, within the cuts discussed above. At $\mathcal{O}(\alpha_s^2)$ this cross section is obtained from the cross section for 2-jet inclusive events by integrating over the full phase space of the additional jets, without any cuts on their transverse momenta or pseudorapidities. Numerical results are shown in the third row of Table 1.

The table exhibits some other remarkable features of forward jet events: the NLO 2-jet inclusive cross section exceeds the LO 2-jet cross section by more than a factor of four and the 3-jet rate at $\mathcal{O}(\alpha_s^2)$ is about as large as the 2-jet rate at $\mathcal{O}(\alpha_s)$. The smallness of the LO 2-jet compared to the NLO 2-jet inclusive cross section means that at least three final-state partons are required to access the relevant part of the phase space. This three-parton cross section, however, has only been calculated at tree level and is subject to the typical scale uncertainties of a tree level calculation. Thus, even though we have performed a full $\mathcal{O}(\alpha_s^2)$ calculation of the forward jet cross section at HERA, including all virtual effects, our calculation effectively only gives a LO estimate of this cross section and large corrections may be expected from higher order effects.

The characteristics of forward jet events are demonstrated in Fig. 1 where the transverse momentum and the pseudorapidity distributions of the recoil jet with the highest p_T^{lab} are shown, subject only to a nominal requirement of $p_T^{lab}, p_T^B > 1$ GeV. Here the recoil system is defined as the complement of the forward jet, in the final state which arises in the photon-parton collision. Almost all forward jet events contain at least one additional jet in the recoil system, with $p_T^{lab} \gtrsim 4$ GeV and, typically, in the central part of the detector.

In the usual cone scheme final-state collinear singularities are regulated by the ΔR separation cut while infrared singularities and initial state collinear emission are regulated by the p_T cut. In $\gamma^* p$ collisions the photon virtuality, Q^2, eliminates any collinear singularities for initial state emission in the electron direction and therefore a large k_T is as good a criterion to define a cluster of hadrons as a jet as its p_T. The dashed line in Fig. 1(a) shows the k_T distribution in the Breit frame of the recoil jet candidate with the largest k_T^B. Basically all forward jet events in this NLO analysis possess a recoil "jet" with $k_T^B > 4$ GeV and would thus be classified as 2-jet inclusive events in a variant of the cone scheme where the $p_T > 4$ GeV condition is replaced by a $k_T^B > 4$ GeV cut. This observation makes intuitively clear why we are able to calculate the 1-jet inclusive forward jet cross section with a program designed for the 2-jet inclusive cross section at NLO: there exists a jet definition scheme in which all forward jet events contain at least one additional hard jet.

An estimate for higher order corrections may be obtained by comparing to BFKL calculations or to existing experimental results. The H1 Collaboration has published such a measurement which was made during the 1993 HERA run with incident electron and proton energies of

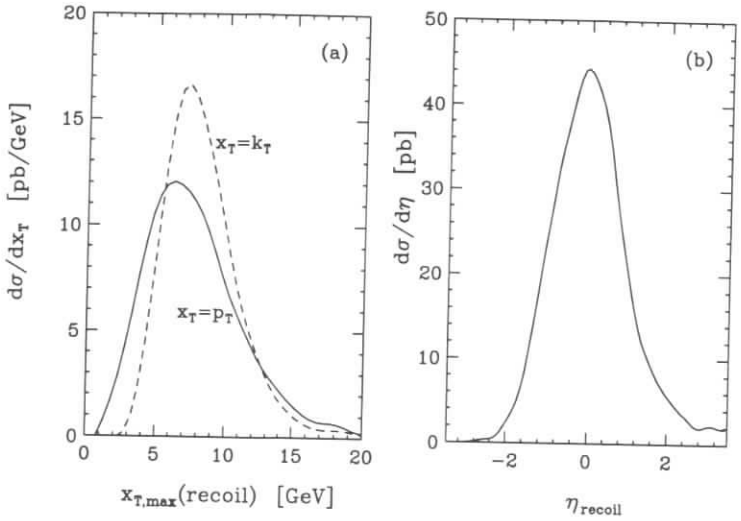

Figure 1: Characteristics of the highest transverse momentum "jet" in the recoil system, i.e. excluding the forward jet. Distributions shown are (a) $d\sigma/dp_T$ in the lab frame (solid line) and $d\sigma/dk_T$ in the Breit frame (dashed line) and (b) the jets pseudorapidity distribution in the laboratory frame. All distributions are calculated at order α_s^2. Jet transverse momentum cuts have been relaxed to $p_T^{lab}, p_T^B > 1$ GeV.

$E_e = 26.7$ GeV and $E_p = 820$ GeV [9]. The acceptance cuts used for this measurement differed somewhat from the ones described before. Because of the lower luminosity in this early HERA run the x_{jet} cut on the forward jet was lowered to 0.025 and defined in terms of the jet energy as opposed to the longitudinal momentum of the jet in the proton direction,

$$x_{jet} = E(j)/E_p > 0.025\,, \tag{3}$$

and the pseudorapidity range of the forward jet was chosen slightly larger, $1.735 < \eta(j) < 2.949$ (corresponding to $6° < \theta(j) < 20°$). Scattered electrons were selected with an energy of $E(l') > 12$ GeV and in the pseudorapidity range $-2.794 < \eta(l') < -1.735$ (corresponding to $160° < \theta(l') < 173°$). Finally the Bjorken-x and Q^2 ranges were chosen as $0.0002 < x < 0.002$ and 5 GeV$^2 < Q^2 < 100$ GeV^2. Within these cuts H1 has measured cross sections of $709 \pm 42 \pm 166$ pb for $0.0002 < x < 0.001$ and $475 \pm 39 \pm 110$ pb for $0.001 < x < 0.002$. These two data points, normalized to bin sizes of 0.0002, are shown as diamonds with error bars in Fig. 2. Also included (dashed histogram) is a recent calculation of the BFKL cross section [10].

As shown before, the MEPJET program allows to calculate the full 1-jet inclusive forward jet cross section[1] for $x \ll x_{jet}$. The LO result is shown as the dash-dotted histogram in Fig. 2 and the NLO result is shown as the solid histogram. The shaded area corresponds to a scale

[1] We have checked that also for the kinematical region considered now almost all forward jet events contain at least one second jet with $p_T^{lab} > 4$ GeV and $k_T^B > 4$ GeV.

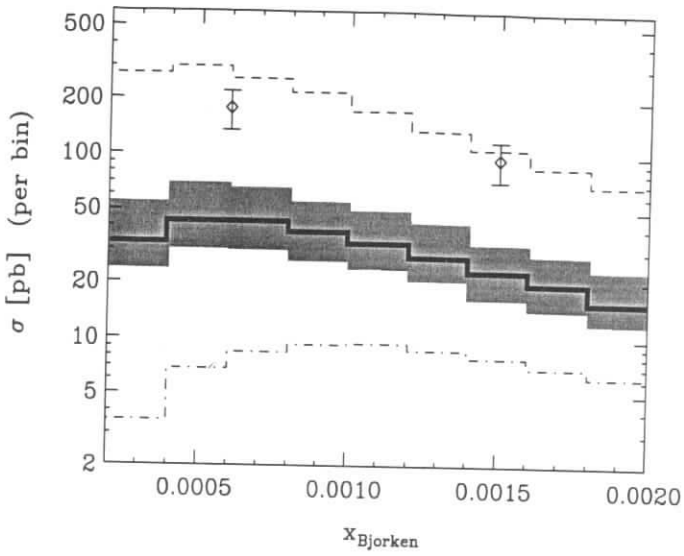

Figure 2: Forward jet cross section at HERA as a function of Bjorken x within the H1 acceptance cuts [9] (see text). The solid (dash-dotted) histogram gives the NLO (LO) MEPJET result for the scale choice $\mu_R^2 = \mu_F^2 = \xi(0.5\sum k_T)^2$ with $\xi = 1$. The shaded area shows the uncertainty of the NLO prediction, corresponding to a variation of ξ between 0.1 and 10. The BFKL result of Bartels et al. [10] is shown as the dashed histogram. The two data points with error bars correspond to the H1 measurement [9].

variation $\mu_R^2 = \mu_F^2 = \xi\ \frac{1}{4}\left(\sum_i k_T^B(i)\right)$, from $\xi = 0.1$ to $\xi = 10$, and indicates a range of "reasonable" expectations for the forward jet cross section at $\mathcal{O}(\alpha_s^2)$.

While the BFKL results [10] agree well with the H1 data, the fixed-order perturbative QCD calculations clearly fall well below the measured cross section, even when accounting for variations of the factorization and renormalization scales. The measured cross section is a factor of 4 above the NLO expectation. The shape of the NLO prediction, on the other hand, is perfectly compatible with the H1 results, and not very different from the BFKL curve in Fig. 2. At LO a marked shape difference is still observed, which can be traced directly to kinematical arguments given in Ref. [11]. Additional details, including a study of the NLO scale dependence of the forward jet cross section, can be found there. First NLO studies for forward jet production have been presented in Ref. [12]. For a study of forward jet cross sections with the ZEUS detector, see Ref. [13].

We conclude that the existing H1 data show evidence for BFKL dynamics in forward jet events via an enhancement in the observed forward jet cross section above NLO expectations. The variation of the cross section with x, on the other hand, is perfectly compatible with either BFKL dynamics or NLO QCD. Since MEPJET provides a full NLO prediction of the 1-jet

inclusive forward jet cross section for arbitrary cuts and jet definition schemes, more decisive shape tests may be possible as additional data become available.

References

[1] E.A. Kuraev, L.N. Lipatov and V.S. Fadin, Sov. Phys. **JETP 45** (1977) 199;
Y.Y. Balitsky and L.N. Lipatov, Sov. J. Nucl. Phys. **28** (1978) 282.

[2] G. Altarelli and G. Parisi, Nucl. Phys. **126** (1977) 297;
V.N. Gribov and L.N. Lipatov, Sov. J. Nucl. Phys. **15** (1972) 438 and 675;
Yu. L. Dokshitzer, Sov. Phys. **JETP 46** (1977) 641.

[3] A.D. Martin, Acta Physica Polonica **B27** (1996) 1287;
A. De Roeck, Acta Physica Polonica **B27** (1996) 1175.

[4] A.H. Mueller, Nucl. Phys. B (Proc. Suppl.) **18C** (1990) 125; J. Phys. **G17** (1991) 1443;
J. Kwiecinski, A.D. Martin and P.J. Sutton, Phys. Rev. **D46** (1992) 921;
W.K. Tang, Phys. Lett. **B278** (1992) 363;
J. Bartels, A. De Roeck and M. Loewe, Z. Phys. **C54** (1992) 635.

[5] E. Mirkes and D. Zeppenfeld, Phys. Lett. **B380** (1996) 205, [hep-ph/9511448].

[6] M. Glück, E. Reya and A. Vogt, Z. Phys. **C67** (1995) 433.

[7] E. Mirkes and D. Zeppenfeld, In the proceedings of the "QCD and QED in Higher Orders" 1996 Zeuthen Workshop on Elementary Particle Theory, April 22-26, 1996 [hep-ph/9606332].

[8] The cuts are similar to the cuts used in the present H1 forward jet analyses. We thank A. De Roeck and E.M. Mroczko for this information.

[9] H1 Collaboration, S. Aid et al., Phys. Lett. **B356** (1995) 118.

[10] J. Bartels, V. Del Duca, A. De Roeck, D. Graudenz, and M. Wüsthoff, preprint DESY-96-036 (1996), [hep-ph/9604272].

[11] E. Mirkes and D. Zeppenfeld, MADPH-96-957, TTP96-38, [hep-ph/9609231].

[12] E. Mirkes and D. Zeppenfeld, Acta Physica Polonica **B27** (1996) 1393, [hep-ph/9604281].

[13] T. Haas and M. Riveline, these proceedings.

Forward Jets Cross Sections

T. Haas[a], M. Riveline[b]

[a] Deutsches Elektronen-Synchrotron DESY, Notkestrasse 85, D-22607 Hamburg, FRG
[b] McGill University, Montreal, Canada

Abstract

We investigate the prospects for a precise measurement of differential forward jet cross sections with the ZEUS detector in order to discriminate between the QCD evolution schemes of DGLAP and BFKL.

At low x-Bjorken (x) and in leading order of α_S the parton evolution is dominated by the Boson-Gluon Fusion process. Higher order terms are usually described by the Altarelli-Parisi equation [1], which sums up leading powers of $\ln Q^2$ and neglects terms with $\ln\frac{1}{x}$ alone. This leads to an emission of partons strongly ordered both in longitudinal (x_i) and transverse momentum (k_T^2) (see fig.1):

$$x \ll x_1 \ll \cdots \ll x_{JET}, \qquad Q^2 \gg k_{T,1}^2 \gg \cdots \gg k_{T,Jet}^2.$$

The resulting gluon distribution is proportional to: $xg(x) \propto exp((2(\frac{3\alpha_S}{\pi} ln Q^2 ln\frac{1}{x}))^{\frac{1}{2}})$.

The BFKL approach [2] resums the $\ln\frac{1}{x}$ terms and leads to parton emissions which are not ordered in transverse momentum. The resulting gluon density grows as a power of x (the *Lipatov* growth): $xg(x) \propto x^{-\alpha_P+1}$ with $\alpha_P - 1 = \frac{12\alpha_S}{\pi} ln 2$.

The effects predicted by the BFKL evolution equation are expected to become important at low x. As a signature of a BFKL-like parton evolution, it has been suggested [4] to study high-E_T jets ($k_{T,Jet}^2 \sim Q^2$) emitted in the forward direction. This relies on the idea that, in the BFKL picture, because of the absence of strong ordering in transverse momentum, the struck quark and the high x_{Jet} parton can be separated by a large rapidity interval, in which the parton emissions are enhanced. In this picture, the cross section for parton emission is dominated by powers of $\alpha_S ln\frac{x_{Jet}}{x}$, while these processes are suppressed in the DGLAP picture.

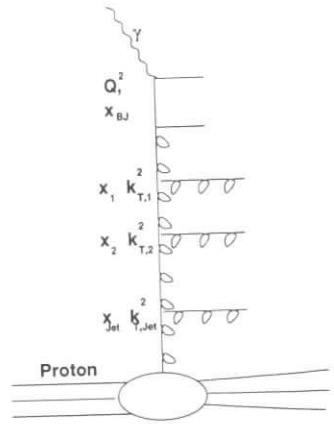

Figure 1: *Gluon ladder in the Boson-Gluon Fusion process.*

In contrast to measurements of the inclusive proton structure function or transverse energy flow, measurements of forward jet cross sections have the advantage that they are sensitive to the explicit details of QCD evolution and have smaller sensitivity to hadronization effects.

However some difficulties still remain. First, because of the kinematics, NLO corrections are large in this region [6]; therefore it is necessary to evaluate the perturbative background to BFKL using NLO calculations of DGLAP. Then the experimental problems are more difficult to handle in the forward region than elsewhere: the purity of the jet sample (i.e. the ratio of the number of jets seen in the detector which also match a jet from the generator level to the total number of jets in the detector) and the jet resolution (i.e. the difference between jet detected and jet generated as a function of various kinematical variables) drop in this region.

Here, as an example, we use the ZEUS detector to show the possibilities and the limits of a forward jet analysis as well as to discuss some luminosity requirements for such an analysis.

In order to reconstruct the jets, the cone algorithm was used, because it leads to small higher order corrections and recombination schemes dependences [6].

In order not to lose energy in the beam pipe, a cut on the pseudorapidity $\eta < 3$ units has been used where η is a function of the polar angle θ ($\eta = -ln(tan(\theta/2))$). A cut on the transverse energy of the jets of 7 GeV has been imposed for better energy resolution and small hadronization effects (for this value of E_T, studies show that the hadronization effects are less than 10%). The present study has been performed for events with $Q^2 > 6$ GeV^2.

In order to evaluate the size of the expected effect of a BFKL type process, the cross section for inclusive one-jet production, where one jet is constrained in the forward region, is calculated with the ARIADNE Monte Carlo [5]. ARIADNE is often used as an approximation to the BFKL effect, although it does not have the exact BFKL evolution process implemented. This cross section is compared to the one found in the LEPTO Monte Carlo [5]. LEPTO implements the DGLAP evolution process.

The results of the comparison are shown in fig.2, where the inclusive one-jet cross section (one jet being constrained in the forward region) is plotted as a function of x. The forward jet has been selected with $2 < \eta_{Jet} < 3$ and the transverse energy of the jets is larger than 7 GeV. For this value of E_T, the hadronization effects are within 10%, as determined with the present generators. The plots show a significantly larger cross section in ARIADNE compared to LEPTO at low x and low Q^2, as expected. This is taken as a sign of the difference between the two parton evolution schemes. Recent comparisons of theoretical calculations using fixed-order NLO QCD calculations [8] and calculation based on a BFKL ladder in the initial state [9] show similar strong differences in the rate of forward jet cross sections. These cross sections have also been evaluated using with other cuts using MEPJET [8] at leading and next-to-leading order. The numerical results of the comparison between LEPTO and ARIADNE are:

Q^2	6-10 GeV^2			10-20 GeV^2			20-100 GeV^2		
x ($\times 10^{-4}$)	1-3	3-7	6-20	1.5-5	5-15	15-40	6-15	15-30	30-80
LEPTO [pb]	120	149	128	136	214	135	177	204	262
ARIADNE [pb]	243	214	196	173	286	140	191	145	229

Table 1: Comparison of cross sections

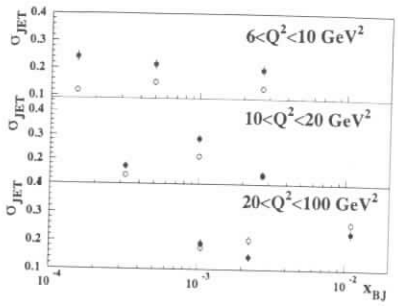

Figure 2: *Comparison of the 1 jet inclusive cross section (in nb) for LEPTO 6.3(○) and ARIADNE 4.08(●) in different Q^2 bins.*

This study is experimentally challenging, as can be inferred from fig.3. There, the purity (defined above) and efficiency (i.e. the ratio of the generated jets which actually match a jet observed at detector level over the total number of generated jets) on a one-to-one jet basis, as well as the correction factors (i.e. the factors needed to get the hadron jet cross section from the detector level value) are shown for an E_T cut of 7 GeV. There is a clear drop in purity at high η, obviously due to the difficulty of reconstructing the jet in this region: Monte Carlo studies show that the angular resolution gets worse in the forward region. As a matter of fact, the granularity of the ZEUS calorimeter sets the limits on the angular resolution of the jet in this region.

In fig.4 the luminosity needed in order to get to 5% for the statistical error as a function of x (for x bins of $2 \cdot 10^{-4}$) is shown for two different sets of cuts.

The first one has requirements only for the jets (a forward jet with $2 < \eta < 3$, $E_{T,Jet} > 7$ *GeV*). The second one requires additionally a cut on p_T^2/Q^2 on the forward jet in order to be in the phase space region of interest ($0.5 < p_T^2/Q^2 < 6$). No detector effect has been taken into account. As can be seen from the figures, the constraint on the momentum of the jet to be within some range around Q^2 severly decreases the statistics and increases the luminosity requirements by a factor between 2 and 5.

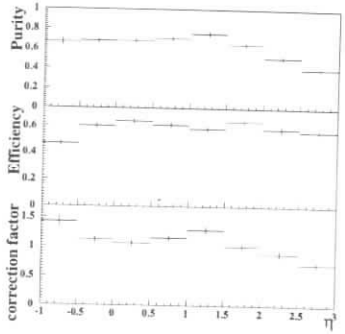

Figure 3: *Purity, efficiency and correction factors as a function of η_{Jet} in a jet by jet basis with $E_{T,Jet} > 7$ GeV.*

Summary and future

Forward jets are expected to be a clear signature to distinguish between BFKL and DGLAP parton evolution. These jets are a challenge to measure, but a sufficient accuracy can be reached with the set of cuts that has been worked out here. The difference predicted for the cross sections in BFKL and DGLAP evolutions are expected to be larger than 10%. A comparison with the NLO calculation seems to be necessary to evaluate the standard QCD background. This could be done by using the MEPJET package.

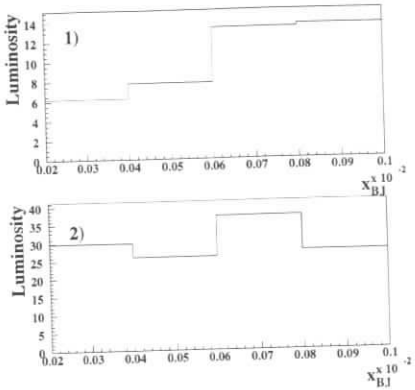

Figure 4: *Luminosity (in pb^{-1}) needed to have a statistical error of 5% in each x bin for two sets of cuts: 1) cuts on rapidity and transverse energy of the jets and 2) same cuts plus constaint on p_T^2/Q^2 on the forward jet.*

References

[1] G.Altarelli and G.Parisi, Nucl.Phys.B 126 (1977) 298

[2] E.A.Kuraev, L.N.Lipatov, V.S.Fadin, Sov.Phys. JETP 45 (1977) 199

[3] J.Bartels, A.DeRoeck, M.Loewe, Z.Phys.C 54 (1992) 634

[4] A.H.Mueller, Nucl.Phys.B (Proc.Suppl.) 18C (1991) 125

[5] G.Ingelman et al., proc 'Physics at HERA' DESY 1991, 1366;
L.Lönnblad, Comput. Phys. Commun. 71 (1992) 15

[6] E.Mirkes, D.Zeppenfeld, TTP96-24, MADPH-96-946, hep-ph/9606332, June 96

[7] J.Kwiencinski, A.D.Martin, P.J.Sutton, Phys.Rev.D 46 (1992) 921

[8] E.Mirkes, D.Zeppenfeld, TTP95-42, MADPH-95-916 (1995), hep-ph/9511448
'Fixed order QCD backgrounds to BFKL dynamics in forward jet production', Erwin Mirkes, Dieter Zeppenfeld

[9] J.Bartels, V.Del Duca, A.DeRoeck, D.Graudenz, M.Wüsthoff, DESY-96-36, CERN-Th/96-83, ANL-HEP-PR-96-23, EDINBURGH-96-2, March 96

Production of Forward Jets at HERA

J. Bartels[1], A. De Roeck[2], M. Wüsthoff[3,a]

[1] II. Institut für Theoretische Physik, Universität Hamburg, D-22761 Hamburg, Germany.
[2] Deutsches Elektronen Synchrotron DESY, D-22603 Hamburg, Germany.
[3] Argonne National Laboratory, 9700 South Cass Avenue, IL 60439, USA.

[a] Partly supported by the U.S. Department of Energy, Division of High Energy Physics, Contract W-31-109-ENG-38.

Abstract: We study predictions for the associated production of forward jets at HERA using the high energy asymptotic expressions derived from the BFKL equation, and compare it with calculations made in the Born approximation. The cuts have been varied to optimize the detection of the BFKL signal. For typical detector cuts we find that the slope of the cross section as a function of x can strongly increase if jets with smaller angles (more forward jets) can be detected.

1 Introduction

A proposed clean footprint of BFKL dynamics [1] at HERA is the measurement of inclusive jet production in the forward direction, in deep inelastic scattering interactions. Jets have to be selected with longitudinal momentum close to the one of the proton (i.e. the fractional momentum of the jet is much larger than the Bjorken-x : $x_{\rm jet} \gg x$), and transverse momentum, $p_{T\rm jet}$, of the order of the virtual photon mass $\sqrt{Q^2}$. These measurements have been proposed in[2] and analytical calculations were performed in[3]. The cross section formula for the process $\gamma^*+g \to g+(n\,g)+q\bar{q}$ or $\gamma^*+q \to q+(n\,g)+q\bar{q}$ has been derived from the BFKL equation which resums the leading logarithms. Details are given in [4]. The results of the BFKL calculations have been compared with the Born diagram calculations, i.e. interactions where no gluons are emitted along the ladder (n=0). Data from the H1 experiment at HERA [5] have shown encouraging agreement with the BFKL parton level calculations presented in [4]. Moreover, recently fixed-order NLO calculations [4, 6] demonstrate that the expected jet cross sections are lower and may have a different x dependence. The BFKL prediction — which, as a result of gluon production between the forward jet and the current jet, rises as a function of $1/x$ — is found to lie above the matrix element calculation. We also find that the Born calculation and matrix element calculation are very similar. In our previous publication we compared the results of the calculation with the H1 data, for exactly the same cuts. In this paper we use the BFKL cross section program to investigate the dependence of the cross section on these cuts.

2 Experimental cuts

In a recent analysis forward jets have been studied by the H1 collaboration[7] for a sample of DIS events with a scattered electron satisfying $E_e > 11$ GeV, $160^0 < \theta_e < 173^0$ and the kinematical conditions $y > 0.1$ and $0.0005 < x < 0.0035$. A cone algorithm is used to find jets in the H1 calorimeter, requiring an E_T larger than 3.5 GeV in a cone of radius $R = \sqrt{\Delta\eta^2 + \Delta\phi^2} = 1.0$ in the space of pseudo-rapidity η and azimuthal angle ϕ in the HERA frame of reference. Preliminary cross sections are measured for events which have a "forward" jet defined by $x_{\rm jet} > 0.035$, $0.5 < {p_{T\rm jet}}^2/Q^2 < 2$, $7^0 < \theta_{\rm jet} < 20^0$ and $p_{T\rm jet} > 3.5$ GeV, where $p_{T\rm jet}$ is the transverse momentum of the jet, and $\theta_{\rm jet}$ the angle of the jet with respect to the proton beam direction. The variable $x_{\rm jet}$ is approximated as $E_{\rm jet}/E_{\rm beam}$ with $E_{\rm jet}$ the energy of the jet and $E_{\rm beam} = 820$ GeV. The data are presented as function of Bjorken-x. The prediction for this experimental cuts is shown in Fig.1 for incident electron and proton beam energies of 27.5 and 820 GeV respectively. Shown is the jet cross section per bin in x. The bins of the histogram are matched to the preliminary bining of the data as they were presented in [7].

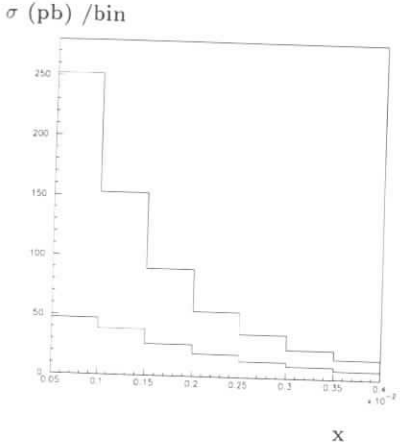

Figure 1: *Cross section per bin from the BFKL calculation (upper curve) and Born calculation (lower curve), for the jet and event selection given in section 2.*

3 Modified cuts

We have varied the cuts described in the section above and studied the behaviour of the Born and BFKL cross sections. We modify the forward jet quantities ${p_{T\rm jet}}^2/Q^2$, $p_{T\rm jet}$, and $\theta_{\rm jet}$ The variables defining the selection of the deep inelastic events have not been varied. It was checked that selecting predominately events with lower x by either changing the minimum scattered electron energy to a few GeV, or by increasing the cut on minimum y from 0.1 to 0.4 does not

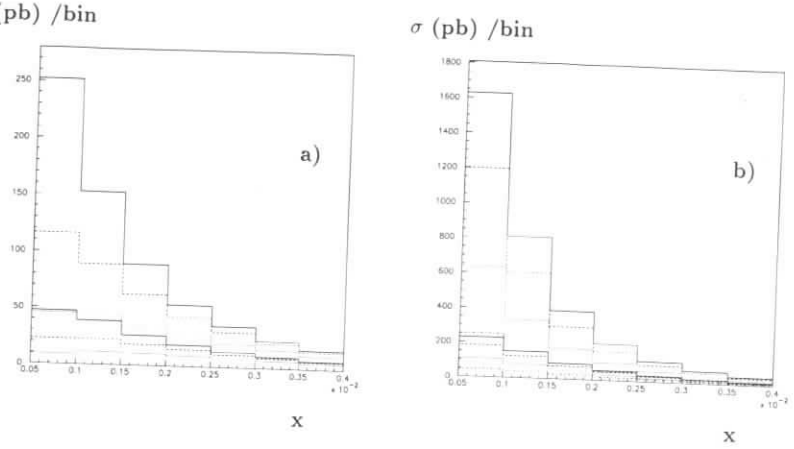

Figure 2: **a)** *Cross section per bin from the BFKL and Born calculations with $p_{T\rm jet} = 3.5$ GeV (solid line), 5 GeV (dashed line) and 6 GeV (dotted line); upper curves are BFKL, lower are Born calculations.* **b)** *Cross section per bin from the BFKL and Born calculations with $\theta_{\rm jet} =$ 2 (solid line), 3 (dashed line) 5 (dotted line) and 7 degrees (dash-dotted line); upper curves are BFKL, lower are Born calculations. All other cuts for both figures are as given in Section 2.*

have a large effect. Beam energies of 27.5 and 820 GeV were assumed for the electrons and protons respectively.

A priori one could imagine that tightening the cut $0.5 < {p_{T\rm jet}}^2/Q^2 < 2$ would result in a more visible difference as one approaches more the 'BFKL' condition. In practice the slope for both the BFKL and Born cross sections do not change much. Reducing the cut to $0.8 < {p_{T\rm jet}}^2/Q^2 <$ 1.2, however reduces the cross section by approximately a factor of 4. It would be of interest to see the effect in a NLO calculation, but the results basically indicate that this cut as used in the experiment at present is sufficiently narrow.

The minimum jet transverse energy required by the set of standard cuts is 3.5 GeV. This could be considered too low to be safe against hadronization effects. Also the predictions of NLO calculations, to be considered as a background to this process, become more reliable at large $p_{T\rm jet}$. Therefor predictions were calculated for higher $p_{T\rm jet}$ cuts. In Fig. 2a results are shown for cuts $p_{T\rm jet} = 3.5, 5$ and 6 GeV. It shows that the slope of the BFKL calculation becomes less steep with increasing $p_{T\rm jet}$. This is in accord with the expectations as presented in [4]. It can understood as being due to the decrease in phase space: the requirement of $p_{T\rm jet}$ to be similar to $\sqrt{Q^2}$ results, for an increase in $p_{T\rm jet}$, to an increase in $\sqrt{Q^2}$, and correspondingly an increase in x. Hence the $x_{\rm jet}/x$ lever arm becomes smaller and the BFKL gluon emission is reduced. Note also that the cross sections are strongly reduced as the cut increases. Hence such an increase reduces the BFKL effect and makes it harder to detect.

The most substantial effect comes from reducing the minimum angle for the jet detection $\theta_{\rm jet}$. In Fig.2b the cross section is shown for $\theta_{\rm jet} = 7, 5, 3$ and 2 degrees. The slope of the BFKL calculation increases strongly at small angles. It would be interesting to see if the

NLO calculations are still in agreement with the Born calculations for these small angles. If so, instrumenting the detectors to cover low angles for jet measurements would be clearly advantageous for these BFKL studies.

The effect of an increased $p_{T\text{jet}}$ cut on a data sample selected with $\theta_{\text{jet}} = 3$ degrees is similar to the one discussed above: the slope gets smaller. However the slope and cross section for a selection with $p_{T\text{jet}} = 5$ GeV and $\theta_{\text{jet}} = 3$ degrees is about the same as for the present selection with $p_{T\text{jet}} = 3.5$ GeV and $\theta_{\text{jet}} = 7$ degrees. Hence detecting jets towards smaller angles allows to put more stringent cuts on the jet energies. It also allows to increase the x_{jet} cut to enlarge the x_{jet}/x lever arm.

4 Conclusions

The dependence of the forward jet cross section as function of x was studied for different jet selections. Increasing the jet energy reduces the sensitivity to the BFKL effect. A substantial gain to observe the BFKL pomeron can be made if the detectors can get upgraded to detect and measure jets at smaller angles.

References

[1] E.A. Kuraev, L.N. Lipatov and V.S. Fadin, *Sov. Phys. JETP* **45** (1977) 199;
Ya.Ya. Balitskij and L.N. Lipatov, *Sov. J. Nucl. Phys.* **28** (1978) 822.

[2] A.H. Mueller, *Nucl. Phys. B* (Proc. Suppl.) **18C** (1991) 125.

[3] J. Bartels, A. De Roeck and M. Loewe, *Z. Phys.* **C54** (1992) 635;
J. Kwiecinski, A.D. Martin and P.J. Sutton, *Phys. Lett.* **B287** (1992) 254; *Phys. Rev.* **D46** (1992) 921;
W.-K. Tang, *Phys. Lett.* **B278** (1991) 363;
J. Bartels, M. Besançon, A. De Roeck and J. Kurzhoefer, in *Proceedings of the HERA Workshop 1992* (eds. W. Buchmüller and G. Ingelman), p. 203.

[4] J. Bartels et al., DESY 96-036, accepted by Phys. lett.

[5] H1 Collab., DESY-95-108 and *Phys. Lett.* **B356** (1995) 118.

[6] E. Mirkes and J. Zeppenfeld, these proceedings

[7] A. De Roeck, to appear in the proceedings of the Workshop DIS96, Rome 1996.

Target Proton Properties in Deep Inelastic Scattering at HERA

I. Gialas[a], J. Hartmann[b]

[a] University and INFN Bologna, Bologna, Italy
[b] McGill University, Dept. of Physics, Montréal, Québec, Canada

Abstract: Leading protons with longitudinal momentum significantly below the proton beam energy are a powerful tool to study the transition of partons to observable hadrons. Some distributions of leading-proton properties are studied which will allow to learn more about this transition process.

Introduction

The fragmentation and hadronisation of partons to observable particles is not calculable in perturbative QCD. Monte Carlo models, which simulate deep inelastic ep scattering events (DIS), first generate the hard scattering process based on perturbative QCD calculations. Then the fragmentation and hadronisation of the colored partons to observable hadrons is modeled differently. Most of the global properties of final state particles are described successfully by the following models: ARIADNE (using the Color Dipole Model and string fragmentation), HERWIG (using parton showers and cluster fragmentation) and LEPTO (using parton showers and string fragmentation). The test of these models in all possible regions of phase space is an important test of our knowledge of nature.

The ZEUS detector has a powerful leading proton spectrometer (LPS). It allows to detect final-state protons, which move with high momentum p_z along the proton beam line. Monte Carlo generators for DIS processes produce such a leading proton in 50-60% of the events. Some of them have about the beam momentum, i.e. $x_l = p_z/820 \text{ GeV} \approx 1$. They are attributed to diffractive scattering processes, where a colorless object, a pomeron, is exchanged between the proton and the virtual photon. The initial state proton does not break up in this case.

A bulk of events have lower x_l: $0.05 \lesssim x_l \lesssim 0.95$. These protons are an excellent tool to study the hadronisation process because they likely have exchanged a colored object with the incoming virtual photon. Thus the proton was left in a colored state (the proton remnant) for a very short time. The way the proton remnant hadronises to a real proton again is not well understood and is modeled differently by the various models. The color forces acting in this process may be studied with high accuracy because these final-state leading protons are not the result of a long fragmentation and hadronisation chain as the rest of the hadrons in the event.

Standard Monte Carlo predictions

The predicted x_l distributions of the LEPTO, HERWIG and ARIADNE Monte Carlo generators [1] are shown in Fig. 1. They differ in shape, offering a handle to investigate the color forces involved by comparing the measured distributions to the different models. Events with a

detected good LPS track from the HERWIG sample are indicated by the dashed-dotted line (scaled by an arbitrary factor). The acceptance of the LPS detector is limited to x_l values above ~ 0.5.

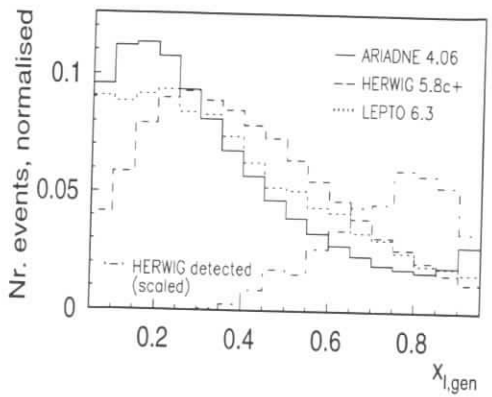

Figure 1: *Generated and detected x_l spectrum from various Monte Carlo Models*

Q^2-dependence of the rapidity distribution of leading protons

The rapidity difference Δy between the incoming and outgoing proton can be used to study the color forces. In DIS Monte Carlo models the initial state QCD radiation decreases the rapidity of the outgoing proton. The Δy distribution is thus shifted to higher values with increasing Q^2. The shift is about 0.25 units when Q^2 changes from 10 to 100 GeV^2. Kopeliovich and Nemchik developed a model [2] to describe QCD effects for partons moving through hadronic matter. Their model leads to a Q^2-dependent retarding force $\kappa = \frac{8}{9\pi} \cdot Q^2 \cdot \alpha_s(Q^2)$ between the colored objects. In [3] the retarding force is related to the rapidity difference of leading particles in pp-collisions so that the differential particle rate $dN/dy = N_o \exp^{-\Delta y/\Delta y_o}$ depends on this force: $\Delta y_o \sim \kappa$. Assuming that in ep-collisions the retarding force between the parton emitted from the proton and the proton remnant is Q^2-dependent as in [2], one finds $\Delta y_o = 2.3 \cdot Q^2/\ln(Q/\Lambda)^2$ (with $\Lambda \approx 0.3$ GeV). This Q^2-dependent retarding force leads to a change of the slope of the Δy distribution with changing Q^2 in contrast to a shift of Δy in the standard DIS models. The slope is expected to change by $\sim$20% when Q^2 rises from 10 to 100 GeV^2. In [3] the slope of the Δy distribution is related to the lifetime of the colored object, i.e. of the proton remnant in our case.

Figure 2a shows the generated Δy distribution for HERWIG events at Q^2 of 10 and 100 GeV^2. The slope of the distribution as shown in logarithmic scale does not change much. In Fig. 2b the Δy distributions for HERWIG and LEPTO events at $Q^2 = 10$ GeV^2 are shown as default. The events are then weighted with a factor corresponding to the retarding force at $Q^2 = 100$ GeV^2. The change of the slope is obvious. The acceptance of the LPS is limited to Δy values below ~ 1, i.e. the exponential fall off, from which the lifetime of the proton remnant would be measurable, is not accessible. However, the study of the Δy distribution in the threshold region will give new information on the Q^2-dependence of the color forces.

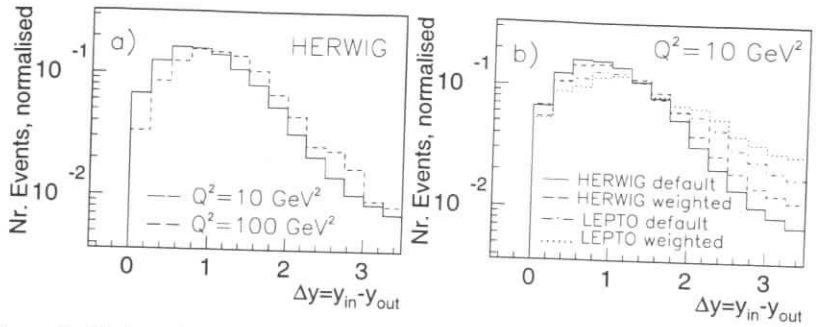

Figure 2: *Q^2 dependence of the Δy distribution of leading protons, see text for details*

Background sources

Events with π^o or ρ^o exchange can result in leading protons too. Contributions of those events have to be subtracted because they are usually not generated in the standard DIS Monte Carlo programs. Figure 3 shows the shapes of generated leading-proton distributions (normalised arbitrarily) of various processes. The EPSOFT-DD sample [4] corresponds to double dissociative events. Background from misidentified π^+ from DIS events is expected to be small. Leading protons from HERWIG -representing the signal- are shown for comparison too.

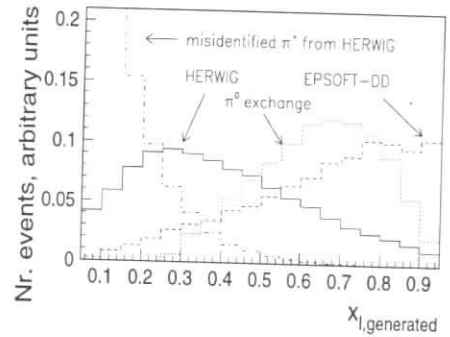

Figure 3: *$x_{l,gen}$ distributions of leading particles from several sources*

Summary

Leading protons are a powerful tool to study hadron formation. The statistics taken with the ZEUS detector from 1994–1996 will give some 10 k events with a good LPS track. This will allow to distinguish between the predictions for the leading-proton properties of various Monte Carlo models and thus improve our understanding of fragmentation and hadronisation. The background from non-DIS events needs to be well understood for this purpose.

Acknowledgements
We thank E. Barberis, N. Cartiglia, M. Erdmann, G. Ingelman, L. Lönnblad, T. Massam, J. Rathsman, R. Sacchi, F. Schrempp and M. Seymour for fruitful discussions during the HERA workshop.

References

[1] L. Lönnblad, Comput. Phys. Commun. 71 (1992) 15;
G. Marchesini et al., Comput. Phys. Commun. 67 (1992) 465;
G. Ingelman, proc. 'Physics at HERA', DESY 1991, p. 1366.

[2] B. Kopeliovich and J. Nemchik, JINR E2-91-150 (1991).

[3] W. Busza, T. Dreyer, M. Erdmann, Z. Phys. C 48 (1990) 167;
T. Dreyer and M. Erdmann, THEP 91/8 (1991).

[4] M. Kasprzak, paper in preparation.

High–p_T Particles in the Forward Region at HERA

M. Kuhlen
Max-Planck-Institut für Physik, Werner-Heisenberg-Institut,
Föhringer Ring 6, D-80805 München, Germany, E-mail: kuhlen@desy.de

Abstract: In order to probe the dynamics of parton evolution in deep inelastic scattering at small x , high–p_T particles produced centrally in pseudorapidity are studied. In the BFKL mechanism gluon radiation is expected to be more abundant than for DGLAP evolution with strong ordering of the gluon transverse momenta, leading to harder p_T spectra. The proposed measurements require charged particle tracking capability as much forward as possible in the HERA laboratory frame, for example with a Very Forward Silicon Tracker, and high luminosity for detailed studies.

HERA allows the study of a new kinematical regime in deep inelastic scattering, reaching very small values of Bjorken-x ($\approx 10^{-5}$) with Q^2 still a few GeV^2 , such that perturbation theory can be applied. It is an open theoretical question whether HERA data can still be described with the conventional DGLAP (Dokshitzer-Gribov-Lipatov-Altarelli-Parisi) parton evolution equations [1] which are derived for not too small x and correspond to a resummation of terms proportional to $(\alpha_s \ln(Q^2/Q_0^2))$, or whether terms proportional to $(\alpha_s \ln 1/x)^n$ become important, which are treated in the BFKL (Balitsky-Fadin-Kuraev-Lipatov) equation [2][1]. The two approximations lead to different constraints for the gluons which can be emitted in the parton evolution chain (Fig. 1a). The leading log DGLAP evolution corresponds to a strong ordering of the transverse momenta k_T (with respect to the proton beam) in the parton cascade ($Q_0^2 \ll k_{T\,1}^{\,2} \ll ...k_{T\,i}^{\,2} \ll ...Q^2$), while in the BFKL evolution arbitrary k_T are possible [4]. It appears that the structure function measurements are too inclusive to distinguish the different evolutions [5]. The hadronic final state emerging from the cascade may be more sensitive to the new type of evolution (see e.g. [6]). However, hadronization effects screen to some extent the parton dynamics from direct observation [7].

QCD predictions for the hadronic final state are extracted from Monte Carlo models, which incorporate the QCD evolution in different approximations and utilize phenomenological models for the non-perturbative hadronization phase. The MEPS (Matrix Element plus Parton Shower) [8] and the HERWIG [11] models invoke leading log DGLAP parton showers with strong k_T ordering. In the colour dipole model (CDM) [9], an unordered parton emission scenario is realized, and in that respect it is similar to the BFKL evolution [12]. Gluon radiation in MEPS and HERWIG is suppressed w.r.t. CDM without the k_T ordering constraint (see Fig. 1b)[2]. However, all models give a satisfactory overall description of current HERA final state data [13].

[1] More recently, in the CCFM approach [3] an equation for both small and large x has been provided.
[2] All distributions shown are in the hadronic centre of mass system (CMS), and are normalized to the number of events N which enter the distribution. The pseudorapidity η in the CMS is defined as $\eta = -\ln\tan\theta/2$, with θ measured with respect to the virtual photon direction.

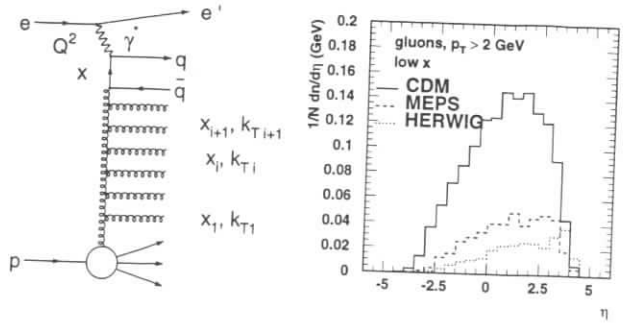

Figure 1: a) *Parton evolution cascade.* b) *The multiplicity of hard gluons with* $p_T > 2$ GeV *as a function of* η *for events at small* x, $\langle x \rangle = 0.00037$ *at* $\langle Q^2 \rangle \approx 14$ GeV^2 . *The proton remnant direction is to the left.*

During the HERA workshop it was found that inclusive charged particle transverse momentum (p_T) spectra offer a handle to disentangle hard perturbative from soft hadronization effects [14]. The hard tail of the p_T spectra (see Fig. 2a) is sensitive to parton radiation from the cascade. The CDM generates a harder tail than LEPTO and HERWIG with suppressed gluon radiation. One can thus hope to study the parton evolution dynamics with high-p_T particles, and discriminate between the different scenarios. Here the implications for the future experimentation at HERA will be investigated.

The measurement of the hard tail of the p_T spectrum shown in Fig. 2a would pose a challenge to QCD (in fact, a QCD calculation for the rate of high p_T forward pions, based upon the BFKL equation, has just become available [15]), and it has been investigated what experimental precision can be achieved. In Fig. 2b the luminosity needed is shown to reduce the statistical error for a given p_T bin to the same level as the expected systematic error [16] for that bin. The luminosity estimate is based upon the CDM. The binning was chosen such that the systematic error is constant ($\approx 5\%$) for all bins. In order to measure the p_T spectrum at p_T =12 GeV with a precision of 5% for both statistical and systematic error an integrated luminosity of 300 pb^{-1} would be needed. The quest for a measurement at large p_T (and large luminosity) is also motivated by the expectation that perturbative QCD will be more reliable there.

As a measure of the rate of hard particles as a function of pseudorapidity, the multiplicity flow of charged particles with $p_T > 2$ GeV is shown vs. η in Fig. 3. Events from two kinematic bins, one at "large x " ($\langle x \rangle$=0.0023) and one at "small x" ($\langle x \rangle$=0.00037) are compared, with $\langle Q^2 \rangle \approx 14$ GeV^2 approximately constant. At high x the differences between the model predictions are not very big, but at small x the models deviate by a large amount. The CDM produces much more particles with $p_T > 2$ GeV than MEPS and HERWIG, and the discrepancy increases with the distance from the current system. That difference has its origin in the very different gluon emission pattern, see Fig. 1b.

The sensitivity to this effect with typical (here H1 [17]) HERA tracking devices is indicated. It is clear that such a measurement requires charged particle tracking capability as far "forward" (into the remnant direction) as possible. The so called "forward" region of the HERA detectors corresponds to the central region in the hadronic CMS. Rather than measuring with

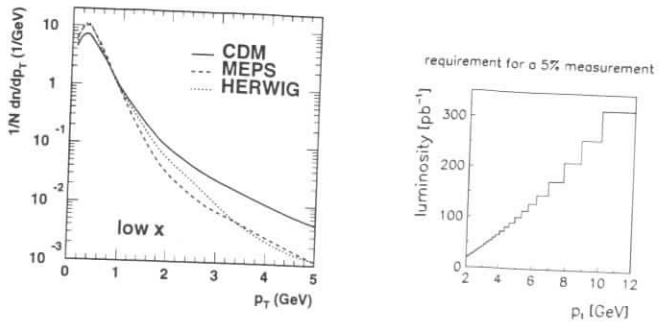

Figure 2: a) *The* p_T *spectra for charged hadrons from* $0 < \eta < 2$ *at* $\langle x \rangle = 0.00037$ *and* $\langle Q^2 \rangle \approx 14$ GeV^2 . b) *The luminosity needed for a statistical precision of 5% for a given bin in* p_T.

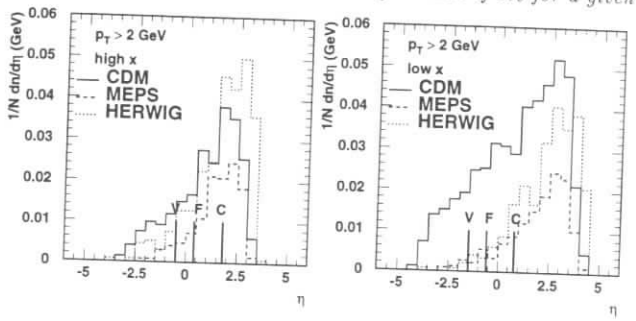

Figure 3: *Multiplicity flow vs.* η *for charged hadrons with* $p_T > 2$ GeV *at* a) *"high" x and* b) *"low" x . The current direction is to the right. Indicated are the acceptance limits of the H1 central tracking system (C,* $\theta_{\rm lab} > 20°$*), the forward tracking system (F,* $\theta_{\rm lab} > 7°$*), and a hypothetical very forward tracking system (V,* $\theta_{\rm lab} > 3°$*). Here* $\theta_{\rm lab}$ *is measured in the laboratory system w.r.t. the proton direction.*

high precision a relatively small effect, which may be masked by hadronization and other uncertainties, it is preferable to measure a large effect with moderate precision. Therefore a "Very Forward Tracker" is proposed which covers angles down to $\theta_{\rm lab} = 3°$.

Here a feasibility study for the case of H1 is presented. A silicon tracker similar to the H1 Backward Silicon Tracker (BST), but with radial ("ϕ") readout strips to measure curvature, could be positioned suitably in the forward region [18]. It would consist of four to eight disks mounted perpendicular to the beam line, and sit in between the central drift chamber and the beam pipe. There is space available between $z \approx 40 - 120$ cm, with z being the longitudinal distance from the interaction point. Radially, the sensitivity would extend from 6 to 12 cm. Angular coverage from $\theta_{\rm lab} = 3°$ to $8°$ would be possible, matching with the end of the H1 forward tracker acceptance at $\theta_{\rm lab} = 7°$. With four readout planes, spaced 0.1 m apart, and with a pitch of 50 μm, a momentum resolution of $\delta p_T / p_T \approx 10\% \cdot p_T$ can be achieved. It can be improved by a vertex constraint. Since the effective HERA beam width is 70 μm (vertical) by 330 μm (horizontal), the event vertex needs to be defined by tracks measured in the existing

central silicon tracker [18] (impact parameter resolution 60 μm), reducing it to roughly 50 μm by 50 μm. When such a vertex constraint is applied, the momentum resolution could be improved to $\delta p_T / p_T \approx 2 - 3\% \cdot p_T$. That is certainly sufficient for the simple measurement of the p_T spectra discussed here. More detailed studies and simulations would be neccessary to study the occupancy in the detector and questions of pattern recognition. The detector would cost 250k-500k DM (estimate based upon the BST costs), depending on the number of silicon planes.

The HERA luminosity upgrade would have an impact on the VFT. When dipoles are inserted into the H1 detector, perhaps up to the faces of the central drift chamber, that would require a larger diameter beam pipe to let out the produced synchrotron radiation. The existing BST could no longer be used, and the VFT would need to be redesigned according to the larger diameter beam pipe. Of course other options could also be explored. For example, H1 is building a Very Low Q-square (VLQ) tracker for the backward region based upon GaAs technology. Again, this device would not fit on a larger diameter beam pipe. However, it may be possible to save on the new detector by re-using the existing electronics.

Initially, for a minimal meaningful measurement a moderate integrated luminosity of 10 pb^{-1} would already be sufficient. For that purpose, one could even think of a short dedicated HERA run with minimal, but optimized instrumentation, including only the trackers and backward electron detection devices.

In this study, however, only the sensitivity of charged particle spectra[3] to suppressed or abundant gluon radiation scenarios has been exploited. It should be possible to construct variables based on correlations between high-p_T particles which probe the gluon dynamics, for example k_T ordering or recombination effects, more directly and locally. Considering the rate of such particles (Fig. 3), high luminosity would be needed to have enough events with pairs of high-p_T particles. Again, a large forward acceptance would increase the evolution length that can be probed, as well as the statistics of high-p_T particle pairs for correlation studies.

References

[1] Yu. L. Dokshitzer, Sov. Phys. JETP 46 (1977) 641;
V.N. Gribov and L.N. Lipatov, Sov. J. Nucl. Phys. 15 (1972) 438 and 675;
G. Altarelli and G. Parisi, Nucl. Phys. 126 (1977) 297.

[2] E.A. Kuraev, L.N. Lipatov and V.S. Fadin, Sov. Phys. JETP 45 (1972) 199;
Y.Y. Balitsky and L.N. Lipatov, Sov. J. Nucl. Phys. 28 (1978) 282.

[3] M. Ciafaloni, Nucl. Phys. B296) (1988) 49;
S. Catani, F. Fiorani and G. Marchesini, Phys. Lett. B234 (1990) 339; Nucl. Phys. B336 (1990) 18.

[4] J. Bartels, H. Lotter, Phys. Lett. B309 (1993) 400;
J. Bartels, H. Lotter and M. Vogt, DESY-95-224.

[3] Other particles could be utilized as well. For example, $\pi^0 \to \gamma\gamma$ could be detected in the forward calorimeter, or K^0_S decays could be identified via secondary vertices. It may even be possible to identify photons either in the calorimeter or via conversions seen in the trackers.

[5] A.D. Martin, to appear in Proc. of the Workshop on Deep Inelastic Scattering and Related Phenomena, DIS96, Rome 1996.

[6] J. Kwieciński, Nucl. Phys. B, Proc. Suppl. 39BC (1995) 58.

[7] M. Kuhlen, hep-ex/9508014; Proc. of the Workshop on Deep Inelastic Scattering and QCD - DIS95, Paris, April 1995, eds. JF. Laporte and Y. Sirois, p. 345.

[8] G. Ingelman, Proc. of the Workshop on Physics at HERA, Hamburg 1991, eds. W. Buchmüller and G. Ingelman, vol. 3, p. 1366;
A. Edin, G. Ingelman and J. Rathsman, Phys.Lett. B366 (1996) 371.

[9] G. Gustafson, Ulf Petterson, Nucl. Phys. B306 (1988);
G. Gustafson, Phys. Lett. B175 (1986) 453;
B. Andersson, G. Gustafson, L. Lönnblad, Ulf Petterson, Z. Phys. C43 (1989) 625.

[10] L. Lönnblad, Computer Phys. Comm. 71 (1992) 15.

[11] G. Marchesini et al., Computer Phys. Comm. 67 (1992) 465.

[12] L. Lönnblad, Z. Phys. C65 (1995) 285; CERN-TH/95-95;
A. H. Mueller, Nucl. Phys. B415 (1994) 373.

[13] T. Carli, to appear in Proc. of the Workshop on Deep Inelastic Scattering and Related Phenomena, DIS96, Rome 1996.

[14] M. Kuhlen, Phys. Lett. B382 (1996) 441.

[15] J. Kwieciński, S.C. Lang and A.D. Martin, Durham preprint DTP/96/62.

[16] W. Hoprich, diploma thesis, Univ. Heidelberg, 1996.

[17] H1 Collab., I. Abt et al., DESY 93-103 (1993).

[18] N. Wulff, H1 internal note H1-09/91-191;
J. Bürger et al., Nucl. Instr. Meth. A367 (1995) 422;
P. Biddulph and D. Pitzl, private communication.

HZTOOL: A Package for Monte Carlo – Data Comparison at HERA (Version 1.0)

J. Bromley[a], N. Brook[a], A. Buniatian[b], T. Carli[c], G. Grindhammer[c], M. Hayes[d], M. Kuhlen[c], L. Lönnblad[e], R. Mohr[c]

[a] Dept. of Physics & Astronomy, University of Glasgow, UK. G12 8QQ
[b] Universitaire Instelling Antwerpen, Wilrijk, Belgium
[c] Max Planck Institut für Physik, D-80805 München, Germany.
[d] H. H. Wills Physics Lab., University of Bristol, UK. BS8 1TL
[e] NORDITA, DK-2100 Copenhagen Ø, Denmark.

Abstract: A library of generic routines (HZTOOL) has been established to allow easy reproduction, by Monte Carlo generators, of the experimental distributions and accessibility to the published data. This package contains a comprehensive collection of published data from H1 and ZEUS .

Many of the physics conclusions and analyses at HERA are limited due to the inability of the Monte Carlo generators to describe some of the distributions published by H1 and ZEUS in the fields of photoproduction and deep inelastic scattering. This is exacerbated by the large range of variations between the models available. This large variation can hinder in the planning of future physics studies. In comparison to the LEP results, the agreement between Monte Carlo event generators for HERA and the experimental data is significantly worse.

Difficulties with the tuning of the event generators arise with the model builders not understanding the experimentalists' cuts and the experimentalists not understanding the generators' various parameters. A consequence of this is a selective tuning of just a few of the available physics distributions. To help remove these problems the HZTOOL project was initiated to provide an easy-to-use environment in which the generators could be tuned and compared to a comprehensive range of the published experimental hadronic final state data, both deep inelastic scattering (DIS) and photoproduction, from the H1 and ZEUS experiments.

The HZTOOL package is fully documented in [1]. It incorporates a collection of jet algorithms commonly used at HERA and a series of tools that allows Monte Carlo studies and comparisons to be made in an uniform environment irrespective of the generator being used. A series of routines are provided that initialize, fill and manipulate the histograms from the published data and creates generator comparisons with the correct experimental cuts. HZTOOL may also be used as a repository for *suggested* measurements where data is not yet available. This enables easy comparison between predictions from different models and may also facilitate the communication between model builders and experimentalists. There are currently five Monte Carlo generators supported in the package: ARIADNE [2], HERWIG [3], LEPTO [4],

PYTHIA [5] and PHOJET [6]. The results of the tuning of these programs, using this package, are discussed in these proceedings [7].

The authors intend to maintain this package and include future hadronic final state distributions produced by H1 or ZEUS. The source code is available on WWW at
`http://dice2.desy.de/~h01rtc/hztool.html`.

References

[1] J. Bromley *et al.* 'HzTool - A Package for Monte Carlo Generator – Data Comparison at HERA (version 1.0)'.
`http://dice2.desy.de/~h01rtc/hztool.ps`

[2] L. Lönnblad, Comp.Phys.Comm. 71 (1992) 15.
`http://www.nordita.dk/~leif/ariadne/`

[3] G. Marchesini *et al.*, Computer Phys. Commun. 67 (1992) 465.
`http://surya11.cern.ch/users/seymour/herwig/`

[4] G. Ingelman, *in* Proc. HERA workshop, Eds. W. Buchmüller and G. Ingelman, Hamburg (1991) Vol. 3, 1366. G. Ingelman, A. Edin and J. Rathsman, DESY-preprint 96057, Hamburg, April 1996 and hep-ph/9605286.
`http://ulrik.tsl.uu.se/thep/src/`

[5] T. Sjöstrand, Comp. Phys. Comm. 82 (1994) 74.
`http://thep.lu.se/tf2/staff/torbjorn/`

[6] R. Engel Z. Phys. C66 (1995) 203.
`http://www.physik.uni-leipzig.de/~engel/`

[7] N. Brook *et al.* 'Tuning Monte Carlo Event Generators to HERA Data' these proceedings.

Tuning Monte Carlo Event Generators to HERA Data

N. Brook[a], T. Carli[b], R. Mohr[b], M. Sutton[c], R.G. Waugh[a]

[a] Dept. of Physics & Astronomy, University of Glasgow, UK. G12 8 QQ
[b] Max Planck Institut für Physik, D-80805 München, Germany.
[c] University College London, UK.

Abstract: The Monte Carlo models ARIADNE, HERWIG and LEPTO are compared to deep-inelastic scattering data measured at the ep-collider HERA. An improved description of the data is achieved for all Monte Carlo models by tuning the available parameters.

1 Introduction

An adequate description of detailed event properties is a key ingredient for a reliable extraction of any physics observable from the data. Precision measurements of the structure function F_2 or the strong coupling constant α_s rely on a correct modelling of the event topology. Observables based on the hadronic final state need to be corrected for detector effects which is only possible if the Monte Carlo simulation describes the data. Therefore, improving the Monte Carlo model description of the large variety of hadronic final state data will play an important rôle in the future physics from HERA.

To allow an easy comparison of HERA data to model predictions, a test facility has been developed [1]. In this contribution, the influence of the model parameters to the hadronic properties of deep-inelastic events (DIS) is systematically investigated. The free parameters of the models are adjusted such that an optimal description of the HERA data is achieved. A list of the various parameters and switches, with a brief description, is given in table 1.

To quantify the description of a given data distribution by the model, a χ^2 is defined as:

$$\chi^2 = \frac{1}{n}\sum_{i=1}^{n}\frac{(\mathrm{MC}(i)-\mathrm{Data}(i))^2}{\sigma^2_{\mathrm{MC}(i)}+\sigma^2_{\mathrm{Data}(i)}} \qquad (1)$$

where Data(i) and MC(i) are the values of the distribution in a given bin i for the data and Monte Carlo respectively. The sum runs over the n data bins.

From the data already published by the H1 and ZEUS experiments, a set of distributions is chosen that is sensitive to variations of the parameters in the Monte Carlo models. Care is taken that the various regions in the (x, Q^2) kinematic plane are covered. Sensitive parameters are identified for each Monte Carlo generator by considering either the variation of the χ^2 or the distribution $S = (\delta MC/MC)/(\delta P/P)$ weighted by the error on the experimental data after an extreme parameter variation (δP). Parameters already constrained by the recent LEP tuning [2] are not independently considered in our optimization procedure. Due to their sensitivity to the model parameters, the following distributions were chosen to perform the tuning on:

- the transverse energy (E_T) flow in function of the pseudo-rapidity ($\eta^* = -\ln\tan(\theta/2)$) and the mean E_T in the central rapidity region $-0.5 < \eta^* < 0.5$ in the hadronic center of mass frame (cms) [3] for selected (x, Q^2) bins;

	PARAMETER	default	tuned	DESCRIPTION
LEPTO	LST(34)	on	on	switch for new seaquark treatment
	PARL(7)	0.5	0.1	probability of soft colour interaction
	PARL(8)	0.01	0.04	cut-off in matrix element z_{qmin}
	PARL(9)	1	25	cut-off in matrix element $\hat{s}_{min}$ in GeV^2
	PYPAR(21)	0.2	0.2	Λ_{QCD} used in initial state parton shower in GeV
	PYPAR(22)	1	1.5	cut-off for initial state parton shower Q_0^2 in GeV^2
ARIADNE	PARA(1)	0.22	0.22	Λ_{QCD} in GeV
	PARA(3)	0.6	0.6	p_t cut-off for parton cascade in GeV
	PARA(10)	1.0	1.5	power in soft suppression for remnant(α)
	PARA(14)	1.0	1.0	factor for k_T to get extension of remnant (μ) in GeV
	PARA(15)	1.0	0.5	power in soft suppression for struck quark (α)
	PARA(25)	2.0	2.0	$\frac{1}{b}$, governs probability of emissions outside the soft suppression cut-off
	PARA(27)	0.6	0.6	square root of primordial k_T^2 in GeV
HERWIG	CLMAX	3.35	5.5	maximum of the allowed cluster mass in GeV
	PSPLT	1.0	0.65	exponent controlling the mass spectra of split clusters

Table 1: *Parameter values before and after tuning for the Monte Carlo models ARIADNE, HERWIG and LEPTO.*

- the scaled longitudinal momentum ($x_F = 2Pz/W$) of single particles in the cms at fixed values of the invariant mass of the hadronic system W [4];
- the logarithm of the inverse scaled momentum ($x_p = 2P/Q$) in the Breit frame in various (x, Q^2) bins [5];
- the transverse momentum of single particles in the positive hemisphere of the cms [6];
- the mean squared transverse momentum versus x_F ($\langle P_T^2\rangle \times x_F$) in the positive hemisphere of the cms ('seagull' plot) [4, 6].

An overall combination of the χ^2 is formed by averaging over these distributions. The distributions entering this overall combination χ^2_{comb} are given in table 2. The typical error on the χ^2 is about 0.04. The parameter combination giving the absolute minimum of χ^2_{comb} is the tuned result. For all Monte Carlo models the parton density functions of GRV 94 is used [7]. The transverse energy-energy-correlation [4] turned out to be very sensitive to parameter variations. However, since the errors of this distribution are highly correlated, they were not included in χ^2_{comb}. Unfortunatley no jet data was included in this tuning procedure because, as yet, there is no published DIS jet data corrected to the hadron level.

2 ARIADNE

In ARIADNE [8] the QCD cascade is modelled by emitting gluons from a chain of independently radiating dipoles spanning colour connected partons [9], correcting the first emission to reproduce the first order matrix elements [10]. Hadronizing the partons into final state hadrons is achieved using the Lund string model as incorporated in JETSET [11]. Since the proton

TYPE of DATA		weight	ARIADNE		HERWIG		LEPTO	
		w_i	$\chi^2_{\rm default}$	$\chi^2_{\rm tuned}$	$\chi^2_{\rm default}$	χ^2_{tuned}	$\chi^2_{\rm default}$	$\chi^2_{\rm tuned}$
$\chi^2_{\rm comb} = \frac{1}{\sum w_i} \sum_{i=1}^{ndis} w_i\ \chi^2$			1.16	0.81	3.26	1.85	1.74	1.36
$\frac{1}{N}\frac{dN}{dx_F}$	at <W>= 77 GeV	0.5	0.58	0.43	0.51	0.14	0.41	0.22
	at <W>= 169 GeV	0.5	1.73	1.57	12.74	2.92	2.56	1.86
$\frac{1}{N}\frac{dN}{dp_T}$		1.0	0.24	0.13	0.70	1.28	0.86	0.75
$< p_T^2 >$ vs x_F	ZEUS	0.5	3.20	0.56	4.82	2.39	0.87	0.74
	H1	0.5	0.69	0.11	3.83	0.16	0.94	0.27
$\frac{1}{N}\frac{dE_T}{d\eta^*}$	low	0.25	1.00	2.47	2.19	1.83	7.25	6.60
	medium	0.25	0.96	0.34	2.81	2.33	2.01	1.35
	high	0.25	2.60	1.32	1.30	1.03	3.08	3.19
$\langle E_T \rangle$	all bins	0.25	0.86	1.85	2.32	1.24	5.33	3.37
$\frac{1}{N}\frac{dN}{d\ln 1/x_p}$	low	0.33	0.53	0.62	2.78	4.38	0.37	0.57
	medium	0.33	0.23	0.19	0.61	0.93	0.16	0.54
	high	0.33	2.13	2.04	2.89	3.49	2.18	1.55

Table 2: *χ^2 values obtained by comparing deep-inelastic HERA data to the prediction of the Monte Carlo models before and after tuning. The first line gives the χ^2 of the overall combination built on weighted data covering different aspects of the hadronic final state listed in the five following lines. Where available, kinematic bins equally distributed over the kinematic plane are selected. For $dE_T/d\eta$ the low bin corresponds to $\langle x \rangle = 1.6 \cdot 10^{-4}$ and $\langle Q^2 \rangle = 6.8$ GeV^2, the medium one to $\langle x \rangle = 6.3 \cdot 10^{-4}$ and $\langle Q^2 \rangle = 14.2$ GeV^2, the high one to $\langle x \rangle = 2.1 \cdot 10^{-3}$ and $\langle Q^2 \rangle = 30.9$ GeV^2. $dN/d\ln 1/x_p$ is calculated within the boundaries $x = 1.2 - 2.5 \cdot 10^{-3}$ and $Q^2 = 10-20$ GeV^2 (low), $x = 1.2-2.5 \cdot 10^{-3}$ and $Q^2 = 20-40$ GeV^2 (medium), $x = 2.4-10 \cdot 10^{-3}$ and $Q^2 = 80-160$ GeV^2 (high).*

remnant at one endpoint of the parton chain is an extended object, the coherence condition allows only a fraction of this source to be involved in gluon radiation. Since the photon probing the proton only resolves the struck quark to a distance $\lambda \sim 1/Q$, the struck quark is also treated as an extended object. As a consequence gluon emissions in the proton and photon directions are suppressed. This phase space restriction is governed by $a = (\mu/k_T)^\alpha$ where a is the fraction of the colour antenna involved in the radiation, μ is a parameter related to a typical inverse size of a hadron and α governs the distribution of the energy along the dipole.

For tuning, the two α parameters for the proton remnant (PARA(10)) and the struck quark (PARA(15)) and the square root of the mean primordial k_T^2 in the proton (PARA(27)) are considered. All other parameters were left at their default values determined from a tuning of EMC and early DELPHI data [12]. The μ parameter, PARA(14), is highly correlated with PARA(10) and PARA(15) so was left at its default. Before the tuning, the $\chi^2_{\rm comb}$ was already acceptable, $\chi^2_{\rm comb}$=1.16, however it could be further reduced to $\chi^2_{\rm comb}$=0.81 by setting PARA(10)=1.5 and PARA(15)=0.5. The "quality" of the description for the individual distributions can be read from table 2. The improvement is mainly due to a much better description of $\langle P_T^2 \rangle \times x_F$. (see Fig. 1/2b). The description of the E_T flows in the high x and Q^2 bin improved mainly in the current region (see Fig. 1/2d) however, at low x and Q^2 the tuned ARIADNE curve now lies slightly below the data (see Fig. 1/2c). The transverse energy-energy correlations are better described after the tuning although not included in $\chi^2_{\rm comb}$ (see Fig. 1/2e and f).

3 HERWIG

HERWIG [13] relies on a coherent parton branching algorithm with additional first order matrix element corrections [14] to populate the extremities of phase space which the partons from the conventional QCD cascade fail to occupy. The partons are transformed into hadrons using the cluster fragmentation model [15], whereby the primary hadrons are produced from an isotropic two body decay of colour-singlet clusters formed from partonic constituents.

All HERWIG parameters that are not constrained by the LEP data and are expected to be relevant to hadronic interactions were inspected for their sensitivity to HERA data. Only few had an impact on the description of the data. The distribution of intrinsic k_T of the incident hadronic constituents driven by PTRMS and the parameter BTCLM determining the mass distribution of the cluster containing the hadronic remnant are found only to modify the E_T flows at low η^* values close to or beyond the detector acceptance. The maximal allowed cluster mass CLMAX and the exponent controlling the mass spectra of split clusters PSPLT turned out to be most sensitive. The E_T flows grow with both increasing CLMAX and PSPLT, while the seagull plot decreases with increasing (decreasing) PSPLT (CLMAX). The x_F and the $\ln 1/x_p$ distributions fall with increasing CLMAX and decreasing PSPLT. However, the $\ln 1/x_p$ spectra in the intermediate (x, Q^2) range are systematically shifted to low values. A reduction in CLMAX, while nicely describing the E_T flows, at the same time reduces the level of the seagull plot such that varying CLMAX alone is unable to describe all data. PSPLT has the opposite effect on the seagull, so that *simultaneously* reducing PSPLT while increasing CLMAX reproduces the data best.

The optimal parameter settings are CLMAX=5.5 and PSPLT=0.65 leading to an improvement of $\chi^2_{\rm comb}$=3.26 to $\chi^2_{\rm comb}$=1.85. This is achieved by ameliorating the x_F spectra, the seagull plot and the E_T flows (see table 2). Such a high value for CLMAX would be potentially worrying, if not taken in conjunction with the reduction of PSPLT to compensate. Since for this HERWIG version and for HERA data it is also necessary to vary the parameter PSPLT, this result may still be consistent with the recent tuning of CLMAX below 4 achieved for LEP data, where the parameter PSPLT is not varied. Varying the parton density functions (GRV92 LO [16], MRS-H [17])) typically yields a variation smaller than 2% at the minimum of $\chi^2_{\rm comb}$. Although the transverse energy-energy correlations are not included in $\chi^2_{\rm comb}$, the new settings lead to a better agreement with the concave shape seen in the data (see Fig. 2e/f).

4 LEPTO

In LEPTO the hard parton processes are described by a leading order matrix element (ME). The soft and collinear divergences are regulated with a lower and upper cut in z_{qmin} where $z_q = p \cdot j_1 / p \cdot q$ where p (q) is the proton (photon) four-vector and j_1 the four-vector of one of the partons produced in the hard subprocess. In addition, the invariant mass squared of the two hard partons is required to exceed a minimal value, $\hat{s}_{min}$. Below the ME cut-offs, parton emissions are treated by parton showers based on the DGLAP evolution equations [20]. The amount of parton radiation depends on the virtuality chosen between a lower cut off (Q_0^2) and a maximum given by the scale of the hard process or the ME cut-off. LEPTO uses JETSET for the hadronization of the partons. In addition to this non-perturbative phase, LEPTO introduces two non-perturbative mechanisms. The first is in events where a sea-quark is involved in the hard subprocess, its partner is not simply rearranged to a meson or a baryon within the target

remnant, but is used to stretch a string to one of the quarks remaining untouched in the proton. The additional E_T produced when hadronizing this string is needed to describe the data. The second is a soft (i.e. at a scale below Q_0^2) colour interaction which assumes that the colour configuration of the partonic system can be changed whilst traversing the colour field of the proton remnant. The probability that a parton pair exchanges their colour is controlled by a parameter, P_{sci}.

In the optimization procedure the parameters of JETSET and the ones governing the final state parton showers were only varied in sets defined by the four LEP collaborations. Sensitive parameters are filtered out by inspecting the relative change of the χ^2 after variation of the parameters within a reasonable range. The remaining parameters are shown in table 1. When increasing z_{qmin} and $\hat{s}_{min}$ the description of the seagull plot and the x_F spectra improves, but then the E_T flows are badly reproduced. The E_T flows do not allow a high value of the cut-off parameter for initial state parton showers Q^2_{ini} and prefer high values of P_{sci}. However, the x_F spectra are better described by low values of P_{sci}. High values of Λ_{QCD} in the initial state parton shower are able to better reproduce the E_T flows at low (x,Q^2), but are disfavored by the x_F spectra and the transverse energy-energy correlations.

When leaving z_{qmin} at the low default value of 0.01, $\hat{s}_{min}$ has to be raised to rather high values up to 100 GeV^2 to get a good χ^2_{comb}. For $0.04 < z_{qmin} < 0.08$ a χ^2_{comb} minimum is found for a large range in $\hat{s}_{min}$ between 4 and 25 GeV^2. The best combination of z_{qmin} and $\hat{s}_{min}$ is used for a simultaneous variation of P_{sci} and Q^2_{ini}. The last improvement is then achieved by varying Λ_{QCD} in the initial state parton shower and a stable χ^2_{comb} minimum for values of 0.2-0.27 GeV is found. The parameter combination giving the lowest χ^2_{comb}=1.36 is shown in table 2. For this set the hadronization parameter used are those defined by L3. If one repeats the optimization procedure using the set from OPAL one gets compatible results, the set from ALEPH only achieved a χ^2_{comb}= 1.56.

The agreement of the E_T flows with the data is improved for all kinematic bins and the scaled longitudinal momenta are better described at high W (see table 2). Replacing the structure function to MRSH results in a worse χ^2_{comb}. In particular, it softens the transverse momentum distribution for single particles and the $\langle P_T^2 \rangle \times x_F$ comes out too low for high x_F. With this parton density function the optimized χ^2_{comb} value is only as good as the one obtained with GRV before tuning. The transverse energy-energy correlations are, even with the tuned parameters, poorly described for $x > 10^{-3}$. The shape of this distribution can be improved by using the parameter set from OPAL. A better description can be achieved by turning off the soft colour interactions or increasing the cut-off parameter of the final state parton shower. However, then the χ^2_{comb} deteriorates mainly because the E_T flows fall below the data.

5 Conclusion

The Monte Carlo event generators ARIADNE, HERWIG and LEPTO have been compared with the hadronic final state of deep-inelastic scattering data from HERA. All the models' descriptions of the published data have improved with tuning, with ARIADNE giving the best fit to the data used in this study. Even though the description of the data has improved the situation is still far worse than that faced at LEP, where there is no initial state radiation or target remnant to model.

References

[1] J. Bromley et al., these proceedings.

[2] A. Blondel et al., 'QCD Event Generators', Proc. of LEP2 workshop, hep-ph/9601212.

[3] H1 Collab., S. Aid et al., Phys. Lett. B356 (1995) 118.

[4] H1 Collab., I. Abt et al., Z. Phys. C63, 377-389 (1994).

[5] ZEUS Collab., M.Derrick et al., Z. Phys. C67 (1995) 93-107.

[6] ZEUS Collab., M.Derrick et al., Z. Phys. C70 (1996) 1-15.

[7] M. Glück, E. Reya and A. Vogt, Z. Phys. C67 (1995) 433.

[8] L. Lönnblad, Comp. Phys. Comm. 71 (1992) 15, version used: 4.08.

[9] G. Gustafson, Ulf Petterson, Nucl. Phys. B306 (1988), G. Gustafson, Phys. Lett. B175 (1986) 453, B. Andersson et al., Z. Phys. C43 (1989) 625.

[10] L. Lönnblad, Z. Phys. C65 (1995) 285.

[11] T. Sjöstrand, Computer Phys. Comm. 39 (1986) 347, T. Sjöstrand and M. Bengtsson, Computer Phys. Comm. 43 (1987) 367,T. Sjöstrand, CERN-TH-6488-92 (1992), CERN-TH 7112/93 Dec. 93.

[12] W. de Boer and H. Fürstenau, Proc. of MC'91 w/s NIKHEF (1991) 616.

[13] G. Marchesini et al., Computer Phys. Commun. 67 (1992) 465, version used: 5.8d.

[14] M. H. Seymour, LU TP 94-17 hep-ph/9410414.

[15] B.R. Webber, Nucl. Phys. B238 (1984) 492.

[16] M. Glück, E. Reya and A. Vogt, Z. Phys. C53 (1992) 127.

[17] A. Martin, R. Roberts and J. Stirling, RAL-93-077.

[18] G. Ingelman, *in* Proc. HERA workshop, Eds. W. Buchmüller and G. Ingelman, Hamburg (1991) Vol. 3, 1366. G. Ingelman, A. Edin and J. Rathsman, DESY-preprint 96057, Hamburg, April 1996 and hep-ph/9605286, version used: 6.4.

[19] M. Bengtson, T. Sjöstrand, Z. Phys. C37 (1988) 465, M. Bengtson, G. Ingelman, T. Sjöstrand, *in* Proc. of the HERA Workshop 1987, Ed. R.D. Peccei, DESY Hamburg 1988, Vol. 1, 149.

[20] Yu. L. Dokshitzer, Sov. Phys. JETP 46 (1977) 641, V.N. Gribov and L.N. Lipatov, Sov. J. Nucl. Phys. 15 (1972) 438 and 675, G. Altarelli and G. Parisi, Nucl. Phys. 126 (1977) 297.

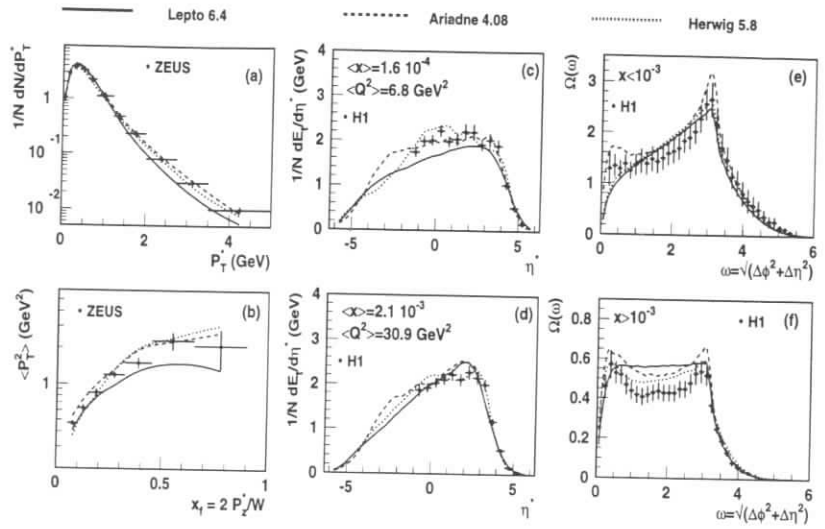

Figure 1: *The transverse momenta dN/dp_T (a) and the 'seagull' plot $\langle P_T^2 \rangle \times x_F$ (b) of single particles in the positive hemisphere of the hadronic center of mass. The transverse energy flow $dE_T/d\eta$ in a low (c) and high (d) x and Q^2 bin. The transverse energy-energy correlations for $x > 10^{-3}$ (e) and $x < 10^{-3}$ (f).*

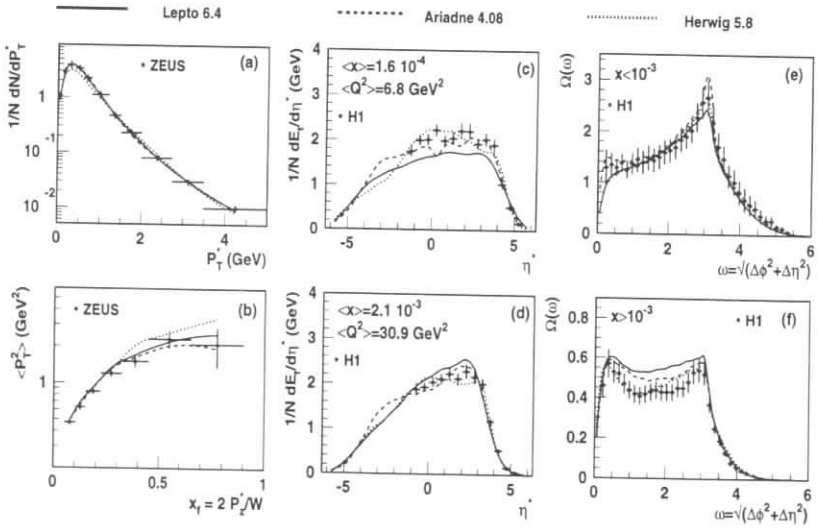

Figure 2: *As Fig.1, but Monte Carlo curves are produced with the tuned parameters.*

The LDC Event Generator

Gösta Gustafson[a], Hamid Kharraziha[a], Leif Lönnblad[c]

[a] Dept. of Theoretical Physics, Sölvegatan 14a, S-223 62 Lund, Sweden, gosta@thep.lu.se, hamid@thep.lu.se
[b] NORDITA, Blegdamsvej 17, DK-2100 Copenhagen Ø, Denmark, leif@nordita.dk

Abstract: We describe briefly a Monte Carlo implementation of the Linked Dipole Chain model and an interface of it to the ARIADNE program for simulation of complete DIS events at HERA. Using this new tool we make some preliminary comparisons to HERA data and find reasonable agreement.

The Linked Dipole Chain model

We here give a brief sketch of the properties of the Linked Dipole Chain (LDC) model, developed by the Lund group. A more detailed description is presented in Refs. [1, 2]. The model is a reformulation and generalization of the formalism developed by Ciafaloni, Catani, Marchesini and Fiorani (CCFM) [3], which interpolates smoothly between the DGLAP and BFKL regions. In the CCFM model there is a specific recipe, which for each possible final state specifies a separation of the produced gluons in what can be called initial-state and final-state radiation. The initial state radiation can be described by a ladder diagram as in Fig. 1. Each set of final states, specified by a definite ladder (but with arbitrary fina-state radiation within the allowed kinematic region), gives a contribution to the cross section, or to the structure function F_2, with a specific weight which includes a non-eikonal form factor.

In the LDC model more of the produced gluons are treated as final-state radiation. This means that the possible final states are grouped in fewer but larger sets. Each set is specified by a chain as in Fig. 1 where the produced (pseudo-real) gluons q_i satisfy the constraint

$$q_{+,1} > q_{+,2} > \ldots q_{+,n}; \qquad q_{-,1} < q_{-,2} < \ldots q_{-,n}; \qquad q_{\perp,i} > \min(k_{\perp,i}, k_{\perp,i-1}). \tag{1}$$

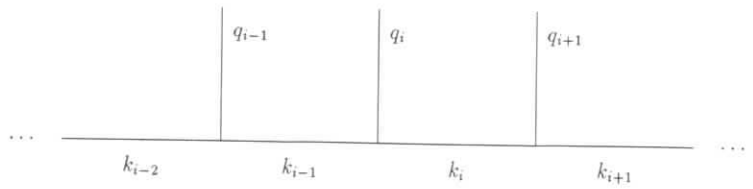

Figure 1: *The notation used for the links and rungs in the ladder.*

To leading order each gluon chain of this type contributes to the cross section, or to F_2, with a weight of the simple form ($z_i = k_{+,i}/k_{+,i-1}$; $\bar{\alpha} = 3\alpha_S/\pi$)

$$(\prod_i \bar{\alpha}\frac{d^2q_{\perp,i}}{dq^2_{\perp,i}}\frac{dz_i}{z_i}) \cdot \delta(\sum_i q_i - P_{\text{tot}}). \tag{2}$$

The non-eikonal form factors are exactly cancelled. The constraint in Eq. 1 means that any gluon with $y_i < y < y_{i+1}$ and $q_\perp < \min(k_{\perp,i}, k_{\perp,i-1})$ will be regarded as final-state radiation. They affect the properties of the final state and can be treated by means of Sudakov form factors, but they can be disregarded in the calculation of the γp cross section or F_2.

To generate events with the weights given in Eq. 2, or to calculate F_2, it is convenient to express the result in terms of the propagators k_i rather than the real momenta q_i. Equation 1 implies that $q^2_{\perp,i} \approx \max(k^2_{\perp,i}, k^2_{\perp,i-1})$, and thus the weight in Eq. 2 can be rewritten as

$$\prod_i \bar{\alpha}\frac{d^2k_{\perp,i}}{k^2_{\perp,i}}\frac{dz_i}{z_i}\min(1, \frac{k^2_{\perp,i}}{k^2_{\perp,i-1}}) \tag{3}$$

If Q^2 is large, the dominant contribution is obtained for the ordered region $k_{\perp,1} < k_{\perp,2} < \ldots < k_{\perp,n}$, and the DGLAP result is recovered. If x is very small for moderate Q^2, also non-$k_\perp$-ordered chains give important contributions, and F_2 increases as a power $x^{-\lambda}$.

In the LDC model it is possible to study both a constant and a running α_S (in the latter case the result is sensitive to a necessary cutoff at small $q^2_\perp$, where α_S is very large). It is also possible to include quark lines and some non-leading contributions by replacing the pole term $1/z_i$ by appropriate splitting functions.

The LDC model is a general scheme, which within the same formalism describes what is often called "normal" DIS events, boson–gluon fusion and hard resolved photon–proton (or photon–photon) scattering. It is symmetric with respect to an exchange of the photon and proton ends of the ladder, and provides, for example, automatically the correct $1/k^4_\perp$ dependence for hard sub-collisions.

Generation of the initial chain

The objective is to produce the initial dipole chain by perturbative initial-state emission of partons, given the momentum fraction x_0 and flavour of the first perturbative incoming parton, the momentum fraction x and flavour of the struck quark and the virtuality Q^2 of the probing photon. For the probability distribution of the chain we use the result from the LDC model. Also quark emissions with the full splitting functions are considered.

The generation is done in three steps. We start out with the leading-log approximation probability for the production of a gluon jet. Also further simplifications are made, at this level, by using constant coupling, allowing the propagators to be below the non-perturbative limit ($Q_0 = 0.6$ GeV) and by neglecting the exponential suppression of emissions where the virtuality of the propagator decreases. These simplifications are corrected for later on, together with corrections to the leading-log approximation.

The path of the chain inside the phase space is specified by choosing the $k^2_\perp$ and k_- for the propagators. With the above simplifications and with logarithmic variables, the probability

distribution for these points becomes flat inside a rectangular area specified by the available phase space and the ordering of k_+ and k_-.

The next step is to throw away all the chains which crawl under the perturbative level since these partons are included in the non-perturbative initial parton density. The surviving chains are then kept with a probability proportional to the suppression of the "going down" steps as in Eq. 3. The ones which are left, about one percent, are now distributed correctly within the leading-log approximation.

The remaining corrections are made in a similar manner: A weight is calculated which is proportional to the probability to keep the chain. Using this weight we are left with a set of chains which are properly distributed. The corrections included at this level are the running of α_s, the full splitting functions and a suppression factor, which is obtained from the integration over azimuthal angles, when the virtuality of two succeeding propagators are almost equal.

Interfacing to ARIADNE

The interface between the C++ code generating the dipole chains and the FORTRAN code of ARIADNE is hidden from the end user so that changing from the standard DIS scheme in ARIADNE [4] to using the LDC model is done by a simple switch in a common block, leaving the current interface to the Lepto generator [5] for generating the electro–weak interaction intact.

The interface consists of three main parts. One for giving the initial parton distributions to the LDC to determine at which x_0 the chain starts. Another deals with converting the initial chain of partonic links to final state on-shell partons, taking care of energy and momentum conservation and the $p_\perp$ limits of subsequent final-state dipole emissions in ARIADNE. The third part is a procedure to correct the emission closest to the electro–weak vertex so that the $\mathcal{O}(\alpha_S)$ matrix elements (taken from Ref. [6]) is reproduced.

The latter turns out to be a minor correction as the main difference as compared to the leading-log splittings is that the matrix elements behaves like $\propto Q^2/k^4_\perp$ when the $k_\perp$ of the first link is much larger than Q^2, which is already taken into account in the LDC part.

The initial parton densities are given as a simple parametrization:

$$xf_i(x) = A_i x^{\alpha_i}(1-x)^{\beta_i}(1 + \gamma_i\sqrt{x} + \delta_i x) \tag{4}$$

And for the preliminary results below, we have simply taken the values presented in [7]. The correct procedure would, of course, be to adjust the parameters in Eq. 4 to fit available data on structure functions using the LDC evolution. This is a future project, which will result in an LDC set of parton density functions which should then, for consistency, also be used to calculate the electro–weak vertex in LEPTO.

The final part, which contains the actual FORTRAN/C++ interface, is a basically straight forward conversion from the momenta k of the generated links, to the momenta q of the (quasi-) real emitted gluons which make up the dipoles and may emit further final-state radiation. There are, however, some ambiguities. First we have to decide how to interpret the $k_\perp$ which in the leading log approximation determines the virtuality of the link. In the original, purely gluonic, formulation we used the relation $dk^2_\perp/k^2_\perp = d\kappa$ where $\kappa \equiv \ln k^2_\perp/\Lambda^2$. In the $z \to 0$ limit the virtuality $-k^2 \approx k^2_\perp/(1-z)$ is the same as $k^2_\perp$. When quarks are introduced, they are massive,

and z is not necessarily close to zero. Here we have used $\kappa = \ln \frac{m^2+k_\perp^2}{\Lambda^2} \equiv \ln \frac{m_\perp^2}{\Lambda^2}$ for simplicity, although a more correct choice might be the "off-shellness", $\kappa = \ln \frac{m^2-k^2}{\Lambda^2} \approx \ln \frac{m_\perp^2}{(1-z)\Lambda^2}$.

The $q_\perp$ of the real emissions are fully determined by the $k_\perp$ of the virtual links only in the leading log approximation, where the dependence upon the azimuthal angles can be neglected. This fact causes some problems with energy–momentum conservation. We have chosen to replace the phase-space factor $dz/z = dk_+/k_+$ in Eq. 3 by dk_-/k_-, and generate the chain from the photon rather than the proton end. Imposing energy–momentum conservation by hand implies that the value x_0' obtained when reaching the proton is not necessarily the same as the x_0 put in from the beginning. Starting from the proton end would give the corresponding, but more serious problem in the photon end.

The final problem arises when we have gluon links, where the outgoing partons must be associated with either the colour or the anticolour flow in the diagram in order to construct the final-state dipoles. This association is simply made randomly, but a complication occurs since two outgoing partons forming a dipole may be connected by more than a single link, in which case the correct limit for the final-state emission depends on the rapidity. In this first version of the LDC generator we have made the simplification that this limit is constant and given by the smallest $k_\perp$ of the connecting links.

Preliminary results

The following results are preliminary in the sense that there are, as mentioned above, still some ambiguities which have not been fully explored, and that the input parton densities may be more or less incompatible with the ones used at the electro–weak vertex and with the LDC evolution.

Besides the parameters in Eq. 4, which should be well constrained by inclusive structure function data, there are no new parameters introduced in the LDC generator. There is, of course, the Λ and cutoff in $k_\perp$ of the links, but these are taken to be the same as in the final-state emissions where they are constrained by LEP data [8]. In principle the $k_\perp$ cutoff should match the virtuality in the input parton densities $f_0(x_0, Q_0^2)$, but we may have a problem as long as no such parton densities satisfying the LDC evolution are available. The only other parameters deal with the fact that the LDC model in principle produces weighted events, which are then normalized to one using a veto. This is a very ineffective procedure and may be speeded up by varying the $\bar{\alpha}$ used internally and a global weight factor. Nevertheless, there is a possibility to have weights bigger than one, in which case the same initial chain may be given several times (although with different final-state radiation), and it is important to check that the distributions studied are insensitive to the choices of these parameters.

Due to lack of space, all distributions available in the HZTool [10] package are not presented here. Instead we only show two distributions in Fig. 2 to indicate how sensitive the result is to the input parton densities. The MRS-like input distributions used behaves like x^α for small x, where $\alpha = -0.17$, and for comparison we have used the same distributions but set α to 0. The result is that in the former case, the generated x_0 is generally smaller, resulting in shorter evolution in x which lowers the $E_\perp$ flow.

Besides these uncertainties, Fig. 2 shows that the LDC generator is working and is giving sensible results, although much more work is needed to get the input parton densities consistent

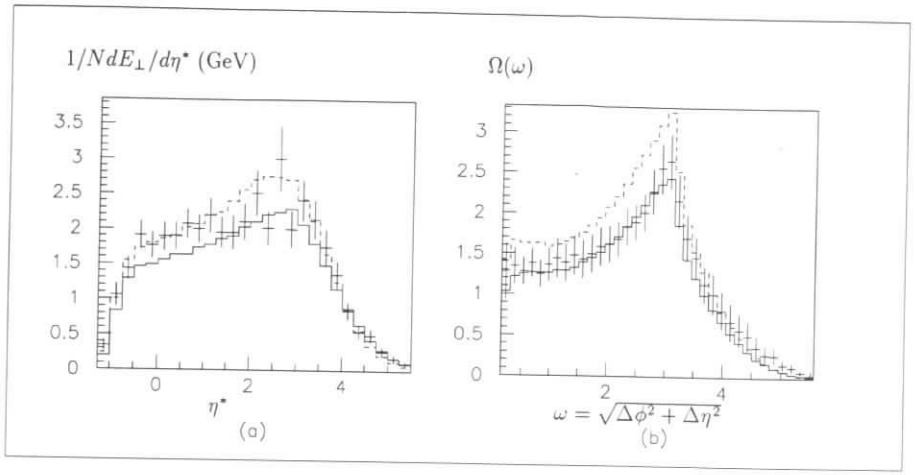

Figure 2: *(a) the $E_\perp$ flow as a function of pseudorapidity in the hadronic c.m.s. and (b) the transverse energy–energy correlations for $x < 0.001$ for the LDC generator compared with data from Ref. [9]. Full line is with input parton density behaving like $x^{-0.17}$ at small x while for dashed they behave like x^0.*

with structure function data and with the LDC evolution before quantitative predictions can be made.

References

[1] B. Andersson, G. Gustafson, J. Samuelsson, *Nucl. Phys.* **B463** (1996) 217.

[2] B. Andersson, G. Gustafson, H. Kharraziha, J. Samuelsson, Lund Preprint LU-TP-95-34, December 1995.

[3] M. Ciafaloni, *Nucl. Phys.* **B296** (1988) 49;
S. Catani, F. Fiorani, G. Marchesini, *Phys. Lett.* **B234** (1990) 339; *Nucl. Phys.* **B336** (1990) 18.

[4] L. Lönnblad, *Comp. Phys. Comm.* **71** (1992) 15.

[5] G. Ingelman, in Proc. HERA workshop, Eds. W. Buchmüller and G. Ingelman, Hamburg (1991) vol. 3, 1366.

[6] R.D. Peccei, R. Rückl, *Nucl. Phys.* **B162** (1989) 125.

[7] A.D. Martin, W.J. Stirling, R.G. Roberts, *Phys. Lett.* **B354** (1995) 155.

[8] I.G. Knowles, et al., 'QCD Event Generators', in Proc. LEP2 workshop, CERN report 96-01, Eds. G. Altarelli, T. Sjöstrand, F. Zwirner.

[9] H1 Collaboration, I. Abt et al., *Phys. Lett.* **B356** (1995) 118.

[10] J. Bromley, et al., "HZTOOL: A package for Monte Carlo – data comparison at HERA", these proceedings.

[11] N. Brook, et al., "Tuning Monte Carlo event generators to HERA data", these proceedings.

The Physics Case for a Forward Detector Upgrade

H. Abramowicz (Tel Aviv), J. Arvieux (Saturne), A. Bamberger (Freiburg), J. Binnewies (Hamburg), S.J. Brodsky (SLAC), N. Brook (Glasgow), J. Butterworth (University College, London), T. Carli (MPI, Munich), S. Catani (INFN, Firenze), G. Cozzika (Saclay), A. De Roeck (DESY, Hamburg), M. Diehl (Cambridge), T. Doeker (Tel Aviv), A. Edin (Uppsala), R. Engel (Leipzig), M. Erdmann (Heidelberg), J. Forshaw (Manchester), L. Frankfurt (Tel Aviv), D. Graudenz (CERN, Geneva), G. Gustafson (Lund), J. Hartmann (McGill), M. Hayes (Bristol), M. Heyssler (Durham), G. Ingelman (DESY, Hamburg & Uppsala), H. Jung (Lund), H. Kharraziha (Lund), W. Koepf (Ohio State University), M. Kuhlen (MPI, Munich), B. Laforge (Saclay), P.V. Landshoff (Cambridge), E. Levin (Tel Aviv), H. Lotter (Hamburg), L. Lönnblad (NORDITA, Copenhagen), M. McDermott (DESY, Hamburg), W.N. Murray (McGill), O. Nachtmann (Heidelberg), N.N. Nikolaev (ITKP, Bonn & Landau Inst., Moscow), N. Pavel (Imperial College, London), R. Pechanski (Saclay), J. Rathsman (SLAC), D. Schildknecht (Bielefeld), D. Simmons (Toronto), L.E. Sinclair (Glasgow), G. Sterman (Stony Brook), E. Strickland (Glasgow), M. Strikman (Penn. State), T. Teubner (Durham), T. Trefzger (LMU, Munich), K. Tokushuku (INS, Tokyo), M. Wüsthoff (Argonne).

Abstract: We summarize the conclusions of a number of contributions to the working groups on *Jets and High–$E_\perp$ Phenomena* and *Diffractive Hard Scattering* concerning issues related to the forward phase space region. They imply strong physics reasons to upgrade the HERA detectors in the forward (proton) direction and we recommend such options to be seriously considered, although they may be in conflict with planned luminosity upgrades.

Introduction. Deep inelastic scattering (DIS) is an excellent way to study the structure of the proton and the HERA results have indeed attracted much attention. This concerns, in particular, the observed rise of the structure function F_2 at small x. Although this had been predicted in perturbative QCD (pQCD), the proper theoretical interpretation is still unclear. There is presently vigorous theoretical research on 'QCD at small x' and different observables based on the hadronic final state are considered in order to improve our understanding. The available experimental data have shown interesting effects, but are not yet sufficient to give clear conclusions.

Confinement and non-perturbative QCD are still major unsolved problems in particle physics. Related to this is the hadronization of the proton remnant in DIS, which has not yet been properly investigated. In particular at small x, this remnant may be a complex many-parton system whose development is far from being understood. General questions such as 'how should the remnant system be described?' and 'what is the proper color-field structure in DIS events?' remain to be answered. These are important problems in their own right and they also have consequences for tests of pQCD issues, since observables can be strongly affected by hadronization effects.

The discovery of large rapidity gap events in DIS at HERA has stimulated enormous interest. Although these events can be phenomenologically described in terms of pomeron models based on Regge concepts, there is no satisfactory understanding of the dynamics creating them. There are conceptual and theoretical problems with the pomeron approach. Efforts are made to use pQCD, which is theoretically better defined, for diffractive processes where a large momentum scale or small size object is present. Furthermore, new ideas have been proposed to describe diffractive scattering in terms of soft color interactions between the scattered partons and the 'background' color field of the proton. Thus, there are fundamental problems to be solved concerning diffractive interactions and their connection to normal DIS, which preferably should both be described in a common theoretical framework. In addition, there are many other unsolved problems concerning various details of the diffractive processes. It is therefore important to experimentally observe as much as possible of the hadronic systems produced in diffractive scattering.

All of these issues, which are elaborated on in the following, require additional measurements and increased forward acceptance to be properly investigated.

Perturbative QCD. In spite of recent results on the structure of the proton we are still far from a satisfactory understanding of the underlying QCD dynamics in the small-x region. Although the rise of the structure function F_2 at small x was predicted by pQCD, it does not yet have a clear and unique theoretical interpretation. A rise is compatible with the BFKL equation [1], but also with conventional DGLAP evolution [2]. To understand the QCD dynamics it is important to sort out which of these approximation schemes are applicable in different regions of phase space. DGLAP should be appropriate for large Q^2 but not too small x and BFKL at small x. It is, however, not theoretically known how far down in x one needs to go in order for the predicted, but not experimentally verified, BFKL dynamics to become noticeable or dominant. In recent theoretical progress these two approximation schemes have been included in a more general one. The CCFM equations [3] incorporate DGLAP and BFKL which are thus reproduced in the relevant limits. The Linked Dipole Chain (LDC) model [4] goes further along this line by also offering an explicit model for Monte Carlo simulation of parton emissions [5].

If the parton density increases without limit as x decreases, it would eventually lead to a violation of unitarity. The high density, or 'overcrowding', of partons in the proton does, however, imply that parton–parton interactions can no longer be neglected. Thus, gluon recombination $gg \to g$, i.e. the reverse of the gluon splitting process, should reduce the parton density and restore unitarity. The GLR equation [6] attempts to describe such gluon recombination effects and predicts novel non-linear phenomena in QCD. Numerical estimates indicate that these effects are too small to be observable at HERA using the inclusive structure function. The effect may, however, be larger if the partons are not distributed evenly in the proton, but there exist smaller regions with higher than average density, so-called 'hot spots'.

To test these theoretical frameworks and develop them further requires detailed comparison with experimental data. Progress in our understanding with inclusive measurements requires very precise data. To be really conclusive, one must exploit the information contained in the hadronic final state, which is of course affected by the radiation processes summed over in the inclusive structure function.

An increased forward transverse energy ($E_\perp$) flow has been suggested as a sign of BFKL dynamics [7]. The observations at HERA are indeed consistent with BFKL dynamics, but can also be reproduced by DGLAP-based models depending on the model for the hadronization of

the proton remnant [8]. This observable is thus sensitive to hadronization corrections. However, as discussed in Ref. [9], the BFKL and DGLAP scenarios are still expected to show differences in the $E_\perp$ flow closer to the proton direction than can presently be observed. Here one should keep in mind that 'forward' in the HERA laboratory frame corresponds to the central region in the hadronic cms, and the large effects are therefore to be found much closer to the proton remnant.

To discriminate between BFKL and DGLAP dynamics it would be advantageous to use observables that enhance the genuine perturbative QCD effects relative to soft hadronization effects. One method is to look for jets with $p_\perp^2 \approx Q^2$ in the forward region [10]. Such a measurement has already been done [11], but the result was not quite conclusive, although it has been shown that a fixed order α_S^2 calculation alone cannot describe the data [12, 13]. According to BFKL, the forward jet cross-section should rise like a power of $x_{\rm jet}/x_B$ for large rapidity intervals $\Delta y = \ln x_{\rm jet}/x_B$ between the current and the forward jet, while for pure DGLAP dynamics, such jets would be heavily suppressed. In Refs. [14, 15, 16] a number of suggestions are made for how to improve this measurement in the future, and it is clear that extending the jet search closer to the proton direction is a vast improvement.

Another way of investigating perturbative effects is to use high$-p_\perp$ particles, which are exponentially suppressed in non-perturbative mechanisms. In Ref. [17] it is shown that such a measurement is feasible and would greatly improve with increased tracking coverage in the forward direction.

Also in photoproduction there are important studies which would benefit greatly from an increase of the forward detector coverage. It is, for example, possible to investigate the important QCD phenomenon of color coherence in the initial state parton emission processes [18]. Such studies are also possible at e.g. $p\bar{p}$ colliders, but γp has the advantage of reduced smearing effects from the underlying event. Another issue is large rapidity gaps between jets or between a jet and a high-$p_\perp$ meson [19, 20] related to the diffractive phenomena discussed below.

Diffraction. Diffractive processes are conventionally related to soft physics, but through the introduction of a large momentum scale in *diffractive hard scattering* [21], perturbative methods may also be used to explore them.

Instead of describing diffraction based on the old Regge formalism, there is a growing field using perturbative QCD methods where the pomeron is represented by Feynman diagrams of gluons. These range from the simplest case of two gluons, via the addition of next-to-leading corrections, to more complicated ladder diagrams. For a special class of hard diffractive processes, vector-meson production by longitudinally polarized photons and high-$p_\perp$ dijet production, it has been shown that perturbative QCD is applicable (for a review see Ref. [22]).

Another approach to understand rapidity gap events has recently been introduced based on non-perturbative soft color interactions [23]. These may be seen as partons interacting with the 'background' color field of the proton [24]. The perturbative phase of the interaction is then supposedly as in usual events, but the color structure is altered through the soft gluon exchanges. In this way the hard scattering system and the proton remnant system may each become color singlets and thereby decouple in the hadronization such that a rapidity gap between them arises. The proper rate of gap events can be obtained and an explicit model [8] seems to reproduce the salient features of the data. This approach may also offer a more 'continuous' theoretical description of all kinds of events, such that gap events and non-gap events can be described in the same framework [8, 9].

Thus, there are different theoretical approaches to the problem and, since they are not on a firm ground, there is a strong need for more experimental information. Ideally, one would like to test the models more generally in comparison to data that covers also the transition from diffractive gap events to 'normal' DIS events, i.e. from large to smaller and vanishing rapidity gaps. Furthermore, the system Y in front of the gap in the process $e + p \to e' + X + Y$, need not be a single proton but can represent proton dissociation or some more general state of higher mass and other quantum numbers. It is desirable to develop a more general description covering also these possibilities. All of this requires as complete detector coverage as possible.

Diffractive events at HERA have mainly been selected by the requirement of a large rapidity gap. This prevents a clear observation of large diffractive masses (M_X) since the X-system is then extending to more forward rapidities. In the present detector configurations it is possible to tag such events with a forward proton spectrometer. However, the only way to study the topology of these events is by extending the angular coverage of the calorimeters. It would then be of interest to establish whether large mass diffraction ($M_X^2 \gg Q^2$) exhibits properties different from those expected in soft diffractive interactions [25]. From a theoretical point of view the regime of large diffractive masses, or small $\beta = Q^2/(Q^2+M_X^2)$, corresponds to the triple regge limit of diffractive scattering and novel effects are expected. An experimental investigation of this regime is important for increasing our understanding of diffractive scattering.

It has been postulated that the study of hard diffractive scattering, in which the virtual photon fluctuates into a small size quark-antiquark configuration which then interacts with the proton, may be a sensitive probe of the deviations from the DGLAP evolution equation [22]. The properties of reactions, such as vector meson production by longitudinally polarized photons [26] or high-$p_\perp$ dijet production [27], may be affected by proton dissociation. Current experimental estimates of this uncertainty are at the 5–10 % level [28]. This percentage can be expected to decrease significantly with an upgrade of the forward region.

The change of regime from soft to hard scattering is expected to affect the slope of the momentum transfer (t) dependence [29]. This in turn may affect the probability of proton dissociation [30]. This calls for a precise measurement of proton dissociation for different configurations of the photon diffracted state X. A clear measurement of the proton fragmentation region is also of experimental importance in order to isolate genuine diffractive events and control the background from non-diffractive events.

If the cross section for inclusive diffractive scattering is mainly due to soft pomeron exchange, then one should observe that the ratio $R_X = \sigma(e + p \to e' + X + Y)/\sigma(e + p \to e' + X + p)$, where Y is the proton dissociation system, should not depend on the system X. The change in the energy dependence of the total $\gamma^* p$ cross section in the DIS regime may be the first indication that the exchange of one or several vacuum poles may not be appropriate and that pomeron-type factorization is violated. This is expected as a consequence of QCD evolution. It is thus of interest to test the factorization hypothesis in the regime of hard diffractive scattering involving interactions of small size configurations (vector meson production by longitudinally polarized photons or high-$p_\perp$ dijet production). The latter are believed to be driven mainly by perturbative QCD [26, 27].

An interesting observation is that the percentage of double dissociation can be related to the level of gluon fluctuations in the wave function of the proton [22]. A systematic study of double dissociation for various configurations of the photon diffracted state, i.e. vector-mesons and high-$p_\perp$ dijets, initiating the diffractive scattering may therefore shed some light on the distribution of color in the proton.

Furthermore, a clear test of color transparency [22] can be made by measuring the probability of survival of large rapidity gaps between two high-$p_\perp$ jets in photoproduction as a function of the transverse size of the "photon" [31]. Since color transparency predicts the suppression of initial and final state interactions, the large rapidity gaps are more likely to survive when the hard interaction is initiated by an unresolved photon as opposed to a resolved one. In order to measure the gap survival probability for resolved photons, an efficient reconstruction of jets in the forward region is essential [19].

Finally, the study of charged current induced diffraction would also profit from extending the coverage of the forward region as shown in Ref. [32].

With a suitable forward detector upgrade, these physics issues (excluding the charged current studies) could be well explored with an integrated luminosity of 100–150 pb^{-1}.

Non-perturbative QCD. To understand soft, non-perturbative strong interaction processes remains a main challenge in QCD. Hadronization is here an important problem which is not solved, although there are well functioning phenomenological models. DIS events provide an interesting source of information since the presence of the initial proton gives a richer structure than e^+e^- annihilation, without giving the full complications of hadron collisions.

Compared to e^+e^- the main new ingredient is the proton remnant. Although it is normally considered a spectator relative to the hard scattering process, it does influence the final state significantly. If the remnant system can be considered as a single color charge, it is natural to have a single color-field connection to the hard scattering system. However, with a more complex remnant the color-field structure may be more complicated leading to another result of the hadronization. An example of this is when the remnant is not a simple diquark, but a more complex parton system remaining when a sea quark or gluon has entered the hard scattering process. Depending on how these cases are described, different final states will result. The effects are not just localized at very large rapidity, but can also have effects rather centrally depending on the model [8]. Although some information will come from the tagging of highly energetic protons which were formed after a hard, non-diffractive interaction [33], more experimental information from the forward region is crucial for an improved understanding of these issues.

In addition, one cannot avoid considering these problems when studying the above perturbative QCD issues since, as mentioned, hadronization corrections may be substantial and must in any case be well controlled in order to reach safe conclusions.

Measuring particles in the forward region would also give data to be used in the context of fracture functions [34]. These are recently introduced theoretical concepts that combine structure function and fragmentation function information. They can, e.g., specify an incoming parton under the condition of a certain particle being produced in the final state. Fracture functions factorize with respect to the hard interaction and their scale evolution is calculable within pQCD.

The target proton wave function may have different types of fluctuations which can be probed. One interesting case is intrinsic charm quarks [35], i.e. the possibility of some (small) probability of having a $c\bar{c}$ pair in the Fock state decomposition of the proton wave function. An interaction with the proton can then realize this charm pair and produce charm particles. At HERA there are two main possibilities for this interaction. The photon can couple directly to either the c or $\bar{c}$, leaving the other in the proton remnant system. The scattered charm quark will typically emerge at a small forward angle due to the large momentum fraction x of intrinsic

charm quarks. Alternatively, the photon couples to a non-charm quark in the proton, such that both the c and $\bar{c}$ are materialized in the proton remnant hadronization, i.e. very forward. Not only open charm (e.g. D-mesons and Λ_c) can be produced, but also large-momentum J/ψ's that could be observed through the decay into a muon pair in the very forward region. Predictions for these processes at HERA are available [36] based on detailed Monte Carlo simulations and show that upgraded forward detectors would be essential.

Monte Carlo models. One should not forget or underestimate the importance of having theoretically well founded event generators which give a good description of data. This is crucial for most measurements at HERA. Although these models are steadily improving, with substantial progress within this workshop [37], there are still important discrepancies with respect to data. To improve these event generators even more, one should compare them with data where they differ the most. These differences are typically found in the treatment of initial-state parton showers, and in the hadronization of the proton remnant. Thus, they mainly affect the hadronic final state in the forward region. Improving generators to better describe the forward region will, however, also set constraints on how they behave in other parts of phase space. Learning more about the forward region will thereby increase our confidence in the generators in general. Indirectly this will also affect the results and conclusions of measurements seemingly unrelated to the forward region.

Conclusions. Taken together the above physics issues make up a compelling case for intensifying the studies of *forward physics* at HERA with an upgraded forward detector. This would also most certainly be beneficial for the study of other issues, which have not been covered in this workshop due to limited time and manpower. Our two working groups have, however, investigated designs of forward detector upgrades, which would be appropriate at ZEUS and H1 as reported in Refs. [16, 17].

Forward detector upgrades are, unfortunately, incompatible with the proposed scheme for increased luminosity with magnets in the forward (and backward) regions. Such magnets placed within the present detectors will severely hinder the above forward physics program and in most cases totally exclude it. Note also that these magnets prevent electrons scattered at very small angles (low Q^2) to be detected, hence the data will not extend to as small x values as are presently reachable. We therefore urge the HERA community to consider these incompatible options in a proper way. It should be stressed that most of the physics issues presented here do not require very large luminosity [22, 38] and could be completed in a fairly limited time. Therefore such a forward upgrade, if speedily implemented, should not exclude a luminosity upgrade, although some delay to the final stage of the latter may be implied.

References

[1] V.S. Fadin, E.A. Kuraev, L.N. Lipatov, *Sov. Phys. JETP* **45** (1977) 199;
Ya. Balitsky, L.N. Lipatov, *Sov. J. Nucl. Phys.* **28** (1978) 822.

[2] V.N. Gribov, L.N. Lipatov, *Sov. J. Phys.* **15** (1972) 438; 675;
L.N. Lipatov, *Sov. J. Phys.* **20** (1975) 94;
G. Altarelli, G. Parisi, *Nucl. Phys.* **126** (1977) 298;
Yu.L. Dokshitzer, *Sov. Phys. JETP* **46** (1977) 641.

[3] M. Ciafaloni, *Nucl. Phys.* **B296** (1988) 49;
S. Catani, et al., *Phys. Lett.* **B234** (1990) 339; *Nucl. Phys.* **B336** (1990) 18.

[4] B. Andersson, G. Gustafson, J. Samuelsson, *Nucl. Phys.* **B463** (1996) 217.
[5] G. Gustafson, et al., "The LDC Event Generator", these proceedings.
[6] L.V. Gribov, E.M. Levin, M.G. Ryskin, Phys. Rep. 100 (1983) 1.
[7] J. Kwiecinski, et al., *Phys. Rev.* **D50** (1994) 217.
[8] A. Edin, G. Ingelman, J. Rathsman, DESY 96-060, *Z. Phys. C* in press.
[9] A. Edin, G. Ingelman, J. Rathsman, "QCD in the forward region", these proceedings.
[10] A.H. Mueller, H. Navelet, *Nucl. Phys.* **B282** (1987) 727;
A.H. Mueller, *Nucl. Phys.* (Proc. suppl.) **18C** (1991) 125.
[11] H1 Collaboration, A. Aid et al., *Phys. Lett.* **B356** (1995) 118.
[12] E. Mirkes, D. Zeppenfeld, "Fixed order QCD backgrounds ...", these proceedings.
[13] J. Bartels, et al., DESY-96-036, April 1996, hep-ph/9604272.
[14] T. Haas, M. Riveline "Forward jet cross-sections", these proceedings.
[15] H. Heßling, "On forward jets and the hot spot limit at HERA", these proceedings.
[16] A. Bamberger, et al., "Diffractive and jet physics ...", these proceedings.
[17] M. Kuhlen, "High-$p_\perp$ Particles in the Forward Region at HERA", these proceedings.
[18] L. Sinclair, et al., "Colour Coherence in hard photoproduction", these proceedings.
[19] M. Hayes, et al., "Rapidity gaps between jets", these proceedings.
[20] J.R. Forshaw and M.G. Ryskin *Z Phys.* **C68** (1995) 137.
[21] G. Ingelman, P. Schlein, *Phys. Lett.* **B152** (1985) 256.
[22] H. Abramowicz, et al., "Diffractive Hard Scattering, Summary Report", these proceedings.
[23] W. Buchmüller, A. Hebeker, *Phys. Lett.* **B355** (1995) 573;
A. Edin, G. Ingelman, J. Rathsman, *Phys. Lett.* **B366** (1996) 371.
[24] W. Buchmüller, M.F. McDermott, A. Hebeker, DESY 96-126.
[25] M. Wüsthoff, *PhD Thesis* 1995, preprint DESY-95-166.
[26] S. Brodsky et al., *Phys. Rev.* **D50** (1994) 3134;
W. Koepf, et al., "Vector Meson production in $ep \to epV$", these proceedings.
[27] J. Bartels, H. Lotter, M. Wüsthoff, *Phys. Lett.* **B379** (1996) 239.
[28] A. Mehta, et al., "Future Diffractive Structure ...", these proceedings.
[29] H. Abramowicz, L. Frankfurt and M. Strikman, DESY 95-047
V. Del Duca, "Diffractive F_2 and t slopes", talk presented at this workshop.
[30] M. Strikman, talk presented at this workshop.
[31] L. Frankfurt, M. Strikman, "Possible evidence for color ...", these proceedings.
[32] J. Pliszka, A.F. Żarnecki, "Diffraction in Charged Current DIS", these Proceedings.
[33] I. Gialas, J. Hartmann, 'Target Proton Properties ...', these proceedings.
[34] L. Trentadue, G. Veneziano, *Phys. Lett.* **B323** (1994) 201;
D. Graudenz, *Nucl. Phys.* **B432** (1994) 351.
[35] S.J. Brodsky, et al., *Phys. Lett.* **B93** (1980) 451;
S.J. Brodsky, C. Peterson, *Phys. Rev.* **D23** (1981) 2745;
S.J. Brodsky, W-K. Tang, P. Hoyer, *Phys. Rev.* **D52** (1995) 6285.
[36] G. Ingelman, L. Jönsson, M. Nyberg, Phys. Rev. D47 (1993) 4872;
G. Ingelman, M. Thunman, hep-ph/9604289, Z. Phys. C in press.
[37] N. Brook, et al., "Tuning Monte Carlo Event Generators ...", these proceedings.
[38] M. Erdmann, et al., "Jets and High-$E_\perp$ Phenomena" summary report, these proceedings.